ADVANCES IN APPLIED CHEMISTRY AND INDUSTRIAL CATALYSIS

Edited by
Binoy K. Saikia

CRC Press
Taylor & Francis Group

ADVANCES IN APPLIED CHEMISTRY AND INDUSTRIAL CATALYSIS

Presenting a collection of papers resulting from the conference on “Applied Chemistry and Industrial Catalysis (ACIC 2021), Qingdao, China, 24-26 December 2021”. The theme of the conference was: “Clean Production and High Value Utilization”, discussing how to reduce the environmental footprint at the source and produce high value-added end products in chemical manufacturing. The conference brought together scholars from the Chinese government, top universities, business associations, research centers and high-tech enterprises, and was committed to building and enabling a platform for the cooperation among the Chinese government, Chemical industry, and scholars. The goal was to build a bridge between R&D results and the Chemical industry.

The conference conducted in-depth exchanges and discussions on relevant topics such as applied chemistry and industrial catalysis aiming to provide an academic and technical communication platform for scholars and engineers engaged in scientific research and engineering practice in the field of chemistry, catalysis and function material. By sharing the research status of scientific research achievements and cutting-edge technologies, it helps scholars and engineers all over the world comprehend the academic development trend and broaden research ideas. So as to strengthen international academic research, academic topics exchange and discussion, and promote the industrialization cooperation of academic achievements.

PROCEEDINGS OF THE 3RD INTERNATIONAL CONFERENCE ON APPLIED CHEMISTRY AND INDUSTRIAL CATALYSIS (ACIC 2021), QINGDAO, CHINA, 24–26 DECEMBER 2021

Advances in Applied Chemistry and Industrial Catalysis

Edited by

Binoy K. Saikia
CSIR-North East Institute of Science & Technology

CRC Press
Taylor & Francis Group
Boca Raton London New York Leiden

CRC Press is an imprint of the
Taylor & Francis Group, an **informa** business

A BALKEMA BOOK

CRC Press/Balkema is an imprint of the Taylor & Francis Group, an informa business

Typeset in Times New Roman by MPS Limited, Chennai, India

Library of Congress Cataloging-in-Publication Data

A catalog record has been requested for this book

First published 2022
Published by: CRC Press/Balkema
Schipholweg 107C, 2316 XC Leiden, The Netherlands
e-mail: enquiries@taylorandfrancis.com
www.routledge.com – www.taylorandfrancis.com

ISBN: 978-1-032-31196-8 (Hbk)
ISBN: 978-1-032-31197-5 (Pbk)
ISBN: 978-1-003-30855-3 (eBook)
DOI: 10.1201/9781003308553

Table of contents

Industrial catalysis and chemical properties research

Chemical devices and environmental chemistry research

Advances in Applied Chemistry and Industrial Catalysis – Saikia (Ed.)

Preface

Due to recent pandemic, 2021 3rd International Conference on Applied Chemistry and Industrial Catalysis (ACIC 2021) was held virtually online during December 24–26, 2021. The decision to hold the virtual conference was made in compliance with many restrictions and regulations that were imposed by countries around the globe. Such restrictions were made to minimize the risk of people contracting or spreading the COVID-19 through physical contact. There were 120 individuals who attended this on-line conference, represented many countries including Canada, America, Singapore and China.

The theme of this conference is "Clean Production and High Value Utilization". It mainly talks about how to reduce environmental footprint at source and produce high value-added end products in chemical manufacturing. At the same time, the conference brings together scholars from the Chinese government, top universities, business associations, research centers and high-tech enterprises. This conference is committed to building an enabling platform for the cooperation among the Chinese government, Chemical industry and scholars. The ultimate goal is to build a bridge between R&D results and the Chemical industry.

During the conference, the conference model was divided into three sessions, including oral presentations, keynote speeches, and online Q&A discussion. In the first part, some scholars, whose submissions were selected as the excellent papers, were given about 5–10 minutes to perform their oral presentations one by one. Then in the second part, keynote speakers were each allocated 30–45 minutes to hold their speeches. In the second part, we invited five professors as our keynote speakers. Prof. Jieshan Qiu, College of Chemical Engineering, Beijing University of Chemical Technology. And then we had Prof. Weidong Zhou, College of Chemical Engineering, Beijing University of Chemical Technology. The others keynote speakers as follow: Prof. Wenbin Yang, Southwest University of Science and Technology; A/Prof. Yang Juan, Xi'an Jiaotong University; Prof. Jun Hu, Northwestern Polytechnical University. Their insightful speeches had triggered heated discussion in the third session of the conference. Every participant praised this conference for disseminating useful and insightful knowledge.

The proceedings are a compilation of the accepted papers and represent an interesting outcome of the conference. Topics include but are not limited to the following areas: Chemical Engineering and Technology, Function Material, Carbon Resources Chemical, Environmental chemical, Industrial catalysis, Energy chemical engineering and other related topics. All the papers have been through rigorous review and process to meet the requirements of international publication standard.

We would like to acknowledge all of those who supported ACIC 2021. The help and contribution of each individual and institution was instrumental in the success of the conference. In particular, we would like to thank the organizing committee for its valuable inputs in shaping the conference program and reviewing the submitted papers.

We sincerely hope that the ACIC 2021 turned out to be a forum for excellent discussions that enabled new ideas to come about, promoting collaborative research. We are sure that the proceedings will serve as an important research source of references and knowledge, which will lead to not only scientific and engineering findings but also new products and technologies.

The Committee of ACIC 2021

Committee member

Conference Chairman
Prof. Xianyong Wei, High-level academic leader of XinJiang University/Xinjiang University/China
University of Mining and Technology, China

Dr. Binoy K. Saikia, Coal Chemistry Division, CSIR-North East institute of Science & Technology, Jorhat-785006, Assam, India

Program Committees
Prof. Xuanke Li, Wuhan University of Science and Technology, China
Prof. Guanghui Wang, Wuhan University of Science and Technology, China
Prof. Jianglong Yu, University of Science and Technology Liaoning, China
Prof. Sergei Manzhos, Université du Québec, Canada
Prof. Jichang Wang, University of Windsor, Ontario, Canada
Prof. Xing Fan, Xinjiang University, China
Prof. Zhimin Zong, China University of Mining and Technology, China
Prof. Jingpei Cao, China University of Mining and Technology, China
Researcher. Xiaoyong Lai,Ningxia University, China
Researcher. Jianli Zhang, Ningxia University, China

Technical Program Committees
Prof. Richard Axelbaum, Washington University in St. Louis, America
Prof. Guangwen Xu, Shenyang University of Chemical Technology, China
Prof. Jieshan Qiu, Beijing University of Chemical Technology, China
Prof. Yiwei Fei, Air Force Logistics University, China
Prof. Xun Hu, University of Jinan, China
Prof. Jun Shen, Taiyuan University of Technology, China
Prof. Ang Zi Yang Adrian, Integrative Built Environment Centre Singapore
Assoc. Prof. Ir. Dr. CHING YERN CHEE, Department of Chemical Engineering, University of Malaya Malaysia

Applied chemistry and chemical analysis techniques

Advances in Applied Chemistry and Industrial Catalysis – Saikia (Ed.)

Optimal analysis of C_4 olefin preparation by ethanol coupling under the influence of multiple factors

Yuzhuo Dang*, Yuxiao Duan** & Shuoshuo Gong
Key Laboratory of Information System Engineering, National University of Defense Technology, Changsha, P.R. China

ABSTRACT: The production of C_4 olefins by petroleum catalytic cracking is costly and harmful to the environment. For the chemical reaction of ethanol coupling to produce C_4 olefin, a Co/SiO_2–HAP catalyst with both acid and base activity was introduced. The ethanol conversion and C_4 olefin selectivity of the reaction under different catalyst ratios were experimentally studied, and a two-factor variance model was constructed to reasonably explain the effects of temperature and catalyst. On this basis, the BP neural network optimization algorithm based on genetic algorithm (BP-GA joint algorithm) was used to study the optimal coupling reaction conditions. The optimal catalyst combination is 265 mg 1.1wt% Co/SiO_2-236 mg HAP, the optimal concentration of ethanol is 1.95 ml/min, and the optimal temperature is 390°C, which are of high similarity to the theoretical analysis results and have strong reliability. Under these conditions, the ethanol conversion rate is up to 97.6%, and the selectivity of C_4 olefin is 64.5%, showing the best target reaction effect, which has practical significance for the actual chemical production.

1 INTRODUCTION

As an important chemical material, C_4 olefin is the basic raw material for preparing other important industrial products. With the global non-renewable resources becoming increasingly scarce, limited oil resources are controlled by a few countries and exploited at unpredictable rates. The production of C_4 olefin by catalytic cracking of petroleum is becoming increasingly expensive and harmful to the environment, so it is gradually not being adopted. Chemical manufacturers are gradually turning their attention to ethanol, a cleaner, more environmentally friendly, more common, and cheaper raw material.

At the end of the 18th century, Dutch chemists discovered that Al_2O_3 could catalyze the dehydration process of ethanol. Subsequently, chemists carried out many experiments on the process, reaction mechanism and catalysts[3], and found that the reaction mechanism under different catalysts was quite different. So far, activated alumina, magnesium oxide, manganese oxide, molecular sieve, cobalt oxide, TiO_2-SiO_2, and other catalysts have good performance, but the catalysts used in industry are mainly activated alumina and molecular sieves. Since the development of the isothermal tubular reaction process in the 1940s and the study of the fixed bed adiabatic reaction process and fluidized bed process in the 1970s, there have been few new studies. Therefore, we focus on the coupling reaction of ethanol to prepare C_4 olefin and obtain the optimal coupling reaction conditions to achieve a high conversion rate.

Corresponding Authors: *1270245602@qq.com and **1228441415@qq.com

DOI 10.1201/9781003308553-1

2 BACKGROUND AND REACTION MECHANISM

In the process of ethanol coupling to produce C_4 olefin, synergistic catalysis by acid-base active sites is usually required. In our experiment, the combination of catalysts (Co/SiO_2 and HAP hydroxyapatite) was used to catalyze the growth of the ethanol carbon chain into four and convert it to olefin. The Co/SiO_2-HAP catalyst has both acid and base active sites, and Co has deoxygenation activity. The C_4 olefin can be produced by adjusting the loading amount of Co and the pH of the catalyst surface. However, due to the inevitable occurrence of other side reactions in the process of ethanol conversion, ketones, aldehydes, and other complex products are produced, resulting in a limited yield of C_4 olefin and a large proportion of other products. Therefore, the research on the design of catalyst combinations has very important industrial environmental protection significance and economic value. In this study, we explored how to improve the conversion rate of ethanol and ensure the C_4 selectivity by controlling the loading ratio of Co/SiO_2 and HAP, the concentration of ethanol, and the experimental temperature.

The Co/SiO_2-HAP catalyst has both acid and base active sites. The specific reaction process is as follows: the reactant ethanol first removes two hydrogen atoms to produce acetaldehyde under the catalysis of alkaline sites, and then removes one water molecule to produce ethylene under the catalysis of acidic sites; or one water molecule can also be directly removed from two ethanol molecules to form an ether molecule, which converts to ethylene by further removing one water molecule; or one molecule of water can be removed from ethanol to form a carbon-carbon double bond to generate ethylene directly. Finally, ethylene (or acetaldehyde) is catalytically converted to butene according to the Prince mechanism.

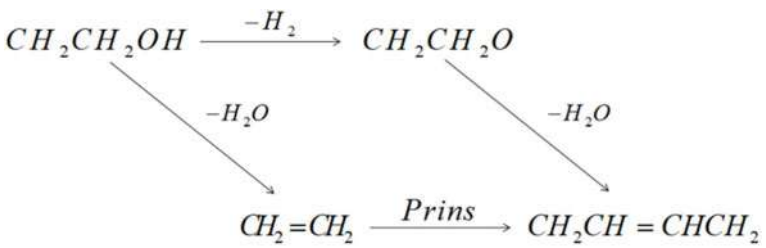

Figure 1. Reaction mechanism of ethanol coupling for the production of C4 olefin.

3 RESULTS AND DISCUSSION

The coupling experiments were carried out using Co/SiO_2-HAP catalyst at different temperatures, and the results are shown in Table 1.

Table 1. Experimental table of coupling reactions.

	Level					
Factor	1	2	3	4	5	6
Reaction temperature/°C	250	275	300	325	350	400
Ethanol concentration/ml· min^{-1}	0.3	0.9	1.68	2.1		
Loading amount of Co/wt%	0.5	1	2	5		
Mass ratio of Co/SiO_2 to HAP/%	0.5	0.556	1			

A series of experiments were carried out at different temperatures using different catalysts. The experimental results are shown in Table 2.

Table 2. Experimental table of coupling reactions.

Entry	Reaction temperature/°C	Ethanol concentration/ $ml \cdot min^{-1}$	Loading amount of Co/wt%	Mass ratio of Co/SiO_2 to HAP/%	Conversion rate of ethanol/%	Selectivity of C_4 olefin/%
1	250	0.3	2	1	14.8	1.96
2	250	0.3	1	1	19.7	5.75
3	250	0.9	2	1	9.7	5.5
4	250	0.9	1	1	6.3	5.63
5	250	1.68	1	1	2.07	34.05
6	250	1.68	2	1	4.60	18.07
7	250	1.68	1	2	1.3	5.19
8	275	0.3	2	1	12.4	6.65
9	275	0.9	1	1	19.2	8.04
10	275	1.68	1	1	5.85	37.43
11	275	1.68	2	1	17.20	17.28
12	275	2.1	5	1	1.0	1.65
13	300	0.3	2	1	20.8	10.12
14	300	0.9	1	1	28.5	13.82
15	300	1.68	1	2	4.1	12.74
16	300	1.68	1	0.5	10.2	3.61
17	325	0.3	2	1	28.3	13.86
18	325	0.9	1	1	37.6	28.72
19	325	1.68	1	1	19.68	49.7
20	325	1.68	2	1	56.38	30.62
21	350	0.3	2	1	36.8	18.75
22	350	0.9	1	1	48.9	36.85
23	350	1.68	0.5	1	60.5	27.25
24	350	1.68	5	1	55.8	10.65
25	350	2.1	5	1	48.7	30.8
26	350	2.1	1	1	13.4	31.04
27	400	0.3	2	1	76.0	38.23
28	400	0.9	1	1	83.7	53.43
29	400	1.68	0.5	1	88.4	41.02
30	400	2.1	1	1	79.3	58.7

For each group of catalyst combinations recorded in the experiment, the relationship between temperature and ethanol conversion and C_4 olefin selectivity was studied respectively under constant Co/SiO_2 and HAP loading ratios. The preliminary study showed that the increase of temperature in the reaction was conducive to ethylene formation. With the change of catalyst combination, the fluctuation degree of ethanol conversion and C_4 olefin selectivity increases gradually.

Ethanol conversion rate and C_4 olefin selectivity are affected by both temperature and catalyst combination. A non-interactive two-factor analysis of the variance model was established. The original hypothesis H_0 is that ethanol conversion rate and olefin selectivity are not affected by temperature and catalyst, and the alternative hypothesis H_1 is that ethanol conversion and C_4 olefin selectivity are affected by both. Here, we ignore the effect of temperature on catalyst activity and think there is no interaction between them. Inter-group error $SS_A = \sum_{i=1}^{r} \sum_{j=1}^{s} (\bar{x}_{i\cdot} - \bar{x})^2 = s\sum_{i=1}^{r} (\bar{x}_{i\cdot} - \bar{x})^2$, intra-group error $SS_E = \sum_{i=1}^{r} \sum_{j=1}^{s} \left[x_{ij} - \left(\bar{x}_{i\cdot} + \bar{x}_{\cdot j} - \bar{x}\right)\right]^2$ and the total error $SS_T = \sum_{i=1}^{r} \sum_{j=1}^{s} \left(x_{ij} - \bar{x}\right)^2$ of the two two-dimensional tables are calculated. Given their respective degrees of freedom, the mean square error can be calculated to obtain the $F = \frac{MS_A}{MS_E} \sim$

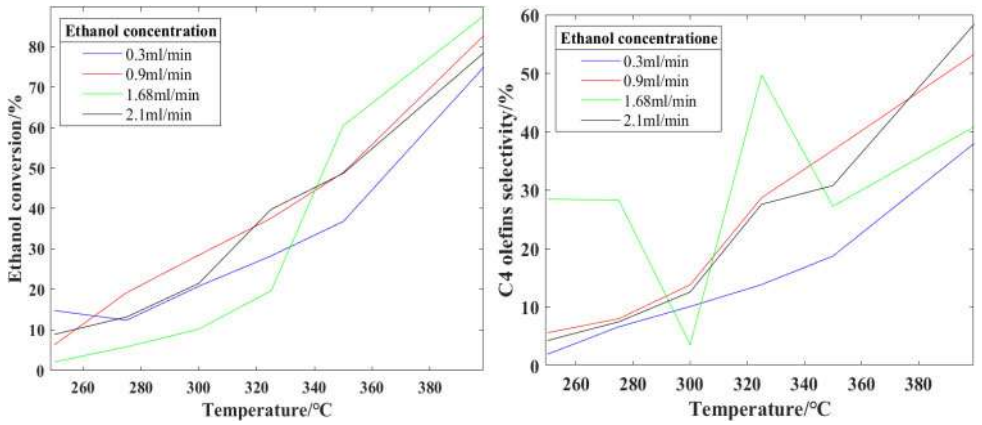

Figure 2. The relationship between ethanol conversion rate and C4 olefin selectivity and temperature at different ethanol concentrations.

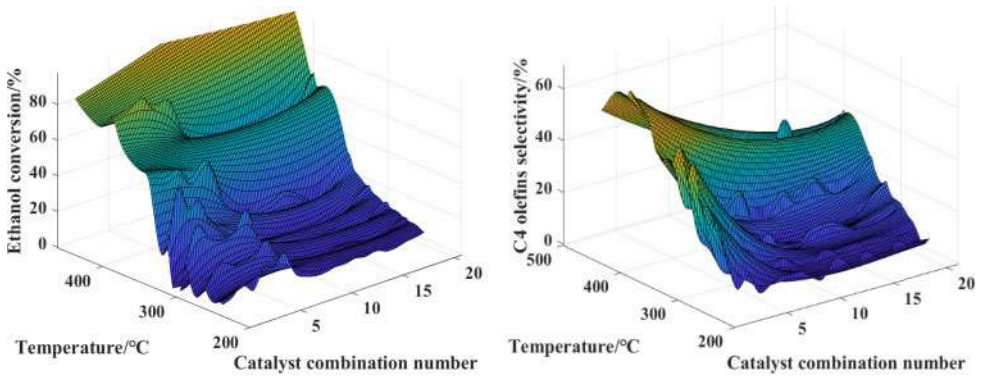

Figure 3. Three-dimensional fitting diagram of the relationship between ethanol conversion and C4 olefin selectivity and temperature under different catalyst combinations.

$F\,(r-1,(r-1)(s-1))$value, and then the P-Value can be calculated to judge the influence of the two factors on ethanol conversion or C_4 olefin selectivity. The results of the two-factor analysis of variance are shown in Tables 3 and 4.

Table 3. Two factor analysis of variance of catalyst combination and temperature on ethanol conversion.

Source	SS	df	MS	F	Prob
Columns	3.06529	6	0.51088	59.2	1.47269e-33
Rows	2.22693	20	0.11135	12.9	2.45503e-29
Error	1.03563	120	0.00863		
Total	6.32785	146			

It can be seen from the last column of the above table that the P-Value is far less than 0.05, so it is fully assured that these two factors have an impact on the ethanol conversion rate. Since the F value is 59.2 > 12.9, the influence of column quantity (temperature) on ethanol conversion rate is greater than that of row quantity (catalyst combination).

Table 4. Two factor analysis of variance of catalyst combination and temperature on C_4 olefin selectivity.

Source	SS	df	MS	F	Prob
Columns	0.95547	6	0.15925	59.25	1.41632e-33
Rows	1.04976	20	0.05249	19.53	9.84214e-29
Error	0.32252	120	0.00269		
Total	2.32776	146			

Table 4 is the same as Table 3. It can be seen from the last column that the P-Value is far less than 0.05, so it is fully assured that these two factors have an impact on the ethanol conversion rate. Since the F value is 59.25 > 19.53, similarly, the influence of column quantity (temperature) on ethanol conversion rate is greater than that of row quantity (catalyst combination).

4 SOLUTION OF OPTIMAL COUPLING REACTION CONDITIONS

According to the experimental data analysis, the best C_4 olefin selectivity is obtained in the combination of a 1:1 ratio of Co/SiO_2 to HAP. With the increase of the mass ratio of HAP, the basic site of the reaction increases, resulting in a large amount of acetaldehyde coupling into olefine aldehyde. When the mass ratio of Co/SiO_2 to HAP reaches 1:1 with the increase of the Co/SiO_2 content, the intermediate reaction will produce acid that promotes the conversion of the olefinic aldehyde into C_4 olefins, increasing the selectivity of C_4 olefin. The selectivity was also maximized at a certain temperature. When the temperature is too high, the selectivity of C_2 olefin is greater; when the temperature is too low, the selectivity of high carbon alcohols is greater. The specific optimal experimental conditions were studied using BP-GA joint algorithm.

Ethanol conversion rate or C_4 olefin selectivity was set as the objective function f, the independent variable X was the catalyst combination and temperature, which contains many influencing factors. The function curve was fitted through a neural network algorithm, and the mathematical model was established to optimize the solution of the problem.

Temperature, loading ratio, loading capacity of Co, and dropping rate of ethanol were respectively represented as x_1, x_2, x_3, and x_4; ethanol conversion rate and C_4 olefin selectivity represented as f_1 and f_2. The regression function was obtained by the neural network, and the optimal solution was obtained by fitting the curve according to the function.

Table 5. Optimal coupling reaction conditions.

	Catalyst combination	Temperature/°C	Conversion rate of ethanol/%	Selectivity of C4 olefin/%
Optimal solution	265 mg 1.1wt%Co/SiO_2-236 mg HAP; ethanol concentration1.95 ml/min	390	97.6%	64.5%

5 CONCLUSION

This study investigated the effects of reaction temperature, loading ratio, loading amount of Co, ethanol dropping rate, and other factors on catalyst content and reaction mechanism. According to the experimental results and the BP-GA algorithm, the following conclusions were obtained:

(1) Temperature is an important factor in the experiment of olefin production by ethanol coupling. Too high or too low temperature will lead to an increase in the selectivity of by-products. The optimal temperature is 390°C, according to experiments and calculations.
(2) The dropping rate of ethanol is also an important factor affecting the experimental results. When the dropping rate is insufficient, there are fewer reactants and low catalyst efficiency. When there is too much ethanol, the catalyst surface is coated with more unreacted ethanol, which reduces the catalyst efficiency. The optimal dropping rate is 1.95 ml/min.
(3) It is found that the content of the catalyst is positively correlated with the concentration of ethanol. When the ratio of Co/SiO_2 to HAP is close to 1, Selectivity of C4 olefin is relatively high. When the loading amount of Co is low, the dispersion of Co on the surface of the catalyst is less, making it difficult to be reduced. Upon increasing the loading amount of Co, it is reduced to a mixed state of oxidation state and elemental cobalt, which accelerates the dehydrogenation of ethanol into acetaldehyde. As the intermediate product, the acetaldehyde then converts to C_4 olefins under the action of the Co/SiO_2-HAP catalyst.

How to control the side reaction, increase the efficiency of the catalyst, and ideally avoid the formation of by-products is the focus of future research. A better understanding of the mechanism of the coupling reaction will not only bring great benefits to industry, but also reduce environmental pollution.

ACKNOWLEDGEMENT

The work was supported by the Key Laboratory of Information System Engineering, National University of Defence Technology, and Professor Chen.

REFERENCES

Chen J. Chemical Reactions Affecting the Composition of FCC Gasoline[J]. Petroleum & Petrochemical Today. 2003; 11: 1–7.

Jiang Y, Fu T, Lu J, Li Z. Effect of SiO_2 Pore size and Additives on Microstructure and Fischer-Tropsch Synthesis of Co/SiO_2 catalysts [J]. Journal of Chemical Engineering of Chinese Universities. 2014; 28(3): 553–560.

Lu S, Lu A. Preparation of Butanol and C_4 Olefins from Ethanol[D]. Dalian: Dalian University of Technology, 2019.

Wang J, Zhong S, Xie Z, Zhang C. Analysis for the Process of Ethanol Dehydration to Olefins[R]. Shanghai: China Academic Journal Electronic Publishing House, 2008.

Zhang J, Chang Y. Studies on the Ethanol to Mixed Hydrocarbons[D]. Lanzhou: Lanzhou University, 2015.

Zhao G, Mao Z, Zhang H, Chen X, Ye M, Wang X, Cheng X. Preparation and Performance Evaluation of the Catalyst for Ethanol Dehydration to Ethylene[J]. Industrial Catalysis. 2016; 24(7): 49–52.

Advances in Applied Chemistry and Industrial Catalysis – Saikia (Ed.)

Study on the extraction of grape seed oil by supercritical carbon dioxide

Yujia Han*
Beijing No. 2 Middle School, Beijing, China

ABSTRACT: It has always been an important problem in industry to seek for a stable and high efficient way to extract oil. However, there are inevitable problems in every traditional technique of oil extraction, such as low efficiency, complicated operations, low productivity, and organic solvent residue which harms people's health in long run, and the operations cannot substitute each other. In this research, we creatively use supercritical CO2 fluid to extract oil from grape seed and discuss the best situation for application in real industry.In this experiment, orthogonal design of four factors three levels was applied. The extracted pressure, temperature and time as the influence factor have been investigated for the optimal parameters of the supercritical CO2 extraction technique. The mass of the oil production is measured and compared using the balance. Targeting on the nine groups of results from the experiment, we use range analysis to process the experimental data. Secondly, we studied the supercritical CO2 extraction process with to achieve the highest anthocyanin content. Grape seed oil was diluted with petroleum ether and scanned with UV-vis spectrophotometer to observe the absorption peak. We observed and compared the absorption peak with the absorption peak with soybean oil and corn oil and find out that there are components including anthocyanin and compare the different absorption peak in different situations to get the appropriate situation which can achieve the highest anthocyanin content. This research provides a theoretical basis for the further production of industrial oil pressing instead of traditional pressing and organic solvent in the future.

1 INTRODUCTION

Edible oil is one of the most important living materials of modern humans. While helping humans maintain physical health, it provides part of the energy needed, which in turn provides an important guarantee for survival and health. Last year, Chinese residents consumed an average of more than 20kg of edible oil every year, and the total consumption reached 29 million tons (Xue 2020). Among them, the oil crops distributed in China mainly involve peanuts, sunflowers, soybeans, rape and flax, with a total planting area of more than 320 million mu (Wang 2019).

The existing industrial edible oil production methods are divided into two kinds, one is the pressing method, which usually squeezes the edible oil from the oil seeds under the physical action of external forces. The input cost of this method is low because it adopts pure physical pressing, the edible oil produced has no solvent residue, and the production process is simple. However, the residual material of this production process has some disadvantages, such as high oil content and low oil production efficiency, so its application atmosphere in industry is greatly limited. Another method is leaching (Sun 2019). This method is mainly based on the principle of similarity compatibility and is extracted by using organic solvents and vegetable oils with similar structures (Wang 2015). This method has been widely used in industrial production at home and abroad because of its high oil production rate, large output, low production cost, high profit, etc.

*Corresponding Author: dingli@niesl.com.cn

DOI 10.1201/9781003308553-2

However, the distillation method cannot completely separate the edible oil from the organic solvent, and the extractant still has trace residues in the product. Among them, the aromatic hydrocarbons and sulfides contained in hexagonal alkanes are highly toxic, which will cause respiratory system dullness, external skin damage, and endanger the stability of the corresponding nervous and blood system and endanger health after exposure. Thus, it can be seen that both the pressing method and the leaching method have their own advantages and disadvantages in the industrial production process, and they are irreplaceable, which implies that it is necessary to find a new process with no solvent residue and high oil yield simultaneously.

Supercritical fluid refers to the fluid above the critical temperature and critical pressure, which is different from the particularity of gas and liquid (Wang 2021). The commonly used supercritical fluids are mainly CO_2, ethane, methanol, ethanol, toluene, water, etc., among which supercritical CO_2 is the most widely used. This is mainly due to the fact that the production of CO_2 is cheap, easy to obtain, stable, non-flammable and explosive, and its critical temperature is 364.2 K and critical pressure is 7.38 MPal, which is easy to be realized in industrial production. In addition, the full use of CO_2 can effectively prevent Greenhouse Effect (Xu 2016). With the rapid development of modern industry, the use of fossil fuels is increasing, the volume of CO_2 gas discharged into the air is also gradually increasing simultaneously. In this regard, the reuse of CO_2 is extremely important to protect the environment on which we live. In addition, the density of supercritical CO_2 fluid is similar to that of ordinary liquid, so it has strong solubility. Compared with the liquid, the viscosity and diffusion coefficient of the supercritical CO_2 fluid is much larger than that of the liquid, which is closer to the gas and has excellent mass transfer performance. Supercritical CO_2 extraction has the advantages of no harm to health due to its simple extraction process and good separation of solvent and solute. Thus, supercritical CO_2 extraction technology has been widely developed in recent years, and has a more in-depth application in the fields of medicine, chemical industry, food, environmental protection, etc.

In this work, supercritical CO_2 fluid technology was used to extract edible oil from grape seeds to find the parameters with the highest extraction rate. The oil content of grape seeds is very high, up to 140.17%, which is comparable to corn and soybeans commonly used to extract oil, so it is a waste of resources if thrown away (Du 2015; Tian 2018). In 2015, China's grape output was 12.628 million tons, making it the second largest producer, indicating it is very important to make full use of its grape seeds to avoid waste of resources. Compared with corn and soybeans, it also contains proanthocyanidins, which can not only facilitate the production of collagen, but also block ultraviolet rays and enhance immunity. Among them, vitamin E has a very obvious skin care effect. Higher levels of unsaturated fatty acids contribute to the prevention of cardiovascular and cerebrovascular diseases. In this experiment, the extraction yield was used as an index to find out the appropriate extraction parameters by designing orthogonal experiments. The second research content is to measure and compare the anthocyanin content in grape seed oil obtained by different extraction processes by using ultraviolet-visible spectrophotometer, and thereby obtaining suitable parameters.

2 METHODOLOGY

2.1 *Experimental reagents*

Drug Name	Purity	Manufacturer
CO_2	>99.95%	Beijing Fudong Gas Products Company
Grape seed	/	Market purchase
Petroleum ether	99%	Tianjin Fuchen Chemical Reagent Factory
Soybean oil	/	Fulinmen, Tianjin
Peanut oil	/	Luhua, Laiyang City, Shandong Province
Absolute ethanol	/	Beijing Chemical Plant

2.2 *Main instruments*

Speed supercritical CO_2 extraction instrument	U.S. Applied Separation Instrument company
One oil-free air compressor	Suzhou Same Electromechanical Company
One low temperature thermostat	Ningbo Xinzhi Biological Technology Co., Ltd.
Universal crusher	Shanghai
UV-Vis Spectrophotometer	Beijing Puxi General Instrument Co., Ltd.
Analytical Balances	Mettler electronic balance LEI04E

2.3 *Supercritical CO_2 extraction process of grape seed oil*

First of all, weigh 50 g of dried grape seeds, rinse with clean water, remove sundries and dry, and put the dried grape seeds into a universal grinder. In order to make the grape seeds come into full contact with CO_2 as far as possible without blocking the extraction pipeline, the grape seed powder with appropriate thickness between 20 mesh and 40 mesh was screened with 20-mesh and 40-mesh sieves in the experiment. Weigh 7 g powder, plug the extraction kettle with filter and polypropylene fiber, put the powder carefully and plug the other end with the same method. Put the extraction kettle loaded into the extraction system vertically, turn on the power supply, open the CO_2 valve, put in the gas, start the air compressor, set the furnace temperature and kettle temperature. When the furnace temperature and kettle temperature are stable, the pressure of the system is adjusted to the needs of the experiment, and the static extraction begins and timing. When the time is up, open the outlet valve for dynamic extraction. After the dynamic extraction is finished, collect the product, reduce the pressure, keep the valve open and keep the gas flowing for one minute, then close the cylinder valve, intake valve, air compressor, mainframe power supply and constant temperature water bath in turn. Finally, the extraction kettle is taken out from the extraction furnace, the material is poured out and cleaned.

Orthogonal experiment: four parameters were changed in the experiment (Table 1), and the data were analyzed by orthogonal test. Supercritical CO_2: the factors affecting the extraction of grape seed oil include extraction temperature (T), extraction pressure (P), flow rate of CO_2 (V), dynamic extraction time (t1) and static extraction time (t2). According to the pre-experimental results, extraction pressure, extraction temperature and extraction time have great influence on the extraction results, so the orthogonal experiment table of four factors and three levels is selected for the experiment (Table 2). In this experiment, we selected three levels of T at 35,40,50°C and P at 150,250,350 bar. We selected three levels of 10, 20 and 30 minutes (Table 1) as the dynamic extraction time. The orthogonal experiment with four factors and three levels was carried out according to the orthogonal table (Table 2).

Table 1. Influencing factors and level setting values of orthogonal test data.

	A pressure (P)/bar	B temperature (T)/°C	C Static extraction time (t_1)/min	D Dynamic extraction time (t_2)/min
1	150	35	5	10
2	250	40	10	20
3	350	50	15	30

Table 2. $L_9\ 3^4$ orthogonal test design table.

	Horizontal combination ABCD	A/bar	B/°C	C/min	D/min
1	1111	150	35	5	10
2	1222	150	40	10	20
3	1333	150	50	15	30
4	2123	250	35	10	30
5	2231	250	40	15	10
6	2312	250	50	5	20
7	3132	350	35	15	20
8	3213	350	40	5	30
9	3321	350	50	10	10

2.4 *Characterization method*

2.4.1 *Determination of extraction yield*

In order to determine the yield of extracted grape seed oil, the dynamic extraction products were collected and the weighing quality was recorded. The ratio of the mass of the dynamic extraction product to the grape seed powder used in the reactor is the extraction yield.

Extraction yield = (the extraction quality of grape seed oil (g)/the quality of grape seed used (g)) *x* 100%

2.4.2 *Determination of anthocyanin content*

The spectrum of diluted grape seed oil solution was determined by UV-vis spectrophotometer, and its anthocyanin content was verified by comparison with soybean oil and corn oil solution under the same conditions (Fu 2002). According to the peak value of anthocyanin in the spectrum of grape seed oil solution under different extraction processes, the supercritical extraction conditions with the highest content of proanthocyanidins were found.

3 RESULTS AND DISCUSSION

3.1 *Determination of the optimal parameters for the extraction of grape seed oil*

We obtained the experimental results in Table 3 by doing the experiments shown in Table 2, and then processed the experimental data using the range analysis method. The processing results are shown in Table 3. Where KI is the sum of all extraction rates at level 1, K2 is the sum of all extraction rates at level 2, and K 3 is the sum of all extraction rates at level 3. k1 is the average value of

Table 3. Measurement results of orthogonal test.

No.	A Pressure/bar	B Temperature/°C	C Static extraction time/min	D Dynamic extraction time/min	Extraction rate/%
1	150	35	5	10	0.31
2	150	40	10	20	0.97
3	150	50	15	30	2.27
4	250	30	10	30	7.42
5	250	40	15	10	2.71
6	250	50	5	20	4.20

(*continued*)

Table 3. Continued.

No.	A Pressure/bar	B Temperature/°C	C Static extraction time/min	D Dynamic extraction time/min	Extraction rate/%
7	350	30	15	20	5.25
8	350	40	5	30	9.67
9	350	50	10	10	2.81
K1	3.54	12.98	14.18	5.83	
K2	14.33	13.35	11.2	10.42	
K3	17.73	9.28	10.23	19.36	
k1	1.18	4.33	4.73	1.94	
k2	4.78	4.45	3.73	3.47	
k3	5.91	3.09	3.41	6.45	
R	4.73	1.36	1.32	4.51	

extraction rate at level 1, k2 is the average value of extraction rate at level 2, k3 is the average value of extraction rate at level 3, and R is the range of each factor.

3.1.1 *Optimization of orthogonal test results*

According to the orthogonal test data, the analysis of the range, the greater the value of the range, the greater the influence of the results. According to the data of orthogonal test in Table 3, P has the greatest influence on the extraction yield, followed by t1 and T, and t2 is the least. There is a great difference between the two levels of extraction pressure and dynamic extraction time, which has a great influence on the extraction rate. Comparatively speaking, the range of static extraction time and temperature is small, and they have relatively little effect on the extraction rate. The extraction rate increases with the increase of pressure, but considering the bearing capacity of the instrument, the high-pressure operation cost increases, so P is set at 350 bar. In addition, the extraction yield is proportional to the dynamic extraction time, but considering the experimental efficiency and production cost, the dynamic extraction time is 30min. The results suggest that temperature and static extraction time have little influence on the experimental results and can be considered as secondary factors. As a result, the optimal process parameters should be to select the corresponding parameters when the K value of each factor is the maximum, indicating that the most suitable conditions are A3, B2, CI, D3, which corresponds to the eighth group in the orthogonal combination of Table 3. Thus, the experiment shows that the optimal process parameters-extraction pressure P is 350 bar, T is 40°C, t1 is 30 min, and t2 is 5 min is the most suitable parameter.

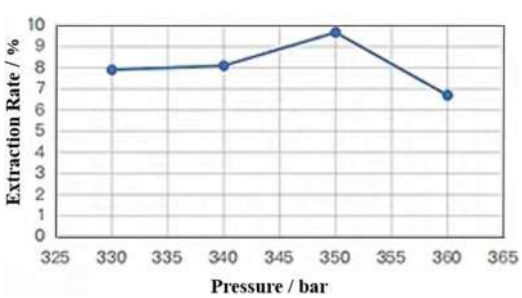

Figure 1. Effect of extraction pressure on extraction rate.

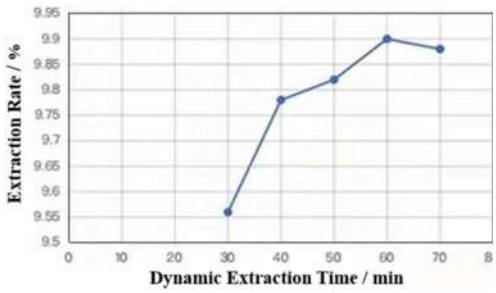

Figure 2. The effect of dynamic extraction time on extraction rate.

3.1.2 *Optimal determination of optimal extraction process parameters*

In order to further obtain the best extraction parameters of grape seed oil, we carried out the optimization and verification of orthogonal experiment. The results of orthogonal experiment showed that the extraction pressure had a great influence on the extraction rate, and the extraction rate was higher at 350bar. As a result, the extraction temperature is set at 40°C, the static and dynamic extraction time is 5 and 30 min respectively, and the extraction pressure is changed (330,340,350, 360bar). Weigh the quality of each group of products and calculate the extraction rate (Figure 1). As shown in the figure, the extraction rate is the highest at 350 bar, and the extraction rate can reach 9.67% under this condition. With the increase of pressure, the yield decreased greatly. This is due to the supercritical CO_2: there is a solution limit for the fluid. Consequently, it is chosen to be 350 bar.

Dynamic extraction time is also an important parameter in our study. At the beginning of extraction, the amount of oil extracted increases rapidly, but with the gradual prolongation of extraction time, the extraction rate slows down. At the same time, the increase of extraction time will also reduce the selectivity of solvents. Thus, after 350 bar, 40°C, t2 is 5 min, dynamic extraction is started, and after 30 min, the product quality is weighed every 10 min, and Figure 3 can be obtained. It can be seen that the highest extraction rate can be obtained after 60 minutes, which can reach 9.90%. Then the extraction yield did not continue to increase with the extension of time.

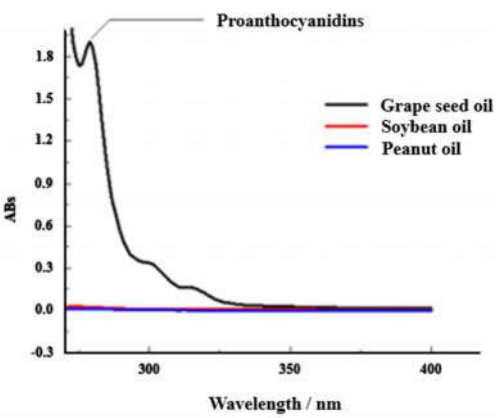

Figure 3. Comparison of UV-Vis absorption spectra of supercritically extracted grape seed oil and commercial edible oil.

According to the experimental results, the extraction rate is less affected by temperature, and the extraction rate is the highest when the temperature is 40PC. Similarly, the static extraction time

has less effect on the extraction rate, which is selected as 5 min. It is concluded that in order to improve the extraction rate, the most suitable parameters are as follows: P = 350 bar, T = 40°C, t1 and t2 = 5 and 60 min, respectively. The final extraction rate is 9.90%.

3.2 *Determination of the supercritical extraction process parameters with the highest proanthocyanidin content*

3.2.1 *Determine the presence of anthocyanins in grape seed oil using ultraviolet-visible spectrophotometer*

In this experiment, the UV-vis spectra of the extracted grape seed oil and the diluted solution of soybean oil and peanut oil were compared to identify the existence of proanthocyanidins. Proanthocyanidins have a characteristic absorption peak at 280 nm. Grape seed oil, soybean oil and peanut oil were diluted 500 times with petroleum ether as reference solution, and the experimental results were shown in Figure 3. The grape seed oil contains proanthocyanidins, while soybean oil and corn oil contain almost no proanthocyanidins.

3.2.2 *Optimization of supercritical extraction process parameters with the highest proanthocyanidin content*

In general, the content of proanthocyanidins in grape seed oil determines its quality. Supercritical CO_2: the content of proanthocyanidins in grape seed oil was affected by extraction temperature and pressure. We chose the content of proanthocyanidins as the optimization goal to study the two extraction parameters of extraction pressure and temperature respectively to find the best supercritical extraction process with the highest content of proanthocyanidins. The experimental conditions are as follows: Take T value of 35, 40, 50°C, P value of 150, 200, 250, 300, 350 bar, t2 value of 5 min, t1 value of 60 min product, dilute them 10,000 times with petroleum ether, use petroleum ether as the reference solution, and use an ultraviolet-visible spectrophotometer to

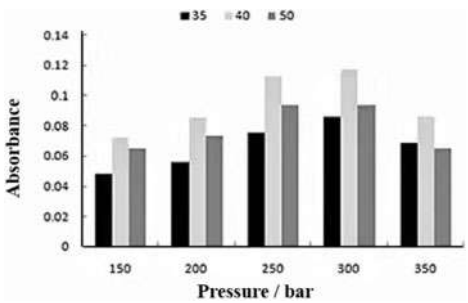

Figure 4. Absorbance of the product at 280nm at different temperatures and pressures.

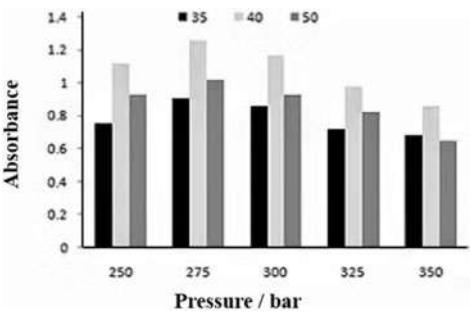

Figure 5. The absorbance of the product at 280nm at different temperatures and pressures.

scan the absorbance value of the product at 280 nm. As shown in Figure 4, all products have the highest proanthocyanidin content under the same pressure and temperature at 40˚C, which is the most suitable temperature.

According to the above results, the proanthocyanidin content is highest when the extraction pressure is 300 bar. Therefore, we are looking for the best extraction process parameters around 300 bar. T Take different samples with T values of 35, 40, 50°C, P values of 150, 200, 250, 300, 350 bar, t2 for 5 min, and t1 for 60 min, dilute them 10,000 times with petroleum ether, use petroleum ether as the reference solution, and use an ultraviolet-visible spectrophotometer to scan the absorbance value of the product at 280 nm. As shown in Figure 5, all the products are at the same temperature and the pressure is the highest when the pressure is 275 bar, indicating that the optimal supercritical extraction pressure is 275 bar.

4 CONCLUSION

In this research, we supercritical CO_2 fluid to extract oil from grape seed and orthogonal design of four factors three levels was applied. The extracted pressure, temperature and time as the influence factor to investigate the optimal parameters of the supercritical CO_2 extraction technique. Also, we studied the supercritical CO_2 extraction process with to achieve the highest anthocyanin content. According to the above experimental results, the optimal process parameters-extraction pressure P is 350 bar, T is 40°C, t1 is 60 min, and t2 is 5 min is the most suitable parameter. The final extraction rate is 9.90%. In addition, the process conditions for supercritical CO_2 extraction of grape seed oil with the highest proanthocyanidin content are 275 bar and 40°C.

REFERENCES

Du Yanshan. Comprehensive utilization of grape seeds [D]. Jiangnan University, 2015.

Fu Wusheng, Zhao Daohui & Huang Jianfeng. Determination of Proanthocyanidin Content in Grape Seed Extract by Ultraviolet Spectrophotometry [J]. Food Research and Development, 2002, 23(6), 90–92.

Sun Bingsuo. Analysis of the reason why the detection value of the solvent residue in crushed fourth-grade rapeseed oil exceeded the standard [J]. Modern Agricultural Science and Technology, 2019, 16, 195–196.

Tian Ye, Chen Guanming, Li Jiafen, Xiang Xiongying, Liu Yang & Li Hongyang. The development status of the world grape industry [J] Tropical Agriculture Science, 2018, 38(06), 96–101.

Wang Lin, Xu Dazhuang, Dai Qixuan, et al. Research progress in the preparation of pharmaceutical preparations based on supercritical fluid technology [J]. Chinese Science Bulletin, 2021, 66(10), 187–1194.

Wang Shaowei Determination of Solvent Residues in Edible Vegetable Oils by Headspace Gas Chromatography-Mass Spectrometry[J]. Food Safety Guide, 2015, 021, 98–100.

Wang Ting. Common sense and development strategy of edible oil consumption [J] China High-tech, 2019, 03, 40–41.

Xu Minghuang. Research on the process of CO2 recovery and reuse technology: dimethyl ether and ethylene carbonate[J]. Master's degree thesis, School of Chemical Engineering and Materials Engineering, Tamkang University, Taiwan, 2016.

Xue Pingping. The status quo and development prospects of China's grain and oil processing industry[J]. Food Economics Research, 2020, 6(02), 65–73.

Advances in Applied Chemistry and Industrial Catalysis – Saikia (Ed.)

Research progress of preservatives in cosmetics and their detection techniques

Jingyuan Chen*
The High School Affiliated to Renmin University of China, Beijing, China

ABSTRACT: Cosmetics are daily chemical industrial products that are applied, sprayed or dispersed by other similar methods on body surface for the purpose of cleaning, skin care, beauty and elimination of bad odors. Cosmetics are exposed to a large number of micro-organisms in the process of production, shipment and use. To mitigate the impacts of microbial contamination on the safety of cosmetics, manufacturers need to add preservatives to cosmetics. However, the excessive use of preservatives may cause skin contact allergy. This paper reviews the classification of preservatives in cosmetics and the detection methods of preservatives, compares and summarizes the research progress and advantages and disadvantages of preservative detection techniques.

1 INTRODUCTION

There are various types of preservatives in cosmetics. According to the limit use regulations of domestic and foreign cosmetic preservatives, preservatives in cosmetics can be divided into three main categories. The first category of cosmetic preservatives is parabens. Parabens, also known as nipagin esters, are used as preservatives in cosmetics because of their low toxicity, non-volatility, good bactericidal ability and stability (European Commission 2007). However, excessive use of parabens in cosmetics may cause contact dermatitis. Both China and the EU indicate in their relevant regulations that the limits for single and mixed esters are 0.4% and 0.8%. In contrast, the US believes that the use of paraben preservatives in cosmetics is safe (European Commission 200); Hu 1994; Wang 2007) The second category of cosmetic preservatives is formaldehyde and formaldehyde releasing compounds. Formaldehyde has high bactericidal activity and low price (Fu 2012). However, excessive amounts of free formaldehyde may irritate the eyes and respiratory tract, trigger allergic reactions, and are even potentially carcinogenic (Critchley 2009). In China's relevant regulations, formaldehyde and its formaldehyde release compounds are stipulated as restricted substances. Both China and Europe stipulate that the concentration of free formaldehyde in cosmetics other than oral hygiene products cannot exceed 0.2%, and the maximum concentration in oral hygiene products is 0.1% (European Commission 2007; Hu 1994; Wang 2007). The third category of cosmetic preservatives is isothiazolinone. Isothiazolinone compounds are highly effective non-oxidizing bactericidal preservatives, including MIT, CMIT and BIT, which have been widely used in various fields such as industrial recycling, cooling water, textile softener and polish, and paper industry. The research shows that these substances are Class I sensitizers which may cause allergic or dermatitis reactions, and excessive exposure may also lead to skin burns, with CMI and MI being the most sensitizing and irritating (Chen 2010; de Groot 1988; Nielsen 2001).

*Corresponding Author: hu.chen@nokia-sbell.com

DOI 10.1201/9781003308553-3

2 NECESSITY FOR PRESERVATIVE DETECTION IN COSMETICS

Although preservatives in cosmetics can slow down the growth of micro-organisms in cosmetics, improper concentrations may cause contact allergies to the skin. In 1998, Nielsen in Denmark reported the research on contact allergies and found that about 6% of contact allergies were caused by the excessive amount of preservatives in the cosmetics used by patients (Goossens 1999; Marks 2000; 2003). According to the patch test on examining skin allergic reactions in the United States from 1996 to 2002, the rate of skin allergic reactions caused by paraben preservatives from 1996 to 1998 was 1.7%. From 2001 to 2002, this figure has decreased to 0.6% due to the widespread use of paraben preservatives in cosmetics. The rate of skin allergy screening caused by formaldehyde or quaternium-15 was about 9%, the rate of contact allergy caused by imidazolidinyl urea was 2.7% to 3.7%, and the rate of contact allergy caused by isothiazolinone was 2.3% (Lu 2014; Pratt 2004; Wilkinson 2002). According to a comprehensive research of patch test in Europe from 1991 to 2000, the rate of skin allergy caused by hydroxybenzoates was 0.5% to 1.0%, the rate of skin allergy caused by formaldehyde or quaternium-15 was about 2% to 2.5%, the rate of skin allergy caused by imidazolidinyl urea was 0.5% to 1.5%, and the rate of skin allergy caused by isothiazolinone was 2.3% (Wu 2007). There are many types of preservatives, and many countries have regulations on the use and detection of preservatives in cosmetics.

3 CONVENTIONAL DETECTION METHODS FOR PRESERVATIVES IN COSMETICS

The analysis methods of HPLC, UV spectrophotometry, capillary electrophoresis and gas chromatography are commonly used in cosmetics. In order to improve the accuracy, stability and efficiency of detection methods for cosmetic components, researchers have been working to improve various methods in recent years.

3.1 *High performance liquid chromatography*

The principle behind HPLC is to use liquid as the mobile phase and inject the mixed solvents with different polarities and ratios into the chromatographic column through the flow pump, so that the different components are separated in the chromatographic column and enter the detector for detection.

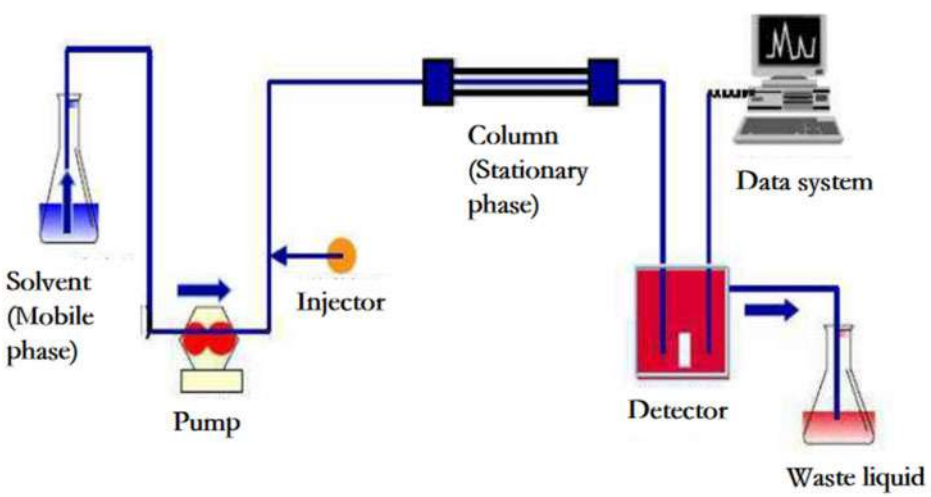

Figure 1. HPLC analytical method for preservatives in cosmetics.

Lu Lin et al. conducted a study on the detection of five restricted preservatives (chlorhexidine, benzoic acid, chlorodimethoate, o-phenylphenol and p-chlorine-m-cresol) in cosmetics. The five preservatives in 10 commercially available cosmetics were extracted with methanol, and saturated sodium chloride solution was used as the precipitant. The results showed that five preservatives such as chlorhexidine presented good linearity in a certain concentration range with the correlation coefficients greater than 0.9990, the limits of detection (LOD) were 0.8–2.2 ng, and the recoveries of the method were 95.0%–104.0%. It was concluded that the method is accurate for the detection of preservatives in cosmetics, and is a useful supplement to the standardized method (Cao 2019).

The goal of chromatographic analysis is to separate the components in the mixture. The resolution of two adjacent chromatographic peaks is defined as the quotient of the retention time difference between the two peaks and the average of the bottom width of the two peaks.

$$\mathbf{R = 2(t_{R2}\text{-}t_{R1})/(W_1 + W_2)}$$

A reversed-phase high performance liquid chromatographic (RP-HPLC) method for the simultaneous detection of 24 preservatives in cosmetics was conducted by Wu Ting et al. The KromasilC18 (4.6 mm × 250 mm, 5 μm) column was used with the phosphate buffer solution (pH=4.26) as the mobile phase and gradient elution. The samples were extracted by methanol ultrasonication, and then determined by RP-HPLC-diode array detector. The sample pretreatment and chromatographic conditions were studied and optimized. The relative standard deviations of the method were found to be 1.3%∼3.3%; the recovery was 90.6%∼97.8%; the linear correlation coefficients of various preservatives were ≥0.9997. The result shows that with high accuracy and precision, HPLC can be used for the analysis of the contents of various preservatives in cosmetics (Liu 2019).

HPLC has many advantages, with a wide range of determination, high separation efficiency, fast analysis speed and high degree of automation, and has become the most common analytical method used by analytical researchers today. HPLC has been widely applied to the separation and determination of various hormones in food, health care products, pharmaceuticals and cosmetics (Patricia 2020). However, this analytical method suffers from extra-column effects. On the one hand, once the elution mode of the mobile phase changes, the dispersion and retention of the target analytes may affect the peak shape of the chromatographic peaks; on the other hand, the limitations of the detector may also limit the detection range (Ebru Türkz Acar 2017).

3.2 *UV spectrophotometry*

UV spectrophotometry is a method to analyze substances by measuring their absorbance within the UV-visible wavelength range. It is used for qualitative analysis, because the absorption spectrum of each substance is determined by its different particle structure; under certain conditions, the absorbance of the substance is linearly related to its concentration and is used for quantitative analysis. Lambert-Beer law was used to calculate the concentration of preservatives in cosmetics (A=kbc), A represented the absorbance.

E Patricia Sheppard et al. determined 16 cosmetic preservatives using partition chromatography separation and UV spectrophotometry. The method was adapted from the official hexachlorophenol first action method 35.023-35.027 and is widely applicable to the determination of preservatives in cosmetics. The chemical categories studied include phenols, parabens, biphenyls, carbonyls, and salicylanilides. The partition chromatography technique can't separate 3,4′, 5-tribromosalicylic acid (TBS) from hexachlorophenol or Irgasan DP 300. However, the UV determination of these compounds was accomplished by using the maximum absorption value of TBS, which was not consistent with the absorption values of the other 2 preservatives. The average recovery of all compounds studied was 97% (Li 2013).

UV spectrophotometry is simple to operate and fast to analyze. However, due to the complexity of the cosmetic matrix, the detection of the target results is susceptible to interference, and cannot be used for the simultaneous detection of multiple types of cosmetic restricted substances, the detection in the actual sample is limited.

3.3 *Capillary electrophoresis*

Capillary electrophoresis is a separation technique that uses capillaries as separation channels and can be used for the detection and analysis of biological macro-molecules.

Yildirim et al. used a capillary electrophoresis (CE) analytical approach for the determination of benzalkonium chloride. The quantitative analysis was performed with an external standard method. The 75 mM (pH 6.0) phosphate buffered solution containing 30% of acetonitrile was used as the electrolyte for the electrophoretic separation. The sample was introduced hydrodynamically into the capillary column within 3 seconds using a pressure of 50.0 mbar. The developed method was validated and applied to samples prepared by wringing out antibacterial wipes containing benzalkonium without further extraction. The linearity of the method was controlled by applying Mandel's test. The LOD values of the developed method were 0.313 and 0.309 μg/ml and the LOQ values for the C10 and C12 derivatives were 1.042 and 1.029 μg/ml respectively (Cho 2019).

Ying Li et al. developed a new mini capillary electrophoresis amperometric assay (mini-CE-AD) for the rapid determination of the fatty aldehyde preservatives formaldehyde and glyoxal in cosmetics. Based on a transient moving chemical reaction boundary online enrichment method, coexisting interferents and their congeners (acetaldehyde and methylglyoxal) can be well separated for both aldehydes, with LOD (S/N=3) up to ng/mL level (1.64–2.80 ng/mL) under optimal conditions. With average recovery between 94–105%, CE should have a wide range of analytical applications (Yang 2018).

Capillary electrophoresis technique has the advantages of high efficiency separation, simple operation and drug saving. However, due to the small capillary diameter and too short optical path, the method has poor preparative ability and low sensitivity; the electrodialysis variation with sample components affects the reproducibility of the separation, which restricts its wide application.

3.4 *Gas chromatography*

GC is a separation and analysis method in which the mobile phase is gaseous and the mixture is separated by using the difference of physical properties such as boiling point and polarity of each substance, which can be used for qualitative and quantitative analysis of thermally stable and volatile substances.

Cho et al. used a gas chromatograph with a flame ionization detector to simultaneously analyze 14 kinds of preservative in cosmetics. The calibration curves of the 14 preservatives, except for dehydroacetic acid (0.9891), showed good linear correlation coefficients above 0.9997, confirming the specificity. The accuracy (% recovery) of the 14 preservatives in cosmetics ranged from 96.9% ~109.2%. The result shows that a series of preservatives can be detected simultaneously by GC (Golden Dividend 2011).

Yang Ming et al. developed a gas chromatographic method for the determination of methanol in polyvinyl alcohol (solid), a raw material used in cosmetics. The head space approach was more suited than distillation and direct dilution methods for the determination of methanol in polyvinyl alcohol. The effects of solvent and salting agent on the determination results were investigated, and the optimal solvent and salting agent were found to be 10m water and 0.5 g sodium chloride respectively. The results showed that the linearity of methanol concentration was good in the range of 10~1000 mg/L with the correlation coefficient up to 0.9995, the recoveries were 92.6%~104.8%, the relative standard deviations were within the range of 1.2%~6.5%, and the limits of detection were 5 mg/L. The experimental results demonstrated that the gas chromatographic method is suitable for the detection of methanol in polyvinyl alcohol, a raw material used in cosmetics (Sun 2019).

Gas chromatography has good separation capacity and reduces the workload of mobile phase preparation. However, the inherent characteristic of not being able to characterize unknown components directly and not being able to apply to a wide range of analytes limits its application.

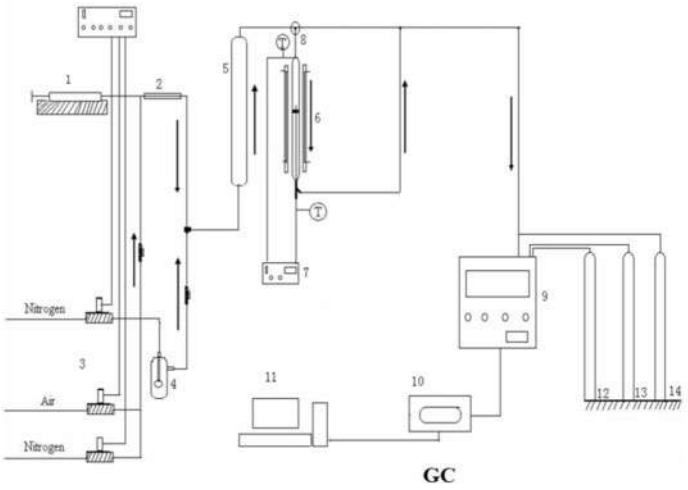

Figure 2. GC analytical method for detection of preservatives in cosmetics.

4 INSTRUMENT COMBINED DETECTION METHOD FOR PRESERVATIVES IN COSMETICS

4.1 *Gas chromatography-mass spectrometry*

Quan et al. conducted a gas chromatography-mass spectrometry method for the simultaneous determination of one preservative, including phenol and benzyl alcohol in cosmetics. The determination of the above 21 preservatives in cosmetics by GC-MS was investigated using ultrasonic extraction. The sample extraction solvent and sonication time selection and experiments on linearity, limit of detection, recovery and precision were carried out. The relative standard deviations of the method were 1.19%–6.68%; the recoveries were 90.46%–9.56%: the minimum limits of detection were 50–250 mg/kg. The result demonstrates that GC-MS is easy to conduct, fast and accurate, and can be utilized for the analysis of the 21 preservatives in cosmetics because of the good separation of the above 21 preservatives (Guerra 2018).

Sun Jing et al. developed a method for the simultaneous determination of 25 preservatives by GC-MS/MS. The cosmetic samples were extracted by ultrasonication with methanolic solution containing 0.1 mg/mLL(+)-ascorbic acid, with 2-octanol, phenol and heptachlor as internal standards, dehydrated with anhydrous sodium sulfate, centrifuged and filtered. Then, the sample was analyzed by GC-MS/MS, and quantified by internal standard method. The limits of detection of the method were 0.08–0.99 μg/kg. 3 types of cosmetic matrices, including water, lotion and cream, were selected to verify the accuracy of the method at 4 spiked levels. The recoveries of 25 preservatives were 82.3%–119.4%, with the RSD of 0.2–14.3% (n=6). The method is qualitatively and quantitatively accurate and can be effectively used for the detection of multiple preservatives in cosmetics products (Qi 2020).

Gas chromatography-mass spectrometry is a combination of chromatographic and mass spectrometric detection techniques, which combines the advantages of gas chromatography for efficient separation and mass spectrometry for providing structural information of analytes, and is widely used in various fields of detection and analysis.

4.2 *Liquid chromatography-mass spectrometry*

EugeniaGuerra et al. improved a formula based on VE and LC-MS/MS for the simultaneous analysis of 22 regulated preservatives and synthetic dyes in cosmetics. The extraction process is performed

in Eppendorf tubes, allowing extraction and clean-up in a single step, reducing sample and reagent consumption for efficient and rapid extraction. The method shows good linearity ($R^2 \geq 0.9918$) and intra- and inter-day precision (%RSD ≤ 13) with the LOQ of preservatives less than 0.587 $\mu g g^{-1}$ and with the LOQ of synthetic dyes less than 3.437 $\mu g g^{-1}$. Quantitative recoveries were obtained at four concentration levels in the range of 2–100 $\mu g g^{-1}$ in cosmetic matrices. The method has been successfully applied to a wide range of cosmetic products, including leave-on and wash-off products, where 13 target compounds could be quantified at concentrations ranging from 0.39 to 442 $\mu g g^{-1}$ for dyes and from 1.89 to 1335 $\mu g g^{-1}$ for preservatives. It is worth highlighting the presence of parabens at concentrations higher than 1000 $\mu g g^{-1}$ in 24 of the 35 samples analyzed in toothpaste.

Li Li et al. Conducted an approach for the determination of the restricted preservatives chlorhexidine, benzyl chloride phenol, chlorodimethoate, o-phenylphenol and p-chlorine-m-cresol in two matrix types of cosmetics by HPLC and liquid chromatography-mass spectrometry respectively. The samples were extracted by solvent ultrasonication, centrifuged at 8000 r/min for 15 min, filtered through a microporous membrane and the renewed filtrate was taken for determination. The two analytical methods were determined using different columns, eluent solvents and elution procedures. The results showed that the linearities of the five restricted preservatives, including chlorhexidine, were good in different linear ranges with linear correlation coefficients greater than 0.990 for HPLC and LC-MS. The relative standard deviations of the method precision were 0.4%∼1.1% and 1.0% ∼2.8% respectively; the recoveries were 103.7%∼119.8% and 71.2% ∼ 117.2% respectively. The limits of detection of the five preservatives were 2.10 ∼ 4.70 $\mu g/g$ and 1.05 ∼ 2.45 $\mu g/g$ respectively. The experimental data indicated that the LC-MS method was more suitable for the qualitative determination of several restricted preservatives in cosmetics, while the LC method was only suited for the quantitative determination of the samples.

Liquid chromatography is not limited by the target analytes and has a wide range of applications. Liquid mass spectrometry takes the advantages of both and makes up for their disadvantages when used alone, making it one of the most effective tools for analyzing mixtures, but it limited by the lack of detectors when used alone.

Figure 3. LC-MS method for detection of preservatives in cosmetics.

5 CONCLUSION

This paper reviews the research progress on detection techniques of preservatives in cosmetics. This paper introduces the principles and research progress of relevant detection techniques used for preservative detection from the basic concept, classification, and necessity of detection. By analyzing the literature, the advantages and disadvantages of each detection method are comprehensively described. The paper describes in detail the conventional detection methods for cosmetics. Some of the methods are easy to operate and have high separation capacity, while some of the detection methods have disadvantages such as low sensitivity, low applicability, and high restriction on the detection object. Compared with conventional detection methods, the combined detection method

has the advantage of being able to provide accurate structural information of analytes while separating phases, but there are disadvantages such as limitations by detector requirements, which require further development of new detection methods.

In addition, there is no comparative assessment of detection methods for specific types of restricted preservatives in cosmetics, and it is necessary to summarize precisely the most effective testing methods for different preservatives by reviewing and organizing the testing of preservatives in cosmetics in various countries.

REFERENCES

Critchley M, Bentham R. Journal of Applied Microbiology, 2009, 106 (3):784.

Chen Y C, XIE X B, SHI Q S, et al. Fine and Specialty Chemicals, 2010, 18 (1): 43.

Cao Hairong. Determination of banned components in cosmetics by ULTRA performance liquid chromatography mass spectrometry [M]. Shanghai University of Applied Technology, 2019.

Cho S H, Jung H R, Kim Y S, etc. Simultaneous Multicomponent Analysis of Preservatives in Cosmetics by Gas Chromatography[J]. 2019, 45(1):69–75.

de Groot A C, Bruynzeel D P, Bos J D, etc. The allergens in cosmetics. Arch Dermatol 1988, 124(10), P1525–1529.

European Commission, Council Directive 76/768/EEC of 27 July 1976 on theApproximation of the Laws of the Member States Relating to Cosmetic Products (Consolidated Version), 2007.

Ebru Türkz Acar, Güne Yldrm. Determination of benzalkonium chloride in wet wipes by using a validated capillary electrophoresis method[J]. Journal of cosmetic ence, 2017, 68(1):1–10.

Fu Z Y, Wang Q, Jia L N, et al. Material Review, 2012, 26 (5):291.

Goossens A, BeckMH, Haneke E, McFadden J P, etc. Adverse cutaneous reactions to cosmetic allergens. Contact Dermatitis 1999, Vol 40, P112–113.

Golden Dividend. Determination of preservatives in cosmetics by gas chromatography-mass spectrometry [D]. Dalian Polytechnic University, 2011. (in Chinese)

Guerra E, Alvarez-Rivera G, Llompart M, etc. Simultaneous determination of preservatives and synthetic dyes in cosmetics by single-step vortex extraction and clean-up followed by liquid chromatography coupled to tandem mass spectrometry[J]. 2018, 188:251–258.

Hu A.X. Application of formaldehyde in the synthesis of heterocyclic cosmetics preservatives [J]. Fragrance and Essence Cosmetics, 1994(04):10–13.

Lu Lin, Li Hui, Gao Yanhong. Determination of five restricted preservatives in cosmetics by high performance liquid chromatography [J]. Health Research, 2014, 43(4):627–629.

Liu Jingxuan. Application of high performance liquid chromatography in cosmetics detection [J]. Metrology and Detection, 2019(3): 62–63.

Li Y, Chen F, Ge J Y, etc. Fast determination of aldehyde preservatives by miniaturized capillary electrophoresis with amperometric detection[J]. Electrophoresis, 2013, 35(2-3):419–424.

Marks JGJr, BelsitoDV, DeLeo V A et al. North American Contact Dermatitis Group patch-test results, 1996–1998. Arch Dermatol 2000: 136: 272–273.

Marks JGJr, BelsitoDV, DeLeo V A et al. North American Contact Dermatitis Group patch-test results, 1998–2000. Am J Contact Dermat 2003: 14: 59–62.

Nielsen N H, Linneberg A, Menne T. Allergic contact sensitization in an adult Danish population: two cross-sectional surveys eight years apart (the Copenhagen Allergy Study). Acta Derm Venereol 2001: 81: 31–34.

Pratt M D, Belsito D V, DeLeo V A et al. North American Contact Dermatitis Group patch-test results, 2001–2002 study period. Dermatitis 2004: 15: 176–183.

Patricia S E, Wilson C H. Preservatives in Cosmetics: Partition Chromatography and Ultraviolet Spectrophotometry[J]. Journal of the Association of Official Analytical Chemists, 2020(5):5.

Qi Aiming, Mao Liqiu, Xiao Shuxiong, et al. Comparative study on simultaneous determination of 5 restricted preservatives in 15 batches of cosmetics by high performance liquid Chromatography and Liquid mass spectrometry [J]. Journal of Natural Science, Hunan Normal University, 2020, V. 43; No.180(01):60–66.

Sun Jing, Tan Li, Cao Ling, et al. Determination of 25 preservatives in cosmetics by gas chromatography-tandem mass spectrometry [J]. Chinese Journal of Chromatography, 2019, 037(003): 331–339.

Wang Ping, Liu Yuhong. Research progress of preservatives and analytical methods for Cosmetics in China [J]. Chinese Journal of Environment and Health, 2007, 24(7):557–559.

Wilkinson J D, w S, Andersen K E et al. Monitoring levels of preservative sensitivity in Europe. A 10-year overview (1991–2000). Contact Dermatitis 2002 46: 207–210.
Wu Ting, Wang Chao, Wang Xing, et al. Determination of 24 preservatives in cosmetics by reversed-phase high performance liquid chromatography [J]. Chinese Journal of Analytical Chemistry, 2007, 35(10):1439–1443.
Yang Ming, ZHANG Lihua, Hu Dan, et al. Determination of methanol content in polyvinyl alcohol used as raw material for cosmetics by gas chromatography [J]. China Surfactant Detergent & Cosmetics, 2018, 048(006):352–355.

Advances in Applied Chemistry and Industrial Catalysis – Saikia (Ed.)

Determination of four acrylates in food packaging paper via high performance liquid chromatography

Yue Qiu*, Dong Xiang, Lu Zhang & Jiaxiong Zhao
Chongqing Academy of Metrology and Quality Inspection, Chongqing, China

ABSTRACT: A method for the determination of four acrylate monomers in food packaging paper was established based on high performance liquid chromatography (HPLC) method. The effects of extraction solvent, ultrasonic time, ultrasonic temperature and other pre-treatment conditions on the extraction efficiency of acrylate monomers were investigated. Under the optimal conditions, the samples of food packaging paper were extracted by ultrasonic treatment, analyzed by HPLC, and quantified by external standard method. The results suggested that the four acrylate monomers showed good linearity in the range of 0.1–50.0 mg/L ($R^2 \geq 0.999$), and the detection limits (LODs) were 0.03–0.08 mg/L. The blank samples were used as the matrix for standard addition experiment, and the recoveries were 89.2%–108.1% with relative standard deviations of 1.3%–4.8%. The method was simple, accurate and reliable, which can provide technical support for daily detection of acrylic monomers in food packaging paper.

1 INSTRUCTIONS

The acrylate polymer has excellent color preservation, light resistance, UV resistance, difficult to oxidation and other advantages (Sengtu 2008; Wei 2009; Zhao 2009). The modified acrylate polymer through functional unit has good paper enhancement effect and water proof performance, therefore it is widely used in the papermaking industry. Acrylate monomer substances have irritant and sensitization to skin, eyes and respiratory tract, which may cause lung, liver and kidney damage. It has been reported that long-term exposure to methyl methacrylate in human body can lead to chronic poisoning, which mainly manifested as comprehensive symptoms of nervous system damage, toxic encephalopathy and even teratogenesis may occur in a few cases (Gong 2013; Liu 2011; Qiu 2021). During the use of food contact materials, harmful substances will migrate into the human body through food.

Since 2008, China has put forward requirements on the migration limit of acrylate monomers in food packaging paper, but there is still lack of research on acrylate monomers in paper packaging materials. At present, the main methods for the determination of acrylate compounds include gas chromatography (Hu 2013), gas chromatography-mass spectrometry (Dai 2012), high performance liquid chromatography (Zuo 2015). Due to the high volatility and low molecular weight of acrylates, liquid chromatography can eliminate the interference of solvents and other impurities.

In this work, high performance liquid chromatography (HPLC) was used to analyze and detect four acrylate monomers in food packaging paper. This method is simple, accurate and reliable, which can provide data reference for the detection of acrylic monomers in plastic food packaging paper in the future.

*Corresponding Author: qiuyuecqu@163.com

DOI 10.1201/9781003308553-4

2 EXPERIMENTAL AND METHODS

2.1 *Materials and reagents*

The standards were acrylic acid-2-hydroxyethyl ester (AAHE), 2-hydroxyethyl-2-methyl-2-acrylate (HEMA), methacrylate (MAA) and methyl methacrylate (MMA), which were all supplied from Dr. Ehrenstorfer (Germany). HPLC grade methanol, acetonitrile and isopropyl alcohol were purchased from Merck (Germany).

2.2 *Instruments and equipment*

Agilent 1260 HPLC with DAD detector (Agilent); SQP electronic analysis balance (Germany Sartorius); N-evap-112 Nitrogen Blower (Organomation, USA); Bilon-2000ct ultrasonic cleaner (Shanghai Bilang Instrument Co., LTD.).

2.3 *Methods*

Each standard substance of 10 mg was accurately weighed and placed in a 10 mL volumetric flask, dissolved with methanol and configured to a standard solution of 1000 ppm. The standard working solution was diluted with methanol with concentrations of 0.1, 1.0, 10.0, 25.0 and 50.0 mg/L. The sample was cut into small fragments with area smaller than 5 mm × 5 mm. The sample of 1.0 g was accurately weighed, and ultrasonic extraction in methanol solution was performed at 40°C for 40 min. The supernatant was filtered through 0.22 μm organic system. The analysis was performed on ZORBAX SB-AQ column (250 mm × 4.6 mm, 5 μm) at 40°C. The mobile phase was the mixture of water and acetonitrile. The detection wavelength was 210 nm, the injection volume was 20 μL, and the flow rate was 1.0 mL/min. Gradient elution procedure: 0–6.5 min, 20%–40%B; 6.5–17 min, 40%–65%B; 17–17.2 min, 65%∼100%B; 22–22.2 min, 100%–20%B, then kept for 6 min.

3 RESULTS AND DISCUSSION

3.1 *Selection of chromatographic conditions*

The effect of chromatographic conditions on the separation of acrylate monomers was investigated. The target compounds were soluble or slightly soluble in water with certain polarity, therefore ZORBAX SB-AQ column was selected as the analysis column for the target compound. The mobile phase system with different polarity for gradient elution was compared, which suggested

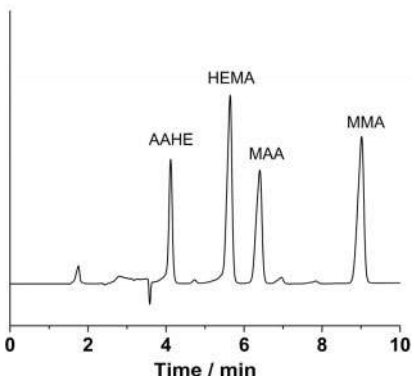

Figure 1. Chromatograms of four acrylate monomers mixed with standard solutions.

acetonitrile-water system had the best separation effect. Moreover, because of the small ultraviolet absorption and weak noise of acetonitrile in short wavelengths, the baseline was smooth during the gradient elution. Hence the best choice was acetonitrile. Under the optimal conditions, the four acrylate monomers could achieve good separation within 10 min, as shown in Figure 1.

3.2 *Selection of extraction fluid*

In this paper, the common and efficient ultrasonic extraction method was used to extract acrylate monomers. Blank food packaging bag samples were selected for standard addition experiments to explore the extraction effects of the target substances with extraction agents of methanol, acetone, ethyl acetate and acetonitrile. The results were shown in Figure 2. It was found that the highest average recovery was obtained with methanol as the extraction agent at the standard level of 0.5 mg/kg. Therefore, methanol was selected as the best extraction agent in this experiment.

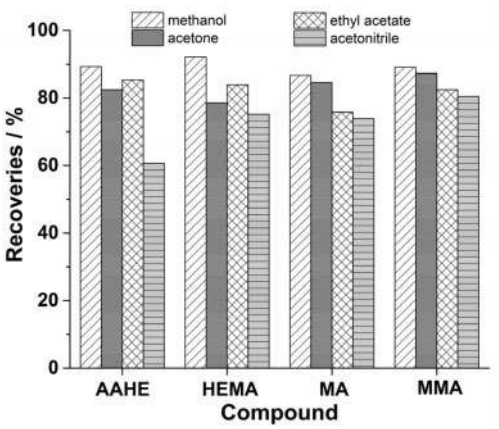

Figure 2. Influence of extraction solvent on recovery of four acrylate monomers.

3.3 *Selection of ultrasound time*

In order to ensure that four acrylate monomers were extracted adequately, the effects of extraction time on extraction efficiency were further investigated, the result was shown in Figure 3. The results showed that the extraction equilibrium time of the four kinds of acrylic monomers was not exactly

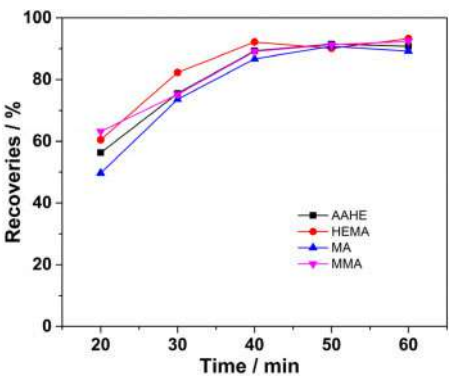

Figure 3. Effect of ultrasonic time on recovery of four acrylate monomers.

the same, but the average recovery tended to be stable after 40 min, so the best extraction time was 40 min.

3.4 *Selection of ultrasound temperature*

Temperature was another important factor affecting extraction efficiency. The influence of ultrasonic temperature on the recovery rate was investigated in the range of 20~60°C. The results were shown in Figure 4. Experimental results showed that with the rise of temperature, the extraction of 4 kinds of acrylic monomers efficiency were improved, but recovery was on the decline with raising the temperature sequentially, this was because the acrylic esters of volatile matter was strong. Therefore, the excessive temperature was not conducive to the extraction of target substances, so the best ultrasonic temperature was set at 40°C.

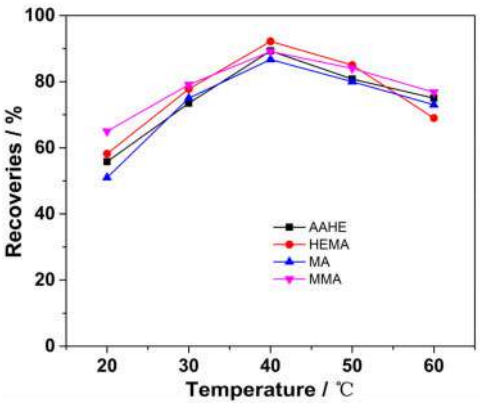

Figure 4. Effect of ultrasonic temperature on recovery of four acrylate monomers.

3.5 *The evaluation of the detection methods*

The standard curves of peak area (y) and sample concentration (x, mg/L) were plotted and linear regression equations were established. The mixed standard solutions of 4 acrylate monomers were added to the blank food paper packaging samples at 50.0, 10.0 and 0.1 mg/kg, respectively. The test was repeated 6 times for each concentration level, and the recovery and precision were calculated. The detection limits (LODs) of the method was calculated as S/N ≥ 3. The results (Table 1)

Table 1. Method evaluation results of four acrylate compounds.

Compounds	Standard curve equation	R^2	LOD (mg/kg)	Spiked (mg/kg)	R (%)	RSD (%)
AAHE	y=36.9x+1.22	0.9993	0.08	0.1	108.1	4.8
				10	93.5	3.1
				50	95.4	2.7
HEMA	y=81.3x+2.54	0.9995	0.03	0.1	91.0	4.0
				10	103.9	3.3
				50	100.8	1.4
MA	y=61.8x+1.95	0.9993	0.03	0.1	89.2	3.5
				10	105.7	2.3
				50	98.1	2.1
MMA	y=81.5x+2.53	0.9993	0.03	0.1	93.7	4.5
				10	94.2	2.4
				50	102.6	1.3

showed that the linear relationship between the concentrations of four acrylate compounds was good ($R^2 > 0.999$) in the range of 0.1–50 mg/kg. The LODs of four acrylate monomers were 0.03–0.08 mg/kg. The recoveries at three spiked levels ranged from 89.2% to 108.1% with relative standard deviations of 1.3% to 4.8%.

4 CONCLUSION

A method for the detection of four acrylate monomers in food packaging paper was established through the optimization of chromatographic conditions and pre-treatment conditions. The method had advantages of simple operation, high extraction efficiency and good accuracy, which could provide a reference for the analysis and detection of acrylates in food packaging materials in the future.

FUNDING

This research was funded by Scientific Research Project of Chongqing Market Supervision Administration [CQSJKJ2019005].

REFERENCES

Dai X. L. (2012). Determination of nine esters compounds in water by chromatographic-mass spectrometry with purge and trap. Admin. Tech. Environ. Monitor. 24, 55–57.

Gong S. G. (2013). Simultaneous determination of 23 ester compounds in cigarette water-borne adhesives by liquid-liquid extraction and gas chromatography-mass spectrometry. Chin. J. Chromatogr 31, 989–994.

Hu W. L. (2013). Determination of acrylates in soil and sediment by head-space gas chromatography. Phys. Test Chem. Anal. Part B: Chem. Anal. 49, 196–198.

Liu D. (2011). Determination of residual acrylate monomers in adhesives by headspace gas chromatography-mass spectrometry. Chin. J. Chromatogr. 29, 1179–1182.

Qiu Y. (2021). Study on migration of two acrylate monomers in plastic food contact materials. E3S Web of Conferences 233, 02045.

Sengtu X. Y. (2008). Determination of residual acrylate monomers in the coatings. Dye Finish 34, 33–35.

Wei Z. (2009). Determination of residual monomer MMA in MMA-CR system by headspace sampling method. Chem. Bioeng. 26, 83–84.

Zhao H. Y. (2009). Head-Space-Gas chromatographic determination of methyl methacrylate released from bone cement. Phys. Test Chem. Anal Part B: Chem. Anal. 45, 707–709.

Zuo Y. (2015). HPLC determination of residual amounts of 13 acrylic esters in living paper products. Phys. Test Chem. Anals. Part B: Chem. Anal. 51, 168–171.

Advances in Applied Chemistry and Industrial Catalysis – Saikia (Ed.)

Influence of pH on efficient removal of naproxen from water

Ying Tang, Wei Yi & Ke Ren
Guangdong Polytechnic of Environmental Protection Engineering, Foshan, P.R. China

Chengyang Hong*
South China Institute of Environment Sciences. Ministry of Ecology and Environment, Guangzhou, P.R. China

ABSTRACT: As a non-steroidal anti-inflammatory drug, naproxen is widely used worldwide. According to the previous investigation and statistics, naproxen has been detected in various environmental media with a concentration of ppt-ppb level, but its environmental risk should not be underestimated. Three types of naproxen removal technologies in the water environment, including physical, chemical and biological technologies, have been reviewed in this paper. Efficient removal methods have been developed in each type of removal technology, but each type has its defects to be solved. This paper further discusses the influence of pH on various removal technologies. Many studies have shown that pH affects naproxen removal in the aqueous phase, and acidic conditions are more conducive to the effective removal of naproxen.

1 INTRODUCTION

As an inhibitor of pepsinogen synthase, naproxen has positive effects on rheumatoid arthritis, osteoarthritis, ankylosing spondylitis, gout, chronic degenerative diseases of the motor system (such as joints, muscles, and tendons) and mild and moderate pain such as dysmenorrhea. Due to its high efficiency and safe pharmacological characteristics, naproxen quickly became the star product of non-steroidal anti-inflammatory drugs (NSAID) once it was developed and launched in the 1970s. Together with paracetamol, aspirin, ibuprofen, and diclofenac, naproxen has become the five pillars of antipyretic and analgesic drugs in the international market, with a very high popularity rate. Naproxen and ibuprofen together occupy nearly half of the market share of non-steroidal anti-inflammatory drugs. In 2016, the production volume of naproxen in China was about 500 tons, and the annual export volume was about 100 tons.

With the production and use of naproxen, naproxen has been widely detected in the environment. The primary sources of naproxen entering the environment are pharmaceutical factory wastewater, hospital wastewater, and domestic sewage. Most of these three types of wastewater are discharged into the environment after being treated by sewage treatment plants, and a small part is discharged directly into the environment without any treatment. Naproxen can be detected in various water environments such as surface water, groundwater, and seawater. Wang et al. studied the distribution characteristics of drugs and personal care products in the Pearl River, the Yellow River, the Haihe River, and the Liaohe River and found that naproxen is one of the PPCPs with a relatively high detection rate, with a concentration range of 0.1–0.25 μg/L (Wang et al. 2010). Naproxen pollution has also been reported in groundwater. Teijon et al. (2010) found that the concentration range of naproxen detected in groundwater in Spain is 0.145–0.263 μg/L. Naproxen has even been detected in drinking water (Benotti et al. 2009). Although the concentration of naproxen detected in the environment is at the ppt-ppb level, its environmental risk cannot be ignored. In addition to the

*Corresponding Author: hongchengyang@scies.org

DOI 10.1201/9781003308553-5

biological toxicity of the parent body, the biological toxicity of naproxen also includes the biological toxicity of degradation products and metabolites. Moreover, studies have shown that the degradation products and metabolites of naproxen are even more biologically toxic (Ma et al. 2014). Studies have also shown that naproxen not only affects the growth and development of aquatic organisms, but also significantly increases the risk of heart disease after long-term use (Baigent et al. 2013).

2 REMOVAL TECHNOLOGY OF NAPROXEN

Various physical, chemical, and biological methods for the degradation of naproxen have been reported. At present, the most widely used treatment technology is the biological method based on the sewage treatment process. However, the preliminary investigation results show that the removal efficiency of naproxen in the sewage treatment process is low. Joss et al. (2005) concluded that the removal rate of naproxen was 50% to 80% through investigation of a number of sewage treatment plants. After removing the interference factors, the removal efficiency of naproxen by activated sludge in the beaker experiment was also not ideal (Tang et al. 2014). Some researchers enhanced biodegradation by domesticating a single dominant flora. Dzionek et al. (2020) introduced Bacillus thuringiensis B1 into a laboratory-scale drip filter to achieve complete biodegradation of naproxen. Although this method significantly improves the removal efficiency, the degradation time is too long. Enzymes are efficient catalysts for biological reactions. In recent years, various extracellular oxidoreductases have been used to degrade pharmaceutical compounds, among which laccase is the most representative one. Ingole et al. (2020) used industrial laccase (LT-100) to degrade naproxen. The degradation rate reached 92% in a degradation time of 5 h under preset experimental conditions.

The principle of the chemical method is to remove naproxen by oxidation with various strong oxides. One is the traditional strong oxidant, such as permanganate, ferrate, hypochlorite and so on. The other is active radicals with strong oxidation ability, such as $^{\bullet}OH$, $SO_4^{\bullet-}$, $O_2^{\bullet-}$ and so on. The former is a chemical oxidation method. Yang et al. (2012) showed that the removal efficiency of naproxen by ferrate was more than 90%, but there were some defects, such as a large amount of oxidant and a great influence on the treatment effect by water quality. The latter is an advanced oxidation technology. The activation of such active oxidation substances is mainly through light, electricity, ultrasound and homogeneous/heterogeneous catalysts. The most widely studied methods for the removal of naproxen are photocatalytic oxidation technology and Fenton oxidation technology. Studies have shown that these two types of technologies have the problems of low light source utilization, narrow pH application range, secondary pollution, etc. At present, heterogeneous advanced oxidation technology based on persulfate activation is more popular. Asmar et al. (2021) activated peroxodisulfate with iron-based metal-organic framework MIL-88-A, and the degradation rate of naproxen could reach 70% after reaction at room temperature for 2 h. Bai et al. (2020) used $CuFe_2O_4$ to activate permonosulfate to degrade naproxen, and the removal efficiency of naproxen could reach 92.3% after 60 minutes of reaction.

Physical methods mainly include the adsorption method and membrane separation method. The principle of adsorption is to transfer pollutants from the water phase to the adsorption material. Membrane separation is a process of intercepting, adsorbing, and concentrating pollutants in an aqueous phase. Although the physical method can effectively remove naproxen, it does not completely degrade it into harmless substances. The subsequent treatment of adsorption materials and membrane materials is still a difficult problem, and it is difficult to popularize the application due to the high cost (Meloza et al. 2020).

3 INFLUENCE OF PH

3.1 *Biotechnology*

There are two main mechanisms for the degradation of target compounds in activated sludge: adsorption and enzymatic degradation. The adsorption of target pollutants by activated sludge

mainly depends on the hydrophobicity of the target and the electrostatic interaction between the target and activated sludge. The pH changes the removal effect of activated sludge on the target compounds by interfering with the electrostatic reaction between the target substances and the activated sludge. Our research group has set up a group of experiments to verify the effect of pH on the adsorption of naproxen by activated sludge. In the experiment, bezafibrate was selected as the reference compound of naproxen. The log K_{ow} values of naproxen and bezafibrate were 3.18 and 4.25, respectively, indicating that bezafibrate was easier to be adsorbed by activated sludge than naproxen. Since the pKa values of naproxen and bezafibrate were 4.15 and 3.6, respectively, both would undergo hydrolysis reaction and exist in aqueous solution as anions under the experimental conditions of pH (6.9 ± 0.1). Bezafibrate dissociates more obviously than naproxen. Therefore, bezafibrate has greater electrostatic repulsion with negatively charged microorganisms in the activated sludge and a stronger obstacle to adsorption. The final comprehensive reflection is that the adsorption and removal effect of naproxen by activated sludge is better than that of bezafibrate (see Table 1). It can be concluded that the electrostatic reaction is an important and non-negligible determinant of the adsorption of naproxen by activated sludge, and it can be further determined that pH will affect the absorption of naproxen by activated sludge.

Table 1. Removal ratio (%) of pharmaceuticals in batch sorption experiments.

C_o (μg/L)		10	50	100	150	200
Removal ratio (%)	Naproxen	26.04	17.77	14.96	15.47	14.8
	Bezafibrate	16.43	14.43	14.8	13.55	8.79

Based on the above research results, our research group further studied the effect of pH on the biodegradation of naproxen by activated sludge. A group of SBR reactors was designed. Two control activated sludge systems (N-SBR and A-SBR) were set up by changing the influent pH value ($pH = 7 \pm 0.2$ and $pH = 3.5 \pm 0.2$). The influence of pH value on activated sludge system is mainly through affecting the life activities of microorganisms, including causing the change of cell membrane charge, thus affecting the absorption of nutrients by microorganisms; affecting the activity of enzymes in the metabolic process; changing the availability of substances in the growth

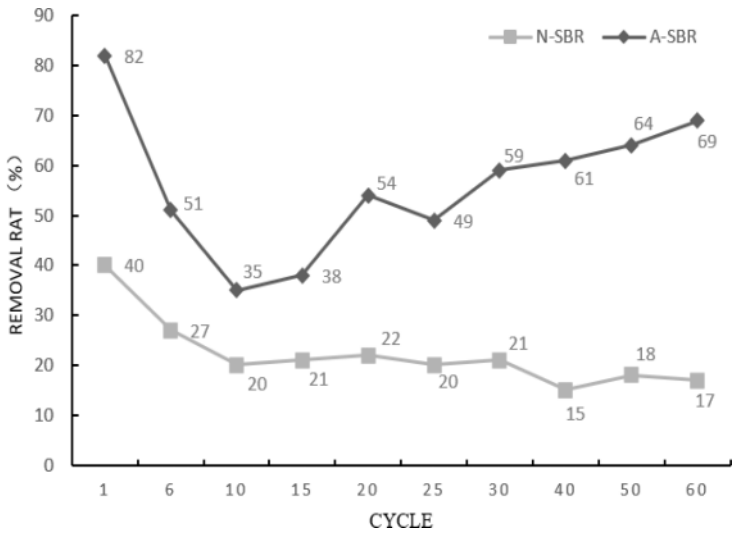

Figure 1. The variety of the efficient removal of naproxen in acidic and nature sequencing batch reactor.

environment and toxicity of harmful substances. The experimental results are shown in Figure 1. The removal effect of the A-SBR system on naproxen is better than that of the N-SBR system. At $pH = 3.5 \pm 0.2$, naproxen mainly exists in molecular form, and at $pH = 7 \pm 0.2$, naproxen mainly exists in anion form. Naproxen is easier to absorb by activated sludge and further absorbed and utilized by microorganisms under acidic conditions than neutral conditions. Compared with the N-SBR system, the A-SBR system has an abiotic limiting factor pH, which can promote the growth of beneficial microorganisms and inhibit the growth of miscellaneous bacteria to a greater extent. Therefore, setting the operating conditions of the activated sludge system to be acidic is beneficial to the effective removal of naproxen.

3.2 *Chemical technology*

Advanced oxidation technology (SRAOPs) based on $SO_4^{\bullet-}$ is leading chemical technology. The active substance $SO_4^{\bullet-}$ is mainly produced by activating persulfate. Persulfate includes peroxymonosulfate (PMS) and peroxydisulfate (PS). The activation methods mainly include thermal activation, alkali activation, ultraviolet (UV) activation, and metal activation.

Thermal activated PS technology is a widely studied and mature method mainly used to remediate in-situ organic pollution of groundwater and soil. The breaking of the O-O bond in the $S_2O_8^{2-}$ molecule can generate $SO_4^{\bullet-}$. In the activation process, the temperature is the main influencing factor, but it is not that the higher the activation temperature, the better the degradation effect of the oxidation system on pollutants. The reaction proceeds slowly at 30°C and can occur very rapidly at 90°C. Superoxide free radicals ($O_2^{\bullet-}$) and hydroxyl free radicals ($^{\bullet}OH$) can be generated at the same time under alkaline conditions. The reaction process is shown in Equation (1 and 2):

$$SO_4^{\bullet-} + OH^- \rightarrow SO_4^{2-} + {}^{\bullet}OH \quad (1)$$

$$S_2O_8^{2-} + 2H_2O \xrightarrow{OH^-} 3SO_4^{2-} + SO_4^{\bullet-} + O_2^{\bullet-} + 4H^+ \quad (2)$$

Therefore, changing the concentration of $SO_4^{\bullet-}$ in the solution by controlling the pH can affect the efficiency of PS degradation of target pollutants.

UV activation is to radiate persulfate by UV light. In the UV/PS system, the O-O bond of PS is homogenously cleaved under UV irradiation (248–254 nm) to form two free $SO_4^{\bullet-}$. Catalysis by UV light is a green and environment-friendly method. Therefore, the generation of $SO_4^{\bullet-}$ is environmentally friendly, has high production efficiency, and is independent of the pH in the solution. In the UV/PMS system, PMS undergoes photolysis at 253.7 nm, and $^{\bullet}OH$ and $SO_4^{\bullet-}$ are generated through the cleavage of oxygen bonds. Studies have shown that in the pH range of 8–10, the generation rate of $^{\bullet}OH$ and $SO_4^{\bullet-}$ through the photolysis of PMS photolysis increases with the increase of the pH value (Guan et al. 2011).

Many transition metal ions, especially divalent metal ions commonly found in soil and groundwater, can act as electron donors to catalyze the decomposition of persulfate through a single electron transfer reaction to generate $SO_4^{\bullet-}$:

$$S_2O_8^{2-} + M^{n+} \rightarrow\rightarrow M^{(n+1)+} + SO_4^{2-} + SO_4^{\bullet-} \quad (3)$$

$$HSO_5^- + M^{n+} \rightarrow\rightarrow M^{(n+1)+} + OH^- + SO_4^{\bullet-} \quad (4)$$

$$HSO_5^- + M^{n+} \rightarrow\rightarrow M^{(n+1)+} + {}^{\bullet}OH + SO_4^{\bullet-} \quad (5)$$

When the solution is neutral or alkaline, transition metal ions are prone to hydrolysis and precipitation. Therefore, this type of oxidation system needs to be carried out under acidic conditions. Given the shortcomings, the improved heterogeneous M_xO_y/persulfate system has become a new research focus, which effectively broadens the pH range for persulfate activation by transition metal ions (Wu et al. 2011).

Zero-valent iron (ZVI)/persulfate is also a heterogeneous oxidation system. Its activation process is a heterogeneous activation process in which the electrons of Fe^0 are transferred to persulfate ions.

Dong et al. (2020) studied the effect of solution pH on the degradation of naproxen by the ZVI/PS system. The experimental results showed that the increase of solution pH would significantly reduce the removal effect of the ZVI/PS oxidation system on naproxen. The influence of pH in the system is mainly in three aspects: ① acidic conditions are conducive to the production of Fe^{2+}; ② Aunder neutral and alkaline conditions, $SO_4^{\bullet-}$ will be converted to $^{\bullet}OH$ (see equation 1), reducing the oxidation capacity of the ZVI/PS oxidation system; ③ When the pH value is higher than the pKa value of naproxen, the deprotonated form of naproxen increases. Studies have shown that the reaction rate of the deprotonated form of naproxen with $SO_4^{\bullet-}$ and $^{\bullet}OH$ is lower than that of naproxen (Wang et al. 2018).

3.3 *Physical technology*

A variety of materials have been developed to adsorb naproxen, and a large amount of data indicates that the influence of pH on adsorption efficiency cannot be ignored. Ozcan et al. (2020) used synthesized activated carbon embedded alginate beads to adsorb naproxen in water. The experimental pH range was set at 3.0–11.0. The study showed that its adsorption capacity dropped sharply with the increase of pH value. Melgoza et al. (2020) studied the ability of non-viable Rhizopus oryzae biomass to absorb naproxen in both dry and wet conditions. The experimental results showed that the adsorption of naproxen by wet biomass increased with the increase of pH value, while dry biomass showed the same trend only in the range of pH > 6. Since the surface of dry biomass is positively charged under acidic conditions, the electrostatic reaction helps dry biomass to show the maximum adsorption capacity of naproxen under the condition of pH 4.7. Karami et al. (2020) used an aluminum-based metal-organic framework to adsorb naproxen, and the adsorption capacity decreased with the increase of pH value in the pH range of 2–8. Kurczewska et al. (2020) used hybridized kaolin and polyaminoamine dendrimer to remove naproxen from water. Since the amine group is protonated under acidic conditions and the adsorbent is positively charged, so in the pH range of 3 to 6, the adsorption capacity increases with the increase of pH value. When the pH value increases, the adsorbent is negatively charged, electrostatic repulsion occurs with negatively charged naproxen, and the adsorption capacity decreases. In summary, the pH dependence of the adsorption of naproxen in the aqueous phase by adsorbents can be rationalized by the electrostatic interaction mechanism.

Table 2. Influence of pH on the adsorption of naproxen by polyethersulfone filter membrane.

2MHCl (μL)		0	10	30	60	100	150
$C_{Naproxen}$ (μg/L)	Before	100.7	93.1	96.4	94.7	95.8	93.1
	After	75.5	23.3	24.0	21.2	19.0	22.5

Our research group has set up a group of experiments to study the influence of pH on the adsorption of naproxen by polyethersulfone filter membrane (see Table 2). The experimental results show that an acidic environment can greatly change the adsorption performance of polyethersulfone filter membrane for naproxen, but there is no linear relationship between the two. The concentration of naproxen in the aqueous solution added with HCl decreased significantly after passing through the polyethersulfone filter membrane, but the adsorption capacity of naproxen by polyethersulfone filter membrane did not increase with the increase of HCl concentration in the aqueous solution.

The pH value of the subsequent experiment was set to 3.5, and the static and dynamic experiments of naproxen adsorption by polyethersulfone filter membrane were further carried out. The results of the static adsorption test showed that the polyethersulfone filter membrane could adsorb naproxen only under acidic conditions. The adsorption performance was the most significant in the initial stage of the experiment, and the adsorption equilibrium can be reached after 7 hours. In the dynamic adsorption test, the removal efficiency of naproxen by the polyethersulfone filter membrane was

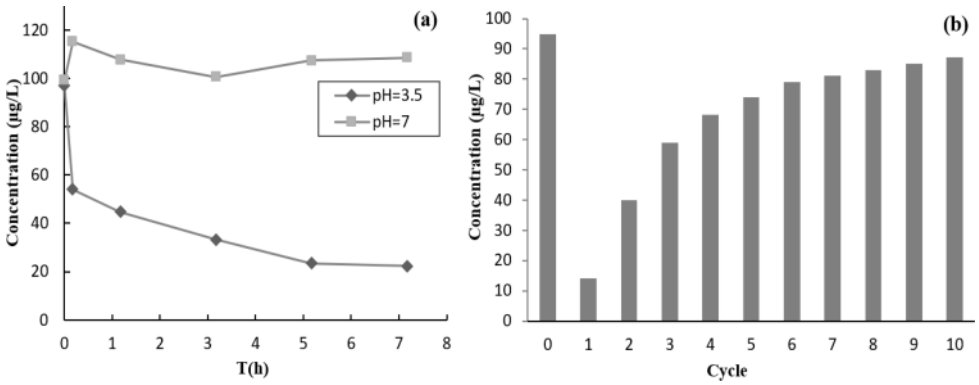

Figure 2. Concentration changes of naproxen in static (a) and dynamic (b) experiments of the adsorption of naproxen by the polyethersulfone filter membrane.

as high as 85.3% for the first filtration of the naproxen aqueous solution. After ten times of filtration, the polyethersulfone filter membrane is saturated and no longer has the adsorption capacity for naproxen. The preliminary experimental results of our research group show that acidic conditions are conducive to the adsorption of naproxen by the polyethersulfone filter membrane. The adsorption principle needs to be analyzed through further experiments.

4 CONCLUSION

Naproxen has entered the environment through a variety of ways from its development, production, and use. In recent years, new trace pollutants have attracted the attention of researchers and society around the world, and research work on naproxen has also been carried out. Naproxen has been detected in various water environments, and its concentration ranges from ng/L to μg/L. Due to the superposition effect of the biological toxicity of its parent body, degradation products, and metabolites in the environment, naproxen brings risks to aquatic organisms and human health. Physical, chemical, and biological removal technologies have been extensively developed to reduce and control naproxen in water environments. PH affects the removal of naproxen by microorganisms by affecting the life activities of microorganisms and changing the existing form of naproxen. Chemical technology mainly affects the removal efficiency by controlling the concentration of active oxidizing substances in the solution. In physical technology, the mechanism of pH influence mainly relies on electrostatic interaction.

ACKNOWLEDGMENTS

This research was financed by the Ordinary Universities Characteristic Innovation Program of Guangdong Province in China (No. 2019GKTSCX061).

REFERENCES

Asmar R E, Baalbaki A, Khalil Z A, Naim S, Bejjani A, Ghauch A. (2021). Iron-based Metal-Organic Framework Mil-88-a for the Degradation of Naproxen in Water Through Persulfate Activation [J]. Chemical Engineering Journal. 405: 126701.

Bai R, Xiao Y, Yan W, Wang S, Ding R, Yang F, Li J, Lu X, Zhao F. (2020). Rapid and Efficient Removal of Naproxen from Water by $CuFe_2O_4$ with Peroxymonosulfate [J]. Journal of Hazardous Materials. 383: 21542–21551.

Baigent C, Bhala N, Emberson J, Merhi A, (2013). Vascular and Upper Gastrointestinal Effects of Non-steroidal Anti-inflammatory Drugs: Meta-analyses of Individual Participant Data from Randomised Trials [J]. The Lancet. 382(9894): 769–779.

Benotti M. J., Trenholm R. A., Vanderford B. J., Holady J. C., Stanford B. D., Snyder S. A. (2009). Pharmaceuticals and Endocrine Disrupting Compounds in U.S. Drinking Water. Environ. Sci. Technol. 43:597–603.

Dong S, Zhai X, Pi R, Wei J, Wang Y, Sun X. (2020). Efficient Degradation of Naproxen by Persulfate Activated with Zero-valent Iron: Performance, Kinetic and Degradation Pathways. Water Science & Technology. 81(10): 2078–2091.

Dzionek1 A, Wojcieszyńska D, Adamczyk-Habrajska M, Guzik U. (2020). Enhanced Degradation of Naproxen by Immobilization of Bacillus Thuringiensis B1 (2015b) on Loofah Sponge. Molecules. 25: 872.

Guan Y, Ma J, Li X, Fang J, Chen L. (2011). Influence of pH on the Formation of Sulfate and Hydroxyl Radicals in the UV/Peroxymonosulfate System [J]. Environmental Science & Technology. 45(21): 9308–9314.

Ingole P M. & Rathod V K. (2020). Naproxen Removal from Wastewater by Enzymatic Degradation using Laccase [J]. Catalysis in Green Chemistry and Engineering. 3(1): 45–56.

Joss A, Keller E, Alder A. C., Gobel A, McArdell C. S., Ternes T, Siegrist H. (2005). Removal of Pharmaceuticals and Fragrances in Biological Wastewater Treatment [J]. Water Research. 39(14): 3139–3152.

Karami A, Sabouni R, Ghommem M. (2020). Experimental Investigation of Competitive Co-adsorption of Naproxen and Diclofenac from Water by an Aluminum-based Metal-organic Framework [J]. Journal of Molecular Liquids, 305: 112808.

Kurczewska J, Cegłowski M, Schroeder G. (2020). Pamam-halloysite Dunino Hybrid as an Effective Adsorbent of Ibuprofen and Naproxen from Aqueous Solutions [J]. Applied Clay Science. 190: 105603.

Ma D, Liu G, Lv W, Yao K, Zhang X, Xiao H. (2014). Photodegradation of Naproxen in Water under Simulated Solar Radiation: Mechanism, Kinetics and Toxicity Variation. Environ. Sci. Pollut. Res. Int. 21:7797–7804.

Meloza B, León-Santiesteban H H, López-Medina R, Tomasini A. (2020). Naproxen Sorption by Non-viable Rhizopus Oryzae Biomass [J]. Environmental Science and Pollution Research. 27(2): 1–13.

Ozcan N, Saloglu D. (2020). Activated Carbon Embedded Alginate Beads for Removing Nonsteroidal Anti-inflammatory Drug Naproxen from Wastewater: Equilibrium, Kinetics, Thermodynamics, Desorption, and Reusability [J]. Water Science and Technology: a Journal of the International Association on Water Pollution Research. 81(7): 1432–1444.

Tang Y, Li X, Xu Z, Guo Q, Hong C, Bing Y. (2014). Removal of Naproxen and Bezafibrate by Activated Sludge under Aerobic Conditions: Kinetics and Effect of Substrates. Biotechnology and Applied Biochemistry. 61(3): 333–410.

Teijon G, Candela L, Tamoh K, Molina A, Ferná A. R. (2010). Occurrence of Emerging Contaminants, Priority Substances (2008/105/CE) and Heavy Metals in Treated Wastewater and Groundwater at Depurbaix Facility (Barcelona, Spain). Science of The Total Environment. 408 (17): 3584–3595.

Wang L, Ying G, Zhao J, Yang X, Chen F, Tao R, Liu S, Zhou L. (2010). Occurrence and Risk Assessment of Acidic Pharmaceuticals in the Yellow River, Hai River and Liao River of North China. Science of The Total Environment. 408(16): 3139–3147.

Wang S, Wu J, Lu X, Xu W, Gong Q, Ding J, Dan B, Xie P. (2018). Removal of Acetaminophen in the Fe^{2+}/Persulfatesystem: Kinetic Model and Degradation Pathways. Chemical Engineering Journal. 358: 1091–1100.

Wu X, Gu X, Lu S, Xu M, Zang X, Miao Z, Qiu Z, Sui Q. (2011). Degradation of Trichloroethylene in Aqueous Solution by Persulfate Activated with Citric Acid Chelated Ferrous Ion [J]. Chemical Engineering Journal. 255: 585–592.

Yang B, Ying G, Zhao J, Liu S, Zhou L, Chen F. (2012). Removal of Selected Endocrine Disrupting Chemicals (EDCs) and Pharmaceuticals and Personal Care Products (PPCPs) during Ferrate (VI) Treatment of Secondary Wastewater Effluents [J]. Water Research. 46(7): 2194–2204.

Advances in Applied Chemistry and Industrial Catalysis – Saikia (Ed.)

Evaluation of biodiesel carbon soot particles as lubricant additives in soybean oil

Hongzhi Luo[1], Chuan Li[1]*, Zhilin Fang, Lei Cheng, Xiaoju Chen, Xuanxuan Wang, Qiaoen He, Jiale Fu, Qiuting Zhao, Qing Qiao & Xue Liang
School of Chemistry and Material Engineering, Hefei, Anhui, P.R. China

ABSTRACT: Tribological properties of biodiesel carbon soot particles (BCSPs) as soybean oil additives were examined utilizing a ball-on-disk reciprocating tribometer. The findings revealed that by adding BCSPs to soybean oil, the lubrication performance can be significantly enhanced. The 0.025 wt% BCSPs simultaneously reduce the friction and wear by 29.0% and 25.4%, respectively, at 10 N for 30 min. The formation of carbon tribofilm containing BCSPs and the rolling bearing effect dominates the lubrication mechanism of soybean oil with BCSPs.

1 INTRODUCTION

The concerns of environmental pollution and ecological damage produced by conventional petroleum-based lubricants have attracted more and more attention as people's knowledge of environmental protection grows and countries around the world pay more attention to the ecological environment (Alves et al. 2013; Syahir 2017). The development of green lubricating oil that meets environmental protection requirements is a pressing issue in today's society. Vegetable oil has received a lot of attention as a potential replacement for conventional petroleum-based lubricants because of its low cost, wide availability, renewable nature, nontoxicity, and biodegradability (Almasi et al. 2021).

Solid lubrication materials have excellent lubrication and reduction wear performance. One of the most effective methods to reduce friction and wear under boundary lubrication is to add solid lubrication substances to lubricating oil (Meng et al. 2015; Singh et al. 2020). Carbon-based lubricating materials are a common solid lubricant that has been widely employed in the lubrication of vegetable oil. Zhang et al. analyzed the tribological performance of vegetable oil utilizing chemically modified graphene additives and observed that graphene nanoparticles greatly improved the tribocapability of the oil (Zhang et al. 2018). Wang et al. investigated the properties of rapeseed oil containing carbon nanotubes and carbon nanotubes decorated with uniform copper nanoparticles and stated that the two kinds of nanoparticles with 0.2% weight fraction remarkably improve the friction reduction and antiwear performance of the oil (Wang et al. 2018). Several studies revealed that low content of soot used as lubricant additives featured good tribological properties in the water, liquid paraffin, and PAO4 oil respectively (Guo et al. 2015; Li et al. 2019). However, the application of soot in vegetable oil is rarely reported. As a result, the current research is devoted to examining the tribological performances of soybean oil with biodiesel carbon soot particles (BCSPs) added under a ball-on-disk reciprocating friction state.

*Corresponding Author: 053039@chu.edu.cn
[1]These authors contributed equally to the work.

DOI 10.1201/9781003308553-6

2 EXPERIMENT

2.1 *Materials*

Soybean oil was procured from China Oil & Food Stuffs Corporation. The BCSPs employed in this research were collected utilizing a self-made soot trap (Li et al. 2019). Boride high molecular weight polyisobutylene succinimide, obtained from Guangzhou Hedao Chemical Co., Ltd, was utilized as a dispersant to solve the agglomeration of soot in soybean oil. The following is the procedure for the preparation of soybean oil with various BCSPs' contents: first, boride high molecular weight polyisobutylene succinimide was added into soybean oil and the prepared oil samples were stirred magnetically for 1 h. Second, BCSPs were dispersed in the soybean oil containing 2 wt% dispersants with 1 h of magnetic stirring, followed by 30 min of ultrasonic oscillation. The dispersant component in soybean oil was 2% by weight. The BCSPs content in soybean oil containing 2 wt% dispersant included 0.0125, 0.025, 0.05, 0.1, 0.2, and 0.4 wt%.

2.2 *Characterization and triological tests*

A ball-on-disk reciprocating tribometer was used in conducting the tribotest (CFT, ZKKH, China). Figure 1 depicts a schematic of tribotests. In the tribotests, the friction pair was chosen to be the GCr15 steel ball and the 304 austenitic stainless steel disk. The morphology of BCSPs was measured with field-emission transmission electron microscopy (FETEM, JEM-2100F, JEOL). On the tribometer, the friction coefficient of the testing process was automatically recorded. Three-dimensional laser scanning microscopy (VK-X100, Keyence) was used to evaluate the optical micrographs, worn surface profiles, and wear area of the disk scars. The chemical compositions of the worn scars were probed by micro-Raman spectroscopy (DXR2, ThermoFisher).

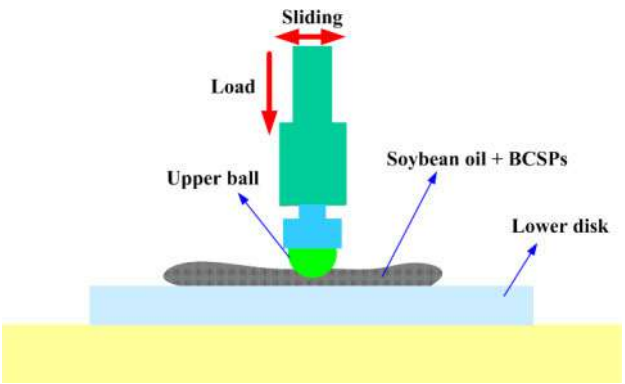

Figure 1. Schematic of tribo-tests.

3 RESULTS AND DISCUSSION

3.1 *Characterization of biodiesel carbon soot particles*

Soot is a small size carbonaceous material (Hu et al. 2013). Figure 2 illustrates the FETEM image of BCSPs. The BCSPs aggregate together to create chain-like structure agglomerates and their sizes were 30-40 nm as shown in Figure 2(a). Figure 2(b) demonstrates that the internal structure of BCSPs has a graphite-like structure, while also possessing an amorphous phase. Moreover, BCSPs have a spherical shape. Thus, BCSPs have the potential to be a solid lubricant in line with the rolling bearing lubrication mechanism.

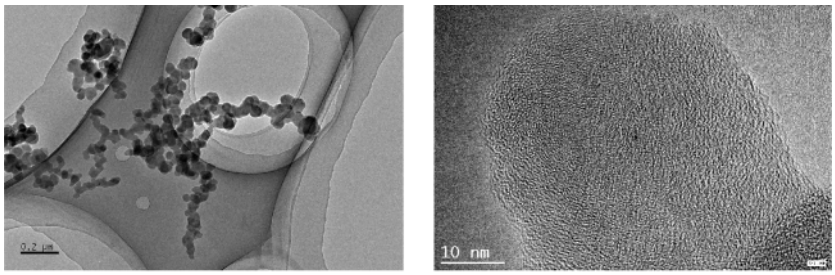

Figure 2. FETEM image of BCSPs.

3.2 *Tribological properties*

Figure 3 displays the impact of BCSPs' contents on average friction coefficient and wear volume under a load of 10 N with a reciprocating speed of 50 mm/s over 30 min. The average friction coefficient dropped with increasing BCSPs' concentration of up to 0.025 wt% and then increased and stabilized afterward, as shown in Figure 3(a). The alteration in the average friction coefficient (in Figure 3(b)) is similar with the fluctuation in the trend of wear volume. The average friction coefficients and wear volume are 0.218 and 4.16×10^7 μm^3, respectively, when BCSPs are added at 0.025 wt%, which are a reduction of 29.0% and 25.4%, respectively, when compared to the soybean oil. Hence, the suitability of BCSPs' content in soybean oil is 0.025 wt% under the chosen test conditions. This reveals that soybean oil with the right amount of BCSPs exhibited good performance in friction reduction and antiwear.

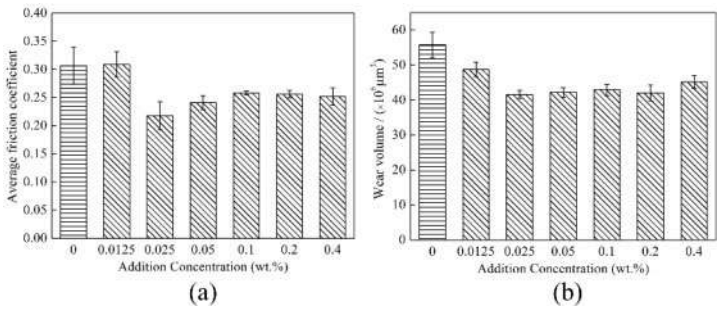

Figure 3. Effect of content of BCSPs on (a) average friction coefficient and (b) wear volume (load: 10 N; reciprocating speed: 50 mm/s; testing time: 30 min).

Figure 4 shows variations of average friction coefficient and wear volume under the different loads under the BCSPs content of 0.025 wt% with a reciprocating speed of 50 mm/s over 30 min. Figure 4 indicates that when BCSPs are added to soybean oil, the average friction coefficient and wear volume reduces at 10, 20, 30, and 40 N. Soybean oil has a rather high friction coefficient with an average value of 0.184 with a load of 40 N. When adding BCSPs at 0.025 wt%, the average friction coefficient is 0.165, which is a reduction of 10.3% compared with the soybean oil. Furthermore, under a load of 40 N, the wear volume of soybean oil with BCSPs was decreased by 24.5% (from 2.78×10^8 μm^3 of soybean oil to 2.10×10^8 μm^3 of soybean oil with BCSPs). Thus, when compared with the soybean oil, soybean oil containing BCSPs offered improved antifriction and antiwear characteristics at different loads.

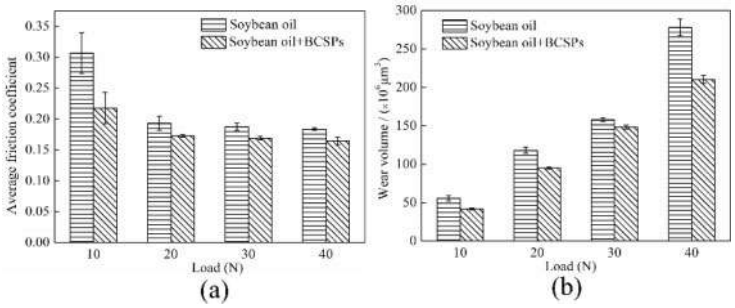

Figure 4. Variations of (a) average friction coefficient and (b) wear volume under the different loads (BCSPs content: 0.025 wt%; reciprocating speed: 50 mm/s; testing time: 30 min).

Figure 5 shows variations of average friction coefficient and wear volume under the different reciprocating speeds under a load of 10 N with a BCSPs' content of 0.025 wt% over 30 min. When comparing soybean oil containing BCSPs to soybean oil alone, the average friction coefficient and wear volume were reduced. Hence, we can conclude that BCSPs are effective in enhancing the tribological performance of soybean oil.

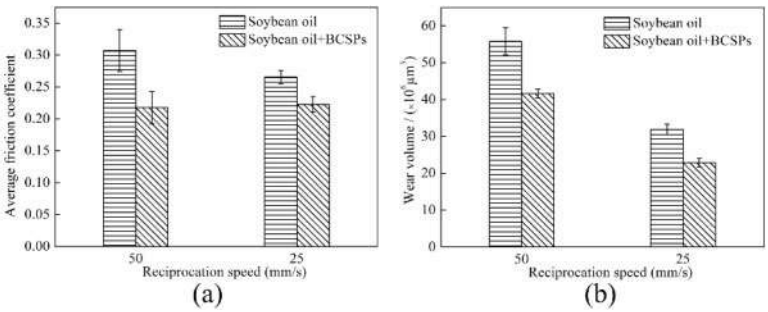

Figure 5. Variations of (a) average friction coefficient and (b) wear volume under the different reciprocating speeds (load: 10 N; BCSPs content: 0.025 wt%; testing time: 30 min).

3.3 *Tribological mechanism*

Figure 6 shows the optical micrographs and worn surface profiles of disks lubricated with various oil samples under a load of 10 N with a reciprocating speed of 50 mm/s over 30 min. Wear scars lubricated with soybean oil seemed to be wider and deeper than those lubricated with soybean oil containing 0.025 wt% BCSPs. For soybean oil, the wear area was 10946.35 μm^2. When compared to soybean oil, the wear area lubricated with soybean oil containing 0.025 wt% BCSPs (8550.39 μm^2) was notably reduced. The results were in line with the previous wear volume findings. The above results also prove that BCSPs enhanced the lubrication capacity of soybean oil.

Figure 7 presents Raman mapping of the worn scars on the disks lubricated with diverse oil samples. When BCSPs were introduced to the soybean oil, the Raman signals of D peak and G peak of worn scars were considerably improved and the distribution area was enlarged, according to Raman maps and spectra on the disk scars. This is due to the formation of more carbon tribofilm forming on the worn surface during friction, which protects the contact surfaces of friction pairs. The corresponding tribological mechanisms are presented below, based on the aforementioned characteristics and analysis. Soybean oil with BCSPs contains spherical particles that have rolling impacts on rubbing surfaces and are better at improving lubrication performance than soybean

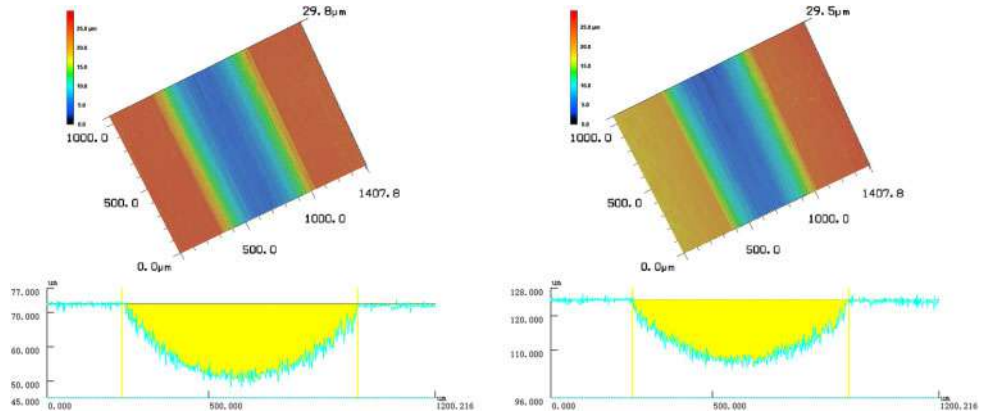

Figure 6. The optical micrographs and worn surface profiles of disks scars lubricated with different oil samples at 10 N and 50 mm/s for 30 min. (a) Soybean oil; (b) soybean oil containing 0.025 wt% BCSPs.

without BCSPs (Zhao et al. 2021). Furthermore, BCSPs could be absorbed on the worn surface during the friction process and participate in the tribofilm. The tribofilm played a crucial role in minimizing friction and preventing wear.

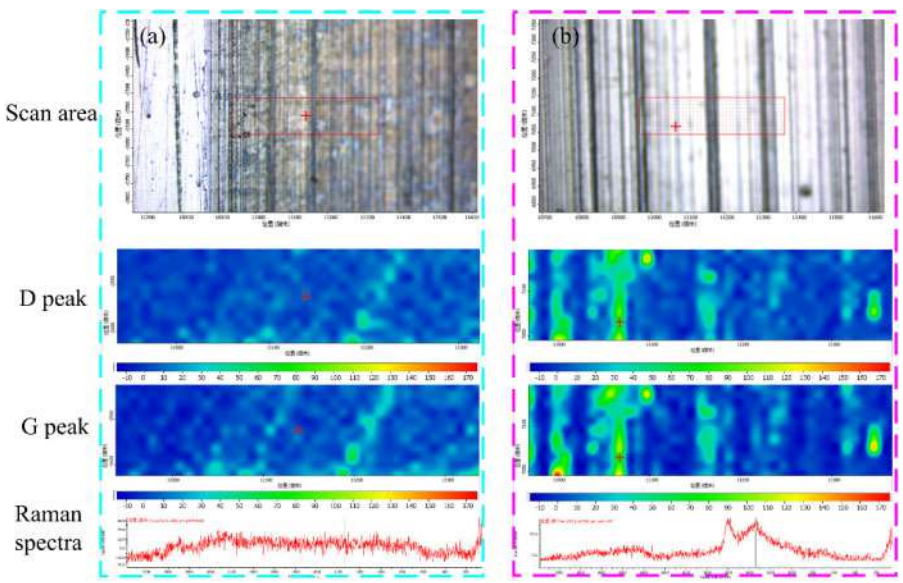

Figure 7. Raman mapping of the worn scars on the disks lubricated by (a) soybean oil; (b) soybean oil containing 0.025 wt% BCSPs.

4 CONCLUSIONS

The impact of BCSPs as soybean oil additives on reducing friction and wear was examined. In contrast to soybean oil, the soybean oil containing BCSPs demonstrated better friction-reducing and antiwear properties. Under a load of 10 N, the BCSPs have the optimum anti-friction and

anti-wear effect at the content of 0.025 wt%, with a friction coefficient reduction of 29.0% and wear volume of 25.4%, respectively. The superior lubricating performance of soybean oil containing BCSPs is directly connected to the more carbon tribofilm that was produced on the friction surface and BCSPs acted as rolling bearing during the friction process.

ACKNOWLEDGMENTS

This work was supported by Discipline Construction Quality Improvement Project of Chaohu University (kj20fdzy01, kj20bskc01, kj21kctd03), the Doctor Start-up Foundation of Chaohu University (KYQD-202001), National College Students' Innovation and Entrepreneurship Training Program of China (202010380012), Teaching Research Project of Chaohu University (ch19jxyj03) and School-level Scientific Research Project of Chaohu University (XLY-202112).

REFERENCES

Almasi, S., Ghobadian, B., Najafi, G., and Soufi, M. D. (2021) A review on bio-lubricant production from non-edible oil-bearing biomass resources in Iran: recent progress and perspectives. J. Clean. Prod., 290: 125830.

Alves, S. M., Barros, B. S., Trajano, M. F., Ribeiro, K. S. B., and Moura, E. J. T. I. (2013) Tribological behavior of vegetable oil-based lubricants with nanoparticles of oxides in boundary lubrication conditions. Tribol. Int., 65: 28–36.

Guo, M. F., Cai, Z. B., Zhang, Z. C., and Zhu, M. H. (2015). Characterization and lubrication performance of diesel soot nanoparticles as oil lubricant additives. RSC Adv., 5: 101965–101974.

Hu, E. Z., Hu, X. G., Liu, T. X., Liu, Y. M., Song, R. H., and Chen, Y. Z. (2013). Investigation of morphology, structure and composition of biomass-oil soot particles. Appl. Surf. Sci., 270: 596–603.

Li, C., Li, M. L., Wang, X. Y., Feng, W. M., Zhang, Q. Q., Wu, B., and Hu, X. G. (2019). Novel carbon nanoparticles derived from biodiesel soot as lubricant additives. Nanomat., 9(8): 1115.

Meng, Y., Su, F. H., and Chen, Y. Z. (2015). A novel nanomaterial of graphene oxide dotted with Ni nanoparticles produced by supercritical CO_2-assisted deposition for reducing friction and wear. ACS Appl. Mater. Interfaces, 7(21), 11604–11612.

Singh, Y., Sharma, A., Singh, N. K., and Chen, W. H. (2020) Development of bio-based lubricant from modified desert date oil (balanites aegyptiaca) with copper nanoparticles addition and their tribological analysis. Fuel, 259: 116259.

Wang, Z., Ren, R., Song, H., and Jia, X. (2018). Improved tribological properties of the synthesized copper/carbon nanotube nanocomposites for rapeseed oil-based additives. Appl. Surf. Sci., 428: 630–639.

Zhang, G., Xu, Y., Xiang, X. Z., Zheng, G. L., Zeng, X. Q., Li, Z. P., Ren T. H., and Zhang, Y. D. (2018). Tribological performances of highly dispersed graphene oxide derivatives in vegetable oil. Tribol. Int., 126: 39–48.

Zhao, J., Huang, Y. Y., He, Y. Y., and Shi, Y. (2021). Nanolubricant additives: A review. Frict., 9(5): 891–917.

Advances in Applied Chemistry and Industrial Catalysis – Saikia (Ed.)

A compound bactericide for industrial circulating water

Yushan Cheng, Runchao Sun*, Jinying Wu & Changshan Huang
Energy research institute Co. Ltd., Henan academy of sciences, Zhengzhou, Henan, China

ABSTRACT: In this paper, the bactericidal properties of three kinds of monomers of oxidizing bactericide NaClO and non-oxidizing bactericide geramine and isothiazolinones were studied. By means of compounding the oxidizing and non oxidizing bactericide monomers with different sterilization mechanisms, the mixture of 10 mg/L isothiazolinones and 1 mg/L NaClO was finally screened out. The circulating water bactericide formula has the characteristics of significant efficiency, stability and durability. The bactericidal performance of the compound bactericide was evaluated from three aspects: dosage, pH application range and environmental temperature. The results showed that the compound bactericide had the advantages of small dosage, wide application range and suitable for different temperatures, which met the requirements of industrial circulating water.

1 INTRODUCTION

Chlorine is a commonly used monomer bactericide at home and abroad, but the by-products of chlorine will cause serious damage to human beings and the environment, and its application will be more and more limited (Zhang et al. 2014). With the deepening of research, more and more oxidizing and non oxidizing fungicides have been applied and promoted, such as NaClO, geramine, isothiazolinone and other monomers have been applied in industrial circulating water (Jia 2006; Ma & Tang; 2016; Zhao 2013). However, these bactericide monomers can't meet the normal requirements of industrial circulating water design within the range of commonly used dosage. Moreover, the long-term use of the same bactericide will make the bacteria resistant, resulting in the increase of the number of bacteria in the water, the deterioration of water quality, the accumulation of slime, and the corrosion caused by microorganisms (Huang et al. 2018; Qiang & Zhang 2003; Sun et al. 2016; Wang et al. 2015). In order to give full play to the best performance of each monomer, it is necessary to carry out the experimental research on the compounding of bactericide monomers to obtain the compound formula with synergistic effect, which will not cause waste, but also meet the design specifications of industrial circulating water, and has become one of the important topics of today's research.

2 EXPERIMENTAL SECTION

2.1 *Test instruments and reagents*

Super clean worktable was purchased from Suzhou purification equipment Co. Ltd.; High-pressure steam sterilization pot was supplied by Zhejiang Xinfeng Medical Equipment Co. Ltd.

*Corresponding Author: hnsnys163@163.cm

DOI 10.1201/9781003308553-7

2.2 *Bactericide*

Oxidizing bactericide: NaClO, mass fraction 12%; Non oxidizing fungicides: isothiazolinone, mass fraction 14%; geramine, mass fraction 45%. They were all purchased from Henan Qingshuiyuan factory. Compound bactericide: the oxidizing bactericide and non oxidizing bactericide were compounded according to different volumes.

2.3 *Experimental methods*

The water sample used was the cooling water of central air conditioning system provided by a hotel in Zhengzhou, and the supplementary water was tap water. The water quality was shown in Table 1.

Table 1. Quality of supplementary water and cooling water.

Test index	Supplementary water	Cooling water
pH	7.04	8.99
Total hardness (mmol/L)	2.71	6.61
Ca^{2+} (mg/L)	64.57	100.70
Cl (mg/L)	18.10	281.34
Total alkalinity (mg/L)	216.20	270.25
Conductivity (us/cm)	809.60	1733.00
Heterotrophic bacteria (cfu/mL)		1.00×10^6
Phenolphthalein alkalinity	nothing	exist

Firstly, the experimental articles were thoroughly sterilized, and then the prepared bactericide solution was added into the sterilized triangular flask containing 200 mL cooling water according to the mass concentration of 100 mg/L. Then, the triangular flask was put into the 29° incubator, and samples were taken at 0 h, 24 h, 72 h and 168 h, respectively. The samples were cultured in the 29° incubator for 72 h, and the average number of colonies was taken. The bactericidal rate was calculated by the change of the number of bacteria in the water sample before and after sterilization (Sun et al. 2012).

3 RESULTS AND DISCUSSION

3.1 *Evaluation on germicidal efficacy of single fungicide*

Aiming at the three monomers of oxidizing bactericide NaClO, non oxidizing bactericide geramine and isothiazolinone, the bactericidal test was carried out by using GB/T 22595-2008 “evaluation method for energy efficiency of biocides heterotrophic bacteria”, and their germicidal efficacy was compared and analyzed (GB/T 22595-2008).

3.1.1 *Germicidal efficacy of NaClO.*

The plate counting results of NaClO monomer fungicide were shown in Table 2.

Table 2. Germicidal efficacy of fungicides with different NaClO dosage.

Test time	mg/L	1.0 mg/L	2.5 mg/L	5.0 mg/L
0h	1.1×10^6	1.1×10^6	1.1×10^6	1.1×10^6
24h	2.3×10^7	3.3×10^5	2.1×10^4	2.5×10^2
72h	1.5×10^7	5.2×10^5	9.1×10^4	9.1×10^4
168h	1.2×10^8	7.4×10^7	2.8×10^5	1.2×10^5

It can be seen from Table 2 that within a certain time range, the number of heterotrophic bacteria in water samples increased with the increase of time. It is because bacteria and algae were rapidly reproducing. When the bactericidal effect of the bactericide was less than or equal to 1.0 mg/L, the bactericidal effect was not ideal, and the duration of the efficacy was short. When the concentration of NaClO was more than 2.5 mg/L, the bactericidal effect increased significantly, at the same time, the bacterial concentration decreased by three orders of magnitude.

Colony characteristics: after the plate test, it is found that there are two obvious colonies in CBD water, one is snowflake like colony, the other is round colony. It can be seen from Figure 1 that there are two obvious bacterial colonies in CBD water. After NaClO treatment, there are still two kinds of colonies on the plate.

Figure 1. Heterotrophic flora.

3.1.2 *Germicidal efficacy of geramine.*
The plate counting results of geramine monomer fungicide were shown in Table 3.

Table 3. Germicidal efficacy of fungicides with different geramine dosage.

Test time	mg/L	10 mg/L	50 mg/L
0h	1.1×10^6	1.1×10^6	1.1×10^6
24h	2.3×10^7	2.1×10^6	2.0×10^2
72h	1.5×10^7	2.1×10^6	1.0×10^5
168h	1.2×10^8	1.6×10^6	4.6×10^5

It can be seen from Table 3 that the bactericidal effect of geramine was not very obvious at the dosage of 10 mg/L. When the dosage reached 50 mg/L, the sterilization rate reached 100% in 24 h. However, After 72 h, the number of heterotrophic bacteria in the water became 10^5 cfu/ mL, which exceeded the requirements of industrial circulating water design specifications and would cause serious corrosion to the pipeline (GB/T 50050-2017).

Colony characteristics: two kinds of colonies were still observed on the plate after killing by geramine.

3.1.3 *Germicidal efficacy of isothiazolinone*

The plate counting results of isothiazolinone monomer fungicide were shown in Table 4.

Table 4. Germicidal efficacy of fungicides with different isothiazolinone dosage.

Test time	mg/L	5 mg/L	10 mg/L
0h	1.1×10^6	1.1×10^6	1.1×10^6
24h	2.3×10^7	3.3×10^4	2.1×10^2
72h	1.5×10^7	7.2×10^5	92×10^4
168h	1.2×10^8	8.4×10^6	1.4×10^5

It can be seen from Table 4 that when the dosage of isothiazolinone was 5 mg/mL, it could not meet the requirements of industrial circulating water design specification. When the dosage reached 10 mg/mL, it could meet the requirements of industrial circulating water design specification within 168h (one week). The reason that the germicidal efficacy first increases and then decreases may be that with the increase of time, the properties of isothiazolinone are consumed, and the remaining concentration of the drug gradually decreases. At the same time, heterotrophic bacteria are also splitting and reproducing. With the increase of time, heterotrophic bacteria splitting and reproducing are dominant, making the bacterial concentration increase.

Colony characteristics: after the killing effect of isothiazolinone, only round colonies were observed on the plate.

3.1.4 *Evaluation on germicidal efficacy of single fungicide*

When NaClO is added at 1mg/L, its germicidal efficacy and lasting efficacy are poor. When NaClO $\geq$ 2.5mg/L, its germicidal efficacy increased obviously, its bacterial concentration decreased by three orders of magnitude, and its efficacy duration increased. When the addition amount of geramine is 50mg/mL, the sterilization rate is almost 100% in 24h, but the efficacy continues to be low. However, when the time lasts for 72h, the number of heterotrophic bacteria in water becomes 105cfu/mL, which exceeds the requirements of industrial circulating water design specifications; Isothiazolinone has good germicidal efficacy, quick action and high germicidal rate. When the dosage of isothiazolinone is 10mg/mL, it can be reduced by four orders of magnitude within 24h, and it can meet the requirements of industrial circulating water design code within 168h hours (one week). Therefore, it is an important direction of experimental research to compound monomer fungicides and exert their synergistic effect to meet the requirements of industrial circulating water design specifications.

3.2 *Analysis of compound effect of two monomer fungicides*

3.2.1 *Combination of NaClO and geramine with fungicide*

The count results of microbicide plate mixed with NaClO and geramine were shown in Table 5.

Table 5. Germicidal efficacy of the mixture of geramine and NaClO.

Number	Geramine (mg/L)	NaClO (mg/L)	0h	24h	72h	168h
Blank	0	0	1.1×10^6	2.3×10^7	1.5×10^7	1.2×10^8
1#	10	5	1.1×10^6	42×10^4	3.0×10^6	46×10
2#	33	1	1.1×10^6	1.0×10^2	1.0×10^5	4.0×10
3#	33	5	1.1×10^6	1.0×10^1	64×10^4	29×10

The germicidal efficacy did not change significantly and showed no synergistic effect after the combination of geramine and NaClO.

Colony characteristics: the existence of two bacteria genera can still be observed after the action of the compound bactericide of NaClO and geramine.

3.2.2 *Combination of NaClO and isothiazolinone with fungicide*

The count results of microbicide plate mixed with NaClO and isothiazolinone were shown in Table 6.

Table 6. Germicidal efficacy of the mixture of isothiazolinone and NaClO.

Number	Isothiazolinone (mg/L)	NaClO (mg/L)	0h	24h	72h	168h
Blank	0	0	1.1×10^6	2.3×10^7	1.5×10^7	1.2×10^8
1#	10	1	1.1×10^6	0	0	0
2#	10	0.5	1.1×10^6	1.9×10^3	2.6×10^2	1.0×10^5
3#	5	1	1.1×10^6	9.6×10^2	7.1×10^5	1.2×10^6
4#	5	0.5	1.1×10^6	1.5×10^3	8.1×10^5	2.5×10^6

It can be seen from Table 6 that when the addition ratio of isothiazolinone is fixed at 10 mg/L, the germicidal efficacy increases with the increase of NaClO addition. The optimum ratio is isothiazolinone 10 mg/L and NaClO 1 mg/L. The bactericide has high bactericidal effect and obvious synergistic effect.

Colony characteristics: only round bacteria were observed on the plate, which indicated that isothiazolinone and NaClO had a good inhibitory effect on the bacteria with snowflake colony characteristics.

3.2.3 *Selection of composite fungicide*

The bactericidal effect of geramine combined with NaClO was not obvious and showed no synergistic effect, and the two kinds of bacteria still existed after bactericidal effect.When the mixture of isothiazolinone and NaClO was 10 mg/L and 1mg/L respectively, the bactericidal effect was very good, and the bactericidal effect was significantly higher than that when the mixture was added with the same isothiazolinone and NaClO alone, showing a synergistic effect, and only a round genus was observed after the bactericidal effect, indicating that it had a better inhibitory effect on the snowflake like genus. Therefore, the mixture of isothiazolinone and NaClO at the ratio of 10 mg/L and 1 mg/L was selected as the fungicide formulation for optimization.

3.3 *Effect evaluation of compound bactericide*

3.3.1 *Effect of compound bactericide addition on germicidal efficacy*

The germicidal efficacy of fungicide was evaluated under different dosage, and the results are shown in Table 7.

Table 7. The bactericidal effect of compound bactericide under different dosage.

Dosage (mg/L)	0h	24h	72h	168h	Sterilization rate (168h)
0	1.01×10^6	2.8×10^7	2.2×10^7	6.2×10^6	
50	1.01×10^6	20	1.5×10^3	5.1×10^4	91.8(%)
75	1.01×10^6	20	10	10	99.9(%)
100	1.01×10^6	0	0	0	100(%)

It can be concluded from Table 7 that when the dosage of compound bactericide and algaecide changes from 0 to 100 mg/L, there is little difference in the effect within 24 h, but with the extension of time, when the dosage of compound bactericide is 50 mg/L, the bactericidal effect begins to get better, and the bacterial concentration is controlled below 10^5cfu/mL. When the amount of compound bactericide was 75 mg/L, the bactericidal effect could last 168h, and after 168h (7D), the bactericidal rate still maintained 99.9%. When the amount of compound bactericide was 100 mg/L, the bactericide still had high bactericidal effect after 168 h.

When the dosage of bactericide was 75∼100 mg/L in 7D, the heterotrophic bacteria in cooling water could be controlled in the range of 10^5 cfu/mL, which meets the industrial design specifications.

3.3.2 *Evaluation of germicidal efficacy of compound fungicides under different pH conditions*

The bactericidal effect of NaClO in water mainly comes from its hydrolysis to HClO in water, and the degree of hydrolysis is greatly affected by the pH of water body. The pH of water body is different in different environmental occasions, some are acidic and some are alkaline. Therefore, the bactericidal effect of composite bactericide in different pH conditions was investigated.

The experimental parameters were as follows: when the dosage of bactericide was 100 mg/L, the sample was taken at different time points, and the dilution method and coating plate method were the same as before.

Table 8. The bactericidal effects of compound fungicides at different pH.

pH	0h	24h	72h	168h
3.05	5.65×10^7	2.85×10^2	4.60×10^3	6.01×10^3
4.10	5.65×10^7	5.65×10^3	1.90×10^4	8.05×10^3
5.03	5.65×10^7	2.76×10^3	2.00×10^3	3.20×10^3
6.20	6.80×10^6	1.58×10^3	3.00×10^4	2.02×10^4
7.02	6.80×10^6	4.52×10^3	7.21×10^3	1.52×10^4
7.97	6.80×10^6	1.67×10^3	2.13×10^3	—
8.90	2.1×10^5	0	0	0

The results showed that the compound bactericide had high germicidal efficacy when pH was in the range of 3-9, and the concentration of heterotrophic bacteria could be controlled within 10^5 cfu/mL within 168 h.

3.3.3 *Germicidal efficacy of compound fungicides at different seasonal temperatures*

Due to the great influence of temperature on the propagation of heterotrophic bacteria, the actual application effect under different seasonal conditions was investigated. The results of heterotrophic bacteria in the central air conditioning cooling water system of international hotels under different seasonal temperatures are shown in Table 9.

Table 9. The bactericidal effect under different ambient temperature.

Date	August (cfu/mL)	Temperature (°C)	October (cfu/mL)	Temperature (°C)
2D	1530	33.4	1260	23.1
5D	4000	35.0	2200	25.2
7D	10000	35.2	4180	23.6

It can be seen from Table 9 that when the ambient temperature is high (about 33°C), the heterotrophic bacteria propagate rapidly, and the concentration of heterotrophic bacteria increases rapidly after adding bactericide for 7D. When the ambient temperature is low (about 23°C), the heterotrophic bacteria propagate slowly, and the number of heterotrophic bacteria is still low after adding bactericide for 7D. However, in any case, the concentration of heterotrophic bacteria in the system can be well controlled below 10^5 cfu/mL.

4 CONCLUSIONS

(1) When the ratio of isothiazolinone and NaClO was 10:1, the bactericidal effect was significant and had synergistic performance. The killing rate was 100% between 24 h and 168 h, and it had a good inhibitory effect on the genus with snowflake like colony characteristics.
(2) When the amount of compound bactericide was 75-100 mg/L, the bactericidal rate remained above 99.9% within 7D, and the heterotrophic bacteria in the cooling water was always controlled within the range of 10^5 cfu/mL.
(3) The bactericide is suitable for circulating water with different pH and temperature, and has the advantages of high bactericidal efficiency, long action time and wide application range.

ACKNOWLEDGEMENTS

This work was supported by the Special project for scientific research and development of Henan Academy of Sciences (200606120).

REFERENCES

GB/T 22595-2008, Test method for efficacy of antimicrobials-Aerobic bacteria [S].
GB/T 50050-2017, Code for design of industrial recirculating cooling water treatment [S].
Huang Changshan, Wu Jinying, Chen Junqiang, et al. (2018) Performance of Corrosion Inhibition Bactericide Based on Phosphono-Salt and Carboxyl Quaternary Ammonium Salt. HENAN SCIENCE, 36(12):1905–1909.
Jia Fengchun. Preparation and Performance Measurement of DG4 Corrosion and Scale Inhibitor and Bactericide [D]. Dalian: Dalian University of Technology, 2006.
Ma Wenjie, Tang Liqiang. (2016) Research Progress of Bactericide with Corrosion Inhibition Performance. CORRSION &PROTECTION IN PETROCHEMICAL INDUSTRY, 33(4):1–5.
Qiang Hui,Z hang jing. (2003) Evaluation of the efficacy of isothiazolinone fungicide. LUTIANHUA KE JI, (3):215–216.
Sun caixia, Chen Yanmin, Huang Changshan, et al. (2016) Bactericidal Property of the Benzalkonium Chloride in Industrial Circulating Water. HENAN SCIENCE, 34(10):1682–1685.
Sun caixia, Chen Yanmin, Zhang Min, et al. (2012) Study on the performance of composite bactericide. Industrial Water Treatment, 32(12):69–71.
Wang Lei, Wu Shaofeng, Gu Xuebin. (2015) Study on the Application of Isothiazolinone Fungicides. Industrial Microbiology, 45(5):60–64.
Zhang Qingdong, Zhou Guoying, Zhao Dongfeng. (2014) Research Progress of New Type bactericides in the oilfield. Guangdong Chemical Industry, 41(5):233–234.
Zhao Wanying. Study on New Type bactericides[D]. Daqing: Northeast Petroleum University, 2013.

Advances in Applied Chemistry and Industrial Catalysis – Saikia (Ed.)

Simulation and application of eutrophication in Hongze Lake

Shixian Ma*, Sichen Tong**, Yongfeng Xiong & Haizhen Hu
School of River and Ocean Engineering, Chongqing Jiaotong University, Chongqing, China

Gang Zhou
Chinese Research Academy of Environmental Sciences, Beijing, China

ABSTRACT: Eutrophication is a common water environmental problem in receiving water bodies. In the case of changing hydrodynamic conditions, excessive input of nutrients may lead to serious eutrophication of water bodies. To solve the problem of eutrophication, a lot of relevant water environment models were generally adopted to simulate the situation in the study area. Based on the EFDC model, this paper takes Hongze Lake as the typical research area. Under the hydrological conditions of a typical hydrological year, the temporal and spatial variation of nitrogen and phosphorus in Hongze Lake under the dual influence of natural inflow and the South-to-North Water Diversion Project was studied to provide a reference for the scientific management and water quality restoration and improvement. Results show that under the influence of natural inflow and water transfer in the Hongze Lake section of the eastern route of the South-to-North Water Diversion in the study area of Hongze Lake, nitrogen and phosphorus have become the main pollutants in Hongze Lake. The seasonal variation of TN concentration was obvious, the highest in spring, followed by summer, and decreased once in autumn and winter. The spatial and temporal distribution characteristics of TP concentration are obvious, and the lake area is generally higher in summer, followed by spring and autumn, and slightly lower in winter.

1 INTRODUCTION

Environmental models are an essential tool for water pollution prevention and water environment management, as well as an important basis for environmental management decisions. Scholars in the field of environmental models have conducted in-depth research on model evaluation methods and review frameworks and pointed out that environmental regulatory model evaluation must also balance model accuracy with model reproducibility, transparency, and usefulness for current regulatory decisions (Holmes et al. 2009). The "Guidelines for Model Quality Assurance" formulated by the US Environmental Protection Agency (EPA) proposed the basic indicators of model evaluation and the basic framework of model evaluation and provided guidelines for model evaluation work (Washington 2002). However, there is no evaluation system based on specific application scenarios and no quantitative evaluation method.

Based on the complexity and uncertainty of water quality models in terms of mechanism, application, and performance, evaluating water quality models is still an extremely complex task (Xu et al. 2017). The water quality model has the advantages of less investment, short operation period, high efficiency, and strong flexibility, and plays an important role in the research of water body eutrophication simulation, evaluation, and prediction (Kong et al. 2021). The common water quality models include QUAL2K, EFDC, HSPF, MIKE, CE-QUAL-W2, WASP, Delft3D, etc (Babamiri et al. 2021; Li et al. 2021; Mishra et al. 2009 , Xu et al. 2017).

Corresponding Authors: *masx@mails.cqjtu.edu.cn and **tongsichen@163.com

DOI 10.1201/9781003308553-8

Eutrophication is the most common and serious water environment problem in today's lakes and reservoirs. China has now become one of the countries with the most serious lake and reservoir pollution and algal blooms in the world (Farnaz et al. 2019; Ma et al. 2020; Yahyaee et al. 2021; Wang et al. 2019). At present, most lakes are already eutrophic and mesotrophic lakes. The existence of eutrophication in lakes has seriously hindered the utilization of these water bodies as resources, resulting in heavy environmental and economic losses. Hongze Lake is the first lake for regulation and storage in the east route of the South-to-North Water Diversion Project. However, Hongze Lake is affected by the water transfer from the Yangtze River and the incoming water from the Huai River. The water quality of Hongze Lake is poor, and the eutrophication problem is more serious. Nitrogen and phosphorus have become the main pollutants of Hongze Lake (Yao et al. 2022). This paper takes the EFDC model as an example to simulate the eutrophication of Hongze Lake.

2 DATA AND METHODS

2.1 *Introduction to the EFDC Model*

The full name of the EFDC model is the environmental fluid dynamics code, originally developed by Dr. John M. Hamrick in 1988 at the Virginia Institute of Marine Science (VIMS) and the School of Marine Sciences at the College of William and Mary. The EFDC model includes 1D, 2D, and 3D modules such as hydrodynamics, sediment transport, material transport, water quality dynamic changes, submerged plants, and sedimentary diagenesis. The eutrophication and water quality module is the main module of EFDC, including 22 water quality variables that are widely used in water bodies such as rivers, reservoirs, lakes, wetlands, estuaries, coasts, and coasts, and the application areas focus on environmental assessment, program decision-making and total allocation (Hamrick 1996; Sun et al. 2021). The model adopts the Mellor-Yamada 2.5-order turbulent closed-form equation, and 1D to 3D calculations can be performed as required.

2.2 *Overview of Hongze Lake research area*

Hongze Lake (N33′06′∼33′40′, E118′10′∼118′52′) located in Huai'an City, Jiangsu Province, is the fourth largest freshwater lake in China. The Hongze Lake Basin has a subtropical monsoon climate, with an average temperature of 14.9°C for many years and an average annual rainfall of 913.3mm, concentrated from April to September. Hongze Lake receives the incoming water from the Huaihe River Basin and has the function of regulating and storing the floods of the Huaihe River. As flood storage and benefit lake, the dead water level of Hongze Lake is 11.5m, the normal water level is 12.5m, and the warning water level is 13.5m. The area of the lake's control basin is 189,000 km2. The Huaihe River is the largest river entering the lake, and the average annual water inflow into the lake is more than 70% of the total water inflow into the lake. The flood gates mainly include Sanhe Gate, Erhe Gate, and Gaoliangjian Gate, with designed flood discharges of 12000 m^3/s, 3000 m^3/s, and 800m^3/s respectively.

In addition to the functions of regulating and storing floods and promoting irrigation, Hongze Lake is also the first lake for regulating and storing the east route of the South-to-North Water Diversion Project. The South-to-North Water Diversion Project is a major national strategic project to build the overall pattern of water resources allocation of "four horizontal and three vertical, north-south allocation, and east-west mutual aid". The completion of the first phase of the East Route Project has played an important role in alleviating the contradiction between the supply and demand of water resources in the water supply area, ensuring economic and social development, and improving the ecological environment. The designed water transfer time of the first phase of the East Route of the South-to-North Water Diversion Project is from October to May of the following year. The designed water transfer scale of the Yangtze River to the Hongze Lake section of the first phase project is 500 m^3/s pumping the Yangtze River and 450 m^3/s entering Hongze Lake. Two lines of water delivery are designed, one way is pumped through Huai'an Station into the Northern Jiangsu Irrigation Canal, and then 300m^3/s is pumped from Huaiyin Station into Hongze Lake; the

other way is westward through Jinbao Channel and Sanhe, and 150 m^3/s is pumped from Hongze Station s into Hongze Lake. The designed water transfer scale of the Hongze Lake to Luoma Lake section of the first phase of the east line is 350 m^3/s out of Hongze Lake and 275 m^3/s into Luoma Lake. The Luonan Middle Canal and Xuhong River are used for water transfer, and Hongze Lake is used for storage.

3 APPLICATION OF EFDC MODEL IN STUDY AREA

3.1 *Basic data collection and mesh*

The terrain, water quality, water quantity, meteorology, and other related data of Hongze Lake were collected for simulation. Inflow and outflow water quality data were collected including Xuyi Station, Hongze Station, Huaishu River, Huaihe Bridge Station, Jiangba Town Station, Laoshan Township Station, and Gaoliangjian Station, Chenghe Township Middle Station, etc. The topographic information such as the elevation of Hongze Lake was obtained to determine the simulated area of about 1324.7 km^2. According to the topographic boundary of the lake area, this model adopts a rectangular grid for simulation calculation. Considering the size of the calculation area and the calculation workload, the selected grid resolution is 516 × 509 m, with a total of 5038 grid cells. The elevation of the lake bottom is 10.18 m, and the topography after interpolation is shown in Figure 1.

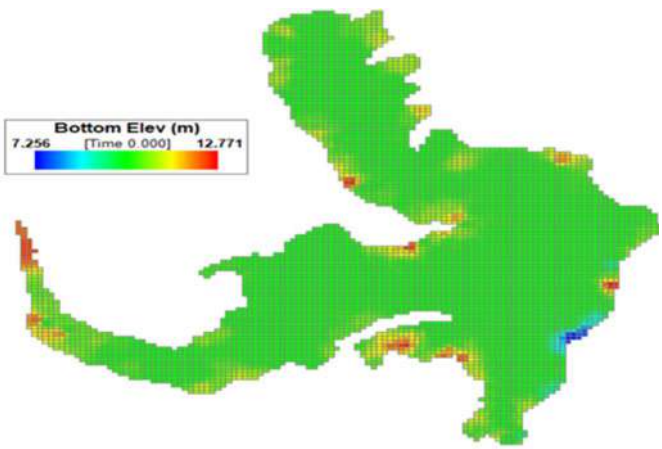

Figure 1. Model grid and bottom elevation of Hongze Lake.

3.2 *Boundary conditions*

The boundary conditions for the discharge of Hongze Lake include the inflow of the Huaihe River system, the water diversion from the South-to-North Water Diversion, and the outflow of Hongze Lake. Due to the limited data, no data on the water volume of other rivers entering the lake except the Huai River was collected. However, the inflow of the mainstream of the Huai River far exceeds that of other rivers entering the lake, so the model simplifies the inflow of the Huai River system as the inflow of the Huai River.

According to the measured water level of Jiangba in Hongze Lake on January 1, 2018, the initial calculated water level of Hongze Lake is set to 13.3m. According to the water temperature measured by the measuring station in the lake, the average water temperature is taken as the initial water temperature, and the initial water temperature is set to 6.6°C. The model run cycle is 1 year from January 1, 2018, to December 31, 2018. There are 11 simulated water quality variables. The

initial value of water quality in the lake is obtained by the weighted average of the data of each water quality monitoring site in the lake, as shown in Table 1.

Table 1. Initial values of water quality variables in Hongze Lake.

Number	Water Quality State Variables	Symbol	Unit	Initial Value
1	Dissolved Organic Phosphorus	DOP	mg/L	0.037
2	Total Phosphate	PO4	mg/L	0.070
3	Dissolved Organic Nitrogen	DON	mg/L	0.35
4	Ammonia Nitrogen	NH4	mg/L	0.27
5	Nitrate Nitrogen	NO2+NO3	mg/L	1.00
6	Chemical Oxygen Demand	COD	mg/L	16.1
7	Dissolved Oxygen	DO	mg/L	11.0

3.3 *Calibration and verification*

Before applying EFDC to build an environmental fluid dynamics model based on the study area, the calculation parameters of the model need to be adjusted appropriately to meet the model simulation accuracy requirements. The model was calibrated and verified by using the water temperature and water quality data of each measuring point in the Hongze Lake area from January 1, 2018, to December 31, 2018. The calibration results of the main parameters of the water quality module are shown in Table 2.

Table 2. Calibration results of main parameters of water quality module.

Parameter Definition	Symbol	Rating Value	Unit	Group
Maximum Nitrification Rate	rNitM	0.07	1/d	Nitration
Reoxygenation Rate Constant	KRO	1	—	DO
Decay Rate of COD	KCD	0.041	1/d	COD
Extinction Coefficient of Suspended Particles	KeTSS	0.052	$m^{-1}/(g{\cdot}m^{-3})$	Illumination
Chlorophyll Extinction Coefficient	KeChl	0.031	$m^{-1}/(g{\cdot}m^{-3})$	
COD Decay Oxygen Semisaturation Constant	KHCOD	1.5	g/L	
Denitrification Semi-saturation Constant	KHDNN	0.1	g/m^3	Ks
Attenuation Temperature Rate Constant of COD	KTCOD	0.041	—	Temperature
Temperature Regulation Constant of Reoxygenation rate	KTR	1.05	—	
Flux constant of Phosphorus Release From Sediment	CBFRP	0.000827	$g/m^2/d$	Sediment Release
SOD Temperature Coefficient	SODTC	1.065	m/d	

According to the purpose of this research, combined with the collected measured data, the water level, temperature, DO, TP, TN, etc. are mainly selected for verification. From the simulation results, the simulated value is relatively close to the measured value and is within the acceptable range. The water level verification of Zehu Lake is shown in Figure 2. The simulated water level is in good agreement with the measured value. The average error and average absolute error of Jiangba water level in Hongze Lake are −0.081 m and 0.17 m, respectively. The average error is small, and the average absolute error is less than 0.2 m.

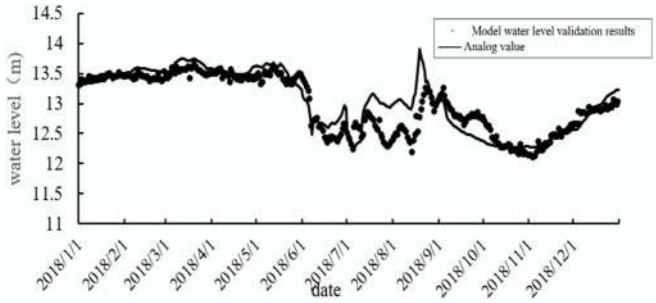

Figure 2. Model water level validation results.

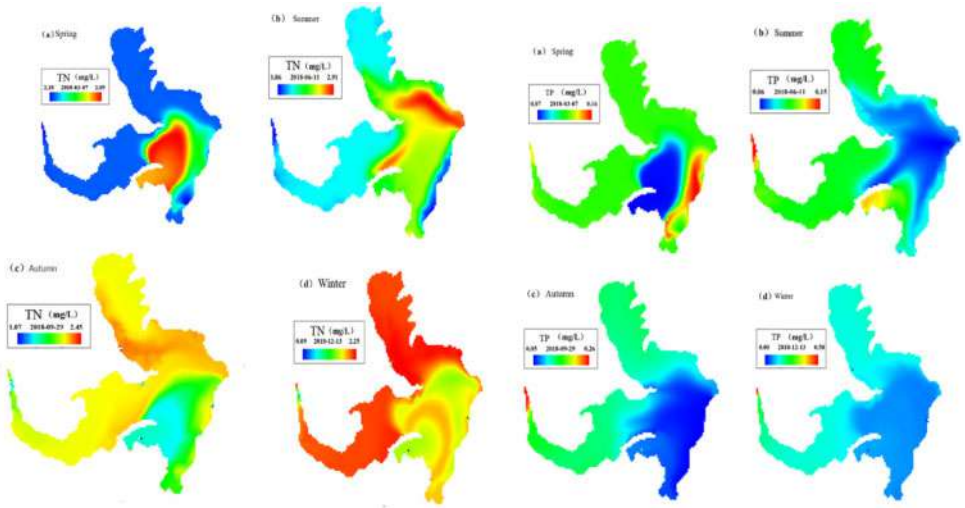

Figure 3. Spatial-temporal distribution of TN and TP in Hongze Lake.

4 CONCLUSION

Based on the results and discussions presented above, the conclusions are obtained as below:

(1) Based on the EFDC model results show that the dissolved oxygen and water temperature simulation results are good, and the simulation of total nitrogen and total phosphorus has certain errors but can reflect the basic trend. It also shows the temporal and spatial distribution of total nitrogen, total phosphorus, and temperature and oxygen in Hongze Lake. The water quality of Hongze Lake is mainly affected by the Yangtze River diversion and Huaihe River inflow. Nitrogen and phosphorus are the main pollutants of Hongze Lake.

(2) The seasonal variation of TN concentration in Hongze Lake is obvious (Figure 3). Except for the location near the lake entry and exit, the four seasons concentration values in the lake area are spring>summer>autumn>winter, and the spatial distribution characteristics of water bodies in different seasons are also different. In the spring lake area, the TN concentration in the eastern lake area is slightly higher than that in the northern lake area and the western lake area. The distribution of TN concentration in the reservoir area in summer and autumn is relatively uniform, and the concentration difference between different areas in winter is more

obvious. The TN concentration in most areas of the northern lake area and the western lake area is higher than 2.0 mg/L, while the eastern lake areas were all lower than 2.0 mg/L.

(3) The spatial and temporal distribution characteristics of TP concentration in Hongze Lake were obvious (Figure 3). The lake area is generally higher in summer, followed by spring and autumn, and slightly lower in winter. The variation range in spring was 0.07–0.16 mg/L; the TP concentration in summer was the highest in the whole year, and the variation range was 0.06–0.15 mg/L, with an average value of 0.09 mg/L. The TP concentration in autumn was between 0.05–0.26 mg/L; and the overall concentration in winter was not high, the concentration ranged from 0.01 to 0.58 mg/L; with an average of 0.021 mg/L.

ACKNOWLEDGMENTS

This work was partly supported by The National Key Research and Development Program of China (2018YFB1600400) and the Basic and Frontier Research Programs of Chongqing, China (cstc2018jcyjAX0534).

REFERENCES

Hamrick JM. User"s Manual for the Environmental Fluid Dynamics Computer Code[J]. Aquatic Ecosystem Health & Management, 1996.

Holmes KJ, Graham JA, Mckone T, et al. Regulatory Models and the Environment: Practice, Pitfalls, and Prospects[J]. Risk Analysis, 2009, 29(2): 159–170.

Kong Yu, SUN Wei, LI Xiaolong, et al. Building and application idea of SWMM-MIKE 11 coupling model in sponge river construction[J]. Water Resources Protection, 2021, 37(6): 74–79.

Li Tianyu, Li Zhenhua, Huang Bingbin, et al. Simulation on water quantity and quality of Shahe Reservoir by MIKE21 model[J]. Acta Scientiae Circumstantiae, 2021, 41(1): 293–300.

Ma Tengfei, Luo Hanjin, Li Zhimin, et al. Eutrophication Trend Analysis and Forewarning Model Construction of Water Source Reservoirs[J]. Environmental Science & Technology, 2020, 43(5): 145–153.

Mishra, A., Kar, S. & N. S. Raghuwanshi (2009). Modeling nonpoint source pollutant losses from a small watershed using hspf model. Journal of Environmental Engineering, 135(2), 92–100.

Nojavan A Farnaz, Kreakie Betty J, Hollister Jeffrey W, Qian Song S. Rethinking the lake trophic state index.[J]. PeerJ, 2019, 7.

Omid B, Safar M. A Multi-objective Simulation–optimization Approach for Water Resource Planning of Reservoir–river Systems Based on a Coupled Quantity–quality Model[J]. Environmental Earth Sciences, 2021, 80(11).

Sun Lina, Ll Yiping, ZHANG Qicheng, et al. Application of EFDC model on two-dimensional numerical simulation of Sanbai Lake[J]. Jiangsu Water Resources, 2021(3): 15–20.

Wang X, Zhou Y, Zhao Z, et al. A Novel Water Quality Mechanism Modeling and Eutrophication Risk Assessment Method of Lakes and Reservoirs[J]. Nonlinear Dynamics, 2019, 96(2).

Washington. Guidance for Quality Assurance Project Plans for Modeling[J], 2002.

Xu C, Zhang J, Bi X, et al. Developing an Integrated 3d-hydrodynamic and Emerging Contaminant Model for Assessing Water Quality in a Yangtze Estuary Reservoir[J]. Chemosphere, 2017, 188.

Xu Jihong. Evaluation on surface water quality based on fuzzy matter-element model [J]. Water Resources Development and Management, 2017(2): 24, 33–36.

Yahyaee AR, Moridi A, Sarang A. A New Optimized Model to Control Eutrophication in Multi-purpose Reservoirs[J]. International Journal of Environmental Science and Technology, 2021, 18(11).

Yao Min, MAO Xiaowen, SUN Ruirui, et al. Study on the spatial and temporal variations of water quality in Hongze Lake from 2010 to 2020[J]. Water Resources Protection:1-9[2022-01-11].

Advances in Applied Chemistry and Industrial Catalysis – Saikia (Ed.)

Comparison of geochemical characteristics of different crude oils from the Huizhou Sag

Jiang Zhao*
Key Laboratory of Earthquake Early Warning, Institute of Seismology, CEA, Wuhan, China
Hubei Earthquake Agency, Wuhan, China

Fang Wang**
Hubei Institute of Geosciences, Wuhan, China

ABSTRACT: Based on the distributions and compositions of various biomarkers within different crude oils from the Huizhou Sag, it can be classified into coal-derived and lacustrine oils. The coal-derived oils from the HZ9-2-1 well are characterized by a higher Pr/Ph ratio (>4.5), abnormally abundant C_{24} tetracyclic terpane, a step-like decreasing pattern for C_{19-26} tricyclic terpanes, more abundant C_{29} norhopane, C_{31} homohopane, and lower neohopanes in C_{27-35} hopanes, absolutely predominant C_{29} rearranged and regular steranes in C_{27-29} steranes. These features are the main indicators to discriminate coal-derived oils from other oils. However, in lacustrine oils, their Pr/Ph ratios are relatively low (<3.0), the abundance of C_{24} tetracyclic terpane and C_{26} tricyclic terpanes are similar, the distribution of C_{19-26} tricyclic terpanes is normal and C_{21} component is the main peak, neohopanes rearranged hopanes are moderate, gammacerane index indicating paleosalinity is very low. It is noted that in this kind of crude oil, 2-methylhopanes and 4-methylsteranes indicating cyanobacteria and dinoflagellates input, respectively, are very abundant, and the variation of the relative abundance has a normal correlation, representing a specific ecosystem condition to be suitable for the growth of two kinds of microbes. They have an important role in oil-source correlation in this study.

1 INTRODUCTION

The Pearl River Mouth Basin (PRMB) is one of the most important petroliferous basins in China, with many oil fields. Previous petroleum exploration in the Huizhou Sag reveals Miocene Zhujiang Formation and the Oligocene Zhuhai Formation are major reservoirs (Fu et al. 2007; Zhu et al. 2008). While the lacustrine facies of the Wenchang mudstone and the coal-bearing sequence of the Enping Formation constitute the source rocks (Fu et al. 1993; Zhang et al. 2004). Few studies concluded that Wenchang Formation was the primary source, while others indicated Enping Formation as a mixed source (Huang 1998; Hu et al. 2015). The parameters used in these studies are pristane/phytane ratios, distribution of C_{27-29} regular steranes, 4-methyl steranes content, the relative abundance of oleanane and bicadinane, and carbon isotopes (Bao et al. 2012; Li et al. 2014; Ma & Hou 2014). Generally, this study provides an overview of the oil characteristics based on a variation of the 2-methylhopanes and 4-steranes relationship. The genetic typing of these crude oils based on this relationship has provided new insight into the petroleum exploration and resource assessment in PRMB.

Corresponding Authors: *863388711@qq.comand **453411740@qq.com

DOI 10.1201/9781003308553-9

2 MATERIALS AND METHODS

A total of 12 crude oil samples from the Huizhou Sag are collected. Firstly, all the crude oil samples were fractionated into saturated, aromatic hydrocarbons, NSOs (nitrogen, sulfur, and oxygen), and asphaltenes, using open column chromatography. Then, saturated hydrocarbons were analyzed using gas chromatography-mass spectrometry (GC–MS) in full scan mode. GC–MS was carried out with an HP 5973 mass spectrometer, coupled to an HP 6890 GC equipped with an HP-5MS fused silica capillary column (30m*0.25 mm i.d., film thicknesses 0.25 μm). The GC temperature was programmed to keep 50°C for 2 min, then increase to 100°C with the rate of 20°C/ min, next from 100 to 310 at a rate of 3°C/min with a final hold of 18 min. Helium was used as the carrier gas with a rate of 1.0 ml/min and the ionization source operated at 70 eV. For the analysis of biomarkers, the fragmentogram for triterpanes (m/z 191) and steranes (m/z 217) was recorded.

3 THE DISTRIBUTION AND COMPOSITION OF CHAIN ALKANES

The pristane/phytane (Pr/Ph) ratio is one of the most commonly used geochemical parameters which has been widely invoked as an indicator of the redox conditions in the depositional environment and source of organic matter (Peters et al. 2005). High Pr/Ph (>3.0) indicates oxic conditions often associated with terrigenous organic matter input, while low values (<1.0) typify anoxic conditions, commonly hypersaline or carbonate environments (Peters et al. 1995, 2005) and values between 1.0 and 3.0 suggest intermediate conditions (suboxic conditions) (Amane & Hideki 1997; Philp 1985).

The chained alkanes within crude oils of Huizhou Sag mainly comprise normal alkane and phytane series. The general distribution characteristics of normal alkane series in all the crude oil samples are similar and shows a wide range of carbon number (C_{9-38}), high abundance of middle to high molecular weight compounds (n-alkanes), none odd-over-even predominance, and CPI value of nearly 1 that characterized it as mature oil (Figure 1). However, there is a significant distinction in the phytane series compositions between the crude oil samples. As shown in Table 1, the coal-derived oils from the HZ9-2-1 well are characteristic of strong pristane prevalence, with the pristane/phytane ratios ranging from 4.57 to 5.29, consisting with that of Enping coal measures as source rocks. However, in lacustrine oils, their pristane/phytane ratios are in the range of 1.40–2.35, in agreement with that of lacustrine facies source rocks of the Wenchang Formation.

The Pr/Ph ratio of crude oil is consistent with that of the corresponding source rock. Therefore, the oils with a high Pr/Ph ratio from HZ9-2-1 Well originated from Enping coal-bearing source rocks, and the rest oils with low Pr/Ph ratio originated from Wenchang lacustrine source rocks. However, some oils also show mixed origins.

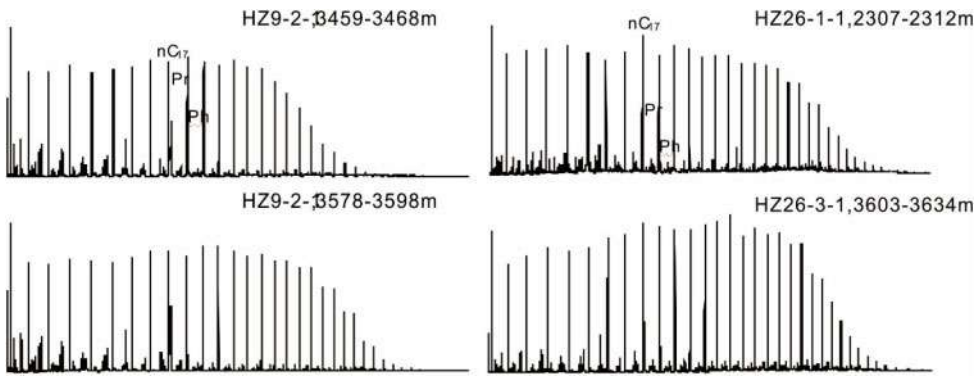

Figure 1. The distribution of chain alkanes in two kinds of crude oils from the Huizhou Sag.

4 TERPANE SERIES

4.1 *Tricyclic terpanes and tetracyclic terpanes*

In the studied crude oil samples, the tricyclic terpanes represent two distribution patterns, suggesting the difference in origin of organic matter and the sedimentary environment of corresponding source rocks. The oils from HZ9-2-1 well display a step-like decreasing pattern for C_{19-26} tricyclic terpanes, whereas in the rest oils, the distribution of C_{19-26} tricyclic terpanes is normal and the C_{21} component is the main peak, suggesting the difference in organic matter origin and sedimentary environment of corresponding source rocks. The C_{19}/C_{23} tricyclic terpane and high C_{24} tetracyclic terpane concentration are usually considered useful indicators of terrestrial organic matter input. The oils from the HZ9-2-1 well are characteristic of a higher $C_{19}TT/C_{23}TT$ ratio (21-32) and abnormally abundant C_{24} tetracyclic terpane with the $C_{24}Te/ C_{26}TT$ ratios are more than 6 (Figure 2), showing a large amount of terrestrial organic matter input i.e. coal-derived oil. While in the rest of the oils, the $C_{19}TT/C_{23}TT$ ratios are less than 3.0, and $C_{24}Te/ C_{26}TT$ ratios are equal to 0.5, with a minor contribution of terrestrial organic matter and are characterized as lacustrine oil. In the cross plot of $C_{24}Te/ C_{26}TT$ versus $C_{19}TT/C_{23}TT$, the oils from HZ9-2-1 well grouped into two distinct regions (Figure 3), which shows that these parameters could divide these oil into genetic types very well. The mixed oil is distributed in the transition zone of these two types of crude oil, and the

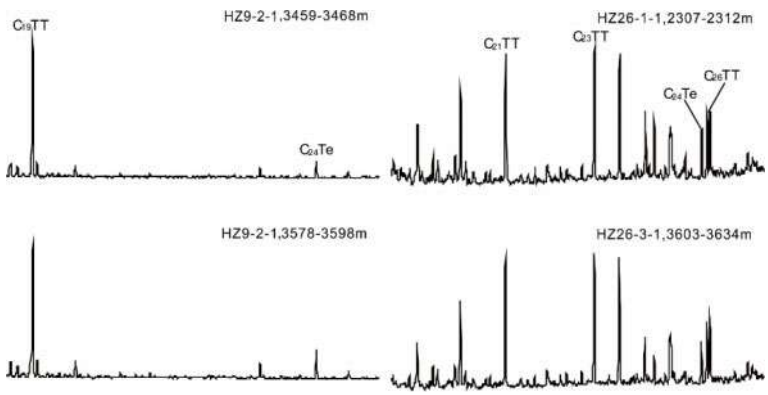

Figure 2. The distribution of tricyclic terpane (TT) series and C_{24} tetracyclic terpane (Te) in two kinds of crude oils from the Huizhou Sag.

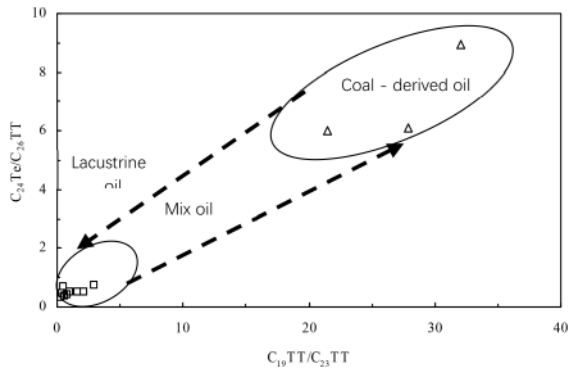

Figure 3. Cross plot of $C_{24}Te/C_{26}TT$ ratio versus C_{19} TT/C_{23} TT ratio in two kinds of crude oils from the Huizhou Sag.

relative contribution of the two types of crude oil determines whether the mixed oil is close to the region of coal-derived oil or lacustrine oil.

4.2 *Triterpane series*

Mass fragmentogram of terpanes (m/z 191) for the studied crude oil samples are shown in Figure 2. Gammacerane contents reflect the salinity and stratification of sediment-water (Peters & Moldowan 1993; Zhang et al. 1999). Ratios of gammacerane/C_{30} hopane for all the studied oils are similar and range from 0.03 to 0.05, indicating that the oils appear to have originated from a source rock deposited in a freshwater environment. The distribution of the extended hopanes or homohopanes (C_{31}-C_{35}) has been used to evaluate redox conditions based on homohopanes index (Peters et al. 2005). The low C_{35}/C_{31}-C_{35} hopane ratios (<0.05) of the oils from the HZ9-2-1 well indicate a suboxic environment. In the other oils, the values of C_{35}/C_{31}-C_{35} hopane are higher than those of oils from the HZ9-2-1 well, and are between 0.05 and 0.07, indicating a suboxic-anoxic sedimentary environment. Brooks noted that high C_{29} norhopane contents can occur in source rocks with terrestrial organic matter input. The oils from HZ9-2-1 well contain more abundant C_{29} norhopane than the other oils with the value of C_{29}/C_{30} hopane being between 0.72 and 0.82, suggesting that the oils derived from the source rocks with terrestrial organic matter input. It is believed that the relative amounts of Ts and C_{29}Ts are influenced by lithology, original organic matter, depositional environment, sedimentary and diagenetic conditions, thermal maturity of hydrocarbon source rocks, etc. (Moldowan et al. 1991; Sieskind et al. 1979; Wang et al. 2000; Zhang et al. 2009). The oils from the HZ9-2-1 well possess the low Ts/Tm ratios and C_{29}Ts/C_{29}H ratios in the range of 0.23–0.35 and 0.12–0.19 respectively (Figure 4). In contrast, the ratios of Ts/Tm and C_{29}Ts/C_{29}H in the other oils are higher than those of oils from the HZ9-2-1 well, ranging from 1.03 to 1.68 and 0.45–0.65, respectively. The C_{29} 20S/(20S+20R) sterane ratios of all the oil samples are identical between 0.42 and 0.48, suggesting that variation in Ts/Tm and C_{29}Ts/C_{29}H for the studied oil samples are controlled by factors other than thermal maturity, i.e. the source rocks and sedimentary organic facies. The biomarker assemblage characteristics analyzed above of the oils from the HZ9-2-1 well are similar to Enping coal-bearing source rocks and typical coal-derived oils, and the rest of the oils indicate the important contribution of Wenchang lacustrine facies source rocks and are characterized as lacustrine oil.

2-methylhopanes are biomarkers for cyanbacteria and their main energy-generating metabolism, and oxygenic photosynthesis. Bao has identified 2-methylhopanes for the first time in the source rocks of the Wenchang Formation and the related crude oils, which were absent in the source rocks of the Enping Formation in Huizhou Sag. There is a significant difference in the concentration of

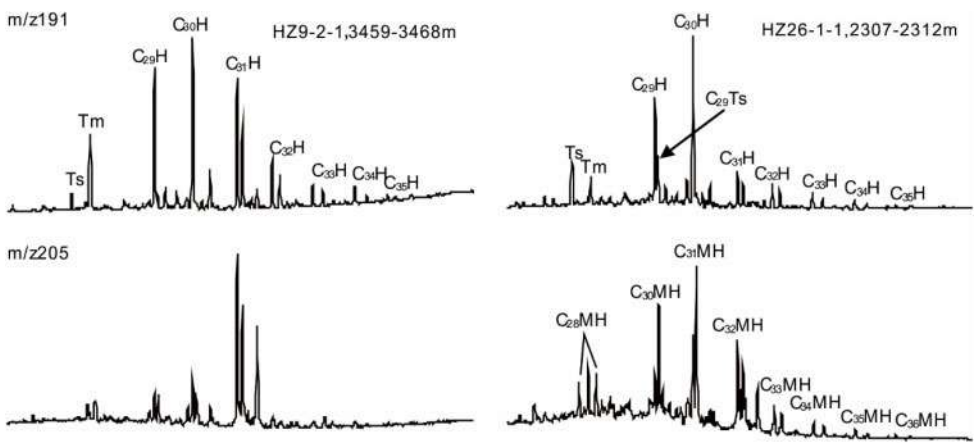

Figure 4. The distribution of triterpane series in two kinds of crude oils from the Huizhou Sag.

2-methylhopanes among all the studied oil samples. In coal-derived oils from the HZ9-2-1 well, the methylhopane indices are less than 0.06, yet the methylhopane indices are larger than 0.10 in the lacustrine oils, thus, suggesting the compositions of 2-methylhopanes are an effective indicator to classify the oil family, coal-derived oil or lacustrine oil, in the Huizhou Sag. Noticeably, different types of oil can be divided based on the characteristics of these triterpane series, which is consistent with the previous knowledge of tricyclic terpene and tetracycline, indicating some triterpane series are an effective indicator to classify the oil family.

5 STERANES

Bicadinane and 4-methyl steranes have been extensively applied in oil–source and oil–oil correlations in the PRMB (e.g., Gong & Li 1997; Huang et al. 2003; Zhang et al. 2003). The m/z 217 mass chromatograms of the crude oils from the HZ9-2-1 well (Figure 5) show a clear regular sterane and diasterane distribution with regard to the high concentration of C_{29} regular steranes and C_{29} diasteranes and low abundance of C_{27}, C_{28} regular steranes, suggesting the oils were derived from source rocks dominated by terrigenous organic matter, which is in agreement with those in the typical coal-derived oils from the Tuha Basin and Tangcan 1 Well of Santanghu Basin. The other oils are characteristic of low concentrations of regular steranes and diasteranes, which are difficult to identify because of the abnormal abundance of 4-Methyl steranes.

In the oils from the HZ9-2-1 well, 4-Methyl steranes are nearly absent, but they occur in high concentration with the C_{30} 4-Methyl steranes/C_{29} regular steranes between 1.23 and 2.78 in the other oils consisting of the feature of lacustrine facies source rocks of Wenchang Formation. In addition, 4-Methyl steranes only occur in relatively high abundance in Pearl River Mouth Basin and Beibuwan Basin, which are common constituents of the Cenozoic lacustrine sediments in eastern China (Fu et al. 1993), suggesting that 4-Methyl steranes possess special significance to the source rocks and related oils in Huizhou Sag. Therefore, as significant as 2-methyl hopanes, 4-Methyl steranes are an effective indicator to discriminate lacustrine oils from coal-derived oils in Huizhou Sag.

As shown in the cross plot of 2-methyl hopane/C_{30} hopane versus C_{30} 4-methyl steranes/C_{29} steranes (Figure 6), as discussed earlier, 2-methyl hopane and 4-methyl steranes are effective

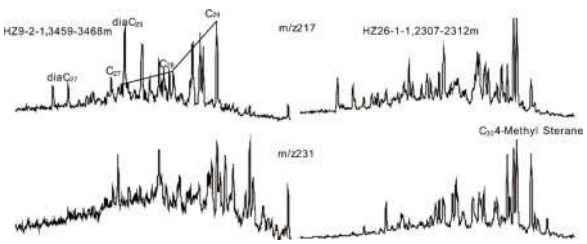

Figure 5. The distribution of sterane series in two kinds of crude oils from the Huizhou Sag.

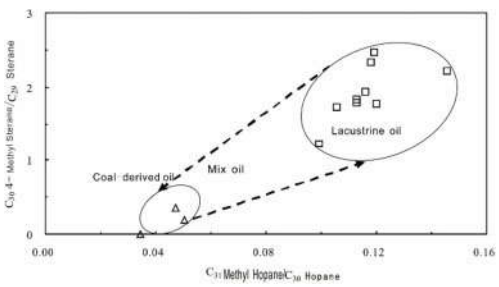

Figure 6. Cross plot of C_{30} 4-methyl sterane/C_{29} sterane ratio versus C_{31} methyl hopane/C_{30}hopane index in two kinds of crude oils from the Huizhou Sag.

indicators to differentiate the genetic types of crude oils in Huizhou Sag, reflecting that they possess significance to crude oil origins. Note that both 2-methyl hopanes and 4-methyl steranes are detected in all the twelve studied oil samples, and the relative abundance of them are in a good relationship, coupled with they occur of much higher relative abundance in the lacustrine oils than the coal-derived oils, suggesting that the sedimentary niche of Wenchang Formation may be responsible for the bloom of cyanobacteria and dinoflagellate. According to the previous studies, static water body, and the occurrence of substantial dinoflagellate, it can be concluded that the sedimentary water body is of eutrophication at the depositional stag of lacustrine source rocks of Wenchang Formation, which is the so-called special niche.

The oils from the HZ9-2-1 well are characterized as typical coal-derived oils, evidenced by high ratios of Pr/Ph, a predominance of C_{29} regular steranes, and diasteranes. However, in those oils, the abundance of oleanane and bicadinane is low, even less than in the lacustrine oils in Huizhou Sag.

6 CONCLUSION

The coal-derived oils from the HZ9-2-1 well are characteristic of a higher Pr/Ph ratio (>4.5), abnormally abundant C_{24} tetracyclic terpane, a step-like decreasing pattern for C_{19-26} tricyclic terpanes, more abundant C_{29} norhopane, C_{31} homohopane, and lower neohopanes in C_{27-35} hopanes, absolutely predominant C_{29} rearranged and regular steranes in C_{27-29} steranes. However, in lacustrine oils, their Pr/Ph ratios are relatively low (<3.0), the abundance of C_{24} tetracyclic terpane and C_{26} tricyclic terpanes are similar, the distribution of C_{19-26} tricyclic terpanes is normal and C_{21} component is the main peak, neohopanes rearranged hopanes are moderate, 2-methylhopanes and 4-steranes are abundant, gammacerane index indicating paleosalinity is very low.

The emergence of water eutrophication at the stage of formation of Wenchang Formation source rocks may be responsible for the normal correlation between the variation of relative abundance of 2-methylhopanes and 4-steranes in the lacustrine oils in Huizhou Sag.

REFERENCES

Bao, J.P. et al. (2012). 2-Methylhopane Series in the Source Rocks and the Related Crude Oils from Wenchang Formation in Huizhou Sag. J. Geochimica. 41(1), 70–77.

Fu, J. M. et al. (1993). A Geochemical Investigation of Crude Oils from Eastern Pearl River Mouth Basin, South China Sea. J. Journal of Southeast Asian Earth Sciences. 8(1/2/3/4), 469–486.

Fu, Ning et al. (2007). Source Rocks and Origin of Oil and Gas in the Northern Baiyun Depression of Pearl River Mouth Basin. Acta Petrolei Sinica. 28(3), 32–38.

Hu, Y. et al. (2015). Origin and Occurrence of Crude Oils in the Zhu1 Sub-Basin, Pearl River Mouth Basin, China. J. Journal of Asian Earth Sciences. 97, 24–37.

Huang, Z.J. (1998). Nonmarine Source Rock and Petroleum Formation of Pearl River Mouth Basin. China Offshore Oil and Gas(Geology). 12(4), 255–261.

Li, Y.C. et al. (2014). Hydrocarbon Zonation and Its Control Factors in Pearl River Mouth Basin. J. China Offshore Oil and Gas, 26(4), 8–14.

Ma, N. & Hou D.J. (2014). The Combination Model of New Tetracyclic Terpane in Source Rock and Crude Oil of Zhujiangkou Basin. J. Special Oil and Gas Reservoir. 21(2), 24–27.

Peters, K.E. et al. (2005). The Biomarker Guide: Biomarkers and Isotopes in Petroleum Exploration and Earth History. M. London: Cambridge University Press. 538–580.

Zhang, S.C. et al. (2004). Geochemistry of Petroleum Systems in the Eastern Pearl River Mouth Basin-I: Oil Family Classification, Oil Source Correlation and Mixed Oil Analysis. J. Acta Sedimentologica Sinica. 22(S), 15–26.

Zhu, W.L. et al. (2008). Geological Characteristics and Exploration Objectives of Hydrocarbons in the Northern Continental Margin Basin of South China Sea. J. Acta Petrolei Sinica. 29(1), 1–9.

Advances in Applied Chemistry and Industrial Catalysis – Saikia (Ed.)

Exploration of the factors affecting the determination of lead content in laboratory ceramic tiles

Fan Zhang, Yujing Zhang* & Bei Shang
China Building Material Test & Certification Group (Shaanxi) Co. Ltd, Xi'an, Shaanxi, China

ABSTRACT: With the improvement of people's living standards, more and more people choose to use some color materials to decorate the tile surface and increase the strength of ceramic tiles. However, the lead and cadmium ceramic tiles will be dissolved out under the action of acid. Moreover, the dissolved lead and cadmium and other heavy metals can affect the liver, nervous system, and hematopoietic function of human, and even paralyze people after respiratory ingestion. In this paper, an experimental control method was adopted to investigate the problems that may occur during the laboratory testing of lead in ceramic tiles. Experimental methods such as single-factor experiments and controlled tests were used in the experiments. By controlling and comparing the variables affecting each step of the experimental pre-treatment, the extraction solution was obtained and the concentration of lead in the extraction solution was determined by an atomic spectrophotometer.

1 INTRODUCTION

Adding lead compounds, such as lead pellets, to ceramic tiles can play a role in fluxing and reducing surface tension, while increasing the gloss of the glaze, and can also effectively promote coloring at lower temperatures. Lead compounds can also be used as a coloring agent, making ceramic tile in the coloring, because of the good effect of having the appearance of bright and vivid hues at high temperatures (Hu 2011). Elements such as lead and cadmium added to ceramic tiles can improve the stability of the pigment, making it possible to maintain the stability of the color of the tile surface even when disturbed by strong oxidizing agents (Yang 2015).

Ceramic tiles can have different degrees of lead dissolved in people's daily use, and the dissolved lead can cause different degrees of damage to the human body and affect physical and mental health. In this paper, the effects of three factors, namely temperature, ceramic powder particle size and concentration of the liquid to be tested, on the laboratory determination of lead content in ceramic tiles are experimentally investigated. Through comparative experiments, the errors in the process of testing the lead content of ceramic tiles are reduced and the accuracy of the test results is improved.

2 EXPERIMENT

2.1 *Experimental instruments*

Experimental instruments	Name	Manufactory
1	Analytical Scales	Sartorius Scientific Instruments Co.
2	Heating plate	Lichen Technology Co.
3	Qualitative filter paper	Hangzhou Special Paper Co.
4	Atomic spectrophotometer	Beijing Pu-Analysis
5	Nitric acid (analytical purity)	Tianjin Damao Chemical Reagent Factory

*Corresponding Author: yjzhang@88.com

DOI 10.1201/9781003308553-10

2.2 *Experimental method*

(1) Prepare 20 different kinds of bricks to be tested. Wash, dry, and grind the bricks to be tested until they pass through 180 mesh aperture sieve.
(2) Weigh 10g of the sample, add 25ml of nitric acid solution and stir well, cover with a surface dish (Hu 2016). Place on a low-temperature heating plate at 200°C for 2h, cool and rest for 1h, immediately filter into a 50ml volumetric flask and rinse to the scale, shake well.
(3) The solutions were collected and measured by atomic absorption spectrophotometry.

2.3 *Experimental influencing factors*

At present, due to the limitations of equipment and laboratory environment, the following factors may exist in the experiments for the determination of lead content in ceramic tiles that affect the accuracy of experimental results:

(1) Heating plate temperature
The heating plate is used to heat the sample with 25 ml of nitric acid in the pre-treatment process, which is efficient and convenient for operation because it has a large area and can be used for batch testing in a small area. However, in the process of specific experiments, the temperature of each point of the heating plate may vary, thus affecting the accuracy of the experimental results.
(2) Ceramic powder particle size
Ceramic tiles are divided into many categories due to the different water absorption, and the differences in process and formula of various types of ceramic tiles can make the ground ceramic powder vary greatly in thickness, which is not conducive to full contact with nitric acid in the process of experimental treatment and also makes the sample unevenly heated in the process of heating. Sieving is the process of separating the ground ceramic powder through a 180 mesh (80 μm aperture) mesh sieve to make it more uniformly mixed in the experiments (Li 2020). Therefore, sieving or not may have some influence on the experimental results.
(3) Concentration of the liquid to be measured
After the sample is heated, 25 ml of the nitric acid solution must be filtered and fixed to 50 ml. However, in practice, due to the heat evaporation of nitric acid, it is not possible to reach the ideal state of 25 ml of filtrate, so the volume of the fixed volume may also affect the accuracy of the experimental results.

3 EXPERIMENTAL ANALYSIS

This paper studies the effects of heating plate temperature, ceramic powder particle size, and concentration of the liquid to be measured on the lead content during the pretreatment process (Li 2016).

3.1 *Samples*

Twenty different sizes and types of bricks were selected and samples were made for experiments.

3.2 *Experimental procedure*

(1) Twenty groups of specimens were subjected to the same pretreatment process to ensure the same experimental environment, specimen specifications, and volume of nitric acid solution added, and the solutions to be measured were extracted for the determination of lead content under the following conditions, respectively.
(2) The twenty groups of samples were heated at 120°C, 140°C, 160°C, and 200°C for two hours using a heating plate to ensure that the other pretreatment conditions remained the same.

(3) Sieving (180 mesh) and not sieving the twenty sets of samples to ensure that the other pretreatment conditions remain the same.
(4) Ensure that other pretreatment conditions remain unchanged, and fix the volume of the twenty groups of samples to 50 ml and fix the volume to 2 times, respectively, after the pretreatment is completed.

3.3 *Experimental results*

3.3.1 *Effect of temperature on the lead content of ceramic tiles*

Table 1. Pb content of ceramic tiles under heating at different temperatures.

	Pb content under different temperature heating (mg/kg)									
Specimen	1	2	3	4	5	6	7	8	9	10
120°C	1.5	1.31	5.7	3.7	1.62	2.7	3.2	2.4	2.02	1.03
140°C	1.2	1.29	5.45	3.2	1.47	2.5	3.02	2.05	1.8	0.95
160°C	1.0	1.26	5.3	2.9	1.3	2.3	2.88	1.9	1.6	0.8
200°C	0.7	1.02	4.9	2.6	1.2	1.9	2.7	1.7	1.4	0.5
Specimen	11	12	13	14	15	16	17	18	19	20
120°C	3.9	1.55	4.02	1.8	3.9	5.2	2.9	4.88	1.5	2.86
140°C	3.5	1.3	3.9	1.58	3.78	5.02	2.78	4.7	1.2	2.7
160°C	3.3	1.0	3.76	1.47	3.69	4.9	2.6	4.5	1.09	2.5
200°C	3.1	0.8	3.5	1.3	3.6	4.7	2.4	4.2	0.93	2.3

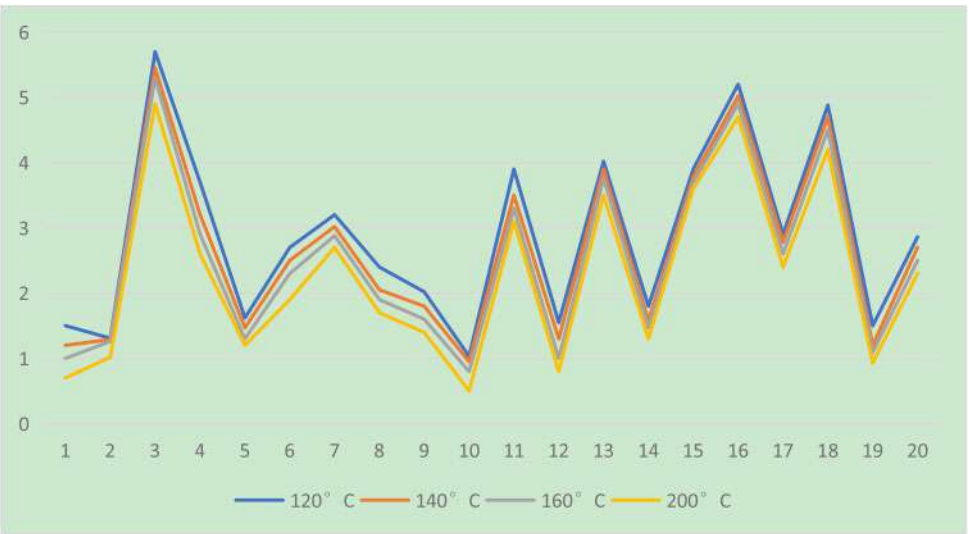

Figure 1. Pb content of ceramic tiles under different temperature heating.

As shown in Table 1, when ceramic tiles were heated at 120°C, 140°C, 160°C, and 200°C, the higher the temperature, the more adequate the acid treatment, the more uniform the heating, and the slightly lower pb content relative to the lower temperature.

3.3.2 *Effect of ceramic powder particle size on the lead content of ceramic tiles*

The group of control tests was heated at 200°C. The ceramic powders with different particle sizes and different contact areas during the experiments will have different degrees of heat uniformity and different acid treatment effects, so the pb content is different. From Table 2, the sieved samples with the larger heating area and contact area tested pb content is larger than the lead content measured by the unsifted samples (Zhi 2015).

Table 2. Pb content of ceramic tiles at different powder particle sizes.

	Pb content of ceramic tiles at different powder particle sizes (mg/kg)									
Specimen	1	2	3	4	5	6	7	8	9	10
Sieved	1.3	0.5	10.2	9.1	1.4	4.2	1.0	1.7	1.6	1.5
Unscreened	0.7	0.1	9.6	8.6	1.0	4.0	0.8	0.6	1.4	0.6
Specimen	11	12	13	14	15	16	17	18	19	20
Sieved	2.6	3.5	1.08	6.6	1.9	7.3	3.1	0.9	7.5	8.6
Unscreened	2.3	3.2	1.02	6.4	1.6	7.1	2.8	0.6	7.3	8.3

Figure 2. Pb content of ceramic tiles at different powder particle sizes.

3.3.3 *Effect of the concentration of the liquid to be measured on the lead content of ceramic tiles*

In the acid treatment process, due to the heat volatilization of nitric acid, the filtrate could not reach the ideal state of 25 ml. Under different fixation methods, the concentration of the solution to be analyzed was different due to the different fixation volumes, so the test results obtained varied greatly. In Table 3, the pb content measured for the sample volume fixed to 50 ml was different from that of the sample volume fixed to twice the filtrate volume. When the volume of the filtrate was small due to excessive evaporation, the pb content measured in the sample fixed to 2 times the volume of the filtrate was smaller compared to the sample fixed to 50 ml.

Table 3. Pb content of ceramic tiles at different concentrations of liquid to be tested.

	Pb content of ceramic tiles at different concentrations of liquid to be tested (mg/kg)									
Specimen	1	2	3	4	5	6	7	8	9	10
Volume fixed to 2 times the volume of filtrate	0.4	2.6	8.1	7.1	1.4	1.2	1.0	1.7	1.6	1.7
Volumizing to 50 ml	0.7	3.2	10.2	9.1	1.9	1.4	1.3	2.0	1.8	2.1
Specimen	11	12	13	14	15	16	17	18	19	20
Volume fixed to 2 times the volume of filtrate	3.2	4.1	7.2	2.5	6.3	5.6	0.9	2.7	1.3	9.0
Volumizing to 50 ml	3.6	4.5	8.0	3.1	6.9	6.2	1.4	3.5	1.6	9.5

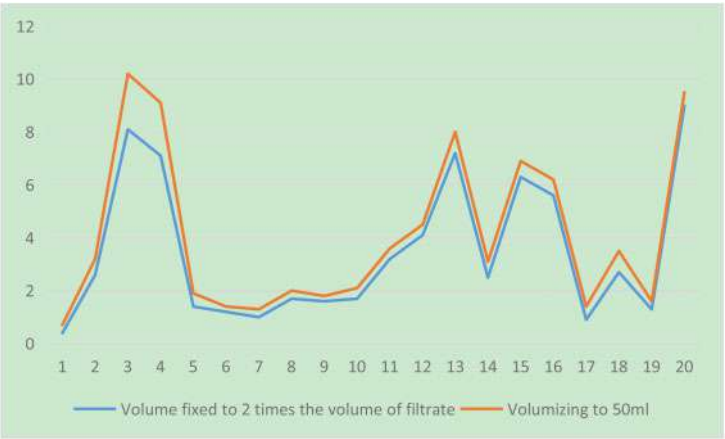

Figure 3. Pb content of ceramic tiles at different concentrations of liquid to be tested.

4 CONCLUSION

This paper investigates the effects of temperature, ceramic powder particle size, and concentration of the liquid to be tested on the lead content of ceramic tiles during the testing process, and draws the following conclusions.

(1) When determining the lead content of ceramic tiles, heating should be carried out at 200°C for more uniform heating.
(2) Ceramic tile powder with 180 mesh sieve should be selected to have a larger contact area, more uniform heating, and better acid treatment effect in the experimental pretreatment.
(3) The volatilization of the liquid to be tested should be reduced as little as possible during the pretreatment process, and the mouth of the beaker can be wrapped with cling film for heating and fixed to 50 ml.

Therefore, heavy metal precipitation detection should be in strict accordance with the national standard requirements, as far as possible to avoid irregularities in the pre-treatment process to reduce the detection error and improve the accuracy of the test results.

ACKNOWLEDGMENTS

This work was supported by the Research on Quality Classification of Building and Sanitary Ceramic Products and Public Service Demonstration Platform of Application Technological Information. (No.2021GY-170)

REFERENCES

Hu Jinbao, Zhang Min, Liang Chao, Liang Xue-Cheng, Hu Li-Hong, Gong Ming. Uncertainty assessment of cadmium dissolution determination in ceramic tiles[J]. Quality Exploration,2016,13(07):40–46.

Hu Jun, Zhuokun Au. Causes, hazards and detection of lead and cadmium dissolution in daily ceramics[J]. Foshan Ceramics,2011,21(11):16–19.

Li WJ, Dong YJ, Wang HT. Study on the effect of sample pretreatment method on the determination of lead and cadmium dissolved in daily ceramics[J]. China Ceramic Industry,2016,23(04): 11-18.DOI:10.13958/j.cnki.ztcg.2016.04.003.

Li Yuelong, Zhang Ting, Chu Xiaoqi, Bai Ji-ri. Evaluation of uncertainty in the determination of lead and cadmium dissolution in daily-use ceramic products by atomic absorption spectrometry[J]. Fujian Analytical Testing,2020,29(03):57–62.

Yang Yi, Xu Rihe. Quality condition of ceramic tile goods and analysis of the reasons for failure [J]. Brand and standardization,2015(09):59–60.

Zhibeng, Xie Yanfang. Risk analysis of lead and cadmium dissolution hazards in daily-use ceramics[J]. Quality Exploration,2015,12(09):52–53.

Advances in Applied Chemistry and Industrial Catalysis – Saikia (Ed.)

The problems with the chemical oxygen demand process and analytical studies

Yan Zhao*, Hong Tang, Yu Wang & Xiao Yan Ge
Shanghai Urban Construction Vocational College, Shanghai, China

Hui Wang
Jiangsu Environmental Monitoring, Jiangsu, China

Yang Li
Shanghai Urban Construction Vocational College, Shanghai, China

ABSTRACT: In this paper, the problems in the practical application of Chemical oxygen demand are studied and analyzed, and the critical point of high and low concentration is determined by the interference analysis of chloride ions to Chemical oxygen demand, the precision test and the effect of titrant on the result of analysis were studied.

1 INTRODUCTION

Chemical Oxygen Demand (COD_{cr}) refers to the mass concentration of oxygen corresponding to that of dichromate consumed by dissolved substances and suspended matter in water samples during Potassium dichromate oxidation under certain conditions, it is an important index to reflect the degree of water pollution (Editorial Board of the Ministry of Environmental Protection of the People's Republic of China 2013; Ministry of Environmental Protection of the People's Republic of China 2017; Sun et al. 2020; Ye et al. 2018). The standard methods for the determination of COD_{cr} in water are HJ 828-2017 and HJ /T70-2001, which are the determination of water quality, the determination of Chemical oxygen demand, the dichromate method and the determination of high chlorine waste water, the determination of Chemical oxygen demand, the chlorine calibration method. The former is mainly used for the analysis of water samples with chloride ion content less than or equal to 1000 mg/l, while the latter is used for the analysis of samples with chloride ion concentration between 1000 and 20000mg/l. These two methods complement each other and basically meet the requirements of COD_{cr} determination in water, but there are still some problems. On the basis of practical application and experimental research, This paper studies and discusses the shortcomings of this method.

2 ANALYSIS MODEL OF HIGH CHLORINE WASTE WATER

In the application scope of HJ828-2017, the standard does not apply to the determination of Chemical oxygen demand in water with chloride concentration greater than 1000 mg/l (diluted). This method can be used if the chloride concentration of the sample is less than 1000 mg/l after dilution. For the same sample size, the amount determined by HJ828-2017 is much less than that determined by HJ/T70-2001. Therefore, many detection units encountered high chlorine waste water samples, the sample diluted to its chloride ion concentration below 1000mg/l after the use of HJ 828-2017.

*Corresponding Author: 113120917@qq.com

DOI 10.1201/9781003308553-11

In this paper, it is found that when the concentration of chloride ion in the waste water sample is between 1000 and 2000 mg/L (Fu et al. 2018), when the concentration of the sample is between 30 and 40 mg/l, the concentration of chloride ion in the waste water sample is between 1000 and 2000 mg/L and the concentration of chloride ion in the waste water sample is between 1000 and 2000 mg/L, the results obtained by the low concentration method of HJ 828–2017 after the sample is diluted twice are quite different from those obtained by the high chlorine waste water method of HJ/T70–2001. The relative deviation between the two methods is about 10% ~ 20%, when the concentration of COD_{cr} in the sample is 40 ~ 100 mg/l, the results of the two methods are close and the deviation is less than 10%. When the concentration of COD_{cr} is more than 100 mg/l and the concentration of chloride ion is between 1000 and 2000 mg/l, the deviation between the high concentration method HJ 828-2017 and HJ/T70-2001 is less than 10%.

Table 1. Determination result of CODcr in water sample of a sewage treatment plant, mg/L.

Sample number	Direct chlorine correction (HJ/T 70-2001)	Double 1 Dilution dichromate method (HJ828-2017)	Approximate concentration of Cl^-	RSD (%)
1–1	42	52	1300–1400	7.1
1–2	46	49	1300–1400	4.2
1–3	46	44	1300–1400	2.3
2–1	32	40	1300–1400	11.1
2–2	30	42	1300–1400	16.7
2–3	30	38	1300–1400	11.8
3–1	55	61	1300–1400	5.2
3–2	74	75	1300–1400	0.7
3–3	51	55	1300–1400	3.8
4–1	92	98	1300–1400	3.2
4–2	89	95	1300–1400	3.3
4–3	96	99	1300–1400	1.5

Table 2. COD_{cr} Determination results of high chlorine standard sample after dilution, mg/L.

Preparation concentration	Dilution multiple	HJ828-2017 RSD%	Approximate concentration of Cl^-
20	8	13.6%~27.3%	<1000
40	4	–4.5%~2.3%	<1000
80	2	–4.6%~2.3%	<1000

In order to further understand the influence of dilution on the determination results of samples, the standard samples with high CODcr were diluted, and the chloride ion concentrations were all less than or equal to 1000 mg/l, and the COD_{cr} concentrations after dilution were 22 mg/l, 44 mg/l and 87 mg/l respectively, the HJ828-2017 method was used to determine three samples in parallel with each concentration. The results showed that the relative errors of 44 mg/l and 87 mg/l were less than ±5%, and the relative errors of 22 mg/l samples ranged from 13.6% to 27.3%, it is much larger than the first two high concentration samples. On the one hand, the error is caused by the large dilution multiple, on the other hand, because the concentration is relatively low, near the lower limit of 16mg/l of the method, the result deviation is relatively large. The experimental results show that when the sample is diluted and the COD_{cr} in the high chlorine wastewater is determined by HJ 828-2017 method, the dilution factor should be reduced as far as possible under the condition that the concentration of chloride ion is diluted to less than 1000 mg/l, and make sure that the

concentration of COD_{cr} is more than 20 mg/l after dilution. Otherwise, the method should not be used, but HJ/T70-2001 method should be used.

3 THE RATIONALITY OF THE CRITICAL CONCENTRATION OF HIGH AND LOW CONCENTRATION

HJ 828-2017 stipulates that less than or equal to 50 mg/l is in the category of low concentration, otherwise it is in the category of high concentration. In the process of analysis, the concentration of titrant ferrous ammonium sulfate (anhydrous) standard solution was 0.005Mol/l and 0.050Mol/l, respectively. 1ml is about 20 drops, and it is calculated that each drop of high concentration and low concentration ferrous ammonium sulfate (anhydrous) is equivalent to 2 and 0.2 mg/l COD_{cr} respectively. It is obvious that the end-point judgment of the analyst has a great influence on the precision of the result, and the absolute deviation is easy to increase (Sun 2020).

In order to investigate the accuracy of the determination of samples in the concentration range of 50–60 mg/l by low concentration determination mode, compare the difference between the two determination modes of high and low concentration, and analyze the rationality of the limit of high and low concentration, the standard samples of 52 mg/l and 58 mg/L COD_{cr} were prepared, and the results were measured by high and low modes in parallel for 6 times, while the results were between 49 and 52 mg/l when low concentrations were used. When the concentration of 58 mg/l is 53–62 mg/l, and when the concentration of 58 mg/l is low, the result is 54–59 mg/l. The results showed that the relative deviation and dispersion of the samples with 52 mg/l and 58 mg/l concentrations were smaller under the low concentration mode. It can be seen that when the concentration of COD_{cr} is between 50–60 mg/L, the precision of low concentration measurement is higher, which is consistent with the expected conclusion of the experiment.

In industries such as the Sewage Treatment or local standards such as the Shanghai municipal sewage standards, 60 mgl is the limit for a certain level of COD_{cr}. When the concentration of water sample is between 50–60 mg/l, the precision of sample determination is very important. The medium and low concentration determination mode HJ 828-2017 is more suitable. Therefore, it is suggested that 60 mg/L should be regarded as the cut-off concentration of high and low concentration.

Table 3. Statistical table of determination results of blank spiked samples under high and low determination modes.

Sample concentration	Low concentration determination		High concentration determination	
52mg/L	Determination results (mg/L)	49 ~ 52	Determination results (mg/L)	49 ~ 56
	average value (mg/L)	50.7	average value (mg/L)	54.0
	SD (mg/L)	1.5	SD (mg/L)	2.9
	Coefficient of variation (%)	3.0	Coefficient of variation (%)	5.4
58mg/L	Determination results (mg/L)	54~59	Determination results (mg/L)	53 ~ 62
	average value (mg/L)	56.3	average value (mg/L)	57.2
	SD (mg/L)	2.0	SD (mg/L)	3.7
	Coefficient of variation (%)	3.5	Coefficient of variation (%)	6.4

4 PRECISION CONTROL INDEX

HJ 828-2017 quality control and quality assurance requires 10% parallel samples per batch, the relative deviation of parallel samples is not more than ±10%. This can be achieved for high-concentration samples, but it is difficult for samples with concentrations near the lower limit of the

method, especially those containing certain suspended solids. The method of water and wastewater monitoring and analysis (4th edition) and the Operation Instruction of the National Surface Water Environmental Quality Monitoring Network (trial) of the Ministry of environmental protection evaluated the precision according to the sample concentration: when the sample concentration is 5 ~ 50mg/l, the relative deviation of the parallel sample is $\leq \pm 20\%$ when the mass concentration of the parallel sample is 50–[100 mg/l, the relative deviation of the parallel sample is $\leq \pm 15\%$ when the mass concentration of the parallel sample is $\geq$100 mg/l, the relative deviation of the parallel sample is $\leq \pm 10\%$ (Bai, 2018), this model is more scientific and objective.

5 FERROUS AMMONIUM SULFATE (ANHYDROUS) CONCENTRATION PROBLEM IN HJ/T70-2001 METHOD

HJ/T 70-2001 method stipulates that the ferrous ammonium sulfate (anhydrous) standard titration solution is implemented with reference to GB11914, which was superseded by HJ828-2017 in 2017, and the sample volume in HJ828-2017 is reduced from 20 ml to 10 ml, the concentration of ferrous ammonium sulfate (anhydrous) standard titration solution was also reduced from 0.10 mol/l to 0.05 mol/l. However, the volume of the sample in hjt 70-2001 is still 20 ml. If the concentration of the ferrous ammonium sulfate (anhydrous) titrant solution is changed from HJ828-2017 to 0.05 mol/l, it is not necessary technically in the first place, secondly, according to the titration principle and formula, the titration volume of the ferrous ammonium sulfate (anhydrous) standard solution of the blank sample will be greater than 50 ml, because the titration tube volume is 50ml, so the need for secondary titration, there is a risk of increasing the method error. Therefore, it is recommended that 0.1 mol/l should still be used for the determination of Chemical oxygen demand in high chlorine waste water by ferrous ammonium sulfate (anhydrous) titration.

6 CONCLUSIONS

The Standard of method is the criterion of laboratory analysis and determination, and the scientific rationality of its provision is of great importance to the monitoring results. In this paper, the shortcomings of the determination method of COD_{cr} in water are studied and discussed, which provides an effective technical reference for revising and perfecting the current standard analysis method of Chemical oxygen demand in water.

ACKNOWLEDGMENTS

The authors would like to thank Shanghai Urban Construction Vocational College and Jiangsu Environmental Monitoring for helpful discussions on topics related to this work. We would like to thank the anonymous reviewers for their helpful remarks. This paper is supported by cjky202102.

REFERENCES

Editorial Board of the Ministry of Environmental Protection of the People's Republic of China methods for monitoring and analysis of water and wastewater. Methods for monitoring and analysis of water and wastewater (fourth edition) [M]. BEIJING: China Environment Press, 2013.

Ministry of Environmental Protection of the People's Republic of China. Water quality-determination of Chemical oxygen demand-dichromate method: Hj 828–2017[S]. BEIJING: China Environmental Sciences Press, 2017.

Minqiang Ye, Cao Lei, Li Qiutong, etc. Comparison of new and old standards for determination of water Chemical oxygen demand by dichromate method [J]. Environmental Monitoring and early warning, 2018,11(1): 26–28.

Sun Juan, Zhang Qinyu, Xu Rong, etc. A review of analytical methods for high chloride wastewater Chemical oxygen demand. Chemometrics, 2020,29(2): 128–131.
Sun Bing. [J] Comparative Study of two methods for determination of Chemical oxygen demand. Guangdong chemical, 2020,47(14): 154–155.
Wang Liang, Sheng Wenlong, Fu Shengnan, et al. Research progress on determination methods of Chemical oxygen demand in high chlorine wastewater. Environmental Research and monitoring, 2018,31(4): 21–25.
Yun-kang Bai. Comparison of three uncertainty evaluation methods for Environmental monitoring-taking the determination of Chemical oxygen demand in water as an example. Environmental Monitoring and early warning, 2018,10(1): 34–41.

Advances in Applied Chemistry and Industrial Catalysis – Saikia (Ed.)

Review on in-situ chemical oxidation technology in groundwater remediation

Xianfeng Sun, Xiaodong Wang* & Lixin Zhao
School of Civil Engineering and Architecture, University of Jinan, Jinan, China

ABSTRACT: With the development of industrialization, more and more pollutants have infiltrated into groundwater, which has been seriously polluted. In-situ chemical oxidation (ISCO) technology has been rapidly developed and widely used in recent years because of its advantages such as wide range of application, complete removal of pollutants, moderate cost, in-situ application and fast processing speed. Combined with the research status of in-situ chemical oxidation technology, this review introduces the research and application of ISCO oxidants such as hydrogen peroxide (H_2O_2), permanganate (MnO_4^-), sodium persulfate ($Na_2S_2O_8$), sodium percarbonate ($2Na_2CO_3{\cdot}3H_2O_2$) and their optimized processes in groundwater remediation, in order to provide theoretical basis for the application of in-situ chemical oxidation technology in the actual remediation of contaminated groundwater.

1 INTRODUCTION

Groundwater is an important part of water resources, which is closely related to human production and life, national economy and the people's livelihood. With the rapid development of economy and the acceleration of urbanization, a large number of organic pollutants are discharged into the environment, causing serious pollution to water resources and posing a major threat to human living environment and health (Zhou et al. 2018). People gradually realize the importance of environmental protection while developing economy.

There are many reasons for groundwater pollution. The main reasons include the direct discharge of industrial wastewater and domestic sewage, the massive use of pesticides and chemical fertilizers, the leakage of fossil fuels during their mining, storage and transportation, and the leakage of landfill leachate. The self-purification capacity of groundwater is relatively weak, which will be difficult to recover after being polluted, causing serious damage to the ecological environment. Therefore, groundwater pollution has become one of the most prominent environmental pollution problems. Many excellent scholars have done a large amount of research on groundwater remediation technology. They have achieved remarkable results in groundwater pollution control through continuous research and exploration, and continue to explore new green remediation technology.

2 GROUNDWATER REMEDIATION TECHNOLOGY

Groundwater remediation technology can be divided into ex-situ remediation technology and in-situ remediation technology.

The ex-situ remediation technology of groundwater is mainly to transfer the polluted groundwater to the ground through extraction and treat the polluted water through physical, chemical or biological water treatment technology to meet the discharge requirements. Pump and Treat (P&T) remediation technology is the most widely used ex-situ remediation technology to deal with

*Corresponding Author: 13853189137@163.com

DOI 10.1201/9781003308553-12

groundwater pollution at present. This method has high treatment cost, tailing and rebound, and the application proportion decreases year by year.

In-situ remediation technology of groundwater pollution refers to a technology that directly restores the groundwater in the contaminated site in situ without damaging the natural environment of groundwater. This technology has the advantages of optimal remediation effect, relatively low cost, relatively short time, friendly to the environment, and it can deal with a variety of pollutants. It has been widely studied and applied in the field of groundwater pollution remediation. In-situ remediation technology mainly includes in-situ chemical reduction technology, in-situ chemical oxidation technology, in-situ microbial remediation technology, in-situ plant remediation technology, in-situ electric remediation technology, in-situ thermal remediation technology, in-situ thermal remediation technology and permeable reactive barrier remediation technology, etc.

3 IN-SITU CHEMICAL OXIDATION TECHNOLOGY

In-situ chemical oxidation (ISCO) technology is to directly inject oxidant into polluted groundwater and oxidize pollutants into less toxic or non-toxic compounds through chemical oxidation (Oh et al. 2011). Its technical principle is shown in Figure 1. This technology has strong pollutant degradation ability, high treatment efficiency, in-situ application, wide application range and low technical cost, it will not damage the groundwater environment. It is recognized as a cost-effective groundwater remediation technology.

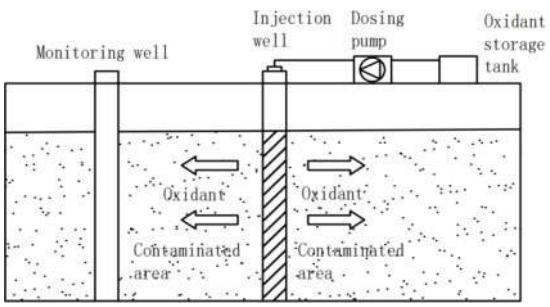

Figure 1. Schematic diagram of in-situ chemical oxidation technology.

The active substances produced by oxidants play a decisive role in the pollutant degradation ability of ISCO technology, so oxidants will directly affect the removal effect of pollutants in groundwater. Oxidants commonly used in ISCO technology include potassium permanganate ($KMnO_4$), hydrogen peroxide (H_2O_2), sodium persulfate ($Na_2S_2O_8$) and sodium percarbonate ($2Na_2CO_3{\cdot}3H_2O_2$, SPC). The remediation effect of ISCO technology is greatly affected by hydrogeological conditions. Therefore, it is necessary to select appropriate oxidants according to the actual situation of the contaminated site and the properties of oxidants.

Table 1. Characteristics of different chemical oxidants.

Oxidant	Chemical formula	Form	Catalyst	Active components (E^0)
Hydrogen peroxide	H_2O_2	Liquid	Fe(II); Fe(III)	H_2O_2(+1.8V); $HO^{\bullet}$(+2.8V); $O_2^{-\bullet}$(−2.4V); $HO_2^{\bullet}$(+1.7V); HO_2^-(−0.88V)
Permanganate	MnO_4^-	Solid	–	MnO_4^-(+1.7V)
Sodium persulfate	$Na_2S_2O_8$	Solid	Fe(II); Fe(III); UV; H_2O_2; Alkali	$S_2O_8^{2-}$(+2.1V); $SO_4^{-\bullet}$(+2.6V)
Sodium percarbonate	$2Na_2CO_3{\cdot}3H_2O_2$	Solid	Fe(II); Fe(III)	H_2O_2(+1.8V); $HO^{\bullet}$(+2.8V); $O_2^{-}\cdot$(−2.4V)

3.1 *Traditional in-situ chemical oxidation technology*

3.1.1 *Fenton oxidation technology*

The traditional Fenton reaction is that Fe^{2+} catalyzes H_2O_2 to produce hydroxyl radical ($HO^{\bullet}$) under acidic conditions. The hydroxyl radical has strong oxidation, it can react quickly with most organic substances, and has the ability to oxidize a variety of pollutants into inorganic substances. Fenton reaction mechanism is very complex. $HO^{\bullet}$ reacts with organic matter to produce organic free radical intermediate ($R^{\bullet}$), which can be finally removed by reacting with H_2O_2 and other substances. The main reactions are shown in equations 1–7 (Watts et al. 2002).

$$Fe(II) + H_2O_2 \rightarrow Fe(III) + HO^{\bullet} + OH^{-} \quad (1)$$

$$RH^{\bullet} + HO^{\bullet} \rightarrow R^{\bullet} + H_2O \quad (2)$$

$$R^{\bullet} + H_2O_2 \rightarrow ROH + HO^{\bullet} \quad (3)$$

$$R^{\bullet} + HO^{\bullet} \rightarrow ROH \quad (4)$$

$$ROH + HO^{\bullet} \rightarrow \text{product} \quad (5)$$

$$R^{\bullet} + Fe(III) \rightarrow Fe\ (II) + \text{product} \quad (6)$$

$$R^{\bullet} + Fe(II) \rightarrow Fe(III) + R^{-} \quad (7)$$

The feasibility of using Fe (II) and Fe (III) catalyzed H_2O_2 to repair groundwater polluted by BTEX was researched (Yang et al. 2011). The research results show that both technologies can effectively remove BTEX in groundwater, and Fe(II) catalyzed H_2O_2 can produce better oxidation effect, and the pH decreases from neutral to strong acidity in the reaction process. Fenton oxidation technology has been widely used in the field of groundwater remediation because of its fast and efficient, wide application range and no secondary pollution. However, the optimal pH of the traditional Fenton reaction is about 3, and the natural groundwater environment is neutral. This condition will cause Fe(II) to be oxidized to form $Fe(OH)_3$precipitation, which will affect the removal effect of pollutants. Moreover, this reaction occurs rapidly and violently, which will produce a large amount of heat and gas, destroy the groundwater environment. The transmission distance of H_2O_2 in groundwater environment is limited, which is not conducive to the continuous degradation of pollutants in groundwater, resulting in the application of this technology in the actual remediation site. Therefore, the technology needs to be optimized to overcome the limitations of Fenton oxidation technology.

3.1.2 *Permanganate oxidation technology*

Permanganate (MnO_4^-) is an oxidant widely used in in-situ chemical oxidation technology. It has good degradation effect on a variety of pollutants. It has the advantages of low price, stable properties, wide application range of pH, easy solubility in water, good durability, safe transportation and use. It is a strong oxidant widely used in groundwater pollution remediation (Chen et al. 2021). The common MnO_4^- are $NaMnO_4$ and $KMnO_4$, both of which are solid, but the application cost of $NaMnO_4$ is high. At present, $KMnO_4$ is widely used in the field of groundwater remediation. $MnO_4^-$is selective for the degradation of pollutants. It can degrade organic compounds containing carbon-carbon double bonds and hydroxyl groups. It is commonly used to treat organic compounds such as chlorinated olefins, polycyclic aromatic hydrocarbons and phenols, but it has poor degradation effect on organic compounds without available electron pairs, such as chlorinated alkanes. The reactions are shown in equations 8–10.

$$MnO_4^- + 8H^+ + 5e^- \rightarrow Mn^{2+} + 4H_2O \qquad pH < 3.5 \quad (8)$$

$$MnO_4^- + 2H_2O + 3e^- \rightarrow MnO_2(s) + 4OH^- \qquad 3.5 < pH < 12 \quad (9)$$

$$MnO_4^- + e^- \rightarrow MnO_4^{2-} \qquad pH > 12 \quad (10)$$

The effect of $KMnO_4$ on remediation of TCE contaminated groundwater was researched (Kao et al. 2008). The research results show that when the TCE concentration is the same, the higher the $KMnO_4$ concentration, the faster the degradation rate of TCE, and the degradation of TCE conforms to the second-order reaction kinetics. MnO_4^- is widely used in the field of groundwater remediation, but the research and practice results show that permanganate oxidation technology has many disadvantages in practical groundwater remediation. MnO_2 produced in the process of permanganate oxidation will block the medium gap, affect the injection of oxidant, hinder the diffusion of oxidant and affect the degradation effect of pollutants. Natural organic matter (NOM) in the underground environment will also consume MnO_4^-, which seriously affects the degradation effect of oxidant on pollutants in the actual site.

3.1.3 *Sodium persulfate oxidation technology*

Sodium persulfate ($Na_2S_2O_8$) is a new oxidant used in the field of groundwater remediation, which has been widely studied and applied in the field of groundwater pollution remediation. The ionization of $Na_2S_2O_8$ in water can produce persulfate ion ($S_2O_8^{2-}$), $S_2O_8^{2-}$contains peroxide bond (-O-O-), and $SO_4^{-\bullet}$ free radical is generated after activation, It has strong oxidation and reaction activity, and finally oxidizes organic pollutants to H_2O and CO_2. The reactions are shown in equations 11–13 (Liang et al. 2004). $SO_4^{-\bullet}$ free radicals can produce $HO^\bullet$ in water. The two free radicals cooperate with each other to improve the degradation efficiency of pollutants. Under strong alkaline conditions (pH > 12), $HO^\bullet$ radical is the dominant radical in the system. Under alkaline conditions (7 < pH < 12), $HO^\bullet$ and $SO_4^{-\bullet}$ work together. Under neutral and acidic conditions (pH < 7), $SO_4^{-\bullet}$ radical is the dominant radical (Mei et al. 2019). At present, the activation modes of $Na_2S_2O_8$ are mainly thermal activation, transition metal activation, strong oxidant activation, alkali activation, etc.

$$S_2O_8^{2-} + \text{activator} \rightarrow SO_4^{-\bullet}/SO_4^{2-} + SO_4^{-\bullet} \tag{11}$$

$$SO_4^{-\bullet} + H_2O \rightarrow SO_4^{2-} + H^+ + HO^\bullet \tag{12}$$

$$SO_4^{-\bullet} + OH^- \rightarrow SO_4^{2-} + HO^\bullet \tag{13}$$

$Na_2S_2O_8$ was activated by thermal activation method and the degradation effects of various organic pollutants at different temperatures were researched (Huang et al. 2005). The research results show that the degradation efficiency of pollutants gradually increases with the increase of oxidant concentration and reaction temperature. With the increase of reaction time, BTEX, vinyl chloride and other organic pollutants can be effectively removed. $Na_2S_2O_8$ is very stable at room temperature and has a long transmission distance in groundwater. However, it is too stable to react with pollutants, so the degradation effect of pollutants becomes worse.

3.2 *Optimization of in-situ chemical oxidation technology*

3.2.1 *Optimization of Fenton oxidation technology*

The traditional Fenton oxidation reaction has some disadvantages, such as narrow pH application range (pH = 3), violent reaction, easy to destroy the ecological environment, easy to form $Fe(OH)_3$ precipitation when Fe(II) is oxidized to Fe(III), low cycle efficiency of Fe(II)/Fe(III) and poor reaction persistence. To solve the above problems, researchers have proposed a variety of optimized Fenton oxidation technologies, mainly including the optimization of Fenton oxidation technology by using iron containing minerals, chelating agents, reducing agents and zero valent iron (ZVI).

There are many kinds of iron containing minerals in nature. Some iron containing minerals have similar catalytic ability to Fe(II), which can efficiently catalyze H_2O_2 to produce $HO^\bullet$. The reaction of H_2O_2 catalyzed by natural iron minerals can overcome the limitation of pH and effectively degrade pollutants under neutral conditions. Chelating agent can expand the pH application range

of the reaction and reduce the formation of $Fe(OH)_3$ precipitation. Reducing agent can promote the circulation of Fe(II)/Fe(III) in the reaction system. Fe^0 can be oxidized to Fe(II), and Fe(III) can also react with Fe^0 to generate Fe(II), which realizes the circulation and regeneration of catalyst Fe(II) in the solution and continuously releases Fe(II) for the actual groundwater remediation. The reactions are shown in equations 14–16.

$$Fe^0 + 2H^+ \rightarrow Fe^{2+} + H_2 \tag{14}$$

$$Fe^0 + H_2O_2 \rightarrow Fe^{2+} + 2OH^- \tag{15}$$

$$Fe^0 + 2Fe^{3+} \rightarrow 3Fe^{2+} \tag{16}$$

The optimization effect of different chelating agents on the degradation of benzene in Fenton system was explored (Georgi et al. 2007). The research results showed that humic acid (HA), hydroquinone polymer (HP) and nitrotriacetic acid (NTA) promoted the degradation of benzene, and the promotion effect of HA on the degradation of benzene was the best. They also explored the effect of chelating agent HA on optimizing the degradation of benzene by Fenton system under the conditions of different initial pH of solution, The results showed that the chelating agent HA can expand the pH application range of the reaction Fenton system.

3.2.2 *Optimization of permanganate oxidation technology*

The traditional permanganate oxidation technology has certain defects, mainly including two aspects: the formation of MnO_2 precipitation in the system reaction and the consumption of MnO_4^- by natural organics. In order to solve the limitations of MnO_4^- in the field of groundwater remediation, researchers have done many studies to improve the remediation effect of MnO_4^- in the field of groundwater remediation. The main methods include inhibiting MnO_2 precipitation and preparing MnO_4^- slow-release material to improve the utilization of MnO_4^- in the system.

$KMnO_4$ sustained-release material was prepared from $KMnO_4$, paraffin, quartz sand and activated carbon to degrade trichloroethylene (TCE) in groundwater (Chen et al. 2021). The research results show that $KMnO_4$ can be well sustained-release and the release rate is controllable. A liquid polymer resin $KMnO_4$ sustained-release material was prepared for the degradation of trichloroethylene (TCE) in groundwater (Lee et al. 2007). The research results show that the slow-release material can slowly release $KMnO_4$ in several years. $NaHPO_4$ can be added to MnO_4^- oxidation system to inhibit the generation of MnO_2 and prevent void from blocking.

3.2.3 *Optimization of sodium persulfate oxidation technology*

Fe(II) is one of the main catalysts for activating $Na_2S_2O_8$. The traditional Fe(II) activated $Na_2S_2O_8$ oxidation technology has similar disadvantages with the traditional Fenton oxidation technology. Fe(II) is easy to be oxidized to Fe(III). Under neutral and alkaline conditions, Fe(III) is easy to form $Fe(OH)_3$ precipitation, which leads to the decrease of Fe(II) concentration in the system and the ability of oxidative degradation of pollutants. In order to solve the above limitations of $Na_2S_2O_8$ in the field of groundwater remediation, The researchers mainly used iron-containing minerals, chelating agents and zero-valent iron (ZVI) to optimize the $Na_2S_2O_8$ oxidation technology.

Optimization of the degradation of trichloroethylene (TCE) by Fe(II) activated $Na_2S_2O_8$ is realized by using various chelating agents (Liang et al. 2004). The research results show that CIT, HEDPA, EDTA and STPP can effectively promote the degradation of trichloroethylene. CIT has the best optimization effect on the degradation of trichloroethylene (TCE) by Fe(II) activated $Na_2S_2O_8$. When the concentration of trichloroethylene was 0.45mM and the molar ratio of Fe(II) to CIT was 5:1, trichloroethylene could be completely degraded within 20 min.

3.2.4 *Sodium percarbonate oxidation technology*

Sodium percarbonate ($2Na_2CO_3{\cdot}3H_2O_2$, SPC) is a new oxidant used in the field of groundwater remediation in recent years. It is an addition compound of H_2O_2 and Na_2CO_3. It is a white crystalline powder. SPC is mainly used as bleach, oxidant and bactericide. It has the advantages of low price, high safety, good stability, convenient storage and transportation, non-toxic and harmless. It is a green oxidant with strong oxidation ability (Liu et al. 2021). SPC is dissolved in water and decomposed into H_2O_2 and Na_2CO_3. H_2O_2 and SPC can effectively degrade organic pollutants in groundwater. SPC and H_2O_2 have similar oxidation properties. However, the pH range of SPC is wider than that of Fenton method. Research shows that SPC can effectively degrade chlorinated hydrocarbons, polycyclic aromatic hydrocarbons and other organic pollutants instead of H_2O_2.

The feasibility, remediation effect and optimization process of Fe(II)/Fe(III) catalyzed SPC for remediation of benzene polluted groundwater were researched (Fu et al. 2016). The results show that chelating agents CIA, GA and OXA can expand the pH application range of the reaction and reduce $Fe(OH)_3$ precipitation from Fe(III). An appropriate amount of reducing agents HYH, ASA and SA promote the circulation of Fe(II)/Fe(III) in the reaction system. The removal effect of pollutants was enhanced, and $HO^{\bullet}$ was the dominant free radical for benzene degradation.

4 CONCLUSION

At present, groundwater resources have been seriously polluted, and the living environment of human health has been seriously threatened. Groundwater pollution has become an urgent problem for human beings. It is very necessary to research and develop groundwater remediation technology. Groundwater pollution remediation technology is developing towards in-situ, green and efficient. In situ chemical oxidation technology has a good application prospect in the field of groundwater remediation because of its wide application range, complete removal of pollutants, moderate cost, in-situ application and fast treatment speed. It is suggested that further research on slow-release material and double oxidation system should be carried out to improve the feasibility of their application in the remediation of groundwater in actual contaminated sites.

REFERENCES

Chen H, Lu J, Wu L, et al. (2021) Developing a new controlled-release KMnO4 for groundwater DNAPL remediation. Environmental Technology & Innovation, 24: 102064.

Fu X, Gu X, Lu S, et al. (2016) Enhanced degradation of benzene in aqueous solution by sodium percarbonate activated with chelated-Fe(II). Chemical Engineering Journal, 285: 180–188.

Georgi A, Schierz A, Trommler U, et al. (2007) Humic acid modified Fenton reagent for enhancement of the working pH range. Applied Catalysis B: Environmental, 72(1): 26–36.

Huang K-C, Zhao Z, Hoag G E, et al. (2005) Degradation of volatile organic compounds with thermally activated persulfate oxidation. Chemosphere, 61(4): 551–560.

Kao C M, Huang K D, Wang J Y, et al. (2008) Application of potassium permanganate as anoxidant for in situ oxidation of trichloroethylene-contaminated groundwater: a laboratory andkinetics study. Journal of Hazardous Materials, 153(3): 919–927.

Liang C, Bruell C J, Marley M C, et al. (2004) Persulfate oxidation for in situ remediation of TCE. II. Activated by chelated ferrous ion. Chemosphere, 55(9): 1225–1233.

Lee E S & Schwartz F W. (2007) Characteristics and applications of controlled-release KMnO4 for groundwater remediation. Chemosphere, 66(11): 2058–2066.

Liu X, He S, Yang Y, et al. (2021) A review on percarbonate-based advanced oxidation processes for remediation of organic compounds in water. Environmental Research, 200: 111371.

Mei Q, Sun J, Han D, et al. (2019) Sulfate and hydroxyl radicals-initiated degradation reaction on phenolic contaminants in the aqueous phase: Mechanisms, kinetics and toxicity assessment. Chemical Engineering Journal, 373: 668–676.

Oh S-Y, Kang S-G, Kim D-W, et al. (2011) Degradation of 2,4-dinitrotoluene by persulfate activated with iron sulfides. Chemical Engineering Journal, 172(2): 641–646.

Watts R J, Stanton P C, Howsawkeng J, et al. (2002) Mineralization of a sorbed polycyclic aromatic hydrocarbon in two soils using catalyzed hydrogen peroxide. Water Research, 36(17): 4283–4292.

Yang L, Zhao Y S, Mang B W, et al. (2011) Treament of BTEX in groundwater by Fenton's and Fen ton-like oxidation reaction and the kinetics. Chinese Journal of Environmental Engineering, 5(05): 992–996.

Zhou Y, Xiang Y, He Y, et al. (2018) Applications and factors influencing of the persulfate-based advanced oxidation processes for the remediation of groundwater and soil contaminated with organic compounds. J Hazard Mater, 359: 396–407.

Advances in Applied Chemistry and Industrial Catalysis – Saikia (Ed.)

Optimization and upgrading of chemical corrosion resistance testing methods for ceramic tiles

Liming Cui
Zibo Product Quality Testing Research Institute, Zibo, Shandong, China

Hui Gao*, Siming Du & Le Zhao
China Building Material inspection and Certificate Group (Shaanxi) Co., Ltd, Xi'an, Shaanxi, China

ABSTRACT: According to the latest edition of the standard content, this paper provides a fast and efficient testing method for the chemical corrosion resistance of ceramic tiles. For the optimization and upgrading of chemical corrosion resistance testing methods of ceramic tiles, two kinds of different testing methods of unglazed tiles and glazed tiles are integrated and optimized. Through process combination optimization, the system of the test process is realized, and the operation is convenient, simple, shortens the test time, improves the test efficiency, high accuracy, small error, high efficiency, and wide application range. The experiment time is shortened but the experiment result is accurate and efficiency is greatly improved.

1 INTRODUCTION

The chemical corrosion resistance of ceramic tile is tested according to GB/T 3810.13-2016 ceramic tile test method, Part 13 "Determination of chemical corrosion resistance", international standard ISO10545-13:2014, and other standards. It is also the detection of 8 kinds of chemical reagents, unglazed brick needs at least 12 + 5 days of detection time, the glazed brick needs to be divided into two categories of the test machine, among which 5 kinds of main hydrochloric acid and potassium hydroxide test needs at least 4 days of the test, resistant to household chemicals, swimming pool salts and citric acid do need additional 24h test. If the chemical corrosion resistance test of unglazed bricks and glazed bricks is carried out in large quantities, a lot of time will be wasted on different types of tiles, different types of chemical reagents, and different test time allocations. Therefore, we need to optimize the test scheme, sort out the test time, allocate chemical reagents reasonably, and be orderly.

2 OPTIMIZED AND UPGRADED THE TEST PROCESS

2.1 *Chemical reagent* [1]

2.1.1 *Household chemicals*

① Ammonium chloride solution: 100g/L

2.1.2 *Swimming pool salts*

② Sodium hypochlorite solution: 20mg/L (Consisting of approximately 0.13 active sodium hypochlorite by a mass fraction)

2.1.3 *Low concentrations of acids and bases*

③ A solution of 0.03 hydrochloric acid with concentrated hydrochloric acid (ρ=1.19g/mL)
④ Citric acid solution: 100g/L
⑤ Potassium hydroxide solution: 30g/L

*Corresponding Author: 13020768556@126.com

DOI 10.1201/9781003308553-13

2.1.4 *High concentration of acids and bases*

⑥ Hydrochloric acid solution with a volume fraction of 0.18 is prepared by concentrated hydrochloric acid ($\rho = 1.19$g/mL)

⑦ Lactic acid solution with a volume fraction of 0.05

⑧ Potassium hydroxide solution 100g/L

2.2 *Optimization and upgrading of unglazed brick experimental steps*

Standard "Take samples of 50*50 mm from each brick sample and keep at least one edge as non-cut edge", indicating that the whole brick can be cut to meet the requirements of the experimental method. To improve the detection efficiency, based on meeting the standard "keep at least one edge as non-cut edge", We can cut the unglazed bricks into strips of 100*25 mm, each sample 40 pieces.

Dry the sample in a drying oven at (110 ± 5)°C until constant weight. The 40 samples were divided into 8 groups with 5 pieces in each group. A 1000mL beaker containing the 8 reagents (①②③④⑤⑥⑦⑧) was put into the beaker. The 8 reagents in each beaker were 25mm high. The samples with a non-cutting surface must be completely immersed in the solution, then all the eight beakers were covered with plastic film and placed in a biochemical incubator at (20 ± 2)°C for 12 days. After 12 days, the sample was taken out and rinsed with running water for 5 days, and then completely soaked in water and boiled for 30 minutes. After that, the sample was removed from the water and gently wiped with wring-dried but still wet suede, and then dried in a drying oven at (110 ± 5)°C.

Under sunlight or 300lx of an artificial light source (but direct irradiation should be avoided), $25 \sim 30$ cm away from the sample, observe the changes of the non-cut edge and the immersed part of the cut edge on the sample surface with naked eyes. It can be divided into the following grades [2].

For ① and ② test fluids:

UA: No visible change

UB grade: visible change on cutting edge

UC class: changes visible on cut edges, uncut edges, and surfaces

For ③, ④, ⑤ test fluids:

ULA: No visible change

ULB class: visible change on cutting edge

ULC class: changes visible on the cut edge, uncut edge, and surface

For ⑥, ⑦, ⑧ test liquid:

UHA: no visible change

UHB: changes visible at the cutting edge

UHC: changes visible on cut edges, uncut edges, and surfaces [3]

2.3 *Optimization and upgrade of glazed brick experimental steps*

The cylinder is cut into a 50mm high PVC pipe with an outer diameter of ϕ40mm, and 8 cut PVC short tubes are used for each group of tests. Glaze tiles are cut into 300*300mm sizes [4].

In the standard, "When testing the corrosion resistance of household chemicals, swimming pool salts, and citric acid, the test solution shall contact the sample for 24h, remove the cylinder and thoroughly clean the sealing material on the glaze with an appropriate solvent. "The test hydrochloric acid and potassium hydroxide corrosion resistance, make the test liquid and sample contact for 4 days, gently shake the device once a day, and ensure the liquid level of the test liquid unchanged. After 2 days, the solution is replaced, and after another 2 days, the cylinder is removed and the sealing material on the glaze is thoroughly cleaned with an appropriate solvent."

According to the repetitions in the above standard, 2 tiles must be cut for each batch of glazed ceramic tile samples to be tested with 8 chemical reagents. After sealing three small cylinders on a glazed ceramic tile, the three chemical reagents (①, ②, ③) were immersed in a biochemical incubator at (20 ± 2)°C for 24h, the sealing materials on the glazed surface were removed and cleaned, and then the visible changes were observed. The five chemical reagents were placed in the

biochemical incubator at (20 ± 2)°C. The solution was replaced after 2 days. The sealing material on the glaze was cleaned after 2 days to observe whether there were visible changes. As for such a complicated operation, it not only wastes time but also is complicated and easy to be disordered. We can complete all the test steps in a short time by optimizing the test operation process with overall planning:

Cut only one 300*300mm sample from the same batch of glazed tiles, as shown in Figure 1. First, five SMALL PVC cylinders are bonded with sealing material (usually petroleum jelly) on the glazed tiles, and then five chemical reagents (③, ⑤, ⑥, ⑦, ⑧) are respectively poured into the biochemical incubator at (20 ± 2)°C. 2 days after the replacement of the corresponding five kinds of chemical reagents, 1 day after adding three adhesive new PVC small cylinder respectively into (1), (2), (4) the three kinds of chemical reagents in the biochemical incubator (20 + 2)°C, 1 day after the end of the test from the biochemical incubator has eight kinds of chemical corrosion of PVC small cylinder, the chemical reagent into special chemical liquid waste processing box, Clean the sealing material on the surface of glazed ceramic tile.

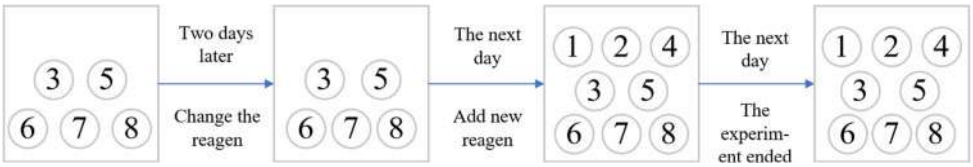

Figure 1. Schematic diagram of chemical corrosion resistance of ceramic tile after optimization.

Mark several lines on the untreated part of the glaze with an HB pencil and wipe the lines with a damp cloth. If pencil marks do not rub off, the bricks will be recorded as "not suitable for the standard grading method" and can only be evaluated by the visual grading method, while the grading system shown in Figure 2 is not suitable.

Bricks that cannot be tested by pencil shall be graded by the following method.

For ① and ② test fluids:

GA (V): no visible change
GB (V) class: there are obvious changes on the surface
GC (V): Partial or total damage to the original surface
For ③, ④, ⑤ test fluids:
GLA (V): no visible change
GLB (V): there are obvious changes on the surface
GLC (V): Partial or total damage to the original surface
For ⑥, ⑦, ⑧ test liquid:
GHA (V): no visible change
GHB (V): there are obvious changes on the surface
GHC (V): Partial or total damage to the original surface [5]

For the bricks that passed the pencil test, the following steps were continued to be evaluated and graded according to the grading system shown in Figure 2. The reflection test involves placing the brick in such a device that the image of a 40W bulb is reflected on an unprocessed surface. The incident angle of the light on the brick surface is about 45°C, and the distance between the brick and the light source is (350 ± 100) mm. The evaluation parameter is the reflection clarity, not the brightness of the brick surface. Adjust the position of the rotation so that the light falls on both the treated and non-treated surfaces, and check whether the image on the treated surface is blurred. This test is not suitable for certain glazes. Especially on a matte glaze. If the reflection is clear, position class B. If the reflection is fuzzy, position class C.

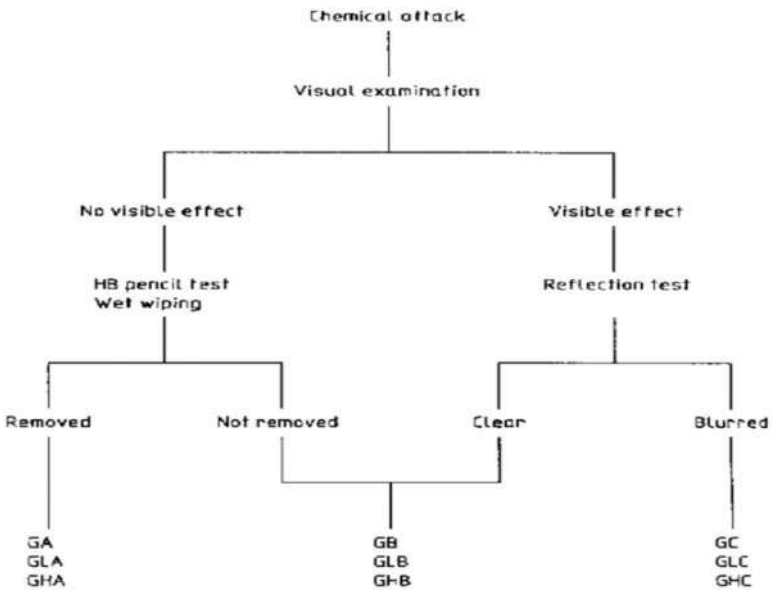

Figure 2. Classification for the chemical resistance of glazed tiles.

It is stipulated in the standard that “the light source can be a solar or artificial light source (about 300lx), but avoid direct sunlight”, “the incidence Angle of light on the brick surface is about 45°C, and the distance between brick and light source is (350±100) mm”. We use the auxiliary lighting is a small desk lamp, but small desk lamp 300 lx light requirements for the indoor environment itself light brightness is not unified, so the small desk lamp auxiliary lighting to reach about 300 lx illumination requirement, so small desk lamp must be an adjustable light source, lamp holder must be a rotating bending lamp holder, and lamplight illuminates area should be more than 300 * 300 mm.

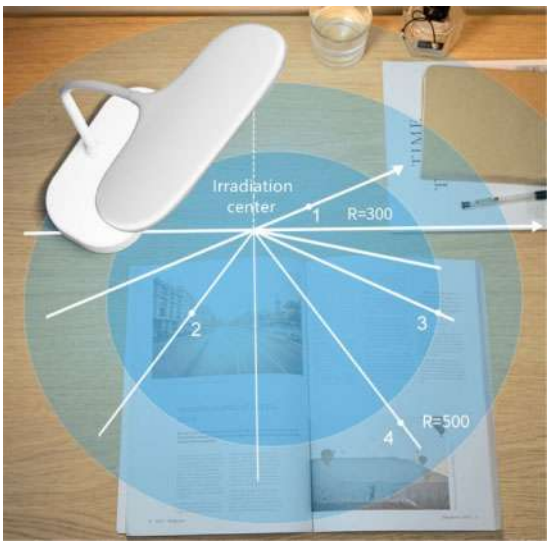

Figure 3. Range of light.

The sealing material recommended in the Standard is plasticine. Compared with vaseline, plasticine has many problems, such as darkening color after repeated use, being difficult to clean, easy to stick to the surface of ceramic brick, and affecting the result of pencil scratch test. Therefore, milky white vaseline is recommended as the sealing material.

Figure 4. Petroleum jelly.

3 CONCLUSION

There are many kinds of test chemical reagents, the test process is complicated, the test period is long, and the judgment basis is messy, so the test is easy causes a confused sense of blindness for the detection personnel. By optimizing the experimental steps and method, there is no glaze tile and brick of pottery and porcelain can be divided into glazed brick two categories, then respectively according to different without glair brick and tile experiment method corresponding optimization steps, especially glazed brick by reasonable planning can not only save the test sample, at the same time efficiently save test time, the use of the overall planning test easy determination results become clear at the same time, reduce the chance of trial errors.

ACKNOWLEDGMENTS

This work was supported by the building and sanitary ceramics technical service standardization innovation platform.

REFERENCES

BS EN ISO 10545-13-1997, Ceramic Tile. Determination of chemical corrosion resistance [S].
GB/T 18749-2019, Chemical corrosion resistance of ceramic tower packing technical conditions [S].

GB/T 3810.13-2016 Ceramic tile Test Method – Part 13 “Determination of chemical corrosion resistance” [S].
Hu Lihong. 2016(07):47-50. Discussion on influencing factors of chemical corrosion resistance determination of ceramic bricks [J]. Quality Exploration.
Li Wenqing. 2017.92-93. Interpretation of new International Standard for determination of chemical corrosion resistance of Ceramic Tiles [C]. China Building Materials Science and Technology Magazine Co., Ltd.

Advances in Applied Chemistry and Industrial Catalysis – Saikia (Ed.)

Research on evaluation system of business model for recovery and reuse of sulfur hexafluoride

Yanming Jin*, Zhuonan Li** & Xinli Xiao***
State Grid Energy Research Institute Co, Ltd, Beijing, China

Yue Zhao# & Feng Zhu##
State Grid Anhui Electric Power Research Institute, Hefei, China

ABSTRACT: Sulfur hexafluoride (SF6) gas has been widely used in high and medium voltage electrical equipment due to its excellent insulation and arc extinguishing properties. According to statistics, the global annual output of sulfur hexafluoride (sulfur hexafluoride) gas is about 20,000 tons, and about 80% is used in the power industry. With the large-scale construction and commissioning of AC/DC UHV projects, the consumption of sulfur hexafluoride gas is increasing. However, the greenhouse effect of sulfur hexafluoride gas is more than 23,900 times that of CO2. It can exist in the air for more than 3,200 years. It is one of the six gases prohibited by the Kyoto Protocol. The controlling and reduction of greenhouse gas emission is an important way to deal with climate change and slow down global warming. This paper constructs an evaluation system for the recovery and reuse of sulfur hexafluoride business model, and evaluates and analyzes the main application scenarios currently available.

1 INTRODUCTION

The recovery and reuse of sulfur hexafluoride gas has become an important manifestation of the State Grid's demonstrating social responsibility. Through the recovery and reuse of sulfur hexafluoride gas, the business concept has been extended, and a sustainable development mechanism based on the recovery and reuse of sulfur hexafluoride has been established. The business model can further refine the commercial value of sulfur hexafluoride gas recovery and reuse, and comprehensively improve the economic, social and transformation benefits [1].

Figure 1. Distribution of sulfur hexafluoride treatment center.

Corresponding Authors: *jinyanming@sgeri.sgcc.com.cn, **lizhuonan@sgeri.sgcc.com.cn, ***xiaoxinli@sgeri.sgcc.com.cn, #285130951@qq.com and ##feng342524@126.com

DOI 10.1201/9781003308553-14

2 BUSINESS MODEL OPTIONS

2.1 *Bidding mode*

The public bidding method is used to publish the bidding announcement of sulfur hexafluoride disposal on the e-commerce platform of State Grid Corporation of China, and invite recyclers who are interested in participating in the bidding and qualified to participate in the bidding activities.

2.2 *Framework agreement model*

Provincial power grid material companies consider all aspects of the business performance and recycling capacity of sulfur hexafluoride recyclers, select enterprises with hazardous waste recycling qualifications, and after comprehensive evaluation by the bidding committee, use entrusted or competitive negotiation methods to determine recyclers and related For the unit price of material disposal, an annual framework agreement is signed with the recycler. Within the term of the agreement, each unit regularly reports the disposal requirements in accordance with the applicable rules. When the storage volume reaches the agreed limit, the material company will notify the recycler to collect it at the agreed price.

2.3 *Extended producer responsibility system*

When bidding for the procurement of some hazardous wastes or related equipment, add recycling requirements to the initial technical specifications, specify the recycling conditions and cycle, clarify the equipment supplier's responsibility for the recycling of sulfur hexafluoride, and require the equipment supplier to regularly or quantitatively review the hexafluoride Sulfur is recovered and disposed of in accordance with the law.

2.4 *Self-utilization and disposal*

The entire production line for recycling and reuse is built independently, and all the work is done by internal units.

2.5 *Paid disposal*

Pay to the recyclers with disposal qualifications, sign a disposal agreement, and dispose of them for a fee. Considering the total amount of sulfur hexafluoride each year, some provincial companies are under greater financial pressure to adopt paid disposal methods (Bucherere 2011; Yong 2006).

3 BUSINESS MODEL EVALUATION INDEX SYSTEM

Based on actual analysis, literature research, preliminary screening and expert evaluation, the evaluation index system for the business model of sulfur hexafluoride recycling and reuse is finally determined. The index system is divided into four first-level indicators: profitability, operation ability, growth ability, and environmental protection ability. A number of second-level indicators are set up under each first-level indicator, thereby establishing evaluation indicators for the business model of sulfur hexafluoride recovery and reuse from multiple dimensions, in order to make a comparison of the business model of sulfur hexafluoride recovery and reuse.

3.1 *Profitability*

Profitability refers to the company's ability to make profits in a certain period of time. Profitability is the most direct and basic index to evaluate the company's profitability, and it is also the prerequisite for analyzing and evaluating the company's profitability quality. Good profitability is the internal

driving force and source of the company's continuous operation and the basic guarantee for obtaining high-quality profits. This article selects the main business profit rate and return on net assets to measure the company's profitability.

①Sulfur hexafluoride recycling business profit margin

Main business profit rate = main business profit/main business income × 100%

② Return on net assets

Return on net assets = net profit/(net assets at the beginning of the year + net assets at the end of the year)/2 × 100%

③ Sales net profit margin

Net sales profit ratio = company net profit/net sales × 100%

④ Market share

Market share = company sales/total market sales × 100%

3.2 *Operational capability*

The performance of the company's operations directly determines the company's current capital use and future capital expansion prospects. This article selects total asset turnover rate, asset return rate and channel channels to measure the company's operating capabilities.

① Total asset turnover rate

Turnover rate of total assets = net operating income/total average assets × 100%

② Return on assets

Return on total assets-net profit before interest and tax/average total assets × 100%

③ Channel access

Channel access is the channel for waste treatment companies to recycle and process solid waste to achieve their own revenue goals.

3.3 *Growth ability*

The company's ability to grow is the company's ability to achieve business expansion and sustainable development through continuous expansion of scale, continuous innovation and change on the basis of its survival. If the company wants to win in the fierce competition in the sulfur hexafluoride recovery market, it must achieve sustainable growth.

① Main business income growth rate

Main business income growth rate = (this period's main business income-last period's main business income)/last period's main business income × 100%

② Net profit growth rate

Net profit growth rate = this year's net profit growth/last year's net profit × 100%

③ The growth rate of net assets

Net assets growth rate = (end net assets-beginning net assets)/beginning net assets × 100%

④ Technological innovation ability

Technological innovation ability refers to the ability to continuously provide new ideas, new theories, new methods and new inventions with economic value, social value, and ecological value in various fields of practical activities.

3.4 *Risk protection*

At present, one of the management bottlenecks encountered by most SF6 service providers in the further development is how to obtain surplus value from cutting corners and irregular operations to fully excavating equipment, staff efficiency and improving service quality to improve profits (Guo 2009).

① Pollutant discharge rate

Pollutant discharge amount = various pollutant discharge amount/income ×100%

② Comprehensive energy consumption rate

Comprehensive energy consumption rate = comprehensive energy consumption/income ×100%

In summary, the business model evaluation system for the recovery and reuse of sulfur hexafluoride is obtained as shown in the following table

Table 1. Evaluation system for business model of sulfur hexafluoride recovery and reuse.

Primary indicators	Secondary indicators
Profitability	Recycling business profit margin Return on net assets Sales net profit margin Market share
Operational capability	Total asset turnover rate Return on assets Channel access
Growth ability	Main business income growth rate Net profit growth rate The growth rate of net assets Technological innovation ability
Risk protection	Pollutant discharge rate Comprehensive energy consumption rate

4 RESULTS AND ANALYSIS

The analytic hierarchy process decomposes the factors related to decision-making into goals, criteria, plans and other levels, and then progressively solves the priority of each element at each level to an element at the upper level. It is a multi-factor decision-making that combines qualitative and quantitative analysis. The analytic process requires the following steps:

4.1 *Establish a hierarchical structure model*

The factors in the actual problem are decomposed into different levels of goals, criteria, and plans from top to bottom. While the factors at the same level are controlled by the lower-level factors, they will also affect the upper-level factors.

4.2 *Construct a pairwise comparison judgment matrix*

When comparing the importance of elements Xi and Xj in the same level relative to a factor of the previous level, use the value aij to describe this relative importance. Assuming that there are n related factors in this level, then A=(aij)n×n Judgement matrix called pairwise comparison:

$$A\left(a_{ij}\right)=\begin{bmatrix} a_{11} & a_{12} & \cdots & a_{1n} \\ a_{21} & a_{22} & \cdots & a_{2n} \\ \cdots & \cdots & \cdots & \cdots \\ a_{n1} & a_{n2} & \cdots & a_{nn} \end{bmatrix} \tag{1}$$

The value of aij in the judgment matrix can be assigned by technical experts according to the scale reference table.

4.3 *Calculation of the relative weight of each indicator*

Sum up each column of the judgment matrix A to get $\sum_{i=1}^{n} a_{ij}$, here

$$b_{ij} = \frac{a_{ij}}{\sum_{i=1}^{n} a_{ij}} \tag{2}$$

$$w_{ij} = \frac{\sum_{j=1}^{n} b_{ij}}{\sum_{i=1}^{n} a_{ij}} \tag{3}$$

$$AW = nW \tag{4}$$

In the formula, W=(w1, w2, wn)T, n is the characteristic value.

4.4 *Consistency test of judgment matrix*

$$CI = \frac{\lambda_{max} - n}{n - 1} \tag{5}$$

$$CR = \frac{CI}{RI} \tag{6}$$

Where is the maximum eigenvalue of the n-th order judgment matrix A.

After calculation, the sub-items of the five types of sulfur hexafluoride recycling business models are as follows:

Table 2. Five types of business model evaluation scores.

Primary indicators	Secondary indicators	Mode 1	Mode 2	Mode 3	Mode 4	Mode 5
Profitability	Recycling business profit margin	0.57	0.32	0.18	0.09	0.76
	Return on net assets	0.19	0.37	0.53	0.29	0.82
	Sales net profit margin	0.52	0.36	0.28	0.13	0.69
	Market share	0.26	0.37	0.68	0.91	0.32
Operational capability	Total asset turnover rate	0.54	0.32	0.28	0.22	0.61
	Net profit growth rate	0.33	0.41	0.27	0.19	0.52
	Channel access	0.63	0.58	0.18	0.85	0.79
Growth ability	Main business income growth rate	0.46	0.55	0.59	0.72	0.39
	Net profit growth rate	0.53	0.44	0.46	0.12	0.72
	The growth rate of net assets	0.50	0.55	0.48	0.63	0.69
	Technological innovation ability	0.35	0.41	0.53	0.61	0.27
Risk protection	Pollutant discharge rate	0.46	0.76	0.84	0.97	0.62
	Comprehensive energy consumption rate	0.62	0.59	0.78	0.47	0.83

After calculation and integration, the scores are as follows:

Table 3. Overall business model evaluation and sub-item scores.

	Mode 1	Mode 2	Mode 3	Mode 4	Mode 5
Profitability	0.836	0.711	0.924	0.968	1.352
Operational capability	1.116	0.867	0.729	0.927	1.341
Growth ability	0.930	0.983	1.035	1.141	1.104
Risk protection	0.772	0.962	1.146	1.078	1.036
Overall score	**2.575**	**2.532**	**2.583**	**2.536**	**2.960**

5 CONCLUSION

It is not difficult to see from the calculation results that the current stage of paid disposal and utilization is the most ideal way. Its main advantages are reflected in profitability and operational capacity, which is because of the convenience of current paid disposal and utilization and the diversity of available suppliers, which creates a huge advantage.

However, from the perspective of growth capabilities, the company's self-use and disposal methods can be applied to Internet platform construction and industry incubation methods, relying on company resources to expand more services, and have strong growth capabilities.

From the perspective of risk protection, the promotion of the extended producer responsibility system has a significant role in promoting the recycling and reuse of solid waste, which facilitates the definition and restriction of its responsibilities at the level of the producer of sulfur hexafluoride gas and related equipment. As a producer, it will also have certain technical advantages or cost advantages in terms of recycling and other related technologies compared to other models. If the system is widely promoted, it will significantly reduce costs for the company and reduce the risk of management and control caused by incomplete qualifications of external manufacturers or poor service quality.

ACKNOWLEDGMENTS

This work is supported by Science and Technology Project of State Grid Corporation of China Research and application of management and control technology for The Recovery and Reuse of Sulfur Hexafluoride Gas (8100-202020149A-0-0-00).

REFERENCES

Bucherere, Ucklemann D. (2011) Business models for the Internet Things. Architecting the Internet of Things. Berlin Heidelberg: Springer-Verlag: 253–277.

Guo P, Huang G H. (2009) Inexact fuzzy-stochastic mixed-integer programming approach for long-term planning of waste management–Part A: methodology. Environ Manage, 91(2): 461–470.

Liang Fangjian, Wang Yu, Wang Zhi long, et al. (2010) The Application Situation of SF6 in Electrical Equipment and Some Problem. Insulating Materials, 43(3): 43–46.

Yong P, Li, Guo H, Huang. (2006) Minimax regret analysis for municipal solid waste management: an interval-stochastic programming approach. Air Waste Manage, 56(7): 931–944.

Advances in Applied Chemistry and Industrial Catalysis – Saikia (Ed.)

The biochemical effects of rhubarb extract's six anthraquinone derivatives in treating lung cancer

Zujie Chen
Peking University, Beijing, China

Suyi Liu
Basis International School, Shenzhen, China

Xiangbo Sun
Experimental High School, Shandong, China

Jingyun Wu*
University of North Carolina at Chapel Hill, Chapel Hill, NC, USA

Hongbo Zhu
SMIC Private School Shanghai, Shanghai, China

Runjin Zhu
University of California Santa Cruz, Santa Cruz, CA, USA

ABSTRACT: Rhubarb, an herbaceous perennial that belonged to the family Polygonaceae, has been a plant of various uses for human consumption worldwide. Rhubarb is regarded as a potential anti-cancer compound in Traditional Chinese Medicine. This study is to evaluate rhubarb and its six major anthraquinone derivatives' effectiveness in treating lung cancer, through *in vitro* (MTT cytotoxicity assay, FACS Annexin V/PI assay, Western blot assay, Boyden chamber assay) and *in vivo* (A549 xenograft in mice and enzyme-linked immunosorbent assay) experiments. Possible results are deduced, interpreted, and discussed.

1 INTRODUCTION

Lung cancer is one of the deadliest health concerns in the 21st century, with a staggering 2.21 million cases in 2020 alone. Smoking, combined with other environmental toxins such as pollution (World Health Organization 2021), contributes heavily to lung cancer diagnosis and deaths; in fact, up to 90% of the 1.80 million people killed by lung cancer in 2020 are associated with tobacco (Huangm et al. 2007; Xiang et al. 2020). Its chemical components are responsible for nicking DNA strands to cause replication errors and damage to other critical cell cycle regulation structures such as P53 tumor suppressor genes with point mutations (especially concerning the nucleotide Guanine) (Chang et al. 2012). Accompanied by the prevalence of COVID-19, lung diseases become a greater concern worldwide. Meanwhile, cyclins and cyclin-dependent kinases (CDK) that are responsible for controlling the interphase of the cell cycle have malfunctioned due to the tar found in cigarettes (Synthergo 2021), resulting in stimulated tumorous growth. As scientists actively develop new treatments to combat this disease, traditional Chinese medicine (TCM) is a potential complementary option. Rhubarb is a noteworthy ingredient whose medical value was explored since ancient times and is still extensively used inf a variety of medications, including Lianhuaqingwen (LHQW), a medicine used to treat influenza and reduce inflammation within the lungs.

*Corresponding Author: jingyun@live.unc.edu

DOI 10.1201/9781003308553-15

Roots and stems of rhubarb contain anthraquinone derivatives among which emodin, aloe-emodin, rhein, chrysophanol, physcion, and danthron are particularly rich. Existing studies have provided evidence suggesting cancer-inhibiting effects of anthraquinone derivatives. Although anthraquinone derivatives share similar chemical structures, they have distinctive bio-activities and should therefore be analyzed separately (Huang et al. 2007). However, few compare each anthraquinone derivative's cancer-inhibiting effects and that of a combination of multiple compounds in rhubarb extract. The primary purpose of our research is to assess the anti-lung cancer effects of anthraquinone-derivative-containing rhubarb extract, and that of each of the six anthraquinone derivatives isolated from rhubarb extract, by measuring their cytotoxicity and apoptosis-inducing effects on A549 cells and HPAEpiC *in vitro* (MTT cytotoxicity test, FACS Annexin V/PI assay, and Western blot assay), metastasis inhibiting effects to A549 cells *in vitro* (Boyden chamber assay), and tumor growth and inflammation inhibiting effects *in vivo* (A549 xenograft in mice and enzyme-linked immunosorbent assay (ELISA)). We hypothesize that increasing concentrations of rhubarb extract or its six anthraquinone derivatives will have the following effects on A549 cells: inhibiting growth and proliferation, inducing apoptosis, regulating cytokines expression, and inhibiting metastasis; without interrupting the growth of normal human pulmonary alveolar epithelial cells (HPAEpiC).

This study not only provides insights into the active compound composition of rhubarb and its biochemical functions in the treatment of lung cancer but also opens the door for more in-depth investigations of possible TCM-based cancer treatments.

2 MATERIALS AND METHODS

2.1 *Chemicals and reagents*

Dried root and rhizome of rhubarb (*Rheum officinale*) are ground and extracted by reflux extraction with diethyl ether. Diethyl ether is removed from the extracted solution with rotary evaporation, and dry solute is collected.

For further separation and identification of the six anthraquinone derivatives from rhubarb extract, high-pressure liquid chromatography apparatus will be set up as well as its associated standard solutions. Reagents used as the separation's mobile phase include 0.01% (v/v) phosphoric acid water solution and at least six methanol solutions of different concentrations, from 15% to 60%, for gradient elution. The HPLC analysis will be carried out using a photodiode-array detector (PDA) and an autosampler under the condition of 25° C on a 150 mm × 4.6 mm column. The flow rate will be set to 1 mL/min, and the injection volume will be 20 μL. To optimize the resolution and separation of the resulting peaks, the quantitation wavelength will be set at 254 nm, and the UV spectra will be taken at multiple points of the peaks to check for peak homogeneity (Panichayupakaranant et al. 2009). The peaks of anthraquinones collected will be identified and analyzed using both a diode-array detector and a series of HPLC standards from ThermoFisher Scientific.

2.2 *Cell culture*

The type of lung cancer cells used in this experiment, A549 cells, can be found in numerous FDA-approved research experiments. The advantageous characteristics of this cell include its relatively short division time and suitability for investigating lung-related infections (Chang et al. 2012). A549 cells are grown inside a culture using a base medium of F12K (Gibco /Invitrogen). 10% fetal bovine serum (FBS) is also added to the base medium to make the complete growth medium that allows for exponential growth (Chang et al. 2012). The cell line is left to grow at 37°C and in a 5% CO2 environment (Li et al. 2018; Synthergo 2021).

Human pulmonary alveolar epithelial cells (HPAEpiC) are used in this study, modeling normal alveolar epithelial cells. HPAEpiC is grown in vitro on an alveolar epithelial cell growth medium, 2% FBS, in T-75 flasks, and incubated at 37°C, under 5% CO2 overnight.

2.3 *MTT cytotoxicity test*

Cytotoxicity of rhubarb extract and each anthraquinone derivative is examined using the MTT cytotoxicity test. A549 cells and HPAEpiC are placed in well plates at 5×10^4 cells/well. Each well is treated with serial dilution of rhubarb extract, an anthraquinone derivative, or 5-fluorouracil as the positive control, or DMSO (concentration < 1%) as the negative control. The final concentration of anthraquinone derivative is 0.1, 0.3, 1, 3, 10, 30 μM in single anthraquinone derivative treated wells. The final concentration of the sum of all six anthraquinone derivatives is 0.1, 0.3, 1, 3, 10, 30 μM in rhubarb extract-treated wells.

The cells are incubated at 37°C, 5% CO2 for 48 hours under treatment. MTT labeling reagent is added to each well, at a final concentration of 0.5 mg/mL. The cells are incubated at 37°C, 5% CO2 for 4 hours, and washed twice with PBS after incubation. 100 μL of DMSO is added to each well. OD570 is measured for each well, and cell survival rate relative to the negative control (DMSO) is calculated as a measure of cytotoxicity. Survival rate (%) = (A negative control - A experiment)/A negative control * 100% (Chang et al. 2012).

2.4 *FACS Annexin V/PI Assay*

To investigate cell apoptosis, cells or tumor samples are divided into 3 groups: a negative control group (treated with DMSO), 6 experimental groups (each treated with one anthraquinone derivative, at various concentrations), and a positive control group (treated with 5-Fluorouracil). For in vitro experiments, A549 cells, at 1×10^6 cells per well, are treated with compounds of assigned groups for 48 h. Cells from each well are then harvested and resuspended with PBS added to a final volume of 500μL. For in vivo tumor experiments, the tumor sample will be pre-processed as mentioned in 2.3 with PBS added to a final volume of 500μL, afterwards the numbers of cells will be counted and 10^6 tumor cells will be used for further analysis.

The cells are incubated with 5μL Annexin V-FITC and 5μL PI double per well at room temperature in the dark. The cells are analyzed by flow cytometry. The results are shown in a 2-dimensional figure with Annexin V intensity as its horizontal axis and PI intensity as its vertical axis (Figures 6 and 7). The lower left area of the figure represents normal cells, while the lower right and upper right regions represent early and late apoptotic cells, respectively. The sum ratio of early and late apoptotic cells can be calculated by FlowJo software.

2.5 *Western blot assay on apoptosis-related proteins*

A549 cells in each well are harvested by RIPA buffer after treatment with one anthraquinone derivative in various concentrations. The samples containing the same weight of the lysate protein are separated using 12% SDS-PAGE electrophoresis for 45 minutes and then are electrotransferred to 0.45μm PVDF membranes. After inhibiting the membrane with 5% bovine serum albumin (BSA) in PBST buffer for 1h at room temperature, the membrane was incubated with primary antibodies (caspase 3/8/9 and PARP) at 4°C overnight or room temperature for 1h. Caspase 3/8/9 and PARP antibodies are diluted at 1:1000 and pretested on the positive control models to determine the final dilution ratio (Altogen Labs 2021). The membranes are then incubated with corresponding fluorochrome-labeled secondary anti-rabbit or mouse secondary antibodies for 1h at room temperature. Finally, the proteins are detected by the Bio-Rad Gel imaging system. 5-Fluorouracil treated A549 cells are used as a positive control. A549 cells treated with fresh F12K containing 0.1%, 0.5%, or 1.0% of DMSO, but without any Rhubarb extract or drug, are used as a negative control.

2.6 *Boyden chamber assay*

The Boyden chamber assay provides a quantitative analysis of migratory responses of the cells. Boyden chamber is made up of chemotaxis chambers, with wells of the upper and lower chambers segregated by membranes with 8 – μm-pores, and 30μg of diluted collagen (10μg/mL) added

to each well of the lower chamber. A549 cells (10^4 cells/well) are placed in the upper chamber and treated with serial dilution of rhubarb extract, or an anthraquinone derivative in the upper compartment. DMSO solvent, serves as the negative control in the experiment, while A549 cells are allowed to migrate through the pores of the membrane into the lower chamber for 48 hours at 37°C. After the incubation time, the membrane is fixed with methanol, and stained by an effective marker β-galactosidase. Micrographs are taken using a digital camera connected to the microscope at 50X magnification, and the numbers of cells in the lower chamber can be calculated on the image. Specifically, the experiment is repeated with three more wells for the calculation of the migrated cells to eliminate the possible existing confounding errors during the experimental process.

2.7 *A549 Xenograft model*

A common C57BL/6 strain of mice kept for 6-7 weeks is used in the experiment (Liu et al. 2012). They have been maintained in pathogen-free and controlled conditions under ethical guidelines. Each mouse receives one injection of the cancer cell amounting to 100 microliters of one million cells (Bidola et al. 2019) directly into the lung through intrathoracic injection (Zhang et al. 2018) and is observed daily until a tumor ranging from 50-150 mm3 forms. The volume of tumors found inside the test subjects is scanned using a Micro-computed tomography protocol (MicroCT) and Iodine dissolved in absolute ethanol (Dai et al. 2018). The mice groups will be separated into ones found in Table 1 and fed with medicine for 3 weeks. After that, the mice are euthanized with their lungs removed for examination and blood drained (Thermo Fisher Scientific 2019). The removed tumors are incubated for 2 hours with collagenase in serum-free DMEM at 37°C. Tissue digestion is stopped with a serum-containing medium. After being filtered by a 40 μm filter, the supernatant is centrifuged and re-suspended in PBS.

Table 1. Experimental groups for *in vivo* experiments.

Experiment Group	Combination of Medicine Used	The dose required for the length of the experiment (Bajic, 2016)
Negative Control	Saltwater treatment	Salt Water
Positive Control	5-Fluorouracil	Injected into mice daily at a dose of 150mg/kg
Group 1	5-Fluorouracil + Rhubarb	Highest dose of Rhubarb at 2000mg/kg + 150mg/kg 5-FU (Concentration is 10mg/ml)
Group 2 (Low Dose)	Rhubarb	Fed twice a day at 200 mg/kg (Concentration 50mg/ml)
Group 3 (Medium Dose)	Rhubarb	Fed twice a day at 1000 mg/kg (Concentration 10mg/ml)
Group 4 (High Dose)	Rhubarb	Fed twice a day at 2000 mg/kg (Concentration 100mg/ml)

2.8 *Enzyme-linked immunosorbent assay (ELISA)*

Phenotypic indicators of a statistically significant treatment will include measuring the inflammation level using a mouse IL-6 cytokine ELISA Kit from ThermoFisher that can detect the level of cytokines present in a sample of mice fluid (urine, blood, etc). The detection will be performed according to the user manual (Bajic et al. 2016).

2.9 *Statistical analysis*

The statistical significance of numerical data from the MTT cytotoxicity test and FACS Annexin V/PI assay is analyzed using Student's t-test. Each experimental or control group of MTT cytotoxicity test and FACS Annexin V/PI assay is repeated 10 times, and data will be considered significant if $p < 0.05$.

3 POSSIBLE RESULTS

3.1 *Possible results of HPLC separation of rhubarb extract*

Possible results of the separation and identification of the anthraquinone derivatives from rhubarb extract are shown in Table 2.

Table 2. Possible results of the separation and identification of the anthraquinone derivatives from rhubarb extract.

Possible Results	Total Number of Desired Anthraquinones Separated	Note
1	6	Complete separation of all six anthraquinones of interest
2	1 to 5	Separation of only a part of six anthraquinones of interest
3	0	Separation yields none of the six anthraquinones of interest

Note: Three kinds of possible results can be obtained from HPLC. Column 2 denotes the number of experimentally separated anthraquinones associated with each possible result, and the third column highlights what each signifies.

3.2 *Possible results of cytotoxicity of an individual anthraquinone derivative of interest or rhubarb extract on A549 cells and HPAEpiC (Table 3 and Figures 1–5)*

In this section, "negligible cytotoxicity" is declared for an anthraquinone derivative or rhubarb extract if its calculated IC50 value is larger than 4μM (Figure 1). "Noticeable cytotoxicity" is declared if the IC50 value is lower than 4μM (Figure 2).

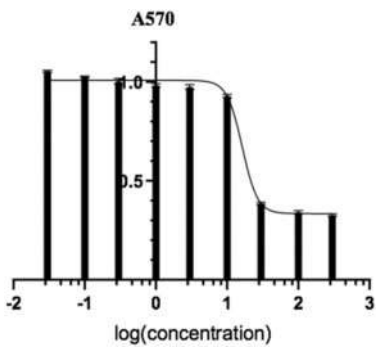

Figure 1. A simulated result of negligible cytotoxicity. The IC50 value is 16.32 μM.

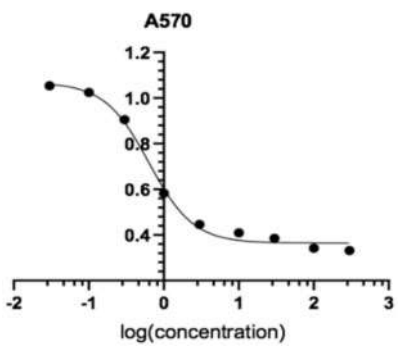

Figure 2. A simulated result of noticeable cytotoxicity. The IC50 value is 0.64 μM.

Possible result 1:

Cytotoxicity of an anthraquinone derivative (emodin, aloe-emodin, rhein, chrysophanol, physcion, and danthron) or rhubarb extract on both A549 cells and HPAEpiC is negligible (Table (1), Figure 1).

Possible Result 2:

An anthraquinone derivative or rhubarb extract shows noticeable cytotoxicity on HPAEpiC (Table 3(2a, 2b), Figure 3, black line). Cytotoxicity of the anthraquinone derivative or rhubarb extract on A549 cells is negligible (Table 3 (2a), Figure 3, blue line), or noticeable, whether it is close to or yet not significantly higher than its cytotoxicity on HPAEpiC (Table 3 (2b), Figure 3 green line & red line).

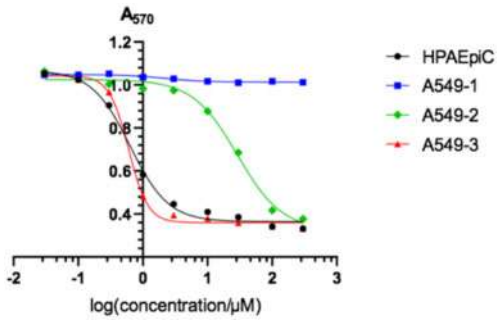

Figure 3. Simulated data of circumstances of possible result 2 illustrating the test object showing significant cytotoxicity to HPAEpiC (IC50=0.635μM), while showing no, low or strong cytotoxicity to A549 cells.

Possible result 3:

An anthraquinone derivative or rhubarb extract shows noticeable cytotoxicity on A549 cells, while the cytotoxicity of the anthraquinone derivative or rhubarb extract to HPAEpiC is neglectable (Table 3(3a & 3b), Figure 4). The cytotoxicity of an anthraquinone derivative or rhubarb extract on A549 cells is compared with the positive control (5-fluorouracil). Its cytotoxicity on A549 cells can be noticeably higher (green line, IC50: 0.158μM, not likely), noticeably lower (black line, IC50: 27.3μM), or close to (blue line, IC50: 1.52μM) the cytotoxicity of 5-fluorouracil (purple line, IC50: 0.82μM) on A549 cells at equivalent concentration.

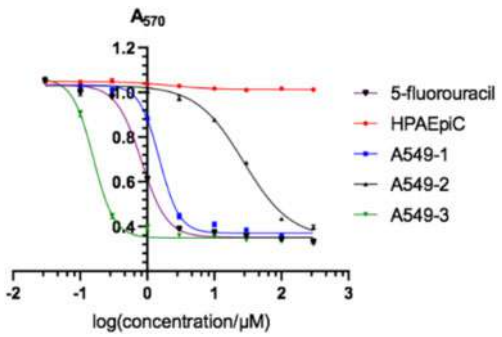

Figure 4. Simulated data of circumstances of possible result 3 illustrating the test object showing no cytotoxicity to HPAEpiC cells while showing near, lower, or higher cytotoxicity to A549 cells compared with the positive control.

If both an anthraquinone derivative and rhubarb extract show Possible Result 3, their cytotoxicity on A549 cells can be compared. Cytotoxicity on A549 cells of the anthraquinone derivative can be noticeably higher, noticeably lower, or close to the cytotoxicity of rhubarb extract on A549 cells at an equivalent dosage (Figure 5 only shows the 2nd possibility).

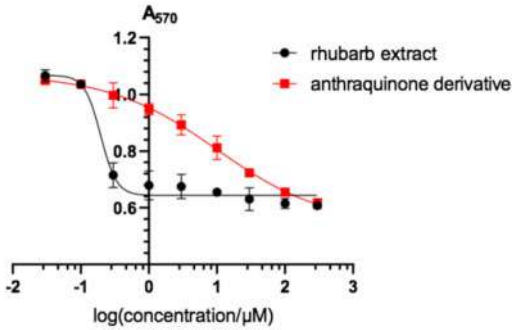

Figure 5. Simulated data of the cytotoxicity of an anthraquinone derivative and rhubarb extract (both showing possible result 3) to A549 cells, when all the other conditions are the same, except for the difference between anthraquinone derivative and rhubarb extract.

Table 3. Possible results of cytotoxicity of rhubarb extract and anthraquinone derivatives on A549 cells and HPAEpiC.

	Cytotoxicity on A549 cells	Cytotoxicity on HPAEpiC
Anthraquinone derivative or rhubarb possible result 1	–	–
Anthraquinone derivative or rhubarb Possible Result 2a	–	++
Anthraquinone derivative or rhubarb Possible Result 2b	+/++	++
Anthraquinone derivative or rhubarb Possible Result 3a	+/++	–
Anthraquinone derivative or rhubarb Possible Result 3b	++	+
Negative control (DMSO)	–	–
Positive control (5-fluorouracil)	++	–

Note: "–" represents negligible cytotoxicity (close to that of the negative control). "++" represents noticeable cytotoxicity, respectively. "+" represents noticeable cytotoxicity, yet significantly lower than the cytotoxicity of the same test object to the other cell.

3.3 *Possible results of cell apoptosis-inducing effects of an individual anthraquinone derivative or rhubarb extract on A549 cells and C57BL/6 mice (Table 4, Figures 6–8)*

Unlike the A549 cells, which can be straightly harvested and performed cell apoptosis assay, the tumor samples must be pre-processed after cultivation in vivo, as the tumors are collected from the C57BL/6 mice and post-processed as we mentioned in methods 2.3. Cell apoptosis assay is firstly carried out by using FACS to determine Annexin V and PI expression.

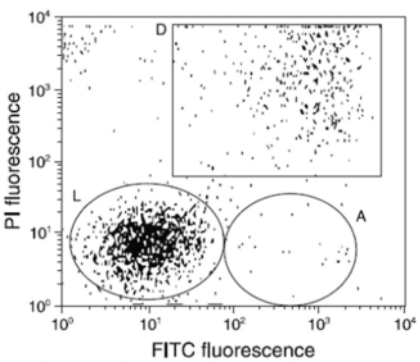

Figure 6. Simulated data of FACS Annexin V/PI assay results of A549 or mouse tumor cells treated with fresh F12K with DMSO (negative control).

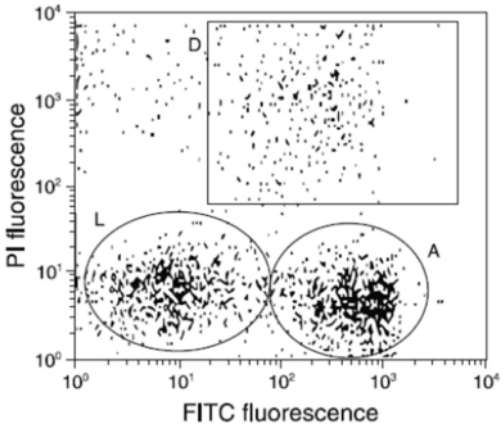

Figure 7. Simulated data of FACS Annexin V/PI assay results of A549 or mouse tumor cells treated with 5-Fluorouracil (positive control).
Note. The horizontal axis represents the fluorescence intensity of Annexin V. The vertical axis represents the fluorescence intensity of PI.

The results of the FACS Annexin V/PI assay may be interpreted as the 2 figures shown above. Figure 6 is simulated data of FACS Annexin V/PI assay results of A549 or mouse tumor cells treated with fresh F12K with DMSO (negative control), and Figure 7 is simulated data of a possible result of A549 or mouse tumor cells treated with 5-Fluorouracil (positive control). Normally growing tumor cells can contain a small number of dead cells, as shown in Figure 6 with a lower proportion of Annexin V(+)-PI(+) cells in the upper right corner. The majority of normal cells located in the lower-left corner showing Annexin V(-)-PI(-). The proportion and possibility of normal cells located in the lower right corner, with Annexin V, highly expressed but PI hardly expressed, is very low. In the early stages of apoptosis, phosphatidylserine, which normally lies on the inner side of the cell membrane, flips to the surface. FITC-labeled Annexin V is a phospholipid-binding protein that is highly specific to phosphatidylserine. The integrity of the cell membrane in the early stage of apoptosis is still good, so the nucleic acid dye PI cannot penetrate the cell membrane and stain the nucleus. Therefore, in cells at the early stage of apoptosis, the Annexin V signal was high but the PI signal was low, so the cells are located in the area circled A in the lower right corner of Figure 7.

For every sample representing cells or mice with different treatments, the sum ratio of apoptotic cells in early and late stages, lying in the region of A&D in Figure 7 can be calculated and analyzed. The ratio Rsample-i is compared with the same ratio from the positive control and the negative control, Rpositive and Rnegative. (R stands for “ratio”. A sample can be A549 cells or C57BL/6 mice, and i stands for samples treated with an anthraquinone derivative)

The possible results of Annexin V-PI assay are shown in Figure 8. For aesthetic purposes, partial abbreviations are used. Drug implies samples treated with 5-Fluorouracil (positive control), while control means samples treated with fresh F12K with DMSO (negative control). The columns of results 1 to 4 are the possible results of the experimental groups. The last column on the right is the “crazy” result likely from mistakes during the experiments, whose validity shall be determined by statistical analysis.

Possible result 1:

The difference between either RA549-i or RC57BL/6-i and Rnegative is not significant. (The relationship between RC57BL/6-i & Rnegative or RA549-i & Rnegative is the same as control and result 1 in Figure 8.)

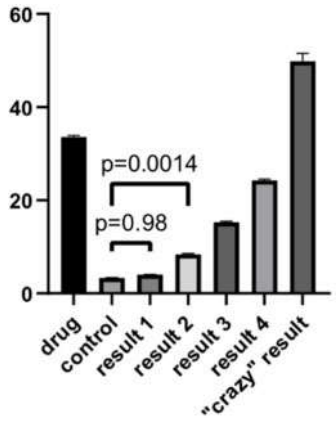

Figure 8. Possible results of apoptotic cell ratio.

Possible result 2:

RA549-i is significantly different from Rnegative and Rpositive, but the difference between RC57BL/6-i and Rnegative is not significant. (The relationship between RC57BL/6-i & Rnegative is the same as control and result 1 in Figure 8, The relationship between RA549-i & Rnegative can be interpreted as result 2/3/4 and control in Figure 8.)

Possible result 3:

RC57BL/6-i is significantly different from Rnegative and Rpositive, but the difference between RA549-i and Rnegative is not significant. (The relationship between RA549-i & Rnegative is the same as control and result 1 in Figure 8, The relationship between RC57BL/6-i & Rnegative can be interpreted as result 2/3/4 and control in Figure 8.)

Possible result 4:

Both RA549-i and RC57BL/6-i are significantly different from Rnegative and Rpositive. (The relationship between RC57BL/6-i & Rnegative and RA549-i & Rnegative can be interpreted as results 2/3/4 and control in Figure 8. The following relationships can be presented between RA549-i and RC57BL/6-i: RA549-i is significantly larger than RC57BL/6-I, RA549-i is significantly smaller than RC57BL/6-i, or the difference between RA549-i and RC57BL/6-i is not significant. (Possible results 4.1–4.3))

Table 4. The possible result of Annexin V/PI assay.

		Difference with Rnegative	Difference with Rpositive
Possible result 1	RA549-i	–	/
	RC57BL/6-i	–	/
Possible result 2	RA549-i	+	+
	RC57BL/6-i	–	/
Possible result 3	RA549-i	–	/
	RC57BL/6-i	+	+
Possible result 4	RA549-i	+	+
	RC57BL/6-i	+	+

Note. "+" *represents a significant difference between* RA549-i/RC57BL/6-i *and* Rnegative/Rpositive *while "–" represents no significant difference between* RA549-i/RC57BL/6-i *and* Rnegative / Rpositive. *"/" represents the difference between* RA549-i/RC57BL/6-i *and* Rpositive *is meaningless in some results.*

3.4 *Possible result of Western Blot assay (Table 5–6); Figure 9))*

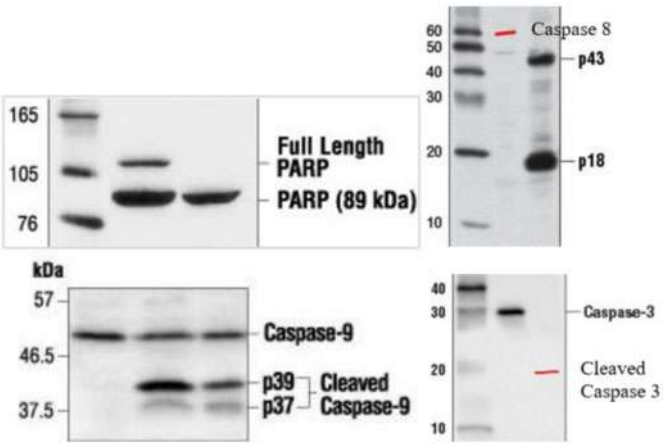

Figure 9. Simulated data of Western blot assay of cell apoptosis-related protein expression.

Figure 9 is a simulated result of four apoptosis-related protein expressions with or without the apoptosis-inducing chemicals. The detail of the picture is shown in Table 5. Western blot assay is performed on cells treated with an anthraquinone derivative or rhubarb extract if cell apoptosis is detected by the Annexin V/PI assay in vitro or in vivo after treatment. In the experiment, one PVDF membrane is cultured with a certain primary antibody. For every membrane, it contains a protein ladder, the samples treated with the positive and the negative control and the samples (both from A549 cells and C57BL/6 mice) treated with anthraquinone derivatives and rhubarb extract.

In all samples treated with 5-Fluorouracil (positive control), a common pattern of bands is observed (performed as the rightest column in Figure 9). If an anthraquinone derivative or rhubarb extract induces cell apoptosis, then a clear band at the position of lower kDa should appear, demonstrating caspase 3/8/9 or PARP cleavage, in contrary no inducement in cell apoptosis will not show the cleaved protein bands. The more obvious the bands are, the more caspase 3/8/9 or PARP expression is.

Table 5. Western blot results.

	MW without cleavage	MW after cleavage
Caspase 3	35kDa	17kDa & 19kDa
Caspase 8	57kDa	18kDa & 13kDa
Caspase 9	49kDa	37kDa & 39kDa
PARP	116kDa	89kDa

Possible result 1:

An anthraquinone derivative or rhubarb extract only induce cell apoptosis in A549 cells compared with the negative control.

Possible result 1a: An anthraquinone derivative or rhubarb extract only induce cell apoptosis in A549 cells in a mitochondria-dependent pathway. The cleavage of Caspase 3, Caspase 9, and PARP is detected.

Possible result 1b: An anthraquinone derivative or rhubarb extract only induces cell apoptosis in A549 cells in mitochondria independent pathway. The cleavage of Caspase 3 and Caspase 8 and PARP is detected.

Possible result 2:

An anthraquinone derivative or rhubarb extract only induce cell apoptosis in C57BL/6 mice compared with the negative control.

Possible result 2a: An anthraquinone derivative or rhubarb extract only induces cell apoptosis in C57BL/6 mice in a mitochondria-dependent pathway. The cleavage of Caspase 3, Caspase 9, and PARP is detected.

Possible result 2b: An anthraquinone derivative or rhubarb extract only induces cell apoptosis in C57BL/6 mice in mitochondria independent pathway. The cleavage of Caspase 3, Caspase 8, and PARP is detected.

Possible result 3:

An anthraquinone derivative or rhubarb extract induce cell apoptosis in both A549 cells and C57BL/6 mice compared with the negative control.

Possible result 3a: An anthraquinone derivative or rhubarb extract induces cell apoptosis in A549 cells and C57BL/6 mice within a mitochondria-dependent pathway. The cleavage of Caspase 3, Caspase 9, and PARP is detected.

Possible result 3b: An anthraquinone derivative or rhubarb extract induces cell apoptosis in A549 cells and C57BL/6 mice within mitochondria independent pathway. The cleavage of Caspase 3, Caspase 8, and PARP is detected.

Possible result 3c: An anthraquinone derivative or rhubarb extract induce cell apoptosis in C57BL/6 mice in a mitochondria-dependent pathway with the cleavage of Caspase 3, Caspase 9 and PARP detected; meanwhile they induce cell apoptosis in A549 cells in mitochondria independent pathway with the cleavage of Caspase 3 and Caspase 8 and PARP detected.

Possible result 3d: An anthraquinone derivative or rhubarb extract induce cell apoptosis in C57BL/6 mice in mitochondria independent pathway demonstrating the cleavage of Caspase 3, Caspase 8, and PARP; meanwhile they induce cell apoptosis in A549 cells in mitochondria-dependent pathway demonstrating the cleavage of Caspase 3 and Caspase 9 and PARP.

Table 6. Possible results of apoptosis-inducing effects of rhubarb extract and anthraquinone derivatives on A549 cells and C57BL/6 mouse.

Cleavage		Caspase 3	Caspase 8	Caspase 9	PARP
Negative control		–	–	–	–
Possible result 1a		+	+	–	+
Possible result 1b		+	+	–	+
Possible result 2a		+	–	+	+
Possible result 2b		+	+	–	+
Possible result 3a		+	–	+	+
Possible result 3b		+	+	–	+
Possible result 3c	A549 cells	+	+	–	+
	C57BL/6 mice	+	–	+	+
Possible result 3d	A549 cells	+	–	+	+
	C57BL/6 mice	+	+	–	+

Note. "+" represents the appearance of cleavage in Western Blot assay. "-" represents no cleavage detected in the Western Blot assay.

3.5 *Possible results of metastasis inhibiting effects of rhubarb extract and anthraquinone derivatives on A549 cells (Table 7)*

By measuring the number of cells in the lower compartment in the Boyden chamber, the result can acquire a quantitative analysis of the migratory response of cells.

Possible result 1

The number of migrated A549 cells after treatment of rhubarb extract or an anthraquinone derivative has no comparable difference compared to the negative control (DMSO).

Possible result 2

The number of migrated A549 cells decreases after the treatment of rhubarb extract or an anthraquinone derivative, compared to the negative control.

Possible result 3

The number of migrated A549 cells increases after the treatment of rhubarb extract or an anthraquinone derivative, compared to the negative control.

Table 7. Possible Results of Metastasis Inhibiting Effects of Rhubarb Extract and Anthraquinone Derivatives on A549 Cells.

	The migration rate of A549 cells treated by Anthraquinone derivative of rhubarb extract	The migration rate A549 cells treated by DMSO	Analysis
Possible result 1	++	++	Similar migratory Response
Possible result 2	+	++	Noticeable reducing migratory response
Possible result 3	-	++	Increasing migratory response

Note: "-" represents migration number increased. "+" represents a noticeable lower migration number in the lower compartment. "++" represents the normal migration number in the lower compartment (negative control).

3.6 *Possible results of cytokine levels and other phenotypic indicators during in vivo experiments (Figures 10 and 11, Table 8)*

Possible result 1: The ingestion of a high dose of rhubarb and 5-Fluorouracil significantly drops the cytokine levels and reduces the weight loss and tumor size associated with cancer.

The amount of IL-6 and TGFβ cytokines used to regulate inflammation caused within the lung drops with a subsequent decrease in M2 Macrophage activity. In addition, the weight of the test subjects in Experimental Group 1 is observed to be at healthier levels than those in the negative control as well as having a significant decrease in the tumor size.

Possible result 2: The uptake of rhubarb in any of the experiment groups only creates a limited impact on the malignant tumor cells due to the inhibition of Angiotensin-converting enzyme 2 (ACE 2) in vivo experiments.

Mice treated with sole rhubarb (experiment groups 2, 3, 4) shows minimum recovery from lung cancer. Tumor size and weight loss of those mice (experiment groups 2, 3, 4) is close to that of the negative control and is not significantly differentiated among those groups. A significant decrease in tumor size and weight loss is observed only in mice treated with 5-Fluoroacil (positive control and experiment group 1).

Possible result 3: Solely using rhubarb as a treatment will drop cytokine levels, and reduce weight loss and tumor size only at high doses.

All three variables will not be expected to have significant change from the control group in the small doses of rhubarb given. The mice given medium dosage rhubarb can be expected to have more positive results in treating cancer, but small. As a result, only the highest dose of rhubarb will see a decrease in cytokine levels, weight loss, and tumor size.

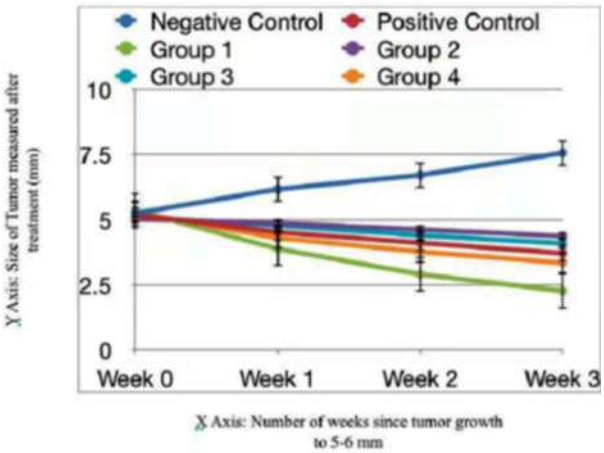

Figure 10. Level of cytokines in experimental groups and control groups. Values are presented as mean ± S.E. and $p<0.01$ (Shang 2017; Yu 2008).

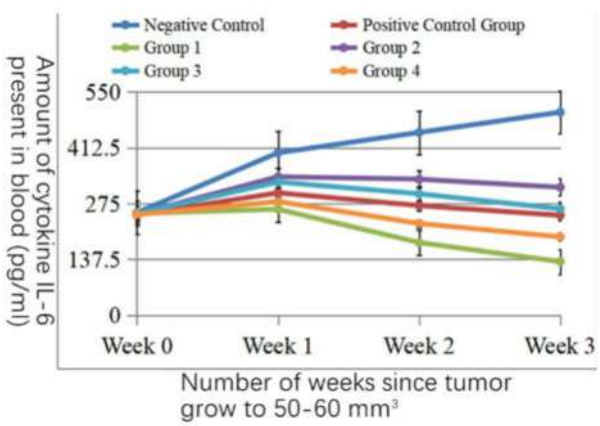

Figure 11. Size of mice lung tumors in experimental groups and control groups. Values are presented as mean ± S.E. and $p<0.01$.

Table 8. Summary of different rhubarb dosages and their impact on cancer cells. Experimental Groups can be referenced in Table 1 above.

Cell Lines	Result 1	Result 2	Result 3
Positive Control	−	+	−
Group 1	+	+	+
Group 2	−	−	−
Group 3	−	−	+
Group 4	−	−	+

Note. "+" represents a significant improvement in the tumor size, weight loss, and cytokine levels of lung cancer mice. "-" represents no significant change detected.

4 DISCUSSION

4.1 *Discussion of HPLC separation of rhubarb extract*

Possible result 1, the complete yielding of all six anthraquinones of interest marks the successful separation and the integrity of the rhubarb extract. The experiment may proceed as intended with the six anthraquinones isolated for treatments. Possible results 2 and 3, however, both represent incomplete separation that only yields some or none of the six anthraquinones expected to exist naturally in rhubarb. Since the design of HPLC used in this experiment has been applied in previous studies for the separation of the six anthraquinones (Li et al. 2018), unexpected results 2 and 3 imply either that there are non-systematic errors in the performance of the HPLC procedures, or that the status of the rhubarb extract is compromised, or both. Repetition of the HPLC separation should be considered for eliminating non-systematic errors, however, there are a number of potential problems that could account for the uncertainties of rhubarb extract: the anthraquinones might be lost during the filtration or centrifugation of rhubarb sample, they might precipitate out of the solution, or they might react with some chemicals involved in the separation. Decomposition of the rhubarb samples prepared is also a possible explanation. Any of the above can potentially produce results 2 and 3 of the HPLC separation, which will prevent this experiment from proceeding, unless possible adjustments can be made, such as using anthraquinones directly bought from a company, or only testing the anthraquinones successfully separated in the case of possible result 2.

4.2 *Cytotoxicity of an individual anthraquinone derivative of interest or rhubarb extract on A549 cells and HPAEpiC*

Cytotoxicity of anthraquinone derivatives and rhubarb extract on A549 cells or HPAEpiC provides insights into the potential therapeutic value of the anthraquinone derivatives and rhubarb extract, against lung cancer.

Possible Result 1 & 2:

A potential drug against lung cancer should specifically inhibit the growth of cancerous cells, without damaging normal cells. Thus if an anthraquinone derivative or rhubarb extract falls into Possible Result 1 (negligible cytotoxicity on A549 cells and HPAEpiC) or 2 (noticeable cytotoxicity on HPAEpiC), one will not expect the anthraquinone derivative or rhubarb extract to have any direct therapeutic value against lung cancer.

It is also possible that certain anthraquinone derivatives might show a pattern of promoting the growth of A549 cells in a dose-dependent manner, as has been observed in past studies (Chang et al. 2012). However, verification of potential growth-promoting effects on cancerous cells of rhubarb anthraquinone derivatives and underlying mechanisms were hardly discussed. Future studies are urgently required for drug development, if patterns of an anthraquinone derivative or rhubarb extract promoting the growth of cancerous cells are observed, to verify the effects, investigate the mechanisms, and improve existing TCM-herb based cancer therapies.

Possible Result 3:

Potential therapeutic value is expected from anthraquinone derivatives or rhubarb extract to fall into Possible Result 3 (noticeable cytotoxicity on A549 cells, negligible or significantly lower cytotoxicity on HPAEpiC), especially if their cytotoxicity was close to, or even beyond (although not likely) the positive control (5-fluorouracil).

Cytotoxicity of rhubarb extract and individual anthraquinone derivatives can be compared if rhubarb extract and one or more anthraquinone derivatives show Possible Result 3, which yields information on how each anthraquinone derivative interacts and contributes to the growth-inhibiting effects on A549 cells of rhubarb extract.

If cytotoxicity of rhubarb extract on A549 cells is higher than any individual anthraquinone derivative at an equivalent concentration:

The growth-inhibiting and apoptosis-inducing effects of anthraquinone derivatives in rhubarb extract overlap and enhance each other, and rhubarb extract can be a more competitive candidate

than any individual anthraquinone derivatives investigated in this study, for drug development against lung cancer.

If rhubarb extract shows similar cytotoxicity to that of the most cytotoxic anthraquinone derivative on A549 cells:

The one anthraquinone derivative may account for most of the growth-inhibiting effects on A549 cells of rhubarb extract. More attention can be paid to that anthraquinone derivative as a potential candidate for drug development against lung cancers.

If the rhubarb extract shows lower cytotoxicity than that of any other anthraquinone derivative on A549 cells:

A certain combination of compounds in rhubarb extract may harm the growth-inhibiting effects on A549 cells. Individual anthraquinone derivatives or alternative combinations of anthraquinone derivatives will be more effective in inhibiting the growth of A549 cells, or against lung cancer.

4.3 *Discussion of FACS annexin V/PI assay and western blot assay*

FACS Annexin V/PI assay follows the MTT cytotoxicity assay described above and mainly is further research of the possible result 3 in MTT cytotoxicity assay (cytotoxicity of an anthraquinone derivative or rhubarb extract is noticeable on A549 cells, and significantly lower or neglectable on HPAEpiC), to determine whether it inhibits the growth of cancerous cells by inducing apoptosis. The functions of a potential drug should induce cancer cell apoptosis in vitro and in vivo.

If an anthraquinone derivative or rhubarb extract falls into possible result 1 in the Annexin V/PI assay, we may not expect the satisfying function in treating lung cancer.

If an anthraquinone derivative or rhubarb extract falls into possible result 2, it shows a induces apoptosis significantly in vitro but it may not induce apoptosis in vivo. Since the localization effect of these substances is not clear and they are not specially designed to target cancer cells, they might be evenly distributed in the whole circulatory system, rather than concentrated near the tumor. Meanwhile, the oxidative environment in the blood is unstable for polyhydroxy anthraquinone, which has strong reducibility. These substances are likely to be partially oxidized in the body. The discussions above can explain why the inhibitory effect of these components on the growth of tumor cells in vivo is not as good as that on the proliferation of A549 cells in culture dishes. For possible result 2, an anthraquinone derivative or rhubarb extract can be a potential drug but some chemical modification or molecular packaging is needed to improve the in vivo effects.

Possible result 3 is not likely to be observed, as the in vivo results usually couldn't be better than the in vitro result. If this result does occur, it may indicate that an anthraquinone derivative or rhubarb extract participates in some other unknown pathway, thus further studies are needed. For the "crazy" result, although there is a tiny possibility that the anthraquinone derivative or rhubarb extract could induce cell apoptosis better than the commercial drug, we should carefully examine the experiment through statistically analysis and repeated experiments, as in most cases the "crazy" result may indicate some cell damage due to the wrong experimental operation.

Anthraquinone derivatives or rhubarb extract showing possible results 4 confirms the hypothesis, as both in vitro and in vivo experiments show significant inducement of apoptosis compared with the negative control group. A higher ratio of apoptotic cells (closer to that of the positive control) in cells treated with those anthraquinone derivatives and rhubarb extract indicates better apoptosis-inducing effects on cancerous cells.

If one or more anthraquinone derivatives and Rhubarb extract show possible result 4, we may try to attribute the effect of Rhubarb extract to one single anthraquinone derivative. HPLC can give us information on the concentration of every anthraquinone derivative by the peak area in the LC part. In our experiment, the apoptosis-inducing effect of the anthraquinone derivatives or rhubarb extract can be compared. (For example, the result of HPLC shows that 500mg Rhubarb extract contains 240mg emodin, thus the result of 10mg/mL Rhubarb extract can be compared with 4.8mg/mL emodin alone). If the apoptosis-inducing effect of rhubarb extract is higher than the sum of individual anthraquinone derivatives at equivalent concentration, it can indicate that the apoptosis-inducing effects of anthraquinone derivatives in rhubarb extract are enhanced by

some mechanism. If the cell apoptosis inducement effect of rhubarb is close to that of the sum of individual anthraquinone derivatives at equivalent concentration, it reveals that one component is independent of the others in inducing cancer cell apoptosis and we may simply choose the best anthraquinone derivative for potential drug development.

Western blot assay follows the Annexin V/PI assay if the apoptosis is detected. Moreover, we aim to detect the molecular mechanism of the cell apoptosis, as well as attribute the pathway to a mitochondrial-dependent or independent pathway. For possible results 3c and 3d, there is a possibility that in vivo mechanism differs from the in vitro mechanism, as usually the in vivo micro-environment is quite different from in vitro experiments.

4.4 *Discussion of Boyden chamber assay*

Possible result 1 contradicts our hypothesis which states that after the treatment of rhubarb extract, metastasis will be inhibited. For possible result 1 where the migratory does not change much compared to the negative control (DMSO), the application of rhubarb extract has no therapeutic effect in inducing cancer cell death. This is probably due to the rhubarb extract did not induce cell death, but rather introducing an anti-inflammatory effect on the A459 cells, which did not change the numbers of migrated cells (Yu et al. 2008).

Possible result 2 is most consistent with our hypothesis that rhubarb extracts are effective in inhibiting lung cancer cells. As the result is observed, the specific components of rhubarb either one emodin, aloe-emodin, rhein, chrysophanol, physcion, and danthron could have a potential therapeutic effect in inhibiting cancer cell proliferation, thus decreasing the migration of A549 cells.

Finally, possible result 3 contradicts the paper's hypothesis that cell viability increases after the application of rhubarb extracts shown in the increased migratory numbers. The certain combination of the compounds in the rhubarb extract introduces an adverse effect in ways of treating lung cancer such as stimulating the transcription factors in cancer cells.

In general, other possible results test the overall effects of rhubarb, for example, certain combinations of anthraquinones promote inhibition of lung cancer cells, but for individual components, the yielded effects may not be as strong as that of their combination, which requires further investigation.

4.5 *Discussion of A549 xenograft*

The *in vivo* experiment most likely gives the conclusion that 5-Fluoroacil and high dose rhubarb yield the most effective treatment against lung cancer that both minimizes the tumor growth in Week 1 as well as uses the properties of anthraquinone to reduce inflammation.

If possible result 2 is observed, it is likely because while rhubarb reduces the inflammation caused by cytokines, it comes at the cost of sacrificing naturally found ACE 2 enzymes found in the body. Recent evidence indicates that overexpression of the enzyme ACE-2 can regulate inflammation and blood pressure (The Conversation 2021), creating inhibition of cancer cell growth (Feng et al. 2010) and preventing inflammatory tissue damage. Emodin inside rhubarb might also inhibit the function of ACE 2 as it is researched to be a potential treatment against COVID-19 (Ho 2007). To confirm the validity of the findings, more trials should be done targeting the expression of ACE-2 in cancerous environments and the long-term effect of rhubarb on cancer patients.

If possible result 3 is observed, it solidifies the claim that TCM should not be taken alone as a treatment. TCM generally requires large doses to act successfully on the body, with only 0.8% of the treatment powder extracted from every 500 grams of rhubarb in one experiment (Synthergo 2021). As a result, only the highest dose of rhubarb sees a decrease in cytokine levels, weight loss, and tumor size. Future experiments should improve their model through extensive material testing to find the proper dosage and balance should TCM ever be used as an alternative method against cancer.

5 CONCLUSION

This study provides an insight into the anti-lung cancer effects of individual anthraquinone derivatives contained by rhubarb, as well as that of rhubarb extract as a whole, in terms of their cytotoxicity and apoptosis-inducing effects on cancerous and normal cells, metastasis inhibiting effects to cancerous cells, and tumor growth and inflammation inhibiting effects. Such understanding of specific functions of rhubarb and compounds associated with those functions can provide basics for future studies, including those into detailed mechanisms and pathways in which those functions are executed, the behavior of active compounds of rhubarb in the distinctive and complex biochemical environment of the human body, and the combined function of rhubarb together with other compounds in multi-compound prescriptions. This study and those mentioned above can be of great aid to the development of new anti-lung cancer drugs. However, since rhubarb is an ingredient commonly used along with other herbs in traditional Chinese medicine, such as in Lianhua Qingwen, the behaviors of these anthraquinones with lung cancer cells in the presence of other molecules still need further investigation. Studying the combined effect of multiple herb ingredients will further people's understanding of Chinese traditional medicine and its relationship with cancer treatment.

ACKNOWLEDGMENTS

Each author was responsible for one or multiple discrete sections of this study, and the work of every author progressed in parallel most of the time, thus each of the six authors contributed equally as the first author. Additionally, Jingyun Wu is also the corresponding author. The authors are grateful for the academic support from Prof. Arthur Salomon.

REFERENCES

Altogen Labs (2021, July 9). A549 Xenograft Model. Retrieved from https://altogenlabs.com/xenograft-models/lung-cancer-xenograft/a549-xenograft-model/

Bidola, P., Silva, J. M. d S. e, Achterhold, K., Munkhbaatar, E., Jost, P. J., Meinhardt, A., Taphorn, K., Zdora, M., Pfeiffer, F., Herzen, J. (2019). A step towards valid detection and quantification of lung cancer volume in experimental mice with contrast agent-based X-ray microtomography. Scientific Reports, 9(1), 1325.

Bajic, E.J., Eden, G.L., Lampton, L.S., Cheah, K.Y., Lymn, K.A., Pei, J.V., Yool, A.J., Howarth, G.S. (2016). Rhubarb extract partially improves mucosal integrity in chemotherapy-induced intestinal mucositis - Rhubarb extract partially improves mucosal integrity in chemotherapy-induced intestinal mucositis. World Journal of Gastroenterol, 22(37), 8322–8333.

Chang, C., Chan, H., Lin, H., Way, T., Kao, M., Song, M., Lin, Y., Lin, C. (2012). Rhein Induces Apoptosis in Human Breast Cancer Cells. Evidence-Based Complementary and Alternative Medicine, 2012, 8.

Dai, H., Chen, Z., Shang, B., Chen., Q. (2018). Identification and Quantification of Four Anthraquinones in Rhubarb and Its Preparations by Gas Chromatography–Mass Spectrometry. Journal of Chromatographic Science, 56.3, 195–201.

Feng, Y., Wan, H., Liu, J., Zhang, R., Ma, Q., Han, B., Xiang, Y., Che, J., Cao, H., Fei, X., & Qiu, W. (2010). The angiotensin-converting enzyme 2 in tumor growth and tumor-associated angiogenesis in non-small cell lung cancer. Oncology reports, 23(4), 941–948.

Huang, Q., Lu, G., Shen, H., Chung, M., Ong, C. (2007). Anti-cancer properties of anthraquinones from rhubarb. Medicinal Research Reviews, 27(5), 609–630.

Ho, T. Y., Wu, S. L., Chen, J. C., Li, C. C., & Hsiang, C. Y. (2007). Emodin blocks the SARS coronavirus spike protein and angiotensin-converting enzyme 2 interaction. Antiviral research, 74(2), 92–101.

Li, X., Li, F., Wang, F., Li, J., Lin, C., & Du, Jx. (2018). Resveratrol inhibits the proliferation of A549 cells by inhibiting the expression of COX-2. OncoTargets and Therapy, 11, 2981–2989.

Liu, X., Liu, J., Guan, Y., Li, H., Huang, L., Tang, H., He, J. (2012). Establishment of an orthotopic lung cancer model in nude mice and its evaluation by spiral CT. Journal of Thoracic Disease, 4(2), 141–145.

Panichayupakaranant, P., Sakunpak, A., & Sakunphueak, A. (2009). Quantitative HPLC Determination and Extraction of Anthraquinones in Senna alata Leaves. Journal of Chromatographic Science, 47(3), 197–200. https://doi.org/10.1093/chromsci/47.3.197

Synthergo (2021, June 30). Everything You Need To Know About A549 Cells. Retrived from https://www.synthego.com/a549-cells#research

Shang, G., Liu, L., Qin, Y. (2017). IL-6 and TNF-α promote metastasis of lung cancer by inducing epithelial-mesenchymal transition. Oncology Letters, 13(6), 4657–4660.

Thermo Fisher Scientific (2019). RPMI 1640 Medium. Retrived from https://www.thermofisher.cn/order/catalog/product/11875093#/11875093

The Conversation. (2021 July 8). What is the ACE2 receptor, how is it connected to coronavirus and why might it be key to treating COVID-19? The experts explain. Retrieved from https://theconversation.com/what-is-the-ace2-receptor-how-is-it-connected-to-coronavirus-and-why-might-it-be-key-to-treating-COVID-19-the-experts-explain-136928

World Health Organization (2021, March 3). Cancer. Retrived from https://www.who.int/en/news-room/ fact-sheets/detail/cancer#:~:text=Cancer%20is%20a%20leading%20cause%20of%20death%20worldwide%2C,%28non-melanoma%29%20%281.04%20million%20cases%29%20Stomach%20%281.03%20million%20cases%29.

Xiang, H., Zuo, J., Guo, F., Dong, D. (2020). What we already know about rhubarb: a comprehensive review. Chinese Medicine, 15(1), 88.

Yu, H., Liu, Y., Cheng, Y., Hu, L., Hou, M. (2008). Effects of rhubarb extract on radiation induced lung toxicity via decreasing transforming growth factor-beta-1 and interleukin-6 in lung cancer patients treated with radiotherapy. Lung Cancer, 59(2), 219–226.

Zhang, S., Liu, Y., Xiang, D., Yang, J., Liu, D., Ren, X., & Zhang, C. (2018). Assessment of dose-response relationship of 5-fluorouracil to murine intestinal injury. Biomedicine & Pharmacotherapy, 106, 910–916.

Advances in Applied Chemistry and Industrial Catalysis – Saikia (Ed.)

Applications of engineered nanoparticles in biomedicine

Wenjin Huang*†
College of Letters & Science, University of California, Santa Barbara, CA, USA

Junqiang Lyu**†
Portsmouth Abbey School, RI, USA

Xuanhua Zhang†
Guiyang No.1 High School, Guizhou, China

Yixiang Zhang†
Changzhou No. 1 High School, Changzhou, China

ABSTRACT: The fascinating application of engineered nanoparticles in biomedicine inspired scientists and engineers to spare no effort in it. Many aspects of the application of nanoparticles in biomedicine have been well studied and developed in the past few decades. Optical images cooperate with different nanomaterials, where organic dyed doped nanoparticle is one type of nanomaterials that have been widely adopted in this field. The applications offer surprising results on target that doctors aim. Light-triggered cancer therapy focuses on 2 kinds of drugs that help the human body to kill cancer cells. Both photothermal therapy (PTT) and photodynamic therapy (PDT) utilise approaches as a photothermal probe to design a new cancer therapy. The use of nanomaterial-based electrochemical biosensors in biomedicine is also summarized in this review. Depending on the different characteristics of various nanoparticles, it is believed that more applications will be invented.

1 INTRODUCTION

Nanotechnology is an interdisciplinary science subject that includes physics, chemistry, biology, and so on. It focuses on studies of microscopic materials, especially various nanoparticles, small particles that range from 1 to 100 nanometers. Gleiter and other scientists successfully synthesized iron nanoparticles by condensing inert gas for the first time, which marked the formal birth of the field of nanotechnology (Das 2011). Binnig and Rohrer invented the scanning tunneling microscope, which displayed aspects of atoms and molecules with extremely high resolution and provided powerful tools for manipulating them and led to the rapid development of nanotechnology (Binnig & Rohrer 1983). Recently, more and more scientists have devoted themselves to nanoparticle researches.

This nanoscale substance appeals to scientists so much because these particles are in the middle ground between the macro system and its micro counterpart, which provides them unique characteristics that can be applied in the field of biomedicine, including quantum tunneling effect, quantum size effect, and larger proportion of the surface area. The Quantum tunneling effect demonstrates the tunneling of microscopic electrons through barriers. Quantum size effect describes two phenomena: electron energy level changes from quasi-continue to discrete energy level near the fermi level of metal, or the band gap widens when the discontinuous exists between the highest orbital energy level and the lowest one. Also, by scaling law, along with the decrease of the size of nanoparticles, the number of atoms on the surface increases dramatically, and there are more dangling bonds. Therefore, they are chemically active as well. On account of these nanoparticles-only characteristics,

Corresponding Authors: *awenjinhuang@ucsb.edu and **bjunqiang_lyu@portsmouthabbey.org
†These authors contributed equally.

DOI 10.1201/9781003308553-16

nanoparticles can have extraordinary stiffness and display special phenomena such as the blue-shift effect.

Nearly all of the known theories of the nanoscale world have been discovered in just the last century, and the material properties have been precisely predicted. At the same moment, tremendous material objects have been constantly built by conscientious scientists and engineers. The further the exploration of insights into the amazing world goes, the more understandings scientists will gain, which forms the cornerstone of nanotechnology's edifice and makes significant changes in the ways we live. The prospect of the field is still uncertain but promising because of its unique characteristics and the opportunity it provides to manufacture lighter, stronger and more effective materials. Therefore, engineered nanoparticles have been consistently and widely adopted in burgeoning industries, especially in the field of biomedicine. In the foreseeable future, engineered nanoparticles can treat problems that were once viewed as maladies or incurable diseases. For instance, recent studies showed that C60 is more effective and harmless than traditional curing methods. The C60 has a high yield of singlet oxygen after photoexcitation, which has an important relationship with physiological and biochemical functions of biological bodies, tissue damage, tumor and actinic therapy techniques.

With the vast advocation and passion devoted by scientists in the application of nanoparticles in biomedicine, three preeminent field studies stand out with sound research: using engineered nanoparticles to form optical imaging, deliver drugs, and cure neoplastic activities. Optical imaging is a device people use to anticipate the responses of tumors to therapies and detect cancers at an early stage (Coll 2011). It is based on quantum dots and is renowned for its extraordinary photostability and ability to label biological tissues and molecules. After that, drugs delivery and specific cures of neoplastic activities take over the following treatments. One purpose of drug delivery, for instance, is to confine therapeutic drugs inside the nanoparticles and let them carry the cure to the damaged tissues, whose nanoparticles have resourceful approaches that expedite the solving rate of certain hydrophobic drugs. Mesoporous silica nanoparticles (MSN) are suitable for this scenario. With a highly hydrophilic outer surface, MSN guarantees fast dissolution of hydrophobic drugs like clotrimazole by accelerating the wetting process and causing a higher dispersion rate of the drug (Zhou 2018). With an adequate engineered drug carrier, therapeutic nanoparticles begin to restore the damage in cells or genes caused by neoplastic activities with certain approaches. In the case of a specific oral squamous cell carcinoma (OSCC), head and neck cancer (HNC), Wang et al. suggested the removal of human antigen R (HuA/HuR). This protein binds RNA but also promotes the survival and escalation of tumors. Encapsulated in solid lipid nanoparticles (SLN) that enable targeted property and are pH-responsive, the system consisting of epirubicin and the plasmid of HuR CRISPR enter the tumor cell, edit the target genetic sequence gradually knockout HuR (Wang et al. 2021). This process can be moderated and observed by the color change of fluorescent proteins GFP and tdTomato. The consequence of HuR removal is the profound hindering of tumor cell growth, as tested by SAS cells, which reduces it by around 69% (Wang et al. 2021). Wang et al. further founded that the application of HuR CRISPR together with epirubicin expedite the death of tumor cells.

This paper will focus on the recent advances in the applications of nanoparticles in biomedical applications. We will demonstrate more examples in the application of optical imaging, drug delivery, cancer therapy, and biosensors and discuss the existing shortage regarding the methodology and mechanisms and provide a perspective prediction of the future development of biomedicine involving nanoparticles potential challenges in this field.

2 OPTICAL IMAGING

2.1 *An introduction to optical imaging*

For centuries, people devoted themselves to studying optical imaging for improving the resolution of pictures. However, people can't reach this goal until the appearance of nanotechnology. Optical imaging applications is one of the most outstanding applications regarding nanoparticles. It is

designed as the tool for the first stage of medical treatment, detecting and diagnosing, and defined as the technique of visualizing nanoscale substances for *in vivo* (Boschi, 2017). The well-known techniques such as computerized tomography and X-ray radiography use the same concept. Still, optical imaging doesn't have the harmful effect these techniques have because of its wave's frequency.

While some photons meet the biological tissues, some of them are reflected, refracted, or scattered, and some can pass through or be absorbed by the biological tissue. This could be determined by the Lambert-Beer Law, which describes that when a beam of parallel monochromatic light passes through a uniform light-absorbing substance, its absorbance value is proportional to the concentration of the substance and the thickness of the absorption layer. The transmittance is inversely proportional to the concentration and thickness. In biological tissue, this light-absorbing substance is usually hemoglobin, or the red substance in our blood that combines with oxygen, water, and lipids. The biological tissue whose thickness is in the range of 650-800 nm allows photons to move through. Optical imaging applications can observe these moving photons and waves created by excited electrons. While using these applications, scientists usually use little confined light boxes. Charge coupled device camera (CCD) in a low-temperature environment simultaneously to ensure the precision of measurement. Cooperating with different kinds of nanomaterials, these applications can offer different surprising results.

2.2 *Nanomaterial in optical imaging*

Fluorophores of nanocrystal serve as an excellent source of nanosized fluorescent "media" to the benefit of observing through microscopes. These optical imaging nanoparticles can be categorized roughly into three categories—organic dyed-doped nanoparticle, quantum dot, and upconversion nanoparticle (Jiang et al. 2009). The organic dyed doped nanoparticle is usually made of silica and some other polymers. It is dyed with many organic dyes such as IRG-023 CY5, fluorescein isothiocyanate (FITC), and rhodamine B isothiocyanate (RITC). They are especially photostable, can't be penetrated by oxygen, and show great biocompatibility and water solubility. Quantum dots are the nanoscale semiconductor crystals made of the elements from groups II to VI, III to IV or IV to VI. Similarly, they are photostable, resistant to photobleaching and long lasting. On the other hand, upconversion nanoparticles are the phosphors, the light absorber in the NIR region and emitters in the visible region. After absorbing energy from infrared light, ions in the nanoparticle is excited and radiate photons. Differently, these nanoparticles are generally insoluble in water, not biocompatible. Their differences are shown in Table 1.

Table 1. Comparison between optical imaging nanoparticles (Boschi 2017).

Parameters	Organic Dye-doped NPs	QDs	UCNs
Size	50–500 nm	2–10 nm	50–200 nm
Autofluorescence	High	High	Low
Light penetration depth	Medium/high	Medium/high	High
Photodamage	Medium/low	Medium/low	Low
Cytotoxicity	Medium	High/medium	Low
Biocompatibility	Good	Good	Good
Photostability	Low	High	High
Excitation wavelength	UV/vis/NIR	UV/NIR	NIR
Cost	Low/medium	High	Low
Excitation radiation toxicity	Low/medium	Low/medium	Low
Multiplexing assays	–	Good	Good

By utilizing these nanoparticles, scientists can analyze the patient's molecular sample images and cure the disease the patient inflicted via surface-enhanced Ramen scattering (SERS), a method used to amplify Raman signals and observe the motion of cancer molecules. For instance, one great example of these outstanding nanoparticles is the gold nanoparticles (AuNPs) (Wu et al. 2019).

By the Raman spectra, the electrode of AuNPs can strengthen the SERS significantly. In the past, observing *in vivo* imaging of mouse ear blood vessels, scientists detected light emission from one AuNPs 58 times greater than that of one rhodamine molecule. Also, the brightness from AuNPs is three orders of magnitude more than that of autofluorescence unlabeled cancer cells. Moreover, AuNPs advance multi-photons imaging. One technique, termed two-photon imaging (TPI), can convert NIR to visible light. Its improved images with great resolution and prevent the scattering of light due to biological tissue. Studies show that the depth of its resolution can reach millimeter level, which is extremely impressive comparing to traditional methods.

The near-infrared persistent luminescence nanoparticle, for example, can complete *in vivo* detection with high sensitivity and obvious marking, as shown in Figure 1 (Liu et al. 2013). From experimental results, this material can last for hours, realizing targeting tumors. Later, from the experiments with the RAW-264.7 macrophages and phagocytic cell line, researches further proved the ability of tracking and monitor injected cells (cells homing *in vivo)* (Maldiney et al. 2014). The reduced damage to humans (unlike the destructive ultraviolet wave and others) makes the technique extraordinary intriguing.

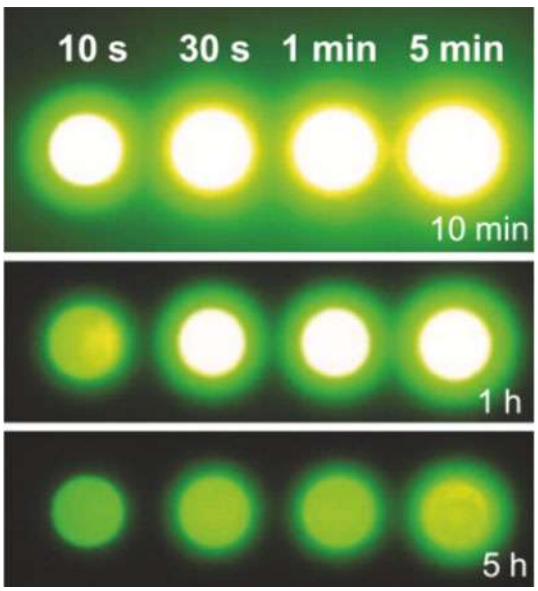

Figure 1. NIR images of four phosphor discs taken at different persistent luminescence time (Liu et al. 2013).

This NIR based method is rather effective and economical because of its low cost and non-radioactive molecule probe. However, it has flaws as well: the majority of biological tissues are too thick to be penetrated. Fortunately, this challenge was solved by scientists Dang et al. recently with the development of a method called dolphin, detection of optically luminescent probes using hyperspectral and diffuse imaging in near-infrared (Dang 2019). This method can reconstruct the 3D image of tumors under the tissue. It emits photons through two modes, hyper spectral imaging (HSI) and hyper diffuse imaging (HDI). As the picture on the left shown, researchers can put the specimen on a quartz platform, and the laser will then excite the photons inside the specimen from the bottom. Consequently, the photons will be emitted from the top and gathered by a liquid nitrogen-cooled InGaAs camera.

After that, researchers use math equations and process the data by forming 3D images in the form of the hyper spectral cube (HPC) or hyper diffuse cube (HDC) and performing the principal component analysis (PCA). Thus, after changing the data set of (x,y, a,b) to 3D fluorescence

imaging, scientists can access the targets in detail regardless of molecular thickness, as shown in Figure 2.

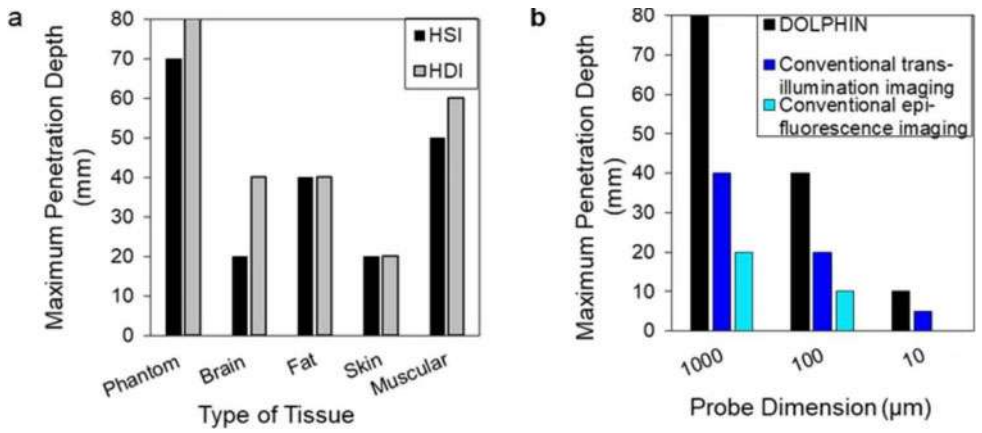

Figure 2. Effect of tissue type and probe size on the maximum depth of detection and comparison of DOLPHIN with conventional imaging systems (Dang 2019).

3 LIGHT-TRIGGERED CANCER THERAPY

Phototherapy founded on light-sensitive nanoparticles develops one of the pioneering methodologies in both drug delivery and therapeutics toward cancerous circumstances. It will introduce the operating mechanism of nanomaterials-based phototherapy. Before being distributed among the targeted cells, the medication with purposely engineered size remains inert so that it won't be recognized and eradicated by the inner defense system. After its arrival, light irradiation with certain wavelengths on the nano-drug will trigger its therapeutic properties and achieve beneficial and convenient results. Currently, two areas of phototherapies are being investigated and tested to enable their utilization: photothermal therapy (PTT) and photodynamic therapy (PDT).

3.1 *PTT utilization*

PTT, accompanied with the application of near-infrared radiation, becomes an optimistic approach to high-precision tumor cell ablation, but maintaining a lower risk of metastasis *in vivo* is still an obstacle needed to be overcome (Guo 2014). With favorable nanoparticle that is eligible for converting radiation energy into thermal energy, the nanoparticles consume near-infrared light with a particular wavelength, applying hyperthermia state to tumor cells and resulting in cell apoptosis.

One of the most typically employed PTT agents is gold nanoparticles. To enhance its capability of energy absorption and conversion, it's used along with its sulfuric compound. Zhou et al. used gold/gold sulfide nanoparticles as a photothermal probe to construct a new cancer therapeutic approach (Gobin et al. 2010). The absorption efficiency of gold/gold sulfide nanoparticles, by calculation, can be up to ∼99%. With this outstanding absorption, gold/gold sulfide performs effectively during in vitro ablation of human prostate cancer cells, as shown in Figure 3.

During the subsequent *in vivo* testing compared to *in vivo* milieu, gold/gold sulfide and another commonly used therapeutic pair, gold/silica nanoshells, are injected into tumor-infected mice; both are treated with polyethylene glycol (PEG) to mitigate the response from the immune defense system. The results showed gold/gold sulfide managed to maintain a higher concentration in the tumor cells compared to that of gold/silica nano shells; this also proved the efficacy of gold/Au_2S to bypass the defense mechanism like the reticuloendothelial system (RES), defense system related to a variety of phagocytic cells.

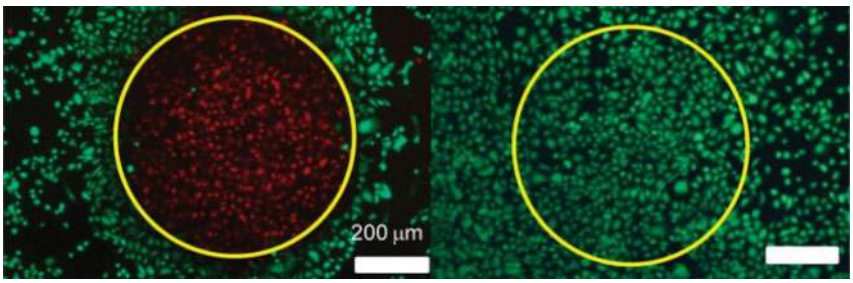

Figure 3. The human prostate cancer cells under laser radiation while untreated (Right) and applied gold/gold sulfide (Left). The scale of both Figures is 200 μm (Gobin et al. 2010).

Besides the composite of gold nanoparticles, polypyrrole (PPy), a type of organic polymeric material, also rivals and even exceeds conventional phototherapeutic agents such as gold nanorods in terms of better performance in the efficacy of energy conversion. Zha et al. attempted to investigate the photothermal characteristics of PPy by triggering it with near-infrared irradiation while observing its temperature increase with RPMI-1640 culture medium (Zha, 2012). Comparing to the samples treated without PPy and applied the same 808 nm radiation, the presence of PPy raised the temperature of the solution to about 34.5°C. In contrast, no significant temperature increase was observed from the solution without PPy. Another experiment similar to the one we have mentioned above also demonstrated the same reddish zone (dead cells) inside the irradiation spot when the laser was applied on the HeLa cells.

3.2 *PDT application*

Utilized light irradiation as well, PDT takes a distinctive mechanism from PTT. While PTT attempts to remove neoplasms via hyperthermia achieved by the light-absorbing nanoparticles, the photodynamic approach aims to activate the neutral drug (a photosensitizer) with light energy, rendering it cytotoxicity toward the targeted tumor cells.

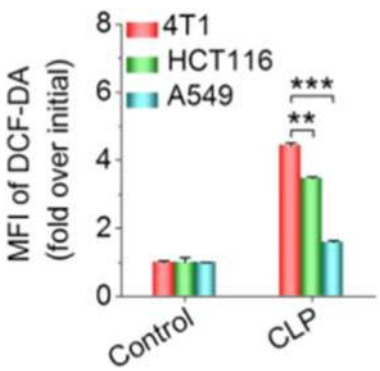

Figure 4. MFI level for the control group (without CLP treatment) and CLP group (treated with CLP) (An 2020).

Upon utilizing the abundance of hydroperoxide produced during the development of cancer, An et al. suggested a nanodrug gained by self-assembly of "an amphiphilic conjugate" to form a CLP nanoparticle, achieved by the conjugation of chlorin e6 (Ce6) and luminol (An 2020). After activating CLP nanoparticles by myeloperoxidase, inner Ce6 produces singlet oxygen $^1O_2$, the form of dioxygen molecules with the lowest excited state and owns strong cytotoxicity toward different

cancer cells. The presence of CLP nanoparticles seemed to induce the increase in reactive oxygen species (ROS) inside cancer cells which, in turn, stimulate $^1O_2$ production. This work selected three types of cancer cells as candidates: 4T1, HCT116 and A549 cells. One group of cells was treated with CLP nanoparticles. The control group was treated with other nutrients instead; the level of ROS inside the cells was indicated by a factor mean fluorescence intensity (MFI). As shown in Figure 4, the group treated with CLP nanoparticles owned a significantly higher ROS level than the control group, indicating the importance of CLP in synthesizing $^1O_2$. Additionally, the illumination produced by the inner luminol unit and the excitation of Ce6 can be applied to both *in vivo* and *in vitro* imaging of the tumor cells, further enhancing the efficacy of the therapeutic function of CLP nanoparticles.

4 ELECTROCHEMICAL BIOSENSORS

Hundreds of years ago, when the subject of biology and engineering had just been developed, biologists and engineers suggested a supposition of placing sensors into the human body and supervising them chronically. Currently, a diverse range of nanomaterials-based biosensors has been widely designed and applied in biomedical fields because these biosensing methods with nanoparticles as probes show excellent sensitivity and selectivity, particularly with respect to electrochemical biosensors. The following is hence mainly focused on the application of different nanomaterials in electrochemical biosensors.

4.1 *Use of metal nanomaterials*

In 2003, Willner et al. reported a new electrochemical biosensor using gold nanocrystal as a probe (Xiao 2003). During the experiment, the auxiliary group of glucose oxidase (GOD) was modified to the surface of gold nanoparticles with a size of 13 nm. The gold nanoparticles were then fixed to the surface of the gold electrode by means of disulfhydryl molecules. And then, the apoenzyme was introduced. Due to the specific combination of the auxiliary group of GOD, the complete GOD virtually maintained its original structure and can be used to catalyze glucose. In the course of collecting electrochemical signals conducted by gold nanomaterials, quantitative analysis and glucose detection are achieved, as shown in Figure 5.

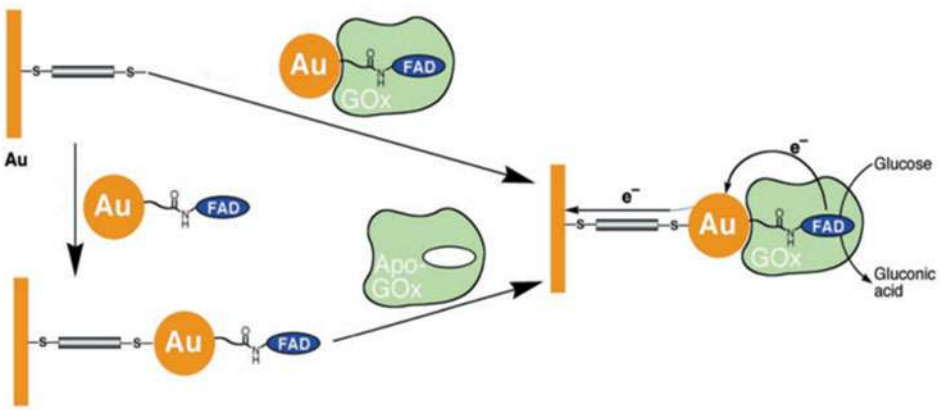

Figure 5. Mechanism of electrochemical biosensor based on gold nanomaterials for detection of glucose (Xiao 2003).

As the application of gold nanoparticles being successfully applied, the focus on other nanoparticles has risen, such as platinum and silver nanoparticles. As shown in Figure 6, generated by the

DNA complementary pairing or two aptamer bindings sites on thrombin, the DNA-modified platinum nanoparticles were modified onto electrode surface through a sandwich structure, where the catalytic current would be obtained by using platinum nanoparticles to catalyze hydrogen peroxide (H_2O_2) substrate (Granot et al. 2005). The results show that the detection limit for thrombin and nucleic acid could reach scales even lower than 1 nM, respectively, because platinum nanoparticles exhibit good catalytic activity.

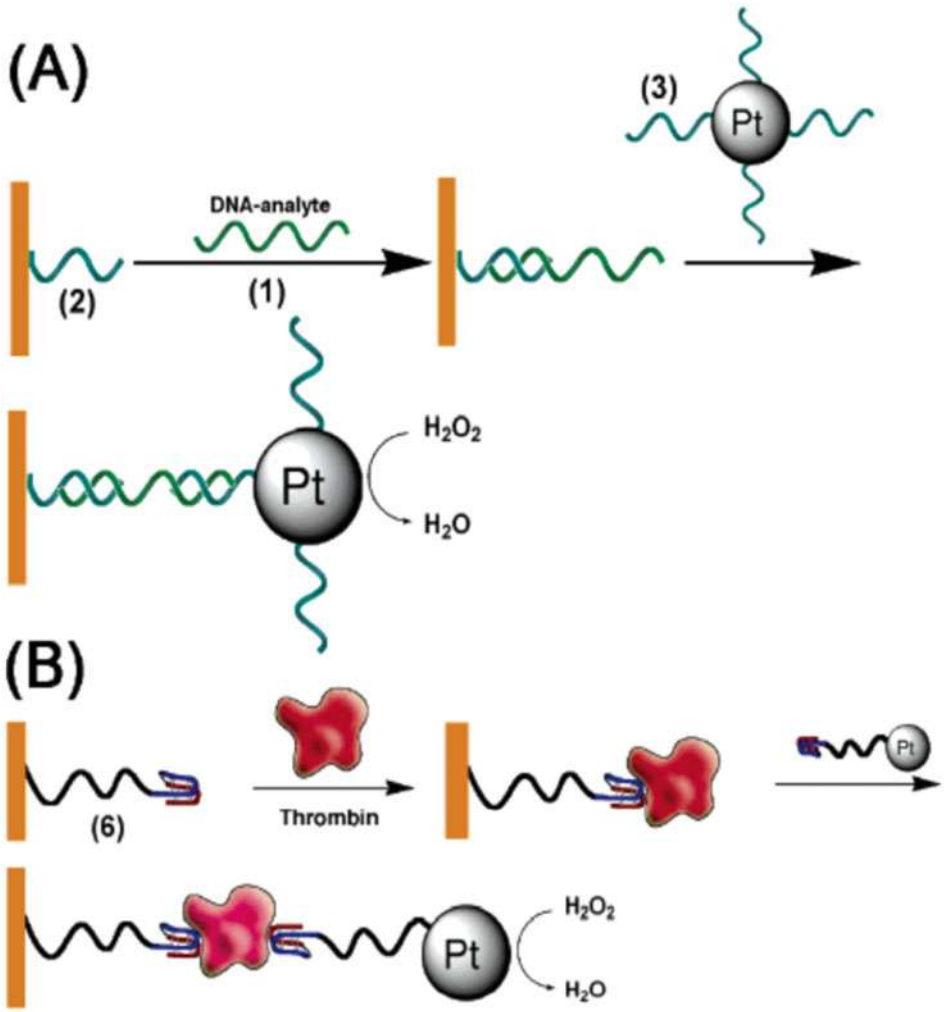

Figure 6. Mechanism of developed electrochemical biosensor for detection of (A) DNA and (B) thrombin (Polsky et al. 2006).

4.2 *Use of oxide nanomaterials*

Li et al. discovered that after modifying the combination of titanium dioxide (TiO_2) and hemoglobin (Hb), the sensitivity of detecting H_2O_2 had tripled after placing the material under UV radiation (Zhou et al. 2005). Meanwhile, the detection limit was two orders of magnitude lower because of the shielding effect provided by TiO_2. A similar effect appeared in the lab again, this time. However, it was stimulated by zinc oxide (ZnO). As shown in Figure 7, Liu et al. suggested that the interaction

among silicon dioxide (SiO_2) nanoparticles, positively charged heme protein hemoglobin (Hb), and the ionic polymer is very curious (Liu 2004). Through a process of layer-on-layer assembling method to modify Hb to the electrode's surface, the application of high sensitivity testing of H_2O_2 succeeded with the protein electrified.

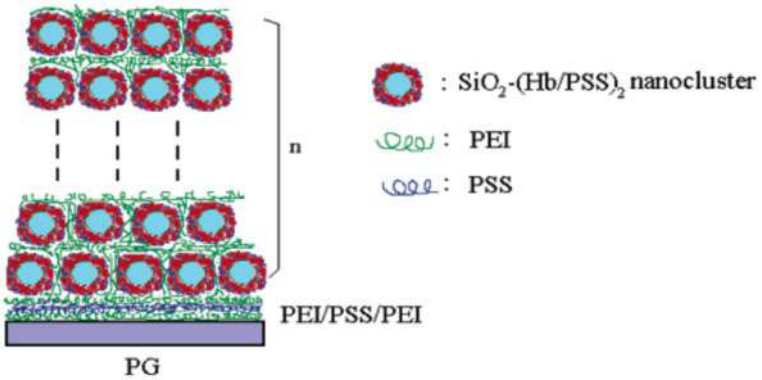

Figure 7. Schematic illustration of the idealized structure on electrode surface (Liu 2004).

4.3 *Use of carbon-based nanomaterials*

Compared to the metal nanomaterial, carbon-based material provides excellent electric conductivity, capability in carrying biopolymers and biocompatibility (BC) since life itself is based on carbon, which offers the variety of its application.

Since it was reported in 1991, carbon nanotubes have become the most widely studied nanomaterial. Davis' team revealed that oxidate singled-walled carbon nanotube (SWNT) is helpful in both the spread of SWNT in the solution and the provision of suitable conditions for the proteins assembling (Azamian 2002). The result showed that even under the condition without any covalent connection activator involved, GOD could be perfectly absorbed onto the surface of SWNT and catalyze glucose efficiently, which is, to be accurate, 10 times more efficient than the circumstance SWNT isn't introduced. This has proved SWNT has a fantastic property in biopolymers transportation and energy transition, but the step of carbon-based biosensors did not stop after the study of SWNT. In 2004, when graphene was discovered and made by both scientists who produced it Nobel prize laureate, a new world was opened and is waiting to be developed.

5 OTHER APPLICATIONS

Nanoparticles have been used as effective drug deliverers because they can deliver the drugs right to the target and thus maximize the benefit of drugs while minimizing their side effects, especially the antineoplastic effect in anticancer therapies. Different nanoparticles have different properties because of their shape and size and thus show distinctive advantages and disadvantages in drug delivery. For instance, titanium dioxide nanoparticles have shown significant potential in drug delivery because of their high stability, high biocompatibility, and low toxicity. Drugs can be taken by TiO_2 and be stored on their surface or inside their reservoir and then be released at the target. As a result, titanium nanoparticles have been used as a mature drug delivery system and have been applied practically with several drugs, such as daunorubicin, cisplatin, and doxorubicin. Traditional nanoparticle synthesis usually uses exorbitant and pernicious chemicals that cause environmental problems and render nanoparticles toxicity. The application of the green synthesis technique enables titanium dioxide nanoparticles to be more environmentally friendly. Moreover, the green synthesis technique uses materials from plant extracts and other biodegradable materials.

6 CONCLUSION

The present paper here summarized the application of engineered nanoparticles in biomedical fields, including optical imaging, cancer therapy, electrochemical biosensors, and other applications. However, the development of engineered nanoparticles still faces certain existing obstacles that may hinder their thorough performance. For instance, the absorption efficiency of nanoparticles regarding energy and heat influences the effectiveness of both the bioimaging and the PDT process. Consequently, nanoparticles with superb absorbance properties ought to be founded or synthesized. Accompanied by the diligence and perseverance of scientists and engineers, the development of nanotechnology will never be overshadowed and will proceed straight to a better future.

REFERENCES

An, Huijie, et al. "Hydrogen Peroxide-Activatable Nanoparticles For Luminescence Imaging and In Situ Triggerable Photodynamic Therapy of Cancer." ACS Appl. Mater. Interfaces, vol. 12, no. 15, 2020, pp. 17230–17243., doi:10.1021/acsami.0c01413.

Azamian, Bobak R., et al. "Bioelectrochemical Single-Walled Carbon Nanotubes." J. Am. Chem. Soc. Au, vol. 124, no. 43, 2002, pp. 12664–12665., doi:10.1021/ja0272989.

Boschi, Federico, and Francesco De Sanctis. "Overview of the Optical Properties of Fluorescent Nanoparticles for Optical Imaging." Eur. J. Histochem., vol. 61:2830, no. 3, 29 Aug. 2017, pp. 245–248., doi:10.4081/ejh.2017.2830.

Coll, Jean-Luc. "Cancer Optical Imaging Using Fluorescent Nanoparticles." Nanomedicine, vol. 6, no. 1, 2011, pp. 7–10., doi:10.2217/nnm.10.144.

Das, Sujoy K., and Enrico Marsili. "Bioinspired Metal Nanoparticle: Synthesis, Properties and Application." Nanomaterials, InTechOpen, 2011, pp. 253–278.

Dang, Xiangnan, et al. "Deep-Tissue Optical Imaging of Near Cellular-Sized Features." Sci. Rep., vol. 9:3873, no. 1, 7 Mar. 2019, pp. 1–12., doi:10.1038/s41598-019-39502-w.

G, Binnig, and Rohrer H. "Scanning Tunneling Microscopy." Surf. Sci., vol. 126, no. 1–3, 1983, pp. 236–244., doi:10.1016/0039-6028(83)90716-1.

Guo, Liangran, et al. "Combinatorial Photothermal and Immuno Cancer Therapy Using Chitosan-Coated Hollow Copper Sulfide Nanoparticles." ACS Nano, vol. 8, no. 6, 2014, pp. 5670–5681., doi:10.1021/nn5002112.

Gobin, André M., et al. "Near-Infrared-Resonant Gold/Gold Sulfide Nanoparticles as a Photothermal Cancer Therapeutic Agent." Small, vol. 6, no. 6, 2010, pp. 745–752., doi:10.1002/smll.200901557.

Granot, Eran, et al. "Enhanced Bioelectrocatalysis Using Au-Nanoparticle/Polyaniline Hybrid Systems in Thin Films and Microstructured Rods Assembled on Electrodes." Chem. Mater., vol. 17, no. 18, 2005, pp. 4600–4609., doi:10.1021/cm050193v.

Jiang, Shan, et al. "Optical Imaging-Guided Cancer Therapy with Fluorescent Nanoparticles." J. R. Soc., Interface, vol. 7, no. 42, 2009, pp. 3–18., doi:10.1098/rsif.2009.0243.

Liu, Feng, et al. Photostimulated near-Infrared Persistent Luminescence as a New Optical Read-out from CR3+-Doped liga5o8." Scientific Reports, vol. 3, no. 1, 2013, https://doi.org/10.1038/srep01554.

Liu, Hongyun, et al. "Electroactive Core-Shell Nanocluster Films of Heme Proteins, Polyelectrolytes, and Silica Nanoparticles." Langmuir, vol. 20, no. 24, 2004, pp. 10700–10705., doi:10.1021/la0488598.

Maldiney, Thomas, et al. "The in Vivo Activation of Persistent Nanophosphors for Optical Imaging of Vascularization, Tumours and Grafted Cells." Nat. Mater., vol. 13, no. 4, 2014, pp. 418–426., doi:10.1038/nmat3908.

Polsky, Ronen, et al. "Nucleic Acid-Functionalized PT Nanoparticles: Catalytic Labels for the Amplified Electrochemical Detection of Biomolecules." Anal. Chem., vol. 78, no. 7, 2006, pp. 2268–2271., doi:10.1021/ac0519864.

Wang, Chen-Shen, et al. "Gene-Editing by CRISPR-Cas9 in Combination with Anthracycline Therapy via Tumor Microenvironment-Switchable, EGFR-Targeted, and Nucleus-Directed Nanoparticles for Head and Neck Cancer Suppression." Nanoscale Horiz., vol. 6, no. 9, 2021, pp. 729–743., doi:10.1039/d1nh00254f.

Wu, Yue, et al. "Gold Nanoparticles in Biological Optical Imaging." Nano Today, vol. 24, 2019, pp. 120–140., doi:10.1016/j.nantod.2018.12.006.

Xiao, Yi, et al. "Plugging into Enzymes": Nanowiring of Redox Enzymes by a Gold Nanoparticle." Science, vol. 299, no. 5614, 2003, pp. 1877–1881., doi:10.1126/science.1080664.

Zha, Zhengbao, et al. “Uniform Polypyrrole Nanoparticles with High Photothermal Conversion Efficiency For Photothermal Ablation of Cancer Cells.” Adv. Mater., vol. 25, no. 5, 2012, pp. 777–782., doi:10.1002/adma.201202211.
Zhou, Hui, et al. “Hemoglobin-Based Hydrogen Peroxide Biosensor Tuned by the Photovoltaic Effect of Nano Titanium Dioxide.” Anal. Chem., vol. 77, no. 18, 2005, pp. 6102–6104., doi:10.1021/ac050924a.
Zhou, Yixian, et al. “Mesoporous Silica Nanoparticles for Drug and Gene Delivery.” Acta Pharm. Sin. B, vol. 8, no. 2, 2018, pp. 165–177., doi:10.1016/j.apsb.2018.01.007.

Advances in Applied Chemistry and Industrial Catalysis – Saikia (Ed.)

Research on the application of chemical analysis technology in the testing of chemical raw materials

Liying Jia*
Dongying Vocational Institute, Dongying, Shandong, P.R. China

ABSTRACT: The correct testing of raw materials in chemical production can further improve the quality of chemical production, which is the basic prerequisite for ensuring the quality of chemical products. At present, in the testing stage of chemical raw materials, the application of chemical analysis technology is very important to improve the quality and efficiency of chemical raw materials. Therefore, it is necessary to thoroughly study the technical characteristics of chemical analysis and its specific application in chemical testing. The study can provide scientific and accurate technical guarantees for the chemical testing process and results, and meet the actual needs of chemical raw material testing.

1 INTRODUCTION

Chemical analysis technology plays a very important role in the testing of chemical raw materials at this stage [1]. Traditional chemical analysis methods still have many limitations. If inaccurate testing is used, it is usually impossible to effectively identify the composition and properties of chemical substances, and it is impossible to develop chemical analysis techniques [2]. The development and research of technology help achieve the expected chemical substance testing results. Effective chemical analysis techniques can not only overcome the original limitations and shortcomings of traditional chemical substance testing techniques, but also can analyze the results of chemical substances more systematically and scientifically [3]. The research on chemical analysis technology effectively combines the testing of raw materials, and accurately adjusts the content and deficiencies of chemical analysis technology, which will help the high-efficiency testing of chemical raw materials in the future.

2 BASIC CONCEPTS AND TECHNICAL STATUS OF CHEMICAL ANALYSIS TECHNOLOGY

2.1 *Basic concepts of chemical analysis techniques*

The chemical analysis method is to carry out experimental testing and research on chemical substances by modern technology. The chemical composition is evaluated mainly based on the initial state, and the composition is carefully analyzed based on the degree of chemical reaction [4]. The requirement of general chemical analysis methods is to identify chemical substances, because the testing work requires a greater demand for chemical analysis techniques. Therefore, the requirements are very strict, and the accuracy of the testing requires comprehensive real-time monitoring. In order to avoid any factors that affect the results of laboratory analysis, it is necessary to use high-quality testing tools and higher requirements for testing technicians. In the testing of chemical materials, the main testing objects are composed of different chemical components. The entire testing process takes a long time, and the current technology is constantly innovating. The testing methods of chemical substances are not only limited to the current testing methods but also include

*Corresponding Author: tg55667788@greenmlie.com

DOI 10.1201/9781003308553-17

the continuous innovation and optimization of the process. The application of technology has also made major breakthroughs to achieve good chemical material testing, ensure greater safety, and promote the continuous research of chemical raw materials.

2.2 *Main features and technical status of the chemical analysis*

In recent years, with the steady development of China's economy, the chemical industry has a lot of room for development. Chemical analysis technology has gradually become the main component of this field, and the testing methods of chemical components are more and more diversified [5]. The traditional single chemical composition analysis is no longer applicable. Especially for the identification of subtle main components, compound analysis, the use of different techniques, there will be deviations in the testing results. In order to accurately distinguish the relationship between the material components, its analysis and practical value lies in the effective use of technology. The current chemical analysis system is constantly improving, and the application level of chemical analysis technology is gradually improving. In general, it penetrates the entire process of industrial raw material production.

3 VALUE AND ROLE OF CHEMICAL ANALYSIS TECHNOLOGY APPLICATION

3.1 *The value of chemical analysis technology application*

In general, chemical analysis technology has two values in detecting chemical substances. First of all, compared with other testing methods for measuring chemical substances, the use of chemical analysis can better capture the properties of chemical substances. The analysis can thoroughly test the state of substances during chemical reactions, and describe the structure of the entire substance and the properties of the chemical substance. Secondly, the use of chemical analysis helps ensure the safety and economic benefits of the production of chemical materials. The above analysis shows that the testing of chemical substances is the basis of chemical production. Because the chemical industry is more dangerous and toxic, it is necessary to fully grasp the properties of chemical materials before using them to ensure the maximum safety and economic benefits of chemical materials production.

3.2 *The application of chemical analysis technology*

3.2.1 *Promote the development of chemical analysis technology*

The use of chemical materials is relatively popular and is almost closely related to people's lives. Therefore, it is necessary to ensure the quality of materials and improve chemical analysis techniques so that the application of chemical analysis in the quality control of chemical materials can satisfy standards for the use of chemicals and reduce the unfavorable factors [6]. Today, many companies are pursuing the maximization of profits in the future development. In the production of related chemical materials, they have not achieved comprehensive processing or comprehensive and accurate testing of chemical materials, completely neglecting people's physical and mental health. For example, some wastewater treatment plants do not consider the quality of the materials of the wastewater treatment plants, and do not conduct adequate chemical material analysis treatments. After being discharged, water pollution would result in the formation of harmful impurities in the water, which are immediately harmful to people's health to a certain extent. Life will have an adverse effect.

In the development stage of the chemical industry, it is necessary to analyze chemical substances carefully and accurately to ensure that the handling of chemical materials meets operating standards, and avoid the production of harmful substances due to reactions between chemical materials and other substances. The popularization of the application of chemical analysis technology can not only promote the accurate development of chemical analysis technology, but also improve the quality of chemical materials and promote the development and application of new chemical materials. Chemical analysts should also persist in learning, build their own chemical testing knowledge base, learn from mistakes and successful experiences, work patiently and meticulously, and promote the progress of the chemical materials industry.

3.2.2 *Accelerate the comprehensive application of chemical analysis technology*

The application of chemical materials is very common. In addition to some frequent chemical experiments, there are also chemical materials used in bridges, construction, medicine and other fields. Therefore, not only the chemical production field must effectively use chemical analysis technology, other industries also need to be able to fully learn to use it to accelerate the comprehensive application of chemical analysis technology [7]. For example, to detect some substances in the oil field, chemical analysis techniques can be used to ensure that the composition of the material does not change the physical and chemical properties of the oil itself. For example, in pipeline production, in order to increase the corrosion resistance and hardness of the pipeline, it is necessary to conduct chemical analysis on materials and other compounds. Pharmaceutical factories use chemicals to ensure safe and non-toxic put into use through advanced chemical analysis technology, and ensure that the production of medicines is linked to the quality of medicines. After the products are sold to consumers, safety risks that may affect the company's economic interests and human health and safety can be avoided.

4 A BRIEF CLASSIFICATION OF CHEMICAL ANALYSIS METHODS

4.1 *Assess the chemical composition of the raw materials*

Chemical analysis method mainly refers to the method of analyzing and describing the composition of analytical object according to a series of chemical reactions and quantitative relationships [8]. Evaluation is the basis of chemical analysis. In the analysis of chemical raw materials, it not only needs to have sufficient theoretical knowledge of chemical analysis methods, but also supplement the accurate measurement of related instruments to achieve the chemical industry's comprehensive basic production. Chemical analysis is different from physical analysis. Chemical analysis cannot simply supplement the appearance of a substance, but deal with it in a timely manner and separation of substances. In order to improve the application effect of technology, analytical technology is constantly updated and testing accuracy is improved, chemical analysis methods have become the core technology in the main application areas. At present, chemical analysis methods are divided into traditional analytical methods and instrument analysis methods.

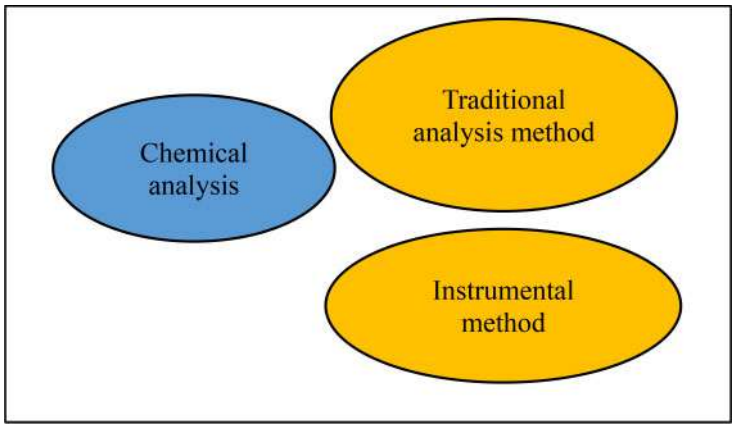

Figure 1. Composition of the chemical analysis methods.

4.2 *Traditional analysis methods*

Based on the existing chemical reactions, the traditional analytical methods clearly distinguish the composition of chemical substances, understand the basic characteristics and properties of their composition, and then qualitatively and quantitatively evaluate the composition of raw materials. In

the identification of chemical raw materials, traditional analytical methods are particularly appropriate means. For the traditional chemical analysis method, the production of chemical materials has a very long application history with the advantages of high efficiency. However, due to the common accuracy of testing, the technology also has some shortcomings. It is commonly used for the basic prediction and general evaluation of general chemical raw materials for environmental experiments. This analysis method is not expensive and can be applied effectively in the laboratory, so this chemical analysis method also plays an important role in the actual chemical production and testing work. If in-depth analysis and evaluation of raw materials are required, the method is a good choice in the analysis process, and basic chemical raw material data can be obtained. Comprehensive analysis, the traditional analysis results can only be used as the basis for raw material analysis, which cannot resolve and detect all the elements of the test objects.

4.3 *Instrumental method*

Instrument analysis is an analytical method to correct the errors and shortcomings of traditional chemical analysis methods. Its accuracy and scientific application are rapid, with speciality compared with the traditional analytical methods. This method of testing is more scientific and accurate, and it is a major part of chemical analysis. The composition and characteristics of chemical raw materials can be analyzed more comprehensively using high-precision instrument analysis methods. In practice, the chemical raw materials can be detected vertically by using relevant instruments to analyze the molecular and even atomic raw materials. Generally, in pure raw material analysis, the application of instrument analysis methods is more important in line with the needs of testing and analysis work. Using other analytical methods or traditional analytical methods is difficult to meet the higher analytical requirements compared with the pre-test method.

Instrumental method:
Using precise instruments, physical or chemical properties, qualitative and quantitative analysis according to the generated test signals.
Features of the instrument analysis:
1 . High sensitivity
2 . Many choices
3 . Expensive and difficult to popularize

Figure 2. Instrument analysis methods and characteristics.

Workers must be more professional and put more effort into the technology. The use of this technology is expensive in the testing of chemical raw materials, which demands the need for specific analysis of specific problems. According to the material requirements, the high-precision analysis method can be selected in the chemical industry. The technology can correctly grasp the basic characteristics of chemical substances, and produce scientific and accurate raw material chemical analysis report.

5 PRACTICAL APPLICATION OF CHEMICAL ANALYSIS METHOD IN CHEMICAL MATERIAL TESTING

5.1 *Assess the chemical composition of the raw materials*

The main task of chemical analysis and testing of chemical materials is to determine and evaluate the chemical composition of raw materials. In order to determine the correct composition of chemical materials, it is often necessary to consider the characteristics of chemical production and complex

environment. Chemical substances are complex in the manufacturing process. Because there is no detailed analysis of chemical materials, the entire chemical production process will appear very dangerous situation. In order to avoid the risk of accidents, it needs to accurately record the chemical analysis method of the testing process, as well as raw material composition analysis reports to ensure production safety.

5.2 *The definition of chemical properties*

Chemical production requires a safe environment. It is possible not only to conduct a comprehensive and thorough analysis and evaluation of the composition of chemical raw materials, but also determine the nature of chemical raw materials. Traditional chemical analysis methods are generally used in the composition analysis of chemical raw materials. There is no scientific and accurate preliminary conclusion. In order to further determine the nature of chemical substances, instrumental analysis is necessary to accurately isolate and analyze the composition and properties of chemical substances. Based on traditional chemical analysis methods, instruments are used to measure the composition of raw materials so that operators can fully understand the general properties of the material and form a very complete scientific report. It should be noted that the selection of instruments should be based on the nature and characteristics of the chemical material. It is important to note that in all cases, the nature of chemical raw materials in the manufacture of chemical products must be determined.

5.3 *Internal structural analysis of chemical materials*

In order to thoroughly analyze chemical raw materials, the internal structure of the components should be tested in addition to measuring and demonstrating their composition and performance. For some chemical products, the internal structural characteristics and structural changes of raw materials need to be understood. In the process of chemical industrial production, the internal structure of chemical raw materials is analyzed by instrument analysis method, which meets the standards of chemical production and greatly improves the accuracy. In the actual experiment, the results of the internal structure analysis of the material basically meet the requirements of the chemical reaction analysis of raw materials. Therefore, according to the actual needs of chemical production, it must fully understand the importance of chemical analysis methods for the testing of industrial chemicals causing chemical reactions, and correctly choose the application of chemical analysis methods.

6 APPLICATION PROSPECT OF CHEMICAL ANALYSIS TECHNOLOGY IN THE TESTING OF CHEMICAL RAW MATERIALS

The rapid development of China's chemical industry has had a great impact on other industries [9]. Modern chemical materials are an important part of people's daily life and are widely used in the production of ordinary products such as plastics and glass. The rapid growth of chemical demand in modern society has promoted the development of social economy and the improvement of chemical level. If no harmful materials are found in the test, once the general market cannot be effectively identified. Physical testing can only provide a preliminary understanding of the appearance and physical properties of raw materials. The application of chemical analysis in chemical testing can accurately analyze the properties of raw materials and predict chemical reactions in the production process. Companies can accurately describe raw materials in post-partum products, and scientifically use chemical analysis techniques to promote the development of the chemical industry.

In the actual chemical production process, chemical analysis has become a commonly used chemical material testing methods. Therefore, taking into account the characteristics of chemical and other production enterprises and the high complexity of production requirements, it is necessary to fully recognize the need to apply the method in raw material testing to have a full understanding

of the method. Therefore, chemical analysis is an indispensable part of chemical raw material testing starting with the in-depth understanding of chemistry and detailed analysis of the correct operation of the instrument. This is a specific analysis and simulation of the chemical production process. Chemical enterprises need to pay attention to the production of chemical products under different conditions to ensure more effective and scientific.

7 CONCLUSION

The material composition of chemical raw materials is tested by chemical analysis, even if its characteristics and internal structure are accurately measured and verified. More importantly, the method itself must be fully understood and applied. In practice, it demands specific analysis of specific problems in view of the particularity of the production environment and the special demand for raw materials. The combination of accurate chemical analysis applications and import chemical control is necessary to make chemical production more safe.

REFERENCES

Huo Yuxin. Research on application of chemical analysis in chemical materials testing [J]. Materials for information record, 2019, 20(09):29–30.

Jiang Haiying. Discussion on chemical analysis technology in chemical materials testing [J]. Chemical Management, 2018(17):186–187.

Liu Yuanheng. Application analysis of chemical analysis in chemical materials testing [J]. China petroleum and chemical standards and quality, 2017, 37(16):35–36.

Pan Xue. Effective application of chemical analysis in chemical material testing [J]. Chemical Industry Management, 2019(33):40–41.

She Huijuan. Explore the effective application of chemical analysis in the testing of chemical materials [J]. Science and technology information, 2020, 18(11):39–40.

Shi Tao. Application of allowable difference in quality control of chemical analysis [J]. Science and technology innovation review, 2018, 15(25):121–122.

Wu Tao. Effective application of chemical analysis in chemical materials testing [J]. Materials for information record, 2019, 20(01):4–5.

Zhang Wengguang. Quality assurance of control based on application inspection of chemical analysis [J]. China New Technology and New Products, 2012(04):24.

Zhang Yin. Research on application of chemical analysis in chemical materials testing [J]. Chemical design communication, 2019, 45(05):74.

Advances in Applied Chemistry and Industrial Catalysis – Saikia (Ed.)

LEAP-based scenario analysis in carbon emission of Jiangsu Province

Xin Wang*
State Grid Jiangsu Economic Research Institute, State Grid Jiangsu Electric Power Co., Ltd, Nanjing, China

Fenghua Zou
State Grid (Suzhou) City & Energy Research Institute Co., Ltd, Suzhou, China

Jing Shi
State Grid Jiangsu Economic Research Institute, State Grid Jiangsu Electric Power Co., Ltd, Nanjing, China

Sheng Wang & Hao Chen
State Grid (Suzhou) City & Energy Research Institute Co., Ltd, Suzhou, China

ABSTRACT: Faced with deteriorating environmental problems dominated by global warming, China is committed to reaching carbon dioxide emissions peak by 2030. This paper proposes a unified structure of emission-oriented scenario analysis based on long-range energy alternatives planning (LEAP) theory at a provincial level which is suitable for regions in China. Numerical analysis is conducted with the example of Jiangsu province under three benchmark scenarios: basic scenario, target scenario, and enhanced scenario. The results reveal the variation trend of carbon emissions from different sectors and demonstrate the feasible path of low-carbon transformation in Jiangsu from 2020 to 2060.

1 INTRODUCTION

With the prevalent concept of low-carbon economy, methods for calculating and decreasing carbon emission attract worldwide attention. State Council of China releases a scheme to reach carbon emission peak before 2030 (State Council of China 2021). Department of Ecology and Environment of Jiangsu Province also issues Emission Peak Action Plan to promote provincial energy transformation (Department of Ecology and Environment of Jiangsu Province 2021). However, the vast quantity of carbon emission produced by developed industry especially the manufacturing industry in Jiangsu increases the pressure of low-carbon transformation. Therefore, precisely measuring the emission and comprehensively analyzing the influence of various factors such as economy, society, policy, and energy utilization technology under different scenarios are effective and meaningful for further emission reduction and policy-making.

Previous studies carried out on emission analysis usually adopt methods such as time series analysis (Jermsittiparsert 2019), multi-objective linear programming (Govindan & Sivakumar 2016), neural network (Patterson et al. 2021), and chaotic dynamics theory (Liu et al. 2017). These mentioned methods focus on finding the short-term relationship between several quantifiable data and overlook long-range macro variables such as technology and policy. To break through the limitation of conventional analysis modes, scenario analysis theory is applied to comparing macro factors in different scenarios and to identifying long-term trends of sustainable development. A novel scenario analysis model based on extended-STIRPAT is established to investigate driving factors of carbon emissions and emission peaking in (Liu & Xiao 2018). The effects of carbon pricing policy including a carbon tax and carbon emission trading are investigated with an improved computable

*Corresponding Author: 595580317@qq.com

DOI 10.1201/9781003308553-18

general equilibrium (CGE) model in (Zhao et al. 2018). With the assistance of the long-range energy alternatives planning (LEAP) model, the energy efficiency and carbon emission reduction potential of the iron and steel industry in Turkey are discussed in (Ates 2015).

However, the mentioned studies conduct scenario analysis in different targets by using distinguished statistical caliber. None of the studies build up a unified emission-oriented scenario analysis model and standard procedures which is appropriate for similar regions. This paper proposes a normative structure of emission-oriented scenario analysis based on LEAP model which is suitable for regions in China at a provincial level.

The rest of the paper is organized as follows. Section 2 introduces the structure of the proposed scenario analysis. Section 3 presents the carbon emission calculation model based on energy balance table. Section 4 indicates the scenario setting and key impact factors outlook. Section 5 introduces the data collection and cleaning methods. Section 6 verifies the effectiveness of the proposed model in cased of Jiangsu Province. Section 7 draws the conclusion.

2 STRUCTURE OF SCENARIO ANALYSIS BASED ON LEAP MODEL

LEAP is a classic bottom-up econometric model which integrates impact factors of energy, economy, and environment. The structure of emission-oriented LEAP differs in different regions due to complex regional characteristics. To comprehensively measure the quantity of carbon emission in China at the provincial level, a normative structure of scenario analysis based on the LEAP model is proposed as Figure 1.

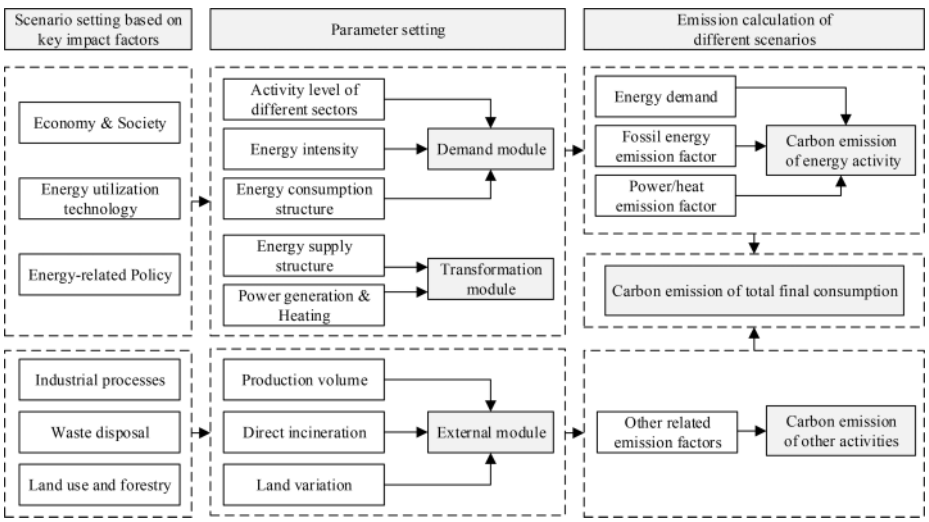

Figure 1. Normative structure of scenario analysis based on LEAP model.

The structure contains three major parts: scenario setting, parameter setting, and emission calculation. The carbon emission of total final consumption in a selected province is divided into two aspects: carbon emission produced by energy activity and other activities. The aspect of energy activity takes emission factors of different energy and final energy demand generated by Demand module and Transformation module into consideration. The Demand module calculates the emission from demand sectors such as industry, construction, and transportation. The Transformation module counts the emission from the energy sector such as power generation and heating. The trend of future energy activity is estimated in terms of economy, society, energy utilization, and policy. The aspect of other activities mainly considers the emission from external modules such as industrial processes, waste disposal, land use, and forestry. It is noted that the partition of three

modules is supported by the provincial energy balance table which can be downloaded from the national bureau of statistics.

3 CARBON EMISSION CALCULATION MODEL BASED ON ENERGY BALANCE TABLE

Emission computation model using energy balance table is a common and practical solution to estimate the quantity of carbon emission at the provincial level (Xie 2020). The model is shown as follows:

$$C_{\mathrm{t}} = \sum_{i \in I} \sum_{j \in J} \left(E_{i,j,t} \cdot F_{i,t} \right) \tag{1}$$

Where C_t is the carbon emission from energy activity of year t, $E_{i,j,t}$ is the total energy consumption at year t, $F_{i,t}$ is the carbon emission factor of energy i at year t, I is the type of the consumed energy, J is the classification of industry.

4 SCENARIO SETTING AND KEY IMPACT FACTORS OUTLOOK

4.1 *Scenario setting*

In consideration of the emission neutrality target announced by the Chinese government, three benchmark scenarios are set up as follows:

(1) Basic scenario: the existing carbon emission reduction policies continue to be implemented and no major policy will be issued after the selected base year; the promotion rates of related technologies remain unchanged; the production and consumption levels of main sectors increase steadily; the direction of the current industrial structure adjustment remains unchanged.
(2) Target scenario: the carbon emission of the selected province peaks at the year 2030 and attains neutrality at the year 2060.
(3) Enhanced scenario: the carbon emission of selected province peaks at the year 2025 and attains neutrality at the year 2055.

4.2 *Outlook of key impact factors*

The assumption of key influence factors is demonstrated in Table 1.

Table 1. Assumption of key impact factors.

Economy& Society:
• Gross domestic product: the growth rates every 5 years from 2020 to 2060 are 5.5%, 4.5%, 4.3%, 4%, 3.8%, 3.5%, 3.3%, and 3%.
• Urbanization rate: the rates every 5 years from 2020 to 2060 are 70.9%, 75.0%, 80.0%, 83.0%, 85.0%, 85.0%, 85.0%, 85.0%, and 85.0%.
• Proportion of employed population: the proportions every 5 years from 2020 to 2060 are 56.1%, 57.0%, 57.5%, 57.2%, 57.0%, 56.8%, 56.6%, 56.4%, and 56.2%.
• Proportion of employment in tertiary industry: the proportion every 5 years from 2020 to 2060 are 43.0%, 48.0%, 52.0%, 55.0%, 57.0%, 58.5%, 60.0%, 60.0%, and 60.0%.
• Proportion of industrial added value: the proportion differs in different scenarios
• Carbon sink: the quantity grows at an average rate of 2.5% from 2020 to 2060.
• Waste disposal: the annual carbon emission generated by disposal counts 1926.7 thousand tonnes from 2020 to 2060.

(Continued.)

Table 1. Continued.

Energy utilization technology:

- Renewable energy generation: the Levelized Cost of Energy declines steadily and the installed capacity increases rapidly from 2020 to 2060.
- Carbon capture, utilization, and storage (CCUS): the emissions caused by CCUS decrease quickly.
- Hydrogen energy: the proportion of hydrogen grows steadily.

Energy-related policy:

- The target years of emission peak and neutrality are set before 2030 and 2060.

5 DATA COLLECTION AND CLEANING

The data of GDP, population, carbon sink, energy consumption, etc., are obtained from the National and Jiangsu statistical yearbook (Jiangsu Bureau of Statistics 2021). GDP and its growth are calculated according to its comparable price. However, current national energy statistics data exist in the form of energy balance table and mix the energy consumption of industry, construction, and transportation into various industrial sectors. For example, transportation energy consumption takes the majority of the energy consumption in traffic, warehousing, and postal industry while construction energy consumption of transportation hubs such as railway stations, terminal buildings, and passenger terminals takes the minority. Therefore, it is necessary to split the mixed data of the energy balance table from the statistical yearbook into corresponding construction and transportation sectors. The principle of adjustment is supported by the Energy Research Institute of National Development and Reform Commission (Price 2017).

6 CASE STUDIES

6.1 *Carbon emission of total final consumption in Jiangsu*

The emission of total final consumption under three benchmark scenarios is shown in Figure 2. In the basic scenario, the emission of Jiangsu peaks at 987 million tonnes around the year 2035. The emission quantity drops 16.39% from 2020 to 2060. In the target scenario, the emission reduces 73% from 2020 to 2060. In the enhanced scenario, the average annual declining rate of emission is 6.8% and the emission reduced by CCUS and carbon sink reaches 64 million tonnes.

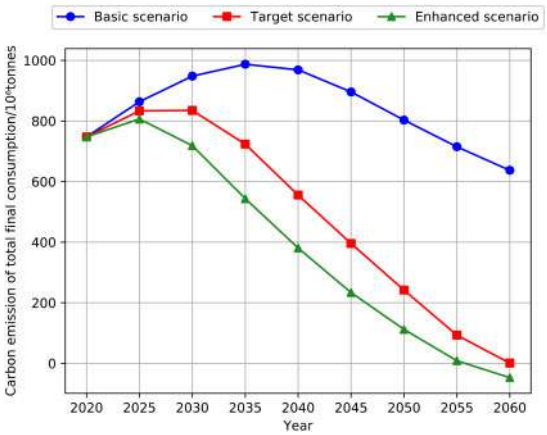

Figure 2. Carbon emission of total final consumption in Jiangsu.

6.2 *Carbon emission of different sectors*

The emissions from four main sectors are indicated in Figure 3. Under target scenario and enhanced scenario, the emissions from the industry sector drop to 32.5% and 12.7% from 2020 to 2050; the emissions from the construction sector peak around the year 2035 and 2030 with peak values of 25 and 21 million tonnes which are approximately 81.84% and 72.40% of the basic scenario; the emissions from transport sector fall to 35.88% and 17.36% of the peak value respectively; the emissions from energy sector peak at 445 and 417 million tonnes. In particular, the quantities of emissions from the energy sector under the target scenario and enhanced scenario exceed the quantity under the basic scenario from 2021 to 2025 due to electrification of final energy consumption in all sectors which forces the energy sector to shoulder reduction pressure from other sectors.

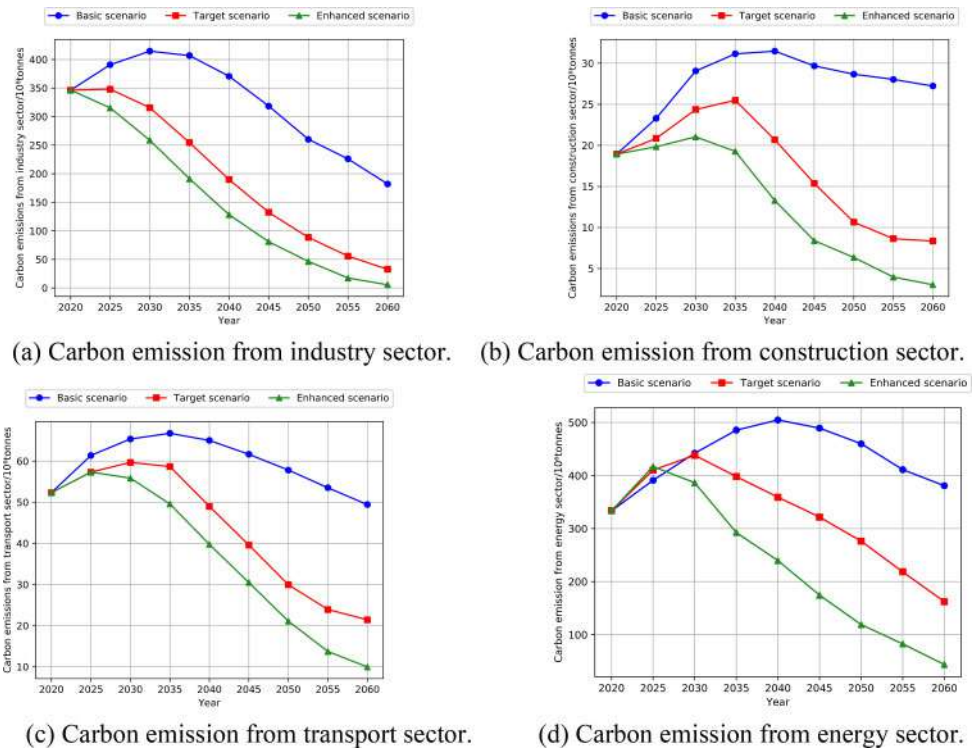

Figure 3. Carbon emission from different sectors.

7 CONCLUSION

This paper proposes a normative structure of emission-oriented scenario analysis based on LEAP theory, which is suitable for provinces in China. The carbon emission in Jiangsu is computed with the provincial energy balance table. Based on the results and discussions presented above, the conclusions are obtained as below:

(1) In the basic scenario, the total final consumption carbon emission in Jiangsu peaks at 987 million tonnes around the year 2035 and drops 16.39% from 2020 to 2060. In the target scenario, the emission reduces 73% from 2020 to 2060. In the enhanced scenario, the average annual declining rate of emission is 6.8%.

(2) Under the target scenario and enhanced scenario, the emissions from the industry sector drop to 32.5% and 12.7% from 2020 to 2050; the emissions from the construction sector peak around the year 2035 and year 2030 with peak values of 25 and 21 million tonnes; the emissions from transport sector fall to 35.88% and 17.36% of the peak value respectively; the emissions from energy sector peak at 445 and 417 million tonnes.
(3) The quantities of emissions from the energy sector in the target scenario and enhanced scenario exceed the quantity in the basic scenario from 2021 to 2025. The results reveal the electrification trend of final energy consumption in all sectors. To reach the emission peak target, the energy sector has to shoulder more reduction pressure from other sectors.

ACKNOWLEDGMENTS

This work was financially supported by the project of State Grid Jiangsu Economic Research Institute (The impact of the "dual carbon" target on Jiangsu's mid-and long-term energy development and suggestions for the development of Jiangsu Electric Power Company).

REFERENCES

Ates S A. 2015. Energy efficiency and CO2 mitigation potential of the Turkish iron and steel industry using the LEAP (long-range energy alternatives planning) system. Energy. 90: 417–428.

Department of Ecology and Environment of Jiangsu Province. 2021. Emission Peak Action Plan. http://sthjt.jiangsu.gov.cn/art/2021/6/30/art_83592_10046357.html.

Govindan K, Sivakumar R. 2016. Green supplier selection and order allocation in a low-carbon paper industry: integrated multi-criteria heterogeneous decision-making and multi-objective linear programming approaches. Annals of Operations Research. 238(1–2): 243–276.

Jermsittiparsert K. 2019. Behavior of tourism industry under the situation of environmental threats and carbon emission: Time series analysis from Thailand. 670216917.

Jiangsu Bureau of Statistics. 2021. Jiangsu Statistic Yearbook. http://tj.jiangsu.gov.cn/col/col83749/index.html.

Liu D, Xiao B. 2018. Can China achieve its carbon emission peaking? A scenario analysis based on STIRPAT and system dynamics model. Ecological indicators. 93: 647–657.

Liu Y, Tian Y, Chen M. 2017. Research on the prediction of carbon emission based on the chaos theory and neural network. International Journal Bioautomation. 21(4): 339.

Patterson D, Gonzalez J, Le Q, et al. 2021. Carbon emissions and large neural network training. arXiv preprint arXiv:2104.10350.

Price L, Khanna N, Fridley D, et al. 2017. Reinventing fire: China–the role of energy efficiency in China's roadmap to 2050. European Council for an Energy Efficient Economy Summer Study. 113–120.

State Council of China. 2021. Carbon Emission Peak Action Plan by 2030. http://www.gov.cn/zhengce/content/2021-10/26/content_5644984.html.

Xie P, Yang F, Mu Z, et al. 2020. Influencing factors of the decoupling relationship between CO2 emission and economic development in China's power industry. Energy. vol.209, pp.118341.

Zhao Y, Li H, Xiao Y, et al. 2018. Scenario analysis of the carbon pricing policy in China's power sector through 2050: Based on an improved CGE model. Ecological indicators. 85: 352–366.

Advances in Applied Chemistry and Industrial Catalysis – Saikia (Ed.)

Profit analysis of virtual power plant in the ancillary service market

Kening Chen[1] & Gao Zhang[2]
State Grid Energy Research Institute, Beijing, China

Liang Xu[3], Xiaoliang Dong[4], Honghai Tang[5] & Yizhe Wang[6]
Beijing Power Exchange Center, Beijing, China

Huiwen Qi[7], Xiangyu Zhang[8] & Zhenbo Xu[9]
State Grid Shanxi Economic Research Institute, Taiyuan, China

ABSTRACT: Under the new power system with a high proportion of renewable energies, the virtual power plant (VPP) can fully motivate different kinds of decentralized controllable resources, therefore the VPP is in the future an important part of participating in the system regulation through the electricity market. This paper comprehensively considers the various costs and profits of the VPP, including income sharing, fixed subsidies, and the competitive relationship with thermal power plants in the ancillary service market. The cost and profit of the VPP are analyzed in different situations, which provides a reference for the investment and operation entities of the VPP.

1 INTRODUCTION

The virtual power plant is a system using advanced information communication technology and software, to realize the aggregation, coordination, and optimization of distributed resources such as distributed generation, energy storage system, controllable load, and electric vehicles. The VPP is a special power plant with a coordinated management system in the electricity market and power system operation. With the access of a large number of distributed generators and flexible loads, the energy management system with virtual power plants will provide security and operation support for the power system.

At present, there are many studies on the market-oriented participation of virtual power plants in system regulation in China and abroad. In reference, the dispatching optimization considering operation uncertainty of a VPP is studied; in some research, the dispatching mode of a virtual power plant connected to the distribution network is designed; the operation mechanisms in the electricity market are also studied in work, as well as in the ancillary service market. Some other research focused on the commercial model of the VPP: In some research, the power purchase and sale strategies of VPP in the electricity market are studied; and the profit of a VPP considering uncertain risks in the electricity market has already been researched, and some work considered the uncertainty of the response capability for the resources aggregated by the VPP.

However, the investment and construction of a VPP require a comprehensive analysis of whether it can be profitable. At present, few studies detail the relationship between the cost and profit of the VPP. This paper establishes the cost and profit model of a VPP in the ancillary service market, considers the competitive advantages compared with traditional power plants, and designs the cost and profit analysis method for the VPP.

Corresponding Authors: [1]chenkening@sgeri.sgcc.com.cn, [2]zhanggao@sgeri.sgcc.com.cn, [3]xu-liang@sgcc.com.cn, [4]xiaoliang-dong@sgcc.com.cn, [5]honghai-tang@sgcc.com.cn, [6]wang-yizhe@sgcc.com.cn, [7]1027722464@qq.com, [8]hdzxy114@163.com and [9]hdzxy114@163.com

DOI 10.1201/9781003308553-19

Table 1. Margin settings for A4 size paper and letter size paper.

	A4 size paper		Letter size paper	
Setting	cm	inches	cm	inches
Top	2.5	0.98"	1.75	0.98"
Bottom	3.0	1.18"	2.01	0.79"
Left	3.0	1.18"	3.28	1.29"
Right	3.0	1.18"	3.28	1.29"
All other	0.0	0.0	0.0	0.0

2 PROFIT ANALYSIS MODEL OF THE VIRTUAL POWER PLANT

2.1 *Analysis of cost and profit factors of the VPP*

The key factors of the virtual power plant profit include the following aspects:

- Within a certain period of time (one year), let Q be the total peak regulation demand of the market, Q_V and Q_h be the total regulation ability of the VPP and thermal power plant respectively.
- λ is the regulation market winning rate for the VPP
- L is the total controllable electricity capacity of a single VPP
- h is the controllable hours of a VPP in a certain period of time (one year)
- η is the proportion of the load that can be controlled by a VPP in the regulation market
- r_m is the kWh income of a VPP participating in the regulation market
- r_0 is the subsidy from the government
- μ is the kWh revenue sharing coefficient for the VPP resource customers in the regulation market
- p is the VPP cost per kW (including the unit cost of fixed investment, and unit variable cost)

1) λ is relevant to the total capacity scale of the VPPs in a certain area, and also relevant to the total regulation requirement in the same area. It is related to the competitive relationship between VPP and thermal power plants.
2) $L{\cdot}h{\cdot}\eta$ is the maximum regulated power of a single VPP in a certain period of time (one year)
3) The unit income r of a VPP can be determined in two ways, one is bidding in the market and the other is from the fixed subsidy. The typical regulation market income in different regions of China is shown in the table below.

Table 2. Typical regulation market unit income in different regions of China (2019).

Region	Type	Price (Yuan/kWh)
Northeast China	down regulation	0.392 for the first level 0.596 for the second level 0.793 for the third level
Northern China	regulation market	0.05
Eastern China	regulation market	0.05
Mid China	regulation market	0.1
VPP trial project in Shanghai	upregulation of the load	1.2
	downregulation of the load	3
VPP trial project in Northern Hebei Province	regulation market	0.22

Table 1 shows that the reward for the regulation service has different modes. The reward mode of the ancillary service market is gradually changing from fixed reward mode to market mode. Due to

many factors to be considered and great uncertainty in the income through the market-oriented mode, the competitiveness between the VPP and the traditional thermal power plants in the market (the ability to bid low prices) can be analyzed by comparing their unit income. While for the fixed reward mode, the competition relationship can be studied considering the market winning rate is a certain hypothetical value.

4) The unit cost of a VPP is composed of the fixed investment cost p0 per kWh and the user reward sharing p1, in which:

• The fixed investment cost p_0 per kWh

$$p_0 = (P_0 - P_g)/L \tag{1}$$

where P_0 is the annual recovery requirement for the total fixed investment of a VPP with scale L, and P_g is the annual government fixed subsidy. P_0 can be divided into several parts, including the annual allocation of fixed investment in software and hardware of a VPP platform $P_{0\_Platform}$, private network/public network fee $P_{0\_Network}$, terminal (concentrator to user/equipment) hardware construction investment $P_{0\_Terminal}$. Annual operating expenses (labor, operation, and maintenance) $P_{0\_Operation}$, etc. Among them, private network/public network cost refers to the annual rental cost of renting a private network/public network or the annual apportionment cost of private network investment and construction cost:

$$p0 = (P_{0\_platform} + P_{0\_network} + P_{0\_terminal} + P_{0\_operation} - P_g)/L \tag{2}$$

• VPP resource customer revenue allocation

5) There are two ways of VPP resource customer income sharing. One is the fixed way: the VPP promises to provide customers participating in the regulation market with rewards of p_c per kWh through contracts, that is, unit cost $p_1 = p_c$; the other way is to allocate a certain proportion of ancillary service revenues to the customers, and $p_1 = r \cdot \mu$.

2.2 *The profit model of the virtual power plants*

(1) Analysis of the VPP profit

The income needs to cover the cost per kWh, which is: $r = r_m + r_0 > p_0 + p_1$

1) If the method of fixed sharing of income is adopted for the resource customers:

$$r_m + r_0 > p_0 + p_c, \quad \textit{which is } r_m + r_0 > (P_0 - P_g)/L + p_c \tag{3}$$

2) If the method of proportional sharing of income is adopted for the resource customers:

$$r_m + r_0 > p_0 + p_1 = p_0 + (r_m + r_0) \cdot \mu, \quad \text{and therefore}: (1-\mu) \cdot (r_m + r_0) > (P_0 - P_g)/L \tag{4}$$

(2) Competition relationship between VPP and thermal power plants:

Whether there is a competitive relationship between the VPP and the traditional thermal power plant in the regulation market, we first need to compare the relationship between Q, $Q_{v,}$ and Q_h. If Q is much larger than $Q_v + Q_h$, there is no competitive relationship between VPP and the traditional thermal power plant, because the total regulation requirement is much larger than the regulation capability of VPP and the traditional thermal power plant.

According to (3) and (4), the net income of virtual power plant per kWh is:

$$\Delta r_v = [r_m + r_0] - [(P_0 - P_g)/L + p_c], \text{or } \Delta r_v = (1-\mu) \cdot (r_m + r_0) - (P_0 - P_g)/L \tag{5}$$

The net income of thermal power plants per kWh is $\Delta r_h = r_m - f(x_o, x_p, x_L)$.

The increased coal consumption cost by output reduction of thermal power plant forms the regulation cost per kWh.

Where, $f(x_o, x_p, x_L)$ refers to the cost of thermal power per kWh in the regulation market, which is a function of the current output power x_o, the current generation proportion x_p, and the down-regulation electricity quantity x_L of the thermal power plant.

$$f(x_o, x_p, x_L) = [\alpha(x_p) - \alpha_0] \cdot x_0 \cdot t / x_L \tag{6}$$

Among which, $\alpha(x_p)$ represents the coal consumption cost per kWh when the power generation ratio is x_p. α_0 is the standard (low) coal consumption cost and t is the operation time (it is considered that the planned power generation of a thermal power plant which is not generated because of the down-regulation, will be supplemented in some way in the later stage).

- If $\Delta r_v < \Delta r_h$ holds no matter which level the thermal power plant is at, the cost of the virtual power plant is always less than the cost of the thermal power plant per kWh, and the virtual power plant is always competitive compared with the thermal power plant. In this case, the standard winning rate of the ancillary service market for the VPP can be set to 100%.
- If $\Delta r_v > \Delta r_h$ holds no matter which level the thermal power plant is at, the cost of the virtual power plant is always more than the cost of the thermal power plant per kWh, and the virtual power plant is always less competitive compared with the thermal power plant. In this case, the standard winning rate of the ancillary service market for the VPP can be set to 0%.
- If Δr_v and Δr_h have uncertain relationships at different regulation levels for the thermal power plants, the competition relationship is also uncertain for the two types of plants. In this case, the standard winning rate of the ancillary service market for the VPP is a value within the range of 0% to 100%.
- If the government gives priority to the VPP to participate in the regulation ancillary market without considering the competitiveness to promote the development of VPP, the standard winning rate can be set to 100%.

(3) Net profit analysis for the VPP

1) Fixed profit mode: $(r_m + r_0) \cdot L \cdot h \cdot \eta \cdot \lambda > (P_0 - P_g) + p_c \cdot L \cdot h \cdot \eta \cdot \lambda$, that is:

$$r_m + r_0 > (P_0 - P_g)/(L \cdot h \cdot \eta \cdot \lambda) + p_c \tag{7}$$

2) Variable profit mode: $(1 - \mu) \cdot (r_m + r_g) \cdot L \cdot h \cdot \eta \cdot \lambda > (P_0 - P_g)$, that is:

$$r_m + r_0 > (P_{0-} P_g)/[(1 - \mu) \cdot (r_m + r_0) \cdot L \cdot h \cdot \eta \cdot \lambda] \tag{8}$$

(3) or (4) are the necessary conditions for a VPP to acquire benefits through the regulation ancillary market. The total benefits that a VPP can acquire in the market regardless of cost are:

$$(r_m + r_0) \cdot L \cdot h \cdot \eta \cdot \lambda \tag{9}$$

3 NUMERICAL CASES

1) Using (7) and (8), we can judge whether the virtual power plant can meet the profit conditions through the regulation service market.

2) Using (9), we can roughly predict the total profit of a VPP through the regulation market (assumptions need to be made about the specific data of relevant variables).

The profit of a VPP under different assumptions is shown in the table below:

Table 2 shows that different types of VPPs with different reward modes, capacity scales, and controlling parameters, are probably getting acceptable profits. If other parameters and modes are selected, the VPP investors or operators can also estimate the profit according to the analysis above.

Table 3. Profit of a VPP under different assumptions.

VPP	Mode of a market	Revenue (Yuan/kWh)	Subsidy	The capacity scale of a VPP (10MW)	Controllable hours each year	Controllable load proportion	Winning rate	Profit each year (10000 Yuan)
A	Bidding	0.45	0	2	1825	30%	100%	492.75
B		0.45	0	5	1825	20%	50%	410.625
C	Fixed-price	0.3	0	10	1825	30%	100%	1642.5
D		0.3	0	3	1825	20%	50%	164.25

4 CONCLUSION

In the future, the virtual power plant is an important part of the new power system. The market-oriented system regulation of the VPP will bring more regulation resources and methods for the system operation. For the VPP investment and operation entities, it is necessary to understand the cost and profit of a VPP and fully analyze the profit share method and competitive ability in the regulating electricity market. This paper gives the relationship between the VPP cost, subsidy, market winning rate, benefit-sharing, and profit. It provides a reference for the construction and development of a virtual power plant. More specific conditions would be considered in our future work, and the VPP cost and profit relationship could be more accurate and practical.

ACKNOWLEDGEMENTS

This work is supported by the Science and Technology Project of State Grid Corporation of China. (Research on market mechanism and business model of the virtual power plant under the background of energy internet; No.: 1400-202057442A-0-0-00).

REFERENCES

Bian X Y, Yang S S, Huang L R, et al. Research on power system scheduling flexibility of virtual power plant accessing to distribution network [J]. Electrical Measurement & Instrumentation, 2020, 57(3): 66–71.

Ghavidel S, Li L, Aghaei J, et al. A review on the virtual power plant: Components and operation systems[C]// IEEE International Conference on Power System Technology. IEEE, 2016.

Jiang Hua, Yang Zhifang, Lin Wei, et al. Probability Distribution of Dispatch Region for a Virtual Power Plant Considering Distributed Renewable Uncertainties [J]. Proceedings of the CSEE, 2021.

Li Bin, Hao Yihao, Qi Bin, el al. Research on key information communication technologies supporting virtual power plant interaction [J]. Power System Technology, 2021.

Niu W J, Li Y, Wang B B. Demand response based virtual power plant modeling considering uncertainty [J]. Proceedings of the CSEE, 2014, 34(22): 3630–3637.

Wang Xuanyuan, Liu Dunnan, Liu Zhen, et al. Operation mechanism and key technologies of virtual power plant under ubiquitous internet of things [J]. Power System Technology, 2019 43(9): 3175–3183.

Yu Xinmei, Liu Shengwei, Wang Xinghua, et al. Decision-making Optimization of Procurement and Sale Strategies for Power Sales Companies Considering Virtual Power Plants [J]. Southern Energy Construction, 8(1): 110–115.

Zhang J L, Xia Y H, Duan D W, et al. Benefit-risk model of virtual power plant in energy market based on WCVaR assessment [J]. Automation of Electric Power Systems, 2017, 41(9): 77–83.

Zhang Kaijie. Research on virtual power plant participation in peak regulation in power market environment [D]. Zhejiang University, 2021.

Advances in Applied Chemistry and Industrial Catalysis – Saikia (Ed.)

Research on the planning and allocation method of smart grid technological transformation investment scale considering operational uncertain factors

Ying Zhou[1], Yun Wang[2], Yaling Jian[3], Qian Wang[4] & Lin Hu[5]
Economic and Technological Research Institute, State Grid Sichuan Electric Power Company, Sichuan, Chengdu, P.R. China

ABSTRACT: Technological transformation investment is an important means for grid companies to ensure the safety of grid operation and improve the level of power grid intelligence. Under the new situation, the scale of technological transformation investment in power grid enterprises is affected by various uncertain factors such as policies, social economy, and corporate profits. Therefore, how to scientifically and rationally plan the future investment scale of technological transformation investment in enterprises is of great significance to ensure the sustainable development of enterprises. Based on this, this article combines the characteristics of technological transformation investment and the high requirements of management substitution, and constructs investment allocation model methods based on different regions, which provides reference and guidance for improving the reasonable level of power grid enterprises' technological transformation investment decision-making and the level of power grid intelligence.

1 INTRODUCTION

With the continuous increase in the operating life of power grid equipment, and affected by many factors such as equipment aging and backward technology, power grid companies need to invest a large amount of money each year to update and transform power grid equipment. At the same time, because different regions have different economic development levels and power grid equipment operating status levels, how to reasonably allocate the scale of technological transformation investment between different regions is to ensure the safety level of grid equipment operation and improve the utilization of electricity technological transformation investment funds. One of the important tasks of efficiency level.

At present, relevant scholars have done certain research on the method of power grid investment allocation among different regions. Literature (Li et al. 2019) takes the medium and low voltage distribution network as the research object, divides the infrastructure investment into three parts: basic distribution investment, deduction investment and adjustment investment, and establishes the investment decision-making distribution of medium and low voltage distribution network infrastructure projects for municipal power grid companies. Model. Literature (Li et al.2020) constructed a hierarchical comprehensive evaluation index system for the investment benefit of the county-level distribution network, built an investment distribution adjustment coefficient model through the comprehensive evaluation results, and combined the future power demand to analyze the investment distribution of the county-level distribution network And calculations. Literature (Liu 2021) introduces the "optimization theory", combined with the future power grid development scale needs, establishes an investment allocation decision method that considers the matching degree

Corresponding Authors: [1]juzen123@163.com, [2]835365213@qq.com, [3]304460740@126.com, [4]zdwan1206@163.com and [5]ncepult2000@163.com

DOI 10.1201/9781003308553-20

and equilibrium degree of the distribution network development. Literature (Liu & Pan, 2020) proposed an investment allocation method based on the evaluation of the distribution network, based on the evaluation score for investment allocation. Literature (Xu et al. 2020) puts forward a method for distribution network investment allocation and project selection based on historical investment results to guide enterprises in making investment decisions.

It can be seen from the above that my country's current research on power grid investment allocation decision-making is mainly focused on distribution network investment projects, while research on investment allocation methods for power grid production technological transformation is relatively lacking. Therefore, this article takes municipal power grid companies as the research object, combines the investment objectives of power grid technology transformation, and constructs a comprehensive evaluation model of technological transformation investment demand from the dimensions of power grid assets, power grid quality, company operation, regional development and plan execution; Comprehensive evaluation scores for technological transformation investment of different county-level units are used as considerations for the initial allocation of technological transformation investment; then, combined with the development needs of power grid companies to improve quality and efficiency under the new situation, the difference in production and operation, operating efficiency, economic benefits, etc.

2 THE BASIC PRINCIPLES OF INVESTMENT ALLOCATION METHODS FOR TECHNOLOGICAL TRANSFORMATION IN DIFFERENT REGIONS

The allocation methods of technological transformation investment in different regions mainly include two parts: the initial allocation plan and the adjustment plan. The initial allocation plan focuses on the actual investment needs of each region, through the construction of a comprehensive evaluation index system for investment needs, comprehensive evaluation and analysis for different regions, and determining the proportion of investment allocation in each region according to the proportion of scores; the adjustment plan mainly takes into account the operation of power grid enterprises In terms of development differences, investment benefits, and asset operation efficiency, the initial allocation plan is revised to a certain extent, so as to ensure the fairness of investment allocation quotas in different regions. The basic principle of the allocation method of technological transformation investment in different regions is shown in the figure below:

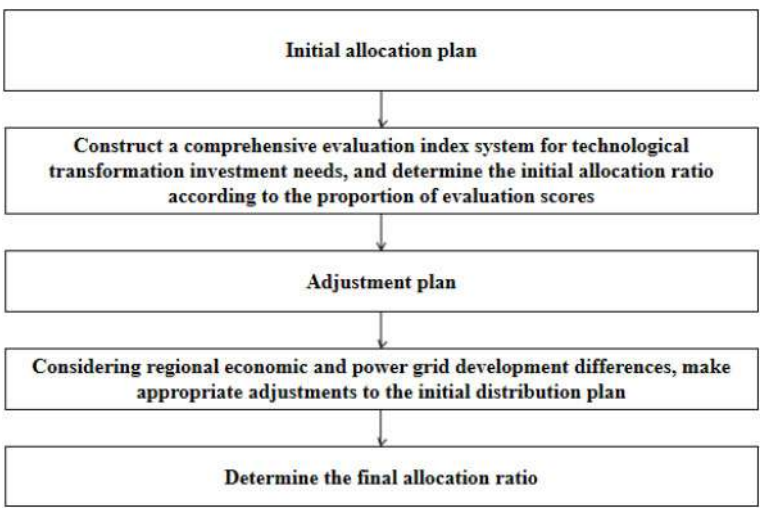

Figure 1. The idea of investment allocation method.

3 RESEARCH ON INVESTMENT ALLOCATION METHODS

3.1 *Research on the initial allocation method based on the comprehensive evaluation of technological transformation investment demand*

(1) Construction of comprehensive evaluation index system

Combining the purpose of power grid investment, constructing a comprehensive evaluation index system from the dimensions of power grid security, regional economic development differences, and corporate operating benefits, as shown in the following table.

Table 1. Comprehensive product improvement index system for technological transformation investment demand.

First level indicator	Secondary indicators	Three-level indicators
Grid assets	Grid asset scale	Original value of assets
Asset status	Asset operation	Asset operating life
	Asset health	Equipment failure rate
Business development	Business contribution	Unit investment increase sales of electricity
		Unit investment increase supply load
Regional Development	Reserve size	Reserve plan
	Electricity demand	Maximum load growth rate of the whole society
		GDP growth rate
		Number of power users
	Local economy	Load density
	Regional characteristics	Terrain coefficient
Plan execution	Plan completion ability	Plan completion rate
		Proportion of historical occurrences

(2) Determination of index weight based on analytic hierarchy process

Hierarchical analysis (Analytic Hierarchy Process for AHP) is a decision-making method that decomposes the elements that are always related to decisions into goals, criteria, schemes, etc., for qualitative and quantitative analysis.

First, a binary comparison judgment matrix is constructed from the importance scaling theory:

$$A = \left(a_{ij}\right)_{n\times n} (i,j = 1,2,\cdots,n) \tag{1}$$

Then the judgment matrix is normalized, and the calculation formula is:

$$\bar{a}_{ij} = a_{ij} / \sum_{k=1}^{n} a_{kj} \ (i,j = 1,2,\cdots,n) \tag{2}$$

The weights are calculated as:

$$w_i = \bar{w}_i / \sum_{i=1}^{n} \bar{w}_i \ (i = 1,2,\cdots,n) \tag{3}$$

Finally, the consistency is judged, if the consistency test, the result is valid. Do not to adjust the result.

(3) Index weight determination

Combining with the basic principles of the analytic hierarchy process, determine the weights of the comprehensive evaluation index of technological transformation investment demand, as shown in the following Table 2.

Table 2. Index weight determination table.

First level indicator	Weights	Secondary indicators	Three-level indicators	Weights
Grid assets	0.0763	Grid asset scale	Original value of assets	0.0763
Asset status	0.1814	Equipment operation	Equipment operating life	0.0341
		Equipment failure situation	Equipment failure rate	0.0409
Business development	0.1673	Business contribution	Unit investment increase sales of electricity	0.0588
			Unit investment increase supply load	0.0476
Regional Development	0.3605	Reserve size	Reserve plan	0.1392
		Electricity demand	Maximum load growth rate of the whole society	0.0281
			GDP growth rate	0.0725
			Number of power users	0.0454
		Local economy	Load density	0.1274
		Regional characteristics	Terrain coefficient	0.0503
Plan execution	0.2145	Plan completion ability	Plan completion rate	0.0341
			Proportion of historical occurrences	0.0308

Score calculation and initial allocation plan

This article combines the expert scoring results of various indicators by experts, and performs a weighted summation with the weights of each indicator to obtain a comprehensive scoring result for each indicator:

$$A = \sum_{i=1}^{14} a_i * b_i \tag{4}$$

In the formula, A represents the comprehensive evaluation score of investment demand for technological transformation in a certain area, table a_i is the score of a certain evaluation index, and table b_i is the index weight.

By calculating the comprehensive evaluation scores of investment demand for technological transformation in different regions, the initial distribution ratio is determined according to the proportion of each region's scores. The specific calculation method is as follows:

$$k = \frac{A_i}{\sum_{t=1}^{t} A_i} \tag{5}$$

In the formula, Table k is the initial allocation ratio of technological transformation investment in a certain area, Table A_i is the comprehensive evaluation score of investment demand for technological transformation in a certain area, and Table t is the number of regions.

3.2 *Initial plan amendment*

Taking into account the increasingly open market environment faced by the distribution network business and the lean requirements of enterprise operations, it is necessary to modify the above plan results to a certain extent from the dimensions of the company's production and operation differences, operational efficiency, and economic benefits. The specific correction plan is shown in the following table:

Table 3. Adjustment ratio.

Area classification	Analysis conclusion	Adjust the ratio
Areas within 10% of the overall evaluation ranking	Appropriately increase the scale of investment	+10%
Comprehensive evaluation ranking within 20%~30%	Appropriately increase the scale of investment	+5%
Areas within 40% to 60% of the overall evaluation ranking	The scale of investment remains the same	0%
Areas within 70%~80% of the overall evaluation ranking	Appropriately reduce the scale of investment	−5%
Regions after 90% of overall evaluation ranking	Appropriately reduce the scale of investment	−10%

4 EMPIRICAL ANALYSIS

This paper collects data related to technological transformation investment of 11 county-level units of City A Power Grid Corporation in 2020, and conducts an empirical analysis according to the above methods.

Table 4. The calculation table of the initial allocation ratio of technological transformation investment of 11 county-level units of Company A in 2020.

Company	Grid asset score	Asset status score	Business development score	Regional Development Score	Plan execution score	Total Score	Initial allocation ratio
H	16.86	40.09	36.97	79.67	47.40	221	20.09%
N	12.03	28.59	26.37	56.83	33.81	158	14.33%
W	10.73	25.50	23.52	50.68	30.15	141	12.78%
J	6.87	16.34	15.07	32.48	19.32	90	8.19%
T	5.51	13.11	12.09	26.05	15.50	72	6.57%
S	6.79	16.14	14.89	32.08	19.09	89	8.09%
G	7.57	18.00	16.60	35.77	21.28	99	9.02%
T	6.15	14.63	13.49	29.07	17.30	81	7.33%
Q	4.13	9.82	9.05	19.51	11.61	54	4.92%
L	4.81	11.43	10.54	22.72	13.52	63	5.73%
Z	2.48	5.89	5.43	11.70	6.96	32	2.95%

Combined with the method for determining the adjustment plan, the revised results of the distribution ratios of 11 county-level units and the final distribution ratios are determined as shown in the following table 4:

Table 5. Final allocation ratio.

Company	Initial allocation ratio	Adjust the ratio	Final allocation ratio
G	9.02%	0%	9.02%
H	20.09%	10%	20.39%
J	8.19%	0%	8.19%
L	5.73%	−5%	5.44%
N	14.33%	5%	14.58%

(*Continued*)

Table 5. Continued.

Company	Initial allocation ratio	Adjust the ratio	Final allocation ratio
Q	4.92%	−5%	4.67%
S	8.09%	0%	8.09%
T	6.57%	0%	6.57%
T	7.33%	0%	7.33%
W	12.78%	5%	13.07%
Z	2.95%	−10%	2.66%

5 CONCLUSION

Improving the reasonable level of future planning and distribution of the investment scale of power grid enterprises' technological transformation is an important way to realize lean management of enterprise investment. In the future, grid companies should dynamically adjust the indicators and weights of indicators for technological transformation investment allocation in accordance with their own development needs and changes in the internal and external environment to meet the needs of business development.

ACKNOWLEDGMENTS

This article was funded by the Science and Technology Project of State Grid Sichuan Electric Power Company (SGSCJY00JJJS2100020).

REFERENCES

Li Ke, Fu Guanghui, Tian Chunzheng, Yu Haozheng, Li Cheng. Distribution network investment allocation method and project optimization based on historical investment results [J]. Computing Technology and Automation, 2019, 38(03): 33–38.

Li Meng, Liu Wei, Li Peng, Tian Chunzheng, Gao Yuqin, Zhang Baodan, Li Zhi, Hu Po. County-level distribution network investment allocation method considering investment benefit evaluation[J]. Journal of Electric Power Science and Technology, 2020,35(06):83–89.

Liu Xiaoguang. Investment decision allocation model for medium and low voltage distribution network infrastructure projects of municipal power grid enterprises [J]. Rural Electrification, 2021(03): 10–14.

Liu Ying, Pan Wei. Research on Optimization of Investment Strategy Considering Distribution Network Development Matching Degree and Equilibrium Degree[J]. Northeast Electric Power Technology, 2020, 41(01): 57-59+62.

Xu Bin, Ma Jun, Liu Hongxin, Chen Qing, Liu Jun, Hu Po. Investment allocation method based on distribution network evaluation [J]. Journal of Wuhan University (Engineering Edition), 2020, 53(03): 248–254.

Advances in Applied Chemistry and Industrial Catalysis – Saikia (Ed.)

Analysis of treating solid waste by pyrolysis and gasification based on building green airports

Bo Li
China Airport Construction Group Co., Ltd, P.R. China
Beijing Super-Creative Technology Co., Ltd, P.R. China

Boyu Zou*
Sichuan Province Airport Group Co., Ltd, P.R. China

Jixiang Su
China Airport Construction Group Co., Ltd, P.R. China
Beijing Super-Creative Technology Co., Ltd, P.R. China

Ran Lei
Beijing Daxing International Airport, P.R. China

ABSTRACT: In 2020, Civil Aviation Administration of China (CAAC) issued a guiding principle for civil aviation to build the four-type airports that are safe, green, smart and culture-oriented. In building green airports, one of the priorities proposed is to reduce waste and other types of pollution, and enable airports and surrounding environment better blend. Allowing for and furthering green airports development, this paper proposes a solid waste treatment technology, i.e., pyrolysis and gasification, suitable for airports to harmless manage and recycle waste.

1 INTRODUCTION

In recent years, China has harvested many fruits in airport infrastructure construction and maintained fast development momentum. Deep-lying contradictions nevertheless emerges between the airport development and the increasing demand in civil aviation, the airport operation safety, the travel demand of passengers, and the environmental and ecological protection, etc. Against the background, the CAAC proposes to build the four-type airports that are safe, green, smart and culture-oriented to practice the new development philosophy and develop high-quality civil aviation comprehensively. A green airport is one with resource intensive utilization and conservation, low-carbon operation and environmental friendliness throughout its service cycle. Among priorities by the outline in building green airports, one is to reduce waste and other pollution aiming at achieving harmony and friendliness between the airport and the surrounding environment. (Action Plan for Constructing Type-four Airports for China Civil Aviation, 2020) Airport waste is an important impairing factor. With passenger throughput increasing annually, heavier pressure is on the airport and the surrounding environment.

*Corresponding Author: zouboyu1218@126.com

DOI 10.1201/9781003308553-21

2 DEMAND OF SOLID WASTE TREATMENT AT AIRPORT

2.1 *Current status of airport waste treatment*

At present, airport solid waste is generally transferred externally for municipal treatment. The outbound transportation requires the waste to be subject to collection, transportation, compression, transfer, end-of-treatment and so on, which is intensive in labor, equipment and vehicle, and high in cost. Further, more people, equipment and vehicles involved may increase the risk of secondary pollution, and health and safety hazards. Waste outbound transportation treatment will also incur higher end-of-treatment costs. Large area of land is also the must, leading to potential problems such as groundwater and air pollution.

2.2 *Conditions for gasification of airport waste*

Airport waste contains aviation waste and domestic waste: the former mainly covers recyclables generated by passengers during the flight, including newspapers, packaging boxes of snacks, bits of food residual, disposable paper cups, etc.; the latter can be further divided into ordinary domestic waste (mainly including waste from the airside and landside of terminals, office waste by organizations settled at airports and domestic waste from airport living areas) and waste after inflight meal processing (waste generated during the production and processing by the airport inflight meal distribution center, which is mainly organic waste generated by inflight meal processing). In general, airport solid waste is of higher quality than urban domestic counterpart and is more viable for gasification. An airport usually generates waste less than 100 ton a day, rendering small gasifiers suitable for treatment.

3 SELECTION OF PYROLYSIS AND GASIFICATION FOR MANAGING AIRPORT SOLID WASTE

3.1 *Pyrolysis and gasification*

Landfill traditionally adopted occupies vast land and exposes soil, groundwater and air to pollution. Large-scale waste incineration has long suffered NIMBY (Not In My Back Yard). Managing waste via pyrolysis outdoes traditional measures for its harmlessness, reduction and resource utilization, and has become a new technology developed by countries all over the world.

This technology first cracks waste into small-molecule combustible gas and then burns them at high temperature in the second combustion chamber, avoiding toxic gases such as dioxins commonly produced by direct waste incineration. The heat generated by the combustion in the second combustion chamber can be recycled to motivate the system, and waste heat can be utilized for power generation, heating, etc. In this way, waste becomes a renewable resource. The organic waste is reduced by more than 90%, and almost no fly ash is produced. The discharged slag can be further used as resources or sent to domestic waste landfills.

3.2 *Ecological benefit analysis*

Compared with direct incineration, pyrolysis equipment can effectively reduce the production of air pollutants such as dioxins, showing obvious benefits in ecological and environmental protection. Estimating and comparing per the cost of processing 240,000 tons of waste per year, as the Table 1 illustrates, pyrolysis, the decentralized waste treatment mode, emits far less pollutants than traditional ones per item. The reduction is even exponential. The pyrolysis equipment can altogether dispose of the leachate in waste, leaving no need for secondary treatment.

Table 1. Ecological Benefit Analysis Indicators (Annualized total value).

Item	Traditional treatment mode	Pyrolysis
CO /kg	50000	6170
NO_x /kg	150000	4900
Particulate matter/kg	15000	6050
SO_2/kg	50000	1620
HCl /kg	30000	3820
PCDD/Fs/g	0.05	0.015
Wastewater discharge/ton	2000	

4 TECHNICAL SOLUTIONS AND BASIC PROCESS OF MANAGING AIRPORT SOLID WASTE VIA PYROLYSIS AND GASIFICATION

Due to its high degree of resource utilization, the airport solid waste can be first subject to unified sorting and recycling. Then, the remaining non-recyclable waste can be managed by pyrolysis and gasification.

4.1 *Principles of waste pyrolysis and gasification*

Pyrolysis and incineration are two completely different processes, mainly featuring the following disparities: First, incineration mainly generates CO_2 and H_2O, while pyrolysis produces flammable low-molecular compounds in gas (such as H_2, CH4, and CO), liquid (methanol, acetone, acetic acid, acetaldehyde and other organic substances, and tar) and solid (coke and carbon black). Second, incineration is an exothermic process, in which the carbon and hydrogen, the main combustible substances in solid waste, undergoes the oxidation reaction. In contrast, pyrolysis is an endothermic process that requires heat to be absorbed to decompose organic compounds. Third, incineration produces a large amount of fly ash, giving toxic gases such as dioxins the chance to synthesize with fly ash as the carrier. A peroxygen reaction is required to generate a large amount of nitrogen oxide compounds after large quantity of air is blown in. Pyrolysis is static with no fly ash produced. An anaerobic environment is required, so the amount of nitrogen involved will be very small (Qian & Han 2014).

Combustion air is supplied with deficit to the primary combustion chamber, allowing domestic waste to be cracked at a certain temperature (650°C∼850°C). Combustible substances within are decomposed into short-chain organic gases (including carbon monoxide, methane, ethane, ethylene, etc.) and trace of hydrogen under high temperature and oxygen deficiency. However, due to lack of oxygen, these organic gases will not burn until they flow into the secondary combustion chamber, and substances remain in the lower part of the primary combustion chamber are fixed carbon and ash. Fixed carbon reacts with enough oxygen to generate CO2 to fully burn and release heat. This heat is used to crack and gasify the waste in the upper part of the primary combustion chamber (He et al. 2019).

4.2 *Process principle of waste pyrolysis equipment*

Airport waste is first fed into the equipment for drying, and then goes through a pyrolysis reaction in the pyrolysis zone. Combustible gas and tar produced are collected and burned to release heat. The heat can enable the rapid pyrolysis of the dry waste even at low temperature. The absence of stirring action commonly seen in the direct-fire incinerator produces little fly ash. This equipment can control the amount of new waste input and the pyrolysis speed in a real time manner, the biggest highlight, so the conservation between the heat generated by the combustion of the combustible gas generated by the pyrolysis and the heat required for pyrolysis can be maintained.

Residues after pyrolysis and the inert substances in the solid waste (such as glass, metals and ceramics) are expelled from the discharge port at the lower part of the equipment. At the same time, the leachate produced in waste storage and treatment will enter the main equipment for complete pyrolysis under the waste heat (the condition that the calorific value of waste is above 1500Kal).

In the thermochemical reaction of incineration, the production of dioxins is related to the temperature environment and the amount of fly ash. The concentration of dioxin produced reaches the peak when the reaction temperature is around 600°C and large quantity of fly ash carriers are produced. The adoption of pyrolysis and gasification enables the waste be cracked and treated in an almost static state, and no fly ash is produced. Collected combustible gas is burned at high temperature, providing a pyrolysis of 850 degrees lasting for more than two seconds. It basically eliminates the possibility of generating harmful substances such as dioxins. The later exhaust gas does not require expensive consumables to deal with (Tao et al. 2015).

4.3 *Waste pyrolysis treatment process*

The collected domestic waste stay in the storage pit for five to seven days and then is transported into the furnace via the waste feeding system. Waste is cracked and gasified in the furnace, lasting for about two hours. The pyrolysis combustible gas then enters the second combustion chamber through the upper flue. The remaining main slag (inorganic non-combustibles) is discharged by the lower wet slag discharger. The waste is reduced by more than 90% and the discharged solid waste meets the standard for pollution control on the landfill site of municipal solid waste.

After entering the second combustion chamber, the pyrolysis combustible gas fully burns in an oxygen-rich environment. Harmful substances such as dioxins can be completely decomposed under 900∼1050°C. This process lasts more than two seconds, and the outlet temperature should be higher than 850°C. The adoption of pyrolysis then allows the waste to be cracked and treated almost statically, generating no fly ash. Collected combustible gas burning at high temperature creates the pyrolysis of more than two seconds under 850°C, basically eliminating the possibility of producing harmful substances such as dioxins.

The waste heat power generation can be divided into two processes: steam-water and flue gas. In the stream-water process, the desalinated water produced by the water carburetor enters the waste heat boiler, and then the steam produced by the waste heat boiler goes into the steam turbine to generate electricity. After the steam works in the steam turbine, it is cooled and condensed into condensed water in the condenser by cooling water. The condensed water then is pumped into the whole-site fill tank through the water pump, and then returns to the boiler for recycling through the boiler feed water pump. (Zuo & Jia 2014) The water carburetor supplements the entire system with demineralized water. Flue gas process works as follows: high-temperature flue gas (850°C∼ 1050°C) produced by waste pyrolysis equipment enters the waste heat boiler through the high-temperature flue gas pipeline. After the heat exchange in the heat exchange pipeline, flue gas drops to about 250°C and exits from the waste heat boiler. Then the flue gas enters the dust removal and purification device through the low-temperature flue gas pipeline. The production can meet the national smoke emission standards. Then the standard-compliant flue gas is sent into the chimney and discharged into the atmosphere via induced draft fan.

The flue gas discharged from the second combustion chamber is subject to neutralization, cooling, absorption by activated carbon by passing a semi-dry reaction tower, and discharged through the chimney after being filtered by a cloth bag. The flue gas emission standard is higher than the current domestic waste incineration pollution control emission one.

The leachate must not be discharged without meeting the standards. The leachate must be sent to the plant's leachate treatment workshop for treatment and the discharged waste water must meet the requirements of the Class I A of the Integrated Wastewater Discharge Standard. When conditions allow (in the case of high calorific value of waste), leachate will be sprayed back to the pyrolysis furnace for high temperature incineration.

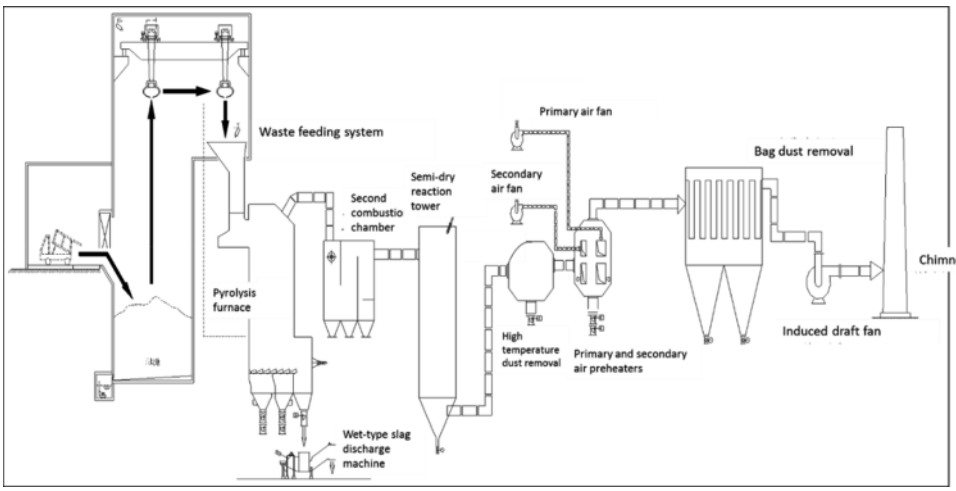

Figure 1. Airport waste pyrolysis and gasification process flow chart.

5 OVERALL BENEFITS

5.1 *Economic benefits*

5.1.1 *Low operating cost*

Waste pyrolysis and gasification is advanced in processing technology, low in energy consumption and operating cost. Because the dust in the flue gas is small and the composition is simple, the flue gas treatment generates less consumables and lower cost.

5.1.2 *Shorter transportation, eliminating the need for construction and operation of transfer stations*

Designed for small and medium tonnage, waste can be transported directly after collection, without the need for compression and transportation. While avoiding multiple secondary pollution incurred by compression and transportation, it saves high waste transportation fees, spares the construction investment of transfer stations, and greatly reduces the front-end cost of the harmless treatment of waste.

5.1.3 *Saving land*

The pyrolysis and gasification equipment is compact in design and small in area occupation, saving valuable land resources.

5.1.4 *Small investment and low maintenance cost*

The complete set of pyrolysis and gasification equipment does not require huge one-off capital investment. Investment and construction can be made as needed, reducing the overall investment. The operation is stable and reliable, and the maintenance cost is low.

5.2 *Environmental benefits*

The waste pyrolysis technology is harmless, able to chemically decompose waste and effectively prevents the generation of dioxin-like harmful gases, leaving no secondary pollution to the air. Residue is small after pyrolysis and gasification, and no large amount of land resources are occupied after being transported externally. The waste heat can be used to generate electricity, saving energy. It is a waste treatment technology that is truly ecological-and-environmental friendly and harmless.

6 CONCLUSION

The gasification of airport waste can fundamentally reverse environmental problems caused by the disposal of airport waste for outbound landfill. Treating airport solid waste through pyrolysis and gasification, and using waste heat to generate power can save energy and improve the comprehensive utilization of airport resources, which is in line with the concept of building green airports. It is worthy of promotion and application.

REFERENCES

Action Plan for Constructing Type-four Airports for China Civil Aviation (2020–2035), 9–10, (2020)

He H, Wang M, Zhang J, Li. Application progress in comprehensive utilization of municipal solid wastes and prospects on its industrialization pattern J., Modern Chemical Industry, 7 06(2019)

Qian R, Han J, Transformation of MSW treatment in Beijing-Pyrolysis and gasification technology of domestic refuse, Environmental Engineering, J.690, 32(2014)

Tao B, Pan W, Chen G Discussion on Anaerobic Pyrolysis Technology of Municipal Solid Wastes, Power Equipment, J. 232, 3(2015)

Zuo Q, Jia L Generating Electricity with Domestic Trash Pyrolysis, Shanxi Metallurgy J.9 06 (2014)

Advances in Applied Chemistry and Industrial Catalysis – Saikia (Ed.)

Application of biochar in amelioration of saline-alkali soil

Jing Zhang, Yan Jiao* & Wenzhu Yang
Key Laboratory of environmental chemistry of Inner Mongolia Autonomous Region, Hohhot, China
Chemistry and Environmental Science College, Inner Mongolia Normal University, Hohhot, China

ABSTRACT: In recent years, there are more and more studies on the application of biochar, and biochar has attracted the attention of researchers at home and abroad. Biochar has been widely applied because most of its raw materials are agricultural wastes, and it has the characteristics of porous, large specific surface area, and rich mineral elements, showing great potential in improving barren soil and repairing polluted soil. Soil salinization is one of the important factors limiting land use. Improving the salinization of soil is beneficial to agricultural production and ecosystem restoration. Therefore, the study on the improvement effect of biochar application on saline-alkali soil can provide a new idea for solving agricultural solid waste and is of great significance to the development of world agriculture. In this paper, the effects of biochar on soil's physical and chemical properties, nutrient content, microorganisms, greenhouse gas emissions, and crop growth, as well as the potential environmental risks of biochar were discussed. The purpose of this paper is to provide new ideas for the application of biochar and reference for the improvement of saline-alkali land.

1 INSTRUCTION

Biochar refers to the biomass in anaerobic conditions, lack of oxygen, or at relatively low-temperature pyrolysis of a carbon-rich of tiny particles porous (Lehmann 2007). International Biochar Association (IBI) in 2013 to further explain the concept and connotation of biochar, biochar is biomass under anoxic conditions is obtained by thermochemical conversion of solid products. It can be used alone or as an additive to improve soil, improve resource efficiency, avoid specific environmental pollution, and as an effective means of reducing greenhouse gas emissions. It mainly contains C, H, O, N and Si, Ca, Al, K, and other inorganic elements (Xu & Fang 2015), among which the carbon content is between 38% and 80% (Yuan et al. 2019). The pH value of biochar is usually between 5-and 12, and it is mostly alkaline (Ahmad et al. 2014) and has many pores and a large specific surface area (Van Zwieten et al. 2010). The composition of biochar is highly aromatic, and it also contains hydroxyl, phenolic hydroxyl, carboxyl, aliphatic double bond, and other special functional groups (Zhou et al. 2016). However, with the change in biomass material or pyrolysis temperature, the pH, pore structure and specific surface area of biochar will change greatly (Campos et al. 2020; Lin et al. 2016).

At the same time, the world existing a lot of saline-alkali lands, saline soil is not suitable for the cultivation of crops, and some soil is even unable to support the growth of any plant. This poor soil seriously limited the agricultural production, and harms the ecological system according to statistics, China has about 340000 km^2 of saline-alkali land, of which about 124000 km^2 of soil can be used for agricultural production after improvement (Wang et al. 2017). Using biochar to improve saline-alkali soil can realize the reuse of agricultural and forestry wastes and reduce their pollution of the environment. At the same time, saline-alkali land modified with biochar will be suitable for crop cultivation, which will be of great help to agricultural development and the improvement of local ecosystems.

*Corresponding Author: Jiaoyan@imnu.edu.cn

DOI 10.1201/9781003308553-22

Take seriously gradually in recent years, scholars at home and abroad using biochar soil improvement this measure, do a lot of related research studies. Studies have shown that biochar increased soil porosity (Major et al. 2010), nutrient and water preserving capability (Sarfraz et al. 2020; Tryon 1948), crop growth and soil nutrient content (Gopal et al. 2020) and carbon emission (Qu et al. 2016) reduction has a positive effect. However, because biochar is mostly alkaline, most studies focus on the improvement effect of biochar on acid soil, and the application of biochar in saline-alkali soil is relatively few. Therefore, its improvement effect on saline-alkali soil needs more long-term research data to prove.

2 EFFECTS OF BIOCHAR IN IMPROVING SALINE-ALKALI SOIL

With the development of science and technology and times, the research on saline-alkali land governance is increasing gradually, and the governance measures are also gradually improved. At present, there is much attention paid to the modifiers made from solid waste reuse at home and abroad, such as biochar (Yang et al. 2014), wood vinegar (Zhang et al. 2014), gypsum (Fang et al. 2012), etc. These materials can reduce the degree of soil salinization, improve the content of soil nutrients, and have a positive effect on reducing soil greenhouse gas emissions. Biochar can not only improve saline soils to make them more suitable for cultivation, but also provide new solutions to solid waste disposal.

The data source of CNKI China Academic Journal Online publication database was used for accurate retrieval with the theme = "biochar + pyrolytic carbon + biochar AND saline-alkali soil + saline soil". From 2010 to 2020, 188 papers were identified, of which 36.17% were in Chinese. See F1 for specific publication year and number of publications. The discipline distribution of the 188 precipitated papers is shown in F2, in which the agricultural science and technology field accounts for 36.17%, basic science 27.13%, and Engineering science series I 5.85%.

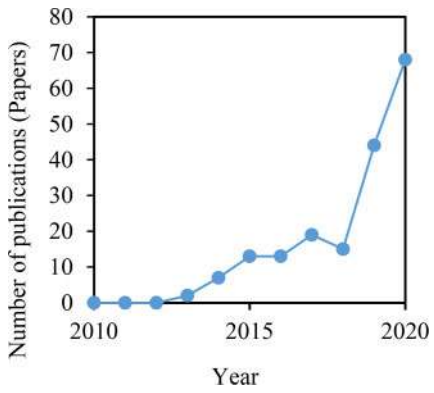

Figure 1. Publication year and the number of articles.

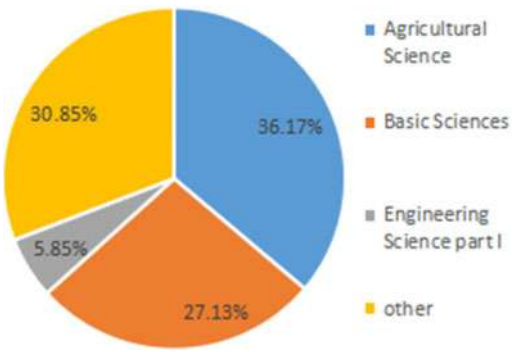

Figure 2. Discipline distribution of published literature.

2.1 *Effects of biochar on the physical and chemical properties of saline-alkali soil*

Biochar applied to saline-alkali soil can improve soil texture and affect physical and chemical properties such as soil water content, pH, and salt content (Table 1).

Biochar has an abundant pore structure. The application of biochar into salt-alkali soil can improve soil capillary porosity, improve soil pore distribution characteristics and connectivity between pores, and promote the development of soil pore structure and the formation of soil stable aggregates. Simultaneous application of biochar can increase the amount of exchangeable base and

base saturation of the soil, reduce the alkalization degree and salt content of saline-alkali soil, and improve the water and salt transport in saline-alkali soil.

Table 1. Effects of biochar on physical and chemical properties of saline-alkali soil.

Water Content	Biochar application can significantly improve soil saturated water conductivity (Zwieten L 2010), reduce tensile strength, and increase field water capacity (Chan 2017). At the same time, soil infiltration rate and cumulative infiltration amount are enhanced [20].
pH	After biochar, the pH value of saline soil could be slightly reduced, and the pH value of soil showed a decreasing trend with the gradual increase of biomass carbon (Kong 2008). Studies have also found that biochar has a negative effect on the pH improvement of saline-alkali soil (Wang 2013).
Saltness	The application of biochar to saline soil can inhibit soil salt return, improve soil water and salt transport, and significantly reduce soil electrical conductivity and ESP (Sun 2020).

2.2 *Effects of biochar on the nutrient content of saline-alkali soil*

After 1.5% biochar was applied to the coastal saline soil, the content of soil organic matter was significantly increased, the proportion of organic carbon and available phosphorus in the total carbon and total phosphorus in the soil was increased significantly, and soil mineral elements were significantly increased (Sun et al. 2020). At a higher biochar application rate (50 t/ha), the organic carbon content and cation exchange capacity of the saline soil increased (Kong et al. 2008). Straw biochar can significantly increase the content of available phosphorus and potassium in the soil with high salinity (Chen et al. 2019). In general, adding biochar can improve the fertility status of salt-affected soils and the nutritional status of plants growing in these soils (Saifullah et al. 2018).

The increase in soil nutrient content may be caused by the fact that biochar is rich in a certain amount of mineral elements, which will increase the soil nutrient content. Moreover, due to its large specific surface area and rich functional groups, biochar has a strong adsorption capacity and can fix part of soil mineral elements through adsorption and pincal action, thus reducing nutrient loss.

2.3 *Effects of biochar on saline-alkali soil microorganisms*

Microorganisms are important participants in soil biochemistry. Their distribution and activity in soil are closely related to the formation of soil structure and the transformation of nutrients and play an important role in the formation of soil fertility. But in saline-alkali soil, the activity of microorganisms will be inhibited, which will affect the growth of crops.

Therefore, the study of microbial activities and changes is of reference value for the application of biochar in saline soil. Studies have shown that adding biochar to salinized rice soil can increase the activity of soil dehydrogenase, sucrase, urease, catalase, alkaline phosphatase, and protease, and significantly promote the microbial activity of the system (Tang et al. 2016). Biochar was applied to alkaline soil with a pH of 8, significantly increasing soil microbial biomass carbon content (Luo et al. 2019). The combination of laboratory simulation and pot maize experiment. The experiment has proved that corn stalk biochar can increase the microbial biomass and microbial biomass carbon of saline and alkaline soil and promote the growth of corn seedlings (Yang & Zhou 2017).

Biochar has a large specific surface area and a porous surface. On the one hand, it can provide better growth and reproduction environment for microorganisms. On the other hand, soil dissolved organic carbon can be adsorbed and stored, providing a new carbon source for microorganisms. Therefore, the application of biochar can increase the microbial abundance of saline-alkali soil.

2.4 *Effects of biochar on greenhouse gas emissions from saline-alkali soils*

The greenhouse effect has seriously affected human development and social progress, causing global warming, sea-level rise, desertification, and other environmental problems. However, greenhouse gases such as CO_2, N_2O, and CH_4 emitted from farmland soil account for 10%–12% of the

global anthropogenic greenhouse gas emissions, and are one of the important emission sources of greenhouse gases.

Therefore, it is of great significance to study the effect of biochar on greenhouse gas emissions from saline soil. Studies have shown that adding biochar to salinized soil can adsorb and fix NH_4^+ in the soil, inhibit the denitrification process, significantly reduce soil CO_2 emission flux and seasonal cumulative total emissions, and at the same time reduce GWP, and effectively mitigate greenhouse gas emissions (Zhang 2019a). The addition of biochar can inhibit the transformation and denitrification of nitrogen microorganisms, and significantly reduce the total seasonal cumulative emissions of CO_2 and N_2O, of which 30 t/hm^2 application has the best carbon sequestration reduction effect (Qu et al. 2016). Similarly, the application of corn stalk biochar can effectively reduce the total greenhouse gas emission of the corn farmland ecosystem (Wang et al. 2019). The application of biochar in alkaline soil increases the content of soil organic matter and effectively inhibits the emission of soil CO_2, with potential carbon sequestration (Hua et al. 2014). Foreign studies have also shown that biochar can reduce the cumulative emission of CO_2 and N_2O, and has the potential to alleviate the flux of CO_2 and N_2O in the actual ecosystem (Pokharel et al. 2018). Adding biochar to paddy soil reduces and increases the cumulative emissions of CH_4 and N_2O respectively, but overall reduces the net emissions and intensity of greenhouse gases (Liu et al. 2014).

The effect of biochar on greenhouse gases could be because it can affect the microorganisms involved in greenhouse gas emissions in the soil, inhibit denitrification, reduce the rate of soil carbon mineralization, and affect the carbon and nitrogen cycle in salt-alkali soil. So collectively, it can slow down greenhouse gas emissions.

2.5 *Effects of biochar on the growth of saline-alkali soil crops*

Because of salt stress and a high degree of alkalinization, saline-alkali soil will inhibit crop growth and reduce yield. It is pointed out that biochar can improve the physical and chemical properties of saline-alkali soil, increase soil fertility, and thus promote crop growth.

When Zhang et al. applied biochar into the soil of alkaline rocky desertification, they found that the bulk density of the soil decreased and the porosity and nutrient content of the soil increased. It also had a significant influence on the growth of aboveground biomass and the total biomass of saplings. Biochar application can improve the physical and chemical properties of soil and promote the growth, dry matter accumulation, and root development of conformational trees at the seedling stage (Zhang et al. 2019b). Biochar applied to the heavy saline soil significantly increased the fresh and dry weight of sorghum seedlings and improved the photosynthetic capacity of sorghum leaves (Liu 2019). Biochar can improve the water permeability of saline-alkali soil and increase soil nutrient content, thus increasing soybean yield (Akhtar et al. 2015). It can alleviate salt stress by adsorbing Na+, increasing the biomass of potato shoots, root length and root volume, and tuber yield (Sun et al. 2020). Zhang Jinhong, Kang He et al. found that 2% biochar could promote the growth of alfalfa and Miscanthus, and significantly increase physiological parameters such as plant height, leaf length, leaf width, and stem fresh weight and dry weight of the plant (Zhang et al. 2020).

Biochar promotes the growth of plants in saline-alkali soil, which may be because the application of biochar improves the physical and chemical properties of saline-alkali soil, increases soil nutrient content, and reduces salinity and alkalinity of saline-alkali soil. Thus, the homeostatic state of Na+ and K+ ions in plants can be changed, reduce the stress damage caused by saline-alkali soil to plant growth, and increase the yield of plants.

3 EFFECTS OF MODIFIED BIOCHAR AND BIOCHAR COMBINED WITH OTHER MATERIALS ON SALINE-ALKALI SOIL

Since biochar itself is mostly alkaline, there is still some debate about its effectiveness in saline-alkaline soil improvement. Some studies at home and abroad focus on the effect of modified biochar or biochar mixture on saline-alkali soil.

Studies have shown that adding a mixture of biochar and polyacrylamide (PAM) to saline soils and applying 1% PAM and 2% biochar can improve soil saturated water conductivity [18]. The mixed application of the two could significantly reduce EC and pH of the soil and significantly increase the biomass and plant height of sunflowers (Wang 2018a). Mixed application of biochar and desulfurized gypsum into saline-alkali soil can reduce soil salinity and alkalinity to a certain extent while increasing soil nutrient content and increasing crop biomass (Han et al. 2017). The combined application of biochar and wood vinegar into saline soil can effectively inhibit salt accumulation in topsoil and increase soil nutrient content and crop yield, which is more effective than soil improvement treated with biochar alone (Wang 2018b). The combination of the two can effectively improve the barrier factors of saline-alkali soil, increase the content of available nutrients, and cation exchange capacity of the soil, which is one of the effective measures for the improvement of saline-alkali soil (Zhao 2017). Biochar combined with hydrochloric acid can reduce pH density and increase crop biomass (Yang et al. 2015). Biochar modified by hydrochloric acid can reduce soil pH (Lu et al. 2017), increase plant height and leaf area of crop dry matter accumulation and absorb soil nutrients, and improve soda saline-alkali soil with the addition of 2% (Guo et al. 2017).

Aromatic hydrocarbon functional groups in biochar can adsorb H+ in soil solution, so that the concentration of H+ in soil solution decreases, which may increase the alkalinization degree of saline-alkali land. Therefore, the research on the combination of biochar with other acidic materials or the modification and reuse of acidic materials is of great significance to the application of biochar in the improvement of saline-alkali land, and it is also one of the new directions of biochar research in the future.

4 POTENTIAL ENVIRONMENTAL RISKS OF USING BIOCHAR

The potential environmental risks of biochar may be due to contaminants in the feedstock, such as volatile heavy metals and toxic and harmful organic compounds, which can accumulate in the biochar during production (Devi & Saroha 2014). The study of He et al. (2019) shows that the concentration of non-volatile metals will continue to increase with the rise of pyrolysis temperature. Some volatile heavy metals, such as Cd, Pb, and Zn, are easy to volatilize at high temperatures. Lyu et al. (2016) showed that at 250–700°C, polycyclic aromatic hydrocarbons, dioxins, and furans were present in the biochar synthesized from pine sawdust, and they found that with the increase in pyrolysis temperature, the content of organic pollutants increased at first and then decreased. Another reason may be that biochar has strong adsorption properties, which can reduce the degradation and mineralization rates of pollutants, thus increasing the retention time of pollutants in the environment (He et al. 2019). Therefore, when biochar is applied to the environment, it may lead to pollution of soil, water, and air environments, and in serious cases, it may harm human health.

Therefore, in the application of biochar, attention should be paid to the selection of raw materials, carbonization conditions, and application amount. It is recommended to test the type and content of heavy metals and organic compounds in biochar before use to determine whether biochar itself is safe. At the same time, the amount of biochar should be appropriate. At present, most of the studies on biochar have proved that biochar has positive effects on the environment, but the potential risk and harm of biochar still need to be paid attention to, and further studies are needed to prove it.

5 RESEARCH PROSPECT

Although in recent years, most of the research results show positive effects on the improvement of saline-alkali soil by biochar, which can improve soil texture and physical and chemical properties, increase soil nutrient content, promote crop growth and reduce soil greenhouse gas emissions.

However, there are still some problems to be further studied and proved in its application in saline-alkali soil. It mainly includes the following aspects:

(1) Since biochar is mostly alkaline, the saline-alkali degree improvement effect of saline-alkali soil is still controversial. Therefore, more in-depth studies and more data support are needed for the interaction process and internal influence mechanism between biochar and saline-alkali soil. At the same time, most of the current studies are on small-scale and short-term effects, and future studies should focus on the long-term effects of large-scale field trials.
(2) To solve the possible negative effects of biochar on saline-alkali soil, the modification of biochar and the combination of biochar with other materials will be one of the research emphases in the future. Future research in this area should focus more on the improvement of saline-alkali soil by combining other wastes with biochar, such as the combination of furfural residue with biochar or the modified application of wood vinegar to biochar.
(3) Because biochar may contain harmful substances such as heavy metals or polycyclic aromatic hydrocarbons (PAHs), the effects of long-term application of biochar on the soil environment are still uncertain. Therefore, the study on the impact of biochar on the soil environment is very urgent, and the study on the environmental toxicity of biochar will be the key direction of its future research.

ACKNOWLEDGMENTS

The National Natural Science Foundation of China (42175038); National Natural Science Foundation of China (41765010); The Program for Young Talents of Science and Technology in Universities of Inner Mongolia Autonomous Region (NJYT-20-A04); Project of Grassland Talent of Inner Mongolia Autonomous Region (2020); Youth Innovation Talent Program of Inner Mongolia Autonomous Region (2016); Inner Mongolia Normal University Graduate student scientific research innovation fund supported project (CXJJS20113); Agricultural Science and Technology Innovation Program of CAAS.

REFERENCES

Ahmad M, Rajapaksha A U, Lim J E, et al. (2014) Biochar as a sorbent for contaminant management in soil and water: A review. Chemosphere, 99: 19–33.

Akhtar S S, Andersen M N, Liu F. (2015) Biochar mitigates salinity stress in potato. Journal of Agronomy and Crop Science, 201(5): 368–378.

Campos P, Mille A Z, Knicker H, et al. (2020) Chemical, physical and morphological properties of biochars produced from agricultural residues: Implications for their use as soil amendment. Waste Management, 105: 256-267.

Chan K Y, van Zwieten L, Meszaros I, et al. (2007) Agronomic values of greenwaste biochar as a soil amendment. Soil Research, 45(8): 629.

Chen Y Y, Wang X Y, Wu H X, et al. (2019) Adsorption and Migration Mechanism of Enteromorphaprolifera Biochar on Na+in Coastal Saline-Alkaline Soil. Periodical of Ocean University of China, 49(S1):85–92. (in Chinese)

Devi P, Saroha A K. (2014) Risk analysis of pyrolyzed biochar made from paper mill effluent treatment plant sludge for bioavailability and eco-toxicity of heavy metals. Bioresour Technol, 162: 308–315

Fang C, Su D L, Duan Y W, et al. (2012) Effects of Coupling of FGD Gypsum and Irrigation on Chemical Properties of Harbor Front Saline Soil. Journal of Soil and Water Conservation, 26(05):59–63. (in Chinese)

Gopal M, Gupta A, Shahul Hameed K, et al. (2020) Biochars produced from coconut palm biomass residues can aid regenerative agriculture by improving soil properties and plant yield in humid tropics. Biochar, 2(2): 211–226.

Guo D Y, Shang D Y, Wang X G, et al. (2017) Effects of Modified Biochar on Growth, Nutrients Uptake of Maize and Soil Physicochemical Properties. Journal of Henan Agricultural Sciences, 46(02):22–27. (in Chinese)

Han J H, Li Y W, Zhang L K, et al. (2017) Effect of biochar and FGD-gypsum application on soil basic physical and chemical properties and maize growth of saline soil. Chinese Journal of Environmental Engineering, 11(09):5291–5297. (in Chinese)
He J, Strezov V, Kan T, et al. (2019) Effect of temperature on heavy metal(loid) deportment during pyrolysis of Avicennia marina biomass obtained from phytoremediation. Bioresour Technol, 278: 214–222.
He Y, Liu C, Tang X Y, et al. (2019) Biochar impacts on sorption-desorption of oxytetracycline and florfenicol in an alkaline farmland soil as affected by field ageing. Sci Total Environ, 671: 928–936.
Hua L, Lu Z Q, Ma H R, et al. (2014) Effect of biochar on carbon dioxide release, organic carbon accumulation, and aggregation of soil. Environmental Progress & Sustainable Energy, 33(3): 941–946.
Kong X Q, Wei J M, Chang G W, et al. (2008) Effect of Biochar on the Physical and Chemical Properties of Saline-alkali Soil and Soybean Yield. Soybean Science, 37(04):647–651. (in Chinese)
L. Van Zwieten, S. Kimber, S. Morris, K. Y. Chan, A. Downie, J. Rust, S. Joseph, A. Cowie. (2010) Effects of biochar from slow pyrolysis of papermill waste on agronomic performance and soil fertility [J]. Plant and Soil, 327(1-2).
Lehmann. (2007) White-crowned sparrow energy investment. Bulletin of the Ecological Society of America, 88(4): 378–388.
Lin J Y, Zhang Y, Liu Y, et al. (2016) Structure and properties of biochar under different materials and carbonization temperatures. Chinese Journal of Environmental Engineering, 10(06),3200–3206. (in Chinese)
Liu H M. (2019) Effects of biochar on the growth and photosynthetic characteristics of Sorghum seedlings in saline-alkali soil. Crop Society of China. A collection of abstract papers from the annual conference of Crop Society of China in 2019. Chinese Crop Society: Chinese Crop Society, 179. (in Chinese)
Liu J Y, Shen J L, Li Y, et al. (2014) Effects of biochar amendment on the net greenhouse gas emission and greenhouse gas intensity in a Chinese double rice cropping system. European Journal of Soil Biology, 65: 30–39.
Lu X R, Chen G S, Li X J. 2017. Experimental Effects of Acidified Biochar on Saline-sodic. Journal of Shenyang Agricultural University, 48(04):462–466. (in Chinese)
Luo Y, Durenkamp M, De Nobili M, et al. (2013) Microbial biomass growth, following incorporation of biochars produced at 350°C or 700°C, in a silty-clay loam soil of high and low pH. Soil Biology and Biochemistry, 57: 513–523.
Lyu H, He Y, Tang J, et al. (2016) Effect of pyrolysis temperature on potential toxicity of biochar if applied to the environment. Environ Pollut, 218: 1–7.
Major J, Rondon M, Molina D, et al. (2010) Maize yield and nutrition during 4 years after biochar application to a Colombian savanna oxisol. Plant and Soil, 333(1–2): 117–128.
Pokharel P, Kwak J H, Ok Y S, et al. (2018) Pine sawdust biochar reduces GHG emission by decreasing microbial and enzyme activities in forest and grassland soils in a laboratory experiment. Science of the Total Environment, 625: 1247–1256.
Qu Z Y, GAO L H, Li C J, et al. (2016) Impacts of Straw Biochar on Emission of Greenhouse Gas in Maize Field. Transactions of the Chinese Society for Agricultural Machinery, 47(12):111–118. (in Chinese)
Saifullah, Dahlawi S, Naeem A, et al. (2018) Biochar application for the remediation of salt-affected soils: Challenges and opportunities. Science of the Total Environment, 625: 320–335.
Sarfraz R, Yang W H, Wang S S, et al. (2020) Short term effects of biochar with different particle sizes on phosphorous availability and microbial communities. Chemosphere, 256: 126862.
Sun H H, Qu Z Y, Wang F, et al. (2020) Impact of Sand Cave Planting on Water and Salt Transport and Tomato Growth Characteristics in Saline-alkali Soil. Journal of Soil and Water Conservation, 34(01):230–235. (in Chinese)
Tang J Y, Jia R, Qu D, et al. (2016) Effects of Biochar on Dehydrogenase Activity and Iron Reduction in Paddy Soils. Journal of Soil and Water Conservation,30(03):262–267. (in Chinese)
Tryon E H. (1948) Effect of charcoal on certain physical, chemical, and biological properties of forest soils. Ecological Monographs, 18(1): 81–115.
Van Zwieten L, Kimber S, Morris S, et al. (2010) Effects of biochar from slow pyrolysis of papermill waste on agronomic performance and soil fertility. Plant and Soil, 327(1–2): 235–246.
Wang C J, Yang F, Xing Y, et al. (2017) Effect of biochar on phosphorus leaching from saline soil in arid area. Sichuan Environment, 36(2): 17–21. (in Chinese)
Wang F. (2018) Experimental Study on the Effects of biochar and wood vinegar on crop growth and Soil and water Environment in Salinized farmland. Inner Mongolia Agricultural University. (in Chinese)
Wang G J, Xu Z W, Tian X L, et al. (2013) Effects of biochar on the physical and chemical properties of salinized soil and the growth of wheat seedlings. Jiangsu Agricultural Sciences, 41(12):390–393. (in Chinese)

Wang G L, Sun T J, LIU T X, et al. (2019) Effects of biochar on carbon footprint of corn fields in arid regions. Journal of Agro-Environment Science, 38(11):2650–2658.(in Chinese)
Wang Q F. (2018) Effects of biochar and polyacrylamide on the growth of Sunflower in salinized soil. Inner Mongolia University. (in Chinese)
Xu Y Z, Fang Z Q. (2015) Advances on remediation of heavy metal in the soil by biochar. Environmental Engineering, 33(2):156–159, 172. (in Chinese)
Yang F, Li X Q, Xing Y, et al. (2014) Effect of Biochar Amendment on Nitrogen Leaching in Saline Soil. Journal of Agro-Environment Science, 33(05):972–977. (in Chinese)
Yang G, Zhou W Y. (2017) Effects of biochar on physical and chemical properties, biomass and growth of maize in saline-alkali soil. Jiangsu Agricultural Sciences, 45(16):68–72. (in Chinese)
Yang Y Y, Li X J, Chen G S, et al. (2015) Effects of Biochar on Saline-sodic Soil Physical and Chemical Properties. Soils and Crops, 4(03):113–119. (in Chinese)
Yuan P, Wang J Q, Pan Y J, et al. (2019) Review of biochar for the management of contaminated soil: Preparation, application and prospect. Science of the Total Environment, 659: 473–490.
Zhang J H, Wu B, Wang G L, et al. (2020) Effects and Evaluation of Biochar on Physical-Chemical Properties of Coastal Saline Soil and Alfalfa Growth. Transactions of the Chinese Society for Agricultural Machinery, 51(08):285–294. (in Chinese)
Zhang Q Y. (2019) A brief introduction of technical measures for improving the Saline-alkali land in Hangjin Banner, Inner Mongolia. Agricultural Engineering Technology, 39(14):45. (in Chinese)
Zhang Y L, SUN J L, Qin C L, et al. (2014) Salinity Analysis of Cotton Fields of Alar in South Xinjiang and the Amelioration Effect of Wood Vinegar. China Cotton, 41(03):30–32+34. (in Chinese)
Zhang Y, QU Z Y, Ding Y H, et al. (2019) Effects of Different Soil Amendment on Soil Amelioration and Greenhouse Gas Emission in Salinization farmland. Water Saving Irrigation, (12):36–41+47. (in Chinese)
Zhao P C. (2017) Effects of biochar and wood vinegar on key chemical barrier factors of saline-alkali soil. Northeast Agricultural University. (in Chinese)
Zhou H J, Geng Y Q, Cong R C, et al. (2016) Effects of wood vinegar on chemical properties, enzyme activities and their correlation in saline alkali soil. Chinese Journal of Soil Science, 47(1): 105–111. (in Chinese)

Advances in Applied Chemistry and Industrial Catalysis – Saikia (Ed.)

Indoor VOC removal method: An analysis for TiO_2-coated activated carbon in air purification process

Zihan Zheng*
University of Florida, Gainesville, FL, USA

ABSTRACT: In recent years, due to the covid-19, people have to spend more time indoors. That makes people pay more and more attention to the problem of indoor air quality. Research shows that indoor air pollution may be more harmful to people's health than outdoor pollution. With the development of air purification technology, people can already treat most of the pollution substances to ensure indoor air quality. However, the removal of tiny doses of VOCs from the air is always a technical challenge. This paper mainly summarizes many different ways to remove VOCs from the air and presents the working concept and significance of an air filtration device that uses activated carbon as its core. By comparing many different treatment technologies, the TiO_2-coated activated carbon grain has the best efficiency to remove VOCs from the air.

1 INTRODUCTION

Water, soil, and air pollution are the world's most widespread and concerning public health issues today. And air pollution has become increasingly well-known and valued by the general public in recent years. However, people have had a misunderstanding about air pollution for a long time. The public always mistakenly thinks that indoor air is cleaner than outdoor air. EPA declared that indoor air pollution was one of the biggest environmental risks as early as 1995. In general, there are three ways to get fresh air: increase airflow, reduce air pollution sources, and set up an air purification system. However, increasing airflow might take more pollutants from outside, and most areas do not have the condition to remove the source of air pollution. Thus, the most viable approach for improving indoor air quality is to explore a higher-efficiency air filtration system.

Nowadays, most of the air purification devices on the market can achieve good purification effects. Because of its excellent adsorption performance, activated carbon is widely used in most air purification systems.

Although activated carbon can remove the majority of dangerous substances from polluted air, it still cannot remove the smallest harmful substance from the air such as VOCs. In all of the indoor pollution sources, VOCs are the most difficult substances to remove. Many research teams have attempted to eliminate this chemical from the air using various approaches. VOCs include a variety of compounds with high vapor pressure and low water solubility, some of which may have acute or long-term negative health consequences. Concentrations of many VOCs are consistently higher indoors (up to ten times higher) than outdoors (U.S. EPA). In recent years, due to the COVID-19 pandemic, people have been forced to stay at home to avoid infection. However, people could avoid the Covid by staying at home, they cannot avoid the risk caused by indoor pollutants. Research shows that VOCs could cause various health problems like reproductive complications, neurological issues, headaches, and even cancer (Lamplugh et al. 2020). Some research teams claim that the deterioration of indoor air quality (IAQ) might result from the current home isolation requirement

*Corresponding Author: zihan.zheng0921@gmail.com

DOI 10.1201/9781003308553-23

that is in place to reduce the spread of coronavirus (Abouleish 2021). To keep our health and reduce the speed of covid-19, air purification devices are very necessary for our home isolation.

In addition to common air purification equipment, the use of air purification materials in the construction process can also achieve a good effect of removing VOCs. Nevertheless, these materials are hard to do the regeneration once installed, and that will cause the efficiency to decrease over time (Lamplugh et al. 2020). Besides, potted plants are also being considered a great method to purify indoor air pollution.

This paper mainly introduces two ways to remove VOCs: using TiO_2-coated activated carbon and using a felt-based living wall, discussing the efficacy, pros, and cons of these methods. After comprehensive comparison of many aspects, this paper gets a conclusion.

2 METHODOLOGY

2.1 *Experiment background*

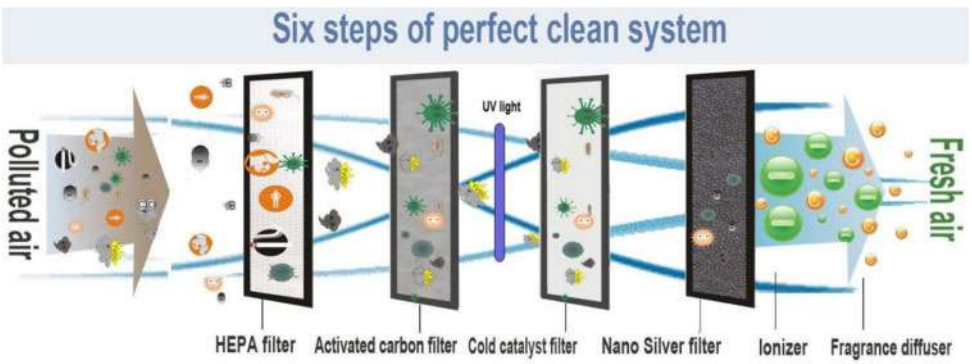

Figure 1. Six steps of air purification.

Common air purification devices are usually divided into six parts, as Figure 1 shown above (Sandle, 1970). The polluted air needs to pass through four filters including an activated carbon filter. However, as we can see in the picture above, ordinary activated carbon filters cannot completely remove pollutants. Therefore, existing air purification equipment with activated carbon as the core actually cannot satisfy people's health needs. To further improve the working efficiency of the air purification device with activated carbon as the core, researchers try to use a variety of metal composites combined with activated carbon. In these studies, nanosilver and TiO_2-coated activated carbon have the most obvious improvement in the performance of activated carbon (Ao & Lee 2005; Chang et al. 2020). Especially the TiO_2 coated activated carbon, can promote the absorption of lower concentration of VOCs by activated carbon.

In addition to the use of air purification equipment to purify the air, the use of plants to absorb VOCs in the air is also a popular research field in recent years. In China, people usually put some green plants in their new homes to remove the smell of paint. These peculiar smells usually come from the residual VOC during the decoration process. Past studies have proved that plants have a good purifying effect on indoor VOCs. Some plants such as palm and Ficus lyrata (fiddle leaf fig), have been proven to have a very high purification effect on VOCs (Pettit et al. 2019; Teiri et al. 2018). Therefore, using plants to remove indoor VOCs is also a good choice.

According to recent studies, indoor pollution levels are higher than those found outside (Robinson & Nelson 1995). Considering people have to spend more time indoors because of covid, the new air purification system is very necessary for every family. The ideal air purification system should balance efficiency and aesthetics. The established manufacturing technique would

also significantly reduce costs. Overall, as people pay more attention to indoor air quality, air purification systems will have a huge potential market.

2.1.1 *TiO_2-coated activated carbon experiment*

Researchers discovered a new approach to combine TiO_2 and activated carbon to boost the efficiency of the activated carbon. Akira Fujishima discovered the photocatalytic capabilities of nanosized titanium dioxide in 1967 (Li et al. 2006). Titanium dioxide has been extensively applied for environmental applications since the first study on its application for photocatalytic cleaning of cyanide-containing waters (Frank & Bard 1977). TiO_2 provides numerous unrivaled advantages. It is quite stable, and it's also thought to be safe for human health. The most essential feature is that it provides excellent catalysis at a low cost. Researchers wrapped TiO_2 around the activated carbon grain to mix TiO_2 and activated carbon. The TiO_2-coated activated carbon (AC) grain (TiO_2/AC) was made by hydrolytically precipitating TiO_2 from Tetrabutyl Orthotitanate and following heat treatment. A recent study looked at the impact of immobilized activated carbon filters on removing indoor air contaminants at part-per-billion (ppb) levels. Researchers devised a series of experiments to demonstrate the advancement of this new air purifying technology. One of the most dependable experiments comes from a Hong Kong Polytechnic University study group. As Figure 2 shows (Ao & Lee et al, 2005), Dr. Ao's research team designed a new combined filter built with both activated carbons, HEPA, and TiO_2-coated filters. By setting up different comparative experiments, they believe that TiO_2-coated filters have a better ability to purify indoor VOCs.

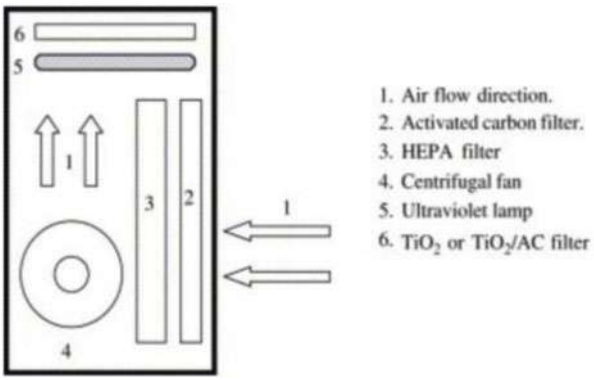

Figure 2. Air purification system design.

2.1.2 *Felt-based living wall*

A Lot of research already confirmed that the ornamental plants have a great purification effect on indoor VOCs (Aydogan & Montoya 2011; Hörmann et al. 2017). However, due to the space limitation of the indoor environment, most houses do not have enough space to place adequate plants to purify the air pollution. Thus, a felt-based living wall would be a better option to solve this problem. A felt-based living wall is a small living wall module that could be set up indoors as a plant purification method. It can be set up on the wall with felt-based vertically. This design could maximize space-saving and purify the air at the same time. Living walls have many advantages, they are both aesthetic and practical. They are also being confirmed to remove the particulate matter (Ottelé et al. 2010).

A research team from Spain designed a novel felt-based living wall. They choose Nephrolepis exaltation as an experiment material to build a living wall. As figure 3 shows, they set up fytotextile, Nephrolepis exaltata, Temperature sensor, TVOCs sensor, portable fan, and a grow lamp in a small plastic box to simulate the growth environment of the plant indoors (Aydogan et al. 2011). After eight months of artificial cultivation, researchers have conducted many experiments on these plants. The results show that the felt-based living wall has a significant improvement effect on indoor air.

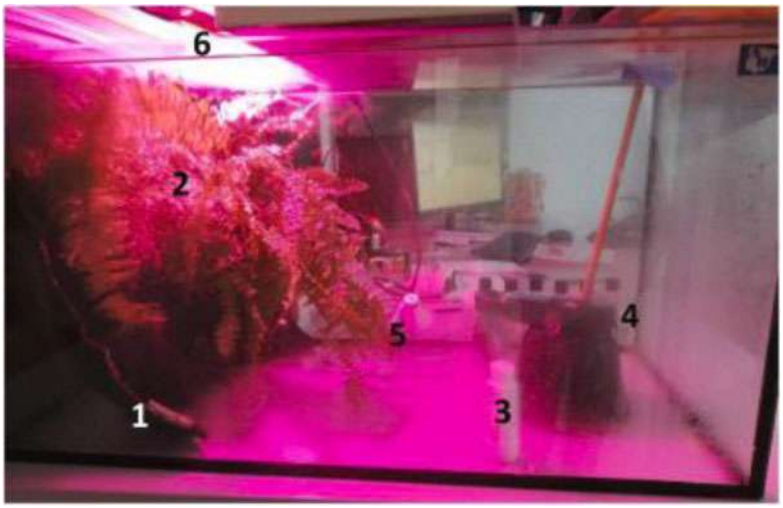

Figure 3. Living wall model.

2.2 *Experiment results*

2.2.1 *Result for TiO_2-coated activated carbon filter experiment*

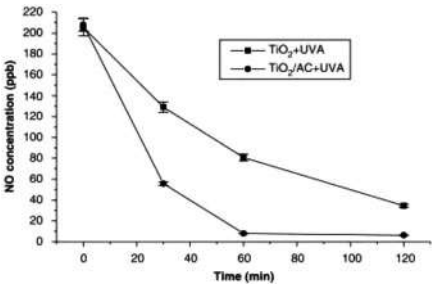

Figure 4. Time vs. NO concentration.

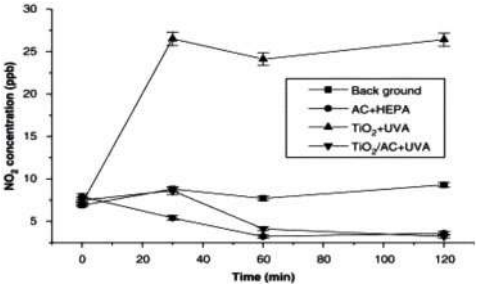

Figure 5. Time vs. NO_2 concentration.

In the experiment, nitric oxide was used as a source of pollution. As we can see from Figure 4 (Ao & Lee 2005), under the purification of TiO_2-coated activated carbon and UVA, the concentration of NO has an extremely quick drop. The NO's concentration reaches 5ppb in just 60 minutes, which means this equipment achieves its pick efficiency in one hour. And for the filter with TiO_2 only, it takes almost 2 hours to decrease the NO concentration under 40 ppb which is much higher than the one with activated carbon. The TiO_2-coated activated carbon has a great working efficiency to purify the indoor VOCs. While conducting research experiments, researchers found that NO_2 was observed as the intermediate from the photodegradation of NO as shown in Eqs(1) and (2).

$$NO + HO_2^{\bullet} \rightarrow NO_2 + OH^{\bullet} \quad (1)$$

$$NO_2 + OH^{\bullet} \rightarrow HNO_3^{\bullet} \quad (2)$$

As shown in Figure 5 (Ao & Lee 2005), there is a clear upward trend in the concentration of NO_2. This trend peaked at the 30-minute mark. By comparing the trendlines, we could find that the TiO_2-coated activated carbon still has the best efficiency to purify the VOCs. After a simple

calculation, the TiO_2-coated activated carbon filter efficiency for NO is as high as 97%, and the purify efficiency for NOx is also over 95% (Ao & Lee 2005).

2.2.2 *Result for felt-based living wall experiment*

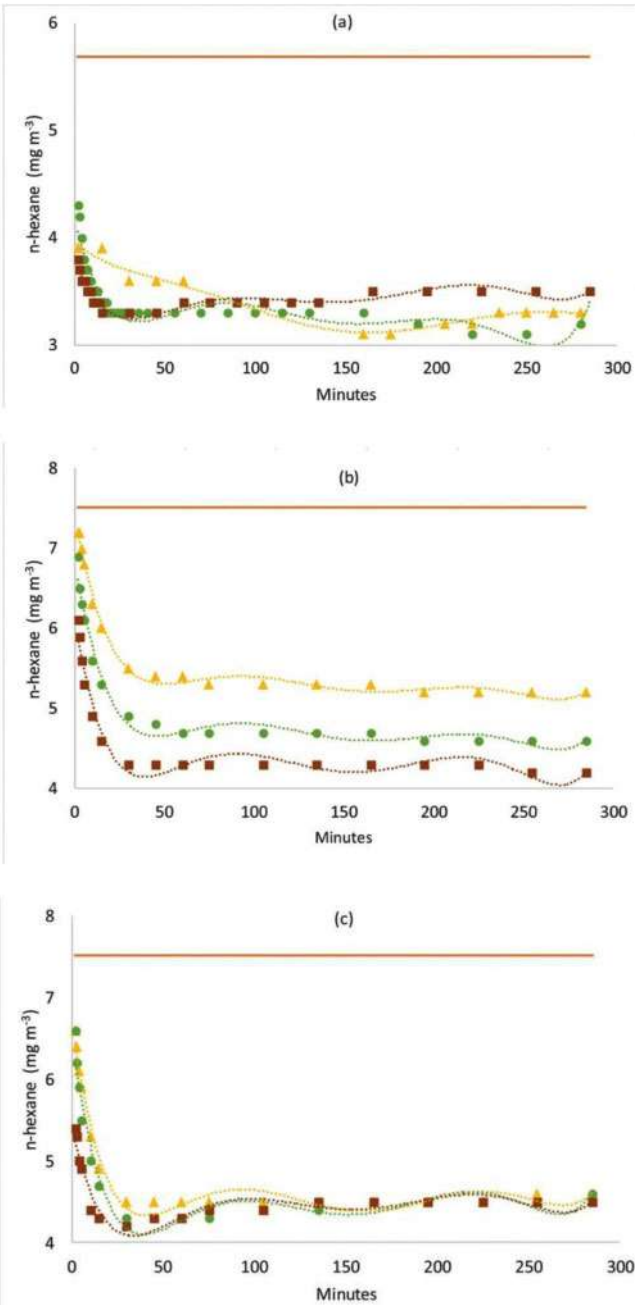

Figure 6. Time vs. n-hexane concentration.

In Suarez's research, she chose n-hexane as a source of pollution. Figure 6 (Fernández-Cañero et al. 2021) shows evolution of VOCs in three different experiment conditions. Respectively as module 1 with 50μl, module 1 with 7μ, and module 2 with 7μl n-hexane. Comparing the result of these three replications, we could find that they have similar trends, the concentration of n-hexane decreases very fast in the first 30 mins and then have some small fluctuations. After calculating the result, the felt-based living wall could remove about 75% of VOCs from the air. In general, the experiment shows a great result that the felt-based wall has an obvious treatment effect on indoor VOCs. In addition, the result also shows the instability of the plant treatment. There are still limitations to tracing small amounts of VOCs. Besides, due to the test subject being plants, their biomass, leaf area, and root volume will all influence the final result. Thus, more study about this subject is necessary for future research (Fernández-Cañero et al. 2021).

3 CONCLUSION

By comparing the traditional activated carbon air purification device with a TiO_2-coated activated carbon filter, we discovered that TiO_2-coated activated carbon has numerous unrivaled advantages. It produces less polluting intermediate generation and has a higher working efficiency. Dr. Ao's experiment took place inside a commercial air purifier. The blank test reveals that there was no pollutant removal due to chamber leaks or experiment mistakes. Because of the original setting, no NO was detected in Part 1, and toluene was eliminated. Activated carbon filters coated with TiO_2 remove 83.2% of NO but create 12.9% of NO_2. The TiO_2-coated activated carbon filter improves working efficiency by 97% while lowering intermediate generation by 1.6% (Ao & Lee 2005). As a result, the TiO_2-coated activated carbon filter not only reduced the amount of intermediate leaving the system but also improved its efficiency. Even though the toluene has a slight photoreactive, the TiO_2-coated activated carbon also presents a great removal efficiency.

Within Dr.Suárez's research, we learned a novel way to deal with indoor VOCs. The advantages of setting up a living wall are obvious, it has great efficiency to remove VOCs from the air and it also has a low cost. Compared with traditional plant treatment methods (Li et al. 2006), a felt-based living wall can save a lot of living space for the householder. Besides, the previous study has already proved that the plant uptake and degradation of VOCs will not produce any harmful co-product (Kim et al. 2008; Teiri et al. 2018).

Compared with using an air purification device to remove indoor VOCs, a felt-based living wall can save a lot of money and will be more aesthetic. Thus, setting up a felt-based living wall is also a great method to respond to indoor air problems.

Overall, the TiO_2-coated activated carbon filter demonstrated a perfect approach to removing indoor contaminated air within a short working period. However, the shortcoming of the TiO_2-coated activated carbon filter is also obvious, the co-product of the treatment process is still bothering the researchers.

Compared to a TiO_2-coated activated carbon filter, although a felt-based living wall has a lower working efficiency and it cannot remove an extremely small amount of VOCs, it will not produce any co-product and has a lower cost. And compared to the traditional air purification device, the TiO_2 coated activated carbon filter is cheaper and has less intermediate generation. Also compared to potted plants, the felt-based living wall could save more space and have a higher working efficiency. These two methods have their own pros and cons.

The author believes that we must explore more ways to respond to indoor air problems. People will spend more time indoors in the future, and the improvement of indoor air quality also has a potential economic impact (Soreanu et al. 2013). Indoor air quality is closely related to human health, and individual health will also affect the development of the entire society. Thus, the author considers that people should take a more cautious attitude towards indoor air pollution.

Although new technology has the potential to improve our lives, the air purifier has the potential to supply us with clean air that has never been tainted. We must understand that air purifiers can only handle dirty air produced by our industrialized development. Maybe we need to rethink the

problem. Is the air purifier really necessary for personal living? Maybe the most important thing we need to do is to cut off the air pollution from the very beginning. The air should never be polluted. The author hopes that there is one day in the future, no one needs an air purifier to protect their health, and people do not need to worry about any environmental problems. As an environmental engineer, the author wants to do their best to achieve these dreams.

ACKNOWLEDGMENTS

This paper is a review based on Ao, C. H, and ç G. P.'s research, thanks for their contribution to the air pollution problems. I would also like to thank Mrs. Yu for her help in the preparation of this paper. And thanks for Alisa Wang's help with the paper corrections.

REFERENCES

Abouleish, M. Z. (2021). Indoor air quality and COVID-19. Public Health, 191, 1.

Ao, C. H., & Lee, S. C. (2005). Indoor air purification by photocatalyst TiO_2 immobilized on an activated carbon filter installed in an air cleaner. Chemical engineering science, 60(1), 103–109.

Aydogan, A., & Montoya, L. D. (2011). Formaldehyde removal by common indoor plant species and various growing media. Atmospheric environment, 45(16), 2675–2682.

Chang, S. M., Hu, S. C., Shiue, A., Lee, P. Y., & Leggett, G. (2020). Adsorption of silver nano-particles modified activated carbon filter media for indoor formaldehyde removal. Chemical Physics Letters, 757, 137864.

Fernández-Cañero, R., ç G. P., Fernández-Espinosa, A. J., Rossini-Oliva, S., Franco-Salas, A., & Pérez-Urrestarazu, L. (2021). Volatile organic compounds removal by means of a felt-based living wall to improve indoor air quality. Atmospheric Pollution Research, 12(3), 224–229.

Frank, S. N., & Bard, A. J. (1977). Semiconductor electrodes. 12. Photoassisted oxidations and photoelectrosynthesis at polycrystalline titanium dioxide electrodes. Journal of the American Chemical Society, 99(14), 4667–4675.

Hörmann, V., Brenske, K. R., & Ulrichs, C. (2017). Suitability of test chambers for analyzing air pollutant removal by plants and assessing potential indoor air purification. Water, Air, & Soil Pollution, 228(10), 1–13.

Kim, K. J., Kil, M. J., Song, J. S., Yoo, E. H., Son, K. C., & Kays, S. J. (2008). Efficiency of volatile formaldehyde removal by indoor plants: contribution of aerial plant parts versus the root zone. Journal of the American Society for Horticultural Science, 133(4), 521–526.

Lamplugh, A., Nguyen, A. & Montoya, L. D. (2020). Optimization of VOC removal using novel, low-cost sorbent sinks and active flows. Building and Environment, 176, 106784.

Li, Y., Li, X., Li, J., & Yin, J. (2006). Photocatalytic degradation of methyl orange by TiO_2-coated activated carbon and kinetic study. Water research, 40(6), 1119–1126.

Ottelé, M., van Bohemen, H. D., & Fraaij, A. L. (2010). Quantifying the deposition of particulate matter on climber vegetation on living walls. Ecological engineering, 36(2), 154–162.

Pettit, T., Irga, P. J., & Torpy, F. R. (2019). The in situ pilot-scale phytoremediation of airborne VOCs and particulate matter with an active green wall. Air Quality, Atmosphere & Health, 12(1), 33–44.

Robinson, J., & Nelson, W. C. (1995). National human activity pattern survey data base. USEPA, Research Triangle Park, NC, 2.

Sandle, Dr Tim. (1970). HEPA Filters in Safety Cabinets. Pharmaceutical Microbiology, 1 Jan. https://www.pharmamicroresources.com/2015/04/hepa-filters-in-safety-cabinets.html.

Soreanu, G., Dixon, M., & Darlington, A. (2013). Botanical biofiltration of indoor gaseous pollutants–A mini-review. Chemical engineering journal, 229, 585–594.

Teiri, H., Pourzamani, H., & Hajizadeh, Y. (2018). Phytoremediation of VOCs from indoor air by ornamental potted plants: A pilot study using a palm species under the controlled environment. Chemosphere, 197, 375–381.

Advances in Applied Chemistry and Industrial Catalysis – Saikia (Ed.)

Application of ultrafiltration-reverse osmosis system double membrane method in advanced treatment of fluoride in raw water

Baoyun Wang*
School of Chemical Engineering, Changchun University of Technology, Changchun, P.R. China

Xilin Dong** & Yunlong Guo
Changchun Water Group, Changchun, P.R. China

Fuqiang Shi & Zhihua Guo
School of Chemical Engineering, Changchun University of Technology, Changchun, P.R. China

He You
Changchun Water Group, Changchun, P.R. China

Hongwu Li***
School of Chemical Engineering, Changchun University of Technology, Changchun, P.R. China

ABSTRACT: The double membrane method of ultrafiltration reverse osmosis system uses the drive of pressure difference to supplement the fluoride removal capacity that cannot be met by conventional treatment process through the selective permeability of membrane. It can stably remove fluoride from water, meet the requirements of national standards and ensure the health of people's drinking water. The water source of a large urban water purification plant is a lake reservoir in the city, with a daily treatment capacity of 250000 tons. The Conventional treatment processes are mechanical mixing tank, small perforated grid reaction tank, lateral flow inclined plate sedimentation and V-shaped filter tank. The advanced treatment process includes ozone and activated carbon filtration. Because the fluoride in the raw water exceeds the standard, the existing process cannot fully meet the needs of national standards. Therefore, the ultrafiltration-reverse osmosis double membrane method is used for advanced treatment of the original process effluent. The water quality of the factory water after the transformation was continuously monitored, and the fluoride concentration was kept below 1 mg/L, the water quality met the national drinking water standard, and the operation was stable. Through the analysis of the monitoring results, the experience of the system operation is summarized, which provides support for the follow-up application of this method.

1 INTRODUCTION

Fluoride is an organic or inorganic compound containing negative fluorine, which is widely found in natural water (Greenlee et al. 2009). Fluorine has both advantages and disadvantages for human health. On the one hand, fluorine is an essential trace element for human body (Cheng & Karthikeyan 2005), and a short time of small dose of fluorine will enhance immune function. On the other hand, long-term excessive intake of fluoride will lead to osteoporosis and bone deformation in the human body (Li et al. 2010), and lack of fluoride intake will make the human body vulnerable to dental caries. When the fluoride concentration in drinking water is 0.5–1.0 mg/l, the fluoride concentration is appropriate. If the fluoride concentration in drinking water exceeds 1.5 mg/l for a long time, the human body will be prone to spot tooth disease. When the fluoride concentration in

Corresponding Authors: *wangbaoyunchn@163.com, **276190286@qq.com and ***younaonao@126.com

DOI 10.1201/9781003308553-24

water exceeds 4 mg/L, the human body will cause skeletal fluorosis (Cheng & Karthikeyan 2005). Fluorine can enter the brain tissue and accumulate in it, damage cells, and produce toxic side effects on it. Therefore, patients with skeletal fluorosis are prone to complicated nerve damage. Excessive fluorine can cause systemic toxicity in the human body. It will not only damage bones and teeth, but also accumulate in various tissues and organs of human body, resulting in toxic and side effects. Fluoride strongly stimulates and corrodes the eyes, skin, throat, nose and other organs, and is easy to cause mucosal congestion and inflammation (Rasool et al. 2018). For example, too high concentration of hydrogen fluoride inhalation will cause bronchitis, pneumonia and other diseases (Fekri & Kasmaei 2013). In order to prevent tooth decay, about 90% of toothpaste products will add fluoride, but the national and related industry standards have strictly controlled the fluoride content to ensure that it does not cause harm to the human body. Daily drinking water with high fluorine content will do harm to human teeth and bones and cause chronic poisoning. At least, it will damage enamel and premature tooth loss (Fekri & Kasmaei 2013). The most important is to cause bone and joint pain, bone deformation, and even spinal bending, and lose the most basic labor ability. Therefore, the damage to the human body caused by excessive fluoride in drinking water cannot be ignored.

The serious over standard of fluoride has caused some harmful events to the environment and human body. For example, the Maas River Valley smog incident in 1930, the air pollution incident in the Maas River Valley industrial area in Belgium from December 1st to December 5th, 1930, caused by a large number of harmful gases such as sulfur dioxide and hydrofluoric acid emitted by industries in the Maas River Valley area Acidic particulate pollution, the incident eventually led to more than 60 deaths. Pollution incidents caused by fluoride have also occurred in China. In May 2011, fluoride and total phosphorus in Wujiang River Basin, especially Wujiangdu Reservoir and its tributary Xifeng River, seriously exceeded the standard, which was known as "Guizhou Wujiang River water pollution event". The incident caused no fish to survive in the 10km section of the lower reaches of the Wujiang River, and even threatened the drinking water safety of 2 million people in Zunyi City, Guizhou Province. In July 2019, the Central Fifth Ecological Environmental Protection Inspectorate was stationed in Gansu's sinking inspection and discovered that 4 chemical companies illegally put into production in Beihewan Circular Economy Industrial Park discharged untreated production wastewater, causing the relevant areas to include fluorine. Many indicators, including chemical compounds, have seriously exceeded the standard.

At present, the commonly used fluoride removal methods are as follows:

(1) The adsorption method is currently the most common method of fluoride removal. It is the adsorption material that determines the adsorption capacity and adsorption efficiency. There are many adsorbent materials, and the adsorbent that is the most effective and most widely used adsorbent for removing fluoride ions is activated alumina (Wang et al. 2017). Because of the strong affinity between fluoride ion and aluminum, activated alumina has a strong adsorption capacity for fluorine. The main factors affecting the adsorption effect are that the regeneration of alumina is complex and cumbersome, and the excessive acidity and alkalinity of water will also greatly reduce the adsorption capacity of fluorine ions.
(2) Ion exchange method is to exchange the fluorine ion in water with the ion on the resin, the ion on the fluorine ion resin and the original resin enters the water, so as to achieve the effect of removing fluorine ion. Chloride ion exchange resin and hydrogen oxygen ion exchange resin are commonly used ion exchange resins. The ion exchange method has a stable fluorine removal effect, and the limitation is that the regeneration of the ion exchange resin consumes a large amount of regenerant. The salt solution regenerated by ion exchange method will contain fluorine ions, which needs appropriate treatment to avoid pollution.
(3) Under the condition of applying constant current, the electro flocculation method takes the iron metal plate as the anode, which is oxidized to produce iron ions through electrochemical reaction, and forms an adsorbent with the hydroxyl ions produced by the cathode. Finally, the fluorine ions are removed by flocculation and precipitation.

(4) The electrodialysis method uses a potential difference to drive the anions and cations between the positive and negative electrodes. By applying a direct current electric field, concentrated water and fresh water are formed in different areas to remove fluoride ions in the water.
(5) The double-membrane method, namely the ultrafiltration-reverse osmosis system double membrane method, is driven by pressure difference to separate fluoride in water. Membrane separation process is a pure physical process, because it does not need heating, so it consumes less energy than the traditional thermal separation process. Membrane separation technology refers to the process of separating pollutants and solutes in solution by using the selective permeability of membrane under the action of external force, such as pressure difference, potential difference and concentration difference. Important applications of membrane separation technology include the production of drinking water. For example, the largest RO desalination plant is located in Solek, Israel, with a daily output of 624,000 cubic meters. Membrane separation technologies include microfiltration, nanofiltration, ultrafiltration, reverse osmosis and other technologies. The double membrane method includes two systems: ultrafiltration and reverse osmosis. Ultrafiltration is a multi-membrane filtration in which pressure or concentration gradient causes the solute to separate through a semi-permeable membrane. High molecular weight suspended solids and solutes are retained in the so-called delayed acid salt, while water and low molecular weight solutes pass through the permeable membrane. Ultrafiltration can remove particulate matter and macromolecular substances from raw water to produce drinking water (A M C et al. 2000). Reverse osmosis is a water purification process that uses a partially permeable membrane to separate ions, unwanted molecules and larger particles from drinking water. In reverse osmosis, pressure is applied to overcome the osmotic pressure, which is a series characteristic driven by the chemical potential difference of solvents. Reverse osmosis can remove many types of dissolved and suspended chemical species and biological species in water, and is used in industrial processes and the production of drinking water. The result is that the solute remains on the pressurized side of the membrane, and the pure solvent can be transferred to the other side. For "selectivity", the membrane does not allow macromolecules or ions to pass through the pores, but allows smaller components of the solution to pass freely (Warsinger et al. 2016).

The double membrane method has the following advantages: The pure water produced is of high quality and is almost unaffected by changes in the quality of raw water. The design is simple, and the membrane manufacturing plant is easier to realize automation. Due to the modular structure, the membrane factory is more flexible, such as the expansion of production capacity. In addition to cleaning the membrane, almost no chemicals are used, which greatly reduces residues and by-products. Due to the physical barrier of the ultrafiltration membrane, the permeate is almost free of viruses and other microorganisms. Therefore, biological pollution or re pollution in subsequent stages is significantly reduced (A M C et al. 2000).

In order to solve the problem of excessive fluoride in raw water and provide residents with drinking water that meets the requirements of national standards. Comprehensively consider the advantages and disadvantages of various fluoride removal methods in raw water. To explore the application of double membrane method in advanced treatment of drinking water in waterworks and provide experience to popularize the law.

2 METHODS AND MATERIALS

The treatment capacity of urban water purification plant is 250000 t/d. The water source is a lake reservoir type reservoir within the jurisdiction, which is located in the middle reaches of large rivers in the urban jurisdiction. The reservoir is mainly used for comprehensive utilization of water supply, flood control, and irrigation to the city, with a total capacity of nearly 1.3 billion cubic meters. The main pollution source of the reservoir is agricultural pollution around and upstream of the reservoir. According to the monitoring results of relevant departments, the water quality of

the reservoir is good, which is class III water all year round. The conventional treatment process of water purification consists of mechanical mixing tank, small hole grid reaction tank, lateral flow inclined plate sedimentation and V-shaped filter. The advanced treatment process consists of ozone and activated carbon filtration. Due to the complex geological conditions of the reservoir and the shallow depth of the water level, it is easy to cause the problem of mutual infiltration between reservoir water and groundwater. The concentration of fluoride ion in urban groundwater has been high, which leads to the exceeding standard of fluoride ion in the influent of water plant. Therefore, it is necessary to add a fluorine removal process. The original treatment process cannot remove excessive fluoride, so it should be upgraded. After comparing the commonly used fluoride removal processes and comprehensively considering the treated water quality, treatment effect and subsequent maintenance, it is finally decided to use ultrafiltration reverse osmosis double membrane method for fluoride removal.

2.1 *Ultrafiltration system*

The double membrane method includes two systems of ultrafiltration and reverse osmosis. Ultrafiltration is the pretreatment of the effluent of the activated carbon filter to ensure the fluoride removal efficiency and service life of the reverse osmosis membrane. Ultrafiltration system includes inlet pump, self-cleaning filter, ultrafiltration device, ultrafiltration water tank, ultrafiltration backwashing pump, etc. Provide water inlet conditions for the normal operation of the next-stage reverse osmosis system. The ultrafiltration membrane adopts internal pressure hollow fiber ultrafiltration membrane. The model of the membrane is DOWTMSFD-2660, the effective membrane area is 33m2, and the designed membrane flux is 45L ($m^2 \cdot h$). Four groups of ultrafiltration filters are used, each group adopts 70 ultrafiltration membranes, and the membrane pore size is 0.1um. The water production capacity of each group was 250m^3, and the recovery rate was $\geq$ 93.5%.

2.2 *Reverse osmosis system*

Reverse osmosis can filter ion level impurities and meet the quality requirements of factory water in water plants. Reverse osmosis system includes scale inhibitor adding device, reverse osmosis inlet pump, security filter, reverse osmosis high-pressure pump, reverse osmosis device, reverse osmosis concentrated water tank, etc. The reverse osmosis membrane adopts cellulose acetate reverse osmosis membrane, the model is Toray TM710D, the effective membrane area is 8m^2, the recovery rate is $\geq$75%, and the designed membrane flux is 21.5L/($m^2 \cdot h$). The system adopts four groups of reverse osmosis devices and operates according to the design of level I and 2 sections. Each group of equipment is equipped with 132 low-pressure reverse osmosis membranes, 22 membrane shells and 6 pieces. The arrangement mode is 15:7. The concentrated water discharge is 3500m^3/d and the water production capacity is 416m^3/h. This process is to remove fluoride in drinking water, so a first-stage reverse osmosis is used. It is designed as a continuous one-time primary reverse osmosis device.

After the ozone-biological activated carbon process, an ultrafiltration-reverse osmosis system combination is added to separate the excess fluoride that cannot be handled by the original process. Make the concentration of fluoride in drinking water reach the level that meets the requirements of national standards.

The specific process flow is shown in the figure 1.

3 RESULTS AND DISCUSSION

3.1 *Monitoring results of original treatment process*

Monitor the factory water and pipe network water of the water plant before transformation, as shown in Figure 2(b). The water concentration of the water plant is between 0.076–1.013 mg/L. The

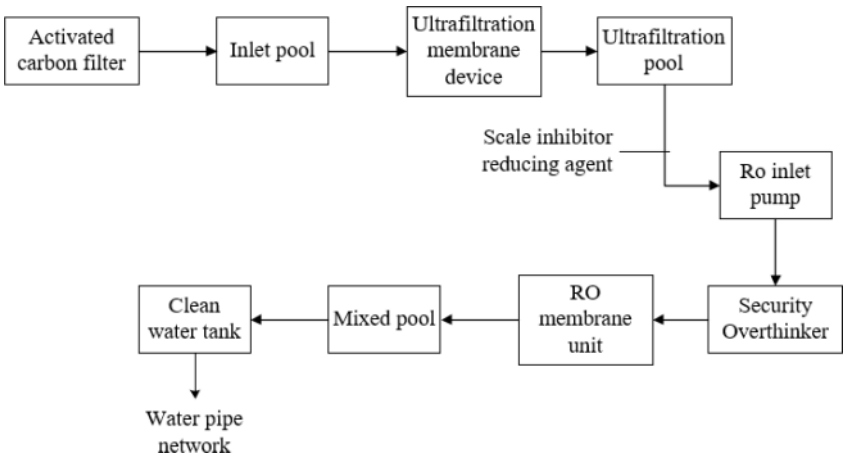

Figure 1. Process flow diagram of double membrane method.

fluoride concentration fluctuates slightly, with an annual average concentration of 0.36 mg/L. The exceeding standard range is within 0.013 mg/l. On the whole, the water purification capacity of the water plant is performing well, basically in line with the national drinking water sanitation standards. However, there are occasional phenomena that slightly exceed the standard concentration, such as January, May, June, and November. The monitoring results of pipe network water show that the fluoride concentration in other months is between 0.099–1.009 mg/l except January. It basically corresponds to the change of the factory water concentration. The annual average concentration is 0.38 mg/L, which is 0.02 mg/L higher than the average concentration of the factory level. The reason may be that the concentration of fluoride has increased due to secondary water supply and aging of the pipe network during the transmission and distribution process.

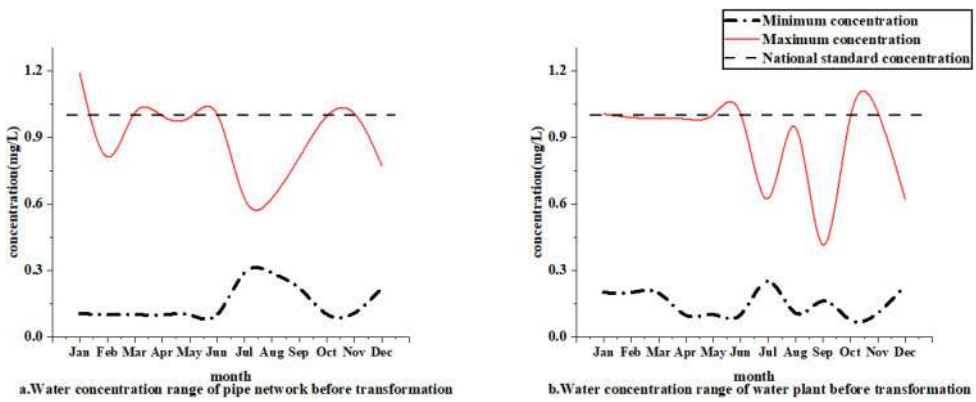

Figure 2. Monitoring range of water quality concentration before transformation.

3.2 *Post treatment effect of adding double membrane method*

After treatment by the ultrafiltration-reverse osmosis system, the fluoride concentration in the water from the water purification plant is stably controlled below 1.0 mg/L. As shown in Figure 4(a) and Figure 4(b). It meets the requirements of drinking water hygiene standards and is within a concentration range suitable for human drinking. Compared with that before the transformation, the

fluoride concentration has reached the standard, and the concentration range has generally decreased by 0.03–0.05 mg/L. After the transformation, the annual variation range of fluoride concentration in factory water is small, and the average value is stable in the range of 0.2–0.4 mg/L. It shows that the ultrafiltration-reverse osmosis system has good fluoride removal stability.

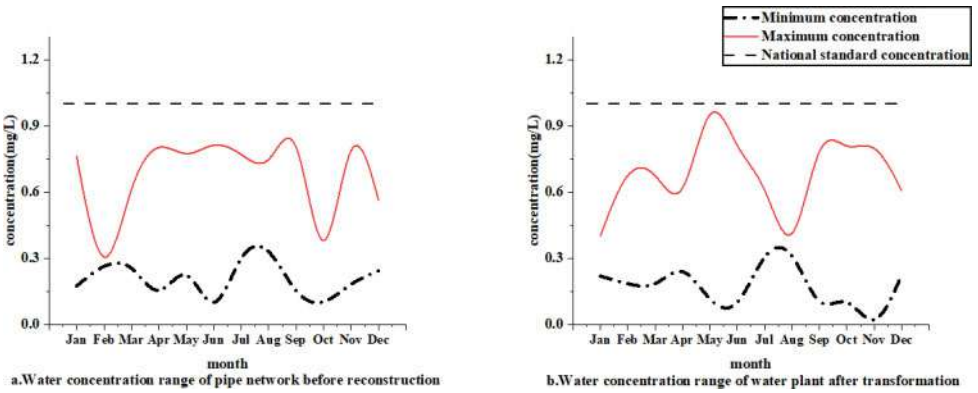

Figure 3. Water quality concentration detection range after transformation.

3.3 *Treatment effect of other substances before and after modification*

In order to control water-borne infectious diseases caused by the presence of carcinogenic microorganisms in water, water plants will perform chlorination and disinfection when treating drinking water. However, while using its disinfection effect, the water plant also needs to control its concentration to prevent excessive content from affecting human health. The national standard requires that the chloride concentration in drinking water shall be controlled within 250 mg/L. Through additional experiments, while monitoring the fluoride removal effect of the original treatment process by the double membrane method, the ability of the method to remove chlorides is monitored at the same time. To explore the further application potential of the double membrane method in water plants. Through the comparison of the monitoring results in Figure 5, it is found that the chloride concentration in the water quality remains basically stable after the water plant undergoes the double-membrane method transformation. There are no obvious signs of reduction. The reason may be that the water plant will add liquefied chlorine gas in order to disinfect the raw water. Chlorine reacts with water to generate hypochlorous acid and hydrochloric acid. Hypochlorous acid destroys the active enzymes in microorganisms and kills microorganisms. The remaining hypochlorous acid will naturally decompose to produce oxygen and hydrochloric acid. Eventually, these hydrochloric acid will naturally volatilize during the process of transporting to the water pipe network. Although the membrane system will remove part of the chloride, the chloride generated by adding chlorine has not been completely volatilized. Therefore, the content did not change significantly. It shows that the double membrane method does not affect the chloride treatment capacity of the water plant and ensures the quality stability of the factory water of the water plant.

3.4 *Effect of temperature on fluoride concentration*

Analyze the water quality monitoring results of each quarter, as shown in Fig.5. It is found that there is a wave crest trend. The concentration of fluoride slowly increased in the first to third quarters, and then decreased in the fourth quarter. The highest average concentration of fluoride was in the third quarter, with a concentration of 0.312 mg/L. The lowest is the fourth quarter, with a concentration of 0.261 mg/L. By comparing and analyzing the change trend of the same temperature, it is not difficult to find that the average concentration of fluoride is basically consistent with the change

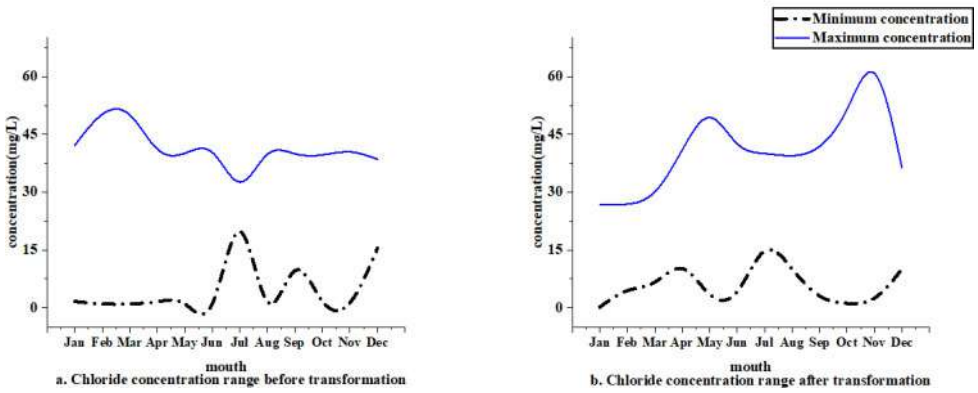

Figure 4. Contrast of chloride concentration before and after the double-membrane method reformation.

trend of temperature. As the temperature increased in the first three quarters, the concentration also increased. In the autumn and winter seasons, the temperature began to drop, and the fluoride concentration also dropped.

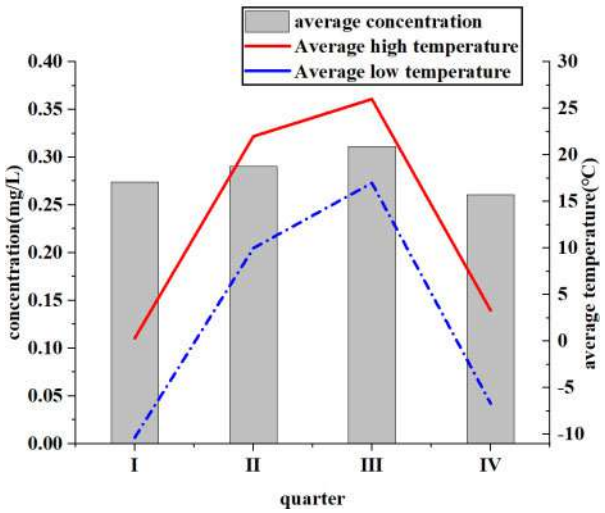

Figure 5. The average concentration changes with temperature.

4 CONCLUSION

Based on the above results and discussion, the following conclusions are obtained:

(1) The ultrafiltration system operates well and provides good conditions for the reverse osmosis system. Fluoride in the effluent of the water plant is between 0.305–0.989 mg/l. The test data shows that the original excess fluoride has reached the limit requirements of the "Drinking Water Hygiene Standard" (GB5749-2006). It can be supplied to residents for daily drinking.
(2) The combined operation of ultrafiltration-reverse osmosis system has good system stability and fluoride removal effect. Compared with before the system transformation, the fluoride

concentration has reached the standard. The concentration range is generally reduced by 0.03–0.05 mg/L, and the concentration is stably controlled below 1.0 mg/L. Meet the requirements of drinking water sanitation standards.

(3) The concentration of fluoride in the raw water keeps the same trend with the change of temperature. As the temperature rises in summer and autumn, the water fluoride concentration increases accordingly. In the third quarter, the average concentration of fluoride reached the highest value of 0.312 mg/L. With the subsequent decrease in temperature, the average concentration of fluoride also decreased to 0.261 mg/L.

(4) Compared with the ability to remove fluoride, the effect of the double-membrane method to remove chloride is not obvious. Chloride concentration has no obvious change before and after system transformation.

For the subsequent improvement of the application of ultrafiltration-reverse osmosis system double membrane method for advanced treatment of fluoride in raw water, this article proposes:

(1) The large-scale urban water purification plant adopts ultrafiltration-reverse osmosis membrane technology to remove fluoride in the water, with advanced technology and good treatment effect. After monitoring and analysis, the removal of fluoride in the factory water from the water plant has achieved the expected effect. The removal efficiency and stability of fluoride are good. The quality of the factory water meets the national standard and can be used as a technology for removing fluoride in water plants and improving and ensuring the quality and safety of drinking water.

(2) In order to increase the application potential of the double membrane method in water treatment in water plants, other substances specified in the "Drinking Water Hygiene Standard" can be tracked and monitored. Improve the economic benefit of the application of double membrane method.

(3) In the second and third quarters, the fluoride concentration will increase with the increase in temperature. In order to ensure the removal rate of fluoride, the effects of influent pressure and other factors can be tested. Ensure that the concentration of fluoride is stable within the national standard.

(4) For the large investment in the initial construction of the system, the operation and maintenance costs of the later system are high. It is necessary to further develop new membrane materials, optimize the system combination and reduce investment costs.

(5) Regarding the reduction in water production caused by pollution after long-term use of the membrane, and the high frequency of chemical cleaning resulting in more consumables. The optimal cleaning parameters can be studied to ensure the membrane permeability and reduce the related cleaning cost.

REFERENCES

A M C, A F J, A R K, et al. Process water production from river water by ultrafiltration and reverse osmosis – ScienceDirect[J]. Desalination, 2000, 131 (1–3):325–336.

Cheng G U, Karthikeyan K G. Sorption of the antimicrobial ciprofloxacin to aluminum and iron hydrous oxides.[J]. Environmental Science & Technology, 2005, 39(23):9166.

Fekri M, Kasmaei L S. Fluoride pollution in soils and waters of Koohbanan region, southeastern Iran[J]. Arabian Journal of Geosciences, 2013.

Fluoride in Drinking Water: A Review on the Status and Stress Effects[J]. Critical Reviews in Environmental Science & Technology, 2006, 36(6):433–487.

Greenlee L F, Lawler D F, Freeman B D, et al. Reverse osmosis desalination: Water sources, technology, and today's challenges[J]. Water Research, 2009, 43(9):2317–2348.

Haji M, Karuppannan S, Qin D, et al. Potential Human Health Risks Due to Groundwater Fluoride Contamination: A Case Study Using Multi-techniques Approaches (GWQI, FPI, GIS, HHRA) in Bilate River Basin of Southern Main Ethiopian Rift, Ethiopia[J]. 2021.

He Z, Lyu Z, Gu Q, et al. Ceramic-based membranes for water and wastewater treatment[J]. Colloids and Surfaces A: Physicochemical and Engineering Aspects, 578.

Jun K. Case study of air pollution episodes in meuse valley of Belgium, donora of Pennsylvania, and London, U.K.

Li Y, Liang C, Slemenda C W, et al. Effect of long-term exposure to fluoride in drinking water on risks of bone fractures.[J]. Journal of Bone & Mineral Research, 2010, 16.

Millar G J, Couperthwaite S J, Dawes L A, et al. Activated alumina for the removal of fluoride ions from high alkalinity groundwater: New insights from equilibrium and column studies with multicomponent solutions[J]. Separation & Purification Technology, 2017, 187:14–24.

Naba Kr. Mondal and Jayanta Kr. Datta and Arnab Banerjee. Fluoride Pollution and its Removal Techniques[J]. Indian Science Cruiser, 2010, 24(5) : 47–55.

Nouri M, Marjani A, Tajdari M, et al. Preparation of cellulose acetate membrane coated by PVA/Fe3O4 nanocomposite thin film: an in situ procedure[J]. Colloid and Polymer Science, 2018, 296(7).

Ottenhall A, Henschen J, Illergard J, et al. Cellulose-based water purification using paper filters modified with polyelectrolyte multilayers to remove bacteria from water through electrostatic interactions[J]. Environmental Science Water Research & Technology, 2018, 4(12):2070–2079.

Rasool, Atta, Farooqi, et al. A review of global outlook on fluoride contamination in groundwater with prominence on the Pakistan current situation[J]. Environmental Geochemistry And Health, 2018.

Rautenbach R, Kopp W, Opbergen G V, et al. Nitrate reduction of well water by reverse osmosis and electrodialysis – studies on plant performance and costs[J]. Desalination, 1987, 65(none):241–258.

Song H M, Zhu L J, Zeng Z X, et al. High performance forward osmosis cellulose acetate (CA) membrane modified by polyvinyl alcohol and polydopamine[J]. Journal of Polymer Research, 2018, 25(7):159.

Wang A, Zhou K, Liu X, et al. Granular tri-metal oxide adsorbent for fluoride uptake: Adsorption kinetic and equilibrium studies[J]. Journal of Colloid & Interface Science, 2017, 505:947.

Warsinger D M, Tow E W, Nayar K G, et al. Energy efficiency of batch and semi-batch (CCRO) reverse osmosis desalination[J]. Water Research, 2016:272–282.

Wei Gao and Heng Liang and Jun Ma and Mei Han and Zhong-lin Chen and Zheng-shuang Han and Gui-bai Li. Membrane fouling control in ultrafiltration technology for drinking water production: A review[J]. Desalination, 2011.

Yi S, Sun Y, Xin H, et al. Porous nano-cerium oxide wood chip biochar composites for aqueous levofloxacin removal and sorption mechanism insights[J]. Environ Sci Pollut Res Int, 2017, 25(26).

Industrial catalysis and chemical properties research

Advances in Applied Chemistry and Industrial Catalysis – Saikia (Ed.)

Comparison of flocculation performance of inorganic ion modified polyferric sulfate

S. Li* & Y. Kang**
Tianjin University, Tianjin, China

ABSTRACT: The flocculation performance of PFS can be improved by introducing different inorganic ions. Polyferric phosphate sulfate (PFPS), polyferric silicate sulfate (PFSiS), and polyferric aluminum phosphate sulfate (PFAPS) with similar content of total iron element [TFe] were prepared in this work. Their properties and particle size distribution were measured, and their flocculation performance on real oily wastewater and coal-gas washing wastewater were compared with that of commercial polyferric sulfate (PFS). The results show that the particle size distributions of three inorganic ion modified PFSs are different, due to the different polymerization mechanisms. These modified PFSs all have certain advantages over PFS. PFAPS has the strongest electric neutralization ability, and the effect of COD removal is the best in the treatment of two kinds of wastewater; PFSiS has the strongest adsorption and bridging capacity, and the effect of removing turbidity is the best in the treatment of two kinds of wastewater.

1 INTRODUCTION

Finding a suitable way to treat industrial and domestic wastewater innocuously can not only avoid pollution to more water bodies but also reuse water resources (Yao et al. 2020), which plays an indispensable role in the sustainable development of human society (Daniele et al. 2019). Coagulation-flocculation is one of the widely used wastewater treatment technologies (Mohtar et al. 2017). Polymeric ferric sulfate (PFS) is a positively charged inorganic polymer flocculant (Butler et al. 2004). Under acidic conditions, the coordination of Fe^{3+} with H_2O can form Fe-monomers through hydrolysis, and these Fe-monomers bridge into Fe-polymers through hydroxyl groups or other anions (Liang et al. 2009). These Fe-polymers have high positive charges on the surface, which can play a role in the flocculation process through electric neutralization, compression of electric double layer, adsorption bridging, and net capture.

In recent years, inorganic or organic modification of PFS to improve its flocculation performance has attracted much research attention. PFPS prepared by introducing PO_4^{3-} into PFS has higher stability, a higher degree of polymerization (Zeng et al. 2007), and stronger flocculation capacity (Zhu et al. 2012); PFSiS prepared by copolymerization of polysilicate (PSi) and PFS not only has strong adsorption and bridging ability of PSi but also has the ability of PFS to destabilize negatively charged pollutants (Fu et al. 2007; Lu et al. 2013; Moussas & Zouboulis 2008; Song & Ren 2008; Zouboulis & Moussas 2008); Under the condition of controlling the content of Al^{3+}, the copolymerization of Al^{3+} and Fe^{3+} to form a composite flocculant of polyaluminumferric (PAF), which can improve the flocculation efficiency of the flocculant on the premise of avoiding Al residue (Mohamed & Mohamed 2020; Sun et al. 2011a, 2011b; Tong et al. 2010). Although there are many research reports on various modified PFS, few comparative studies on flocculation performance and action mechanisms on different modified PFS have been released.

Corresponding Authors: *825669635@qq.com and **ykang@tju.edu.cn

DOI 10.1201/9781003308553-25

In this work, PFPS, PFSiS, and PFAPS with similar content of a total iron element ([TFe]) were prepared, and their properties and particle size distribution were measured. And their flocculation performance on oily wastewater from Tianjin Petrochemical and coal-gas washing wastewater from Benxi Iron & steel was compared with those of commercial PFS.

2 EXPERIMENTAL

2.1 *Materials*

$FeSO_4 \cdot 7H_2O$ (Tianjin Kermel, China), H_2O_2 (Tianjin Chemical Reagent Supply and Marketing Co., China), H_2SO_4 (Tianjin Damao, China), H_3PO_4 (Tianjin Kermel, China), Na_2SiO_3 (Tianjin Fengchuan, China) and $Al_2(SO_4)_3 \cdot 18H_2O$ (Tianjin Damao, China) used in this study were analytical grade reagents. Commercial PFS was purchased from Energy Chemical, China. The solvents used are deionized water (the conductivity 2.55 μS/cm, Tianjin Yongqingyuan, China).

2.2 *Preparation of flocculant samples*

2.2.1 *Preparation of PFPS*

0.05 mol $FeSO_4 \cdot 7H_2O$ was dissolved in 80 ml deionized water, and then add 0.0075 mol H_2SO_4 into it. In a 30°C water bath, 0.04 mol H_2O_2 was dropped into it under stirring for oxidation. After oxidation for 30 min, H_3PO_4 was added to it according to $PO_4^{3-}/Fe = 0.1$ under stirring conditions. And then it was aged in a 50°C water bath for 2 h to obtain a liquid PFPS sample.

2.2.2 *Preparation of PFSiS*

0.05 mol $Na_2SiO_3 \cdot 7H_2O$ was added into 40ml deionized water and dissolved in a water bath at 50°C to prepare the Na_2SiO_3 solution. Under the condition of stirring in a 40°C water bath, Na_2SiO_3 solution was dropped into 20 ml 30% H_2SO_4 solution. After adjusting the pH value of the prepared solution to 2.9–3.0 with 4 mol/L NaOH solution, it was placed in a 40°C water bath for 1.5 h to obtain PSi. 0.05 mol $FeSO_4 \cdot 7H_2O$ was dissolved in 10ml deionized water and added 0.0075 mol H_2SO_4 in it. In a 30°C water bath, 0.04 mol H_2O_2 was dropped into it under stirring for the oxidation of Fe^{2+}. After oxidation for 30 min, $Fe_2(SO_4)_3$ solution was generated. Under the conditions of a 50°C water bath and stirring, $Fe_2(SO_4)_3$ solution was dropped into PSi and aged for 2.5 h at the same temperature to prepare a liquid PFSiS sample.

2.2.3 *Preparation of PFAPS*

$Fe_2(SO_4)_3$ solution was obtained as the preparation of PFPS. Under the condition of stirring, add H_3PO_4 according to $PO_4^{3-}/Fe = 0.1$. After stirring for 10 min, add $Al_2(SO_4)_3 \cdot 18H_2O$ according to $Al/Fe = 0.15$. After stirring for 10min, it was aged for 2 h in a 50°C water bath to obtain a liquid PFAPS sample.

2.2.4 *Dissolution of commercial PFS*

13.4g commercial PFS with [TFe] = 22.4% was dissolved in 86.6 ml deionized water under stirring to obtain a liquid PFS sample with [TFe] = 3%.

2.3 *Analytical methods on flocculants*

The [Fe^{2+}], [TFe], and basicity of the flocculant samples were determined according to China Standard GB/T14591-2016 *Water treatment chemicals—Poly ferric sulfate*. The particle size distribution of Fe-polymer in liquid flocculant samples was measured by a nanoparticle size analyzer (Zetasizer Nano ZS, Malvern Panalytical Co., Ltd., UK).

2.4 *Actual wastewater*

Oily wastewater (Tianjin Petrochemical, China) and coal-gas washing wastewater (Benxi Iron & steel, China) were used to compare the flocculation effects of PFPS, PFSiS, PFAPS, and commercial PFS. The basic properties of two actual wastewaters are shown in Table 1.

Table 1. Characteristics of actual wastewaters.

Name	Turbidity (NTU)	COD (mg/L)	pH
Oily wastewater	53.77	584	7.8
Coal-gas washing wastewater	463.1	1230	8.6

2.5 *Flocculation experiments*

A flocculation experiment was carried out at 25°C on the coagulation test mixer (MY3000-6M, Wuhan Meiyu Co., Ltd., China). In each experiment, 200 ml actual wastewater in a 300 ml beaker was added liquid flocculant sample with a certain dosage and stirred at 250 rpm for 1 min, then at 35rpm for 15min, finally, the flocculated wastewater stood for a certain time (oily wastewater for 20 min, coal-gas washing wastewater for 2 h), and take the supernatant for determination. Its pH value was measured by a pH meter (PHS-3C, Shanghai Youke Instrument Co., Ltd., China), and its COD was measured by a COD tester (COD-571, Shanghai Yidian Scientific Instrument Co., Ltd., China). Turbidimeter (WGZ-4000, Shanghai Yidian physical optical instrument Co., Ltd., China) was used to measure its turbidity, and a nanoparticle analyzer (Zetasizer Nano ZS, Malvin Co., Ltd., UK) was used to measure its zeta potential.

3 RESULTS AND DISCUSSION

3.1 *Properties of sample*

The properties of PFPS, PFAPS, and PFSiS are shown in Table 2. The [TFe] of the three samples are similar and the [Fe^{2+}] of them are lower than 0.01wt%, indicating that Fe^{2+} was completely oxidized in the preparation of these flocculant samples. The basicity of PFAPS is slightly higher than that of PFPS, indicating that the addition of Al^{3+} promotes the hydrolysis of H_2O and the formation of OH^-.

Table 2. Properties of PFPS, PFAPS and PFSiS.

Name	[Fe^{2+}] (wt.%)	[TFe] (wt.%)	Basicity
PFPS	0.00334	3.11	0.242
PFAPS	0.00921	2.85	0.253
PFSiS	0.00439	2.80	—

3.2 *Particle size distribution of Fe-polymers*

The particle size distribution of three inorganic ions modified PFS is shown in Figure 1. The results show that the size of Fe-polymers in liquid samples of PFPS and PFAPS are mainly distributed around 1–5 nm and 1000 nm, while the Fe-polymers size of PFSiS is mainly distributed around 50–1000 nm. This is due to the copolymerization between Si-polymer in pre-aging PSi and $Fe_2(SO_4)_3$ to form Fe-polymer with a particle size of 50–1000 nm. The proportion of Fe-polymer with a particle size of 1–5 nm in PFPS is higher than that in PFAPS, while the proportion of Fe-polymer with a

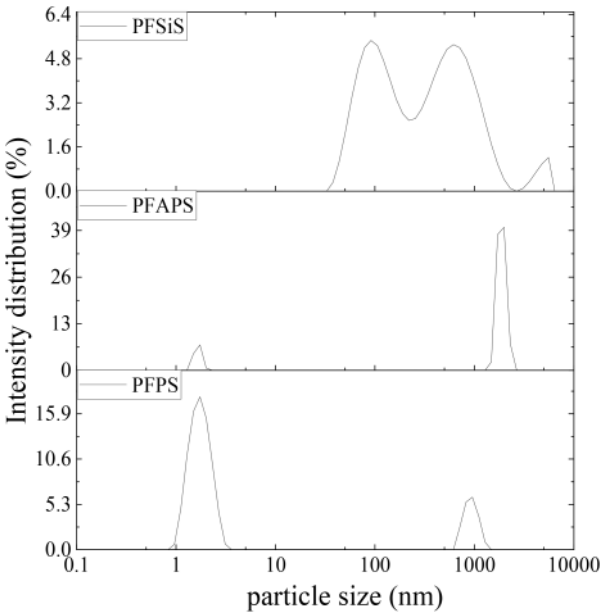

Figure 1. Particle size distribution of PFPS, PFAPS, and PFSiS.

particle size of 1000 nm is lower than that in PFAPS. This is because the added Al^{3+} can compete with Fe^{3+} for PO_4^{3-}, thus weakening the substitution effect of PO_4^{3-} on OH^- in the process of Fe^{3+} polymerization, which affects the stability of the flocculant sample, making the polymerization process of PFAPS easier to develop towards the formation of uncharged precipitation with large particle size.

3.3 *Flocculation performance on actual wastewater*

3.3.1 *Oily wastewater*

The turbidity, COD, zeta potential, and pH value of the supernatant of treated oily wastewater are shown in Figure 2. As shown in Figure 2(c), the electric neutralization capacity of PFAPS is significantly better than that of other flocculants for oily wastewater flocculation, that of commercial PFS is similar to that of PFPS, while PFSiS is the worst. This is because the addition of Al^{3+} increases the positively charged metal polymers in PFAPS, and then improves its electric neutralization ability. Although the entry of PO_4^{3-} into PFPS can reduce the electric neutralization ability of a single Fe-polymer, the promotion of PO_4^{3-} to polymerization will increase the number of Fe-polymers in PFPS and make its electric neutralization close to PFS. The combination of negatively charged PSi and $Fe_2(SO_4)_3$ makes the neutralization ability of PFSiS inferior to other flocculants. As shown in Figure 2(a), the removal effect of PFPS, PFAPS, and PFSiS on the turbidity of oily wastewater is better than that of commercial PFS. Due to the best electric neutralization capacity, the supernatant turbidity of oily wastewater treated by PFAPS reaches the lowest value earlier than other flocculants., when the dosage of PFPS, PFAPS or commercial PFS added is large, the supernatant turbidity increases slightly. This is because some pollutants adsorb excessive positively charged Fe-polymers, which make them exist stably in wastewater. While, due to the excellent adsorption bridging capacity and poor electric neutralization capacity of PFSiS, it has the best turbidity removal of oily wastewater. As shown in Figure 2(b), the COD removal effect of PFPS, PFAPS, and PFSiS on oily wastewater is better than that of commercial PFS, indicating that the active components in the three inorganic ion modified flocculants are higher than that of commercial PFS. While the

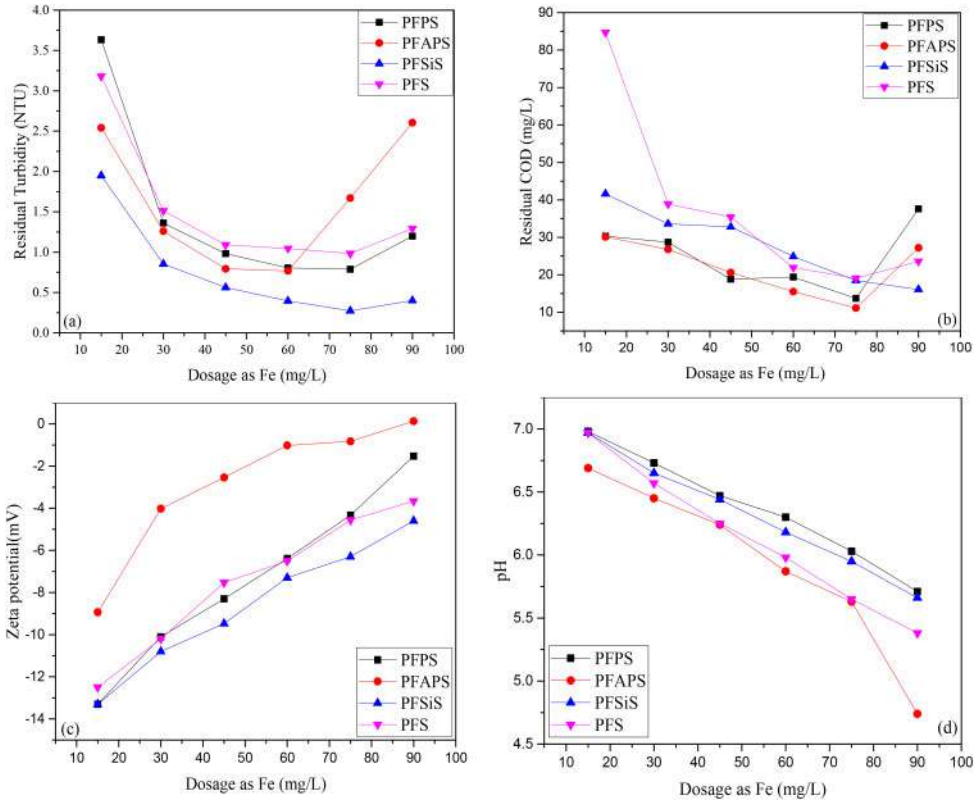

Figure 2. Turbidity (a), COD (b), zeta potential (c), and pH (d) of the supernatant of flocculated oily wastewater.

COD removal effect of PFPS and PFAPS is similar and better than that of PFSiS. As shown in Figure 2(d), the pH value of the supernatant decreases gradually with the increase of flocculant dosage, especially does significantly when the dosage of PFAPS is large. This is because the addition of Al^{3+} increases the concentration of metal cations in PFAPS and improves its hydrolysis ability in the water.

3.3.2 *Coal-gas washing wastewater*

The turbidity, COD, zeta potential, and pH value of the supernatant of treated coal-gas washing wastewater are shown in Figure 3. As shown in Figure 3(c), the neutralization capacity of PFAPS is still significantly better than that of other flocculants for coal-gas washing wastewater flocculation. The neutralization capacity of commercial PFS is better than that of PFPS and PFSiS, while the neutralization capacity of PFPS and PFSiS is similar. This is because the coal-gas washing wastewater with high turbidity contains a large amount of negatively charged solid particles, which will absorb a large amount of 1–5 nm positivity charged Fe-polymers in PFPS, weaken its electric neutralization ability, and make its electric neutralization ability of coal-gas washing wastewater similar to that of PFSiS. As shown in Figure 3(a), the order of the turbidity removal effect of coal-gas washing wastewater from good to bad is PFPS, commercial PFS, PFSiS, and PFAPS. This is because the coal-gas washing wastewater has high turbidity and contains more solid suspensions. And PFSiS has strong adsorption and bridging ability, which has an obvious effect on the turbidity removal of the wastewater. Although PFAPS has a strong electric neutralization ability, Fe^{3+} and

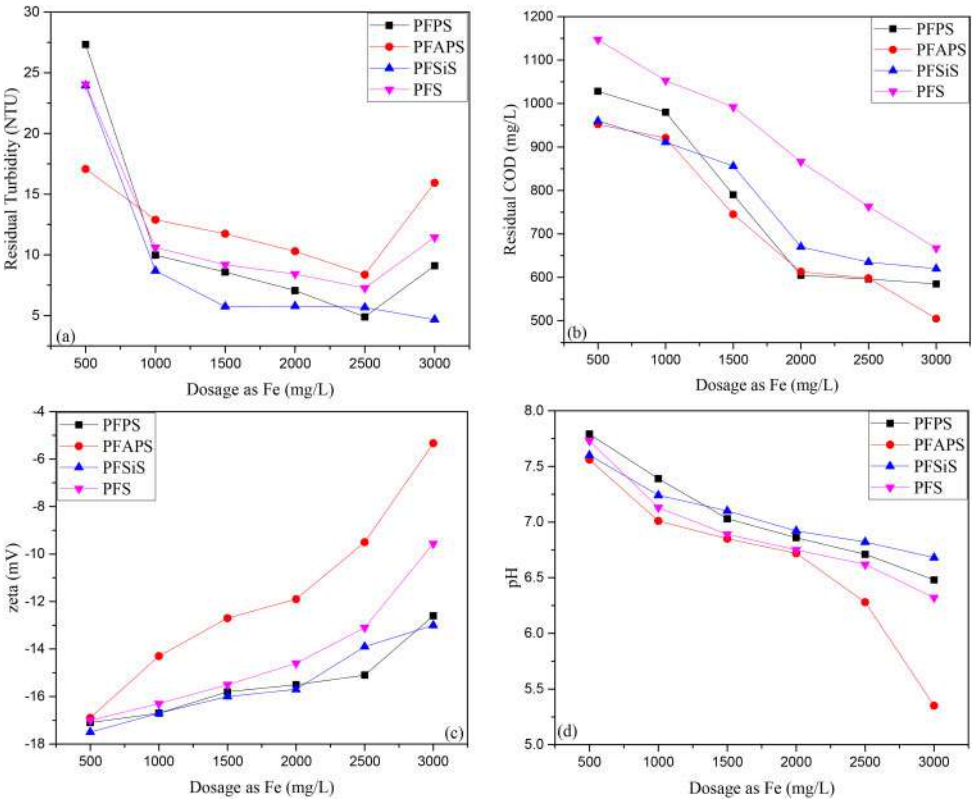

Figure 3. Turbidity (a), COD (b), zeta potential (c), and pH (d) of the supernatant of flocculated coal-gas washing wastewater.

Al^{3+} can form many flocs in the wastewater, which is adverse to the removal of turbidity. Except for PFSiS, the supernatant turbidity of coal-gas washing wastewater treated by other flocculants also increases when the dosage of flocculant is large. Figure 3(b) shows that the COD removal effect of PFPS, PFAPS, and PFSiS on the coal-gas washing wastewater is better than that of commercial PFS, while the COD removal effect of PFPS and PFAPS is similar and better than that of PFSiS. As shown in Figure 3(d), the pH value decreases gradually with the increase of flocculant dosage, and the supernatant pH value of the wastewater treated by PFAPS decreases significantly when the flocculant dosage is large.

4 CONCLUSION

The flocculation effects of PFPS, PFAPS, PFSiS, and commercial PFS on real oily wastewater and coal-gas washing wastewater were compared and studied in this work, which compares the flocculation mechanism of three kinds of inorganic ion modification PFS and provides guidance for its practical application. The results show that the size distributions of Fe-polymer in three ion modified PFS solutions are different, due to the different polymerization mechanisms. These modified PFSs all have certain advantages over commercial PFS. PFAPS has the strongest electric neutralization ability, and the effect of COD removal is the best in the treatment of two kinds of wastewater; PFSiS has the strongest adsorption and bridging capacity, and the effect of removing turbidity is the best in the treatment of two kinds of wastewater.

REFERENCES

Butler A D, Fan M, Brown R C, et al. (2004) Absorption of dilute SO_2 gas stream with conversion to polymeric ferric sulfate for use in water treatment. Chemical Engineering Journal, 98(3), 265–273.

Daniele M, Giulia E, Enrico Antonio C, et al. (2019) A procedure for designing natural water retention measures in new development areas under hydraulic-hydrologic invariance constraints. Hydrology Research, 50(5), 1293–1308.

Fu Y., Yu S.L., Yu Y.Z., et al. (2007) Reaction mode between Si and Fe and evaluation of optimal species in poly-silicic-ferric coagulant, Journal of Environmental Engineering. 19, 678–688.

Liang Z, Wang Y, Zhou Y, et al. (2009) Hydrolysis and coagulation behavior of polyferric sulfate and ferric sulfate. Water Science & Technology, 59(6), 1129–1135.

Lu D., Zhang Y., J. T. Zhou. (2013) Properties and Coagulation Behaviour of Polyferric Silicate Sulphate by Different Preparation. Asian Journal of Chemistry, 25(15), 8383–8387.

Mohamed F. M., Mohamed F. M. (2020) The effectiveness of activated silica derived from rice husk in coagulation process compared with inorganic coagulants for wastewater treatment. The Egyptian Journal of Aquatic Research. 46(2), 131–136.

Mohtar S S, Zulaikha T, Noor A M, et al. (2017) Optimization of coag-flocculation processes of a newly synthesized quaternized oil palm empty fruit bunch cellulose by response surface methodology toward drinking water treatment process application. Clean Technologies & Environmental Policy, 19(1), 1–14.

Moussas P A, Zouboulis A I. (2008) A study on the properties and coagulation behaviour of modified inorganic polymeric coagulant—Polyferric silicate sulphate (PFSiS). Separation & Purification Technology, 63(2), 475–483.

Song Z, Ren N. (2008) Properties and coagulation mechanisms of polyferric silicate sulfate with high concentration. Journal of Environmental Sciences. 2, 129–134.

Sun C, Yue Q, Gao B, et al. (2011a) Effect of pH and shear force on flocs characteristics for humic acid removal using polyferric aluminum chloride-organic polymer dual-coagulants. Desalination. 281(20), 243–247.

Sun T, Sun C, Zhu G, et al. (2011b) Preparation and coagulation performance of poly-ferric- aluminum-silicate-sulfate from fly ash. Desalination. 268(1-3), 270–275.

Tong S, Liu L L, Wan L L, et al. (2010) Effect of silicon dose on preparation and coagulation performance of poly-ferric-aluminum-silicate-sulfate from oil shale ash. Chemical Engineering Journal. 163(1–2), 48–54.

Yao J, Wang G, Xue B, et al. (2020) Identification of regional water security issues in China, using a novel water security comprehensive evaluation model. Hydrology Research, 51(5), 854–866.

Zeng K, XU XG, Wei P, Huang SF. (2007) Formation Kinetics and Hydrolysis Species of Polyferric Phosphatic Sulfate and Polyferric Sulfate. Hydrometallurgy of China, 26(2) 96–98.

Zhu G, Zheng H, Chen W, et al. (2012) Preparation of a composite coagulant: Polymeric aluminum ferric sulfate (PAFS) for wastewater treatment. Desalination, 285 315–323.

Zouboulis A I, Moussas P A. (2008) Polyferric silicate sulphate (PFSiS): Preparation, characterisation and coagulation behaviour. Desalination, 224, 307–316.

Advances in Applied Chemistry and Industrial Catalysis – Saikia (Ed.)

Effect of Pb^{2+} in pulp on the separation of lead-zinc sulfide minerals

Hongxiang Xu*
Postdoctoral Research Station, China Tin Group Co., Ltd., Guangxi, P.R. China
School of Chemical & Environmental Engineering, China University of Mining and Technology, Beijing, P.R. China

Zengrui Pang
School of Chemical & Environmental Engineering, China University of Mining and Technology, Beijing, P.R. China

Quan Li & Mingzhen Hu
Postdoctoral Research Station, China Tin Group Co., Ltd., Guangxi, P.R. China

Jiushuai Deng & Bozeng Wu
School of Chemical & Environmental Engineering, China University of Mining and Technology, Beijing, P.R. China

Runzhi Huang
Postdoctoral Research Station, China Tin Group Co., Ltd., Guangxi, P.R. China

Shenzhou Li
School of Chemical & Environmental Engineering, China University of Mining and Technology (Beijing), Beijing, P.R. China

ABSTRACT: The influence mechanism of Pb^{2+} on the separation of lead-zinc sulfide minerals was studied by micro-flotation test and XPS analysis. The micro-flotation test shows that when butyl xanthate was used as a collector, Pb^{2+} could significantly improve the recovery of sphalerite in a certain concentration range, which was also confirmed by XPS analysis. The influence of Pb^{2+} on the flotation separation of lead-zinc sulfide ore can be weakened by adjusting the pH in the pulp or by precipitation.

1 INTRODUCTION

Lead and zinc minerals play an important leading role in China's non-ferrous metal industry, but their flotation separation process is often affected by the presence of ions in the pulp. There may be some unavoidable ions introduced by mineral self-dissolution and fluid inclusion release in flotation pulp of sulfide ore[1]. These ions will inevitably have a significant effect on the separation of lead-zinc sulfide minerals. Pb^{2+} is an unavoidable ion introduced into the flotation pulp due to the self-dissolution of galena, which has a certain influence on the separation of lead-zinc sulfide ore. Therefore, the focus of this study is the separation and mechanism analysis of Pb^{2+} on lead-zinc sulfide ore.

*Corresponding Author: 201535@cumtb.edu.cn

DOI 10.1201/9781003308553-26

2 MATERIALS AND METHODS

2.1 *Samples and reagents*

The samples were ground and screened to obtain 38–74μm grain size products as flotation feed. XRD results (Figure 1) showed that galena and sphalerite had high purity and met the requirements of the test.

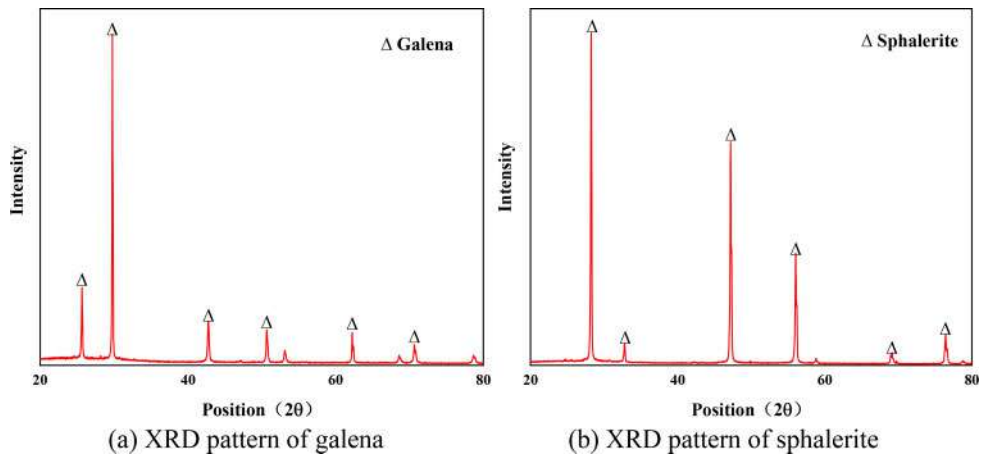

Figure 1. XRD patterns of test ore samples.

The test reagent details are shown in Table 1. Butyl xanthate was used as collector, sodium cyanide as depressor, and lead nitrate was used to provide Pb^{2+}. Acid and sodium hydroxide was used as pH regulator, terpineol oil as foaming agent.

Table 1. Test reagents.

Drug name	Reagent grade
$C_4H_9OCSSNa$	technical grade
NaCN	technical grade
$Pb(NO_3)_2$	analytically pure
HCl	analytically pure
NaOH	analytically pure

2.2 *Micro-flotation test*

A single mineral flotation test was carried out by the XFG flotation machine (Rock Equipment Factory, China) at room temperature. The single mineral sample (2.0g) was added to a 40ml flotation cell containing 35ml deionized water. The deionized water was pre-adjusted to the pH of the test, and the main shaft speed of the flotation machine was fixed at 1608r/min. Then the required concentration of lead nitrate, sodium cyanide, and butyl xanthate was added to the pulp and reacted for 3min respectively, then the recovery of a single mineral was calculated after the foam and the products in the tank were filtered, dried, and weighed after 4min manual scraping[2].

2.3 *XPS analysis*

The XPS analysis was detected with the Thermo Scientific K-Alpha Instrument (Thermo Fisher, USA) using Al Kα radiation (1486.6eV). The vacuum degree of the analysis room is about 3×10^{-7}mbar, and the sputtering voltage is 12kV and 6mA. All components present in samples were determined by the scanning method, and then high-resolution XPS spectra of sphalerite components were collected. The required spectral and atomic concentration information was calculated and analyzed using Advantage spectroscopy software[3].

3 TEST RESULTS AND ANALYSIS

3.1 *Micro-flotation test*

The influence of Pb^{2+} content in flotation pulp on the separation of lead-zinc sulfide minerals is shown in Figure 2. In the flotation process, the dosage of butyl xanthate and sodium cyanide was 10 and 24.5mg/L respectively with the pH value of 8[4].

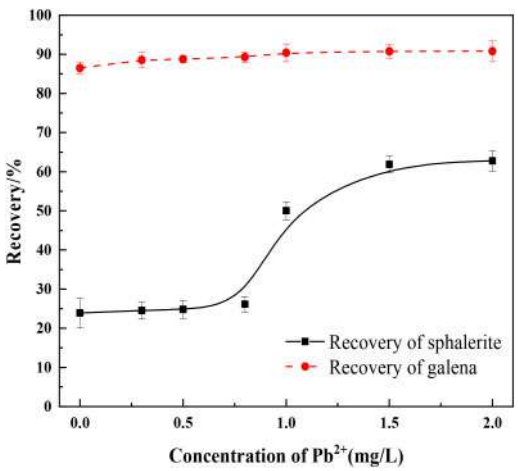

Figure 2. Results of the micro-flotation test.

Figure 2 shows that the content of Pb^{2+} has a little effect on the recovery rate of galena. Whereas the recovery rate of sphalerite increased significantly. When the Pb^{2+} content in the pulp is 2mg/L, the sphalerite recovery tends to be stable, reaching the maximum value of 62.78%, which is about 30% higher than that in the blank system. Therefore, when there is a certain amount of Pb^{2+} in the flotation pulp, it will have a great influence on the separation of lead-zinc sulfide minerals.

3.2 *XPS results analysis*

According to the above test results, Pb^{2+} may be on the surface of sphalerite through chemical adsorption, to increase the active sites on the surface of sphalerite. Therefore, XPS detection was used to further confirm the activation mechanism of Pb^{2+} and sphalerite surface. Table 2 lists the atomic concentrations of untreated and treated sphalerite samples with collectors, depressors, and added ions.

After butyl xanthate reacted with sphalerite, the carbon atom concentration increased by 4.27% compared with that of sphalerite without additives, indicating that butyl xanthate adsorbed on the surface of sphalerite. When the sphalerite is treated with Pb^{2+}, the concentration of carbon atoms on the surface of sphalerite increases by 1.87% compared with that treated with collector, indicating

Table 2. Atomic concentrations of sphalerite samples treated with the following flotation reagents: (a) untreated, (b) Butyl xanthate and NaCN, (c) Pb(II), Butyl xanthate, and NaCN.

	Atomic concentration/%			
Samples	C 1s	O 1s	S 2p	Zn 2p
a	42.26	12.92	21.59	23.23
b	46.53	13.07	19.53	20.87
c	48.4	12.52	19.18	19.29

that butyl xanthate is more easily adsorbed on the surface of sphalerite treated with Pb^{2+}. To obtain more details about the adsorption of butyl xanthate on the sphalerite surface in the presence of Pb^{2+}, Zn 2p XPS high-resolution spectra of the sphalerite sample were plotted, as shown in Figure 3.

The Zn 2p XPS spectral fitting results of sphalerite samples treated with Pb^{2+}, butyl xanthate, and sodium cyanide are shown in Figure 3. The Zn 2P 3/2 and 2P 1/2 spectra can be adjusted appropriately by two components and corresponding satellite characteristics. Compared with bare sphalerite surface (a), the binding energies of Zn 2p 3/2 and 1/2 peaks move from 1022.05eV and 1045.05eV to 1022.55 eV and 1045.51eV, respectively, with positive shifts of 0.5eV and 0.46eV, respectively, on the mineral surface treated with chemical agent (b). The zinc sites on the sphalerite surface can interact with butyl xanthate. After treating sphalerite with Pb(II), Zn 2p 3/2 and Zn 2p 1/2 XPS peaks were positively offset by 0.2eV and 0.25eV, respectively, compared with (b), indicating that butyl xanthate is more easily adsorbed on the surface of Sphalerite treated with Pb(II). This is also consistent with the research results of Sarvaramini et al.[5].

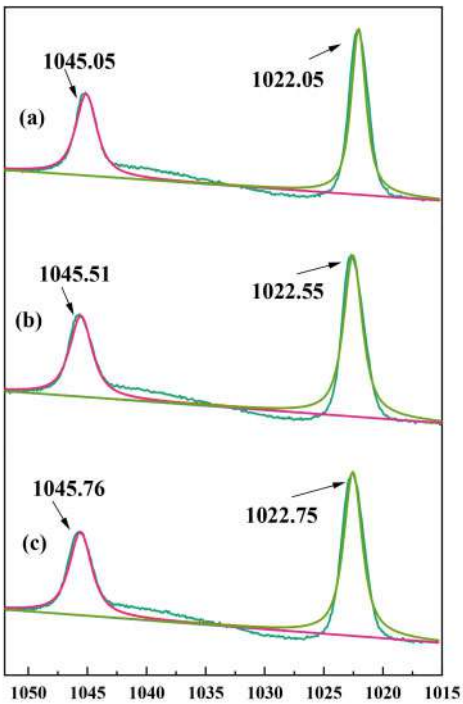

(a) untreated, (b) Butyl xanthate and NaCN, (c) Pb(II), Butyl xanthate and NaCN.

Figure 3. XPS high-resolution spectra of Zn 2p doublet for sphalerite samples.

4 CONCLUSION

The adsorption mechanism of Pb^{2+} on the sphalerite surface and its influence on the flotability of sphalerite were studied through micro-flotation test and XPS analysis. The test results show that:

(1) When there is a certain content of Pb^{2+} in the pulp, the sphalerite can be activated to a certain extent, and the separation of lead-zinc sulfide minerals is affected to a certain extent. The activation mechanism is further explored by XPS.
(2) XPS results show that the presence of Pb^{2+} leads to an increase in the atomic content of carbon and a decrease in the atomic content of zinc on the mineral surface, indicating that a small part of Pb^{2+} replaces Zn^{2+} in the pulp. The migration of XPS peak binding energy further firmed that butyl xanthate is more easily adsorbed on the surface of Sphalerite treated by Pb(II).
(3) The influence of Pb^{2+} on the flotation separation of lead-zinc sulfide ore can be weakened by adjusting the pH of the pulp or eliminating the Pb^{2+} through the precipitation method. The flotation separation of lead-zinc sulfide ore by activated ions in weakened pulp is of high economic value in practical application.

ACKNOWLEDGMENTS

This work was financially supported by the China Postdoctoral Science Foundation (2020M673551XB).

REFERENCES

Deng J, Bai Z, Zhao B, et al. Opportunities and challenges in microwave absorption of nickel-carbon composites[J]. Physical Chemistry Chemical Physics, 2021.

Deng Jiu-shuai, Mao Ying-bo, Wen Shu-ming, et al. New influence factor inducing difficulty in selective flotation separation of Cu-Zn mixed sulfide minerals[J]. International Journal of Minerals, Metallurgy, and Materials, 2015, 22(2): 111–115.

Guanghua Ai, Kaihua Huang, Cheng Liu, Siyuan Yang. Exploration of amino trimethylene phosphonic acid to eliminate the adverse effect of seawater in molybdenite flotation. International Journal of Mining Science and Technology, 2021.

Liang Y, Mao M, Song T, et al. Application of a New Depressant in the Flotation Separation of a Lead-zinc-sulfur Bulk Concentrate[J]. Conservation and Utilization of Mineral Resources, 2020, 40(5): 109–115.

Popov S.R, Vučinić D.R., Kačanik J.V. Floatability and adsorption of ethyl xanthate on sphalerite in an alkaline medium in the presence of dissolved lead ions[J]. International Journal of Mineral Processing,1989, 27(3–4).

Advances in Applied Chemistry and Industrial Catalysis – Saikia (Ed.)

Effect of storage time on the change of physicochemical properties of stored sludge from a sewage plant

Diannan Huang, Rui Li, Li Zhang*, Rubing Bai, Xinyuan Hou & Jinxiang Fu
Municipal and Environmental Engineering Institute, Shenyang Jianzhu University, Shenyang, Liaoning, China

ABSTRACT: With the accelerated urbanization process, the accumulation of stored sludge in wastewater treatment plants is increasing year by year, and the stored sludge is likely to pose a potential and long-term threat to the surrounding environment. To identify the pollution characteristics of stored sludge sources and to analyze the changes in the physicochemical properties of stored sludge at different storage times, this study sampled sludge stored in a sludge storage site in north China for nearly ten years and analyzed its moisture content, pH value, TOC, TN, TP, TK. The results showed that all the indicators showed different downward trends with the increase in storage time. The moisture content decreased by 14.4%. The pH value decreased from 7.3 to 6.9, and the overall sludge was weakly alkaline. The TOC content decreased significantly, from 286.4 g/kg to 171.3 g/kg. The TN, TP, and TK content decreased in the range of 50.1～20.3 g/kg, 29.1～25.3 g/kg, and 8.4～4.9 g/kg.

1 INTRODUCTION

Storage sludge usually refers to the sludge whose moisture content is about 80% after mechanical dehydration of the sewage treatment plant, which has not yet reached the access requirements of 60% specified in the landfill and is directly stored in the natural environment by artificial ditch or storehouse. This kind of sludge is usually not treated stably and harmlessly. Long-term stacking in the natural environment will affect the surrounding water, soil, and air environment in various ways such as rainfall-runoff, groundwater seepage, and atmospheric dispersion, and thus threaten human health. However, the storage sludge in the environment is bound to change its physical and chemical properties with the extended storage time through physical, chemical, and biological reactions. Chen Yun et al. studied the spatial and vertical variation of moisture content and organic matter content of the sludge in a landfill site in Jiangsu Province (Chen et al. 2020). Kaixi et al. studied the geotechnical characteristics of sludge density, moisture content, and organic matter content in 5 landfill sites, including Shanghai and Guangzhou (An et al. 2021). Wang Selan studied the change of sludge moisture content and organic matter with landfill depth in the Lao Gang comprehensive landfill area (Wang 2018). O'Kelly has studied the geotechnical characteristics of landfill sludge engineering from the perspective of physics and microorganisms (Kelly & Brendan 2006). But now, there is still a lack of identification of pollution characteristics of the sludge stored in the wastewater treatment plant, which has restricted the reasonable formulation of sludge treatment and disposal technology to a certain extent.

In this study, the sludge stored in a sludge storage site in northern China for nearly ten years was taken as the research object. Due to the different storage times of sludge in different sludge pits, the moisture content, pH value, TOC, total alkalinity, TN, TP, and TK of sludge in different sludge pits were analyzed to reveal the influence of storage time on the changes of the physicochemical properties of sludge.

*Corresponding Author: 77377200@qq.com

DOI 10.1201/9781003308553-27

2 MATERIALS AND METHODS

2.1 *Materials*

Sludge: The sludge is collected from a storage sludge landfill in the north of China, and is sampled based on the landfill time order. All samples were stored in sealed bags away from light. The moisture content and TOC content of the sludge were measured immediately after the sample was retrieved. The rest of the samples were dried naturally in a dark place to remove impurities, stones, and other wastes, ground in a mortar, and sieved, then stored in a 4°C refrigerator for further use, and the pH, TN, TP, and TK measurements were completed as soon as possible.

Main chemical reagents: sodium hydroxide, concentrated sulfuric acid, concentrated nitric acid, 30% hydrogen peroxide, ammonium molybdate, potassium persulfate, anhydrous ethanol, ascorbic acid, potassium antimony tartrate, etc.

2.2 *Chemical analysis*

Sludge TN: Take 0.01g sludge sample in 250 ml conical flask, add 100ml distilled water, 30ml alkaline potassium persulfate, heat to 120°C in a medical portable sterilizer, maintain for 1h and cool to room temperature, and add with 10 mL of 10% HCl to measure the content of TN on the ultraviolet spectrophotometer. Sludge TP: Take 0.25 g of sludge sample and put it in the crucible. The temperature of the muffle furnace is raised to 400°C, suspended for 15 minutes, and then heated to 650°C for 15 minutes. After cooling, add 10 mL of 3mol / L HCl and dilute the volume to 50 ml. Take 5 ml solution and add indicator and molybdenum antimony anti-coloring agent, and measure the content of TP on the ultraviolet spectrophotometer. Sludge TK: 0.2 g of sludge sample was taken, digested with nitric acid, hydrogen peroxide, and hydrochloric acid, filtered, and fixed to 50 ml and the TK content was measured on a flame atomic absorption spectrophotometer. Sludge moisture content was adopted by the weight method, the pH value was adopted by the electrode method, and the content of TOC has adopted by the burning method (CJ/T221 2005).

3 TEST RESULTS AND DISCUSSIONS

3.1 *Analysis of the effect of storage time on sludge moisture content*

The variation of sludge moisture content with storage time is shown in Figure 1. The original storage sludge has a relatively high moisture content of 80.8%. After 7 years of storage, the sludge moisture content drops to 66.4%, a decrease of 14.4%. It can be seen from the trend line of the moisture content of the stored sludge that the moisture content of the stored sludge gradually decreases with the increase of the storage time, but the decline is not obvious, and the moisture content of sludge stored for about ten years still maintains a high level.

This is because the stored sludge is placed in the open air for a long time, and the landfill time is longer. During this process, it is affected by meteorological factors such as rain, snow, sunshine, and natural evaporation. At the same time, the bio-heat generated by the growth and reproduction of microorganisms in this process will also reduce the water content. The change in the moisture content of sludge is the result of the combined effects of natural precipitation, evaporation, and microorganisms (Liu et al. 2018). Therefore, the moisture content of the stored sludge decreases slightly.

3.2 *Analysis of the effect of storage time on pH value and total alkalinity of sludge*

The variation of sludge pH value and total alkalinity with storage time is shown in Figure 2. The initial pH value of sludge is 7.3. With the increase in landfill time, the pH value of stored sludge gradually decreases. After 6 years of storage, the pH value of sludge remains at around 6.9. The reason for this phenomenon may be that microorganisms are constantly decomposing organic

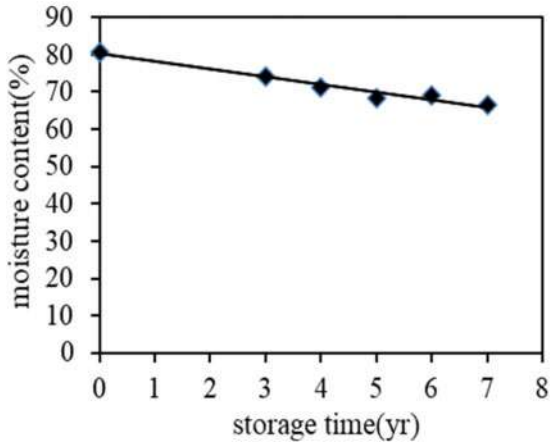

Figure 1. Change of sludge water moisture content with storage time.

matters in sludge and generating a large number of organic acids through metabolic reactions, which leads to the decrease of the pH value of sludge. With the extension of storage time, the total pH of the sludge is weakly alkaline, and the total alkalinity of the sludge reaches the lowest value of 8.3 in the sixth year of storage, and then gradually increases to 8.86. The reason for this phenomenon may be that with the extension of the landfill time, the sludge in the landfill pit occurs a methanogenic reaction under anaerobic conditions. Organic acids are constantly being consumed, causing the pH of the sludge to rise. Methanogenic bacteria synthesize methane by using the organic acids generated in the early stage, which leads to the continuous consumption of organic acids in the sludge, increasing the pH value of the sludge. In addition, the addition of bleaching powder can effectively reduce the stench odor produced by the sludge in the process of the landfill, but the bleaching powder will produce a large amount of OH^- after hydrolysis with water, resulting in the overall weak alkalinity of sludge in landfill pit (Huang et al. 2017). With the increase in landfill time, the sludge in the landfill pit gradually tends to be stable. Some studies have pointed out that when the sludge pile reaches the maturity level, the pH value in the sludge remains in the neutral or alkaline range (Ridha et al. 2009).

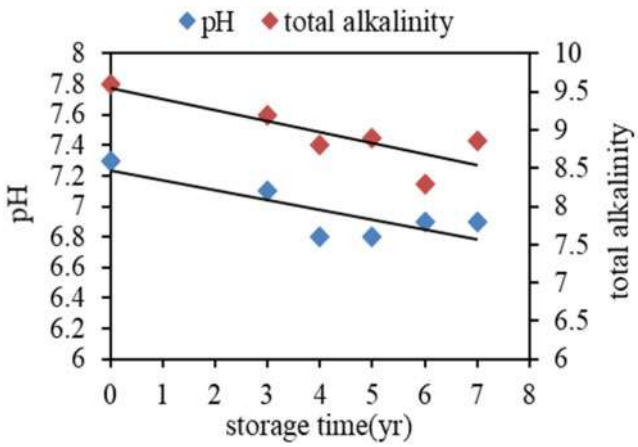

Figure 2. Change of sludge pH value and total alkalinity with storage time.

3.3 *Analysis of the effect of storage time on sludge TOC*

The variation of sludge TOC content with storage time is shown in Figure 3. According to the diagram, the TOC content of the stored sludge tends to decrease at different rates with increasing storage time, with the TOC of the sludge decreasing rapidly from 286.4 g/kg in the early stages of the landfill to 210.5 g/kg in the third year, and decreasing slowly from 210.5 g/kg to 171.3 g/kg in the later stages of landfill. Because the stored sludge contains a large number of microorganisms, the nutrients needed by the microorganisms for life activities are provided by the organic carbon in the sludge. The microorganisms decompose the organic carbon in the sludge so that the carbon source can be released, at the same time, the organic carbon is also needed for aerobic and anaerobic biological reactions in the sludge, so the TOC content in the sludge is decreasing year by year. As the storage time increases, the TOC in the sludge gradually decreases, the number of microorganisms also decreases, and the degradation of organic carbon by microorganisms decreases, so the rate of decline of organic carbon gradually slows down. In addition, some scholars have pointed out that the organic matter content of sludge is closely related to the degradation degree of sludge. The longer the sludge landfill time, the higher the degradation degree and the lower the organic matter content (Feng et al. 2013).

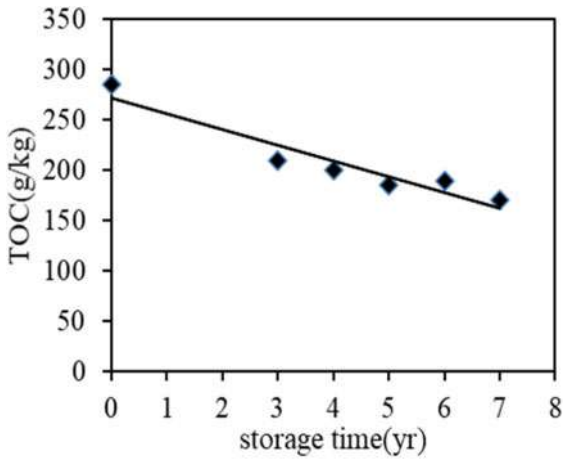

Figure 3. Change of sludge TOC content with storage time.

3.4 *Analysis of the effect of storage time on sludge TN, TP, and TK*

The variation of sludge TN, TP, and TK content with storage time is shown in Figures 4 and 5. During the storage period of nearly ten years, the TN content of sludge varied from 50.1 to 20.3 g/kg, TP content varied from 29.1 to 25.3 g/kg and TK content varied from 8.4 to 4.9 g/kg. The results of the second Chinese soil census show that the average content of TN in Chinese soil is 2.9 g/kg, the average content of TK in the soil is 10 g/kg, and the average content of TP in the soil is 0.17 g/kg∼1.1 g/kg, which is less than that of nitrogen and potassium. Compared with the normal soil, the content of TK in the stored sludge is lower, which may be caused by the lower TK content of the sludge at the initial stage of landfilling. The content of TN and TP is much higher than the average content of the normal soil. The stored sludge contains more nitrogen and phosphorus, it can be used as a good repair material for wasteland, sandy land, garden land, and other soils.

With the increase in storage time, the contents of TN, TP, and TK in sludge all showed a decreasing trend in different degrees. TP content was less affected by storage time, indicating that the presence of phosphorus in the environment was more stable, while TN and TK were more significantly affected by storage time. The loss of nitrogen in sludge may be due to the continuous decomposition

of organic nitrogen by microorganisms in the initial stage of landfilling. At the same time, with the extension of storage time, nitrate-nitrogen continues to undergo denitrification under hypoxic conditions, which further leads to nitrogen loss. The continuous decrease of TK content may be because the potassium in the stored sludge is relatively active, and it is easy to gradually dissolve in rainwater with the rainfall process, and the potassium in sludge is easy to change into water-soluble available potassium with the increase of storage time (Wang et al. 2016), so the content of potassium in storage sludge decreased obviously.

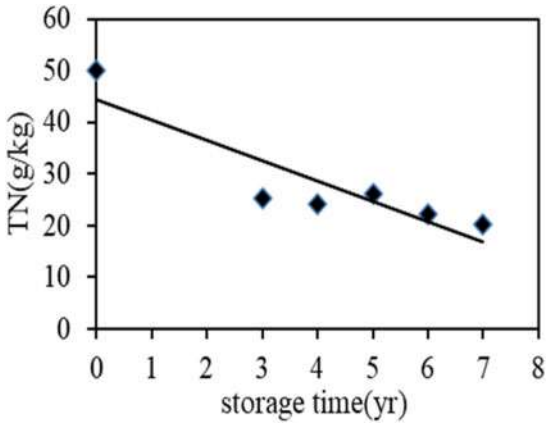

Figure 4. Change of sludge TN with storage time.

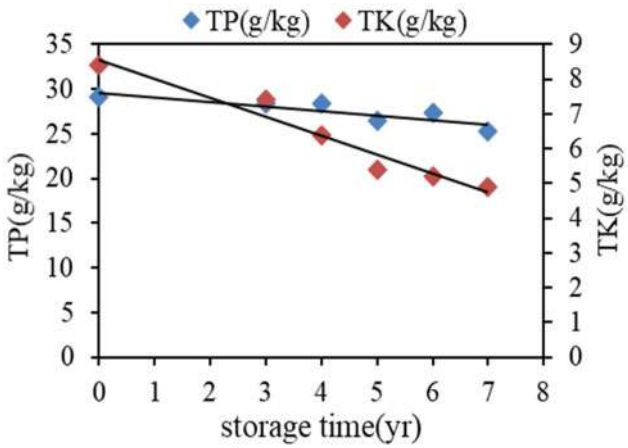

Figure 5. Change of sludge TP and TK with storage time.

4 CONCLUSION

In this paper, the effect of storage time on the change of physicochemical properties of stored sludge from sewage plants was analyzed. The main conclusions can be summarized as follows:

(1) With the increase of storage time, the moisture content of sludge does not change significantly, the pH value decreases from 7.3 to 6.9 and then remains stable, the total alkalinity of sludge

decreases significantly, but the whole sludge is weakly alkaline and the total alkalinity remains above 8.

(2) With the increase in storage time, the TOC content decreased significantly, and the decreasing speed changed from fast to slow, from 210.5 g/kg to 171.3 g/kg.

(3) The stored sludge is rich in nitrogen, phosphorus, and potassium, and the content of TN and TP is much higher than the average value of normal soil, which has a high potential for resource utilization. With the increase of storage time, TN decreased from 50.1 g/kg to 20.3 g/kg, TP from 29.1 g/kg to 25.3 g/kg, and TK from 8.4 g/kg to 4.9 g/kg. Nitrogen and potassium in sludge are easily lost in the environment, while phosphorus is relatively stable in the environment.

In terms of future work, indexes of heavy metals and microorganisms in stored sludge should be carried out to enhance the completeness of research results.

ACKNOWLEDGMENTS

This work was financially supported by the General project of scientific research plan of Liaoning Provincial Department of Education (no: LJKZ0601).

REFERENCES

An K. X., Xu W. J., Lan J. W., Zhang M. L., Tang J., Zhan L.T., Ke H., Chen Y.M. (2021). Study on geotechnical characteristics of landfill sludge in China. J. Environmental sanitation engineering. 29 (04), 78–85.

Chen Y., Wang L., Zheng Z. J., Wu J. J., Xie H. J. (2020). Analysis and evaluation of specific soil in sludge storage of a landfill site in Jiangsu province. J. Environmental sanitation engineering. 28 (01), 43–49.

Feng Y., Luo X. Y., Lin W. A., Zhan L.T., Ke H., Chen Y. M. (2013). Study on engineering characteristics test of sludge in disposal depot. J. Rock and soil mechanics. 34 (01), 115–122.

Huang D. N., Tan J., Li W., Zhao Y. C., Fu J. X., Yu P. F., Zhang H. K. (2017). Property analysis of stored sludge in a sludge dumpsite in Shenyang. J. Journal of Shenyang Jian zhu University. 33 (02), 371–377.

Kelly, O. & Brendan, C. (2006). Geotechnical properties of municipal sewage sludge. J. Geotechnical and geological engineering. 24 (4), 833–850.

Liu T. T., Cui C. W., He J. G., Tang J. (2018). Composition characteristics and evolution of stored sludge in Hun he River Basin. J. Environmental science. 39 (01), 276–283.

Ridha H., Salma H., Imen T. S. (2009). Evolution of the fatty fraction during co-composting of olive oil industry wastes with animal manure: Maturity assessment of the end product. J. Chemosphere. 75 (10).

Test method for sludge of the municipal sewage treatment plant. (2005). S. CJ/T 221-2005.

Wang X. D., Lin J. J., Li Z.W., Zhao H. P., Yu G.W., Wang Y. (2016). Effect of hydrothermal treatment time on the migration of nitrogen, phosphorus, potassium and heavy metals in sludge. J. Environmental science. 37 (03), 1048–1054.

Wang, S. L. (2018). Comparison, selection and stability study on capacity enhancement scheme of sludge landfill reservoir in Lao gang Comprehensive Landfill Site. J. Environmental sanitation engineering. 26 (04), 51–55.

Advances in Applied Chemistry and Industrial Catalysis – Saikia (Ed.)

Study on nitrogen removal of surface water by MBBR process coupled with sulfur autotrophic denitrification

Y.L. Han, M.L. Zhu*, H. Jiang, J.B. Zhang & P.L. Xu
School of Environmental Science and Engineering, Xiamen University of Technology, Xiamen, Fujian, China
The Key Laboratory of Water Resources Utilization and Protection of Xiamen, Xiamen University of Technology Xiamen, Fujian, China

ABSTRACT: In recent years, nitrate nitrogenous pollution in surface waters has been extremely serious, while micro-polluted surface water has insufficient carbon sources and high dissolved oxygen levels. Traditional heterotrophic denitrification technology was insufficient to remove nitrate pollution. Therefore, the use of biological autotrophic denitrification technology without additional carbon sources and the formation of an anaerobic environment are the keys to nitrogen removal. In this paper, a sulfur autotrophic denitrification system coupled with the MBBR process was used to study the denitrification of micro-polluted surface water. The results showed that under the condition of influent COD concentration of 62.45 mg/L, after 34 days of stable operation of MBBR-sulfur autotrophic system, the removal rates of NO_3^--N reached 51.90%, the removal rate of TN reached 31.65%, and the effluent DO was 6.23 mg/L. The single MBBR process had no nitrogen removal effect and even accumulated a certain amount of nitrogen pollution, and the effluent DO was 6.20 mg/L.

1 INTRODUCTION

With the rapid development of industry and agriculture in China and the improvement of people's living standards, a large number of industrial wastewater, nitrogen-containing pollutants caused by agricultural non-point source pollution, and domestic sewage are discharged into the water body. The main pollution of surface water comes from agricultural non-point source pollution, and the main form of total nitrogen is nitrate-nitrogen (Gao & He 2012; Miao & Jiang 2019). Micro-polluted surface water has the characteristics of low BOD_5 content, low C/N ratio, and high dissolved oxygen (DO) content. However, the traditional heterotrophic denitrification technology is difficult to remove nitrate-nitrogen under the condition of insufficient carbon sources in surface water. Therefore, the use of autotrophic denitrification technology without additional carbon sources is the key to nitrogen removal.

At present, the existing nitrogen removal technology has no obvious effect on the removal of high nitrogen polluted surface water: Huang (Huang 2012) used the Multi-pond-artificial wetland coupling system to conduct nitrogen removal research on Qiantang River, and the TN removal rate of the system effluent was about 10%. Jia (Jia 2018) used the multi-enhanced biological denitrification technology in the pond to study the water purification of Longhong Stream in Hangzhou West Lake, which was mainly characterized by "low phosphorus and high nitrogen". The average removal rates of TN and NO_3^--N in the water were 27.64% and 23.34%. Biological autotrophic denitrification can economically and efficiently remove nitrate-nitrogen. Because of its advantages of no additional carbon source, less sludge production, and no secondary pollution, it has attracted the attention of scholars at home and abroad (Yan & Liao 2006). Sulfur-limestone

*Corresponding Author: 292890310@qq.com

DOI 10.1201/9781003308553-28

autotrophic denitrification (SLAD) has been studied for decades to treat nitrate-nitrogen pollution (Wan & Liu 2008). The principle of the sulfur autotrophic denitrification process was that sulfur denitrifying bacteria used reduced sulfur (S^0, S^{2-}, $S_2O_3^{2-}$, et al) as electron donor and nitrate as an electron acceptor to reduce nitrate-nitrogen to nitrogen under anoxic or anaerobic conditions (Deng & Wang 2008; Zhang & Yang 2020). Domestic and foreign scholars mostly studied the effect of sulfur autotrophic denitrification by infiltration system. Wang (Wang 2018) carried out a detailed study on the removal of nitrate-nitrogen from micro-polluted surface water through the autotrophic denitrification process. According to the experimental results, when the S/N ratio was 1.0, 1.2, and 1.5, the total nitrogen removal rate was 20.2%, 66.4%, and 80.3% respectively.

The nitrogen removal effect of sulfur autotrophic denitrification system with filtration was excellent, but its application in practical engineering still needs to take into account the site problems of large-scale filtration device construction and the operation cost of water pumps that extract surface water into the filtration device purification. The practical application feasibility is poor. The MBBR process (moving bed biofilm method) can effectively solve the site problems. MBBR uses filler as the carrier to provide growth conditions for microorganisms, improve the type and quantity of microorganisms, degrade organic pollutants in water, purify water quality, and form an anaerobic environment in the membrane (Geng & Zhang 2003; Gong & Pan 2021). The process can throw fillers directly into the water without the need for additional construction facilities and power consumption for large areas of land. Xu et al. (Xu & Xia 2004) studied the treatment effect of MBBR on micro-polluted surface water in the Huangpu River. The results showed that the maximum suspended nitrification volume load was 72 g/(m^3/d). Zhou et al. (Zhou & Sun 2020) used a "six-stage MBBR biological oxidation tank" to treat the micro-polluted water in the river, the removal rate of ammonia nitrogen was 57.4%, simultaneous nitrification and denitrification accounted for 7.97%. Therefore, in this study, MBBR and sulfur autotrophic denitrification technology were combined for high dissolved oxygen and micro-polluted surface water with high nitrate-nitrogen as the main pollution characteristics. One was to provide anaerobic conditions for denitrification in the biofilm after the formation of MBBR biofilm, and the other was to realize sulfur autotrophic denitrification by filling sulfur in the MBBR ball to solve the problem of insufficient carbon source and difficulty in autotrophic denitrification of micro-polluted surface water.

2 MATERIAL AND METHODS

2.1 *Experimental device*

In this experiment, a bucket with a height of 32 cm, a diameter of 34.5 cm, a bottom of 26 cm, and a total volume of 18 liters was used as the experimental device. The experiment was divided into three groups, each group of water sample volume12L, study on the removal effect of MBBR, sulfur autotrophic denitrification process, and MBBR coupled with sulfur autotrophic denitrification process on high dissolved oxygen micro-polluted surface water. The experiment was static, and the experimental scheme is shown in Table 1.

Table 1. The experimental scheme.

Process	Material
The blank group	/
MBBR	Polyurethane spherical biological filler
MBBR-Sulfur autotrophic	Polyurethane spherical biological filler + sulfur + limestone

Sulfur as an electron donor, has a small density, large specific surface area, and is easy to be attached to by organisms. Limestone is used to adjust the pH value of the effluent. The particle sizes of sulfur and limestone are 3–5 mm. To make the filler ball suspend in water, a total of 2 g

sulfur/limestone was added according to the mass ratio of 1:1. MBBR filler ball was polyurethane spherical biological filler, diameter 150 mm, large specific surface area, easy to film, adding rate was 30% (V_{filler}: V_{water}). Sulfur and limestone were filled into polyurethane spherical biological filler, and *thiobacillus denitrificans* were added to the device to improve the microbial content in water and accelerate the operation of denitrification. The inoculation amount of bacterial liquid was 0.1% ($V_{bacteria}$:V_{water}), and the bacteria were cultured in the laboratory. In samples from secondary sedimentation tank sewage, the element of the medium was (Che et al. 2008): 5.0g $Na_2S_2O_3 \cdot 5H_2O$, 2.0g KNO_3, 2.0g KH_2PO_4, 1.0g $NaHCO_3$, 0.5g $MgSO_4 \cdot 6H_2O$, 0.005g$CaCl_2$, 0.5gNH_4Cl, constant volume in 1000ml distilled water, adjusted pH to 7 and sterilization at 120°C for 20min.

2.2 *Experimental water and inoculated sludge*

Experimental water using an artificial configuration of nitrate-nitrogen pollution characteristics of high dissolved oxygen micro-polluted surface water, water quality as shown in Table 2.

Table 2. Water quality of influent (unit: mg/L).

Water quality indexes	NO_3^--N	TN	COD	DO
Concentration	7.11	7.925	62.45	6.45

The inoculated sludge was taken from the secondary sedimentation tank of a sewage treatment plant in Xiamen, and the sludge was a sludge-water mixture.

2.3 *Analysis project and methods*

The measurement items include NO_3^-, -TN, COD, and DO. Table 3 describes the analysis methods.

Table 3. Analysis project and methods.

Analyze project	Analysis method
NO_3^--N	Ultraviolet spectrophotometry
TN	Nondispersive infrared detection method
COD	Potassium dichromate digestion spectrophotometric method
DO	Electrochemical probe method

3 RESULTS AND DISCUSSION

The experiment lasted 12 days from 2021.9.7 to 2021.9.18. Subsequently, the laboratory was closed due to the new coronavirus, and the experiment was suspended. The laboratory was unsealed on 2021.10.9 and continued for two days (2021.10.9-2021.10.10).

3.1 *Change of DO concentration*

Changes in DO concentrations in three different nitrogen removal processes (Figure 1).

Denitrification requires a dissolved oxygen concentration of less than 1 mg/L, too high a dissolved oxygen concentration will inhibit denitrification. As shown in Figure 1, due to the water having a certain self-purification capacity, the oxygen consumption rate of the blank group was greater than the reoxygenation rate in the first 5 days, and the DO concentration continued to decline. When DO reached the lowest point on the fifth day, the reoxygenation rate was greater

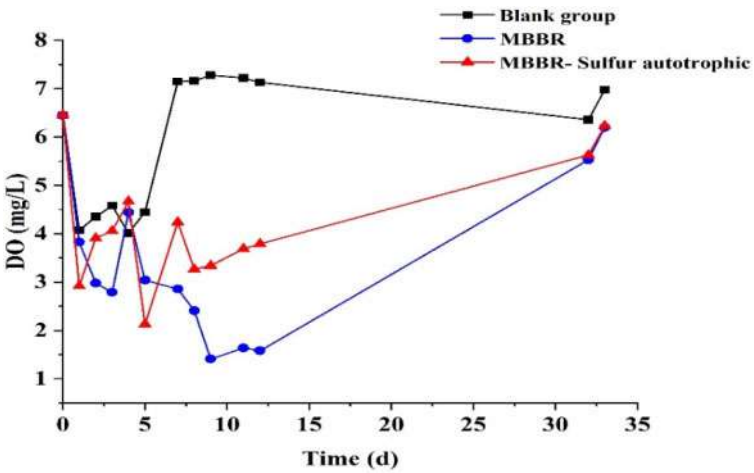

Figure 1. Variation of DO concentration in different denitrification processes.

than the oxygen consumption rate, and DO gradually rose, and remained at 7 mg/L after 34 days. The DO concentration of MBBR gradually decreased, remained relatively stable at about 1.5 mg/L after 9 days, and increased to 6.20 mg/L after 34 days. The DO concentration of MBBR-sulfur autotrophic fluctuated up and down. With the decrease of organic matter in water, the oxygen consumption rate gradually decreased. After 8 days, it was relatively stable at 3–4 mg/L, and then the DO recovered to 6.23 mg/L on the 34th day. three groups of DO concentration returned to normal after 34days, maintained in an aerobic state.

As the water body has a certain self-cleaning ability, DO concentration in the blank group decreased to the lowest point and then gradually recovered. The DO content of MBBR and MBBR-sulfur autotrophs both decreased, while the DO content of MBBR was lower than that of MBBR-sulfur autotrophic, which may be because the sediment deposited in the MBBR device contained a large number of protozoa. These protozoans may have used up some dissolved oxygen to breathe in water, but returned to normal after 34 days.

3.2 *Change of NO_3^--N concentration*

Changes in NO_3^--N concentrations in three different nitrogen removal processes (Figure 2).

It can be seen from Figure 2 that after 34 days of water purification, MBBR-sulfur autotrophication had an absolute removal effect on NO_3^--N. The blank group and MBBR had no removal effect but had the accumulation of NO_3^--N.

The initial concentration of NO_3^--N in the blank group was 7.11 mg/L, the concentration of NO_3^--N on the 12th day was 6.39 mg/L, and the removal rate was 10.13%. The epidemic prevention and control experiment was stopped. At the end of the experiment, the concentration of NO_3^--N was concentrated due to nearly half of the evaporation of water. On the 34th day, the concentration of NO_3^--N was increased to 10.32 mg/L. The concentration of NO_3^--N in MBBR was 5.91 mg/L on the 12th day, and the removal rate was 16.88%. At the end of the experiment, the concentration of NO_3^--N began to increase gradually due to the concentration caused by large evaporation of water, and the concentration of NO_3^--N was 14.36 mg/L on the 34th day. The concentration of NO_3^--N in MBBR-sulfur autotrophic system gradually decreased on the fifth day. After 34 days of water purification, the concentration of NO_3^--N in the effluent was 3.42 mg/L, and the removal rate was 51.90%. After 34 days of stable operation, the concentration accumulation of NO_3^--N in MBBR was higher than that of the blank group. It may be because the experiment was carried out in an unventilated room, and the DO concentration of the experimental device was only between

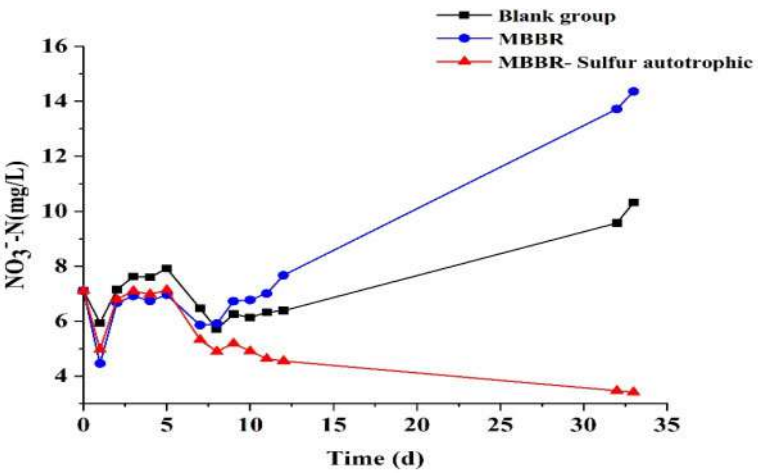

Figure 2. Variation of NO_3^--N concentration in different denitrification processes.

1 and 2 mg/L on the 8th day, so MBBR could not effectively conduct an aerobic reaction. It can be seen that each group of processes had removal effects on NO_3^--N in the first 12 days. After 12 days, due to evaporation of water and concentration, the nitrate-nitrogen accumulation rate of MBBR was higher than that of the removal rate. MBBR-sulfur autotrophic removal of NO_3^--N was excellent.

3.3 *Change of TN concentration*

Changes in TN concentrations in three different nitrogen removal processes (Figure 3).

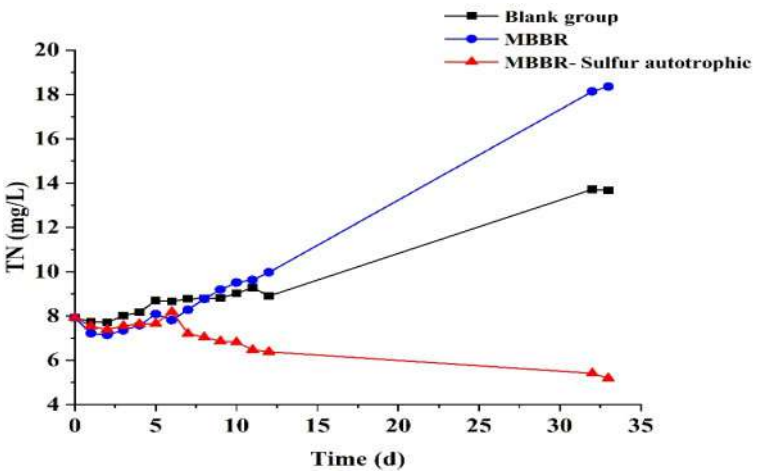

Figure 3. Variation of TN concentration in different denitrification processes.

It can be seen from Figure 3 that MBBR-sulfur autotrophic had an obvious nitrogen removal effect. On the 12th day, the effluent TN concentration was 6.39 mg/L, and the removal rate was 19.40%. On the 34th day, the effluent TN concentration was 5.42 mg/L, and the removal rate was 31.65%. Both the blank group and MBBR had TN accumulation. The accumulation degree of MRRR (the 34th day TN concentration was 18.38 mg/L) was higher than that of the blank

group (the 34th day TN concentration was 13.67 mg/L). The main reason for TN accumulation was evaporation concentration. After 34 days, the water was concentrated by nearly half, resulting in a nearly double increase in TN concentration in water. In addition, the accumulation degree of MBBR was higher than that of the blank group, which may be caused by dust pollution in the air. This experiment was carried out in the laboratory. There were many sand water purification filters in the laboratory, and sand drifted into the bucket during ventilation, resulting in the accumulation of TN in the water.

4 CONCLUSIONS

(1) The combined process of MBBR and sulfur autotrophic denitrification was used to treat high dissolved oxygen micro-polluted surface water. The MBBR filler ball was used for aerobic nitrification outside the ball, and the sulfur was used as an electron donor for anaerobic denitrification inside the ball. When the influent COD concentration was 62.45 mg/L, the stable operation for 34 days had an excellent denitrification effect. The removal rates of NO_3^--N could reach 51.90%, and the removal rate of TN could reach 31.65%.
(2) A single MBBR process has no removal effect on NO_3^--N and TN. Due to water evaporation, a large amount of NO_3^--N and TN accumulated after 34 days of operation. MBBR process was affected by DO. High DO content would inhibit the denitrification process, while low DO would breed filamentous bacteria and affect effluent water quality.
(3) MBBR and MBBR-sulfur autotrophic would consume dissolved oxygen in water, and tend to be stable after consumption to a certain extent. Finally, the DO concentration returned to normal levels and remained in an aerobic state.

ACKNOWLEDGMENT

This work was financially supported by “the research project funds of the removal technology of total nitrogen in surface water with high dissolved oxygen and micro-pollution under normal and low-temperature conditions” from “Yellow River Survey, Planning and Design Institute Co., Ltd.”

REFERENCES

Che, X. & Luo, G. Z. (2008). Isolation, Identification and Denitrification Characterization of Thiobacillus denitrificans. J. Chinese J Journal of Environmental Science. 29(10), 2931–2937.
Deng, X. L. & Wang, A. J. (2008). Present state of the sulfur-autotrophic denitrification technique and its developing trend. J. Industrial Water Treatment. 28(3), 13–16.
Gao, J. W. & He, S. B. (2012). Nitrogen Removal from Micro-polluted Surface Water by Combined Process of Biofilter and Ecological Gravel Bed. J. China Water & Wastewater. 28(1), 26–30.
Geng, Y. H. & Zhang, M. (2003). Study on membrane hanging process of micro-polluted raw water pretreatment by moving bed biofilm reactor. J. North Environment. 1, 51–54.
Gong, W. J. & Pan, W. L. (2021). Application research and development prospect of MBBR process. J. Applied Chemical Industry. 50(3), 780–783, 788.
Huang, F. M. (2012). Research for Qian Tang River micro-polluted oligo Carbon water Nitrogen Demonstration Engineering. D. Hu Bei: Wuhan University of Technology.
Jia, R. K. (2018). Study on the Purification Technology of the Eutrophic Water in Longhongjian Watershed.D. Shan Xi: Xi’an University of Architecture and Technology.
Miao, B. & Jiang Y. (2019). Effect of Low Temperature on Sulfur Autotrophic Denitrification and Its Improvement. J. China Water & Wastewater. 35 (5), 105–109.
Wan, D. J. & Liu, H. J. (2008). Using the combined bioelectrochemical and sulfur autotrophic denitrification system for groundwater denitrification. J. Bioresource Technolog.100(1), 142–148.
Wang, Z. (2018). Comparison of autotrophic and heterotrophic denitrification processes for nitrateremoval from micro-polluted surface water. D. Shanghai Jiao Tong University.

Xu, B. & Xia, S. Q. (2004). MBBR Technology for Pretreatment of Micro-polluted Raw Water in Huangpu River. J. China Water & Wastewater. (08), 5–9.
Yan, Z. Y. & Liao T Z. (2006). Progress in Research of Biological Removal of Nitrogen. J. Chinese Journal of Applied & Environmental Biology. 12(2), 292–296.
Zhang, L. T. & Yang, C. J. (2020). Research and progress of Sulfur autotrophic denitrificationfor advanced treatment of Nitrogen removal. J. Yunnan Chemical Technology. 47(3), 1–4,6
Zhou, Z. X. & Sun, X. Y. (2020). Study on Nitrification Performance of MBBR Process in Treatment of Micro Polluted Water. J. Technology of Water Treatment. 46(8), 121–125.

Advances in Applied Chemistry and Industrial Catalysis – Saikia (Ed.)

Hydrogenolysis of 2, 4, 6, 8, 10, 12-hexabenzyl-2, 4, 6, 8, 10, 12-hexaazaisowurtzitane (HBIW) with PdX (X=Fe, Ni, Co, Ag, Pt)/mpg-C_3N_4 catalysts

Wei Liu* & Kun Chen
School of Materials Science and Engineering, Beijing Institute of Technology, Beijing, China

Zhengzheng Zhang
Research Institute, Gansu Yin Guang Chemical Industry Group Co. Ltd., Baiyin, China

Huanming Liu, Na Li, Shaohua Jin & Siwei Zhao
School of Materials Science and Engineering, Beijing Institute of Technology, Beijing, China

ABSTRACT: Palladium-based bimetallic catalysts were synthesized and characterized. These catalysts were applied to 2, 4, 6, 8, 10, 12-hexabenzyl-2, 4, 6, 8, 10, 12-hexaazaisowurtzitane (HBIW) hydrogenolysis. PdNi/mpg-C_3N_4 catalysts had a better 78% yield of 2, 6, 8, 12-tetra acetyl-4,10-dibenzyl-2, 4, 6, 8, 10, 12-hexaazaisowurtzitane (TADBIW) than the 53% yield with PdFe/mpg-C_3N_4 catalysts. The introduction of Co, Ag, and Pt to the metal Pd could completely inhibit the activity of hydrogenolysis of HBIW.

1 INTRODUCTION

2, 4, 6, 8, 10, 12-Hexanitro-2, 4, 6, 8, 10, 12-hexaazaiso wurtzitane (HNIW or CL-20) is the highest-energy explosive that is currently produced and applied in engineering applications, and its synthesis has always been the focus of attention by scientists from all over the world. Although many synthetic methods of CL-20 had been found, the most concise and economical synthesis route is still the routes: (1) the synthesis of 2, 4, 6, 8, 10, 12-hexabenzyl-2, 4, 6, 8, 10, 12-hexaazaiso wurtzitane (HBIW) by condensation of glyoxal and benzamide, (2) HBIW undergoes hydrogenolysis and nitration to synthesize CL-20 (Koskin 2017; Simakova 2012). These routes remove the benzyl group by hydrogenolysis, which uses H_2 as a reducing agent and can reduce the cost of this route. However, precious metals of Pd are necessary as a catalyst for the hydrogenolysis of HBIW. At the same time, the catalyst cannot be reused resulting in an increase in the production cost of CL-20 and limiting its application. Therefore, the catalysts for the use of hydrogenolysis of HBIW have always been a research hotspot.

Studies have proved that the palladium hydroxide containing water is an efficient catalyst for HBIW hydrogenolysis, and it can be directly used in HBIW hydrogenolysis without a carrier (Fotouhi-Far 2017). At the same time, metal palladium also has a good catalytic effect on the hydrogenolysis of HBIW. However, metal catalysts will agglomerate reducing the activity. So palladium metal is often loaded on various supports and dispersed as nanoparticles (Dong 2017). The force between the carrier and metal can improve the stability of the catalyst to avoid the metal particles agglomerating and falling off during the reaction. At present, many carriers have been studied, such as activated carbon, silicon dioxide, titanium dioxide, and carbon nitride (Zhao 2020).

The Pd nanoparticles loaded on titanium dioxide had a good performance in the hydrogenolysis of HBIW with a low ratio of palladium to HBIW (<1‰) under high pressure of H_2, which

*Corresponding Author: {a_Wei Liu}506021682@qq.com

 DOI 10.1201/9781003308553-29

benefited from the superior dispersion of palladium. The palladium-iron alloy loaded on titanium dioxide can also reduce the amount of palladium usage (Lou 2018). The Pd nanoparticles loaded on mesoporous graphite carbon nitride (mpg-C_3N_4) can be used three times to solve the problem of catalyst deactivation in the hydrogenolysis of HBIW. As a carbon-nitrogen carrier, mpg-C_3N_4 has a rich nitrogen ring in its structure and can coordinate with the metal. These nitrogen rings are not only conducive to the good dispersion of palladium but also improve the stability of the loaded metal. In this paper, mpg-C_3N_4 was used as a support, and a variety of palladium-based bimetals were loaded (Ong 2016). The hydrogenolysis of HBIW with these bimetallic catalysts was studied and the PdNi/mpg-C_3N_4 showed a good performance.

2 EXPERIMENT

2.1 *Materials*

The HBIW was synthesized with the condensation of glyoxal with benzamide and was recrystallized with acetone to increase purity. The carrier of mpg-C_3N_4 was prepared in our laboratory by the thermal polymerization method with cyanamide as precursor and SiO_2(12nm) as a hard template. The metal salts of $PbCl_2$, $FeCl_2{\cdot}4H_2O$, $NiClO_4{\cdot}6H_2O$, $AgClO_4$, $Co(NO_3)_2{\cdot}6H_2O$, and $H_2PtCl_6{\cdot}6H_2O$ were purchased from the Aladdin reagent company and used without purification.

2.2 *Preparation of catalysts*

The 200mg mpg-C_3N_4, 30.5mg $FeCl_2{\cdot}2H_2O$, 33.3mg $PdCl_2$ and 60ml water were added to 250mL four-necked flask. The temperature of the mixture was raised to 90°C under magnetic stirring with the water bath. The color of mpg-C_3N_4 was changed due to the adsorption of metal ions. After stirring for 6h at 90°C, the pH of the solution was adjusted to 10 with 1M NaOH solution. The $NaBH_4$(2mg/mL) solution freshly prepared, the amount of which was five times the theoretical amount to reduce all metals, was slowly dripped into the mixture for ensuring the complete reduction of Pd^{2+} and Fe^{3+}. The mixture was kept stirring at 90°C for 4 hours, cooled to room temperature, and stirred overnight. After that, the above mixture was centrifuged, washed with water to neutral, and vacuum dried at 65°C for 6 hours to obtain the catalyst named as PdFe/mpg-C_3N_4.

Other bimetallic catalysts were prepared by the same method, except that the metal salt was replaced according to the following Table 1.

Table 1. The raw materials and their dosage in the preparation of catalysts.

Catalysts	The dosage of $PdCl_2$/mg	X metal	The dosage of X metal/mg	The dosage of mpg-C_3N_4/mg	The mass ratio of Pd:X/(mg:mg)
PdFe/mpg-C_3N_4	33.3	$FeCl_2{\cdot}4H_2O$	30.5	200	7:3
PdNi/mpg-C_3N_4	33.3	$NiClO_4{\cdot}6H_2O$	16.5	200	7:3
PdAg/mpg-C_3N_4	33.3	$AgClO_4$	16.5	200	7:3
PdCo/mpg-C_3N_4	33.3	$Co(NO_3)_2{\cdot}6H_2O$	42.6	200	7:3
PdPt/mpg-C_3N_4	33.3	$H_2PtCl_6{\cdot}6H_2O$	22.8	200	7:3
Pd小/mpg-C_3N_4	33.3	–	–	200	7:0

2.3 *Catalytic performance for hydrode benzylation*

The 10mg catalysts, 100mg HBIW, 0.3mlDMF, 0.15mlAc_2O and 1.8μl BrPh were added to the two-neck bottle. The air in the bottle was replaced with N_2 three times and then replaced with H_2 three times. The reactor was connected with an H_2 balloon. The mixture was magnetically stirred at 18°C for 1h and then 45°C for 7h. After the reaction, the mixture of TADBIW and catalysts

was centrifuged, washed with acetone three times, and dried in a vacuum for 6h at 60°C. The yield of TADBIW was obtained by subtracting the mass of catalysts from the mass of the above solid mixture. The CCl_3 was used as the solvents to extract the solid mixture to get the TADBIW. HR-MS (EI): m/z = 539.2374 $[M + Na]^+$, calcd. for $[C_{28}H_{32}N_6O_4+Na]^+$:539.2377. ^1H NMR (DMSO-d_6) δppm 1.75–2.16 (m, 12H, Me), 3.93–4.10 (d, 4H, CH2), 5.26–5.56 (m, 4H, CH3), 6.21–6.62 (m, 2H, CH) 7.3–7.51 (m. ph, 10 H).

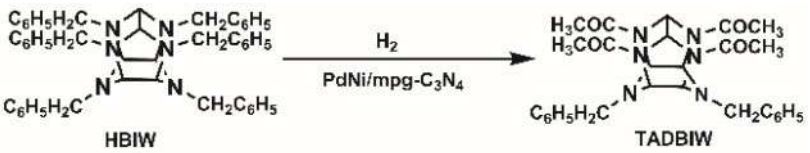

Figure 1. The hydrogenolysis of HBIW to TADBIW.

2.4 *Characterization of catalysts*

The metal contents of each catalyst were determined by the plasma–optical emission spectroscopy (ICP–OES) analysis with Agilent 5110 Instrument. The topography and element distribution of the catalysts was observed by the scanning electron microscope (SEM) and an energy dispersive spectrometer (EDS).

3 RESULTS AND DISCUSSION

3.1 *The metal content of catalysts*

The metal contents of each catalyst were determined by the plasma–optical emission spectroscopy (ICP–OES) analysis with Agilent 5110 Instrument. The topography and element distribution of the catalysts was observed by the scanning electron microscope (SEM) and an energy dispersive spectrometer (EDS).

Table 2. The metal content of the catalysts.

Catalysts	Content of Pd/%	Content of metal X/%
PdFe/mpg-C_3N_4	5.94	2.3
PdNi/mpg-C_3N_4	5.48	2.9
PdAg/mpg-C_3N_4	5.72	3.0
PdCo/mpg-C_3N_4	5.93	2.4
Pd/Pt/mpg-C_3N_4	6.10	2.7

3.2 *The topography and element distribution of catalysts*

As can be seen in Fig2, the PdNi/mpg-C_3N_4 showed an irregular block morphology. The surface of the catalysts is loose and porous, which provides a large specific surface for the metal deposition or material transfer. The loading of Pd and Ni is confirmed in figure 3. It showed that these two elements were evenly distributed on the surface of the catalyst and the existence of the O element was due to the oxidation of the Pd and Ni.

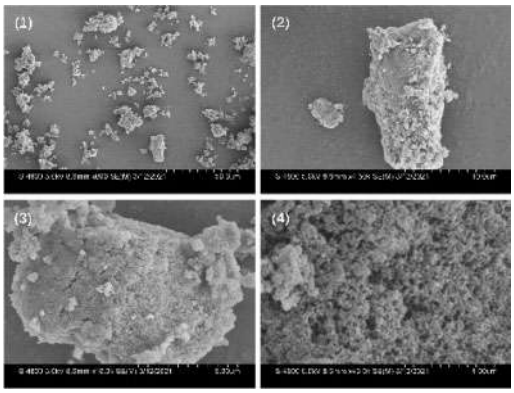

Figure 2. The SEM of PdNi/mpg-C_3N_4.

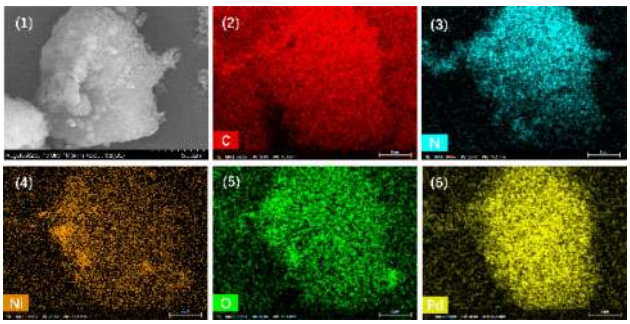

Figure 3. The SEM-EDS of PdNi/mpg-C_3N_4.

3.3 *The hydrogenolysis of HBIW*

The above bimetal catalysts were used in the hydrogenolysis of HBIW and the results were shown in Table 3. The formation of an alloy of Pd with Ag, Pt, or Co can inhibit the activity of palladium in the hydrogenolysis of HBIW. But the Pd/Fe and Pd/Ni alloy loaded on the mpg-C_3N_4 showed a good performance in the hydrogenolysis of HBIW. The yield of TADBIW with PdFe/mpg-C_3N_4 as catalyst was 53%, while the yield of TADBIW with PdNi/mpg-C_3N_4 as catalyst was 78%, which was bigger than the yield with Pd (5.4%)/mpg-C_3N_4 as catalysts when the mass ratio of Pd to HBIW was 0.6%.

Table 3. The hydrogenolysis results of HBIW.

Catalysts	Massratio (Pd/HBIW)/%	Yield/%
PdFe/mpg-C_3N_4	0.59	53
PdNi/mpg-C_3N_4	0.55	78
PdAg/mpg-C_3N_4	0.57	–
Pd/Pt/mpg-C_3N_4	0.61	–
PdCo/mpg-C_3N_4	0.59	–

4 CONCLUSIONS

PdX (X=Fe, Ni, Co, Ag, Pt)/mpg-C_3N_4 catalysts were synthesized by the chemical reduction method and characterized by ICP and SEM-EDS. The hydrogenolysis of HBIW with the above catalysts was carried out. The PdFe/mpg-C_3N_4 and PdNi/mpg-C_3N_4 catalysts were effective for the hydrogenolysis of HBIW, while the introduction of Co, Ag, and Pt can completely inhibit the activity of the catalyst.

REFERENCES

Dong, K. (2017). The Highly Effective Hydrogenolysis-Based Debenzylation of Tetraacetyl-Dibenzyl-Hexaazaisowurtzitane (TADBIW) Using a Palladium/Dowex Catalyst Having a Synergistic Effect. J. Energ Mater. 45, 1–9.

Fotouhi-Far, F. (2017). Study of Deactivation of Pd(OH)2/C Catalyst in Reductive Debenzylation of Hexabenzylhexaazaisowurtzitane. Propell Explos Pyrot. 42, 213–219.

Koskin, A. P. (2017). Reductive debenzylation of hexabenzylhexaazaisowurtzitane – the key step of the synthesis of polycyclic nitramine hexanitrohexaaza isowurtzitane. Russ. Chem. Bull. 56, 2370–2375.

Lou, D. (2018). PdFe bimetallic catalysts for debenzylation of hexabenzylhexaazaisowurtzitane (HBIW) and tetraacetyldibenzylhexaazaisowurtzitane (TADBIW). Catal Commun. 109, 28–32.

Maksimowski, P. (2016). Palladium Catalyst in the HBIW Hydrodebenzylation Reaction. Deactivation and Spent Catalyst Regeneration Procedure. Central European Journal of Energetic Materials. 13 (2), 333–348.

Ong, W. J. (2016)., Graphitic Carbon Nitride (g-C3N4)-Based Photocatalysts for Artificial Photosynthesis and Environmental Remediation: Are We a Step Closer To Achieving Sustainability? Chem Rev. 116, 7159–329.

Simakova, I. L. (2012). The effect of preparation conditions on the catalytic and physical-chemical properties of Pd/C in reductive debenzylation of hexabenzylhexaazaisowurtzitane. J. Sib. Fed. Univ., Chem. 5, 239–250.

Zhao, W. (2020). Ultrasmall Pd Nanoparticles Supported on TiO2 for Catalytic Debenzylation via Hydrogenative C–N Bond Cleavage. ACS Appl Nano Mater. 4, 159–161.

Advances in Applied Chemistry and Industrial Catalysis – Saikia (Ed.)

Determination of 13 bisphenol compounds in plastic food contact materials by gas chromatography-mass spectrometry

Yue Qiu*, Genrong Li, Qing Zhang, Jiali Lu & Mei Long
Chongqing Academy of Metrology and Quality Inspection, Chongqing, P.R. China

ABSTRACT: A method was established for simultaneous determination of 13 bisphenol compounds in plastic food contact materials by gas chromatography-mass spectrometry (GC-MS). The optimal conditions of gas chromatography and mass spectrometry were investigated by evaluating the main factors affecting the separation effect. Finally, the rapid and effective separation of 13 bisphenol compounds was achieved within 10 min. The results showed that the limits of detection were 0.01–0.05 mg/kg, the average recoveries ranged from 81.3% to 115.5%, and the precision was in the range of 1.3%–6.7%. The method had high sensitivity and accuracy, which was suitable for the qualitative and quantitative analysis of bisphenol compounds in plastic food contact materials.

1 INSTRUCTIONS

Bisphenol compounds are commonly used in the manufacture of food contact materials such as milk bottles and microwave lunch boxes, which can be transferred into food and enter human body. Studies have shown that bisphenol compounds are "environmental hormones", also known as "exogenous endocrine disruptors", which may cause harm to human reproductive system and fetal development even at very low intake (Delfosse 2012; Hu 2014; Kitamura 2005). In view of the possible harm caused by bisphenol epoxy derivatives to human beings, many countries have begun to strictly restrict the use of these compounds in packaging materials, organic coatings and adhesives, and their detection methods have become a research focus of food safety testing in various countries.

At present, there are many researches on the detection methods of bisphenol residues (Brunete 2009; Gallart-ayala 2011; Tollback 2006; Wang 2013). With the increasing variety of bisphenol compounds, the existing analytical methods of bisphenol compounds will be difficult to meet the requirements of multi-residue detection of bisphenol compounds in food and its contact packaging materials (He 2015). Therefore, it is necessary to study the residue analysis methods for more kinds of bisphenol compounds.

In view of this, the paper studied the detection method of 13 bisphenol compounds in plastic food contact materials via gas chromatography-mass spectrometry, which can provide technical support for the detection of bisphenol compounds in food contact materials in the future.

2 EXPERIMENTAL AND METHODS

2.1 *Materials and reagents*

Standard samples: Hexafluorobisphenol A (BPAF), bisphenol F (BPF), bisphenol E (BPE), bisphenol A (BPA), bisphenol B (BPB), tetramethylbisphenol A (TMBPA), bisphenol C (BPC), bisphenol Z (BPZ), tetrachlorobisphenol A (TCBPA), bisphenol F diglycidyl ether (BFDGE), bisphenol AP (BPAP), bisphenol A diglycidyl ether (BADGE) and bisphenol P (BPP) purchased from Germany

*Corresponding Author: qiuyuecqu@163.com

DOI 10.1201/9781003308553-30

Dr. Ehrenstorfer company. Methanol, isopropyl alcohol and acetonitrile were all chromatographic pure, which purchased from Tedia Company in the United States.

2.2 *Instruments and equipment*

Gas chromatography-mass spectrometer (Trace 1310-ISQ7000, Thermo Fisher Technologies Co., LTD.); Electronic balance (MS105DU, Mettler Toledo International Trade Co., LTD.); Ultrasonic cleaning instrument (Bilon-2000CT, Shanghai Bilang Instrument Co., LTD.); Nitrogen blower (N-EVAP-112, Organomation, USA).

2.3 *Methods*

Each standard substance of 10 mg was weighed and dissolved with methanol to obtain a single standard reserve liquid of 1000 ppm. The standard working solution was diluted with methanol with concentrations of 0.2, 0.5, 2.0, 5.0 and 10.0 mg/L. The sample was cut into small particles with weight smaller than 0.02 g. The sample of 1.0 g was extracted by ultrasound with methanol. The supernatant was filtered through 0.45 μm organic membrane and analyzed by GC-MS. The chromatographic column was HP-5MS (30 m × 0.25 mm × 0.25 μm). Injector temperature was 300°C. Injection volume was 1 μL. The flow rate was 1.5 mL/min. Carrier gas was high purity helium (99.999% purity). Ion source temperature was 300°C and the interface temperature of mass spectrometry was 280°C.The electron energy was 70 EV with solvent delay of 5 min. The range of full scan (m/z) was 40–400.

3 RESULTS AND DISCUSSION

3.1 *Selection of chromatographic conditions*

Firstly, the effects of chromatographic column, inlet temperature, heating rate, carrier gas flow rate and ion source temperature on the separation of acrylate compounds were investigated. It was found that HP-5MS column had the best separation effect for bisphenol compounds. Generally speaking, when the column heating rate increase, the retention time become faster and the peak is sharper, but the separation degree between analytes may become worse. In this experiment, the initial column temperature of 65°C was used to investigate the effects of different heating rates on the separation of target compounds. After comprehensive consideration of peak time, peak shape and separation degree, 13 bisphenol compounds could achieve good baseline separation within 10 min under optimal conditions, as shown in Figure 1.

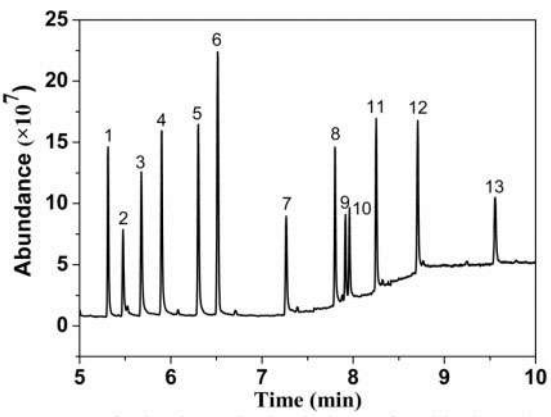

Figure 1. Chromatograms of mixed standard solutions of 13 bisphenol compounds (peak numbers the same as Table 1).

3.2 *Standard curve and detection limit*

The linear equation and correlation coefficient of each target substance obtained by referring to 1.3.2 were shown in Table 1. The results suggested that the 13 bisphenol compounds showed good linearity in the range of 0.2–10 mg/L, and the linear correlation coefficients (R^2) were all higher than 0.998. The detection limits (LODs) of 13 target compounds were 0.01–0.05 mg/kg by using the method of 3 times signal-to-noise ratio (S/N≥3) method.

Table 1. The linear regression equations, correlation coefficients (R^2) and detection limits (LODs) of 13 bisphenol compounds.

No.	Compound	linear regression equations	R^2	LOD (mg/kg)
1	BPAF	Y=44348.7X-2105.7	0.9988	0.01
2	BPF	Y=21168.9X-1390.5	0.9985	0.02
3	BPE	Y=144546.4X-13851.2	0.9996	0.01
4	BPA	Y=92561.4X-3188.4	0.9987	0.01
5	BPB	Y=111627.7X-7912.5	0.9981	0.01
6	TMBPA	Y=185437.8X-13046.2	0.9991	0.01
7	BPC	Y=19558.4X-1085.7	0.9990	0.01
8	BPZ	Y=28952.3X-1388.1	0.9995	0.01
9	TCBPA	Y=32173.0X+2011.5	0.9905	0.05
10	BFDGE	Y=41530.7X-1935.1	0.9993	0.05
11	BPAP	Y=67450.1X-2840.2	0.9888	0.01
12	BADGE	Y=52914.7X-1894.9	0.9917	0.01
13	BPP	Y=22751.7X-1239.2	0.9989	0.02

3.3 *Precision and recovery*

Blank plastic food contact material samples were selected for spiked recovery and precision tests at 0.2, 2.0 and 10.0 mg/kg, respectively. Each concentration level was determined for 7 times repeatedly, and the results were shown in Table 2. The experiment showed that the recoveries (R) of 13 bisphenol compounds at three spiked levels ranged from 81.3% to 115.5%, and the relative standard deviations (RSD) were 1.3%–6.7%, which could meet the actual detection requirements.

Table 2. Recoveries (R) and RSDs (n=7) for bisphenol compounds.

		0.2 mg/kg		2.0 mg/kg		10.0 mg/kg	
No.	Compound	R/%	RSD/%	R/%	RSD/%	R/%	RSD/%
1	BPAF	81.3	4.0	86.9	2.4	93.8	1.6
2	BPF	107.0	3.6	92.6	1.9	97.5	1.4
3	BPE	84.6	4.2	107.4	2.7	101.5	2.0
4	BPA	82.9	4.8	94.5	2.4	103.6	1.9
5	BPB	89.3	5.1	105.2	3.9	98.7	1.6
6	TMBPA	90.4	3.7	96.1	2.5	99.0	1.3
7	BPC	108.5	4.4	103.0	2.6	98.1	1.5
8	BPZ	83.7	5.3	90.0	3.8	94.2	1.8
9	TCBPA	115.5	6.7	109.1	4.5	97.5	2.3
10	BFDGE	82.2	5.6	94.7	3.4	95.2	2.1
11	BPAP	90.7	4.9	103.8	2.8	97.5	1.6
12	BADGE	106.1	4.7	94.7	2.6	96.8	1.7
13	BPP	84.4	5.0	105.4	3.1	100.6	1.5

3.4 *Actual sample testing*

Actual samples of ten plastic food contact materials were selected for analysis by this method. The results showed that a certain amount of bisphenol compounds were detected in three samples. As shown in Table 3, a small amount of BPF was found in Sample 1, BPF and TCBPA were detected in Sample 2, and BPA and BADGE were found in Sample 3, with the content ranging from 0.18 mg/kg to 6.77 mg/kg.

Table 3. Average contents (mg/kg) of bisphenol compounds in commercial samples.

No.	Compound	Sample 1	Sample 2	Sample 3
1	BPAF	—	—	—
2	BPF	0.18	6.77	—
3	BPE	—	—	—
4	BPA	—	—	4.08
5	BPB	—	—	—
6	TMBPA	—	—	—
7	BPC	—	—	—
8	BPZ	—	—	—
9	TCBPA	—	2.17	—
10	BFDGE	—	—	—
11	BPAP	—	—	—
12	BADGE	—	—	1.59
13	BPP	—	—	—

4 CONCLUSION

A method for the determination of 13 bisphenol compounds in plastic food contact materials was established by gas chromatography-mass spectrometry. The detection limits of the method were in the range of 0.01–0.05 mg/kg, the average recoveries were 81.3%–115.5%, and the precision was 1.3%–6.7%. The method had high sensitivity and accuracy, which was suitable for the qualitative and quantitative analysis of bisphenol compounds in plastic food contact materials.

FUNDING

This research was funded by Scientific Research Project of Chongqing Market Supervision Administration [CQSJKJ2019005].

REFERENCES

Brunete C. S. (2009). Determination of tetrabromobisphenol-A, tetrachlorobisphenol-A and bisphenol-A in soil by ultrasonic assisted extraction and gas chromatography-mass spectrometry. J. Chromatogr. A 1216, 5497–5503.

Delfosse V. (2012). Structural and mechanistic insights into bisphenols action provide guidelines for risk assessment and discovery of bisphenol A substitutes. Proc. Natl. Acad. Sci. USA 109, 14930–14935.

Gallart-ayala H. (2011). Analysis of bisphenols in soft drinks by on-line solid phase extraction fast liquid chromatography-tandem mass spectrometry. Anal. Chim. Acta 683, 227–233.

He D. (2015). Rapid Determination of Seven Bisphenols in Edible Oils with Dispersive Liquid-Liquid Microextraction and Ultra Performance Liquid Chromatography-Tandem Mass Spectrometry. Food Research and Development 36, 102–106.

Hu X. J. (2014). Determination of Bisphenolic and Halogenated Bisphenolic Compounds in Human Urine by High Performance Liquid Chromatography-Tandem Mass Spectrometry. Chin. J. Anal. Chem. 42, 1053–1056.

Kitamura S. (2005). Comparative Study of the Endocrine-Disrupting Activity of Bisphenol A and 19 Related Compounds. Toxicol. Sci. 84, 249–259.

Tollback J. (2006). Determination of the flame retardant tetrabromobisphenol A in air samples by liquid chromatography-mass spectrometry. J. Chromatogr. A 1104, 106–112.

Wang X. M. (2013). Rapid determination of tetrabromobisphenol A and its main derivatives in aqueous samples by ultrasound-dispersive liquid-liquid microextraction combined with high-performance liquid chromatography. Talanta 116, 906–911.

Advances in Applied Chemistry and Industrial Catalysis – Saikia (Ed.)

Supercritical water oxidation of tributyl phosphate

Shenghan Sun, Shuzhong Wang*, Yanhui Li, Tiantian Xu, Jianna Li, Fan Zhang & Chao He
Key Laboratory of Thermo-Fluid Science and Engineering of MOE, School of Energy and Power Engineering, Xi'an Jiaotong University, Xi'an, Shaanxi, China

ABSTRACT: Supercritical water oxidation (SCWO) treatment of tributyl phosphate (TBP) has been implemented on a batch reactor in a sand bath, and experiments were investigated at a reaction pressure of 23∼29 MPa, reaction temperature of 400∼490°C, oxidation coefficient (OC) of 1.0∼3.0, and residence time of 1∼21 min. The experimental results indicate that reaction pressure does not have an obvious influence on chemical oxygen demand (COD) removal efficiency, but OC, residence time, and reaction temperature have. Most of the TBP was degraded at 460°C, 25 MPa, OC of 3.0 within residence time of 10 min, which reached up to 99.32% of COD removal efficiency. The study proves that the SCWO method has an excellent degradation effect on TBP and can be used as a potential choice.

1 INTRODUCTION

Tributyl phosphate (TBP) is usually used as an extractant during spent fuel reprocessing (El-Dessouky et al. 2001). In the process of extraction and re-extraction, TBP will be exposed to radiation and chemical action, as well as light and heat. Affected by these, TBP will be destroyed, and chemical reactions such as degradation and polymerization will occur, with the extraction performance decreasing. The performance of the extractant deteriorates severely after being used repeatedly, and a small number of radioactive elements will be retained, which makes TBP a kind of waste and harms the environment as well. TBP is not only used as an extractant in the PUREX process but also as a plasticizer and defoamer due to its excellent physical and chemical properties (Berne et al. 2004). These are the paths for TBP to enter the environment, so an environment-friendly method to degrade TBP is a must.

At present, there are many available methods for the degradation of TBP, including incineration, electrochemical oxidation, Fenton oxidation, plasma treatment, and so on (Feng et al. 2019). However, these methods have various problems. For example, the incineration method produces a lot of pollutants, the operation cost is high, also the equipment is corroded. As for the electrochemical oxidation method, the electrode materials used are also expensive and this method consumes more energy. What's more, the Fenton oxidation method has a long reaction time and produces a large amount of secondary waste liquid. Therefore, we need a TBP degradation method, that is, the supercritical water oxidation (SCWO) method with a short reaction time, less secondary pollution, and energy saving.

The concept of SCWO technology was first proposed by American scientific researcher Modell in the 1980s. SCWO is a kind of high-temperature, high-pressure wet oxidation technology. When water is in a supercritical state ($T > 374.15°C$, $P > 22.1$ MPa), it will become a kind of non-polar fluid. TBP can react with oxidants in supercritical water. SCWO technology has many advantages. It can treat different kinds of wastewater, including pesticide wastewater, phenol, and municipal sludge. Also, through the process of SCWO, many kinds of organics will be completely degraded,

*Corresponding Author: sunshenghan@stu.xjtu.edu.cn

 DOI 10.1201/9781003308553-31

with a degradation rate of 99.99% (Calzavara et al. 2004). More importantly, for radioactive wastes (Xu et al. 2021), such as radioactive waste resins (Xu et al. 2020), the method of SCWO can also separate the nuclides in it to accomplish the goal of volume reduction.

2 APPARATUSES AND PROCEDURES

2.1 *Apparatus and materials*

The experiment uses a set of sand-bath batch reactors, which was introduced in our previous research (Li et al. 2020).

NOVA60A water quality analyzer and Spectroquant® TR320 heating digester from Merck were used to determine the chemical oxygen demand (COD) of the liquid product. TBP (analytically pure), NaOH (analytically pure), and hydrogen peroxide solution (30 wt%) were purchased from Beijing Reagent Company of Sinopharm.

2.2 *Analysis methods*

We use the COD removal efficiency to reflect the effect of SCWO to degrade TBP, which is defined by the following equation:

$$X_{\mathrm{COD}} = \frac{[\mathrm{COD}]_0 - [\mathrm{COD}]}{[\mathrm{COD}]_0} \times 100\% \tag{1}$$

where X_{COD} means the COD removal efficiency, $[\mathrm{COD}]_0$ means the COD concentration in TBP before reaction, and [COD] means the COD concentration in the liquid after the SCWO reaction.

The OC is calculated by dividing the actual oxygen added by the stoichiometric specific oxygen demand. The calculation formula is as follows:

$$\mathrm{OC} = \frac{[\mathrm{O_2}]_{\mathrm{init}}}{[\mathrm{O_2}]_{\mathrm{stoi}}} \tag{2}$$

where $[\mathrm{O_2}]_{\mathrm{init}}$ is the actual oxygen addition, and $[\mathrm{O_2}]_{\mathrm{stoi}}$ is stoichiometric specific oxygen demand.

3 RESULTS AND DISCUSSIONS

The four crucial factors we choose in this paper are reaction temperature, OC, residence time, and reaction pressure, and their ranges are shown in Table 1. To ensure the accuracy of the experimental data, each group of the experiments was repeated 3 times before the average data was taken as the final data.

Table 1. Ranges of temperature, pressure, residence time, and OC.

Temperature (°C)	Pressure (MPa)	Residence time (min)	OC
400 ~ 490	23 ~ 29	1 ~ 21	1.0 ~ 3.0

3.1 *Effect of reaction pressure*

When the reaction temperature is 460°C, the OC is 1.2 and the residence time is 10 min, the influence of reaction pressure on the degradation effect of TBP is explored. Figure 1 shows the COD concentration of the liquid products and the COD removal efficiency. When the reaction pressure is 23, 25, 27, 29 MPa, the COD removal efficiency is 96.30%, 96.86%, 97.34%,97.59%,

respectively. As the reaction pressure increases, the COD removal efficiency increases as well. As we can see from Figure 1, when the reaction pressure is up to 27 MPa, the promotion effect of the reaction pressure on COD removal efficiency is weakened accordingly.

Reaction pressure has two different influence mechanisms on the COD removal efficiency. On the one hand, increased pressure increases the density of supercritical water, which can increase the concentration of reactants in the reactor and speed up the reaction. On the other hand, the dielectric constant that rises with the rise of pressure reduces the dissolving ability of supercritical water to organics and hinders their decomposition of them. The combined effect of density and dielectric constant causes the efficiency to increase slightly with the increase of pressure. Compared with other factors, reaction pressure limits promoting effect on COD removal efficiency, and increased pressure increases the reactor cost as well. Considering the pressure should be stabilized above the supercritical point and that the cost of the reactor should be avoided increasing, the reaction pressure is recommended to be set to 25 MPa.

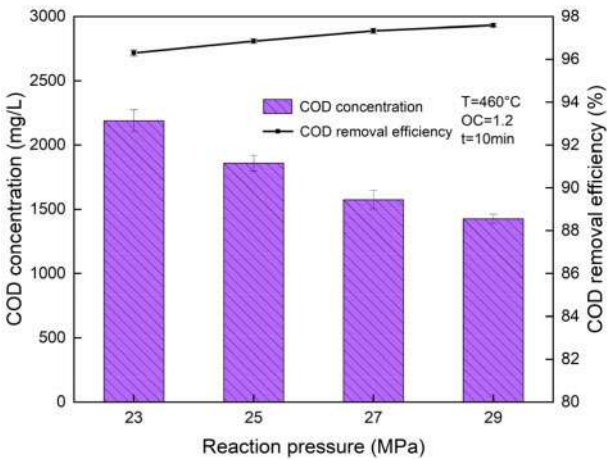

Figure 1. The effect of reaction pressure on the degradation of TBP.

3.2 *Effect of oxidation coefficient*

When the reaction temperature is 460°C, the reaction pressure is 25 MPa, and the residence time is 10 min, the influence of OC on the degradation effect of TBP is explored. Figure 2 shows the COD concentration of the liquid products and the COD removal efficiency under different conditions. When the OC is 1.0, 1.2, 1.5, 2.0, 3.0, the COD removal efficiency is 95.31%, 96.86%, 97.71%, 99.04%, 99.32%, respectively.

As we can see, when the OC becomes higher than before, there is a steady increase accordingly for the removal efficiency. After the OC reaches 2.0, the increase in COD removal efficiency shows a slowing trend. The reason is that in the SCWO process, the generation of free radicals in the system is simultaneously affected by the concentration of organics and oxidants. When the OC is high enough and limited by the concentration of organics, the excess oxidant can not generate more free radicals, so the curve of COD removal efficiency tends to be flat with the rise of OC. From the perspective of pollutant removal, the OC of TBP should not be greater than 2.

3.3 *Effect of reaction temperature and residence time*

When the reaction pressure is 25MPa and OC is 1.2, the influence of reaction temperature and residence time on the degradation effect of TBP is explored. Figure 3 shows the COD removal

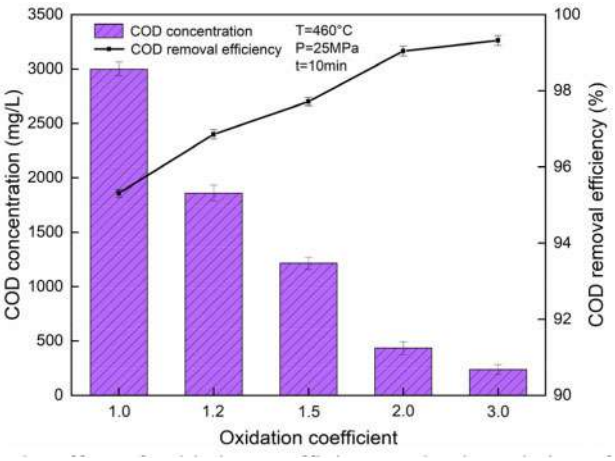

Figure 2. The effect of oxidation coefficient on the degradation of TBP.

efficiency under different conditions. As we can see, although the reaction temperature gradually increases, the residence time has the same influence on the COD removal efficiency. The efficiency increases rapidly in the first 1 to 6 minutes, and then the growth rate decreases. In the end, there is no change after 10 minutes. The extension of the residence time can increase the COD removal efficiency to a certain extent, but the removal of COD is still limited in the later stage of the reaction. This is because the concentration of residual organics in the system decreases, which in turn causes the reaction rate to decrease too. When the reaction temperature rises from 400°C to 460°C, the efficiency changes significantly, when the reaction temperature rises from 460°C to 490°C, the removal efficiency increases slightly.

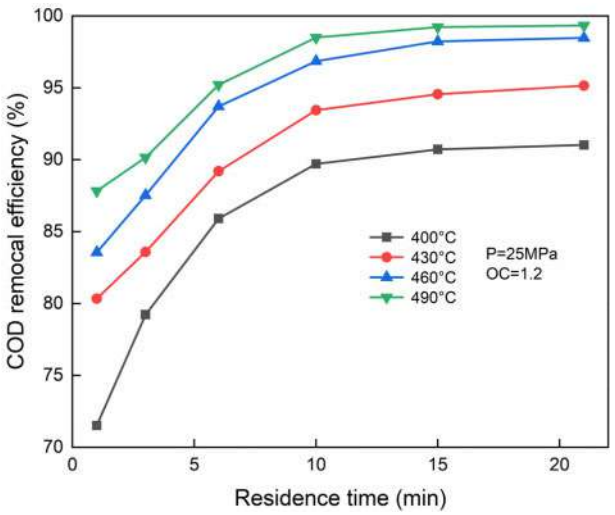

Figure 3. The effect of reaction temperature and residence time on the degradation of TBP.

In the SCWO reaction, increasing the reaction temperature has two effects on the promotion of COD removal efficiency. Firstly, increasing the reaction temperature increases the number of activated molecules in the reaction system and the molecular diffusion coefficient as well, which in

turn leads to an increase in the TBP degradation rate. Then, increasing the temperature can accelerate the free radical reaction induction stage, shorten the reaction induction period, and increase the degradation rate of organics. The inhibition effect of high temperature on COD removal efficiency is mainly reflected in the decrease of supercritical water density as the temperature increases. At 25 MPa, when the temperature increases from 400°C to 490°C, the density decreases from 166.53 kg/m^3 to 92.69 kg/m^3. The decrease in density reduces the concentration of reactants, which in turn reduces the reaction rate. The effect of increasing the number of activated molecules and molecular diffusion coefficient on the reaction rate is much greater than the effect of decreasing the concentration of reactants on the reaction rate, so the COD removal efficiency increases significantly with the increase of temperature from 400°C to 460°C. However, the efficiency increases slowly when the temperature rises from 460°C to 490°C, and the promoting effect of temperature is further weakened with the extension of residence time. This is because TBP is degraded into inorganic substances of small molecules under high temperatures and the concentration of organics in the reaction system is greatly reduced, leading to the slow increase of the reaction rate. High reaction temperature has a limited promoting effect on TBP degradation and increases energy consumption and reaction system requirements. Therefore, the degradation temperature of TBP is recommended to be set to 460°C. In this way, we can degrade it well and reduce the cost at the same time.

The effect of residence time is manifested in prolonging the reaction time, with COD removal efficiency rising rapidly, and then changing slowly. This is because under supercritical conditions, TBP, oxidant, and supercritical water become one phase, and TBP can be degraded in a short time, so the efficiency increases significantly in the early stage of the reaction. As the reaction goes on, the concentration of organics in the reaction system decreases, so the degradation rate decreases, and the efficiency changes slowly in the later stage of the reaction. In summary, to ensure a good degradation, we had better set the residence time to 10 minutes.

4 CONCLUSION

Aiming at the refractory substance TBP in the natural environment, the effects of reaction temperature, residence time, reaction pressure, and OC on the degradation efficiency of TBP in the SCWO reaction are explored. The reaction temperature has the most significant influence on the degradation effect, increasing the reaction temperature can significantly raise the COD removal efficiency. The effect of residence time on the removal rate of COD is fast first and then slow. When the residence time is less than 6 minutes, prolonging the residence time has a significant impact on the COD removal efficiency, but after 10 minutes, the COD removal efficiency changes slowly. At the same time, increasing the OC can also increase the COD removal efficiency greatly, but the rise in reaction pressure promotes the COD removal efficiency slightly. This work provides basic data and guidance for the design of the SCWO treatment device of TBP, and the following work is to study the system consumption and process design.

ACKNOWLEDGEMENT

This work was supported by the National Natural Science Foundation of China [51871179].

REFERENCES

Berne C, Montjarret B, Guountti Y, et al. (2004) Tributyl phosphate degradation by Serratia odorifera[J]. Biotechnology Letters, 26(8): 681–686.

Calzavara Y, Joussot-Dubien C, Turc H A, et al. (2004) A new reactor concept for hydrothermal oxidation[J]. Journal of Supercritical Fluids, 31(2): 195–206.

El-Dessouky M I, El-Aziz M M A, El Mossalamy E H, et al. (2001) Wet-oxidation of spent organic waste tributyl phosphate/diluents[J]. Journal of Radioanalytical and Nuclear Chemistry, 249(3): 643–647.

Feng W, Wang R, Ye D, et al. (2019) Review on treatment technologies of radioactive waste organic phase (TBP/OK) [J]. Environment Engineering, 37(5): 92–98,104.
Li J N, Wang S Z, Li Y H, et al. (2020) Experimental research and commercial plant development for harmless disposal and energy utilization of petrochemical sludge by supercritical water oxidation[J]. Chemical Engineering Research & Design, 162: 258–272.
Xu T T, Wang S Z, Li Y H, et al. (2020) Optimization and Mechanism Study on Destruction of the Simulated Waste Ion-Exchange Resin from the Nuclear Industry in Supercritical Water[J]. Industrial & Engineering Chemistry Research, 59(40): 18269–18279.
Xu T T, Wang S Z, Li Y H, et al. (2021) Review of the destruction of organic radioactive wastes by supercritical water oxidation[J]. Science of the Total Environment, 799.

Advances in Applied Chemistry and Industrial Catalysis – Saikia (Ed.)

Response of cadmium enrichment and free amino acids content in seedlings of two castor varieties to cadmium stress

Guangxu Zhu*, Xingfeng Wang, Dandan Cheng, Meiling Peng, Qing Chen, Jianglan Li, Ling Xia & Xue Wang
College of Biology and Environment Engineering, Guiyang University, Guiyang, P.R. China

ABSTRACT: As important primary nitrogen metabolites in plant tissue, free amino acids have been widely used to understand the nitrogen metabolism mechanism of plants under different environmental stress. To reveal the changes of cadmium (Cd) absorption and free amino acids in castor under the stress of Cd, a hydroponic experiment was performed to study the effect of Cd stress (0, 1, 2, and 5 $mg \cdot L^{-1}$) on the biomass and free amino acids secretion of two castor varieties seedlings (Zibo-3 and Zibo-9). The results indicated that the biomasses of the two castor varieties under 1 and 2 $mg \cdot L^{-1}$ Cd addition were not decreased significantly ($p<0.05$) compared with the control, while 5 $mg \cdot L^{-1}$ of Cd treatment reduced the biomass of Zibo-3 and Zibo-9 by 23.3% and 11.8%, respectively. Additionally, when spiked with higher Cd dose addition, the bioaccumulation factors for Cd in Zibo-9 were higher than those in Zibo-3, thus Zibo-9 showed higher tolerance and absorption ability to Cd. The comparison between both studied castor varieties indicated that Cd stress resulted in a differential but coordinated response of amino acid levels, which are playing a significant role in plant adaptation to Cd stress.

1 INTRODUCTION

Phytoremediation technology, which is characterized by low cost, good effect, safety, reliability and easy operation, has become a promising remediation technology (Sarwar et al. 2017; Sierra et al. 2021). The key effect of this remediation technique depends on how to screen or cultivate plant species with strong vitality and wide adaptability, which can tolerate external heavy metal stress environment and enrich heavy metals in vivo (Mahar *et al.* 2016). Castor (*Ricinus communis* L.) is an oil crop with high economic value. It has large biomass, developed root system, strong tolerance and adaptability to drought, cold, barren and saline- alkali. It is planted all over China. Previous studies have shown that castor has good tolerance and remediation effect to heavy metals (Khan et al. 2018; Zhang *et al.* 2015). Planting castor on heavy metal contaminated soil can not only control heavy metal pollution but also provide renewable energy, which obtain economic, energy and environmental benefits and has a wide application prospect.

The tolerance of plants to heavy metal stress is usually manifested at multiple levels of morphological structure, biochemical metabolism and gene regulation. It mainly tolerates and relieves the toxicity of heavy metals through antioxidant defense, root efflux, cell wall fixation, vacuole compartmentation, metal ligand chelation, biotransformation, and osmotic adjustment (Kushwaha et al. 2016; Sytar et al. 2013). Free small molecular substances in plants, such as organic acids, polyamines and amino acids, can act as signal molecules in plants and play an important role in osmotic regulation, structural protection and metabolic regulation (Seneviratne et al. 2019).

Nitrogen metabolism is an important nutrient metabolism pathway in plant growth and development. The intensity and dynamic changes of nitrogen metabolism directly affect the content and

*Corresponding Author: ad32@qq.com

DOI 10.1201/9781003308553-32

composition ratio of various chemical components in plants. A variety of intermediate metabolites or nitrogen-containing organic compounds of plant nitrogen metabolism play an important role in alleviating adverse environmental factors (Meng et al. 2016; Kataria et al. 2015). Amino acids are important compounds of nitrogen metabolism in plants, and their changes can reflect the nitrogen metabolism in plants. Therefore, amino acid metabolism plays an important role in plant growth and development as well as in coping with environmental stress, and specific free amino acids can more sensitively respond to changes in certain environmental stress (Sangwan et al. 2015). Studies have shown that adversity stress can significantly change the amino acid composition of plants, which is often accompanied by the accumulation of certain amino acids during the process of adversity adaptation (Zafari et al. 2016). The free amino acids produced in plants under stress conditions can maintain cellular water potential, eliminate toxicity and store nitrogen, and also play a key role in the mechanism of heavy metal enrichment in hyperaccumulator plants (Zemanová et al. 2015).

In the present study, two castor varieties (Zibo-3 and Zibo-9) were used as materials for hydroponic experiments. Different concentration gradients of Cd stress were set to analyze the response of the types and quantities of free amino acids in castor to heavy metal stress, and the sensitive amino acids with significant changes were screened out, so as to further reveal the physiological mechanism of plant tolerance and accumulation of heavy metals, and provide a scientific basis and theoretical basis for further research and utilization of castor for phytoremediation of heavy metal contaminated soil.

2 MATERIALS AND METHODS

The test plant was castor (Zibo-3 and Zibo-9), purchased from Zibo Academy of Agricultural Sciences.

The experiment was carried out in the green house of the College of Biology and Environment Engineering, Guiyang University, with a day/night temperature of 25°C (12h)/20°C (12h), photosynthetic photo flux density of 1.30×10^5lux, and a relative humidity of 70%. The seeds were surface sterilized in 2% H_2O_2 for 10 min, rinsed with deionized water, and then germinated in plastic containers, filled with wet sand. When roots were 2∼3 cm long and the first two leaves were developed, plants were transferred to a continuously aerated hydroponics Hoagland's solution and 0, 1, 2 and 5 mg·L^{-1} of Cd solution (labeled as T0, T1, T2 and T3, respectively). There were four replicates of each treatment and each replicate consisted of one plantlet. The level of the solution was maintained by adding deionized water and renewing once every 7 d. The pH of the solution was maintained at 5.8±0.1 with 1 M HCl or 1 M KOH.

Plant leaves were harvested 10 days after addition of Cd in nutrient solution. Plants were then washed with tap water and rinsed with deionized water. The fresh weights of the individual plant were subsequently determined after blotting to remove excess water. Near half of the samples were dried at 105°C for 30 min, then at 70°C in a drying oven to a constant weight. The dried plant samples were ground to a fine powder in a stainless box mill. The plant samples were digested in a mixture of concentrated $HClO_4$ and HNO_3 (1:4, by volume). The Cd concentration was determined by inductively coupled plasma mass spectrometry (ICP-MS, ELAN DRC-e, PerkinElmer company, US).

The remaining half of the samples were frozen in liquid nitrogen and immediately lyophilized for free amino acid extraction. For total soluble amino acids extraction, the procedure was performed as follows: about 150 mg plant sample (200 μL, 1 nmol·μL^{-1} α-aminobutyric acid and sarcosine added as internal standards) was homogenized with 1.8 mL of trifluoroacetic acid (TFA) 10% (v/v) under sonication for 5 min at 4°C. The homogenate was centrifuged at 12,000 rpm for 15 min (4°C), and the supernatant solution was collected. After that, the remaining sample was reextracted using 2 mL TFA (10% v/v) in the same manner. The supernatants were combined and filtered through a 0.22 mm membrane, and the collected solution was purified using 4 mL Amicon Ultra 3 K centrifugal filter tubes (Millipore, US). The purified supernatant was used for the determination

of free amino acids (FAA) by High performance liquid chromatography (HPLC, 1260, Agilent company, US). Seventeen different FAAs were identified and quantified: alanine (Ala), arginine (Arg), asparagine (Asp), cystine (Cys), glutamate (Glu), glycine (Gly), histidine (His), isoleucine (Ile), leucine (Leu), lysine (Lys), methionine (Met), phenylalanine (Phe), proline (Pro), serine (Ser), threonine (Thr), tyrosine (Tyr), valine (Val).

The experimental data were processed and plotted using Excel 2017, and the statistical analysis was carried out by two-way ANOVA using LSD (SPSS 26.0) to test the difference of the means among Cd treatments.

3 RESULTS AND ANALYSIS

3.1 *Effects of cadmium stress on plant biomass*

In the concentration gradient experiments, the average biomasses yield of the two tested plants are shown in Figure 1. Overall, the biomass of the two cultivars under different cadmium treatments was comparable. For both of the plants, the biomasses yield growing in the solutions spiked with 1, and 2 mg·L^{-1}Cd were not decreased significantly ($p<0.05$) compared with the control (CK), though the yield reduced significantly ($p<0.05$) under higher Cd concentrations of 5 mg·L^{-1} Cd spiked, which implied that there was a tolerance limitation for the plant to Cd. The biomasses yield of Zibo-3 and Zibo-9 treated with T3 was 23.3% and 11.8% lower than that of the control, respectively, which indicated that Zibo-9 had relatively high tolerance to cadmium stress.

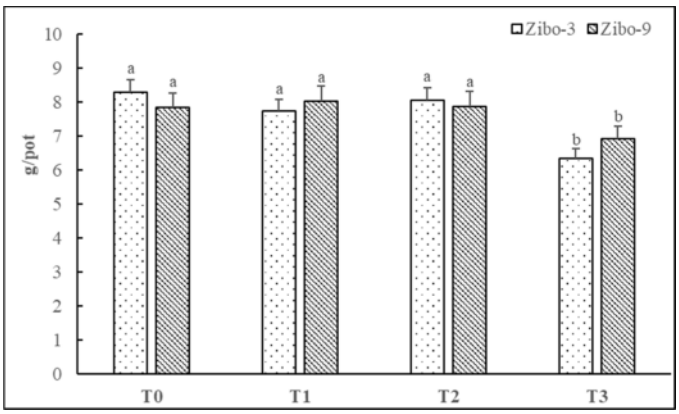

Figure 1. Effect of the Cd treatments on the plant biomass of the two plant cultivars; letters a and b represent significant differences between treatments ($P<0.05$).

3.2 *Cadmium concentrations and enrichment capacity in the plants*

Cadmium concentrations in the studied plants under different treatments are shown in Table 1. Generally, Cd concentrations in the test plants exhibited a linear increase in response to an increasing amount of Cd does. Whereas the extent of the increase also differed between the plant species. In comparison to Zibo-9, Zibo-3 recorded a higher Cd concentration at treatment T1, however, after exposure to 2 and 5 mg·L^{-1} of Cd, the contents of accumulated Cd in Zibo-9 were higher than those in Zibo-3.

The bioaccumulation factor (BCF) was calculated to investigate the accumulation ability of trace metals in the solution-plant system. BCF refers to the ratio of concentration of metals in the plant and the corresponding available content of heavy metals in the solution. A greater BCF indicates a stronger accumulation ability of heavy metals (Buscaroli 2017). Table 1 also compare BCF values

Table 1. Concentrations and BCF of Cd in the studied plant species; letters a, b and c represent significant differences between treatments (P <0.05).

	Cd concentration (mg/kg)		BCF	
Treatment	Zibo-3	Zibo-9	Zibo-3	Zibo-9
T1	14.11±0.71c	10.65±0.53c	14.11±0.71a	10.65±0.53c
T2	24.65±1.23b	29.61±1.48b	12.33±0.62b	14.81±0.74b
T3	60.82±3.04a	103.71±5.19a	12.16±0.61b	20.74±1.04a

for Cd in the two test plants. As expected, the BCF values in the Zibo-3 decreased with increased Cd application. However, Zibo-9 showed the opposite trend. The higher Cd levels in treatments from T1 to T3 led to even more marked increases in BCF values for Cd in Zibo-9, suggesting a higher enrichment ability of Cd.

3.3 *Effects of Cd on free amino acid profile*

The data regarding the effect of Cd stress on the concentrations of FAA in the two studied plants are shown in Figure 2 and Table 2. For Zibo-3, there was no significant difference in total FAA contents among Cd treatments. In the case of Zibo-9, with the increase of Cd addition, the total FAA content in plants spiked with T1 and T2 treatment was significantly higher than that of the control (T0), while decreased significantly under T3 treatment, which had no significant difference with the control.

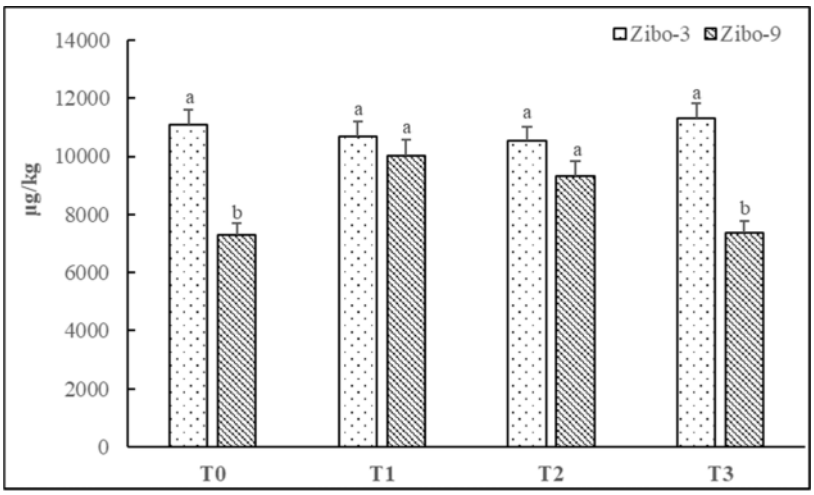

Figure 2. Effect of the Cd treatments on the total FAA concentrations of the two plant cultivars; letters a and b represent significant differences between treatments (P <0.05).

As for the specific amino acid, the addition of Cd to the two study plants altered clearly the FAA composition and concentration. However, the changes of FAA were not consistent with Cd treatments (Table 2). In control seedlings of Zibo-3, the most abundant FAA was Glu (30.9% of total FAA), followed by Asp (15.2%), Ala(14.9), His (9.5%), Met (7.6%) and Ser (6.4%). Under Cd stress, these amino acids remained the major FAA, while a considerable reduction was observed for Glu, Met and Ser. In contrast, the amount of His, Thr, Phe, Ile, Pro and Arg clearly increased,

Table 2. Effects of Cd treatments on individual FAA concentration (μg/kg) in the studied plants, different letters (a, b, c, d) indicate significantly different between treatments ($P < 0.05$).

	Zibo-3				Zibo-9			
Amino Acid	CK	T1	T2	T3	CK	T1	T2	T3
Asp	1684.7a	1594.1a	1627.2a	1361.3b	1246.9c	1917.1a	1672.3b	1133.9c
Glu	3429.2a	2876.2b	2734.6b	2400.4c	3080.8b	3645.4a	3385.7ab	2557.0c
Ser	715.3a	596.6b	509.5c	526.6bc	592.2b	744.9a	685.7a	510.9c
His	1058.4c	1271.0b	1251.3b	1464.9a	423.8d	738.1b	872.7a	638.7c
Gly	146.4a	92.9c	77.5d	114.2b	55.9b	104.9a	61.3b	42.7c
Thr	268.6b	333.9a	335.7a	353.5a	230.6b	287.3a	301.8a	221.2b
Arg	319.0c	997.8b	1112.9ab	1201.2a	254.1d	517.8b	451.7c	615.7a
Ala	1652.3b	1266.2c	1048.7d	1906.6a	490.1b	627.8a	575.0a	465.8b
Tyr	71.8c	147.9a	94.9b	98.3b	23.4a	12.3b	3.2b	2.4c
Cys	17.3a	17.5a	19.0a	12.7b	10.9a	7.6c	3.8d	9.7b
Val	441.7a	255.9c	398.3ab	386.7b	148.9d	361.1a	217.6b	188.3c
Met	827.7a	636.6b	594.85b	555.17b	405.47b	571.2a	561.7a	545.0a
Phe	111.6c	121.3c	182.8b	202.5a	79.7c	110.6b	124.4a	103.9b
Ile	53.0c	73.9b	124.6a	123.9a	24.8c	80.5b	100.9a	77.3b
Leu	85.2b	86.7b	122.6a	119.1a	64.8c	84.0b	100.1a	86.1b
Lys	80.5b	79.2b	114.8a	79.1b	54.9b	78.0a	77.4a	77.3a
Pro	138.6d	254.1b	187.5c	420.4a	119.9b	134.0a	117.b	93.5c

especially for Pro and Arg, whose contents were enhanced up to 2.0 and 2.8 times higher than those in the control treatment, respectively.

In the case of Zibo-9, Glu, Asp, Ala, Met, Ser, His were still the main FAA encountered in the plants among the Cd treatments. Glu dominated the most abundant FAA in the plants, whose amount varied from 34.7% ~ 42.2% of the total FAA among the Cd treatments of plant, which were higher than those in Zibo-3 (21.2%~30.9%). The majority of FAA and total FAA contents in Zibo-9 exhibited an increase with increasing external Cd concentrations at lower doses of Cd (T0~T2). The exposure of 2 mg·L^{-1} Cd in solution induced a maximum increase of 307% for Ile, followed by Val (143%) and His (106%), compared with the control treatment. When treated with the highest amount of Cd (5mg·L^{-1}), Zibo-9 exhibited a decrease for most of the FAA contents in the seedlings, resulting in a decline of 20.9% for total FAA content compared with that under T2 treatment. Note that unlike other amino acids, Arg exhibited a linear increase in response to an increasing amount of Cd addition.

Glu and Asp, the main amino acids presented in the present study, are involved in nitrogen assimilation and transport processes within the plants. Furthermore, they are used to build up reserves during periods of nitrogen availability for subsequent use in growth, defense, and reproductive processes (Zemanová et al. 2015). In the present study, at lower Cd exposure, increasing Cd doses were associated with clearly increasing Glu and Asp contents in Zibo-9 and with decreasing Glu contents in Zibo-3, indicating a different pathway of nitrogen utilization of both plants. A higher accumulation fraction of Glu and Asp in Zibo-9 may be associated with the observed higher Cd tolerance and Cd accumulation in Zibo-9 than inZibo-3. Under T3 treatment, the declines of both amino acids can be caused by intensive syntheses of plant defense elicitors. These two amino acids are quickly transformed into the required products or incorporated into a protein without increased accumulation in plant when exposed to Cd stress.

In this study, His, Thr, Phe, Ile, Pro, Arg, and Leu were found to accumulate in plants under lower Cd stress. Studies have shown that functional groups such as carboxyl, amino, thiol and phenolic groups in free amino acids in plants can combine with metal ions to form stable chelates, which have passivation and detoxification effects on toxic heavy metals. Pro is also precursors to

the synthesis of plant chelates, which are believed to play an important role in plant heavy metal tolerance (Christopher 2000). When treated with high doses of Cd, some of those amino acids decreased significantly, which may be ascribed to the direct biological response of Zibo-9 to Cd stress.

4 CONCLUSION

In this paper, a hydroponic experiment was adopted to reveal the changes of cadmium absorption and free amino acids in two castor varieties under the stress gradient of Cd. The main conclusions are obtained as follows:

(1) Compared with the control, there was no significant decrease for the biomasses yield of both castor varieties seedlings growing in the solutions spiked with 1, and 2 $mg \cdot L^{-1}$ Cd, while the biomasses were significantly inhibited by high concentration of Cd stress (5 $mg \cdot L^{-1}$), Zibo-9 showed higher tolerance and absorption ability to Cd.
(2) The majority of the free amino acid detected were found to alter in response to Cd stress, However, there was no significant difference in the concentrations of total free amino acids of Zibo-3 between the Cd treatments, and low dose of Cd addition promoted the secretion of amino acids in Zibo-9, while high dose inhibited it. A higher accumulation fraction of Glu and Asp in Zibo-9 may be associated with the higher Cd tolerance and Cd accumulation in Zibo-9 than in Zibo-3.

ACKNOWLEDGEMENTS

This research was financially supported by the National Natural Science Foundation of China (No. 41803018), Youth Science and Technology Talent Growth Project of Education Department of Guizhou Province (KY [2018] 294), and PhD Research Startup Foundation of Guiyang University (GYU-ZRD [2018] 008).

REFERENCES

Buscaroli, A. (2017). An overview of indexes to evaluate terrestrial plants for phytoremediation purposes (Review). Ecol. Indic. 82, 367–380.

Christopher, S. C. (2000). Phytochelatin biosynthesis and function in heavy metal detoxification. Curr. Opin. Plant Biol. 3, 211–216.

Kataria, S., Baghel, L., Dubey, A., et al. (2015). Effect of cadmium on growth, nitrogen metabolism, photosynthesis and yield of soybean. Inter. J. Trop. Agr. 33, 993–1001.

Khan, M. M., Islam, E., Irem, S., et al. (2018). Pb-induced phytotoxicity in para grass (*Brachiaria mutica*) and Castor bean (*Ricinus communis* L.): Antioxidant and ultrastructural studies. Chemosphere. 200, 257–265.

Kushwaha, A., Rani, R., Kumar, S., et al. (2016). Heavy metal detoxification and tolerance mechanisms in plants: Implications for phytoremediation. Environ. Rev. 24, 39–51.

Mahar, A., Wang, P., Ali, A., et al. (2016). Challenges and opportunities in the phytoremediation of heavy metals contaminated soils: A review. Ecotox. Environ. Safe. 126, 111–121.

Meng, S., Li, S., Li, Y., et al. (2016). Nitrate and ammonium contribute to the distinct nitrogen metabolism of *Populus simonii* during moderate salt Stress. Plos One, 11(3), e0150354.

Sangwan, P., Kumar, V., Gulati, D., et al. (2015). Interactive effects of salicylic acid on enzymes of nitrogen metabolism in clusterbean (*Cyamopsis tetragonoloba* L.) under chromium (VI) toxicity. Biocatal. Agr. Biotech. 4(3), 309–314.

Sarwar, N., Imran, M., Shaheen, M. R., et al. (2017). Phytoremediation strategies for soils contaminated with heavy metals: modifications and future perspectives, Chemosphere. 171, 710–721.

Seneviratne, M., Rajakaruna, N., Rizwan, M., et al. (2019). Heavy metal-induced oxidative stress on seed germination and seedling development: a critical review. Environ. Geochem. Hlth. 41(3), 1635.

Sierra, B., Guerrero, J. M., Sokolski, S. (2021). Phytoremediation of heavy meta1s in tropical soils an overview. Sustainability. 13(5), 2574.
Sytar, O., Kumar, A., Latowski, D., et al. (2013). Heavy metal-induced oxidative damage, defense reactions, and detoxification mechanisms in plants. Acta Physiol. Plant. 35, 985–999.
Zafari, S., Sharifi, M., Ahmadian, C. N., et al. (2016). Modulation of Pb-induced stress in Prosopis shoots through an interconnected network of signaling molecules, phenolic compounds and amino acids. Plant Physiol. Bioch. 99, 11–20.
Zemanová, V., Pavlík, M., Pavlíková, D., et al. (2015). Responses to Cd stress in two Noccaea species (*Noccaea praecox* and *Noccaea caerulescens*) originating from two contaminated sites in Mezica, Slovenia and Redlschlag, Austria. Arch. Environ. Con. Tox. 70, 1–11.
Zhang, H. Z., Guo, Q. J., Yang, J. X., et al. (2015). Subcellular cadmium distribution and antioxidant enzymatic activities in the leaves of two castor (*Ricinus communis* L.) cultivars exhibit differences in Cd accumulation. Ecotox. Environ. Safe. 120, 184–192.

Advances in Applied Chemistry and Industrial Catalysis – Saikia (Ed.)

Study on preparation of C4 alkenes by ethanol coupling

Zhongzheng Wang
College of Horticulture and Landscape, Tianjin Agricultural University, Tianjin, China

Xin Zhang & Yi Zheng
College of Food Science and Bioengineering, Tianjin Agricultural University, Tianjin, China

Hong Fang*
College of Basic Sciences, Tianjin Agricultural University, Tianjin, China

ABSTRACT: The catalyst and temperature in the production of C4 olefins by ethanol coupling are the core factors affecting the yield of C4 olefins. Therefore, we need to explore the process conditions for preparing C4 olefins by the catalytic coupling of ethanol. We construct a multivariable linear regression model and perform a heteroscedasticity White test, multicollinearity VIF test, and t-test. The linear regression equations of each dependent variable on ethanol conversion rate and C4 olefin selectivity were obtained. The ethanol conversion rate and C4 olefin selectivity were affected by different catalyst combinations and the temperature was quantitatively analyzed according to the regression coefficients.

1 INTRODUCTION

Ethanol molecules can prepare C4 olefins with excellent application prospects and economic benefits. C4 olefins, as necessary chemical raw materials, have received extensive attention at home and abroad, and have been widely used in the production of chemical products and pharmaceutical intermediates. Therefore, we need to explore the process conditions for preparing C4 olefins by the catalytic coupling of ethanol. In the reaction of ethanol coupling to produce C4 olefins, it is necessary to determine the effect of catalyst combination, and temperature on the yield of C4 olefins. We first select three factors that affect the catalyst combination, namely Co loading, Co/SiO_2 and HAP charging ratio, ethanol concentration, and temperature. As independent variables, ethanol conversion rate and C4 olefin selectivity were used as dependent variables. Through the analysis of references, we established a multiple linear regression model, obtained the linear regression equations of their variables on ethanol conversion and C4 olefin selectivity, and carried out a heteroscedasticity test and t-test.

2 EXPLORING THE INFLUENCE OF AN INDEX ON TWO DEPENDENT VARIABLES BASED ON A MULTIVARIABLE LINEAR REGRESSION MODEL

2.1 *Data processing for A and B loading methods*

The data of this work comes from question B of the 2021 China Higher Education Association CupNational College Students Mathematical Contest in Modeling.

*Corresponding Author: fanghong681019@126.com

DOI 10.1201/9781003308553-33

By consulting the literature, we know that SiO_2 alone has no activity to catalyze ethanol (Lu 2018). Therefore, we will remove the data related to silica.

First, consider using Spearman's rank correlation coefficient to explore the relationship between temperature and ethanol conversion rate and the relationship between temperature and C4 olefin selectivity in the two charging modes A and B, that is, to find the two charging methods in A and B, respectively. In this way, the correlation coefficient between temperature and ethanol conversion rate and the correlation coefficient between temperature and C4 olefin conversion rate. Quantitative analysis shows whether the difference in charging affects the temperature and ethanol conversion rate and whether temperature and C4 olefin selectivity.

Spearman's rank correlation coefficient, Used to reflect the degree of correlation between two ordinal or hierarchical variables. When calculating Spearman's correlation coefficient, it is required to rank the variable value first. After the measured values of the variables x and y of the two paired measurements are organized, if the rank variables have no results after sorting, the calculation formula of Spearman's correlation coefficient Rs is:

$$R_s = 1 - \frac{6\sum_{i=1}^{n} d_i^2}{n(n^2-1)}$$

where $d_i = x_i - y_i (i = 1, 2, \cdots, n)$.

It is calculated that the correlation coefficients between the temperature and the conversion rate of ethanol under the two charging modes A and B are 0.7798 and 0.865, respectively, and the correlation coefficients between the temperature and the selectivity of C4 olefins under the two charging modes A and B are 0.664 and 0.9255, respectively. Because these two pairs of correlation coefficients are both positive correlation values, and both are within the range of solid correlation coefficients, it can be analyzed that the difference in the charge does not affect the conversion rate of temperature and ethanol, and the selectivity of temperature and C4 olefins.

2.2 *Establishment of the model*

To explore the influence of different catalyst combinations and temperatures on the ethanol conversion rate and the selectivity of C4 olefins, it is understood that the factors that affect the catalyst combination during the preparation process are: Co loading, Co/SiO_2, and HAP charging ratio, and ethanol concentration. Through the above step research and analysis, it is found that the loading methods of A and B do not affect the dependent variable, so the data in Annex 1 can be integrated and analyzed. The overall situation of the indicators of this model is introduced in Table 1:

Table 1. Overview of indicators.

Quantitative Target	Dependent variables	Ethanol Conversion Rate (g_1)
		C4 Olefin Selectivity (g_2)
	Independent variables	Co load (h_1)
		Co/SiO_2 and HAP Charging Ratio (h_2)
		Ethanol Concentration (h_3)
		Temperature (h_4)

$$g_i = \beta_0 + \beta_1 h_1 + \beta_2 h_2 + \beta_3 h_3 + \beta_4 h_4 + \mu$$

Where $i = 1, 2$ and μ is an unobservable and completely random disturbance term.

2.3 *Model solution for the influence of quantitative targets on ethanol conversion rate*

2.3.1 *Based on the OLS regression model*

First, the joint significance test of the regression coefficients before the four independent variables shows that $p = 0.0001 < 0.05$ (Qing 2019). Therefore, under the 95% confidence interval, the null hypothesis that β_i is all 0 is rejected and β_i is not all 0.

The regression results are as follows:

Table 2. Regression analysis results based on OLS.

Ethanol conversion rate	Coef.	Std.Err.	t	P>|t|	[95% Conf.	Interval]
Co load	1.9104	1.0519	1.82	0.072	−0.1745	3.9953
Co/SiO_2 and HAP Charging Ratio	−1.3932	4.6672	−0.30	0.766	−10.6435	7.8570
Ethanol Concentration	−13.9202	2.3606	−5.90	0.000	−18.5988	−9.2417
Temperature	0.3316	0.0231	14.34	0.000	0.2858	0.3775
cons	−63.3375	9.5716	−6.62	0.000	−82.3081	−44.3670

The t-test is performed on the obtained regression coefficient β_i. From the results of the above table, it can be seen that the h_1, h_2 variable is not significant, and the confidence interval contains all zeros. And SSR = 40901.9263, SSE = 17999.9749, SST = 58901.901. According:

$$R^2 = 1 - \frac{SSE}{SST}$$

$$SSE = \sum_{i=1}^{n} \left(Y_i - \hat{Y}_i\right)^2$$

$$R^2_{adjusted} = 1 - \frac{SSE/(n-k-1)}{SST/(n-1)}$$

(k is the number of independent variables)

$R^2 = 0.6944$, $R^2_{adjusted} = 0.6832$, At the same time, the more independent variables we introduce, the greater the goodness of fit. But our regression is explanatory, and the requirement for the square of R is not very high. We aim to focus on the overall significance of the model and the statistical significance of the independent variables. And because the square of R and the square of adjusted R is not much different, it is preliminarily considered that there is no problem of multicollinearity.

So the OLS model obviously cannot meet our requirements. Because of the above problems, we plan to perform the heteroscedasticity White test and multicollinearity VIF test on the data.

2.3.2 *White test*

To determine the result more accurately, we perform a White test on the OLS model and get that $P = 0.0024 < 0.05$, So we can reject the null hypothesis that there is heteroscedasticity (Liu 2012).

2.3.3 *Use the OLS regression model and robust standard error to correct heteroscedasticity*

It can be seen that the P-value h_2 has been reduced, and the heteroscedasticity problem has been better solved.

2.3.4 *VIF test of multicollinearity*

To test the existence of multicollinearity, we use the variance inflation factor VIF

$$VIF_i = \frac{1}{1 - R^2_{1-k/i}}$$

Table 3. Regression analysis results based on OLS and robust standard errors.

Ethanol conversion rate	Coef.	Std.Err.	t	P>|t|	[95% Conf. Interval]	
Co load	1.9104	1.2926	1.48	0.142	−0.6515	4.4723
Co/SiO_2 and HAP Charging Ratio	−1.3932	3.1426	−0.44	0.658	−7.6217	4.8352
Ethanol Concentration	−13.9202	1.9750	−7.05	0.000	−17.8347	−10.0057
Temperature	0.3316	0.0245	13.52	0.000	0.28301	0.3802
cons	−63.3375	8.7752	−7.22	0.000	−80.7298	−45.9453

$R^2_{1-k/i}$ is to use the i-th independent variable as the dependent variable, and regress on the remaining independent variables to get the goodness of fit. Defining the regression model is VIF = max{VIF, VIF, VIF, VIF, VIF}, if VIF>10, it can be considered that there is multicollinearity(Ge 2011).

The test results are as follows:

Table 4. VIF inspection results.

Variables	VIF	1/VIF
Co load	1.02	0.979934
Co/SiO_2 and HAP Charging Ratio	1.00	0.999942
Ethanol Concentration	1.02	0.978679
Temperature	1.00	0.998443
The average value of VIF	1.01	

From this, we see that the mean value of VIF = 1.01<10, so it is considered that there is no multicollinearity.

2.3.5 *Linear regression equation*

Through the above steps, a linear regression model of the influence of the quantitative target on the ethanol conversion rate is obtained (Watada 1988):

$$g_1 = -13.9202h_3 + 0.3316h_4 - 63.3375$$

2.4 *Model solution for the influence of quantitative targets on the selectivity of C4 olefins*

2.4.1 *Based on the OLS regression model*

First, the joint significance test of the regression coefficients before the four independent variables shows that $P = 0.0001 < 0.05$. Therefore, under the 95% confidence interval, the null hypothesis that β_i is all 0 is rejected and β_i is not all 0.

The regression results are shown in table 5.

The t-test is performed on the obtained regression coefficient β_i. From the results of the above table, it can be seen that the h_2 variable is not significant, SSE = 9720.033, SST = 20691.0106. According to the above formula: $R^2 = 0.5302$, $R^2_{adjusted} = 0.5130$, the same reason is that the difference between the square of R and the square of Rafter adjustment is not significant, so it is preliminarily considered that there is no multicollinearity problem.

Therefore, the OLS model can meet the requirements, and the data is further tested by the white test of heteroscedasticity and the VIF test of multicollinearity.

2.4.2 *White test*

To determine the result more accurately, we perform a White test on the OLS model and get that $P = 0.7291 > 0.05$, So we can reject the null hypothesis that there is heteroscedasticity.

Table 5. Regression analysis results based on OLS.

Ethanol conversion rate	Coef.	Std.Err.	t	P>|t|	[95% Conf. Interval]	
Co load	−1.7020	0.7730	−2.20	0.030	−3.2341	−0.1700
Co/SiO_2 and HAP Charging Ratio	5.9396	3.4297	1.73	0.086	−0.8580	12.7371
Ethanol Concentration	−1.5755	1.7347	−0.91	0.366	−5.0136	1.8626
Temperature	0.1799	0.0170	10.59	0.000	0.1462	0.2136
cons	−41.5250	7.0336	−5.90	0.000	−55.4654	−27.5845

2.4.3 *VIF test of multicollinearity*
The test results are as follows:

Table 6. VIF inspection results.

Variables	VIF	1/VIF
Co load	1.02	0.979934
Co/SiO_2 and HAP Charging Ratio	1.00	0.999942
Ethanol Concentration	1.02	0.978679
Temperature	1.00	0.998443
The average value of VIF	1.01	

From this, we see that the mean value of VIF = 1.01<10, so it is considered that there is no multicollinearity.

2.4.4 *Linear regression equation*
Through the above steps, a linear regression model of the influence of the quantitative target on the ethanol conversion rate is obtained:

$$g_2 = -1.7020h_1 + 0.1799h_4 - 41.5250$$

3 CONCLUSION

The regression coefficient in the regression equation of this question represents the parameter of the degree of h's influence on g. The larger the regression coefficient, the greater the influence of h on g. The positive regression coefficient indicates that g increases with the increase of h, and the negative regression coefficient indicates that g increases with h.

3.1 *Analysis of the effect of quantitative targets on ethanol conversion rate*

$$g_1 = -13.9202h_3 + 0.3316h_4 - 63.3375$$

According to the linear regression equation, the order of the independent variable index that affects the degree of ethanol conversion is $h_3 > h_4$, and the ethanol conversion rate shows an upward trend with the increase of temperature and a downward trend with the addition of ethanol concentration.

3.2 *Analysis of the effect of quantitative targets on the selectivity of C4 olefins*

$$g_2 = -1.7020h_1 + 0.1799h_4 - 41.5250$$

According to the linear regression equation, the order of the independent variable index that affects the degree of C4 olefin selectivity is $h_1 > h_4$, and the selectivity of C4 olefin presents an upward trend with increasing temperature and a decreasing trend with increasing Co loading.

REFERENCES

Ge Jinxin. (2011). Research on the selection of ratios in the Distress Prediction of Listed Companies[D]. Nanjing University.

Liu M. (2012). Some Application Problems of White Heteroscedasticity Test[J]. Statistics & Information Forum.

Lu Sharpie. (2018). Preparation of butanol and C4 olefins from ethanol [D]. Dalian University of Technology.

Qing, Yang P L, Yuan Q, et al. (2019). Mobile Phone User Behaviour Prediction Base on Multivariable Linear Regression Model[C]//

Watada H T. (1988). Possibilistic linear systems and their application to the linear regression model[J]. Fuzzy Sets and Systems.

Advances in Applied Chemistry and Industrial Catalysis – Saikia (Ed.)

Experimental research of mercury thermal desorption in high-mercury gold separation residue

R.Y. Li
Shanxi Lipu Innovation Technology Co., Ltd, Taiyuan, Shanxi, China

X.X. Gao
School of Environmental Science and Engineering, Taiyuan University of Technology, Taiyuan, Shanxi, China

X.H. Liu & N. Cao
Shanxi Lipu Innovation Technology Co., Ltd, Taiyuan, Shanxi, China

X. Kong*
School of Environmental Science and Engineering, Taiyuan University of Technology, Taiyuan, Shanxi, China

ABSTRACT: The high mercury concentration in gold separation residue is a main limiting factor to realizing the collaborative disposal of gold separation residue in cement kiln. In this study, the horizontal tubular furnace system was used as the heat source to simulate the high-temperature flue gas of a cement kiln, meanwhile, the removal of mercury in gold separation residue by thermal desorption was studied from influence factors such as temperature, time, flow rate and atmosphere. Combining with the experimental results and the actual operating conditions of the cement kiln, it is determined that the optimal temperature for thermal desorption of high concentration mercury pollutants (640 mg/kg) in gold separation residue is 300°C, the optimal time is 20 min, the flow rate is 300 ml/min, pH is 9, and the mercury removal rate is 97.64%.

1 INTRODUCTION

Gold has a high economic value, which can be separated by mercury mixing, cyanidation, and other methods (Schmidt 2012). Mercury mixing is the most commonly used method for gold separation because of its low technical requirements and simple operation process (Cordy et al. 2011). However, a large amount of gold separation residue containing a high concentration of mercury was produced, which posed a serious threat to the surrounding ecological environment and human health (Nyanza et al. 2021; Tabelin et al. 2020). The common treatment methods of gold separation residue include landfill, harmless disposal, and resource utilization, in which the collaborative disposal of cement kiln had attracted people's attention because of its advantages such as large treatment capacity, small secondary pollution, harmlessness, and recycling (Baidya & Ghosh 2020; Jian et al. 2020). However, the high concentration of mercury in gold separation residue has become a main factor limiting collaborative disposal, so it is necessary to pretreat the gold separation residue for mercury removal.

The common methods of mercury removal include a physical method, chemical method, and biological method (Wang et al. 2020; Xing et al. 2020), in which thermal desorption was widely used because it can quickly remove and recover mercury. Combined with the

*Corresponding Author: 476288645@qq.com

DOI 10.1201/9781003308553-34

conditions of the cement kiln, the high-temperature flue gas of the cement kiln can be used as the heat source to thermally desorb the high-mercury gold separation residue, and then carry out the collaborative disposal of the cement kiln to realize the resource utilization of the waste residue.

Given this, this paper used thermal desorption technology to simulate the flue gas temperature of a cement kiln under laboratory conditions to study the thermal desorption removal of mercury in gold separation residue, to solve the problem of high concentration mercury limiting the collaborative disposal of cement kiln, and provide technical reference for the collaborative disposal of high mercury-gold separation residue in cement kiln.

2 EXPERIMENTAL MATERIALS AND METHODS

2.1 *Description of specimens*

The gold separation residue used in this experiment was taken from the gold spot of mercury mixing method in a county of Shanxi Province, the physical and chemical analysis results showed that the gold separation residue is acidic, the mercury concentration is 640mg/kg and the main mineral components are SiO_2 (quartz), $CaSO_4 \cdot 2H_2O$ (crystalline calcium sulfate, commonly known as raw gypsum) and $CaAlSi_2O_8 \cdot 4H_2O$ (anorthite), which can be used as raw materials of cement production.

2.2 *Experimental method*

The thermal desorption experiment of gold separation residue was carried out in a horizontal tubular furnace system. The whole system consists of a gas cylinder, mass flowmeter, temperature controller, horizontal tubular furnace, thermocouple, and flue gas absorption device. The sample was calcined in a corundum boat, the nitrogen flow rate was adjusted by a flowmeter, the heating temperature and time were controlled by a temperature controller, and the gaseous mercury in the flue gas was absorbed by the Ontario method. The experimental device is shown in Figure 1, and the DMA80 mercury analyzer was used to determine the mercury concentration of gold separation residue before and after pyrolysis.

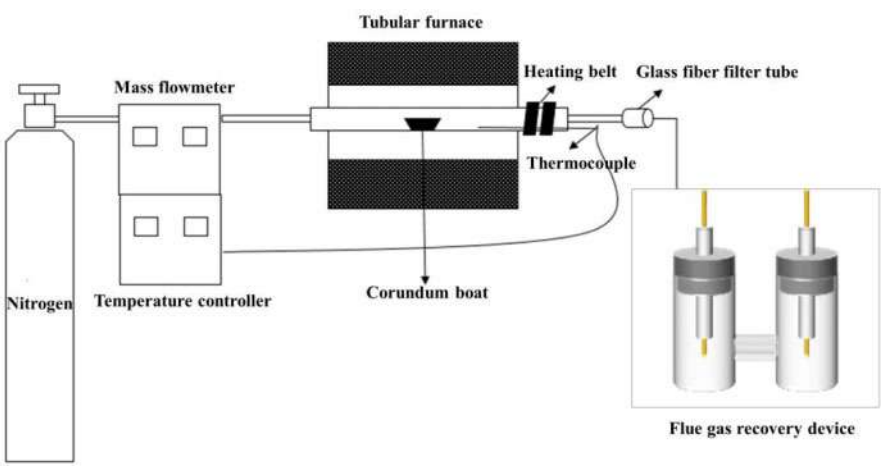

Figure 1. Experimental device diagram of thermal desorption and mercury removal.

3 RESULTS AND DISCUSSIONS

3.1 *Effect of temperature and time on mercury removal*

The heating temperature ranged from 200°C to 800°C, and the gold separation residue was subjected to constant temperature thermal desorption from 5 min to 30 min to obtain the removal effect of mercury. As shown in Figure 2, the mercury removal rate changed significantly at 200°C and 300°C within 5 min to 20 min, and the concentration of mercury after pyrolysis at 300°C and 20 min reduced to 61.805 mg/kg, with the removal rate reached 90.79%, which proved that time was an important factor affecting the effect of mercury thermal desorption. The pyrolysis effect was obvious in the first 10 minutes at 400°C, and the thermal desorption effect was not obvious with the extension of time, which was similar to Sierra's study (Sierra et al. 2016). Nearly 80% of the mercury was released at 280°C, and the rest of which was released when the temperature was added from 360°C to 560°C. Between 500°C to 800°C, the mercury concentration after thermal desorption was less than 5 mg/kg, indicating that temperature was also the main factor affecting the thermal desorption effect, which is consistent with the research results of Park(Park et al. 2020), who proved that the heat treatment process is endothermic, and the increase of temperature will promote the removal of mercury in soil. Combined with the operating conditions of the cement kiln, 300°C and 20 min were selected as the optimum temperature and time of thermal desorption.

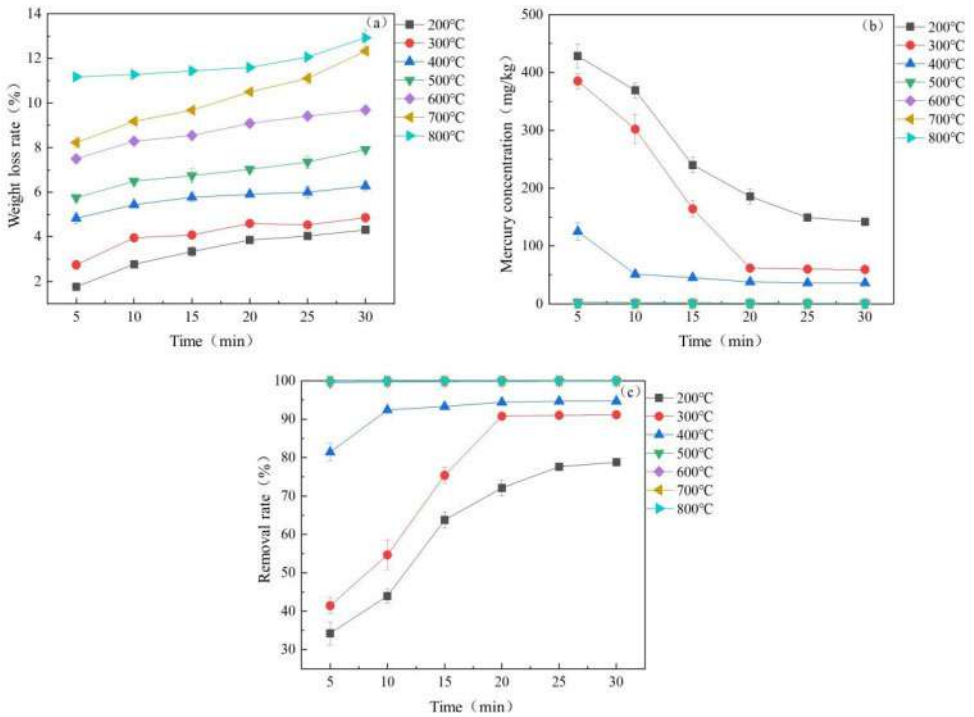

Figure 2. Weight loss rate (a), mercury concentration (b), and mercury removal rate (c) of gold separation residue during the pyrolysis experimental process.

3.2 *Effect of flow rate on mercury removal*

At 300°C and 20 min, the mass flowmeter was used to control the flow rate of high-purity nitrogen to explore the effect of flow rate on mercury thermal desorption of gold separation residue, Figure 3 showed the removal effect of mercury.

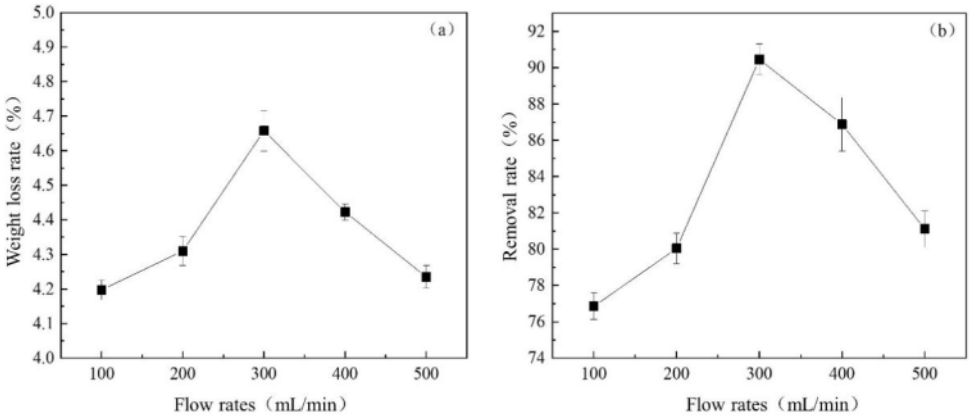

Figure 3. Weight loss rate (a) and mercury removal rate (b) of gold separation residue at different flow rates.

At 300°C and 20 min, with the increase of flow rate, the weight loss rate and removal rate increased first and then decreased, meanwhile, the removal effect changed significantly. At the flow rate of 300 ml/min, the Weight loss rate and mercury removal rate of gold separation residue reached the maximum value, with a concentration of mercury after thermal desorption of 64.05 mg/kg and the removal rate of more than 90%. And then the flow rate continued to increase and the desorption effect of mercury decreased. The results showed that 300 ml/min was the optimum flow rate condition.

3.3 *Effect of atmosphere on mercury removal*

The pH of the sample used in this experiment was 2.36, because of the alkaline atmosphere in the cement kiln, the pH of the sample needed to be adjusted. 1 mol/L NaOH solution was used to adjust the pH of gold separation residue to 7, 8, 9, 10, 11, 12, and 13 in this experiment, and the adjusted samples with different pH were thermally desorbed at 300°C and flow rate of 300 ml/min for 20 min at, Figure 4 shows the removal effect of samples at different pH.

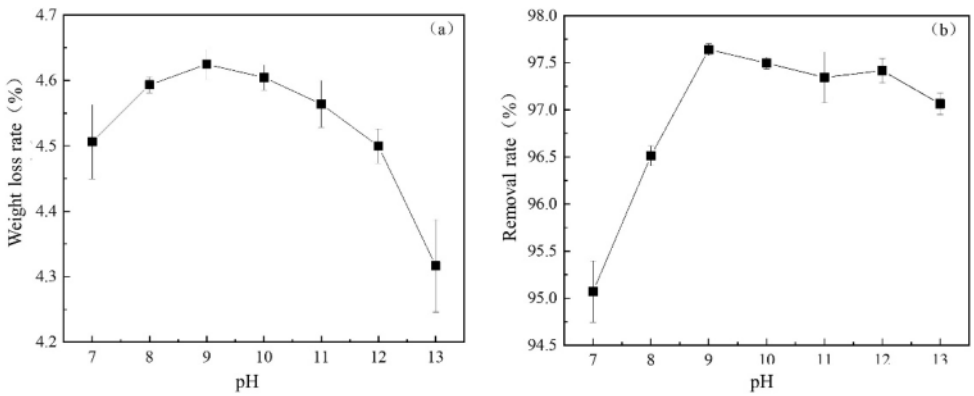

Figure 4. Weight loss rate (a) and mercury removal rate (b) of gold separation residue at different pH.

Between pH = 7 to 9, the removal rate of mercury increased obviously, when pH = 9, the mercury concentration after thermal desorption was 15.83 mg/kg, and the removal rate reached the highest of 97.64%. When pH was greater than 9, the mercury removal effect did not change significantly,

indicating that the alkaline atmosphere can improve the thermal desorption effect of mercury. Mineral components analysis of gold separation residue after thermal desorption at pH = 9 is shown in Figure 5. The main components are SiO_2 and $CaSO_4$, which can be used as alternative raw materials for cement production.

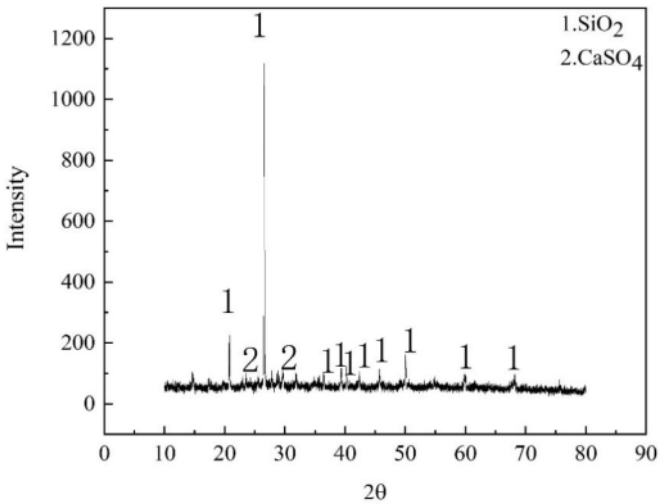

Figure 5. XRD composition of gold separation residue sample after thermal desorption at pH = 9.

4 CONCLUSION

The collaborative disposal of cement kiln can realize the harmlessness and resources recycling of gold separation residue, but the high mercury concentration in gold separation residue is a main limiting factor for which. Therefore, mercury removal needs to be carried out before it enters the kiln. By simulating the waste heat of high-temperature flue gas of a cement kiln, this experiment explored the mercury thermal desorption conditions of high-mercury gold separation residue. The results showed that the mercury removal of high-mercury gold separation residue can be realized by controlling the thermal desorption time for 20 min, the induced air temperature of the cement kiln at 300°C, flow rate at 300 ml/min, and pH = 9. After the removal of mercury, the mercury concentration reduced to 15.83 mg/kg and the removal rate reached 97.64%, which meets the entry requirements of cement kiln. Meanwhile, the main mineral components of the gold separation residue after mercury removal were SiO_2 and $CaSO_4$, which can replace some raw materials in cement production, and the resource disposal of high-mercury gold separation residue can be realized.

ACKNOWLEDGMENTS

This work was financially supported by the Key R & D projects in Shanxi Province (201903D321076)

REFERENCES

Baidya, R., Ghosh, S.K. (2020). Co-processing of industrial trade rejects in cement plant. Waste Manage. Res. 38 (12), 1314–1320.

Cordy, P., Veiga, M.M., Salih, I., Al-Saadi, S., Console, S., Garcia, O., Alberto Mesa, L., Velasquez-Lopez, P.C., Roeser, M. (2011). Mercury contamination from artisanal gold mining in Antioquia, Colombia: The world's highest per capita mercury pollution. Sci. Total Environ. 410, 154–160.

Jian, S., Gao, W., Lv, Y., Tan, H., Li, X., Li, B., Huang, W. (2020). Potential utilization of copper tailings in the preparation of low heat cement clinker. Construction and Building Materials 252.

Nyanza, E.C., Bernier, F.P., Martin, J.W., Manyama, M., Hatfield, J., Dewey, D. (2021). Effects of prenatal exposure and co-exposure to metallic or metalloid elements on early infant neurodevelopmental outcomes in areas with small-scale gold mining activities in Northern Tanzania. Environ. Int. 149.

Park, M.-o., Kim, M.-H., Hong, Y. (2020). The kinetics of mercury vaporization in soil during low-temperature thermal treatment. Geoderma 363.

Schmidt, C.W. (2012). QUICKSILVER & GOLD: Mercury Pollution from Artisanal and Small-Scale Gold Mining. Environ. Health Perspect. 120 (11), A424–A429.

Sierra, M.J., Millan, R., Lopez, F.A., Alguacil, F.J., Canadas, I. (2016). Sustainable remediation of mercury contaminated soils by thermal desorption. Environmental Science and Pollution Research 23 (5), 4898–4907.

Tabelin, C.B., Silwamba, M., Paglinawan, F.C., Mondejar, A.J.S., Ho Gia, D., Resabal, V.J., Opiso, E.M., Igarashi, T., Tomiyama, S., Ito, M., Hiroyoshi, N., Villacorte-Tabelin, M. (2020). Solid-phase partitioning and release-retention mechanisms of copper, lead, zinc and arsenic in soils impacted by artisanal and small-scale gold mining (ASGM) activities. Chemosphere 260.

Wang, L.W., Li, X.R., Tsang, D.C.W., Jin, F., Hou, D.Y. (2020). Green remediation of Cd and Hg contaminated soil using humic acid modified montmorillonite: Immobilization performance under accelerated ageing conditions. J. Hazard. Mater. 387.

Xing, Y., Wang, J.X., Shaheen, S.M., Feng, X.B., Chen, Z., Zhang, H., Rinklebe, J. (2020). Mitigation of mercury accumulation in rice using rice hull-derived biochar as soil amendment: A field investigation. J. Hazard. Mater. 388.

Advances in Applied Chemistry and Industrial Catalysis – Saikia (Ed.)

Migration and transformation of heavy metals during pyrolysis of printing and dyeing sludge

Ruihua Zhao, Yang Yu, Juan Chen* & Yun Luo
School of Energy and Power Engineering, Shandong University, Jinan, China

ABSTRACT: The effects of pyrolysis conditions and sludge water content on the distribution of heavy metals, Cr and Cu, in the pyrolysis residues of printing and dyeing sludge were studied through the horizontal tube furnace pyrolysis experiments, and the release trend of heavy metals in the pyrolysis residues was discussed. Experiments show that under N_2 atmosphere, the release rate of Cr in the sludge is basically not released with the increase of temperature, but the form of chromium in the printing and dyeing sludge can be converted to more stable Cr^{3+} due to the reducing atmosphere provided by it. In the simulated dry flue gas atmosphere containing oxygen, the chromium in the printing and dyeing sludge was oxidized, so that the release was promoted. The copper in the printing and dyeing sludge has a very low pyrolysis volatilization under N_2 atmosphere, while in dry flue gas, the CO_2 generated by CO_2 pyrolysis reduces Cu to form CuCl, which increases the release of copper. At the same time, the increase of sludge water content is conducive to the fixation of the two heavy metals in the coke. The inhibition of Cr release by water is mainly achieved by providing a reducing atmosphere; while for copper, water can promote the chlorine in the sludge to generate HCl, thereby reducing the Volatilization of CuCl.

1 INTRODUCTION

In China, population growth and the rapid development of urbanization have led to a surge in the number of sewage treatment plants, and the amount of sludge generated by cities and towns is also increasing. Printing and dyeing sludge is confirmed as a kind of hazardous waste containing harmful heavy metals, as well as organic matter and inorganic minerals, some of which can be recycled as energy materials. In the secondary utilization process, since the heavy metals such as Cu, Zn, Ni in the printing and dyeing sludge, it is highly toxic to the environment and cause great harm to the environment.

At present, there are three sludge treatment methods: sanitary landfill, composting, and incineration. Some problems of traditional treatment methods were exposed, such as secondary pollution, poor treatment effect, and inability to recover energy, which limit their application and development. The method by using high-temperature flue gas in coal-fired power plants to dispose sludge can not only kill pathogens in the sludge, but also retain heavy metals in the pyrolysis residue to a great extent. Furthermore, the generated pyrolysis residue also has a rich pore structure which can be used for preparation of adsorbent material. Combustible gases such as H_2 and CO generated by further sludge pyrolysis could by recycled and reused. Sludge has high moisture content with gigantic volume. As sludge is utilized as a resource, drying treatment is often required to facilitate storage management and transportation. The energy consumption is dynamic due to the moisture range of sludge removal is different. When the sludge moisture is from 80% to 60% and below 35%, it is low energy consumption. However, it is viscous sludge which is formidable to treatment,

*Corresponding Author: juanchen@sdu.edu.cn

DOI 10.1201/9781003308553-35

and the energy consumption of drying increases sharply as the sludge moisture is 60-35%. The presence of H_2O has a beneficial effect on the preparation of adsorbent materials and combustible gases from pyrolysis sludge. It could promote the formation of the pore structure charcoal and generate more combustible gases such as H_2. Therefore, the direct pyrolysis of wet sludge helps to reduce the energy consumed by drying and dehydration in the sludge pretreatment process and facilitate the subsequent utilization of pyrolysis products.

In this work, the effect of pyrolysis conditions and sludge moisture on the speciation distribution of two heavy metals (Cr and Cu) was deeply investigated. In the pyrolysis residue of printing and dyeing sludge and release trends of heavy metals were studied through the pyrolysis experiment of a horizontal tube furnace. It provides theoretical guidance for the harmless pyrolysis of printing and dyeing sludge.

2 EXPERIMENTAL RAW MATERIALS AND PYROLYSIS EXPERIMENTS

2.1 *Experimental raw materials*

The sludge used in the experiment was obtained from the compressed and dehydrated sludge of the sewage treatment plant of a large-scale printing and dyeing plant in Jinan, and the moisture content was about 86%. After the recovered sludge was ventilated and dried in a cool place, it was placed in a drying oven at 80°C for 48 hours. After dried, it was ground to 45∼105μm for use. The industrial analysis and elemental analysis of sludge were shown in Table 1.

Table 1. Proximate and ultimate analysis of dyeing sludge.

Proximate analysis/% (mass, ad)				Ultimate analysis/% (mass, ad)					Cr	Cu
M	V	A	FC	C	H	O*	N	S	(mg/kg)	(mg/kg)
3.34	34.11	53.18	9.36	39.27	3.60	51.09	4.02	2.02	1002.73	1031.72

* by difference.

2.2 *Horizontal tube furnace pyrolysis experiment*

The sludge pyrolysis experiments were carried out on the settling furnace test bench. Before each experiment, the ground sludge was placed in an oven at 80°C for constant temperature drying for 12 hours. The pyrolysis temperature was set at 700°C, 800°C, 900°C, and 1000°C, respectively. The pyrolysis experiments in N_2, simulated dry flue gas (CO_2 15%, O_2 3.5%/N_2), and simulated dry flue gas atmosphere at 900°C were carried out respectively. The pyrolysis experiments with sludge moisture of 0%, 40%, 50%, and 60% were carried out to explore the effect of different working conditions and sludge moisture on the migration and transformation of Cr and Cu. The samples after the experiment were processed by microwave digestion, and the concentration of each heavy metal was detected by ICP-AES.

The relative enrichment factor RE (relatively enrichment factor) was defined to represent the enrichment effect of heavy metals in char samples under different pyrolysis conditions.

$$RE = \frac{C_{char}}{C_s} \times Y_{char} \times 100\% \tag{1}$$

Where C_{char} is the concentration of heavy metals in the coke sample, C_s is the concentration of heavy metals in the sludge sample, and Y_{char} is the ratio of the mass of the coke sample to the experimental sludge after the experiment.

3 RESULTS AND DISCUSSION

3.1 *Effect of pyrolysis atmosphere on Cr and Cu release*

Figure 1 (a) showed the release of Cr after the sludge was pyrolyzed in N_2 and dry flue gas atmospheres. In different atmospheres, the release rules of heavy metal Cr in the process of sludge pyrolysis were different. Sludge pyrolysis made the organic matter in the sludge undergo thermochemical reactions such as thermal cracking and converted it into a partial reducing gas. In this atmosphere, the Cr in the sludge was reduced. Although the total amount of Cr in the sludge before and after pyrolysis rarely changed, it achieved a more toxic Cr^{6+} direction from Cr^{3+} conversion during the pyrolysis process in a nitrogen atmosphere. Compared with pyrolysis in the N_2 atmosphere, the release of Cr in dry flue gas increased significantly, and in the temperature range of 700–900°C, the release gradually increased with the pyrolysis temperature getting higher. The recovery was the lowest and the release was slightly inhibited at 1000°C. Because of the simulated dry flue gas atmosphere, oxygen played a major role. The presence of oxygen made the Cr in the sludge oxidize, and the Cr hexavalent compound is oxidized to Cr^{6+} which volatilization temperature was lower.

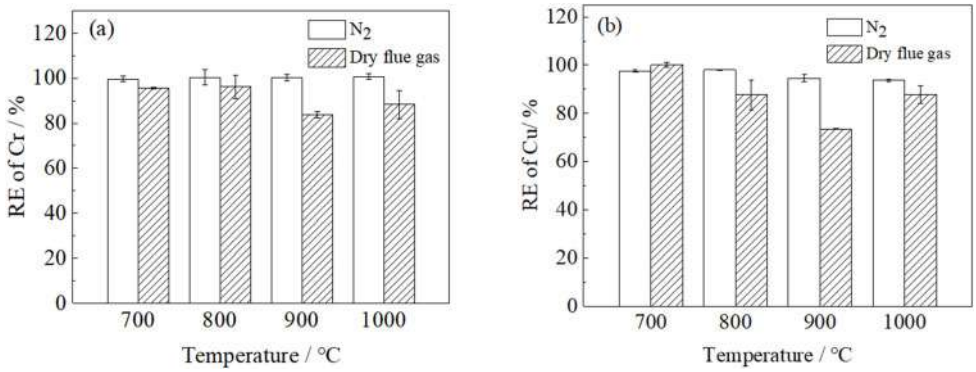

Figure 1. Enrichment rate of Cr (a) and Cu (b) in sludge pyrolysis under different atmosphere.

Figure 2 (b)showed the pyrolysis results of sludge in N_2 and dry flue gas atmosphere. It could be seen that with the increase of pyrolysis temperature, Cu volatilization in different atmospheres was various. Cu in nitrogen atmosphere hardly volatilized instead of that in dry flue gas at 700–900°C, while it was inhibited at 900-1000°C. The release part of Cu in the sludge was mainly in the form of copper chloride. In the N_2 atmosphere, the release of Cu increased with the increase of the pyrolysis temperature, but the effect was not obvious. Compared with the almost non-volatile nitrogen atmosphere, the Cu emission in dry flue gas got higher. This was because the CO generated by the reaction of CO_2 and the carbon in the sludge at high temperatures promoted the reduction of copper oxides. The stable CuO was reduced to Cu and Cu_2O. The chlorine in the sludge reacted with Cu^0 and began to generate CuCl gas and volatilized in large quantities at 900°C. When the pyrolysis temperature was 1000°C, the reduction of CuO in the sludge tended to develop towards the formation of Cu_2O, which greatly reduced the copper released in the form of CuCl and inhibited the release of Cu.

3.2 *Effect of sludge water content on heavy metal release*

As shown in Figure 3, the moisture in the sludge also affected on the volatilization of Cr and Cu. It could be seen that when the sludge with different moisture content was pyrolyzed, the higher the moisture content in the sludge, the less chromium was released. Because when the wet sludge was pyrolyzed at high temperature, the steam generated greatly increased the proportion of reducing

gases (H_2, CO) generated in the furnace, which promoted the reduction of Cr and converted it to a more stable Cr^{3+} form. Thus, the volatilization of Cr was inhibited. With the increase of sludge moisture content from 0 to 60%, the recovery of Cu in pyrolysis coke increased by 13.2%. This was because the sludge was mainly released into the flue gas as CuCl gas under the dry flue gas atmosphere of 900°C, and the increase of moisture promoted the reaction of H_2O with Cl in the sludge to generate HCl gas release which inhibited the release of Cu.

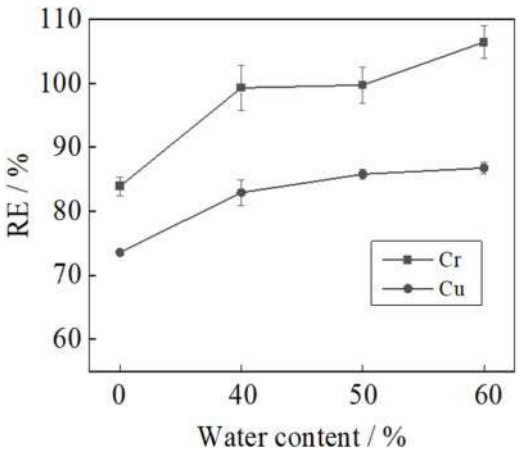

Figure 2. Enrichment rate of Cr and Cu during pyrolysis of sludge with different water content.

4 CONCLUSION

In this work, the effects of pyrolysis temperature, atmosphere, and sludge moisture content on the release characteristics of Cr and Cu during sludge pyrolysis were studied through the horizontal tube furnace experimental bench. The main conclusions were as follows:

(1) When the sludge was pyrolyzed in the N_2 atmosphere, Cr was hardly released. In the simulated dry flue gas atmosphere, the Cr in the sludge reacted with O_2 to generate more volatile Cr^{6+}, which led to an increase in the amount of Cr released with the increase of the pyrolysis temperature. When the printing and dyeing sludge was pyrolysis in the N_2 atmosphere, the Cr in the sludge was reduced to Cr^{3+} due to the reducing gas generated by the high temperature, which not only inhibited the volatilization but also reduced the biological toxicity of chromium in the sludge.

(2) The Cu in the printing and dyeing sludge is released in a small amount during pyrolysis in the N_2 atmosphere. However, in the dry flue gas, the release of Cu was significantly increased, and at 900°C, the recovery rate reached a minimum of 73.55%. This was closely related to the CO generated by the pyrolysis of CO_2 at high temperatures. At 900°C, the reduction of Cu^0 by CO began to generate CuCl gas, which leads to the release of a large amount of Cu. This temperatures should be avoided in the actual application process. When the pyrolysis temperature continued to increase to 1000°C, Cu_2O began to dominate the reduction reaction which inhibited the volatilization of Cu.

(3) During the pyrolysis process, the higher the moisture content of the sludge, the more conducive to the fixation of Cr and Cu in the sludge. As the sludge moisture content gradually increased from 0 to 60%, the RE of Cr increased from 83.88 to 99.70% and the RE of Cu increased from 73.55 to 86.76% during the pyrolysis of sludge. For Cr, the reducing gas generated by H_2O and CO_2 at high temperature promoted the reduction of Cr and fixed it in the coke. For Cu,

H_2O was more likely to form HCl with chlorine in sludge at high temperatures which reduced the release of CuCl. On the whole, the increase of sludge moisture content was conducive to the transformation of the heavy metals (Cr and Cu) to the direction of less toxicity and was also conducive to the inhibition.

ACKNOWLEDGMENTS

This work was financially supported by National Natural Science Foundation of China (51776112), the Shandong Provincial Natural Science Foundation, China (2018GGX104019) and Foshan research project of characteristic innovation of University Teachers (2020JNHB04).

REFERENCES

Abrile Mariana Guadalupe, Fiasconaro María Laura, Orecchia Daiana Soledad, et al. Utilization of sludge derived from landfill leachate treatment as a source of nutrients for the growth of Nicotiana alata L. Journal of Environmental Management. 2021;289:112488.

Chanaka Udayanga W. D., Veksha Andrei, Giannis Apostolos, et al. Fate and distribution of heavy metals during thermal processing of sewage sludge. Fuel. 2018;226:721–44.

Chou Baoxing. The Development Status and Challenges of Urban Sewage Treatment in China. Water & Wastewater Engineering. 2010;46(02):1–3.

Kasina Monika, Kajdas Bartłomiej, Michalik Marek. The leaching potential of sewage sludge and municipal waste incineration ashes in terms of landfill safety and potential reuse. Science of The Total Environment. 2021;791:148313.

Li Xiaoge, Pan Jing, Xi Danli, et al. Bioavailability and speciation analysis of heavy metals in textile dyeing sludge. Rock and Mineral Analysis. 2009;28(01):10–4.

Mahtab Mohd Salim, Farooqi Izharul Haq, Khursheed Anwar. Zero Fenton sludge discharge: a review on reuse approach during wastewater treatment by the advanced oxidation process. International Journal of Environmental Science and Technology. 2021.

Raj Abhay, Yadav Ashutosh, Arya Shashi, et al. Preparation, characterization and agri applications of biochar produced by pyrolysis of sewage sludge at different temperatures. Science of The Total Environment. 2021;795:148722.

Shen Boxiong, Guo Caixia, Wu Shunwei. Research progress of heavy trace metal migration during the incineration of sludge Power System Engineering. 2008(01):15-6+40.

Wu Qingrong, Zhang Xukun, Wang Gaomin. Adwances on low temperature drying technology of municipal sewage sludge. Environmental Engineering. 2017;35(03):127–31.

Xiong S., Zhang B., Jia X., et al., editors. Feasibility Study on the Pyrolysis Production for Hydrogen-Riched Fuel Gas from the Wet Sewage Sludge. 2009 3rd International Conference on Bioinformatics and Biomedical Engineering; 2009 11–13 June 2009.

Zhao Weifan, Dai Liang, Wang Gang, et al. Research progress in preparation and modification of heavy metal adsorbents for sludge biochar. Functional materials. 2020;51(11):11083-8+115.

Advances in Applied Chemistry and Industrial Catalysis – Saikia (Ed.)

Electrokinetic motion of a particle at PEG-dextran interface in a microchannel

Zewu Liu, Junyan Zhang & Yonxin Song*
Department of Marine Engineering, Dalian Maritime University, Dalian, China

ABSTRACT: The aqueous two-phase system (ATPS) composed of polymers is often used for the separation of cells and other biomolecules due to its compatibility with bioparticles. In this paper, an ATPS composed of 5% polyethylene glycol (PEG) and 11% dextran was used to study the electrokinetic (EK) movement of polystyrene particles at the interface. The results show that the EK velocities of particles at the ATPS interface both decrease with the increase in particle size. EK velocity of the droplet formed by one phase (PEG or dextran) in the other phase was investigated, indicating that the surface of the dextran droplet in the PEG-rich phase is negatively charged and the surface of the PEG droplet in the dextran-rich phase is positively charged. The experimental results provide a method for bioparticle separation based on different electrokinetic velocities at the ATPS interface.

1 INTRODUCTION

The aqueous two-phase system (ATPS) composed of polyethylene glycol (PEG) and dextran (DEX) is mainly used for cell culture (Han 2015, Teixeira 2019, Sinha 2000), as well as the separation of cells (Tsukamann 2009; Zimmermann et al. 2017), biomacromolecules (Asenjo & Andrews 2011; Chavez-santoscoy et al. 2010; Iqbal et al. 2016; Umakoshi et al. 1996), and particles in existing studies due to its ability to preserve the activity of biological substances. The use of ATPS in biomacromolecule separation is mainly to achieve the purpose of enrichment in a certain phase solution by the difference in the hydrophobicity of the substance and the two-phase solution. For example, Ki-Hwan Nam et al. used ATPS composed of PEG and dextran to enrich cells in the PEG phase by the difference in the hydrophobicity of the biphasic solution to dead and live Chinese hamster ovary cells, and dead cells were enriched in the interface (Nam et al. 2005). Masatoshi Tsukamoto et al. used a two-phase system consisting of PEG and dextran to separate polystyrene particles and whole blood cells according to their hydrophilicity (Tsukamoto et al. 2009). Mohammad Mastiani et al. achieved encapsulation of individual cells and particles by setting a special microchannel using a biphasic system consisting of polyethylene glycol and saline solution (Mastisni et al. 2019). Hiroshi Umakoshi et al. studied the effect of using the relative cellular activity of dihydrate composed of PEG and dextran and separated heat-sensitive proteins from E.coli by this biphasic system, in which, cells were enriched into the interface and dextran phase, while heat-sensitive proteins were enriched into the PEG phase (Umakoshi et al. 1996). S. Hardt et al. used a two-phase system consisting of PEG and dextran to separate the difference in affinity for the two-phase solution by using whole blood cells (Hardt 2012). However, in these studies, to achieve the purpose of enrichment, complicated structures are required for separation.

At the same time, some researchers also employ an electric field (Hahn 2011; Ohshima & Hiroyuki 2012; Raghavarao et al. 2010), or magnetic field (Flygare et al. 1990) to accelerate the enrichment process of particles or the phase separation process in ATPS. However, in this process,

*Corresponding Author: yongxin@dlmu.edu.cn

DOI 10.1201/9781003308553-36

the applied direction of the electric field is mainly perpendicular to the biphasic interface, and the main application scenario is also within the microchannel. For example, Mengqi Li et al. determined the difference in the voltage required to transfer polystyrene particles of different sizes from the PEG phase to the dextran phase and from the dextran to the PEG phase by applying a pulse voltage, providing a basis for the next separation by this method. However, in its study, the interface needs to be controlled at a specific position, which makes its operation more complex (Li & Li 2019). In G. Munchow et al.'s study, the bovine serum protein was mixed in PEG or dextran (Münchow et al. 2006). By applying the electric field strength perpendicular to the interface, it was shown that the transfer of bovine serum protein from the PEG-rich phase to the dextran-rich phase was much easier than that from the dextran-rich phase to the PEG-rich phase.

In this study, an ATPS composed of 5% PEG and 11% Dextran was employed. By applying an electric field paralleling the ATPS interface, the electrokinetic velocity of polystyrene particles at the ATPS interface in a single straight microchannel was investigated. At the same time, the velocity of the dextran droplet in the PEG-rich phase and the velocity of the PEG droplet in the dextran-rich phase were also measured to figure out the charging mechanism of the PEG/dextran interface.

2 MATERIAL AND METHOD

2.1 *Materials*

Polyethylene glycol (PEG, Mw, 6,000 g/mol), dextran (DEX, Mw, 450,000–650,000 g/mol), and polystyrene particles (3μm, 5μm, 8μm, 10μm, and 20μm in diameter) were purchased from Sigma-Aldrich China. The particles were purified in deionized water (18.2 MΩ·cm) by centrifugation five times before use. Sodium chloride (NaCl) was analytically pure and purchased from Tianjin Fucheng Chemical Reagent Factory. All solutions were prepared with deionized water prepared by a Mili-Q purification system (Japan Millipore, Japan).

2.2 *Preparation of ATPS*

PEG and dextran powder were diluted in deionized water respectively to prepare the stocked solution of dextran and PEG with the mass fraction of 20%, and weigh the required mass of PEG and dextran stocked solution, buffer solution, and other agents by the electronic balance in the next step, successively add them into a 15 mL centrifuge tube, fully mix them, allow to stand for 24 h or more after mixing well, so that the two are fully separated, and then take out the upper phase solution and the lower phase solution successively through the pipette.

2.3 *Experimental containers and systems*

Figure 1 shows schematically the components and working principle of an electrokinetic velocity measurement system, which consists of two microfluidic chips with different widths and a DC power supply, with the two electrodes connected to the DC power supply and inserted into the two holes of the lower container, respectively. The channel width of the lower chips is designed to be 800 μm, while the length of the channel is designed 2 cm and the height of the channel is 3 mm. The sample cell in the lower phase is designed to be a cylinder with a radius of 2.5 mm. To slow down the difference of the pressure between the two sides during the application of voltage. The width size of the upper phase channel is designed to be 700 μm. The length was 1 cm, the height of the channel was 2 mm, and the radius of the sample cell was 1.5 mm.

2.4 *Determination of particle movement velocity*

During the experiment, add the solution to the container as shown in Figure 2. First, add a certain mass fraction of dextran solution in the lower phase container; Second, add a certain amount of

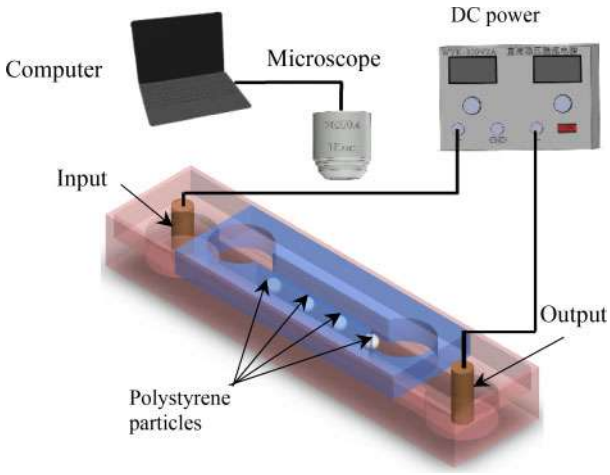

Figure 1. The experimental system for the measurement of particles' electrokinetic velocity.

PEG solution in the upper phase container. 2.5 μL of pure water droplets containing polystyrene particles were added to the PEG phase, two platinum electrodes were sequentially inserted into the holes on both sides and an electric field was applied. At the same time, the electrokinetic movement of the particles was recorded using a CCD camera of an inverted fluorescence microscope imaging system (Ti-E Nikon), and in the subsequent process, the movement distance of the particles over a period of time was calculated by this software.

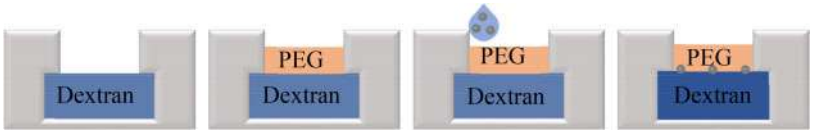

Figure 2. The process of loading solutions and sample.

To avoid the effect of interface disturbance on the particle movement speed in the process of applying an electric field, when applying an electric field, only record the movement of polystyrene particles in the first 10–20 seconds after applying the electric field, which is used to calculate the speed. For each group of conditions, measure at least 4 particles, and then calculate the average speed.

3 RESULT AND DISCUSSION

3.1 *Position of PS particles on ATPS interface*

In this part, 5% PEG-11% dextran is used as the research object, and the positions of polystyrene particles with different particle sizes on the interface were studied. Most of the polystyrene particles are in the PEG phase, and with the increase in particle size, the height of the polystyrene particles in the lower phase also increases, which will change the dynamic viscosity of the particle surface.

For a polystyrene particle at the interface, its position on the interface is the result of force balance. The particles at the interface are mainly affected by the combined action of gravity G, buoyancy F_b, interfacial tension $F_{c,}$ and static pressure F_p. And these four forces should satisfy:

$$G = F_b + F_c + F_p \tag{1}$$

It can be seen that for the aqueous two-phase composed of PEG and DEX, the interfacial tension and the density of the two-phase solution are constant under the condition that the concentration of the two polymers is determined, so the left side of the above equation is a constant, while the right side is a function of h and θ_2. For a specific particle, its position is relatively determined.

3.2 *Comparison of EK velocities on the interface and in the bulk phases*

The velocity of 5 μm polystyrene particle at the interface or two-phase solution had shown in Figure 3. With the electric field input, the polystyrene particles in the PEG phase move in the same direction as the particles on the interface, while the polystyrene particles in the DEX phase move in opposite direction compared with the particles at the interface.

Compared with the polystyrene particles at the interface, the force of the solution on the polystyrene particles in the PEG or DEX phase changes, and the dynamic viscosity of the solution around the particles also changed. In the PEG phase, the force of solution on polystyrene particles is the same as the electrophoretic movement of particles, and the dynamic viscosity of fluid around the particles is lower than that of the solution at the interface, which makes the polystyrene particles move faster in PEG phase. However, for polystyrene particles in the DEX phase, the solution has the smallest force on them, and the dynamic viscosity of the solution in which the particles are located is very high, which makes the movement speed of polystyrene particles in the DEX phase decrease.

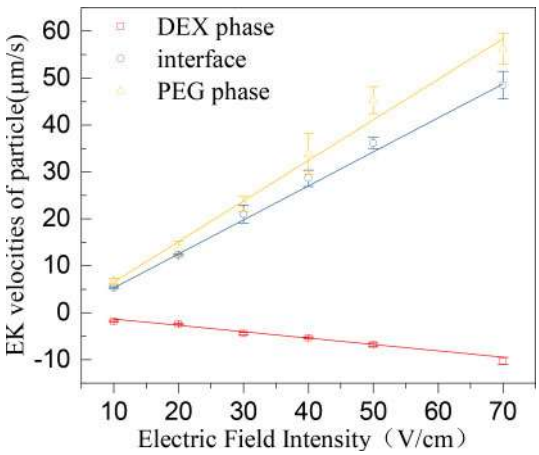

Figure 3. The EK velocities of particles at the ATPS interface and in the bulk.

3.3 *Size effect on the EK velocity of particles on the ATPS interface*

Figure 4 shows the electrokinetic velocities of the different size (3 μm, 5 μm, 8 μm, 10 μm, 20 μm) of polystyrene particles at the interface which consist of 5% (wt %) PEG and 11% (wt %) DEX. With the particle size of polystyrene particles increasing, the velocity of polystyrene particles decreases at the same electric field strength. This is due to the different resistance exerted by the two-phase solution on the polystyrene particles of different particle sizes at the interface, for different particle sizes, the height of the polystyrene particles in the dextran phase is also different, with the particle size increased, the height of the polystyrene particles in the lower phase also increases, which in turn changes the dynamic viscosity of the particle surface, making the velocity of the polystyrene particles with the polystyrene particle size decreases with increasing particle size.

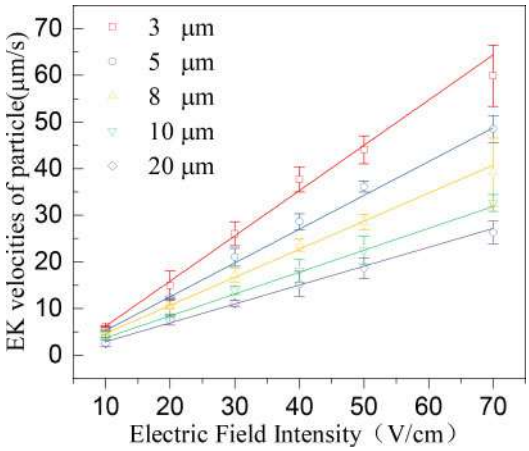

Figure 4. The EK velocity of particles on the ATPS interface.

3.4 *EK velocities of ATPS droplet*

The motion of the droplet can reflect the charged situation of the interface between the two water phases. As shown in Figure 5. For the DEX droplet in the PEG phase, the droplet's motion is opposite to the anode. However, the PEG droplet in the DEX phase moves to the cathode. For the DEX droplet in the PEG phase, the droplet is subjected to electrophoretic force, electric field force, and force of surrounding fluid on the droplet in the process of applying an electric field, and the droplet moves under the combined action of these three forces. As for the droplet appearing in the opposite direction from the theoretical analysis, the existing studies mainly believe that it is due to the electroosmotic flow inside the droplet, and the electroosmotic flow inside the droplet, in turn, causes the cycle relative to the DEX phase at the interface.

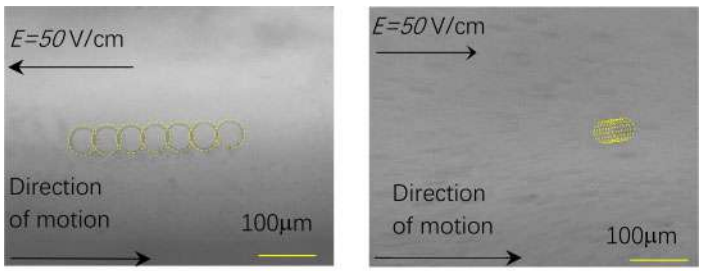

(a) DEX droplet in PEG phase (b) PEG droplet in DEX phase

Figure 5. The EK movement of the droplet.

4 CONCLUSION

A method for particle separation based on two-phase electrophoresis is proposed in this paper. The electrokinetic movement velocity of particles and microalgae on the two-phase interface composed of 5% PEG and 11% Dextran is measured. The experimental results show that the DEX droplet in the PEG phase moves to the negative order, while the PEG droplet in the DEX phase moves to the positive order. The electrokinetic velocity of polystyrene particles decreases with the increase of particle size. When the applied electric field intensity was 50 V/cm, the motion speed of 3μm

particles compared with that of 20μm particles increased 127.6%. The samples can be electrically separated into two aqueous phases by using the difference in the particles' electrokinetic velocity at the interface.

ACKNOWLEDGMENTS

The authors wish to thank the financial support of the National Natural Science Foundation of China (51979019, 52001049)

REFERENCES

A. Chavez-santoscoy, J. Benavides**,** W. Vermaas & M. Rito-Palomares (2010). Application of aqueous two-phase systems for the potential extractive fermentation of cyanobacterial products. J. Chemical Engineering & Technology. 33(1), 177–182.

C. Han, S. Takayama, & J. Park(2015). Formation and manipulation of cell spheroids using a density adjusted PEG/DEX aqueous two phase system. 5(11891), 2015.

G. Münchow, S. Hardt, J. P. Kutter & K. S. Drese(2006). Electrophoretic partitioning of proteins in two-phase microflows. J. Lab on a Chip. 7(1), 98–102.

H. Umakoshi, K. Yano, R. Kuboi & I. Komasawa(1996). Extractive cultivation of recombinant escherichia coli using aqueous two-phase systems for production and separation of intracellular heat shock proteins. J. Biotechnology Progress. 12(1), 51–56.

J. A. Asenjo, B. A. Andrews(2011). Aqueous two-phase systems for protein separation: a perspective. J. Chromatogr A. 1218(49), 8826–8835.

J. Sinha J, P. K. Dey & T. Panda(2000). Aqueous two-phase: the system of choice for extractive fermentation. J. Applied Microbiology & Biotechnology. 54(4), 476–486.

K. H. Nam, W. J. Chang, H. Hong, S. M. Lim, D. I. Kim & Y. M. Koo(2005). Continuous-flow fractionation of animal cells in microfluidic device using aqueous two-phase extraction. J. Biomedical Microdevices. 7(3), 189–195.

K. S. M. S. Raghavarao, R. M. Stewart, S. R. Rudge & P. Todd(2010). Electrokinetic demixing of aqueous two phase systems. 3. drop electrophoretic mobilities and demixing rates. J. Biotechnology Progress. 14(6), 922–930.

M. Iqbal, Y. Tao, S. Xie, Y. Zhu, D. Chen, X. Wang, L. Huang, D. Peng, A. Sattar, M. A. B. Shabbir, H. I. Hussain, S. Ahmed & Z. Yuan(2016). Aqueous two-phase system (ATPS): an overview and advances in its applications. J. Biological Procedures Online. 18(1), 1–18.

M. Li & D. Li(2019). Bidirectional transfer of particles across liquid-liquid interface under electric pulse. J. Colloid and Interface Science. 560, 436–446.

M. Mastisni, N. Firoozi, N. Petrozzi, S. Seo & M. Kim(2019). Polymer-salt aqueous two-phase system (ATPS) micro-droplets for cell encapsulation J. Scientific Reports. 9(1).

M. Tsukamoto, S. Taira, S. Yamamura, Y. Morita, N. Nagatani, Y. Takamura & E. Tamiya(2009). Cell separation by an aqueous two-phase system in a microfluidic device. J. Analyst. 134(10), 1994–1998.

Ohshima & Hiroyuki (2012). Electrical phenomena at interfaces and biointerfaces. Wiley.

S. Flygare, P. Wikstrm, G. Johansson & P. O. Larsson(1990). Magnetic aqueous two-phase separation in preparative applications. J. Enzyme and Microbial Technology. 12(2), 95–103.

S. Hardt & T. Hahn. Microfluidics with aqueous two-phase systems. J. Lab on a Chip. 12(3), 434–442.

S. Zimmermann, S. Gretzinger, P. K. Zimmermann, A. Bogsnes, M. Hansson & J. Hubbuch (2017). Cell separation in aqueous Two-phase systems influence of polymer molecular weight and tie-line length on the resolution of five model cell lines. Biotechnology Journal. 13(2).

T. Hahn & S. Hardt. Concentration and size separation of DNA samples at liquid-liquid interfaces. J. Analytical Chemistry. 83(14), 5476–5479.

Teixeira, Alyne G., R. Agarwal & J. P. Frampton(2019). Confinement of suspension-cultured cells in polyethylene glycol/polyethylene oxide-albumin aqueous two-phase systems. J. Frontiers in Chemistry. 7(441).

Advances in Applied Chemistry and Industrial Catalysis – Saikia (Ed.)

Determination of the composition of imported recycled polyamide/polyethylene blends by differential scanning calorimetry

KaiDong Lin
CCIC Physical and Chemical Testing Co., LTD, ShangHai, P.R. China

Chao Zhang & FengPing Ni
Ningbo Joysun Product Testing Service Company, NingBo, P.R. China

Chuan Luo*
Ningbo Customs District Technology Center, NingBo, P.R. China

ABSTRACT: A determination method of the composition of polyamide/polyethylene blends was studied by differential scanning calorimetry. Through the study of the influence factors such as heating rate, cooling rate, sample mass and sample thickness, the best thickness is (0.7±0.1)mm, the best sample mass is (5±1)mg, and 10°C/min is the optimum temperature rise and fall rate. The comparative study of actual blend samples found that, the accuracy of melting enthalpy normalization method is better. For PE/PA blend system, the repeatability of PE and PA is between 0.65% and 5.85%.

1 INTRODUCTION

With the gradual closure of domestic supervision on imported waste plastics, major waste plastics exporting countries such as Europe and the United States have lost the world's largest solid waste market. Many countries have invested their production capability in Thailand, Malaysia, Vietnam and other countries. After processing waste plastics into recycled plastic particles, they continue to be exported to the Chinese market. The quality of imported recycled plastic particles is mixed. In order to standardize the product quality of recycled plastics, the plastic standards committee has put forward and formulated a series of standards for recycled plastics. With the gradual release and implementation of GB/T 40006 series of national standards for recycled plastics, further requirements are put forward for the quality of recycled plastics. The premise of testing according to GB/T 40006 series national standards is to judge the polymer composition of the sample, so the method of testing the polymer composition becomes the key.

Polyamide is usually called nylon, which is mainly used in the production of films, fibers, engineering plastics, etc., and is the largest consumption of the five engineering plastics in the world so far. According to the statistical data of recycled particles imported from several major ports in China in recent years, some recycled plastic particles from composite film materials may contain polyethylene and polyamide at the same time. When those two different types of polymers are blended, they may be reconstituted particles of many different batches of film materials, the composition of recycled particles may be inconsistent, which will affect the subsequent use.

For the composition test of polymers, Dai et al. have determined PE/PP blends by infrared spectrum, Zhang et al. have determined by pyrolysis gas chromatography mass spectrometry (GC/MS), and Luo et al. have determined the composition of ABS and other plastics by element analyzer. Since

*Corresponding Author: luochuan@customs.gov.cn

DOI 10.1201/9781003308553-37

most polyamides are crystalline polymers, the composition of crystalline polymers can be effectively determined by differential scanning calorimetry. Therefore, the composition of polyamide blends was studied by differential scanning calorimetry.

2 EXPERIMENT

Equipment: Differential Scanning Calorimeter (Switzerland METTLER TOLEDO, DSC 3+), 40ul standard aluminum crucible (CHINA), In standard material (Switzerland METTLER TOLEDO), Sn standard material (Switzerland METTLER TOLEDO), high purity nitrogen, LLDPE (BAOFENG ENERGY, S1003), Polyamide 6 (Mitsubishi, Japan, 1030), polyamide 66 (DuPont, USA, 101L).

Select the sample, flatten it to (0.7±0.1) mm, cut a sample of (5.0±1.0) mg, put it into a 40ul standard aluminum crucible, punch the lid, press it, and perform the DSC test according to the above mentioned procedure. The melting peak of the second heating section was selected for analysis.

3 RESULTS AND DISCUSSION

3.1 *Influence of temperature rising program on enthalpy determination*

Referring to GB/T 19466.3-2004 standard, establish the temperature program, select the same cooling for crystallization after the heating section, and then select different heating rates for heating, and study the changes of enthalpy and peak type of various polymers. The specific temperature program is as follows: The heating program is as follows: 50°C, heat to 280°C at a rate of 10°C/min, stay constant for 2 min, cool to 50°C at a rate of 10°C/min°C/min, stay constant for 2 min, and then heat to 280°C at a rate of 1/2/5/10/20/30°C/min°C/min again, stay constant for 2 min, and cool down to 50°C at a rate of 10°C/min°C/min.

Weigh about 5mg of various polymers for analysis them according to the above temperature program, select LLDPE for polyethylene research, and the normalized melting enthalpy is listed in Table 1, as follows:

Table 1. Effect of different heating rates on melting enthalpy.

	raise temperature rate °C/min					
Sample	1	2	5	10	20	30
PE	424.93	409.84	372.07	409.38	369.93	385.09
PA6	379.58	320.26	317.46	316.85	299.34	284.83
PA66	291.89	341.39	288.53	324.74	309.26	250.3

It can be seen from the above Table 1 that different heating rates have different effects on the melting enthalpy of different polymers. The melting enthalpy of polyolefins such as polyethylene decreases first and then increases with the increase of heating rate. The melting enthalpy of polyamide 6 decreases gradually, and the melting enthalpy of polyamide 66 fluctuates. And low heating rate will lead to detection efficiency. Based on the above, 10°C/min is selected as the heating rate.

3.2 *Effect of cooling rate on polymer crystallization*

Under different cooling programs, the regular arrangement of polymer molecular chains will change, resulting in different crystallinity of polymer, which will affect the subsequent melting determination.

Therefore, the study of the effect of cooling rate on melting enthalpy is tested according to the following procedures: the first and second raise temperature rate and second cool temperature rate is as same as the 2.1 temperature grogram, the first cool temperature rate is 1/2/5/10/20/30°C/min.

Weigh about 5mg of various polymer and analyze them according to the above temperature programs, and list the normalized melting enthalpy in Table 2 as follows:

Table 2. Effect of different heating rates on melting enthalpy.

	Cool temperature rate °C/min					
Sample	1	2	5	10	20	30
PE	292.84	440.58	431.13	382.32	439.77	400.64
PA6	390.23	316.01	320.69	284.42	296.49	302.27
PA66	314.07	330.18	339.4	338.63	336.42	306.95

It can be seen from the above Table 2 that a lower cooling rate is conducive to the regular arrangement of polymer molecular chains, but too low a cooling rate will affect the test efficiency. Therefore, the cooling procedure of 10°C/min shall be selected comprehensively.

3.3 *Effect of sample thickness*

For the influence of sample's thickness and mass, press samples of different thicknesses, and then cut another batch of samples of different mass on the samples for testing. The results are shown in Table 3:

Table 3. Effect of different test plate thickness on melting enthalpy.

	PE		PA6		PA66	
No	thickness, mm	Enthalpy	thickness, mm	Enthalpy	thickness, mm	Enthalpy
1	0.829	95.81	0.930	19.33	0.938	53.87
2	0.706	104.75	0.807	19.48	0.720	54.06
3	0.574	89.57	0.703	20.33	0.606	45.91
4	0.475	91.60	0.430	14.90	0.513	55.04
5	0.401	85.82	0.348	22.08	0.373	58.59

The above data are plotted separately. It can be saw that the enthalpy of various polymers varies with the thickness of the test piece. Considering the above, when the thickness of the test piece is (0.7 ± 0.1) mm, most polymers have better enthalpy, so the sample thickness is set as (0.7 ± 0.1) mm.

3.4 *Effect of sample mass*

Weigh four kinds of polymers with different mass, press them into (0.7 ± 0.1) mm sheets, test them according to the above method, and study the relationship between polymer mass and standard enthalpy. The results are shown in Table 4:

From the above results, the sample mass and melting enthalpy of polyethylene, polyamide 6 and polyamide 66 basically show a linear relationship, and the sample mass has little effect on the test results of melting enthalpy. When the sample mass is greater than 10mg, the sample will occupy the whole crucible and cannot be placed. Therefore, the sample mass is 5 mg $\pm$ 1 mg.

Table 4. Effect of different sample amounts on melting enthalpy.

No	1	2	3	4	5	6
PE, m, mg	1.00	2.03	4.94	7.95	10.00	11.74
Enthalpy	103.09	189.1	439.37	681.1	837.69	1012.77
Standard enthalpy	103.09	93.15	88.94	85.67	83.77	86.27
PA6, m, mg	1.03	2.01	5.03	7.92	10.01	11.94
Enthalpy	38.6	73.03	174.87	206.66	309.85	311.34
Standard enthalpy	37.48	36.33	34.77	26.09	30.95	26.08
PA66, m, mg	1.06	1.99	4.87	7.96	9.70	12.02
Enthalpy	49.08	109.56	254.46	504.99	550.17	776.41
Standard enthalpy	46.30	55.06	52.25	63.44	56.72	64.59

3.5 *Accuracy testing of polyamide and polyethylene*

Since there is no suitable solvent to dissolve PE and PA66 at the same time, the standard sample is prepared by physical blending. Mix PE and PA66 with appropriate weight, mix them with the high-speed mixer, and then use a small injection molding machine for injection molding. Take the standard sample after 10 molds for testing and analyze according to the similar steps of PE / PP. The results are shown in Table 5.

Table 5. PE/PA66 standard mixture composition test results.

Unit: % (Mass fraction)

Standard mixture	Actual ratio		Standard enthalpy method				Melting enthalpy normalization method			
			PE		PA66		PE		PA66	
	PE	PA66	test	Def.	test	Def.	test	Def.	test	Def.
PE/PA R1	10.46	89.54	6.58	3.88	84.84	4.70	9.77	0.70	90.23	−0.70
PE/PA R2	20.72	79.28	16.39	4.34	80.97	1.70	22.01	−1.28	77.99	1.28
PE/PA R3	38.83	61.17	33.82	5.01	60.35	0.81	43.86	−5.03	56.14	5.03
PE/PA R4	48.91	51.09	45.03	3.88	51.88	0.79	54.76	−5.85	45.24	5.85
PE/PA R5	59.16	40.84	51.76	7.40	45.06	4.22	61.57	−2.40	38.43	2.40
PE/PA R6	79.26	20.74	72.81	6.45	23.65	2.91	81.10	−1.85	18.90	1.85
PE/PA R7	90.06	9.94	84.73	5.33	12.10	2.16	90.71	−0.65	9.29	0.65

It can be seen from Table 5 that, using the standard enthalpy method, the absolute difference between the test value and the actual value of PE fluctuates between 3.88% ~ 7.40%, and the average absolute difference is 5.18%, both of they are positive deviations without any rules. The absolute difference between the test value and the actual value of PA66 fluctuates between 0.79% ~ 4.70%, and the average absolute difference is 2.47%, both of they are positive deviations without any rules. Using the melting enthalpy normalization method, the absolute difference is between 0.65% ~ 5.85%, and the average absolute difference is 2.54%. When the PE/PA66 content is close, the deviation is large, and when it is low, the deviation is small. In conclusion, it can be saw that the accuracy of melting enthalpy normalization method is better, and for PE/PA blend system, the repeatability of PE and PA should not exceed 6%.

4 CONCLUSION

A determination method of the composition of polyamide/polyethylene blends was established by differential scanning calorimetry. Through the study of the influence factors, the best thickness is (0.7±0.1) mm, the best sample mass is (5±1) mg, and 10°C/min is the optimum raise and cool temperature rate. The comparative study of actual blend samples found that, the accuracy of melting enthalpy normalization method is better. For PE/PA blend system, the repeatability of PE and PA is between 0.65% and 5.85%.

ACKNOWLEDGEMENTS

This work was financially supported by the science research project of General Administration of Customs, P. R. CHINA (Fund No.: 2020HK245) and the Zhejiang basis public science research project (Fund No.: LGC20B040001).

REFERENCES

An L.H. (2003) Technologies and Future of Recycling of Polyamide. China Plastics, 17(5):65–69.

Dai S.J, Luo C, Zhang C., etc. (2021) Determination of Small-Amount Polypropylene in Imported Regenerated Polyethylene-Polypropylene Blends by Fourier Transform Infrared Spectroscopy. E3S Web of Conferences 261, 02067 (2021).

Luo, C., Dai, S., Zhang, Y., Yuan, L., Zhang, C., & Lin, Z. (2021). Identification Method of Solid Waste Characteristic for Imported Recycled Engineering Plastics. In IOP Conference Series: Earth and Environmental Science (Vol. 621, No. 1, p. 012050). IOP Publishing.

Luo, C., Wang, H., Wang, Q., Liu, ZH, etc., (2020). Application of Instrumental in the Identification of Solid Waste Characteristic of Imported recycled ABS Plastic. In IOP Conference Series: Earth and Environmental Science (Vol. 508, No. 1, p. 012205). IOP Publishing.

Luo, C., Wang, Q., Liu, Z., Wang, H., Chen, T., & Lin, Z. (2020). Application of Fusion sample preparation X Ray Fluorescence Spectrometry in the Identification of Solid Waste Characteristic of Imported Coated Fibre Cloth. In IOP Conference Series: Earth and Environmental Science (Vol. 508, No. 1, p. 012214). IOP Publishing.

Yuan LF, Luo C, Xu SH, etc., (2020) Quantitative analysis of blend ratio of polycarbonate to acrylonitrile-butadiene-styrene copolymer by pyrolysis gas chromatography – mass spectrometry using solid dispersant for sample preparation, Journal of Instrumental Analysis 39(6):69–773.

Zhang, Y., Luo, C., Yuan, L., Xu, SH, etc., (2021). Pyrolysis-gas chromatography/mass spectrometry to identification of the solid waste characteristic of imported polyamide recycled plastics. In IOP Conference Series: Earth and Environmental Science (Vol. 621, No. 1, p. 012038). IOP Publishing.

Advances in Applied Chemistry and Industrial Catalysis – Saikia (Ed.)

Microporous aeration induced performance enhancement of electrochemical softening for circulating cooling water

Yiyong Tang* & Wenxing Li**
School of Economics and Management, Beijing Jiaotong University, Beijing, China

ABSTRACT: In this study, the aeration-assisted electrochemical reactor with two-dimensional plate electrodes was employed to soften the simulated circulating cooling water. Results show that microporous aeration could accelerate the mass transfer process of scaling ions, making the precipitation rate rise and the energy consumption decrease. A high precipitation rate of 55 $g \cdot m^{-2} \cdot h^{-1}$ is obtained at the current density of 100 $A \cdot m^{-2}$ and the flow rate of 1.2 $L \cdot min^{-1}$. Commonly used as scale inhibitor, ATMP has little impact on the precipitation rate, only a decline of 14% is observed at the concentration of 5 $mg \cdot L^{-1}$. The accumulation of precipitates on the cathodes is hindered by the microporous aeration, and the precipitates with readily detached lamellar morphology facilitates the increasing of precipitation rate.

1 GENERAL INSTRUCTIONS

Due to continuous concentration, the circulating cooling water often contains high hardness, which often leads to the scaling problem of the system. Water softening can remove Ca^{2+}, Mg^{2+} and other scaling ions, and eliminate the possibility of scaling from the root (Hasson 2008). Lime treatment is the most commonly used water softening method (Gabrielli 2006), but the softening process requires continuous consumption of chemicals. Although ion exchange method has high softening efficiency (Zhi 2014), it is difficult to treat the secondary wastewater generated by regeneration. With the continuous development of membrane technology, nanofiltration technology is gradually applied to water softening (Yu 2018). Circulating cooling water contains a certain concentration of suspended solids and COD. Pretreatment is required before nanofiltration, which will greatly increase the treatment cost.

Recently, electrochemical softening technology has become a research hotspot in the field of water quality softening because of its environmental friendliness and versatility (Jin 2019). The basic principle of electrochemical softening is as follows: firstly, the cathode generates OH^- through electrochemical reduction reaction, creating an alkaline environment with high pH value near its surface (formula1∼2). Subsequently, Ca^{2+}, Mg^{2+} and $HCO_3{}^{2-}$ in the solution diffuse into the environment and undergo chemical precipitation reaction (formula3∼5). Finally, the precipitates gather on the cathode surface, nucleate and crystallize.

$$O_2 + 2H_2O + 4e^- \rightarrow 4OH^- \tag{1}$$

$$2H_2O + 2e^- \rightarrow H_2 + 2OH^- \tag{2}$$

$$HCO_3^- + OH^- \rightarrow CO_3^{2-} + H_2O \tag{3}$$

$$Ca^{2+} + CO_3^{2-} \rightarrow CaCO_3 \downarrow \tag{4}$$

$$Mg^{2+} + 2OH^- \rightarrow Mg(OH)_2 \downarrow \tag{5}$$

Corresponding Authors: *16113121@bjtu.edu.cn and **wxli@bjtu.edu.cn

DOI 10.1201/9781003308553-38

At present, there are two main problems in the application of electrochemical softening technology: one is the difficulty in removing the sediment on the cathode surface. With the progress of the reaction, a large amount of sediment will accumulate, resulting in passivation of the cathode surface, which must be removed regularly by physical or chemical means. Second, when the current density is large and more OH^- is generated, the precipitation process is controlled by the mass transfer of scaling ions such as Ca^{2+}, Mg^{2+} and HCO_3^{2-}, and there is an upper limit on the precipitation rate. The limitation of sedimentation rate leads to the need for larger cathode area in the treatment process, so more water treatment equipment is needed. For the circulating cooling water system with large water flow, the investment cost is high. Therefore, it is necessary to find a simple and effective method to remove cathode sediment and strengthen scaling ion mass transfer at the same time.

2 EXPERIMENTAL DESIGN

2.1 *Experimental device*

The device used in the experiment is shown in Figure 1. The shell of electrochemical reactor is made of transparent plexiglass. After adding microporous aeration disk, the water volume can be retained by 1.2 L. Three ruthenium titanium iridium coated titanium anode plates and three mirror stainless steel cathode plates are staggered, fixed on the reactor wall through slots, and connected with the positive and negative poles of external DC power supply respectively. Electrode plate size 10 cm×10 cm×1 mm, the distance between the plates is 1 cm, and the effective cathode plate area is regarded as 0.05 m^2. The cooling water is sent from the water inlet at the bottom of the reactor through the peristaltic pump and overflows from the upper water outlet. The microporous aeration disk is fixed at the bottom of the reactor and connected with the external air pump (air flow 1 $L \cdot min^{-1}$, Power 3W). Duringoperation, a large number of small particle size bubbles are generated.

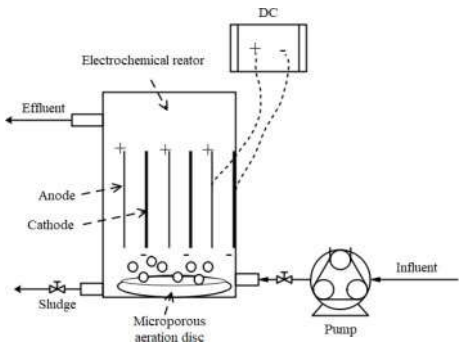

Figure 1. Schematic diagram of experimental device.

2.2 *Influent quality*

The simulated circulating cooling water prepared in the laboratory is used as the inlet water. Dissolve 1 mol $CaCl_2$ and 2 mol $NaHCO_3$ in 400 L tap water, and then stand for 12h. Finally, the conductivity of the simulated water sample is about 1300 $\mu S \cdot cm^{-1}$, pH value 8.0, total alkalinity 6.7 $mmol \cdot L^{-1}$, total hardness 3.7 $mmol \cdot L^{-1}$, including calcium hardness 3.4$mmol \cdot L^{-1}$.

2.3 *Analytical method*

Hardness was determined by EDTA titration. The conductivity and pH were measured by HACH portable conductivity and pH meter respectively. The morphology of the precipitates was observed by scanning electron microscope (SEM, FEI, Quanta-200).

2.4 *Performance evaluation*

The precipitation rate of $CaCO_3$ (the precipitation rate of hardness measured by $CaCO_3$) is used as the evaluation index of electrochemical softening performance, and the calculation formula is as follows:

$$v = 6 \times (H_e - H_i) \times Q/A \tag{6}$$

Where, v is the precipitation rate of $CaCO_3$, $g \cdot m^{-2} \cdot h^{-1}$; Hi and He are the total hardness of inlet and outlet water, $L \cdot min^{-1}$; Q is inflow flow, $L \cdot min^{-1}$; A is the effective cathode plate area, with a value of 0.05 m^2.

The precipitation energy consumption of $CaCO_3$ consists of DC energy consumption and aeration energy consumption. The calculation formula is as follows:

$$W = (U \times I + E)/(v \times A) \tag{7}$$

Where, W is the precipitation energy consumption of $CaCO_3$, $kWh \cdot kg^{-1}$; U is electrolytic voltage; I is the total current; E is aeration power, which is 3 W.

3 RESULT

3.1 *Effect of current density*

When the flow rate is 0.4 $L \cdot min^{-1}$, the effects of current density on the sedimentation rate and energy consumption of the reactor are shown in Figures 2 and 3 respectively. It can be seen that without aeration, the sedimentation rate increases with the increase of current density. When the current density is greater than 100 $A \cdot m^{-1}$, the precipitation rate tends to a limit value of 21 $g \cdot m^{-2} \cdot h^{-1}$. At this time, the chemical precipitation process is controlled by the mass transfer of scaling ions. At the same time, with the increase of current density, the utilization rate of OH^- decreases greatly, resulting in a sharp increase in precipitation energy consumption. When there is microporous aeration, the sedimentation rate still increases with the increase of current density. However, due to the acceleration of scaling ion mass transfer, the precipitation rate under the same current density is higher than that without aeration. When the current density reaches 140 $A \cdot m^{-1}$, the sedimentation rate tends to the limit value, which is 42 $g \cdot m^{-2} \cdot h^{-1}$, which is twice higher than that without aeration. The increase of sedimentation rate is only the result of turning on the 3W aeration pump, so the energy consumption under the same current density is greatly reduced compared with that without aeration. It is worth noting that when the current density is 0, the precipitation rate is almost 0, indicating that the effect of simple microporous aeration softening is very low, but it only strengthens the chemical precipitation process. In fact, many methods to accelerate ion

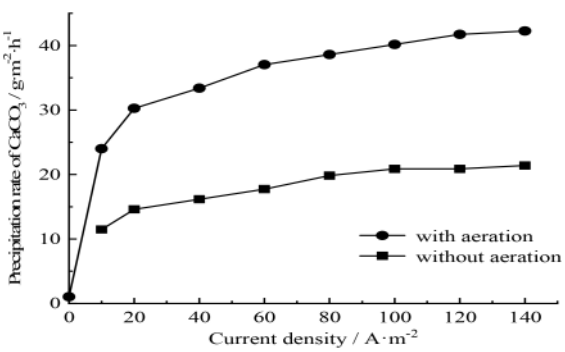

Figure 2. Effect of current density on precipitation rate.

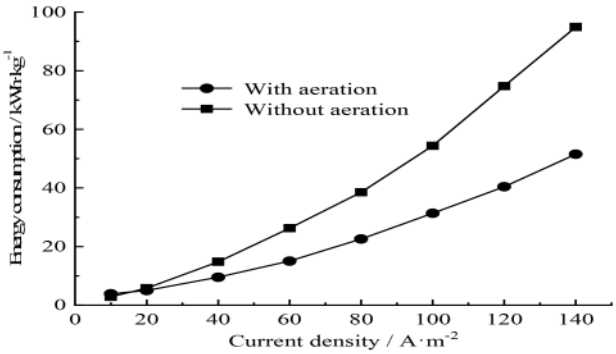

Figure 3. Effect of current density on energy consumption.

mass transfer, such as ultrasound and rotating electrode plate, can improve the precipitation rate. Microporous aeration is one of these methods with the lowest cost and energy consumption.

3.2 *Effect of flow rate*

When the current density is 100 $A \cdot m^{-1}$, the effects of flow rate on the precipitation rate and energy consumption of the reactor are shown in Figures 4 and 5 respectively. Under both conditions, the precipitation rate increases with the increase of flow rate, and the energy consumption decreases with the increase of flow rate. This is because when the flow rate increases, the cooling water treated by the reactor increases at the same time, resulting in an increase in the total amount of hardness removed and an increase in the precipitation rate. When the flow rate increases, the electrolytic voltage of the reactor basically does not change, so the electrolytic power does not change and the precipitation energy consumption decreases. It can be seen that under the same flow rate, the sedimentation rate with aeration is higher than that without aeration. When the flow rate is1.2 $L \cdot min^{-1}$, the sedimentation rate is as high as 55 $g \cdot m^{-2} \cdot h^{-1}$, and only 32 $g \cdot m^{-2} \cdot h^{-1}$ without aeration. In practical application, electrochemical softening equipment generally adopts the form of side flow treatment. Increasing the cooling water volume of side flow treatment can improve the sedimentation rate of aeration auxiliary equipment and bring better softening and scale inhibition effects. Accordingly, more water pumps need to be put into operation.

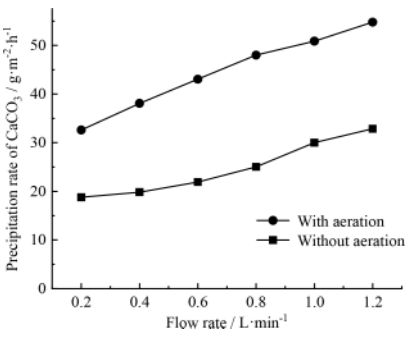

Figure 4. Effect of flow rate on precipitation rate.

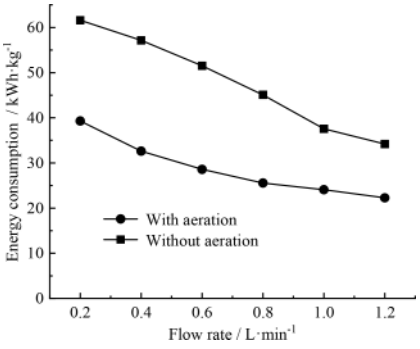

Figure 5. Effect of flow rate on energy consumption.

3.3 *Effect of scale inhibitor concentration*

In the process of practical application, in order to prevent the adverse consequences caused by water quality fluctuation, electrochemical softening and low concentration scale inhibitor will be used together. The chemical precipitation process involved in electrochemical softening is very similar to the general scaling process, so the scale inhibitor will also have an effect on it. Therefore, the effect of the concentration of common scale inhibitor ATMP on the precipitation rate of the reactor is studied, and the results are shown in Figure 6. When the flow rate was 0.4 $L \cdot min^{-1}$ and the current density was 100 $A \cdot m^{-1}$, the precipitation rate decreased with the increase of ATMP concentration. The reasons for this phenomenon are complex. The obstruction of mass transfer process and the inhibition of $CaCO_3$ crystal growth process after complexation of scale inhibitor with Ca^{2+} and Mg^{2+} will lead to the decrease of precipitation rate. When the concentration of ATMP is 5 $mg \cdot L^{-1}$, the precipitation rate under aeration is 33 $g \cdot m^{-2} \cdot h^{-1}$, which is only 14% lower than that without scale inhibitor, and 27% lower than that without aeration. Therefore, it is certain that microporous aeration can not only improve the sedimentation rate, but also reduce the impact of scale inhibitors on the sedimentation rate. It also shows that the auxiliary means of microporous aeration can be used together with low concentration scale inhibitor in theory.

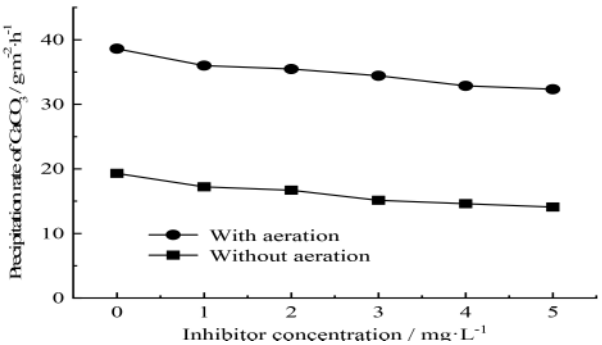

Figure 6. Effect of scale inhibitor concentration on precipitation rate.

3.4 *Cathode weight gain and precipitate morphology*

The weight gain of the cathode plate of the electrochemical reactor was weighed after 12 hours of operation under the conditions of flow rate of 0.4 $L \cdot min^{-1}$ and current density of 100 $A \cdot m^{-1}$. The results showed that the total weight gain of the plate without aeration was 2.52 g, accounting for 19% of the total hardness removed. Under the condition of aeration, the weight of the plate increased by 3.12 g, accounting for only 12% of the total hardness removed. The scouring effect of microporous aeration on the sediment attached to the cathode plate reduces the accumulation of sediment on the cathode plate and delays the passivation process of the cathode plate, which is also one of the reasons for the high sedimentation rate under aeration conditions. The morphology of the precipitates under the two conditions was also observed by SEM, and the results are shown in Figure 7. It can be seen that the precipitates without aeration are massive and densely stacked together. When the precipitate with this morphology is covered on the cathode surface, it will not only hinder the continuous progress of electrochemical reaction, make the cathode completely passivated, but also difficult to remove from the cathode surface. Under the condition of microporous aeration, the interconnected flakes were observed. The thickness of these flakes was in the nano scale, and there were a large number of voids between them. The gap provides a channel for the mass transfer of scaling ions to the cathode surface, so that the surface covered by these precipitates is not completely passivated, which improves the precipitation rate on the other hand. It is speculated that the formation of these thin films is related to the friction effect of microbubbles on the precipitates. Loose flake deposits are also easier to remove than dense blocks.

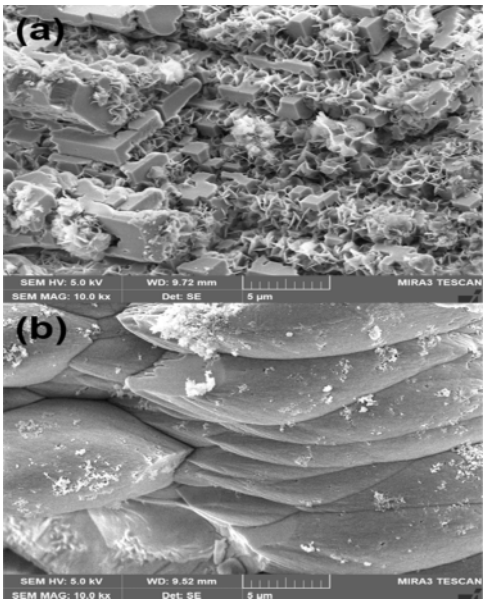

Figure 7. Morphology of sediment (a) with and (b) without aeration on cathode surface.

4 CONCLUSION

Based on the results and discussions presented above, the conclusions are obtained as below:

(1) Microporous aeration can accelerate the mass transfer of scaling ions, improve the precipitation rate of electrochemical reactor and reduce energy consumption. When the current density is 100 A·m-1and the flow rate is 1.2 L·min^{-1}, the precipitation rate is as high as 55 g·m^{-2}·h^{-1}.
(2) When there is5 mg·L^{-1}ATMP in the cooling water, the sedimentation rate of the reactor under microporous aeration decreases by only 14%.
(3) Microporous aeration reduces the accumulation of sediment on the cathode plate, and the sediment with thin morphology helps to improve the precipitation rate and is easier to be removed.

REFERENCES

Gabrielli, C. & Maurin, G. et al. (2006) Electrochemical water softening: principle and application. Desalination, 201(1): 150–163.
Hasson, D. & Lumelsky, V. et al. (2008). Development of the electrochemical scale removal technique for desalination applications. Desalination, 230(1–3): 329–342.
Jin, H. & Yu, Y. & Zhang, L. et al. (2019) Polarity reversal electrochemical process for water softening. Separation and Purification Technology, 210: 943–949.
Yu, Y. & Jin, H. & Jin, X. et al. (2018) Current pulsated electrochemical precipitation for water softening. Industrial & Engineering Chemistry Research, 57(18): 6585–6593.
Yu, Y. & Jin, H. & Meng, P. et al. (2018) Electrochemical water softening using air-scoured washing for scale detachment. Separation and Purification Technology, 191: 216–224.
Zhi, S. & Zhang, S. (2014) A novel combined electrochemical system for hardness removal. Desalination, 349: 68–72.

Advances in Applied Chemistry and Industrial Catalysis – Saikia (Ed.)

Retrosynthesis of undescribed sesquiterpene lactone

Lujie Pu*
School of Natural Sciences, The University of Manchester, Manchester, England, UK

Jingsong Chen
The Quarry Lane School, Dublin, CA, USA

Weichen Tang
Shenzhen College of International Education, Shenzhen, Guangdong, China

Jiawei Li
Dulwich International Zhuhai High School, Zhuhai Guangdong, China

Haozhe Xu
Ulink college of Shanghai, Shanghai, China

ABSTRACT: This paper discussed some possible routes for the retrosynthesis of a specific sesquiterpene lactone in detail. Some differences between the routines are compared to select the best reaction pathway for it. Our main aim of the paper is the demonstration with details of three possible retrosynthesis routes of a specific sesquiterpene lactone from plants. All these routes are following the rule that simplifies the complex molecule into the simplest ones. Our designs don't include the consideration of stereochemistry, while we are concentrated on the practicability of the routes, including the availability of the starting materials and stability of fragments. Finally, the comparison between the routes brings the best one. Our designs aren't too innovative, but hopefully, they can provide or motivate more competitive and powerful ideas. The retrosynthetic routes design is the basis to reach the studies of undefined organic molecules, which is an essential tool for organic studies.

1 INTRODUCTION

Centipeda minima is an annual prostrate aromatic herb ranging in China, Japan, India, Thailand, Indonesia, Philippines New Guinea, Australia, and the Pacific Islands; It is commonly known for its value in Traditional Chinese Medicine for treating colds, allergies, and headaches. Recent studies have shown sixteen new sesquiterpene lactones present in centipeda minima, and the bioactivities of centipeda minima most likely come from the sesquiterpene lactones present in the herb because of the sesquiterpenes' significant cytotoxicity against human cancer cells and anti-inflammatory activities (Wu et al. 1985). In an investigation of compounds with new structures and potent bioactivities, a systematic phytochemical investigation of Centipeda minima was conducted, and 16 new and 13 known sesquiterpenes were isolated and determined structurally (Qiu & Feng 2021). As shown in Figure 1, Molecule (1) is one of the sesquiterpene lactones that consists of 3 rings – 2 carbocycles and 1 heterocycle. The olefin on the right heterocycle is directly conjugated to a carbonyl group embedded in the heterocycle, which makes the structure an exo-methylene-lactone. This structure is well-known to be a bio-conjugating reagent because the β carbon of

*Corresponding Author: Lujie.pu@postgrad.manchester.ac.uk

DOI 10.1201/9781003308553-39

the olefin is extremely electrophilic, and in biological systems, nucleophiles tend to add in and form a new bond with the β carbon which may inhibit enzymes or cancer cells. Therefore, the molecule (1) extracted from centipeda minima has potential biomedical value. The molecule (1) can be extracted and purified from centipeda minima, but the process is not only time-consuming but also expensive, therefore a feasible chemical synthesis of this molecule is needed to create this molecule in laboratories. In this paper, several retrosynthetic routes for molecule (1) will be designed and examined.

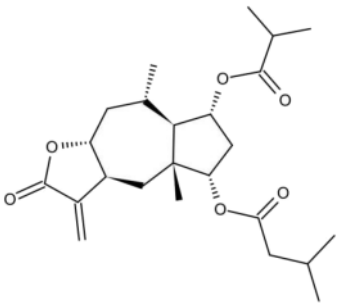

Figure 1. Molecule (1) (Qiu 2021).

2 RETROSYNTHESIS ANALYSIS

The exo-methylene-lactone on the right side of the molecule (1) is extremely electrophilic which makes the molecule sensitive to nucleophiles. Such high electrophilicity might be problematic in the synthesis of the target molecule therefore it is critical to remove the exo-methylene-lactone at an early stage of retrosynthesis; as a result, the exo-methylene-lactone will be installed toward the end of synthesis to prevent interferences due to its high electrophilicity. It is not hard to achieve by assigning the oxidation level to each carbon of the molecule (1) and performing the very first retrosynthetic step - breaking the molecule into basic functional groups according to the oxidation level analysis below.

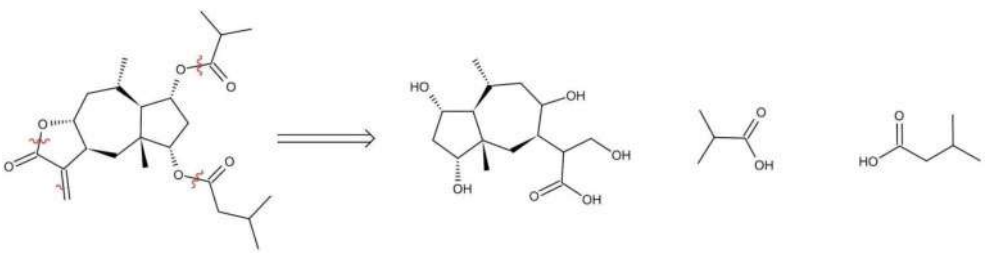

Figure 2. The initial disconnection of exo-methylene-lactone.

There are some esters in molecule (1) that can be retrosynthetically hydrolyzed to carboxylic acids in aqueous solutions of strong acids. (SCRIBD 2021) In short, nucleophilic substitution reactions (including ester hydrolysis and saponification) can deconstruct the molecule into three main parts as shown in Figure 2. The compound now gets much simpler with the two carboxylic acids subtracted from the main part as well as the five-membered ring in the main part opening up.

As we know, hydrogens at the a-carbon of carbonyl compounds are somewhat acidic. (SCRIBD, https://www.scribd.com) When an a-proton is removed, a conjugate-base anion is formed at the a-carbon which is called an enolate ion involved in the formation of enol. Consequently, breaking the carbon-carbon single bond attached to a seven-membered ring can be retrosynthetic hydrolyzed to two carbonyl compounds as shown in Figure 3.

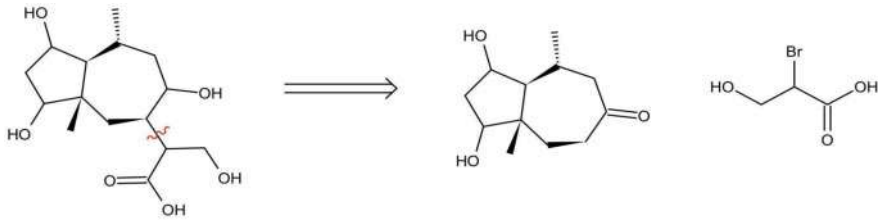

Figure 3. The process of subtracting carbolic acid from the main part.

It is worth mentioning that, during the formation of two compounds, the hydrogen on the lower side can be more easily to be removed than those above the carbonyl group because of the methyl group on the upper side in the seven-membered ring. When a conjugate base on the lower side is formed, it would attack the carbon bound to bromine and make the bromine group leave.

Several retrosynthetic routes can be designed by finding different Di-oxygenation patterns or doing operations on the functional groups including functional groups addition, inter-conversation, disconnection, intramolecular condensation, and removal.

3 RETROSYNTHETIC ROUTE 1

As shown in Figure 4, by firstly changing the OH group on the five carbons ring into an alkene, then disconnecting the $\alpha - \beta$ unsaturated carbonyl along with the double bond, writing CH_2 at one end and C=O at the other to open the five carbons ring. A 1,4 Di-oxygenation pattern is available, by using the pattern, disconnecting the bond between carbon 2 and carbon 3. This step opens the seven-carbon ring into a straight chain, not only minimizing the ring strain but also simplifying the molecule. Finally, two 1, 5 Di-oxygenations can be used, disconnecting the bond between carbons

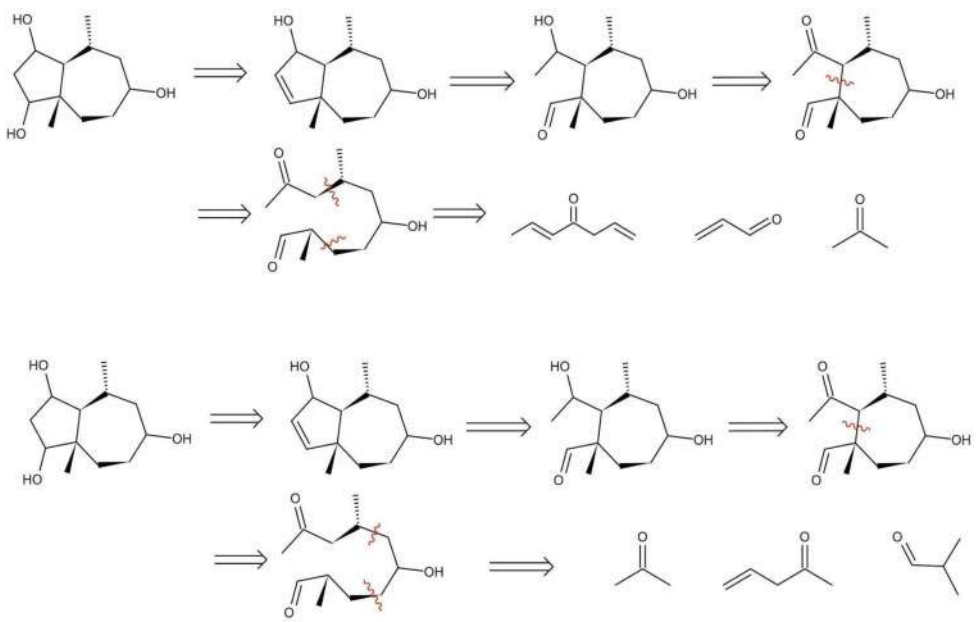

Figure 4. Retrosynthetic route 1.

3 and carbons 4 to simplify the long chain into three shorter chains. The chains are raw materials that can be obtained.

4 RETROSYNTHETIC ROUTE 2

Figure 5 shows one route is to disconnect the seven-membered ring first, breaking the molecule into a 5-methyl-1,3-cyclopentanedione and a long chain called 1,4-ene-3-hexanol which is a complicated molecule. (This step is involved in enolization). The long-chain could be simplified by undergoing a prins reaction under acidic conditions to obtain a propyne and a 2-ene-1-propanol. Because the dicarbonyl compounds can self-condensate through cyclization if it will generate a 5 or 6-membered ring (based on the knowledge of enolization and intramolecular condensation). When we decide to disconnect the 5-methyl 1,3-dicarbonyl cyclopropane, there are two options displayed in the following flow chart. (involved in enolization). Although the resulting carbonyl groups are slightly different from the position of the methyl, both of them can cyclize themselves to produce the 5-membered ring.

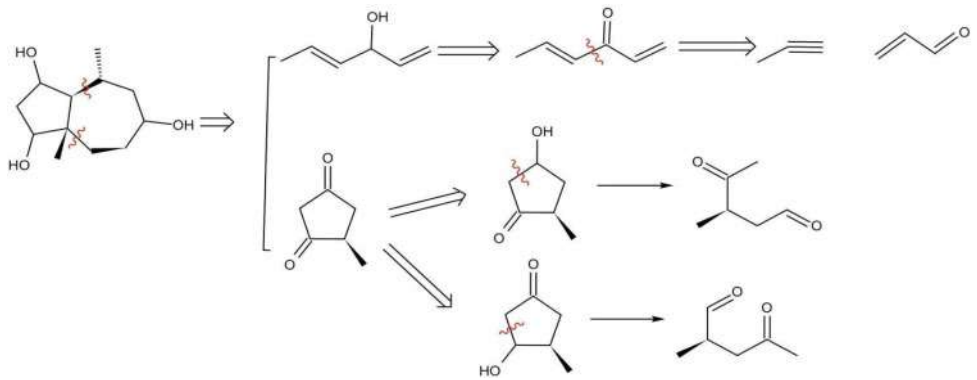

Figure 5. Retrosynthetic route 2.

5 RETROSYNTHETIC ROUTE 3

As shown in Figure 6, the other way begins with eliminating the methyl group which is at the common carbon of two rings, so that a double bond can be formed at the common side (W.H. Freeman and Company 2016). After that, electrons on the pi bond will be attracted into the seven-membered-ring, and leave the single bond which will break to give a 1,3-cyclopentanedione and

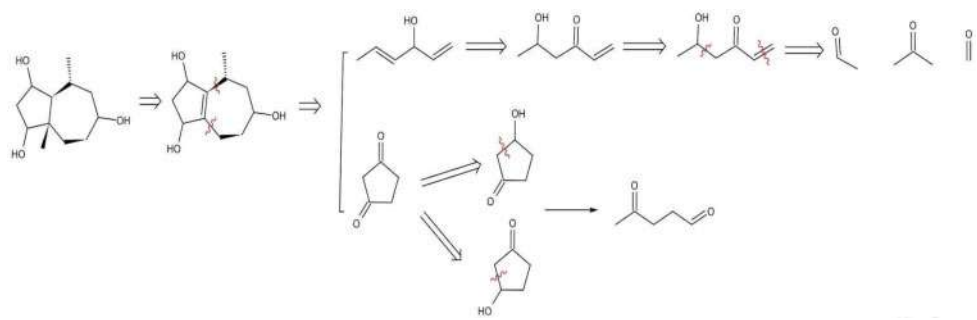

Figure 6. Retrosynthetic route 3.

1,4-ene-3-hexanol. To simplify the chain, the hydroxyl at carbon 3 is transferred to carbonyl group, then another hydroxyl group is added to break the double bond at carbon 4, and with the breakage of the double bond at carbon 1, an ethanal and a methanal and one acetone will be formed as the raw materials for this route. (Ungar & Dorfman 1952) As for the breakage of the 1,3-cyclopentanedione, it is the same process as route 2.

6 COMPARISON

Specifically looking at some factors affecting the feasibility that are particular in each routine. Just simply focusing on the reactants would be needed for each reaction first, it is not hard to find that the reactants with both double bond and carbonyls in routes 1 and 2 are more complicated than the carbonyls in route 3. From another perspective, we could look at the yielding of each route. One unique reaction in route 1 could be the formation of $\alpha - \beta$ unsaturated carbonyl using aldol reaction which has also taken place in route 3 for two times. But it should be having a better yield in route 3 since reactants are relatively simple. In contrast, the prins reaction in route 2 has a high possibility to give a mixture of different products which indicates the yielding won't be high and it would be difficult to separate them from each other.

7 CONCLUSION

In conclusion, the passage proposed three routes for the synthesis of sesquiterpene lactone. The common idea in all three routines is to gradually disconnect final molecule bonds in different ways by divergent thinking at first, to explore which path is reasonable. Through a relative literature review, It can be argued that all three routines are feasible according to their mechanisms although route 3 might be more suitable since it has a relatively higher yield and simple reactants compared to the other two routes. On the whole, the highlight of this paper is to disassemble molecules by the retrosynthetic thinking way, starting from the final molecule, which is an effective method to figure out reactants and synthetic paths. All the retrosynthetic processes can effectively cultivate the ability of logical and divergent thinking and the three different retrosynthetic routines presented above can provide a theoretical basis for future research. Hopefully, all three routines discussed above can be verified in the experiment in the near future to explore which method is the most convenient, effective, and environmentally friendly.

REFERENCES

F. Ungar, R. I. Dorfman. "Metabolism of Dgr1-Androstene-3,17-Dione", Science, 1952

Jinbin Wu, Yuito Chun and Yutaka Ebizuka, Biologically active constituents of Centipeda minima: Isolation of a new plenolin ester and the antiallergy activity of sesquiterpene lactones, 1985, 33, 4091–4094

Loudon, Parise, Organic Chemistry [six edition], W.H. Freeman and company, 2016

Qiu, Feng (2021/02/26). Cytotoxic and Anti-Inflammatory Sesquiterpenes from the Whole Plants of Centipeda minima. Journal of Natural Products, 84, 247–258. doi: 10.1021/acs.jnatprod.0c00884

SCRIBD, https://www.scribd.com, [accessed 10th November 2021]

Advances in Applied Chemistry and Industrial Catalysis – Saikia (Ed.)

Occurrence and transformation of arsenic from coal to ash fly via combustion

L. Jiang*
North China Electric Power Research Institute Co., Ltd, Beijing, China

Y. Xu**
Beijing Huake Tonghe Technology Co., Ltd, Beijing China

L. Du***
North China Electric Power Research Institute Co., Ltd, Beijing, China

ABSTRACT: The harmful element arsenic was selected as the research object, and the total amount and occurrence forms of arsenic in pulverized coal, fly ash, and desulfurization gypsum of four coal-fired power plants distributed in different regions were detected via a step-by-step extraction experiment. The main forms of arsenic in pulverized coal are reducible arsenic and residual arsenic, and the main forms of arsenic in fly ash are reducible arsenic. After combustion of pulverized coal, residual arsenic in pulverized coal changes to reducible arsenic in fly ash. The activity of arsenic after combustion is strengthened, which is more conducive to the migration of arsenic. The occurrence forms of arsenic in coarse ash and fine ash are the same, but the total amount of arsenic adsorbed by fine ash is larger, which is due to the larger specific surface area and stronger adsorption capacity of fine powder. The content of arsenic in fly ash is higher under low load than high load. The occurrence law of arsenic in pulverized coal and coal-fired solid waste was summarized, and the occurrence from the transformation process of arsenic in pulverized coal through high-temperature combustion was explored, which can guide restraining the environmental risk of arsenic in coal-fired solid waste.

1 INTRODUCTION

Coal burning is one of the main ways to release heavy metals in China, and coal-fired power station is the largest coal-consuming industry in China (Gong et al. 2020). The emission control of heavy metals in thermal power can control the problem of heavy metal pollution to a great extent (Shi et al. 2016). At present, the policies of ultra-low emission, energy conservation, and emission reduction of coal-fired power plants have effectively controlled the pollutant emission in flue gas (Hua et al. 2019; Zheng et al. 2017). However, the released heavy metals will not disappear out of thin air but will be transferred to the by-products of environmental protection measures such as dust removal and desulfurization, and then re-enter the environment. The output of desulfurized gypsum and fly ash in China is huge, and the resource utilization rate increases year by year (Jiang 2020). The existing heavy metals will be released again in the process of resource utilization, which has a great risk of secondary pollution (Tchounwou et al. 2012).

The environmental toxicity effects of different forms of compounds are quite different. The study on the total amount and occurrence forms of heavy metals (especially arsenic with strong toxicity) in solid waste of coal-fired power plants are helpful to understand and prevent their potential secondary pollution in the process of resource utilization (Mastalerz & Drobniak 2007; Shah et al. 2008). Exploring the occurrence forms of arsenic in coal-fired solid wastes can effectively solve

Corresponding Authors: *kaveykikiy@163.com, **675728887@qq.com and ***furanbotu@hotmail.com

DOI 10.1201/9781003308553-40

the possible secondary pollution caused by the stacking and comprehensive utilization of solid wastes in power plants, and provide a theoretical basis for the emission control of heavy metals in the recycling of desulfurization gypsum.

In this paper, the harmful element arsenic with high environmental risk was selected as the research object, and the total amount and occurrence forms of arsenic in pulverized coal, fly ash, and desulfurization gypsum of four coal-fired power plants distributed in different regions were detected via step-by-step extraction experiment. The occurrence law of arsenic in pulverized coal and coal-fired solid waste was summarized, and the occurrence from the transformation process of arsenic in pulverized coal through high-temperature combustion was explored, to guide restraining the environmental risk of arsenic in coal-fired solid waste.

2 EXPERIMENT AND METHODS

The improved Tessier process is adopted in the occurrence experiment, and the controlled element forms in fly ash are analyzed in five forms (Chen et al. 2020). The step-by-step extraction experiment shall be carried out according to the following steps.

(1) Ion exchange state (FR1)

Dry fly ash sample (5g) and 30ml $MgCl_2$ solution were put into 50ml polyethylene pipe for vibrating continuously for 30min at room temperature with the shaking speed of 200 r/min and then centrifuge for 15min. The supernatant was transferred into a 50ml volumetric flask with a pipette and stored at 4°C for ICP elemental analysis. The residue is washed and dried for the next step.

(2) Acid soluble state (FR2)

The remaining residue in step 1 and 30ml sodium acetate buffer solution (pH = 5) was put into a 50ml polyethylene pipe. After shaking the above solution at room temperature for 1h, refer to step 1 for subsequent steps.

(3) Reducible state (FR3)

The residue in step 2 is put into a 50ml polyethylene pipe, then 10ml hydroxylamine hydrochloride solution (0.1M) is added. After 80°C water bath for 1h, it is centrifuged at high speed for 15min. The supernatant was transferred into a 50ml volumetric flask and stored at 4°C.

(4) Oxide bound state (FR4)

The residue in steps 3 and 10ml H_2O_2 (30%) was put into a 50ml polyethylene pipe to seal and heat in a 90°C water bath for 1H. When the residue is evaporated to dryness at least, take it out and cool it, and 30ml ammonia acetate solution (1m) was added. Then repeat the above oscillation and centrifugation process.

(5) Residue state (R)

The residual residue in step 4 was digested by microwave in the HNO_3-HF-H_3BO_3 system. The digestion procedure refers to the raw ash digestion method.

The residue of each step shall be completely evaporated and weighed for mass balance analysis. The content of controlled elements in the extract was tested by ICP-MS.

3 RESULTS AND DISCUSSIONS

3.1 *Occurrence form of arsenic*

Different state contents of arsenic (As) in fly ash and coal were listed in Table 1. The main existing form of arsenic in the four coal-fired powders of four coal-fired power plants is reducible arsenic, accounting for 43.24%∼65.95%. The second is residual arsenic, accounting for 20.43%∼33.77%. The second is oxide-bound arsenic, accounting for 11.87%∼23.65%. The form with the lowest arsenic content in the four pulverized coal is ion-exchange arsenic, accounting for no more than 0.27%. On the whole, the form difference in pulverized coal is not as obvious as that of other metal elements.

Table 1. Different state content of arsenic in fly ash and coal (10^{-6}).

Power plant	Substance	FR1	FR2	FR3	FR4	R
1	Fine ash	0.32	1.36	6.84	0.86	1.8
	Coarse ash	0.02	0.78	2.74	0.15	0.37
	Coal	0	0.01	0.64	0.35	0.48
2	Fine ash	0.97	4	19.69	3.27	4.36
	Coarse ash	0.36	3.6	13.62	1.31	2.7
	Coal	0	0.12	1.05	0.36	0.78
3	Fine ash	3.26	12.3	78.27	9.82	8
	Coarse ash	0.35	11.2	106.31	14.36	12.97
	Coal	0.04	0.22	9.78	1.76	3.03
4	Fine ash	0.13	2.05	8.72	0.77	0.53
	Coarse ash	1.64	5.93	29.09	1.37	1.24
	Coal	0	0.02	3.43	1	1.18

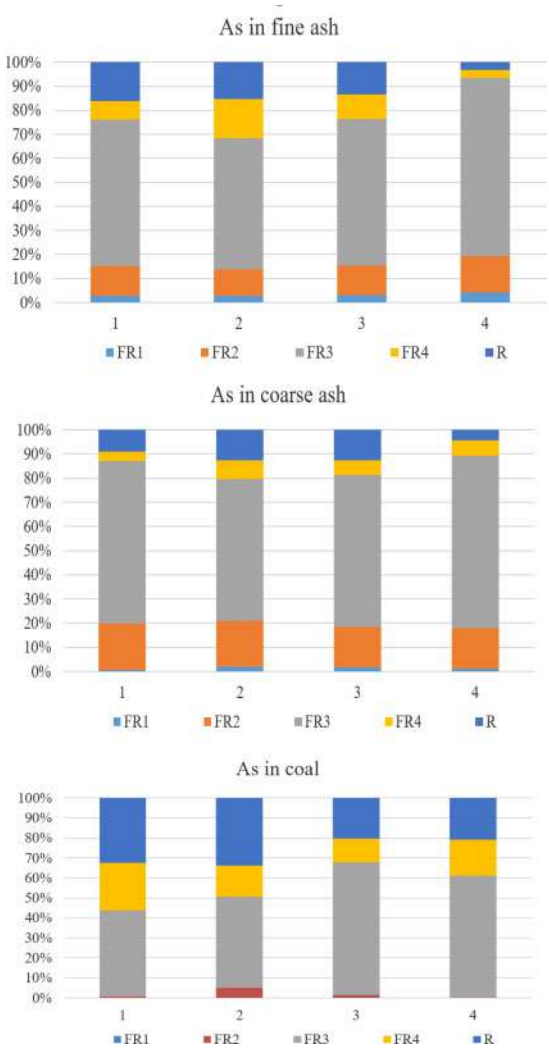

Figure 1. Different state proportions of arsenic in fly ash and coal (%).

The main existing form of arsenic in coarse ash and fine ash produced by the four coal-fired power plants is reducible arsenic, in which the proportion of fine ash is 54.59%~74.08%, and that of coarse ash is 58.76%~71.48%, which is 118.91% and 124.58% higher than that of reducible arsenic in pulverized coal respectively. The secondary occurrence form of arsenic in ash is residual arsenic, accounting for 3.16%~16.10% in fine ash and 4.34%~12.59% in coarse ash. It shows that the activity of arsenic is strengthened after combustion, which is more conducive to the migration of arsenic.

3.2 *Occurrence and transformation of arsenic*

The comparison of arsenic content in a unit mass of pulverized coal and fly ash of four coal-fired power plants shows that the arsenic content in fine ash > arsenic content in coarse ash > arsenic content in pulverized coal. With the consumption of other elements in the combustion of pulverized coal, the content of arsenic is enriched, especially in the fine ash with a smaller specific surface area. The distribution of arsenic on fly ash with different scales is significantly different, and the removal efficiency of arsenic by dust removal device is also affected by the scale and morphology of particulate arsenic. Particles with particle sizes in the range of 0.1~1 μm are easier to escape, so fine particles of this scale may also be easier to carry particulate arsenic to escape to the flue gas purification device behind the dust collector or into the atmosphere. Fly ash with different particle sizes will only change the content of arsenic adsorbed, but the occurrence form of arsenic will not change significantly.

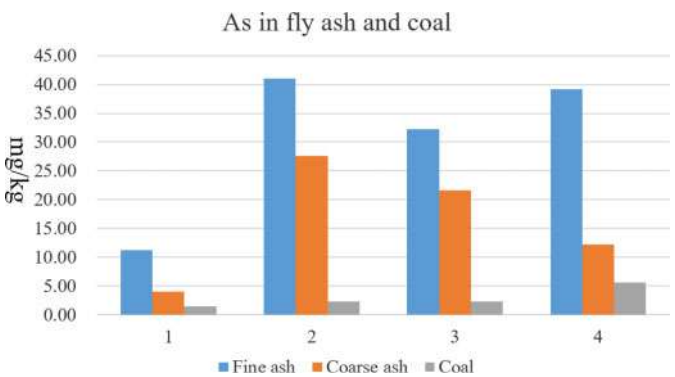

Figure 2. Comparison of arsenic content between fly ash and coal (mg/kg).

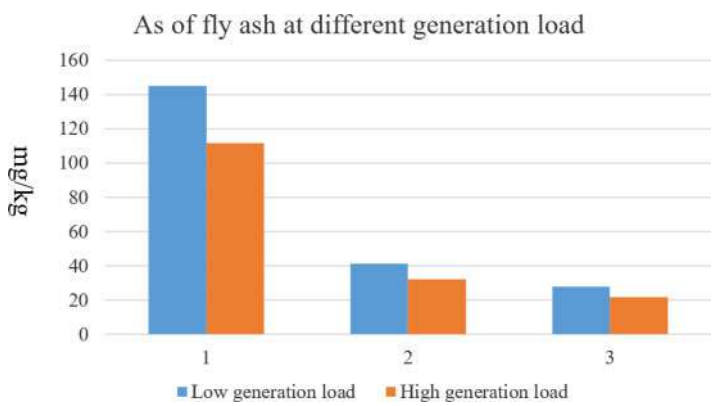

Figure 3. Arsenic content of fly ash at different generation loads (mg/kg).

Under the high-temperature environment of coal combustion, arsenic mainly migrates into the flue gas in the form of gas As_2O_3 (g). Many scholars have shown that gaseous arsenic is enriched in ash mainly through interaction with mineral components in coal (Sterling & Helble 2003). Arsenic migrated into fly ash can be captured together with particles under the action of a dust removal device, to reduce the emission of arsenic to the atmosphere during coal combustion.

Through the comparison of arsenic content in fly ash under different loads, it can be seen that the arsenic content in fly ash under low load is higher than in high load.

4 CONCLUSIONS

(1) The main forms of arsenic in pulverized coal are reducible arsenic and residual arsenic, and the main forms of arsenic in fly ash are reducible arsenic. After combustion of pulverized coal, residual arsenic in pulverized coal changes to reducible arsenic in fly ash. The activity of arsenic after combustion is strengthened, which is more conducive to the migration of arsenic.
(2) The occurrence forms of arsenic in coarse ash and fine ash are the same, but the total amount of arsenic adsorbed by fine ash is larger, which is due to the larger specific surface area and stronger adsorption capacity of fine powder.
(3) The content of arsenic in fly ash is higher under low load than high load.

REFERENCES

Chen, L. W., Chen, H. Y., Wu, J., Chao, S. L., & Q. Wei (2020) Comparative study on speciation of Cu, Pb and Zn from mining tailings via Tessier 5-step sequential extraction and improved BCR method. Journal of Safety and Environment. 20(2), 735–740.

Gong, H. Y., Hu, H. Y., Liu, H. M., Li, S., Huang, Y. D., Fu, B., Luo, G. Q., & H. Yao (2020) Review of arsenic transformation and emission control during coal combustion. Proceedings of the CSEE. 40(22), 7337–7351.

Hua, W., Sun, H. T., Qi, J. M., Huang, Z. J., Shi, Z. P., & L. B. Duan (2019) Emission characteristics of Pb and As from an ultra-low emission coal-fired power plant. Thermal Power Generation. 48(10), 65–70.

Jiang, L. (2020) Comprehensive utilization situation of fly ash in coal-fired power plants and its enlightenment to China. Clean Coal Technology. 26(4), 31–39.

Mastalerz, M., & Drobniak, A. (2007) Arsenic, cadmium, lead, and zinc in the Danville and Spring field coal members (Pennsylvanian) from Indiana. International Journal of Coal Geology. 71(1), 37–53.

Shah, P., Strezov, V., & K. Prince (2008) Speciation of As, Cr, Se and Hg under coal fired power station conditions. Fuel. 87(10–11), 1859–1869.

Shi, Y. H., & H. C. Wu (2016) Emission characteristics of Pb in coal-fired plants: research development. Thermal Power Generation. 45(1), 1–8.

Sterling, R. O., & J. J. Helble (2003) Reaction of arsenic vapor species with fly ash compounds: kinetics and speciation of the reaction with calcium silicates. Chemosphere. 51(10), 1111–1119.

Tchounwou, P. B., Yedjou, C. G., & A. K. Patlolla (2012) Heavy metals toxicity and the environment. EXS. 101, 133–164.

Zheng, T. T., Zhou, Y. G., & Q, Y. Jin (2017) Integrated removal and ultra-low emission of multiple pollutants for coal-fired power plants. Thermal Power Generation. 46(4), 10–15.

Advances in Applied Chemistry and Industrial Catalysis – Saikia (Ed.)

Preparation and properties of straw-based water absorbent materials

Yanping Qu*, Xueying Cao** Yuhe Bai*** & Fengyao Tian****
Environmental Science of Qilu Institute of Technology, China

ABSTRACT: Using corn straw as raw material, the water solution polymerization method was used to synthesize water absorption resin, and analyzed the initiator potassium persulfate dosage, crosslinking agent N-hydroxymethyl acrylamide (MBA) dosage, straw and acrylic acid mass ratio and temperature of four factors, selected three influential factors for an orthogonal test. The results showed that the optimum single factor preparation conditions were as follows: the mass ratio of acrylic acid to corn stalk was 5, the mass ratio of acrylic acid to acrylamide was 5, the crosslinking agent was 1.0%, the initiator was 1.0%, the reaction temperature was 70°C, the water absorption rate, was 17.232 $g \cdot g^{-1}$ and the water retention rate was 90.96%. The optimum preparation conditions were as follows: mass ratio of acrylic acid to straw was 5, initiator dosage ratio was 1.5%, and the reaction temperature was 70°C. Under these conditions, water absorption was 18.844 $g \cdot g^{-1}$ and water retention was 97.73%, indicating that the resin had good water absorption and water retention.

1 INTRODUCTION

Water absorption resin is a new type of functional polymer water absorption material with a very broad market prospect (Bai et al. 2015). It is insoluble in water, but with a large number of hydrophilic groups, can absorb dozens or even hundreds of times its weight of water, and then slowly solidified into a hydrogel, and can reuse (Cai et al. 2015; Karlsson et al. 2016; Tang et al. 2017). Using plant straw to prepare resin water-absorbent material can not only effectively utilize this rich renewable resource, but also reduce the preparation cost of the water-absorbent resin, so that it is easier to be promoted, and also provide a good reference for the utilization of other resources. Therefore, this paper takes corn straw as raw material and carries on the appropriate alkalization treatment to it (Wang et al. 2015). In the preparation process, the aqueous solution polymerization method was used to prepare a new type of corn straw water absorption resin (Wang et al. 2017; Zhao et al. 2015). The optimum preparation conditions of water-absorbing resin were determined by an orthogonal test, and the water-absorbing properties, water-retaining properties, and repeated water-absorbing properties of resin were studied. It is of great significance to reduce resource waste and prevent environmental pollution and provides an effective way for the resource utilization of corn straw in China.

2 SYNTHESIS OF STRAW-BASED WATER-ABSORBENT RESIN

Add an appropriate amount of straw into the prepared beaker, add 10% NaOH solution at a ratio of 10:1 by volume, put it into a 95°C water bath, stir it slowly with a glass rod, and heat it for 120 min. After alkali cooking, wash the modified straw with distilled water to neutral and then dry it in the air-blast drying oven at 55°C∼60°C for later use.

Corresponding Authors: *805025846@qq.com, **1219295424@qq.com, ***2357333170@qq.com and ****3196312541@qq.com

DOI 10.1201/9781003308553-41

3 RESULT AND ANALYSIS

3.1 *Effects of different conditions on properties of a straw-based water-absorbent resin*

3.1.1 *Analysis of the influence of straw to acrylic acid mass ratio on water absorption performance*

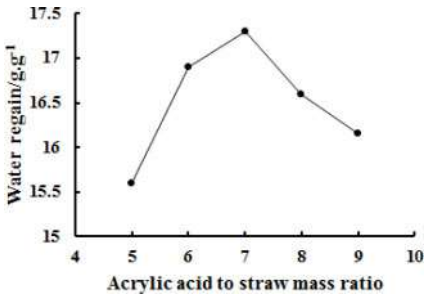

Figure 1. Effect of the acrylic acid and straw mass ratio on the resin water absorption rate.

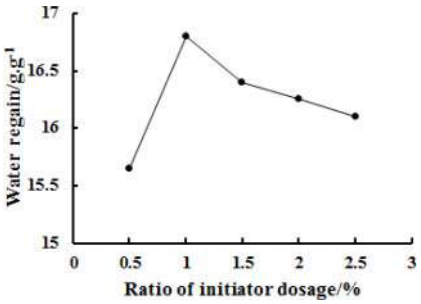

Figure 2. Effect of the initiator dosage on the water absorption rate of the resin.

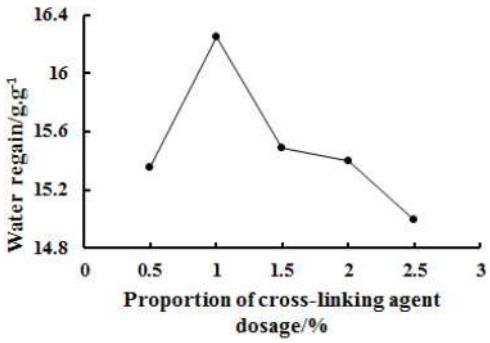

Figure 3. Effect of crosslinker dosage on resin absorption of water.

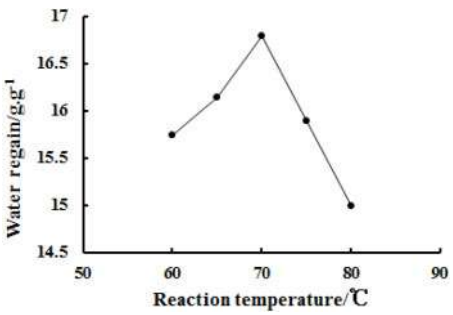

Figure 4. Effect of reaction temperature on resin absorption of water.

According to the changing trend in Figure 1 when the mass ratio of acrylic acid to straw is 5–7, the water absorption rate of the resin increases with the increasing mass ratio of acrylic acid to straw. When the mass ratio of acrylic acid to straw was 7 to 9, the water absorption decreased with the increase of the mass ratio of acrylic acid to straw. This is because the skeleton structure of water absorption resin is mainly composed of cellulose, and the resin monomer takes place in graft copolymerization reaction on the cellulose skeleton. Acrylic acid contains hydrophilic groups, which are closely related to the hydrophilic groups on the water absorption resin. When the mass ratio of acrylic acid to straw is not large, these groups will graft and copolymerize on the skeleton structure, which will improve the water absorption capacity of the water absorption resin. But when the acrylic acid and straw quality is relatively large, the formation of the network structure of the skeleton is relatively close, other monomers are difficult to graft copolymerization to the skeleton structure of cellulose, slowly improving the amount of acrylic acid, not only will not make the water absorption resin water absorption performance becomes high but also reduce. Through the analysis of experimental results, acrylic acid and straw mass ratio of 7 water absorption resin water absorption effect are the best.

3.1.2 *Analysis of the influence of initiator proportion on water absorption and water retention*
As can be seen from Figure 2, water absorption is significantly correlated with the initiator, which increases first and then decreases when the latter increases. The highest water absorption rate was reached when the initiator dosage was 1.0%. This is because the initiator can prompt the scion grafting polymerization reaction, and can form a stable three-dimensional reticular structure, helps to improve response speed and bibulous rate, early in the process of the initiator dosage began to increase, bibulous rate is kept fast growth the tendency, but when the dosage of initiator has reached a certain level, still keep increasing trend, Will cause the polymerization reaction rate is too fast, cause detonation so that the internal part of the hygroscopicity resin self-polymerization crosslinking, thus forming a large number of low molecular polymer, water absorption resin harms the water absorption performance, the water absorption rate decreased significantly. The experimental results show that the water absorption property of the resin reaches the highest value when the initiator ratio reaches 1.0%.

3.1.3 *Analysis of the influence of the proportion of crosslinking agents on water absorption and water retention*
Figure 3 shows that water absorption is also correlated with the amount of crosslinker. In general, the water absorption rate of water absorption resin increased first and then decreased with the increase of the amount of crosslinking agent. When the proportion is between 0.5% and 1.0%, there is a positive correlation between the two, because at this time, with the increase of the amount of crosslinking agent, the polymer network structure will polymerize more closely and the crosslinking degree of the polymer will increase. The polymer is easy to form an expansion network structure, so the corresponding water absorption rate will also increase; In the case of 1.0%∼2.5%, the two are in a negative correlation. At this time, due to a large number of crosslinking points, the complexity of the mesh structure is increased and the water absorption performance is reduced. The experimental results show that the maximum water absorption rate appears at 1.0%, the best water absorption effect.

3.1.4 *Analysis of the effect of reaction temperature on water absorption and retention*
Figure 4 shows that the water absorption rate of water absorption resin is also significantly correlated with the reaction temperature. In general, the increase in reaction temperature shows a trend of increasing first and then decreasing. This is because in the case of low temperature, increasing the temperature can form a lot of heat, and promote the degree of molecular activity and the fluidity of the solvent, so that the polymerization reaction can be more fully completed, to improve the water absorption of the resin. However, when the temperature is too high, it is easy to cause high polymerization or even burst polymerization, which affects the progress of graft copolymerization reaction, resulting in an unstable reaction and thus adversely affecting the water absorption performance of the obtained water absorption resin. In addition to the above effects, the state of high temperature may produce unnecessary side reactions, the by-products will also affect the water absorption capacity of the water absorption resin. By observing the experimental results, it is shown that the water absorption of the resin reaches the best effect when the reaction temperature is 70°C.

3.2 *Analysis of orthogonal test results*

Experimental results of the analysis of single-factor experiment found that the factors for the bibulous rate of water absorption resin can produce different effects, including the dosage of crosslinking agent on water absorption resin absorption performance of minimal impact, so choosing the best crosslinking agent accounted for as a fixed amount of orthogonal test, and then the other three factors as orthogonal experimental parameters were analyzed, and each factor set three levels.

At this time, the maximum water absorption of the hydro absorbent resin was 18.844 $g \cdot g^{-1}$ (mass ratio of acrylic acid to straw, initiator dosage ratio of 1.5%, reaction temperature of 70°C), and the water retention rate decreased to 12.082 $g \cdot g^{-1}$ on the third day.

Table 1. Results of orthogonal test.

Number	The quality ratio of acrylic to straw	Evocator/%	Reaction temperature/°C	Water absorption/g·g^{-1}	Retention rate/%
1	5	1.0	65	16.228	95.68
2	5	1.5	70	18.844	97.73
3	5	2.0	75	15.026	93.02
4	6	1.0	70	18.836	96.92
5	6	1.5	75	15.404	97.84
6	6	2.0	65	15.324	96.34
7	7	1.0	75	15.950	97.93
8	7	1.5	65	16.148	96.25
9	7	2.0	70	15.066	95.20
K_1	50.098	51.014	47.700	33	
K_2	49.564	50.396	52.746		
K_3	46.804	45.416	46.38		
R	3.294	6.598	6.3660		

4 CONCLUSION

(1) After selecting and comparing the results of a single-factor experiment, the ranking order of influencing factors is as follows Acrylic acid to straw mass ratio>Initiator>Reaction temperature>Crosslinking agent. Among single factors, the optimum preparation conditions for water absorption were as follows: the mass ratio of acrylic acid to straw was 5, the ratio of initiator and the crosslinking agent was 1%, and the reaction temperature was 70°C.

(2) Select three of the four single factors in the absorbent resin water absorption and water retention performance influential factors in the orthogonal experiment, because of the influence of crosslinking agent in the single factor experiments to a minimum, so that the dosage of crosslinking agent and acrylic acid as straw quality than as an experiment in which a fixed amount, then further to explore other factors, The optimum preparation conditions were as follows: the mass ratio of acrylic acid to corn straw was 5, the mass ratio of acrylic acid to acrylamide was 5, the initiator accounted for 1.5% of the total mass of the resin, and the reaction temperature was 70°C. Under these conditions, the water absorption rate of the resin was 18.844 g·g^{-1}, and the water retention rate was 97.73%, indicating that the resin had good water absorption and water retention properties.

REFERENCES

Bai, M., Wilske, B., Buegger, F., J Esperschütz, Bach, M., & Frede, H. G., et al. (2015). Relevance of nonfunctional linear polyacrylic acid for the biodegradation of superabsorbent polymer in soils. Environ. Sci. Pollut. Res. Int., 22(7), 5444–5452.

Cai, S. T., Zhou, M., & Qian, X. (2015). β-cyclodextrin modified hybrid magnetic nanoparticles as an adsorbent for phenol removal. Adv. Mater. Res., 1095, 63–66.

Karlsson, K., R Kádár, Stading, M., & Rigdahl, M. (2016). Processing window for extrusion foaming of hydroxypropyl methylcellulose. Cellulose, 23(3), 1–11.

Tang, X., Zuo, F., Tang, X., & Wang, H. (2017). Preparation of liquor flavoring from yellow water based on water absorbent resin. Agric. Biotechnol., v.6(06), 62–68.

Wang, K. Y., Cen, R. F., & Shu, W. W. (2015). Preparation and performance of super-absorbent resin using polyacrylonitrile fiber wastes. Adv. Mater. Res., 1120–1121, 498–501.

Wang, Z., Ning, A., Xie, P., Gao, G., Xie, L., & Li, X., et al. (2017). Synthesis and swelling behaviors of carboxymethyl cellulose-based superabsorbent resin hybridized with graphene oxide. Carbohydr. Polym., 157, 48–56.

Zhao, F., Repo, E., Yin, D., Meng, Y., Jafari, S., & Sillanpaeae, M. (2015). Edta-cross-linked β-cyclodextrin: an environmentally friendly bifunctional adsorbent for simultaneous adsorption of metals and cationic dyes. Environ. Sci. Technol., 49(17), 10570.

Advances in Applied Chemistry and Industrial Catalysis – Saikia (Ed.)

Collaboration between C-H activation and pericyclic reactions for constructing fused eight- and four-membered carbocycles

Zuhong Wang*
Harrow International School Beijing, Beijing, China

ABSTRACT: Pericyclic reactions are often highly regio- and stereoselective. Approaches involving these reactions are often high-yielding for synthesising fused eight- and four-membered carbocycles. Unfortunately, most of these methods suffer from highly functionalised starting materials and sometimes involve expensive catalysts. This article reviews Xingwei Li and co-workers' novel approach for synthesising fused eight- and four-membered carbocycles, which broke through the above two problems the traditional pericyclic approaches faced when constructing the two carbon frameworks above. It is via the C-H activation of less functionalised starting materials catalysed by a manganese(I) catalyst, followed by pericyclic reactions. Manganese is readily available and has low toxicity. This article also introduces the past development of synthesising these two carbon frameworks via pericyclic reactions and the synthesis of the starting materials for these pericyclic reactions via C-H activation.

1 INTRODUCTION

The ability to synthesise fused carbocycles is of great importance, as many natural products possess such structure frameworks. For example, cananodine (Figure 1), a guaipyridine alkaloid, possesses a fused carbocycle (Hsieh et al. 2001).

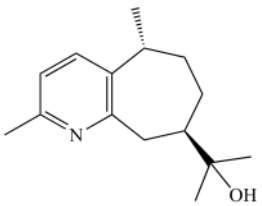

Figure 1. Structure of cananodine.

Cananodine exhibits high anti-cancer activity against hepatocarcinoma. However, it is isolated from the fruits of *Cananga odorata* only in small quantities (10 mg per 3.5 kg) (Hsieh et al. 2001). Many other useful natural products consisting of a fused carbocycle possess a similar problem, hence the need for developing efficient methods for synthesising fused carbocycles.

Many efforts of preparing fused eight- and four-membered carbocycles were made in recent decades (He et al. 2016; Hoyt et al. 2015; Smith & Baran 2015; Wang & Lu 2018; Wang & Yu 2015; Willcox et al. 2016; Yet 2000); some are via pericyclic reactions that are often highly regio- and stereoselective, such as the following two approaches.

2 USING PERICYCLIC REACTIONS TO PREPARE FUSED EIGHT- AND FOUR-MEMBERED CARBOCYCLES

In 2006, S. Ma and co-workers discovered that cycloisomerisation would occur favourably in β-(1, 2-Allenyl) butenolides and 2-Allyl-3-allenylcyclohex-2-enones when heated in xylene solvent under specific

*Corresponding Author: xinbabj@163.com

DOI 10.1201/9781003308553-42

temperature, resulting in fused eight-membered carbocycles at high yield (Gu & Ma, 2006). The mechanism of this cycloisomerisation was proposed to be as shown in Figure 2 (Gu & Ma, 2008). The structure of 2-Allyl-3-allenylcyclohex-2-enone is shown in Figure 3.

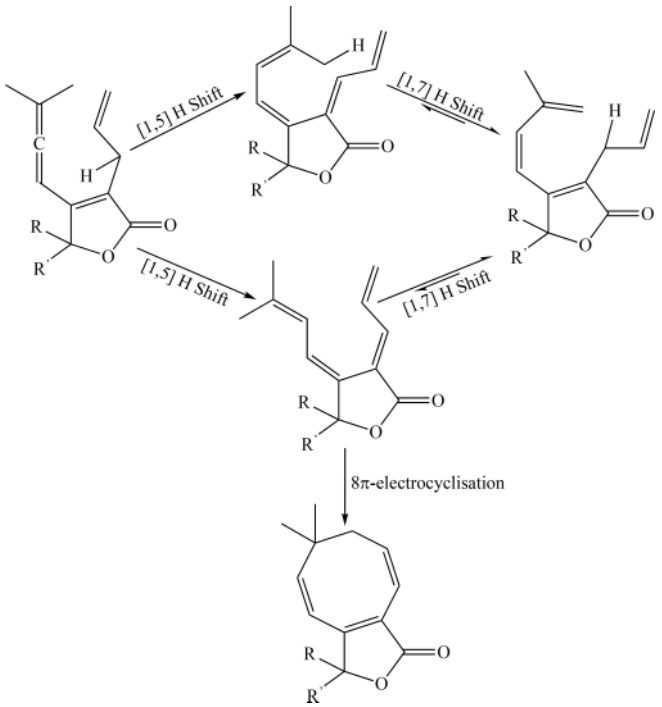

Figure 2. Plausible pathway for the cycloisomerisation of β-(1,2-Allenyl) butenolides (Gu & Ma 2008).

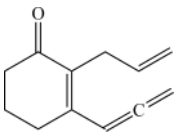

Figure 3. Structure of 2-Allyl-3-allenylcyclohex-2-enone.

In 2007, F.D. Toste and co-workers reported that gold(I)-catalysed intramolecular formal [2+2] cycloaddition would occur in various allenenes, which results in the production of fused four-membered carbocycles. This cycloaddition is not typical, as it is stepwise, with an ionic intermediate (Figure 4). Despite this, F.D. Toste's reaction is still high-yielding and highly enantioselective (Luzung et al. 2007).

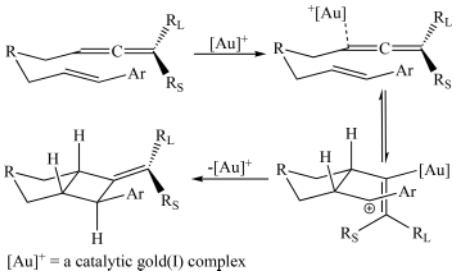

Figure 4. Plausible mechanism of F.D. Toste's approach (Luzung et al. 2007).

A common problem with these pericyclic methods is that they involve highly functionalised starting materials. This problem was sufficiently resolved by X. Li and co-workers in 2019.

3 THE ROLE OF C-H ACTIVATION

X. Li successfully developed a method to carry out S. Ma or F.D. Toste's approach while preparing the starting materials in situ via the C-H activation of less functionalised materials (Figure 5) (Kong; Li; Xu & Zheng, 2019).

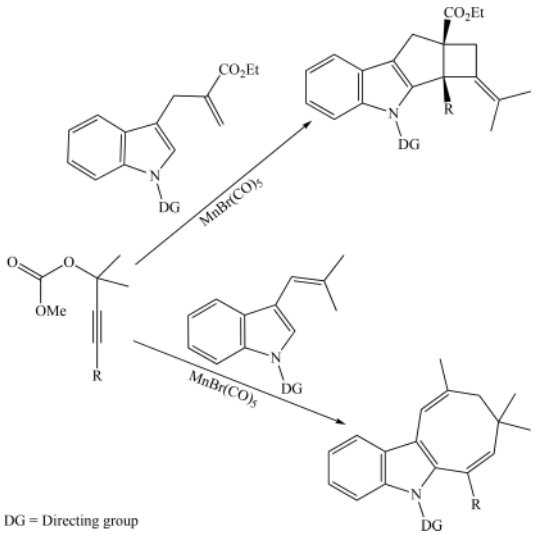

Figure 5. X. Li's novel approach (Xu et al. 2019).

C-H activation has recently emerged as a possible methodology to functionalise one of the most common inert bonds in organic compounds: the C-H bond. S. Ma and co-workers pioneered allene synthesis via C-H activation of arenes in 2015 at a high yield by applying propargyl esters and using a rhodium (III) catalyst (Figure 6) (Wu et al. 2015).

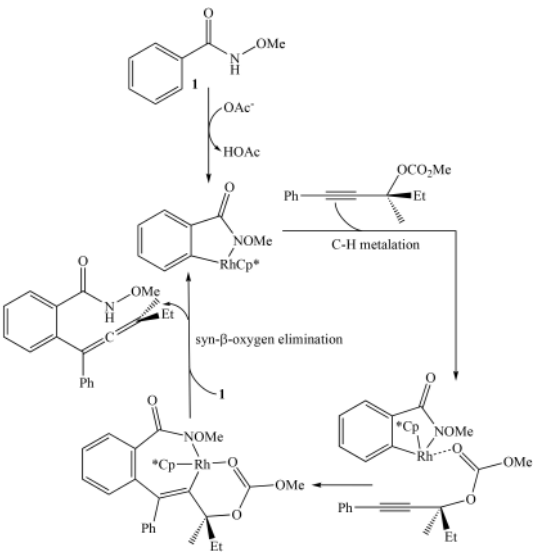

Figure 6. Possible mechanism of S. Ma's approach (Wu et al. 2015).

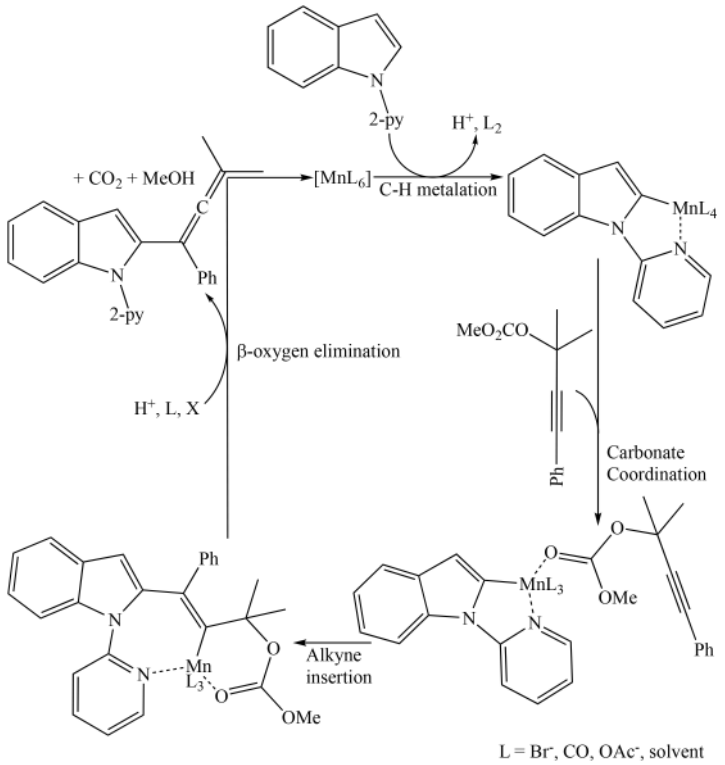

Figure 7. Plausible mechanism of F. Glorius' approach (Lu et al. 2017).

In 2017, F. Glorius and co-workers realised that in an indole system, with the nitrogen atom connected to certain directing groups and using a manganese(I) catalyst, S. Ma's allene synthesis would take place while maintaining a high yield (Figure 7). This method is more practical since manganese(I) is readily available and has low toxicity (Lu et al. 2017), and is therefore employed by X. Li in his approach (Xu et al. 2019).

4 INTEGRATED APPROACH

X. Li's integrated approach has considerable potential, as it utilises less functionalised starting materials while being highly regio- and stereoselective, possessing a high functional group and steric hindrance tolerance, and it avoids the use of expensive gold(I) catalyst and instead employs a manganese(I) catalyst. For three products produced by his method, X. Li, in his paper, demonstrated their synthetic utility, each in a different existing reaction, which all turned out to be selective, with good yields (Figure 8) (Xu et al. 2019).

Despite the advance, X. Li's approach still faces some limitations. For example, the preinstalled olefin group creates steric hindrance, precluding the application of some rhodium (III) or cobalt (III) catalysts in this reaction. Besides, his method fails when constructing a fused eight-membered carbocycle if the preinstalled olefin group is monosubstituted. This indicates the need for future studies in X. Li's methodology (Xu et al. 2019).

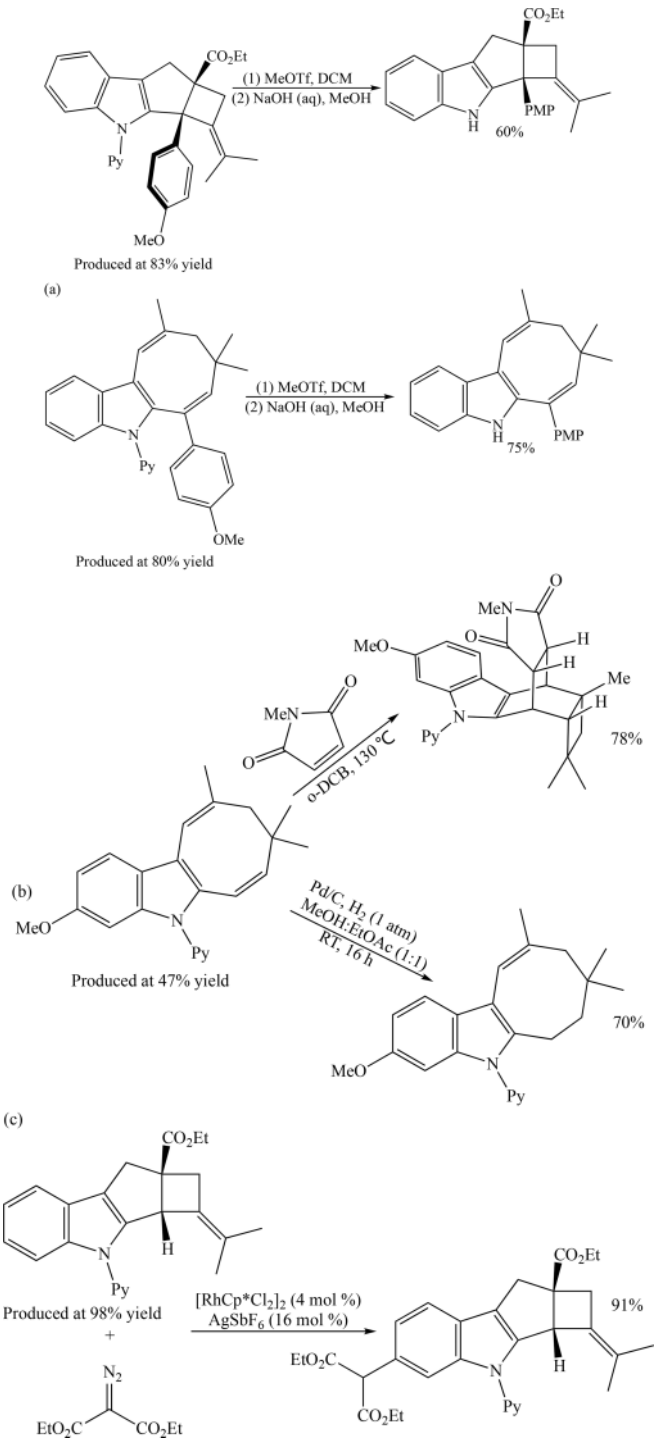

Figure 8. Applications of X. Li's approach (Xu et al. 2019).

5 CONCLUSION AND FUTURE PERSPECTIVES

In conclusion, X. Li's novel method for synthesising fused eight- and four-membered carbocycles via merging C-H activation and pericyclic processes sufficiently resolved two major problems of the traditional pericyclic methods, that are using highly functionalised starting materials, and in the case of synthesising fused four-membered carbocycles – the use of an expensive gold(I) catalyst. It is believed that in the future, more catalytic systems other than those involving manganese(I) and more substrates would be applicable for X. Li's integrated approach. Besides, it would be growingly common for C-H activation to be combined with pericyclic approaches at constructing a broader range of carbocycles to make these pericyclic methods less costly and more efficient.

REFERENCES

Gu, Z., Ma, S. (2008) Studies on Thermal Reactivity of β-(1,2-Allenyl) butenolides and 2-Allyl-3-allenylcyclohex-2-enones. Chem. Eur. J., 14: 2453–2464.

He, G., Lu, G., Guo, Z., Liu, P., Chen, G. (2016) Benzazetidine synthesis via palladium-catalysed intramolecular C-H amination. Nat. Chem., 8: 1131–1136.

Hoyt, J.M., Schmidt, V.A., Tondreau, A.M., Chirik, P.J. (2015) Iron-catalyzed intermolecular [2+2] cycloadditions of unactivated alkenes. Science, 349: 960–963.

Hsieh, T.J., Chang, F.R., Chia, Y.C., Chen, C.Y., Chiu, H.F., Wu, Y.C. (2001) Cytotoxic Constituents of the Fruits of Cananga odorata. J. Nat. Prod., 64: 616–619.

Lu, Q., Greßies, S., Klauck, F.J.R., Glorius, F. (2017) Manganese(I)-Catalyzed Regioselective C-H Allenylation: Direct Access to 2-Allenylindoles. Angew. Chem. Int. Ed., 56: 6660–6664.

Luzung, M.R., Mauleón, P., Toste, F.D. (2007) Gold(I)-Catalyzed [2 + 2]-Cycloaddition of Allenenes. J. Am. Chem. Soc., 129: 12402–12403.

Ma, S., Gu, Z. (2006) Sequential Rearrangement of 1,2,4Z,7-Tetraenes Involving [1,5]-Hydrogen Migration and Electrocyclization: An Efficient Synthesis of Eight-Membered Cyclic Compounds. J. Am. Chem. Soc., 128: 4942–4943.

Smith, M.W., Baran, P.S. (2015) As simple as [2+2]. Science, 349: 925–926.

Wang, M., Lu, P. (2018) Catalytic approaches to assemble cyclobutane motifs in natural product synthesis. Org. Chem. Front., 5: 254–259.

Wang, Y., Yu, Z.X. (2015) Rhodium-Catalyzed [5+2+1] Cycloaddition of Ene–Vinylcyclopropanes and CO: Reaction Design, Development, Application in Natural Product Synthesis, and Inspiration for Developing New Reactions for Synthesis of Eight-Membered Carbocycles. Acc. Chem. Res., 48: 2288–2296.

Willcox, D., Chappell, B.G.N., Hogg, K.F., Calleja, J., Smalley, A.P., Gaunt, M.J. (2016) A general catalytic β-C–H carbonylation of aliphatic amines to β-lactams. Science, 354: 851–857.

Wu, S., Huang, X., Wu, W., Li, P., Fu, C., Ma, S. (2015) A C–H bond activation-based catalytic approach to tetrasubstituted chiral allenes. Nat. Commun., 6: 7946.

Xu, Y., Zheng, G., Kong, L., Li, X. (2019) Manganese(I)-Catalyzed Synthesis of Fused Eight- and Four-Membered Carbocycles via C-H Activation and Pericyclic Reactions. Org. Lett., 21: 3402–3406.

Yet, L. (2000) Metal-Mediated Synthesis of Medium-Sized Rings. Chem. Rev., 100: 2963–3008.

Advances in Applied Chemistry and Industrial Catalysis – Saikia (Ed.)

A proposed synthesis routine of akuammicine, one of the akuamma alkaloids from the seeds of the akuamma tree

Yangyi Gu*
School of Chemistry, Chemical Engineering, and Life Sciences, Wuhan University of Technology, Wuhan, Hunan, China

Tianhe Zheng
Guanghua Cambridge International School, Shanghai, China

Jiongchen Guo
Shanxi Cambridge international school, Jinzhong, Shanxi, China

ABSTRACT: In this paper, a synthesis routine of akuammicine is proposed. The akuammicine is synthesized by indoles within a few steps. The chirality of carbon 13 is ensured by Chiral HPLC Columns technology, which is the focus of the whole synthetic analysis. What's more, the two rings of akuammicine are generated by the Diels-Alder reaction and Heck reaction, which is the innovation of this approach. Akuammicine is a kind of indole alkaloid from akuamma tree seed extract and it can treat various diseases, such as malaria, dysmenorrhea, and gastrointestinal diseases. Therefore, it is of great significance to study the rapid and effective synthesis method of akuammicine for the medical industry and even the future development of human beings.

1 INTRODUCTION

For centuries, people of Western Africa use the akuamma tree to treat ailments and the seeds of the akuamma tree have been used as a traditional treatment for pain and fever. Recent studies have confirmed that the effective constituent comes from a series of indole alkaloids within the seed extracts and akuammicine is one of them. The research of preparation methods of it can help us create new drugs that have unique pharmacologic properties and therapeutic utility. (Creed Simone et al. 2020).

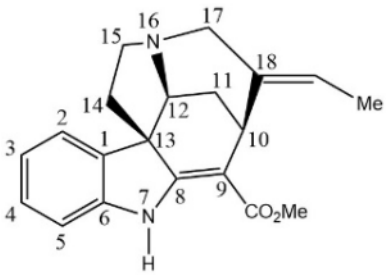

Scheme 1. The structure of akuammincine.

Akuammicine is a monoterpenoid indole alkaloid with the formula $C_{20}H_{22}N_2O_2$, isolated from several plant species including Alstonia spatula, Catharanthus roseus, and Vinca major. It is found in the Apocynaceae family of plants including Picralima nitida, Vinca minor, and the Aspidosperma. It has the role of plant metabolite

*Corresponding Author: 957342149@qq.com

DOI 10.1201/9781003308553-43

and has a melting point of 182°C and pKa of 7.45 whose IUPAC Name is methyl (19E)-2,16-didehydrocur-19-en-17-oate (Scheme 1). In this paper, a synthesis method of akuammicine is proposed (Christophe Wiart PharmD 2013).

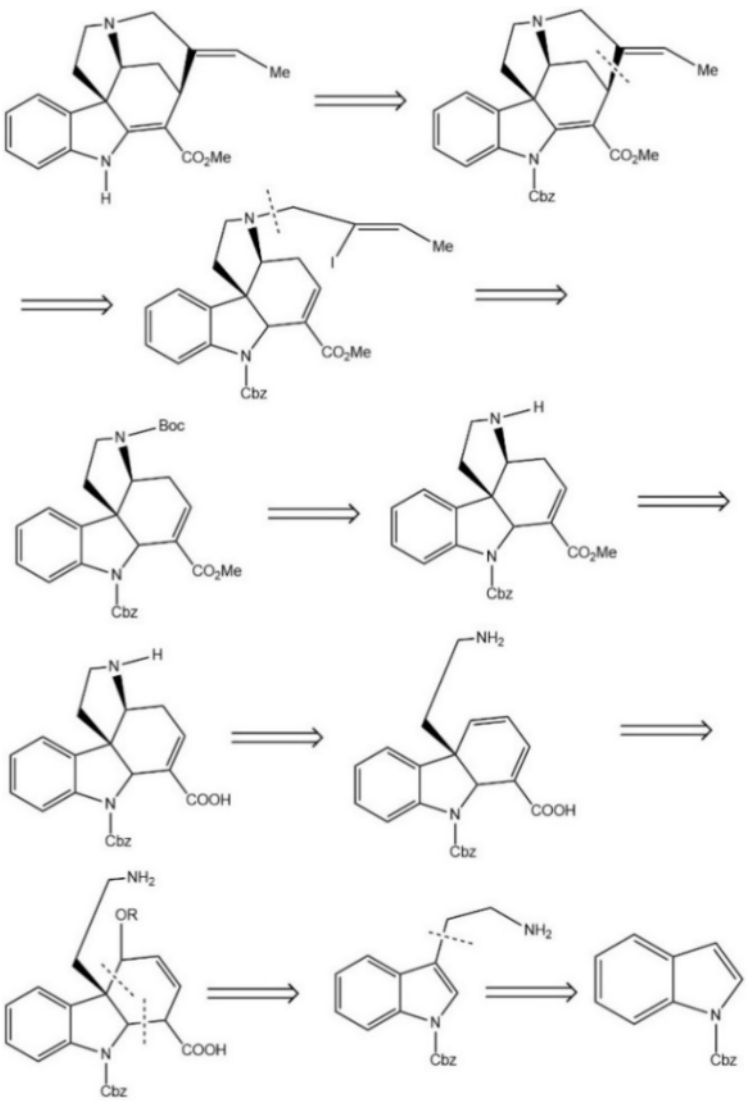

Scheme 2. Retrosynthetic analysis of akuammicine.

2 SPECIFIC CONTENT AND DISCUSSION

The first step of the proposed retrosynthesis is to make a disconnection of the carbon-carbon bond between positions 10 and 18, which is based on the Heck cyclization reaction. The advantage of this disconnection is that the reaction of an alkene by alkylation or arylation can easily happen. The second step is to break the carbon-nitrogen single bond between positions 16 and 17. Then, the third step is also the breaking of the carbon-nitrogen single bond but between positions 12 and 16. This shows the electrophilic addition reaction between amines and alkenes. After that, the fourth step is the key to the whole retrosynthesis. It is shown that

two carbon-carbon single bonds are connected at the same time, which is related to the Diels-Alder reaction. The final step is the electrophilic substitution of indole, so it is obvious that the raw material is indole. However, the indole molecule contains an amino group that could take participate in side reactions, so it is necessary to protect it at the beginning. (scheme 2).

Akuammicine is one of the indole alkaloids found within the seed extracts, to obtain this structure, indole is chosen as the material because of its structural similarity to the target product and high accessibility in the laboratory. The retrosynthesis shows that the amidogen may participate in side reactions, so indole can be treated with Cbz-Cl to protect the secondary amine as **9**. The Cbz group is a very old amino protecting group discovered by Bergmann in 1932 but is still in use today. Its advantages are as follows: the preparation of reagents and the introduction of protective groups are relatively easy; Benzyloxycarbonyl amino acids are not easily racemized during activation. It can also be selectively removed in a variety of mild ways. Then, **9** can be converted into **8** by electrophilic substitution of indoles. Position 13 will be much more favored than position 8 due to the difference in nucleophilicity. (scheme 3)

After that, **8** could be directly treated with **12** to achieve a cyclization reaction by using the Diels-Alder reaction. As for **7**, the carbon-carbon double bond is attached to the alkoxy group so that the double bond will be activated, making the DA reaction easier to happen successfully. However, it is worth noting that there will be two paths in the tautomerism, providing a pair of enantiomers. These two paths show that the chirality of carbon 13 can be various. Thus, **7a** and **7b** will be separated in a special method such as "Chiral HPLC Columns Technology" and so on. (scheme 4)

After **7a** is obtained, the alcohol can be easily eliminated in an acidic condition to get **6**. This step reflects the conversion of olefin to conjugated diene. At the same time, a carboxyl group is attached to it, making the three double bonds a conjugated system, so the structure is more stable and the reaction is more conducive to happening. Then, nitrogen has a lone pair that allows it to attack the carbon-carbon double bond, so the primary amines undergo addition reactions with alkenes to get **5**. By the way, the double bond between positions 9 and 10 plays an electron-withdrawing role in the double bond between positions 11 and 12, which also facilitates the Michael addition between the amino group and the double bond. The mechanism of the reaction is shown below. (scheme 5)

Next, **4** can be easily gotten by a simple esterification reaction. The volatiles was removed and replaced with fresh MeCN before the solution of the crude free amine was treated with Hünig's base and bromide **11** to give N-alkylated tetracycle **3**. (Snaddon et al. 2020) Conversion to **2** was then achieved in the usual manner using Rawal's Heck cyclization (Rawal et al. 1993) (scheme 6). The coupling reaction between aryl or vinyl halides

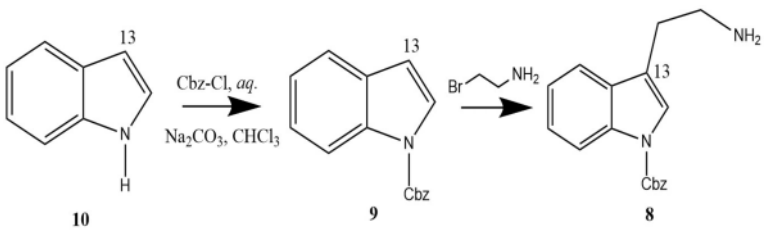

Scheme 3. Synthesis of 8 by the protection of imine and then electrophilic substitution reaction.

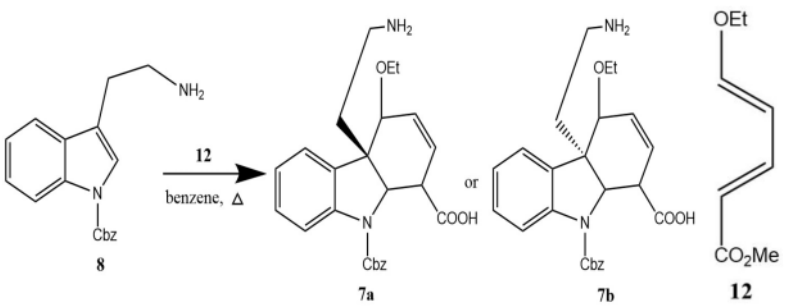

Scheme 4. Synthesis of 8 by Diels-Alder reaction.

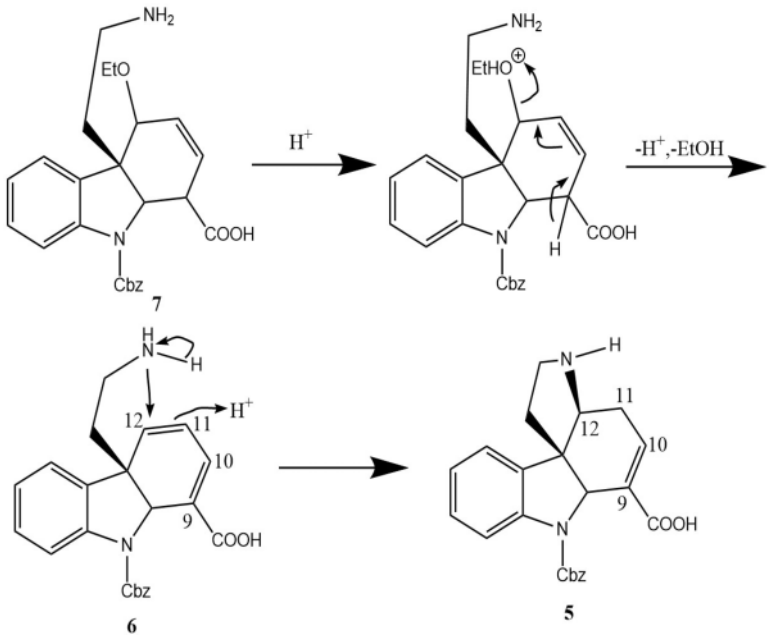

Scheme 5. The mechanism of synthesis of 5.

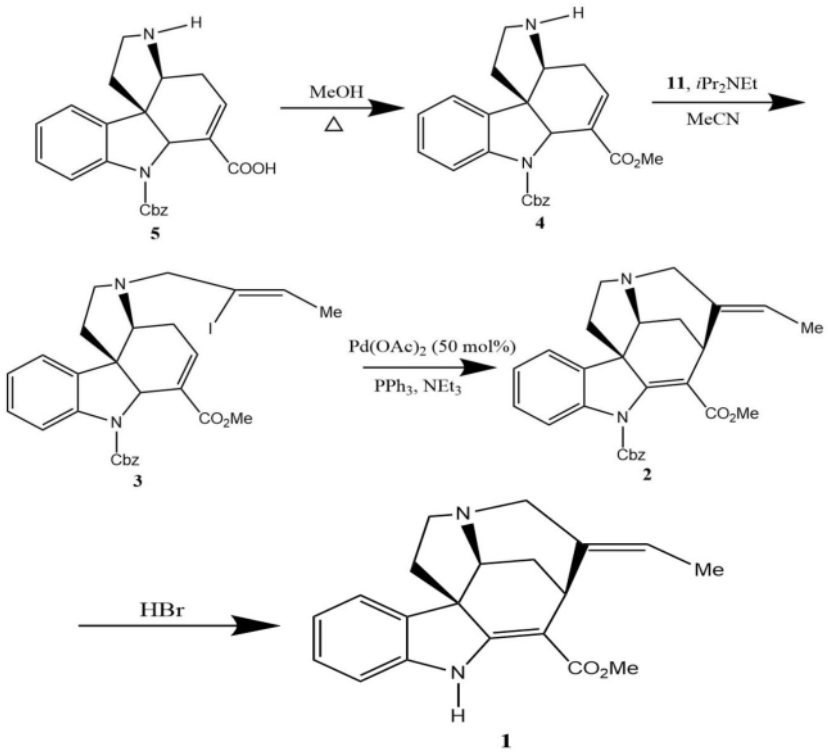

Scheme 6. Synthesis of 2 by electrophilic substitution of amines and Rawal's Heck cyclization reaction.

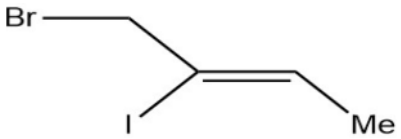

Scheme 6. continued.

and active olefin catalyzed by palladium under alkaline conditions is usually called the Heck reaction. Since Heck and Morizoki independently discovered this reaction in the late 1960s, the continuous improvement of catalysts and reaction conditions has made its application range more and more extensive, making this reaction become one of the most important reactions that constitute C-C bond. In addition, Heck reaction has good Trans selectivity. Finally, the akuammicine can be acquired through the step of removal treatment of Cbz group. The method is acidolysis by using HBr.

3 CONCLUSION

This paper provides a new idea and method of synthesis of akuammicine, the study shows that akuammicine is a kind of indole alkaloids, from akuamma tree seed extract, and akuamma tree seed has been used as a tradition in the treatment of pain and fever, used to treat various diseases, including malaria, dysmenorrhea, and gastrointestinal diseases. Therefore, the synthesis of this molecule through organic chemistry can help us to develop new opioids with unique pharmacological characteristics and therapeutic effects, which is of great significance to the development of human society.

ACKNOWLEDGMENT

Yangyi Gu, Tianhe Zheng, Jiongchen Guo gratefully acknowledge Professor Brian M. Stoltz.

AUTHOR CONTRIBUTION

Yangyi Gu: conceived the study, pathway retrosynthesis, communicated with team members and participated in the discussion, searched for information, wrote the paper

Tianhe Zheng: pathway retrosynthesis, writing-reviewing and revising the essay, communication with team members and participation in the discussion, searched for information

Jiongchen Guo: pathway retrosynthesis, writing-reviewing and revising the essay, communication with team members and participation in the discussion.

REFERENCES

Christophe Wiart PharmD, PhD, in Lead Compounds from Medicinal Plants for the Treatment of Cancer, 2013.

Creed Simone M, Gutridge Anna M, Argade Malaika D, Hennessy Madeline R, Friesen J Brent, Pauli Guido F, van Rijn Richard M, Riley Andrew P. Isolation and Pharmacological Characterization of Six Opioidergic Picralima nitida Alkaloids. [J]. Journal of natural products, 2020:

Snaddon Thomas Neil, Hutchings-Goetz Luke, Yang Chao, Fyfe James. (2020) Enantioselective Syntheses of Strychnos and Chelidonium Alkaloids via Regio- and Stereocontrolled Cooperative Catalysis. [J]. Angewandte Chemie (International ed. in English).

V. H. Rawal, C. Michoud, R. F. Monestel. (1993) J. Am. Chem. Soc. 115, 3030–3031.

Advances in Applied Chemistry and Industrial Catalysis – Saikia (Ed.)

Experimental study on coalescing and separation to remove trace water from jet fuel

H.F. Dong*, J. Hu** & C.A. Huang***
System Engineering Research Institute, Beijing, China

X.W. Tian****
College of Chemistry and Chemical Engineering, China University of Petroleum (East China), Qingdao, China

ABSTRACT: The hygroscopic nature means that jet fuel will inevitably be mixed with water during the process of storage, transportation, and filling, which can seriously affect flight safety. Therefore, this water needs to be removed reasonably. Three methods of gravity sedimentation, adsorption separation, and coalescence separation were used to remove traces of emulsified water from jet fuels. The effects of filtration velocity and concentration of continuous phase and dispersed phase on coalescence dewatering efficiency were investigated. The results show that with the increase in coalescence flow rate, the coalescence separation efficiency decreases gradually. For the jet fuels with water content from 22 to 1393 ppm, the free water content in the fuels at the outlet is all less than 15 ppm, With the increase of water before treatment, the dehydration efficiency of the equipment gradually increased. Gravity sedimentation and adsorption separation method have been limited by working conditions, large flow, and flexible operation of coalescence separation equipment, so it is an ideal method for traces of water treatment at present.

1 INTRODUCTION

Jet fuel will inevitably be mixed with water during the process of storage, transportation, and filling. The fuel in the oil tank is connected to the atmosphere. The fuel has high water solubility when the temperature is high during the day and can absorb moisture from the atmosphere at night. When the water solubility is low, free water is generated. This free water will be deposited on the bottom of the tank. The above process continues, and a considerable amount of water will appear in the fuel of the tank. Safe navigation. The tanker needs to fill with ballast water when unloading the oil and returning to the voyage. It is difficult to remove the water when reloading the oil. This will also cause the fuel to be mixed with water (Hua 2010; Zhang 2016).

Water in jet fuel mainly exists in the form of dissolved water and insoluble water, which insoluble water includes free water, emulsified water, and so on. Hydrogen bonds are formed between water and part of the aromatic hydrocarbons in the fuel to become dissolved water (Joseph 2014). When the fuel is cooled below the saturation temperature, the excess water is precipitated in the form of fine water droplets with a diameter of 2–10 m to form insoluble water (Mathias 2018). The trace moisture in jet fuel will cause a large number of microorganisms to grow, which will affect the relevant quality indicators of the oil product and corrode the fuel tank and engine components (Cui 2017; Shen 2018; Su 2021; Zhu 2016); trace moisture will easily form ice crystals and accumulate at low temperatures, thereby blocking the fuel system The filter seriously affects flight safety (Chen 2014; Wang 2018). The separation methods of water in jet fuel mainly include the gravity sedimentation method, adsorption separation method, and coalescence separation method.

Corresponding Authors: *hfdong@163.com, **hujing526@126.com, ***553158539@qq.com and ****17863928195@163.com

 DOI 10.1201/9781003308553-44

The gravity sedimentation method is a physical method that uses the density difference between the oil and water phases, and the incompatible water droplets and oils are separated under static or low-speed flow to achieve separation. This method can only remove free water, which is very effective for emulsification The removal of water and dissolved water is extremely limited and is generally used in the oil pretreatment process. When jet fuel is disturbed, especially in the case of pumping, free water will form emulsified water and become turbid. The adsorption separation method is a method to realize the separation of non-dissolved water and oil by the water absorption of materials with special water absorption functions, such as polymer water-absorbing resins, molecular sieves, and other materials. However, the material adsorption capacity is limited, regeneration is difficult, the adsorption medium needs to be replaced frequently, and the cost is high.

Coalescence separation is a physical method that uses the difference in affinity between oil and water to coalesce fiber materials to achieve emulsion droplets demulsification and growth, and finally, achieve oil-water separation through gravity sedimentation (Yang 2019). The coalescence process mainly includes droplet capture, droplet coalescence, and droplet release processes (Hu 2019). (1) The droplet capture process can be achieved by interception, diffusion, sedimentation, van der Waals force, and inertial collision (Hazlett 1969; Othman 1988). For smaller droplets, diffusion is the main influencing factor. As the droplet size increases, the diffusion effect is weakened, the interception effect is enhanced, and the inertial collision has little effect on the approach mechanism; (2) The coalescence process mainly includes wetting coalescence and collision coalescence, and the main resistance comes from the oil phase film between the fiber and the droplet. When the oil film is thin to a certain thickness and subsequently ruptured, coalescence occurs (Basu 1993), and proper wetting characteristics should be maintained between the two, which can ensure that water droplets can replace the oil phase and adhere to the fiber, and allow coalescence of droplets. Release (Angelov 1984; Li 2015; Pang 2016; Robert 1997); (3) The release process is mainly related to the liquid flow rate and fiber size (Hazlett 1969). When the fluid drag force overcomes the adhesion between the droplet and the fiber, separation occurs. Compared with other methods, coalescence separation has the advantages of high oil-water separation efficiency, low energy consumption, low processing cost, simple equipment, small footprint, and no secondary pollution.

This study compares and analyzes the effects and feasibility of the three methods of gravity sedimentation, adsorption separation, and coalescence separation to remove trace water in jet fuel through experiments, to find the best jet fuel trace water treatment method. And explore the influence of factors such as feed flow rate, continuous phase, and dispersed phase concentration (different water content in the fuel) on the coalescence and dehydration performance and the change law of dissolved water in jet fuel.

2 TEST PART

2.1 *Equipment*

Coalescing separator (self-made coalescing filter element and separation filter element), air compressor (Autus S1600), pneumatic diaphragm pump (Desheng QMJ-HL2002), precision electric agitator (Tianrui JJ-1A), high-power CNC Ultrasonic cleaner (Shumei KQ-40KDE), Karl Fischer moisture analyzer (Swiss Metrohm 831).

2.2 *Process flow*

The process flow is shown in Figure 1. The stirring device is used to uniformly mix the oil and water in the feed barrel. The air compressor drives the pneumatic diaphragm pump to press the fuel into the coalescence and dehydration equipment to separate the trace water. The separated water is discharged from the water collector.

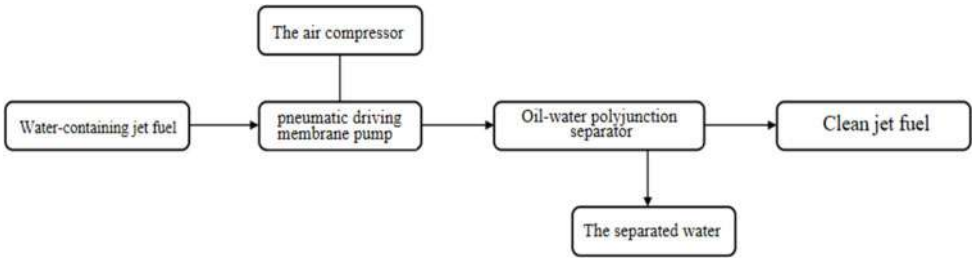

Figure 1. Process flow chart.

Jet fuel and the solid particles and moisture it carries flow into the inside of the coalescing filter element from the inlet of the filter separator. The coalescing filter element has both the functions of filtering solid particles and breaking the emulsion and coalescing water droplets. The solid particles are blocked by the filter layer. The inside of the knot filter element realizes the separation of solid and liquid; after the small water droplets are coalesced into large water droplets by the demulsification layer and the coalescence layer, they are blocked by the separation filter element and settle on the bottom of the equipment by gravity to realize the separation of oil and water; The treated jet fuel flows from the outside into the inside of the separation filter element, and the water droplets that may coalesce in the future are blocked by the separation filter element outside the filter element, and finally, the clean jet fuel flows out from the outlet. A simplified diagram of the coalescence and separation process is shown in Figure 2.

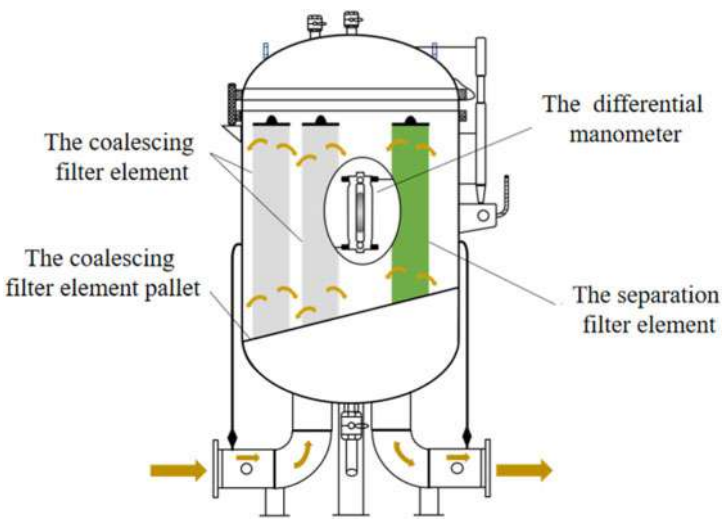

Figure 2. Schematic diagram of coalescence and separation process.

3 RESULTS AND DISCUSSION

3.1 *Research on the influence of coalescence and separation efficiency*

3.1.1 *The influence of filtration flow rate on the efficiency of coalescence and dehydration*

Ultrasonic equipment is used to emulsify the trace water in jet fuel to simulate the existence of emulsified water droplets under actual working conditions. The comparison before and after

treatment is shown in Figure 3. It can be seen from Figure 3 that most of the emulsified water droplets have a particle size below 20 μm. Figure 3(a) is the fuel oil with trace water after emulsification, and Figure 3(b) is the fuel sampled from the water collecting port of the coalescing equipment after treatment. From the figure, we can see the large water droplets that coalesce and settle together at the bottom.

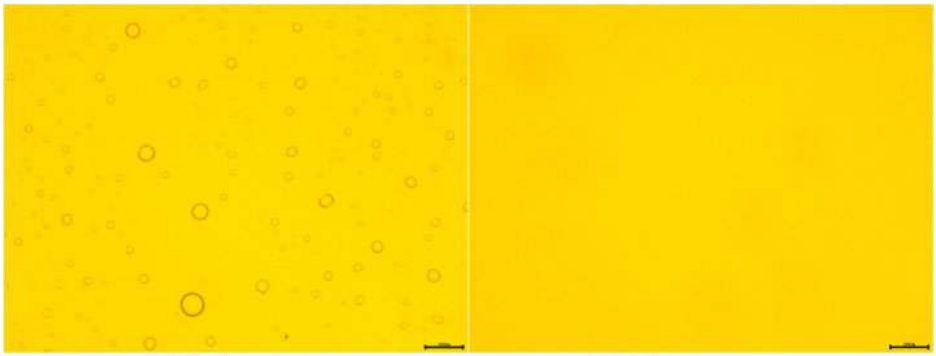

Figure 3. A microscopic view of emulsified water droplets before and after treatment (fuel water content of 251.4 ppm).

Previous studies have shown that when the flow velocity of the continuous phase is in the range of $2.78 \times 10^{-3} \sim 1.67 \times 10^{-2}$m/s, for droplets with a size of 46~106 μm, the flow velocity has little effect on the efficiency of coalescence and separation[17]. For droplets with a size of 2-12 μm, the efficiency of coalescence and separation decreases significantly as the flow rate increases[18]. The separation efficiency of glass fiber is relatively stable in the flow rate range of $3.89 \times 10^{-3} \sim 7.22 \times 10^{-3}$ m/s[19]. In this test, the inner diameter of the filter element is 80 mm, the length is 500 mm, and the surface area of a single filter element is 0.126 m^2. The continuous phase flow rate is within the range of $3.89 \times 10^{-3} \sim 7.22 \times 10^{-3}$ m/s, which corresponds to the treatment flow range of the single filter element. It is 29.42 L/min~54.58 L/min. To ensure a higher separation efficiency in the actual application process, the flow velocity of the continuous phase is far less than 3.89×10^{-3} m/s. To explore the influence of filtration rate on coalescence efficiency, the test results are shown in Table 1. To reduce the test error, parallel measurement is performed 3 times, and the average value is taken.

Table 1. The influence of filtration flow rate on the efficiency of coalescence and separation.

Water content before treatment/ppm	Flow rate/(L/min)	Water content after treatment/ppm	Separation efficiency/%
251.4	2.86	9.6	96.18
250.7	5.88	10.6	95.77
259.9	6.27	14.3	94.49

It can be seen from Table 1 that the water content in the system after treatment is less than 15 ppm (in line with API/IP 1581 testing standards). With the increase of the coalescence flow rate, the coalescence and separation efficiency gradually decreases, but the decrease is not large. This may be because water droplets of various sizes are mixed in the system, water droplets of different particle sizes are affected by the flow rate to different degrees, and the overall efficiency of coalescence and separation is less affected by the flow rate of the material.

3.1.2 *The influence of continuous phase and dispersed phase concentration on the efficiency of coalescence and dehydration*

An oil-water mixing system containing different quantitative and trace amounts of water is prepared, and the water in jet fuel is emulsified by ultrasonic equipment to obtain jet fuel with different water content. The oil-water separation test is carried out at the same flow rate. The test results are shown in Table 2.

Table 2. Jet fuel coalescence and dehydration efficiency under different water content.

Order	Water content before treatment/ppm	Water content after treatment/ppm	Dehydration efficiency/%
1	1393.8	13.8	99.00
2	971.6	13.8	98.57
3	495.7	10.3	97.92
4	251.4	9.6	96.18
5	173.3	10.3	94.05
6	72.8	3.3	95.46
7	53.8	6.9	87.17
8	46.7	7.8	83.29
9	22.1	15.0	32.12

It can be seen from Table 2 that the higher the water content before treatment, the higher the dehydration efficiency of the equipment. For jet fuel with a water content of more than 1000 ppm, the dehydration efficiency is greater than 98%, and the free water content in the system after the treatment is less than 15 ppm, which fully meets the API/IP 1581 testing standard; for the water content below 100 ppm Jet fuel coalescence and dehydration efficiency is relatively low; in particular, for oil-water mixing systems with extremely low water content, the coalescence and dehydration effect decreases sharply. This is because the less water, the easier it is to form a stable emulsified state, thereby reducing the "wetting of the glass fiber". The efficiency of coalescence and the very small amount of water will reduce the probability of "collision coalescence", and it is difficult to form large water droplets that are sufficient to settle quickly.

3.2 *Research on the separation of trace water from jet fuel by gravity sedimentation method*

The gravity sedimentation method uses the density difference between the oil and water phases, and the incompatible water droplets and oil are stratified under static or low-speed flow to achieve oil-water separation. The sedimentation process of water droplets in the oil conforms to the stokes law, according to the law:

$$u = \frac{d^2(\rho_w - \rho_o)g}{18\mu} \tag{1}$$

in the formula: u-the sinking speed of water droplets, m/s;

d – Water droplet size, m;

ρ_w – Density of water, kg/m^3;

ρ_o – Density of oil, kg/m^3;

g – Acceleration of gravity, m/s^2;

μ – The dynamic viscosity of the oil, Pas.

The jet fuel used in this test has a density of 810.5 kg/m^3 and a dynamic viscosity of 1.4767×10^{-3} Pa·s. According to the above formula, the sinking velocity of water droplets with a particle size of 20 μm can be calculated $= 0.2795 \times 10^{-4}$ m/s ≈ 0.1 m/h, which shows that the separation by gravity sedimentation is a long process. The temperature or humidity of the environment in the early and late stages of settlement may be quite different, which has a greater impact on

the amount of dissolved water in jet fuel. Therefore, this part of the experiment examines the total water content in the fuel at a fixed height in the system (including dissolved water and dissolved water). Insoluble water) to investigate the oil-water separation efficiency of the gravity sedimentation method. In the experiment, the middle part of the container was taken as the sampling point, each time point was measured 3 times, and the average value was taken as the measurement result. The results are shown in Figure 4. The free water in the final states of a, b, c, and d in the figure are respectively 20.2 ppm, 37.9 ppm, 23.6 ppm, and 33.2 ppm, which does not meet the detection standard API/IP 1581 for low free water content in jet fuel It is less than 15 ppm.

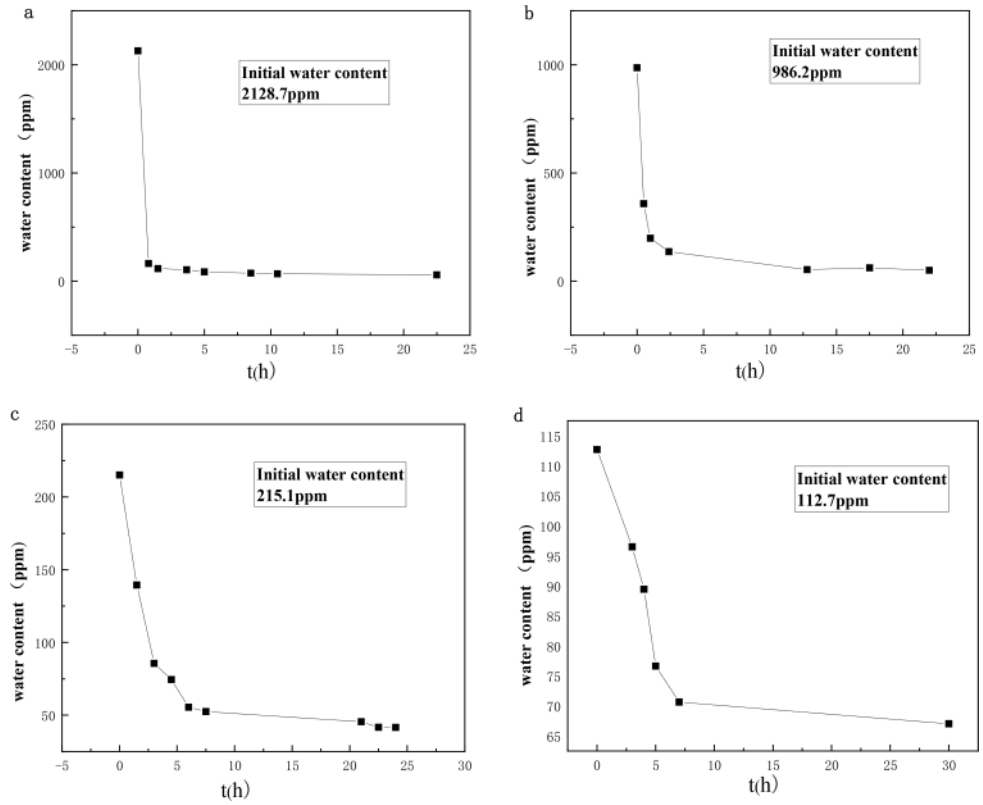

Figure 4. The change of water content in jet fuel over time (gravity sedimentation method).

3.3 *Study on the separation of trace water from jet fuel by adsorption*

In this part of the experiment, a spherical 4A molecular sieve was used as the adsorbent, the particle size range was 1.6～2.5 mm, and the saturated water adsorption was 215 mg/g. 4A molecular sieve is a synthetic alkali metal aluminosilicate with a microporous cubic lattice, and its effective pore size is 0.4 nm. Molecular sieves determine the order of preferential adsorption according to the polarity of molecules of different substances. The selective adsorption is based on the size and shape of the molecules, that is, only those molecules smaller than the pore size of the molecular sieve are adsorbed. Small polar molecules and unsaturated molecules, it has selective adsorption properties. The greater the polarity, the higher the degree of unsaturation, and the stronger its selectivity. The selective adsorption performance of the 4A molecular sieve for water is higher than that of other molecules.

Put the excess molecular sieve into the oil-water mixing system. Take a static adsorption test, and continue to stir during the test to ensure that the adsorbent is in full contact with the liquid

phase. Record the free water content in jet fuel at different adsorption times, take the middle of the container as the sampling point, measure 3 times at each time point, and take the average value as the measurement result. It can be seen from Figure 5 that molecular sieves can quickly adsorb trace water in jet fuel, and after sufficient time of adsorption, they can meet the API/IP 1581 free water content detection standard of less than 15 ppm.

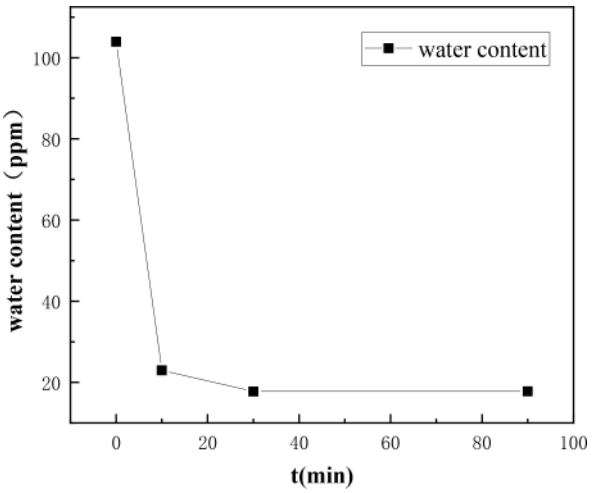

Figure 5. The water content in jet fuel changes with time (adsorption method).

3.4 *Analysis of the pros and cons of the three methods for separating trace water in jet fuel*

After the above tests, it was found that the gravity sedimentation method has a longer processing time and has a significant effect on fuel oil with large water content, but it is difficult to meet the relevant standards in the end. In actual use, the sedimentation separation equipment mainly includes water removal tanks, water removal tanks, etc., which require a large container and a very low flow rate. This method can be used as a pretreatment method in conjunction with other methods.

The adsorption separation method utilizes the high selectivity of a molecular sieve or polymer water-absorbing resin to water molecules, and can quickly remove trace water in jet fuel in a short time under the condition that the adsorbent and the fuel are fully contacted. The separation capacity is limited by the saturated water absorption of the adsorbent, and the adsorbent needs to be replaced frequently. The cost of regeneration and desorption is relatively high. For example, a 4A molecular sieve requires high-temperature activation and regeneration, the activation temperature is 500°, and the time is 5 hours. It is suitable for occasions that require extremely high-water content and do not require high-speed liquid flow.

The coalescence separation method uses the different affinity of oil and water relative to the surface of the coalescing material. Tiny water droplets converge and merge on the surface of the material. When the size of the water droplet reaches a certain level, it will be separated from the surface of the coalescing material under the action of gravity and flow field to form free. To realize the separation of the insoluble water in the fuel, it can effectively treat the suspension or emulsion with the density difference of the two phases not less than 0.01 g/cm^3. The coalescing filter element adopts a layer-by-layer winding structure, and its filtering effect not only effectively removes free water but also enables the solid impurities and fiber content in the fuel to reach relevant standards. Its water removal efficiency is high, the coalescing filter element and the separation filter element have a long service life; the structure is compact and small, the size of the filter element can be designed according to the needs, and the processing capacity is up to 500 m^3/h, which can meet the needs of long-term high-speed fuel filtration.

4 CONCLUSION

(1) Through the oil-water separation test, it is found that the gravity sedimentation separation method has a longer processing process and poor separation effect, and it can be used as a pretreatment method in combination with other methods;
(2) The adsorption separation method has a good water removal effect, and the oil-water separation efficiency in the fluid state is unknown, and the adsorbent needs to be replaced frequently, which is suitable for occasions with extremely high-water content requirements;
(3) The coalescing separation method has high separation efficiency for emulsified water, and for jet fuels with a water content of 22～1393 ppm, the free water content in the outlet fuel can be no more than 15 ppm; and the equipment has a large processing flow rate, flexible operability, and coordination. Other filters can greatly prolong the service life and the filtering effect of solid particles and are currently more ideal micro-water treatment methods.

REFERENCES

Angelov, G., Boyadzhiev, L., G. Kyutchoukov, G. (1984) Separator for liquid-liquid dispersions. Chemical Engineering Communications,25:1–6.

Basu, S. (1993) A Study on effect of wetting on mechanism of coalescence in a model coalescer. Academic Press,159: 68–76.

Chen, K., Xiang, H., Sun, T., Dian, D.M. (2014) Research on the icing behavior of water in the jet fuel. Petrochemical Application, 33:1–5.

Cui, Y.Y., Wang, N. (2017) Status of study on microbial contamination in aviation fuel system. Oil and Gas Storage and Transportation, 36: 651–656.

Hazlett, R. N. (1969) Fibrous bed coalescence of water. steps in the coalescence proces. Industrial & Engineering Chemistry Fundamentals, 8:4–4.

Hu, D., Zhang, Q., Yang, C. F., Wang, X.L. (2019) Process diagnosis of coalescence separation of oil-in-water emulsions-two case studies. Journal of Dispersion Science and Technology, 40: 1–11.

Hua, G.S. (2010) Research on coalesence technology of removal water from jet fuel. Beijing University of Chemical Technology.

Joseph, K.W., Lam, M. D., Carpenter, C. A., Williams, J. I. H. (2014) Water solubility characteristics of current aviation jet fuels. Fuel,133:26–33.

Li, X., Hu, D., Cao, L. (2015) Sensitivity of coalescence separation of oil-water emulsions using stainless steel felt enabled by LBL self-assembly and CVD. Rsc Advances,5:71345–71354.

Mathias, S., Gerhard, S. (2018) Experimental study on the accretion and release of ice in aviation jet fuel. Aerospace Science and Technology,83:294–303.

Othman, F.M., Fahim, M.A., Jeffreys, G.V., Mumford, C.J. (1988) Prediction of predominant mechanisms in the separation of secondary dispersions in a fibrous bed. Journal of Dispersion Science and Technology,9:2–2.

Pang, F.L. (2016) Experimental study on coalescence separation and optimization for water in oil emulsion. East China University of Science and Technology.

Robert, M. (1997) Separation of liquid-liquid dispersion by flow through fibre beds. Filtration and Separation,34: 369–376.

Shen, S.Q., Xu, J.H., Li, Z.G. (2018) Formation mechanism and discussion of suspended solids in jet fuel. Petrochemical Technology, 25: 254–258.

Su, P., Niu, M.M., Xiong, Y., Gu, K.C., Xu, T.Y., Han, S. (2021) Influence of characteristic fungi on properties of jet fuel. Petroleum Refining and Chemical Industry,52:77–82.

Wang, Y., Wang, L. (2018) Research of solution behaviors of water in jet fuel. Contemporary Chemical Industry, 47:792–794+801.

Yang, Y.J., Chen, W.W., Zhang, Q., Li, L., Lin, S., Wang, Z.Q., Li, W.L. (2019) Coalescence technology and its application in the separation of oil and water emulsion. Progress in Chemical Industry, 38: 10–18.

Zhang, Y. (2016) Experimental and numerical study of coalescence dehydration and two phase flow of corrugated plates for aviation kerosene. China University of Petroleum (East China).

Zhu, J.J., Wang, L. (2016) Introduction to the source and the harm of the contaminant in the jet fuel. Chemical Industry Times, 30: 39–42.

Advances in Applied Chemistry and Industrial Catalysis – Saikia (Ed.)

Catalytic activity for hydrogen evolution reaction in phosphene nanoribbons: A first-principles study

Hao Chen & Luwu He*
School of Mechanical and Power Engineering, East China University of Science and Technology, Shanghai, China

ABSTRACT: Phosphene has been reported to be a promising nanocatalyst for hydrogen evolution reaction (HER) in recent years. For this study, we investigated the catalytic performance of phosphene nanoribbons (PNRs) by using first-principles calculations. The results revealed that PNRs are suitable for HER because of their highly active edges. And it was found that the width does not affect the catalytic activity of both APNRs (Armchairs phosphene nanoribbons) and ZPNRs (Zigzag phosphene nanoribbons). On the other hand, strain engineering is an effective method to significantly improve the catalytic activity of APNRs. It is expected that the insights obtained from this study could be helpful to further improve the activity of catalysts.

1 INTRODUCTION

As a clean and renewable energy source, hydrogen has always been regarded as the most promising new energy source in the future. The electrochemical hydrogen evolution reaction (HER) is an efficient and cheap method among the many current hydrogen production technologies. (Lasia 2019) Efficient hydrogen evolution electrode materials should have the characteristics of good electrical conductivity, large specific surface area, low hydrogen evolution overpotential, high electrocatalytic activity, good electrochemical stability, and strong corrosion resistance. (Jin et al. 2018) At present, although some precious metal catalysts (Pt) have excellent catalytic activity for hydrogen production, their scarcity and high cost limit their wide application. (Wang et al. 2012) So scientists have been looking for efficient and low-cost hydrogen evolution electrocatalysts, however, the stability and catalytic activity of these materials are difficult to compare with Pt. Two-dimensional materials have many unique electronic properties, are low in price, and have large specific surface areas, which have gradually attracted people's attention.

Black phosphorene (BP) is the most stable allotrope of phosphorus in terms of thermodynamics and chemistry (Zhang et al. 2017), it has semiconducting properties, high carrier mobility, and tunable bandgap. These unique properties make black phosphorene have good application prospects in photocatalysis and electrocatalysis (Zhang et al. 2016). However, the surface of BP lacks the catalytic activity of hydrogen evolution reaction, so pure phosphene is not suitable for electrocatalyst. Sofer (Sofer et al. 2016) et al. studied the catalytic performance of phosphene in the hydrogen evolution reaction through ab initio calculations and electrochemical measurements, found that the edge of phosphene has high catalytic activity than in the plane. Shao (Shao et al. 2018) et al. reported a new method to prepare NH_2-functionalized few-layer black phosphorus (BP) nanosheets. Its electrocatalytic activity in alkaline electrolytes greatly outperforms that in acidic electrolytes attributed to the unique structure which exposes more edges and dangling bonds and favors charge transfer. Wang et al. (2018) used a simple solvothermal method to synthesize in-plane BP/Co_2P heterostructures for electrocatalysis, the BP/Co_2P nanosheets exhibit better and more stable electrocatalytic activities in the hydrogen evolution. Lin et al. (2017) constructed a

*Corresponding Author: chen_hao97@163.com

DOI 10.1201/9781003308553-45

novel hybrid catalyst based on the in-situ growth of Ni_2P nanoparticles on 2D black phosphorus, that exhibits high HER electrocatalytic activity and good stability in acid solution.

Based on previous studies, it can be concluded that although the surface catalytic activity of black phosphene is low, it can be greatly improved by doping with metal elements or forming a heterojunction with other two-dimensional materials. Herein we studied the catalytic activity of two catalytic sites (top and side sites) on two different types of PNRs (APNR and ZPNR). Then, we consider the width effect for PNRs and discuss the effect of strain engineering on the catalytic activity of APNRs. The calculations show that the reconstructed PNRs may become highly active catalysts for HER.

2 MODEL AND CALCULATION METHOD

All calculations in this study were performed using DFT implemented in the Vienna ab initio simulation package (VASP). The generalized gradient approximation (GGA) with the Perdew–Burke–Ernzerhof (PBE) functional is employed. A 450 eV cut-off energy was set for the plane-wave basis set. The convergence accuracy for energy was set to 10^{-5} eV. A $7 \times 1 \times 1$ gamma point catered k-mesh was selected for the structure relaxation. To avoid the interaction between neighboring units, we set at least 15 Å vacuum in both two directions perpendicular to the periodic direction.

The structure of two types of PNRs and a 4×3 supercell of phosphene is given (see Figure 1(a)). The primitive cell is indicated by a dashed black rectangle. Two different types of PNRs, that is, APNRs and ZPNRs, can be obtained by cutting phosphene along the armchair and zigzag directions, respectively in Figure 1(b, c) Here, the width of the black phosphene nanoribbon is defined as the number of primitive cells, 3-ZPNR and 3-APNR are marked with a red dashed line. In addition, PNRs with a width of 4 to 7 were considered to clarify the influence of the width on the

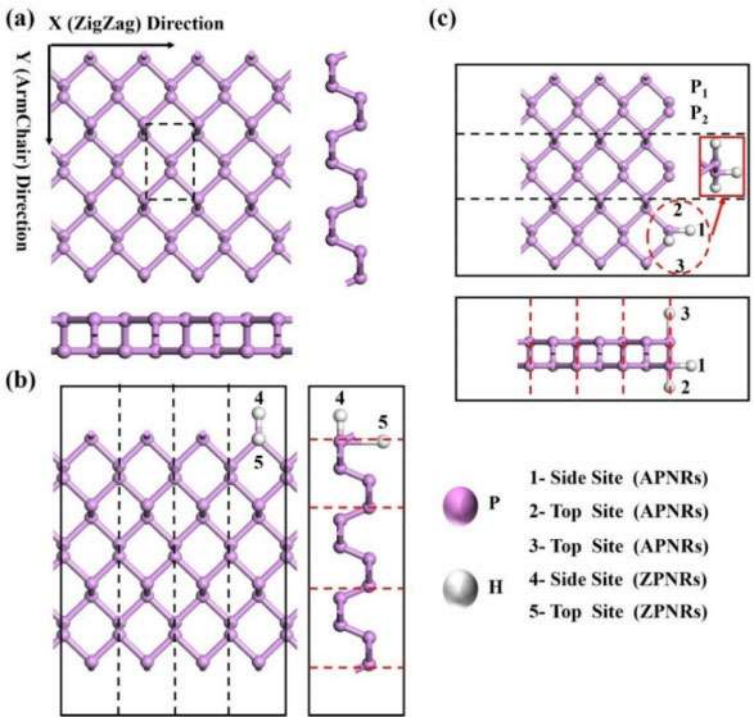

Figure 1. The atomic structures of (a) black phosphorene, (b) ZPNRs, and (c) APNRs.

hydrogen evolution catalytic performance. The APNRs and ZPNRs are extended to 3 × 1 and 1 × 4 supercells to keep around 10 Å between hydrogen atoms according to the lattice constants. To study the edge catalysis of PNR, we selected two different edge sites, that is, the top sites (marked as 2, 3, 5) and the side sites (marked as 1, 4), where white balls at the edge of PNRs indicate H atoms.

3 RESULTS AND DISCUSSION

All calculations should be performed after structures are relaxed. The stabilities of the black phosphorene nanoribbons were evaluated with the averaged cohesive energy (E_{coh}):

$$E_{coh} = E_{nano}/n - E_P \tag{1}$$

Where E_{nano} and E_P are the free energies of phosphor nano-structures and an isolated phosphor atom in a vacuum, respectively and n represents the number of boron atoms in the phosphor nanostructures. The average cohesive energy of the two types of nanoribbons decreases as the width of the nanoribbons increases as shown in Figure 2, APNR cohesive energy is always lower than ZPNR. This is because the edge atoms of ZPNR contain an unreconstructed bond (we called a dangling bond), and the edge atoms in the APNR allow dangling bond reconstruction (which reduces the edge energy), so ZPNR is more stable than APNR. In general, width is inversely proportional to cohesive energy. In Figure 2(c, d), the red dashed box represents the part of edge reconstruction in 3-APNR and 3-ZPNR.

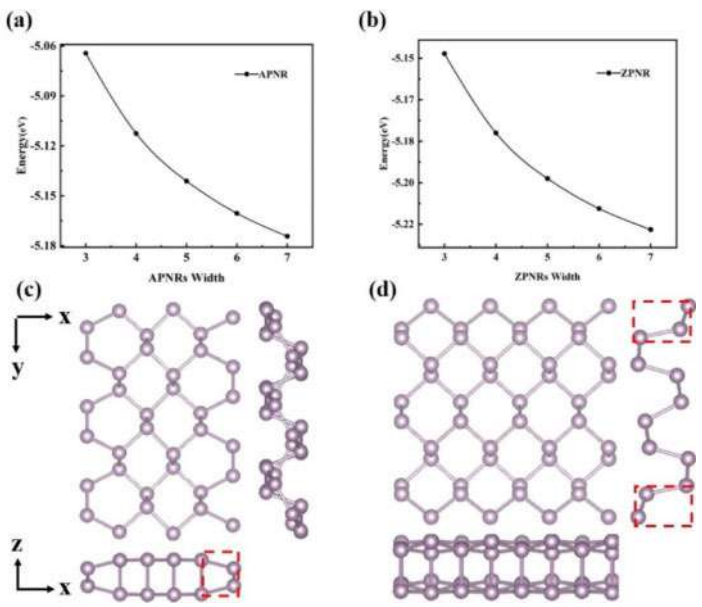

Figure 2. The averaged cohesive energies of (a) APNRs and (b) ZPNRs with width increased from 3 to 7, and the atomic structure of relaxed (c) APNR and (d) ZPNR.

It can be observed that the distance between the atoms in the middle of APNR in the z-direction becomes larger, that is, the thickness of the nanoribbon increases, but the bond angle does not change much in the same plane. The edge atoms change greatly in the z-direction, showing a tendency to shrink inward. In the y-direction, the distance between the edge atoms becomes larger and opens to both sides, resulting in a smaller out-of-plane buckling. But for edge atoms in ZPNR, the distance between the atoms in the z-direction is reduced, having a greater out-of-plane buckling, which makes it more stable than APNR.

The Gibbs free energy of hydrogen adsorption (ΔG_H) is calculated to evaluate the catalytic activity of PNRs for HER. Nørskov et al. (2005) proposed Eq. (2) and verified it for most metals and certain sulfides. The closer the calculated ΔG_H to 0 eV, the higher the HER activity (Chen et al. 2019). Where E_H is the adsorption energy of hydrogen atoms on the surface of the black phosphorene nanoribbons.

$$\Delta G_H = E_H + 0.24 \tag{2}$$

The results of Gibbs free energy at the five sites of 3-ABNR and 3-ZBNR as shown in Figure 3. We found that 1, 2, and 3 sites belong to symmetry points, and their average Gibbs free energy is −0.366 eV, while the value of Gibbs free energy at site 4,5 is −0.361 and −0.399 eV, respectively. In addition, the figure also lists the data of typical hydrogen evolution reaction catalysts (including Pt, MoS_2, and 2-Pmmn-borene with Gibbs free energies of -0.09, 0.08, and −0.46 eV, respectively) for comparison (Liu et al. 2018; Wang et al. 2021). The data of monolayer black phosphorus are also listed in Figure 3. The results show that the HER activity on the BP surface is weak, which is not conducive to H* adsorption and H_2 desorption, but nanoribbons can expose more active edge sites and enhance the interaction between H atoms and adsorption sites to promote HER activity.

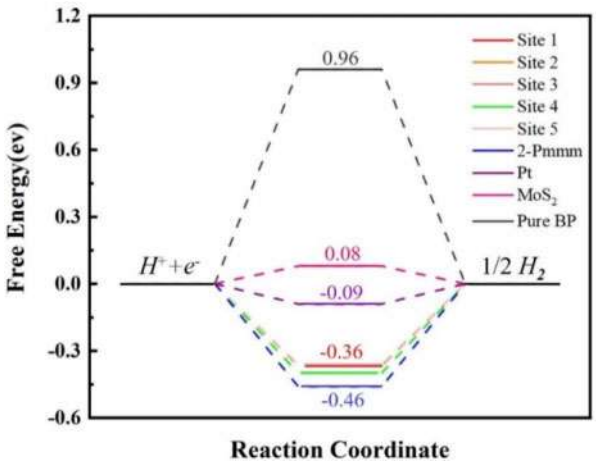

Figure 3. The calculated free energy diagram for HER of sites 1 to 5 in PNRs and cited data including Pt, MoS_2, and 2-Pmmn-borene for comparison.

Although PNR may be a highly active hydrogen evolution catalyst, the above results are obtained under the width of 3. The width effect for PNRs also needs to be taken into account. As shown in Figure 4(a–e) APNRs of all widths have undergone similar edge reconstructions, with the edge atoms

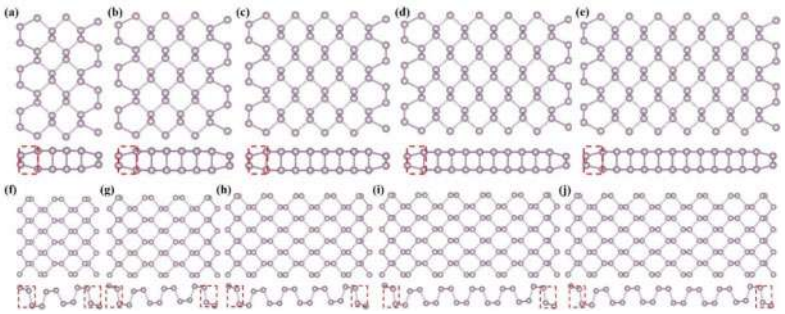

Figure 4. (a–e) APNRs and (f–j) ZPNRs with widths increased from 3 to 7.

shrinking inward, while the central phosphorous atom can roughly maintain the original structure. A similar edge reconstruction phenomenon also appears in ZPNRs, where the edge atoms only have a larger undulating angle along the width of the nanoribbon in Figure 4(f–j). In summary, the number of phosphor atoms undergoing edge reconstruction remains unchanged as the width increases (marked by the red dashed line), so the edge reconstruction is nearly independent of the width.

After discussing the structure of PNRs with different widths, we calculated the Gibbs free energy of PNRs with widths from 4 to 7 in Figure 5(a,b). For APNRs, as its width increases from 3 to 7, the Gibbs free energy at the catalytic site is -0.27 ± 0.1 eV; while on ZPNR, the Gibbs free energy at the top and side sites are -0.31 ± 0.05 eV, and -0.36 ± 0.05 eV respectively. The fluctuation range of the Gibbs free energy of PNRs with different widths is relatively small, indicating that their catalytic activity remains unchanged with the increase of the width, that is, the catalytic performance of PNRs is independent of the width factor. The ZPNRs have a smaller variation range than APNRs because their structure is more stable. Therefore, it can be guessed that the edge reconstruction of the nanobelt has nothing to do with its width, resulting in their hydrogen evolution catalytic performance being almost insensitive to the width.

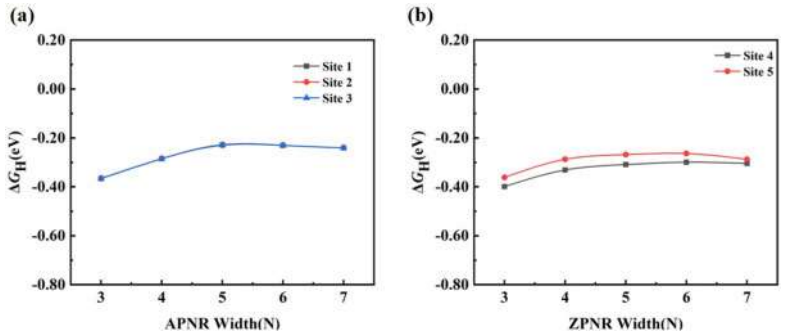

Figure 5. The hydrogen adsorption free energies of (a) APNRs and (b) ZPNRs with widths increased from 3 to 7.

To further improve the hydrogen evolution catalytic performance of PNRs, we selected APNR with a width of 5 to apply strain in the direction of periodic extension. For the tensile simulation, a small incremental strain is applied step by step. The internal atomic positions in the other two directions are fully relaxed under a small strain applied along the stretch direction. The strain-stress curve of APNRs (see Figure 6(a)) indicates that the PNRs can sustain the tensile strain from -5% (compressive stains) to 7% (tensile strains) and an increment of 1%. During the entire strain engineering process, the Gibbs free energy of hydrogen adsorption increases monotonically with tensile strain. It is notable that when a tensile strain of about 7%, the Gibbs free energy can reach -0.03 eV, which is almost close to zero in Figure 6(b).

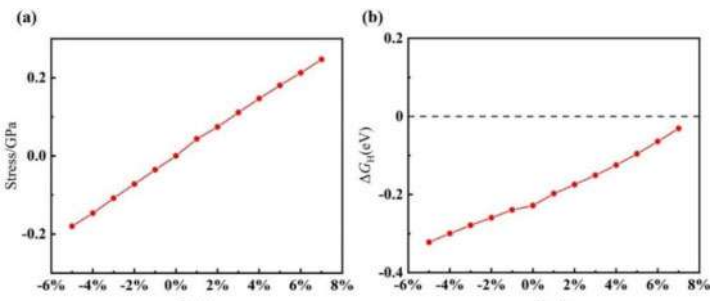

Figure 6. The stress-strain relationship of (a) 5-APNR, and the strain engineering of the HER performance of (b) 5-APNRs.

The results show that by applying strain, not only the catalytic performance of APNR can be effectively improved, but also a highly active catalytic site with almost zero Gibbs free energy can be obtained, which indicates that there will be a certain prestressed PNRs can be used as catalysts to obtain an ultra-fast hydrogen evolution reaction.

4 CONCLUSION

The current study used first-principles calculations to analyze the width of nanoribbons and strain engineering on the hydrogen evolution activity of the PNRs catalyst. The following conclusions can be drawn. Black phosphene nanoribbon is a good catalyst for hydrogen evolution reaction because the edge structure exposes higher active sites. However, due to the independent edge reconstruction, it is found that the width of the PNR hardly affects the catalytic HER of the PNR. Furthermore, strain engineering has proven to be an effective way to enhance the catalytic performance of APNRs probably, and a Gibbs free energy of almost zero may be achieved at a tensile strain of 7%. This study provided insights into the catalytic performance of PNRs and an effective methodology to improve the catalytic activity of phosphene and other two-dimensional materials as well.

REFERENCES

Chen, C.-H., Wu, D., Li, Z., Zhang, R., Kuai, C.-G., Zhao, X.-R., Dong, C.-K., Qiao, S.-Z., Liu, H. & Du, X.-W. 2019. Ruthenium-Based Single-Atom Alloy with High Electrocatalytic Activity for Hydrogen Evolution. *Advanced Energy Materials*, 9, 1803913.

Jin, H., Guo, C., Liu, X., Liu, J., Vasileff, A., Jiao, Y., Zheng, Y. & Qiao, S. Z. 2018. Emerging Two-Dimensional Nanomaterials for Electrocatalysis. Chem Rev, 118, 6337–6408.

Lasia, A. 2019. Mechanism and kinetics of the hydrogen evolution reaction. *International Journal of Hydrogen Energy*, 44, 19484–19518.

Lin, Y., Pan, Y. & Zhang, J. 2017. In-situ grown of Ni 2 P nanoparticles on 2D black phosphorus as a novel hybrid catalyst for hydrogen evolution. *International Journal of Hydrogen Energy*, 42, 7951-7956.

Liu, C., Dai, Z., Zhang, J., Jin, Y., Li, D. & Sun, C. 2018. Two-Dimensional Boron Sheets as Metal-Free Catalysts for Hydrogen Evolution Reaction. *The Journal of Physical Chemistry C*, 122, 19051-19055.

Nørskov, J. K., Bligaard, T., Logadottir, A., Kitchin, J. R., Chen, J. G., Pandelov, S. & Stimming, U. 2005. Trends in the Exchange Current for Hydrogen Evolution. *Journal of The Electrochemical Society*, 152.

Shao, L., Sun, H., Miao, L., Chen, X., Han, M., Sun, J., Liu, S., Li, L., Cheng, F. & Chen, J. 2018. Facile preparation of NH_2-functionalized black phosphorene for the electrocatalytic hydrogen evolution reaction. *Journal of Materials Chemistry A*, 6, 2494-2499.

Sofer, Z., Sedmidubsky, D., Huber, S., Luxa, J., Bousa, D., Boothroyd, C. & Pumera, M. 2016. Layered Black Phosphorus: Strongly Anisotropic Magnetic, Electronic, and Electron-Transfer Properties. *Angew Chem Int Ed Engl*, 55, 3382-6.

Wang, C., Dekrafft, K. E. & Lin, W. 2012. Pt nanoparticles@photoactive metal-organic frameworks: efficient hydrogen evolution via synergistic photoexcitation and electron injection. *J Am Chem Soc*, 134, 7211-4.

Wang, J., Liu, D., Huang, H., Yang, N., Yu, B., Wen, M., Wang, X., Chu, P. K. & Yu, X. F. 2018. In-Plane Black Phosphorus/Dicobalt Phosphide Heterostructure for Efficient Electrocatalysis. *Angew Chem Int Ed Engl*, 57, 2600-2604.

Wang, X., Wu, R., Tian, P., Yan, Y., Gao, Y. & Xuan, F. 2021. Borophene Nanoribbons via Strain Engineering for the Hydrogen Evolution Reaction: A First-Principles Study. *The Journal of Physical Chemistry C*, 125, 16955-16962.

Zhang, Y., Rui, X., Tang, Y., Liu, Y., Wei, J., Chen, S., Leow, W. R., Li, W., Liu, Y., Deng, J., Ma, B., Yan, Q. & Chen, X. 2016. Wet-Chemical Processing of Phosphorus Composite Nanosheets for High-Rate and High-Capacity Lithium-Ion Batteries. *Advanced Energy Materials*, 6.

Zhang, Y., Zheng, Y., Rui, K., Hng, H. H., Hippalgaonkar, K., Xu, J., Sun, W., Zhu, J., Yan, Q. & Huang, W. 2017. 2D Black Phosphorus for Energy Storage and Thermoelectric Applications. *Small*, 13.

Advances in Applied Chemistry and Industrial Catalysis – Saikia (Ed.)

Ni-based catalyst for phenol and its derivative selective hydrodeoxygenation

Shiqi He*
College of Chemistry, Beijing University of Chemical Technology, Beijing, China

ABSTRACT: Phenol and its derivatives are model compounds for the pyrolysis of biomass oil. The study of the hydrodeoxygenation reaction of these compounds is of great significance to the utilization of biomass resources. Ni-based catalysts have good HDO reaction activity and are one of the choices of catalysts used in the conversion and utilization of biomass resources. This article reviews several recent studies on the application of different Ni-based catalysts to the HDO reaction of phenol and its derivatives, discusses the effects of catalyst support and preparation methods on reaction activity and selectivity, and also mentions the effect of catalyst surface acidity on product distribution. It can be concluded that the structure of the reactant, the form of the catalyst, and the conditions for the preparation of the catalyst all have an impact on the choice of the catalytic reaction pathway.

1 INTRODUCTION

Phenol and its derivatives are common by-products in petrochemical and coal tar production, where output is huge and the cost of raw materials is low. Cyclohexanol and cyclohexanone, the hydrogenated products of phenol, are industrial raw materials widely used in the manufacture of paint, fiber, rubber, and other solvents and nylon-66 intermediates.

Fossil energy is depleted day by day. There is no good solution to the environmental problems caused by the development and utilization of fossil energy. Therefore, it is the top priority for the development of mankind to find new sustainable energy sources. In recent years, many renewable energy sources have been developed. Biomass energy has the characteristics of wide sources, large reserves, low price, renewable, low pollution, diverse conversion paths, and alternative petroleum resources. The use of biomass energy as raw materials is in line with green development. The concept and application prospects are broad. Among them, the biomass oil converted from the biomass pyrolysis reaction has many advantages: carbon neutral, easy to obtain, can be converted into liquid, etc. Phenol and its derivative are representative products of biomass oil pyrolysis, researching the catalytic hydrogenation of phenolic compounds has far-reaching significance and can promote the reuse of biomass resources. And for the simplest phenol among the phenolic compounds, the basic method of selective hydrogenation is to hydrogenate phenol on a supported metal catalyst. However, the metal palladium with the best catalytic effect at present is relatively expensive and radioactive, and the number of uses it is a little enormous so it is not widely used for the higher cost of catalyzed preparation. The metal Ni is similar to the noble metal Pd and both have an affinity for hydrogen. Pd-based catalysts are mainly used in the current industrial catalytic hydrogenation reaction, but it has the disadvantage of being expensive. Therefore, it is economical and possible to use the metal Ni instead of the noble metal Pd. This essay aims to talk about the reported way of phenolic derivative hydrodeoxygenation and to discuss how different Ni-based catalysts affect this reaction path by analyzing some experiments on these catalysts' development over the last 5 years.

*Corresponding Author: shiqi_h0104@163.com

DOI 10.1201/9781003308553-46

2 EFFECTS

Adjusting the catalyst carrier, preparation method, and environmental conditions in the preparation process can control the activity of the Ni-based catalyst and its distribution of the hydrodeoxygenation (HDO) reaction product. The use conditions of the catalyst, such as temperature, pressure, solvent, etc., will also affect its choice of reaction route. The different product distribution also means that the catalyst affects the progress of the reaction through different activation pathways.

It was reported that hydrodeoxygenation of guaiacol occurred by two main pathways including catechol to benzene and methyl catechol to toluene (Jonathan et al. 2015). The first way is to form catechol and methane by demethylation, then to form phenol by hydrodeoxygenation, and form benzene in the same way finally. The second way is to form methyl catechol by transalkylation of guaiacol, and then to form cresol by hydrodeoxygenation, and to produce methylbenzene eventually by the second hydrodeoxygenation.

2.1 *Different reactant*

The study of Vinicius et al. studied the Ni_2P/SiO_2 catalyst prepared by the incipient wetness impregnation method and its application in the hydrodeoxygenation reaction of the hydrodeoxygenation of ortho, meta, and para cresol (Vinicius et al. 2017). The difference in the positions of methyl and phenolic hydroxyl groups will lead to different distributions of HDO reaction products. However, under the action of the catalyst, the reaction products of the three cresols are mainly methylcyclohexane, which may be due to the adsorption of hydrogen and adsorption on the surface of the catalyst. There is a competitive advantage in the process of interaction between the benzene ring the benzene ring. The selectivities of ortho, meta, and para cresols to methylcyclohexane are 55.7%, 62.9%, and 64.8%, respectively (Vinicius et al. 2017).

Table 1. Reaction features of cresol at 340°C, 4 MPa over Ni_2P/SiO_2 (conversion near 20%) (Vinicius, Priscilla, Victor, Fabio Noronha, FrédéricRichard, 2017).

Model molecule	τ (gh mol^{-1})	Conversion (%)	Selectivity (mol%)						1=MCHe/MCHes
			Tol	MCHnone	MCHols	MCHes	MCH	ECP	
o-cresol	11.0	18.7	8.2	13.6	7.4	14.4	55.7	0.7	65
m-cresol	8.0	20.2	20.6	1.6	0.0	13.8	62.9	1.1	65
p-cresol	9.3	19.4	10.2	4.1	7.1	10.0	64.8	3.8	63

The hydroxyl oxygen is adsorbed on the surface of the catalyst, and the adsorbed hydrogen attacks the carbon where the hydroxyl group is located, thereby completing deoxygenation. This process is affected by the positional relationship between methyl and phenolic hydroxyl groups. Both hydroxyl and alkyl groups are electron-donating groups, which activate the ortho and para positions of the benzene ring. Reaction kinetics studies show that meta-cresol has the highest activity, ortho-methyl Phenol has the lowest activity, and the latter has low reactivity probably because it is also affected by methyl steric hindrance. The weak acidity on the surface of the Ni_2P/SiO_2 catalyst also affects the rate of the deoxygenation reaction. The intermediate product methyl cyclohexanol is more likely to be directly hydrogenated to methylcyclohexane.

Xuefang Lan et al. studied the Ni_2P/SiO_2 catalyst prepared by the incipient wetness impregnation method and its application in the HDO reaction of o-methoxy phenol (Lan et al. 2018). In this reaction, the distribution of products changes with time.

Phenol and anisole are the reaction products of 0.033h. When the reaction proceeds to 0.5h, benzene becomes the main product. The removal of methoxy and hydroxyl is the first process of

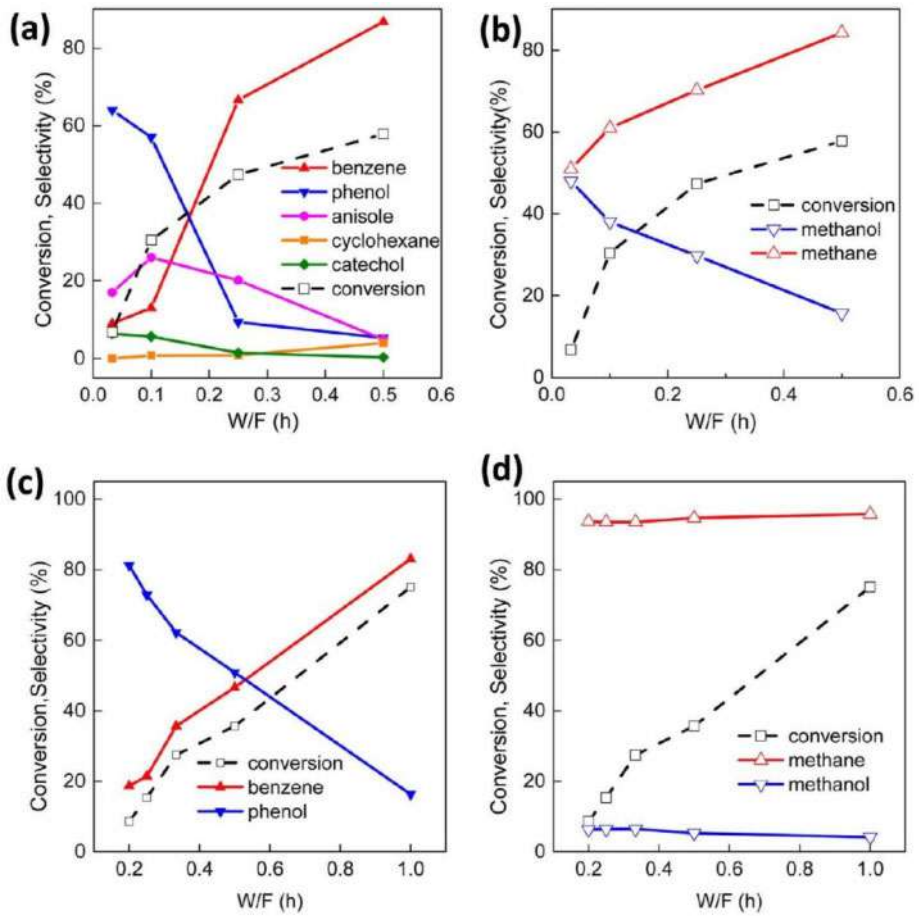

Figure 1. Products selectivity in guaiacol HDO (a), selectivity of initial products in guaiacol HDO (b), selectivity of initial products in anisole HDO (c), and selectivity of initial products in anisole HDO (d) over Ni_2P/SiO_2 at 300°C (Lan et al. 2018).

o-benzyl phenol HDO. After it becomes phenol and anisole, the anisole is dealkylated to phenol, and phenol hydrogenolysis becomes a benzene ring the condition of preparing catalysts.

O.U. Valdés-MartínezaC et al. (2019) prepared the bimetallic Ni-Ru/TiO_2 catalyst by the co-impregnation method. The catalytic activity of the bimetallic Ni-Ru/TiO_2 catalyst is strongly affected by the calcination. The average particle size of Ni increases significantly after calcination, from 2.14nm to 9.9nm.

The benzene hydrogenation reaction rate before calcination is about 8 times higher than that after calcination. Although calcination changes the distribution of acidic sites on the catalyst surface, it has almost no effect on the selectivity of the catalytic reaction. These catalysts tend to hydrogenate the benzene ring first in the phenol hydrogenation reaction, and the main product obtained is saturated alkanes, which are less affected by calcination.

The research of Chi-CongTrana et al. uses the hard template method in nano-casting technology to prepare unsupported bimetallic NiMo, CoMo catalysts, and trimetallic NiMoW catalysts for the hydrodeoxygenation of o-methoxy-phenol (Tran et al. 2017). The effects of the specific surface area of the catalyst and the support on the number of active sites, the effect of the active metal components of the catalyst on the activity, and the role of the acidity of the catalyst surface in the dehydration

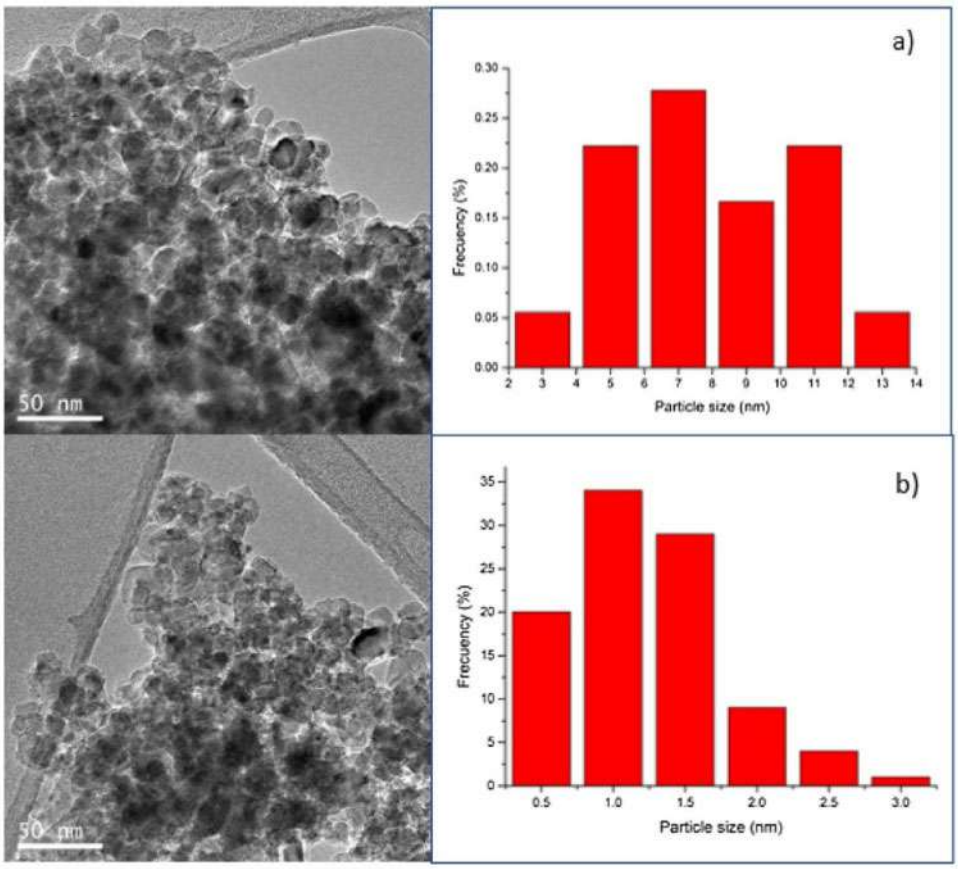

Figure 2. HRTEM images and particle size distribution for $NiRu/TiO_2$ catalysts a) after calcination and b) before calcination (Vald s-Mart et al. 2019).

process are discussed. The unsupported catalyst prepared by the nano-casting technology exhibits higher specific surface area and activity than the unsupported catalyst prepared by the chemical deposition method. The selectivity of the HDO reaction product of o-hydroxycresol is related to the surface acidity of the catalyst. There are more acidic sites on the surface of the trimetallic NiMoW catalyst, which leads to an increase in the distribution of deoxidation products.

The experiments of Xiangping Li et al. studied the Ni/Al-SBA-15 catalyst prepared by the incipient wetness impregnation method and its application in the hydrodeoxygenation reaction of eugenol (Li et al. 2019). The carrier Al-SBA-15 mesoporous zeolite was prepared using water and ethanol as the solvent. The framework structure of the catalyst was obtained by using the former as the carrier changed, but the framework structure of the latter did not change significantly. The difference between the two catalysts in the HDO reaction of eugenol is not obvious. However, the catalyst obtained by loading Ni on the carrier Al-SBA-15 prepared with ethanol as a solvent does not contain oxygen-containing substances in the reaction product, and the selectivity of saturated cycloalkanes is higher, possibly because of its strong surface acidity For another kind of catalyst.

Yanchun Shi et al. synthesize a series of Ni-based catalysts with the wet impregnation method and the in situ encapsulation method using different silicon compounds as supports (He et al. 2017). In addition, phenol HDO reaction has also been researched with three Ni-based catalysts.

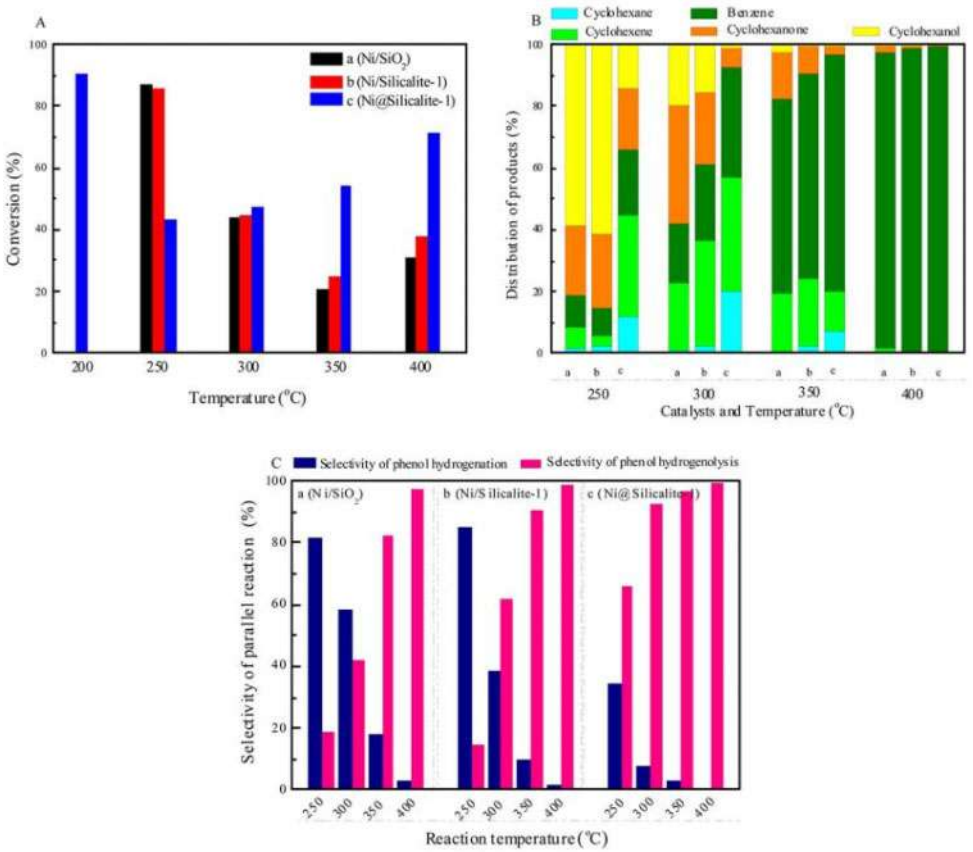

Figure 3. Phenol conversion (A), product distribution (B), hydrogenation, and hydrogenolysis selectivity of parallel reaction (C) over three Ni-based catalysts under increasing temperature (1.0 g catalysts; 0.1 mL/min phenol flow rate; 300 mL/min H_2 flow rate; 0.25 MPa H2) (J. He 2017).

The particle size of the active sites in the encapsulated Ni@Silicalite-1 catalyst is smaller than the two impregnated catalysts (Ni/SiO_2, Ni/Silicalite-1), and the dispersion of Ni is more uniform. Apart from that, the stability of the encapsulated Ni@Silicalite-1 catalyst is stronger than that of the catalyst prepared by the other two impregnation methods. With the increase of the catalytic reaction temperature of phenol, the selectivity of the reaction product benzene increased significantly, the selectivity of cyclohexanol and cyclohexanone decreased significantly, and the deoxygenation process became the most important reaction path. The increase in temperature can increase the reaction rate while inhibiting the adsorption of the benzene ring on the catalyst surface. The two processes compete with each other to cause the conversion rate to decrease first and then increase.

3 COMPARISON

Comparing the work of Vinicius and Xuefang Lan, the same catalyst is used to catalyze the HDO reaction of different phenol derivatives. The selectivity of the reaction products is very different. The main product obtained by catalyzing cresol is methylcyclohexane while catalyzing o-methoxyphenol. The main product obtained is a benzene ring. Both are deoxidation products, which proves that under the action of Ni_2P/SiO_2 catalyst, there is a competitive advantage in the

process of completing the HDO reaction through the deoxidation process. The reason for the obvious difference in reaction products may be that different sites of the reactants are adsorbed on the surface of the catalyst resulting in different reaction paths. The steric hindrance of the methoxy group is significantly greater than that of the methyl group, which may cause the process of the benzene ring of the o-methoxyphenol is absorbed on the surface of the catalyst to be hindered.

The activity of the catalyst will be affected by the dispersibility of the active components. The highly dispersible catalysts show higher activity. Supported catalysts prepared by uniformly dispersing the active metal components on the surface of the carrier usually have higher specific surface area and activity. Different supports can add different properties to the catalyst, and the acidity and basicity of the support will promote the conversion of reactants to different reaction pathways, which affects the selectivity of the catalytic reaction products. In addition, the carrier has a large specific surface area and rich pore structure, and the obtained supported catalyst will also have the same characteristics. However, after long-term use, the coke deposited on the surface of the carrier will block the good pore structure of the carrier and cause the deactivation of the catalyst. Using different methods to prepare the support will have different effects on the framework structure of the support, thereby affecting the stability of the catalyst. Calcination is an important process for preparing catalysts, usually used to remove unnecessary organic compounds in the preparation process, but it will affect the activity of the catalyst. Choosing different synthesis methods will make the surface structure of the catalyst very different. Compared with the catalyst prepared by the impregnation method, the catalyst prepared by the in-situ encapsulation method has higher stability, better dispersion of active components, and smaller particle size. The unsupported catalyst prepared by the nano-casting technology can also show a higher specific surface area, and it may be promising to replace part of the supported catalyst in the future.

4 CONCLUSION

This study summarizes the characteristics of the reaction of phenol and its derivatives under different Ni-based catalysts in the past few years. Therefore, the following result could be obtained. The spatial position resistance and electron effect of the reaction substrate affect the choice of the reaction pathway. Choosing a suitable synthesis method could also improve the activity and stability of the catalyst. The surface acidity of the catalyst affects the selectivity of phenol and its derivatives to catalyze the reaction. While the support brings high dispersibility to the active components, it will also be inactivated during long-term use. The research lays the foundation as well for choosing how to prepare high-efficiency Ni-based catalysts for the HDO reaction of biomass oil.

ACKNOWLEDGEMENT

Thanks for the support of the internet of Beijing University of Chemical Technology and all people who helped me during the research.

REFERENCES

Chi-Cong Tran, Filip Stankovikj, Manuel Garcia-Perez, Serge Kaliaguine. Unsupported transition metal-catalyzed hydrodeoxygenation of guaiacol[J]. Catalysis Communications 101 (2017) 71–76.

J. He, X.-H. Lu, Y. Shen, R. Jing, R.-F. Nie, D. Zhou, Q.-H. Xia. Highly selective hydrogenation of phenol to cyclohexanol over nano silica supported Ni catalysts in aqueous medium[J]. Molecular Catalysis 440 (2017) 87–95.

Jonathan E. Peters, John R. Carpenter, and David C. Dayton. Anisole and Guaiacol Hydrodeoxygenation Reaction Pathways over Selected Catalysts[J]. Energy Fuels 2015, 29, 2, 909–916.

O.U. Vald s-Mart nez, C.E. Santolalla-Vargas, V. Santes, J.A. de los Reyes, B. Pawelec, J.L.G. Fierro. Influence of calcination on metallic dispersion and support interactions for NiRu/TiO_2 catalyst in the hydrodeoxygenation of phenol[J]. Catalysis Today 329 (2019) 149–155.

Vinicius O.O. Gonçalves, Priscilla M. de Souza, Victor Teixeira da Silva, Fabio B. Noronha, FrédéricRichard. Kinetics of the hydrodeoxygenation of cresol isomers over Ni_2P/SiO_2: Proposals of nature of deoxygenation active sites based on anexperimental study[J]. Applied Catalysis B: Environmental 205 (2017) 357–367.

Xiangping Li, Jianguang Zhang, Bin Liu, Juping Liu, Chuanbin Wang, Guanyi Chen. Hydrodeoxygenation of lignin-derived phenols to produce hydrocarbons over Ni/Al-SBA-15 prepared with different impregnants[J]. Fuel 243 (2019) 314–321.

Xuefang Lan, Emiel J.M. Hensen, Thomas Weber. Hydrodeoxygenation of guaiacol over Ni_2P/SiO_2–reaction mechanism and catalyst deactivation[J]. Applied Catalysis A, General 550 (2018) 57–66.

Advances in Applied Chemistry and Industrial Catalysis – Saikia (Ed.)

How effective is feather degradation solution as a fertilizer in soilless lettuce cultivation

Mimu Chen*
Utahloy International School, Guangzhou, China

ABSTRACT: Fertilizers are an indispensable part of agriculture. Currently, numerous researches have been done on feather degradation methodologies, including hydrolysis by high-pressure cooking, extruding method, acid, and base hydrolysis, enzymatic hydrolysis, and microbial fermentation — turning agricultural waste into useful fertilizers. Feather degradation solution obtained from microbial fermentation using chicken feathers contains rich amino acids related to a context that could greatly benefit vegetable cultivation by improving their yield and quality. The effectiveness of feather solution in soilless cultivation for lettuces will be investigated. Two groups of 6 lettuces are cultivated in nutrition solution for 35 days, the experiment group added feather degradation solution in this process. As a result, the lettuces cultivated with feather degradation solution had significant improvements in their fresh weight, total soluble solids concentration, amino acids concentration, and polypeptides concentration. This solution is successful as a fertilizer used for soilless cultivation. It has great potential in the future to be developed into a sustainable fertilizer for both in-soil and soilless farming.

1 INTRODUCTION

In agriculture worldwide, fertilizers play an extremely important role and are often indispensable. They contribute to food quality and food security. Therefore, as the industries developed and mature, the need and pursuit of more eco-friendly fertilizers are becoming more common. Currently, numerous researches have been done on feather degradation methodologies, including hydrolysis by high-pressure cooking, extruding method, acid and base hydrolysis, enzymatic hydrolysis, and microbial fermentation. Among them, microbial fermentation effectively uses microorganisms or keratinase to destroy its spatial structure, which increased the solubility of keratin. It is a biodegradation method, also known as the enzymatic hydrolysis method which increased the solubility of keratin. The product—keratin, could be used in a variety of fields including stock farming (animal feed), beauty industry (cosmetics), and agriculture (fertilizers). Up to now, much research about how to degrade and utilize feathers effectively by using microbial fermentation has been done. This essay further investigates how effective is feather degradation solution when it is used in vegetable cultivation.

2 RELEVANT CONCEPTS

Chicken feathers are abundantly being produced — a hundred million annually. Currently, a small amount of these feathers are been used as a source of animal fodder or agricultural fertilizers, yet the larger proportion is been disposed of as waste. This is not only a huge squander of renewable resources, but also resulted in the emission of greenhouse gases, and is an occupation of land resources. In chicken feathers, they contain more than 95% of keratin (Akhter & Marzan 2020), which is a very precious source of fodder and fertilizers. Moreover, keratin in feathers could be

*Corresponding Author: mimuchen@outlook.com

DOI 10.1201/9781003308553-47

used to obtain amino acid relating agents to enhance the utilization rate of micro-elements in crops. Microbial keratinase could be obtained from microbially hydrolyzed feathers using fungi, bacteria, and actinomycetes. It has great effects on increasing the production and quality of crops whilst decreasing the cost (Adetunji 2012).

Soilless farming is a relatively new way of cultivating plants, and it is considered a more efficient way of cultivating crops than traditional farming. In the former, crops do not need to waste energy on developing complex root systems to search for nutrients or water in the soil. Instead of being planted in soil, crops are cultivated in mineral-rich nutrient solutions, so that all the needed components a crop needs to grow are provided to it directly. Therefore, these crops convert more energy into growing usable (edible in most cases) parts rather than useless root systems. Hence, in a soil farming system, the nutrient solution is the key and will directly affect the quantity and quality of the crops cultivated.

Lettuces (Lactuca sativa L), which belongs to a genus of lettuce in the Composite family, is an annual or biennial herbaceous crop. Lettuces are a very commonly used crop in soilless farming and are a salad crop that is been cultivated worldwide. This crop has very high commercial values for its diet and medicinal usage (Agri Farming 2018).

Currently, microbial fermentation is developed as an effective method to degrade feathers and transfer them into amino acid-related substances. In theory, solutions attained from degraded feathers will improve vegetable quality when used as fertilizers. In this experiment, an investigation on the effectiveness of feather degradation solution in lectures in soilless farming will be taken.

3 MATERIALS AND METHODS

3.1 *Chicken feather and its degradation process*

Chicken feathers, used as the primary source of the feather degradation solution are collected from local farms in Guangzhou (23.13°N, 113.26°E) China. All feathers collected come from Field Broilers, which is originated in Qingyuan China, and mainly used as a source of commercial poultry.

Before doing any experiments, the feathers are to be washed and cleaned completely. First, all feathers are washed thoroughly with water to remove any blood and dirt. Second, clean feathers are laid on a flat surface indoors where the sunlight could hit and are exposed under the sun to let dry

Table 1. Nutrient Solution Ingredients.

Categories	Compound	Amount (mg/L)
A Solution	Calcium nitrate tetrahydrate	472
	Potassium nitrate	202
	Ammonium nitrate	80
B Solution	Dipotassium hydrogen phosphate	100
	Potassium sulfate	174
	Magnesium sulfate heptahydrate	246
C Solution	Ethylenediaminetetraacetic acid sodium iron	20
	Boric acid	2.86
	Manganese sulfate tetrahydrate	2.13
	Zinc sulfate heptahydrate	0.22
	Copper sulfate pentahydrate	0.08
	Ammonium molybdate tetrahydrate	0.02

completely. This was done in May of 2020 in Guangzhou. The average room temperature was 26 degrees Celsius, and the average outdoor temperature was between 24 to 30 degrees Celsius. Third, after all, dried naturally by the sun, feathers are transferred into an oven of 75 degrees Celsius for an 8-hour second-time drying. Fourth, a ball mill of 60 mesh particle size standard sieve was used to grind dried feathers. Finally, the final degradation solution is obtained by fermented fine feather power with SCUT-3— a feather degrading bacteria. The fermentation process was completed under 40 degrees Celsius in 48 hours.

3.1.1 *Preparing nutrient solution for soilless farming*

In this experiment, a controlled nutrient solution is added to all subjects, and 100 mg/L of feather degradation solution is added to the controlled solution to experiment group subjects.

The controlled nutrient solution used in this study uses leafy vegetable recipe B from South China Agricultural University. The solution is a mixture of 3 different sub-nutrient solutions.

3.1.2 *Planting lettuces*

The soilless farming device used 2 blue plastic boxes of length 385mm, width 280 mm, and height 150 mm, covered with a 20 mm thick foam board, on which opened 6 symmetrical and equal size holes of 55 mm in diameter. One of the boxes is controlled, and one of the boxes experiments.

In this experiment, Romaine Lettuces are used. After seeds germinated to produce 3-4 leaves, transplant the subjects into individual engraftment cups, then placed into prepared holes in the soil farming device; 1 plant in each hole, and 6 plants in a box. A controlled nutrition solution was added to two of the plastic box, and all the roots of the subjects are submerged in the solution. An extra 100 mg/L feather degradation solution was added into the experimented box and was mixed with the controlled nutrition solution thoroughly. To guarantee equal access to nutrient solutions for all subjects, the solution amount inside each box is checked daily to ensure the roots of all lettuces are submerged by it. When too much solution is absorbed, and roots are exposed to air, a more controlled nutrition solution is added to the box.

4 MEASURING DATA

After 35 days of transplanting, the final result is measured for the 6 lettuces in each box. Within the final results, the 3 more average data out of the 6 plants in each box are taken. In this study, 4 parameters of the lettuces are measured—fresh weight, total soluble solids concentration, amino acids concentration, and polypeptides concentration.

The fresh weight of all controlled and experimented subjects are measured with 1% electronic balances after directly picked from the engraftment cup and extra liquid on the roots removed. A total soluble solid percentage is acquired by using an ATAGO N-1α saccharometer (refractometer). Amino acid concentration is measured using an amino acid analyzer according to China National food safety standards GB 5009.124-2016—the protein in food was hydrolyzed into free amino acids by hydrochloric acid, separated by ion-exchange column, and then reacted with ninhydrin solution to produce a color reaction, and the amino acid content was determined by visible light spectrophotometry detector. Polypeptide concentration is acquired by using 15% trichloroacetic acid solution to completely precipitate the large molecule protein in the lettuce sample, while the small molecule peptide remained in the solution, removing the protein precipitation, the supernatant following China National food safety standards GB/T5009.5-2003 to determine the total nitrogen content.

This figure shows how the lettuces are cultivated.

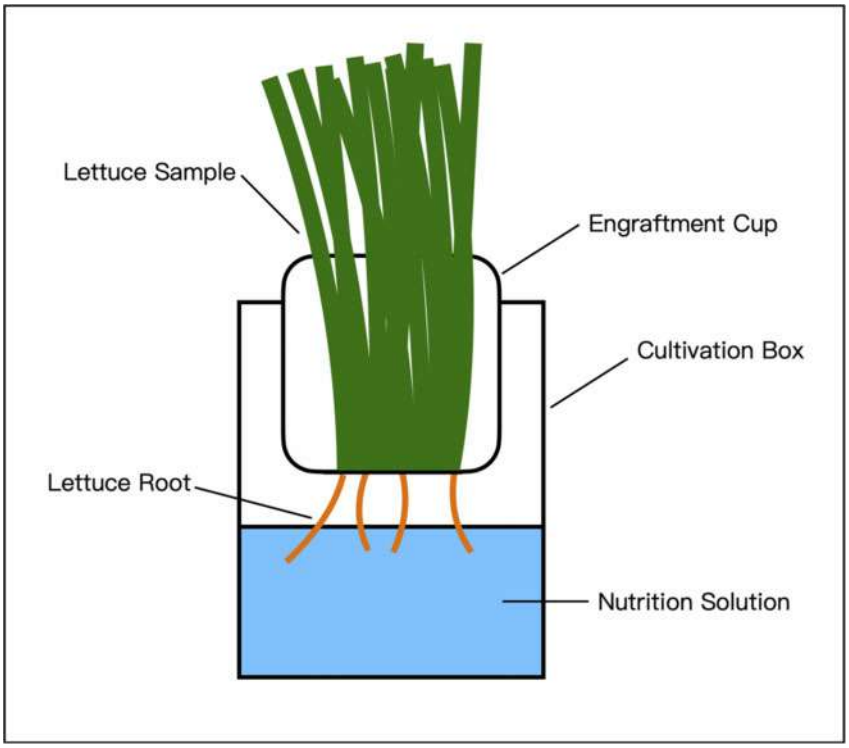

Figure 1. Lettuce in cultivation box.

Table 2. Lettuce quality.

	Fresh Weight (g)				Total Soluble Solid Concentration (%)			
	Group 1	Group 2	Group 3	Average	Group 1	Group 2	Group 3	Average
Controller	160.97	154.05	159.85	158.29	3.51	3.98	4.3	3.93
Experimented	213.54	220.24	225.06	219.61	5.42	5.37	6.39	5.73
	Animo Acid Concentration (mg/g)				Polypeptide Concentration (mg/g)			
	Group 1	Group 2	Group 3	Average	Group 1	Group 2	Group 3	Average
Controlled	1.57	1.36	1.24	1.39	21.8	21.35	19.1	20.75
Experimented	3.01	2.66	2.83	2.83	31.69	28.09	26.07	28.62

5 RESULTS

In the experiment, soilless cultivated lettuces showed a significant improvement in all the parameters measured when 100 mg/L of feather degradation solution is added to the controlled nutrition solution for soilless lettuces cultivation. The fresh weight of controlled lettuces is 158.29 ± 3.71 grams, and the fresh weight of experimented lettuces is 219.61 ± 5.79 grams—138.74% of the former. The soluble solid in this study refers to all compound in the vegetable that is soluble in

water, including sugar, acids, minerals, and vitamins. With the controlled subjects, the concentration is 3.93 ± 0.40 percent; and in the experimented subjects, the concentration is 5.73 ± 0.58 percent. In total double solid concentration, lettuces cultivated with feather degradation solution is 146.17% of lettuces without this solution. Controlled subjects had 1.39 ± 0.17 mg/g in amino acid concentration and experimented subjects had 2.83 ± 0.18 mg/g—203.60% of controlled subjects. Polypeptide concentration for controlled lettuces is 20.75 ± 1.45 mg/g, and for experimented lettuces is 28.62 ± 2.85 mg/g, which is 137.92% of the former.

As shown in Figure 2, the impact of feather degradation solution on lettuce development is very significant. Improvements in all four indicators could be seen in the results for the experimented groups.

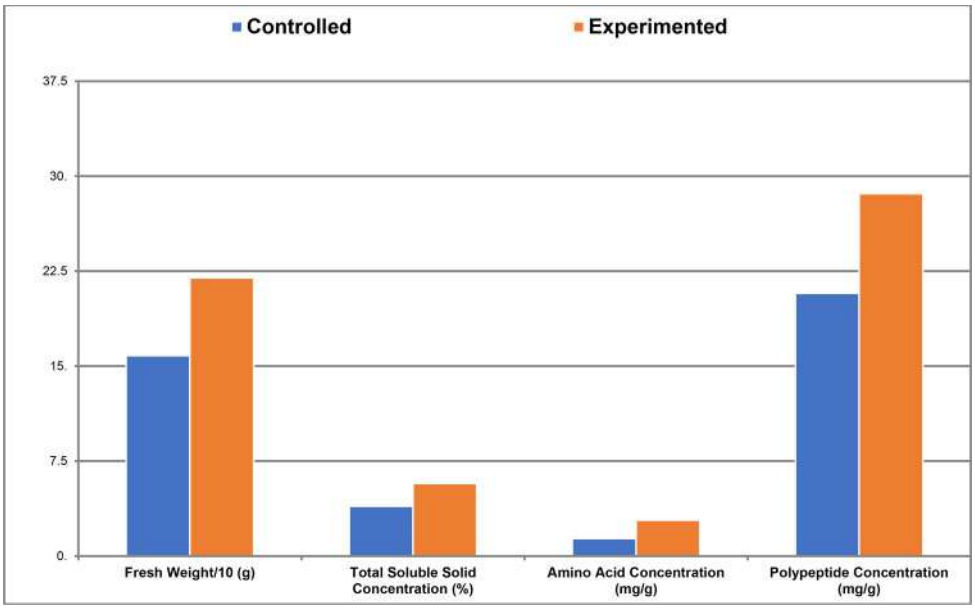

Figure 2. Lettuce quality.

6 DISCUSSION

Feather, being the most important source of feather degradation solutions, is a readily valuable resource, but presently, a huge source of pollution. Feathers have an abominable nature, ordinary proteolytic enzymes such as pepsin and trypsin have extremely tiny effects on this substance; so they are very difficult to be degraded in the natural environment. Moreover, because they usually contain grease, blood, or other animal-related substances, they are usually pathogenic microorganisms carriers which is a potential menace to public health. Moreover, feathers also produce huge emissions of greenhouse gases, like nitrous oxide, ammonia, and hydrogen sulfide (Li 2019). Presently, there are three common and popular methodologies for feather disposal. One in the two being incineration. It is effective in eliminating the threat of diseases and other health concerns caused by feathers, yet expensive plus not environmentally friendly. The second method is to bury them in landfills or dumpsites. This also provides opportunities for greenhouse gases emission while giving people extra work to carefully avoid staining underground water systems. The third method is less popular and mostly done in some countries in Europe and USA—hydrolyze feathers at high temperatures to obtain protein. This is extremely expensive and is a huge waste of

electricity and water resources (Acda 2010). Consequently, feather disposal is a difficult task to deal with.

Nevertheless, many recent studies investigated another more efficient and more environmentally friendly method of treating this substance — microbial degradation, which provides a new and more efficient way of disposing of feathers by converting them into a bio-fertilizer. This is a progress of degrading keratin in feathers by using keratinases, which are faster, cheaper, and less pollutant than most methods. Therefore, as soilless farming becomes more developed and popular, the demand for relative products like nutrition solutions will increase in proportion. Therefore, the validity of feather degradation solution as not only soil fertilizers but soilless farming fertilizers is as important and worth investigating.

In this experiment, some variables weren't perfectly kept controlled. When cultivating lettuces, the nutrition solutions level is controlled, and experimented cultivation box is checked daily to make sure all roots are submerged by the liquid. However, when roots are exposed in either of the boxes, only recipe B nutrition solution was added. Hence, the concentration of feather degradation solution in the experimented box wasn't kept constant since there was a 531 ml of controlled nutrition solution added to the box on day 12, and 479 ml addition on day 29. This will cause a decrease in feather degradation concentration in the box. As a result, the present data of experimented lettuces sample may be slightly lower than the results in reality.

7 CONCLUSION

In conclusion, this study investigates the potential of feather degradation solution in the soilless cultivation of lettuces. This experiment took place in the wintertime, in Guangzhou, China. Raw materials of the feather degradation solution include feathers from Field Broilers and SCUT-3 as the degradation bacteria. Romaine Lettuces are used for this investigation, and the entire soilless cultivation process took 35 days. The controlled nutrition solution was recipe B of leafy vegetables from South China Agricultural University, while experimented groups had feather degradation solution added. Results of the experiments showed significant improvements in fresh weight, total soluble solids concentration, amino acid concentration, and polypeptide concentration of subjects with father degradation solution added in the process of cultivation.

Feather degradation solution—eco-friendly, efficient, and cost-effective—has great potential to be developed into an ideal agricultural fertilizer in the future for both soilless and soil cultivation. In this investigation, the effectiveness of feather degradation solution in soilless cultivation is proven, yet more research on its ability in enhancing plant development in soil cultivation conditions could be done. This cheap and sustainable fertilizer could be used on large scale in the future.

REFERENCES

Acda, M. N. (2010). (PDF) sustainable use of waste chicken feather for durable and low cost building materials for tropical climates. ResearchGate. Retrieved October 30, 2021, from https://www.researchgate.net/publication/287694572_Sustainable_use_of_waste_chicken_feather_for_durable_and_low_cost_building_materials_for_tropical_climates.

Adetunji. (2012). Production and application of keratinbased organic …– IJSER. Retrieved October 30, 2021, from https://www.ijser.org/researchpaper/Production-and-Application-of-KeratinBased-Organic-Fertilizer-from-Microbially-Hydrolyzed-Feathers-to-cowpea.pdf.

Akhter, M., & Marzan, L. W. (2020). Microbial Bioremediation of Feather Waste for Keratinase Production: An Outstanding Solution for Leather Dehairing in Tanneries. Microbiology insights. Retrieved October 30, 2021, from https://pubmed.ncbi.nlm.nih.gov/32440139/.

Lettuce cultivation information guide. Agri Farming. (2018, April 7). Retrieved October 30, 2021, from https://www.agrifarming.in/lettuce-cultivation.

Li, Q. (2019, December 5). Progress in microbial degradation of feather waste. Frontiers in microbiology. Retrieved October 30, 2021, from https://www.ncbi.nlm.nih.gov/pmc/articles/PMC6906142/.

Advances in Applied Chemistry and Industrial Catalysis – Saikia (Ed.)

Research on low temperature NO conversion over Mn-TiO_2 catalysts

Quanming Liang*, Penglai Zuo**, Ziwen Yang*** & Li Tong****
Institute of Urban Safety and Environmental Science, Beijing Academy of Science and Technology, Beijing, China

Lijuan He*****
Beijing Municipal Research Institute of Eco-environmental Protection, Beijing, China

ABSTRACT: The effect of different MnO_x loadings on NO conversion over MnO_x-TiO_2 catalysts prepared by the impregnation method was investigated. The NO conversion increased firstly and then tended to be stable with the increase of MnO_x loading. When the MnO_x loading reached 20 wt%, the conversion of NO reached 89.0% at 140°C. However, the N_2 selectivity showed a downward trend as the increase of MnO_x loading (0–30 wt%). This indicated that MnO_x increased the NO conversion over the catalyst as well as widened the temperature window toward activity, but decreased the N_2 selectivity. Afterward, the catalysts were characterized by BET, XRD, NO-TPD, NH_3-TPD, and H_2-TPR methods. The results showed that the addition of MnO_x blocked the porous structure, further decreasing the specific surface area and pore volume of catalysts. However, a small amount of MnO_x loading could be uniformly dispersed on the surface of the catalyst as a single layer, facilitating to enhancing the NO adsorption performance, NH_3 adsorption performance, and redox performance of the catalysts, thereby increasing the catalysts' NO conversion efficiency, the catalytic reaction path of which conformed to the Langmuir-Hinshelwood mechanism. When the content of MnO_x exceeded 20%, the MnO_x would exist on the surface of the carrier in a crystalline form, and the NO conversion was difficult to continue to improve.

1 INTRODUCTION

Nitrogen oxide (NO_x) is one of the main air pollutants, which can produce a series of environmental problems such as acid deposition, photochemical smog, O_3 enrichment, fine particulates generation, and eutrophication of water body. At present, the most widely used technology in the industry is selective catalytic reduction (SCR), the core of which is a catalyst. The SCR reaction equation with NH_3 as reducing agent is as follows: $4NO + 4NH_3 + O_2 \rightarrow 4N_2 + 6H_2O$; $2NO_2 + 4NH_3 + O_2 \rightarrow 3N_2 + 6H_2O$.

With the strict limits of NO_x emissions and the increase of environmental protection supervision, the power industry using medium and high-temperature catalysts can meet the emission standards. In contrast, the flue temperature of the non-electric industrial boiler is mostly below 300°C, and the operation condition is not stable, leading to that the medium and high-temperature catalysts are not effective for NO_x removal. Therefore, the development of environmentally friendly catalysts with low temperature and high activity is the current research hotspot in the denitration of industrial boiler flue gas in non-electric industries.

Due to the high NH_3-SCR activity under low-temperature conditions, the manganese-based catalysts can improve the adsorption and activation of NO_x and NH_3 in the reaction atmosphere on the catalyst surface, making it the most commonly studied alternative to V_2O_5-MoO_3/TiO_2 and V_2O_5-WO_3/TiO_2 catalyst (Jiang et al. 2020; He et al. 2021; Thirupathi & Smirniotis 2012; Zhang et al. 2019a, 2021). Fang (Fang et al. 2015) investigated the NH_3-SCR activity of Mn-based

Corresponding Authors: *liangquanming@163.com, **zuopenglai@126.com, ***184236865@qq.com, ****tongli12042009@163.com and *****helijuan@cee.cn

DOI 10.1201/9781003308553-48

catalysts prepared by different precursors or pure MnO_x. Mn_2O_3 and Mn_3O_4 had good catalytic activity for NO_x. Through the XRD, TG, and H_2-TPR test analysis, the catalyst surface contained a large amount of crystalline and/or amorphous MnO_x. Xin (Xin et al. 2018) prepared the Mn_2O_3 catalyst to promote the activation of NH_3 to form NH_2 intermediates, meanwhile, capturing gaseous NO to form NH_2NO, which was finally converted to N_2.

Yang (Yang et al. 2018) found that highly dispersed active sites, abundant surface Lewis acid sites, and strong interaction between Mn and Ti significantly improved the low-temperature SCR activity of the Mn-Ti catalyst. $Mn_{0.5}Ti_{0.5}$ catalyst exhibited the best low-temperature NH_3-SCR performance and excellent H_2O/SO_2 resistance. In-situ FTIR was used to study the reaction mechanism, and the results showed that both Langmuir-Hinshelwood and Eley-Rideal reaction mechanisms existed in the NH_3-SCR reaction process, among which Langmuir-Hinshelwood reaction played a dominant role at low temperature (Chen et al. 2016; Yang et al. 2016). Wei (Wei et al. 2018) concluded that the main active substance was Mn^{4+} species dispersed on the surface of the catalyst. The addition of MnO_x promoted the adsorption of the reaction atmosphere and the formation of oxygen vacancies. The Lewis acid site reaction followed the Eley-Rideal reaction mechanism, and the Bronsted acid site reaction followed the Langmuir-Hinshelwood mechanism. Zhang (Zhang et al. 2019b) further found that oxygen vacancies not only activated reactive species but also promoted the desorption of NO_2 molecules from metal sites, providing conditions for subsequent fast SCR reactions. Li (Li et al. 2019) pointed out that NH_3 could not only adsorb on the Lewis acid site and participate in SCR reaction in the form of NH_3 but also adsorb on the Bronsted acid site and participate in SCR reaction in the form of NH^{4+}.

Based on the above discussions, this paper investigated the NO conversion and N_2 selectivity of MnO_x-TiO_2 catalyst with MnO_x as the active component and optimized the formulation of high activity denitration catalyst. On this basis, BET, XRD, NO-TPD, NH_3-TPD, and H_2-TPR methods were used to analyze the pore structure, crystal structure, NO adsorption performance, NH_3 adsorption performance, and redox performance of MnO_x-TiO_2 catalyst. Finally, the SCR catalytic reaction path was revealed to guide the preparation of the catalyst.

2 EXPERIMENTAL

2.1 *Catalyst preparation*

The preparation method for Mn-TiO_2 catalyst was as follows: Manganese acetate tetrahydrate (Sinopharm Chemical Reagent Co., Ltd.) and TiO_2 (industrial grade, ≥96.0%) were added to 50 mL deionized water with the desired proportion by stirring for 2 h at 60°C. Subsequently, the formed viscous solids were oven-dried at 105°C for 3 h and then calcined at 350°C for 3 h.

In this paper, MnO_x was recorded as the final species of manganese compound in the fresh catalysts, and the Mn-TiO_2 catalysts with 0%, 5%, 10%, 20%, and 30 wt% MnO_x were denoted as 0Mn, 5Mn, 10Mn, 20Mn and 30Mn, respectively.

2.2 *Catalyst activity test*

The catalyst performance evaluation system included a high-pressure cylinder, mass flow controller, gas mixer, quartz reactor, tubular furnace, temperature control instrument, mass spectrometer, 42I nitrogen oxide analyzer, computer, etc. The pipeline was connected by a PTFE pipe with a diameter of 3 mm.

The catalyst NO conversion was measured in a fixed-bed quartz micro-reactor with the catalyst amount of 1 mL, and the gas hourly space velocity (GHSV) was 30,000 h^{-1} at a flow rate of 500 mL/min for each test. The reaction gas consisted of 0.07% NO, 0.07% NH_3, 5% O_2, and Ar as balance gas, and the test temperature was 80-360°C. A high-level 42I Nitrogen oxide analyzer (Thermo Electron Co., American) was used to measure the imported and exported concentration toward NO and to calculate the NO conversion. The mass spectrometer was applied to test the vacuum degree of N_2O to represent the production of N_2O, which was used to analyze the selectivity of N_2.

$$\text{NO conversion} = ([NO]_{in} - [NO]_{out})/[NO]_{in} \times 100\%$$

2.3 *Catalyst characterization*

The specific surface area and pore volume of the catalyst were tested on ASAP 2020 physical adsorption instrument (Micromeritics Co., American), and the samples were vacuum-pretreated at 120°C for 4 h and adsorbed statically at −196°C by N_2. BET (Brunauer-Emmett-Teller) method was used to calculate the specific surface area (S_{BET}) of samples (Liang et al. 2020). Crystal structures of the samples were carried out on the D8 advanced X-ray diffractometer (Bruker Co., Germany) with a Cu Kα radiation in the 2θ range of 10°–80°.

The NO temperature-programmed desorption (NO-TPD), NH_3 temperature-programmed desorption (NH_3-TPD), and H_2 temperature-programmed reduction (H_2-TPR) experiments were performed on AutoChem1 II Model 2920 chemisorption instrument (Micromeritics Co., American). The NO-TPD and NH_3-TPD experimental procedures were as follows: 50 mg of the sample (40–60 mesh) were firstly pretreated at 300°C for 60 min under a He atmosphere, and then switched to 10% NO/He or 10% NH_3/He atmosphere for 60 min. Finally, the temperature was increased at a rate of 10 °C/min, and the TCD signal was detected. The H_2-TPR experiment steps were as follows: 50 mg samples (40-60 mesh) were pretreated at 400°C in pure O_2 atmosphere for 30 min, subsequently cooled to room temperature for 15 min after He purging. Then the 10% H_2/Ar was introduced, and the temperature was raised to 600°C at a rate of 10°C/min, and the H_2 consumption was detected by TCD.

3 RESULTS AND DISCUSSION

3.1 *Effect of MnO_x loading on NO conversion over the $MnO_x - TiO_2$ catalyst*

Figure 1(a) showed the effect of MnO_x loading on NO conversion over the MnO_x-TiO_2 catalyst. It could be seen that when the reaction temperature was 140°C, the NO conversion of 0Mn, 5Mn, 10Mn, 20Mn, and 30Mn catalysts were 21.2%, 59.2%, 80.6%, 89.0%, and 89.5%, respectively, indicating that with the increase of MnO_x loading, NO conversion gradually increased. However, when the MnO_x loading reached 20 wt%, the NO conversion tended to be stable, and the catalyst exhibited excellent low-temperature catalytic reduction activity. Above 280°C, the NO conversion decreased to varying degrees as the reducing agent NH_3 was oxidized by a catalyst.

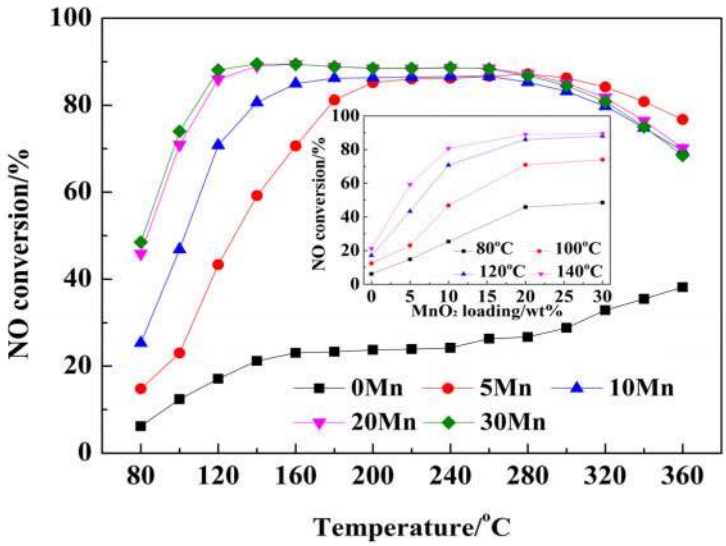

Figure 1(a). NO conversion of different MnO_x loadings over the catalysts.

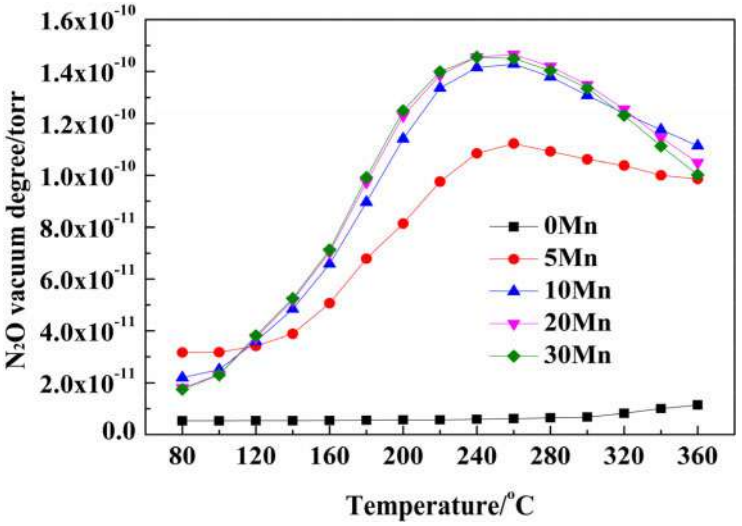

Figure 1(b). N_2O vacuum degree of different MnO_x loadings over the catalysts. Reaction conditions: $[NH_3] = [NO] = 0.07\%$, $[O_2] = 5\%$, Ar balance, GHSV = 30,000 h^{-1}.

The N_2O production of MnO_x-TiO_2 catalyst was shown in Figure 1(b). It could be seen that, compared with the 0Mn catalyst, the N_2O production of the catalysts with different MnO_x loadings showed a trend of rising firstly and then stable. In the temperature range of 240∼260°C, the N_2O production reached an extreme value. Subsequently, due to the oxidation of NH_3, the N_2O content generated by the side reaction between NO and NH_3 was greatly reduced. Therefore, the addition of MnO_x improved the catalyst NO conversion, and widen the temperature window toward the activity of the catalyst, but it made the N_2 selectivity worse.

3.2 *Physical and chemical properties of MnO_x-TiO_2 catalyst*

Characterization techniques including BET, XRD, NO-TPD, NH_3-TPD, and H_2-TPR were used to analyze the physical and chemical properties of MnO_x-TiO_2 catalysts.

3.2.1 *BET analysis*

Table 1 showed the results of specific surface area, pore volume, NO desorption amount, NH_3 desorption amount, and H_2 consumption for the MnO_x-TiO_2 catalyst. It was seen that with the increase of MnO_x loading, the specific surface area and pore volume of MnO_x-TiO_2 catalysts showed a downward trend, from 94.1 m^2/g and 0.53 cm^3/g for 0Mn catalyst to 54.2 m^2/g and 0.29 cm^3/g for 30Mn catalyst. The results suggested that adding MnO_x blocked the pore structure of the carrier and reduced the specific surface area and pore volume of the catalyst. When MnO_x was overloaded, the catalytic reaction process of NO, NH_3, O_2, and the other reaction atmospheres on the catalyst surface would be affected, resulting in NO conversion being difficult to continue to increase (Wei et al. 2018).

Table 1. Physical and chemical properties of catalysts.

Classification	0Mn	10Mn	20Mn	30Mn
Specific surface area (m^2/g)	94.1	66.1	64.6	54.2
Toatal pore volume (cm^3/g)	0.53	0.36	0.33	0.29
NO desorption amount (mmol/g)	0.92	1.26	1.42	1.44
NH_3 desorption amount (mmol/g)	0.66	0.75	0.95	0.92
H_2 consumption (mmol/g)	2.34	5.20	7.47	8.24

3.2.2 *XRD analysis*

Figure 2 illuminated the XRD patterns of the catalysts. The diffraction peaks of the four catalysts were attributed to typical anatase TiO_2 with the corresponding characteristic peaks appearing at 25.3°, 37.8°, 48.0°, 53.8°, 55.3°, 62.7°, 68.8°, 70.4° and 75.0°. As the increase of MnO_x addition, 20Mn and 30Mn catalysts showed obvious MnO_x diffraction peaks at 18.1°, 28.9°, 32.5°, 36.2°, 58.4° and 60.0°. The results demonstrated that the appropriate amount of MnO_x could be uniformly dispersed on the surface of the catalyst in a single layer. However, when the MnO_x content exceeded 20%, MnO_x existed on the surface of the carrier in the form of crystallinity, due to the excessive loading of the active component (Fang et al. 2015).

3.2.3 *NO-TPD analysis*

To explore the reaction mechanism during the NH_3-SCR reaction over the MnO_x-TiO_2 catalyst, the NO-TPD and NH_3-TPD characterization of the catalysts was performed. Figure 3 showed the NO-TPD profiles for the NO adsorption performance of the catalysts. The NO desorption peaks of the four catalysts were mainly concentrated in the temperature range of 50–400°C. With the increase of MnO_x loading, the NO desorption amount of the catalyst increased from 0.92 mmol/g for the 0Mn catalyst to 1.44 mmol/g for the 30Mn catalyst, and the maximum desorption peak gradually shifted to the middle and high temperature, expanding NO adsorption temperature range of catalyst. The results showed that adding MnO_x enhanced the adsorption capacity of NO on the catalyst surface, which was positively correlated with the NO conversion. Therefore, it was inferred that the adsorption of NO on the catalyst surface contributes to the occurrence of NO selective catalytic reduction reaction.

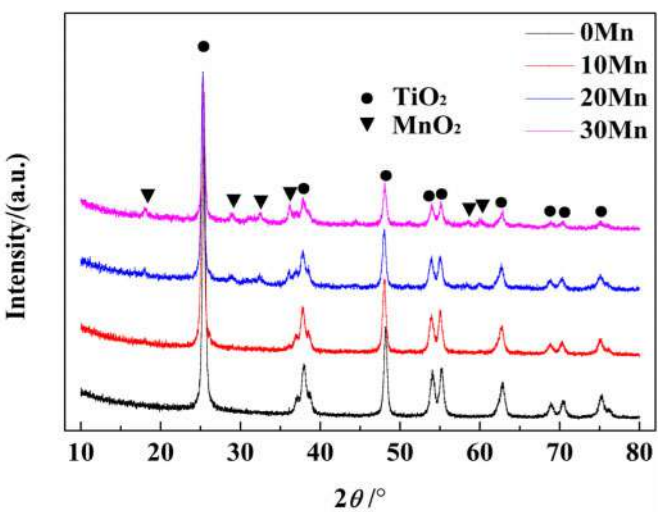

Figure 2. X-ray diffraction patterns of catalysts.

3.2.4 *NH_3-TPD analysis*

Figure 4 showed the NH_3-TPD profiles of MnO_x-TiO_2 catalysts with different MnO_x loadings. It was seen that the catalyst had a wide NH_3 desorption peak in the range of 50–650°C. As the loading of MnO_x increased, the NH_3 desorption capacity of the catalyst increased from 0.66 mmol/g of 0Mn catalyst to 0.92 mmol/g of 30Mn catalyst. Among them, the temperature range of 50–400°C belonged to NH_3 species with weak desorption at the Bronsted acid site (Pan et al. 2013), facilitating to enhancing the catalyst's low-temperature NH_3 adsorption performance, the result of which was similar to that of NO-TPD. Therefore, it was inferred that NH_3 was firstly adsorbed on the surface

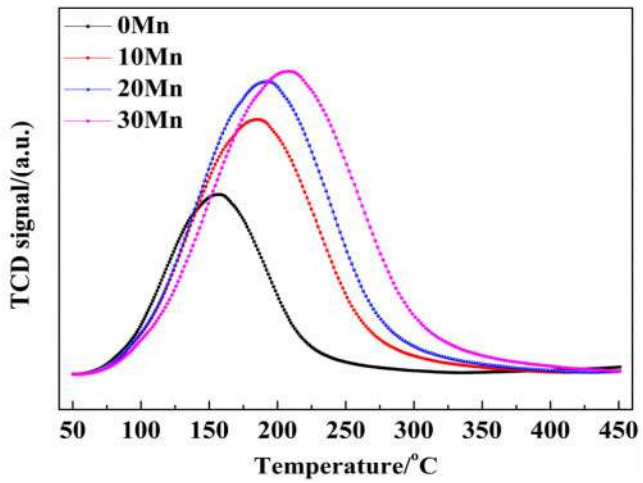

Figure 3. NO-TPD profiles of catalysts.

of the catalyst and participated in the catalytic reaction of NO. In other words, the adsorbed NH_3 and NO on the surface of the material were conducive to improving the catalytic reduction reaction of NO. Therefore, the reaction path conformed to the L-H mechanism.

3.2.5 *H_2-TPR analysis*

H_2-TPR characterization was used to investigate the redox performance of MnO_x-TiO_2 catalysts with different MnO_x loadings, and the specific results were depicted in Figure 5. All the MnO_x-TiO_2 catalysts showed two reduction peaks, which were concentrated in the temperature range of 150–340°C and 340–550°C. There was no obvious reduction peak for 0Mn catalyst at low temperature, but the overall reduction peak area increased with the increase of MnO_x loading with the H_2 consumption increased from 2.34 mmol/g for 0Mn catalyst to 8.24 mmol/g for 30Mn catalyst, indicating that the addition of MnO_x enhanced the redox performance of the catalyst, to improve the catalyst NO conversion.

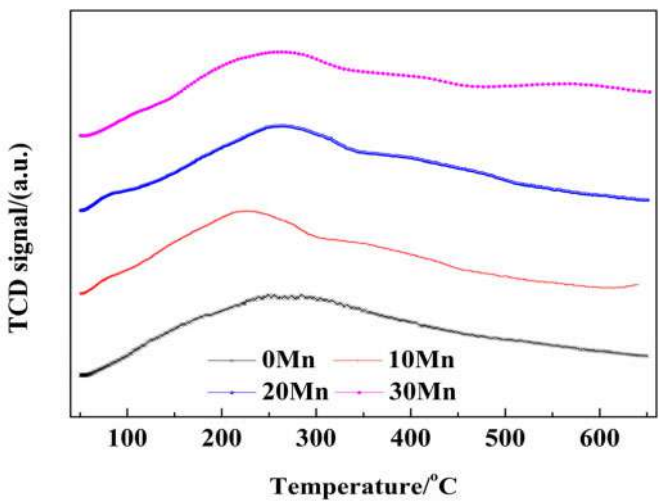

Figure 4. NH_3TPD profiles of catalysts.

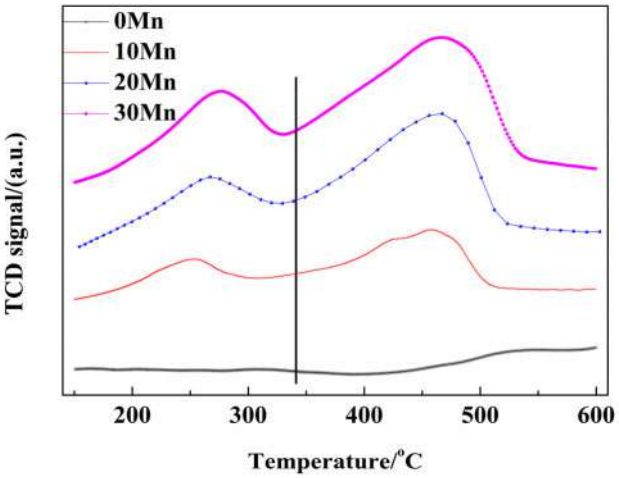

Figure 5. H_2-TPR profiles of catalysts.

4 CONCLUSION

The NO conversion of MnO_x-TiO_2 catalyst increased with the increase of MnO_x loading, as the MnO_x loading reached 20 wt%, the NO conversion reached 89.0%, at 140°C. As the MnO_x loading continued to increase, the NO conversion stabilized. However, the N_2 selectivity decreased with the increasing MnO_x loading (0–30 wt%). The results indicated that MnO_x could improve the NO conversion, and widen the temperature window toward activity, but made the N_2 selectivity worse. The addition of MnO_x blocked the pore structure of the carrier, thus reducing the specific surface area and pore volume of the catalyst. An appropriate amount of MnO_x uniformly dispersed on the surface of the catalyst could enhance the NO adsorption performance, NH_3 adsorption performance, and redox performance, thus improving the catalyst NO conversion. When the MnO_x content exceeded 20%, MnO_x existed on the surface of the carrier in the form of crystallization, resulting in the NO conversion was difficult to continue to improve. Combined with the results of NO-TPD and NH_3-TPD experiments, the catalytic reaction path accorded with the L-H mechanism.

ACKNOWLEDGMENTS

This work was supported by the Youth Talents Plan of the Beijing Academy of Science and Technology (BGS202107) and the S&T Program of Hebei (No. 19273706D).

REFERENCES

Chen, Q.L., et al. (2016) The promotion effect of Co doping on the K resistance of Mn/TiO_2 catalyst for NH_3-SCR of NO. J. Taiwan. Inst. Chem. E. 64, 116–123.

Fang, D., et al. (2015) Identification of MnO_x species and Mn valence states in MnO_x/TiO_2 catalysts for low temperature SCR. Chem. Eng. J. 271(1), 23–30.

He, G.Z., et al. (2021) Superior oxidative dehydrogenation performance toward NH_3 determines the excellent low-temperature NH_3-SCR activity of Mn-based catalysts. Environ. Sci. Technol. 55(10), 6995–7003.

Jiang, B.Q., et al. (2020) Mn/TiO_2 catalysts prepared by ultrasonic spray pyrolysis method for NO_x removal in low-temperature SCR reaction. Colloid. Surface. A. 586(5).

Li, X., et al. (2019) DFT analysis of the reaction mechanism for NH_3-SCR of NO_x over Mn/gamma-Al_2O_3 catalyst. J. Phys. Chem. C. 123(41), 25185–25196.

Liang, Q.M., et al. (2020) Effects of SO_2 and H_2O on low-temperature NO conversion over F-V_2O_5-WO_3/TiO_2 catalysts. J. Environ. Sci. 90, 253–261.
Pan, Y.X., et al. (2013) Promotional effect of Si-doped V_2O_5/TiO_2 for selective catalytic reduction of NO_x by NH_3. J. Environ. Sci. 25(8), 1703–1711.
Thirupathi, B. & Smirniotis, P.G. (2012) Nickel-doped Mn/TiO_2 as an efficient catalyst for the low-temperature SCR of NO with NH_3: Catalytic evaluation and characterizations. J. Catal. 288, 74–83.
Wei, L., et al. (2018) Study on the role of Mn species in low temperature SCR on MnO_x/TiO_2 through experiment and DFT calculation. Mol. Catal. 445, 102–120.
Xin, Y., et al. (2018) Molecular-level insight into selective catalytic reduction of NO_x with NH_3 to N_2 over a highly efficient bifunctional Va-MnO_x catalyst at low temperature. ACS. Catal. 8(6), 4937–4949.
Yang, N.Z., et al. (2016) Deactivation of Mn/TiO_2 catalyst for NH_3-SCR reaction: effect of phosphorous. RSC. Adv. 6(14), 11226–11232.
Yang, Y.R., et al. (2018) Mesoporous Mn-Ti amorphous oxides: a robust low-temperature NH_3-SCR catalyst. Catal. Sci. Technol. 8(24), 6396–6406.
Zhang, M.H., et al. (2019b) A DFT study on the effect of oxygen vacancies and H_2O in Mn-MOF-74 on SCR reactions. Phys. Chem. Chem. Phys. 21, 19226–19233.
Zhang, N.Q., et al. (2019a) Polytetrafluoroethylene modifying: A low cost and easy way to improve the H_2O resistance ability over MnO_x for low-temperature NH_3-SCR. J. Environ. Chem. Eng. 7(3).
Zhang, W.J., et al. (2021) Comparison study of the SCR performance over Mn-TiO_2 and Ce-TiO_2 catalysts: An experimental and DFT study. Energ. Fuel. 35(18), 14681–14691.

Advances in Applied Chemistry and Industrial Catalysis – Saikia (Ed.)

Graphited mesoporous carbon as polysulfide host by chemical vapor deposition for high-rate Li-S batteries

Xiaoqiang Liang*,#
China North Vehicle Research Institute, Beijing, China

Cai yun Chang#
Center on Nanoenergy Research, School of Physical Science and Technology, Guangxi University, Nanning, China

Yadong Chen, Jun Tian, Yituo Wang & Na Liu
China North Vehicle Research Institute, Beijing, China

Yadi Liu**
Beijing Swift New Energy Technologies Co., Ltd., Jiancaicheng, Haidian District, Beijing, China

ABSTRACT: Graphitized mesoporous carbon materials have highly conductive paths, which can accelerate the electrochemical reaction rate and electron movement speed, thus providing sufficient internal structure cavity for the volume expansion generated in the process of lithium intercalation and deactivation. In this paper, we further researched the effect of the graphitization degree of carbon materials filled with mesoporous for high-rate performance Li-S batteries. Graphitized mesoporous carbon materials are synthesized through Chemical Vapor Deposition (CVD) approach where acetonitrile serves as a carbon source and SBA-15 as a template, which is named CVD-C. Compared with CMK-3, the CVD-C materials display superior cycling and high-rate performance for Li-S batteries. Hence, when the temperature reached 1000°C and the current rate increased to 5°C over 300 cycles, an optimized CVD-C material electrode exhibited a low capacity decay rate of 0.13% each cycle.

1 INTRODUCTION

Lithium-sulfur (Li-S) batteries, in which the cathode is sulfur and the anode is lithium, are regarded as one of the most encouraging candidates for the future-oriented novel energy-storage system to meet the growing demand for large-scale energy consumption because of the high energy density (1675 mAh g^{-1}) and the rich sulfur element in the plant (Azimi et al. 2015; Barghamadi et al. 2013; Eftekhari & Kim 2017; Kumar et al. 2018; She 2016). Despite its advantages, the disadvantages of the Li-S battery also cannot be ignored. The specific drawbacks include sulfur's low conductivity, large volumetric fluctuation, and shuttling effects, resulting in severe self-discharge phenomenon, sulfur's irreversible loss, limited coulombic efficiency, and shortened cycling performances (Azimi et al. 2015; Gao et al. 2020; Guo et al. 2019; Gupta & Sivaram 2019; Li et al. 2014; Liang et al. 2019; Wen et al. 2019; Zhao et al. 2020; Zhang et al. 2016). The three main problems directly restrict the commercial development of Li-S batteries (Zhu et al. 2019).

To solve these problems, researchers have carried out studies on several aspects, mainly consisting of two techniques solutions: (1) fabrication cathode with sulfur and high conductivity material,

Corresponding Authors: *liangxiaoqiang15@mails.ucas.ac.cn and **lyd912@126.com
# Two authors contributed equally to this work.

DOI 10.1201/9781003308553-49

such as carbon materials or conductive polymers (Chang & Chung 2015; Duan et al. 2016; Yang et al. 2011; Zhang et al. 2016), leading to increase the cathode conductivity. (2) application for interlayer or catalyst layer, such as metallic nitrides/oxides/sulfides additives (Liu et al. 2020; She 2013; Wang et al. 2020; Wu et al. 2015; Tao et al. 2014; Tian et al. 2019), porous structure or adsorbing function materials, which can inhibit the lithium polysulfides (Li_2S_n, $4 \leq n \leq 8$) through chemical or physical actions.

Porous carbon is considered a promising sulfur cathode carrier because of its high conductivity and superior adsorption performance. The Nazar group (Ji et al. 2009) demonstrated that cathodes S/commercial ordered mesoporous carbon materials (CMK-3) exhibited high, stable, and reversible capacities (1320 mAh g^{-1}) with excellent rate performance and cycling life. After that, various carbon materials have demonstrated enhanced stability performance, specifically, porous carbon, carbon nanotubes (CNT), graphene, graphene oxide, carbon nanofibers (CNF), and so on (Chen et al. 2020; Liang et al. 2011; Liang et al. 2019; Liu et al. 2020; Schuster et al. 2012; Wang et al. 2012; Wang et al. 2020; Zhao et al. 2020; Zheng et al. 2011; Zheng et al. 2013; Zeng et al. 2014). It is considered that the porous structure of carbon materials confined polysulfides transport and supplied an excellent electron/ion channel. Therefore, the porous structure of carbon materials, including macro-, meso-, mico- or hierarchical (Gao et al. 2020; Liang et al. 2011; Long et al. 2018; Qi et al. 2015; Schuster et al. 2012; Wang et al. 2012; Zeng et al. 2014) have all been researched through high-temperature carbonization with various carbon sources via different templates (Manawi et al. 2018; Kim et al. 2003). However, the effect of graphitization degree on carbon materials as cathodes has been neglected (Ji et al. 2009; Liang et al. 2011; Wang et al. 2001; Xia & Mokaya 2004).

In our previous study, we had preliminarily prepared graphitic carbon via Chemical Vapor Deposition (CVD), where Mn7C3 was utilized as composite cathode material (Liang et al. 2019). Herein, we further investigated the effect of the graphitization degree of mesoporous carbon which was directly deployed as the cathode. Through the traditional CVD method, we synthesize different graphitized mesoporous carbon materials whose carbon source is acetonitrile and template is SBA-15 by controlling the temperature and time.

Compared with traditional carbon material (CMK-3), synthetic graphitized carbon material with carbonization temperature at 1000°C displayed brilliant high-rate capacity and stable cycling life, corresponding to graphitized mesoporous carbon skeleton which promotes the Li-ion/electron conductivity.

2 EXPERIMENTS

2.1 *Materials preparation*

Synthesis of graphited carbon rods (CVD-C): Graphited carbon rods were synthesized via a CVD process named CVD-C (as shown in Table 1). 0.2 g commercial SBA-15 template (Nanjing XFNANO Materials Tech) was situated in an alumina boat. Then, these were placed into a tube furnace under the atmosphere of nitrogen and acetonitrile vapor (99.8%, aladdin) at 25°C. Next, the temperature was increased to 950°C and maintained for 3 h at the heating rate of 20°C/min for CVD-C-1. The CVD-C-2 was synthesized by the same reagent which was calcined at 1000°C and maintained for 20 h. The furnace was then cooled to 25°C and the sample was thoroughly cleaned with hydrofluoric acid (HF) to etch out the silica.

S/CVD-C composites: To prepare the S/CVD-C composites, a melt-diffusion strategy is adopted herein. CVD-C and sulfur (Aladdin, 99.99%) (2:3 by mass ratio) were milled together and heated to 155°C for 15 h under an Ar.

Commercial ordered mesoporous carbon materials (CMK-3): CMK-3 was obtained from Nanjing XFNANO Materials Tech. S/CMK-3 composite was carried out in the same way as the S/CVD-C composites.

Table 1. Preparation parameters of CVD-C materials.

Samples ID	Temperature/°C	Times/h
CVD-C-1	950	3
CVD-C-2	1000	20

2.2 *Materials characterization*

To characterize the samples' morphologies and microstructure, field emission scanning electron microscopy (FESEM, Hitachi SU8020) and high-resolution transmission electron microscopy (HRTEM, JEOL JEM-2010) are used. Small-angle X-ray Scattering (SAXS) was collected by the D8 Advance instrument. An X-ray diffractometer (XRD) (Panalytical Instrument X′Pert 3 Powder) with Cu Kα radiation (40 kV, 40 mA) is utilized to accomplish XRD patterns. The samples' surface areas and pore size distributions were measured using a Quantachrome instrument (Autosorb iQ USA). The thermogravimetric analysis (TGA) measurement is conducted using a TGA/DSC 1 instrument in argon flow at a heating rate of 5°C min^{-1}.

2.3 *Electrochemical preparing*

To composite, the cathode, synthesized powder, super P, and poly-(vinyldifluoride) (PVDF) are ground with a ratio of 8:1:1. Before vacuum drying at 60°C for 12h, the cathode film was coated on the aluminum foil. The active materials of the cathode electrodes' area were about 2.7 mg cm^{-2}. The mass of sulfur in cathode electrodes is about 1.3 mg cm^{-2}. The packing density of composite material in the cathode electrodes was about 1.4 g cm^{-3}. To obtain the specific capacities, the sulfur mass is used to calculate it. To assemble type 2032 Li-S coin cells, the working environment is a glove box filled with ultrahigh purity argon with water and oxygen contents below 0.01 ppm. The Li metal foil is the anode and Celgard 2500 membrane is the separator. To obtain the electrolyte, lithium bis(trifluoromethane) sulfonamide (LiTFSI) (Sigma Aldrich, 99.99 %) and $LiNO_3$ into 1, 3-dioxolane (DOL) and dimethoxyethane (DME), where the concentration of LiTFSI and $LiNO_3$ is 1 M and 0.5 M respectively, and the volume ratio of DOL and DME is 1:1. Neware instrument (CT-4008, Shenzhen, China) is adopted to measure the different rate cycle performance of Li-S cells at the voltage range of 1.7–2.8 V.

3 RESULTS AND DISCUSSIONS

Here we present a novel approach for fabricating ordered mesoporous graphitic carbon material via the traditional Chemical Vapor Deposition (CVD) with SBA-15 as a frequently-used template and acetonitrile as a carbon source. It has been reported and explored in this paper that carbonization temperatures are suitable for the fabrication of well-ordered mesoporous carbon materials above 950°C with varying degrees of graphitic character (Xia & Mokaya 2004).

The carbons powder's X-ray diffraction (XRD) patterns via the CVD method with 950°C (named CVD-C-1), 1000°C (named CVD-C-2), and CMK-3 materials, are illustrated in Figure 1 a-b. The specific angle portions of the XRD patterns (below $2\theta = 5°$) show (100) peak that indicates the mesostructured of the carbons, which indicates a long-range structure ordering of materials (Jun et al. 2000). However, the low-angle region of the CVD-C-2 sample does not show any peaks, which are reduced deeply at higher CVD temperatures and long holding times (Xia & Mokaya 2004). Furthermore, the specific angle portions (above $2\theta = 10°$) of all the samples show peaks at $2\theta = 26$, 43, and 54° which can be respectively attributed to (002), (101), and (004) diffraction peaks from graphitic pore walls (Kim et al. 2003). According to the Bragg equation, the corresponding crystal plane spacing can be calculated, be 0.34 nm, 0.21 nm, and 0.17 nm, respectively. The XRD

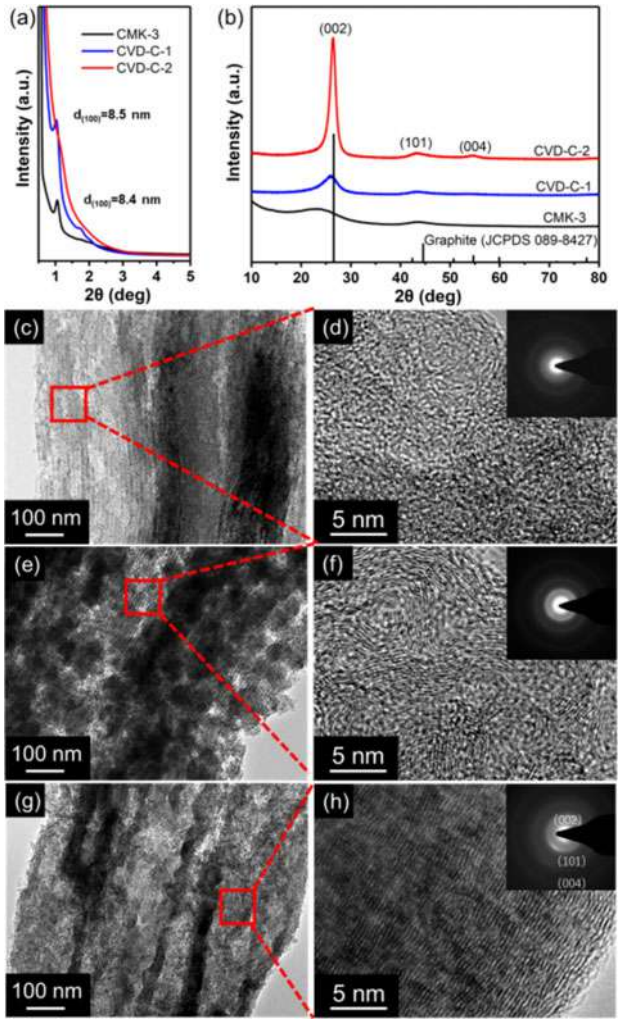

Figure 1. (a-b) XRD patterns of CVD-C and CMK-3, (c-d) TEM images of CMK-3, (e-f) TEM images of CVD-C-1, (g-h) TEM images of CVD-C-2.

patterns indicated that the CVD-C-2 carbon holds graphitic (i.e., crystalline) rather than amorphous pore walls. The narrow peaks (002) because of graphitic ordering in the pore walls increased at higher carbonization temperatures. The results of powder XRD with the Raman spectra of different carbons shown in Figure S1 are consistent. The Raman spectra indicate two bands at ca. 1350 cm^{-1} (D-band) and ca. 1580 cm^{-1} (G-band), respectively. The intensity ratios of the D and G bands (I_D/I_G) value of the CVD-C-2 sample was 1.11. It can be concluded that CVD-C-2 samples have abundant defects, which are conducive to the diffusion of lithium ions. The results proved that the carbonization temperature increased, the higher level of crystalline character of carbons formed, in accordance with the XRD patterns.

The graphitic mesoporous materials' excellent structure ordering was also proved by transmission electron microscopy (TEM) as illustrated in Figure 1 c-h. From Figure 1d, the high-resolution TEM images and the corresponding electron diffraction pattern (inset) display the CMK-3 material has many amorphous structures and a little graphitic structure. Compared with that, the HRTEM images of CVD-C-1 show more graphitic structure and diffraction rings. With the carbonization

temperature increased, the CVD-C-2 sample has a completely graphitic structure and obvious diffraction rings in accordance with the information of graphite crystalline that can facilitate electron conduction.

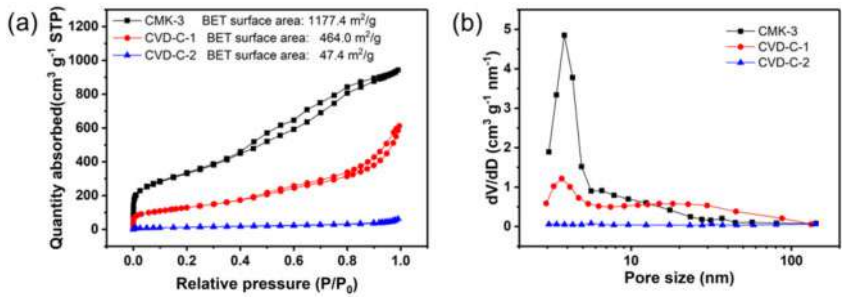

Figure 2. (a) N_2 adsorption/desorption isotherms and (b) pore volume distribution of carbon materials: CMK-3 and CVD-C.

To verify the porosity of CVD-C materials, N_2 adsorption/desorption isothermal analysis was performed. As illustrated in Figure 2, it displayed that all isotherms of all materials were type-IV curves with clear capillary condensation steps, suggesting that samples had typical mesostructure with uniform pore size distribution. The Brunauer-Emmett-Teller (BET) specific surface areas for all the samples are about 1177.4 m^2 g^{-1}, 464.0 m^2 g^{-1}, and 47.4 m^2 g^{-1}, respectively, with a total pore volume, are 1.46 cm^3 g^{-1}, 0.9 cm^3 g^{-1}, and 0.09 cm^3 g^{-1}. The pore size distribution curve (Figure 2(b)) showed uniform pore size distribution with the mesoporous, which was due to the eradication of the SBA-15 template inserted in the carbon matrix. The average pore size of the samples was 5.00 nm, 7.07 nm, and 8.13 nm, respectively, which favored the fast migration of solvated lithium ions, contributing to a high specific capacity and cycling stability (Zhang 2019). The SEM images displayed the same results (as illustrated in Figures S2 and S3). The morphologies of the CVD-C-2 sample showed the fiberlike close stacking structures, which provided the channel of lithium ions and electrons.

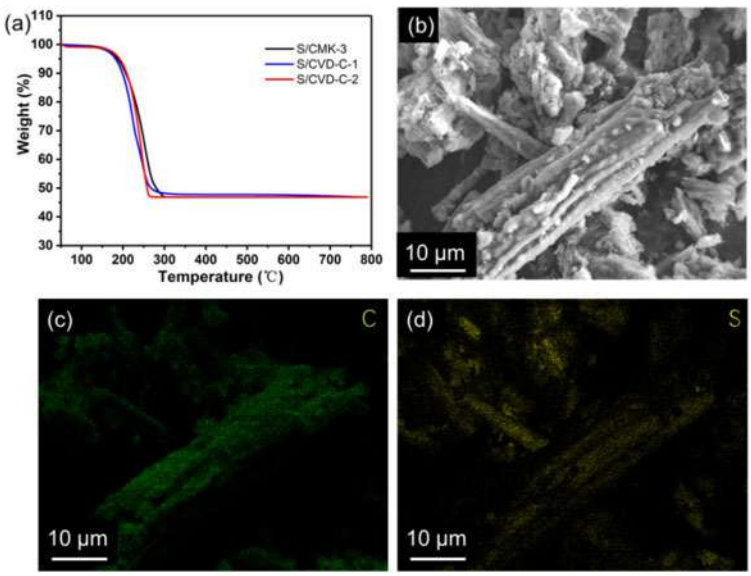

Figure 3. (a) TGA data of S/CVD-C and S/CMK-3 composites, (b-d) The elemental mapping of S/ CVD-C-2 composites.

The sulfur-carbon composite materials were prepared through a simple melt-diffusion strategy with heating to 155°C for 15 h in an Ar atmosphere. The sulfur begins to evaporate above ~155° in the Ar, but the carbon is stable in the inert gases before 800°C. To obtain the sulfur content in S/C composite cathodes, the samples were examined by thermogravimetric analysis (TGA) in an argon atmosphere, as illustrated in Figure 3(a). The results show that the sulfur content of all S/C composites is about 53%, which is close to the added amount. There is no obvious noticeable morphological difference between S/C composite materials and carbon materials (as shown in Figures 3(b), S3, and S4 (a and d)), which proves that the sulfur is homogeneously distributed on the carbon materials. The EDS images also prove this point (as demonstrated in Figures 3(c-d) and S4 (b-c, e-f)).

To study the capability of different current densities and the cycling life of the S/CVD-C-2 composite cathode, the CR2032 Li-S battery coin cells are assembled using the approach mentioned above. To demonstrate the advantages of highly graphitized carbon material (CVD-C-2), the S/CMK-3 and S/CVD-C-1 composites were also synthesized for comparison. The characteristics of the batteries were tested with galvanostatic charge/discharge at 1.7 V to 2.8 V, which can prevent side reactions deriving from the diminution of LiNO3 (Qu et al. 2014). Capacity values in our paper were calculated based on sulfur mass, which was in cathode electrodes about 1.1–1.5 mg cm^{-2}. The different capability of all batteries is shown in Figure 4a. The results show that the discharge capacity declined with the increase of current density from 0.5 C to 5 C, while 1 C is 1675 mA g^{-1}. The initial discharge capacities of S/CVD-C-2 composite cathode at discharge rates of 0.5 C, 1 C, 2 C and 5 C are 939.4, 861.9, 773.2, 601.9 mAh g^{-1}. Compared with that, the S/CMK-3 composite cathode's initial discharge capacities at different rates are 1351.5, 834.9, 718.8, and 181.5 mAh g^{-1}. The initial discharge capacities of the S/CVD-C-1 composite cathode are 1081.6, 970.2, 649.5, and 226.6 mAh g^{-1}, respectively. It can be concluded that the S/CVD-C-2 composite cathode proves superior electrochemical performance at high rate discharge conditions (2 C and 5 C), which was caused by the graphitic carbon and mesoporous structure to increase the electronic/ionic transport and augment reaction kinetics in the cathode (Qu et al. 2014). The normalization of specific capacity for the three batteries displays that the S/CVD-C-2 composite cathode has the minimum decay rate, even at a 5 C rate, discharge the capacity maintains 70% of the beginning capacity (as shown in Figure 4b). The initial cycle charge and discharge plots of the S/CVD-C-2 composite cathode at different rates (0.5 C, 1 C, 2 C, 5 C) depict the two representative charge/discharge plateaus of the cathode including sulfur, representing the establishment of long-chain polysulfides (Li_2Sx, $4 \leq x \leq 8$) at the high plateau and the formation of short-chain Li_2S_2/Li_2S at the low plateau, which shows in Figure 4c. The first discharge platform at 2.3 V is in connection with the transformation from sulfur cathode to $Li_2Sx(4 \leq x \leq 8)$, while the second one is due to the formation of short-chain lithium polysulfides at 2.1 V vs. Li/Li^+, at a lower current rate about 0.5 C. With the increase of discharge rate, the second charge/discharge plateaus steadily rise/drop, but two representative plateaus retain in the discharge curves even at high current rates (5 C), demonstrating low kinetic barrier in the electrode process and high rate capability. This could be attributed to mesoporous structure and graphitic carbon skeleton, which enhanced electronic and ionic transport at the cathode.

To further analyze the cycling life of the composite cathode under high discharge rate conditions. The initial discharge capacity of the S/CMK-3 composite cathode is 113.9 mAh g^{-1} at a current density of 5 C as illustrated in Figure 4d and provides a capacity of 68.2 mAh g^{-1} after 100 cycles. Compared with that, the initial discharge capacity of the S/CVD-C-1 composite cathode presents a good reversible capacity of 328.7 mAh g^{-1} after 100 cycles. Whereas the S/CVD-C-2 composite cathode demonstrates a beginning discharge capacity of 777 mAh g^{-1} at a current density of 5 C and still maintains a capacity of 598 mAh g^{-1} after 100 cycles, which is the best of the three prepared cathodes. More importantly, the discharge capacity of the S/CVD-C-2 composite cathode remains 439.7 mAh g^{-1} after 300 cycles, as shown in Figure 4e. However, after 300 cycles, the S/CMK-3 and the S/CVD-C^{-1} composite cathode are 76.7 mAh g^{-1} and 291.5 mAh g^{-1}, respectively. Obviously, at a high discharge rate (5 C), the S/CVD-C-2 composite cathode displays an excellent

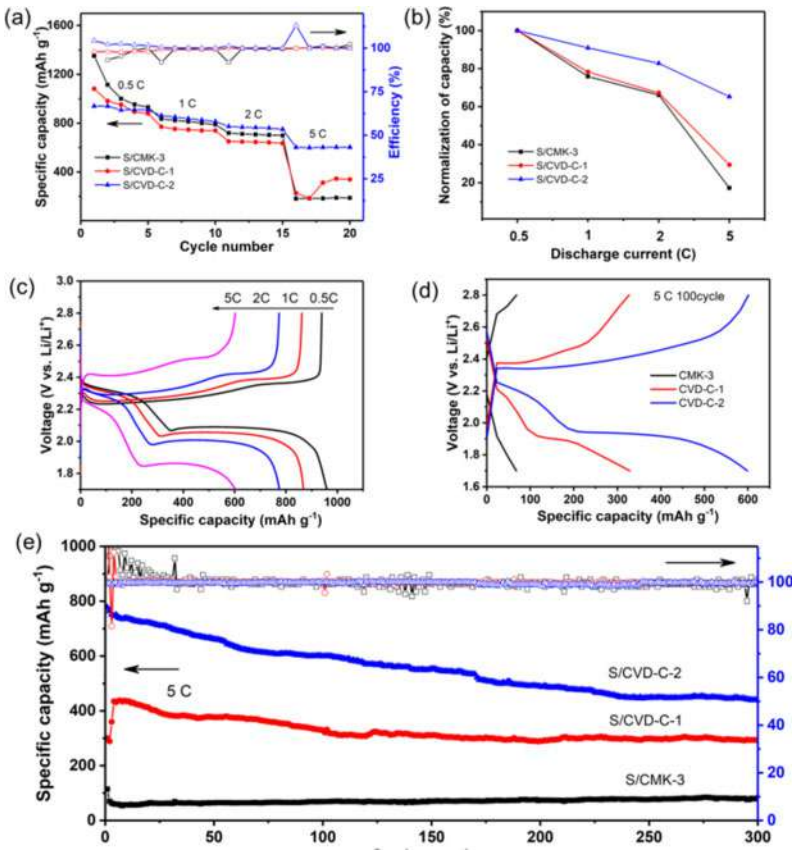

Figure 4. Electrochemical performances of S/CVD-C and S/CMK-3 cathodes. (a) Rate performances at 0.5 C, 1 C, 2 C and 5 C; (b) Normalization of capacity in different discharge currents;(c) Galvanostatic charge/discharge profiles of S/CVD-C-2 at 0.5 C, 1 C, 2 C and 5 C.; (d) Galvanostatic charge/discharge profiles of S/CMK-3 and S/CVD-C at 5 C. (e) Cycling performances and coulombic efficiency at 5 C (1 C = 1675 mA g^{-1}).

cycling performance, its columbic efficiency reaching 100% in each cycle. The excellent high rate capacity and long cycling stability performance of the S/CVD-C-2 composite cathode can be explained by its mesoporous structure and graphitic carbon skeleton, which provide channels for electron transportation and electron transport.

The Electrochemical Impedance Spectra (EIS) was also performed before and after 300 cycles at a discharge rate of 5 C, and the corresponding conclusions were illustrated in Figure 5. The Nyquist plots of both before and after cycles are made up of two parts, a depressed semicircle in the high-frequency part and a slope line in the low-frequency part. The intercept at the horizontal axis resistance represents the combined resistance (R_{ohm}), including the electrolyte's ionic resistance, the active material's intrinsic resistance, and the contact resistance. In high frequency, the semicircle represents the charge-transfer resistance (R_{ct}) through the boundary between electrode and electrolyte. The slope line is related to the electrode's Li-ion diffusion. After 300 cycles, the charge-transfer resistance of all the batteries decreased compared with that before cycling, which is related to the electrolyte fully infiltrated into the electrode. Figure 5(b) exhibits that the S/CVD-C-2 composite cathode possesses a smaller R_{ct} and faster Li-ion diffusion compared with others, which can be ascribed to improved conductivity corresponding to the degree of graphitization and the

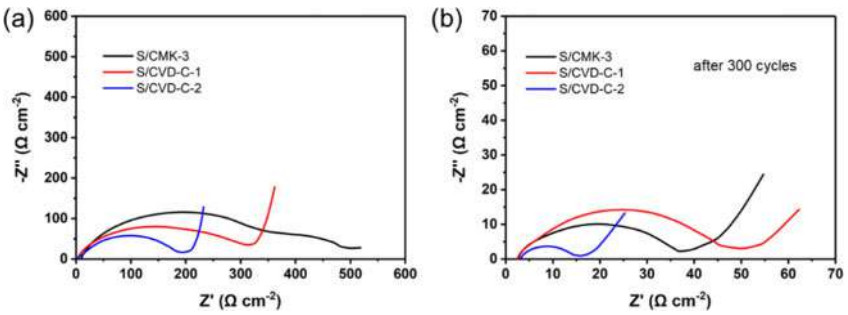

Figure 5. Nyquist curves of AC impedance spectra from 1000 kHz to 100 MHz at room temperature (a) and after 300 cycles (b) at 5C.

mesoporous structure. Therefore, its capacity and cycling performance at a high rate of discharge can be improved.

4 CONCLUSION

In summary, the extremely graphitic carbon with a mesoporous structure was prepared through a simple CVD template approach. With the calcined temperature reaching 1000°C, the CVD-C-2 exhibited a completely graphitic structure. The composite cathode (S/CVD-C-2) material was synthesized by the melt-diffusion method which was utilized for the Li-S battery. Compared with the traditional S/CMK-3 composite cathode, the S/CVD-C-2 composite cathode battery shows much more reversible capacities and a more attractively high rate and cycling life. This battery not only holds a high specific capacity of 777 mAh g^{-1} at 5 C but also keeps a stable cycling performance after 300 cycles which remains 439.7 mAh g^{-1} at 5 C. The superior electrochemical characteristics are described by the graphitic and mesoporous structure which can increase the electronic/ionic transport. The approach and strategy developed here maybe provide a novel idea for the carrier materials of Li-S battery at a high rate and cycling condition.

REFERENCES

N. Azimi, Z. Xue, S. S. Zhang, Z. Zhang, in Rechargeable Lithium Batteries, 2015, pp. 117–147.
M. Barghamadi, A. Kapoor, C. Wen, Journal of The Electrochemical Society 2013, 160, A1256–A1263.
C. H. Chang, S. H. Chung, A. Manthiram, Journal of Materials Chemistry A 2015, 3, 18829–18834.
J. Chen, Y. Liu, Z. Liu, Y. Chen, C. Zhang, Y. Yin, Q. Yang, Z. Shi, C. Xiong, Colloids and Surfaces A: Physicochemical and Engineering Aspects 2020, 603.
L. Duan, F. Zhang, L. Wang, in Alkali-ion Batteries, 2016.
A. Eftekhari, D.-W. Kim, Journal of Materials Chemistry A 2017, 5, 17734–17776.
X. Gao, Y. Huang, Z. Guang, X. Li, Energ Fuel 2020, 34, 3931–3940.
D. Guo, F. W. Ming, H. Su, Y. Q. Wu, W. Wahyudi, M. L. Li, M. N. Hedhili, G. Sheng, L. J. Li, H. N. Alshareef, Y. X. Li, Z. P. Lai, Nano Energy 2019, 61, 478–485.
Gupta, S. Sivaram, Energy Technol-Ger 2019, 7.
X. Ji, K. T. Lee, L. F. Nazar, Nat Mater 2009, 8, 500–506.
S. Jun, S. H. Joo, R. Ryoo, M. Kruk, M. Jaroniec, Z. Liu, T. Ohsuna, O. Terasaki, Journal of the American Chemical Society 2000, 122, 10712–10713.
T. W. Kim, I. S. Park, R. Ryoo, Angew Chem Int Ed Engl 2003, 42, 4375–4379.
R. Kumar, J. Liu, J.-Y. Hwang, Y.-K. Sun, Journal of Materials Chemistry A 2018, 6, 11582–11605.
X. Li, X. Li, M. N. Banis, B. Wang, A. Lushington, X. Cui, R. Li, T.-K. Sham, X. Sun, Journal of Materials Chemistry A 2014, 2.

X. Q. Liang, W. B. Guo, P. P. Zhang, Y. D. Liu, G. Y. Chen, X. M. Lu, X. Pu, Journal of the Electrochemical Society 2019, 166, A2028–A2034.
X. A. Liang, Z. Y. Wen, Y. Liu, H. Zhang, L. Z. Huang, J. Jin, Journal of Power Sources 2011, 196, 3655–3658.
J. T. Liu, S. H. Xiao, Z. Y. Zhang, Y. Chen, Y. Xiang, X. Q. Liu, J. S. Chen, P. Chen, Nanoscale 2020, 12, 5114–5124.
L. Long, X. Jiang, J. Liu, D. Han, M. Xiao, S. Wang, Y. Meng, Rsc Adv 2018, 8, 4503–4513.
Ouyang, J. Liu, M. Zhu, Small 2020, 16.
Y. M. Manawi, Ihsanullah, A. Samara, T. Al-Ansari, M. A. Atieh, Materials (Basel) 2018, 11.
J. Qi, X. Lai, J. Wang, H. Tang, H. Ren, Y. Yang, Q. Jin, L. Zhang, R. Yu, G. Ma, Z. Su, H. Zhao, D. Wang, Chem Soc Rev 2015, 44, 6749–6773.
Y. Qu, Z. Zhang, X. Zhang, G. Ren, X. Wang, Y. Lai, Y. Liu, J. Li, Electrochimica Acta 2014, 137, 439–446.
Z. W. Seh, W. Y. Li, J. J. Cha, G. Y. Zheng , Y. Yang, M. T. McDowell, P. C. Hsu, Y. Cui, Nature Communications 2013, 4.
Z. W. Seh, Y. M. Sun, Q. F. Zhang, Y. Cui, Chemical Society Reviews 2016, 45, 5605–5634.
D. Tian, X. Q. Song, M. X. Wang, X. Wu, Y. Qiu, B. Guan, X. Z. Xu, L. S. Fan, N. Q. Zhang, K. N. Sun, Advanced Energy Materials 2019.
J. Schuster, G. He, B. Mandlmeier, T. Yim, K. T. Lee, T. Bein, L. F. Nazar, Angew Chem Int Ed Engl 2012, 51, 3591–3595.
X. Y. Tao, J. G. Wang, Z. G. Ying, Q. X. Cai, G. Y. Zheng, Y. P. Gan, H. Huang, Y. Xia, C. Liang, W. K. Zhang, Y. Cui, Nano Letters 2014, 14, 5288–5294.
Y. Xia, R. Mokaya, Advanced Materials 2004, 16, 1553–1558.
C. Wang, A. J. Appleby, F. E. Little, Electrochimica Acta 2001, 46, 21.
X. Wang, W. Lei, R. Hu, P. Xia, Y. Pan, Z. Ma, N. Zhao, Y. Wang, Ionics 2020, 26, 4473–4477.
Z. Wang, X. Xu, Z. Liu, S. Ji, S. O. Ahmed Idris, J. Liu, Electrochimica Acta 2020, 332.
Z. S. Wang, J. D. Shen, S. M. Ji, X. J. Xu, S. Y. Zuo, Z. B. Liu, D. C. Zhang, R. Z. Hu, L. Z.
Z. S. Wang, J. D. Shen, S. M. Ji, X. J. Xu, S. Y. Zuo, Z. B. Liu, D. C. Zhang, R. Z. Hu, L. Z. Ouyang, J. Liu, M. Zhu, Small 2020, 16.
Z. Wang, X. Xu, Z. Liu, S. Ji, S. O. Ahmed Idris, J. Liu, Electrochimica Acta 2020, 332.
D. W. Wang, G. Zhou, F. Li, K. H. Wu, G. Q. Lu, H. M. Cheng, I. R. Gentle, Phys Chem Chem Phys 2012, 14, 8703–8710.
X. Wen, X. Lu, K. Xiang, L. Xiao, H. Liao, W. Chen, W. Zhou, H. Chen, J Colloid Interface Sci 2019, 554, 711–721.
M. Wu, Y. Cui, Y. Z. Fu, Acs Appl Mater Inter 2015, 7, 21479–21486.
Y. Yang, G. H. Yu, J. J. Cha, H. Wu, M. Vosgueritchian, Y. Yao, Z. A. Bao, Y. Cui, Acs Nano 2011, 5, 9187–9193.
L. Zeng, F. Pan, W. Li, Y. Jiang, X. Zhong, Y. Yu, Nanoscale 2014, 6, 9579-9587.J. Zhang, C. P. Yang, Y. X. Yin, L. J. Wan, Y. G. Guo, Adv Mater 2016, 28, 9539–9544.
Y. P. Zhang, R. Gu, S. Zheng, K. X. Liao, P. H. Shi, J. C. Fan, Q. J. Xu, Y. L. Min, Journal of Materials Chemistry A 2019, 7, 21747–21758.
Z. Zhao, J. Wang, M. Cheng, J. Wu, Q. Zhang, X. Liu, C. Wang, J. Wang, K. Li, J. Wang, Electrochimica Acta 2020, 349.
G. Y. Zheng, Y. Yang, J. J. Cha, S. S. Hong, Y. Cui, Nano Letters 2011, 11, 4462–4467.
G. Y. Zheng, Q. F. Zhang, J. J. Cha, Y. Yang, W. Y. Li, Z. W. Seh, Y. Cui, Nano Letters 2013, 13, 1265–1270.
K. Zhu, C. Wang, Z. Chi, F. Ke, Y. Yang, A. Wang, W. Wang, L. Miao, Front Energy Res 2019, 7.

Advances in Applied Chemistry and Industrial Catalysis – Saikia (Ed.)

Experiments and thermodynamic models for ternary liquid-liquid equilibrium systems of water + furfuryl alcohol-ethyl acetate at different temperatures

Mai Han*, Mingyi Xu**, Song Lin***, Houchun Yan**** & Qingsong Li*****
State Key Laboratory of Heavy Oil, China University of Petroleum (East China), Qingdao, Shandong, China

ABSTRACT: To explore the ability to separate the water-furfuryl alcohol azeotrope by extraction, the liquid-liquid equilibrium data of the water + furfuryl alcohol + ethyl acetate system at 303.2 K, 313.2 K, and 323.2 K were measured under atmospheric pressure with ethyl acetate as the extractant. The calculated separation factor is far greater than 1, indicating that ethyl acetate is a good extractant for this system. At the same time, the equations of Bachman and Hand were used to perform the consistency test to the experimental data, and the linear correlation coefficients R^2 were all greater than 0.99. Finally, the NRTL and UNIQUAC thermodynamic models were used to correlate experimental data, and the relative root mean square deviation (RMSD%) was less than 0.53, indicating that NRTL and UNIQUAC can correlate experimental data well.

1 INTRODUCTION

Furfuryl alcohol (FA) is an important organic compound, mainly used to produce furfural resin, phenolic resin, FA-urea-formaldehyde resin, etc. In addition, it can also be used to prepare fruit acid, plasticizer, solvent, and rocket fuel, etc. (Albouchi & Murkovic 2018; Herold & Pfriem 2013; Herold et al. 2013; Kang 2015; Swasti 2012). FA is expensive, and it is widely used in industry, construction, and other fields. However, FA can form an azeotrope with water (Herold & Pfriem 2013; Herold et al. 2013; Kim 2011), which cannot be separated by conventional distillation methods. Therefore, it is necessary to explore a new method for the extraction process of FA.

At present, few literatures reported on the research on the water + FA system. Dong et al. (Dong 2020) used some polar solvents, such as isopropyl ether, tert-butyl methyl ether, dichloromethane, and methyl-isobutyl methanol, to extract FA in water. Yan et al. (2021) used chloroform and methyl isopropyl ketone as extractants to explore the liquid-liquid equilibrium at 303.2, 313.2, and 323.2 K. Through regression verification of the experimental data, they found that the above solvents are excellent extractants for the water + FA system. Due to the wide application of FA, it is necessary to choose a new extractant to separate FA from aqueous solutions.

To study the possibility of separating FA-water azeotropic system with more extractants, the liquid-liquid equilibrium of the water + FA + ethyl acetate system was carried out at 303.2 K, 313.2 K, and 323.2 K under 101.3 kPa. In addition, the Bachman and Hand equations are used to detect the linear correlation of the experimental results after the phase equilibrium data is measured. Besides, the NRTL (Renon & Prausnitz 1968) and UNIQUAC (Abrams & Prausnitz 1975) models are used to perform regression processing on the experimental data, and the binary interaction parameters are calculated.

2 EXPERIMENTAL PART

2.1 *Experimental reagents*

The properties of the reagents used in the liquid-liquid equilibrium experiment are listed in Table 1.

Corresponding Authors: *hanmai55@126.com, **xmy1218myx@163.com, ***17863958922@163.com, ****yanhouchun1996@vip.qq.com and *****licup69@163.com

 DOI 10.1201/9781003308553-50

Table 1. Properties of chemical reagents.

Reagents	CAS number	Supplier	*w*/%	UNIQUAC *r*	UNIQUAC *q*
furfuryl alcohol	98-00-0	Aladdin	>99.5	3.3784	2.6760
ethyl acetate	141-78-6	Aladdin	>99.5	3.4786	3.1160
deionized water	7732-18-5	lab-made		0.9200	1.3997

2.2 *Operation and analysis*

The liquid-liquid equilibrium experiment of water + FA + ethyl acetate was carried out at 303.2 K, 313.2 K and 323.2 K. A certain quality of the mixture was added to the phase equilibrium kettle, and after being vigorously stirred for 2 hours, it was placed for another 4 hours to make the system reach a phase equilibrium state. The temperature of the system was maintained constant through a constant temperature water bath with an accuracy of ±0.1°C. The GUM standard was used to measure the uncertainty of the mass composition of the two enriched phases.

After a certain period of rest, the mixture was divided into an aqueous phase and an organic phase. The samples obtained in this experiment were all applicable to gas chromatograph (Agilent GC6820) equipped with thermal conductivity detector (TCD) and Porapak N (3m×3mm) water column resistance for detection, and each sample was tested at least three times. Finally, the average value was recorded as the sample component content.

The chromatographic analysis conditions are: the carrier gas is hydrogen; the detector and vaporization chamber are maintained at 493.2 K. The initial temperature of the column was 393.2 K and held for 1 minute, and then the temperature was programmed to 493.2 K at a rate of 20 K per minute and held for 6 minutes.

3 RESULT AND DISCUSSION

3.1 *Experimental data*

The liquid-liquid equilibrium data of water + FA + ethyl acetate is shown in Table 2. It can be seen from the table that the mass fraction of FA in the two phases gradually increases with the increase of its mass fraction, and the mass fraction of FA in the organic phase increases more than in the water phase, indicating that ethyl acetate has excellent selectivity and extraction ability in the system.

Table 2. Liquid-liquid equilibrium data of water (1) + FA (2) + ethyl acetate (3) ternary system.

	organic phase			water phase				
T/K	w1	w2	w3	w1	w2	w3	D	S
303.2	0.0346	0	0.9674	0.9320	0	0.0690		
	0.0390	0.0509	0.9101	0.9211	0.0107	0.0682	23.78	112.63
	0.0472	0.0965	0.8563	0.9115	0.0195	0.0690	23.40	95.40
	0.0504	0.1170	0.8326	0.9054	0.0251	0.0695	21.60	83.79
	0.0597	0.1558	0.7845	0.9035	0.0302	0.0662	22.77	78.01
	0.0659	0.2000	0.7341	0.8928	0.0389	0.0682	21.77	69.50
	0.0783	0.2484	0.6732	0.8855	0.0505	0.0639	19.61	55.57
	0.0845	0.2835	0.6320	0.8614	0.0625	0.0761	17.22	46.26
	0.1071	0.3154	0.5776	0.8719	0.0664	0.0617	16.76	38.66

(*continued*)

Table 2. Continued.

	organic phase			water phase				
T/K	w1	w2	w3	w1	w2	w3	D	S
313.2	0.0364	0			0	0.0628		
	0.0419	0.0485	0.9097	0.9247	0.0105	0.0649	22.83	102.03
	0.0579	0.0909	0.8512	0.9087	0.0180	0.0733	22.74	79.03
	0.0604	0.1284	0.8112	0.9148	0.0251	0.0601	22.88	77.53
	0.0709	0.1735	0.7556	0.9027	0.0345	0.0628	21.22	64.13
	0.0846	0.2085	0.7069	0.8966	0.0420	0.0613	19.63	52.51
	0.0896	0.2465	0.6638	0.8901	0.0495	0.0604	19.15	49.45
	0.1170	0.2839	0.5991	0.8766	0.0622	0.0612	15.72	34.20
	0.1291	0.3243	0.5466	0.8696	0.0717	0.0587	14.82	30.45
323.2	0.0390	0			0	0.0620		
	0.0398	0.0764	0.8838	0.9254	0.0142	0.0604	26.78	125.22
	0.0516	0.1218	0.8266	0.9141	0.0235	0.0624	24.06	91.90
	0.0624	0.1488	0.7888	0.9099	0.0288	0.0613	22.71	75.28
	0.0737	0.1962	0.7301	0.8988	0.0390	0.0622	20.84	61.40
	0.0976	0.2267	0.6756	0.8881	0.0490	0.0629	17.31	42.08
	0.1101	0.2559	0.6340	0.8703	0.0578	0.0718	15.54	34.96
	0.1494	0.2719	0.5787	0.8675	0.0659	0.0666	12.77	23.97
	0.1860	0.3269	0.4871	0.8079	0.1158	0.0763	6.70	10.09

* $u(t)$=0.1°, $u(p)$=1.5 kPa, $u(w)$=0.0005.

The ternary phase diagram and its connecting lines are shown in Figure 1. It can be observed that the region of two-phase in the ternary phase diagram is extremely large, indicating that ethyl acetate can extract more FA from water. It can be seen that as the temperature increases, the two-phase region has no changes, indicating that the temperature has little effect on the system.

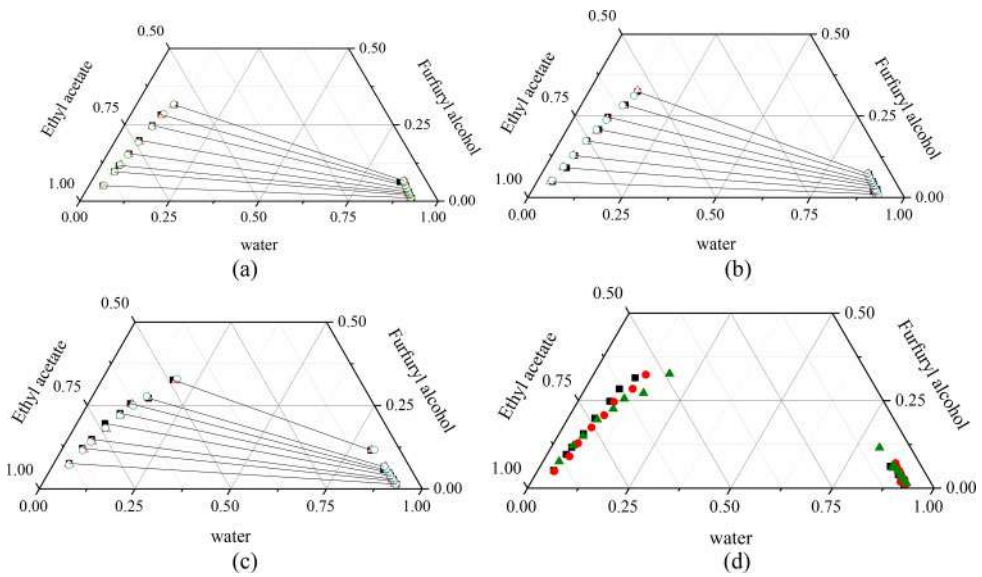

Figure 1. The ternary phase diagram of water + FA + ethyl acetate. (a) 303.2 K, (b) 313.2 K, (c) 323.2 K. (■) Experimental value, (△) NRTL model; (◯) NRTLmodel.

3.2 *Selectivity*

In order to evaluate the extraction effect of ethyl acetate, the distribution coefficient (D) and the separation factor (S) (Stephenson et al. 1984; Xu et al. 2017) were calculated using the following equations:

$$D = w_2^I / w_2^{II} \tag{1}$$

$$S = (w_2^I \cdot w_1^{II}) / (w_2^{II} \cdot w_1^I) \tag{2}$$

where w_1^I and w_2^I are the mass fractions of water and FA in the organic phase, respectively; w_1^{II} and w_2^{II} are the mass fractions of water and FA in the water phase, respectively.

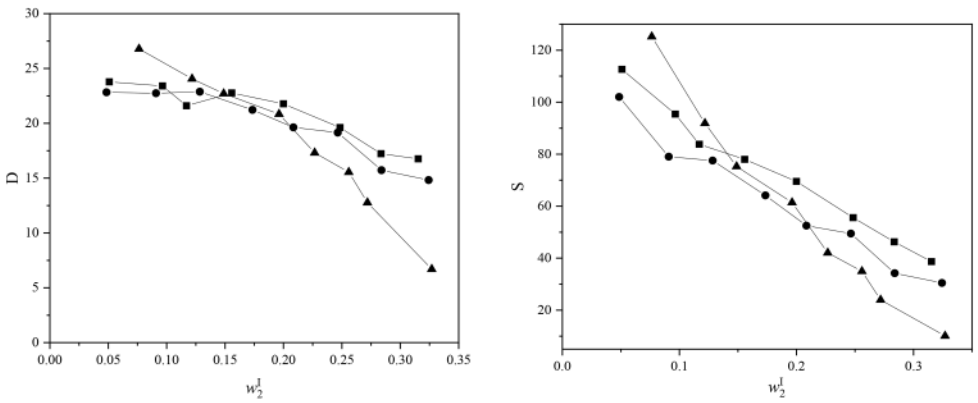

Figure 2. The change trend graph of distribution coefficient (D) and separation factor (S). (■)303.2 K; (●)313.2 K; (▲)323.2 K.

The values of D and S are shown in Figure 2. It can be seen from Figure 2 that the separation factor of each system gradually decreases with the increase of FA in the organic phase, indicating that the extraction effect of the extractant is weakened. This is because the increase in the mass fraction of FA leads to a decrease in the area of the two-phase region. The distribution coefficient and separation factor can fully reflect the separation ability of the extractant. The separation factors are far greater than 1, indicating that ethyl acetate has better extraction capacity and higher selectivity, which is more beneficial for subsequent separation.

3.3 *Consistency test of phase balance data*

To evaluate the reliability of the data, the consistency test of the experimental data, which is of great significant, was used in this experiment. The Bachman and Hand equations are used to perform the consistency test of the phase equilibrium data.

$$w_2^I = A + B(w_2^I / w_3^{II}) \tag{3}$$

$$\ln(w_2^I / w_i^I) = a + bln(w_2^{II} / w_1^{II}) \tag{4}$$

where A, B and a, b are the parameters of Bachman equation and Hand equation respectively. w_2^I is the mass fraction of FA in the organic phase, and w_1^{II}, w_2^{II} and w_3^{II} respectively represent the mass fractions of water, FA and ethyl acetate in the water phase. The parameters of the equation and the linear correlation coefficient R2 are listed in Table 3, R2>0.99, indicating that the phase balance data meets the consistency requirements (Yang et al. 2014).

Table 3. The parameters of Bachman and Hand equation.

		Bachman equation			Hand equation		
extractant	T/K	A	B	R^2	a	b	R^2
ethyl acetate	303.2	–0.1155	1.0345	0.9976	2.3975	1.1907	0.9951
	313.2	–0.0937	1.0159	0.9992	2.4640	1.2021	0.9995
	323.2	–0.1477	1.0797	0.9995	1.7087	0.9806	0.9913

3.4 *Thermodynamic model*

The NRTL and UNIQUAC models were used to regress the experimental data of the phase equilibrium of the research system, and the mentioned parameter r and surface area parameter q of the UNIQUAC model are listed in Table 5. The best fixed value of the NRTL non-randomness parameter a is 0.3. By minimizing the objective function (OF) (Mafi et al. 2017; Saien & Razi Asrami 2017), the best binary interaction parameters of the NRTL and UNIQUAC models are obtained:

$$OF = \sum_{n=1}^{M}\sum_{m=1}^{2}\sum_{l=1}^{3}(w_{lmn}^{exp} - w_{lmn}^{cal})^2 \tag{5}$$

where w_{lmn}^{exp} and w_{lmn}^{cal} are the component mass fractions measured by model fitting and experiment respectively, the subscripts n, m and l respectively represent the number of conjugate junctions, the phase number and the component number in the liquid-liquid equilibrium; M represents the number of junctions.

The root mean square deviation (RMSD) (Amparo et al. 2016; Behroozi et al. 2017) is used to estimate the consistency of experimental data and simulated data:

$$RMSD\% = 100\left\{\sum_{n=1}^{M}\sum_{m=1}^{2}\sum_{l=1}^{3}\frac{(w_{lmn}^{exp} - w_{lmn}^{cal})^2}{6M}\right\}^{0.5} \tag{6}$$

M, xexp, xcal, l, m, n have the same meaning as the OF equation. As is shown in Table 4, the value of RMSD is $\leq 0.34\%$. The calculated data is in good agreement with the experimental data, indicating that the NRTL and UNIQUAC models can predict the experimental data more accurately.

Table 4. NRTL and UNIQUAC parameters of water (1)-FA (2)-ethyl acetate (3) ternary system.

			NRTL parameters				UNIQUAC parameters		
extractant	T/K	$i-j$	gij-gjj /j/mol	gji-gii /j/mol	α	RMSD/%	uij-ujj /j/mol	uji-uii /j/mol	RMSD/%
ethyl acetate	303.2	1-2	8537.17	−1022.49	0.3	0.4971	−1084.11	−48.35	0.4700
		1-3	9512.20	2857.52	0.3		−748.13	−3211.02	
		2-3	−4408.61	7704.66	0.3		−27337.21	2247.92	
	313.2	1-2	9355.20	−2311.71	0.3	0.4280	−13.05	625.19	0.5227
		1-3	9749.93	3556.14	0.3		−788.67	−3547.27	
		2-3	−5264.93	8492.79	0.3		−27800.77	4211.24	
	323.2	1-2	10173.22	−3600.93	0.3	0.5205	1058.01	1298.73	0.4722
		1-3	9987.66	4254.76	0.3		−829.20	−3883.52	
		2-3	−6121.25	9280.92	0.3		−28264.33	6174.56	

1) g and u are the binary interaction parameters obtained by NRTL and UNIQUAC, J /mol;
2) α is the non-randomness parameter of NRTL.

4 CONCLUSION

Based on the results and discussions presented above, the conclusions are obtained as below:

(1) In this study, the liquid-liquid equilibrium of the water + FA + ethyl acetate ternary system under normal pressure is explored at different temperatures. By analyzing the data, it is found that ethyl acetate has a large separation factor when used as an extractant, and it is an excellent extractant. When the Bachman and Hand equations are used to correlate the experimental data, the correlation coefficients obtained are all greater than the requirement of 0.99, indicating that the experimental data has good thermodynamic consistency.
(2) The NRTL and UNIQUAC models are used to regress data to calculate binary interaction parameters. The RMSD% calculated by the two models are both lower than 0.53, and the correlation is strong. The phase equilibrium data in this study can support the separation design of water-FA azeotrope.
(3) Ethyl acetate can be used for the treatment of furfuryl alcohol wastewater and is a good extractant.

ACKNOWLEDGMENTS

This work was financially supported by the National Natural Science Foundation of China (51172284).

REFERENCES

D.S. Abrams, J.M. Prausnitz, Statistical thermodynamics of liquid mixtures: A new expression for the excess Gibbs energy of partly or completely miscible systems, AIChE J. 21 (1975) 116–128.

A. Albouchi, M. Murkovic, Formation kinetics of furfuryl alcohol in a coffee model system, Food Chem. 243 (2018) 91–95.

Amparo, Cháfer, Javier, de, la, Torre, Estela, Lladosa, Sonia, Loras, Study of liquid–liquid equilibria at different temperatures of water + ethanol + 1-butyl-1-methylpyrrolidinium bis(trifluoromethylsulfonyl)imide ternary system, Fluid Phase Equilib. (2016).

M. Behroozi, P. Armozd, M. Mohhamadi Sarab Badieh, Determination of liquid–liquid equilibria data for (water + propanoic acid + 3-methylbutan-1-ol) ternary mixture at 293.15 K to 313.15 K, J. Mol. Liq. 243 (2017) 513–518.

S. Dong, W. Sun, Y. Jiang, B. Jia, Liquid-liquid equilibrium study for ternary systems of (water + furfuryl alcohol + solvents) at 298.2 K: Measurement and thermodynamic modelling, J. Chem. Thermodyn. 148 (2020) 106136.

N. Herold, A. Pfriem, Impregnation of veneer with furfuryl alcohol for an improved plasticization and moulding, Eur. J. Wood Wood Prod. 71 (2013) 281–282.

N. Herold, T. Dietrich, W.J. Grigsby, R.A. Franich, A. Winkler, B. Buchelt, A. Pfriem, Effect of Maleic Anhydride Content and Ethanol Dilution on the Polymerization of Furfuryl Alcohol in Wood Veneer Studied by Differential Scanning Calorimetry, BioResources. 8 (2013) 1064–1075.

C. Kang, T. Jin, H.J. Park, M. Wen, H.Y. Kang, J. Matsumura, Changes in The Dynamic and Static MOE of Furfuryl Alcohol–Treated Wood, Summary of the Graduate School of Agriculture, Kyushu University. 60 (2015).

T. Kim, R.S. Assary, C.L. Marshall, D.J. Gosztola, L.A. Curtiss, P.C. Stair, Acid-Catalyzed Furfuryl Alcohol Polymerization: Characterizations of Molecular Structure and Thermodynamic Properties, ChemCatChem. 3 (2011) 1451–1458.

M. Mafi, M.R. Dehghani, B. Mokhtarani, Liquid-liquid equilibrium data for extractive desulfurization using 1-butyl-3-methyl imidazolium thiocyanate, n- alkane and thiophene, Fluid Phase Equilib. 456 (2017).

H. Renon, J.M. Prausnitz, Local compositions in thermodynamic excess functions for liquid mixtures, AIChE J. 14 (1968) 135–144. https://doi.org/10.1002/aic.690140124.

J. Saien, M. Razi Asrami, Liquid-Liquid Equilibrium of the Ternary System of Water + Phenol + (Propan-2-yl) Benzene at Several Temperatures, J. Chem. Eng. Data. 62 (2017) 3663–3670.

R. Stephenson, J. Stuart, M. Tabak, Mutual solubility of water and aliphatic alcohols, J. Chem. Eng. Data. 29 (1984) 287–290.
Y.R. Swasti, M. Murkovic, Characterization of the polymerization of furfuryl alcohol during roasting of coffee, Food Funct. 3 (2012) 965.
D. Xu, L. Zhang, J. Gao, D. Pratik, L. Zhao, Z. Cui, Liquid-liquid equilibrium for ternary systems of ethyl acetate/isopropyl acetate+2,2,3,3-tetrafluoro-1-propanol+water at 298.15, 318.15K, J. Chem. Thermodyn. 106 (2017) 218–227.
C. Yang, Y. Qian, J. Guo, J. Chen, Liquid-liquid equilibria for the ternary system methyl isobutyl ketone + 1,2-benzenediol + water, J. Chem. Eng. Data. 59 (2014) 3663–3667.
H. Yan, Y. Han, M. Han, W. Wang, J. Han, T. Xing, B. Li, Q. Li, Liquid-Liquid Equilibrium Study of Ternary Systems of (Water plus Furfuryl Alcohol plus Solvents) at 303.2, 313.2, and 323.2 K, J. Chem. Eng. Data. 66 (2021) 3590–3597.

Advances in Applied Chemistry and Industrial Catalysis – Saikia (Ed.)

Study on synthesis of polycarbonate by melt transesterification

E. Yongsheng*, Bin Liu** & Fang Yang***
School of Biological and Chemical Engineering, Liaoning Institute of Science and Technology, Benxi, China

ABSTRACT: Polycarbonate is a widely used thermoplastic engineering plastic with excellent properties. In this paper, bisphenol A and diphenyl carbonate are used as raw materials to synthesize polycarbonate by melt transesterification. The effects of catalyst type, catalyst dosage, molar ratio of raw materials and heating rate, reaction temperature, reaction time and vacuum on the molecular weight of the product are investigated, and the optimal reaction conditions are obtained. The structure of the product is verified by infrared absorption spectroscopy. The rotary viscometer measures the intrinsic viscosity of the sample and calculates the viscosity average molecular weight of the sample to be 30000. The glass transition temperature of the product is detected to be 150.5°C by dilatometer.

1 INTRODUCTION

Polycarbonate (PC) is a kind of excellent thermoplastic engineering plastics with outstanding impact resistance and creep resistance, and good heat resistance and cold resistance. It is widely used in automobile, electrical and electronic, communication equipment, packaging and other fields (Luo & Xiao 1997).

At present, there are two main production methods of polycarbonate: phosgene interfacial polycondensation and non-phosgene melt transesterification (Zhang & Niu 2018). The phosgene interfacial polycondensation method uses toxic phosgene and dichloromethane solvents, which is not conducive to environmental protection. The melt transesterification method does not use phosgene and solvent, and uses bisphenol A (BPA) and diphenyl carbonate (DPC) as raw materials to directly produce products under melting conditions, which is a green synthesis process. In this paper, polycarbonate is synthesized by melt transesterification.

2 EXPERIMENT

2.1 *Reagents and instruments*

The experimental drugs include bisphenol A, diphenyl carbonate, sodium hydroxide, potassium hydroxide, lanthanum acetylacetonate and tetraphenylphosphine phenolate, all of which are analytical reagents; the experimental instruments include Beijing Ruili WQF-510A FTIR infrared spectrometer, DHJ-8s type rotational viscometer, 30cm long dilatometer.

2.2 *Synthesis of polycarbonate*

45.66g bisphenol A and 44.98g diphenyl carbonate are added into A three-way flask, 0.6mg catalyst is added, and nitrogen is passed through. Turn on the electric heating mantle and heat it to 140°C, then the reactants have melted. Turn on the stirring, start the vacuum pump, adjust the nitrogen input. The reaction temperature is gradually increased to 270°C at a heating rate of 4°C/min, the vacuum degree is increased to above –0.09MPa, and the reaction is continued for 70 minutes.

Corresponding Authors: *eyongsheng@lnist.edu.cn, **596236638@qq.com and ***eys73@126.com

DOI 10.1201/9781003308553-51

The phenol distilled out during the reaction is condensed by the condenser and then recovered. After the reaction is over, the product is poured out while it is hot, and the transparent solid obtained after cooling is the polycarbonate.

The reaction equation is shown in Figure 1:

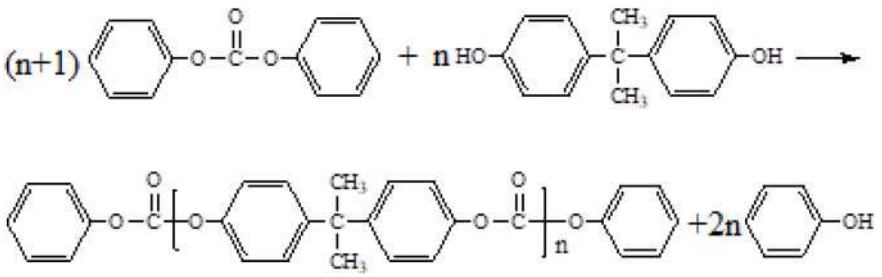

Figure 1. Polycarbonate reaction equation.

2.3 *Testing and characterization*

DHJ-8s type rotary viscometer is used to measure the intrinsic viscosity of the sample at 20°C, and then the viscosity average molecular weight of the sample is calculated by the Mark-Houwink formula (Jin & Hau 2000).

Mark-Houwink formula:

$$[\eta] = \mathrm{kM}^{\alpha} \Rightarrow M = ([\eta]/k)^{1/\alpha} \tag{1}$$

Where, $[\eta]$ is the intrinsic viscosity, M is the viscosity average molecular weight, k is the proportional constant, $\mathrm{k} = 1.11 \times 10 - 2$, α is the expansion factor, $\alpha = 0.82$ (Wang & Chen 2013).

The structure of the product is characterized by the infrared spectrometer. The dilatometer is used to detect the glass transition temperature of the product.

3 RESULTS AND DISCUSSIONS

3.1 *The effect of catalyst type on product molecular weight*

The molecular weight reflects the degree of polymerization of the polymer and has a direct impact on its performance. Therefore, this experiment uses the molecular weight of the product as the basis for selecting the optimal reaction conditions.

The reaction needs to be carried out smoothly under catalytic conditions. At present, the most commonly used catalysts are alkaline metal hydroxides, alkali metal salts and quaternary phosphonium salts. At the same time, due to the high reaction temperature, it is necessary to consider whether the catalyst will change color at high temperature and whether it is decomposed at high temperature. Based on the above factors, this experiment selected sodium hydroxide (NaOH), potassium hydroxide (KOH), lanthanum acetylacetonate (La(C5H7O2)3) and tetraphenylphosphine phenolate (C30H25OP) as candidate catalysts.

Take bisphenol A 45.66g, diphenyl carbonate 44.98g and catalyst 0.6mg. Keep the heating rate at 4°C/min, the final reaction temperature at 270°C, and the reaction time for 70 min. Investigate the effect of different catalysts on the molecular weight of the product.

It can be showed from Figure 2 that lanthanum acetylacetonate has the best catalytic effect, and the molecular weight of the product can reach 30,000. In this experiment, lanthanum acetylacetonate is used as the catalyst.

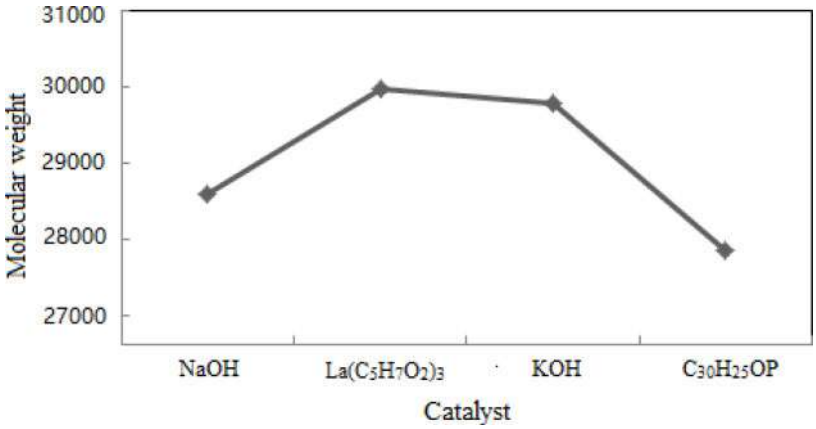

Figure 2. The effect of catalyst type on product molecular weight.

3.2 *The effect of catalyst dosage on product molecular weight*

Take bisphenol A 45.66g, diphenyl carbonate 44.98g. Catalyst is lanthanum acetylacetonate. Keep the heating rate at 4° C/min, the final reaction temperature at 270° C, and the reaction time for 70 min. Investigate the effect of different catalysts dosage on the molecular weight of the product.

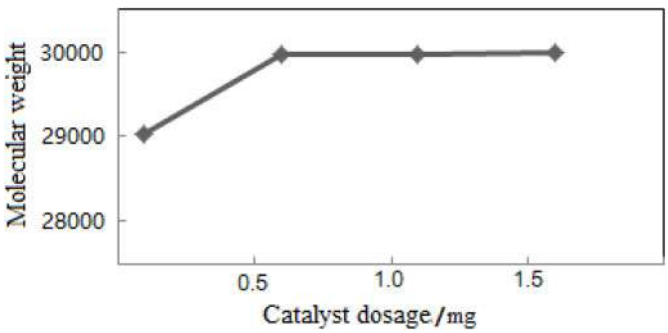

Figure 3. The effect of catalyst dosage on product molecular weight.

It can be showed from Figure 3 that the amount of catalyst is very small, only 0.6mg is needed to achieve the catalytic effect, that is, $1.3 \times 10 - 5$ g/g (BPA). It is meaningless to increase the amount of catalyst, and the residual catalyst will also affect the color of the product.

3.3 *The effect of raw material molar ratio and heating rate on product molecular weight*

According to the reaction equation, the molar ratio of the raw material diphenyl carbonate and bisphenol A is 1:1. Because the reaction temperature is relatively high, and the reaction system is under the vacuum condition, diphenyl carbonate will volatilize to a certain extent, so it should be appropriately excessive. The molar ratio of diphenyl carbonate and bisphenol A is directly related to the heating rate. A slower heating rate allows the diphenyl carbonate to react fully into the oligomer, which reduces its volatilization.

Take bisphenol A 45.66 g (0.2 mol), lanthanum acetylacetonate 0.6 mg. Keep the final reaction temperature at 270°C, and the reaction time for 70 min. Investigate the effect of raw material molar ratio and heating rate on product molecular weight.

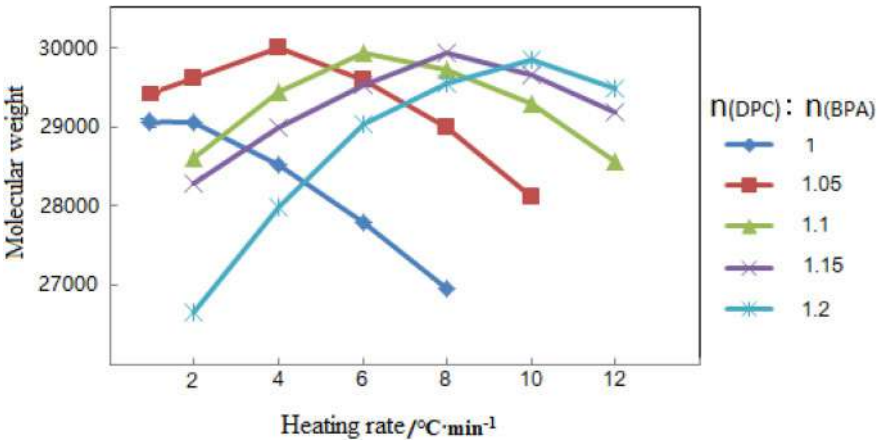

Figure 4. The effect of raw material molar ratio and heating rate on product molecular weight.

It can be showed from Figure 4, that different heating rates correspond to different suitable molar ratios of raw materials. The experiment takes the heating rate of 4°C/min as the best heating rate, and the molar ratio of raw materials n (DPC): n (BPA) = 1.05 as the best raw material molar ratio. At this time, the amount of diphenyl carbonate is 44.98 g (0.21 mol).

3.4 *The effect of the final reaction temperature on product molecular weight*

Take the optimum other reaction conditions, investigate the effect of the final reaction temperature on product molecular weight.

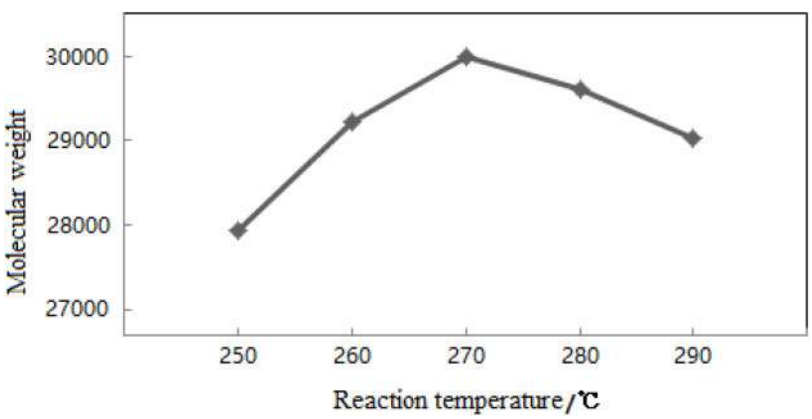

Figure 5. The effect of the final reaction temperature on product molecular weight.

It can be showed from Figure 5 that with the increase of the final reaction temperature, the molecular weight of the product first increases and then decreases. When the reaction temperature is low, the reaction rate is slow and the reaction system is sticky, which is not conducive to the reaction. However, if the temperature is too high, side reactions such as branching, cross-linking and rearrangement will be aggravated, the degree of polymerization will be destroyed, the molecular weight will decrease, and the color of the product will turn yellow. The best final reaction temperature for this experiment is 270°C.

3.5 *The effect of reaction time on product molecular weight*

Take the optimum other reaction conditions, investigate the effect of reaction time on product molecular weight.

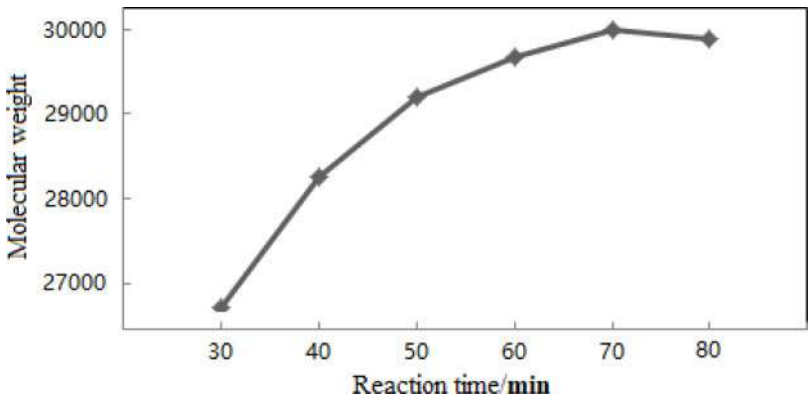

Figure 6. The effect of reaction time on product molecular weight.

It can be showed from Figure 6, with the extension of reaction time, the degree of polymerization and molecular weight gradually increased. When the reaction time reaches 70min, the molecular weight of the polycondensation reaction is the highest. Continue to extend the reaction time, the continued high temperature intensifies the side reaction, the molecular weight of the product decreases, and the color becomes darker. The optimal reaction time is 70min.

3.6 *Product characterization*

3.6.1 *Product structure analysis*

Figure 7 shows the infrared absorption spectrum of the product. In the figure, 1774 cm^{-1} is the characteristic absorption peak of C=O stretching vibration; the absorption peak at 1502 cm^{-1} is caused by the stretching vibration of the benzene ring skeleton; 1230 cm^{-1}, 1191 cm^{-1} and 1160 cm^{-1} are caused by the stretching vibration of C-O (Sweileh & Al-Hiari 2010); 1016 cm^{-1} and 825 cm^{-1} correspond to the fingerprint peaks of the para aromatic ring; 2969 cm^{-1} is saturated with C-H stretching vibration peak (Ning 2000). It can be seen from the infrared absorption spectrum that the product is polycarbonate.

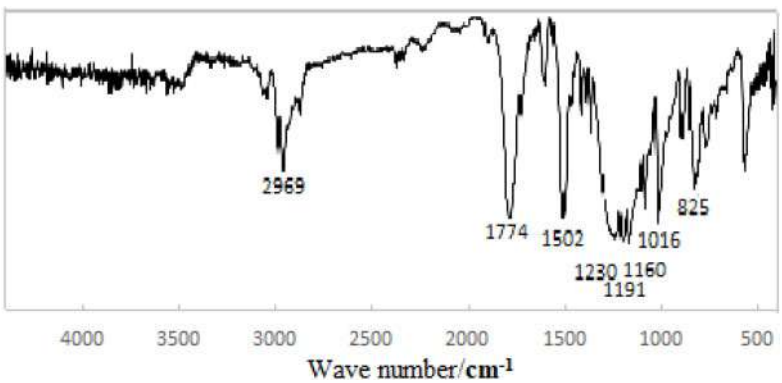

Figure 7. FT-IR spectrum of polycarbonate.

3.6.2 *Product glass transition temperature determination*

Figure 8 is the relationship graph of capillary liquid column height and temperature. The temperature corresponding to the turning point of the slope of the two straight lines in the figure is the glass transition temperature of the product, which is 150.5°C, which is consistent with the polycarbonate prepared by the phosgene interface polycondensation method.

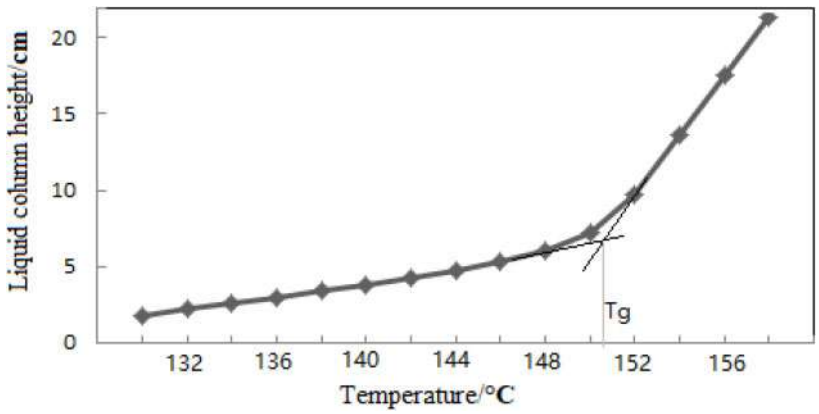

Figure 8. Relationship graph of capillary liquid column height and temperature.

4 CONCLUSION

Based on the results and discussions presented above, the conclusions are obtained as below:

(1) Using bisphenol A and diphenyl carbonate as raw materials, lanthanum acetylacetonate as a catalyst, the melt transesterification method is used to synthesize polycarbonate. The optimal reaction conditions are: the molar ratio of raw materials n (DPC): n (BPA) is 1.05: 1, the amount of catalyst is 1.3×10^{-5} g/g (BPA), the heating rate is 4°C/min, the final reaction temperature is 270°C, and the reaction time is 70 min.
(2) The product is proved to be polycarbonate by infrared absorption spectrum. The viscosity of the product is measured by rotary viscometer and the maximum viscosity average molecular weight is calculated to be 30000. The glass transition temperature of the product is measured by a dilatometer to be 150.5°C.
(3) The melt transesterification process is simple and environmentally friendly, which is a development trend. Improving the catalyst to increase the molecular weight and transparency of polycarbonate is the focus of future research.

REFERENCES

Jin Riguang & Hua Youqing (2000). Polymer Physics, 2nd ed., Beijing: Chemical Industry Press, 92.

Luo Yi & Xiao Qinsha (1997). Engineering Plastics Polycarbonate and Its Developing Trends. Plastics 26 (5), 12–15.

Ning Yongcheng (2000). Structure Identification of Organic Compounds and Organic Spectroscopy, 2nd ed., Beijing: Science Press, 332–340.

Sweileh B.A. & Al-Hiari Y.M. (2010). Synthesis and Characterization of Polycarbonates by Melt Phase Interchange Reactions of Alkylene and Arylene Diacetates with Alkylene and Arylene Diphenyl Dicarbonates. Molecules 15 (5), 3661–3682.

Wang Xiaoyu & Chen Meijun (2013). Research on the relationship between molecular weight and viscosity of polycarbonate. Gansu Science and Technology 29 (12), 18–19.

Zhang Guihua & Niu Jianzhou (2018). Analysis of Polycarbonate Production and Market Application Prospect in China. Chemical Industry 36 (5), 45–56.

Advances in Applied Chemistry and Industrial Catalysis – Saikia (Ed.)

Determination and correlation of liquid-liquid equilibrium of water + furfuryl alcohol + extractant

Houchun Yan, Qingqing Yin, Yuanyuan Han, Mai Han & Qingsong Li*
State Key Laboratory of Heavy Oil, China University of Petroleum (East China), Qingdao, Shandong, P.R. China

ABSTRACT: In order to provide data support for the recovery and treatment of furfuryl alcohol wastewater, the liquid-liquid equilibrium data of water + furfuryl alcohol + methyl acetate system at 303.15 K, 313.15 K and 323.15 K were investigated at 101.3 kPa. The extraction effect was evaluated by the calculated partition coefficient and separation factor, and the calculated results were all greater than 1, indicating that methyl acetate has good extraction capacity and extraction effect as an extractant. Hand and Othmer-Tobias empirical equations were used to test the consistency of the experimental data, and the linear correlation coefficient R^2 was ≥ 0.99. NRTL and UNIQUAC thermodynamic models were used to correlate the experimental data, and the relative root mean square deviation (RMSD) and average absolute deviation (AAD) were both lower than 0.0085, indicating that NRTL and UNIQUAC can correlate the experimental data well.

1 INTRODUCTION

Furfuryl alcohol is a significant raw material for the production of furan resin. The purity of its industrial products is greater than 98%, and the water content is less than 0.3%. Due to the low requirement for water content, a large amount of wastewater needs to be removed in the production of furfuryl alcohol (Meng et al. 2016; Sharma et al. 2013; Vargas-Hernández et al. 2014). In addition, in the production process of 2-methylfuran and other products, wastewater will also be produced, which contains about 10% furfuryl alcohol. Based on the annual output of 5000 tons of 2-methylfuran, the furfuryl alcohol contained in the produced furfuryl alcohol wastewater was calculated to be about 420 t/a (Zhao et al. 2020). According to GC-MS analysis of furfuryl alcohol wastewater, there are more than 40 kinds of organic substances (furfuryl alcohol, acetic acid, furfural and other alcohols, aldehydes, ketones, esters and organic acids). Furfuryl alcohol wastewater is difficult to treat, with low biodegradability and great damage to the environment and ecology. It is a highly difficult organic wastewater. At present, there are few studies on the treatment of furfuryl alcohol wastewater (Xiong et al. 2020). Generally, the wastewater containing furfuryl alcohol will be biochemically treated with other heavy phase organics together in industry. The cost of this treatment method is high, requiring about 2000-3000 RMB per ton (Zhao et al. 2020). Therefore, the reasonable treatment of these wastewater is very important.

As an effective separation method, liquid-liquid extraction technology is suitable for separation processes that require energy saving. At present, some literatures have reported the exploration of the liquid-liquid equilibrium relationship between furfuryl alcohol wastewater and extractant system. Wongsawa et al. used ethyl acetate, methyl isobutyl ketone, 2-furfural, and 1-butanol as extractants to determine the ternary liquid-liquid equilibrium data between each extractant and water and furfuryl alcohol at 298.2 K (Wongsawa & Hronec 2014). Dong et al. explored the liquid-liquid equilibrium data for water + furfuryl alcohol + methyl tert-butyl ether/isopropyl ether/dichloromethane/4-methyl-2-amyl alcohol at 298.2K (Dong et al. 2020). Yan et al. used chloroform and methyl isopropyl ketone as extractants to determine the liquid-liquid equilibrium data (Yan et al. 2021).

*Corresponding Author: licup69@163.com

DOI 10.1201/9781003308553-52

In order to investigate the effect of methyl acetate on the separation of furfuryl alcohol from water, the liquid-liquid equilibrium data of water + furfuryl alcohol + methyl acetate at 303.15, 313.15, and 323.15 K were measured in this work. The extraction effect was evaluated by partition coefficient and separation factor. The consistency of the experimental results was tested by Hand and Othmer Tobias equations (Zhu et al. 2020). In addition, NRTL and UNIQUAC thermodynamic models (Cui et al. 2020) were used to fit the measured data, so as to obtain binary interaction parameters and provide data basis for subsequent industrial design.

2 MATERIALS AND METHODS

2.1 *Materials*

The physicochemical properties, suppliers, and the mass fractions obtained by chromatographic analysis of the chemicals used in this work are listed in Table 1.

Table 1. Chemical reagents.

				UNIQUAC	
Chemicals	CAS	Supplier	$w^{1)}$/%	$r^{2)}$	$q^{3)}$
furfuryl alcohol	98-00-0	Sinopharm Chemical Reagent Co., Ltd	> 99.5	3.3784	2.6760
methyl acetate	79-20-9	Sinopharm Chemical Reagent Co., Ltd	> 99.5	2.8042	2.5760
distilled water	7732-18-5	self - made	–	0.9200	1.3997

1) w is the mass fraction; 2) r is the volume parameter of UNIQUAC; 3) q is the surface area parameter of UNIQUAC.

2.2 *Process and Method*

A certain quality of reagent was added to the phase equilibrium kettle, fully mixed for 4 hours, and then left to stand and stabilize more than 6 hours to achieve the stable state of the ternary system (Fan et al. 2020). The temperature of the system was maintained constant through a constant temperature water bath, and the temperature of the balance kettle liquid was measured with a high-precision thermocouple with an accuracy of ±0.1°C.

When the two phases in the system reach equilibrium, samples were taken for the aqueous phase and the organic phase respectively. At the same time, the content of components was detected by gas chromatography, which used a thermal conductivity detector (TCD) and a Porapak N column (3 m in length and 3 mm in inner diameter). The carrier gas of the chromatography was hydrogen, and the flow rate was 60 mL/min. The temperature of the detector and gasification chamber was 513.2 K. The initial temperature of the column was 393.2 K, then increased to 493.2 K at a rate of 30 K/min, and then maintained at 493.2 K for 3 minutes. Each sample was analyzed more than 3 times, and the final result was the average of the qualified data. The standard uncertainty of the components was calculated according to GUM and related standards (Fan et al. 2020), and the value did not exceed ±0.0035.

3 RESULTS AND DISCUSSION

3.1 *Phase Equilibrium Data*

The liquid-liquid equilibrium data of water + furfuryl alcohol + methyl acetate system measured at 303.15, 313.15, and 323.15 K are shown in Table 2. According to the data, with the increase of furfuryl alcohol content, the mass fraction of furfuryl alcohol in both aqueous phase and methyl acetate phase gradually increases, and the content of furfuryl alcohol in methyl acetate phase is greater than that in aqueous phase. This indicates that methyl acetate can be used as an extractant for extracting furfuryl alcohol from water.

The ternary phase diagram, phase equilibrium connection line and feed composition of the system are shown in Figure 1. The feed composition point is located on the connection line, indicating that the ternary system complies with the law of mass conservation. The phase diagram of the investigated water + furfuryl alcohol + methyl acetate system belongs to the type I system (Jia et al. 2021), that is, water and furfuryl alcohol, methyl acetate, and furfuryl alcohol belong to completely miscible pairs, while water and methyl acetate belong to a partially miscible pair. It can be seen from Figure 1 that there is a large two-phase region in the ternary phase diagram, indicating that methyl acetate has great operability as an extractant and is suitable for extraction and separation.

3.2 *Selectivity*

The following equation was used to calculate the partition coefficient (D) and separation factor (S) to evaluate the extraction effect of methyl acetate (Li 2020).

$$D = w_2^I / w_2^{II} \tag{1}$$

$$S = (w_2^I / w_2^{II}) / (w_1^I / w_1^{II}) \tag{2}$$

Where w_1 represents the mass fraction of water, w_2 represents the mass fraction of furfuryl alcohol; Superscript I indicate methyl acetate phase and superscript II indicates aqueous phase.

The values of the partition coefficient and the separation factor are shown in Table 2, and their variation trend with the furfuryl alcohol in the methyl acetate phase is shown in Figure 2. The results show that as the temperature of the ternary system increases, the partition coefficient and separation factor of each system first decrease and then increase, and the extraction effect is the best at 50°C; as the content of furfuryl alcohol in the organic phase increases, the partition coefficient and separation factor of each system decrease gradually. The results show that the extraction effect of extractant decreases with the increase of furfuryl alcohol content in the feed, which is due to the decrease of the area of the two-phase region by the increase of furfuryl alcohol concentration. The partition coefficient and the separation factor can reflect the extraction ability. Since their values are both greater than 1, indicating that methyl acetate has relatively good extraction ability and high selectivity, which is favorable for subsequent separation.

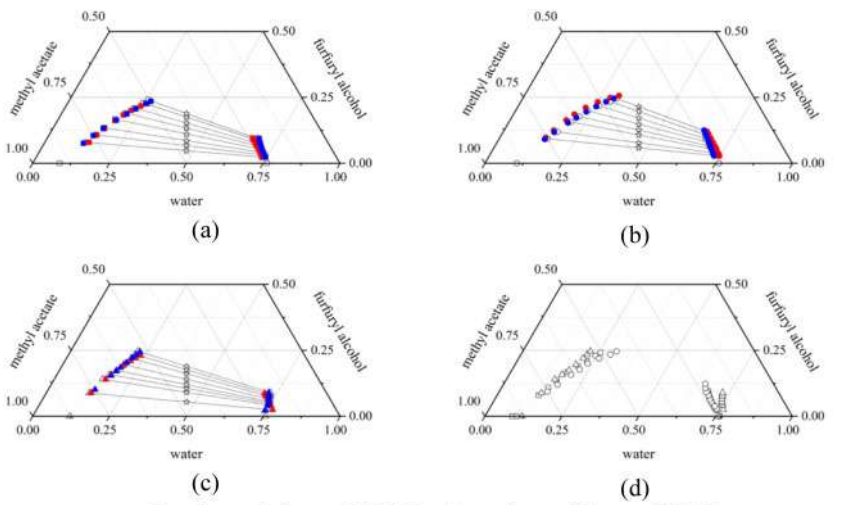

Figure 1. Ternary phase diagram of water + furfuryl alcohol + methyl acetate at (a) 303.2 K, (b) 313.2 K, and (c) 323.2 K. (d) Temperature comparison diagram.

Table 2. Liquid-liquid equilibrium data of water (1) + furfuryl alcohol (2) + methyl acetate (3) system.

	organic phase			aqueous phase				
T/K	x_1^{I}	x_2^{I}	x_3^{I}	x_1^{II}	x_2^{II}	x_3^{II}	D	S
303.2	0.0884	0	0.9116	0.7628	0	0.2372	–	–
	0.1347	0.0796	0.7857	0.7425	0.0227	0.2348	3.51	19.33
	0.1511	0.1086	0.7403	0.7318	0.0321	0.2361	3.38	16.39
	0.1656	0.1351	0.6993	0.7223	0.0418	0.2359	3.23	14.10
	0.1846	0.1674	0.6480	0.7102	0.0546	0.2352	3.07	11.80
	0.2069	0.1910	0.6021	0.7003	0.0654	0.2343	2.92	9.89
	0.2268	0.2099	0.5633	0.6919	0.0754	0.2327	2.78	8.49
	0.2447	0.2299	0.5254	0.6835	0.0878	0.2287	2.62	7.31
	0.2562	0.2406	0.5032	0.6772	0.0955	0.2273	2.52	6.66
313.2	0.1040	0	0.8960	0.7612	0	0.2388	–	–
	0.1567	0.0936	0.7497	0.7399	0.0286	0.2315	3.27	15.45
	0.1761	0.1197	0.7042	0.7281	0.0388	0.2331	3.09	12.76
	0.2015	0.1571	0.6414	0.7096	0.0543	0.2361	2.89	10.19
	0.2193	0.1774	0.6033	0.6994	0.0647	0.2359	2.74	8.74
	0.2347	0.1998	0.5655	0.6887	0.0787	0.2326	2.54	7.45
	0.2625	0.2184	0.5191	0.6742	0.0921	0.2337	2.37	6.09
	0.2908	0.2343	0.4749	0.6636	0.1074	0.2290	2.18	4.98
	0.3052	0.2460	0.4488	0.6552	0.1226	0.2222	2.01	4.31
323.2	0.1208	0	0.8792	0.7570	0	0.2430	–	–
	0.1400	0.0882	0.7718	0.7628	0.0245	0.2127	3.60	19.61
	0.1572	0.1403	0.7025	0.7524	0.0419	0.2057	3.35	16.03
	0.1714	0.1585	0.6701	0.7469	0.0492	0.2039	3.22	14.04
	0.1865	0.1741	0.6394	0.7429	0.0556	0.2015	3.13	12.47
	0.1974	0.1964	0.6062	0.7385	0.0649	0.1966	3.03	11.32
	0.2098	0.2201	0.5701	0.7344	0.0747	0.1909	2.95	10.31
	0.2158	0.2347	0.5495	0.7312	0.0821	0.1867	2.86	9.69
	0.2200	0.2467	0.5333	0.7285	0.0898	0.1817	2.75	9.10

Note:1 u is standard uncertainty, $u(T) = 0.1°$ C, $u(P) = 1.0$ kPa, $u(w) = 0.0035$.

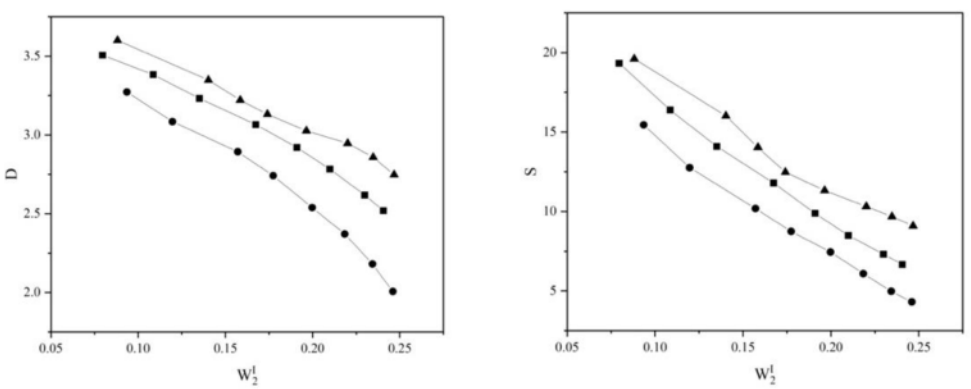

Figure 2. Variation trend of partition coefficient (D) and separation factor (S) (■)303.2 K; (●)313.2 K; (▲)323.2 K.

3.3 *Consistency test of phase equilibrium data*

The Hand and Othmer-Tobias empirical equations (Zhu 2020) were used to test the consistency of the phase equilibrium data:

$$\ln\left(w_2^{\mathrm{I}}/w_3^{\mathrm{I}}\right) = a + b\ln\left[w_2^{\mathrm{II}}/w_1^{\mathrm{II}}\right] \tag{3}$$

$$\ln\left[\left(1 - w_3^{\mathrm{I}}\right)/w_3^{\mathrm{I}}\right] = c + d\ln\left[\left(1 - w_1^{\mathrm{II}}\right)/\left(w_1^{\mathrm{II}}\right)\right] \tag{4}$$

Where a, b, c, and d are the parameters of the above equation respectively. w_1 represents the mass fraction of water, w_2 represents the mass fraction of furfuryl alcohol, w_3 represents the mass fraction of methyl acetate; superscript I represents the methyl acetate phase and superscript II represents the aqueous phase.

The parameters and linear correlation (R^2) of the equation are listed in Table 3. The R^2 is ≥ 0.99, indicating that the measured phase equilibrium data have good consistency.

Table 3. Parameters of Hand and Othmer-Tobias equations.

		Hand Equation			Othmer-Tobias Equation		
Extractant	T/K	a	b	R^2	c	d	R^2
methyl acetate	303.2	1.0188	1.2638	0.9999	4.0524	3.0151	0.9989
	313.2	0.9469	1.0123	0.9992	3.1916	2.2626	0.9990
	323.2	1.0536	1.4398	0.9993	6.0497	5.8514	0.9990

3.4 *Thermodynamic model*

In this paper, Aspen Plus V10 software was used to regress the measured liquid-liquid equilibrium data through NRTL and UNIQUAC models (Cui et al. 2020). The binary interaction parameters obtained by NRTL and UNIQUAC models were summarized in Table 4. The parameters of NRTL and UNIQUAC models were correlated by nonlinear regression method, and the objective function (OF) is calculated as follows:

$$OF = \sum_{k=1}^{M}\sum_{j=1}^{2}\sum_{i=1}^{3}\left(w_{ijk}^{exp} - w_{ijk}^{cal}\right)^2 \tag{5}$$

Where w^{exp} denotes the experimental mass fraction of each component, w^{cal} denotes the mass fraction of each component calculated by the thermodynamic model; subscript k denotes the connecting line, j denotes the phase, $i$represents the component; M denotes the phase equilibrium connection lines.

Table 4. NRTL and UNIQUAC parameters of water (1) + furfuryl alcohol (2) + methyl acetate (3) system.

	NRTL parameters					UNIQUAC parameters			
$i-j$	a_{ij}	b_{ij}(K)	α	*RMSD*	*AAD*	a_{ij}	b_{ij}(K)	*RMSD*	*AAD*
1-2	1.40	822.57	0.3	0.0085	0.0066	5.84	−1970.52	0.0083	0.0062
2-1	−1.76	264.41				3.41	−919.34		
1-3	5.09	−747.72	0.3			0.03	−79.62		
3-1	−0.18	243.71				0.01	−297.78		
2-3	1.90	1342.00	0.3			23.08	−7401.67		
3-2	−3.95	775.91				2.61	−568.30		

The relative root mean square deviation (*RMSD*) and mean absolute deviation (*AAD*) were used to estimate the consistency between the experimental data and the simulated data. It can be seen from Table 4 that the *RMSD* and *AAD* values are both less than 0.0085, indicating that the NRTL and UNIQUAC models are suitable for this ternary system.

$$RMSD = \left\{ \sum_{k=1}^{M} \sum_{j=1}^{2} \sum_{i=1}^{3} \left(w_{ijk}^{exp} - w_{ijk}^{cal} \right)^2 / 6M \right\}^{1/2} \tag{6}$$

$$AAD = \sum_{k=1}^{M} \sum_{j=1}^{2} \sum_{i=1}^{3} \left| x_{ijk}^{exp} - x_{ijk}^{cal} \right| / 6M \tag{7}$$

Where k, j, i, M, w^{exp}, and w^{cal} are the same as Equation (5).

4 CONCLUSION

The liquid-liquid equilibrium data of water + furfuryl alcohol + methyl acetate system at 303.15, 313.15, and 323.15 K at 101.3 kPa were determined in this paper. The results showed that methyl acetate had good extraction ability for furfuryl alcohol in aqueous solution. The thermodynamic consistency of the experimental data was verified by the Hand and Othmer-Tobias empirical equations. At the same time, the experimental data was fitted through the NRTL and UNIQUAC thermodynamic models. The results showed that the deviation between the fitted data and the measured phase equilibrium data was small, and the relative root mean square deviation (*RMSD*) and mean absolute deviation (*AAD*) were both lower than 0.0085. Therefore, the phase equilibrium data measured in this paper can provide a basis for the process design and process simulation calculation of the extraction and recovery of furfuryl alcohol from wastewater using methyl acetate as the extractant.

ACKNOWLEDGMENTS

This work was financially supported by the National Natural Science Foundation of China (51172284).

REFERENCES

Cui Y, Zhang Z, Shi X, Guang C, Gao J. Triple-Column Side-Stream Extractive Distillation Optimization via Simulated Annealing for the Benzene/Isopropanol/Water Separation. Sep. Purif. Technol. 2020; 236: 116303.

Dong S, Sun W, Jiang Y, Jia B. Liquid-Liquid Equilibrium Study for Ternary Systems of (Water + Furfuryl Alcohol + Solvents) at 298.2 K: Measurement and Thermodynamic Modelling. J. Chem. Thermodyn. 2020; 148: 106136.

Fan W, Yan H, Huang X, Liao Z, Li Q, Ma Z. Liquid-Liquid Equilibria for Ternary Systems n-Hexane + 1-Hexene + Furfural (or N, N-Dimethylformamide) at 298.2, 308.2, and 318.2 K. J. Chem. Eng. Data. 2020; 65(1): 146–152.

Jia B, Jiang X, Chen X, Dong S. Experimental Determination and Modeling of Liquid-Liquid Equilibrium for Ternary Mixtures Composed of Water, Epichlorohydrin and Different Solvents. J. Mol. Liq. 2021; 322: 114984.

Li Q, Fan W, Yan H, Huang X, Zhang L, Ma Z. Experimental Determination and Modeling of Liquid-Liquid Equilibrium for Water + Diethoxymethane + Methyl Tert-Butyl Ether (or Methyl Isobutyl Ketone) at 298.15, 308.15, and 318.15 K. Fluid Phase Equilib. 2020; 505: 112353.

Meng Q, Zheng H, Zhu Y, Li Y. Study on the Reaction Pathway in Decarbonylation of Biomass-Derived 5-Hydroxymethylfurfural over Pd-Based Catalyst. J. Mol. Catal. A Chem. 2016; 421: 76–82.

Sharma R V, Das U, Sammynaiken R, Dalai A K. Liquid Phase Chemo-Selective Catalytic Hydrogenation of Furfural to Furfuryl Alcohol. Appl. Catal. A Gen. 2013; 454: 127–136.

Vargas-Hernández D, Rubio-Caballero J M, Santamaría-González J, Moreno-Tost R, Mérida-Robles J M, Pérez-Cruz M A, Jiménez-López A, Hernández-Huesca R, Maireles-Torres P. Furfuryl Alcohol from Furfural Hydrogenation over Copper Supported on SBA-15 Silica Catalysts. J. Mol. Catal. A Chem. 2014; 383–384: 106–113.

Wongsawa T, Hronec M. Fluid Phase Equilibria Ternary (Liquid – Liquid) Equilibrium Data of Furfuryl Alcohol with Organic Solvents at T = 298. 2 K: Experimental Results and Thermodynamic Models. Fluid Phase Equilibria J. 2014; 365: 88–96.

Xiong G, Zhang L, Cai Y. Wastewater Treatment Methods in the Production of Furfuryl Alcohol. CN110655627A[P]. 2020.

Yan H, Han Y, Han M, Wang W, Han J, Xing T, Li B, Li Q. Liquid–Liquid Equilibrium Study of Ternary Systems of (Water + Furfuryl Alcohol + Solvents) at 303.2, 313.2, and 323.2 K. J. Chem. Eng. Data. 2021; 66(9): 3590–3597.

Zhao C, Xu J, Zhan J. Method for Recovering Furfuryl Alcohol in 2-Methylfuran Wastewater. CN202010447386.6[P]. 2020.

Zhu Z, Xu Y, Li H, Shen Y, Meng D, Cui P, Ma Y, Wang Y, Gao J. Separation of Isopropyl Alcohol and Isopropyl Ether with Ionic Liquids as Extractant Based on Quantum Chemical Calculation and Liquid-Liquid Equilibrium Experiment. Sep. Purif. Technol. 2020; 247 (January): 116937.

Advances in Applied Chemistry and Industrial Catalysis – Saikia (Ed.)

Study on a structure of $C_8H_{20}O_{20}Tb_2$

Hai-Xing Liu[#]
Chemistry & Chemical and Environmental Engineering College, Weifang University, Weifang, P.R. China

Xiao-Ping Zhang[#]
Chemistry & Chemical and Environmental Engineering College, Weifang University, Weifang, P.R. China
Huarui Quality Inspection Technology Service Company, Weifang, P.R. China
Weifang University, College of Chemistry and Chemical Engineering, 2016 graduates

Ying Liu*
Chemistry & Chemical and Environmental Engineering College, Weifang University, Weifang, P.R. China

ABSTRACT: The Tb complex $C_8H_{20}O_{20}Tb_2$ was synthesized by hydrothermal technology and the crystal structure was determined utilizing single-crystal X-ray diffraction. The Tb atom is coordinated by nine O atoms. The molecular structure is stabilized by the O-H…O hydrogen-bonding interactions.

1 INTRODUCTION

Zheng (2021) et al. obtained the Nd MOF complex {[Nd(biphenyl3,4′,5tricarboxylic acids)(N, N-dimethylformamide)(H_2O)]·2H_2O}$_n$ and characterized with X-ray diffraction, IR and elemental analysis. Meanwhile, the luminescent, magnetic, and photocatalytic properties of the compound were analyzed. Yang (2021) et al. established the hydrothermal reaction method of MOF [Cd(benzene tetracarboxylic acid)$_{0.5}$(1,3-bis(1H-imidazole-1-ylmethyl)benzene)(H_2O)]·H_2O and characterized X-ray diffraction, IR, elemental and thermogravimetric analysis. They also discussed the fluorescent property of the matter. Zhang (2021) et al. synthesized Pr compound (piperazine)$_{1.5}$[Pr(pyridine2,6dicarboxylate)$_3$]·7H_2O and analyzed by elemental analysis, IR, and X-ray diffraction. The matter had antitumor property. Yu QunYing (2021) reported the anticancer activity and structure of Ru complex (NH_4)$_2$[Ru(1isopropyl4methylbenzene) (1,1dimethyl biguanide)]$_2Cl_2$·4H_2O. Wei (2021) et al. synthesized two manganese complexes [Mn(2,2′-bicinchoninic acid)(1,10-phenanthroline)(H_2O)$_2$]$_n$ and [Mn(2,2′-bicinchoninic acid) (H_2O)]$_n$ and characterized by IR, UV, fluorescence, X-ray diffraction, elemental and thermogravimetric analysis. It was shown that the complexes had obvious fluorescence properties and thermal stability. Zhang (2021) et al. synthesized polymer {[Co(4-(4-(1H-imidazole-1-yl) phenyl) pyridine) (4,4′-diphenyl ether dicarboxylic acid) (H_2O)]·H_2O}$_n$ with a hydrothermal method and studied its UV absorption and thermal stability. Li (2021) et al. explored the arginine-cobalt complex ($C_6H_{14}N_4O_2$·3Co·H_2O) and characterized by the infrared spectrometer, thermal differential analyzer, energy spectrometer, and scanning electron microscope. They also studied the complex activity for the anti-tumor aspect. Xie (2021) et al. synthesized silver complex [{Ag(1,3,5-benzene tricarboxylic acid)} {Ag$_2$(1,3,5-benzene tricarboxylic acid)}]$_n$ and characterized with X-ray powder diffractometer, scanning electron microscope and infrared spectroscopy. The compound had also fine photocatalytic and antibacterial properties. Li (2021) et al. synthesized copper complex {[Cu(1,1′-bis(4-carboxybenzyl)-4,4′bipyridinium dichloride)$_{1.5}$(H_2O)$_2$]·SO_4}$_n$ and characterized using IR, elemental analysis and X-ray diffraction. The matter was effect by the inhibition of protein tyrosine phosphatases 1B. Xu Yan (2021) synthesized trinuclear Mn

*Corresponding Author: ydliuying@163.com
#Co-first author

 DOI 10.1201/9781003308553-53

complex {[Mn(N,N′-(ethylene) bis-(salicylideneiminato))]$_3$(5-(ethoxycarbonyl-naphthalene-1-yl) phosphonic acid)}ClO_4 and characterized by X-ray analysis, infrared spectrometer and elemental analysis. The matter was a supramolecular one-dimensional chain structure by $\pi - \pi$ interaction and showed antiferromagnetic interactions. In this paper, the $C_8H_{20}O_{20}Tb_2$ structure is reported.

2 EXPERIMENTAL

All commercially obtained reagent-grade chemicals were used without further purification. A mixture of Tb_4O_7 (0.009g), dilute HNO_3, 4-amino-2-chloropyridine (0.01g), $K_2S_2O_8$ (0.01g), boric acid (0.01g) and vitamin C (0.01g) were added into 15 mL water with 10%(v/v) ethanol and heated for 6h at 404K. The solution was obtained by filtration after cooling the reaction to room temperature. Colorless block single crystals suitable for X-ray measurements were obtained after a few weeks.

3 RESULTS AND DISCUSSIONS

The title complex crystal structure is shown in Figure 1. The crystal data and structure refinement is shown in Table 1. The Tb atom is coordinated by nine O atoms. The distances d(Tb-O) are in the range of 2.397-2.537 Å. The angles of O3-Tb1-O5, O5-Tb1-O7, O1-Tb1-O9 are 125.19, 69.29, 94.47°, respectively. The torsion angles of O9-Tb1-O3-C2, O7-Tb1-O5-C3, and O5-Tb1-O3-C2 are 171.0, 92.0, 46.6°, respectively. Selected bond lengths and bond angles are shown in Table 2.

The molecular structure is stabilized by the O-H…O hydrogen-bonding interactions.

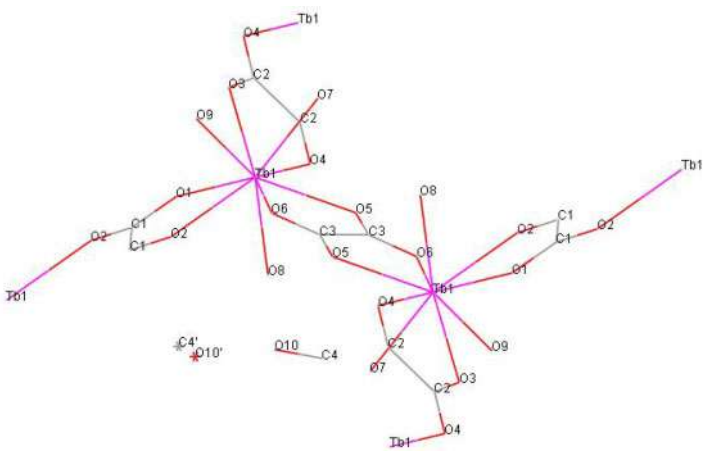

Figure 1. The molecular structure of $C_8H_{20}O_{20}Tb_2$.

Table 1. Crystal data and structure refinement for $C_8H_{20}O_{20}Tb_2$.

Empirical formula	$C_8H_{20}O_{20}Tb_2$
Formula weight	754.08
Temperature	298(2) K
Wavelength	0.71073 Å
Crystal system, space group	Monoclinic, P2(1)/c
Unit cell dimensions	a = 11.0327(11) Å alpha = 90°.
	b = 9.6517(8) Å beta = 114.347(2)°.
	c = 10.0602(10) Å gamma = 90°.

(*continued*)

Table 1. Continued.

Volume	975.98(16) Å^3
Z, Calculated density	2, 2.566 Mg/m^3
Absorption coefficient	7.286 mm^{-1}
F(000)	716
Crystal size	0.21 × 0.15 × 0.11 mm
Theta range for data collection	2.93 to 25.00°.
Limiting indices	$-13 <= h <= 13$, $-8 <= k <= 11$, $-10 <= l <= 11$
Reflections collected / unique	4697 / 1716 [R(int) = 0.0443]
Completeness to theta = 25.00	99.8 %
Absorption correction	Semi-empirical from equivalents
Max. and min. transmission	0.5012 and 0.3099
Refinement method	Full-matrix least-squares on F^2
Data / restraints / parameters	1716 / 0 / 156
Goodness-of-fit on F^2	1.085
Final R indices [I>2sigma(I)]	R1 = 0.0290, wR2 = 0.0685
R indices (all data)	R1 = 0.0355, wR2 = 0.0730
Largest diff. peak and hole	0.980 and -1.420 e. Å^{-3}

Table 2. Select bond lengths [Å] and angles [°] for $C_8H_{20}O_{20}Tb_2$.

Tb(1)-O(9)	2.397(5)
Tb(1)-O(8)	2.414(5)
Tb(1)-O(1)	2.437(5)
Tb(1)-O(7)	2.463(5)
Tb(1)-O(5)	2.469(4)
Tb(1)-O(3)	2.471(4)
O(1)-C(1)	1.274(8)
O(2)-C(1)	1.239(8)
O(3)-C(2)	1.267(7)
O(5)-C(3)	1.247(7)
O(10)-C(4)	1.43(2)
O(10′)-C(4′)	1.42(3)
O(9)-Tb(1)-O(4)#	1 137.40(15)
O(9)-Tb(1)-O(6)#	2 73.48(15)
O(9)-Tb(1)-O(8)	143.56(17)
O(6)#2-Tb(1)-O(8)	89.79(15)
O(9)-Tb(1)-O(1)	94.47(17)
O(4)#1-Tb(1)-O(1)	82.46(15)
O(6)#2-Tb(1)-O(1)	130.79(15)
O(8)-Tb(1)-O(1)	71.99(15)
O(9)-Tb(1)-O(7)	72.87(18)
O(4)#1-Tb(1)-O(7)	83.75(16)
O(8)-Tb(1)-O(7)	137.22(17)
O(1)-Tb(1)-O(7)	142.06(15)
O(9)-Tb(1)-O(5)	127.93(16)
O(8)-Tb(1)-O(5)	68.71(16)
O(1)-Tb(1)-O(5)	136.91(16)
O(7)-Tb(1)-O(5)	69.29(16)
O(9)-Tb(1)-O(3)	72.39(14)
O(4)#1-Tb(1)-O(3)	66.72(14)
O(6)#2-Tb(1)-O(3)	141.38(15)
O(8)-Tb(1)-O(3)	128.71(15)

(*continued*)

Table 2. Continued.

O(1)-Tb(1)-O(3)	69.68(14)
O(7)-Tb(1)-O(3)	72.40(14)
O(5)-Tb(1)-O(3)	125.19(14)
O(9)-Tb(1)-O(2)#3	69.72(16)
O(4)#1-Tb(1)-O(2)#3	140.59(15)
O(6)#2-Tb(1)-O(2)#3	66.45(14)
O(8)-Tb(1)-O(2)#3	73.94(16)
O(1)-Tb(1)-O(2)#3	64.65(14)
O(7)-Tb(1)-O(2)#3	135.60(16)
O(3)-Tb(1)-O(2)#3	116.39(14)
C(1)-O(1)-Tb(1)	122.7(4)
C(2)-O(3)-Tb(1)	118.0(4)
C(2)-O(4)-Tb(1)#1	120.8(4)
C(3)-O(5)-Tb(1)	119.2(4)
O(4)-C(2)-O(3)	125.7(6)
O(4)-C(2)-C(2)#1	117.6(7)
O(5)-C(3)-O(6)	127.0(6)

4 CONCLUSIONS

The Tb complex $C_8H_{20}O_{20}Tb_2$ was synthesized by hydrothermal technology. The crystal packing is stabilized by O-H...O hydrogen bonding interaction.

ACKNOWLEDGMENTS

This study was supported by the Open Project of State Key Laboratory of Supramolecular Structure and Materials (No: sklssm201323) (Jilin University), State Key Laboratory of Inorganic Synthesis and Preparative Chemistry (No: 2011-13) (Jilin University).

REFERENCES

Li, C. Guo, Q.-F. Zhu, X.-H. Dong, K.-X. Zeng, Z.-J. Ji, Y.-H. (2021). Study on Synthesis and Properties of Complexes of Arginine and Cobalt, Chemical Reagents. 43(10), 1348–1352.

Li, L. Gao, X.-L. (2021). Synthesis and Protein Tyrosine Phosphatase 1B Inhibition of Copper (II) Complex with Bipyridinium Carboxylate, Chemical Reagents. 43(3), 365–369.

Wei, W.-C. Liu, Z. Wei, R.-Z. Liang, C.-X. Tang, Q. (2021). Synthesis, Crystal Structure and Properties of Manganese Complexes Constructed by 2,2′-Bicinchoninic Acid, Chemical Reagents. 43(2), 235–242.

Xie, R.-R. Yang, T.-H. Feng, J. Zhang, M.-Y. (2021). Photocatalytic and Antibacterial Properties of Silver Complex with 1,3,5-Benzenetricarboxylic Acid, Chemical Reagents. 43(1), 16–21.

Xu, Y. (2021). Phosphonate Bridged Mn(III)-Schiff Base Compound: Synthesis, Structure and Magnetic Properties, Chemical Reagents. 43(11), 1575–1579.

Yang, H. Wu, Y.-Z. Cui, H.-L. Liu, L. Wang, J.-J. Chen, X.-L. (2021). Three-Dimensional Cd-MOF Based on Benzenetetracarboxilic Acid and Bis(imidazolylmethyl)benzene Ligands: Synthesis, Structure and Fluorescence Property. Chinese Journal of Inorganic Chemistry. 37(3), 465–472.

Yu, Q.Y. (2021). Symmetrical Diruthenium Complex Based on 1-Isopropyl-4-methylbenzene and Dimethylbiguanide: Synthesis and Anticancer Activity in Vitro. Chinese Journal of Inorganic Chemistry. 37(5), 899–904.

Zhang, L. Guo, L.F. Huang, S. Kang, J. Sun, W.M. (2021). Synthesis, Characterization and Biological Activity of Pr Complex Constructed by Pyridine-2,6-dicarboxylate. Chinese Journal of Inorganic Chemistry. 37(7), 1269–1276.

Zhang, Z.-L. Jin, D.-J. Zhang, F.-F. Yao, X.-Q. (2021). Synthesis, Crystal Structure and Properties of One-dimensional Co(II) Coordination Polymer Based on 4,4′-Diphenyl Ether Dicarboxylic Acid Bridged Ligand, Chemical Reagents. 43(4), 529–533.

Zheng, H. Jiao, Y. Feng, S.S. (2021). Synthesis, Structure, Luminescence, Photocatalytic and Magnetic Properties of a Neodymium Complex Constructed from Biphenyl-3,4′,5-tricarboxylic Acid. Chinese Journal of Inorganic Chemistry. 37(9), 1691–1699.

Advances in Applied Chemistry and Industrial Catalysis – Saikia (Ed.)

Effects of crop straw on manganese, boron, and iron uptake of *Amygdalus davidiana* seedlings

Jinrong Zhang & Panhong Zou
School of Agriculture and Horticulture, Chengdu Agricultural College, Chengdu, Sichuan, China
Jinrong Zhang and Panhong Zou contributed equally to this work.

Xiangting Xu, Junjiang Shu, Wanjia Tang, Lijin Lin & Huashan Lian*
College of Horticulture, Sichuan Agricultural University, Chengdu, Sichuan, China

ABSTRACT: Explore the effects of rape, rice, corn, and wheat straw on the Mn, B, and Fe content of *Amygdalus davidiana* seedlings. The *A. davidiana* seedlings were used as test materials, and 6–8 true leaves were transplanted into basins containing different straws to determine the Mn, B, and Fe contents of the *A. davidiana* seedlings. Wheat straw and corn straw significantly increased the Mn content in the roots, stems, and leaves of *A. davidiana* seedlings, while rape straw and rice straw reduced the Mn content of *A. davidiana* seedlings. Four kinds of straw (rape, rice, wheat, corn) were used to treat the *A. davidiana* seedlings so that the B content in the roots, stems, and leaves was lower than the control in varying degrees. Four kinds of straw increased the Fe content in the roots of *A. davidiana* seedlings. Only wheat straw increased the Fe content in the stems of *A. davidiana* seedlings. Rice straw and rape straw significantly increased the Fe content in the leaves of *A. davidiana* seedlings, the Fe content in the leaves of *A. davidiana* seedlings treated with wheat straw and corn straw was significantly lower than that of the control. This provides an important theoretical basis for returning straw to the field to increase trace elements in plants.

1 INTRODUCTION

Amygdalus davidiana has lush branches and leaves, a developed root system, and a strong role in maintaining water and soil. It can be used as a grafting rootstock for *A. davidiana* plum and other fruit trees, it can be cultivated as an ornamental tree, and the fruit can be eaten raw, as wine. At present, it is widely distributed in western Liaoning in our country (Zhang 2000, 2019). Increasing the content of trace elements in *A. davidiana* seedlings has many benefits for its use as a rootstock and food.

Trace elements are indispensable for the growth and development of the human body and plants, for example, manganese (Mn), boron (B), iron (Fe), and so on. These elements can not be synthesized in the human body and can be obtained through plant trace elements. The trace elements in plants originate from the soil (Ma et al. 2020). The human pituitary gland contains the richest Mn content. The pituitary gland is the control center of all advanced life activities of the human body. At the same time, Mn also participates in the synthesis and activation of various human enzymes, promotes human growth and development, and regulates the endocrine system. Therefore, the role of Mn is very important (Wu 2007; Yan et al. 2002). Mn in plants can promote the synthesis of auxin, maintain the stability of chlorophyll, participate in the process of photosynthetic cleavage

*Corresponding Author: 49939450@qq.com

DOI 10.1201/9781003308553-54

and oxygen evolution, and act as an enzyme catalyst (Rao et al. 2012). The World Health Organization recommends that the intake of B for adults is 1-13 mg/d. B is an important antidote for human and animal fluorosis (Aguilar et al. 2013; Ma et al. 2020). B is closely related to plant cell structure, tissue differentiation, carbohydrate synthesis and transportation, and protein and nucleic acid metabolism (Tang et al. 1998). Fe is the highest content of essential trace elements in the human body. Fe is a component of human hemoglobin and myoglobin and participates in the transportation and storage of human oxygen, as well as the synthesis of cytochrome oxidase and catalase (Sun & Guo 2011). Fe plays a major role in chlorophyll synthesis, photosynthesis, respiration, and other processes.

Returning crop straws to the field is conducive to promoting the development of green organic agriculture, which can change the soil structure and improve soil nutrients. Yu et al. found that returning straw to the field promotes the absorption of Mn and Fe in red pepper, significantly increases the yield of rice and the Fe content in rice; Wang et al. showed that the amount of Fe detected during the pyrolysis of wheat straw is higher than that Mn and B (Yu et al. 2015; Yuan et al. 2013; Wang et al. 2020). Increasing the content of trace elements in fruits and vegetables is conducive to human health, and also promotes the growth and development of the plant itself. This experiment aimed to study the changes of Mn, B, and Fe in *A. davidiana* seedlings by adding different straws, to increase the trace elements in *A. davidiana* and the production of high-quality rootstocks provides a theoretical basis. It is also useful for reference to increase the trace elements in different parts of the plant by returning straw to the field.

2 MATERIALS AND METHODS

2.1 *Materials*

The test material is *A. davidiana* seedlings, which were purchased in the market. After the *A. davidiana* seeds germinate, transplanted in plastic basins, with a moisture content of 2%-6%. Rape, rice, wheat, and corn straw were collected from farmland around Sichuan Agricultural University, dried, and crushed for later use. The test soil was fluvo-aquic soil, taken from farmland around the Chengdu campus of Sichuan Agricultural University.

2.2 *Experimental design*

The basin experiment was conducted on the Chengdu campus of Sichuan Agricultural University from April to October 2019. The seedlings were grown in 50-hole high-bottom trays with perlite, the bottom plate was irrigated with 1 L of Hoagland nutrient solution, the nutrient solution is changed every 3 days, and cultivated day and night in an artificial climate room at 21°C–23°C. The soil was air-dried and crushed, passed through a 5 mm sieve, and each plastic basin (20 cm high and 20 cm diameter) was filled with 3 kg of air-dried soil. There were 5 treatments in the experiment, adding rape straw, adding rice straw, adding wheat straw, adding corn straw, and adding no straw (control). The ratio of adding straw to the soil in each basin is 10 g/kg, the mixture was evenly mixed, and each treatment is repeated 4 times (4 basins). All potted plants were watered every day, and the soil moisture content was always maintained at about 80% of the field water holding capacity. A. davidiana seedlings will be transplanted after two weeks. At the beginning of May 2019, when the seedlings grew to 6 to 8 true leaves (6-9 cm plant height), selected seedlings with the same growth and transplant them into basins, planting 4 plants in each basin (in four directions). Place plastic basins (with a spacing of about 15 cm) completely randomly and change positions randomly to reduce the influence of edge effects. The A. davidiana seedlings were watered in time to ensure that the soil is moist. At the same time, we also paid attention to the removal of weeds and the prevention and control of pests and diseases. After 60 days, the whole plant was sampled, and various indexes were determined.

2.3 *Measurement items and methods*

Divided the sampled *A. davidiana* seedlings into three parts: roots, stems, and leaves. Plant samples were rinsed with tap water and then rinsed repeatedly with deionized water. They lost roots, and stem leaves activity at 105°C for 15 min, then dried to constant weight at 80°C and weighed. Nitration of the sample by nitric acid perchloric acid (4:1 by volume), ICAP6300 ICP spectrometer determinates Mn, B, Fe content in roots, stems, and leaves.

2.4 *Statistical analysis*

Statistical analyses were performed using SPSS 22.0 statistical software. Data were analyzed using a one-way analysis of variance with the least significant difference test ($p \leq 0.05$).

3 RESULTS

3.1 *The effect of different straws on Mn content of A. davidiana seedlings*

The treatments of wheat straw and corn straw significantly increased the Mn content in the roots of the *A. davidiana* seedlings by 64% ($p > 0.05$) and 50% ($p > 0.05$), respectively, compared with the control. The treatments of rape straw and rice straw were not significantly different from the control. The Mn content in the stems of *A. davidiana* seedlings treated with wheat straw and corn straw was significantly higher than that of the control, 51% ($p > 0.05$) and 39% ($p > 0.05$) increased over the control, there was no significant difference between the rape straws treatment and the control, while the rice straw treatment significantly reduced the Mn content in the stems. The change of Mn content in the leaves of *A. davidiana* seedlings treated with different straws was similar to that in the stems. Wheat straw and corn straw significantly increased the Mn content in the leaves, while rape straw and rice straw significantly reduced the Mn content in the leaves.

Table 1. Effects of different straws on Mn content of *A. davidiana* seedlings.

Treatment	Roots (μg/g)	Stems (μg/g)	Leaves (μg/g)
Control	33.01±2.32c	35.97±3.08c	109.82±5.53c
Rape	29.48±3.11c	33.27±2.47c	63.25±2.50d
Rice	29.78±2.37c	27.34±1.34d	35.12±3.41e
Wheat	91.90±2.58a	73.40±3.79a	352.49±6.20a
Corn	65.82±2.14b	58.51±1.45b	249.66±5.17b

Different lowercase letters within a column indicate significant differences based on a one-way analysis of variance and the least significant difference test ($p \leq 0.05$).

3.2 *Effects of different straws on the B content of A. davidiana seedlings*

The content of B in the roots, stems and leaves of *A. davidiana* seedlings treated with different straws was lower than that of the control. Wheat straw treatment *A. davidiana* seedlings had the lowest B content, with 58% ($p > 0.05$), 34% ($p > 0.05$) and 78% ($p > 0.05$) lower than control in roots, stems and leaves, respectively.

3.3 *The effect of different straws on Fe content of A. davidiana seedlings*

Compared with the control, different straw treatments of *A. davidiana* seedlings significantly increased the Fe content in the roots, and the rice straw treatment had the highest Fe content in the roots, which was 39% ($p > 0.05$) higher than the control. The wheat straw treatment of *A. davidiana*

seedlings significantly increased the Fe content in the stems, which was 25% ($p > 0.05$) higher than the control. Other straw treatments significantly reduced the Fe content in the stem. The corn straw treatment had the lowest Fe content in the stem, which was 66% ($p > 0.05$) lower than the control. Compared with the control, the treatments of rice straw and rape straw significantly increased the Fe content in the leaves of *A. davidiana* seedlings by 24% ($p > 0.05$) and 6% ($p > 0.05$), respectively. Wheat straw and corn straw significantly reduced the Fe content in the leaves.

Table 2. Effects of different straws on the B content of *A. davidiana* seedlings.

Treatment	Roots (μg/g)	Stems (μg/g)	Leaves (μg/g)
Control	324.64±6.13a	233.80±7.50a	352.77±6.04a
Rape	285.41±6.68b	189.37±4.61b	223.59±5.07b
Rice	156.65±4.40d	164.83±5.03d	93.03±3.31c
Wheat	135.02±3.63e	155.23±3.71d	77.12±4.27d
Corn	205.54±5.89c	179.38±5.44c	94.94±5.73c

Different lowercase letters within a column indicate significant differences based on a one-way analysis of variance and the least significant difference test ($p \leq 0.05$)

Table 3. Effects of different straws on Fe content of A. davidiana seedlings.

Treatment	Roots (μg/g)	Stems (μg/g)	Leaves (μg/g)
Control	251.62±5.20d	133.39±7.90b	292.86±8.42c
Rape	320.19±4.17c	77.73±3.41d	311.62±10.04b
Rice	411.68±9.13a	99.89±4.62c	386.38±9.95a
Wheat	372.98±8.53b	178.57±6.46a	274.61±4.40d
Corn	359.67±8.67b	45.92±4.78e	263.35±7.85d

Different lowercase letters within a column indicate significant differences based on a one-way analysis of variance and the least significant difference test ($p \leq 0.05$).

4 DISCUSSION

Straw returning to the field can return the nutrient elements in the crop to the soil, and to a certain extent, it can alleviate the lack of soil nutrients and reduce the number of chemical fertilizers (Dai et al. 2010). Straw is rich in organic carbon and medium and traces elements. After the straw is returned to the field, it decomposes under the action of soil microorganisms, and the released medium and trace elements are absorbed and utilized by crops (Huang et al. 2005). Experiments such by Wang et al. (Wang et al. 2006) showed that the combined application of straw and chemical fertilizers increased the content of zinc and manganese in the soil; Wang et al. (Yu et al. 2015) experiments showed that the technology of returning straw to the field promoted the absorption of Mn, Zn, and Fe by pepper plants, thereby increasing crop yield.

This study's results showed that wheat straw and corn straw significantly increased the Mn content in the roots, stems, and leaves of *A. davidiana* seedlings; all four kinds of straw could increase the Fe content in the roots of *A. davidiana* seedlings, but only wheat straw increased the Fe content in the stems. *A. davidiana* leaves treated with rice straw and rape straw contained more Fe. The above results of increasing Mn and Fe in *A. davidiana* seedlings are the same as previous experimental studies, indicating that straw is a good source of trace elements and plays an important role in the

absorption of trace elements in some plants. The B content in the roots, stems, and leaves of the four kinds of straw treated *A. davidiana* seedlings were lower than the control, indicating that the lack of trace elements in the straw was absorbed by the plant through the soil after decomposing. It may be absorbed and utilized by the soil or microorganisms in the soil.

It is speculated from the experimental results that wheat straw was used to increase plant Mn content and Fe content in roots and stems, corn straw was used to increase plant Mn content and Fe content in roots, and rice straw or rape straw increased plant Fe content in roots and leaves. It provides a theoretical basis for adding a specific trace element to the straw returning to the field, and different crop straws also play a certain role in the increase of manganese and iron content in *A. davidiana* seedlings.

5 CONCLUSION

Wheat straw and corn straw had a significant effect on increasing Mn content in roots, stems, and leaves of *A. davidiana* seedlings, wheat straw increased Fe content in *A. davidiana* stems. Rice straw and rape straw increased Fe content in *A. davidiana* leaves. The four straws (rape, rice, wheat, corn) all significantly increased the Fe content in the roots of *A. davidiana* seedlings. The B content in the roots, stems, and leaves of the seedlings in the treatment group was lower than the control. Part of the straw treatment increased the Mn and Fe content in the *A. davidiana* seedlings, and it had reference significance in increasing the Mn and Fe content in the *A. davidiana*, the physiological effects of the trace elements need to be further tested and demonstrated.

ACKNOWLEDGMENTS

This work was financially supported by the Youth Fund Project of Chengdu Agricultural College (20QN04).

REFERENCES

Aguilar, F., Crebelli, R., Dusemund, B. (2013) Scientific opinion on the re-evaluation of boric acid (E 284) and sodium tetraborate (borax) (E 285) as food additives. EFSA Journal, 11(10): 3407.

Dai, Z.G., Lu, J.W., Li, X.K. (2010) Nutrient release characteristic of different crop straws manure. Transactions of the Chinese Society of Agricultural Engineering, 26(6): 272–276.

Huang, Y.X., Wang, G.L., Feng, Y.H. (2005) Changes of organic matter in red paddy soil derived from red soil in a long-term located experiment. Chinese Journal of Soil Science, 36(2): 181–184.

Ma, Y.P., Shi, L., He, Y. (2020) Trace elements iron, manganese, boron, zinc, copper, molybdenum and human health. Fertilizer and Health, 47(5): 12–17.

Rao, Y.C., Zheng, T.T., Ma, B.J. (2012) The effect of trace elements iron, manganese and copper on rice growth and the prevention and cure of element deficiency. Chinese Rice, 18(4): 31–35.

Sun, C.F., Guo N. (2011) Trace element iron effects on human health. Studies of Trace Elements and Health, 28(2): 64–66.

Tang, S.W., Xu, X. L. (1998) Physiological function and yield-increasing effect of trace element boron on plants and application technology of boron fertilizer. Agricultural Research and Application, (3): 38–41.

Wang, G., Zhao, L.X., Meng, H.B. (2020) Law for migration and transformation of carbon and trace elements during the pyrolysis of wheat straw. Transactions of the Chinese Society of Agricultural Engineering, 36(7): 256–263.

Wang, J.F., Liu, Y.J., Li, B.Y. (2006) Effects of returning crop straw into vertisol on the physical and chemical properties and availability of manganese, zinc, copper. Chinese Journal of Eco-Agriculture, (3):49–51.

Wu, M.J. (2007) Manganese and human health. Studies of Trace Elements and Health, (6):69–70.

Yan, SH.M., Li, Z.X., Xiong, L.P. (2002) Essentials of trace element medicine | . Physiological role and balance of trace elements in human body. Guangdong Trace Elements Science, (09): 1–48.

Yu, M., Wang, Z.X., Wu, H.Y. (2015) Effect of straw returning technology on red pepper plants and trace elements in soil. Journal of Anhui Agricultural Sciences, 43(2): 32–35.
Yuan, L., Zhang, Y., Yang, J. (2013) Effects of different cultivation methods and straw incorporation on grain yield and nutrition quality of rice. Acta Agronomica Sinica, 39(2): 350–359.
Zhang, J.Y. (2000) *Amygdalus davidiana* seedlings and cultivation management techniques. The Journal of Hebei Forestry Science and Technology, (S1): 59–62.
Zhang, L.G. (2019) High-efficiency management and cultivation techniques of *Amygdalus davidiana* in western Liaoning. Rural Technology, (6): 89–90.

Advances in Applied Chemistry and Industrial Catalysis – Saikia (Ed.)

Experimental study on electrochemical corrosion of tubing wall in flowing liquids

Han Wang, Huali Zhang, Yufei Li & Lin Zhang
Engineering Technology Research Institute, Petro China Southwest Oil and Gas Field Company, Chengdu, P.R. China

Jiarui Cheng* & Wenlan Wei
Xi'an Key Laboratory of Wellbore Integrity Evaluation, Xi'an Shiyou University, Xi'an, P.R. China

ABSTRACT: Corrosion damage is one of the causes of downhole tubular column failure, and its reaction process is influenced by factors such as ambient temperature, pressure, medium concentration and flow velocity. In order to study the corrosion pattern of P110 steel pipe wall in flowing liquid environment, this study conducted multi-point online electrochemical corrosion parameter measurements using a circulating flow experimental setup. The electrochemical corrosion behavior of P110 steel in flowing NaCl solution was analyzed, and the effects of different flow velocities and different concentrations of NaCl solution on the corrosion behavior of P110 steel were discussed. The experimental results show that in the flowing 2wt.% NaCl solution, the corrosion rate of P110 steel increases with the increase of flow velocity, and the corrosion reaction in the process is mainly controlled by the cathodic oxygen diffusion and anodic dissolution reaction together; in the high flow velocity NaCl solution, the shear force of the liquid on the wall and Cl^- act together to destroy the corrosion product film, resulting in a continuous decrease of charge transfer resistance after the increase of Cl^- concentration, the corrosion rate increases.

1 INTRODUCTION

Corrosion damage of metal surface is one of the main factors of equipment and pipeline damage in the production of petroleum and petrochemical industries. Oil well pipe is mostly the only channel for oil and gas extraction, which is damaged by the corrosion reaction of various substances, resulting in spike leakage of the pipe column and reduced (Zhang et al. 2012) service life. P110 steel, as a commonly used pipe for oil pipe and casing, has good comprehensive mechanical properties, with yield strength reaching 840–860 MPa and tensile strength reaching 925 ~ 935 MPa (Chen 2015; Nestor 2012), playing an important role in oil and gas extraction. However, P110 steel in the recovery medium is susceptible to corrosion by brine containing Cl^-, which produces uniform corrosion or pitting and triggers cracking and puncture leakage of the pipe column.

Existing studies, which mainly focus on the corrosion behavior of P110 petroleum casing steel in static NaCl solution, are dominated by the study of Cl^- concentration changes, and less for the corrosion in flowing liquids. In static NaCl solution, due to the small $^-$radius of Cl, it can penetrate the surface of the metal substrate by penetrating the corrosion product film and promote Fe^{3+} hydrolysis, thus promoting the occurrence of electrochemical corrosion. Wu Dandan et al. (Liu

*Corresponding Author: cjr88112@163.com

DOI 10.1201/9781003308553-55

et al. 2003; Wu et al. 2014) experimentally proved that the increase in Cl^- concentration makes the corrosion tendency of P110 steel increase, and the corrosion rate first increases and then decreases. In the flow of NaCl solution, on the one hand, the liquid cutting force to promote the stripping of corrosion products, thinning the oxide film on the surface of the material, so that the base metal is exposed to the corrosive medium, increasing the reaction area and accelerating the corrosion rate; on the other hand, due to the corrosion reaction, the surface of the metal wall becomes rough, promoting the effect of fluid shear scouring, the synergistic effect of the two will accelerate the surface material damage. Existing flow corrosion research, to pipe flow type, rotating disc type and jet type three flow experiments (Bi et al. 2013; Bo et al. 2019). Liu Jingjun et al. used tubular flow type and rotating disc type flow simulator (Deng et al. 2017) in 3.5 wt. % NaCl solution to test the variation law of corrosion rate of carbon steel surface with flow velocity, and the results showed that the corrosion rate of carbon steel showed a continuous increasing trend in a certain flow velocity range.

In this paper, a homemade miniature three-electrode test system was used to carry out online flow corrosion experiments on P110 steel pipes for different flow velocities of NaCl solutions using a multi-channel electrochemical workstation, and the flow corrosion pattern of P110 steel was obtained by analyzing the test data.

2 EXPERIMENTAL MATERIALS AND METHODS

2.1 *Experimental materials*

The material used in this experiment is oil tubing P110 steel grade pipe, and the chemical composition of this material is detailed in the table1. A cylindrical annular specimen of 2.5 mm outer diameter, 1.5 mm inner diameter and 30 mm length was intercepted from the wall of the oil well tubing. The outermost layer of the miniature triple electrode is an epoxy resin cured insulation layer, followed by an auxiliary electrode (carbon rod) with an outer diameter of 6 mm and an inner diameter of 3mm. The inner layer consists of a P110 steel working electrode and a 0.4 mm diameter silver wire (reference electrode), with epoxy resin cured insulation between each layer. Copper wires are used to connect with the working electrode and auxiliary electrode respectively to form the test circuit. The reference electrode is connected to the saturated glycerol electrode. Surface polishing and two surface distilled water rinsing before the experiment, and then the specimen with chemically pure anhydrous ethanol dipped in degreasing cotton scrubbed two times, dried with filter paper, blowers cold air dry spare. Corrosion medium is NaCl analytical pure and distilled water preparation solution, NaCl mass fraction of 2 wt. %.

Table 1. Chemical component of P110 steel (mass fraction/wt %).

C	Si	Mn	P	S	Cr	Ni	Cu	Fe
0.32	0.42	1.47	0.013	0.006	0.0036	0.01	0.05	97.69

2.2 *Experimental equipment*

The experiments were completed in a homemade flow experimental platform, as shown in Figure 1a for the schematic diagram of the main setup. The experimental section (Figure 1(b)) was made of Plexiglas with a 6 mm diameter through-hole in the wall, and the three electrodes were glued so that the test surface of the three electrodes was flush with the inner wall of the tube. The PARSTAT-MC1000 multi-channel electrochemical workstation was used for electrochemical testing, and the weight loss was measured by an electronic balance with an accuracy of 0.1 mg.

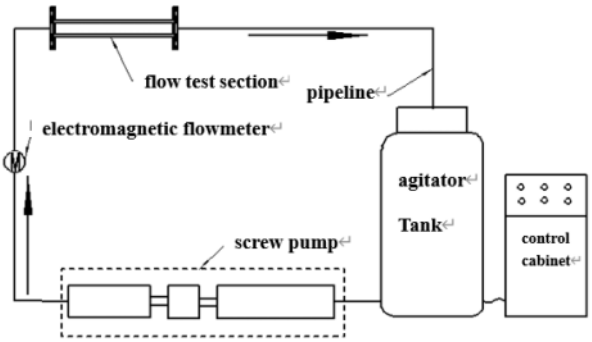

a Schematic diagram of the circulating flow experimental setup

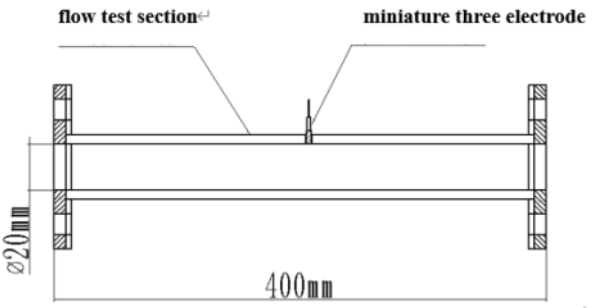

b Diagram of miniature three-electrode installation

Figure 1. Circulating flow test device.

2.3 *Experimental steps*

Before the experiment, the electrode working surface was polished with 800#, 10#00, 1500#, 2000# sandpaper step by step, rinsed with distilled water, wiped with alcohol, and dried with cold air. Install the miniature triple electrode into the circulating flow experimental apparatus to ensure that the annular working surface is in full contact with the experimental medium, while the Princeton electrochemical workstation is connected to the miniature triple electrode. The prepared NaCl solution was filled into the circulating flow experimental apparatus, and the flow velocity was adjusted, and electrochemical tests were performed after the flow velocity stabilized for 10 min. The electrochemical polarization curves were scanned from -1.5V (vs Ref) to1.5 the end of V at a rate of 5mV/s. The electrochemical impedance spectra (EIS) were tested in the frequency range of 1.0×(10-105-2) Hz. After the experiments, the specimens were rinsed with distilled water to remove the corrosive medium, wiped with alcohol and then blown dry and encapsulated.

3 EXPERIMENTAL RESULTS

The polarization curves of P110 steel in different flow velocities (1, 3, 5, 7, 9, 11 m/s) 2wt. % NaCl solutions are shown in Figure 2 shows the electrochemical polarization measurement parameters. The self-corrosion potential, current density, anodic and cathodic Tafel slopes were obtained by Tafel fitting of the polarization curves. The test results showed that the self-corrosion potential showed a continuous positive shift with the increase of flow velocity, from -874.832 mV at the flow velocity of 1m/s to 11 - 430.164mV at m/s, while the self-corrosion current density also increased continuously with the increase of flow velocity. In addition, the polarized anodic curves showed the

dissolution characteristics of material activation reaction, i.e., the anodic current density increased with the increase of polarization potential, which indicated that no dense and stable passivation film was formed on the metal surface during the anodic dissolution. The anodic polarization curves with different flow velocity polarization curves were smoother, and the fitted cathodic Tafel slope showed that the increase of flow velocity had no significant effect on the anodic Tafel slope, but the cathodic polarization curve showed a backward trend and the cathodic Tafel slope increased significantly. This is due to the fact that the concentration of dissolved oxygen on the surface of the material and the flow velocity of the solution are related, and when the flow velocity of the solution is increased to help oxygen diffuse on the surface of the material, the cathode appears to be characterized by oxygen diffusion control at this time.

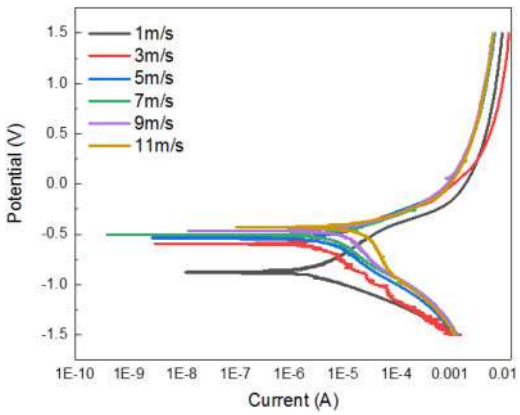

Figure 2. Polarization curves of P110 solution steel under different flow velocities of 2wt.% NaCl solution.

The impedance spectra of P110 steel in 2 wt.% NaCl solution at different flow velocities are shown in Figure 3(a). The test results show that the impedance spectrum has only one time constant and presents an incomplete semicircle, with a decreasing trend of semicircle diameter from 1 m/s to 11 m/s, and an increasing semicircle diameter only at 7m/s. This indicates that there is a significant effect on the surface film formation characteristics of P110 steel with the flow velocity. Based on the measurement results, a circuit diagram was established as shown in Figure 3(b), where R_s is the resistance of the solution, CPE is the constant phase element, R_{ct} is the resistance of charge transfer, and Table 2 shows the fitted parameters of each equivalent circuit element. The calculated results show that both the resistance of the solution and the resistance of the charge transfer fluctuate with the flow velocity, and the resistance of the solution is maximum at the flow velocity of 9m/s; the resistance of the charge transfer decreases first, where the resistance of the charge transfer is maximum at 1 m/s and reaches the second peak at the flow velocity of 7 m/s.

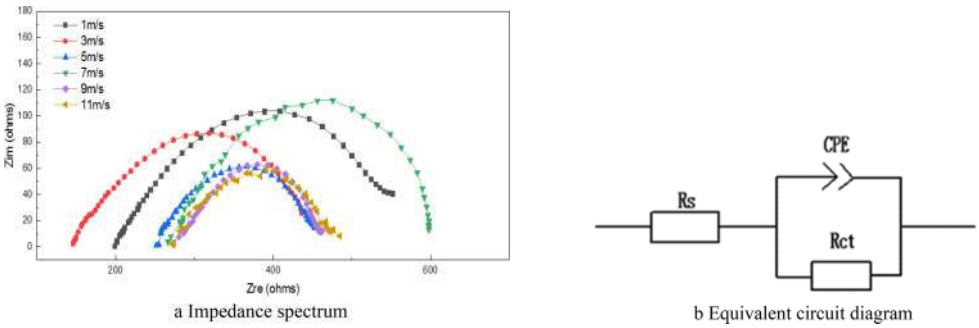

Figure 3. Impedance spectroscopy and equivalent circuit of P110 steel under different flow velocities of 2wt.% NaCl solution.

Table 2. Fitting parameters of impedance spectrosc110 steel under different flow velocities of 2wt.% NaCl solution.

flow velocity	1	3	5	7	9	11
$Rs/(\Omega\cdot cm^2)$	201.4	145.7	252.1	273.4	282.7	272.5
CPE-T	3.67×10^{-4}	2.07×10^{-4}	2.08×10^{-4}	4.75×10^{-5}	1.2×10^{-4}	1.92×10^{-4}
CPE-P	0.61	0.59	0.64	0.72	0.72	0.61
$R_{ct}/(\Omega\cdot cm^2)$	380.4	323.2	210.7	340.1	183.9	210.7

4 DISCUSSION

For the corrosion process of metals, some scholars equate the metal in corrosion to a short-circuit cell or energy production system, where there is energy consumption in the production of corrosion products, thus equating the oxidation phase of the metal to the corrosion of the metal. At this point the corrosion rate can represent the rate of weight loss or permeability, which is calculated as follows (Nesic et al. 1995).

$$C_R = \frac{R_P}{\rho} = \frac{i_{corr} A_W}{zF\rho} \tag{1}$$

where, C_R—corrosion rate, mm/a.

i_{corr}—self-corrosion current density, mA/cm^2

A_W—atomic weight of the substance, g/mol.

F—Faraday's constant, C/mol.

R_p— polarization resistance in Ωcm^{-2}, the linear polarization resistance can be expressed as follows

$$R_P = \frac{\beta_a \beta_b}{2.303 i_{corr}(\beta_a + \beta_b)} \tag{2}$$

β_a—anodictafel slope, obtained by extrapolation of the anodic tafel curve.

β_c—cathodictafel slope, obtained by extrapolation of the cathodic tafel curve.

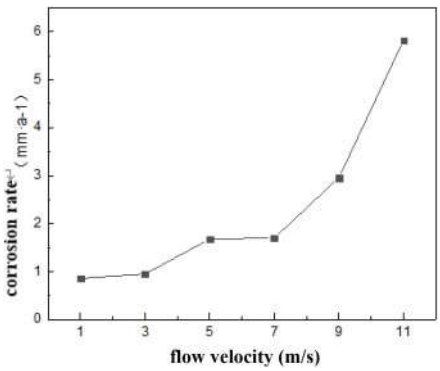

Figure 3. Corrosion rate of P110 steel under different flow velocities of 2wt.% NaCl solution.

Figure 4 shows the corrosion rate of P110 steel at different flow velocities. With the increase in flow velocity, P110 steel corrosion rate shows an overall rising trend, in 1 m/s to 3 m/s corrosion rate is relatively flat, 3 m/s to 5 m/s corrosion rate has increased, 5 m/s to 7 m/s corrosion rate again into the plateau period, and when the flow velocity is greater than 7 m/s corrosion rate began to increase significantly, which is consistent with Figure 4 in the impedance spectrum semicircle

diameter at greater than 7 m/s sudden change in the results are consistent. Can be initially judged in this flow velocity interval, 7 m/s flow velocity in 2% NaCl solution corrosion rate increase in the sudden change point, the corrosion rate at this time for 1.701 mm/a. In 1 m/s P110 steel corrosion rate of the smallest 0.859 mm/a, 11 m/s corrosion rate of the largest 5.817 mm/a, the flow velocity increases 10 m/s corrosion rate increased by 6.78 times. Through Figure 6 can be seen that the increase in flow velocity on the corrosion of P110 has a catalytic effect, but the corrosion rate and the solution flow velocity is not a simple linear relationship, in this process the corrosion of P110 steel by the cathodic oxygen diffusion and anodic dissolution reaction jointly controlled.

5 CONCLUSION

In this paper, the corrosion rate of the wall surface of P110 steel was obtained by multi-point electrochemical corrosion measurements with the change of flow velocity and Cl^- concentration, and the polarization curves and impedance spectra were obtained from the tests. The results showed that in the flowing 2wt.% NaCl solution, the corrosion rate of P110 steel increased with the increase of flow velocity, where there was a critical point of corrosion increment, and the corrosion increment changed significantly when it was greater than that flow velocity. Increased flow velocity will change the corrosive medium and charge transfer, will not only increase the corrosion rate, but also affect the corrosion product film denseness and stability, resulting in the material again exposed to the corrosive medium. The laws obtained in this paper can guide the prediction of pipe wall damage in flowing salt solutions. In addition, the results of the flow velocity effect investigation can guide the selection of construction parameters in the field.

ACKNOWLEDGMENTS

This work was supported by National Natural Science Foundation of China grant number 52105209 and 51901180, and it was made possible by Open Fund (PLC 20210401) of State Key Laboratory of Oil and Gas Reservoir Geology and Exploitation (Chengdu University of Technology).

REFERENCES

Bi Z.Y., He S.L., Li Z.B. (2013) Research and development of new SEW P110 casing. Welded Pipe, 36: 5–9.

Bo, S.C. Qu, D.R., Liu, Y. (2019) Experimental study on flow-induced corrosion of carbon steel in petrochemical circulating water. Petrochemical Corrosion and Protection, 36: 6–7.

Chen, B. (2015) Process equipment corrosion and protection. Beijing: Sinopec Press.

Deng, Q. Wang Y.C., He, W. (2017) Synergistic influence of anions and temperature on corrosion behavior of P110 steel in oilfield water. Materials Protection, 50: 12–17.

Liu J.J., Yong X.Y., Lin Y.Z. (2003) Erosion-corrosion behavior of carbon steel in different simulated flowing apparatuses. Materials Protection, 9: 25–27.

Nesic, S. Solvi, G.T. Enerhaug, J. (1995) Comparison of the rotating cylinder and pipe flow tests for flow-sensitive carbon dioxide corrosion. Corrosion, 10: 773–787.

Nestor, P. (2012) Electrochemistry and corrosion science. Beijing: Chemical Industry Press.

Wu D.D., Xiao Qi, Wang S.T. (2014) Corrosion behavior of sulfide-resistant casing steel P110SS under condition of high containing H2S/CO2 and Cl^-. Corrosion and Protection, 35: 112–115.

Zhang X.Y., Zhu B., Sun L.L. (2012) Erosion and corrosion behavior of P110 steel in chloride ions solution. Weapon Materials Science and Engineering, 35: 1–5.

Advances in Applied Chemistry and Industrial Catalysis – Saikia (Ed.)

Electrochemical corrosion behavior of steel in acid solution with some tetrazole derivative

Xulingjie Teng
Jiangxi Vocational College of Finance and Economics, Jiujiang, China
School of Materials and Energy, University of Electronic Science and Technology of China, Chengdu, China

Baohua Wu
School of Materials and Energy, University of Electronic Science and Technology of China, Chengdu, China

Xuefei Tao*
Jiangxi Vocational College of Finance and Economics, Jiujiang, China

Zhihua Tao**
School of Materials and Energy, University of Electronic Science and Technology of China, Chengdu, China

ABSTRACT: Tetrazolium violet (TV) is a tetrazole fungicide with an important pharmaceutical intermediate and it can be used as the corrosion inhibitor in steel pickling has been analyzed by electrochemical methods. electrochemical impendence spectroscopy (EIS) shows that TV is an effective inhibitor and the inhibition efficiency raised and reached 91.0% at max when the inhibitor concentration is 10^{-3}M. In addition, with the decrease of temperature and the increase of corrosion inhibitor concentration, TV's inhibition efficiency goes up.

1 INTRODUCTION

Mild steel gets extensive use in construction, industry, and other fields because of its high output and low price. (Quraishi et al. 2008) Steel is extremely liable to corrosion in practical applications due to its features of this metal. So, the corrosion inhibition of mild steel becomes extremely important. Lately, various anti-corrosion methods have been proposed. Using organic corrosion inhibitors is a kind of useful method (Qin et al. 2018). The use of corrosion inhibitors will bring many benefits, such as low price, high efficiency, and low consumption. In general, organic molecules containing specific structures such as -C=O, -C=S and -C=N have good corrosion resistance (Verma et al. 2021). Under the guidance of this idea, it is found that some tetrazole compounds have certain anticorrosion properties.

2 MATERIALS AND PREPARATION AND ELECTROCHEMICAL EXPERIMENTS

Inhibitor is tetrazolium violet (TV), namely 3-(naphthalene-1-yl)-2,5-diphenyl-2*H*-tetrazole-3-ium. Fig. 1 shows TV's molecular structure. During the experiment, the concentration gradient of TV ranges from 1×10^{-5} to 1×10^{-3}M in an acidic solution with 0.5M H_2SO_4.

The electrochemical test includes two parts: EIS and potentiodynamic polarization. Tests use a three-electrode system with a volume of 200 ml. Measurements were carried out through a CHI760E electrochemical workstation at 288 K, 298 K, 308 K, and 318 K. Reference electrode use saturated mercurous sulfate electrode (SMSE). The working electrode adopted a cylindrical low carbon steel sample with a diameter of 1.5 cm, an exposed surface area is 1.767 cm^2, and a platinum electrode as a counter electrode. The testing methods can see in reference to RSC Adv., 2020, 10, 21517 for an electrochemical model. (Tao et al. 2020).

Corresponding Authors: *Xuefei2003@126.com and **Tzh3595@uestc.edu.cn

DOI 10.1201/9781003308553-56

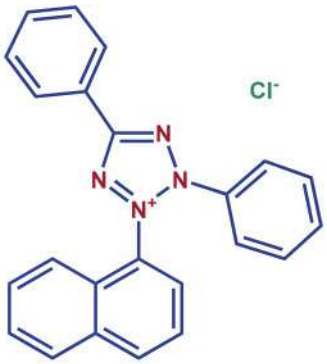

3-(naphthalen-1-yl)-2,5-diphenyl-2*H*-tetrazol-3-ium

Figure 1. Tetrazolium violet's molecular structure.

3 RESULTS AND DISCUSSION

3.1 *Electrochemical experiments*

Cathode and anode's Tafel curves for mild steel in H_2SO_4 medium with the different concentrations of TV inhibitor at 288,298,308,318K are presented in Table 1. Corrosion current density (I_{corr}) and potential (E_{corr}) are obtained via extrapolating the linear part of the cathode and anode's polarization curves. The inhibitive efficiency can be calculated from Eq. (1) (Tao et al. 2020).

$$I_{EI}\% = \frac{I_{corr} - I_{corr(inh)}}{I_{corr}} \times 100 \quad (1)$$

where I_{corr} is the corrosion current density without myclobutanil and $I_{corr(inh)}$ is the corrosion current density with different concentrations of TV in 0.5 M H_2SO_4 solution, respectively.

The inhibition efficiency increased both the decrease of temperature and the increase of corrosion inhibitor concentration as shown in Table 1. With the increase in TV concentration, corrosion inhibition efficiency changes from 10.6% to 90.9%. Along with temperature elevation, leading to serious corrosion rate as shown in Table 1, which could be attributed to the diffusion coefficients of corrosion products increasing linearly with the increase of temperature.

Table 1. Corrosion of steel in 0.5 M H_2SO_4 with different concentrations of TV base on the Tafel extrapolation.

Temperature (K)	Concentration (M)	E_{corr} (mV vs. SMSE)	β_c (mV·dec^{-1})	β_a (mV·dec^{-1})	I_{corr} (μA·cm^{-2})	I_{EI} %
	Blank	−921	148.7	132.5	3119.2	–
	1.0×10^{-5}	−919	162.2	147.1	2789.2	10.6
	3.2×10^{-5}	−910	136.9	98.9	1407.9	54.9
288	1.0×10^{-4}	−907	137.5	118.7	1132.3	63.7
	3.2×10^{-4}	−903	127.9	123.5	1070.1	65.7
	1.0×10^{-3}	−883	100.8	88.0	283.50	90.9
	Blank	−914	163.3	131.3	3550.9	–
	1.0×10^{-5}	−907	150.5	116.6	3125.9	12.0
	3.2×10^{-5}	−907	155.3	119.2	2911.5	18.1
298	1.0×10^{-4}	−911	155.7	156.2	2579.3	27.4
	3.2×10^{-4}	−904	136.4	134.7	1835.7	48.3
	1.0×10^{-3}	−892	110.4	86.0	361.0	89.8

(*continued*)

Table 1. Continued.

Temperature (K)	Concentration (M)	E_{corr} (mV vs. SMSE)	β_c (mV·dec^{-1})	β_a (mV·dec^{-1})	I_{corr} (μA·cm^{-2})	I_{EI} %
	Blank	−924	181.3	154.7	8414.7	–
	1.0×10^{-5}	−924	185.4	158.6	7220.7	14.2
	3.2×10^{-5}	−924	188.4	154.8	6949.1	17.4
308	1.0×10^{-4}	−913	180.9	137.6	5551.3	34.0
	3.2×10^{-4}	−906	152.1	152.6	4073.8	51.6
	1.0×10^{-3}	−899	129.1	117.3	1430.6	83.0
	Blank	−932	199.7	183.1	15658.0	–
	1.0×10^{-5}	−927	198.6	184.3	13954.7	10.9
	3.2×10^{-5}	−927	200.5	183.5	12964.4	17.2
318	1.0×10^{-4}	−910	228.6	165.2	11430.9	27.0
	3.2×10^{-4}	−904	165.4	151.2	6230.4	60.2
	1.0×10^{-3}	−899	165.5	163.7	3620.5	76.9

The Nyquist impedance parameters at different temperatures with and without a TV at 288, 298, 308, and 318K are shown in Table 2. EIS shows that the radius of the impedance spectrum increases when inhibitor concentration raises and reached a maximum at 10^{-3} M as shown in Figure 2.

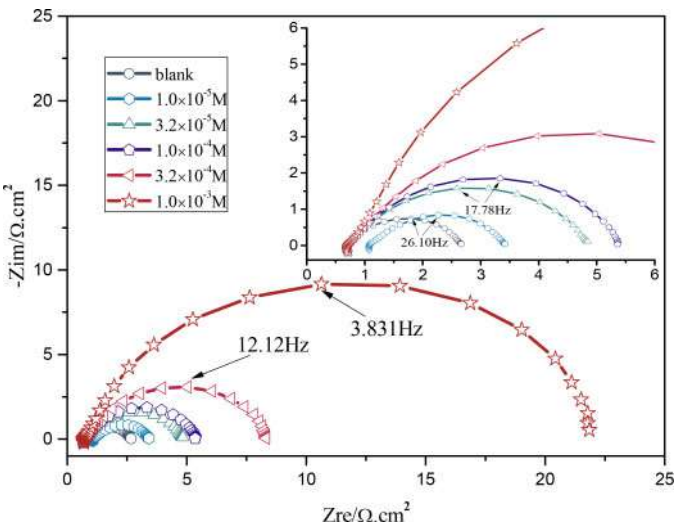

Figure 2. Nyquist plots for mild steel in 0.5 M H_2SO_4 with various concentrations of the TV at 288K.

Nyquist spectra show only one capacitive loop, and thus there are just one-time constants, so Nyquist plots can be fitted by Randle equivalent circuit like Figure 3. And R_s means solution

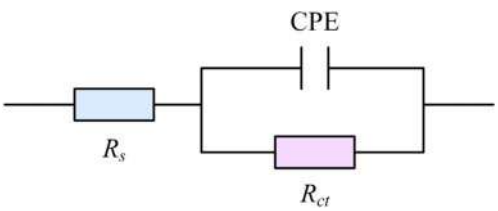

Figure 3. Equivalent circuit diagram for fitting.

resistance, CPE is a capacitance and R_{ct} is charge-transfer resistance. For a circuit including a CPE, the double-layer capacitance values (C_{dl}) can be calculated from CPE parameter values Y_0 and n by the following equation:[4]

$$C_{\mathrm{dl}} = \frac{Y_0 \omega^{n-1}}{\sin\left(n(\pi/2)\right)} \tag{2}$$

Thus, all of the Nyquist plots were fitted by Randle equivalent circuit, and fitting parameters at different temperatures are shown in Table 2. The value of C_{dl} decreased with increasing the TV inhibitor concentration at the same temperature, C_{dl} values are negatively correlated with inhibitor concentration. Generally, organic molecules are bigger and have a smaller dielectric constant than a water molecules.In the Helmholtz model, the thickness of the double layer is determined by C_{dl}. (Ehsani et al. 2015)

$$C_{\mathrm{dl}} = \frac{\varepsilon^0 \varepsilon}{d} S \tag{3}$$

d is the thickness of C_{dl}, S is the electrode's surface area, ε^0 is the permittivity of air and ε is local permittivity. C_{dl}'s change is mainly because organic molecules substitute for water molecules adsorb on the electrode's surface. (Ramazan et al. 2018)

Table 2. Impedance parameters and inhibition efficiency for the corrosion of copper in 0.5 M H_2SO_4solution with different concentrations of Tetrazolium Violet.

Temperature	Concentration	R_s	CPE		C_{dl}	R_{ct}		
K	(M)	(Ω cm^2)	$Y(\mu\Omega^{-1}s^n cm^{-2})$	n	(μF cm^{-2})	(Ω cm^2)	Error (%)	I_{EZ} %
	Blank	0.683	7.601	0.80	2.882	1.999	0.913	–
	1.0×10^{-5}	1.104	8.717	0.76	2.757	2.346	1.068	14.8
288	3.2×10^{-5}	0.737	6.285	0.80	2.573	4.168	1.024	52.0
	1.0×10^{-4}	0.742	4.087	0.82	1.821	4.722	1.139	57.7
	3.2×10^{-4}	0.763	3.526	0.81	1.620	7.824	1.560	74.5
	1.0×10^{-3}	0.748	3.489	0.85	2.227	22.20	2.125	91.0
	Blank	0.867	3.227	0.84	82.5	1.557	0.685	–
	1.0×10^{-5}	0.501	2.916	0.86	1.14	1.932	0.695	19.4
298	3.2×10^{-5}	0.702	3.185	0.86	1.47	2.209	0.743	29.5
	1.0×10^{-4}	0.644	1.255	0.80	0.329	3.645	1.137	57.3
	3.2×10^{-4}	0.657	3.052	0.82	1.27	5.049	1.307	69.2
	1.0×10^{-3}	0.852	2.705	0.84	1.48	13.80	1.607	88.7
	Blank	0.751	5.853	0.82	4.62	0.7998	0.899	–
	1.0×10^{-5}	0.740	9.506	0.77	4.64	0.8426	1.029	5.1
308	3.2×10^{-5}	0.687	5.523	0.83	3.74	0.9359	0.865	14.5
	1.0×10^{-4}	0.555	2.162	0.84	122	1.5660	1.117	48.9
	3.2×10^{-4}	0.600	3.764	0.82	5.81	2.4200	1.164	67.0
	1.0×10^{-3}	0.751	3.202	0.83	5.77	6.4740	1.806	87.6
	Blank	0.567	18.76	0.78	4.62	0.2998	1.912	–
	1.0×10^{-5}	0.601	21.09	0.78	5.199	0.3066	2.210	2.2
318	3.2×10^{-5}	0.665	17.27	0.78	4.64	0.3815	1.835	21.4
	1.0×10^{-4}	0.635	23.90	0.76	6.29	0.3829	1.872	21.7
	3.2×10^{-4}	0.624	21.15	0.75	5.81	0.5409	1.911	44.6
	1.0×10^{-3}	0.664	18.25	0.76	5.77	1.0470	1.960	71.4

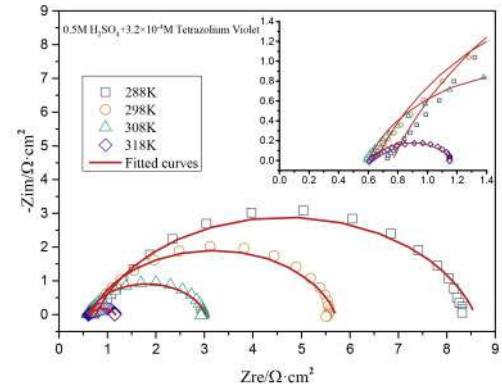

(a)

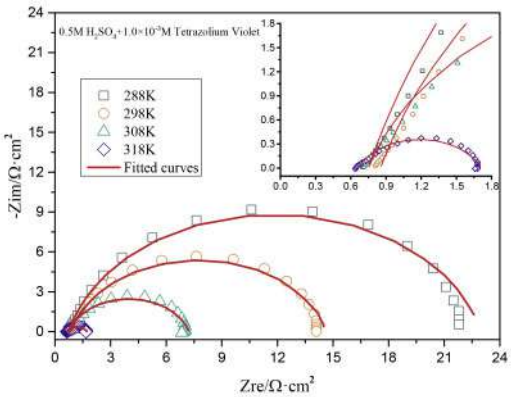

(b)

Figure 4. The fitting results of EIS data at different temperatures: **(a)** 3.2×10^{-4} M and **(b)** 10^{-3} M TV.

Fitting Nyquist diagrams of EIS data in 0.5 M H_2SO_4 containing 3.2×10^{-4}M and 1.0×10^{-3} MTV at 288 K, 298 K, 308 K, and 318 K are shown in Figure 4. From diagrams, we find that experimental data fit nicely with an equivalent circuit, this result shows that the radius of the impedance spectrum increases when inhibitor concentration raises.

From Table 2, we can find that corrosion efficiency calculated by R_{ct} increases when TV concentration increases. As a result, inhibition efficiency raised and reached 91.0% at max when the inhibitor concentration is 10^{-3}M, which reveals strong inhibition ability. This result greatly supports the results obtained by the potentiodynamic polarization method.

3.2 *SEM*

To observe the inhibition effect of TV more intuitively. Mild steel blocks' surface morphologies etched in H_2SO_4 solution at 308 K for 3 hours are demonstrated in Figure 5. Figure 5(a) shows mild steel blocks' surface morphology that has not been corroded. Figure 5(b) and (c) shows the surface morphology of blocks corroded in sulfuric acid medium without corrosion inhibitor and sulfuric acid solution with 10^{-3} M TV, respectively. Figure 5b shows obvious corrosion compared with Figure 5(a). Compared with Figure 5(b), Figure 5(c) shows that the corrosion situation is reduced after adding a corrosion inhibitor. Therefore, the corrosion was inhibited by the presence

of a TV in the corrosion solution. The scratches shown in the photos were caused by polishing before corrosion.

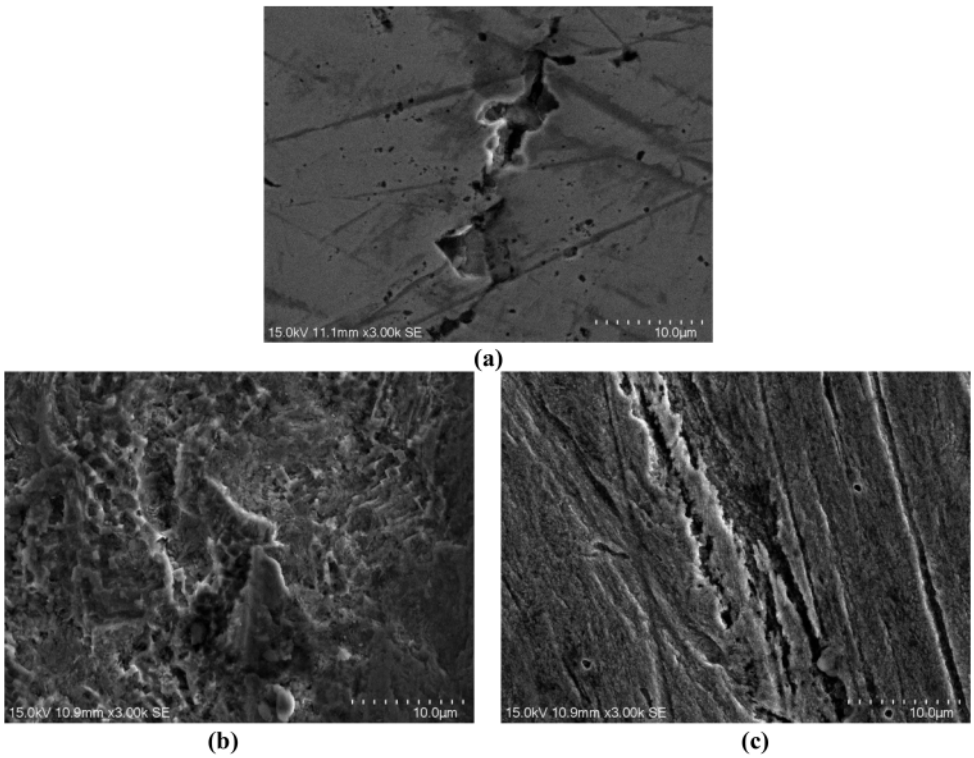

Figure 5. SEM morphology of steel specimens: **(a)** only surface polishing, immersed in 0.5 M H_2SO_4 solution for 3 h without **(b)** and with 10^{-3} M TV **(c)**.

4 CONCLUSION

The TV as steel inhibitor in 0.5 M H_2SO_4 was found to have a promising inhibition performance and Corrosion inhibition efficiency depends on the concentration of inhibitor and temperature. Corrosion inhibition efficiency is significantly improved with the increase of the corrosion inhibitor concentration. However, with the increase in temperature, the corrosion inhibition efficiency decreases slightly. The corrosion inhibition efficiency of steel is in acceptable agreement with those obtained from potentiodynamic polarization and EIS studies. The SEM tests have shown that steel corrosion could be inhibited by the TV inhibitor.

ACKNOWLEDGMENTS

The authors gratefully acknowledge the support of the Natural Science Foundation of Jiangxi Province of China under Grant No. 20212BAB204046.

AUTHORS' BIOGRAPHY

Taoxuefei is an Associate Professor at the Jiangxi Vocational College of Finance and Economics. Taoxuefei has been working as a low-carbon engineering management expert and his engineering management degree from the school of mechanical engineering, Chongqing University.

Taozhihua is an Associate Professor at the University of Electronic Science and Technology of China. His research interests include advanced material and process for PCB manufacture, reliability in Cu interconnection, and corrosion electrochemistry.

REFERENCES

A. Ehsani, R. Moshrefi, M. Ahmadi, Electrochemical Investigation of Inhibitory of New Synthesized 3-(4-Iodophenyl)-2-Imino-2,3-Dihydrobenzo d Oxazol-5-yl 4-Methyl-benzenesulfonate on Corrosion of Stainless Steel in Acidic Medium, Journal of Electrochemical Science and Technology, **2015**, 6, 7–15.

M.A. Quraishi, I. Ahamad, A.K. Singh, S.K. Shukla, B. Lal, V. Singh, N-(Piperidinomethyl)-3- (pyridylidene)amino isatin: A new and effective acid corrosion inhibitor for mild steel, *Materials Chemistry and Physics,* **2008**, 112, 1035–1039.

T.T. Qin, J. Li, H.Q. Luo, M. Li, N.B. Li, Corrosion inhibition of copper by 2, 5-dimercapto-1, 3, 4-thiadiazole monolayer in acidic solution. *Corros. Sci.* **2018**, 53, 1072–1078.

Ramazan Solmaz, Ece Altunbaş Şahin, Ali Döner, Gülfeza Kardaş, The investigation of synergistic inhibition effect of rhodanine and iodide ion on the corrosion of copper in sulphuric acid solution. *Corros. Sci.* **2018**, 53, 3231–3240.

C. Verma, S.H. Alrefaee, M.A. Quraishi, E.E. Ebenso, C.M. Hussain, Recent developments in sustainable corrosion inhibition using ionic liquids: A review, Journal of Molecular Liquids, **2021**, 321.

Zhihua Tao, Yuanxun Li, Yi Xiao Peng, Hua Su, et al, Electrochemical studies of prothioconazole as a novel corrosion inhibitor for copper in acidic solutions. *RSC Adv.* **2020**, 10, 21517.

Advances in Applied Chemistry and Industrial Catalysis – Saikia (Ed.)

Adsorption of different plant straws on congo red

Y. Qu*, S. Wang**, L. Wang & X. Xu
Department of Environmental Science, Qilu Institute of Technology, Jinan, China

ABSTRACT: Maize straw, rice straw, and soybean straw were modified with citric acid to prepare citric acid modified straw adsorbent and simulate adsorption of Congo red dye wastewater. The effect of adsorbent on the adsorption of Congo red dye wastewater under different conditions was studied. The results showed that the adsorption effect of the modified straw adsorbent was the most obvious under the acidic environment of 25°C temperature, 40 mg/L initial concentration of Congo red, and pH between 2 and 6.

1 INTRODUCTION

Plant straw accounts for about 80% of the earth's plant biomass (Haudin 2007), which is rich in nitrogen, phosphorus, cellulose, lignin, and other substances (Liu 2021). Plant straw is not only a renewable biomass resource (Girgis 2002) but also a material basis for maintaining ecological balance. However, due to the lack of relevant knowledge and technology, for a long time, a large amount of straw was left idle, resulting in the waste of straw resources.

The printing and dyeing industry has always been an important traditional industry in China, which has developed rapidly in the past 20 years. With the increasingly strict wastewater discharge standards, higher requirements and challenges have been put forward for the treatment of printing and dyeing wastewater (Su 2020). At present, the treatment methods of dye wastewater include chemical oxidation (Pje 2019) and membrane separation (Polizzi 2020). However, most of these methods have some disadvantages, such as complicated technology and high cost. The adsorption method is a traditional sewage treatment method, whose principle is to use porous adsorption materials to adsorb pollutants (Gazaille 2020). The development of traditional adsorbents is limited due to their high price, while the plant straw has the advantages of wide source, low price, and easy acquisition, which makes the plant straw have a great development prospect in the field of preparing new adsorbents.

To realize the maximum utilization of straw resources, the paper uses corn, rice, and soybean straw as raw materials and uses citric acid to prepare modified corn straw adsorbent, modified rice straw adsorbent, and modified soybean straw adsorbent. The adsorption effect of modified plant straw on dye wastewater under different conditions was studied, and the adsorption and regeneration performance of the adsorbent was explored.

2 EXPERIMENTAL METHODS

2.1 *Preparation of adsorption materials*

2.1.1 *Straw pretreatment*

Corn straw, rice straw, and soybean straw were cut into small sections, washed with deionized water, dried and crushed, sieved straw powder was washed with deionized water and dried in the oven to obtain corn straw sorbent (CS), rice straw sorbent (RS) and soybean straw sorbent (SS).

Corresponding Authors: *805025846@qq.com and **3105992718@qq.com

 DOI 10.1201/9781003308553-57

2.1.2 *Preparation of modified straw adsorbent*

CS, RS, and SS were boiled in 0.5 mol/L sodium hydroxide solution for 1 h. After cooling, they were washed with deionized water until neutral. Finally, the materials were dried in a 65°C oven to obtain the alkalized corn straw sorbent, rice straw sorbent, and soybean straw sorbent. Then, weigh the alkalized corn straw adsorbent, rice straw adsorbent, and soybean straw adsorbent into three beakers, then weigh citric acid and potassium dihydrogen phosphate in proportion and pour them into three beakers, then add an appropriate amount of deionized water. After full agitation, an ultrasound was performed. After cooling, the modified soybean straw adsorbent (MSS), modified corn straw adsorbent (MCS), and modified rice straw adsorbent (MRS) were obtained by deionizing water washing to neutral and drying.

2.2 *Study on adsorption performance of modified straw*

The Congo red solution with a volume of 50 mL and a concentration of 40 mg/L was added into a conical flask with 150 mL, followed by MCS, MRS, MSS, CS, RS, and SS of the same volume. The solution was put on a shaking table and shaken for 60 min. The absorbance of the supernatant was measured at 497 nm.

3 RESULTS AND DISCUSSION

3.1 *Comparative analysis of adsorption properties of straw adsorbent before and after modification*

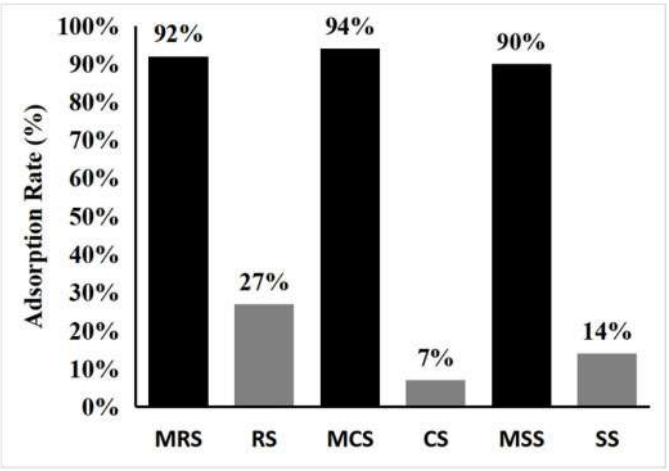

Figure 1. Comparison of straw adsorption rate before and after modification methods.

It can be seen from Figure 1 that the adsorption rates of RS, CS, and SS are lower than those of MRS, MCS, and MSS, among which the adsorption rates of MCS and CS change the most. The reason why the adsorption rates of the three kinds of straw after modification are higher than before modification is that the internal structure of straw changes due to the alkalization of sodium hydroxide (Xing 2021). In addition, the activation of the straw with citric acid can provide carboxyl functional groups for ion exchange (Gamoudi 2019), which improves the adsorption performance of the straw and increases the absorption rate of the modified straw.

3.2 *Analysis of the influence of dosage on adsorption performance*

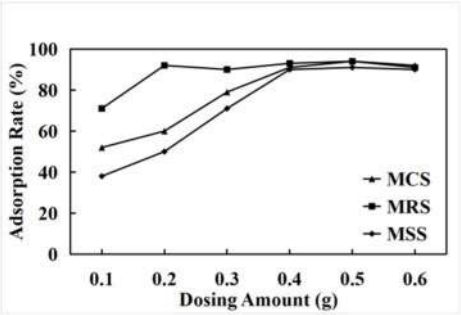

Figure 2. The effect of dosing amount on the adsorption performance of MCS, MRS, and MSS.

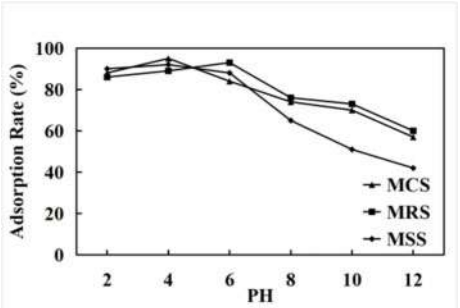

Figure 3. The effect of PH on the adsorption performance of MCS and MRS and MSS.

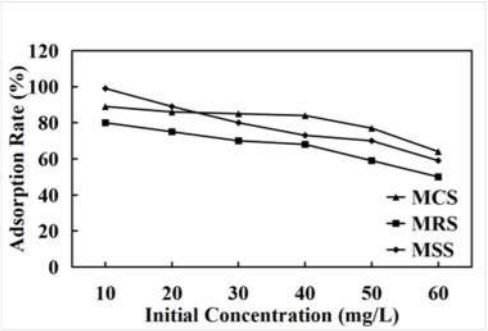

Figure 4. The effect of initial concentration on the adsorption performance of MCS and MRS and MSS.

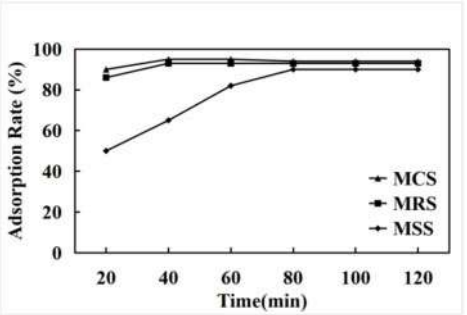

Figure 5. The effect of time on the adsorption performance of MCS and MRS and MSS.

As shown in Figure 2, in general, the change of the adsorption rate of MCS, MSS, and MRS for Congo red showed an upward trend at the beginning, and then gradually slowed down. The adsorption rate increases with the increase of the dosage because the number of sites available for dye adsorption increases with the increase of adsorbents[10]. The reason why the latter adsorption effect remained unchanged was that the adsorption equilibrium state was reached between the sites of straw adsorbent and dye. Considering economic factors, 0.2g MRS, 0.4g MCS, and MSS were selected in the experiment.

3.3 *Analysis of the influence of system pH on adsorption performance*

As shown in Figure 3, when pH is between 2 and 6, the adsorption effect of MSS, MRS, and MCS on Congo red is better. With the increase in pH, the adsorption rate of Congo red on MSS, MRS and MCS decreased from acid to alkali. In general, straw adsorbent has a good adsorption effect on Congo red dye solution under acidic conditions, which is due to the strong electrostatic attraction between cations on the surface of the modified straw adsorbent and anionic dyes in the solution (Zaitseva 2019), thus improving the removal rate of anionic dyes. With the increase of pH, the solution system is in an alkaline environment. At this point, the surface of the adsorbent is negatively charged, which generates electrostatic repulsion with Congo red molecules (Yang 2021), and the adsorption rate of Congo red decreases. Therefore, the pH of MSS and MCS is between 2 and 4, and the pH of MRS is 6.

3.4 *Analysis of the influence of initial dye concentration on adsorption performance*

As shown in Figure 4, the adsorption rates of MSS, MRS, and MCS decreased with the increase of the initial concentration of Congo red. The reason is that with the increase of the initial concentration of dye, the number of dye molecules in the solution keeps increasing, and the dye molecules gradually occupy the adsorption sites on the surface of the adsorbent (Mohan 2007). When the adsorption reaches saturation, the amount of adsorbent will not change, but the initial concentration keeps increasing, leading to a decrease in the adsorption rate (Marzin 2020). When the initial concentration of MSS, MRS, and MCS is greater than 10 mg/L, the adsorption rate begins to decline, indicating that the modified straw is more suitable for the treatment of Congo red dye wastewater with a lower concentration. Therefore, 40 mg/L Congo red solution was selected for the experiment.

3.5 *Analysis of the influence of time on rigid adsorption performance*

It can be seen from Figure 5 that when the adsorption time of MRS and MCS is between 20 min and 40 min, the adsorption rate increases rapidly, and then slows down after 40 min, indicating that the adsorption equilibrium has been reached at this time (Peng 2019). This phenomenon may be caused by the fact that the adsorption site on the surface of the adsorbent at the initial stage of adsorption is not saturated, so adsorption is relatively easy to carry out. Thereafter, as the adsorption time increases, the adsorption sites on the surface of the adsorbent are basically in a saturated state, which leads to the slowing down of the adsorption rate. Therefore, the adsorption time of MRS and MCS was 40 min, and that of MSS was 80 min.

4 CONCLUSION

(1) The adsorption performance of MRS, MCS, and MSS on Congo red dye solution is better than that of RS, CS, and SS, and the change of adsorption rate of MCS and CS is 87%. Soybeans followed at 76 percent. The adsorption rate of rice straw before and after modification was the lowest, which was 65%.
(2) When MRS dosage was 0.2 g, the initial concentration of Congo red was 40 mg/L, pH was 6, and the reaction time was 40 min at 25°C, the adsorption effect was the best. When the dosage of MCS was 0.4 g, the pH was between 2 and 4, and the reaction time was 40 min at 25°C, the adsorption effect reached its best. When the dosage of MSS was 0.4 g, the pH was between 2 and 4, and the reaction time was 40 min at 25°C, the adsorption effect was the best.

REFERENCES

Gamoudi S (2019). Adsorption of organic dyes by HDPy+-modified clay: Effect of molecular structure on the adsorption. J. Journal of Molecular Structure, 77(03): 522–531.

Gazaille C (2020). Characterization of Biological Material Adsorption to the Surface of Nanoparticles without a Prior Separation Step: a Case Study of Glioblastoma-Targeting Peptide and Lipid Nanocapsules. J. Pharmaceutical Research, 38(4): 681–691.

Girgis B S (2002). Cereal straw as a resource for sustainable biomaterials and biofuels. J. Materials Letters, 7: 57–164.

Hattori H (2010). AntiReflection Surface with Particle Coating Deposited by Electrostatic Attraction. J. Advanced Materials, 13(1):51–54.

Haudin, CS (2007). Effect of aeration on mobility of selenium in columns of aggregated soil as influenced by strawamendment and tomato plant growth. J. GEODERMA, 141(1-2): 98–110.

Jia D (2015). Adsorption of Pb (II) from aqueous solutions using corn straw. J. Desalination & Water Treatment, 56(01): 223–231.

Liang X (2021). Hydroxyl/amino and Fe (III) co-grafted graphite carbon nitride for photocatalytic removal of volatile organic compounds. J. Environmental Research, 197:111044.

Marzin T (2020). Using Microfluidic Set-Up to Determine the Adsorption Rate of Sporosarcina pasteurii Bacteria on Sandstone. J. Transport in Porous Media, 132(11).
Mohan D (2007). Pittman C U. Arsenic removal from water/wastewater using adsorbents–A critical review. J. Journal of Hazardous Materials, 142(1–2): 1–53.
Na S (2020). Concentrations and Seasonal Variations of Perfluorinated Compounds in Sludge from Three Wastewater Treatment Plants in China. J. Analytical Letters, 53(15): 1–13.
Peng H (2019). Orthotropic mechano-sorptive creep behavior of Chinese fir during the moisture adsorption process determined in tensile mode via dynamic mechanical analysis (DMA). J. Holzforschung, 73(3): 229–239.
Pje A (2019). Slow-release permanganate versus unactivated persulfate for long-term in situ chemical oxidation of 1,4-dioxane and chlorinated solvents. J. Chemosphere, 221: 802–811.
Polizzi V (2020). Molecular weight-based fractionation of lignin oils by membrane separation technology. J. Holzforschung, 74(2): 166–174.
Yang Z (2021). Anomalous phonon softening of G-band in compressed graphitic carbon nitride due to strong electrostatic repulsion. J. Applied Physics Letters, 118(2): 023103.
Zaitseva E S (2019). Self-Consistency in Calculating the Rates of Adsorption and Desorption and an Isotherm of Adsorption on a Rough Surface of Aerosols. J. Russian Journal of Physical Chemistry A, 93(4): 631–638.

Chemical devices and environmental chemistry research

Advances in Applied Chemistry and Industrial Catalysis – Saikia (Ed.)

Constructed wetland systems vegetated with different plants applied to the treatment of nitrobenzene wastewater

Diannan Huang* & Baofeng Zhang
Municipal and Environmental Engineering Institute, Shenyang Jianzhu University, Shenyang, Liaoning, China

Kui Jing
School of Environment, Liao Ning University, Shenyang, Liaoning, China

Li Zhang, Rubing Bai & Rui Li
Municipal and Environmental Engineering Institute, Shenyang Jianzhu University, Shenyang, Liaoning, China

ABSTRACT: Constructed wetlands (CWs) were often built for municipal wastewater treatment. However, there have been few reports on the refractory organics industrial wastewater treatment, such as nitrobenzene (NB) wastewater. In this paper, four laboratory-scale CWs (CW only, CWs planted with *Echinodorus amazonicus* (EA), *Calamus,* and *Water hyacinth* were set up to treat artificial NB wastewater in this study. An inflow NB load was between 10.00 and 30.00 mg/L. The results showed that higher NB degradation efficiency was got in CWs with plant groups. The highest NB removal reached 92.8% in CW planted with EA. This investigation indicated that the potential application of CWs for NB wastewater treatment and a proper choice of plants can further increase NB removal efficiency.

1 INTRODUCTION

Nitrobenzene (NB) is massively produced and widely used in manufacturing organic products, such as aniline, lubricating oils, explosives, dyes, solvents, drugs, pesticides, and synthetic rubber. Nitrobenzene is one of the organic compounds listed as a priority pollutant by the US Environmental Protection Agency (USEPA) based on known or suspected carcinogenicity, mutagenicity, teratogenicity, and high acute toxicity. Several previous investigations found that NB concentrations in rivers were frequently detected at significant values, especially in the rivers of North China. The detection rate of NB was 83.2% for all the samples, with a mean value of 18.1 $ng{\cdot}L^{-1}$ and a range from <0.3 to 8450.0 $ng{\cdot}L^{-1}$ (Gao et al. 2008). The popular presence of NB in the aquatic environment would threaten the health of an aquatic ecosystem. Therefore, the treatment of NB wastewater is an arduous task.

At present, wastewater containing NB could be treated by physical-chemical and biological methods. Physical-chemical methods such as ozonization (Zhao et al. 2008), electrochemical reduction (Liu et al. 2012), adsorption (Qin et al. 2007), ultrasonic irradiation (Hung et al. 2000; Zhao et al. 2009), Fenton oxidation (Jiang et al. 2011), photochemical reduction (Makarova et al. 2000), and radiolytic degradation (Zhang et al. 2007), etc. have been reported. However, physical-chemical methods were often with the character high operating costs and complex control requirements. These limited their successful application on NB contaminated wastewater treatment, especially in economically undeveloped areas.

Compared to physical-chemical methods, the biological method to its low cost, no second product, and environmental friendliness has become an advantaged method for NB removal. Among

*Corresponding Author: 7nan@163.com

DOI 10.1201/9781003308553-58

the numerous biological technologies, constructed wetlands (CWs) as a cost-effective, and efficient alternative biological method have increasingly become globally granted for wastewater treatment (Garcia et al. 2010; Vymazal & Cycling 2005). Traditionally, CWs were mainly used for nutrient and organic matter retention in domestic and municipal sewage, stormwater, and agricultural runoff (Kadlec & Knight 1996; Vymazal et al. 1998). However, there were few studies on NB wastewater treatment utilizing CWs. Lin (Lin et al. 2012) applied Anaerobic Baffled Reactor (ABR) coupled with CWs treated NB wastewater. According to their studies, the focus of the study was NB removal efficiency. Few of them investigated the effects of plants and media during CW treatment.

In this study, CWs with different plants (*Echinodorus amazonicus* (EA), *Calamus,* and *Water hyacinth*) were used to test NB degradation efficiency. The aim of this study was to investigate whether the constructed wetland system coupled with plants has a higher NB removal efficiency than conventional CWs. In addition, NB removal efficiency under varying NB loads was examined to test the tolerance of CWs for NB pollution.

2 MATERIALS AND METHODS

2.1 *Multimedia constructed wetland*

The multi-media constructed wetlands (CWs) systems (each with three parallel) were established in a PVC container with 1.00m length× 0.50 m width× 0.40 m depth. The container was packed with multiphase packing. The following composition comprised the surface to bottom layer: the rhizosphere layer (0∼15 cm), filled with native loam soil; 15∼20 cm layer was covered with grit (grain size:1∼5 mm); 20∼40 cm layer was filled with quartzite (grain size:10∼45 mm). The water inlet pipe was connected to a piezometer to control the water level within the CWs. Four perforated PVC pipes were placed in front of the constructed wetland reactors for sampling. The sketch of constructed wetland was shown in Figure 1.

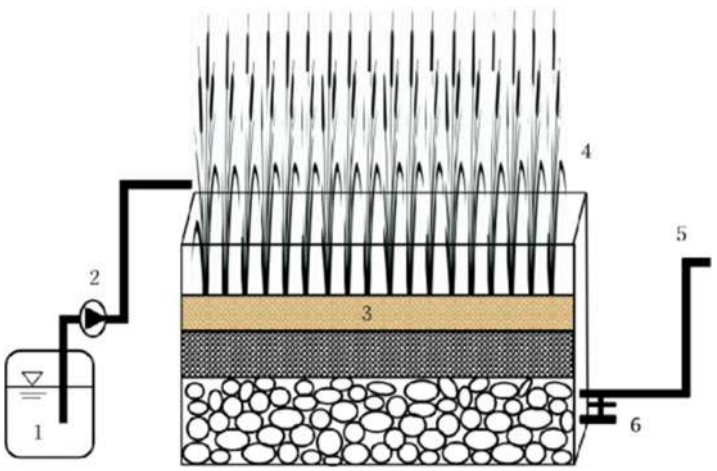

Figure 1. Laboratory-scale constructed wetlands (1, feeding tank; 2, peristaltic pump; 3, sample outlet; 4, plants; 5, outflow; 6, drain valve).

2.2 *Experimental materials*

Modified artificial wastewater containing nitrobenzene (NB), ammonium, chemical oxygen demand (COD), and phosphate concentrations were used in this study. Influent artificial wastewater was prepared by using $C_6H_{12}O_6$, NH_4Cl, and $K_2HPO_4{\cdot}3H_2O$ dissolved in deionized water according to the required concentrations (Table 1). Moreover, a trace mineral solution containing

EDTA-Na, $FeSO_4 \cdot 7H_2O$, $CaCl_2 \cdot 6H_2O$, $ZnCl_2$, $CuCl_2 \cdot 5H_2O$ was added to the artificial wastewater (1 ml/L). Since NB was a relatively water-insoluble liquid at room temperature, it was prepared by dissolving in ethanol, and then the nitrobenzene–ethanol mixture was added to deionized water to get artificial NB wastewater. The equalized wastewater was delivered to the CW system continuously at a rate of approximately 54.0 L/d to yield an HRT of 1d. Table 1 presents the corresponding influent loads and operation characteristics of the wetland reactors.

Table 1. The character of artificial wastewater quality.

Operation characteristics	NH_4^+-N(mg/L)	PO_4^{3-}-P(mg/L)	COD (mg/L)	Pollution load ($g \cdot m^{-2} \cdot d^{-1}$)
	13±3	5±1	150±22	1.34, 2.01, 2.69, 3.35 and 4.03

2.3 *Experimental design*

Four experiments (CW only, CWs planted with *Echinodorus amazonicus* (EA), *Calamus,* and *Water hyacinth*) were designed to investigate the variation of NB concentration under different treatments.

2.4 *Data analysis*

All experiments were carried out in triplicate to obtain reliable data and the results are presented here as mean±standard deviation (SD). Statistical analyses were performed using the statistical software package SPSS 16.0, and the P-value was used to assess the statistical significance and quantitative differences.

3 TEST RESULTS AND DISCUSSIONS

3.1 *Performance of CWs for NB removal under different NB loads*

The effect of nitrobenzene loading on the performance of the CW is shown in Figure 2. The CW reactor performance was studied under various nitrobenzene loads (1.34∼4.03 $g \cdot m^{-2} \cdot d^{-1}$) at an influent nitrobenzene concentration between 10.00 and 30.00 mg/L. The hydraulic retention time (HRT) was 24 h. CW, CW-W, CW-EA, and CW-C were carried out to test the removal efficiencies of NB under CW only, CW with *Water hyacinth*, *Echinodorus amazonicus* (EA), and *Calamus* plant treatment. The result showed that, when the NB organic load was low, the nitrobenzene

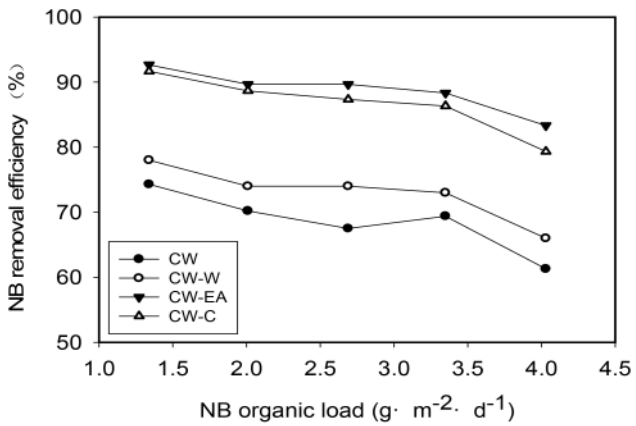

Figure 2. Nitrobenzene removal efficiency in CW at various NB organic loads.

removal efficiency was high to 74.0∼92.7%. With the increasing NB pollution load, the degradation rate decreased to 61.3∼83.3%. This phenomenon may be due to the toxic NB inhibited in the phytodegradation and the higher concentration of NB caused higher inhibition of the activity of plant growth, thus resulting in a relatively low NB removal efficiency. This result conformed to the study reported by Zhao that high influent NB concentration can decrease the biodegradation efficiency of NB (Zhao et al. 2011).

3.2 *Removal of NB under different treatments*

The performances of NB degradation in the four experimental phases of different CW treatments are shown in Figure 3. Influent NB concentration gradually increased from 10mg/L to 30mg/L. When NB wastewater was treated with unplanted CW (Figure 3(a)), the effluent NB concentration ranged from 2.4 to 13.2 mg/L, accordingly, the NB removal efficiency was from 56.6% to 77.9%. To test plant effects to NB removal, NB concentration variation in CW planted with *Water hyacinth, Echinodorus amazonicus,* and *Calamus* were shown in Figure 3(b–d), respectively. The result showed that NB removal efficiencies kept high during NB concentration ranging from 10 mg/L to 25 mg/L, however, with the increase of influent NB to 30 mg/L, NB removal efficiency decreased sharply. It may be the high influent NB concentration induced deleterious effects on the plant and thus inhibited its purification for NB wastewater. In CW-W, CW-EA, CW-C test, NB removal efficiency was ranged from 65.9% to 80.8%, 82.0% to 92.8%, and 78.5% to 91.7%, respectively. Through comparing these three kinds of a plant to NB removal ability, it is seen that their purification ability is *Echinodorus amazonicus* > *Calamus* >*Water hyacinth.* It was seen that NB removal efficiency was influenced by the species of plant. This phenomenon might be due to that the different plants always have different roots; while various root types would form discrepancy rhizosphere ecological environment, thus influencing the NB removal.

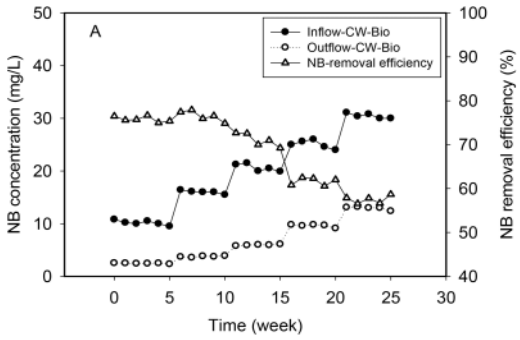

(a) NB removal in unplanted CW

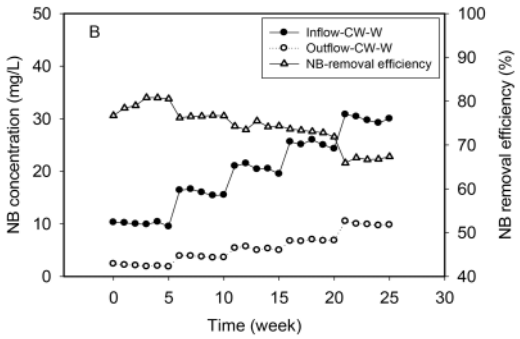

(b) NB removal in CW planted with water hyacinth

Figure 3. NB removal efficiency in various CW treatments.

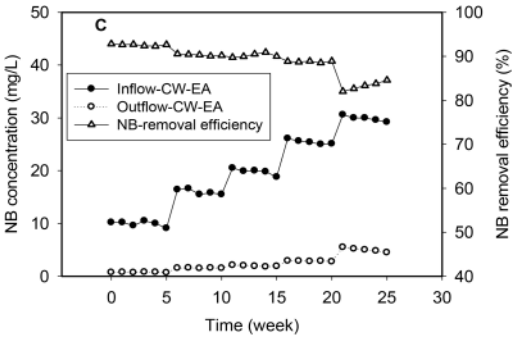

(c) NB removal in CW planted with EA

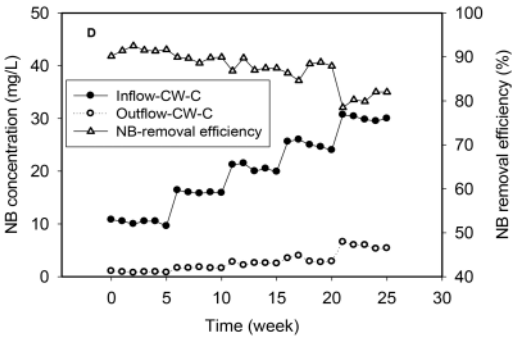

(d) NB removal in CW planted with calamus

Figure 3. Continued.

4 CONCLUSION

The results of the study indicated that NB wastewater can be treated efficiently by CWs. Adding plants can enhance NB removal efficiency in the CW system. The highest NB removal reached 92.8%. Plant species would affect NB removal efficiency in the CW system Their purification ability is *Echinodorus amazonicus* > *Calamus* >*Water hyacinth.* Plants play an important role in improving the removal rate of NB.

ACKNOWLEDGMENTS

This work was financially supported by the general project scientific research plan of the Liaoning Provincial Department of Education (no: LJKZ0601) and water pollution control and treatment of major national science and technology projects (no: 2015ZX07202-012).

REFERENCES

Gao J. J., Liu L. H., Liu X. R., Zhou H. D., Wang Z. J., Huang, S. B (2008). Concentration level and geographical distribution of nitrobenzene in Chinese surface waters, J. Environ. Sci. (China) 20, 803–805.

Garcia J., Rousseau D. P. L., Morato J., Lesage E., Matamoros V., JOSEP M.B (2010). Contaminant removal processes in subsurface-flow constructed wetlands: a review. Crit Rev. Env. Sci. Tec. 40, 561–661.

Hung H. M., Ling F. H., Hoffmann M (2000). Kinetics and mechanism of the enhanced reductive degradation of nitrobenzene by elemental iron in the presence of ultrasound, Environ Sci. Technol. 34, 1758–1763.

Jiang B. C., Lu Z. Y., Liu F. Q., Li A. M., Dai J. J., Xu L., Chu L. M (2011). Inhibiting 1,3-dinitrobenzene formation in Fenton oxidation of nitrobenzene through a controllable reductive pretreatment with zero-valent irliangon. Chem Eng. J 64, 1385–1392.

Kadlec R. & Knight R (1996). Treatment Wetlands. Lewis Publishers, Boca Raton, lorida.

Lin Y., Yin J., Wang J., Tian W (2012). Performance and microbial community in hybrid anaerobic baffled reactor-constructed wetland for nitrobenzene wastewater. Bioresour. Technol. 118, 128–135.

Liu X. B., Lu H. Y., Huang W. M., Kong H. S., Ren X. B., Lin H. B (2012). Electrochemical degradation of nitrobenzene. Curr. Org. Chem. 16, 1967–1971.

Makarova O. V., Rajh T., Thurnauer M (2000). Surface modification of TiO_2 nanoparticles for photochemical reduction of nitrobenzene, Environ Sci. Technol. 34, 4797–4803.

Qin Q. D., Ma J., Liu K. (2007). Adsorption of nitrobenzene from aqueous solution by MCM-41, J. Colloid. Interf. SCI. 315, 80–86.

Vymazal, J. & Cycling N (2005). Natural and Constructed Wetlands: Nutrients, Metals and Management. Backhuys.

Vymazal J., Brix H., Cooper P., Green M., Haberl R (1998). Constructed Wetlands for Wastewater Treatment in Europe. Backhuys Publishers, Leiden.

Zhang S. J., Jiang H., Li M. J., Yu H. Q., Yin H., Li Q. R (2007). Kinetics and mechanisms of radiolytic degradation of nitrobenzene in aqueous solutions, Environ Sci. Technol. 41, 1977–1982.

Zhao D., Liu C., Zhang Y., Liu Q (2011). Biodegradation of nitrobenzene by aerobic granular sludge in a sequencing batch reactor (SBR). Desalination 281, 17–22.

Zhao L., Ma J., Sun Z. Z (2008). Oxidation products and pathway of ceramic honeycomb-catalyzed ozonation for the degradation of nitrobenzene in aqueous solution, Applied Catalysis B. 79, 244–253.

Zhao L., Ma J., Zhai X (2009). Synergetic effect of ultrasound with dual fields for the degradation of nitrobenzene in aqueous solution. Environ. Sci. Technol 43, 5094–5099.

Advances in Applied Chemistry and Industrial Catalysis – Saikia (Ed.)

Research on pretreatment of organic sulfur compounds in garlic wastewater by coagulation

Kun You*, Jie Li** & Diannan Huang
Municipal and Environmental Engineering Institute, Shenyang Jianzhu University, Shenyang, Liaoning, P.R. China

Weiwei Zhou
Department of Municipal Engineering and Equipment Engineering, Shandong Urban Construction Vocational College, Jinan, Shandong, P.R. China

Dongyue Shen
Shenyang Urban Architectural Design Company, Shenyang, Liaoning, P.R. China

ABSTRACT: The organic sulfide in garlic wastewater has a strong antibacterial and bactericidal effect, which leads to the difficulty of efficient biochemical degradation of garlic wastewater. The effects of PAC dosage, pH value, reaction time, and stirring speed on organic sulfur removal were analyzed by coagulation static experiment. When the mass concentration of organic sulfur in the influent is 204 mg/L when the dosage of PAC is 1.5g/L, pH value is 9, reaction time is 30min, and stirring speed is 120r/min, the removal effect of organic sulfur is the best, the removal rate reaches 99.50%, and the mass concentration of organic sulfur in the effluent is 1mg/L. PAC can effectively reduce the organic sulfur concentration of garlic wastewater, increase the B/C value of wastewater from 0.34 to 0.44, improve the biodegradability of garlic wastewater, and provide favorable conditions for subsequent biochemical treatment of wastewater.

1 INTRODUCTION

According to incomplete statistics, every 1t garlic finished product produced will produce 30–40t garlic wastewater. Garlic wastewater contains a high concentration of organic sulfur with a strong pungent smell. Zhang Xiaoxi and others believe that garlic wastewater contains organic sulfide mainly allicin, which has a strong bacteriostatic and bactericidal effect, further increasing the operation difficulty of sewage treatment. The problem with bacteriostatic organic sulfide, it is difficult to degrade efficiently. Li Song et al. added PAC to the wastewater, which can remove colloidal substances and greatly reduce the organic sulfide of the wastewater. Therefore, the pretreatment of garlic wastewater with PAC effectively reduces the concentration of organic sulfide in garlic wastewater, reduces the bacteriostatic and bactericidal effect of garlic wastewater, and provides favorable conditions for subsequent biochemical treatment.

2 MATERIALS AND METHODS

2.1 *Test water*

The garlic processing wastewater is artificially simulated, and the water quality indexes of the simulated wastewater are shown in Table 1.

Corresponding Authors: *466755432@qq.com and **943702009@qq.com

DOI 10.1201/9781003308553-59

Table 1. Test water quality index.

Project	COD (mg/L)	NH_3-N (mg/L)	Organic sulfur (mg/L)
Numerical value	10000±1000	50±5	220±30

2.2 *Experimental method*

The control variable method was used to explore the effects of PAC dosage, pH value, reaction time, and stirring speed on the removal effect of organic sulfur in garlic wastewater. When exploring each influencing factor, the other three factors remained unchanged to determine the best influencing factors.

3 RESULTS AND DISCUSSION

3.1 *Effect of PAC dosage on organic sulfur removal*

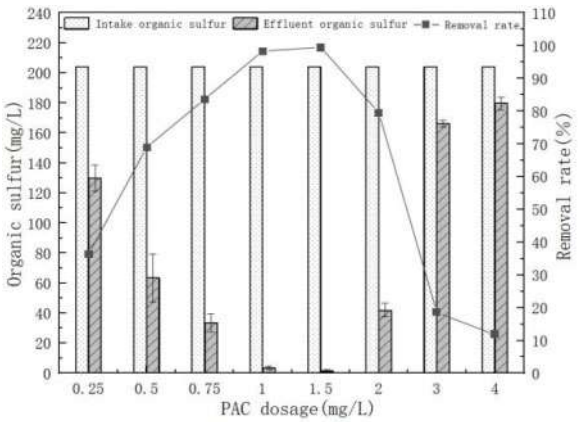

Figure 1. The influence of PAC dosage on the removal rate of organic sulfur.

As shown in Figure 1, when the pH value is 8, the reaction time is 30min, and the stirring speed is 120r/min when the influent organic sulfur concentration is 204mg/L when the PAC dosage is maintained at 0.25g/L, the organic sulfur removal rate is 36.28%, and the effluent organic sulfur concentration is 130mg/L. too small PAC dosage will also lead to poor removal effect of garlic wastewater and insufficient ions hydrolyzed by PAC flocculant, As a result, colloidal bridging is difficult to connect, and the removal effect of organic sulfur is poor; When the dosage of PAC increased to 1.5g/L, the organic sulfur removal rate was 99.51%, and the organic sulfur concentration in the effluent was 1mg/L, When the dosage of PAC increases to 4g/L, the removal efficiency of organic sulfur decreases to 11.77%, while the concentration of organic sulfur in the effluent is 180mg/L. when the dosage of PAC is too large, the suspended solids in wastewater will be positively charged again, and the positive charges will repel each other to re-establish a stable state. At this time, the suspended particles in garlic wastewater will also be covered by PAC, resulting in colloidal protection, The coagulation effect becomes worse and the removal effect of organic sulfur is poor.

3.2 *Effect of pH value on organic sulfur removal*

As shown in Figure 2, when the PAC dosage is 1.5g/Ll, the reaction time is 30min, the stirring speed is 120r/min, and the pH value is 5, the organic sulfur concentrations in the inlet and outlet water are 246mg /L and 110mg/L respectively, and the organic sulfur removal rate is 55.40%. The pH value of the water body is acidic. Al ions in the wastewater cannot form Al $(OH)_3$ colloid, which usually exists in the form of free Al^+, Furthermore, the treatment efficiency of garlic wastewater under acidic conditions is low; When the pH value is 9, the concentration of organic sulfur in influent is 254mg/L and the concentration of effluent is 4mg/L. at this time, the highest removal rate of organic sulfur is 98.43%; When the pH value increases to 10, the influent organic sulfur concentration is 259mg/L and the effluent concentration is 55mg/L, and the removal rate decreases to 78.76%. The pH value in the water body is strongly alkaline. At this time, the aluminum hydroxide colloid formed in garlic wastewater will react with hydroxyl in the water body to form meta aluminate ions, which will lose the role of adsorption and coprecipitation, resulting in the poor treatment effect of garlic wastewater.

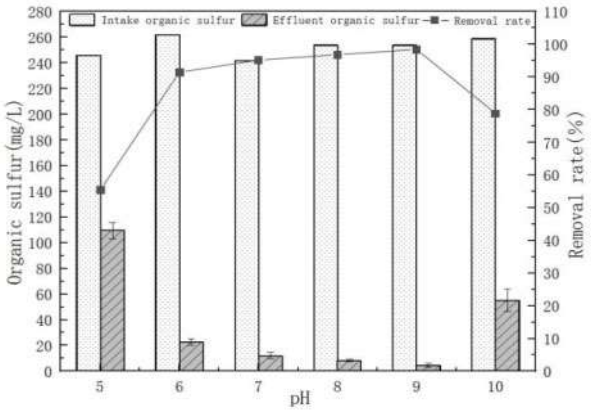

Figure 2. Effect of pH value on organic sulfur removal rate.

3.3 *Effect of reaction time on organic sulfur removal*

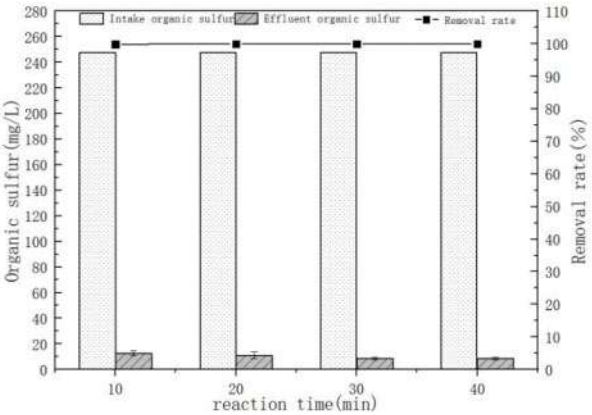

Figure 3. Effect of reaction time on organic sulfur removal rate.

As shown in Figure 3, when PAC dosage is 1.5g/L, pH value is 9, and stirring speed is 120r/min, when the influent organic sulfur concentration is 248mg/L and the reaction time is 10min, the minimum removal rate of organic sulfur is 94.89%. At this time, the maximum effluent concentration is 13mg/L. if the reaction time is too short, it will lead to insufficient mixing between coagulant and garlic wastewater, The removal effect of organic sulfur failed to reach the best; When the reaction time increased to 30min, the highest removal rate of organic sulfur was 96.64%, and the effluent concentration was 8mg/L; When the reaction time continues to increase to 40min, the removal rate of organic sulfur remains at 96.64%. If the reaction time is too long, the removal rate of organic sulfur does not increase further, which will increase the unnecessary economic cost.

3.4 *Effect of stirring speed on organic sulfur removal*

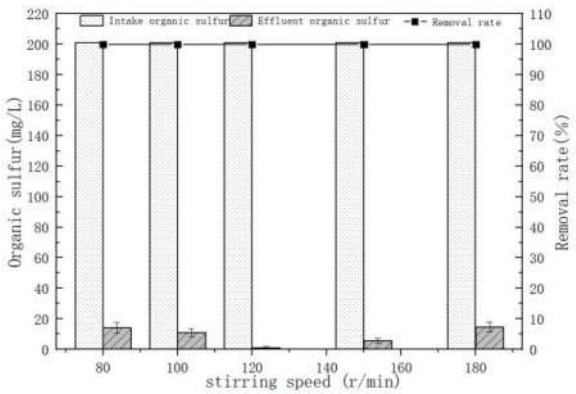

Figure 4. Effect of stirring speed on organic sulfur removal rate.

As shown in Figure 4, when the dosage of PAC is 1.5g/L, the pH value is 9 and the reaction time is 30min, under the condition that the influent organic sulfur concentration is 201mg/L when the stirring speed is 80r/min, the removal rate of organic sulfur is 93.04%, the effluent concentration is 14mg/L, the stirring speed is low, and the mixing of PAC and garlic wastewater is not thorough enough, When one end of the extended part of the polymer adsorbs a colloidal particle, the other end cannot play the role of bridging due to the adhesion of the second colloidal particle, so the effect of coagulation cannot be achieved; When the stirring speed is 120r/min, the treatment efficiency of organic sulfur is the highest 99.50%, and the effluent concentration is 1mg/L; When the stirring speed is 180r/min, the effluent concentration of organic sulfur in garlic wastewater is 15mg/L, and the removal rate is reduced to 92.70%. When the stirring speed is too high, the precipitated flocs formed in the wastewater will be broken, resulting in bridging fracture, flocs breaking, and secondary adsorption destabilization particles, which will deteriorate the effluent quality of garlic wastewater.

3.5 *Biochemical analysis of garlic wastewater pretreated by coagulation method*

As shown in Figure 5, it can be seen from the figure that the influent B/C value ranges from 0.32 to 0.35, with an average value of 0.34, and the effluent B/C value ranges from 0.42 to 0.46, with an average value of 0.44, which increases the BOD/COD value of wastewater from 0.34 to 0.44. The average removal rates of COD and BOD were stable at 24.88% and 3%, respectively, which improved the biodegradability of garlic wastewater and stabilized the removal of COD and BOD, which provided favorable conditions for the subsequent biochemical treatment of wastewater.

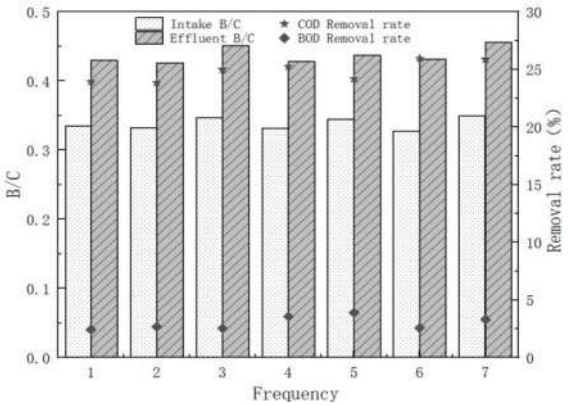

Figure 5. B/C and removal rate change graph.

4 CONCLUSIONS

Based on the results and discussions presented above, the conclusions are obtained as below:

(1) When PAC dosage is 1.5g/L, pH value is 9, reaction time is 30min and stirring speed is 120r/min, the removal effect of organic sulfur in garlic wastewater is the best, and the removal rate reaches 99.50%. When the mass concentration of organic sulfur in the influent is 204mg/L, the mass concentration of organic sulfur in the effluent is 1mg/L.

(2) After PAC pretreatment of garlic wastewater, the organic sulfur concentration, bacteriostatic and bactericidal effects are greatly reduced, and the B/C value is increased from 0.34 to 0.44. The effluent quality of garlic wastewater is stable, which improves the biodegradability of garlic wastewater and provides favorable conditions for subsequent biochemical treatment of wastewater.

REFERENCES

Chen Xiliang. (2019). Research progress on garlic processing wastewater treatment [J]. Shandong chemical industry, 48 (23): 225–226.

Li Song, He Yibo, Yu Kunxing, et al. (2019). Effects of different drip irrigation fertilization rates on sugarcane yield and economic benefits [J]. Hunan Agricultural Sciences, (3): 33–36.

You Kun, Bi Dongfang, Shen Dongyue, et al. (2020). Efficiency Analysis of SBR Process for Treating High Concentration Garlic Processing Wastewater [C]. Proceedings of the 17th Shenyang Scientific Academic Annual Meeting. Shenyang Municipal Committee of CPC, Shenyang Municipal People's Government: Shenyang Science and Technology Association 198–202.

Zhang Huifeng, Wang Yaxi, Liu Kaili. (2020).Study on wastewater treatment of garlic food processing enterprises [J]. Environment and Development, 32(12):40–41.

Zhang Xiaoxi, Zhao Yan, Li Gen, Chu Le, Ding Chen, Ma Yinfei. (2020).Research progress on comprehensive utilization of garlic processing wastewater [J]. Chinese Journal of Fruits and Vegetables, 40(05):71–74+97.

Advances in Applied Chemistry and Industrial Catalysis – Saikia (Ed.)

Spatial distribution characteristics of five heavy metals elements in rice: A case study for different basins in Heilongjiang Province

Wei Zhao
School of Chemistry and Chemical Engineering, Harbin Institute of Technology, Harbin, Heilongjiang, P.R. China

Yujuan Shan
School of Public Health and Management, Wenzhou Medical University, Wenzhou, Zhejiang, P.R. China

Lan Zhao*
Heilongjiang Provincial Center for Disease Control and Prevention, Harbin, Heilongjiang, P.R. China

Lanshun Nie
Faculty of Computing, Harbin Institute of Technology, Harbin, Heilongjiang, P.R. China

ABSTRACT: In this paper, we study the contents of five heavy metal elements found in rice from five basins situated in Heilongjiang Province, and we analyze the distribution of these heavy metal elements in rice for different basins under consideration. Microwave digestion-inductively coupled plasma mass spectrometry (ICP-MS) analysis was used to determine the contents of five heavy metals in rice, including total chromium (Cr), cadmium (Cd), total arsenic (As), lead (Pb), and total mercury (Hg). The single factor pollution index and comprehensive pollution index were employed as an evaluation approach to assess the heavy metal pollution index of rice. For different basins, there were diverse characteristics of heavy metal elements found in rice. The over standard rate of heavy metal elements was low, but the detection rate was high. It was noticed that the rice from Wusuli River Basin was heavily polluted, while that from the Songhuajiang River Basin was slightly polluted. It was suggested that pollution was localized. The heavy metal content of rice in Heilongjiang Province is generally at a low level of food safety risk. However, it is still necessary to further control the sources of heavy metal pollution in the environment and monitor and assess the risk of heavy metal levels in rice.

1 INTRODUCTION

Rice is a cereal crop of the genus Oryza, one of the two major food crops and utilized as a staple food for nearly half of the worldwide population. Heavy metal pollution is an imperative aspect of rice quality and safety. In recent years, due to the indiscriminate discharge of industrial wastewater, waste gases, and waste residues, as well as the abundant application of chemical fertilizers and pesticides, large quantities of pollutants containing heavy metals are discharged into the environment, which aggravates the situation of heavy metal pollution (Lewandowski et al. 2006; Sun et al. 2011). During rice growth, heavy metals can be absorbed and enriched from the growing environment. The metals entry into the human body during food intake exist mainly in the original form and reported its transformed state into highly toxic compounds (Entry et al. 1991; Ivan et al. 1990; Li et al. 2007).

*Corresponding Author: Zhaolan1970@126.com

 DOI 10.1201/9781003308553-60

Most metals are accumulated in vivo with a long half-life, which can produce acute and chronic toxic reactions but are also responsible for teratogenic, carcinogenic, and mutagenic effects. The element content in rice is mainly affected by geographical and geological factors (Williams et al. 2007; Zeng et al. 2008). Thus, whether the distribution of rice elements detected in different regions will show different distribution characteristics for different basins is a scientific problem worthy of further discussion (Fangmin et al. 2006; Ke et al. 2005; Li et al. 2008; Yu et al. 2013; Zhang & Ke 2004).

Rice is one of the grains with a wide planting range, and large consumption in Heilongjiang Province. At present, there are few studies on heavy metal content in rice available for Heilongjiang Province. Hence, in this study, rice samples of planting links directly collected from five main river basins in Heilongjiang Province were selected as the research object. Five heavy metal elements (Cr, Cd, As, Hg, and Pb) were detected by using inductively coupled plasma mass spectrometry (ICP-MS) (Lei et al. 2010; Zhen et al. 2008; Zhu et al. 2009). The single factor pollution index and comprehensive pollution index were employed to analyze the heavy metal pollution index for rice. In this study, the pollution status of heavy metals in rice and the distribution characteristics of rice heavy metals in five basins were studied, which would provide technical guidance and data support for ensuring the food safety of rice in Heilongjiang Province (Xiao et al. 2014).

2 MATERIALS AND METHODS

2.1 *Sample collection*

During rice harvesting, 154 rice samples of planting link were collected from five river basins of Heilongjiang Province, including 30 from the Mudanjiang river basin, 30 from the Wusuli river basin, and 30 from the Songhuajiang river basin, 33 from the Heilongjiang river basin, and 31 from Nenjiang river basin.

2.2 *Instruments and reagents*

ICAP Q inductively coupled plasma mass spectrometer (Thermo company, USA); Mars X microwave digestion instrument (CEM company, USA); CP324S 1/10000 electronic balance (Sartorius company, Germany); B-400 homogenizer (BUCHI company, Switzerland); Milli-Q Academic ultrapure water machine (Millipore Company, USA).

Hg single element standard solution (1000 μg/mL, National Institute of Metrology); multi-element mixed standard solution (Cr, As, Cd, Pb) (1000 μg/mL, Agilent company, USA); standard quality control material (Liaoning rice GBW 10043, national standard reference material center); internal standard solution (10 μg/mL, Agilent company, USA); mass spectrometer tuning solution (Thermofisher Scientific company, USA); nitric acid (GR, Merck Company, USA).

2.3 *Experimental methods*

Sample pretreatment. The rice samples were hulled, ground by a pulverizer, screened, and treated with microwave digestion apparatus. An accurate amount of a 0.5 g rice sample was taken and put into a polytetrafluoroethylene (PTFE) digestion tank. Add 5 mL nitric acid to perform the digestion in a microwave digestion instrument. The overall microwave digestion procedure has presented in Table 1. After digestion and cooling, ultrapure water was used to adjust the volume up to 25 mL. The sample was mixed well before taking the measurement. Two parallel samples were prepared for each trial, and the average value was taken as the ultimate value. At the same time, the blank experiment was conducted. The ICP-MS was adopted for sample detection purposes.

Instrument parameters. RF power: 1 550 W, analog voltage: 1 925 V, pulse voltage: 1 175 V, flow rate of collision gas (He): 4.0 L/min, atomizer (Ar) flow rate: 1.05 L/min, cooling gas (Ar) flow rate: 14 L/min, auxiliary gas (AR) flow rate: 0.8 L/min, sampling depth: 5.0mm, peristaltic pump velocity: 40 rpm, the sampling duration: 45 s.

Solution preparation. Hg standard series solution: dilute the single element standard solution of Hg with 5% HCl and 2% HNO3 solution to prepare the required concentration of 0.00 μg/L, 0.05 μg/L, 0.10 μg/L, 0.50 μg/L, 1.00 μg/L, and 2.00 μg/L. Mixed (Cr, As, Cd, and Pb) standard series solution: dilute the mixed standard solution (Cr, As, Cd, and Pb) step by step with 5% nitric acid solution to prepare the required concentration of 0.0 μg/L, 5.0 μg/L 10.0 μg/L, 20.0 μg/L, 50.0 μg/L, and 100.0 μg/L. Internal standard solution: Ultrapure water was used to dilute the internal standard solution to a concentration of 10 ng/mL.

2.4 *Data statistics*

According to the national standard GB 2762-2017 "Quantity of pollutants in food", the expression of the analysis results was evaluated. The single factor pollution evaluation index and comprehensive evaluation index method were used as the evaluation methods during this study. The expression of the single factor pollution evaluation index is as follows:

$$Pi = Ci/Si. \tag{1}$$

Where Pi denotes the calculated single heavy metal pollution index, Ci refers to the measured value of pollutant i in the sample, Si assigns to the evaluation standard value of pollutant i. When $Pi < 1$ indicates no pollution, and for the case when $Pi \geq 1$ indicates that the sample has been polluted. The larger the Pi value, the more serious the heavy metal pollution. According to the classification standard of the pollution index, it can be divided into 4 grades, as shown in Table 1.

Table 1. Classification standard of pollution index.

Grade	Single-factor pollution index	Judgment of pollution grade
1	Pi < 1	Clean
2	1 <= Pi < 2	Light pollution
3	2 <= Pi < 3	Moderate pollution
4	Pi >= 3	Heavy pollution

To highlight the role of the pollution index of different heavy metals present in the samples, the comprehensive evaluation index of samples was introduced, that is, based on the single pollution index. The Nimelow pollution index method was employed to comprehensively evaluate the sample and to determine the pollution status of different heavy metals in the sample [5]. For calculation purposes, the employed equation is presented as follows:

$$P_{comprehensive} = \sqrt{\frac{(P_{\text{mean}})^2 + (P_{\max})^2}{2}} \tag{2}$$

Where P_{mean} denotes the mean value of each single pollution index P_i in the sample, and $P_{\max}$ denotes the maximum value of each single pollution index in the sample. Moreover, a comprehensive pollution index was used to reflect the comprehensive pollution level of the measured heavy metal element content. Table 2 shows the classification criteria for the comprehensive evaluation.

Table 2. Comprehensive evaluation criteria.

Table Head	*Pcomprehensive*	*Determination of pollution grade*	*Pollution level*
1	P<=0.85	Non pollution	Clean
2	0.85<P<=1.71	Light pollution	Contaminated
3	1.71<P<=2.56	Moderate pollution	Some pollutants exceed the standard
4	P>2.56	Heavy pollution	The pollution is quite serious

3 RESULTS AND ANALYSIS

3.1 *Linear relationship and quality control of heavy metal elements*

After the ICP-MS was tuned and the instrument was confirmed to be in a normal and stable state, the prepared samples were injected in sequence. As listed in Table 3, the correlation of five heavy metal elements was good with $R \geq 0.999$. The national standard reference materials of Liaoning rice GBW 10043 (GSB-21) and Hunan rice GBW10045 (GSB-23) were selected for quality control purposes. The measured values for all 5 heavy metal elements were within the range of the reference amount, indicating that the applied method was accurate and reliable. The obtained measurement results are shown in Table 4.

Table 3. Linear correlation diagram of standard curve of 5 heavy metal elements.

Element	*Linear equation*	*Linear range (ng/ml)*	*Correlation coefficient*
Cr	Y=5033.226X+720.558	0–100.0	1.000
As	Y=400.871X+11.107	0–100.0	1.000
Cd	Y=2678.364X+9.444	0–100.0	1.000
Hg	Y=6350.627X+102.378	0–2.0	0.9994
	Y=16973.18X+1065.511	0–100.0	0.9995

Table 4. Determination of standard reference meterial.

	GBW10043(GSB-21)			GBW10044(GSB-22)		
Element	*Detection value 1 mg/kg*	*Detection value 2 mg/kg*	*Standard value mg/kg*	*Detection value 1 mg/kg*	*Detection value 2 mg/kg*	*Standard value* mg/kg
Cr	0.1362	0.1415	0.14±0.05	0.1567	0.1921	0.17±0.05
As	0.1163	0.1117	0.114±0.018	0.1187	0.1290	0.12±0.03
Cd	0.0103	0.0131	0.012±0.003	0.0178	0.0200	0.018±0.002
Hg	0.00501	0.00496	0.0048±0.0008	0.0017	0.0018	0.0022±0.0005
Pb	0.0739	0.0782	0.075±0.025	0.0752	0.0931	0.09±0.03

3.2 *Contents of heavy metal elements in rice*

After microwave digestion of 154 rice samples, the contents of cadmium, total chromium, total arsenic, lead, and total mercury were detected using the ICP-MS instrument. The detection results are shown in Table 5. The limit value of heavy metals was determined according to the "National food safety standard Quantity of pollutants in food (GB 2762-2017)" [18]. It can be seen from the obtained results that the contents of five heavy metal elements in rice were at a lower level, and the average contents of cadmium, total chromium, total arsenic, total mercury, and lead were 0.003793, 0.3013, 0.2118, 0.008294, and 0.0322 mg/kg, respectively. Among the 154 samples tested, 4 samples have exceeded the standard value. Among these 4 samples, there were two samples for the total chromium content, and two samples were for total mercury content, with the over standard rate of 2.6%. There were no lead and cadmium samples that exceeded the standard value. Among the 154 samples, the total arsenic obtained value for 55 samples was more than 0.2 mg/kg.

3.3 *Analysis of heavy metal pollution in rice*

According to the single factor pollution index evaluation method, the heavy metal pollution of rice in five basins has presented in Table 6. For the Mudanjiang river basin and Songhuajiang river

Table 5. Results of different element contests in samples.

Contaminants	*Sample quantity (copies)*	*Sample quantity (copies)*	*Average (mg/kg)*	*Minimum (mg/kg)*	*Maximum (mg/kg)*
Cr	154	154	0.3013	0.0317	1.6302
As	154	154	0.2118	0.0200	0.4996
Cd	154	154	0.003793	0	0.01784
Hg	154	154	0.008294	0.002806	0.143519
Pb	154	154	0.0322	0.0016	0.1442
Contaminants	*Detected quantity (copies)*	*Detection rate(%)*	*Limit value (mg /kg)*	*Over standard quantity (copies)*	*Over standard rate (%)*
Cr	154	100	1.0	2	1.3
As	154	100	–*	–	–
Cd	137	88.96	0.2	0	0
Hg	25	16.23	0.02	2	1.3
Pb	154	100	0.2	0	0

a. * means that the limit standard of inorganic arsenic in rice is 0.2 mg/kg in GB 2762-2017, and a recheck is required if the detected value exceeds 0.2 mg/kg when monitoring the total arsenic.

basin, one rice sample with light pollution of total Cr was found. Similarly, the Wusuli river basin had found a rice sample with a heavy pollution level of total Hg, and the Nenjiang river basin had exhibited a rice sample with a light pollution level of total Hg. The remaining other samples were found clean. To further investigate the pollution situation of the various samples, the comprehensive pollution index was calculated according to the Nimero comprehensive pollution index evaluation model. As shown in Table 6, the rice from the Wusuli River basin was heavily polluted, that obtained from the Songhuajiang River basin was slightly polluted, and that collected from the other three river basins was not polluted. No contamination was noticed for the remaining 150 samples.

Table 6. Results of different element contents in samples.

Table Head	*Cr pollution index*	*Cd pollution index*	*Hg pollution index*	*Pb pollution index*	*Mean value (mg/kg)*	*Maximum value (mg/kg)*	*comprehensive pollution index*
Mudanjiang River	1.6302	0.0268	0.2457	0.0625	0.4913	1.6302	1.204
Wusuli River	0.5952	0.01265	7.17595	0.196	1.99495	7.17595	5.269
Songhuajiang River	1.0748	0.0174	0.1403	0.553	0.446375	1.0748	0.8229
Nenjiang River	0.0957	0.07605	1.1163	0.077	0.3371875	1.1163	0.8246
Mudanjiang River	1.6302	0.0268	0.2457	0.0625	0.4913	1.6302	1.204

a. There is no limit standard for total arsenic in rice in GB 2762-2017, and the arsenic is not included in the statistics when calculating the index in the table.
b. The pollution index of the remaining 150 samples is all less than 1, which is not listed in the table.

3.4 *Distribution of heavy metal elements in rice of different basins*

The highest value of average total chromium content in rice was 0.4066 mg/kg found in the Songhuajiang River basin, while the lowest was 0.1621 mg/kg for the Mudanjiang River basin. The highest value of total chromium was found in the Mudanjiang River basin, which was 1.6302 mg/kg. The total chromium content in the Songhuajiang River basin was relatively higher, and the content of total chromium in specific locations of Mudanjiang River Basin and Heilongjiang River Basin was

higher, and the other basins were mainly in a low-level area. One sample from both the Songhuajiang River basin and Mudanjiang River basin exceeded the standard value, and the exceeded limit was 3.33%. The highest average total arsenic content in rice was found for 5 major basins located in the Heilongjiang River basin, which was 0.2813 mg/kg, and the lowest value of 0.1511 mg/kg was assigned for the Mudanjiang River basin. The highest arsenic content was 0.4804 mg/kg found in the Mudanjiang River basin. The total arsenic content in the Songhuajiang River basin and Heilongjiang River basin was higher, while for Mudanjiang River Basin was lower.

Moreover, some samples needed further determination of inorganic arsenic to determine whether they exceeded the standard value. Among five major basins, the highest average cadmium content found in rice was for the Heilongjiang River basin, which was 0.00524 mg/kg, while the lowest was 0.00249 mg/kg noticed for the Mudanjiang River basin. The highest content was 0.01784 mg/kg for the Nenjiang River basin. The cadmium content in rice was mainly distributed in low-level areas, and the overall situation was comparatively good.

In addition, the highest average total mercury in rice was found in the Wusuli River basin, which was 0.008185 mg/kg, while the lowest was 0.002 956 mg/kg for the Songhuajiang River basin. The highest content was 0.143519 mg/kg noticed for the Wusuli River basin with the highest detection rate of 33.33%. The cleanliness of total mercury in rice was good, only a few samples exceeded the standard value. The mercury content for the Wusuli River basin was relatively higher, and other basins were mainly in low-level areas. One sample from the Wusuli River basin and Nenjiang River basin exceeded the standard value, with an over standard rate of 3.00%. The highest average lead content in rice was obtained for the Songhuajiang River basin, which was 0.058 6 mg/kg, while the lowest was 0.0111 mg/kg for the Mudanjiang River basin. The highest content was 0.1442 mg/kg for the Heilongjiang River basin. The lead content in the Songhuajiang River basin and Heilongjiang River basin was relatively higher and other basins were mainly located in low-level areas. The cleanliness of lead in rice was good. The detection results of heavy metal elements in rice from different river basins are shown in Table 7.

Table 7. Results of different element contents in rice from different basins.

Element	*Statistical items*	*Mudanjiang River basin*	*Wusuli river basin*	*Songhuajiang river basin*	*Heilongjiang river basin*	*Nenjiang river basin*
Cr	Sample quantity (copies)	30	30	30	33	31
	Detection quantity (copies)	30	30	30	33	31
	Over standard quantity (copies)	1	0	1	0	0
	Average value (mg/kg)	0.1621	0.3405	0.4066	0.3372	0.2530
	Maximum value (mg/kg)	1.6302	0.8772	1.0748	0.9750	0.6759
	Minimum value (mg/kg)	0.0425	0.0317	0.1212	0.1364	0.0761
As	Sample quantity (copies)	30	30	30	33	31
	Detection quantity (copies)	30	30	30	33	31
	Over standard quantity (copies)	–	–	–	–	–
	Average value (mg/kg)	0.1511	0.1849	0.2616	0.2813	0.1742
	Maximum value (mg/kg)	0.2991	0.3082	0.4804	0.4996	0.3988
	Minimum value (mg/kg)	0.0837	0.0200	0.1442	0.0875	0.0428
Cd	Sample quantity (copies)	30	30	30	33	31
	Detection quantity (copies)	16	29	29	33	30
	Over standard quantity (copies)	0	0	0	0	0
	Average value (mg/kg)	0.00249	0.00440	0.00404	0.00524	0.00422
	Maximum value (mg/kg)	0.01437	0.01381	0.01543	0.01505	0.01784
	Minimum value (mg/kg)	0	0	0	0.00133	0

(*Continued*)

Table 7. Continued.

Element	Statistical items	Mudanjiang River basin	Wusuli river basin	Songhuajiang river basin	Heilongjiang river basin	Nenjiang river basin
Hg	Sample quantity (copies)	30	30	30	33	31
	Detection quantity (copies)	5	10	4	5	1
	Over standard quantity (copies)	0	1	0	0	1
	Average value (mg/kg)	0.002990	0.008198	0.002941	0.003119	0.003436
	Maximum value (mg/kg)	0.004914	0.143519	0.004565	0.006905	0.022326
	Minimum value (mg/kg)	0.002886	0.002806	0.002806	0.002806	0.002806
Pb	Sample quantity (copies)	30	30	30	33	31
	Detection quantity (copies)	30	30	30	33	31
	Over standard quantity (copies)	0	0	0	0	0
	Average value (mg/kg)	0.0111	0.0268	0.0586	0.0391	0.0250
	Maximum value (mg/kg)	0.0189	0.0750	0.1252	0.1442	0.1209
	Minimum value (mg/kg)	0.0037	0.0016	0.0189	0.0127	0.0095

4 CONCLUSIONS AND DISCUSSION

In this study, heavy metals were detected in rice samples of planting link collected directly from five main basins located in Heilongjiang Province, and the contents of various heavy metals elements in rice from different basins were analyzed. The results manifested that the over standard rate of heavy metal elements in rice for Heilongjiang Province was low, but the detection rate was higher. The single factor pollution index and comprehensive pollution index were employed to analyze the heavy metal pollution index of rice. The results demonstrated that the rice in the Wusuli River basin was heavily polluted, and the rice in the Songhuajiang River basin was slightly polluted. The pollution is localized; it is suggested to find out and control the source of heavy metal pollution in the environment and continue to monitor and assess heavy metal levels in rice.

ACKNOWLEDGMENT

This research is supported by the National Key Research and Development Program of China (No. 2018YFB1703403).

REFERENCES

Chujun Li, Jianping Liu, Liying Jia. Present situation and Prospect of rice breeding in China [J]. China Seed Industry, 2007(1):11–12.

Entry J. A., Donnelly P. K., K. Cromack Jr. Influence of ectomycorrhizal mat soils on lignin and cellulose degradation[J], Biology and fertility of soils, 1991, 11(1): 75–78.

Fangmin C., Ningchun Z., Haiming X. et al., Cadmium and lead contamination in japonica rice grains and its variation among the different locations in southeast China[J], Science of the Total Environment, 2006, 359(1–3): 156–166.

Gexin Xiao, Hui Xiao, Yang Liu. Thinking about Big Data Analysis of Food Safety[J]. China Digital Medicine. 2014, 9(1): 4–7.

Ivan J. Fernandez, Lindsey E. Rustad. Soil response to S and N treatments in a northern New England low elevation coniferous forest[J], Water Air Soil Pollution, 1990, 52: 23–39.

Jian Zhu, Nanping Shi, Hongjuan Wang. Content and analysis of Arsenic, Lead, Cadmium and heavy metals in Rice [J]. Liangyou Cangchu Keji Tongxun, 2009, 1: 50–52.

Ke Qingming, Liang, Kangjing, Zheng Luduan, Zhu Yan1, Fang Hui , Liang Yiyuan, GUO Yuchun, LIN Wenxiong. Corresponding analysis on rice grain heavy metal pollution in Fuj ian Province. Chinese Journal Of Applied Ecology, Oct .2005, 16 (10): 1918～1923

Lei Ming, Zeng Min, Wang Lihong, Williams Paul. Arsenic, lead, and cadmium pollution in rice from Hunan markets and contaminated areas and their health risk assessment [J]. Acta Scientiae Circumstantiae, 2010, 30(11): 2314–2320.

Lewandowski I, Schmidt U, Londo M, et al. The economic value of the phytoremediation function – Assessed by the example of cadmium remediation by willow (Salix ssp) [J]. Agricultural Systems, 2006, 89(1):68–89.

Liyou-qin, LIRong-lin, Shizhi-qi. Pollution and Risk Evaluation of Heavy Metals in Rice [J]. Jiangsu.ofAgr.Sci 2008, 24(6): 977–978.

Sun B, Zhao F J, Lombi E. Leaching of heavy metals from contaminated soils using EDTA[J]. Environmental Pollution, 2011, 113(2):111–20.

Williams P N, Villada A, Raaba A, et al. Greatly Enhanced Arsenic Shoot Assimilation in Rice Leads to Elevated Grain Export: Comparison With Wheat and Barley[J]. Environment Science&Technology, 2007, 41(5): 6854–6859.

Yanhong Zhen, Yanjun Chen, Genxing Pan. Cd, Zn and Se content of the polished rice samples from some Chinese open markets and their relevance to food safety [J]. Journal of Safety and Environment, 2008, 8(1): 119–122.

Yu Feng-Xiang, Lin Qin-Lu, Chen Xu. Contents and Distributions of Cadmium and Lead in Rice From Main Rice Cultivation Areas in China [J]. Journal of Ecology and Rural Environment 2013, 29(1): 24–28

Zeng F R, Mao Y, Cheng W D, et al. Genotypie and Environmental Variation in Chromiu. Cadmium and Lead Concentrations in Rice [J]. Environmental Pollution, 2008, 153(6): 309–314.

Zhang M K, Ke Z X, Heavy metals, phosphorus and some other elements in urban soils of Hangzhou City, China, Pedosphere, vol. 14, no. 2, pp. 177–185, 2004.

Advances in Applied Chemistry and Industrial Catalysis – Saikia (Ed.)

Expanded application study on the treatment of dye wastewater by ozone advanced oxidation

Minquan Feng
State Key Laboratory of Eco-hydraulics in Northwest Arid Region, Xi'an University of Technology, Xi'an, China

Yibo Wang*
College of Environment and Chemical Engineering, Xi'an Polytechnic University, Xi'an, China

Yu Xiao
Hanjiang to Weihe River Valley Water Diversion Project construction Co., Ltd., Xi'an, China

Qian Yin
College of Environment and Chemical Engineering, Xi'an Polytechnic University, Xi'an, China

ABSTRACT: In this paper, ozone advanced oxidation technology was used to degrade the simulated acidic red GR and activated red X-3B wastewater. The treatment conditions were optimized, and ozone advanced oxidation was expanded with other technologies. The main conclusions as follows: when alone ozone was used to treat acid red GR dye wastewater, the removal rate reached 95.4% at pH 6-8, and the best degradation effect was achieved by ozone/UV coupled treatment technology, with 99.8% removal rate at pH 7. The treatment of reactive red X-3B by ozone advanced oxidation technology showed the highest removal rate of 97.13% at pH of 8, and the removal rate of ozone/UV coupled treatment technology was up to 99.95% at pH 7. The experiments of ozone-coupled metal catalyst show that the order of treatment effect as follow $TiO_2 > MnO_2 > Fe_2O_3$.

1 INTRODUCTION

The quality of dye wastewater is complex, with the characteristics of high chromaticity, drastic changes in water quality, large amount of water, great changes in pH, high content of organic pollutants and so on (Bhatia et al., 2017; Michael-Kordatou et al., 2015). Dye is the main factor causing the color change of printing and dyeing wastewater. The dyes in wastewater can absorb light, reduce the transparency of water, seriously interfere with the growth of microorganisms and aquatic organisms, inhibit the self-purification of water, and indirectly produce human visual pollution. Seriously polluted water is harmful to human health (Kim et al. 2017). Therefore, the discharge of dyes must be strictly monitored, and more attention should be paid to the treatment of toxic dyes, such as some azo dyes and phthalein bronze dyes. There are many kinds of organic matter, the color is dark and changeable, the pH value and the water quality and quantity change greatly, especially the dye wastewater is one of the industrial wastewaters which is difficult to degrade. The rise of imitation silk and chemical fiber fabrics, as well as the improvement of printing, dyeing and finishing process, bring PVA size, alkaline hydrolysis of viscose fiber, auxiliaries, new dyes and refractory organic compounds into a large number of dye wastewater, which makes the traditional wastewater treatment process face severe challenges. The concentration of COD in the wastewater is increased from hundreds mg/L to 3000∼5000 mg/L (Sun et al. 2019; Wang et al. 2018;. Therefore, this paper studies the degradation efficiency of printing and dyeing wastewater

*Corresponding Author: 20180719@xpu.edu.cn

DOI 10.1201/9781003308553-61

by ozone advanced oxidation technology (Ruan et al. 2010), and takes acid red GR and reactive red X-3B dye wastewater as the research object to study the treatment effect of advanced ozonation and its extended coupling process on the dye wastewater, so as to provide new ideas and processes for the treatment of printing and dyeing wastewater.

2 MATERIALS AND METHODS

Ozone Generator, YX-3.5g, Tianchang Yunxiao Household Appliances sales Co., Ltd.; UV-vis Spectrophotometer, 752N, Shanghai Youke Instruments Co., Ltd.; adjustable Air pump, ACO-9602, Guangdong Haili Group Co., Ltd.; Magnetic Mixer, HJ-6A, Zhengji instrument Co., Ltd.; Analytical balance, 1/1000 Precision, Shanghai Youke Instruments Co., Ltd. All the drugs used in the experiment were analytically pure, and the data measured in the experiment was the average of three tests.

3 RESULTS AND DISCUSSION

3.1 *Study on the degradation of acid red GR and reactive red X-3B by advanced ozone oxidation*

The reaction conditions of pH were optimized, and the active red X-3B and acid red GR dye wastewater with the concentration of 100 mg/L and 150 mg/L was prepared, respectively, and the wastewater treated in the follow-up experiment was prepared according to this concentration. The pH of the adjusting wastewater was 4, 7 and 10, respectively. Six samples were aerated with ozone generator and a total of 20min was used to test the treatment results under different pH conditions.

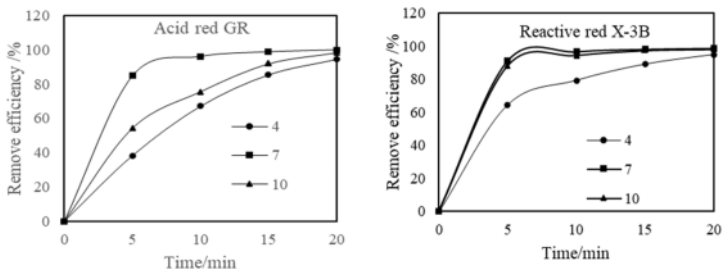

Figure 1. Effect of treatment under different pH and time.

As can be seen from the above Figure 1, the removal rate increased with the increase of ozone aeration time, and under the condition of pH 7, the removal rate of both acid red GR and reactive red X-3B reached more than 80% after 5 min of ozone treatment. In the same treatment time, the treatment effect of the two kinds of dye wastewater as follow: neutral > alkaline > acidic. Under neutral conditions, the removal effect was the highest after 20 min treatment, and the removal rates of acid red GR and active red X-3B reached 99.99% and 98.84%, respectively.

3.2 *Ozone/microelectrolysis coupling experiment*

The optimum amount of iron-carbon micro-electrolysis materials was determined, and 50 g, 75 g and 100 g iron-carbon micro-electrolysis materials were added to the two solutions of the same dye (Wang et al., 2019), respectively. Under the condition of pH 4, treatment time was 30 min, and the dye concentration was measured by sampling every 5 min.

As can be seen from the above Figure 2, the treatment rate and effect of iron-carbon micro-electrolysis material adding 100 g is obviously better than that of 75 g and 50 g. However, the effect

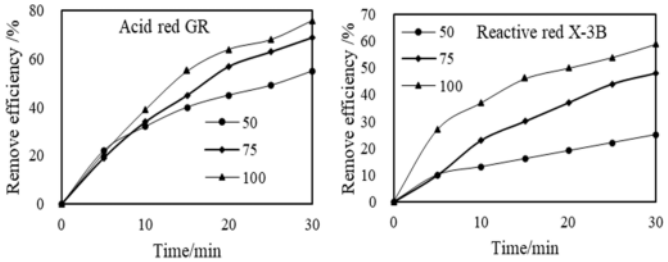

Figure 2. Effect of treatment under different iron-carbon material dosage and treatment time conditions.

of increasing the iron-carbon micro-electrolytic material from 75 g to 100 g on the removal rate was not as effective as that of increasing from 50 g to 75 g. Therefore, the amount of iron-carbon micro-electrolytic material added was selected as 100 g for the subsequent coupling experiments.

The optimal reaction pH was determined by adding 100 g of iron-carbon micro-electrolytic material to the two dye wastewaters, and the pH of the solution was 4, 7 and 10, respectively. The dye wastewater was treated with ozone generator aeration for a total of 20 min, and the absorbance was measured by sampling at 5 min intervals.

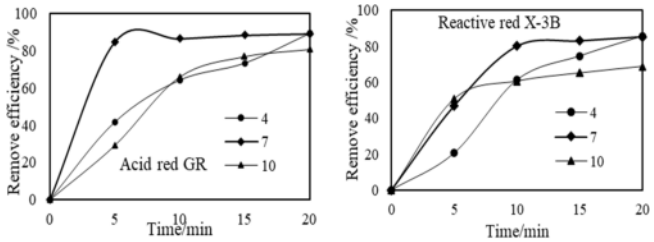

Figure 3. Ozone/micro-electrolysis coupling under different pH conditions.

As can be seen in Figure 3, under the condition of pH 7, the acid red GR solution was treated by ozone micro-electrolysis with the best effect, and the removal rate was as high as 89.15%. Compared with acidic and alkaline conditions, the degradation rate of wastewater is the fastest when it is neutral, the removal rate is as high as 84.76% at 5 min. Under the condition that pH is 4, the effect of ozone/micro-electrolysis coupling treatment of reactive red X-3B solution is the best, and the removal rate is as high as 85.71%. The treatment effect from large to small is acidic, neutral and alkaline. The degradation rate is the fastest when the solution is neutral, and the removal rate is as high as 80.05% at 10 min. After the treatment of two kinds of dye wastewater by ozone coupled micro-electrolysis, it was found that the coupling process did not have a positive effect on the degradation.

3.3 *Ozone/hydrogen peroxide coupling experiment*

The optimum dosage of hydrogen peroxide alone was determined, and 1 mL, 2 mL, and 3 mL hydrogen peroxide were added to the two kinds of dye wastewater respectively. The pH of all solutions was adjusted to 4 by acid, and the treatment was stirred by aeration with a commissionable air pump, and the absorbance was measured by sampling after 30 min.

When the amount of additive is 2 mL of hydrogen peroxide solution has the best treatment effect, the removal rate of acidic red GR is 5.41% and the removal rate of activated red X-3B is 8.97%. The amount of hydrogen peroxide added in the subsequent coupling experiment was selected as 2 mL.

To optimize the reaction pH of ozone coupled with hydrogen peroxide, 2 mL of hydrogen peroxide was added to the two dye wastewaters. The pH of the solution was adjusted to 4, 7 and 10, respectively. Ozone oxygen aeration treated the wastewater, the treatment time was 25min, and the dye concentration was measured by sampling every 5min.

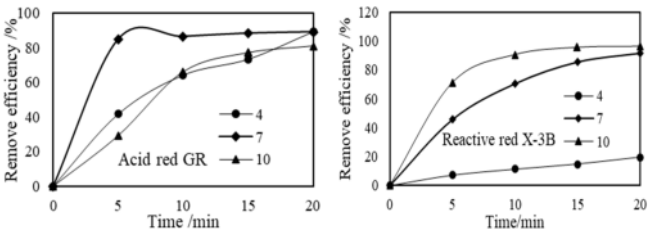

Figure 4. Ozone/hydrogen peroxide coupling data processing diagram.

It can be seen from Figure 4, when pH is 7, the acid red GR solution is treated by ozone/hydrogen peroxide coupling at the fastest rate and the best effect. It is concluded that when the solution is neutral, the removal rate is as high as 94.80% when the reaction is in 5min, and the final removal rate is 99.18%. The treatment effect is neutral, alkaline and acidic from high to low. Compared with the ozone treatment alone, the ozone/hydrogen peroxide coupling treatment effect is 0.81% different from the removal rate under its neutral condition, and does not have a positive coupling effect on the reaction. Under the condition that pH is 10, the active red X-3B solution is treated by ozone/hydrogen peroxide coupling, the speed is the fastest and the effect is the best. It is concluded that when the solution is alkaline, the reaction carries on 10 min, the removal rate is as high as 90.60%, and the best removal rate is 96.83%. The treatment effect is alkaline, neutral and acidic from high to low. Compared with ozone treatment alone, the removal rate of ozone/hydrogen peroxide coupling treatment is 1.44% different from that under alkaline condition, and does not have a positive effect on the reaction.

3.4 *Ozone/UV/ultrasonic experiment*

The pH of the wastewater was set to 4, 7 and 10, respectively, the dye wastewater was treated with ozone generator aeration under the action of UV curing lamp irradiation/ultrasonication for a total of 30 min, and samples were taken at 10 min intervals to measure and add the dye concentration.

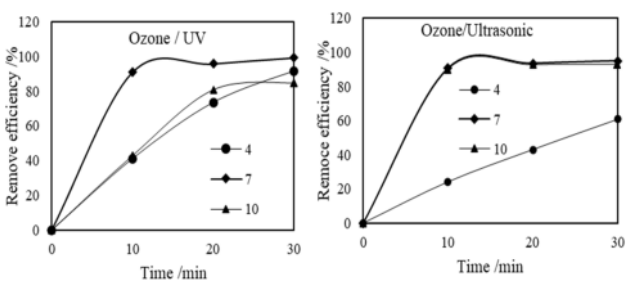

Figure 5. Ozone/UV and right ozone/ultrasonic coupling (acidic red GR).

As can be seen from Figure 5, when pH is adjusted to neutral, the coupling process of ozone/UV was used to treat acidic red GR wastewater. The degradation rate of dye was the fastest and the removal rate was the highest. The removal rate of dye reached 90.83% at 10 min and 99.16% at 30 min. The removal rate was 91.6% under acidic condition. Compared with the ozone treatment alone, the removal rate of ozone/UV treatment was 0.83% lower than that of neutral treatment, and

there was no positive catalytic effect on the reaction. When pH is adjusted to neutral, the coupling process of ozone/ultrasonic was used to treat acidic red GR wastewater. The degradation rate of dye was the fastest and the removal rate was the highest. The removal rate of dye reached 90.72% at 10 min and 95.00% at 30 min. The removal rate was 91.6% under alkaline condition, and the lowest under acidic condition. Compared with ozone treatment alone, the removal rate of ozone/ultrasonic treatment was 4.99% different from that of neutral treatment, and there was no positive catalytic effect on the reaction.

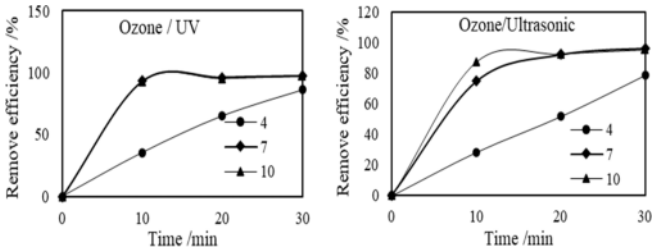

Figure 6. Ozone/UV and right ozone/ultrasonic coupling (activated red X-3B).

As can be seen from Figure 6, when the ozone/UV coupling treatment is adjusted, the treatment speed of reactive red X-3B wastewater is the fastest and the degradation effect is the strongest under the neutral condition, the removal rate is as high as 93.04% when the reaction time is 10 min, and the final removal rate is as high as 99.23%. When the solution is alkaline, the removal rate is 97.13%. Compared with ozone treatment alone, the ozone/UV treatment effect was 0.31% higher than the removal rate under its neutral condition, which had a positive catalytic effect on the reaction. When ozone and ultrasonic wave are coupled to treat reactive red X-3B wastewater, the treatment speed is the fastest under alkaline conditions, and the removal rate is as high as 87.46% when the reaction time is 10 min, and 95.39% when the treatment time is 30 min. Under neutral conditions, compared with ozone treatment alone, the removal rate of ozone/ultrasonic coupling treatment decreased by 3.53%, and did not produce a positive catalytic effect on the reaction.

3.5 *Ozone/metal catalyst treatment experiments*

MnO_2 catalytic treatment experiment:500 mL of acid red GR solution with a concentration of 100 mg/L and 500 mL of reactive red X-3B solution with a concentration of 150 mg/L were prepared in triplicate, and 4 mg, 8 mg and 12 mg of MnO_2 were added to the three solutions of the same dye. The samples were treated with ozone generator aeration for a total of 30 min, and the dye concentrations were measured at 10 min intervals.

Table 1. Experiments of MnO_2-catalyzed treatment of acidic red GR.

	4 mg	8 mg	12 mg
Time/min	Effect/%	Effect/%	Effect/%
0	0.00%	0.00%	0.00%
10	82.01%	79.88%	83.80%
20	95.94%	95.05%	97.18%
30	98.62%	98.35%	99.24%

The TiO_2 catalytic treatment experiment was performed in the same way as the MnO_2 catalytic experiment, 0.5 mg, 1 mg and 1.5 mg of TiO_2 were added to the dye wastewater.

The Fe_2O_3 catalytic treatment experiment was performed in the same way as the MnO_2 catalytic experiment by adding 2 mg, 4 mg, and 6 mg of Fe_2O_3 to three solutions of the same dye, respectively (Qian et al. 2019).

Table 2. Experiments on MnO_2-catalyzed treatment of activated red X-3B.

	4 mg	8 mg	12 mg
Time/min	Effect/%	Effect/%	Effect/%
0	0.00%	0.00%	0.00%
10	87.51%	89.07%	88.66%
20	96.13%	96.60%	96.40%
30	97.96%	98.37%	98.23%

Table 3. TiO_2-catalyzed treatment of acidic red GR.

	0.5 mg	1 mg	1.5 mg
Time/min	Effect/%	Effect/%	Effect/%
0	0.00%	0.00%	0.00%
10	93.79%	92.36%	91.75%
20	98.49%	97.68%	97.34%
30	99.52%	99.31%	99.24%

Table 4. TiO_2-catalyzed treatment of activated red X-3B.

	0.5 mg	1 mg	1.5 mg
Time/min	Effect/%	Effect/%	Effect/%
0	0.00%	0.00%	0.00%
10	92.09%	92.69%	93.09%
20	96.58%	97.38%	97.72%
30	98.18%	98.32%	98.59%

Table 5. Fe_2O_3-catalyzed treatment of acidic red GR.

	2 mg	4 mg	6 mg
Time/min	Effect/%	Effect/%	Effect/%
0	0.00%	0.00%	0.00%
10	62.74%	55.12%	68.54%
20	83.49%	82.37%	82.44%
30	92.05%	91.11%	92.13%

Table 6. Fe_2O_3-catalyzed treatment of activated red X-3B.

	2 mg	4 mg	6 mg
Time/min	Effect/%	Effect/%	Effect/%
0	0.00%	0.00%	0.00%
10	66.84%	66.37%	62.05%
20	86.99%	85.07%	84.23%
30	93.22%	92.77%	91.88%

(1) Acid red GR, as shown in Table 1, the best removal rate of 99.24% was achieved when the catalyst MnO_2 was added in the amount of 12 mg. The treatment effect was 12 mg, 4 mg and 8 mg in descending order, and the amount of catalyst added was 4 mg, which was the most cost effective from the point of view of lower cost. As shown in Table 3, the best removal rate of 99.52% was achieved with the addition of 0.5 mg of TiO_2 catalyst. As shown in Table 5,

the best removal rate of 92.13% was achieved when the catalyst Fe_2O_3 was added at 6 mg. Comparing the catalytic efficiencies of the three metals, it is concluded that TiO_2> MnO_2> Fe_2O3.

(2) Activated red X-3B, as shown in Table 2, when the catalyst MnO_2 was added at 8 mg, the best removal rate was 98.37%. The treatment effect was 8 mg, 12 mg, 4 mg in descending order. As shown in Table 4, the best removal rate was 98.59% when the catalyst TiO_2 was added in the amount of 1.5 mg. As shown in Table 6, the best removal rate of 93.22% was achieved when the catalyst Fe_2O_3 was added in the amount of 2 mg. Comparing the catalytic efficiency of the three metals, it is concluded that TiO_2> MnO_2> Fe_2O_3.

In summary, the experiments with ozone-coupled metal catalysts showed that the ranking of treatment effects in treating both dye wastewaters was: TiO_2> MnO_2> Fe_2O_3.

4 CONCLUSIONS

In this paper, advanced ozonation coupling technology was adopted to treat acidic red GR and reactive red X-3B dye wastewater. The main conclusion can be summarized as follows:

(1) The two kinds of dye wastewaters were treated by ozone oxidation alone. When the reaction pH was in the range of 6-8 and the treatment time was 20min, the removal rate of acid red GR wastewater and active red X-3B wastewater could reach 99.99% and 98.84%, respectively.
(2) In the treatment of dye wastewater by ozone-coupled technology, it is found that the coupling effect of treating acid red GR is in the order of ozone/UV light > ozone/hydrogen peroxide>ozone/ultrasonic>ozone/micro-electrolysis.
(3) For reactive red X-3B: ozone/UV light > ozone/hydrogen peroxide > ozone/ultrasonic > ozone/micro-electrolysis.
(4) When metal oxide catalyzed ozone was used to treat two dye wastewater, it was found that the order of treatment effect as follow TiO_2 > MnO_2 > Fe_2O_3.

ACKNOWLEDGMENT

This work was financially supported by the Basic Research Program of Natural Science in Shaanxi province (No. 2019JLM-60 and 2021JQ-670).

REFERENCES

Bhatia D, Sharma N R, Singh J, et al. (2017). Biological methods for textile dye removal from wastewater: A review. Crit. Rev. Environ. Sci. Technol. 47 1836–1876.

Kim H, Yang S, Rao S R, et al. (2017). Water harvesting from air with metal-organic frameworks powered by natural sunlight. Science. 356 430–434.

Michael-Kordatou I, Michael C, Duan X, et al. (2015). Dissolved effluent organic matter: Characteristics and potential implications in wastewater treatment and reuse applications. Water Res. 77:213–248.

Qian J, Chen M, Li J, et al. (2019). Study on CuO/Al_2O_3 catalytic ozone treatment of acid red B solution. J. Chin. Chem. Soc. 66 1484–14889.

Ruan X C, Liu M, Zeng Q, et al. (2010). Degradation and decolorization of reactive red X-3B aqueous solution by ozone integrated with internal micro-electrolysis. Sep. Purif. Technol. 74 195–201.

Sun Z, Liu Z, Han L, et al. (2019). Study on the treatment of simulated azo dye wastewater by a novel micro-electrolysis filler. Water Sci. Technol. 79 2279–2288.

Wang B, Tian K, Xiong X, et al. (2019). Treatment of overhaul wastewater containing N-methyldiethanolamine (MDEA) through modified Fe–C microelectrolysis configured ozonation: Investigation on process optimization and degradation mechanisms. J. Hazard. Mater. 369: 655–664.

Wang R, Jin X, Wang Z, et al. (2018). Amultilevel reuse system with source separation process for printing and dyeing wastewater treatment: A case study. Bioresour. Technol. 247 1233–1241.

Advances in Applied Chemistry and Industrial Catalysis – Saikia (Ed.)

Preliminary study on purification of wastewater from liquor production

Xiaoyan Lan* & Xueling Chen
Wuliangye Technical College, Yibin Vocational and Technical College, Yibin, Sichuan, China

ABSTRACT: This study used the Fenton oxidation process to treat Baijiu production wastewater based on the original anaerobic fermentation process. The $FeSO_4$ dosage and the H_2O_2 addition amount in the Fenton oxidation method were investigated, respectively. The single factor test and orthogonal test were carried out to obtain the optimum combination conditions. The orthogonal test showed that the aerobic fermentation conditions were 1ml H_2O_2, 0.05g $FeSO_4$, 6 ml anaerobic bacteria, and the time was nine days. The aerobic fermentation condition was: pH6, 0.2 mL nitrifying bacteria, the temperature of 30°C, and eight days. The denitrifying fermentation condition was: pH7, 0.15 ml denitrifying bacteria, the temperature of 35°C, and seven days.

1 INTRODUCTION

Baijiu is a traditional liquor with a long history that is unique to China. Behind the huge scale of production, there are potential severe environmental pollutions. The wastewater during Baijiu production can be divided into high concentrated organic wastewater and low concentrated organic wastewater. High concentrated wastewater has high COD, BOD_5 and SS values, complex components, and acidic pH, which are the main pollutants. Baijiu wastewater treatment has achieved great success in recent years, but it is only limited to large and medium-sized Baijiu enterprises. The wastewater of many small workshops and wineries is discharged directly without any treatment. Many wineries have been upgraded and expanded to increase production capacity, but the wastewater treatment capacity is insufficient. The technology is backward, the cost is high, and the management requirement is high. The production training base in our college-the Baijiu production laboratory has relatively low efficiency in wastewater treatment. This experiment aims to solve the environmental impact of wastewater during the production of Baijiu.

2 EXPERIMENTAL METHOD

2.1 *Reagents and instruments*

Nessler's reagent, potassium sodium tartrate reagent, ammonia nitrogen standard solution, ammonia nitrogen standard working solution, 0.12 g/mL mercury sulfate solution, 1.5 g/100 mL silver acid solution, 1.0 mol/L potassium dichromate standard solution, potassium hydrogen phthalate standard solution, 10% concentrated sulfuric acid, polyferric sulfate, potassium nitrate standard stock solution, potassium nitrate standard solution, alkaline potassium persulfate, hydrochloric acid solution, $FeSO_4$, H_2O_2.

UV-200 ultraviolet spectrophotometer, 20mm cuvette, water bath, pipette, incubator, shaking incubator, glass rod, electronic balance, ear ball, gauze, PH test paper, sodium hydroxide solution, beaker.

Test strain:

There were 3×10^6 anaerobic bacteria/mL, 2×10^8 nitrifying bacteria/mL, and 1×10^8 denitrifying bacteria/mL.

*Corresponding Author: lanxiaoyan2000@163.com

DOI 10.1201/9781003308553-62

2.2 *Experimental process*

Wastewater → filtration → PH adjustment → (first stage) adding anaerobic bacteria, H_2O_2, $FeSO_4$ for anaerobic fermentation → stirring evenly → (second stage) adding nitrifying bacteria for aerobic fermentation → filtration → (third stage) adding denitrifying bacteria for denitrifying fermentation → filtration.

2.3 *Experimental methods for treatment of wastewater from Baijiu production*

2.3.1 *Single factor test and orthogonal test of anaerobic fermentation*

Investigation of the effects of anaerobic bacteria content on anaerobic fermentation: 200 mL wastewater from Baijiu production, 0.1 g $FeSO_4$, and 1 mL H_2O_2 were added in 5 fermentation tanks; then 1, 2, 3, 4, 5, 6, 7 mL anaerobic bacteria were added into the tanks respectively; after being stirred evenly, the mixtures were left for seven days for fermentation.

Investigation of the influence of the additive amount of $FeSO_4$ on anaerobic fermentation: 200 mL wastewater from Baijiu production, 5 mL anaerobic bacteria, and 1 mL H_2O_2 were added in 5 fermentation tanks; then 0.05, 0.1, 0.15, 0.2, and 0.25 g $FeSO_4$ were added into the tanks respectively; after being stirred evenly, the mixtures were left for fermentation for seven days.

Investigation of the influence of the additive amount of H_2O_2 on anaerobic fermentation: 200 mL wastewater from Baijiu production, 0.1 g $FeSO_4$, and 5 mL anaerobic bacteria were added in 5 fermentation tanks; then 0.5, 1, 1.5, 2, and 2.5 mL H_2O_2 were added into the tanks respectively; after being stirred evenly, the mixtures were left for fermentation for seven days.

Investigation of the influence of fermentation time on anaerobic fermentation: 200 mL wastewater from Baijiu production, 5 mL anaerobic bacteria, 0.1 g $FeSO_4$, and 1 mL H_2O_2 were added in 5 fermentation tanks; after being stirred evenly, the mixtures were left for fermentation for 5, 6, 7, 8, and 9 days respectively.

The orthogonal experiment of anaerobic fermentation

The approximate range of the added number of anaerobic bacteria, $FeSO_4$ and H_2O_2 and the fermentation time was analyzed by single factor test. According to the values measured by the single factor experiment, the orthogonal experiment of L9(34) was designed. The levels of orthogonal factors of anaerobic fermentation are shown in Table 1.

Table 1. The levels of orthogonal factors of anaerobic fermentation.

	Factor			
	A H_2O_2 (mL)	B $FeSO_4$(g)	C Anaerobic Bacteria (mL)	D Time (d)
1	0.5	0.05	4	7
2	1	0.1	5	8
3	1.5	0.15	6	9

2.3.2 *Single factor test and orthogonal test of aerobic fermentation*

Investigation of the influence of pH on aerobic fermentation: 200 mL wastewater from Baijiu production and 0.02 mL nitrifying bacteria were added in 5 fermentation tanks; the pH values of the mixtures were adjusted to be 5, 6, 7, 8, and 9, respectively; then 0.2 mL nitrifying bacteria was added to the five tanks; after being stirred evenly, the mixtures were left for fermentation for seven days in an incubator at 30°C.

Investigation of the influence of the additive number of nitrifying bacteria on aerobic fermentation: 200 mL wastewater from Baijiu production was added in 5 fermentation tanks; the pH value of the wastewater was adjusted to be 7; then 0.01, 0.02, 0.03, 0.04-, and 0.05- mL nitrifying bacteria were added to the five tanks respectively; after being stirred evenly, the mixtures were left for fermentation for seven days in an incubator at 30°C.

Investigation of the influence of temperature on aerobic fermentation: 200 mL wastewater from Baijiu production was added in 5 fermentation tanks; the pH value of the wastewater was adjusted to be 7; then 0.02 mL nitrifying bacteria was added to the five tanks; after being stirred evenly, the mixtures were left for fermentation for seven days in incubators at 20, 25, 30, 35, and 40°C respectively.

Investigation of the influence of time on aerobic fermentation: 200 mL wastewater from Baijiu production was added in 5 fermentation tanks; the pH value of the wastewater was adjusted to be 7; then 0.02 mL nitrifying bacteria was added to the five tanks; after being stirred evenly, the mixtures were left for fermentation for 5, 6, 7, 8 and 9 days respectively in incubators at 30°C.

The orthogonal experiment of aerobic fermentation

The suitable pH range of nitrifying bacteria, the number of nitrifying bacteria, the temperature range, and the time were studied through a single factor experiment. The orthogonal experiment of L9(34) was designed. The levels of orthogonal factors of aerobic fermentation are shown in Table 2.

Table 2. The levels of orthogonal factors of aerobic fermentation.

	Factor			
Level	A PH	B nitrifying bacteria (mL)	C Temperature (°C)	D Time (d)
1	6	0.01	25	6
2	7	0.02	30	7
3	8	0.03	35	8

2.3.3 *Single factor test and orthogonal test of denitrification fermentation*

Investigation of the influence of denitrifying bacteria content on denitrifying fermentation: 200 mL wastewater from Baijiu production was added in 5 fermentation tanks; the pH value of the wastewater was adjusted to be 7; then 0.05, 0.1, 0.15, 0.2-, and 0.25-mL denitrifying bacteria were added to the five tanks respectively; after being stirred evenly, the mixtures were left for fermentation for eight days in incubators at 30 ˚C.

Investigation of the influence of pH on denitrifying fermentation: 200 mL wastewater from Baijiu production was added in 5 fermentation tanks; the pH values of the mixtures were adjusted to be 5, 6, 7, 8, and 9 respectively; then 0.1 mL denitrifying bacteria was added to the five tanks; after being stirred evenly, the mixtures were left for fermentation for seven days in an incubator at 30°C.

Investigation of the influence of temperature on denitrifying fermentation: 200 mL wastewater from Baijiu production was added in 5 fermentation tanks; the pH value of the wastewater was adjusted to be 7; then 0.1 mL denitrifying bacteria was added to the five tanks; after being stirred evenly, the mixtures were left for fermentation for eight days in incubators at 20, 25, 30, 35, and 40°C respectively.

Investigation of the influence of time on denitrifying fermentation: 200 mL wastewater from Baijiu production was added in 5 fermentation tanks; the pH value of the wastewater was adjusted to be 7; then 0.1 mL denitrifying bacteria was added to the five tanks; after being stirred evenly, the mixtures were left for fermentation for 5, 6, 7, 8 and 9 days respectively in incubators at 30°C.

The orthogonal experiment of denitrification fermentation

The range of the added number of denitrifying bacteria, the pH range of the survival of denitrifying bacteria, the range of temperature and fermentation time were analyzed through the single factor test. According to the values measured by the single factor experiment, the orthogonal experiment of L9(34) was designed. The levels of orthogonal factors of denitrification fermentation are shown in Table 3.

Table 3. The levels of orthogonal factors of denitrification fermentation.

	Factors			
Level	A PH	B Temperature (°C)	C Denitrifying Bacteria (mL)	D Time (d)
1	6	25	0.05	7
2	7	30	0.1	8
3	8	35	0.15	9

3 RESULTS AND DISCUSSION

3.1 *Analysis of anaerobic fermentation experiment*

3.1.1 *The influence of anaerobic bacteria content on anaerobic fermentation*

Table 4. The influence of anaerobic bacteria content on anaerobic fermentation.

Anaerobic Bacteria Content 3 × 10^6/mL	1	2	3	4	5	6	7
Ammonium Nitrogen Content (ug/L)	3616	3624	3776	4616	5537	5558	5547

It can be seen from Table 4 that as the content of anaerobic bacteria increases, anaerobic bacteria decompose macromolecular organic matter in Baijiu wastewater into ammonium nitrogen, and the content of ammonium nitrogen gradually increases. When the number of anaerobic bacteria is 5 mL, the ammonium nitrogen content tends to rise slowly, indicating that the optimum additive content of anaerobic bacteria is 5 mL.

3.1.2 *The influence of $FeSO_4$ content on anaerobic fermentation*

Table 5. The influence of $FeSO_4$ content on anaerobic fermentation.

$FeSO_4$ (g)	0.05	0.1	0.15	0.2	0.25
Ammonium Nitrogen Content (ug/L)	4659	5346	5425	5390	5415

It can be seen from Table 5 that the anaerobic bacteria can convert organic matter into ammonium nitrogen, and adding $FeSO_4$ can convert difficult-to-decompose organic matter into ammonium nitrogen. The content of ammonia nitrogen can be measured. The higher the content of ammonium nitrogen is, the more organic matter is transformed. According to the figure above, when 0.1 g $FeSO_4$ was added, the increase of ammonium nitrogen content tended to be gentle, indicating that the addition amount of 0.1 g maximized the organic matter conversion.

3.1.3 *The influence of H_2O_2 content on anaerobic fermentation*

Table 6. The influence of H_2O_2 content on anaerobic fermentation.

H_2O_2 (mL)	0.5	1	1.5	2	2.5
Ammonium Nitrogen Content (ug/L)	4724	5735	5545	5684	5547

It can be seen from Table 6 that the anaerobic bacteria convert organic matter into ammonium nitrogen, and adding H_2O_2 catalyzes the conversion of difficult-to-decompose organic matter into ammonium nitrogen. The content of ammonia nitrogen can be measured. The higher the content of ammonium nitrogen is, the more organic matter is converted. According to the figure above, when 1 mL H_2O_2 was added, the increase of ammonium nitrogen content tended to be gentle, indicating that the addition amount of 1 mL maximized the organic matter conversion.

3.1.4 *The influence of fermentation time on anaerobic fermentation*

It can be seen from Table 7 that as anaerobic bacteria continue to convert decomposable organic matter into ammonium nitrogen, H_2O_2 and $FeSO_4$ will continuously transform the difficult-to-decompose organic

Table 7. The influence of fermentation time on anaerobic fermentation.

Time (d)	5	6	7	8	9
Ammonium Nitrogen Content (ug/L)	4215	4972	5491	5576	5595

matter. As time goes on, ammonium nitrogen continues to accumulate. On the 7th day, the accumulation of ammonium nitrogen reaches a plateau, indicating that seven days of fermentation are appropriate.

3.1.5 *Analysis of anaerobic fermentation orthogonal test results*

Table 8. Anaerobic fermentation orthogonal test results.

	Factor				
Test No.	A	B	C	D	COD
1	1	1	1	1	1201
2	1	2	2	2	1138
3	1	3	3	3	778
4	2	1	2	3	681
5	2	2	3	1	1181
6	2	3	1	2	1009
7	3	1	3	2	1089
8	3	2	1	3	936
9	3	3	2	1	1331
K1	3117	2971	3146	3713	
K2	2871	3255	3150	3236	
K3	3356	3118	3048	2395	
k1	1039	990	1048	1237	
k2	957	1085	1050	1078	
k3	1118	1039	1016	798	
R	161	95	34	439	
Order	C>B>A>D				
Optimal level	A_2	B_1	C_3	D_3	
Optimal combination	A_2 B_1 C_3 D_3				

As shown from Table 8, the effects of $FeSO_4$, H_2O_2, time, and anaerobic bacteria on the COD content of Baijiu production wastewater are studied through orthogonal experiments. From range R, it can be seen that the content of anaerobic bacteria reduces COD the most, followed by the content of $FeSO_4$, the content of H_2O_2, and time. The optimal combination obtained is A_2 B_1 C_3 D_3, namely, 1 mL H_2O_2, 0.05 g $FeSO_4$, 6 mL anaerobic bacteria, and nine days.

3.2 *Aerobic fermentation test and analysis*

3.2.1 *Analysis of the effect of pH on aerobic fermentation*

Table 9. The effect of pH on aerobic fermentation.

pH	5	6	7	8	9
Ammonium Nitrogen Content (ug/L)	4798	4337	4074	3978	4012

According to Table 9, when 0.02 mL nitrifying bacteria was added, the ability of nitrifying bacteria to convert ammonium nitrogen into nitrate nitrogen is different under different pH conditions. The higher the content of ammonium nitrogen, the lower the conversion of ammonium nitrogen. Thus, the conversion effect of ammonium nitrogen under different pH conditions can be measured. The ammonium nitrogen conversion rate is the highest when the nitrifying bacteria are at pH7.

3.2.2 *Analysis of the effect of nitrifying bacteria content on aerobic fermentation*

Table 10. The effect of nitrifying bacteria content on aerobic fermentation.

Nitrifying Bacteria Content 2×10^8/mL	0.01	0.02	0.03	0.04	0.05
Ammonium Nitrogen Content (ug/L)	5592	5457	5413	5397	5407

As shown from Table 10, nitrifying bacteria transform ammonium nitrogen into nitrate nitrogen, and the measured ammonium nitrogen content is the remaining that was not converted by nitrifying bacteria. If the ammonium nitrogen content is high, the conversion efficiency is low. The conversion rate is the maximum when the added number of nitrifying bacteria is 0.02 mL.

3.2.3 *Analysis of the effect of temperature on aerobic fermentation*

Table 11. The effect of temperature on aerobic fermentation.

Temperature (°C)	20	25	30	35	40
Ammonium Nitrogen Content (ug/L)	5416	4656	4150	4214	4614

As can be seen from Table 11, nitrifying bacteria transform ammonium nitrogen into nitrate nitrogen, and the measured ammonium nitrogen content is the remaining that was not converted by nitrifying bacteria. When the temperature is too low, the conversion efficiency of ammonium nitrogen is very low because the nitrifying bacteria are inhibited by temperature. When the temperature is 30°C, the remaining amount of ammonium nitrogen is the least, indicating that the conversion rate of nitrifying bacteria is the best under this temperature condition.

3.2.4 *Analysis of the effect of time on aerobic fermentation*

Table 12. The effect of time on aerobic fermentation.

Time (d)	5	6	7	8	9
Ammonium Nitrogen Content (ug/L)	4567	4145	3976	3897	3945

According to Table 12, with the accumulation of time, the content of ammonium nitrogen gradually decreases and tends to be stable, and the decrease is most apparent on the 6th day. On the 7th day, the reduction and change tend to slow down. Therefore, when the fermentation time is seven days, the conversion efficiency of ammonium nitrogen is good.

3.2.5 *Analysis of orthogonal test results of aerobic fermentation*

As can be seen from Table 13, the effects of nitrifying bacteria content, pH, time, and temperature on the COD content of Baijiu production wastewater were studied through orthogonal experiments of aerobic fermentation. After the anaerobic fermentation processing, the nitrifying bacteria were added immediately, the immediate addition of nitrifying bacteria overtakes anaerobic fermentation to aerobic fermentation, and the ammonium nitrogen produced by anaerobic fermentation is converted to nitrate nitrogen and nitrate. According to range R, pH has the most significant influence on aerobic fermentation, followed by the content of nitrifying bacteria and time. The temperature has little effect on aerobic fermentation. The optimal combination obtained by the orthogonal test is A_1 B_3 C_2 D_3, namely, pH6, 0.2 mL nitrifying bacteria, the temperature of 30°C, and eight days.

Table 13. Orthogonal test results of aerobic fermentation.

	Factor				
Test No.	A	B	C	D	COD
1	1	1	1	1	841
2	1	2	2	2	732
3	1	3	3	3	648
4	2	1	2	3	554
5	2	2	3	1	948
6	2	3	1	2	825
7	3	1	3	2	846
8	3	2	1	3	742
9	3	3	2	1	645
K1	2221	2241	2408	2434	
K2	2327	2422	1931	2403	
K3	2233	2118	2442	1944	
k1	740	747	802	811	
k2	775	807	643	801	
k3	744	706	814	648	
R	35	101	171	163	
Order	A>B>D>C				
Optimal level	A_1	B_3	C_2	D_3	
Optimal combination	A_1 B_3 C_2 D_3				

3.3 *Denitrification and fermentation test results and analysis*

3.3.1 *The influence of denitrifying bacteria content on denitrifying fermentation*

Table 14. The influence of denitrifying bacteria content on denitrifying fermentation.

Denitrifying Bacteria Content 1 × 10^8/mL	0.05	0.1	0.15	0.2	0.3
Nitrate Nitrogen Content (mg/L)	304	257	243	226	229

Denitrifying bacteria transform and decompose nitrate nitrogen into nitrogen and release it. The nitrate-nitrogen content can be measured. The lower the nitrate-nitrogen content, the better the decomposition effect. It can be seen from Table 14 that when denitrifying bacteria convert nitrate nitrogen and nitrite into nitrogen, the transformation capacity of denitrifying bacteria can be determined by the remaining content of nitrate-nitrogen in the water. According to the above table, the transformation effect is the best when the added number of denitrifying bacteria is 0.1 g.

3.3.2 *The influence of pH on denitrification fermentation*

Table 15. The influence of PH on denitrification fermentation.

PH	5	6	7	8	9
Nitrate Nitrogen Content (mg/L)	479	420	307	398	459

Denitrifying bacteria transform and decompose nitrate nitrogen into nitrogen and release it. The nitrate-nitrogen content can be measured. The lower the nitrate-nitrogen content, the better the decomposition effect. It can be seen from table 15 that too low pH values will inhibit the conversion of nitrate-nitrogen and affect the survival of denitrifying bacteria, leading to a low conversion rate of nitrate nitrogen. High pH values will also inhibit the conversion of nitrate-nitrogen. When pH is 7, the conversion rate of nitrate-nitrogen is the highest.

3.3.3 *The influence of temperature on denitrification fermentation*

Table 16. The influence of temperature on denitrification fermentation.

Temperature (°C)	20	25	30	35	40
Nitrate Nitrogen Content (mg/L)	573	431	364	348	490

Denitrifying bacteria transform and decompose nitrate nitrogen into nitrogen and release it. The nitrate-nitrogen content can be measured. The lower the nitrate-nitrogen content, the better the decomposition effect. It can be seen from Tables16 that the conversion of denitrifying bacteria will be inhibited when the temperature is too low or too high. When the denitrifying bacteria is at 35°C, the conversion rate of denitrifying bacteria is the highest, and the remaining nitrate nitrogen is the lowest.

3.3.4 *The influence of time on denitrification fermentation*

Table 17. The influence of time on denitrification fermentation.

Time (d)	5	6	7	8	9
Nitrate Nitrogen Content (mg/L)	389	340	261	247	256

Denitrifying bacteria transform and decompose nitrate nitrogen into nitrogen and release it. The nitrate-nitrogen content can be measured. The lower the nitrate-nitrogen content, the better the decomposition effect. It can be seen from Table 17 that the content of nitrate nitrogen gradually decreases with the accumulation of time and days. On the 7th day, the conversion of nitrate-nitrogen tends to be gentle, and the production and decomposition of nitrate-nitrogen reached dynamic equilibrium.

3.3.5 *Analysis of orthogonal test results of denitrification fermentation*

Table 18. Orthogonal Test Results of Denitrification Fermentation.

	Factor				
Test No.	A	B	C	D	COD
1	1	1	1	1	674
2	1	2	2	2	489
3	1	3	3	3	482
4	2	1	2	3	649
5	2	2	3	1	365
6	2	3	1	2	387
7	3	1	3	2	608
8	3	2	1	3	496
9	3	3	2	1	377
K1	1645	1931	1557	1416	
K2	1401	1350	1515	1484	
K3	1481	1246	1455	1627	
k1	548	643	519	472	
k2	467	450	505	494	
k3	493	415	485	542	
R	81	228	34	70	
Order	C>A>D>B				
Optimal level	A_2	B_3	C_3	D_1	
Optimal combination	A_2B_3 C_3 D_1				

The influence of denitrifying bacteria content, pH, time, and temperature on COD content of Baijiu production wastewater was studied through the orthogonal test of denitrifying fermentation. After aerobic fermentation, the denitrifying bacteria were immediately added to convert nitrate nitrogen and nitrite generated by aerobic fermentation into nitrogen to purify water. It can be seen from Table 18 that the content of denitrifying bacteria has the greatest impact on denitrifying fermentation, followed by pH, time, and temperature. The optimal orthogonal combination of denitrifying fermentation is A2 B3 C3 D1, namely, 0.15 mL of denitrifying bacteria, pH7, the temperature of 35°C, and seven days.

4 CONCLUSION

After preliminary experiments, the odor of wastewater with the smell of distiller grains can be reduced through anaerobic fermentation, aerobic treatment, and denitrification fermentation. At the same time, the color of the original dark brown wastewater from Baijiu production becomes lighter. Subsequent addition of flocculation agent polyferric sulfate further improves the smell and color of the wastewater, and biochemical treatment gradually reduces the COD of Baijiu wastewater. The high content amino acids, proteins, and higher alcohols in Baijiu wastewater are decomposed into ammonium nitrogen, which is then decomposed by nitrifying bacteria and denitrifying bacteria. As a result, the content of highly concentrated organic matter in wastewater is reduced, so as to achieve the purpose of purification.

FOUNDATION

Scientific and Technological Innovation Team Project of Yibin Vocational and Technical College (ybzy21cxtd-03); College Level Scientific Research Project of Yibin Vocational and Technical College (ZRKY21YB-10, ZRKY21YB-11); Key Laboratory of Meat Processing of Sichuan Province (21-R-27)

REFERENCES

Chinese Hydraulic Engineering Society. Water Quality-Determination of Ammonia Nitrogen -Automatic Determination by Nessler's Reagent Spectroscopy. Beijing: Standards Press of China, 2008.

Fang J, Liu G, Li H, Tang Y, Li X. Comparison of Aerobic Treatment Methods for Liquor-making Wastewater[J]. Liquor-Making Science & Technology. 2015; (1): 62–64.

Li Q. Selection of Treatment Processes of Wastewater from Baijiu (Liquor) Production[J]. Liquor-Making Science & Technology. 2014; (09): 69–70.

Li X, Zhang J. Application of rapid digestion spectrophotometry in the determination of COD in industrial wastewater[J]. Petrochemical Industry Application. 2017; (04):127–130.

Zhang C, Wang P, Lyu S, Fan H, Lan S, Zhao X. Study on Treatment of Wastewater by Fenton Oxidation Technology[J]. Shandong Chemical Industry. 2019; (02):174–176.

Zhou J, Zhou J. Present Applications and Prospects of the Treatment of Distilled Spirit Wastewater[J]. Journal of Sichuan University of Science & Engineering (Natural Science Edition). 2008; 21(6):74-77+87.

Zhu J. The Determination of COD in Wastewater by the Rapid Spectrophotometric Method[J]. Environment and Sustainable Development. 2015; (03): 207–208.

Advances in Applied Chemistry and Industrial Catalysis – Saikia (Ed.)

Treatment of amoxicillin wastewater by Fe/Cu micro-electrolysis and the COD removal kinetics: Effects of Fe filler particle size and shape

Liheng Liu*
Guangxi Key Laboratory of Environmental Pollution Control Theory and Technology, Guilin University of Technology, Guilin, China

Jinchao Wang** & Dongwei He***
College of Environmental Science and Engineering, Guilin University of Technology, Guilin, China

ABSTRACT: In this study, the optimal process conditions for the treatment of simulated amoxicillin wastewater by Fe/Cu micro-electrolysis systems were preliminarily determined through batch experiments. According to the optimal process conditions, the effects of Fe particle size and shape on COD removal rate and kinetics were also discussed. The experimental results showed that the optimal process conditions were as follows: the electrode material dosage was 45 g/L, the initial pH was 3, and the reaction temperature was 293K. The micro-electrolysis systems with smaller-size particles and spherical particles had greater COD removal rates. The COD removal of the micro-electrolysis system constructed with different size particles was more preferably matched to the pseudo-second-order kinetic model, and their dominant speed-controlling steps were liquid film diffusion. The COD removal of micro-electrolysis systems with flaky and irregular particles was more in accordance with the pseudo-first-order kinetic model, while the COD removal of micro-electrolysis systems with columnar and spherical particles could be better described by the pseudo-second-order kinetic model. The main speed-controlling steps of micro-electrolysis systems constructed with different shape particles were chemical reaction (flaky particles), liquid film diffusion (columnar particles), liquid film diffusion/chemical reaction (irregular particles), and liquid film Diffusion (spherical particles), respectively.

1 INTRODUCTION

Pharmaceuticals are a new type of contaminant in water, which harm the environment due to their special physical and chemical properties or toxicity (Park et al. 2017). In addition, pharmaceuticals in water may enter the food system or human body through irrigation and water supply systems, causing a potential threat to food safety and human health (Fu et al. 2019, Malvar et al. 2019). The main sources of pharmaceuticals in water are various wastewaters, such as domestic sewage, hospital wastewater, and pharmaceutical wastewater (Becker et al. 2020; Guedes-Alonso et al. 2020; Huang et al. 2019). Among them, pharmaceutical wastewater is considered to be the most harmful to the water environment, because of its enormous emissions, complexity, and harmful substances (Changotra et al. 2020). The effective treatment of pharmaceutical wastewater can significantly reduce the content and types of pharmaceuticals in the water, ensuring the safety of the water environment and human health.

Although many techniques (e.g., photoelectrocatalysis, membrane bioreactor, adsorption) of have good treatment effects on pharmaceutical wastewater (Camiré et al. 2020; Chen et al. 2020; Collivignarelli et al. 2020), micro-electrolysis is still considered to be an attractive approach due to better pollutant removal efficiency, more simple operation and lower cost (Xu et al. 2016; Yuan et al. 2018). A previous study showed that the removal rate of oxytetracycline by micro-electrolysis

Corresponding Authors: *deanhenry_liu01@126.com, **652324870@qq.com and ***296132986@qq.com

DOI 10.1201/9781003308553-63

was higher than 95%, and the removal rate of COD was greater than 40% (Qi 2016). This may be attributed to a large amount of F^{2+} and [H] produced in the process of micro-electrolysis reactions, which have a strong reduction capacity (Xu et al. 2016). The possible reactions of micro-electrolysis are as follows (He et al. 2016; Sun et al. 2019):

$$Fe - 2e \rightarrow Fe^{2+} \tag{1}$$

$$Fe^{2+} - e \rightarrow Fe^{3+} \tag{2}$$

$$2H^{+} + 2e \rightarrow 2[H] \rightarrow H_2 \uparrow \tag{3}$$

$$O_2 + 4H^{+} + 4e \rightarrow 2O \cdot + 4[H] \tag{4}$$

$$H_2O + e \rightarrow [H] + OH \tag{5}$$

According to the above reactions, the amount of iron, hydrogen ion concentration (pH), and oxygen content all have an impact on the production of Fe^{2+} and [H], which further affect the treatment effect of micro-electrolysis on pharmaceutical wastewater (Qin et al. 2016). In addition, the contact time and temperature also have a greater impact on the treatment efficiency of pharmaceutical wastewater by micro-electrolysis (Mahdizadeh & Malakootian 2019; Xu et al. 2019). Therefore, many previous studies have focused on the effect of these process conditions on pharmaceutical removal (Malakootian et al. 2019; Liu et al. 2018, 2020; Yang et al. 2017). However, the influence of the physical properties of the electrode material (such as size and shape) on the removal of contaminants cannot be underestimated. Unfortunately, there are only a few studies on this aspect. Zhu et al. discussed the effect of activated carbon size and shape on the treatment effect of sunset yellow wastewater by Fe/C micro electrolysis, and showed that the sunset yellow degradation rate and COD removal rate of micro electrolysis system with 3∼6 mm spherical coal-based activated carbon particles were maximum (99% and 77.5%) (Zhu et al. 2018). Sun et al. (2019) constructed different Fe/C micro-electrolysis systems with iron particles and iron shaving as anodes, which were used to treat textile wastewater, and the TOC and chroma removals of iron particle Fe/C micro-electrolysis system were greater. Based on cathode materials, binary micro-electrolysis mainly has two types Fe/C micro-electrolysis and Fe/Cu micro-electrolysis (Lin et al. 2016). Due to the acceleration of iron corrosion, the pollutants removals of Fe/Cu micro-electrolysis are generally better than that of Fe/C micro-electrolysis under the same conditions (Yang et al. 2019). Nevertheless, there are few reports on the influence of electrode material physical properties on Fe /Cu micro-electrolysis to remove pollutants.

In this study, different Fe/Cu micro electrolysis systems were constructed and used to treat simulated amoxicillin wastewater. Through batch experiments, the optimal process conditions for the treatment of simulated amoxicillin wastewater by Fe/Cu micro-electrolysis system were preliminarily determined. Based on optimal process conditions, the effects of anode material (iron) size and shape on COD removal efficiency and COD removal kinetics were discussed.

2 MATERIALS AND METHODS

2.1 *Materials*

Various iron particles, copper powder, and amoxicillin were purchased from Shandong Lubei Metal Products Co., Ltd. (China), Shanghai Aladdin Bio-Chem Technology Co., Ltd. (China), and Hu'nan Kamp Medicine Co., Ltd. (China), respectively. Hydrochloric acid, sulfuric acid, silver sulfate, and sodium hydroxide were all from Xilong Chemical Co., Ltd. (China), and their purity was analytically pure.

The experimental wastewater was simulated amoxicillin wastewater of which COD concentration was 1243.22 mg/L and initial pH was 4.8.

2.2 *Experimental*

The mixtures of iron particles and copper powders of different qualities were added to Erlenmeyer flasks containing 50 mL of amoxicillin simulated wastewater. The mass ratio of iron particles to copper powder was 4: 5. And the initial pH of amoxicillin simulated wastewater was in the range of 2–6. Then, these Erlenmeyer flasks were shaken in a water bath thermostat for a certain period of time (2–72 h). The speed of the water bath thermostatic oscillator was 150 rpm/min, and its temperature was controlled within the range of 15–40°C. Subsequently, the wastewater after the reaction was transferred to centrifuge tubes and centrifuged for 20 min (4500 rpm/min). Finally, the microwave digestion method of potassium dichromate was used to measure the COD concentration of the supernatant. The COD removal rate (ϕ, %) was calculated according to formula (6) (Zhou et al. 2019):

$$\phi = (C_0 - C)/C_0 \times 100\% \tag{6}$$

where C_0 (mg/L) is the initial COD concentration of simulated amoxicillin wastewater; C (mg/L) is the COD concentration of supernatant.

2.3 *Kinetics models*

Pseudo-first-order kinetics, pseudo-second-order kinetics, liquid membrane diffusion, particle diffusion, and chemical reaction models were used to describe the process of COD removal. Their linear mathematical expressions are as follows (Lin et al. 2016; Liu et al. 2020):

$$\text{Pseudo-first-order kinetics model: } \ln(q_{r,\max} - q_{r,t}) = \ln q_{r,\max} - k_1 t \tag{7}$$

$$\text{Pseudo-second-order kinetics model: } t/q_{r,t} = 1/(k_2 q_{r,\max}^2) + t/q_{r,\max} \tag{8}$$

$$\text{Liquid film diffusion model: } \ln(1 - q_{r,t}/q_{r,\max}) = k_f t \tag{9}$$

$$\text{Particle diffusion model: } 1 - 3(1 - q_{r,t}/q_{r,\max})^{2/3} + 2(1 - q_{r,t}/q_{r,\max}) = k_p t \tag{10}$$

$$\text{Chemical reaction model: } 1 - (1 - q_{r,t}/q_{r,\max})^{1/3} = k_c t \tag{11}$$

where $q_{r,t}$, and $q_{r,max}$ (mg/g) are the COD removal at time t (h) and the maximum COD removal, respectively, and $q_{r,t}$ can be calculated by the following formula: $q_{r,t} = C_0\phi_t V/(100M)$; ϕ_t (%) is the COD removal rate at time t (h); V (L) is the volume of simulated amoxicillin wastewater; M (g) is the internal electrolysis filler mass; k_1 (1/h), k_2 (h·mg/g), k_f (1/h),k_d (1/h) and k_c (1/h) are the pseudo-first-order kinetics, pseudo-second-order kinetics, liquid film diffusion, particle diffusion, and chemical reaction rate constants, respectively.

3 RESULTS AND DISCUSSIONS

3.1 *Effects of multiple factors on COD removal*

3.1.1 *Filler dosage*

In general, a higher dosage of micro-electrolytic filler can provide more active sites and produce more Fe^{2+}, which is conducive to the removal of pollutants (Liu et al. 2020; Zhou et al. 2019). The results shown in Figure 1a were consistent with the above rules. The removal rate of COD generally showed an upward trend with the increase of micro-electrolysis filler dosage. When the

filler dosage was 45 g/L, the COD removal rate was 55.88%. Similar results have been reported in previous studies (Ren et al. 2018; Yu et al. 2019).

3.1.2 *Initial pH*

Micro-electrolysis is an acid-promoting process and the initial pH of the solution will significantly affect the corrosion of iron and the production of [H], which indicates that the removal of pollutants decreases with the increase of the pH of the solution (Ao et al. 2019). However, the results presented in Figure 1b were contrary to this theory. When the initial pH of the solution was in the range of 2–6, the maximum COD removal rate was 96.19% (when the initial pH was 3). This may be attributed to the higher concentration of H^+ (pH=2) which would cause polarization of the anode and slow down its corrosion reaction rate (Yuan et al. 2018).

3.1.3 *Reaction temperature*

Previous studies have shown that higher reaction temperatures are beneficial for contaminant removal (Chen et al. 2012; Wu et al. 2018). However, as the reaction temperature increased, the COD removal rate of simulated amoxicillin wastewater by Fe/Cu micro-electrolysis (Figure 1(c)) was undulant. The reason may be that the electron migration, hydrogen evolution, and reaction area of the micro-electrolysis reaction process depended on the reaction temperature (Li et al. 2017). Based on Figure 1c, the optimized reaction temperature was 293K, and the corresponding COD removal rate was 97.47%.

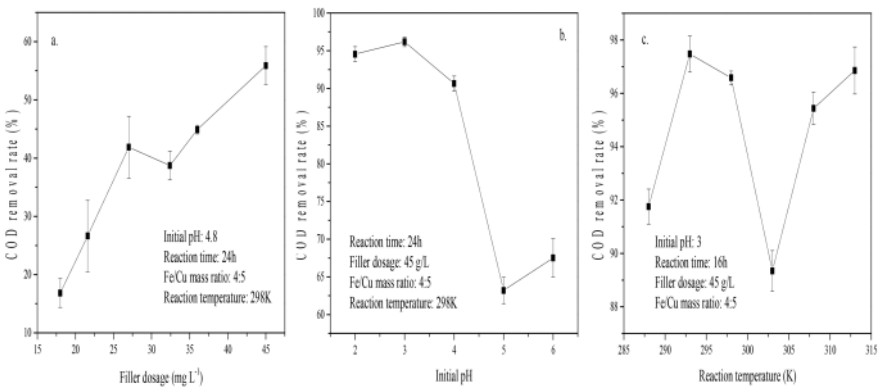

Figure 1. Effect of filler dosage (a), initial pH (b), and reaction temperature (c) on COD removal.

3.2 *Effect of Fe particle size on COD removal rate and kinetics*

3.2.1 *COD removal*

To explore the effect of anode material particle size on pollutant removal, a series of Fe/Cu micro-electrolysis systems were constructed with spherical iron particles of different particle sizes (r = 0.2 mm, 0.6 mm 1.0 mm, 1.4 mm, and 2.0 mm). Depending on the size of the iron particles, these micro-electrolysis systems were named MES-0.2, MES-0.6, MES-1.0, MES-1.4, and MES-2.0, respectively. The COD removal rates of these micro-electrolysis systems to simulated amoxicillin wastewater under the optimized process conditions determined by batch experiments are presented in Figure 2.

As shown in Figure 2, the effect of iron particle size on COD removal was more obvious when the reaction time was less than 48 h. This effect could be divided into three stages. In the first stage (the reaction time was in the range of 0–6 h), the COD removal rate of MES-0.2 was the lowest. The reason may be that more fine iron particles enhance the interaction strength between the particles, causing the reduction of the fluidity of the electrode material/wastewater system and the

migration ability of the pollutants to the electrode. With the extension of the reaction time, micro electrolysis was into the second stage (6–24 h). Due to the corrosion of the anode, the degradation of amoxicillin, and sufficient shock, the rheological properties of the electrode material/wastewater system were significantly changed. The MES-0.2 could provide a more effective reaction area, resulting in a higher COD removal rate (except for MES-0.4). In the third stage (reaction time was greater than 24h), the COD removal rates of MES-0.6, MES-1.0, and MES-2.0 continued to increase, while the COD removal rates of MES-0.2 and MES-1.4 showed a downward trend. This may be due to the desorption of contaminants adsorbed on the electrode materials of MES-0.2 and MES-1.4 escaped into the liquid phase, which was not removed (Lin et al. 2016). The Logistic function of Origin software was used to fit the data in Figure 2, and the maximum COD removal rates of MES-0.2, MES-0.6, MES-1.0, MES-1.4, and MES-2.0 were 99.31%, 97.52%, 97.38%, 97.22%, and 97.00%, respectively.

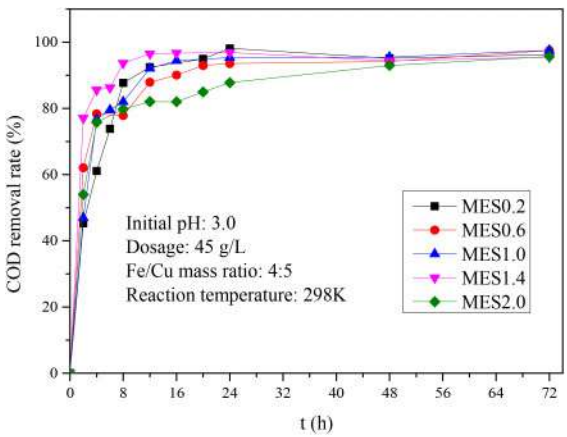

Figure 2. The effect of Fe particle size on COD removal.

3.2.2 *COD removal kinetics*

The fitting results of pseudo-first-order kinetics and pseudo-second-order kinetics models for COD removal of MES-0.2, MES-0.6, MES-1.0, MES-1.4, and MES-2.0 are shown in Figure 3 and

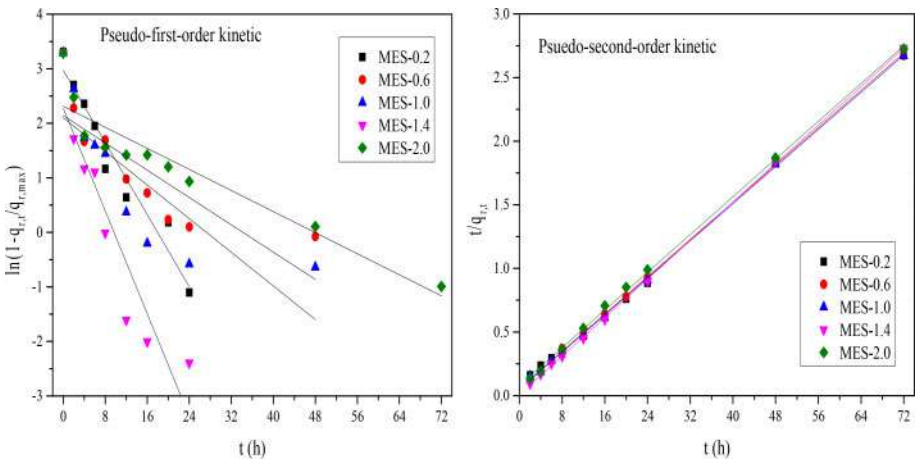

Figure 3. Kinetics fittings of COD removals by MES-0.2, MES-0.6, MES-1.0, MES-1.4 and MES-2.0.

Table 1. From the R^2 values, the COD removals of all micro-electrolysis systems were more in line with the pseudo-second-order kinetic model. Moreover, the values of qr, max calculated by the pseudo-second-order dynamic model ($q_{r,max,cal}$) were closer to the experimental values ($q_{r,max,exp}$). These indicated that the iron particle size had little effect on COD removal kinetics.

Table 1. COD removal kinetic parameters of MES-0.2, MES-0.6, MES-1.0, MES-1.4 and MES-2.0.

		Pseudofirstorder kinetic			Pseudosecondorder kinetic		
Micro electrolysis	$q_{r,max,exp}$	$q_{r,max,cal}$	k_1	R^2	$q_{r,max,cal}$	k_2	R^2
MES-0.2	27.44	19.57	0.1655	0.9409	27.31	0.0243	0.9987
MES-0.6	26.94	8.519	0.0626	0.6442	27.29	0.0247	0.9995
MES-1.0	26.90	8.178	0.0771	0.6216	27.45	0.0259	0.9995
MES-1.4	26.86	9.766	0.2357	0.8511	26.45	0.1568	0.9997
MES-2.0	26.80	10.11	0.0483	0.8648	26.98	0.0171	0.9990

Figure 4 and Table 2 show the fitting results of liquid film diffusion, particle diffusion, and chemical reaction models for COD removal. The mass transfer processes of the other micro-electrolysis systems were two-stage except for MES-0.2. The stages of the mass transfer process of MES-0.6, MES-1.0, MES-1.4, and MES-2.0 were also significantly different. According to the R^2 values, the main speed control steps of these five micro-electrolysis systems were all liquid film diffusion. However, the intercepts of these fitted curves are not zero, indicating that the mass transfer process was also affected by other processes. After comprehensive judgment, the speed control steps of MES-0.2, MES-0.6, and MES-1.0 should be liquid film diffusion/particle diffusion, while the speed control steps of MES-1.4 and MES-2.0 might be liquid film diffusion/chemical reaction.

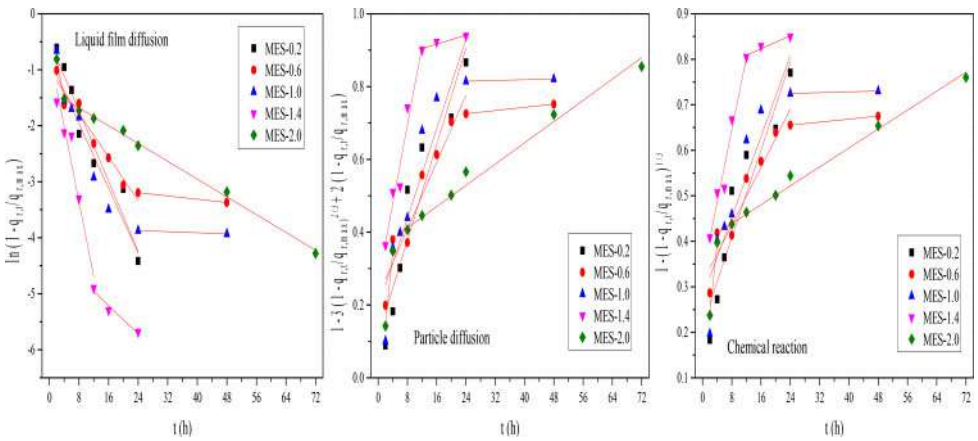

Figure 4. Mass transfer process fittings of COD removals by MES-0.2, MES-0.6, MES-1.0, MES-1.4 and MES-2.0.

3.3 *Effect of Fe particle shape on COD removal rate and kinetics*

3.3.1 *COD removal*

Combined with the above research, four Fe/Cu micro-electrolysis systems of MES-F, MES-C, MES-I, and MES-S were constructed with flaky iron particles, columnar iron particles, irregular iron

Table 2. Mass transfer process parameters of MES-0.2, MES-0.6, MES-1.0, MES-1.4 and MES-2.0.

Microelectrolysis	Time range	Liquid film diffusion			Particle diffusion			Chemical reaction		
		k_f	A_f	R^2	k_p	A_p	R^2	k_c	A_c	R^2
MES-0.2	2-24h	−0.1567	−0.4819	0.9338	0.0329	0.1142	0.8761	0.0241	0.2154	0.8719
MES-0.6	2-24h	−0.0971	−1.0046	0.9466	0.0230	0.2247	0.9111	0.0159	0.3087	0.9061
	24-48h	−0.0074	−3.0180	1.0000	0.0011	0.6990	1.0000	0.0008	0.6355	1.0000
MES-1.0	2-24h	−0.1445	−0.8046	0.8992	0.0308	0.1922	0.8180	0.0221	0.2762	0.8042
	24-48h	−0.0025	−3.8110	1.0000	0.0003	0.8080	1.0000	0.0002	0.7194	1.0000
MES-1.4	2-12h	−0.3352	−0.6707	0.9313	0.0540	0.2630	0.9470	0.0398	0.3261	0.9546
	12-24h	−0.0629	−4.2031	0.9259	0.0031	0.8678	0.8670	0.0036	0.7658	0.8949
MES-2.0	2-4h	−0.3530	−0.1069	1.0000	0.1029	−0.0636	1.0000	0.0800	0.0774	1.0000
	4-72h	−0.0397	−1.3652	0.9957	0.0073	0.3533	0.9783	0.0052	0.3971	0.9866

particles, and spherical iron particles, respectively. Their COD removals of simulated amoxicillin wastewater are shown in Figure 5. It could be seen that the COD removal rate of MES-S was significantly higher than that of MES-F, MES-C, and MES-I because of the higher effective reaction area (Sun 2019). The maximum COD removals of MES-F, MES-C, MES-I, and MES-S from the Logistic function of Origin software were 77.74%, 91.46%, 92.75%, and 97.22%, respectively. These indicated that the shape of Fe particles had an obvious effect on the removal of pollutants by Fe/Cu micro-electrolysis.

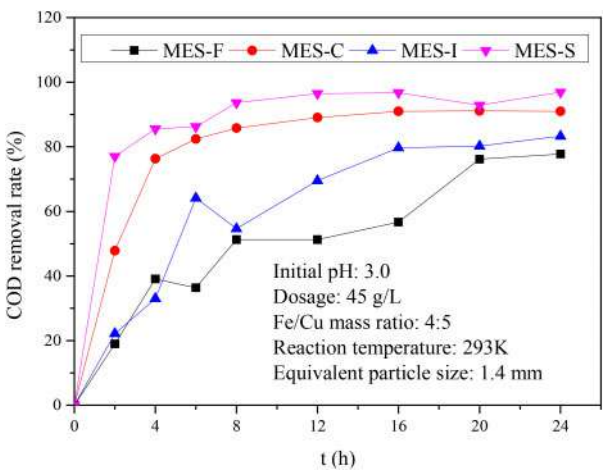

Figure 5. The effect of Fe particle shape on COD removal.

3.3.2 *COD removal kinetics*

From the fitting results of pseudo-first-order kinetics and pseudo-second-order kinetics models (Figure 6 and Table 3), the COD removals of MES-F, MES-C, MES-I, and MES-S could be better described by the pseudo-second-order kinetic model due to the higher R^2 values. However, the errors between qr, max, cal values of MES-F and MES-I from the pseudo-first-order kinetic model and the experimental values ($q_{r,max,exp}$) were less, which indicated that the pseudo-first-order kinetic model may be more suitable for COD removal processes of MES-F and MES-I. These suggested that the shape of Fe particles had a great impact on the contaminant removal kinetics of Fe/Cu micro-electrolysis.

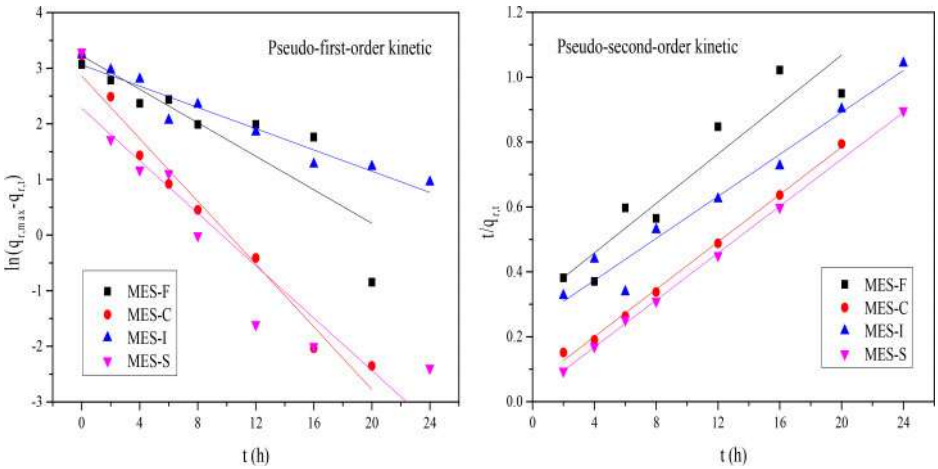

Figure 6. Kinetics fittings of COD removals by MES-F, MES-C, MES-I, and MES-S.

Table 3. COD removal kinetic parameters of MES-F, MES-C, MES-I, and MES-S.

		Pseudofirstorder kinetic			Pseudosecondorder kinetic		
Micro electrolysis	$q_{r,max,exp}$	$q_{r,max,cal}$	k_1	R^2	$q_{r,max,cal}$	k_2	R^2
MES-F	21.48	25.13	0.1506	0.7184	26.25	0.0047	0.8694
MES-C	25.27	17.46	0.2818	0.9710	27.37	0.0248	0.9966
MES-I	25.60	21.32	0.0956	0.9261	30.89	0.0043	0.9579
MES-S	26.86	9.766	0.2357	0.8511	27.63	0.0558	0.9994

The fitting results of liquid film diffusion, particle diffusion, and chemical reaction models for MES-F, MES-C, MES-I, and MES-S are listed in Figure 7 and Table 4. The mass transfer processes of these four micro-electrolysis systems were two-stage. Similarly, due to the non-zero intercept, the mass transfer process of MES-F was mainly affected by particle diffusion/chemical reaction, while the mass transfer processes of MES-C, MES-I, and MES-S were mainly controlled by liquid film diffusion/chemical reaction. According to the R2 values, the dominant speed-controlling steps of MES-F, MES-C, MES-I, and MES-S were a chemical reaction, liquid film diffusion, liquid film diffusion/chemical reaction, and liquid film diffusion, respectively.

4 CONCLUSION

The different Fe/Cu micro-electrolysis systems were constructed and successfully used to treat simulate amoxicillin wastewater. Through batch experiments, the optimal process conditions of the Fe/Cu micro-electrolysis system were determined. And on this basis, the influences of Fe particle size and shape on COD removal efficiency and kinetics were also discussed. The optimal process conditions for the treatment of simulated amoxicillin wastewater by Fe/Cu micro-electrolysis system were as follow: the electrode material dosage was 45 g/L, the initial solution pH was 3, and the reaction temperature was 293K. The COD removal efficiency of the Fe/Cu micro-electrolysis system with a small iron particle size was higher. The COD removals of the micro-electrolysis systems with different sizes of iron particles were more in line with the pseudo-second-order kinetic model, and their main speed-controlling step was liquid film diffusion. Compared with

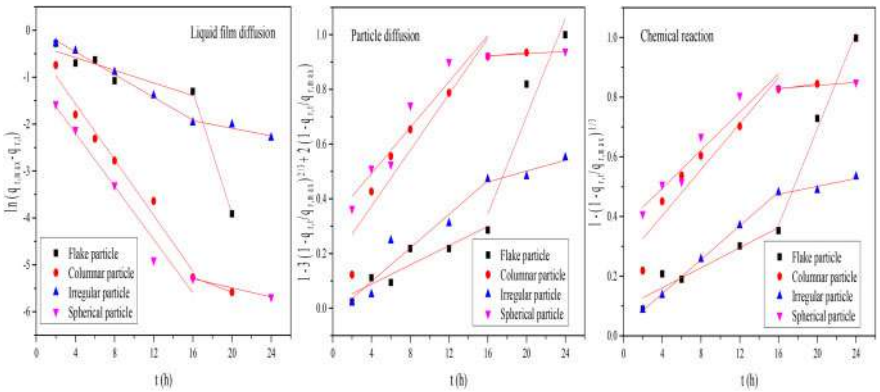

Figure 7. Mass transfer process fittings of COD removals by MES-F, MES-C, MES-I, and MES-S.

Table 4. Mass transfer process parameters of MES-F, MES-C, MES-I and MES-S.

Micro electrolysis	Time range	Liquid film diffusion			Particle diffusion			Chemical reaction		
		k_f	A_f	R^2	k_p	A_p	R^2	k_c	A_c	R^2
MES-F	2-12h	−0.0677	−0.3110	0.7778	0.0176	0.0178	0.8398	0.0168	0.0937	0.8797
	12-24h	−0.6520	9.1261	1.0000	0.0893	−1.0842	0.8498	0.0807	−0.9201	0.9821
MES-C	2-12h	−0.2972	−0.3779	0.9755	0.0512	0.1683	0.8699	0.0385	0.2487	0.8835
	12-24h	−0.0795	−3.9937	1.0000	0.0036	0.8634	1.0000	0.0044	0.7576	1.0000
MES-I	2-12h	−0.1212	0.0264	0.9926	0.0308	−0.0258	0.8912	0.0284	0.0277	0.9995
	12-24h	−0.0404	−1.2811	0.6928	0.0099	0.3030	0.7016	0.0066	0.3685	0.7015
MES-S	2-12h	−0.2833	−1.0592	0.9640	0.0420	0.3250	0.8936	0.0319	0.3669	0.9172
	12-24h	−0.0487	−4.5168	1.0000	0.0021	0.8884	1.0000	0.0026	0.7872	1.0000

flake particles, columnar particles, and irregular particles, the Fe/Cu micro electrolysis system of spherical iron particles was more conducive to COD removal. The COD removal of micro-electrolysis systems with flaky and irregular particles was more in accordance with the pseudo-first-order kinetic model, while the COD removal of micro-electrolysis systems with columnar and spherical particles could be better described by the pseudo-second-order kinetic model. The main speed-controlling steps of micro-electrolysis systems constructed with different shape particles were chemical reaction (flaky particles), liquid film diffusion (columnar particles), liquid film diffusion/chemical reaction (irregular particles), and liquid film Diffusion (spherical particles), respectively.

ACKNOWLEDGMENTS

This work was financially supported by Guangxi Key Laboratory of Environmental Pollution Control Theory and Technology Fund Projects (Guikeneng1801Z009, Guikeneng1401Z004), the Project of High-Level Innovation Team and Outstanding Scholar in Guangxi Colleges and Universities (002401013001), and Special Funding for Guangxi 'BaGui Scholar' (2016A10) Construction Projects.

REFERENCES

Ao, L. & F. Xia & Y. Ren & J. Xu & D. Shi & S. Zhang & L. Gu & Q. He (2019). Enhanced nitrate removal by micro-electrolysis using Fe0 and surfactant modified activated carbon. *Chem. Eng. J.* 357,180–187.

Becker, R.W. & M. Ibáñez & E.C. Lumbaque & M.L. Wilde & T.F. da Rosa & F. Hernández & C. Sirtori (2020). Investigation of pharmaceuticals and their metabolites in Brazilian hospital wastewater by LC-QTOF MS screening combined with a preliminary exposure and in silico risk assessment. *Sci. Total Environ.* 699, 134218.

Camiré, A. & J. Espinasse & B. Chabot & A. Lajeunesse (2020). Development of electrospun lignin nanofibers for the adsorption of pharmaceutical contaminants in wastewater. *Environ. Sci. Pollut. Res.* 27, 3560–3573.

Changotra, R. & H. Rajput & J.P. Guin & S,A. Khader & A. Dhir (2020). Techno-economical evaluation of coupling ionizing radiation and biological treatment process for the remediation of real pharmaceutical wastewater. *J. Clean. Prod.* 242, 118544.

Chen, L. & P. Cheng & L. Ye & H. Chen & X. Xu & L. Zhu (2020). Biological performance and fouling mitigation in the biochar-amended anaerobic membrane bioreactor (AnMBR) treating pharmaceutical wastewater. *Bioresource Technol.* 302, 122805.

Chen, R.H. & L.Y. Chai & Y.Y. Wang & H. Liu & Y.D. Shu & J. Zhao (2012). Degradation of organic wastewater containing Cu-EDTA by Fe-C micro-electrolysis. *T. Nonferr. Metal. Soc. China* 22, 983–990.

Collivignarelli, M.C. & A. Abbà & M.C. Miino & H. Arab & M. Bestetti & S. Franz (2020). Decolorization and biodegradability of a real pharmaceutical wastewater treated by H_2O_2-assisted photoelectrocatalysis on TiO_2 meshes. *J. of Hazard. Mater.* 387, 121668.

Fu, Q. & T. Malchi & L.J. Carter & H. Li & J. Gan & B. Chefetz (2019). Pharmaceutical and Personal Care Products: From Wastewater Treatment into Agro-Food Systems. *Environ. Sci. Technol.* 53, 14083–14090.

Guedes-Alonso, R. & S. Montesdeoca-Esponda & J.A. Herrera-Melián & R. Rodríguez-Rodríguez & Z. Ojeda-González & V. Landívar-Andrade & Z. Sosa-Ferrera & J.J. Santana-Rodríguez (2020). Pharmaceutical and personal care product residues in a macrophyte pond-constructed wetland treating wastewater from a university campus: Presence, removal and ecological risk assessment. *Sci. Total Environ.* 703, 135596.

He, Y.M. & K.Y. Chen & T.Y. Zhang (2016). Advanced treatment of heavy oil wastewater for reuse by the combination of microwave enhanced coagulation and iron/carbon micro-electrolysis. *J. Water Reuse Desal.* 6, 40–49.

Huang, S. & X. Shi & X. Bi & L.Y. Lee & H.Y. Ng (2019). Effect of ferric hydroxide on membrane fouling in membrane bioreactor treating pharmaceutical wastewater. *Bioresource Technol.* 292, 121852.

Li, P.N. & A.V. Ghule & J.Y. Chang (2017). Direct aqueous synthesis of quantum dots for high-performance $AgInSe_2$ quantum-dot-sensitized solar cell. *J. Power Sources* 354, 100–107.

Lin, H. & Y. Lin & L. Liu (2016). Treatment of dinitrodiazophenol production wastewater by Fe/C and Fe/Cu internal electrolysis and the COD removal kinetics. *J. Taiwan Inst. Chem. Eng.* 58, 148–154.

Liu, L. & D. He & F. Pan & R. Huang & H. Lin & X. Zhang (2020). Comparative study on treatment of methylene blue dye wastewater by different internal electrolysis systems and COD removal kinetics, thermodynamics and mechanism. *Chemosphere* 238, 124671.

Liu, Y. & C. Wang & Z. Sui & D. Zou (2018). Degradation of chlortetracycline using nano micro-electrolysis materials with loading copper. *Sep. Purif. Technol.* 203, 29–35.

Liu, Y. & Y. Gao & B. Yao & D. Zou (2020). Removal of chlortetracycline by nano- micro-electrolysis materials: Application and mechanism. *Chemosphere* 238, 124543.

Mahdizadeh, H. & M. Malakootian (2019). Optimization of ciprofloxacin removal from aqueous solutions by a novel semi-fluid Fe/charcoal micro-electrolysis reactor using response surface methodology. *Process Saf. Environ. Prot.* 123, 299–308.

Malakootian, M. & K. Kannan & M.A. Gharaghani & A. Dehdarirad & A. Nasiri & Y.D. Shahamat & H. Mahdizadeh (2019). Removal of metronidazole from wastewater by Fe/charcoal micro electrolysis fluidized bed reactor. *J. Environ. Chem. Eng.* 7, 103457.

Malvar, J.L. & J.L. Santos & J. Martín & I. Aparicio & E. Alonso (2019). Routine analytical method for monitoring the main metabolites for a recurrent group of parabens and pharmaceuticals in wastewater and tap water. *Anal. Bioanal. Chem.* 411, 6625–6635.

Park, J. & N. Yamashita & C. Park & T. Shimono & D.M. Takeuchi & H. Tanaka (2017). Removal characteristics of pharmaceuticals and personal care products: comparison between membrane bioreactor and various biological treatment processes. *Chemosphere* 179, 347–358.

Qi, Y. & S. Wu & F. Xi & S. He & C. Fan & B. Dai & J.C. Huang & L. Gao (2016). Performance of a coupled micro-electrolysis, anaerobic and aerobic system for oxytetracycline (OTC) production wastewater treatment. *J. Chem. Technol. Biotechnol.* 91, 1290–1298.

Qin, Z. & S. Liu & S.X. Liang & Q. Kang & J. Wang & C. Zhao (2016). Advanced treatment of pharmaceutical wastewater with combined micro-electrolysis, Fenton oxidation, and coagulation sedimentation method. *Desalin. Water Treat.* 57, 25369–25378.

Ren, L. & J. Dong & Z. Chi & H. Huang (2018). Reduced graphene oxide-nano zero value iron (rGO-nZVI) micro-electrolysis accelerating Cr(VI) removal in aquifer. *J. Environ. Sci.* 73, 96–106.

Sun, Z. & Z. Xu & Y. Zhou & D. Zhang & W. Chen (2019). Effects of different scrap iron as anode in Fe-C micro-electrolysis system for textile wastewater degradation. *Environ. Sci. Pollut. Res.* 26, 26869–26882.

Wu, Y. & Q. Yue & Z. Ren & B. Gao (2018). Immobilization of nanoscale zero-valent iron particles (nZVI) with synthesized activated carbon for the adsorption and degradation of Chloramphenicol (CAP). *J. Mol. Liq.* 262, 19–28.

Xu, L. & Y. Yang & W. Li & Y. Tao & Z. Sui & S. Song & J. Yang (2019). Three-dimensional macroporous graphene-wrapped zero-valent copper nanoparticles as efficient micro-electrolysis-promoted Fenton-like catalysts for metronidazole removal. *Sci. Total Environ.* 65, 219–233.

Xu, X. & Y. Cheng & T. Zhang & F. Ji & X. Xu (2016). Treatment of pharmaceutical wastewater using interior microelectrolysis/Fenton oxidation-coagulation and biological degradation. *Chemosphere* 152, 23–30.

Yang, B. & Y. Qi & R. Liu (2019). Pilot-Scale Production, Properties and Application of Fe/Cu Catalytic-Ceramic-Filler for Nitrobenzene Compounds Wastewater Treatment. *Catalysts*, 9, 11.

Yang, K. & Y. Jin & Q. Yue & P. Zhao & Y. Gao & S. Wu & B. Gao (2017). Comparison of two modified coal ash ferric-carbon micro-electrolysis ceramic media for pretreatment of tetracycline wastewater. *Environ. Sci. Pollut. Res.* 24, 12462–12473.

Yu, W. & Y. Sun & M. Lei & S. Chen & T. Qiu & Q. Tang (2019). Preparation of micro-electrolysis material from flotation waste of copper slag and its application for degradation of organic contaminants in water. *J. Hazard. Mater.* 361, 221–227.

Yuan, D. & Y. Liu & X. Mao & Y. Xiong & Z. Hong & J. Wang & X. Yin (2018). Treatment Performance and Degradation Process of Contaminants in Vitamin B12 Wastewater. *Environ. Eng. Sci.* 35(7), 673–683.

Zhou, D. & Y. Hu & Q. Guo & W. Yuan & J. Deng & Y. Dang (2019). Decomplexation efficiency and mechanism of Cu(II)-EDTA by H_2O_2 coupled internal micro-electrolysis process. *Environ. Sci. Pollut. Res.* 26, 1015–1025.

Zhu, X. & X. Chen & Z. Yang & Y. Liu & Z. Zhou & Z. Ren (2018). Investigating the influences of electrode material property on degradation behavior of organic wastewaters by iron-carbon micro-electrolysis. *Chem.l Eng. J.* 338, 46–54.

Advances in Applied Chemistry and Industrial Catalysis – Saikia (Ed.)

Application of staged flocculation sedimentation process in treatment of wastewater from copper concentrator

Xingfu Xue*
Sichuan University Jinjiang College, Pengshan, P.R China

ABSTRACT: For mine wastewater and mine tailings wastewater from copper mine concentrator, considering the characteristics and economic utilities of the physical treatment, chemical treatment, physical chemistry treatment and biological treatment, the mixed wastewater after reaction was neutralized and coagulated by using aluminium chlorohydrate iron as flocculant, and the flocculating properties of poly aluminium chloride and polyacrylamide were compared to achieve the function of treating the wastewater. The results show that the combined treatment technology of the first stage neutralizing, second stage neutralizing, poly aluminium chloride coagulation reaction, polyacrylamide flocculation reaction should be selected so as to make the effluent water quality meet the standard of reuse or discharge and the natural sedimentation has a good effect on the removal of suspended solids in wastewater.

1 INTRODUCTION

The problem of environmental protection in copper concentrator has been perplexing the sustainable development of the enterprise. The mine wastewater is mainly the underground wastewater gushing out from the mine hole in the process of mining. The mine tailings wastewater is a kind of wastewater produced in the tailings pond. The mine tailings wastewater produced by the concentrator is not only large in quantity and fine in particle, but also contains many kinds of chemicals. The acidic and alkaline wastewater is mainly neutralized by the method of mutual neutralization of wastewater and by the alkalinity of tailings. Heavy metal ions can be removed by adjusting pH value of raw water, co-precipitation or flotation, sulfide precipitation, lime-flocculation precipitation, adsorption (including biological adsorption), chelating resin, ion exchange and constructed wetland. Xanthate named for light yellow powder, is pungent odor and easy to decompose and the smell valve is 0.005 mg/L. The fish and shrimps in the water polluted by xanthate have an unpleasant smell of xanthate. Xanthate is soluble in water and unstable in water, especially in acidic conditions, its decomposition products can be sulfur pollutants. Therefore, the maximum allowable concentration of butyl xanthate in surface water of China is 0.005 mg/L. The black powder is mainly composed of dihydroxydisulfide phosphate, including formic acid, phosphoric acid, thiocresol and hydrogen sulfide. It is dark brown oily liquid, slightly soluble in water, with hydrogen sulfide odor. It is also the source of phenol, phosphorus and other pollution in mineral processing wastewater. Terpineol oil, known as 2# floatation oil and the main component is terpene alcohol. Yellow-brown oily transparent liquid, insoluble in water, is a non-toxic dressing reagent with a rosin flavour and it can cause changes in water sensory properties. Because terpineol oil is a foaming agent, it tends to cause unpleasant foam on the surface of the water. Xanthate and black powder are mainly removed by iron salt coagulation, precipitation, bleaching powder oxidation, Fenton oxidation degradation and artificial wetland technology. Sulfides are mainly removed by the methods of mutual precipitation, air stripping, air oxidation, chemical precipitation and biochemical oxidation. According to the national environmental protection standard, the related mine wastewater and mine tailings wastewater from concentrator must meet the first grade standard of comprehensive

*Corresponding Author: xuexingfu1980@163.com

DOI 10.1201/9781003308553-64

sewage discharge standard (GB8978-1996). In practical wastewater treatment, poly aluminium chloride (PAC) and polyacrylamide (PAM) are widely used. The difference between PAC and PAM is that aluminium chlorohydrate is coagulant, which acts as a bridging agent in wastewater treatment and thus attracts and flocculates each other to form clumps. The polyacrylamide is a kind of polymer organic flocculant, which can effectively promote the reaction between sewage and organic molecules in sewage treatment, and form a colloid flocculation group to achieve the removal effect. In this study, the mixed wastewater after reaction was neutralized and coagulated by using aluminium chlorohydrate iron as flocculant, and the flocculating properties of PAC and PAM were compared to achieve the function of treating the wastewater, make the wastewater meet the discharge standard finally.

2 RELATED WORK

According to the different stages of production, the wastewater from copper mine can be divided into mining wastewater and mineral processing wastewater. The mining wastewater is mainly acid wastewater, while the mineral processing wastewater is mainly tailings and middling wastewater produced in flotation stage. Lime is added to the flotation pulp to restrain the flotation of sulfur minerals and copper, which makes the wastewater alkaline. Acidic wastewater from copper mine is formed by oxidation, decomposition and microbial action of sulfide in ore or slag, and then combined with water. This kind of acid wastewater is mainly sulfuric acid, metal sulfate, and the ore in a variety of metal elements such as copper, lead, iron, aluminum, zinc, cadmium to form a solution containing these ions. The harm degree of this kind of wastewater to the water body is mainly determined by the acidity of the wastewater and the content of metal ions in the wastewater. The treatment of acidic copper-containing wastewater by ion exchange method was studied by Xu Xinyang et al. and the results shown that the treated wastewater could meet the national discharge standard. However, the ion exchange method needs periodic desorption and regeneration of the ion resin, which makes the cost of the ion exchange method increase and its application is limited. It has been shown that the treatment of mineral processing wastewater with low arsenic content and non-settling suspended matter by using aluminium chlorohydrate as flocculant is very effective, and that most of the mine wastewater contains heavy metal ions, in order to separate various heavy metal ions and eliminate their mutual interference, the method of fractional precipitation is usually adopted. For example, a two-stage neutralization-flocculation method was used to treat the acid wastewater from pyrite mine. The results showed that the method not only could make the metal ions in the effluent reach the standard at a lower pH value, but also was better than the one-stage neutralization-flocculation method and the amount of lime used is only 2/3 of the latter. The commonly used sulfiding agents are Na_2S, NaHS, H_2S, CaS and FeS. The main collectors for sulfide precipitation flotation are xanthate, amine and amphoteric collectors. Chitosan has abundant amino and hydroxyl groups which can chelate with many metal ions and can effectively adsorb and remove metal ions from wastewater, therefore, it is often used alone or in coordination with other substances as adsorbent, flocculant in water treatment for wastewater decolorization, heavy metal ion recovery. Li Q et al studied the flocculation and sedimentation of chitosan to Pb^{2+} and Cu^{2+} in wastewater. The results showed that chitosan could remove Cu^{2+} and Pb^{2+} from wastewater effectively. When the dosage of 0.8% chitosan was only 0.32 ml, the removal rates of Cu^{2+} and Pb^{2+} were 98.3% and 98.0% respectively. At present, the most up-to-date method of treating mine wastewater is microbial method, which has the advantages of low cost, strong applicability, no secondary pollution and recovery of elemental sulfur. The sulfate-reducing bacteria process is the reduction of sulfate to hydrogen sulfide by use of sulfate-reducing bacteria (SRB) and the further oxidation of hydrogen sulfide to elemental sulfur by biological oxidation. The iron ions can be completely precipitated in the form of $Fe(OH)_3$ at pH 3.0～5.0 due to the oxidation of Fe^{2+} to Fe^{3+} by iron oxidizing bacteria, which can further neutralize the treatment and save reagent. The successful use of thiobacillus ferrooxidans in the treatment of mine wastewater has been proven by the environmental protection institute of Beijing general research institute of

mining and metallurgy at its application in the Wushan copper mine wastewater. Compared with traditional chemical methods, this method can greatly reduce the cost of Fe^{2+} oxidation process.

3 MATERIALS AND METHODS

3.1 *Wastewater*

The wastewater comes from the mine wastewater and mine tailings wastewater of Sichuan Liwu copper industry Co., Ltd. The altitude of the concentrator is 2500M above sea level, the altitude of the mine wastewater is 2552M and 2400M above sea level, the altitude of the tailing pond is 2000M above sea level, the distance from the concentrator is 3000M. the volume of mine wastewater is $1100M^3/d$ ($50M^3/h$) and the volume of mine tailings wastewater is $1000M^3/d$ ($50M^3/h$). The wastewater contains impurities such as Pb, Zn, Cu, Fe and mineral processing reagents. The preliminary test data of wastewater samples are shown as in Table 1.

Table 1. The preliminary test data of wastewater samples.

test item	mine tailings wastewater	1#mine	2#mine	emission standard	unit
pH	4.5∼5.2	3.2∼3.5	4.5∼5.2	6.0∼9.0	
COD	15.05	19.56	9.030	100	mg/L
SS	98	142	136	70	mg/L
NH_3-N	11.16	8.761	7.512	15	mg/L
TP	1.8	0.79	0.46	0.5	mg/L
Hg	0.573	0.429	0.357	0.05	mg/L

The chemical oxygen demand (COD) of the two kinds of wastewater is low. The main reason is that the organic reagent in the wastewater is decomposed under acid condition, and the remaining part is organic polymer which is difficult to be degraded, if the wastewater needs to be reused, the problem that the concentration of organic matter will affect the mineral processing index during the reuse of intermediate water should be considered. The tailing pond of the project has good selfpurification ability, except ammonia nitrogen (NH_3-N) and mercury are high, other indicators are low. The metal ions in mine gushing wastewater are high, especially 1# mine gushing water, and Fe, Zn and Cu are much higher than national standard. The remaining indexes of wastewater, such as Pb, Cd, Ni, As, Fe, Cr, Fluoride, volatile phenol meet the first grade standard of comprehensive sewage discharge standard (GB8978-1996). Because the COD value of the wastewater reaches the standard and is very small, the previous test analysis report shows that the wastewater has no biochemical property, so the wastewater is not treated by biochemical method.

3.2 *Methodology and experimental procedure*

Investigate the natural settling effect of the mine tailings wastewater. Through the observation of the wastewater sample, the natural sedimentation effect of the mine tailings wastewater and mine gushing wastewater is good, if the sedimentation time is long enough (about one day), suspended solids (SS) can be reduced below 100 mg/L to reach the standard of reuse. However, the chromaticity of 1# mine wastewater is high, so the chromaticity of wastewater should be removed in the process. Investigate the removal method of COD of the mine tailings wastewater. If the mine tailings wastewater is used circularly, the flotation reagents such as xanthate and 2#Oil will be enriched continuously in the process of mineral processing, which will result in variable dosage and affect the ore processing index. It is difficult to detect the single amount of these drugs, but the single amount of these drugs can be inferred from the determination of COD, NH_3-N, total phosphorus (TP) and other indicators. Therefore, how to remove COD, NH_3-N, TP in the mine tailings wastewater is

the key to determine whether the tailings wastewater can be reused. Explore how to remove metal ions. The concentration of metal ions, especially Fe and Zn ions which can be used as activators or inhibitors in the continuous cycle, will affect the mineral processing index.

3.3 *Materials and analytical methods*

The concentration of all metal ions in the wastewater sample was determined by instrumental analysis ICP2060T single-channel scanning inductively coupled plasma-atomic emission spectrometer from Skyray instrument. COD, NH_3-N, TP were determined by multi-parameter water quality tester 5B-3B(V11) produced by Beijing Lianhua YongXing Science and Technology Development Co., Ltd. The pH measurements were performed using a laboratory table-top pH meter (Model PHS-3, Shanghai Leici instrument Co., Ltd. China). The nanometer aerator equipped with peristaltic pump as gas source was adopted. Polyacrylamide, aluminium chlorohydrate, which were used during experiments, were purchased from Henan Gongyi Huaming water treatment materials Co., Ltd. All reagents were analytically pure.

4 RESULTS AND DISCUSSION

4.1 *COD and NH_3-N remover*

Table 2. Experimental data of COD and NH_3-N remover.

	test item	raw water	aeration	removing reagent
1 # mine wastewater	COD (mg/L)	19.56	19.34	10.53
	NH_3-N (mg/L)	8.761	8.772	6.099
	COD removal rate (%)	–	–	46.17%
	NH_3-N removal rate (%)	–	–	30.38%
2 # mine wastewater	COD (mg/L)	9.030	9.15	7.51
	NH_3-N (mg/L)	7.512	7.13	3.158
	COD removal rate (%)	–	–	16.84%
	NH_3-N removal rate (%)	–	–	57.96%
mine tailings wastewater	COD (mg/L)	15.05	14.31	12.31
	NH_3-N (mg/L)	11.16	10.78	2.952
	COD removal rate (%)	–	4.9%	18.2%
	NH_3-N removal rate (%)	–	3.4%	73.54%

Because of the acidity of the wastewater, most of the organic chemicals and organic matters which are easy to be degraded have already been degraded, while the removal of COD and NH_3-N by aeration is not effective, which proves that the residual COD and NH_3-N are difficult to be decomposed organic polymers. The reagents such as COD and NH_3-N remover have good effect on the mine tailings wastewater, and can be used together according to requirements.

4.2 *Removal of metal ions*

Lime neutralization method, PAC coagulation method, PAM flocculation method and some physical methods were used to test the wastewater samples. The experimental data are shown as in the Tables 3, 4 and 5.

The result of experiments shows that most metal ions can be removed by these three methods, but the lime neutralization method has a large amount of mud and a little worse effect than the other two methods, and the operating cost of the PAM flocculation method is higher. The modified coagulation-sedimentation method was used to recycle the sludge to increase the sludge particle

Table 3. Experimental data of mine tailings wastewater.

test item	mine tailings wastewater	lime neutralization	PAC coagulation	PAM flocculation	emission standard	unit
pH	4.5∼5.2	8.0∼9.5	7.0∼9.0	7.0∼8.0	6.0∼9.0	
Hg	0.573	0.297	0.381	0.397	0.05	mg/L

Table 4. Experimental data of of 1#mine wastewater.

test item	1# mine	lime neutralization	PAC coagulation	PAM flocculation	emission standard	unit
pH	3.2∼3.5	8.0∼9.5	7.0∼9.0	7.0∼8.0	6.0∼9.0	
Zn	22.25	1.97	0.628	0.785	2.0	mg/L
Cu	7.93	0.741	0.163	0.93	0.5	mg/L
Hg	0.429	0.257	0.368	0.242	0.05	mg/L

Table 5. Experimental data of of 2#mine wastewater.

test item	2# mine	lime neutralization	PAC coagulation	PAM flocculation	emission standard	unit
pH	4.5∼5.2	8.0∼9.5	7.0∼9.0	7.0∼8.0	6.0∼9.0	
Zn	9.19	2.79	0.096	0.12	2.0	mg/L
Cu	2.01	0.76	0.149	0.155	0.5	mg/L
Hg	0.357	0.294	0.243	0.314	0.05	mg/L

size, increase the heavy metal removal rate, reduce the dosage of chemicals and save the operation cost.

5 CONCLUSIONS

The following conclusions can be drawn from this study:Under certain conditions, based on the function of natural settlement, the mine tailings wastewater can be clarified quickly and the SS and chromaticity can be removed by physical or chemical methods. The concentration of the reagents in the backwater can be controlled by physical method and chemical method. The mine tailings wastewater can be used to remove the metal ions in the backwater by coagulation sedimentation and adsorption. For the treatment and reuse of mine wastewater, it is suggested that the combined treatment technology of the first stage neutralizing, second stage neutralizing, PAC coagulation reaction, PAM flocculation reaction should be selected to make the effluent water quality meet the standard of reuse or discharge stably. In conclusion, coagulation sedimentation method has been widely used in the treatment of copper mineral processing wastewater. Combining coagulation-sedimentation technology with mineral processing technology, according to the actual operation of mineral processing plant, proper treatment and reasonable reuse of mineral processing wastewater can minimize the influence of wastewater on mineral processing indexes and maximize the reuse rate of wastewater, it is of great significance to reduce the discharge of wastewater in order to realize circular economic development and the establishment of the green mine. In the future, the copper enterprises should combine coagulation-sedimentation with natural sedimentation of tailings pond and high-efficiency thickener technology to work out a reasonable process according

to the actual operation of concentrators, such as mineral technological process, reagent system, etc. The technology will bring great contributions to the establishment of a stable wastewater treatment system to achieve zero discharge of wastewater finally.

ACKNOWLEDGMENTS

The author gratefully acknowledges financial support from Sichuan Economic and Information Commission for the program research and development of various heavy metal wastewater treatment technology in 2019 and on-site support in water sample analysis, engineering practice from Sichuan Liwu copper industry Co., Ltd.

REFERENCES

Begbie M, Craw D, Rufaut C, et al. Temporal and spatial variability of acid rock drainage in a rehabilitated coal mine, Wangaloa, South Otago, New Zealand [J]. S New Zealand Journal of Geology and Geophysics, 2007, 50(3): 227–238.

Lei Z W Sun Y Yang G Y Study on waste water management and resource utilization in Non-ferrous metal [J]. Safety and Environmental Protection in Mining Industry, 2006, 33(4): 40–41.

Li Q, Xi D L. Adsorption of lead ions from wastewater by Chitosan [J]. Chemical Environmental Protection, 2005, 25(5): 350–352.

Li Q, Yu Y P, Wang Z D. Adsorption of Cu^{2+} in wastewater by Chitosan [J]. Industrial Water Treatment, 2003, 23(4): 30–32.

Liu Z Y, Chen J Z. Study on the treatment of acidic mine wastewater [J]. Yunnan Environment Science, 2005, 23(A01):152–156.

Luptakova A, Kusnierova M Bioremediation of acid mine drainage contaminated by SRB [J]. Hydrometallurgy, 2005, 77(1): 97–102

McAnally S, Benefield L, Reed R B. Nickel removal from a synthetic nickel-plating wastewater using sulfide and carbonate for precipitation and coprecipitation [J]. Separation Science and Technology, 1984, 19 (2–3): 191–217

Wang W Gui X Y Water pollution and prevention in mining area [J] Safety and Environmental Protection in Mining Industry, 2001, 28(5): 48–49.

Wang Y M. Treatment of mineral processing wastewater by lime-flocculation sedimentation process [J]. Hunan Non-ferrous Metal 2005, 21(2):32–33.

Xu X Y Study on the treatment of Acidic copper-bearing mine wastewater [J]. Metal Mine, 2006 (11):76–78.

Yin A J Liu Z H Treatment of mine acid water by two-stage neutralization-flocculation process [J]. Hunan Metallurgy 1996, 71(2):137–143.

Advances in Applied Chemistry and Industrial Catalysis – Saikia (Ed.)

Fenton-neutralization-coagulation process for the treatment of SDBS wastewater

Lintang Yu*, Hang Su**,Yong-guang Wang***& Jun Wu****
College of Environmental Science and Engineering, Yangzhou University, Yangzhou, P.R. China

ABSTRACT: Fenton-neutralization-coagulation process was used to treat SDBS wastewater, The results show that: When the mass ratio of Fe^{2+} to H_2O_2 is 4.5: 1, PH value is 3, reaction time is 6h, neutralization reaction pH value is 10 and neutralization reaction time is 75min, The total removal rates of COD (Chemical Oxygen Demand) and SS (suspended solids) were 90.32% and 96.7% respectively.

1 INTRODUCTION

SDBS (Sodium dodecyl benzene suifonate), its chemical structure is:

The structure of SDBS is composed of a variety of chemical bonds such as benzene ring and double bond, which is not easy to be oxidized and is more sensitive to water hardness. Its chemical structure composed of hydrophobic non-polar molecules and hydrophilic polar molecules is an amphiphilic structure (Liu 2020) relatively stable in acidic solution and it has the functions of dispersion, foaming, emulsification, wetting (Li et al. 2015), strong degreasing ability, and high decontamination ability. SDBS has a significant decontamination effect on particle dirt and oily dirt. It is an excellent anionic surfactant (Shen & Wang1991). It is often used as a raw material for various detergents and has broad application prospects in detergents in the textile industry. SDBS is mainly linear sodium alkylbenzene sulfonate (LAS), and the production of LAS accounts for more than 90% of the total synthetic detergent (Wang et al. 2006). SDBS wastewater enters the discharged water body, adsorbing other pollutants to form colloidal particles by generating a large amount of foam, which can inhibit and kill microorganisms, thereby inhibiting the degradation of other toxic substances. In addition, SDBS has a solubilizing effect and improves other pollutants. The concentration of SDBS in the water can cause indirect pollution (Ye 2019), and SDBS in the water may cause great harm to humans in the form of dermatitis, irritation and respiratory diseases (Li et al. 2015).

At present, the processing technologies of SDBS mainly include physical method, biodegradation, membrane separation, and advanced oxidation, etc. (Su et al. 2019), and the commonly used physical methods include flocculation/coagulation sedimentation and air flotation, etc. The flocculation/coagulation sedimentation method has good effect, low cost and mature technology, and it is generally used as a pretreatment process for high-concentration surfactant wastewater, but its coagulant dosage is large, covering a large area and producing a large amount of waste residue and sludge (Feng et al. 2011); Air flotation is to produce a large number of microbubbles in the water

Corresponding authors: *ltyu@yzu.edu.cn, **su18895369824@163.com, ***003152@yzu.edu.cn and ****005407@yzu.edu.cn

DOI 10.1201/9781003308553-65

to form a three-phase mixture of water, gas and the removed substance. The density of the adhesive is less than water and floats to the surface of the water so that the organic pollutants in the water are separated and removed (Song 2000). The air flotation method has simple process flow and equipment structure, convenient operation and management, low investment, but its cost is high and secondary pollution cannot be avoided. The biodegradation method applies microorganisms to decompose organic carbon compounds and convert them into biological substances, which has the advantages of clean and environmental protection, low cost, thorough purification and no secondary pollution. However, its treatment time is long, and it has high environmental requirements, which requires a suitable temperature and pH, and can only treat low-concentration wastewater. If the concentration is too high, its toxicity will inhibit biodegradation and is unsatisfactory for industrial production (Yu et al. 2014). Advanced oxidation technology known as deep oxidation technology is characterized by the generation of hydroxyl radicals (OH) with strong oxidizing ability. Fenton oxidation is the most common type of advanced oxidation technology, which is used in reaction conditions such as high temperature and high pressure, light irradiation, and reaction with catalysts. It can effectively make macromolecules difficult to degrade organic oxygen, and it has a wider range of applications in the treatment of refractory wastewater.

Fenton's reagent composed of H_2O_2 (hydrogen peroxide) and Fe^{2+} ions is a chemical system with strong oxidizing properties. Under acidic conditions, H_2O_2 generates ·OH with the catalysis of Fe^{2+}. The oxidation potential of ·OH is as high as 2.73 V, making its oxidation ability very strong; ·OH has high electronegativity or electrophilicity, and its electron affinity is as high as 569.3 KJ, making it have strong addition reaction characteristics (Wu 2016). The electrophilic ·OH attacks an electron donating alkyl group, breaks it to form a small molecule compound, and finally oxidizes it to CO_2 and H_2O (Chen et al. 2004).

The oxidation product Fe^{3+} of the Fenton reaction is a flocculant with high adsorption and flocculation activity, which can cross-link the organic macromolecules in the wastewater to form colloidal particles or microflocs, and finally form larger flocs precipitation (Fan & Jin 2009), so as to remove organic molecules and reduce the SS in the wastewater. After neutralization and precipitation, the supernatant is taken to adjust the pH to 8 with sulfuric acid. By adding aluminum sulfate as a coagulant, the fine particles that are not easy to be separated from the wastewater can be changed into flocs, which are easy to be separated from the water through sweeping flocculation, so as to separate from the water.

2 TEST

2.1 *Test wastewater*

The main chemical composition of the industrial cleaning agent used in the washing of textile machines in a textile factory is SDBS. The production wastewater containing SDBS is weakly acidic. The quality of the wastewater is shown in Table 1.

Table 1. Wastewater quality.

COD/mg·L^{-1}	pH range	SS/mg·L^{-1}	Colour
6440	5.3	1420	/mg·L^{-1}

2.2 *Test reactor*

The test reactor has a specification of Φ200 mm×500 mm (diameter × height), the effective water depth is 350mm, and the effective volume is about 10L. The center of the pool is mechanically stirred and made of plexiglass.

2.2.1 *Fenton reaction*

Add an appropriate amount of 1 mol/L concentrated sulfuric acid to adjust the pH value, then add a certain amount of H_2O_2 and $FeSO_4$ in proportion, and stir to react.

2.2.2 *Neutralization precipitation*

After the Fenton reaction, add $Ca(OH)_2$ to stir and neutralize, then settle down after the reaction, and take the supernatant for COD and SS detection.

2.2.3 *Coagulation reaction*

After neutralization and sedimentation, the sludge is discharged through the sludge valve, 1mol/L sulfuric acid is added to adjust the PH value to 8, and $Al_2(SO_4)_3$ is added. After the reaction is completed, the COD and SS values are measured.

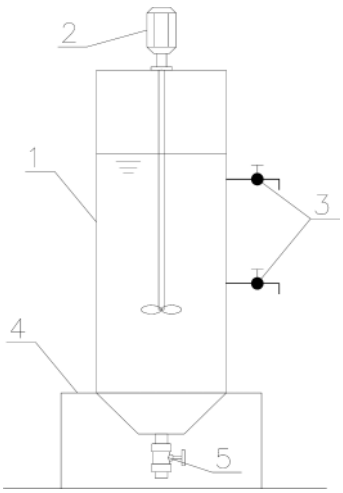

Figure 1. Reacto diagram of the test. 1. Reactor body 2. Stirrer 3. Sampling port 4. Support 5. Mud discharge valve.

2.3 *Test method*

The Fenton-neutralization test was designed by orthogonal experiment. The pH value is an important parameter in the process of Fenton reaction. The pH value controls the generation of OH· radicals and the concentration of Fe in Fe^{2+} or Fe^{3+} (Kang & Hwang 2000), H_2O_2 and Fe^{2+} also play an important role in the formation of OH· radicals. OH· radicals combine with organic compounds and oxidize them, thereby degrading them. Therefore, the optimal molar ratio of Fe^{2+}/H_2O_2 must be determined (Mohajeri et al. 2010). The main factors in this experiment are: Fe^{2+} dosage, pH value of Fenton reaction and pH value of neutralization reaction. 3 different levels of them were respectively selected to carry out orthogonal test according to Table 2. In this experiment, the wastewater containing 6‰ SDBS was taken under the conditions of Fenton reaction time of 4h and neutralization precipitation time of 2h. To ensure the test results, each COD data is measured three times, and the test results were averaged.

Table 2. Level – factor design table.

Level factor	Fe^{2+}:H_2O_2	Fenton reaction pH range	Neutralization reaction pH range
1	4:1	1	8
2	4.5:1	2	10
3	5:1	3	12

Table 3. L(3^4)Orthogonal experiment analysis table.

Experimental factor	Fe^{2+}:H_2O_2	Fenton reaction pH range	Neutralization reaction pH range	COD Removal rate
1	4:1	1	8	78.3
2	4:1	2	10	83.5
3	4:1	3	12	82.7
4	4.5:1	1	10	83.3
5	4.5:1	2	12	82.8
6	4.5:1	3	8	83.2
7	5:1	1	12	79
8	5:1	2	8	80.2
9	5:1	3	10	82.8
K_1	244.5	240.6	241.7	
K_2	249.3	246.5	249.6	
K_3	242	248.7	244.5	
R_j	7.3	8.1	7.9	

A simple and intuitive analysis of the results of the orthogonal experiment, the K_i row in Table 3 is the sum of the COD removal rate of the i-th level of each factor, and the R_j row is the range of K_i column. The larger the range, the greater the influence of this factor on the removal rate. It can be concluded that the influence of the three factors on the removal rate is Fenton pH value>neutralization pH value>Fe^{2+}: H_2O_2 mass ratio, and the best combination of factors for COD removal rate is Fe^{2+}:H_2O_2 =4.5:1. The pH value of the Fenton reaction is 3, and the pH value of the neutralization reaction is 10. The experiment was carried out under these conditions.

3 TEST PART

3.1 *Fenton-neutralization test*

3.1.1 *Fenton reaction*

In this experiment, the Fenton reaction was controlled to have a water inlet of 10L, Fenton's pH value of 3, $FeSO_4$ (concentration 10%) dosage of 100 ml, reaction time is 4h, neutralization reaction PH=10, and neutralization reaction time of 2h. The experiment was carried out under these conditions. Figure 2 shows the effect of different H_2O_2 dosage on COD removal rate and SS removal rate. It can be seen from the figure that the COD removal rate peaks is at when the H_2O_2 dosage is 12.5ml, and the higher H_2O_2 dosage will also cause the COD removal rate to decrease, which has little effect on the SS removal rate. Under this condition, the removal rate of SS is basically stable at about 94.5%.

Figure 2 shows that the dosage of H_2O_2 has a certain effect on the COD removal rate in the COD Fenton neutralization sedimentation tank. When the dosage of H_2O_2 is too low, fewer hydroxyl radicals are produced, and there are a series of intermediate reactions in the reaction. The reaction rate is too low, so the low dosage of H_2O_2 cannot decompose enough ·OH to attack the organic molecules in the water, resulting in a low COD removal rate. As the concentration of H_2O_2 increases, the reaction rate tends to increase. Because a series of intermediate reactions occur during the reaction, enough H_2O_2 must be added to make the reaction beyond this point (Gunes 2018). The high dosage of H_2O_2 cannot improve the degradation efficiency of organic matter, which may be due to the decomposition of H_2O_2 in water and the recombination of OH (Mane et al. 2007; Xue et al. 2009). In addition, excessive H_2O_2 may cause free radicals to be reduced to non-radicals, and it will reduce the removal efficiency of organic matter. At the same time, excessive H_2O_2 dosage will also cause the COD detection value to be higher. Therefore, the H_2O_2 dosage of 12.5ml has the greatest impact on the COD removal rate. In this case, the mass ratio Fe^{2+}:H_2O_2 of about 4.5:1 is confirmed by the results of orthogonal experiments.

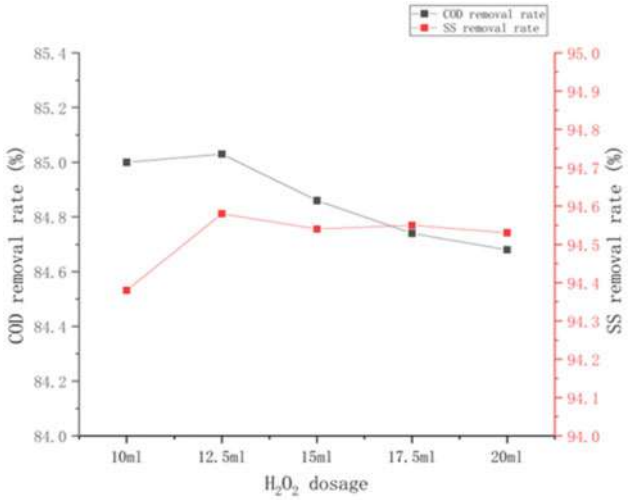

Figure 2. Relationship between H_2O_2 dosage and removal rate.

3.1.2 *The relationship between Fenton reaction time and removal efficiency*

In this experiment, the Fenton reaction pH value is 3, the mass ratio of Fe^{2+}:H_2O_2 is 4.5:1, the neutralization reaction pH value is 10, and the neutralization time is 2h. The Fenton reaction time is adjusted by measuring the effluent COD value and effluent water. The SS value determines the best Fenton reaction time, and the test results are shown in Figure 3. As the Fenton reaction time increases, the COD removal rate and the SS removal rate increase significantly. Until the Fenton reaction time is 6h, the COD removal rate increases gradually, the COD removal rate is basically stable at about 85%, and the SS effluent value gradually stabilizes after 4 hours of reaction. Since when the reaction time is short, Fenton's reagent fails to generate enough hydroxyl radicals to fully react with organic molecules. When the reaction time is longer, Hydroxyl radicals and organic molecules can fully react. Then as time increasing, hydroxyl radicals cannot effectively attack the remaining organic molecules, and the COD removal rate will also tend to stabilize. During the first 4 hours of the reaction, most of the organic molecules are mineralized to inorganic substances and stripped from the wastewater. At the same time, a large amount of suspended matter in the wastewater forms colloids or flocs with the neutralizing reagent, and finally forms a larger floc precipitation. As the reaction time increasing, the suspended matter that is easily removed in the wastewater begins to decrease, causing the SS removal rate to slowly increase until stable. When the reaction time is 6h, the COD and SS removal effects are both at the best. Therefore, the 6-hour reaction is the best Fenton reaction time for this test.

3.1.3 *The relationship between neutralization reaction time and removal efficiency*

This experiment was carried out under the conditions that the pH value of the Fenton reaction was 3, the mass ratio of Fe^{2+}:H_2O_2 was 4.5:1, and the pH value of the neutralization reaction was 10. The neutralization reaction time was adjusted to determine the removal rate of COD and SS, and the optimal neutralization reaction time was determined. The test results were shown in Figure 4. When the neutralization reaction time is 30 min to 45 min, most of the pollutants are cross-linked under the action of neutralization reagent and Fe^{3+} to form large flocs precipitation. As the neutralization reaction time increases, the micro flocs adsorb each other to form larger flocs and continue to precipitate. After 75 minutes, the COD effluent value is basically stable at about 970 mg/L, and the effluent value of SS is basically stable at 80 mg/L after 60 min. Therefore, this experiment selects 75 min as the best reaction time for neutralization.

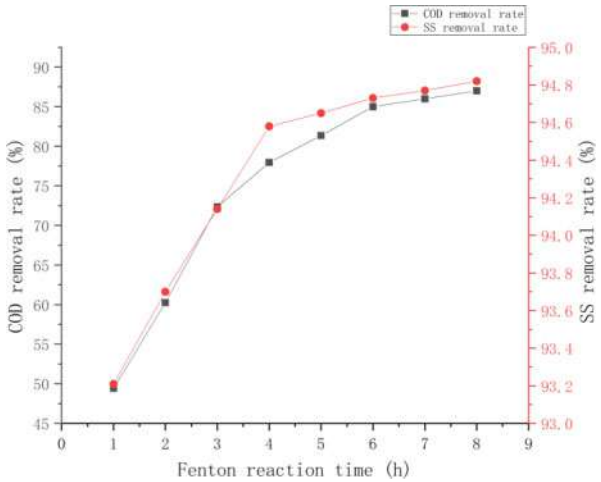

Figure 3. The relationship between Fenton reaction time and removal rate.

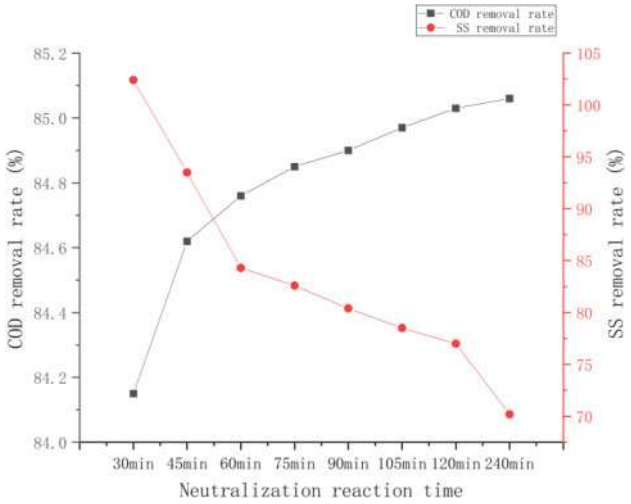

Figure 4. The relationship between neutralization reaction time and removal rate.

3.2 *Coagulation test*

After the wastewater is treated under the treatment conditions determined by the above Fenton - Neutralization Test, the pH value is adjusted to 8 by adding sulfuric acid, and 10ml of aluminum sulfate coagulant with a concentration of 10% is added for every 1L of wastewater, and then quickly stirred. After producing a large alum flower, the coagulant PAM is added at the proportion of 0.1%. Then it is stirred slowly for a period of time, and then stand still. After the surface of wastewater is cleared, the liquid supernatant is taken to conduct numerical detection of COD and SS.

As shown in Table 4, when the coagulant collides with the remaining SDBS molecules in the water, it can effectively remove the colloidal particles in the wastewater and the SDBS molecules adsorbed on the surface of the colloid, and further remove the small organic molecules in the water. Therefore, the concentration of SDBS in the wastewater can be reduced. After the wastewater

is processed by the Fenton-neutralization-coagulation process, the removal rate of COD reaches 90.32%, and the removal rate of SS reaches 96.7%.

4 CONCLUSION

(1) It is feasible to use Fenton-neutralization-coagulation process to pre-treat SDBS wastewater. When the influent COD is 6440mg/L and the influent SS is 1420mg/L, the COD removal rate after treatment can reach 90.32%, and the SS removal rate can reach 96.7%.

(2) The best operating conditions for Fenton-neutralization process to treat SDBS wastewater are pH=3, Fe^{2+}: H_2O_2 mass ratio 4.5:1, reaction time 6h, neutralization pH=10, and neutralization reaction time is 75 min.

REFERENCES

Chen Yufeng, Chen Riyao, Zheng Xi, Chen Xiao, Chen Zhen. Study on electro-generated Fenton reagent and its degradation of sodium dodecylbenzene sulfonate[J]. Technology and Equipment for Environmental Pollution Control, 2004(11):42–47.

Fan Jinchu, Jin Zhaofeng. Water Quality Engineering[M]. Beijing: China Construction Industry Press, 2009:28–35.

Feng Huixia, Zhang Juan, Zhang Ting. Research progress in the application of surfactant wastewater treatment technology[J]. Applied Chemical Industry, 2011, 40 (10): 1828–1832.

Güneş Elçin and Çifçi Deniz İzlen and Çelik Suna Özden. Comparison of Fenton process and adsorption method for treatment of industrial container and drum cleaning industry wastewater. [J]. Environmental technology, 2018, 39(7): 824–830.

Kang YW, Hwang KY (2000) Effects of reaction conditions on the oxidation effciency in the Fenton process. Water Res 34:2786–2790.

Li Yue, Wang Baohui, Lao Xin. Research progress of new methods for the treatment of sodium dodecylbenzene sulfonate in sewage[J]. Energy Chemical Industry, 2015, 36(6): 33.

Lílian Cristina Pereira et al. A perspective on the potential risks of emerging contaminants to human and environmental health[J]. Environmental Science and Pollution Research, 2015, 22(18): 13800–13823.

Liu Pengfei, Research on the removal of surfactants in wastewater by coagulation-electrocatalytic oxidation combined method[D]. Shenyang University of Technology, 2020.

Mane VS, Mall ID, Srivastava VC (2007) Use of bagasse fly ash as an adsorbent for the removal of brillant green dye from aqueous solution. Dye Pigment 73:269–278.

Mohajeri S, Aziz HA, Isa MH, Zahed MA, Adlan MN (2010). Statistical optimization of process parameters for landfill leachate treatment using electro-Fenton technique.J Hazard Mater 176:749–758.

Shen Zhong, Wang Guoting. Colloid and Surface Chemistry[M]. Beijing: Chemical Industry Press, 1991, 305.

Song Qin. Treatment of wastewater containing anionic surfactants by foam separation method[J]. Pollution Control Technology, 2000, 13 (2): 123–124.

Su Guiping, Xiang Jin, Zheng Wenjiang, et al. Treatment of wastewater containing sodium dodecylbenzene sulfonate by adsorption-foam separation combined technology[J]. Journal of Sichuan University of Science & Technology, 2019, 32(3): 20.

Wang Jun, Pan Zhijun, Zhang Chaohong, et al. Study on the ultrasonic degradation of sodium dodecylbenzene sulfonate (SDBS) catalyzed by ordinary anatase TiO2[J]. Environmental Science Research, 2006, 19(3): 81–87.

Wu Peng. Exploration of Fenton Reaction Treatment of Organic Wastewater[J]. Xinjiang Nonferrous Metals, 2016, 39(S1):72–73.

Xue, X., et al. (2009). Fenton-like oxidation of Rhodamine B in the presence of two types of iron (II, III) oxide. J Hazard Mater 166(1): 407–414.

Ye Xue. The harm of surfactant wastewater to the environment and its treatment technology[J]. Sichuan Chemical Industry, 2019, 22(03):11–13.

Yu Shan, Li Changhai, Jia Dongmei. Research progress on alkylbenzene sulfonate wastewater treatment technology[J]. Applied Chemical Industry,2014,43(08):1477–1481.

Advances in Applied Chemistry and Industrial Catalysis – Saikia (Ed.)

Research on disinfection technology of medical wastewater based on chlorine dioxide

Xingfu Xue*
Sichuan University Jinjiang College, Pengshan, China

ABSTRACT: Disinfection is a necessary link in the treatment of medical wastewater. Traditional chlorine-containing disinfectants play a leading role in the treatment of medical wastewater, but with the increasingly stringent water quality standards, the requirements for disinfection technology are also getting higher and higher. In this study, a specific mixture of agent A and agent B was used to generate chlorine dioxide to disinfect the treated wastewater, the fecal coliform group of the treated wastewater can meet the national standard of wastewater pollutant discharge (GB18466-2005). Therefore, the process has better practical application value and obvious economic benefit for the treatment of medium and small-sized hospital wastewater.

1 INTRODUCTION

Wastewater from small and medium-sized hospitals contains toxic and harmful substances such as organic substances, infectious bacteria, viruses, parasitic eggs, medicines, disinfectants, and detergents. If the medical wastewater is discharged directly without treatment, it will seriously pollute the water environment and affect people's health. Compared with ordinary domestic wastewater, medical wastewater also has the characteristics of space pollution, and acute and latent infection, especially the highly infectious virus such as the novel coronavirus (COVID-19). For example, the concentration of suspended matter in the effluent is unstable, the secondary pollution of residual sludge, the pollution of aerosol, the excessive addition of disinfectants, and the destruction of ecological safety. On January 30, 2020, the general office of the ministry of ecology and environment of China issued a circular on emergency monitoring of the ecological environment in response to the epidemic situation of COVID-19 and a monitoring plan for the epidemic situation of pneumonia caused by a new type of coronavirus infection. In addition to the monitoring of 61 routine indicators, two additional indicators of epidemic prevention and control, residual chlorine, and biological toxicity were added. On February 1, the ministry of ecology and environment also issued a circular on the supervision of medical sewage and urban sewage in the epidemic situation of COVID-19, the residual chlorine content in the medical wastewater of the designated hospital for epidemic prevention and control, and the effluent from the sewage treatment where the medical wastewater was collected were determined as emergency monitoring, biotoxicity can be unpredictable if conditions are not met. Therefore, the government departments concerned pay great attention to the monitoring of residual chlorine in the water during the epidemic. Residual chlorine refers to the chlorine-containing disinfectant in the water. After a certain period of contact, in addition to a small part of chlorine with bacteria, microorganisms, and viruses in the water, there is still a part of chlorine left and the amount of chlorine added exceeds the required amount of chlorine, this means the amount of total chlorine such as active chlorine, hypochlorous acid, organic chloride that remains after the chlorine agent is added to the treated water and is acted upon by reducing substances such as pathogenic microorganisms and viruses. The effect of residual chlorine is to ensure continuous sterilization, but also to prevent water from secondary pollution. The disinfection efficacy of chlorine preparation only depends on the residual chlorine concentration. In the

*Corresponding Author: xuexingfu1980@163.com

DOI 10.1201/9781003308553-66

water supply and drainage industry, residual chlorine is an important parameter to evaluate the quality of water and it is also an important index for water environmental monitoring. According to the research and analysis of related data, liquid chlorine disinfection, ozone disinfection, sodium hypochlorite disinfection, and membrane biological treatment are widely used in China at present. However, liquid chlorine is simply used to sterilize microorganisms and it is easy to form organochloride and cause secondary pollution to the water body. Ozone disinfection does not have the effect of continuous disinfection and the equipment is complicated and the management is difficult, it must be used in combination with other disinfectants to increase the cost of treatment. Based on this, given the problems of the high residue of disinfection by-products, low degree of automation, poor mechanization, poor tightness, and insufficient sanitary protection conditions in the traditional disinfection process by adding chlorine dioxide, this paper proposes an improved chlorine dioxide disinfection process for medical wastewater treatment.

2 RELATED WORK

Chlorine dioxide is a member of the oxychloride family and was discovered by a British chemist named Humphry Davy in 1811. When he discovered that potassium chloride reacted with hydrochloric acid to produce a green gas called chlorine dioxide, the relative molecular weight is 67.452 g/mol. It is a yellow-green or orange gas and its color varies with the concentration. It has a pungent odor similar to chlorine and ozone at normal temperature and pressure. Its solubility in water is 8.3 g/L, under pH-neutral conditions, the dissociation constant is 1.2×10^7 and it remains in the state of non-dissociation. The chlorine dioxide is highly volatile and escapes from the solution as soon as it is slightly aerated. When cooled to $-40°C$, it becomes a dark red liquid and when the temperature drops to $-59°C$, it becomes an orange solid. Chlorine dioxide is an explosive gas. To solve the problem of chlorine dioxide storage and transportation, stability chlorine dioxide has been developed. Using its morphological properties which change with temperature, it cools down to a liquid chlorine dioxide, under $-5 \sim 9°C$ the property is stable and the effective ClO_2 content is kept at about 2%. The solid chlorine dioxide is easily soluble in water, contains the effective ClO_2 2%∼5%, and is easy to use and carry. Chlorine dioxide is one of the best water disinfectants and has been used in pulp and fiber bleaching, disinfection of drinking water, sterilization and preservation of food processing, industrial wastewater treatment sterilization, clinical sterilization, sterilization and bleaching of food packaging paper, sanitation and epidemic prevention disinfection, oil and fat bleaching and sterilization in flour and rice processing, water disinfection and disease prevention and treatment in aquaculture since its inception. Chlorine dioxide is a highly effective, broad-spectrum, safe, fast, and multifunctional disinfectant, which has also been used to disinfect drinking water and hospital sewage in China in recent years, many developed countries already use chlorine dioxide as a common disinfectant for drinking water and hospital sewage. Chlorine dioxide is recognized internationally as the most ideal new alternative to chlorine series disinfectant with very low residual chlorine production and almost no halocarbon such as carcinogenic trihalomethane. A combination process of chlorine and chlorine dioxide, ozone, and chloramine has been developed to produce a synergistic effect and enhance the efficacy of disinfection. There are many explanations for how chlorine dioxide works. It has been found that the outer layer of the molecular structure of chlorine dioxide has a pair of unpaired electrons-an active free radical that has strong oxidation. It can rapidly oxidize and destroy the tyrosine in the protein of the virus capsid, inhibit the specific adsorption of the virus and prevent its infection to host cells. Chlorine dioxide redox with some amino acids in bacterial and other microbial proteins which break down amino acids, controlling microbial protein synthesis and ultimately killing bacteria. In addition to inactivating common bacteria, chlorine dioxide can kill heterotrophic bacteria such as Escherichia coli, iron bacteria, sulfate-reducing bacteria, and autotrophic bacteria such as fungi, poliovirus, hepatitis virus, giardia lamblia cyst, and its disinfection effect is not affected by the pH value. Unlike other disinfectants, chlorine dioxide's oxidation of organic matter rarely interacts with the water's organic matter to produce harmful chlorinated organics. Its main organic by-products

include low molecular weight acetaldehyde and carboxylic acid and its effect on reducing anions and cations is mainly from its toxic state to a non-toxic state. The main inorganic by-products of ClO_2 disinfection are ClO_2^-, ClO_3^- and Cl^-. The toxicity of ClO_2^- and ClO_3^- is still controversial. Other recent studies have shown that the main mechanism of chlorine dioxide disinfection is not the inhibition of protein synthesis but rather the effect on the outer membrane of microorganisms by changing the structure of protein and lipid in the outer membrane, the permeability of the outer membrane can be changed to cause the abnormal metabolism of microorganism and kill the microorganism. Studies have shown that in the process of chlorine dioxide disinfection, the effect of time is greater than that of concentration and time is the most important factor in the disinfection of chlorine dioxide, therefore, prolonged disinfection time can improve the disinfection effect of chlorine dioxide. Like liquid chlorine, chlorine dioxide is more effective at killing bacteria as the temperature increases. In general, the inactivation efficiency of chlorine dioxide to microorganisms increases with the increase of system temperature. According to a recent study by LeChevalliert, when the temperature of the system was lowered from 20°C to 10°C, the inactivation efficiency of cryptosporidium chlorine dioxide was reduced by 40% under the same conditions, this is similar to the effect of chlorine dioxide inactivating giardia lamblia and the virus.

3 MATERIALS AND METHODS

3.1 *Wastewater*

The wastewater comes from a hospital in Chengdu which has 20 clinical departments, 10 medical technology departments, 10 functional departments (departments), and 100 existing beds. The main departments and facilities of hospital wastewater discharge are the clinic, laboratory, ward, laundry room, and operating room. In addition to the separate treatment of radioactive wastewater in the hospital, the wastewater from the dining hall is treated by the grease trap, the domestic wastewater is treated by the septic tank, and treated by the sewage treatment station. After the wastewater is treated by the sewage treatment station, it is discharged into the municipal pipe network, when it finally enters the sewage treatment, the medical wastewater discharged shall comply with the pretreatment standards of the water pollutant discharge standard for medical institutions (GB18466-2005). The preliminary test data of batch sample data for 7 consecutive days of medical wastewater samples are shown in Table 1.

Table 1. The preliminary test data of medical wastewater samples.

test item	pH	COD	BOD_5	SS	fecal coli group count	total residual chlorine
value	8.6	328.0	121.0	65.0	8.75×10^4	—
	8.5	326.7	118.2	70.2	9.45×10^4	
	8.5	330.2	123.6	65.8	9.25×10^4	
	8.6	332.2	125.4	64.9	8.55×10^4	
	8.6	320.5	124.8	68.0	9.35×10^4	
	8.6	333.2	126.4	65.9	8.65×10^4	
	8.6	321.5	125.8	69.0	9.35×10^4	
unit		mg/L	mg/L	mg/L	MPN/L	mg/L

Table 2. The discharge standard of medical wastewater.

test item	pH	COD	BOD_5	SS	fecal coli group count	total residual chlorine
value	6∼9	250.0	100.0	60.0	5000	2.0∼8.0
unit		mg/L	mg/L	mg/L	MPN/L	mg/L

3.2 *Methodology and experimental procedure*

The sewage treatment process is a hydrolysis acidification+filtration+disinfection process. The synthetic sewage from the hospital flows into the regulating tank after the large suspended matter is intercepted by the grille. After the peak load of sewage is eliminated by adjusting, homogenizing, and equalizing quantity, part of the chemical oxygen demand (COD) is removed and the sewage pump is used to lift it into the hydrolysis tank and the secondary biochemical tank. Through hydrolysis and acidification, biodegradation, metabolism, oxidation, adsorption, and other functions, toxic and harmful, refractory organic matter can be transformed into non-toxic and harmless, stable, non-secondary pollution organic matter and achieve sewage purification. The effluent is settled by a secondary clarifier and the upper clear water is drained into an intermediate clarifier, filtered through a filter, and then discharged after quantitative chlorine dioxide sterilization. The requirement of residual chlorine in the effluent is ensured by using chlorine dioxide disinfection technology. To ensure the full play of disinfectant, it will be divided into agent A and agent B, agent A general is a chlorine dioxide disinfectant while agent B is an activator, the main ingredient is citric acid to help a full dissolution of the disinfection effect. Agent A and agent B are packed separately mixed with water according to a certain proportion and then reacted with a diaphragm metering pump according to a certain proportion to produce dissolved chlorine dioxide.

3.3 *Materials and analytical methods*

COD, BOD_5, and SS were determined by multi-parameter water quality tester 5B-3B(V11) produced by Beijing Lianhua YongXing science and technology development Co., Ltd. The pH measurement was performed using a laboratory table-top pH meter (Model PHS-3, Shanghai Leici instrument Co., Ltd. China). The diaphragm metering pump was Seko Komba series microprocessor-based electromagnetic driven metering pump with a maximum pressure of 10.0bar and a maximum flow rate of 9L/H. The analytical methods used in fecal coliform count tests refer to the methods for monitoring and analyzing water and wastewater.

4 RESULTS AND DISCUSSION

4.1 *Comparison of sterilization efficacy of different concentrations of chlorine dioxide*

The fecal coliform bacteria in the water was measured at different concentrations after 30 minutes of disinfection, as shown in Table 3. The sterilization effect of different concentrations of chlorine dioxide is shown in Figure 1 and the total residual chlorine in the treated sewage with different concentrations of chlorine dioxide is shown in Figure 2.

Table 3. The germidical efficacy at different concentrations of chlorine dioxide.

test item	unit	1	2	3	4	5	6	7
concentrations of chlorine dioxide	mg/L	5	10	15	20	25	50	100
fecal coli group count	MPN/L	4800	3500	2300	1100	500	0	0
Total residual chlorone	mg/L	2.4	2.7	2.8	3.2	4.0	4.5	5.6

As can be seen from Figures 1 and 2, under the condition of disinfection time of 30 minutes, the total number of bacteria in and out of the water decreased gradually with the increase of the concentration, and the total number of bacteria in the water was zero at the concentration of 50mg/L, which achieved complete elimination When the concentration was 50mg/L, the number of bacteria in the effluent was zero and the bacteria could be eliminated. Similarly, the fecal coliform count decreased with the increase of the concentration and at the concentration of 50mg/L, the

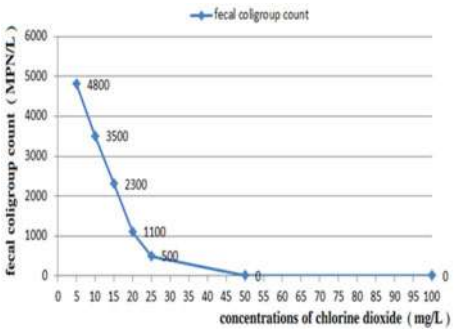

Figure 1. The sterilization effect of different concentrations of chlorine dioxide.

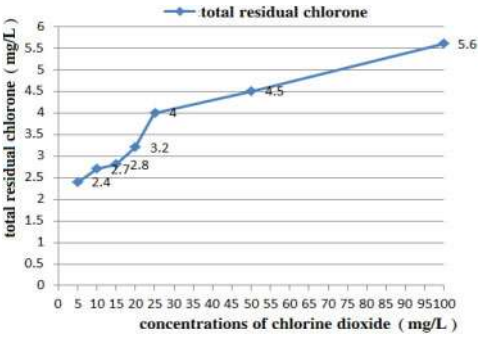

Figure 2. The total residual chlorine with different concentrations of chlorine dioxide.

fecal coliform group in the effluent was 0MPN/L. When the concentration of chlorine dioxide was 45～50mg/L, the total residual chlorine in the wastewater increased obviously.

4.2 *Comparison of germicidal efficacy of chlorine dioxide in different time*

The chlorine dioxide was put into the wastewater treatment system for 60 minutes and determined at a different time and the experiment result was shown in Table 4. The sterilization effect of different contact times of chlorine dioxide is shown in Figure 3 and the total residual chlorine in the treated sewage with a different contact time of chlorine dioxide is shown in Figure 4.

Table 4. The germidical efficacy at a different contact time of chlorine dioxide.

test item	Unit	1	2	3	4	5	6	7
contact time of chlorine dioxide	h	0.5	1.0	1.2	1.8	2.0	2.2	2.5
fecal coligroup count	MPN/L	2800	1300	800	650	300	0	0
total residual chlorone	mg/L	2.9	2.6	2.5	2.3	2.2	2.1	2.0

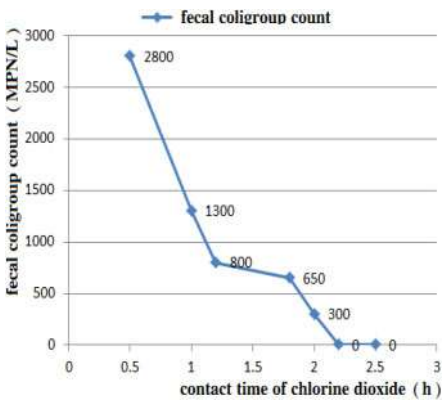

Figure 3. The sterilization effect of different contact time of chlorine dioxide.

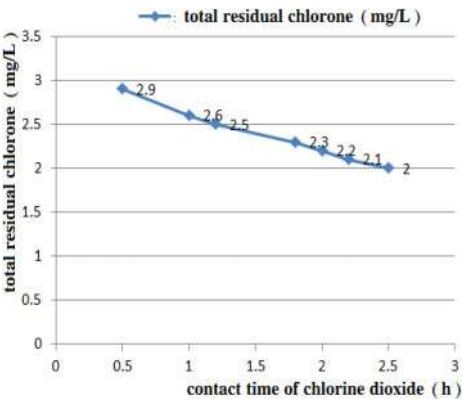

Figure 4. The total residual chlorine with a different contact time of chlorine dioxide.

As can be seen from Figures 3 and 4, with the disinfection contact time increased, the total number of bacteria in and out of the water decreased gradually with the extension of time, and the

total number of bacteria in the water reached zero when the disinfection time was 2.2 hour. When the disinfection time is 2.2 hours, the total number of bacteria in the influent and outlet water is zero, and the total number of bacteria in the influent and outlet water is zero, complete elimination was achieved, and at the time of disinfection for 2.2 hours, the fecal coliform count in the effluent was zero and complete elimination was achieved. When the contact time of chlorine dioxide was 45～50mg/L, with the increased contact time of chlorine dioxide, the total residual chlorine in the wastewater decreased obviously.

5 CONCLUSIONS

The chlorine dioxide disinfection process for treatment of medical wastewater has the advantages of a simple treatment process, good effluent effect, less production of disinfection by-products, and complete disinfection. The process can reduce the formation of disinfection by-products, optimize the quality of effluent, reduce the harm to the environment after disinfection of hospital wastewater, and meet the requirements of medical wastewater discharge standards and environmental ecological safety. For chlorine dioxide to enter the broader market for commodities and applications, the issue of chlorine dioxide's stability must be addressed. The chlorine dioxide is made by absorbing chlorine dioxide gas in inert solutions such as sodium carbonate, sodium percarbonate, and borate to form a liquid containing more than 2% chlorine dioxide which can be activated by acid before use. As technology advances, CIO_2 in chlorine dioxide aqueous solutions is adsorbed on porous materials such as molecular sieves and calcium silicates to form solid chlorine dioxide, sometimes supported by excipients such as agar or gelatin, the stability of the solid-state slow-release chlorine dioxide was further improved.

REFERENCES

Chen C L, Zhang X, Lin Y X. Research and application of disinfection mechanism of chlorine dioxide[J]. Journal of Medical Engineering Design, 2002, 23(4).

Editorial board of water and wastewater monitoring method of state environmental protection bureau. Methods of water and wastewater monitoring and analysis (4th edition) [H]. Beijing: China Environmental Science Press, 2002.

Emmamuel E, Perrodin Y, Keck G, et a1. Ecotoxicological risk assessment of hospital wastewater. A proposed framework for raw effluents discharging into urban sewer network[J]. Journal of Hazardous Materials, 2005, 117(1):1–11.

Feng X X. Study on treatment of hospital wastewater by MBR+ chlorine dioxide disinfection system [D]. Nankai University, 2011:16–17.

Gu J W. Application of CASS and CIO_2 in hospital wastewater treatment[J]. Applied Journal of General Practice, 2005, 3(6).

Guay Cynthia, Rodriguez Manuel, Serodes Jean. Using ozonation and chloramination to reduce the formation of trihalomethanes and haloacetie acids in drinking water[J]. Desalination, 2005, 176(1～3):229–240.

Lechevallier M, Norton W D. Giardia and eryptosperidium in raw and finished water[J]. AWWA, 1995, 87(9):54–63.

Li X Z. Study on new technology of preparation of high effective disinfectant dioxidochlorine [D]. Kunming University of Science and Technology, 2009.

Narkis N, Katz A, Orshansky E, et al. Disinfection of effluents by combinations of chlorine dioxide and chlorine[J]. Water Science and Technology, 1995, 31(5):105–114.

Zhu M, MaL S, Wang S W et al. Study on the kinetics of water disinfection in chlorine dioxide[J]. Hebei Chemical Industry, 2010, 33(10):34–36.

Advances in Applied Chemistry and Industrial Catalysis – Saikia (Ed.)

Optimization of low temperature plasma system for the degradation of UDMH wastewater through response surface methodology

Ziwen Hou, Zelong Xu* & Yi Wu
Joint Laboratory of Liquid Propellant Application Technology, China Jiuquan Satellite Launch Center, Jiuquan, China

ABSTRACT: Using suspended electrode dielectric barrier discharge (FE-DBD) technology, a low temperature plasma system for the disposal of unsymmetrical dimethyl hydrazine (UDMH) wastewater was designed and built. To study the mechanism and optimization of the system, the discharge gap, pH value of solution and dosage of alkali solution were taken as the influencing factors, while the degradation rates of UDMH and COD were taken as the response values. The relation between each influencing factor and the response values was analysed through response surface methodology. Combined with the central composite design method, the experiment conditions were designed, the quadratic polynomial regression model of response value and influencing factor was established, and the reliability of the model was analysed through variance analysis and experimental verification. Finally, the response surface analysis and system optimization of the response values were carried out, and the optimal operating conditions and degradation rates of UDMH and COD were obtained, which were verified by experiments. The results showed that the optimal operating conditions of the system were as follows: the discharge gap was 2 mm, the pH value of the solution was 10, and the dosage of alkali solution was 1.00 g/L. Under the conditions above, the actual degradation rates reached 95.00% and 87.40% respectively, which were higher than the predicted values of 88.54% and 82.16%, and the error was 5.99% ∼ 6.80%.

1 GENERAL INSTRUCTIONS

UDMH is the fuel for most of China's liquid launch vehicles in service, and will still be widely used in China's space launch missions for a long time in the future (Li 2020). In daily propellant supplying tasks, thousand tons of wastewater with different concentrations of UDMH is produced every year. If the wastewater is not treated timely and effectively, it will cause immeasurable damage to the environment, personnel and equipment (NUDT 1993).

At present, the conventional treatment methods for UDMH wastewater mainly include heating, physical adsorption, chemical oxidation and microbial degradation (Qiao 2004; Yuan 1991). Most of these methods can remove UDMH in wastewater to a certain extent. However, it is easy to cause secondary pollution. In addition, these methods have various disadvantages like high energy consumption and cost, long treatment cycle, and poor effect when the concentration of pollutants is low (Bu 2015; Liu 2010; Jia 2009; Wang 2002; Zhang 2013). Therefore, there is an urgent need to seek new technologies and methods for the treatment of UDMH wastewater to realize non-toxic treatment and achieve the purpose of reducing environmental pollution and enhancing the environmental safety protection capability of the launch site. Plasma has a stronger ability to degrade organic substances, making it a better oxidizing agent (Li 2020). It can efficiently degrade organic substances into non-toxic molecules through high-energy electronic shocks, ultraviolet photolysis catalysis, and chemical kinetics. The efficient degradation of organics into non-toxic

*Corresponding Author: 422412620@qq.com

DOI 10.1201/9781003308553-67

small molecules is one of the hotspots in the field of environmental treatment in recent years (Li 2020). It is expected to be applied to the efficient treatment of UDMH wastewater and solve relevant safety problems of launch sites.

Generally speaking, traditional researches on the optimization of process parameters of wastewater treatment system tend to adopt analysis methods with a single factor, which fail to analyze the interaction between process parameters. However, the response surface method can be used to study the relations between various influencing factors (Li 2015). At present, there is little literature on its application to the experimental study of UDMH wastewater treatment, and the optimization parameters studied in the literature only include temperature, pH value, etc., and do not involve parameters relevant to plasma discharge. Therefore, a low temperature plasma system for the treatment of UDMH wastewater was built in this paper. The discharge gap, pH value of solution and dosage of alkali solution were selected as the influencing factors, and the degradation rates of UDMH and COD were selected as the response values. Central composite design method was selected to design the experiment conditions (Zhen 2021) and Design-Expert software was used to analyze the experiment data. At the same time, a second-order model was established for regression fitting, and the reliability of the model was analyzed through analysis of variance and experimental verification. The impact of operating parameters on response values and the interaction between parameters in the response surface diagram were studied as well. The optimal operating conditions and degradation rates of the system were obtained, and the optimal operating conditions of the system were verified by experiments. This study can provide a theoretical basis for the experimental research and engineering application of low temperature plasma in the degradation of UDMH wastewater.

2 CONSTRUCTION OF LOW TEMPERATURE PLASMA SYSTEM FOR UDMH WASTEWATER TREATMENT

2.1 *System design and process*

As shown in Figure 1, the treatment system is composed of three subsystems: box, water circulation system and reaction module. To ensure the treatment capacity and efficiency, the method of circulating treatment is adopted for the degradation of UDMH wastewater. Only the wastewater flowing through the discharge area will be disposed by plasma. The box is made of 304 stainless-steel with an effective capacity of 500L, which is used to contain wastewater; the water circulation system

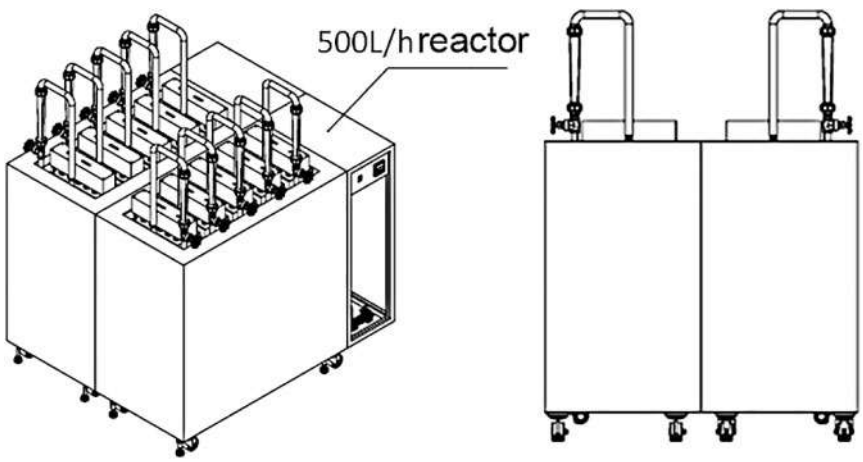

Figure 1. Diagram of low temperature plasma system for UDMH wastewater treatment.

includes water pump, water pipe and flow meter. The UDMH wastewater in the tank is pumped to the deflector by the pump, shunted to each discharge area through the deflector, and returned to the tank after treatment; the reaction module is constructed based on the principle of cylindrical dielectric barrier discharge, which is mainly composed of reaction tube, insulating protective cover, liquid inlet, grounding rod, insulating protective cover fixing rod and liquid holding frame.

2.2 *Plasma discharge components*

As shown in Figure 2, Figure 2(a) is a schematic diagram of a plasma discharge assembly, and Figure 2(b) is a schematic diagram of a reaction tube. Each reaction module contains 6 reaction tubes in an array arrangement. The six reaction tubes are fixed on a stainless-steel plate which act as a ground pole, and the stainless-steel plate has a grounding rod to ensure the reliability of the grounding of each reaction tube. The reaction tube is the core of the entire system. The cylindrical dielectric barrier discharge structure is adopted to fill the entire cylindrical cavity with plasma. It is a typical dielectric barrier discharge unit, which can improve the plasma concentration and realize the efficient treatment of the wastewater. A notch is set on the guide sleeve, and the size determines the efficiency of each reaction tube. When the water circulation system draws the wastewater into the liquid inlet, it flows into the liquid holding rack and flows back to the tank through the notch on the reaction pipe. Once the wastewater flows into the notch, the discharge phenomenon will occur inside the reaction tube, generating a large amount of plasma.

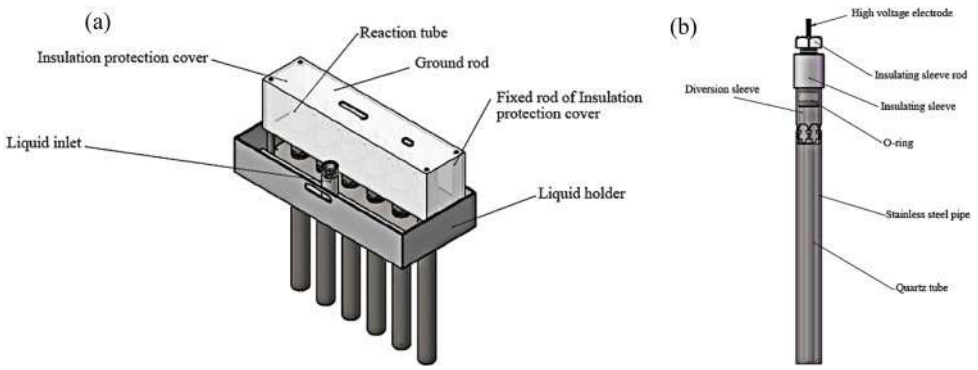

Figure 2. Schematic diagram of the reaction module and discharge tube.

2.3 *System electrical parameters and measurement of energy utilization efficiency*

A suspended electrode dielectric barrier discharge plasma device was used to dispose UDMH wastewater. The optimal working conditions were studied. The operating parameters of FE-DBD and auxiliary measures were studied to enhance the degradation of wastewater through plasma. When the power frequency was 10 kHz and the effective value of discharge voltage was 11kv, FE-DBD could stably generate strong low temperature plasma. The discharge power of FE-DBD device could be measured by Lissajous graphic method (Cong 2018), and the discharge parameters were shown in Figure 3.

The expression of the discharge power is shown in the following formula, where P is the discharge power of the device, and f is the power supply frequency, which is 10 kHz, and C is the measuring capacitance, which is 10^3 pF, and S is the parallelogram area in the Lissajous figure, which is $10^4 \times 10^3$ V^2.

$$P = \frac{1}{T}\int_0^T UIdt = \frac{C}{T}\int_0^T U\frac{dUc}{dt}dt = fC\oint UdUc = fCS \tag{1}$$

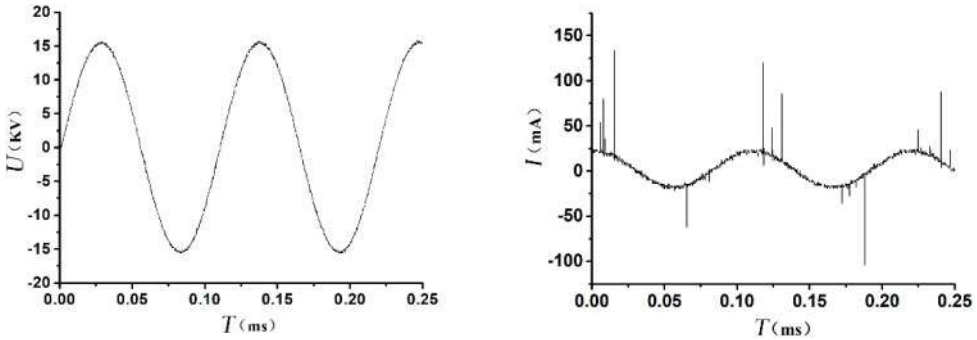

Figure 3. Discharge parameters of FE-DBD during operation. (a) Voltage waveform. (b) Current waveform.

$$SED = \frac{P}{V} \tag{2}$$

$$G_{50} = \frac{0.5 \cdot C_0}{SED \cdot t_{50}} \tag{3}$$

$$S = \frac{P \times \mathrm{t}}{V} \tag{4}$$

In the formulas above, the energy utilization efficiency G_{50} refers to the mass of pollutants degraded per unit of energy when the target pollutant degradation rate is 50%, in g/(kW·h); *SED* (specific energy density) is the relative energy density, which represents the energy injected by unit volume solution, in kW/L; V is the volume of the wastewater disposed, in L; t_{50} is the time it takes for the reactant to be degraded by 50%, in h; C_0 is the initial mass concentration of the reactant, in g/L; S is the energy density, in kJ/L; t is the time taken to complete the treatment process, in s. Combining formulas (1) ~ (4), the energy utilization efficiency G_{50} is calculated to be 14.42~144.2g/(kW·h), and the energy density for degradation of UDMH is 254.4 kJ/L.

2.4 *Analytical instruments, methods and reagents*

UV-Vis spectrophotometer, HP8453E, Agilent, USA; pH meter, PHSJ-3F type, Shanghai Leici. The concentration of UDMH was determined by sodium ferrocyanide spectrophotometry, and the COD value was determined through potassium permanganate method.

UDMH, Jiangxi Xinghuo Organic Silicone Plant, with a mass fraction of 99.59%; the wastewater sample was prepared with reverse osmosis water. Sodium hydroxide and hydrochloric acid of analytical grade from Sinopharm Group.

3 EXPERIMENT DESIGN FOR RESPONSE SURFACE METHODOLOGY

3.1 *Introduction to response surface methodology*

Response surface method (RSM) has been widely used in experimental design and optimization in recent years. It is a collection of mathematical and statistical methods that can establish the correlation between independent variables and dependent variables (responses). Through the analysis of the mathematics established by RSM model, the optimal working conditions can be determined. Central composite design (CCD) is one of the most widely used experimental design methods in RSM. It helps to reduce the number of experiments required to achieve the optimal conditions and analyze the interaction between parameters.

3.2 *Determination of factors and levels*

The influencing factors of the low temperature plasma system for UDMH wastewater treatment determined through the experiment were the discharge gap (D), the pH value of the solution (pH) and the dosage of alkali solution (C_{OH}), and the response values in the experiment were the degradation rates of UDMH (X_{UDMH}) and COD (X_{COD}). These two response values were defined as: X=1-C_t/C_0.

3.3 *Central composite design*

Central composite design (CCD) was introduced to optimize the design of the low temperature plasma system for UDMH wastewater treatment, using three-factor three-level RSM analysis. The factor levels are listed in Table 1 and the design plan and results are listed in Table 2. Unless otherwise specified: in the experiment, the concentration of UDMH wastewater was 1000 mg/L, and the treatment capacity was 500L, and the treatment time was 60 min, and the energy consumption of each reaction tube was 43W; the actual value and code value of each level were calculated by formulas (5) and (6):

$$X_i = \frac{Z_i - Z_i^0}{\Delta Z_i}, i = 1, 2, 3 \tag{5}$$

$$\Delta Z_i = \frac{Z_{max} - Z_{min}}{2} = Z_{max} - Z_i^0 = Z_i^0 - Z_{min} \tag{6}$$

In the formulas above, Z is the actual value of the factor; X is the code value; Z_{max} is the maximum actual value, and the corresponding code value is X=+1; Z_{min} is the minimum actual value, and the corresponding code value is $X = -1$. The subscript i=1 represents the discharge gap (D), i=2 represents the pH value (pH) of the solution, and i=3 represents the dosage of alkali solution (C_{OH}).

Table 1. Code levels of influencing factors.

		Levels				
Independent variables	codes	$-\alpha$	-1	0	1	α
D/mm	X_1	1	2	3	4	5
pH	X_2	4	6	8	10	12
C_{OH}(g/L)	X_3	0.25	0.50	0.75	1.00	1.25

There were 20 groups of operation sequences in CCD experiment design. Groups 1 to 8 in Table 2 were orthogonal designs, and groups 9 to 14 formed a composite design of the upper and lower horizontal α. α was the distance of the axial point to the center, $\alpha=2^{k/4}$, The value of k represented the number of influencing factors. In this experiment, k=3, $\alpha=2^{3/4}=1.68$, so α determined the effective range of the experiment parameters, $\Omega=[X_j \in \Omega; -\alpha \le X_j \le +\alpha; \forall j=1,2,3]$. 15–20 groups were designed as central points, which were used to estimate experiment errors.

4 ESTABLISHMENT OF QUADRATIC RESPONSE SURFACE REGRESSION MODEL AND RESPONSE SURFACE ANALYSIS

4.1 *Establishment of the quadratic regression model for the degradation rate of UDMH X_{UDMH}*

The data in Table 2 were entered into Design-Expert software for processing, and p the response values of the X_{UDMH} were coded and converted and a quadratic polynomial regression model of the

Table 2. Design and results of CCD experiments.

No	Experiment type *	D/mm		pH		C_{OH}/(g/L)		Response		
		actual value	code value	actual value	code value	actual value	code value	actual value	code value	actual value
1	O1	4	1	6	−1	0.50	−1	9.44	8.68	27.33
2	O2	4	1	10	1	1.00	1	47.85	45.34	5.39
3	O3	4	1	10	1	0.50	−1	41.36	39.00	6.24
4	O4	4	1	6	−1	1.00	1	10.94	10.17	23.58
5	O5	2	−1	1	1	0.50	−1	81.82	75.27	3.15
6	O6	2	−1	6	−1	1.00	1	21.75	20.31	11.86
7	O7	2	−1	1	1	1.00	1	95.00	87.40	2.72
8	O8	2	−1	6	−1	0.50	−1	18.77	17.49	13.75
9	S1	5	1.68	8	0	0.75	0	1.38	1.27	186.96
10	S2	1	−1.68	8	0	0.75	0	59.78	55.60	4.32
11	S3	3	0	12	1.68	0.75	0	48.82	46.26	5.28
12	S4	3	0	4	−1.68	0.75	0	6.21	5.71	41.55
13	S5	3	0	8	0	1.25	1.68	47.87	45.36	5.39
14	S6	3	0	8	0	0.25	−1.68	36.78	34.61	7.01
15	C1	3	0	8	0	0.75	0	45.78	43.38	5.64
16	C2	3	0	8	0	0.75	0	44.96	42.71	5.74
17	C3	3	0	8	0	0.75	0	45.56	43.17	5.66
18	C4	3	0	8	0	0.75	0	46.02	43.72	5.61
19	C5	3	0	8	0	0.75	0	45.63	43.24	5.65
20	C6	3	0	8	0	0.75	0	4524	42.87	5.70

*O—orthogonal design point; S—star point or pivot point; C—center point.

relations between the response values and each factor at the code level and the actual level were obtained. Regression model of UDMH code level for X_{UDMH} was obtained as well.

According to the central composite design principles, the value range of each factor was: 1 mm$\leq D \leq$5 mm, 4$\leq pH \leq$12, 0.25 g/L$\leq C_{\mathrm{OH}} \leq$1.25g/L. Table 3 shows the ANOVA data of the degradation rate of UDMH. The value of F was used to determine the statistical significance of the second-order regression model. When P<0.05, the corresponding parameters were all significant. Since P was lower than 0.0001 and F was equal to 15.67 in the degradation rate model of UDMH, the model was significant. In addition, R^2=0.9338, indicating that more than 93.38% of the data deviation could be explained. R^2_{adj} could test the adequacy of the model. R^2_{adj}=0.8742 indicated that there was a strong interaction between the predicted X_{UDMH} and the experimental X_{UDMH}. AP was used to reflect the ratio of signal to noise. It was acceptable when AP was larger than 4. In this experiment, AP of the model was 14.183, indicating that the regression equation had better adaptability than predicted.

Table 3. Variance analysis of response surface model for X_{UDMH}.

Source	Degree of freedom	Sum of squares	Mean square	Value of F	Value of P	R^2	R^2_{adj}	AP
Model	9	82.62	9.18	15.67	< 0.0001	0.9338	0.8742	14.1833
Residual error	10	5.86	0.5860	—	—	—	—	—
Total	19	88.48	—	—	—	—	—	—

4.2 *Establishment of the quadratic regression model for the degradation rate of COD X_{COD}*

Similarly, the data in Table 2 was entered into Design-Expert software for processing, and X_{COD} response value was coded and converted, and a quadratic polynomial regression model of the relation between the response value and each factor at the coding level and the actual level was obtained. The regression model of the code level for X_{COD} was determined as well.

According to the central composite design principles, the value range of each factor was: 1 mm$\leq D \leq$5 mm, 4$\leq pH \leq$12, 0.25 g/L$\leq C_{OH} \leq$1.25 g/L. The ANOVA data of X_{COD} were listed in Table 4. The value of F was used to determine the statistical significance of the second-order regression model. When P was lower than 0.05, the corresponding parameters were all significant. In the X_{COD} model, P<0.0001 and F=16.11, indicating that the model was significant. In addition, R^2=0.9355, indicating that more than 93.55% of the data deviation could be explained. R^2_{adj} could test the adequacy of the model. R^2_{adj} =0.8774 showed that there was a strong interaction between the predicted X_{COD} and the experimental X_{COD}. AP was used to reflect the ratio of signal to noise. It is acceptable when AP is larger than 4. In this experiment, AP of the model was 14.330, indicating that the regression equation had better adaptability than predicted.

Table 4. Variance analysis of response surface model for X_{COD}.

Source	Degree of freedom	Sum of Mean squares	square	Value of F	Value of P	R^2	R^2_{adj}	AP
Model	9	77.50	8.61	16.11	< 0.0001	0.9355	0.8774	14.330
Residual error	10	5.34	0.5345	—	—	—	—	—
Total	19	82.85	—	—	—	—	—	—

4.3 *Response surface analysis of X_{UDMH} and X_{COD}*

During the experiment, the reduction of the discharge gap led to a significant increase in the discharge area, the discharge filaments were more uniform and denser, and the discharge phenomenon was more obvious. Shortening the discharge gap could enhance the electric field strength and power density, which was conducive to the generation of stronger low-temperature plasma. Secondly, low temperature plasma could produce high-reactivity short-lived active particles. By shortening the discharge gap, these particles were easier to reach the liquid phase and react with pollutants to achieve the purpose of degradation. In addition, the pH value was increased during the treatment process, and the low temperature plasma generated a large amount of ozone which dissolved in the waste liquid. The ozone would undergo a series of reactions under the catalysis of hydroxyl groups to generate a large number of hydroxyl radicals with high oxidation value. The active substance could effectively oxidize organic pollutants. By increasing the dosage of alkali solution, amount of the hydroxyl and pH value, more free hydroxyl radicals could be generated to improve the degradation of UDMH; if the pH value was too high, the hydroxyl radicals produced by plasma would be easy to quench, which lowered the degradation rate of UDMH; it was easier to oxide protonated UDMH while high pH would hinder the protonation of UDMH; the change in pH value may affect the reaction mode of UDMH, thus affecting the degradation rate.

For the three-dimensional surface diagram of response value obtained by Design-Expert software, if the contour is circle, the interaction between the two factors shall be viewed as not significant, and if the contour is ellipse, the interaction shall be viewed as significant, as shown in Figures 4 and 5.

It can be seen from Figures 4 and 5 that X_{UDMH} and X_{COD} were not significantly affected by the interaction between the discharge gap and the pH value. With the decrease of discharge gap and the increase of pH value, the degradation rate increased gradually but not significantly. The

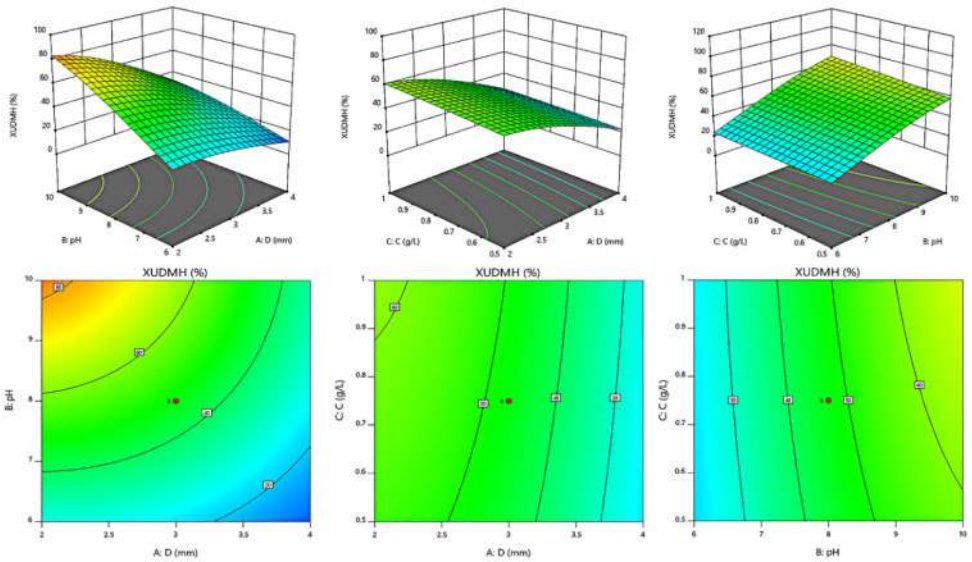

Figure 4. Interaction of various process parameters on the degradation rate of UDMH.

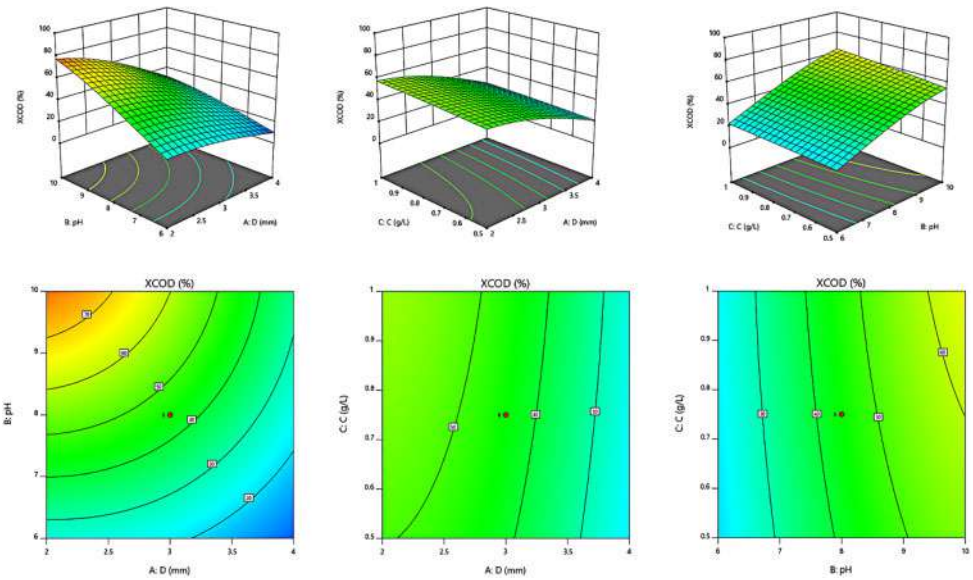

Figure 5. Interaction of various process parameters on the degradation rate of COD.

approximately parallel contour lines show that the degradation rate X was significantly affected by the interaction between dosage of alkali solution, discharge gap and pH value. This may be attributed to the increase of the number and activity of active factors in the discharge process as the dosage of alkali solution increased.

5 SYSTEM OPTIMIZATION ANALYSIS

The system optimization analysis was carried out by using Design-Expert software to determine the optimal influencing factor levels and degradation rates of the system. The predicted degradation rates were 88.54% and 82.16%, and the optimal levels of each influencing factor obtained by optimization analysis were: D=2mm, pH=10, C_{OH}=1.00g/L. During the experiment, the process parameters were adjusted to the optimal conditions, and then the degradation rates of UDMH and COD of the system were tested and analyzed. After the processing and analysis of the data, it was concluded that the degradation rates under the optimal operating conditions were 95.00% and 87.40% respectively. The results are listed in Table 5.

Table 5. The values of X_{UDMH} and X_{COD} of the system under the optimal process conditions.

			X_{UDMH}/%		X_{COD}/%		
D/mm	pH	C_{OH}/(g/L)	Predicted value	Experiment value	Predicted value	Experiment value	Error
2	10	1.00	88.54	95.00	82.16	87.40	6.80%(UDMH) 5.99%(COD)

6 CONCLUSION

In this paper, a low temperature plasma system for the disposal of UDMH wastewater was designed and built. The discharge gap, pH value and dosage of alkali solution were selected as variables, and the degradation rates of UDMH and COD were selected as target values. The response surface method was used to optimize the target values, and the following conclusions were obtained:

(1) In this paper, CCD was used to design the experiment conditions. The data were imported into Design-Expert software to obtain the quadratic polynomial regression model of the degradation rates of UDMH and COD. The analysis of variance showed that the regression model was significant. Through the comparison analysis of the experiment and predicted values of the degradation rates of UDMH and COD, it was further proved that the model had high reliability in fitting the degradation rates of UDMH and COD within the whole experiment.
(2) The response surface method was used to analyze the impact of each factor on the response value. Among them, the discharge gap had a great influence on X_{UDMH} and X_{COD} response value of the system. The interaction between the discharge gap and the dosage of alkali solution had a greater impact on X_{UDMH} and X_{COD}. It was improper to reduce the discharge gap to a value too low since it needed to be matched with the pH value and the dosage of alkali solution.
(3) The optimal operating conditions of the system obtained by the analysis of the optimal module of Design-Expert software were: D=2mm, pH=10, C_{OH}=1.00g/L. Under such operating conditions, the predicted values of the degradation rates were 88.54% and 82.16%, and the error was 5.99%∼6.80%.

REFERENCES

Bu, X. Y. & X. X. Liu (2015). Study on the oxidative degradation mechanism of UDMH wastewater by ultraviolet spectroscopy. Energetic materials. 23(10), 977–981.

Cong, X. M. & Y. T. Wu (2018). Research on the stability of Lissajous figure and improvement of experimental method. College Physics Experiment. 31(05), 52–55.

Jia, Y. & Y. Li (2009). UV-Fenton method to treat UDMH wastewater. Energetic materials, 2009, 17(3): 365–368.

Li, H. & J. Liu (2020). Activated carbon-microwave-Fenton combined technology to treat UDMH wastewater. Journal of Propellants. 43(01), 104–109.
Li, L. & S. Zhang (2015). Application of response surface methodology in experimental design and optimization. Laboratory Research and Exploration. 34(008), 41–45.
Li, X. & X. Q. (2020). Research on Dielectric Barrier Discharge Plasma Degradation of Wastewater Pollutants in Pharmaceutical Enterprises. New Technology of Electrical Engineering and Energy. 28, 354–358.
Li, X. Y (2020). Research progress of plasma technology in wastewater treatment. Modern Salt Chemical Industry. 47(05), 8–9.
Liu, Y. & B. L. Xia (2010). Degradation of UDMH Wastewater by Acidic Redox Potential Water. Energetic Materials. 18(3), 359–360.
Logistics Department (1993). Commission of Science, Technology and Industry for National Defense. Rocket Propellant Monitoring and Protection and Pollution Control. Changsha: National University of Defense Technology Press, 650–788.
Qiao, H. & C. L. Zhou (2004). The hazards and treatment of rocket propellant wastewater. Journal of Logistics Engineering Institute. (1), 55–58.
Wang, Z. Y. & M. D. Zhang (2009). Status and development of treatment technology for refractory organic wastewater. Industrial Water Treatment. 22(12), 1–4.
Yuan, X. X. & M. F. Luo (1991). Catalysts and processes for purifying nitrogen-containing organic pollutants. Environmental Science. 13(1), 58–61.
Zhang, S. J. & X. J. Chen (2013). Microwave-enhanced Fenton degradation of UDMH wastewater. Energetic Materials. 21(4), 455–459.
Zhen, H. & Y. L. Wu (2021). The combined effect of temperature and salinity on the early embryonic development rate of Strongylocentrotus intermedius. Journal of Ecology. 40(2), 460–469.

Advances in Applied Chemistry and Industrial Catalysis – Saikia (Ed.)

High-alkali lime method combined with flue gas neutralization for the removal of low-concentration chloride ions in dye wastewater

Haixin Zheng, Jinyun Xu, Zhaohui Ren, Minjing Li, Guoqiang Zhong & Di Zhao
School of Chemical Engineering, Tianjin Key Laboratory of Green Chemical Technology and Process Engineering, State Key Laboratory of Separation Membrane and Membrane Processes, Tiangong University, Tianjin, China

Xudong Hu
School of Materials Science and Engineering, Key Laboratory of Advanced Ceramics and Machining Technology, Ministry of Education, Tianjin University, Tianjin, China

Xiangyin Cheng, Jianing Guo, Guanwei Yao & Chunming Zheng*
School of Chemical Engineering, Tianjin Key Laboratory of Green Chemical Technology and Process Engineering, State Key Laboratory of Separation Membrane and Membrane Processes, Tiangong University, Tianjin, China

Xiaohong Sun**
School of Materials Science and Engineering, Key Laboratory of Advanced Ceramics and Machining Technology, Ministry of Education, Tianjin University, Tianjin, China

ABSTRACT: Chloride ions could corrode drainage pipes and buildings, causing serious damage and environmental pollution. In this work, the high alkali lime method combined with simulated flue gas was used to remove chloride ions from industrial dye wastewater. Calcium oxide and sodium aluminate were added to wastewater according to the mole ratio and then the simulated flue gas was also added to the above reaction solution to achieve the best removal effect. The optimized removal rate of chlorine ions in the dye wastewater could reach 64.1% at n(Ca2+): n(Al3+): n(Cl-) of 12:3.5:1, the reaction time of 60 minutes, and the pH value of 9. By adding lime, and reduce the air pollution. This method conforms with the concept of carbon emission reduction and carbon neutralization, which achieves the effect of using waste to treat waste.

1 INTRODUCTION

Chloride ions mainly come from wastewater discharged from petrochemical, metallurgical, pharmaceutical and other industries (Heikkinen et al. 2008). High concentrations of chloride ions could corrode drainage pipes and buildings, which hinder the growth of aquatic plants and animals. It is of great significance to find a simple, efficient, and economical method to remove the chloride ions in industrial dye wastewater (Kameda et al. 2005). The flocculation is to add a certain amount of metal salts and/or polymers to form insoluble salt precipitation, thereby removing the pollutants in the wastewater (Pang et al. 2018). An industrial boiler would generate a large amount of flue gas, which is difficult to be recycled. The flue gas contains carbon dioxides and sulfur dioxide, which could be used for the neutralization of alkali wastewater (Rao et al. 2007). In this work, the high soda-lime method and simulated flue gas processes were combined to remove chloride ions in wastewater. Friedel's salt precipitations could be formed after the neutralization of industrial dye wastewater with high alkali conditions.

*Corresponding Authors: *zhengchunming@tiangong.edu.cn and **sunxh@tju.edu.cn

DOI 10.1201/9781003308553-68

2 EXPERIMENTAL

2.1 *Experimental drugs*

Calcium oxide (AR,>99.9%), sodium aluminate (AR,>98%), and cationic polyacrylamide (cPAM,>99%) were purchased from Shanghai Aladdin Biochemical Technology Co., Ltd. The industrial dye wastewater was collected from Fujian Shishi Textile Dyestuff Co., Ltd., and the Cl- content in the dye wastewater was 260 mg/L. All chemicals were used without further purification and deionized water was used throughout this study.

2.2 *Experiment preparation*

The required solution is prepared as follows: 3 g CaO is weighed and dissolved in 27 mL of deionized water to prepare a calcium oxide solution with a mass fraction of 10%; 3 g of $NaAlO_2$ is weighed and dissolved in 27 mL of deionized water to prepare a mass fraction of 10% aluminate Sodium solution; weigh 0.062 g of polyacrylamide and dissolve it in 62 mL of deionized water to prepare a polyacrylamide solution with a mass fraction of 0.1%.

2.3 *Flocculation processes*

Take 100 mL of dye wastewater and place it in a beaker to stir with an electromagnetic stirrer. Add the prepared calcium oxide solution and sodium aluminate solution to the wastewater in a predetermined proportion. After a certain period of reaction, the simulated flue is introduced into the solution. The pH value of the solution system was adjusted by gas, then a polyacrylamide (PAM) solution was added to the solution system, the stirring was stopped after the reaction was completed, and the precipitate was separated by filtration after standing for precipitation. Take 10 mL of supernatant, and calculate the chloride ion content and chloride ion removal rate in the supernatant after the reaction by silver nitrate titration.

3 RESULTS AND DISCUSSION

3.1 *The effect of $n(Ca^{2+})$: $n(Cl^-)$ ratio on Cl^- removal effect*

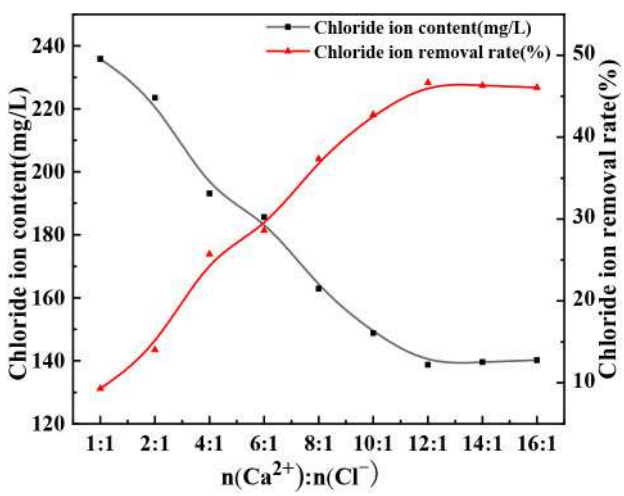

Figure 1. The effect of $n(Ca^{2+})$: n(Cl) ratio on Cl removal effect.

Take 100 mL of dye wastewater in a beaker, determine the stirring speed of 500 r/min; the reaction time is 30 min; pass the simulated flue gas to adjust the pH value of the solution to 7; n(Al^{3+}): n(Cl) is 3:1, change the amount of CaO solution added; after the reaction, PAM solution was added to settle for 30 min. After the supernatant was filtered, the Cl content in the supernatant was measured and the chloride ion removal rate was calculated.

As shown in Figure 1, when n(Ca^{2+}):n(Cl)<12:1, the removal rate increases with the increase of the amount of Ca^{2+} added to the solution, and the increase of the amount of Ca^{2+} will generate more $Ca_4Al_2Cl_2(OH)_{12}$ precipitation; when n(Ca^{2+}):n(Cl)>12:1, there is a lot of OH in the solution, and the excess OH will react with $Ca_4Al_2Cl_2(OH)_{12}$ again to generate $Ca_4Al_2(OH)_{14}$, which makes chloride ions entering the solution again, the removal rate decreases. When n(Ca^{2+}): n(Cl) was 12:1, the removal rate of chloride ions was the highest, which was 46.64%.

3.2 *The effect of n(Al^{3+}): n(Cl^-) ratio on Cl^- removal effect*

Take 100 mL of dye wastewater in a beaker, stir at a speed of 500 r/min; the reaction time is 30 min; pass simulated flue gas to adjust the pH of the solution to 7; determine the optimal n(Ca^{2+}): n(Cl^-) is 12:1, change the addition amount of sodium aluminate solution. After the reaction was completed, PAM solution was added for precipitation for 30 min, the supernatant was filtered, the Cl^- content in the supernatant was determined, and the chloride ion removal rate was calculated.

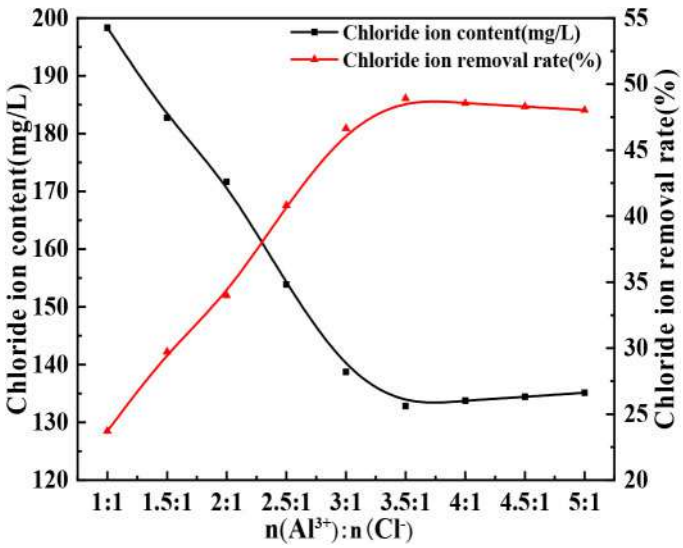

Figure 2. The effect of n(Al^{3+}):n(Cl^-) ratio on Cl^- removal effect.

As shown in Figure 2, it is determined that n(Ca^{2+}):n(Cl^-) is 12:1. When n(Al^{3+}):n(Cl^-)<3.5:1, with the increase of the amount of Al^{3+}, more A large amount of $Ca_4Al_2Cl_2(OH)_{12}$ precipitates, and the Cl^- removal rate increases gradually; when n(Al^{3+}):n(Cl^-)>3.5:1, there is a large amount of $Al(OH)_4^-$ in the solution, and excess $Al(OH)_4^-$ reacts with $Ca_4Al_2Cl_2(OH)_{12}$ to generate $Ca_3Al_2(OH)_{12}$, and the chloride ion returns to the solution, so the removal rate is reduced.

3.3 *Effect of simulated flue gas addition on chloride ion removal*

As shown in Figure 3, when the pH value is between 7 and 9, the removal rate of chloride ions increases with the increase of the pH value of the solution; when the pH value of the solution is greater than 9, the removal rate of chloride ions gradually decreases. When the pH of the solution was 9, the removal efficiency was the highest, reaching 64.01%.

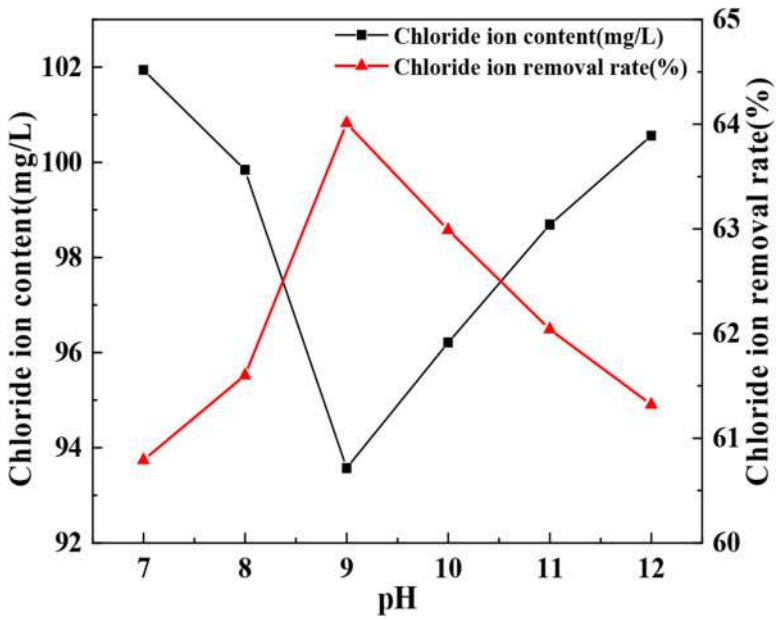

Figure 3. Effect of simulated flue gas influx on Cl^- removal.

3.4 *Characterization and analysis*

3.4.1 *SEM*

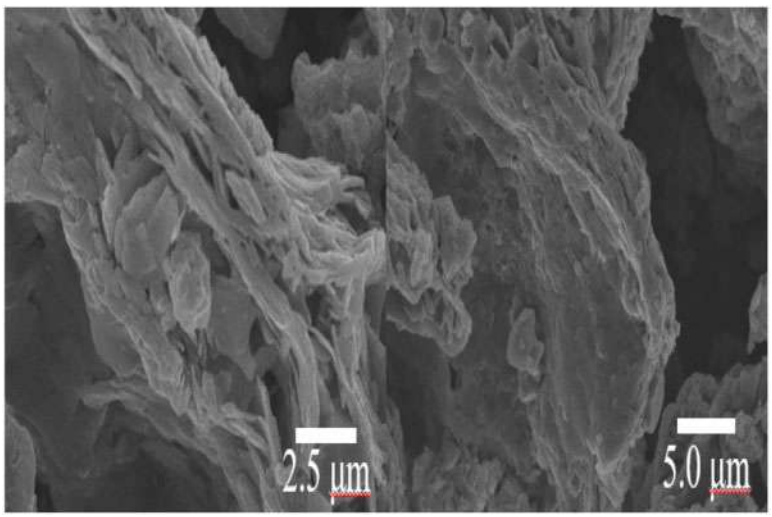

Figure 4. SEM spectrum of solid precipitate.

As can be seen from Figure 4, a layered compound formed by the calcium-aluminum salt is the main body, and chloride ions are inserted between the layers of the layered compound. The sediment is a layer of flaky substances stacked on each other, and other particles of different sizes can be seen on the surface.

3.4.2 *XRD*

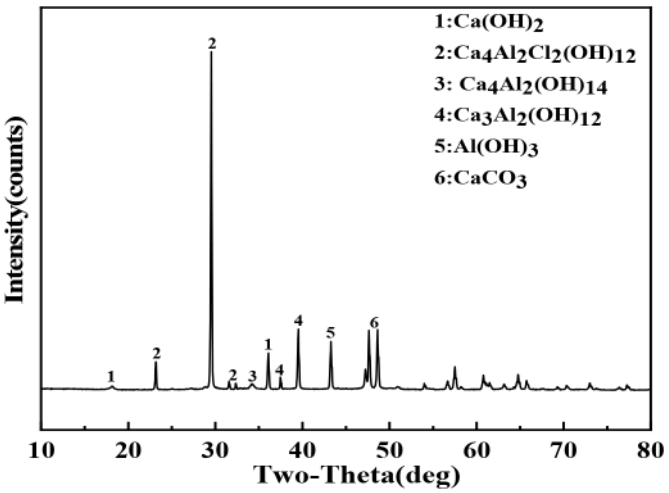

Figure 5. XRD pattern of solid precipitate.

It can be seen from the XRD pattern in Figure 5 that the characteristic peaks of the Friedel salt layered compound are consistent with those in the literature, but there are slight differences. It can be determined that the reaction produces Friedel's salt-$Ca_4Al_2Cl_2(OH)_{12}$. From the XRD analysis, it can be found that in addition to the diffraction peak corresponding to $Ca_4Al_2Cl_2(OH)_{12}$, there are other diffraction peaks. The diffraction peaks correspond to the precipitation of $Ca_4Al_2(OH)_{12}$, $Ca_4Al_2(OH)_{14}$, $Ca_3Al_2(OH)_{12}$, etc. The unreacted $Ca(OH)_2$ and the $CaCO_3$ precipitation generated by the reaction with simulated flue gas, excess $NaAlO_2$ present in the solution is precipitated as $Al(OH)_3$.

4 CONCLUSIONS

(1) In this study, when the molar ratio of $n(Ca^{2+}):n(Al^{3+}):n(Cl^-)$ was 12:3.5:1; the reaction time was 30 minutes; the settling time was 30 minutes; the solution was adjusted by introducing simulated flue gas when the pH reaches 9, the removal rate of chloride ions in dye wastewater can reach 64.1%.
(2) The method can remove chloride ions well, and has the advantages of low cost, simple operation, no secondary pollution, and low energy consumption. At the same time, the flue gas of the coal-fired boiler is involved in the reaction, and the flue gas can be recycled and used to achieve the purpose of treating waste with waste.

ACKNOWLEDGMENTS

This work was supported by the State Scholarship Fund of the China Scholarship Council (201709345012).

REFERENCES

Heikkinen P M, Noras P, Salminen R, et al. Mine Closure Handbook. Environmental Techniques for the Extractive Industry [J]. 2008.

Kameda T, Yoshioka T, Hoshi T, et al. The removal of chloride from solutions with various cations using magnesium-aluminum oxide [J]. Separation & Purification Technology, 2005, 42(1): 25–9.
Pang W L, Hao L W, Man T S, et al. Removal of Chloride Ions from an Aqueous Solution Containing a High Chloride Concentration through the Chemical Precipitation of Friedel's Salt [J]. Materials Transactions, 2018, 59(2): 297–302.
Rao A G, Reddy T, Prakash S S, et al. pH regulation of alkaline wastewater with carbon dioxide: A case study of treatment of brewery wastewater in UASB reactor coupled with absorber[J]. Bioresource Technology, 2007, 98(11):2131–2136.

Advances in Applied Chemistry and Industrial Catalysis – Saikia (Ed.)

A summary of the sources, pathways, environmental impacts, and implications of ZnO and TiO_2 nanoparticles

Guangyu Zhu*
Shanghai Dayu Electrics Co., Ltd., Shanghai, China

ABSTRACT: An interest in nanotechnology has burgeoned due to the emergence of numerous applications of nanoparticles (NPs). Consequently, increased production, use, and disposal of NPs might result in a massive menace to the environment, making it urgent to critically assess their potential releases and risks. In this paper, the main source, pathway, impact, and implication of No. 1 and No. 3 most produced NPs: TiO_2 NPs and ZnO NPs, are overviewed, taking into account the possible transformations they can undergo. Based on our findings, it is clear that three dominant entry routes of those NPs are the wastewater effluent discharge, landfills, and agricultural application in form of biosolids. In addition, chemical transformations eliminated ZnO NPs during waste treatment highlighting the need to shift our focus from pristine to transformed ZnO NPs when conducting ZnO NP risk assessment. Finally, numerous NP toxicity cases and simulated high predicted exposure concentration (PECs) of NPs in some areas underscore the necessity to develop more advanced NP removal technologies as well as more severe and detailed regulations in the future.

1 INTRODUCTION

The term nanoparticles (NPs) refers to particles with diameters between 1 nm and 100 nm. NPs have drawn huge interest due to their unique physicochemical properties which set them apart from their bulk counterparts. For instance, depending on NPs size, gold can increase its melting point from 200 to more than 1000 degrees Celsius (Tian et al. 2014). This growing interest has led to the emergence of numerous applications in various fields such as cosmetics, cleaning, textiles, and agriculture (Donia & Carbone 2019). Consequently, higher production, use, and disposal of NPs result in huge NPs released into the environment, making it urgent to assess the impact they can have on the environment.

Among different types of NPs, TiO2 NPs and ZnO NPs are two typical NPs that are No. 1 and No. 3 most produced NPs globally (Martínez et al. 2020). With their widespread use in miscellaneous household and industrial products, TiO_2 and ZnO NPs are either released directly to different environmental compartments (air, soil, water) or indirectly released from technical facilities such as wastewater treatment plants (WWTPs), incineration plants, and landfills (Bundschuh et al. 2018; Donia & Carbone 2019; Llana et al. 2021; Sun et al. 2016; Tian et al. 2014). For example, some ZnO NPs in paint is directly released into the air while almost all ZnO NPs in cosmetics go to WWTPs (Sun et al. 2016).

After being released, NP's impact on the environment is the next important problem. Currently, many studies have been conducted to analyze the effects of NPs on different environmental compartments (Cohen et al. 2018; Giese et al. 2018; Mahmoodzadeh et al. 2015; Rashid et al. 2021). A number of different toxic mechanisms were mentioned, including oxidative stress, dissolution, redox reactions, etc. (Cohen et al.2018; Giese et al. 2018; Mahmoodzadeh et al. 2015; Rashid et al. 2021).

However, there are some drawbacks to most studies. Firstly, most research on the NP effects focused on organisms in aquatic systems while NP accumulation in other environmental compartments was also identified (Donia & Carbone, 2019). For instance, an article mentioned that a

*Corresponding Author: zhuguangyu3574@163.com

 DOI 10.1201/9781003308553-69

majority of ZnO NPs were found in the soil and farmland (Donia & Carbone, 2019). Thus, without knowing the main source of each type of NPs, their release pathways, and consequently predicting their environmental concentration and impact, the research aiming for NP risk assessment cannot purposefully help address the real-world problem of NP pollution. In addition, the majority of the research conducted on the NP impact made use of pure NPs, the so-called pristine NPs (Starnes et al. 1987). In real situations, some types of NPs undergo an extensive transformation before causing environmental impact (Dale et al. 2015). Thus, determining whether TiO_2 and ZnO NPs are transformed and how the transformation of NPs affects their environmental impact is indeed important when conducting NP risk assessment.

Even though there exist a number of studies discussing NP risk, a systematic overview of the sources, pathways and the complex impact of the NPs on the environment is lacking. In this paper, instead of focusing on the impact of a particular type of NPs under a single environmental condition, different phases of the life cycle of two typical NPs are illustrated, including several individual sections: NP sources and releases, pathways of NPs into the environment, NP environmental impact, implications and recommendations for NPs risk mitigation. To address the drawbacks mentioned above, the main source, release, and pathway for ZnO and TiO_2 NPs are comprehensively overviewed, compared, and analyzed. Also, possible transformations of NPs in different compartments are taken into consideration when discussing their environmental impact.

2 MAIN BODY

In the last decade, the unique properties of NPs enable a wide range of possible applications. Among all types of NPs, TiO_2 and ZnO NPs are the highest and third-highest utilized nanomaterials (Bundschuh et al. 2018). The broad use and increased release of NPs can cause potential environmental risks. More disturbing is the fact that the exponentially increasing production of those NPs may exacerbate the problem. Statistics show that the annual ZnO NP production was around 1600 tons in 2010, which was increased to 58,000 tons by 2020 (Khan et al. 2019). Therefore, to meet the urgent need for assessing the environmental risks of NPs, it is critical to identify and analyze their sources, pathways, and environmental impact.

2.1 *NP Sources and releases*

Identifying recent NP sources can greatly aid in assessing the environmental impact of NPs and determining corresponding regulations and safety strategies. TiO_2 and ZnO NPs, as the No. 1 and No. 3 most produced NPs, offer a wide range of uses (Martínez et al. 2020). In this section, the top three product sources of TiO_2 and ZnO NPs and their corresponding releases to different compartments are illustrated.

Cosmetics dominate the utilization of ZnO and TiO_2 NPs, accounting for around 82.6 and 59.4 percent of NP use, respectively (Sun et al. 2016). One widely used application is sunscreen. Because those NPs are so good at absorbing ultraviolet (UV) radiation, they can be a great addition to sunscreens and other sun protection products (Martínez et al. 2020). Another broadly used application is toothpaste which may contain up to 10% titanium by weight (Donia & Carbone 2019). NPs act as a white pigment in toothpaste to make it white and aesthetic.

Paints and coatings are ranked No. 2 for TiO_2 and ZnO NPs use (5.9% and 14.3% NP use) (Sun et al. 2016). This application is beneficial for products that must withstand the potential environmental adverse effects. NPs merged with paints can not only promote UV protection but also protect against physical deterioration like abrasion and corrosion (Llana et al. 2021). There are examples from the textile industries where the fabrics coated with ZnO NPs exhibited amazing functions of UV resistance and antibacterial property (Hatamie et al. 2015). Another study reported that corrosion resistance of steel is increased by nearly ten times by coating TiO_2 NPs on the surface of steel compared with bare steel (Abdeen et al. 2019).

TiO_2 NPs have become popular materials in electronics and the demand for TiO_2 NPs is steadily growing (6.9% of TiO_2 NPs use. Ranked No. 3) (Sun et al. 2016). For example, they are ideal for biosensors because of their high surface area, quantum confinement, and biocompatibility (Bertel

et al. 2021). Nano-TiO_2 biosensors can be used to detect numerous important species like urea, protein, glucose, and DNA for food control or disease prevention (Bertel et al. 2021).

ZnO NPs can be used to improve different functionalities for plastics (2.0% of ZnO NPs using. Ranked No. 3) (Sun et al. 2016). Many common plastic materials have mediocre elongation value and poor durability against UV radiation. One study showed that adding ZnO NPs can promote UV protection and improve the elongation property of plastics (Putra et al. 2017). Plastics with the highest elongation value of 2.154% were obtained with the addition of 20 wt% ZnO NPs (Putra et al. 2017).

There are two possible outcomes for TiO_2 and ZnO NPs when being used for different applications shown above. Some of them are directly released into different environmental compartments (air, water, soil). The remaining non-released NPs at the end of product use phases become the end of life (EOL) materials treated in technical compartments (waste incineration plants, recycling processes, landfills).

2.2 *Summary of key statistics for NP sources and releases*

Some key statistics in terms of NPs sources and releases are displayed (Sun et al. 2016) (Figures 1 and 2 and Table 1). For both NP types, cosmetics are their major use (59.4% for TiO_2 NPs and 82.6% for ZnO NPs, respectively). The most dominant release pathway for those NPs occurs via wastewater. This is in accordance with other papers indicating that most of the NPs used in cosmetics like shampoos or sunscreens do not penetrate the skin but are washed off in the shower and go to WWTPs (Johnson et al. 2011).

In addition, those two types of NPs also share the same No. 2 use which is paints. In this case, only 1% of TiO_2 NPs and 35% of ZnO NPs are directly released into the environmental compartments during the use phase due to weathering or leftover disposal. Instead, most of NPs in paints end up in technical treatment like recycling processes.

Furthermore, there is a difference between TiO_2 NPs and ZnO NPs in terms of their No. 3 use (6.9% for TiO_2 NPs in electronics and 2.0% for ZnO NPs in plastics, respectively). For TiO_2 NPs in electronics, 30% of them are released into wastewater, the remaining 70% will go to EOL treatment. For ZnO NPs used in plastics, 80% of NPs enter wastewater.

Based on the statistical summary above, the most prominent release is via technical compartments (WWTPs) contributed by both NPs used in cosmetics and 80% ZnO NPs in plastics use. For the next step, it is reasonable to give top priority to identifying possible pathways of NPs in WWTPs into environmental compartments. Followed by No. 1 cosmetic application, lots of NPs are used in paints and electronics ending up in EOL treatment where more than 70% of them are treated in recycling processes and around 30% of them are in landfills. Thus, tracking the release of NPs during WWTPs, recycling and landfills should be our focus in the next section.

Table 1. Proportion of NPs released during the use phase and non-released NPs by the top three product categories (Sun et al. 2016). Detailed allocation for use release and EOL treatment are also shown (Sun et al. 2016).

			Allocation after use release					Allocation during EOL treatment		
Share of TiO2 NPs use	Product categories	Use Release (x)	Waste water	EOL Air	Surface Water	Treatment Soil		Landfill	Incineration	Recycling
59.4	Cosmetics	0.95	0.9		0.1		0.05	0.35	0.25	0.4
8.9	Paints	0.01	0.5	0.25		0.25	0.99	0.3		0.7
6.9	Electronics	0.3	1				0.7	0.15	0.1	0.75
Share of ZnO NPs use										
82.6	Cosmetics	0.95	0.9		0.1		0.05	0.35	0.25	0.4
14.3	Paints	0.35	0.5	0.25		0.25	0.65	0.3		0.7
2.0	Plastics	0.8	1				0.2	0.35	0.25	0.4

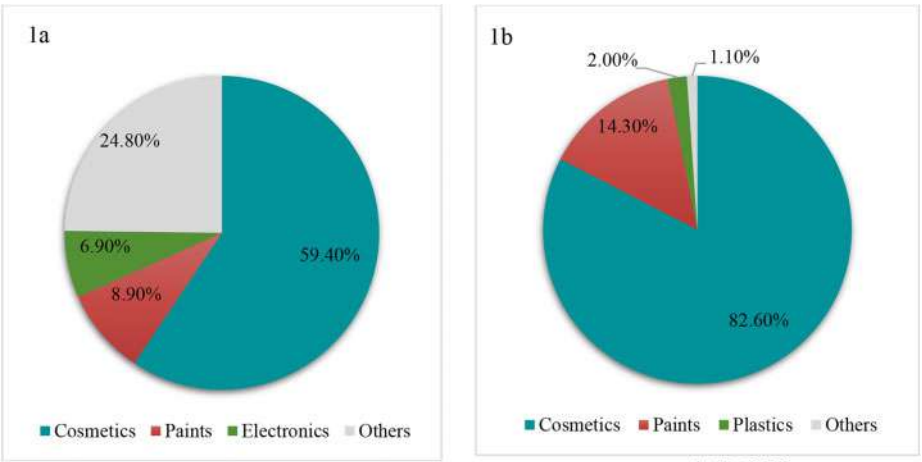

(a) TiO_2 NPs (b) ZnO NPs

Figure 1. Share of production for TiO_2 NPs and ZnO NPs (Sun, 2016).

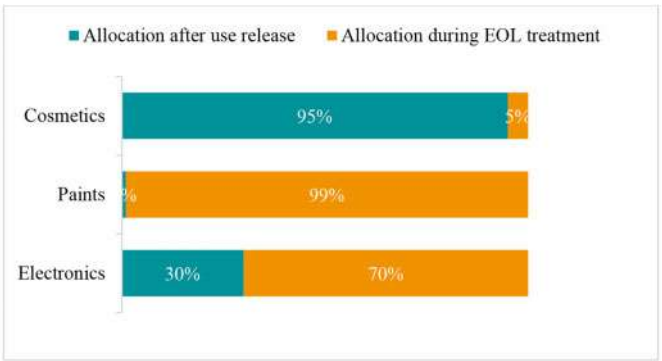

(a): Proportion of TiO_2 NPs released in use phase and enter EOL treatment by top three product categories (Sun, 2016).

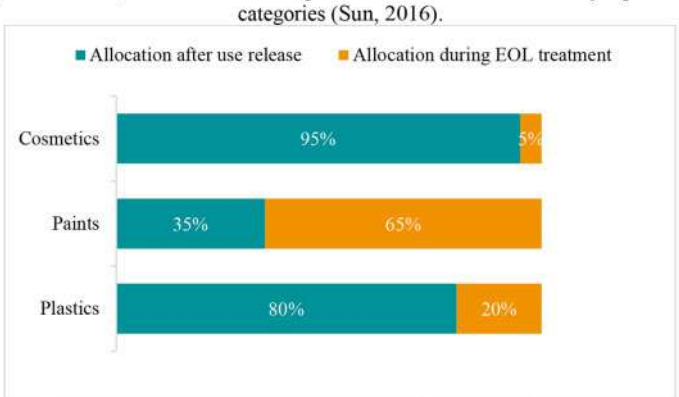

(b): Proportion of ZnO NPs released in use phase and enter EOL treatment by top three product categories (Sun, 2016).

Figure 2. The proportion of TiO_2 and ZnO NPs released in use phase and enter EOL treatment by top three product categories.

2.3 *Pathways of NPs into natural ecosystems*

Increasing application of TiO_2 and ZnO NPs and consequent high production volume will lead to huge NP releases either directly into the environment or indirectly through technical compartments (Donia & Carbone 2019).

From the section above, a major recipient of NPs for different applications is identified. For both NPs, direct environmental releases during product use are insignificant. Release pathways of NPs related to technical processes including wastewater treatment, recycling, and landfills are brought into focus.

Firstly, the most dominant flow for these two types of NPs from manufacturing and consumption to wastewater needs to be discussed.

In the case of TiO_2 NPs, it was estimated that 75%∼87% of TiO_2 NPs are removed from secondary settling tanks during wastewater treatment (Bundschuh et al. 2018; Zvimba et al. 2016). Part of those treated TiO_2 NPs captured in sewage sludge end up in landfills. However, since sewage sludge is often used as fertilizer (application of biosolids to soil), TiO_2 NPs accumulated in sewage sludge also go into the soil and potentially contaminate the environment. This pathway account for approximately 36% of TiO_2 NP emissions (Bundschuh et al. 2018). Other releases through either wastewater effluent or landfills account for roughly 33% and 30%, respectively (Bundschuh et al. 2018).

ZnO NPs, according to some findings, were treated so well with only an insignificant amount discharged into the environment through the wastewater effluent (Martínez et al. 2020; Zvimba et al. 2016). A study showed that more than 98% of Zn were adsorbed onto the activated sludge for subsequent application of biosolids to soil (Zvimba et al. 2016). In other words, the dominant pathway for ZnO NP environmental release is through the agricultural use of sewage sludge.

However, not like TiO_2 which is chemically inert in water, ZnO NPs are almost completely transformed into different Zn-containing species during wastewater treatment (Chen et al. 2020; Dale et al. 2015). A study also reported that ZnO NPs were present at lower than 0.05 wt % relative to transformed ZnO NPs in WWTPs (Dale et al. 2015). Because wastewater and sewage sludge are enriched in SH- and PO_4^{3-}, two dominant transformations for ZnO NPs which are phosphatization and sulfidation will lead to the formation of $Zn_3(PO_4)_2$ Zn-ferrihydrite and ZnS (Starnes et al. 1987). Thus, transformed ZnO NPs appear to be the relevant species when analyzing the impact of ZnO NPs from the application of biosolids.

Another possible release pathway is related to recycling. Unfortunately, few studies have focused on the behavior of NPs during the recycling process. One article reported that after recycling, most NPs will flow to landfills or incineration plants rather than be recovered during recycling processes (Caballero-Guzmán et al. 2015). During incineration, metallic NPs accumulate in the incinerator bottom ash and are typically sent to landfills (Caballero-Guzmán et al. 2015). Therefore, risk assessment for NP recycling processes should focus on cases related to the potential leaching behavior of NPs in landfills.

2.4 *Impact of TiO_2 and ZnO NPs on the environment*

As mentioned in Section 2.3, one main point of entry for TiO_2 and ZnO NPs after being treated by WWTPs is soil due to the application of biosolids.

Various beneficial bacteria and fungi such as nitrogen-fixing bacteria and arbuscular mycorrhizal fungi (AMF) play vital roles in maintaining both soil and plant health (Ameen et al. 2021). Due to these, the impact of NPs on the soil microorganisms growth has been studied (Ameen et al. 2021; Jalvo et al. 2017; Judy et al. 2015; Priyanka et al. 2017; Rashid et al. 2021; Shah et al. 2014; Starnes et al. 1987).

2.4.1 *TiO_2 and ZnO NPs in soil environment and implication*

Lots of articles have reported results indicating that TiO_2 NPs can alter the growth of soil bacteria which are summarized in Table 2 (Ameen et al. 2021; Jalvo et al. 2017; Judy et al. 2015; Priyanka

et al. 2017; Rashid et al. 2021; Shah et al. 2014). In a study, TiO_2 NPs had more than 99% inhibitory effect on *Pseudomonas putida* (Jalvo et al. 2017). Furthermore, TiO_2 NPs caused a significant reduction in the viability of AMF in rice roots (Priyanka et al. 2017). Also, another article showed that both anatase and rutile TiO_2 in biosolids have a time-dependent toxic impact on bacterial composition (Shah et al. 2014). Additionally, another report suggested that TiO_2 NPs also disrupted the gene expression of bacteria, making bacteria unable to complete the decomposition of organic pollutants (Rashid et al. 2021). Factors such as time, size, surface charges, capping agent, and cell wall composition influence NP impact (Priyanka et al. 2017).

As being mentioned, transformed ZnO NPs such as phosphatized ZnO NPs (pZnO NPs) and sulfidized ZnO NPs (sZnO NPs) present in biosolids are relevant species for ZnO NPs risk assessment in the environment. However, currently, there are few papers published on beneficial soil microorganisms that use those transformed ZnO NPs (Starnes et al. 1987) (Table 2). In a study, a 17-19% decrease in mortality of *Caenorhabditis elegans* after 24 hours of exposure to transformed ZnO NPs was reported (Starnes et al. 1987). Although they mentioned that transformed ZnO NPs had an initial lower toxic effect compared to pristine ZnO NPs due to the low dissolution rate of transformed ZnO NPs, it is expected that all transformed ZnO NPs will be dissolved in the end after uptake of NPs in acidic bacteria cell (Starnes et al. 1987). Another study showed that uptake of transformed ZnO NPs has caused toxic effects in the plant directly by suppressing its nutrient acquisition rather than impacting the viability of the nitrogen-fixing bacteria (Judy et al. 2015).

The detection of the negative impact of NPs in biosolids indicates that people need to take action to limit them to a boundary. A study indicated that predicted exposure concentration (PECs) of both NPs in soil with biosolids do not exceed but are close to no observed effect concentration (NOEC) threshold (Keller & Parker 2019). To mitigate potential NP risk, a more efficient WWTP process with more advanced NP treatment methods and technologies is needed before land application. Regulations also need to be revised to include limitation levels of different types of NPs in biosolids before agricultural use.

Although we lack insufficient knowledge about environmental impact, especially for transformed ZnO NPs which make regulation difficult to revise, there are no pristine ZnO NPs present after wastewater treatment resulting in further studies needed to determine if regulations for NPs risk in agricultural use should be influenced by the utilization of zinc in nano form versus its bulk counterparts. Also, based on the current study, it seems that transformed ZnO NPs have a lower toxic effect in the short-term scenario, people may have more time to address problems once excessive ZnO NPs are detected.

2.4.2 *Impact of TiO_2 NPs in aquatic environment and implication*

TiO_2 NPs have another main entry point which is surface water from wastewater effluent discharge. The release of TiO_2 NPs has a great impact on many microorganisms in an aquatic environment which plays a crucial function in sustaining the balance of biogeochemical processes (Bertel et al. 2021).

Many articles studied the responses of TiO_2 NPs in different concentrations on various microorganisms (Jovanović et al. 2015; Velzeboer 2014; Wang et al. 2011). A study reported that the egg production and embryo survival rate of zebrafish exposed to 0.1 mg/L TiO2 NPs was negatively affected after 13 weeks (Wang et al. 2011). Another article looked at the effects of TiO2 NPs smaller than 25nm on Pimephales promelas fish. Results showed that fish treated with TiO_2 NPs were more susceptible to infections and had a higher death rate (Jovanović et al. 2015). However, some articles got unexpected results due to the stability and aggregation behavior of TiO_2 NPs (Velzeboer 2014). A study showed that no toxicity on *Vibrio fischeri* was observed with an addition of 100 mg/L of TiO2 NPs (Velzeboer 2014). Low bio-active concentrations caused by fast NP aggregation could be the possible reason for the absence of expected toxicity (Velzeboer 2014). Another article reported that with a significant increase in the stability of TiO_2 NPs dispersion, a decreased toxicity on the growth of microalgae was observed (Rashid et al. 2021).

Similar to the biosolids application case, the detection of the negative impact of TiO_2 NPs in the aquatic environment indicates that people need to take action. Again, for risk assessment,

environmental concentrations of NPs need to be known. An article showed that the predicted environmental concentration for TiO_2 NPs is 0.047 ug/l in 2025 in Europe which is not that bad (Velzeboer 2014). However, a simulation from another article showed that TiO_2 NPs will occasionally exceed the surface water NOEC threshold in San Francisco meaning that some effects from TiO_2 NPs may already be noticeable for the most sensitive species (Keller & Parker 2019). Although that result is only from a simulation, people should at least be alert about NP concentration in some specific places and take actions similar to what I mentioned for risk mitigation of NPs in biosolids as soon as possible to address the potential risk of TiO_2 NPs in wastewater effluent.

A good point for TiO_2 NPs is that, based on some findings under lab conditions, the behavior of NPs in water is often dominated by aggregation which can stabilize TiO_2 NPs and diminishes NPs toxicity effects (Rashid et al. 2021; Velzeboer 2014). However, in a real scenario, TiO_2 NPs mostly come from WWTPs. The release of TiO_2 NPs via wastewater suggests that NPs will be mixed with significant quantities of household and industrial detergents, and this could help to disaggregate these NPs (Klaine et al. 2008). Thus, the determination of the actual form of TiO_2 NPs and their subsequent impact should also be emphasized in environmental risk assessment.

2.4.3 *Impact of NP leaching from landfills*

There is little information regarding landfills leachate. A study examined the behavior of TiO_2 NPs indicating no significant leaching behavior and TiO_2 NPs are strongly retained as clusters in landfill environments (Dulger et al. 2016). But another study indicated that ZnO NPs during landfills revealed very low leaching rates even after 6 months (Dulger et al. 2016).

Table 2. Effect of NPs on different organisms in soil.

NPs	Size	Bacteria/Fungi	Effect	References
Photo-activated TiO_2-NPs	5.6 nm	*Pseudomonas putida*	Membrane damage and significant production of reactive oxygen species	(Jalvo, 2017)
TiO_2 NPs	7.4, 5.2, and 4.5 nm	AMF-rice	Inhibition of AMF symbiosis in rice roots	(Priyanka, 2017)
Anatase and rutile TiO_2 NPs	10 and 12 nm	Soil bacterial community	Time-dependent toxic effect changing the bacterial composition in wavering pattern	(Shah, 2014)
Phosphatized and sulfidized ZnO NPs	30 nm	*Caenorhabditis elegans*	Damage by dissolution and mechanical damage to the intestinal wall were found after 24 exposure to NPs.	(Starnes, 1987)
Combination of ZnS adsorbed Zn ions, and $Zn_3(PO_4)_2$ NPs	<5 nm	*Medicago truncatula*	Large reductions in modulation frequency, plant growth, and microbial composition changes were found	(Judy, 2015)

2.5 *Summary of important and common findings*

TiO_2 and ZnO NPs are attracting a lot of interest with numerous applications. Consequently, huge NP production and release make it potentially risky to the environment. Dealing with such a challenge begins with accurately understanding the main sources of NPs and their corresponding pathways of release into the environment.

Some articles in this paper have found their major use and sources. Cosmetics, paints, and electronics are the primary sources of TiO_2 NPs. For ZnO NPs, cosmetics, paints, and plastics are their top three product categories.

For both TiO_2 and ZnO NPs, most of them enter WWTPs due to the same major sources in cosmetics. However, they behave differently during the wastewater treatment process. While TiO_2

NPs are chemically inert and almost no titanium ions are found, ZnO NPs experience extensive transformation processes forming different Zn compounds.

There are three main pathways accounting for TiO_2 and ZnO NPs released from WWTPs into the environmental compartments. Almost all transformed ZnO NPs and part of TiO_2 NPs end up in the soil environment. The remaining TiO_2 NPs move to surface water. Of course, the possibility of landfills leaching should not be excluded.

For environmental impact studies, there is evidence of both TiO_2 NP and transformed ZnO toxicity in a wide variety of organisms in the soil and aquatic environment. For transformed ZnO NPs, they had an initial lower toxic effect compared to pristine ZnO NPs due to the low dissolution rate, but it is expected that all transformed ZnO NPs will be dissolved and damage organisms at last. For TiO_2 NPs, whether they form aggregation or not will largely impact their degree of toxicity. For landfills leaching impact, currently, there are few studies for that with one article mentioning possible ZnO NP leaching behavior.

Regarding the environmental concentration of NPs, some models predicted that the concentration for both ZnO and TiO_2 NPs in soils is close to the toxic threshold while the concentration for TiO_2 NPs in surface water has already exceeded limits in certain areas.

3 DISCUSSION

3.1 *Future focus*

Firstly, some models have shown that the current NP concentration is at least approaching the toxic threshold. Given the fact that production and use of the investigated NPs are inevitably increasing, the expected concentration of NPs will be higher and higher. Meanwhile, we get the major recipient which is WWTPs for No.1 and No.3 most used NPs. Thus, for NP risk mitigation purposes, future research has to figure out the potential advanced NP removal technologies during wastewater treatment processes which will be discussed in the next section. For model accuracy purposes, lacking data is a major issue (Keller & Parker 2019). Thus, more actual field data are needed to validate those models and simulations.

In addition, although few articles are talking about NP leachate, a study did find ZnO NP leaching behavior in landfills. Future research has to investigate if TiO_2 NPs leaching and the further dissipation is possible or not. Also, more analysis should be done on the impact of ZnO NP leachates on groundwater supplies and subsequently human health.

Furthermore, many studies used commercially available pristine ZnO NPs for toxicity tests. This paper showed that transformations of ZnO NPs in the wastewater treatment process change the physicochemical properties of NPs leading to an environmental impact that is often distinct from what non-transformed NPs may have. Thus, transformations play an important role and should be taken into consideration in future studies when analyzing the environmental impact of ZnO NPs.

3.2 *Recommendations for potential technologies for NP risk mitigation*

Creating advanced removal technologies is an effective way for NP risk mitigation. For TiO_2 NP removal, it is suggested to use coagulation treatment (Punzi et al. 2020). The use of chitosan and alum together in wastewater treatment could be a promising treatment technology (Punzi et al. 2020). For ZnO NP treatment mainly found in activated sludge, the use of sludge combined with biochar can be an effective method that can promote the transition of Zn into their residual forms and subsequently mitigate Zn impact on the soil environment (Bogusz & Oleszczuk 2018).

4 CONCLUSION

The incorporation of NPs in various products leads to the release of NPs in the environment. As the No. 1 and the No.3 most produced NPs, the risks of TiO_2 and ZnO NPs to the environment cannot

be accurately assessed without knowing their main sources, release pathways, and environmental impacts.

Due to the NPs being widely used in cosmetics, three dominant entry routes of NPs to the environment are the wastewater effluent discharge, landfills, and agricultural application in form of biosolids. Regarding environmental impacts, there are many studies indicating evidence of the toxicity of both types of NPs in a wide variety of organisms. It's worth noting that pristine ZnO NPs undergo various transformations in the wastewater treatment process which can modify their environmental impacts. In addition, many simulation results indicated that the NP concentration is close to or has exceeded the toxicity threshold in a certain area.

For NP risk mitigation purposes, future studies should focus on finding more advanced NP removal technologies during wastewater treatment processes as well as revising regulations for NP concentration limitation. In addition, future research needs to investigate if landfill leaching of NPs is possible or not as well as to conduct more research on the impacts of NP leaching on groundwater supplies. Lastly, transformed ZnO NPs have different properties compared to pristine ZnO NPs which are neglected in most studies. Thus, it should be taken into consideration when analyzing the impact of ZnO NPs in future research.

REFERENCES

Abdeen, D., El Hachach, M., Koc, M., & Atieh, M. (2019). A Review on the Corrosion Behaviour of Nanocoatings on Metallic Substrates. Materials, 12(2), 210.

Ameen, F., Alsamhary, K., Alabdullatif, J., & ALNadhari, S. (2021). A review on metal-based nanoparticles and their toxicity to beneficial soil bacteria and fungi. Ecotoxicology and Environmental Safety, 213, 112027.

Bundschuh, M., Filser, J., Lüderwald, S., McKee, M., Metreveli, G., Schaumann, G., . . . Wagner, S. (2018). Nanoparticles in the environment: Where do we come from, where do we go to? Environmental Sciences Europe, 30(1), 1-17.

Bertel, L., Miranda, D., & García-Martín, J. (2021). Nanostructured Titanium Dioxide Surfaces for Electrochemical Biosensing. Sensors (Basel, Switzerland), 21(18), 6167.

Bogusz, A., & Oleszczuk, P. (2018). Sequential extraction of nickel and zinc in sewage sludge- or biochar/sewage sludge-amended soil. The Science of the total environment, 636, 927–935.

Cohen, Y., Bilal, M., & Liu, H. (2018). Comment on "Assessing the Risk of Engineered Nanomaterials in the Environment: Development and Application of the nanoFate Model". Environmental Science & Technology, 52(9), 5509–5510.

Chen, C., Unrine, J.M., Hu, Y., Guo, L., Tsyusko, O.V., Fan, Z., Liu, S., & Wei, G. (2020). Responses of soil bacteria and fungal communities to pristine and sulfidized zinc oxide nanoparticles relative to Zn ions. Journal of hazardous materials, 124258.

Caballero-Guzmán, A., Sun, T.Y., & Nowack, B. (2015). Flows of engineered nanomaterials through the recycling process in Switzerland. Waste management, 36, 33–43.

Donia, D. T., & Carbone, M. (2019). Fate of the nanoparticles in environmental cycles. International Journal of Environmental Science and Technology, 16(1), 583–600.

Dale, A.L., Lowry, G.V., & Casman, E.A. (2015). Stream dynamics and chemical transformations control the environmental fate of silver and zinc oxide nanoparticles in a watershed-scale model. Environmental science & technology, 49 12, 7285–93.

Dulger, M., Sakallioglu, T., Temizel, I., Demirel, B., Copty, N.K., Onay, T.T., Uyguner-Demirel, C.S., & Karanfil, T. (2016). Leaching potential of nano-scale titanium dioxide in fresh municipal solid waste. Chemosphere, 144, 1567–72.

Giese, B., Klaessig, F., Park, B., Kaegi, R., Steinfeldt, M., Wigger, H.,. . . Gottschalk, F. (2018). Risks, Release and Concentrations of Engineered Nanomaterial in the Environment. Scientific Reports, 8(1), 1565–18.

Hatamie, A., Khan, A., Golabi, M., Turner, A., Beni, V., Mak, W., . . . Willander, M. (2015). Zinc Oxide Nanostructure-Modified Textile and Its Application to Biosensing, Photocatalysis, and as Antibacterial Material. Langmuir, 31(39), 10913–10921

Johnson, A., Bowes, M., Svendsen, C., Thompson, I., Barnes, R., Williams, R., Spurgeon, D. (2011). An assessment of the fate, behaviour and environmental risk associated with sunscreen TiO2 nanoparticles in UK field scenarios. The Science of the Total Environment, 409(13), 2503–2510.

Jalvo, B., Faraldos, M., Bahamonde, A., & Rosal, R. (2017). Antimicrobial and antibiofilm efficacy of self-cleaning surfaces functionalized by TiO2 photocatalytic nanoparticles against Staphylococcus aureus and Pseudomonas putida. Journal of hazardous materials, 340, 160–170.

Judy, J.D., McNear, D., Chen, C., Lewis, R.W., Tsyusko, O.V., Bertsch, P.M., Rao, W., Stegemeier, J.P., Lowry, G.V., McGrath, S.P., Durenkamp, M., & Unrine, J.M. (2015). Nanomaterials in Biosolids Inhibit Nodulation, Shift Microbial Community Composition, and Result in Increased Metal Uptake Relative to Bulk/Dissolved Metals. Environmental science & technology, 49 14, 8751–8.

Jovanović, B., Whitley, E.M., Kimura, K., Crumpton, A.C., & Palić, D. (2015). Titanium dioxide nanoparticles enhance mortality of fish exposed to bacterial pathogens. Environmental pollution, 203, 153–164.

Khan, R., Inam, M., Khan, S., Park, D., & Yeom, I. (2019). Interaction between Persistent Organic Pollutants and ZnO NPs in Synthetic and Natural Waters. Nanomaterials (Basel, Switzerland), 9(3), 472.

Keller, A.A., & Parker, N. (2019). Innovation in procedures for human and ecological health risk assessment of engineered nanomaterials. Exposure to Engineered Nanomaterials in the Environment.

Klaine, S.J., Alvarez, P.J., Batley, G.E., Fernandes, T.F., Handy, R.D., Lyon, D., Mahendra, S., Mclaughlin, M.J., & Lead, J.R. (2008). Nanomaterials in the environment: behavior, fate, bioavailability, and effects. Environmental toxicology and chemistry, 27 9, 1825-51.

Llana, M., Tolentino, M., Valeza, N., Reyes, J., & Basilia, B. (2021). Release Analysis of Nano-Titanium Dioxide (TiO2) from Paint: An Accelerated Weathering Experiment. IOP Conference Series. Materials Science and Engineering, 1117(1), 12029.

Martínez, G., Merinero, M., Pérez-Aranda, M., Pérez-Soriano, E., Ortiz, T., Begines, B., & Alcudia, A. (2020). Environmental Impact of Nanoparticles' Application as an Emerging Technology: A Review. Materials, 14(1), 166.

Mahmoodzadeh, H., Nabavi, M., & Kashefi, H. (2015). Effect of Nanoscale Titanium Dioxide Particles on the Germination and Growth of Canola (Brassica napus). Journal of Ornamental plants, 3, 25–32.

Putra, B., Juwono, A., & Rochman, N. (2017). Effect of addition of butyl benzyl phthalate plasticizer and zinc oxide nanoparticles on mechanical properties of cellulose acetate butyrate/organoclay biocomposite. AIP Conference Proceedings, 1862(1), AIP conference proceedings, 2017-07-10, Vol.1862 (1).

Priyanka, K.P., Harikumar, V.S., Balakrishna, K.M., & Varghese, T. (2017). Inhibitory effect of TiO2 NPs on symbiotic arbuscular mycorrhizal fungi in plant roots. IET nanobiotechnology, 11 1, 66–70.

Punzi, V.L., Kungne, V.Z., & Skaf, D.W. (2020). Removal of titanium dioxide nanoparticles from wastewater using traditional chemical coagulants and chitosan. Environmental Progress, 39.

Rashid, M., Forte Tavčer, P., & Tomšič, B. (2021). Influence of Titanium Dioxide Nanoparticles on Human Health and the Environment. Nanomaterials (Basel, Switzerland), 11(9), 2354.

Sun, T., Bornhoöft, N., Hungerbuühler, K., & Nowack, B. (2016). Dynamic Probabilistic Modeling of Environmental Emissions of Engineered Nanomaterials. Environmental Science & Technology, 50(9), 4701–4711.

Starnes, D., Unrine, J., Chen, C., Lichtenberg, S., Starnes, C., Svendsen, C.,. . . Tsyusko, O. (2019). Toxicogenomic responses of Caenorhabditis elegans to pristine and transformed zinc oxide nanoparticles. Environmental Pollution (1987), 247(C), Environmental pollution (1987), 2019-04-01, Vol.247 (C).

Shah, V., Jones, J., Dickman, J., & Greenman, S. (2014). Response of soil bacterial community to metal nanoparticles in biosolids. Journal of hazardous materials, 274, 399–403.

Tian Yin Sun, Gottschalk, F., Hungerbühler, K., & Nowack, B. (2014). Comprehensive probabilistic modelling of environmental emissions of engineered nanomaterials. Environmental Pollution (1987), 185, 69–76.

Velzeboer, I. (2014). Implications of nanoparticles in the aquatic environment.

Wang, J., Zhu, X., Zhang, X., Zhao, Z., Liu, H., George, R.M., Wilson-Rawls, J., Chang, Y., & Chen, Y. (2011). Disruption of zebrafish (Danio rerio) reproduction upon chronic exposure to TiO2 nanoparticles. Chemosphere, 83 4, 461–7.

Zvimba, J., Musee, N., Chauque, E., & Ngila, J. (2016). Fate, behaviour, and implications of ZnO nanoparticles in a simulated wastewater treatment plant. Water S. A., 42(1), 72–81.

Advances in Applied Chemistry and Industrial Catalysis – Saikia (Ed.)

Methodological verification of determination of TVOC in indoor air

Mengying Zhang, Wenqing Li*, Xianbian Mao, Xingfang Li & Huanhuan Gou
China Building Material Test & Certification Group (Shaanxi) Co., Ltd., Shaanxi, China

ABSTRACT: TVOC is one of the most serious types of indoor air quality pollution. In the indoor decoration process, TVOC mainly comes from the building and decoration materials of adhesives, coatings, paints, panels, wallpaper, and so on. In the decoration, especially in the improper decoration, the TVOC content in the indoor air often exceeds the standard, causing damage to the human body. The procedures and results of determination of TVOC in indoor air were described in this article to provide a reference for the scientific and reasonable verification of the determination of TVOC.

1 INTRODUCTION

TVOC refers to an organic substance with a saturated vapor pressure exceeding 133.32 Pa at room temperature. Its boiling point is between 50°C and 250°C. It can be present in the air in the form of evaporation at room temperature. TVOC can cause an imbalance of the body's immune level, affect the function of the central nervous system, and experience headache, drowsiness, weakness, chest tightness, and other conscious symptoms; it may also affect the digestive system, loss of appetite, nausea and can damage the liver and hematopoietic system in severe cases (Pang 2019; Wu 2010). The World Health Organization (WHO), and the National Academy of Sciences/National Research Council (NAS/NRC) have always emphasized that TVOC is an important type of air pollutant.

TVOC is one of the most serious types of indoor air quality pollution. It mainly comes from the building and decoration materials of adhesives, coatings, paints, panels, wallpaper, and so on. When the concentration of TVOC indoors is 0.16 mg/m^3∼0.3 mg/m^3, it is harmless to human health, but it is often exceeded in decoration, especially in the case of improper decoration[2]. Determine the content of TVOC in indoor air can measure whether the decoration is appropriate, whether the use of decoration materials is environmentally friendly, and whether indoor air will affect human health, and minimize the impact of TVOC on indoor air quality (Sun et al. 2011).

This experiment confirms the technical capabilities of GB 50325-2020 (Ministry of Housing and Urban-Rural Development of the People's Republic of China 2020) Appendix E of the TVOC testing method in indoor air. According to GB/T 27417-2017 (China National Accreditation Service for Conformity Assessment 2017) and HJ 168-2020 (Ministry of Ecology and Environment of the People's Republic of China 2020), the standard curve, detection limit, precision, and accuracy are verified to ensure that the method meets the testing requirements, to provide a reference for the scientific and reasonable verification of determination of TVOC.

2 TEST

2.1 *Instruments and reagents*

Agilent 7820A Gas Chromatograph, FID detector. Column: Agilent DB-WAX Capillary column, 30m × 0.25mm × 0.25μm; JX-5 thermal analysis instrument; CNW T-C composite thermal analysis tube.

*Corresponding Author: 18821795290@gmail.com

 DOI 10.1201/9781003308553-70

Standard solution: 16 kinds of VOC standard solutions in carbon disulfide (n-hexane, 1-octene, n-nonane, benzene, trichloroethylene, toluene, n-butylacetate, n-undecane, ethylbenzene, p-xylene, m-xylene, o-xylene, styrene, n-tetradecane, 2-ethyl-1-hexanol, n-hexadecane), the concentration is 2000 mg/L, manufacturer: ANPEL.

2.2 *Instrument conditions*

GC: The inlet temperature is 220°C, the detector temperature is 250°C, and the flow rate is 1.5 mL/min. Temperature program: initial 35°C, holding time 10 minutes, rising to 110°C at 5°C/min, then rising to 200°C at 20°C/min, holding time 2 minutes.

Thermal analysis: analysis temperature 320°C, enrichment 5 minutes, desorption 3 minutes.

2.3 *Preparation of standard adsorption tube*

Standard series of 50mg/l, 100mg/l, 400mg/l, 800mg/l, 1200mg/l, and 2000mg/l of standard solutions were prepared, take 1 μL and inject it into the adsorption tube to make a standard adsorption tube with the content of each component of 0.05 μg, 0.1 μg, 0.4 μg, 0.8 μg, 1.2 μg, 2 μg. Pass nitrogen through the adsorption tube with 100 mL/min, take it off and seal it after 5 minutes, and use it as a series of standard adsorption tube samples.

2.4 *Testing*

The adsorption tube is placed in the thermal analysis instrument, and after full analysis at 320°C, the analysis gas is directly fed into the GC for qualitative and quantitative chromatographic analysis.

3 RESULTS

3.1 *Standard curve*

Make a standard curve based on the peak area and content of each component to obtain a linear regression equation. The results are as Table 1.

Table 1. The linear regression equation of the concentration, peak area, and standard curve of 16 kinds of volatile organic compounds standard solution.

Parameters	Peak area						Linear regression equation	Correlation coefficient R^2
	0.05 μg	0.1 μg	0.4 μg	0.8 μg	1.2 μg	2.0 μg		
n-Hexane	6.566	12.694	50.94	90.282	120.94	200.9	y = 98.272x + 5.864	0.9962
1-Octene	28.571	46.708	236.649	460.209	708.787	1164.038	y = 585.92x - 3.4922	0.9998
n-Nonane	36.051	53.997	252.639	488.786	727.056	1196.06	y = 597.76x + 5.7958	0.9997
Benzene	82.905	98.416	274.55	461.764	668.793	1044.521	y = 495.94x + 62.401	0.9991
Trichloroethylene	5.366	8.745	50.316	95.766	146.834	239.822	y = 120.99x - 0.6117	0.9995
Toluene	53.004	61.021	266.765	517.152	767.817	1273.253	y = 631.07x + 11.273	0.9997
n-Butylacetate	17.642	26.479	141.253	283.117	414.585	690.296	y = 346.7x - 0.6844	0.9997
n-Undecane	30.986	50.186	205.417	395.925	568.127	924.886	y = 459.38x + 14.224	0.9992

(*continued*)

Table 1. Continued.

Parameters	Peak area						Linear regression equation	Correlation coefficient R^2
	0.05 μg	0.1 μg	0.4 μg	0.8 μg	1.2 μg	2.0 μg		
Ethylbenzene	31.952	54.477	254.416	504.928	744.708	1239.263	y = 620.62x + 0.984	0.9998
p-Xylene	36.949	54.753	255.996	512.033	757.844	1264.718	y = 632.55x + 0.6985	0.9999
m-Xylene	38.954	58.096	256.464	512.134	760.996	1269.942	y = 634.01x + 1.9727	0.9999
o-Xylene	40.842	60.168	268.551	526.727	779.468	1291.394	y = 644.14x + 6.0555	0.9999
Styrene	39.613	55.554	264.732	530.882	781.316	1302.719	y = 651.39x + 1.8318	0.9998
n-Tetradecane	49.685	50.205	198.749	409.251	605.323	1029.816	y = 508.06x + 5.2256	0.9991
2-Ethyl-1-hexanol	44.65	47.601	197.783	385.94	571.175	951.877	y = 469.8x + 10.237	0.9996
n-Hexadecane	95.024	117.19	189.306	279.086	375.719	558.437	y = 235.06x + 90.87	0.9994

The standard curve of 16 kinds of volatile organic compounds is shown below:

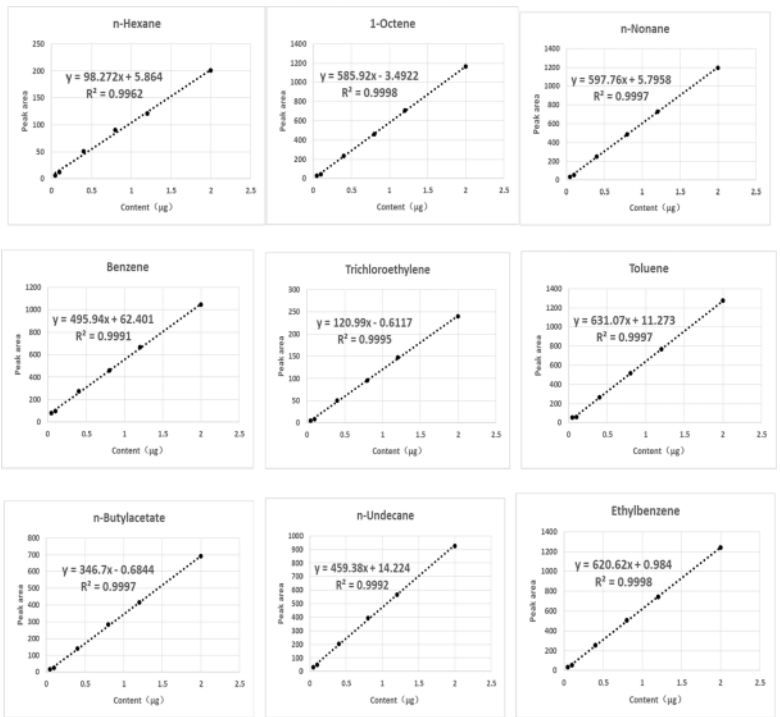

Figure 1. The standard curve of 16 kinds of volatile organic compounds.
(The picture shows the standard curve of n-hexane, 1-octene, n-nonane, benzene, trichloroethylene, toluene, n-butylacetate, n-undecane, ethylbenzene, p-xylene, m-xylene, o-xylene, styrene, n-tetradecane, 2-ethyl-1-hexanol, n-hexadecane in sequence).

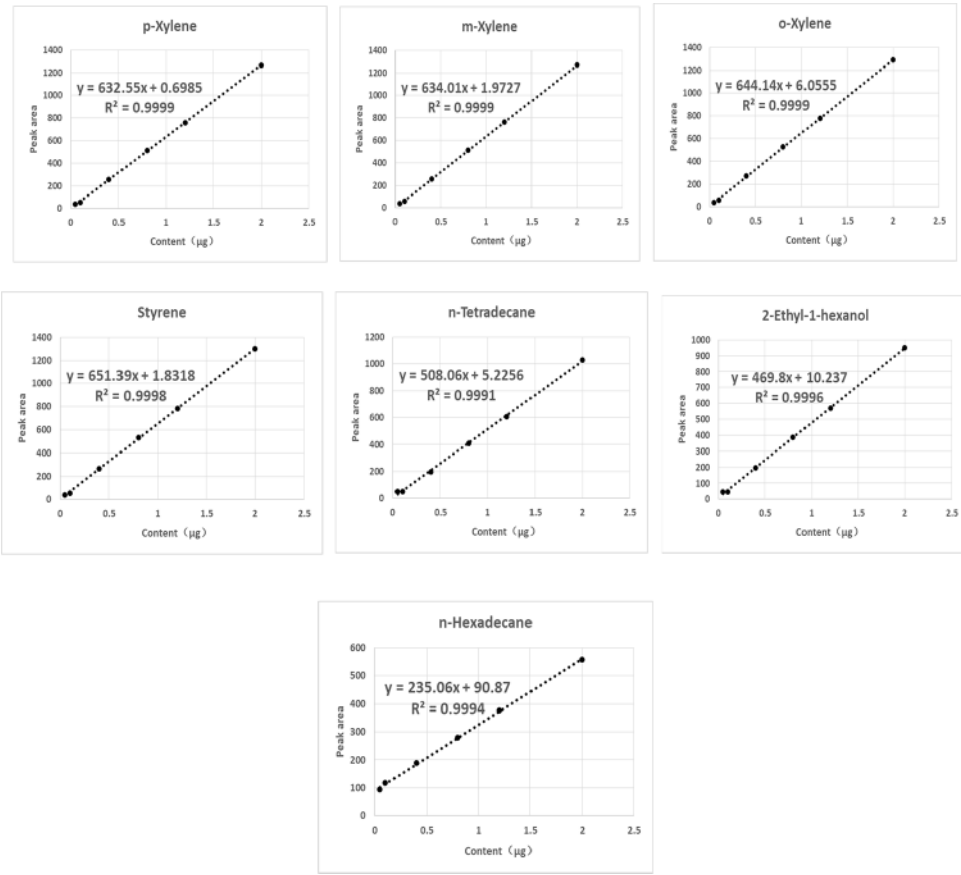

Figure 1. continued.

It can be seen from Table 1 and Figure 1 that the correlation coefficients of the standard curve linear regression equations are all above 0.995, and the standard curve accords with the use requirement.

3.2 *Detection limit*

According to the qualitative principle of three times the S/N and the quantitative principle of ten times the S/N, perform 6 parallel experiments on the minimum content of the standard curve of 0.05 μg and calculate the S/N and detection limit of the instrument. The results are as Table 2:

Table 2. The results of detection limit.

Parameters	S/N						Average	Detection limit (mg/m^3)
	1	2	3	4	5	6		
n-Hexane	0.902	0.978	0.977	0.948	0.964	0.878	0.941	0.016
1-Octene	1.511	1.123	1.520	1.587	1.594	1.547	1.480	0.010
n-Nonane	1.259	1.437	1.204	1.294	1.274	1.294	1.294	0.012
Benzene	3.644	4.264	4.387	4.261	4.217	3.947	4.120	0.004
Trichloroethylene	0.237	0.176	0.208	0.254	0.264	0.248	0.231	0.065

(*continued*)

Table 2. Continued.

Parameters	S/N 1	2	3	4	5	6	Average	Detection limit (mg/m^3)
Toluene	2.139	2.936	1.257	2.419	2.461	2.487	2.283	0.007
n-Butylacetate	0.574	0.352	0.426	0.531	0.462	0.541	0.481	0.031
n-Undecane	0.931	0.587	0.762	0.846	0.841	0.885	0.809	0.019
Ethylbenzene	1.057	0.522	0.811	0.847	0.746	0.864	0.808	0.019
p-Xylene	1.184	1.024	1.031	1.120	1.103	1.111	1.096	0.014
m-Xylene	1.368	0.879	0.995	1.025	0.987	1.035	1.048	0.014
o-Xylene	1.635	0.971	0.986	1.512	1.421	1.321	1.308	0.011
Styrene	1.572	0.842	1.227	1.512	1.024	1.063	1.207	0.012
n-Tetradecane	1.207	0.551	0.697	1.021	0.845	0.731	0.842	0.018
2-Ethyl-1-hexanol	2.399	1.548	1.566	1.697	1.784	1.697	1.782	0.008
n-Hexadecane	6.294	3.507	4.330	4.316	3.974	5.457	4.646	0.003

The detection limit of n-hexane is 0.016 mg/m^3, the detection limit of 1-octene is 0.010 mg/m^3, the detection limit of n-nonane is 0.012 mg/m^3, the detection limit of benzene is 0.004 mg/m^3, the detection limit of trichloroethylene is 0.065 mg/m^3, the detection limit of toluene is 0.007 mg/m^3, the detection limit of n-butylacetate is 0.031 mg/m^3, the detection limit of n-undecane is 0.019 mg/m^3, the detection limit of ethylbenzene is 0.019 mg/m^3, the detection limit of p-xylene is 0.014 mg/m^3, the detection limit of m-xylene is 0.014 mg/m^3, the detection limit of o-xylene is 0.011 mg/m^3, the detection limit of styrene is 0.012 mg/m^3, the detection limit of n-tetradecane is 0.018mg/m^3, the detection limit of 2-ethyl-1-hexanol is 0.008 mg/m^3, and the detection limit of n-hexadecane is 0.003 mg/m^3.

3.3 *Precision*

The determination is repeated 6 times for a sample with content of 0.4μg, and the standard deviation and coefficient of variation are calculated. The results are as Table 3.

Table 3. The results of precision.

Parameters	Measured value 1	2	3	4	5	6	Average (μg)	Standard deviation	CV (%)
n-Hexane	0.386	0.375	0.366	0.384	0.384	0.374	0.378	0.0078	2.1
1-Octene	0.394	0.391	0.386	0.381	0.386	0.377	0.3856	0.0062	1.6
n-Nonane	0.381	0.384	0.384	0.391	0.367	0.387	0.382	0.0082	2.2
Benzene	0.384	0.374	0.385	0.347	0.367	0.39	0.374	0.0158	4.2
Trichloroethylene	0.355	0.355	0.368	0.371	0.341	0.346	0.356	0.012	3.3
Toluene	0.374	0.369	0.384	0.382	0.38	0.376	0.378	0.0056	1.5
n-Butylacetate	0.374	0.394	0.38	0.386	0.376	0.371	0.3808	0.0085	2.2
n-Undecane	0.348	0.342	0.355	0.361	0.381	0.375	0.3608	0.015	4.2
Ethylbenzene	0.371	0.377	0.372	0.379	0.382	0.386	0.378	0.0058	1.5
p-Xylene	0.385	0.38	0.376	0.383	0.381	0.371	0.379	0.0051	1.3
m-Xylene	0.374	0.372	0.37	0.388	0.382	0.384	0.378	0.0073	1.9
o-Xylene	0.388	0.394	0.381	0.382	0.377	0.388	0.385	0.0061	1.6
Styrene	0.376	0.38	0.37	0.366	0.361	0.384	0.373	0.0087	2.3
n-Tetradecane	0.324	0.35	0.334	0.343	0.351	0.344	0.341	0.010	3.0
2-Ethyl-1-hexanol	0.371	0.361	0.356	0.381	0.346	0.356	0.362	0.012	3.4
n-Hexadecane	0.347	0.358	0.349	0.366	0.361	0.375	0.359	0.011	2.9

The coefficient of variation of n-hexane is 2.1%, the coefficient of variation of 1-octene is 1.6%, the coefficient of variation of n-nonane is 2.2%, the coefficient of variation of benzene is 4.2%, the coefficient of variation of trichloroethylene is 3.3%, the coefficient of variation of toluene is 1.5%, the coefficient of variation of n-butylacetate is 2.2%, the coefficient of variation of n-undecane is 4.2%, the coefficient of variation of ethylbenzene is 1.5%, the coefficient of variation of p-xylene is 1.3%, the coefficient of variation of m-xylene is 1.9%, the coefficient of variation of o-xylene is 1.6%, the coefficient of variation of styrene is 2.3%, the coefficient of variation of n-tetradecane is 3.0%, the coefficient of variation of 2-ethyl-1-hexanol is 3.4%, and the coefficient of variation of n-hexadecane is 2.9%. According to the requirements of Appendix B of GB/T 27417-2017[2], the coefficient of variation of each component in the laboratory meets the requirements.

3.4 *Accuracy*

Use the stock solution to add standard, the concentration is 200 μg/mL, the additional volume is 1μL, calculate the recovery rate of each component. The results are as Table 4:

Table 4. The results of recovery.

Parameters	Added scalar (μg)	Background value (μg)	Measured value (μg)	Recovery (%)	Average recovery (%)
n-Hexane	0.2	N.D	0.176	88	88.5
		N.D	0.178	89	
1-Octene	0.2	N.D	0.181	90.5	91
		N.D	0.183	91.5	
n-Nonane	0.2	N.D	0.184	92	93
		N.D	0.188	94	
Benzene	0.2	N.D	0.176	88	87
		N.D	0.172	86	
Trichloroethylene	0.2	N.D	0.165	82.5	83.25
		N.D	0.168	84	
Toluene	0.2	N.D	0.171	85.5	86
		N.D	0.173	86.5	
n-Butylacetate	0.2	N.D	0.168	84	85.25
		N.D	0.173	86.5	
n-Undecane	0.2	N.D	0.17	85	82.75
		N.D	0.161	80.5	
Ethylbenzene	0.2	N.D	0.186	93	94.25
		N.D	0.191	95.5	
p-Xylene	0.2	N.D	0.189	94.5	92.75
		N.D	0.182	91	
m-Xylene	0.2	N.D	0.184	92	92.5
		N.D	0.186	93	
o-Xylene	0.2	N.D	0.194	97	94.25
		N.D	0.183	91.5	
Styrene	0.2	N.D	0.184	92	93
		N.D	0.188	94	
n-Tetradecane	0.2	N.D	0.167	83.5	82.25
		N.D	0.162	81	
2-Ethyl-1-hexanol	0.2	N.D	0.184	92	90
		N.D	0.176	88	
n-Hexadecane	0.2	N.D	0.172	86	87.25
		N.D	0.177	88.5	

The recovery of n-hexane is 88.5%, the recovery of 1-octene is 91%, the recovery of n-nonane is 93%, the recovery of benzene is 87%, the recovery of trichloroethylene is 83.25%, the recovery of toluene is 86%, the recovery of n-butylacetate is 85.25%, the recovery of n-undecane is 82.75%, the recovery of ethylbenzene is 94.25%, the recovery of p-xylene is 92.75%, the recovery of m-xylene is 92.5%, the recovery of o-xylene is 94.25%, the recovery of styrene is 93%, the recovery of n-tetradecane is 82.25%, the recovery of 2-ethyl-1-hexanol is 90%, and the recovery of n-hexadecane is 87.25%. According to the requirements of Appendix A of GB/T 27417-2017[2], the recovery of each component in the laboratory meets the requirements.

4 CONCLUSION

According to the actual conditions of the laboratory, this article confirms the technical capabilities of the TVOC test method in Appendix E of GB 50325-2020 and verifies the standard curve, detection limit, precision, and accuracy. The results show that the laboratory has the conditions and capabilities for indoor air TVOC measurement. At the same time, the following points need to be paid attention to in the determination:

(1) Since n-hexane is volatile easily, it is best to configure a standard solution series with a certain concentration, and inject it into the adsorption tube quantitatively, to avoid the influence of n-hexane volatilization and make the curve more linear.
(2) The temperature and airtightness of the thermal analysis transfer tube must be ensured. Too low temperature will cause the loss of n-tetradecane and n-hexadecane, and there will be no peaks. Therefore, the transfer tube must be insulated.
(3) The T-C tube should be activated with nitrogen before use, the activation temperature should be higher than the analytical temperature, and not more than 320°C, and the activation time should not be fewer than 30 minutes.

REFERENCES

Bin Wu (2010) Indoor Environment Formaldehyde, Ammonia, Hydrazine, Benzene, TVOC Detection and Quality Control. Resources and Environment, 2018, 44(11):214.

China National Accreditation Service for Conformity Assessment. (2017) GB/T 27417-2017 Comformity assessment-Guidance on validation and verification of chemical analytical methods.

Guanhua Pang (2019) Analysis of Quality Control in Detection of Indoor Environment Contaminants Radon, Formaldehyde, Ammonia, Benzene and TVOC. Guangdong Chemical Industry, 2019, 46(22):125–126.

Ministry of Ecology and Environment of the People's Republic of China. (2020) HJ 168-2020 Technical guideline for the development of environmental monitoring analytical method standards.

Ministry of Housing and Urban-Rural Development of the People's Republic of China. (2020) GB 50325-2020 Standard for indoor environmental pollution control of civil building engineering. Beijing: China Planning Press.

Xiuping Sun, Shuping Hou, Xifeng Liu (2011) Effectible Factor of Nicety for Indoor Air Test of TVOC [J]. Construction Quality, 2011, 29(05):23–24.

Advances in Applied Chemistry and Industrial Catalysis – Saikia (Ed.)

Research progress of nitrogen removal in low C/N wastewater by constructed wetlands: Mechanism and influencing factors

Xiaoyan Ge*
Shanghai Urban Construction Vocational College, Shanghai, China
College of Environmental Science and Engineering, State Environmental Protection Engineering Center for Pollution Treatment and Control in Textile Industry, Donghua University, Shanghai, China

Yanwei Guo** & Jian Zhai
Shanghai Urban Construction Vocational College, Shanghai, China

Xinshan Song & Xin Cao
College of Environmental Science and Engineering, State Environmental Protection Engineering Center for Pollution Treatment and Control in Textile Industry, Donghua University, Shanghai, China

ABSTRACT: Constructed wetland is an effective and low-cost method to treat low C/N wastewater. There are many factors that can influence the performance of constructed wetland. This paper elucidates the main microbial mechanism of nitrogen removal in low C/N wastewater by constructed wetlands, analyses the influencing factors of nitrogen removal and summarizes the improved methods. In addition, the challenges during removal process are prospected.

1 INTRODUCTION

Excessive nitrogen (N) discharged into the natural environment can lead to severe water eutrophication and the deterioration of aquatic ecosystems. Nitrogen compounds accumulated in sewage treatment plant effluent or non-point source pollution are considered to be the inducement of water eutrophication and ecotoxicity in China (Bednarek 2014). This kind of water has the characteristics of low C/N (BOD_5/N=2.5∼3), large fluctuation and discharge, which requires strong impact resistance of the treatment process (Guan et al. 2019).

Constructed wetland has the endowment of deep nitrogen removal and control of non-point source pollution. Since the 1970s, CWs have been widely used to remove SS, COD, N, P, algae, and heavy metal ions due to their cost-effectivity, efficiency, and stability in operation (Fu et al. 2017). Given the above advantages and landscaping effect on the environment, constructed wetlands serve as a promising alternative for other traditional wastewater treatment processes. The constructed wetland technology can further reduce pollutant load and protect water quality before wastewater enters water body (Kivaisi 2001). In recent years, to enhance the treatment effect of wetland, researchers put forward enhanced constructed wetland (Enhanced wetland), such as CW-MFC, CW-MEC, artificial aerated CWs and photovoltaic electrolysis enhanced constructed wetland (Li et al. 2019).

After the low C/N wastewater enters the constructed wetland, the pollutants are efficiently removed under the synergistic action of wetland vegetation (macrophytes), substrates and microorganisms (Gao et al. 2019). However, low C/N ratio or insufficient carbon source are the main factors that restrict the treatment of wastewater by constructed wetland. In addition, low temperature in winter and inappropriate reactor structure both can reduce the performance of contaminants removal in constructed wetland. At present, the purification technology of constructed wetland is increasingly mature, but the treatment of nitrogen in low C/N wastewater needs further research.

Corresponding Authors: *gexiaoyan09@126.com and **guoyanwei@succ.edu.cn

DOI 10.1201/9781003308553-71

The objectives of this study were to 1) conclude the structure type of constructed wetlands; 2) elucidate the main treatment mechanisms of low C/N wastewater in constructed wetlands; 3) analyze the influencing factors of contaminants removal; 4) summarize the improved methods.

2 THE REMOVAL MECHANISMS OF NITROGEN IN CONSTRUCTED WETLAND

In constructed wetlands, nitrogen removal pathways mainly include plant, substrate and microorganism. The previous study in free-surface constructed wetlands to treat low-pollution water, showed that microbial (mainly denitrification) contributed 58.6% to nitrogen removal, soil adsorption accounted for 25.2% of nitrogen, and plant absorption contributed 16.2% to nitrogen removal (ABE et al. 2017). Many previous studies indicated that the microorganisms contributed the most to nitrogen conversion and removal in low C/N wastewater. Microbial nitrogen removal pathway is considered as the main mechanism of constructed wetlands to treat nitrogen in low C/N wastewater (Zhuang et al. 2019).

The inorganic forms of nitrogen are ammonium (NH_4^+), nitrite (NO_2^-), nitrate (NO_3^-), nitrous oxide (N_2O) and nitrogen (N_2). Conventional microbial nitrogen conversion approaches mainly include ammonification, nitrification, denitrification, dissimilar nitrate reduction to ammonium (DNRA), and unconventional denitrification approaches, such as partial nitrification and denitrification (PND), and anaerobic ammonia oxidation (anammox). The transformation pathways of microbial nitrogen are shown in Figure 1.

2.1 *Simultaneous Nitrification and Denitrification (SND)*

Nitrification and denitrification are the most common microbial nitrogen removal processes. In the nitrification process, *amo*A is a functional gene of aerobic ammoxidation, and *nxr*A is a functional marker of NO_2^- oxidation to NO_3^-. Denitrification is the main microbial mechanism of TN removal in constructed wetlands. In the denitrification process, NO_3^- acts as an electron acceptor which gets electrons from organic carbon, eventually producing N_2 under anoxic conditions. *Nar*G and *nap*A are the genes encoding nitrate reductase, *nir*K and *nir*S are the main genes encoding nitrite reductase, and *nos*Z is the gene encoding nitrous oxide reductase. They are used as functional markers to study the denitrification process. The lack of sufficient carbon source results in the low TN removal efficiency (Zhou et al. 2018). The previous studies indicated that the introducing of S, Fe and H_2 can change microbial community structure and further intensify the biological denitrification (Ma et al. 2020). In the biofilm reactor, a special biofilm with oxygen gradient is formed due to the uneven distribution of dissolved oxygen. Bacteria on the biofilm surface firstly contact wastewater and dissolved oxygen, and then convert ammonia into nitrite or nitrate. Under anoxic conditions, nitrite or nitrate enters the deep layer of biofilm and is reduced to N_2, which shortens the reaction time of nitrogen removal process.

2.2 *Autotrophic denitrification*

According to different electron donors, the autotrophic denitrification process is mainly divided into sulfur autotrophic denitrification, iron autotrophic denitrification and hydrogen autotrophic denitrification. Under anoxic conditions, Sulfur autotrophic denitrification is that inorganic chemotrophic or phototrophic bacteria use reduced sulfur as electron donor, NO_3^- acts as an electron acceptor to produce N_2 and sulfate (SO_4^{2-}) (Chen et al. 2018). Iron autotrophic denitrification is a process in which phototrophic and chemotrophic denitrifying bacteria use Fe^{2+} as electron donor and NO_3^- as electron acceptor to produce N_2 under anaerobic conditions (Jia et al. 2020). Hydrogen autotrophic denitrification is a process in which hydrogen autotrophic denitrification bacteria use H_2 as electron donor and NO_3^- as electron acceptor for denitrification (Gao et al. 2017).

2.3 *Dissimilatory Nitrate Reduction to Ammonium (DNRA)*

Unlike the denitrification, DNRA is a biological process in which dissolved organic carbon is used as the electron donor and NO_3^- /NO_2^- as the electron acceptor under anaerobic conditions, and nitrogen is ultimately retained as NH_4^+-N. Then, NH_4^+-N is absorbed by plants or oxidized to NO_3^--N by microorganisms. In constructed wetlands, electron donor is an important and decisive factor, such as organic carbon, Fe^{2+}, sulfide and H_2. The research showed that the higher the ratio of total carbon to NO_3^--N concentration, the more conducive to the occurrence of DNRA process. In most cases, DNRA and denitrification processes occur simultaneously in wetlands, but when the concentration ratio of total carbon to NO_3^--N is greater than 12, DNRA process can exist alone (Jahangir et al. 2017).

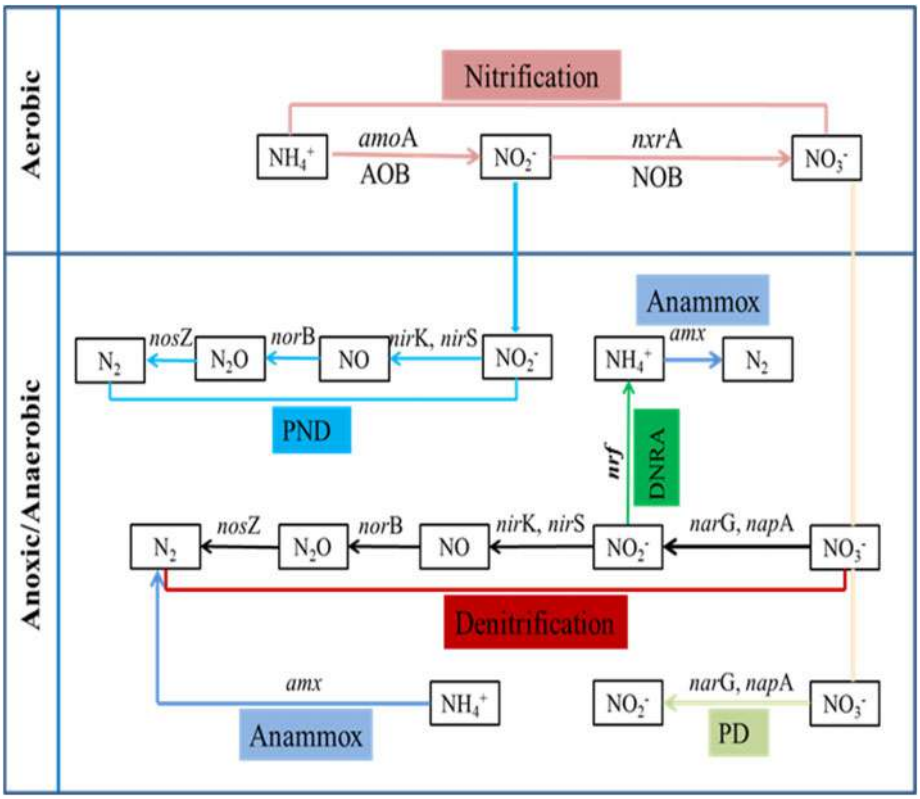

Figure 1. Transformation pathway of microbial nitrogen. [Wang et al. 2021].
PND: Partial nitration and denitrification.
DNRA: Dissimilatory nitrate reduction to ammonium.
PD: Partial denitrification.

2.4 *Partial Nitration and Denitrification (PND)*

This process involves translation of NH_4^+-N to NO_2^--N which is called nitrification (Eq.1) after that the denitrification of NO_2^--N to N_2 gas (Eq. 2) takes place (Kumar et al. 2019).

$$NH_4^+ + 1.5O_2 \rightarrow NO_2^- + H_2O + 2H^+ \quad (1)$$

$$NO_2^- + 1/2CH_3OH + H^+ \rightarrow 1/2N_2 + 1/2CO_2 + 1.5H_2O \quad (2)$$

2.5 *Anammox*

In addition to denitrification, anammox also provides another permanent nitrogen removal pathway. Anammox is a process that uses NH_4^+ as electron donor and reduces nitrite to N_2. Anammox bacteria are anaerobic autotrophs, and *amx* is a functional gene of anammox. Compared with traditional nitrification-denitrification, anammox has been widely studied as it rarely requires external carbon. Further, oxygen and energy requirements are also very low and nitrogen is removed at greater speed.

3 THE MAIN INFLUENCING FACTORS OF NITROGEN REMOVAL PERFORMANCE

3.1 *Wetlands type and structure*

According to different water distribution modes, constructed wetlands can be divided into surface flow constructed wetlands and subsurface flow constructed wetlands. Subsurface flow constructed wetland has better removal effect on TP, TN and algae. Meanwhile, owing to its better sanitary conditions, it is suitable to be used as the main treatment unit for repairing eutrophic water bodies (Flores et al. 2019). Based on the wastewater flow direction, subsurface flow constructed wetlands can be divided into horizontal flow constructed wetlands (HFCWs) and vertical flow constructed wetlands (VFCWs). The application of constructed wetland system has many forms, such as hybrid constructed wetland (Hybrid CWs) and multi-stage CWs, which usually consists of two parallel or multiple constructed wetlands.

3.2 *Hydraulic operating condition*

Hydraulic Residence Time (HRT), hydraulic load and operation mode can influence the nitrogen removal performance in constructed wetlands. Generally, appropriate prolongation of HRT can increase the nitrogen removal efficiency. Hydraulic load refers to the amount of sewage water passing through per unit area per unit time. Low hydraulic load means that the sewage water stays in the wetland for a long time, which is conducive to the coordinated removal of nutrients and organic matter in the eutrophic water by plants, substrates and microorganisms (Wu et al. 2015). Continuous flow and intermittent flow are the mainly operation modes of constructed wetland. These two operation modes are both applied in engineering practice.

3.3 *The ratio of carbon to nitrogen*

Low influent carbon/nitrogen (C/N) cannot provide sufficient carbon to microbial growth, and results in lower total nitrogen (TN) removal efficiency. To address this problem, researches have proposed many methods to increase carbon source or electron donors: ① Introducing solid carbon source, such as crop straw, bark, waste wood chips, etc.; biodegradable polymer, such as PHBV (3-hydroxybutyrate-co-3-hydroxyvalerate), PBS (Polybutylenesuccinate) and PCL (Polycaprolactone), etc. (Tao et al. 2020; Yang et al. 2018), ② Using inorganic electron donors, such as S, Fe and H_2; ③ Applied the enhanced CWs, such as iron carbon microelectrolysis enhanced constructed wetland technology, CW-MFC, CW-MEC (Shen et al. 2019).

3.4 *Other factors*

Plants and substrates are two important components of constructed wetlands. Plants with strong pollution resistance and developed root systems are crucial to enhance removal performance of constructed wetlands. Meanwhile, substrate selection is one of the key technical issues for constructed wetlands. Except for the conventional three substrates of soil, sand and gravel, the emerged substrates (ion-exchange substrates, P-sorption substrates, and electron donor substrates) are developed and applied in constructed wetlands due to the strong adsorption capacity and economic availability (Yang et al. 2018).

4 CONCLUSION

Based on the above discussions, the conclusions are obtained as below:

(1) Sewage treatment plant effluent or non-point source pollution has the characteristics of low C/N, large fluctuation and discharge, which requires strong impact resistance of the treatment process.
(2) Nitrogen removal pathways mainly include plant, substrate and microorganism. Conventional microbial nitrogen transformation pathways include ammonification, nitrification, denitrification and DNRA and partial nitration and denitrification.
(3) The wetlands type and structure, hydraulic operating condition, the ratio of carbon to nitrogen, plants and substrate all can influence the removal performance of constructed wetlands. In order to improve the performance of constructed wetlands, it is necessary to consider the above factors in the design process.
(4) CW-MFC, CW-MEC, artificial aerated CWs and photovoltaic electrolysis are used to enhance nitrogen removal.
(5) Regarding the sustainable development of constructed wetlands, future research on avoiding substrate clogging to extend their lifetime, the mechanism and influencing factors of microbial removal and the coupling mechanism between CWs and other technologies are needed.

ACKNOWLEDGEMENTS

This study was financially supported by the scientific research project of Shanghai Urban Construction Vocational College (Grant No.cjky202111), the Fundamental Research Funds for the Central Universities and Graduate Student Innovation Fund of Donghua University (Grant No.CUSF-DH-D-2020074).

REFERENCES

Abe, K. Komada, M. Ookuma, A (2014). Purification performance of a shallow free-water-surface constructed wetland receiving secondary effluent for about 5 years. *Ecological Engineering*, 69:126–133.

Bednarek, A. Szklarek, S & Zalewski, M (2014). Nitrogen pollution removal from areas of intensive farming—comparison of various denitrification biotechnologies. *Ecohydrology & Hydrobiology,* 14(2), 132–141.

Chen, F. M. Li, X. Gu, C (2018). Selectivity control of nitrite and nitrate with the reaction of S^0 and achieved nitrite accumulation in the sulfur autotrophic denitrification process[J]. *Bioresource Technology*, 266:211–219.

Flores, L. García, J. Pena, R (2019). Constructed wetlands for winery wastewater treatment: A comparative Life Cycle Assessment. *Science of the Total Environment*, 659:1567–1576.

Fu, G. Huang, S. L. Guo, Z. Zhou, Q. Wu, Z (2017). Effect of plant-based carbon sources on denitrifying microorganisms in a vertical flow constructed wetland. *Bioresource Technology*, 224: 214–221.

Gao, Y. Xie, Y. W. Zhang, Q (2017). Intensified nitrate and phosphorus removal in an electrolysis-integrated horizontal subsurface-flow constructed wetland. *Water Research*, 108:39–45.

Gao, Y. Yan, C. Wei, R. P (2019). Photovoltaic electrolysis improves nitrogen and phosphorus removals of biochar-amended constructed wetlands. *Ecological Engineering*, 138: 71–78.

Guan, L. Hai, Y. Peng, Y. J. Xiao, J & Yan Y (2019). Enhanced nitrogen removal of low C/N wastewater in constructed wetlands with co-immobilizing solid carbon source and denitrifying bacteria. *Bioresource Technology,* 280:337–344.

Jahangir, M. M. R. Fentono, M. C (2017). In situ denitrification and DNRA rates in groundwater beneath an integrated constructed wetland. *Water Research*, 111:254–264.

Jia, W. Sun, X. Gao, Y (2020). Fe-modified biochar enhances microbial nitrogen removal capability of constructed wetland. *Science of the Total Environment*, 740:139534.

Kivaisi A. K (2001). The potential for constructed wetlands for wastewater treatment and reuse in developing countries: a review. *Ecological Engineering*.,16(4):545–560.

Kumar, S & Dutta, V (2019). Constructed wetland microcosms as sustainable technology for domestic wastewater treatment: an overview. *Environmental Science and Pollution Research*, 26:11662–11673.

Li, X. Li, Y. Y. Li, Y (2019). Enhanced nitrogen removal and quantitative analysis of removal mechanism in multistage surface flow constructed wetlands for the large-scale treatment of swine wastewater. Journal of Environmental Management, 246:575–582.

Ma, Y. H. Zheng, X. Y. Fang, Y. Q (2020). Autotrophic denitrification in constructed wetlands: Achievements and challenges. *Bioresource Technology,* 318:123778.

Shen, Y. H. Zhuang, L. L. Zhang, J (2019). A study of ferric-carbon micro-electrolysis process to enhance nitrogen and phosphorus removal efficiency in subsurface flow constructed wetlands. *Chemical Engineering Journal*, 359(1): 706–712.

Tao, M. N. Guan, L. Jing, Z. Q (2020). Enhanced denitrification and power generation of municipal wastewater treatment plants (WWTPs) effluents with biomass in microbial fuel cell coupled with constructed wetland. *Science of the Total Environment*, 709:136159.

Wang, Y.N. Guo, X C. Lu S Y. Liu, X. H. Wang, X. H (2021). Review of nitrogen removal in low-polluted water by constructed wetlands: Performance, mechanism, and influencing factors. *Journal of Agricultural Resources and Environment,* 38(5):722–734.

Wu, H. M. Zhang, J. Ngo, H. H (2015). A review on the sustainability of constructed wetlands for wastewater treatment: Design and operation. *Bioresource Technology,* 175, 594–601.

Yang, Y. Zhao, Y. Liu, R & Morgan, D (2018) Global development of various emerged substrates utilized in constructed wetlands. *Bioresource Technology*, 261:441–452.

Yang, Z C. Yang, L H. Wei, C J (2018). Enhanced nitrogen removal using solid carbon source in constructed wetland with limited aeration. *Bioresource Technology,* 248:98–103.

Zhang, L L. Yang, T. Zhang, J (2019). The configuration, purification effect and mechanism of intensified constructed wetland for wastewater treatment from the aspect of nitrogen removal: A review. *Bioresource Technology,* 293:122086.

Zhou, X. Wu, S.B. Wang, R.G. Wu, H. M (2018). Nitrogen removal in response to the varying C/N ratios in subsurface flow constructed wetland microcosms with biochar addition. *Environmental Science and Pollution Research*, 26: 3382–3391.

Advances in Applied Chemistry and Industrial Catalysis – Saikia (Ed.)

Screening of nitrogen removal bacteria and its application in aquaculture wastewater treatment

Sirui Chen*
University of Wisconsin, Madison, Wisconsin, USA

ABSTRACT: In this study, a bacteria strain with strong nitrogen removal capability was isolated from the sediment of the aquaculture pond. Based on morphological observation and 16S rRNA gene sequence analysis, the strain was identified as *Pseudomonas* sp. and named *Pseudomonas* sp. DC1. The nitrogen removal performances of strain DC1 were evaluated using shake flasks method. When the strain DC1 was inoculated into simulated wastewater with ammonia nitrogen as the sole nitrogen source, the ammonia nitrogen concentration was decreased from 603.6mg/L to 58.55 mg/L within 24 h, and the removal efficiency of ammonia nitrogen reached 90.3%. In the flask experiment with nitrate nitrogen as the sole nitrogen source, the removal efficiency of nitrate nitrogen reached 67.6% within 30 h. Using strain DC1 to treat California perch aquaculture wastewater, the ammonia nitrogen concentration was decreased from 78.06 mg/L to 32.94 mg/L within 5 d, and the removal efficiency of ammonia nitrogen reached 57.3%. The above results revealed that strain DC1 is a new strain with strong nitrogen removal capability and could tolerate a high concentration of ammonia nitrogen, representing a great potential to treat aquaculture water and urban sewage.

1 INTRODUCTION

China is a large aquaculture country, but the high-density and intensive modern aquaculture leads to the serious exceeding of ammonia nitrogen (NH_4^+-N), nitrite nitrogen (NO_2-N), and nitrate nitrogen (NO_3-N) in the water body, which causes serious eutrophication of the water body. With the enhancement of people's awareness of environmental protection and China's great attention to the construction of ecological civilization, how to purify aquaculture wastewater to meet the discharge standard is becoming the focus of management departments, society, and researchers.

At present, the main methods of treating nitrogen-containing wastewater include physical, chemical, and biological methods. Among them, microbial technology is the most efficient and green way to remove nitrogen-containing wastewater (Jiang 2013), and is becoming a hotspot of wastewater remediation. The traditional microbial denitrification technology is divided into two processes, aerobic nitrification, and anaerobic denitrification, which need to be carried out under aerobic and anaerobic conditions respectively, increasing the operation cost and construction area and limiting its popularization and application. In order to overcome the shortcomings of traditional microbial denitrification processes, people began to study new biological denitrification technologies. In the 1980s, Robertson et al. first reported a bacterial strain that can simultaneously do heterotrophic nitrification-aerobic denitrification (HN-AD) under aerobic conditions (Robertson 1984). This strain can simultaneously use NH_4^+-N, NO_2-N, and NO_3-N as nitrogen sources to carry out nitrification and denitrification under aerobic conditions. Therefore, screening bacteria with high nitrogen removal performance in different environments has become a research hotspot in recent years (Ji 2015). At present, the HN-AD bacteria isolated by researchers in different

*Corresponding Author: chenserena26@163.com

DOI 10.1201/9781003308553-72

environments mainly include *Pseudomonas* (Chen 2016; Song 2018; Sun 2016 & Tang 2021), *Acinetobacter* (Huang 2015; Zhang 2019), *Bacillus* (Zhao 2015), *Alcaligenes* (Shen 2017), and *Klebsiella* (Zhang 2018). For example, the removal rate of NO_3^--N in simulated wastewater culture medium by strains screened from the soil by Wang et al. under completely aerobic conditions can reach 97.67% (Wang 2011), and the NH_4^+-N removal rate of an HN-AD bacteria ZB612 isolated from landfill leachate by Zou et al. can reach 90% (Zou 2011).

Although there are many newly isolated HN-AD bacteria strains, and some of them have a denitrification capacity of more than 90%, there is a widespread problem of the long denitrification cycle. Since most of the strains are sensitive to harsh environments such as high load nitrogen-containing water, low temperature, and extreme pH values and the complex composition of wastewater itself, most researches are still at the stage of degrading simulated wastewater in the laboratory, and the research on using strains to treat real wastewater is rare. Guangdong is located in a coastal area with a very developed aquaculture industry. At present, aquaculture enterprises are actively promoting the transformation of tailwater discharge in response to the requirements of the government by establishing microbial remediation ponds. Therefore, this study isolated strains with high denitrification ability from the sediment of five different aquaculture ponds in Guangzhou. The nitrogen removal performance of the strains in simulated wastewater and real aquaculture wastewater was studied, in the hope of providing strain resources and remediation technology for treating aquaculture wastewater or municipal sewage.

2 METHODS

2.1 *Sample collection sites and methods*

The sediment samples were collected from Nanhai tilapia aquaculture ponds, Sanshui California perch aquaculture ponds, Zhongshan grass carp aquaculture ponds, secondary and tertiary ponds of Dongyong grouper aquaculture pond in Guangzhou, Guangdong Province. The sediment was sampled with a cylindrical mud extractor in accordance with the five-point sampling method. 50 g sediment was taken from each aquaculture pond according to the sampling point, collected in sterile sampling tubes respectively, and stored in a refrigerator at 4°C. When returned to the laboratory for separation, 5 tubes of sediment from each pond were mixed for further use.

2.2 *Screening methods of nitrogen-removing bacteria*

Sediment (10 g) was diluted with sterile normal saline into 10^{-1} diluent. 100-μL sample was coated on BTB medium, and then incubated in a constant temperature incubator at 28°C for 2d. Single colonies were selected and streaked 3-4 times for single staining microscopy to determine whether they were pure or not. The pure strains were inoculated in denitrification medium and nitrification medium respectively, and incubated at 28°C for 2 d. According to the size of the blue halo around the bacterial colony and the depth of red color after adding Gris reagent to the culture medium, the strains with denitrification ability and nitrification ability were preliminarily identified.

The formula of each medium used for screening is as follows: (1) BTB screening medium (Zhan 2017) (g/L): KH_2PO_4 1.5, Na_2HPO_4 7.9, $MgSO_4 \bullet 7H_2O$ 0.01, sodium citrate 5.66, $NaNO_3$ 0.8415, NH_4Cl 0.192, $NaNO_2$ 0.362, trace element solution 2 mL, BTB solution (i.e., bromomethyl phenol blue dissolved in ethanol at 1%) 1 mL, 2.0% AGAR, pH 7.2; (2) denitrification identification medium (g/L): on the basis of BTB medium, only $NaNO_3$ 1.3 was used as the nitrogen source; (3) nitrification identification medium (g/L): $(NH_4)_2SO_4$ 0.5, sodium citrate 5.0, K_2HPO_4 1.0, $MgSO_4 \bullet 7H_2O$ 0.3, NaCl 0.3, $FeSO_4 \bullet 7H_2O$ 0.03, $CaCO_3$ 7.5, pH 7.0-7.5; (4) NH_4^+-N simulated wastewater medium (g/L): K_2HPO_4 1.5, $MgSO_4 \bullet 7H_2O$ 0.01, Na_2HPO_4 7.9, sodium citrate 5.66, NH_4Cl 0.6036, trace element solution 2 mL; (5) NO_3^--N simulated wastewater medium (g/L): K_2HPO_4 1.5, $MgSO_4 \bullet 7H_2O$ 0.01, Na_2HPO_4 7.9, sodium citrate 5.66, $NaNO_3$ 0.9590, trace element solution 2 mL. Trace element solution (g/L): EDTA 50, $ZnSO_4$ 2.2, $CaCl_2 \bullet 2H_2O$ 5.5, $MnCl_2 \bullet 4H_2O$ 5.06, $FeSO_4 \bullet 7H_2O$ 5.0, $(NH_4)_6Mo_7O_2 \bullet 4H_2O$ 1.1, $CuSO_4 \bullet 5H_2O$ 1.57, $CoCl_2 \bullet 6H_2O$ 1.61, pH 6.0.

2.3 *Determination of nitrogen removal performance of the strain DC1 in simulated wastewater*

The strain DC1 with strong nitrogen removal ability were selected to determine the nitrogen removal performance in simulated wastewater. Specific methods: 24-hour slant cultures of strain DC1 were inoculated into 300-mL bottles filled with 60 mL nutrient broth, and cultured in a constant temperature incubator with 160 rpm/min at 30°C for 24 h. The seed solution was inoculated into 500-mL bottles containing 100-mL ammonia-rich simulated wastewater or nitrate-rich simulated wastewater with 1.0% inoculation amount, and incubated with 160 rpm/min at 30°C for 2 d. The content of NH_4^+-N in the culture medium of simulated wastewater and the OD600 value of wastewater were determined by taking 2-mL samples every 6 h. Three parallel experiments were set up and repeated three times. NH_4^+-N was determined by Nessler's Reagents spectrophotometry (GB HJ535-2009), NO_3-N was determined by ultraviolet spectrophotometry (GB HJ/T346-200). The NH_4-N content of NH_4^+-N simulated wastewater sample solution is measured at OD420 nm, the NO_3-N content of NO_3-N simulated wastewater sample solution is measured at OD220 and OD275 nm. The standard curve was drawn to calculate the removal rate of NH_4^+-N by strains at different times. The nitrogen removal rate was calculated according to the following formula:

$$\eta = \frac{C_0 - C_i}{C_0} \times 100\%$$

Where C_0 is the corresponding nitrogen content (mg/L) in fermentation broth 0 h after inoculation, C_i is the corresponding nitrogen content (mg/L) in fermentation broth after inoculation for i h.

2.4 *Nitrogen removal performance of strain DC1 in real aquaculture wastewater*

The contents of NH_4^+-N, NO_3-N, and NO_2-N in the real wastewater from five aquaculture ponds were measured. According to the nitrogen content in the wastewater, the wastewater with high nitrogen content was selected and sub-packed in 500-mL bottles, with 100-mL wastewater in each bottle. The experimental group with strain DC1 and the control group without strain were set up, and repeated experiments for 3 times. According to the content of NH_4^+-N in the wastewater, sodium citrate was added with a C/N of 15 as the carbon source. Samples were taken to measure the initial values of each indicator before the addition of the strain. 2-mL DC1 seed solution cultivated to logarithmic period was inoculated into the experimental group, which was then incubated in a constant temperature incubator with 160 rpm/min at 30°C for 5 d. Samples were taken regularly every 24 h to determine the content of NH_4^+-N in the wastewater.

2.5 *Morphological identification of the strain DC1*

The strain DC1 were inoculated into a nutrient agar medium and cultured at 28°C for 24 h to observe the morphology of the colony. Single colonies were selected for single staining, and the individual morphology of the strain was observed by scanning electron microscopy (SEM).

2.6 *16S rRNA gene sequence analysis and phylogenetic tree construction*

The 16S rDNA sequence of the strain was amplified with general primers. The forward primer (27F) is 5'-AGAGTTTGATCCTGGCTCAG-3' and the reverse primer (1492r) is 5'-GGCTACCTTGTTACGACTT-3'. The total volume of the PCR reaction system was 25 uL, which contains 1 μL of DNA template lysate, 12.5 μl of 2X Unique TM Taq Master Mix (With Dye), 9.5 μl of RNase Free Water, 1 μL of 27F, and 1 μL of 1492R. The PCR reaction procedure was as follows: 94°C for 5 min, 94°C pre denaturation for 30 sec, 53°C annealing for 30 sec, 72°C extension for 90 sec, 72°C for 10 min, 30 cycles, and cooling at 4°C. The amplified products were analyzed by agarose gel electrophoresis. The amplified products were sent to Shanghai Shenggong Bioengineering Co., Ltd. for sequencing. The sequences obtained were analyzed by Blast homology in the GenBank database of NCBI. The phylogenetic tree was constructed by MEGA7.0 software and the Neighbor-joining method.

3 RESULITS

3.1 *Screening results of nitrogen removal bacterial strains*

BTB medium was used to isolate strains of the sediment samples of the five aquaculture ponds in the South China Sea. According to whether the color of BTB medium changes from green to blue (Figure 1), 66 strains were preliminarily screened. The 66 strains were cultured in the denitrification medium and nitrification medium respectively for 2 d. Three strains numbered DC1, ZS16, and SS5 were screened, which had strong HN-AD ability. Among them, the strain numbered DC1 not only had strong nitrification and denitrification ability but also grew faster than ZS16 and SS5. Considering that the fast growth rate has more application advantages in wastewater treatment, strain DC1 was selected for nitrogen removal experiments of simulated wastewater and real wastewater in subsequent experiments.

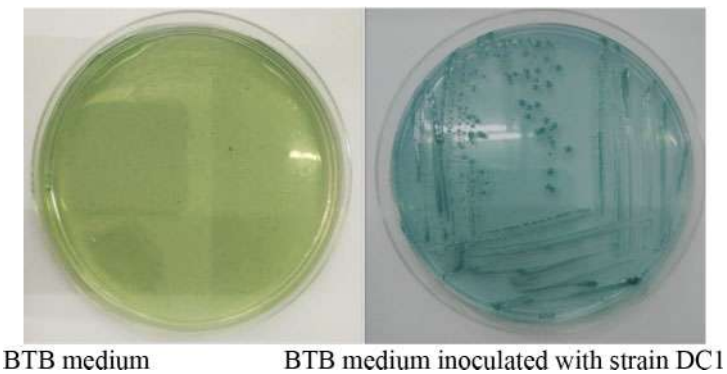

Figure 1. The denitrification ability of the strain DC1on the BTB plate.

3.2 *Nitrogen removal performance of strain DC1 in ammonia-rich simulated wastewater*

The simulated wastewater was prepared with high concentration of NH_4Cl (603.6 mg/L) as the only nitrogen source. The OD_{600} value and NH_4^+-N content of the wastewater culture medium were measured regularly every 6 h. The results are shown in Figure 2.

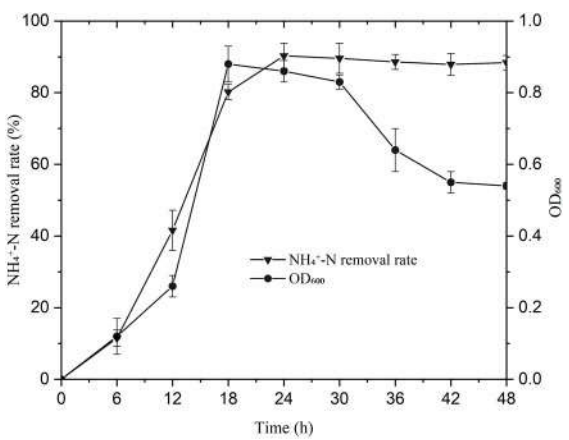

Figure 2. Growth curve and NH_4^+-N removal rate of strain DC1 in simulated wastewater.

The strain DC1 grew slowly during 0-6 h, and bacterial biomass reached the maximum at 18 h. The strain entered the stable stage after18 h. When the strain DC1 was inoculated into simulated wastewater with ammonia nitrogen as the sole nitrogen source, the ammonia nitrogen concentration was decreased from 603.6mg/L to 58.55 mg/L within 24 h, and the removal efficiency of ammonia nitrogen reached 90.3%. The curve of ammonia nitrogen removal rate was basically positively correlated with the growth curve of the strain, indicating that the strain used NH_4^+-N as a nitrogen source to make the bacteria grow and reproduce in large quantities, so as to remove NH_4^+-N from the wastewater. Zou et al. (Zou 2011) isolated an HN-AD bacteria ZB612 of *rhizobia* from landfill leachate. The ammonia nitrogen removal efficiency was 90% within 48 h and the initial NH_4^+-N concentration was only (98.23 ± 1.57) mg/L. The ammonia nitrogen removal rate of 8 nitrifying bacteria screened by Si et al. was between 65% and 80% in 72 h (Si 2011). The initial concentration of ammonia nitrogen in our simulated wastewater was 603.6 mg/L, and the ammonia nitrogen removal efficiency in 24 h was 90.3%, indicating that the strain DC1 has high nitrogen removal efficiency, short cycle, and can withstand a high concentration of ammonia nitrogen. It is not only suitable for the remediation and treatment of general aquaculture wastewater and domestic wastewater (NH_4^+-N content is 20–80 mg/L) but also can be used for the denitrification treatment of coking wastewater and fertilizer plant wastewater with high nitrogen concentrations.

3.3 *Nitrogen removal performance of strain DC1 in nitrate-rich simulated wastewater*

The simulated wastewater of nitrate nitrogen was prepared with high concentration of $NaNO_3$ as the only nitrogen source. The OD_{600} value and NO_3-N content of the wastewater culture medium were determined regularly every 6 h. The results are shown in Figure 3.

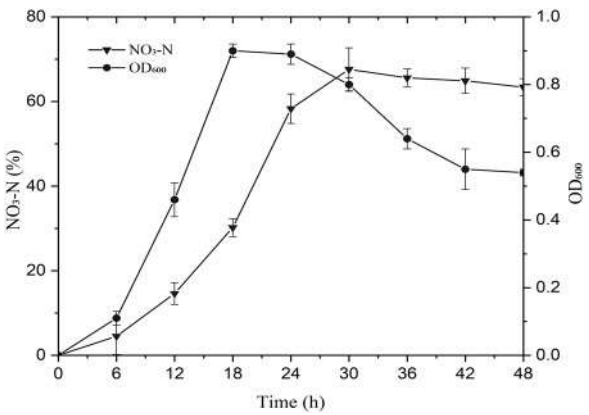

Figure 3. Growth curve and nitrate rate of strain DC1 in simulated wastewater.

The strain DC1 grew well in the nitrate-rich simulated wastewater, and its growth curve was similar to that in the simulated-rich simulated wastewater, but its NO_3-N removal curve was not completely consistent with the NH_4^+-N removal curve. The NO_3-N removal rate of DC1 increased rapidly during 18-24 h and reached the maximum of 67.6% at 30 h, with the content of NO_3-N decreasing from 959 to 310.7 mg/L. Compared with the NH_4^+-N removal rate, the NH_4^+-N removal effect of strain DC1 was significantly better than that of NO_3-N.

3.4 *Nitrogen removal performance of strain DC1 in real aquaculture wastewater of Sanshui California perch*

The nitrogen content of wastewater from five aquaculture ponds was measured in this study. The results are shown in Table 1 below.

Table 1. Pollution status of aquaculture wastewater

Sample Water	NH_4^+-N (mg/L)	NO_3-N (mg/L)	NO_2^-N (mg/L)
Zhongshan	26.30	3.02	2.64
Sanshui	78.06	1.94	9.32
Nanhai	16.88	0.81	2.92
Dongchong (Secondary pond)	35.12	3.54	12.46
Dongchong (Tertiary pond)	31.59	0.87	5.75

As can be seen from Table 1, the ammonia pollution of the real wastewater from five different aquaculture ponds is extremely serious, which far exceeds the national standard (total nitrogen $\leq$ 3 mg/L). Among them, the ammonia nitrogen content of aquaculture wastewater from Sanshui California perch pond is as high as 78.06 mg/L. The overall situation of nitrate nitrogen is slightly better. The accumulation of NO_2-N is an important cause of large-scale illness and massive deaths of fish. All five aquaculture ponds have exceeded the standard, especially the Dongchong tertiary pond using container farming technology is seriously polluted, which is not consistent with their claim of zero-emission. According to the status of ammonia nitrogen pollution in aquaculture wastewater in Table 1, we selected the aquaculture wastewater of Sanshui California perch as the treatment object. The real wastewater of the Sanshui California perch pond was treated using strain DC1. The OD_{600} and NH_4^+-N content of the wastewater were continuously measured every day within 5 days. The results are shown in Figure 4.

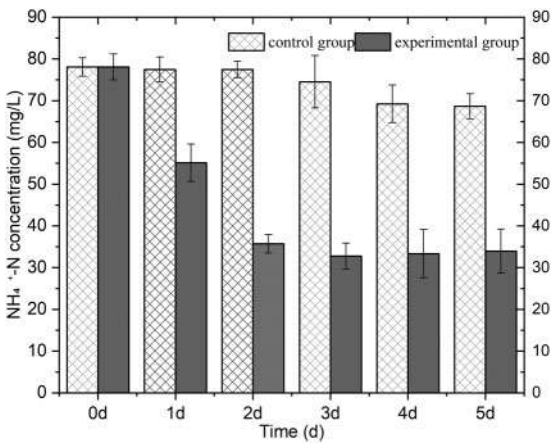

Figure 4. Ammonia nitrogen removal rate of strain DC1 in California perch aquaculture wastewater.

As can be seen from Figure 4, 2 days after inoculation of strain DC1, the NH_4^+-N content in the experimental group was significantly lower than that in the control group. After 3 days, the NH_4^+-N content in the experimental group decreased from the initial 78.06 to 35.70 mg/L, and the NH_4^+-N removal rate reached 55.6%. From day 4 to 5, the NH_4^+-N content in the experimental group was removed slowly. On the 5th day, the NH_4^+-N content decreased from 78.06 to 32.94 mg/L, and the NH_4^+-N removal rate reached 57.3%. Due to the complexity of the real wastewater components, many new isolated denitrifying strains have a good denitrification effect in simulated wastewater, but they do not grow at all in real wastewater, so they have no denitrification effect. At present, it has been reported that the NH_4^+-N removal rate of most screened strains in the treatment of real wastewater is usually less than 40% (Si 2010). The NH_4^+-N removal rate of strain DC1 in the

wastewater of Sanshui California perch pond is 57.3%, which is higher than the reported level. For example, Zheng screened a strain with strong denitrification ability that had only a 13.3% NH_4^+-N removal rate for soybean products processing wastewater (Zheng 2018); Zhang used the screened *Pseudomonas* to remove NH_4^+-N from closed industrial circulating aquaculture wastewater, with a removal rate of 30% (Zhang 2010). The NH_4^+-N removal rate of wastewater treated by strain DC1 was more than 50% in 2 days, and the period of NH_4^+-N removal was significantly shorter than that of similar literature. Since the denitrification efficiency of strain DC1 in the real aquaculture wastewater of California perch pond is far from the removal rate of simulated wastewater, we plan to explore the influencing factors of wastewater denitrification such as rotating speed, dissolved oxygen, bacterial dosage, and carbon source supplement to further improve the NH_4^+-N removal rate of the strain in real wastewater. At the same time, it is planned to combine strain DC1 with other strains screened in the same period to treat wastewater to improve denitrification efficiency. On the basis of the improved NH_4^+-N removal rate of wastewater, the denitrification test of glass tank wastewater will be carried out in the future.

3.5 *Morphological identification results of strain DC1*

The colony of strain DC1 inoculated in nutrient agar medium for 24 h is shown in Figure 6 (left). The colony is round with a diameter of 0.5–1.5 mm, most of which are central uplift, milky white, and opaque, with smooth and moist surfaces and neat edges. The SEM result of the strain are shown in Figure 5 (right). The shape of the DC1 strain is a long rod, blunt at both ends, with a single scattered arrangement, about 1.5 μm long and 0.43 μm wide.

Figure 5. Colony morphology and scanning electron micrograph of DC1.

3.6 *16S rRNA gene sequence analysis and phylogenetic tree construction of strain DC1*

The genomic DNA of DC1 was extracted and its 16S rDNA was amplified by PCR using general primers 27F and 1492R. The results of agarose gel electrophoresis of the amplified products are shown in Figure 6. It can be seen from the figure that a clear and bright band appeared at about 1500 bp. The sequencing results of amplified products showed that the 16S rDNA sequence length of strain DC1 was 1439 bp. The sequence was submitted to the GenBank database for Blast homology analysis with related species and a phylogenetic tree was drawn. The results are shown in Figure 7. The 16S rDNA sequence of strain DC1 was 99.72% homologous to *Pseudomonas Koreensis* with the accession number of NR025228.1. Therefore, DC1 was preliminarily determined as *Pseudomonas* and was named *Pseudomonas sp.* DC1.

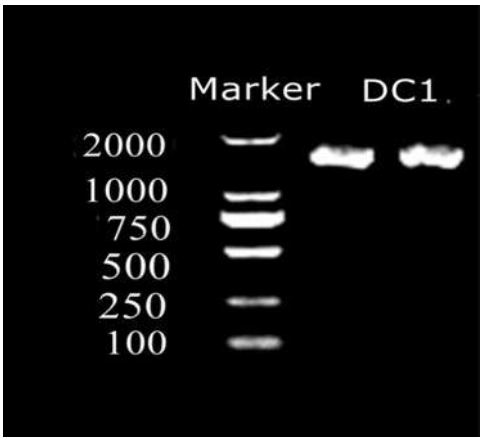

Figure 6. Amplification of strain DC1 of 16S rDNA by PCR.

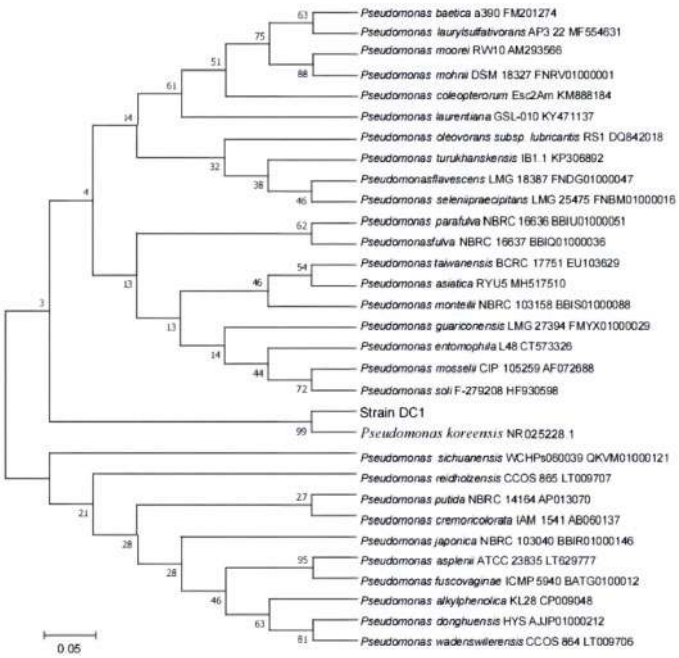

Figure 7. Phylogenetic tree of strain DC1 based on 16S rDNA sequence homology.

4 CONCLUSIONS

In this study, the HN-AD strain DC1 with high nitrogen removal ability was screened from the bottom sediment of the tertiary pond of Dongchong in Guangzhou. The strain was identified as *Pseudomonas* by morphology and named *Pseudomonas sp*. DC1. Strain DC1 has high nitrogen removal efficiency and short denitrification cycle, and can tolerate high NH_4^+-N concentration. When treating high concentration of ammonia-rich simulated wastewater and nitrate-rich simulated wastewater at 30°C and 160 rpm/min, the NH_4^+-N removal rate can reach 90.3% within 24 h, and the NO_3^--N removal rate can reach 67.6% within 30 h. The strain was applied to the real wastewater

denitrification and made a breakthrough. Within 5 days of treating the aquaculture wastewater of Sanshui California perch with high NH_4^+-N content, the NH_4^+-N in the wastewater decreased from 78.06 to 32.94 mg/L, and the ammonia-nitrogen removal rate reached 57.3%. The above results show that the strain DC1 has a good application prospect in the treating aquaculture wastewater.

ACKNOWLEDGEMENTS

This work was financially supported by Department of Biological Sciences, Guangzhou University and was under the guidance of Professor Hu Shu from Guangzhou University.

REFERENCES

Chen L., Bai J., Zhao Y.G., et al. 2016. Identification and denitrification characteristics of an aerobic denitrifier in estuary phragmites wetland. *Acta Microbiologica Sinica* 56(8):1314–1325.

Huang T.L., He X.X., Zhang H.H., Zhou S.L., et al. 2015. Nitrogen removal characteristics of the heterotrophic nitrifier cation-aerobic denitrification bacterium *Acinetobacter* sp. Sxf14. *Chin J Appl Environ Biol* 21 (2): 201–207.

Ji B., Yang K., Zhu L., et al. 2015. Aerobic denitrification: a review of important advances of the last 30 years. *Biotechnology and Bioprocess Engineering* (20): 643–651.

Jiang L., Xu C.B., Ma X.P., et al. 2013. Identification and denitrification characteristics of anaerobic denitirfier. *Environmental Science & Technology* 36 (3): 12–15.

Robertson L.A., Kuenen J.G. 1984. Aerobic denitrification: A controversy revived. *Archives of Microbiology* 139 (4): 351–354.

Shen H., Wan X.H., Jiang G., et al. 2017. Identification and nitrogen removal characteristics of two nitrifying-aerobic denitrifying bacteria strains newly isolated from marine sediments. *Chin J Appl Environ Biol* 23 (1): 0157–0163.

Si W.G., Lu Z.G., Xu C. 2011. Isolation of Heterotrophic Nitrifiers Which Can Tolerate High Concentration of Ammonia-nitrogen and the Optimization of Their Nitrogen Removal Efficiency in Wastewater. *Environmental Science* 32(11): 3448–3454.

Song M.l., Li C., Liu C.J., et al. 2018. Screening, identification, and immobilization of an Aerobic Denitrifier. *Jiangsu Agricultural Sciences* 46(13): 271–275.

Sun Q.H., Yu D.S., Zhang P.Y., et al. 2016. Isolation, Identification, and Nitrogen Removal Characteristics of a Heterotrophic Nitrification-Aerobic Denitrification Strain y3 Isolated from Marine Environment. *Environment Science* 37(3): 1089–1097.

Tang M.R., Li R.Y. 2021. Isolation of heterotrophic nitrification-aerobic denitrification bacteria strains and purification of river water by mixed cultures. J. *Acta Scientiae Circumstantiae* 41(7): 2657–2663.

Wang Y.L., Lei X.L., Chen L.J., et al. 2011. Screening aerobic denitrifiers from soil and study on characteristics of denitrification. *Chinese Journal of Environmental Engineering* 5(8): 1902–190.

Zhan H., Wang G.J., Chen C.X. 2017. Identification and Denitrification Ability of an Aerobic Denitrifier. *Journal of Tianjin Agricultural University* 24(2): 44–48.

Zhang M., Bi J.T. 2019. Preliminary Study on Effect of A Denitrifying Bacterium on Purifying and Remediation for Black and Odorous Water Bodies. *Environmental Engineering* 37(8): 32–36.

Zhang W.J. 2010. Study on Denitrification of Aquaculture Wastewater. Zhejiang: Ningbo University.

Zhang Y. 2018. Isolation and Preliminary Identification of Native Denitrification Bacteria from an Aquaculture Pond. *Journal of Hydro ecology* 39(5): 111–114.

Zhao J.H., Huang S.B. 2015. Isolation and characteristics of a thermophilic aerobic denitrifier. *Environmental Science & Technology* 38 (1): 6–10.

Zheng Y.Y., Xiao H.Y., Wang X.H. 2018. Screening and preliminary application of low-temperature denitrifying bacteria. Food Engineering (3): 29–32.

Zou Y.Y., Zhang Y., LI M.Z., et al. 2016. Isolation and identification of a heterotrophic nitrification-aerobic denitrification bacterium and its denitrification ability. *China Environmental Science* 36(3): 887∼893.

Advances in Applied Chemistry and Industrial Catalysis – Saikia (Ed.)

Pilot scale experimental study on fluoride removal by chemical precipitation combined with high efficiency solid-liquid separator

Xin Song*, Gang Zhang** & Fuwei Zhou***
University of Jinan, Jinan, China

ABSTRACT: With the rapid economic development and frequent industrial production, more and more wastewater is generated from industrial production, and the problem of fluorine-containing wastewater has become more and more serious. Therefore, it is particularly important to be able to effectively treat fluorine wastewater and optimize the existing fluorine removal technology at this stage. The pilot study aimed at the high-efficiency and low-cost de-fluoridation treatment of industrial fluorine-containing water, and used a high-efficiency solid-liquid separator to optimize the chemical precipitation method with a chemical plant in Shandong Province's refrigerant production alkali washing wastewater as the object of treatment. A pilot study on fluoride removal was carried out. The test results show that the best operating condition of the process is when the pH is 6, the water flow rate is 100 L/h, the stirring speed is 200r/min, and the calcium chloride dosage is Ca^{2+}: F^- reaches 10:1. The residual fluoride ion concentration in the effluent is 0.66 mg/L, which can effectively remove the fluoride ion concentration in the fluorine-containing wastewater and ensure the long-term stable operation of the equipment.

1 INTRODUCTION

With the rapid economic development and frequent industrial production, more and more wastewater is produced in industrial production. A large number of fluorine-containing wastewater discharge problems occur in the chemical fields such as metal smelting, electroplating, aluminum electrolysis, ceramics, pharmaceutical semiconductors, etc. a large number of fluorine-containing industrial wastewater will be discharged in many of the above production processes, and the content of fluorine ion can reach more than 150 mg/L, Even in some industrial fields, fluoride ions in wastewater can reach more than thousands of mg/L. Therefore, it is particularly important to effectively treat Fluorine Wastewater and optimize the existing fluorine removal technology at this stage.

In China, according to the first level standard of integrated wastewater discharge standard (GB8978-1996), the fluorine ion concentration should be less than 10 mg/L. however, many enterprises can only use high treatment cost to meet the fluorine ion standard in the absence of efficient and low-cost fluorine removal technology, which is not conducive to plant operation, but also inconsistent with our concept of resource-saving and sustainable development. Therefore, using chemical precipitation method to remove fluorine ions and high-efficiency solid-liquid separator to achieve high-efficiency fluorine removal has become the goal of this pilot test.

Calcium chloride is a calcium containing compound with good treatment effect for fluoride removal by chemical precipitation. Under stirring conditions, calcium chloride and fluoride ions will form CaF_2 precipitation, which is a fluoride with relatively high solubility product constant. When the temperature is 18°C, the solubility of calcium fluoride in water is 16.3 mg/l, that is, the concentration of fluoride ion is 7.9 mg/L, calcium fluoride above this concentration will form sediment (Aoudj 2012, Reardon 2000, Jadhav 2014, Parthasarathy 1996, Toyoa 2000). At the

Corresponding Authors: *940647941@qq.com, **cea_zhangg@ujn.edu.cn and ***780879648@qq.com

DOI 10.1201/9781003308553-73

same time, the same ion effect will appear between fluorine ions and chloride ions. When soluble calcium salts such as calcium chloride and calcium nitrate are dissolved in the wastewater, the ionization balance of calcium fluoride will move towards the direction of calcium fluoride molecular precipitation due to the increase of calcium ion concentration in the wastewater, resulting in the same ion effect and reducing the solubility of calcium fluoride (Halogens 2019). This is conducive to the precipitation and removal of fluorine ions. No matter what pH, the fluorine ion concentration will decrease with the increase of calcium ion concentration in water (Mooney 2010; Tripathy 2006). Under the laboratory test conditions, the hardness removal rate can be increased to 95%∼98% within 12-15 minutes, which can better meet the requirements of fluorine removal in fluorine-containing industrial wastewater (Bhatnaga 2011; Cai 2018).

In this study, the alkali washing wastewater from refrigerant production in a refrigerant factory in North China was treated. In the pilot test, considering that the industrial wastewater has complex components and contains a large amount of CO_3^{2-}, the solubility of both calcium salts is lower than that of calcium fluoride. From the analysis of solubility product constant, it can also be concluded that calcium fluoride cannot be precipitated directly, Therefore, before the pilot test, hydrochloric acid is added to blow off the pretreatment to remove CO_3^{2-}, and the water treatment volume of the pilot test is 100L/h. on the basis of the small-scale test in the laboratory, considering that calcium chloride is generated as waste in the production process of the plant, the pilot test study of calcium chloride de-fluorination is carried out with a high-efficiency solid-liquid separator, The operation effect of high-efficiency solid-liquid separation equipment applied to scale removal of fluorine-containing wastewater under pilot test conditions and the influence law of process parameters such as rising flow rate and stirring speed on the operation effect are verified, which provides an important basis for the design and operation of subsequent production test devices.

2 MATERIALS AND METHODS

2.1 *Influent quality*

The influent for the pilot test of fluorine removal by chemical precipitation method is taken from the alkali washing water of the refrigerant production system of a refrigerant production plant in North China. The average fluorine ion concentration of the influent is 4000 mg/L.

2.2 *Test materials and devices*

The high-efficiency solid-liquid separation equipment consists of water inlet and outlet pipes, dosing pipes, mud discharge pipes, stirring paddles and triangular weirs. The effective volume is 50L. The reactor is equipped with partitions, and the G value is strictly controlled according to the small-scale experimental data. The high-efficiency solid-liquid separator is shown in Figure 1.

2.3 *Detection and analysis method*

In the test, the hardness was measured by the ion selective electrode method (GB7477-89); the pH value of the solution was measured by a pH meter (METTLER TOLEDO, Germany); the ion concentration was measured by the fluoride ion selective electrode (Shanghai, Hach, PF-2-01) and the reference electrode (Shanghai, Hach, 232-01) to cooperate with the acidity meter (Ray magnetic, PHS-3C) for determination; all chemicals are of analytical grade.

3 RESULTS AND DISCUSSION

3.1 *Results and discussion*

In the test, the rising flow rate was adjusted by changing the inlet water flow. Under the conditions of controlling the stirring speed to 200 r/min, the PAM dosage of 10 mg/L, and the calcium to fluoride ratio of 20:1, the residence time of F^- was 50 L/h, 100 L/h, 150′ L/h, 200 L/h, and 250 L/h

chemical precipitation method for fluoride removal pilot test. After 1 hour of stable operation, samples were taken to determine the fluoride ion concentration in the inlet and outlet water, and the effect of the rising flow rate on the fluoride ion concentration in the outlet water was explored. Influence, the test result is shown in Figure 2.

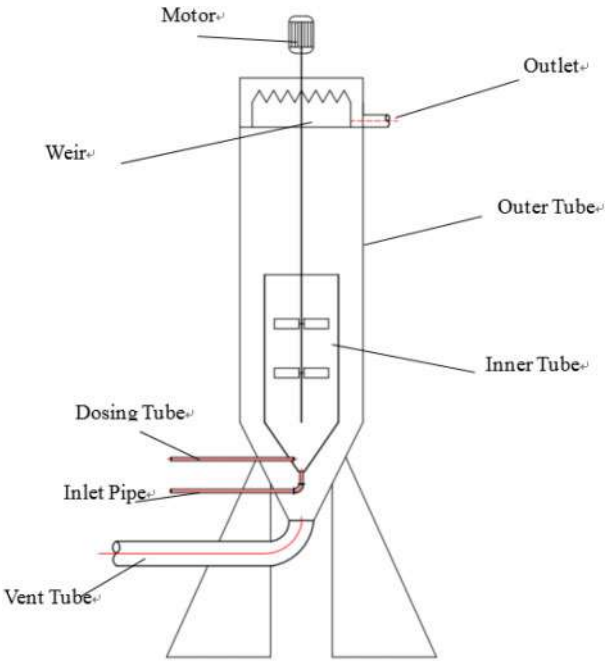

Figure 1. High-efficiency solid-liquid separator.

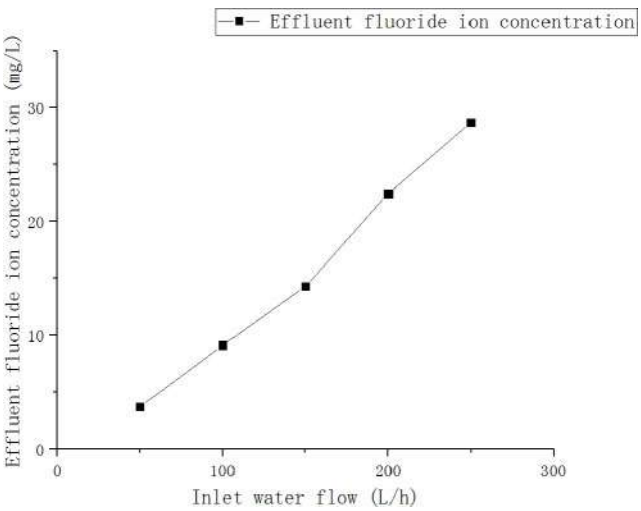

Figure 2. Influence of rising flow rate on the effect of fluoride removal.

It can be seen from Figure 2 that under the same other conditions, the rising flow rate has the following influence on the fluoride ion concentration in the effluent: With the increase of the

inlet water flow rate, the rising flow rate gradually increases, and the reaction time of Ca^{2+} and F^- gradually increases. Insufficient, resulting in the incomplete reaction of the two, the residual fluoride ion concentration in the effluent will also increase.

3.2 *The influence of stirring speed on the effect of fluoride removal*

In the process of this pilot test, an important factor that affects the fluoride removal effect is the stirring speed of the stirring blade in the reactor. In order to study the influence of the stirring speed on the fluoride removal effect of the high-efficiency solid-liquid separator, the inlet water flow rate is controlled to 100 L/h, the dosage of PAM is 10 mg/L, the ratio of calcium to fluoride is 20:1, and the chemical precipitation de-fluoridation experiment with the stirring speed increased from 120 r/min to 440 r/min was carried out. After 1 hour of stable operation, the fluorine in the inlet and outlet water was measured. The ion concentration, the test result is shown in Figure 3.

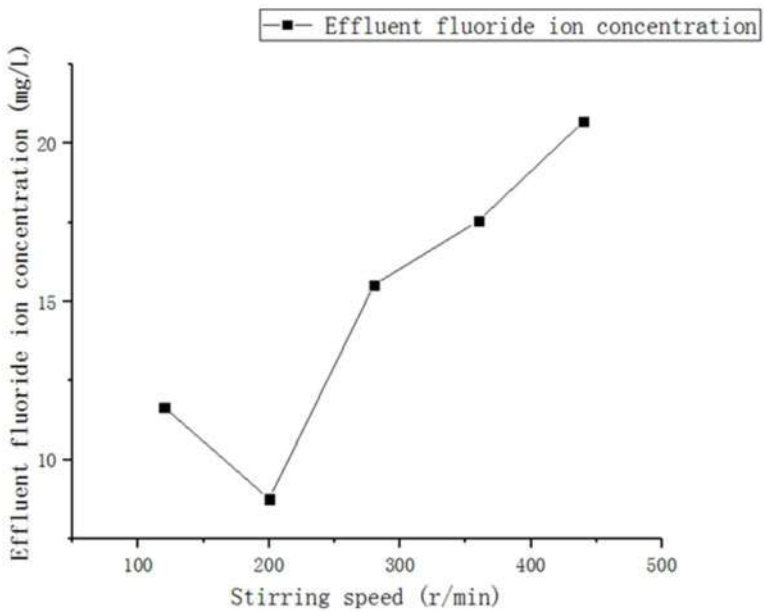

Figure 3. Influence of stirring speed on the effect of fluoride removal.

Figure 3 reflects the influence of the stirring speed on the residual fluoride ion in the effluent in the actual fluorine-containing wastewater treatment project using calcium chloride chemical precipitation technology. It can be seen that higher or lower stirring speed is unfavorable for the removal of fluoride ions. When the stirring speed is about 200r/min, the fluoride ion removal effect is better. When the stirring speed is less than 200r/min, the mixing of Ca^{2+} and F^- is not complete enough, so the expected treatment effect is not achieved; when the stirring speed is greater than 200r/min, the mixing of Ca^{2+} and F^- is more complete than before However, at this time, the water flow in the reactor moves violently, and the hydraulic shear force is too large, which increases the sludge settlement load, and fails to achieve a good solid-liquid separation effect, and therefore affects the removal effect of fluoride ions.

3.3 *The effect of calcium chloride dosage on the effect of fluoride removal*

In the high-efficiency solid-liquid separator coupled with chemical precipitation method to remove fluoride in the pilot test process, Ca^{2+}: F^- also has a very important effect on the fluoride removal

effect. The higher the dosage of calcium ions, the higher the removal rate of fluoride ions. In order to achieve the fluoride ion concentration at a lower cost, control the inlet water flow to 100 L/h, the PAM dosage 10 mg/L, and the stirring speed at 200L/min to determine the effect of the $CaCl_2$ dosage on the fluoride ion removal rate Influence, the test result is shown in Figure 4.

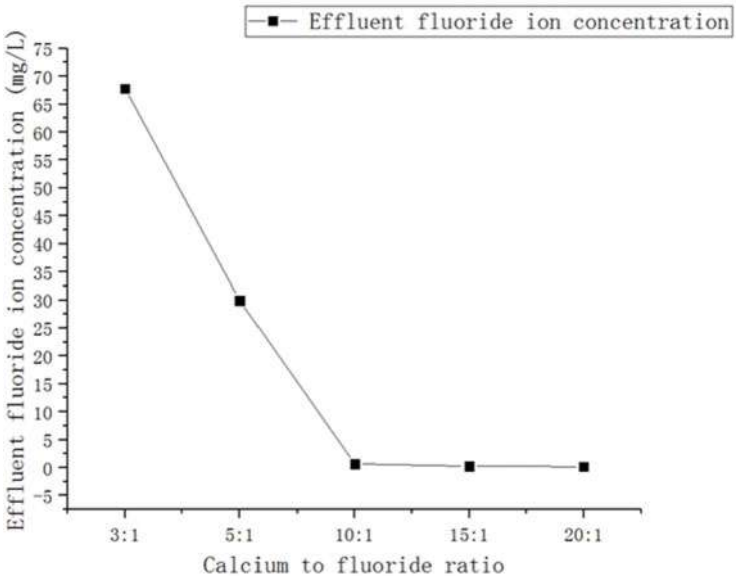

Figure 4. Influence of calcium chloride dosage on the removal effect of fluoride ion.

Figure 4 shows the influence of calcium chloride dosage on the removal effect of fluoride ions. It can be seen from the figure that when Ca^{2+}: F^- is less than 10:1, as the dosage of calcium chloride increases, the fluoride ion concentration in the effluent is gradually Decrease, and when Ca^{2+}: F^- reaches 10:1, the fluoride ion concentration is already below 1mg/L.

4 CONCLUSION

Based on the results and discussions presented above, the conclusions are obtained as below:

(1) When the stirring speed is 200r/min-440r/min, as the stirring speed increases, the residual fluoride ion concentration in the effluent decreases and becomes slower. When the stirring speed is lower than 200r/min, the residual fluoride ion concentration in the effluent drops the speed becomes faster as the stirring speed increases, and the stirring speed that can achieve a better effect of removing fluoride ions should be around 200r/min.
(2) The residual fluoride ion concentration in the effluent decreases linearly with the increase of the rising flow rate, but the linear decrease of the residual fluoride ion concentration in the effluent is approximately the same at different rising flow rates.
(3) The increase in the dosage of calcium chloride does enhance the removal effect of fluoride ions, but this enhancement effect is no longer significant after Ca^{2+}: F^- reaches 10:1. This is also due to the fact that fluoride ions have already been removed at this stage. Reaching a very low content, it is difficult for the chemical precipitation method to have a significant treatment effect on it.
(4) Considering the rising flow rate, the stirring speed and the calcium chloride dosage, the optimal operating conditions under the pilot test conditions are determined to be the inlet water flow

rate of 100L/h, the stirring speed of 200r/min, and the calcium chloride dosage of When Ca^{2+}: F^{-} reaches 10:1, the residual fluoride ion concentration in the effluent is 0.66mg/L, which can effectively remove the fluoride ion concentration in the fluorine-containing wastewater and ensure the long-term stable operation of the equipment.

REFERENCES

Aoudj S., Drouiche N. Hecini M. (2012). Coagulation as a Post-Treatment Method for the De-fluoridation of Photovoltaic Cell Manufacturing Wastewater. J. Procedia Engineering. 33(1), 111–120.

Bhatnaga R.A., Kuma R.E., Sillanp M. (2011). Fluoride removal from water by adsorption-a review. J. Chemical Engineering Journal, 171 (3), 811–840.

Cai J.G., Zhao X., Zhang Y.Y. (2018). Enhanced fluoride removal by La -doped Li /Al layered double hydroxides. J. Journal of Colloid and Interface Science, 509, 353–359.

Halogens, Fluorine (2019). Findings from Central South University in the Area of Fluorine Described (Separation and recovery of NaF from fluorine containing solution by the common ion effect of Na). J. Chemicals & Chemistry.

Jadhav S.V., Gadipelly C.R., Marathe K.V. (2014). Treatment of fluoride concentrates from membrane unit using salt solutions. J. Journal of Water Process Engineering, 2(31–36).

Mooney G.A., Nogueria A.T., Cope D.C. (2010). Two-stage lime treatment in practice. Proper operation of a twostage treatment system can meet EPA guidelines for fluoride and phosphorous. J. Environmental Progress and Sustainable Energy, 1(4), 274–280.

Parthasarathy N., Buffle J. (1996). Combined use of calcium sails and polymeric aluminium hydroxide for de-fluoridation of wastewater. J. Water Research, 29(4), 443–448.

Reardon E.J., Wang Y. (2000). A Limestone Reactor for Fluoride Removal from Wastewaters. J. Environmental Science & Technology, 34(15), 3247–3253.

Toyoa A., Trata T. (2000). New method for treating fluorine waste water to reduce sludge and running costs. J. IEEE transaction on semiconductor manufacturing, 13(3), 305–309.

Tripathy S.S., Bersillon J.L., Gopal K. (2006). Removal of fluoride from drinking water by adsorption onto alum-impregnated activated alumina. J. Separation and Purification Technology, 50(3), 310–317.

Advances in Applied Chemistry and Industrial Catalysis – Saikia (Ed.)

Inter-monthly change and climatic zoning of sea surface temperature in the South China Sea and the adjacent Northwest Pacific Ocean

Mengjuan Zhang, Jiancheng Kang*, Yutong Hua, Xiangchun Meng & Li Zhou
School of Environmental and Geographical Sciences, Shanghai Normal University, Shanghai, China

Zhiwei Chen
School of Business, Shanghai Normal University TianHua College, Shanghai, China

ABSTRACT: Using the Global Ocean Assimilation Database (SODA2.2.4) to extract the monthly sea surface temperature (SST) and ocean current (OC) data during the climatic reference period (CRP) from 1981 to 2010, and to analyze the multi-year average monthly and monthly difference characteristics of the South China Sea (SCS) and the adjacent Northwest Pacific Ocean (NPO), then to study the regional climate zoning (area), the results show that: (1) The monthly average highest temperature in the study area occurs in the eastern part of the NPO near the equator (29.9°C); the lowest temperature occurs in the north coastal area of the SCS (22.5°C). The temperature difference is the smallest in the NPO and the largest on the north coast of the SCS. (2) The temperature difference in the study area increases from low latitude to high latitude; and the higher the latitude, the more obvious the change in temperature difference; it also shows the characteristics of increasing from east to west. (3) at the sea area near 18.75°N south of the Tropic of Cancer, the inter-monthly and monthly change of the SST shows the characteristics of temperate climate, which may be suggested that the boundary between the tropical and temperate (subtropical) zones in the study area is lower than the land latitude, 17.75°N maybe roughly regarded as the climate boundary between the tropical and temperate (subtropical) zones in this sea area.

1 INTRODUCTION

Today, Climate Change has been a major challenge faced by the sustainable development of human society (Zeng et al. 2008). To adapt to the research on accelerating climate change, the World Meteorological Organization (WMO) proposed in 2015 that the 30 years from 1981 to 2010 be used as the new CRP for climate change research.

The ocean is an important part of the earth's climate system. The influence of the ocean on the climate is mainly realized through the change of the ocean's thermal state (Wu et al. 2011). The SST is an important indicator that characterizes the thermal and dynamic conditions of the ocean surface, and an important parameter for studying the hydrological climate environment. The anomalies in the SST can affect atmospheric circulation and climate change (Qiu et al. 2011; Zhou & Wang 2015). The SCS and the NPO are one of the main areas that affect climate change in China and Southeast Asia.

This paper uses the SST and OC data in the CRP from 1981 to 2010 to comprehensively analyze the distribution characteristics, monthly and monthly difference changes of the SST in the SCS and the adjacent NPO, to delineate the Climate Zones, and select feature points in the study area for focusing research, providing the basis for further revealing the process of climate change, temporal and spatial differentiation and influence mechanism.

*Corresponding Author: kangjc@shnu.edu.cn

DOI 10.1201/9781003308553-74

2 STUDY AREA AND DATA SOURCE

See Figure 1(a), the scope of the study area: 0.25°N–25.25°N, 105.25°–140.25°E, including most of the SCS, the northwestern part of the NPO, the Sulu Sea, and the Celebes Sea.

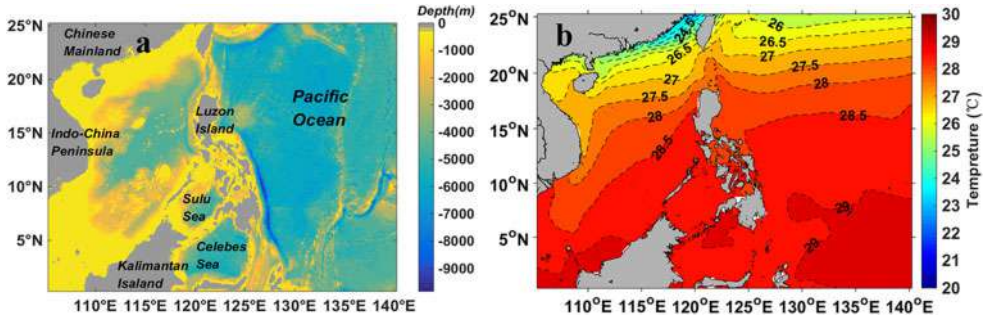

Figure 1. (a) Topographic map of the SCS and the adjacent NPO; (b) The average SST distribution at the SCS and the adjacent NPO for 30 years from 1981 to 2010.

The study area belongs to a part of the Tropical Western Pacific Warm Pool (WPWP) (Cravatte et al. 2009). The abnormal change in the heat content of the WPWP will cause a change in the atmospheric circulation and ocean circulation in the entire Pacific, and then affect global climate change (Hu et al. 2015; Lu et al. 2014; Yang et al. 2017).

The SCS is the largest and deepest marginal sea in China. It is connected to adjacent sea areas through multiple channels. The changes in the ocean heat content of the upper layer of the SCS have an extremely important impact on the atmospheric circulation, especially the East Asian monsoon and climate anomalies in the south of China (Zhu et al. 2003).

For this research, the topographic data selected comes from the Global Seabed Topographic Depth Database (1-Minute Gridded Global Relief Data, ETOPO1), which was released by the National Geophysical Data Center (NGDC) (Amante & Eakins 2009). The data of the SST and flow field come from the Simple Ocean Data Assimilation (SODA) jointly developed by the University of Maryland (UMD) and Texas A&M University (TAMU), referred to as SODA_2.2.4. The SODA_2.2.4 data set is a data set with an assimilation time from 1871 to 2010, the latitude and longitude coverage range is 75.25°S–89.25°N, 0.25°E–359.75°E, and the horizontal grid accuracy is 0.5°*0.5°, the time resolution is monthly average (Carton & Giese 2008).

3 THE SST CHARACTERISTICS

3.1 *The SST distribution characteristics in the CRP (1981–2010)*

From the average SST of 30 years from 1981 to 2010, see Figure 1(b), in the study area, the temperature range is about between 22°C–29°C, and the temperature difference is 7°C. The lowest sea temperature appears near the northeast coast of the SCS, where the isotherms are densest and the SST changes the most in the study area. There are three areas with the highest temperature in the study area, where are in the southwestern waters of Kalimantan Island, the southwestern side of the Philippine Islands, and the southeastern Pacific Equatorial waters.

According to the temperature field distribution displayed by isotherms in Figure 1(b), the SST decreases from low latitudes to high latitudes in the study area. In the SCS, the isotherm presents a trend of the southwest to northeast distribution, which can be divided into three regions: from 15°N to the north coast of SCS, the isotherm is distributed in parallel with the coastal zone and coastal current direction; being perpendicular to the coastline, the isotherms are denser and the

temperature difference is larger. Near the coast of the Indo-China Peninsula to the south of 15°N, the isotherm is parallel to the coastline, almost perpendicular to the latitude. In the south of 15°N at the middle of the SCS, the temperature is higher, the isotherms are sparse and the temperature difference is small. The main factors affecting the distribution of temperature fields in the SCS are solar radiation, sea-land distribution, and ocean current. Due to the Kuroshio, the temperature in Bashi Channel is significantly higher than in areas in the same latitude. In the NPO, at the north of 12°N, the isotherms are distributed along the latitudinal direction, and the temperature difference is obvious with the change of latitude. In the south of 12°N and the Celebes Sea, influenced by the North Equatorial Warm Current and equatorial countercurrent, where the temperature difference is small. The isotherm distribution characteristics east of Taiwan Island and the Philippine Islands are different, the isotherm to the north of Luzon Island is prominent towards high latitude, indicating that the temperature of the isotherm to the south of Luzon Island is higher than that of the SCS and the NPO; while the isotherm to the south of Luzon Island is opposite, and there is even a relatively low-temperature area.

To discuss the seasonal variation of the SST in the study area, the SST of July, when the highest average SST has for 30 years, subtracts the SST of February with the lowest average SST, and the annual variation amplitude (AVA) of the SST at each grid point has been obtained, as shown in Figure 2(a). The spatial distribution characteristics of the AVA of the SST can be seen in Figure 2(a): in the study area, the range of the AVA of the SST is between 0.19°C and 8.6°C. It shows an increasing trend from southeast to northwest; the most significant variation is in the northern part of the SCS, that is, the coastal area of Guangdong of China to northern Vietnam; the smallest of the AVA of the SST is near the equator. In the SCS, the AVA of the SST in the northern part of 12°N is more than 3°C. The AVA of the SST along the Coast of the Indo-China Peninsula is larger than that in the sea area at the same latitude, and the smallest of the AVA of the SST occurs in the waters near the Kalimantan Island at about 110°E. In the Bashi Channel, the AVA of the SST is between 2.6°C and 3°C, which is significantly smaller than that in the SCS and NPO at the same latitude. In the NPO, the AVA of the SST is between 0.4°C and 3.4°C, which is smaller than that in the SCS. The AVA of the SST in the north of 12°N increases with the increase of latitude, and there are four peak areas of annual variation in the NPO between 20°N and 25°N. The AVA of the SST is small at the south of 12°N and less than 1°C near the equator.

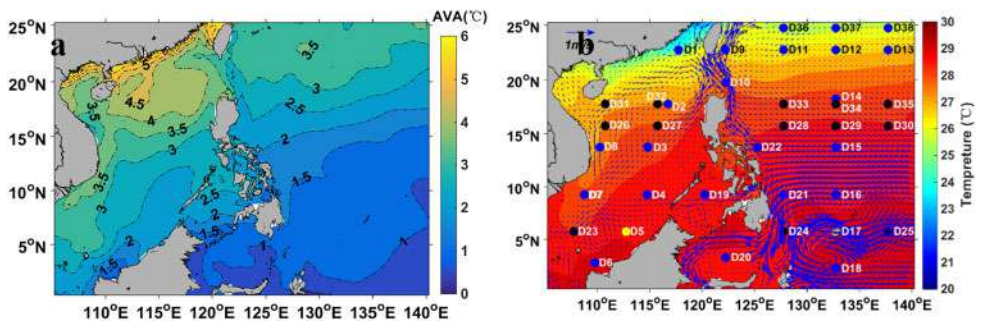

Figure 2. (a) Annual variation amplitude (AVA) of the SST at the SCS and adjacent NPO for 30 years from 1981 to 2010; (b) The SST, flow field diagram, and the feature points in the study area. (The blue arrow in the figure represents the flow field, the arrow points to the direction of flow velocity, and the arrow length is the size of flow velocity.)

3.2 *Monthly changing process and differences of the SST at Feature Points*

3.2.1 *Selection of feature points in the study area*

To better explore the inter-monthly and monthly differences in the different climate zones in the study area, 38 characteristic points have been selected as shown in Figure 2(b) and Table 1.

Table 1. Coordinates 38 characteristic points and the reasons for their selections.

Feature points	(Coordinate)	Reasons for choosing points
D1	22.75°N,117.75°E	These points are uniformly distributed in the SCS, synthetically observed the SST changing trend with longitude and latitudinal variation. In particular, D1 is located in the central margin of the maximum positive value of temperature variation, which can observe the changes caused by the difference in the thermal properties of the sea and land in the coastal area of South China
D2	17.75°N,116.75°E	
D3	13.75°N,115.75°E	
D4	9.25°N,114.75°E	
D5	5.75°N,112.75°E	
D6	2.75°N,109.75°E	
D7	9.25°N,108.75°E	These points are located near the Indo-China Peninsula, its SST is significantly lower than that of the SCS at the same latitude, further observing regional changes.
D8	13.75°N,110.25°E	
D9	22.75°N,122.25°E	These points are located on the eastern side of Luzon Strait, near the entrance of the Kuroshio, the characteristics of the SST influenced by the Kuroshio were observed.
D10	19.75°N,121.75°E	
D11	22.75°N,127.75°E	These points are located at the same latitude and different longitudes in the northern part of the NPO, the changes in the SST a long longitude were observed.
D12	22.75°N,132.75°E	
D13	22.75°N,137.75°E	
D14	18.25°N,132.75°E	These points are located at the same longitude and different latitudes in the NPO. The changes in the SST are observed in different latitudes with the same longitude.
D15	13.75°N,132.75°E	
D16	9.25°N,132.75°E	
D17	5.75°N,132.75°E	
D18	2.25°N,132.75°E	
D19	9.25°N,120.25°E	These points are located in enclosed water bodies (Sulu Sea) and semi-enclosed water bodies (Celebes Sea).
D20	3.25°N,122.25°E	
D21	9.25°N,127.75°E	These points are located in the north and south branches of the North Equatorial Warm Current, to observe the variation caused by different trends
D22	13.75°N,125.75°E	
D23–D38		These points use to discuss climatic zone boundaries, see Figure 5.

3.2.2 *Monthly changing process of SST at the feature points*

The monthly distribution curves of the SST at the feature points are drawn in a group according to different sea areas, for conveniently compared and discussion, as shown in Figures 3 and 4.

The monthly temperature change curves of the eight points (D1-D8) located in the SCS can be roughly divided into three different distribution states:

The change curves of D6, D5, D4, and D3 are the same; their highest temperature occurs in May and June, the lowest temperature occurs in February, and there is the second low temperature occurred in August; showing typical tropical climate characteristics. (2) D7 and D8 locate near the Indo-China Peninsula, they have larger monthly difference changes compared with D4 and D3 at the same latitude, as affected by the difference in thermal properties between land and sea, and ocean currents. (3) D1 and D2 present a mode of increasing first and then decreasing, with a unimodal waveform in a year. Especially, the D1, its lowest temperature is in February, and the highest temperature occurs in August, showing the characteristics of a temperate climate.

The inter-monthly and monthly variations of the feature points in the SCS show latitudinal zonality, and the variation amplitude is small at the low latitude and large at the high latitude. Although the latitude of the Indo-China Peninsula is not high, it is similar to where that of the north coast of the SCS due to the influence of land and ocean currents. The sea area close to the equator

is affected by the movement of the direct point of the sun (experiencing twice direct irradiation), resulting in sub-high and sub-low temperature, which has not appeared near the north coast of the SCS.

Compared to the inter-monthly and monthly change characteristics of the average SST in the SCS, it may indicate that there may be a boundary between temperate (subtropical) and tropical zones near D2.

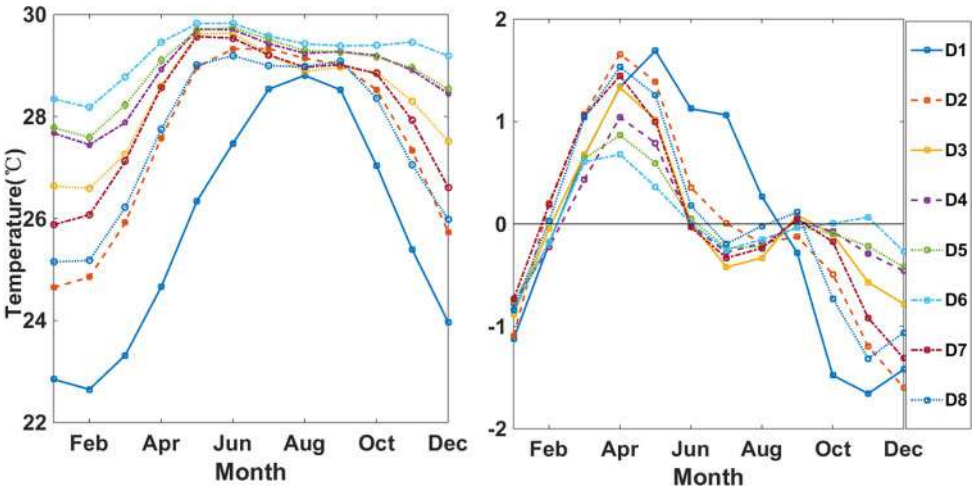

Figure 3. Monthly change curves and inter-monthly change curves of 8 feature points in the SCS (The left is monthly change, the right is inter-monthly change curves (monthly difference change)).

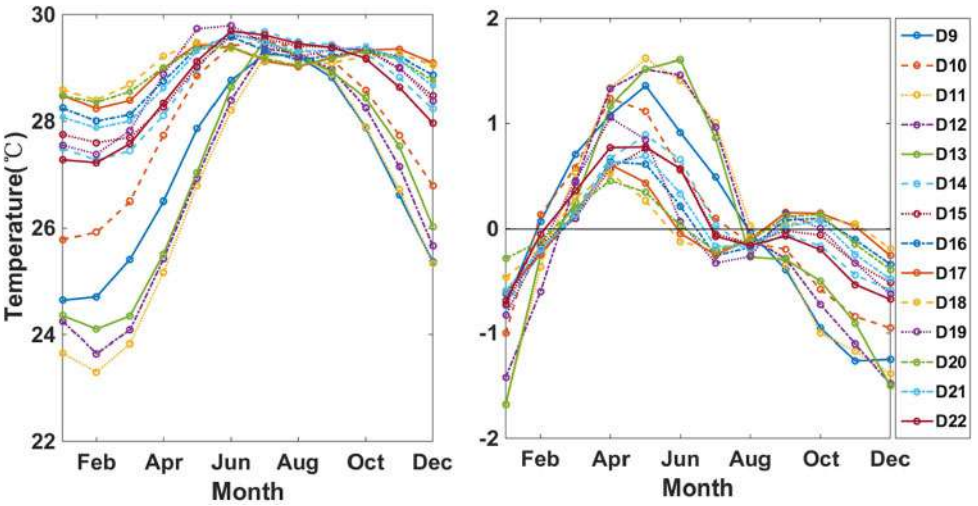

Figure 4. Monthly change curves and monthly difference change curves of 14 feature points in the NPO. (The left is monthly change, the right is monthly difference change curves (monthly difference change).)

The monthly change curve of D9-D22 can be roughly divided into two categories: (1) Among the five points D9-D13, D10 has the highest annual temperature and the smallest monthly change, followed by D9. The temperature on D9 and D10 is higher than the sea area at the same latitude because it is located near the Bashi Strait having been affected by the Kuroshio warm current.

The temperature difference at the other three points (D11, D12, D13) shows an increasing trend from east to west. (2) D19 is located in the Sulu Sea, where the annual temperature difference of 2.41°C is greater than that of the characteristic point in the adjacent sea area at the same latitude (the temperature difference of D4 in the SCS is 2.26°C, and the temperature difference of D21 in the NPO is 1.76°C); but D20, located in the Celebes Sea, its temperature change is 1.02°C, it is the smallest in the study area, mainly because of the intrusion of the North Equatorial Warm Current and the blocking of the islands, which caused the warm water flow to stay in the Celebes Sea resulting in a small temperature change. In addition, the annual temperature difference at each point increases from low latitude to high latitude and from east to west. D11, D12, and D13, which are located at the same latitude as D1 in the SCS, have the same characteristics with a unimodal waveform in a year. It maybe suggests, that near the latitude of D1 in SCS and D11, D12, D13 in the NPO, there is a boundary between temperate (subtropical) and tropical zones.

From the monthly difference change curves (monthly difference curves) of D9-D22, it can get: (1) For all points of D9-D22, the maximum negative value of the monthly difference appears in November, December, and next January, which shows, that at these three months, the temperature drop is the largest; the maximum positive value of the monthly difference occurs in April, May, and June, shows, that the maximum temperature increase in these three months; (2) At the two points of D17 and D18, their minimum negative value of the monthly difference appears in June, indicating that the two points began to cool in June; but at other points, the smallest monthly difference appeared in August and September when began to cool. The smallest positive value of the monthly difference appeared in February and March, indicating that it started to heat up in these two months, this is caused by two direct shots from the sun's direct point.

The monthly and monthly difference changes of characteristic points in the NPO not only show latitude zonality but also show an increasing trend from east to west, that is, from the outer sea to the inner sea. The relatively closed waterbody—Sulu Sea has a higher temperature difference than that of the same latitude, and the semi-closed waterbody—Celebes Sea's temperature difference is the smallest in the entire study area. The warming and cooling of the surface water in the study area are following the direction of the direct sun's movement.

4 DISCUSSION: THE CLIMATE ZONING (AREA) AT THE STUDY AREA

To study the process of regional climate change and the temporal and spatial differentiation of climate change, it is necessary to carry out detailed climate zoning (regions) for the study area.

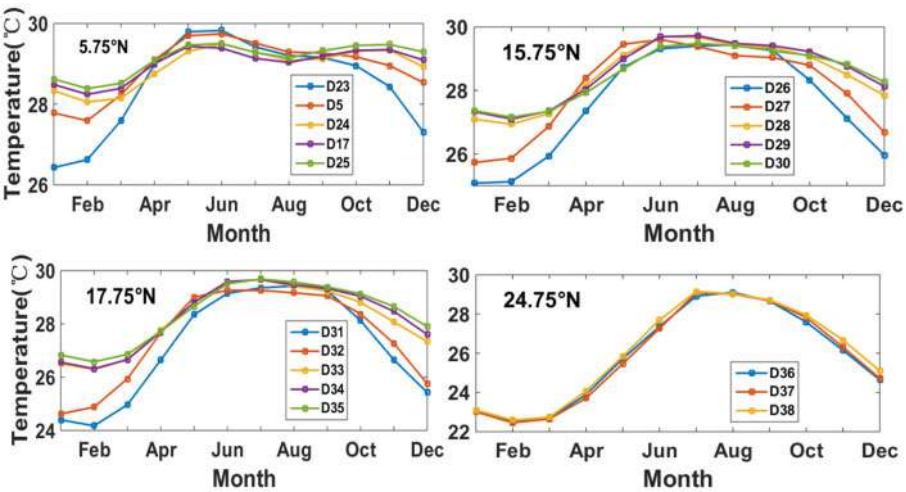

Figure 5. Monthly change curve of characteristic points at a different latitude.

The climate zone on the earth is mainly controlled by solar radiation. On a global scale, the Tropic of Cancer is used as the boundary between the temperate zone and the tropical zone. So, in this way, the study area of this article belongs to the tropical area.

From the view of the inter-monthly temperature changes and physical mechanism, in the tropics, the earth's surface is exposed to direct sunlight twice a year, and the temperature is high throughout the year; the annual change is small, and the monthly difference is small. In the temperate zone, the earth's surface is exposed to direct sunlight once a year, and the inter-monthly temperature changes show only one high temperature and one low temperature, the monthly temperature change curve is approximately a horizontal "S" waveform; the temperature changes seasonally, and the amplitude of change increases with increasing latitude.

If the monthly change of the SST is used as an indicator for the division of climatic zones, the multi-year average inter-monthly change of the SST in the studied sea area is examined, see Figure 5, and combining Figures 3 and 4, it can be seen that the sea area south of 13.75°N is a typical tropical feature; in the sea area of 15.75°N–17.75°N, the inter-monthly tropical characteristics of the SST have gradually weakened, and the highest temperature shifted from April to May to June then July. By the 18.75°N sea area, see Figures 3 and 4, the sub-low temperature and sub-high temperature disappeared; the characteristics of the temperate zone have appeared.

Therefore, this paper uses the inter-monthly SST change characteristics as an indicator for further division of the regional climate zone. In the SCS and the adjacent NWP, the boundary is roughly near 17.75°N, the south side belongs tropical, and the north side is temperate (subtropical); thus, it lays the foundation for further research on the process and temporal and spatial differentiation of regional climate change.

5 CONCLUSION

In this paper, the monthly distribution characteristics of annual mean SST over the SCS and the adjacent NPO during the CRP from 1981 to 2010 are analyzed. Based on the characteristic, further climatic zonation (zone) of the study area is carried out. The study can be concluded as:

1) In the study area, the highest monthly mean SST is about 29.9°C, which occurs in the eastern NPO near the equator. The lowest temperature of 22.5°C occurred on the north coast of the SCS. In the south of 12°N and the Celebes Sea, influenced by the North Equatorial Warm Current and equatorial countercurrent, where the temperature difference is the smallest. And the temperature difference in the north coastal area of the SCS is the largest.
2) In the study area, from low latitudes to high latitudes, the change of temperature difference increases and becomes obvious. The variation of temperature difference also shows an increasing trend from east to west, that is, the variation of temperature difference outside the sea is small, and it is greater in the inland sea; the greatest the change of temperature difference is near the north coast of the SCS.
3) In the SCS, the isotherm tends to be southwest to northeast. In the northern part of the SCS, the isotherm is approximately parallel to the coast. In the north-central NPO, isotherms are distributed parallel to the latitudes.
4) Through the analysis of temperature variation of inter-monthly and monthly differences, it can be seen that the average inter-monthly and monthly temperature variation of the sea area located near 18.75°N south of the Tropic of Cancer shows the characteristics of temperate climate. It has been suggested that the boundary between the tropical zone and temperate zone (subtropical zone) in the study area is lower than the latitude on land, and may be about 17.75°N as the climate boundary between tropical zone and temperate zone (subtropical zone) in the study area.

ACKNOWLEDGMENT

This research was supported by the Scientific Research Development Foundation of Shanghai Normal University (KF201824, KF2021106).

REFERENCES

Amante, C., Eakins, B.W. (2009). ETOPO1 1 Arc-Minute Global Relief Model: procedures, data sources and analysis. Psychologist. 16 (3), 20–25.

Carton, J.A., Giese, B.S. (2008). A Reanalysis of Ocean Climate Using Simple Ocean Data Assimilation (SODA). Monthly Weather Review. 138 (8), 2999.

Cravatte, S., Delcroix, T., Zhang, D., et al. (2009). Observed freshening and warming of the western Pacific warm pool. Climate Dynamics. 33 (4), 565–589.

Hu, D.X., Wu, L.X., Cai, W.J., et al. (2015). Pacific western boundary currents and their roles in climate. Nature. 522 (7556), 299.

Lu, C.H., Huang, L., He, J.H, et al. (2014). Interannual variation of heat content in the Western Pacific Warm Pool and its impact on climate anomalies in East Asia. Journal of Tropical Meteorology. 30 (01), 64–72.

Qiu, F.W., Fang, W.D., Guo, P. (2011). Interannual and spatial variability of the Sea surface temperature in the South China Sea during 2000–2008. Acta Oceanologica Sinica. 33 (03), 11–18.

Wu, X.F., Xu, J.P., Zhang, Q.L., et al. (2011). CSEOF analysis of the upper ocean heat content over tropical western Pacific. Journal of Tropical Oceanography. 30 (06), 37–46.

Yang, X.X., Wu, X.F., Xu, J.P. (2017). A review on the upper ocean heat and salt content in the Western Pacific Warm Pool. Transactions of Oceanology and Limnology. (05), 18–30.

Zeng, N., Ding, Y., Pan, J., et al. (2008). Climate change–the Chinese challenge. Science. 319 (5864), 730–731.

Zhou, M.P., Wang, G.H. (2015). Responses of atmospheric circulation to sea surface temperature anomalies in the South China Sea. Ocean Science. 11 (4), 1693–1710.

Zhu, X.H., Wang, W.Q., Zhou, W.D., et al. (2003). The interannual mode of sea surface temperature in the South China Sea and its relationship with monsoon forcing. Journal of Tropical Oceanography. (04), 42–50.

Advances in Applied Chemistry and Industrial Catalysis – Saikia (Ed.)

Research progress on the mechanisms of tropical cyclone intensity changes

Hanyan Wu, Jun Peng*, Jun Zhao & Lifeng Zhang
College of Meteorology and Oceanography, National University of Defence Technology, Changsha, Hunan, P.R. China

ABSTRACT: Changes in the intensities of tropical cyclones (TCs) are a complex multiscale problem. Not only external atmospheric environmental factors, such as the ocean thermal environment and environmental vertical wind shear, but also internal dynamic processes, such as small-scale processes, balanced and unbalanced dynamics and multiscale interaction processes, result in changes in TC intensity. These factors interact in a nonlinear form, resulting in difficulty regarding TC intensity forecasts. At present, studies on the effects of external environmental factors are relatively complete and certain. As the key to breaking through the limitation of TC intensity prediction, most of the internal dynamic processes have not been unified. From the two aspects of environmental factors and internal dynamics, this paper reviews, summarizes and discusses the above main physical factors affecting changes in TC intensity by investigating the latest literature in the last decade to provide a theoretical basis and ideas for the further study of TC intensity changes.

1 INTRODUCTION

A tropical cyclone (TC) is a strong cyclonic vortex with a warm core structure generated on the tropical ocean surface and often causes serious disasters. The occurrence of TC disasters in China is high in frequency, wide in scope and severe in degree (Xu & Gao 2005). Extensive and in-depth research on TCs can improve prediction accuracy to reduce their disastrous impacts. Research on TCs mainly focuses on two aspects: track forecasts and intensity forecasts. In the past two decades, significant progress has been made in research on improving the accuracy of TC track forecasts (Zhang & Weng 2015), but little progress has been made in regard to research on intensity forecasting (Elsberry 2014). Track forecasts of TCs are mainly dependent on the large-scale flows in which the vortex is embedded; therefore, track forecasts can be improved by utilizing a global prediction model. Unlike path prediction, TC intensity forecasts is more dependent on multiscale processes that span many orders of magnitude (Montgomery & Smith 2017). To date, the accurate forecasting of the rapid intensification of TCs still faces great challenges.

The rapid intensity (RI) of a tropical cyclone is defined as a 15.4 ms^{-1} (30 kt) increase in maximum sustained wind within 24 hours (Kaplan et al. 2010). The occurrence of RI is influenced not only by the large-scale environmental background and mesoscale convective system but also by the dynamic processes of TCs (Gary 1968). In addition, tropical cyclones have convective motion and the typical interaction characteristics of moist convection with larger-scale circulation (Marks & Shay 1998), which lead to the complex thermal and dynamic mechanisms of their intensification processes. A number of theories have been proposed regarding the intensification of TCs. Examples include the CISK paradigm (Charney & Ellassen 1964), the cooperative-intensification paradigm (Ooyama 1982), the WISHE intensification paradigm (Emanuel 1986), and vortical hot towers (i.e., the three-dimensional asymmetry paradigm) (Hendricks et al. 2004).

*Corresponding Author: pengjun@nudt.edu.cn

DOI 10.1201/9781003308553-75

In the early stage of TC research, although detailed studies on the cores of tropical cyclones were not sufficiently in-depth, researchers made it clear through observation that ocean heat transfer played a key role in intensifying tropical cyclones (Riehl 1950). In addition, the higher relative humidity in the middle and lower troposphere, the higher trough, cold vortex forcing, and the weaker environmental vertical wind shear are more conducive to the occurrence of rapid intensification (Gary 1968; Merrill 1988).

In recent years, increasing attention has been given to the role of the core dynamics of TCs in intensity changes (Ruf et al. 2016). Many observations have shown that the core structure of a rapidly intensifying tropical cyclone has distinctive characteristics compared with that of a tropical cyclone without RI. For example, a TC experiencing RI has a deeper and stronger inflow in the boundary layer and a stronger outflow in the upper layer, accompanied by a large number of strong convective bursts (Rogers et al. 2013).

With the improvement of observations and the development of high-performance computing, many achievements have been made in research on the mechanisms of TC intensity change. In this paper, the main research progress on TC intensity changes in the last ten years is reviewed from the two aspects of external factors and internal dynamic processes, and some scientific problems that need to be studied at present are proposed.

2 EXTERNAL FACTORS

Developing tropical systems often first exhibit a mesoscale vortex in the middle troposphere, which is considered to be a precursor of tropical cyclones (Simpson et al. 1997). This mesoscale vortex is combined with favourable external environmental fields: warm sea surface temperature, large ocean heat content (OHC), high humidity in the lower troposphere and weak vertical wind shear (Gary 1968; Merrill 1988), which can cause the vortex to intensify and eventually reach the intensity of a tropical cyclone. The ocean thermal environment, ambient wind vertical shear, and the interaction between the ambient low trough and TC are discussed later.

2.1 *Ocean thermal environment*

As early as 1950, Riehl (1950) studied the formation of TCs and made a ground-breaking realization: he clearly recognized that ocean thermal transmission played a key role in TC intensification. The formation of TCs is possible only when the sea surface temperature (SST) reaches 26.5°C (Gary 1968). When the SST exceeds 28°C, more heat flux and water vapour flux are transferred to the atmosphere, and the TC intensifies at a faster rate. However, when the SST reaches 30°C, the growth rate of the TC decreases (Chan et al. 2001). The physical quantity derived from SST to measure the contribution of the ocean to TC intensity also includes the tropical cyclone heat potential (TCHP), which refers to the heat contained in seawater with a temperature higher than 26°C. Its increase also leads to an increase in the frequency of TCs experiencing RI (Zhao et al. 2018). In addition to SST, the ocean heat content (OHC), the depth of the ocean mixing layer and the vertical structure of SST also affect the sea surface heat flux and ultimately the intensity of the TC. The more OHC there is, the deeper and warmer is the sea water in the mixing layer; therefore, SST remains high when sea water is mixing, which has a positive effect on the intensification of TCs (Leipper & Volgenau 1972). The barrier layer (fresh water pool at the top of the mixing layer) inhibits mixing and is conducive to TC intensification (Balaguru et al. 2012). Turbid sea water can also block solar shortwave radiation, causing sea water below the surface to cool, thus counteracting the effect of fresh water (Newinger & Toumi 2015). In addition, salinity stratification can also reduce sea surface cooling and is conducive to the RI of TCs, and this effect increases with the increase in the TC intensification rate (Balaguru et al. 2020).

The effect of the ocean on TC intensification can also be indirect. A moving storm can bring cold deep water to the surface through upwelling, entrainment, and shear-induced vertical mixing, resulting in a decline in SST, which in turn affects the development of TCs (Stramma et al. 1986). Recent research points of interest include the role of mesoscale warm and cold vortices in the ocean

(Ma et al. 2017). In addition, TCs will also cause the upturning of sea water on the ocean surface, bringing sea water from the lower layers of the ocean to the sea surface in the form of turbulence and forming a cold ocean wake, which will have an impact on the changing intensity of tropical cyclones (Cione & Uhlhorn 2013). Studies show that cold wakes often weaken TC intensity.

2.2 *Environmental wind vertical shear*

Vertical wind shear (VWS) is defined as the vector difference of the wind between 850 hPa and 200 hPa in the vertical direction. Studies have shown that the VWS affects the structure and development of TCs (Ramage 1959) and that continuous strong vertical wind shear is not conducive to maintaining the warm core structure of TCs. Among the physical mechanisms by which VWS affects TC strength, the "ventilation effect" (Simpson & Riehl 1958) was recognized early on. The ventilation effect refers to the inflow of low-entropy ambient air into the TC core. However, there is some debate as to exactly where the "ventilation effect" occurs. The initial "ventilation effect" is thought to occur in the middle troposphere and is therefore known as the "mid-troposphere ventilation" effect. Later, many researchers verified the "middle ventilation" effect in numerical simulations (Cram et al., 2007). The "upper ventilation" effect (Kwon & Frank 2008) is proposed based on the "top-down" effect of VWS. The "low-level ventilation effect" (Riemer et al. 2013) is proposed based on the "bottom-up" effect of VWS. In general, strong vertical wind shear is not conducive to TC intensification (Wood & Ritchie 2015) and may even result in a rapid weakening (RW) TC (Ma et al. 2019).

In recent years, there has been new discoveries regarding the study of VWS. Under the influence of VWS, some TCs will experience RI, which may be related to other environmental factors. For example, Rios-Berrios et al. (2016) conducted research on Hurricane Katia (2011) and found that under moderate vertical wind shear, high humidity in the middle and low troposphere is conducive to TC intensification; Rios-Berrios (2020) found that radiation will reduce the tilt of the vortex and will also lead to the intensification of TCs under strong shear. In fact, most of the intensification of TCs under shear is related to their internal structure (Rios-Berrios et al. 2016), which is mainly related to the intensification of deep convection. This will be explained in detail in the next section. Ching and Gabriel (Ching & Gabriel 2020) studied the large-scale environmental factors that control the RIs of tropical cyclones in the North Atlantic and found that when the vertical wind shear decreases, the probability of TCs experiencing RI increases significantly, but this characteristic is not found in the Gulf of Mexico, western Caribbean Sea or Sargasso Sea, which indicates that the influence of vertical wind shear is also related to the region.

2.3 *Other atmospheric environmental factors*

Other atmospheric environmental factors, such as external baroclinic pressure disturbances and cold air, often interact strongly with TCs, causing intensity changes in TCs.

Simpson and Riehl (1958) used aircraft observational data to prove the "ventilation effect" and pointed out that the degree of circulation is related to the baroclinicity of the large-scale environment in the middle troposphere. The interaction between the upper troposphere system and TCs is also one of the most challenging factors affecting TC intensity forecasting (Molinari & David 1990). Some studies have shown (Bosart et al. 2000) that high-level troughs have a positive impact on hurricanes, but other studies have pointed out that the impact of troughs is negative due to the presence of vertical wind shear (Lewis & Jorgensen 1978). Intensification mechanisms of high-level troughs may be through high-level vortex angular momentum flux forcing (Molinari & Vollaro 1989), high-level divergence intensification (Bosart et al. 2000), or superposition of potential vortices (Molinari & Skubis 1995). The relative position of the TC and high-altitude trough determines whether the influence of the high-altitude trough is positive or negative (Yu & Kwon 2005). When the relative position remains the same, the intensity of the high-altitude trough has almost no effect on the peak intensity of the TC. However, it does affect the rate of intensification. However, Li et al. (2006) conducted a numerical study on Typhoon Winnie and found that the stronger the trough was, the

colder the advection, and the stronger the positive vorticity advection and high-altitude divergence in front of the trough, which is conducive to the maintenance and strengthening of the TC.

As one of the ambient airflows, cold air also has an impact on the occurrence and development of TCs. The kinetic energy brought by the invasion of cold air can promote the formation of typhoons; the strong cold air invading the Northern Hemisphere is the main reason for the large-scale, highly humid and unstable air releasing a large amount of potential energy. Based on the CISK mechanism, Li (1983) explained that strong dry cold air is not conducive to the occurrence and development of TCs from the perspective of dynamics, while cold air of moderate intensity is conducive to the occurrence and development of TCs. Niu et al. (2005) used the MM5 model to numerically simulate Typhoon 0216 (Sinlaku) and found that cold air intruding into the periphery of the TC can greatly increase precipitation in the periphery of the TC and inverted trough, but cold air intruding near the centre of the TC can cause the TC to weaken. Therefore, the influence of cold air on the strength of the TC is related to the strength of the cold air and location of the invasion.

In addition, the relative humidity of the middle troposphere was considered to be a necessary condition for the occurrence and development of TCs in their early stage. If the relative humidity of 500 hPa is lower than 40%, it is difficult to generate TCs (Gary 1968). Therefore, it is generally believed that conditions that reduce relative humidity, such as the intrusion of dry air in the middle layer, will weaken the strength of TCs (Wood & Ritchie 2015), while increasing humidity in the middle layer will increase the intensity of TCs (Gao et al. 2020). However, it is also believed that humidity does not play a dominant role in the intensity change of TCs (Liang et al. 2018). Ma et al. (2019) found that the humidity of the middle layer of the environment exhibits different characteristics of contribution in different regions: it shows a significant role in the Atlantic Ocean and other regions, but it is not significant in the Northwest Pacific. This phenomenon may be related to the absence of a mid-level dry air layer prevailing over the Northwest Pacific.

3 INTERNAL DYNAMIC PROCESSES

Lee et al. (2015) developed a set of probabilistic multiple linear regression models to predict the intensity of tropical cyclones using environmental factors that have been proven to be related to the intensity of TCs as predictors, and these models showed good results. However, the relative importance of the factors that affect the change in TC intensity is uncertain; therefore, the linear regression model has limitations. Hendricks et al. (2010) pointed out that under favourable environmental conditions, the RI processes of TCs are more likely to depend on their internal dynamic structure. Observational analysis shows that some storms can intensify rapidly in relatively strong VWS (>10 ms^{-1}) or moderate VWS (7–10 ms^{-1}) (Nguyen & Molinari 2015). The main reason for this is that the core processes of TCs reduce the adverse impact of environmental VWS on their intensification. The importance of internal dynamics in the processes of TC intensification is self-evident, but there is not much unified understanding regarding internal dynamics.

3.1 *Small-scale convective motion*

In the study of RI processes of TCs, the previous theories are all based on a two-dimensional model (Charney & Ellassen 1964; Emanuel 1986; Oyama 1982). However, with the improvement of observational ability and numerical resolution, a new paradigm of rotating convection is proposed, which emphasizes the asymmetric nature of the spin-up process and notes that TC intensification is carried out along a three-dimensional path. The rotating convective cells, namely, vortical hot towers (VHTs), develop through local conditional instability, then move to the core along the average vorticity gradient and are absorbed in the centre, resulting in upscaled angular velocity flux and average flow strengthening (Hendricks et al. 2004)[11]. In addition to VHTs, convective bursts (CBs), in which long and narrow convective cells in the vertical direction inside TCs are also a common convective activity in TCs. Observations have shown that VHTs and CBs are often accompanied by the RI of TCs. Both VHTs and CBs are small-scale convective cells with a strong

ascending velocity in the tropical atmosphere. However, VHTs are called hot towers because of the large amount of latent heat released during the ascending process (Zhuge et al. 2015).

A large number of studies have shown (Guimond et al. 2010) that large-area, long-lasting CBs are often accompanied by RI processes of TCs. Many researchers believe that CBs are the cause of TC intensification and are related to the location of CBs. Chen and Fang (Chen & Fang 2012) found in numerical simulations that deep convection within the radius of maximum wind (RMW) will lead to the intensification of TCs, while deep convection outside the RMW will inhibit the intensification of TCs. Similarly, Rogers et al. (2013) pointed out in an analysis of observational data that the intensified TC not only has more CBs but also that the CBs tend to appear on the inner side of the RMW, while for the stable TC, CBs are fewer, and more appear on the outside of the RMW. Zhang and Tao (2013) further studied the influence of the position of deep convection on intensification and found that the position of organized deep convection determines the vertical tilt of the vortex. When the tilt angle reaches 90° to the left of the environmental shear, the TC immediately increases. Many studies have analysed the specific role of CBs in RI processes of TCs, and the main conclusion is that CBs will cause sinking airflow at the inner boundary of the eye wall, intensifying the warm core of TCs, and causing the RI of TCs (Guimond et al. 2010).

However, some studies have proposed the opposite view that small-scale convective motion is not the cause of RI. Jiang (2012) found that for TCs with VHTs in the inner core, although the probability of RI and slow intensification (SI) had both increased and the probability of slow and rapid weakening had also decreased, but the increase in the probability of intensification and weakening was not large; therefore, he believed that the VHTs were not a sufficient and necessary condition for RI. DeMaria et al. (2012) studied the relationship between lightning activity and RI using a 6-year Worldwide Lightning Location Network (WWLLN) of TCs in the Atlantic and eastern North Pacific and found that the lightning density of the rapidly weakening storm in the core (0–100 km) is greater than that of the RI storm, and within the following 24 hours, the lightning density of the RI storm is higher in the rain belt (200–300 km). Zagrodnik and Jiang (2014) analysed the relationship between precipitation and convection and latent heat of TCs using 14-year TRMM data and found that in the period close to the beginning of RI, the TC core area does not necessarily require strong and extensive deep convection; in contrast, after RI lasts for at least 12 hours, there is more deep convection than before the start of RI. Therefore, they believed that small-scale convective motion is more likely to be a product of the RIs of TCs.

3.2 *Balanced and unbalanced dynamics*

In previous studies, the gradient wind balance in the boundary layer of TCs was often acquiesced (Emanuel et al. 1994). However, Smith et al. (2009) pointed out that the boundary layer is a shallow layer, and its inflow is mainly caused by the unbalanced gradient wind in the radial momentum equation. Based on this, they proposed a more complete boundary layer formula, in which the tangential wind speed in the inner core becomes supergradient wind; that is, nonequilibrium boundary layer dynamics. The so-called supergradient wind indicates that in the boundary layer, due to the frictional deceleration of tangential wind, the centrifugal force and Coriolis force near the ocean surface are reduced, resulting in the imbalance of radial pressure gradient force, centrifugal force and Coriolis force. The unbalanced force is radially inward, which in turn causes the tangential wind in the boundary layer to increase with decreasing radius. The influence of unbalanced flow cannot be ignored in some cyclones, and it has a significant contribution to the maximum intensity (Bryan & Rotunno 2009). Smith and Vogl (2008) calculated the boundary layer and showed that supergradient wind is a common feature of the inner core boundary layer of mature storms. Therefore, as shown in Figure 1, Smith et al. (2009) divided the boundary layer into two regions according to whether the top of the boundary layer is inflow or outflow. In the inflow boundary layer, the radial pressure gradient at the top of the layer and the downward advection of free vortex properties (such as moisture, heat, and momentum) are directly affected by the upper vortex (Smith & Vogl 2008). In the outflow boundary layer, the vertical advection of the characteristic boundary layer enters the free vortex and has a profound impact on its structure (Smith et al. 2009). For a long time,

people generally believed that surface friction only plays an inhibitory role in the intensification of TCs. Planetary boundary layer circulation is mainly controlled by the balance between the convergence of environmental vorticity and surface friction. The former tends to accelerate the storm, and the latter tends to slow down the storm (Marin et al. 2009). The proposal of supergradient wind recognizes the importance of surface friction in TC spin-up.

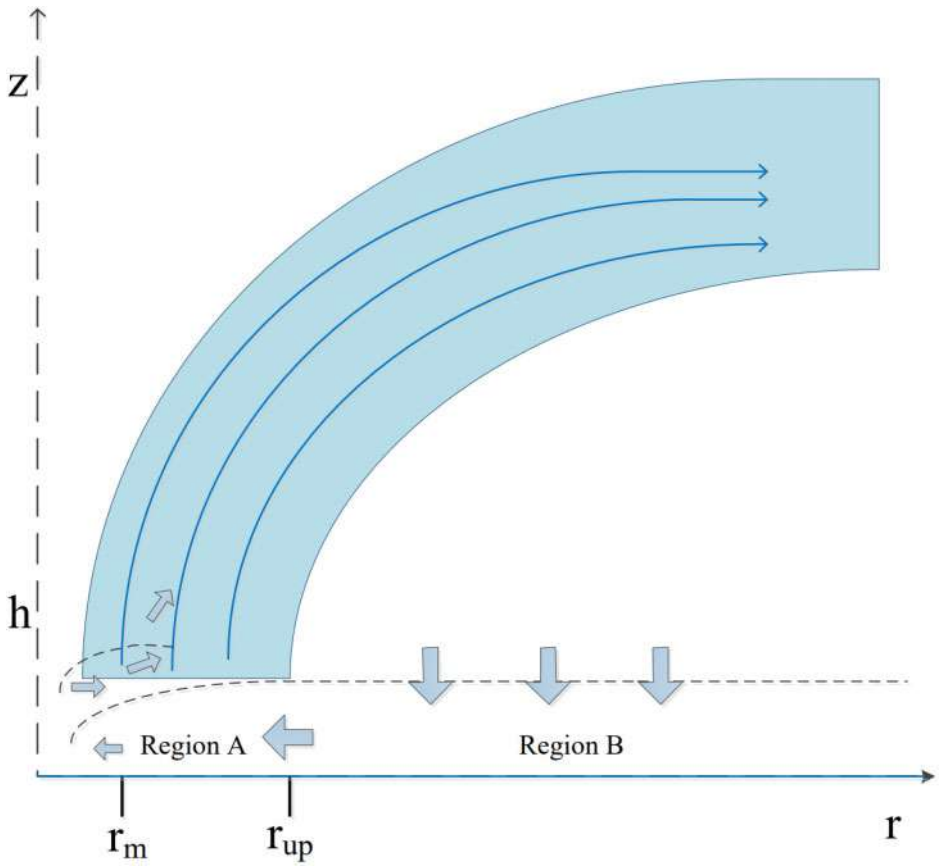

Figure 1. Conceptual model for the boundary layer in the inner-core region of the TC. The boundary layer is divided into two regions depending on the flow direction at the top of the boundary layer (Region B: inflow, $r > r_{up}$; Region A: outflow, $r < r_{up}$), where r is the radius. This figure is re-edited with permission from Smith et al. (2009).

In the case of supergradient winds, vertical advection and vertical diffusion are the main processes for maintaining supergradient winds and will lead to stronger, deeper and more radially constrained secondary circulation in the boundary layer (Williams 2015). When supergradient winds are advected vertically out of the boundary layer by the updraft of the eye wall, they are also considered to be the momentum source of the eye wall above the boundary layer in the TC (Montgomery & Smith 2017). Therefore, many researchers have believed that the boundary layer mechanism proposed by Smith et al. (2009) can explain the intensification process of TCs (Montgomery & Smith 2014) and the asymmetric model can be used to provide supporting evidence (Montgomery et al. 2020). However, it has also been pointed out that unbalanced motion cannot explain the intensification process of TCs (Fei et al. 2021). Starting from TC intensification being mostly related to axisymmetric dynamics, they used an axisymmetric model and showed

that although the vertical advection of radial wind contributes more than 50% to the intensity and height of boundary layer supergradient flow, the final TC intensity is not affected. They believed that although the traditional balancing process greatly underestimates the intensity of the inflow and intensification rate in the boundary layer and cannot capture the important inertial effects of the boundary layer in the inner core region (Bui et al. 2009), it explains the important role of the heating effect in the eye wall in stimulating and enhancing secondary circulation (Pendergrass & Willoughby 2009). Moreover, the supergradient wind is not a unique phenomenon during TC intensification but exists throughout the life of TCs. Therefore, the balanced and unbalanced dynamics should be a unified view.

3.3 *Multiscale interactions*

TCs have convective motion and typical interactions between moist convection and larger-scale systems (Marks & Shay 1998), which makes it more difficult to predict their intensity. In the process of influencing the intensity of TCs, multiscale interactions include interactions between external environmental factors and TCs, but the focus of this section is on multiscale interactions of TCs.

The classical second-class conditional instability (CISK) theory (Charney & Ellassen 1964) has actually described interactions between convective-scale motion and large-scale vortex motion. Dunkerton et al. (2009) proposed three hypotheses resulting in TC genesis ("marsupial paradigm") that link synoptic scale, subsynopic scale, mesoscale and convective scale processes. In the past two decades, research on the interaction between different scale systems in the process of TC genesis has attracted attention, mainly focusing on the interactions between the mesoscale convective vortex (MCV) and convective scale systems. MCVs are thought to cause the concentration and increase of cyclonic vorticity in the lower troposphere. In the early days, researchers believed that their influence mechanisms were top-down (Simpson et al. 1997). With the discovery of VHTs, the bottom-up impact mechanism has been increasingly recognized (Hendricks et al. 2004).

Multiscale interactions not only manifest during the genesis of TCs but also have an important role in later development. Among the several paradigms regarding the intensification of TCs, the three-dimensional asymmetric paradigm (VHT) recognizes the growth and randomness of local, buoyant, rotating deep convection (Montgomery & Smith 2014), which can form deep and aligned vortices in the vertical direction by reducing tilt or forming vortices above (below) the existing low-level (middle-level) circulation centre. They are critical in the intensification of TCs (Wang 2012). Even TCs in moderate shear can experience RI with the high-level cyclone circulation centre aligned with the low-level centre (Rogers et al. 2015). When Fang and Zhang (2011) studied Dolly (2008), they found that the thermal forcing of small-scale convection could lead to secondary circulation, causing the intermediate-scale and convective-scale vorticity to concentrate in the centre of the storm, which in turn led to large-scale vorticity intensification. These results are the same as those of Nolan (2007) and Montgomery et al. (2006). Ge et al. (2015) found that in the process of self-organization of small-scale convection into mesoscale structures, the high core vorticity and negative radial vorticity gradient of the initial vortex play important roles.

In recent years, studies based on spectral analytical methods have further deepened the understanding of multiscale internal dynamic TC processes (Bhalachandran et al. 2020; Wang et al. 2018; 2019). Wang et al. (2018, 2019) studied the characteristics of the mesoscale kinetic energy spectrum at different heights based on the ideal TC simulation and found that the slow intensification period is mainly manifested as the growth and saturation of the mesoscale kinetic energy spectrum, and this growth characteristic during the RI period gradually expands to small scales. This energetic feature seems to support the WISHE mechanism. The proposed conceptual model for the horizontal kinetic energy budgets at different heights and scales is given in Figure 2. Bhalachandran et al. (2020) studied the multiscale asymmetry characteristics during tropical cyclone RI and found that the main mechanism of the growth/decay of the asymmetric characteristics is the baroclinic conversion of effective potential energy to kinetic energy on various asymmetric scales and the exchange of kinetic energy between different asymmetric scales, rather than the normally assumed positive pressure mean-eddy interaction.

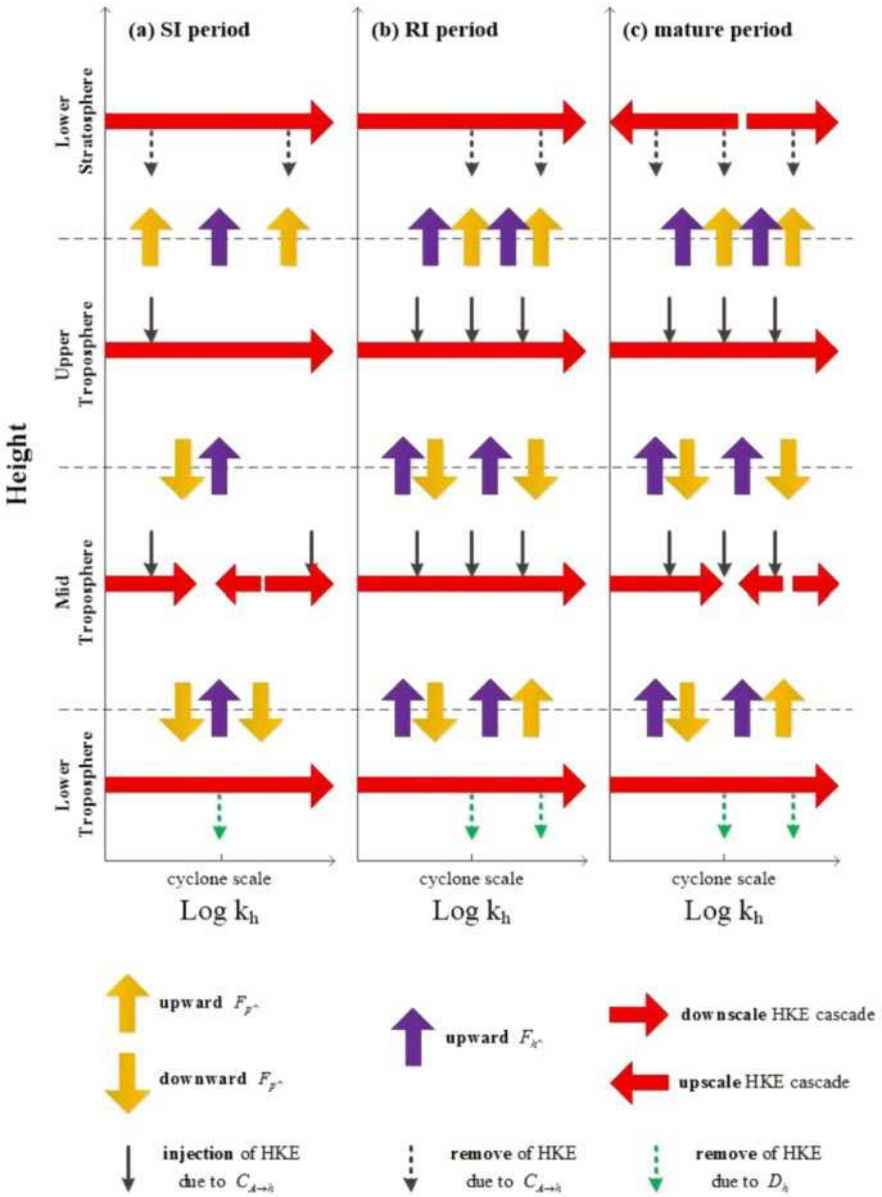

Figure 2. Schematic of the horizontal kinetic energy (HKE) budgets vs horizontal wavenumber during the (a) slow intensification (SI), (b) rapid intensification (RI), and (c) mature periods of the TC. $F_{p\uparrow}$ and $F_{h\uparrow}$ are the vertical fluxes of pressure and HKE, respectively; $C_{A\to h}$ represents the spectral conversion of available potential energy to HKE; D_h is the diffusion term. This figure is directly reproduced with permission from Wang et al. (2018).

4 CONCLUSION

Predicting the intensity changes of TCs is currently a major problem worldwide. This process involves a large-scale environment and internal dynamics. This paper discusses and summarizes some influential factors that affect the intensity change of TCs from the above two aspects.

Current research on the influence of environmental factors on the intensity of TCs is gradually improving. Warm sea surface temperature, large ocean heat capacity, high humidity in the lower troposphere, weak vertical wind shear, weak upper-level forcing from troughs or cold advection, and upper-level easterly winds (Gary 1968; Merrill 1988) are undoubtedly conducive to the development of TCs. The main contradiction regarding the influence of the external environment on the intensity of TCs lies in that some storms can be strengthened in relatively strong VWS, while weak VWS is more conducive to TC intensification in general. However, current research confirms that it is related to the core processes of TCs.

Hendricks et al. (2010) pointed out that under favourable external environmental conditions, RI processes of TCs are more likely to depend on their internal dynamic structure. Similar to RI processes of TCs in strong VWS mentioned above, internal dynamics can sometimes even affect the role of environmental factors. Therefore, to break through the bottleneck of the existing intensity prediction model, we must give more attention to its internal dynamic processes, although this research is more complicated. The current research on the internal dynamics of TCs is limited to either observational analysis or a highly idealized environment. This research may only provide insights into certain aspects of tropical cyclone intensification processes (Rogers 2015), leading to most studies on internal dynamics not yet forming a unified understanding.

(1) Although small-scale convective motion has been discovered during the intensification of TCs, it is controversial whether it is the cause or product of TC intensification;
(2) Whether the boundary layer spin-up mechanism is the main physical mechanism of TC intensification in balanced and unbalanced dynamics;
(3) In terms of multiscale interactions, is the energy between different scales upscaled or downscaled? Or what are the similarities and differences in the energy cascade characteristics at different stages of TC development? What are the scale-dependent characteristics of the vertical energy transport between different heights of the troposphere?

In recent years, the newly developed spectrum analytical theory has provided a new perspective for the internal dynamic processes of TCs. It has shown theoretical advantages of certain aspects in the energy spectrum distribution and cascade characteristics of the TC system and the growth/attenuation of multiscale asymmetric characteristics. It is reasonable to believe that multiscale analytical angles with the development of comprehensive observational experiments for TCs and the use of high-resolution numerical forecasting models, the theoretical understanding of TCs will become increasingly solid, and the ability to predict TC intensity will also gradually improve.

ACKNOWLEDGMENTS

This research is supported by National Natural Science Foundation for Young Scientists of China (Grant No. 41705037) and partly supported by the National Natural Science Foundation of China (Grant No. 41975066 and 42005053).

REFERENCES

Balaguru, K., G.R. Foltz, L.R. Leung, J. Kaplan, W. Xu, N. Reul & B. Chapron (2020) Pronounced impact of salinity on rapidly intensifying tropical cyclones. Bulletin of American Meteorological Society, 101: E1497–E1511.

Balaguru, K., P. Chang, R. Sarabanan, L.R. Leung, Z. Xu, M. Li & J.S. Hsieh (2012) Ocean barrier layers' effect on tropical cyclone intensification. Proceeding of the National Academy of Sciences of the United States of America, 109: 14343–14347.

Bhalachandran, S., D.R. Chavas, J. Marks, D. Frank, S. Dubey, A. Shreevastava & T.N. Krishnamurti (2020) Characterizing the Energetics of Vortex-Scale and Sub-Vortex-Scale Asymmetries during Tropical Cyclone rapid intensity changes. Journal of the Atmospheric Sciences,77:315–336.

Bosart, L.F., C.S. Velden, W.E. Bracken, J.E. Molinari & P.G. Black (2000) Environmental influences on the rapid intensification of Hurricane Opal (1995) over the Gulf of Mexico. Mon. Wea. Rev., 128: 322–352.
Bryan, G.H. & R. Rotunno (2009) Evaluation of an analytical model for the maximum intensity of tropical cyclones. J. Atmos. Sci., 66:3042–60.
Bui, H.H., R.K. Smith, M.T. Montgomery & J. Peng (2009) Balanced and unbalanced aspects of tropical cyclone intensification. The Quarterly Journal of the Royal Meteorological Society. 135:1715–1731.
Chan, J.C.L., Y.H. Duan & L.K. Shay (2001) Tropical cyclones intensity change from a simple ocean-atmosphere coupled model. J. Atmos. Sci., 58: 154–172.
Charney, J.G. & A. Ellassen (1964) On the Growth of the Hurricane Depression. Journal of the Atmospheric Sciences, 21: 68–75.
Chen, Q. & J. Fang (2012) Effects of vertical wind shear on intensity and structure of tropical cyclone. J. Trop. Meteor., 18, 172–186.
Ching, H.J.N. & A.V. Gabriel (2020) Large-scale environmental controls on the seasonal statistics of rapidly intensifying North Atlantic tropical cyclones. Climate Dynamics, 54: 3907–3925.
Cione, J. J. & E.W. Uhlhorn (2003) Sea surface temperature variability in hurricanes: Implications with respect to intensity change. Mon. Wea. Rev., 131: 1783–1796.
Cram, T.A., J. Persing, M.T. Montgomery & S.A. Braun (2007) A Lagrangian trajectory view on transport and mixing processes between the eye, eyewall, and environment using a high-resolution simulation of Hurricane Bonnie (1998). J. Atmos. Sci., 64:1835–1856.
DeMaria, M., R.T. DeMaria, J.A. Knaff & D. Molenar (2012) Tropical cyclone lightning and rapid intensity change. Mon. Wea. Rev., 140: 1828–1842.
Dunkerton T.J., M.T. Montgomery & Z. Wang (2009) Tropical cyclogenesis in a tropical wave critical layer: Easterly waves. Atmos. Chem. Phys., 9: 5587–5646.
Elsberry, R. L. (2014) Advances in research and forecasting of tropical cyclones from 1963–2013. Asia-Pacific Journal of Atmospheric Sciences, 50: 3–16.
Emanuel, K.A. (1986) An air-sea interaction theory for tropical cyclones. Part I: Steady state maintenance. Journal of the Atmospheric Sciences, 43: 585–604.
Emanuel, K.A., J.D. Neelin & C.S. Bretherton (1994) On large-scale circulations in convecting atmospheres. Q. J. R. Meteorol. Soc., 120: 1111–1144.
Fang, J. & F. Zhang (2011) Evolution of multiscale vortices in the development of hurricane dolly (2008). Journal of the Atmospheric Sciences, 68: 103–122.
Fei, R., Y. Wang & Y. Li (2021) Contribution of Vertical Advection to Supergradient Wind in Tropical Cyclone Boundary Layer: A Numerical Study. Journal of the Atmospheric Sciences. 78: 1057–1073.
Gao, J., H. Zhao, P.J. Klotzbach, C. Wang, G.B. Raga & S. Chen (2020) Possible Influence of Tropical Indian Ocean Sea Surface Temperature on the Proportion of Rapidly Intensifying Western North Pacific Tropical Cyclones during the Extended Boreal Summer, Journal of Climate, 33: 9129–9143.
Gary, M.W. (1968) Global view of the origin of tropical disturbances and storms. Mon. Wea. Rev., 96: 669–700.
Ge X., W. Xu & S. Zhou (2015) Sensitivity of tropical cyclone intensification to inner-core structure. Advances in Atmospheric Sciences, 32: 1407–1418.
Guimond, S.R., G.M. Heymsfield & F.J. Turk (2010) Multiscale observations of Hurricane Dennis (2005): The effects of hot towers on rapid intensification. J. Atmos. Sci., 67: 633–654.
Hendricks, E.A., M.S. Peng, B. Fu & T. Li (2010) Quantifying evironmental control on tropical cyclone intensity change. Monthly Weather Review, 138: 3243–3270.
Hendricks, E.A., M.T. Montgomery & C.A. Davis (2004) On the role of 'vortical' hot towers in formation of tropical cyclone Diana (1984). Journal of the Atmospheric Sciences, 61: 1209–1232.
Jiang, H. (2012) The relationship between tropical cyclone intensity change and the strength of inner-core convection. Mon. Wea. Rev., 140: 1164-1176.
Kaplan, J., M. DeMaria, & J.A. Knaff (2010) A Revised Tropical Cyclone Rapid Intensification Index for the Atlantic and Eastern North Pacific Basins. Wea Forecasting, 25: 220–241.
Kwon, Y.C. & W.M. Frank (2008) Dynamic instabilities of simulated hurricane-like vortices and their impacts on the core structure of hurricanes. Part II: Moist experiments. J. Atmos. Sci., 65: 106–122.
Lee, C.Y., M.K. Tippett, S.J. Camargo & A.H. Sobel (2015) Probabilistic Multiple Linear Regression Modeling for Tropical Cyclone Intensity. Mon. Wea. Rev., 143: 933–954.
Leipper, D.F. & D. Volgenau (1972) Hurricane Heat Potential of the Gulf of Mexico. Journal of Physical Oceanography. 12: 218–224.
Lewis, B.M. & D.P. Jorgensen (1978) Study of the dissipation of Hurricane Gertrude (1974). Mon. Wea. Rev., 106: 1288–1306.

Li, C. (1983) The effect of ambient flow on generation and development of typhoon. Acta Meteorologica Sinica, 3: 21–30.
Li, Y., L.S. Chen & X.T. Lei (2006) Numerical study on impacts of upper-level westerly trough on the extratropical transition process of typhoon winnie(1997). Acta Meteorologica Sinica, 64: 552–563.
Liang, J., L.G. Wu & G. Gu (2018) Rapid weakening of tropical cyclones in monsoon gyres over the tropical western North Pacific. Journal of Climate, 31:1015–1028.
Ma, Z., J. Fei, & X. Huang (2019) A definition of rapid weakening for tropical cyclones over the western North Pacific. Geophysical Research Letters, 46:11471–11478.
Ma, Z., J. Fei, L. Liu, X. Huang & Y. Li (2017) An investigation of the influences of mesoscale ocean eddies on tropical cyclone intensities. Mon Wea Rev, 145: 1181–1200.
Marin, J.C., D.J. Raymond & G.B. Raga (2009) Intensification of tropical cyclones in the GFS model. Atmos. Chem. Phys., 9: 1407–1417.
Marks, F.D. & L.K. Shay (1998) Landfalling tropical cyclones: forecast problems and associated research opportunities. Bulletin of the American Meteorological Society,79:305–305.
Merrill, R.T. (1988) Environmental influences on hurricane intensification. J. Atmos. Sci., 45: 1678–1687.
Molinari, J. & D. Vollaro (1989) External influences on hurricane intensity. Part I: Outflow layer eddy angular momentum fluxes. J. Atmos. Sci., 46: 1093–1105.
Molinari, J. & S. Skubis (1995) External Influences on Hurricane Intensity. Part III: Potential vorticity structure. Journal of the Atmospheric Sciences, 52: 3593.
Molinari, J. & V. David (1990) External Influences on Hurricane Intensity. Part II: Vertical Structure and Response of the Hurricane Vortex. Journal of the Atmospheric Science, 47:1902–1918.
Montgomery M.T., G. Kilroy, R.K. Smith & N. Crnivec (2020) Contribution of mean and eddy momentum processes to tropical cyclone intensification. Quarterly Journal of the Royal Meteorological Society. 146: 3101–3117.
Montgomery M.T. & R.K. Smith (2014) Paradigms for tropical cyclone intensification. Austrialian Meteological and Oceanographic Journal, 64: 37–66.
Montgomery, M.T., & R.K. Smith (2017) Recent Developments in the Fluid Dynamics of Tropical Cyclones. Annual Review of Fluid Mechanics, 49: 541–574.
Montgomery, M.T., M.E. Nicholls, T.A. Cram & A.B. Saunders (2006) A vortical hot tower route to tropical cyclogenesis. J. Atoms. Sci.,63: 355–386.
Newinger, C. & R. Toumi (2015) Potential impact of the colored Amazon and Orinoco plume on tropical cyclone intensity. Journal of Geophysical Research: Oceans. 120: 1296–1317.
Nguyen, L.T. & J. Molinari (2015) Simulation of the Downshear Reformation of a Tropical Cyclone. Journal of the Atmospheric Sciences, 72: 4529–4551.
Niu, X., H. Du & J. Liu (2005) The numerical simulation of rainfall and precipitation mechanism associated with typhoons sinlaku (0216). Acta Meteorologica Sinica, 63: 57–68.
Nolan, D.S. (2007) What is the trigger for tropical cyclogenesis? Aust. Meteor. Mag., 56:241–266.
Ooyama, K.V. (1982) Conceptual evolution of the theory and modeling of the tropical cyclone. Journal of the Meteorological Society of Japan, 60: 369–380.
Pendergrass, A.G. & H.E. Willoughby (2009) Diabatically induced secondary flows in tropical cyclones. Part I: Quasi-steady forcing. Mon. Wea. Rev., 137: 805–821.
Ramage, C.S. (1959) Hurricane development. Journal of the Atmosphereic Science,16:227–237.
Riehl, H. (1950) A model of Hurricane Formation. Journal of Applied Physice,21: 917–925.
Riemer, M., M. T. Montgomery & M.E. Nicholls (2013) Further examination of the thermodynamic modification of the inflow layer of tropical cyclones by vertical wind shear, Atmospheric Chemistry and Physics, 13: 327–346.
Rios-Berrios, R. (2020) Impacts of Radiation and Cold Pools on the Intensity and Vortex Tilt of Weak Tropical Cyclones Interacting with Vertical Wind Shear, Journal of the Atmospheric Sciences, 77: 669–689.
Rios-Berrios, R., R.D. Torn & C.A. Davis (2016) An Ensemble Approch to Investigate Tropical Cyclone Intensification in Sheared Environments. Part I: Katia (2011), Journal of the Atmospheric Sciences, 73:71–93.
Rios-Berrios, R., R.D. Torn & C.A. Davis (2016) An Ensemble Approach to Investigate Tropical Cyclone Intensification in Sheared Environments. Part II: Ophelia (2011), Journal of the Atmospheric Sciences, 73: 1555–1575.
Rogers, R., P.D. Reasor & S. Lorsolo (2013) Airborne Doppler observation of the inner-core structural differences between intensifying and stead-state tropical cyclone. Mon. Wea. Rev., 141: 2970–2991.
Rogers, R.F., P.D. Reasor & J.A. Zhang (2015) Multiscale structure and evolution of hurricane earl (2010) during rapid intensification. Monthly Weather Review, 143: 536–562.

Ruf, C.S., R. Atlas, P.S. Chang, M.P. Clarizia, J.L. Garrison, S. Gleason, S.J. Katzberg, Z. Jelenak, J.T. Johnson, S.J. Majumdar, A. Obrien, D.J. Posselt, A.J. Ridley, R.J. Rose & V.U. Zavorotny (2016) New ocean winds satellite mission to probe hurricanes and tropical convection. Bulletin of the American Meteorological Society, 97:385–395.

Simpson, J., E. Ritchie, G.J. Holland, J. Halverson & S. Stewart (1997) Mesoscale interactions in tropical cyclone genesis, Mon. Wea. Rev., 125: 2643–2661.

Simpson, R.H., & H. Riehl (1958) Mid-tropospheric ventilation as a constraint on hurricane development and maintenance. Technical Conf. on Hurricanes, Amer. Meteor. Soc., D4–10.

Smith, R.K., M.T. Montgomery & N.V. Nguyen (2009) Tropical cyclone spin-up revisited. Q. J. R. Meteorol. Soc., 135:1321–1335.

Smith, R.K. & S. Vogl (2008) A simple model of the hurricane boundary layer revisited. The Quarterly Journal of the Royal Meteorological Society, 134: 337–351.

Stramma, R.S., P. Cornillon, & J.F. Price (1986) Satellite observation of sea surface cooling by hurricanes. J. Geophys. Res., 91: 5031–5035.

Wang, Y., L.F. Zhang, J. Peng & S.S. Liu (2018) Mesoscale horizontal kinetic energy spectra of a tropical cyclone. Journal of the Atmospheric Sciences, 75: 3579–3596.

Wang, Y., L.F. Zhang, J. Peng, Y. Zhang & T.F. WEI (2019) Investigation of mesoscale available potential energy spectra in a simulated tropical cyclone. Journal of Meteorological Research, 33: 1098–1112.

Wang, Z. (2012) Thermodynamic aspects of tropical cyclone formation. J. Atmos. Sci., 69: 2433–2451.

Williams, G.J. (2015) The effects of vortex structure and vortex translation on the tropical cyclone boundary layer wind field. J. Adv. Model. Earth Syst., 7:188–214.

Wood, K.M., & E.A. Ritchie (2015) A definition for rapid weakening of North Atlantic and eastern North Pacific tropical cyclones. Geophys. Res. Lett., 42: 10091–10097.

Xu, L. & Gao,G. (2005). Features of typhoon in recent 50 years and annual disaster assessment. Meteorological Monthly, 31: 41–45.

Yu, H. & H.J. Kwon (2005) Effect of TC-trough interaction on the intensity change of two typhoons. Wea. Forecasting, 20: 199–211.

Zagrodnik, J.P. & H. Jiang (2014) Rainfall, convection, and latent heating distributions in rapidly intensifying tropical cyclone. J. Atmos. Sci., 71: 2789–2809.

Zhang, F. & D. Tao (2013) Effects of vertical wind shear on the predictability of tropical cyclones. Journal of Advances in Modeling Earth Systems, 7:1534–1553.

Zhang, F. & Weng, Y. (2015) Predicting hurricane intensity and associated hazards: A five-year real-time forecast experiment with assimilation of airborne Doppler radar observations. Bull. Am. Meteor. Soc, 96: 25–32.

Zhao, H., X. Duan, G.B. Raga & P.J. Klotzbach (2018) Changes in characteristics of rapidly intensifying western North Pacific tropical cyclones related to climate regime shifts. J. Climate, 31: 8163–8179.

Zhuge, X., J. Ming & Y. Wang (2015) Reassessing the use of inner-core hot towers to predict tropical cyclone rapid intensification. Wea. Forecasting, 30: 1265–1279.

Advances in Applied Chemistry and Industrial Catalysis – Saikia (Ed.)

Research on scenario construction and dynamic deduction model of major hazardous chemicals disaster based on stochastic petri net

Xunqing Wang*, Kun Liu** & Yujie Zhou***
School of Public Administration, Shandong Technology and Business University, Yantai Shandong, China

ABSTRACT: Major hazardous chemical accidents have unconventional characteristics such as sudden destruction, complexity of evolution, and unpredictability. The traditional 'prediction response' decision-making model is difficult to effectively deal with, so it is urgent to change to the 'scenario response' emergency mode. Based on the theory of scenario analysis and structural description, this paper constructs the scenario of the evolution process of hazardous chemical accidents from the logical structure dimension of 'scenario state(s)-element attribute(I)-emergency response (R)', and analyzes the dynamic causal relationship among the scenario elements. Secondly, based on the scenario construction, random Petri net are used according to the isomorphic relationship between stochastic Petri net and Markov chain, the stochastic Petri net model and equivalent Markov chain model of hazardous chemical disaster scenario evolution are constructed, and the stable state probability of the system is calculated. Finally, taking Qingdao '11·22' oil pipeline leakage and explosion accident as an example, Markov chain and its related mathematical methods are used to carry out the case. This paper studies the development and evolution trend of hazardous chemical disasters and accidents, and analyzes the evolution and variation rules, so as to provide scientific support for the scenario response emergency decision-making of major hazardous chemical disasters.

1 INTRODUCTION

With the development of economy and the increase of social demand, more and more dangerous chemicals are used. However, due to the loopholes in safety supervision and production process, dangerous chemical disasters and accidents occur frequently. For example, the Tianjin Port accident in 2015 and the Jiangsu Flood accident in 2019 had a serious impact on social life. General Secretary Xi stressed that "in the face of public safety accidents, it is not only to blame, but also to sort out the common problems behind them." These serious accidents revealed that there are still some outstanding problems in the management of hazardous chemicals, such as weak safety awareness and negligence of safety supervision, and the situation of safety management of hazardous chemicals is very grim.

At present, there are many studies on the evolution of hazardous chemical disaster accidents at home and abroad. Ohtani and Kobayashi (2005) analyzed the hazardous chemical disaster accidents in Japan and pointed out that the incidence of hazardous chemical disaster accidents is closely related to the safety and professional quality of employees engaged in hazardous chemical accidents. From the analysis of the above literature, it can be seen that the prevention and reduction of dangerous chemical accidents caused by human factors have become an important problem to be solved urgently. The evolution process of hazardous chemical accidents is characterized by random uncertainty. Yuan Xiongjun et al. (2014) established an event tree model for the evolution mechanism of hazardous chemical leakage accidents based on the basic parameters of event number

Corresponding Authors: *xunqingwang@163.com, **1392695953@qq.com and ***1040793841@qq.com

DOI 10.1201/9781003308553-76

by adopting the general event tree analysis method. Sun Kang et al. (2015) constructed a directed weighted network for hazardous chemical disaster events in the chemical park based on complex network theory. The above methods, such as event tree and complex network, have discussed the evolutionary process of hazardous chemical accidents, but the evolutionary mechanism of hazardous chemical disaster accidents is not discussed from the perspective of dynamic causality among the internal driving factors of event scenarios. In the aspect of emergency decision-making technology and model of chemical disaster accident, researchers at home and abroad have done a lot of research. Bhardwaj et al. (Bhardwajjr & Chawlar 2007) pointed out that there were problems such as errors in emergency handling methods in the process of emergency handling of hazardous chemical disasters. There are also people pointed out that different methods should be adopted for different types of hazardous chemicals in hazardous chemical disaster accidents (Song 2015). Therefore, how to formulate targeted emergency response measures based on scenario analysis has become an important problem to be solved in dealing with major hazardous chemical disasters.

In research, for the evolvement of disasters and accidents and emergency decision-making research is still in the exploratory stage, focusing on the existing literature on the case studies and historical data of "prediction – in the face of the" decision model research, due to the evolution of the complexity and uncertainty for disaster accident, needs to be handled through the scenario analysis and deal with such unusual for disasters and accidents. Different from previous studies, the innovation of this paper is mainly reflected in :(1) according to the characteristics of scenario evolution of hazardous chemical disaster accidents, based on scenario analysis and structured description theory, from the logical structure dimension of "scenario state (S)-element attribute (I)-emergency response (R)"; (2) The stochastic Petri net model and the equivalent Markov chain model are used to construct the evolution of the scenario of chemical disaster accident, and the stable state probability of the system is calculated. (3) Dynamic scenario simulation was carried out by Markov chain and related mathematical methods to deduce the development and evolution of hazardous chemical disasters and accidents and analyze the evolution and change rules.

2 MAJOR HAZARDOUS CHEMICAL ACCIDENT SCENARIO CONSTRUCTION

2.1 *Construct a structured description of the situation*

The definition of an emergency is the basis of studying its related problems. Through case study, it is determined that the chemical disaster accident is formed by internal and external factors. In the face of complex event description, the set is used to structurally construct the evolution scenario of dangerous chemical disasters and accidents. Therefore, from the logical structure dimension of "scenario state (S)- element attribute (I)- emergency response (R)", the scenario construction of the evolution process of hazardous chemical disaster accident was carried out. The situation state is the initial situation of the emergency. Element attribute is the key element, subordinate element and environmental element that play an important role in the evolution of the situation. Emergency response refers to the emergency intervention measures for specific situations. Finally, the scenario is constructed as follows: scenario state, key factors, subordinate factors, environmental factors and emergency response. Expression is as follows: for disaster accident scene = {{scene state (S)}, {key elements (KI)}, {subordinate elements (DI)}, {environmental elements (EI)}, {emergency response (R)}}:

$$
\begin{aligned}
S &= State \\
KI &= KeyIngredient \\
SI &= SencodaryIngredient \\
EI &= EnvironmentalIngredient \\
R &= Response
\end{aligned}
$$

Case Introduction: The incident started at 2:12 on November 22, 2013. Weifang Oil Transportation Department's dispatching center found that the outbound pressure of Huangdao oil depot of East Yellow River pipeline dropped, and judged that the pipeline leaked after it was confirmed that there was no operation factor in Huangdao oil depot. Enterprises and government departments took measures, but at 10:25 am, an explosion occurred while working at the spill site, and caused the drainage culverts and the burning of spilled oil at sea. From the on-site enterprise headquarters to municipal or even provincial headquarters, from the enterprise's general production accident to a particularly serious accident.

Taking the "11·22" East Yellow Oil pipeline leakage explosion accident of Sinopec in Qingdao, Shandong Province in 2013 as an example, the above structured description framework was used to construct scenario description: S = {pipeline oil spill (S1), pipeline burst into flames (S2), ground ice fire (S3), marine pollution (S4)}; KI = {pipeline corrosion is serious (kI1), pipeline complex (KI2), illegal use of non-explosion-proof electric apparatus (KI3)}; SI = {pipeline hidden trouble investigation is not thorough (SI1), leaking oil into the drainage culvert (SI2), oil spill recoil road (SI3), leakage area not set the alert (SI4)}; EI = {pipeline and urban drainage pipeline overlapping (EI1), Jiaozhou bay tidal flow backward of crude oil (EI2), marine hydrology environment (EI3)}; R = {turn off valve (R1), put out the fire (R2), notification and evacuate people (R3), with the nozzle block the leakage of crude oil (R4), the leaked area set up effective alert and containment (R5), use high-spray vehicle, vehicle-mounted foam cannon, etc. to put out the fire (R6), isolate the oil boom (R7), and add cleaning agent (R8)}

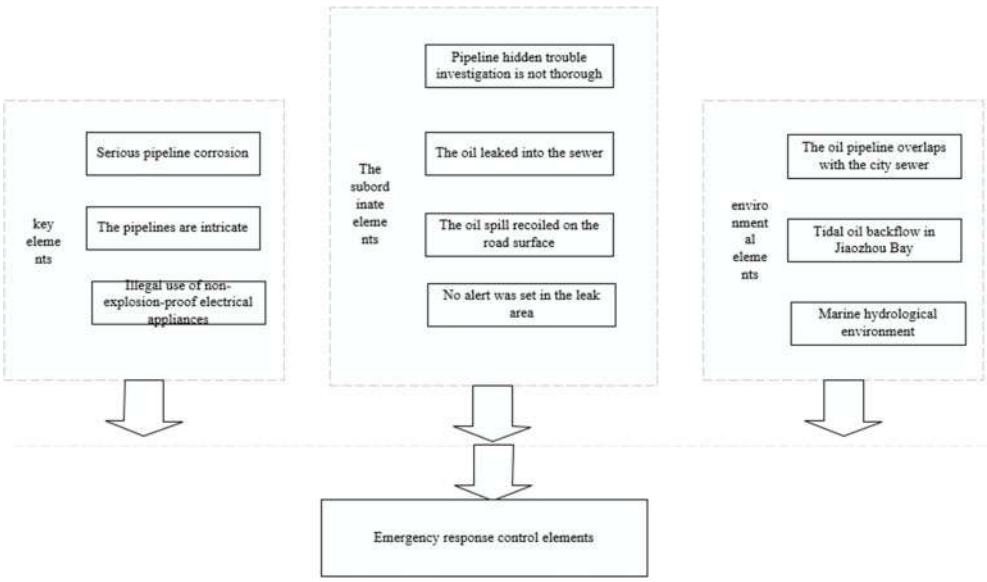

Figure 1. Scene elements of fire and explosion accident caused by crude oil leakage of Qingdao 11.22 oil pipeline.

Through scenario analysis, structured thought and collective form, a structured description framework is studied on the evolution scenario construction of hazardous chemical disaster accidents, as shown in Figure 1.

3 A STOCHASTIC PETRI NET MODEL FOR MAJOR CHEMICAL ACCIDENT SCENARIOS

Taking the "11.22" oil leakage fire and explosion accident of Qingdao oil pipeline as an example, the structural analysis of the hazardous chemical disaster accident scenario is constructed, and it is found that the evolution process of the hazardous chemical disaster fire and explosion scenario is a complex system. Stochastic Petri Net (SPN) is a graphical tool suitable for modeling, simulation and analysis of complex systems (Lin, 2000).

3.1 *steps of stochastic Petri net modeling*

The steps of stochastic Petri net modeling are as follows: Step1: establish the SPN model and associate the time delay with the corresponding changes; Step2: Analyze the reachable graph R(m) of SPN model. Each arc in the graph is marked with the average implementation rate corresponding to the arc, the isomorphic Markov Chain (MC) is constructed, the reachable graph is calculated and the model is determined to be active and bounded. Denoting all identifiers or states as m_1, m_2, …, m_n, n is the standard start total.; Step3: Analyze Markov chain. In a Markov chain isomorphic to SPN, where all standard initial sets are denoted as $[M_0>$, then $[M_0>$ have n elements, and the Markov chain has n states. Define a n by n transfer matrix $Q=[q_{ij}]$, $i \geq 1, j \leq n$.

When i ≠ j,

$$\begin{aligned} &if\ \exists t_k \in T : M_i[t_k > M_j\ \ then \\ &\quad q_{ij} = d(1-e^{-\lambda_k \tau})/d\tau\Big|_{\tau=0} = \lambda_k \\ &\quad else\ \ q_{ij} = 0 \end{aligned}$$

When i = j,

$$\begin{aligned} q_{ij} &= d\prod_k (1-(1-e^{-\lambda_k \tau}))/\ d\tau|_{\tau=0} \\ &= d(e^{-\tau}\sum_k \lambda_k))/d\tau\ |_{\tau=0} \\ &= -\sum_k \lambda_k \end{aligned}$$

Among it, $k \neq i$ and $\exists M' \in [M_0 > \exists T : M_i[t_k > M'$, λ_k is the rate of t_k. $M_i[t_k >$ means that change t_k has the right to occur in M_i, $M_i[t_k > M_j$ means that change t_k occurs new M_j in M_i. The steady-state probability is obtained by solving the following linear matrix equation, denoted as $P=(P(m_1), P(m_2), \ldots, P(m_n))$, and can be obtained according to the correlation theorem of Markov chain stationary distribution and The Chipman-Kolmogorov equation:

$$\begin{cases} P\Gamma = 0 \\ \sum_{i=1}^{n} P(m_i) = 1 \end{cases}$$

Step4: After the stability probability is obtained, the performance of the scene system of fire and explosion of dangerous chemical disasters described by SPN is analyzed.

3.2 *Stochastic petri net model of major hazardous chemical accidents*

Taking the "11.22" oil pipeline fire and explosion accident in Qingdao as an example, a structural framework was constructed based on the above hazardous chemical disaster scenarios, and the corresponding stochastic Petri net model was established according to the steps in Section 3.1, as shown in Figure 2. The model shown in Figure 2 consists of 15 libraries and 9 transitions:

In Figure 2, each depot and change set are respectively represented: (1) the finite set of depot P,

P1: pipeline transporting hazardous chemicals (crude oil); P2: pipeline corrosion is serious; P3: The oil pipelines are intricate; P4: Pipeline identification confusion; P5: Illegal use of non-explosion-proof electrical appliances; P6: Leakage of crude oil into drainage culverts; P7: Oil

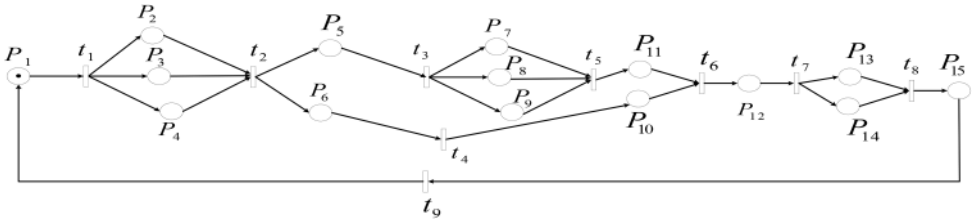

Figure 2. SPN model diagram of hazardous chemical accident scenario evolution.

pipeline explosion; P8: oil pollution sea deflagration; P9: Ground flowing crude oil fire; P10: Oil is no longer leaking; P11: The open fire is extinguished; P12: The oil spill was cleaned up; P13: Restoring order at the site of the explosion; P14: treatment of polluted waters; P15: The incident subsided. (2) Change of the limited set t.

t1: pipeline hidden trouble investigation is not thorough; t2: Oil spill; t3: generate impact sparks; t4: Close the valve and use the dc water gun to intercept the leaking crude oil; t5: the use of vehicle-mounted foam, high spraying vehicles, etc.; t6: containment boom isolation; t7: Add cleaning agent; t8: End of fire fighting and rescue; t9: Handling the aftermath.

The initial identification of the random Petri net is M1 = (1, 0, 0, 0, 0, 0, 0, 0, 0, 0, 0,0,0,0,0), indicating that P1 has a Token. Therefore, the reachable set triggered by different transitions can be obtained as follows:

$$M_1 = (1,0,0,0,0,0,0,0,0,0,0,0,0,0,0);$$

$$M_2 = (0,1,1,1,0,0,0,0,0,0,0,0,0,0,0);$$

$$M_3 = (0,0,0,0,1,0,0,0,0,0,0,0,0,0,0);$$

$$M_4 = (0,0,0,0,0,1,0,0,0,0,0,0,0,0,0);$$

$$M_5 = (0,0,0,0,0,0,1,1,1,0,0,0,0,0,0);$$

$$M_6 = (0,0,0,0,0,0,0,0,0,1,1,0,0,0,0);$$

$$M_7 = (0,0,0,0,0,0,0,0,0,0,0,1,0,0,0);$$

$$M_8 = (0,0,0,0,0,0,0,0,0,0,0,0,1,1,0);$$

$$M_9 = (0,0,0,0,0,0,0,0,0,0,0,0,0,0,1).$$

Nine states based on stochastic Petri net model M_1, M_2, M_3, M_4,..., M_9 can obtain the isomorphic Markov chain, as shown in Figure 3.

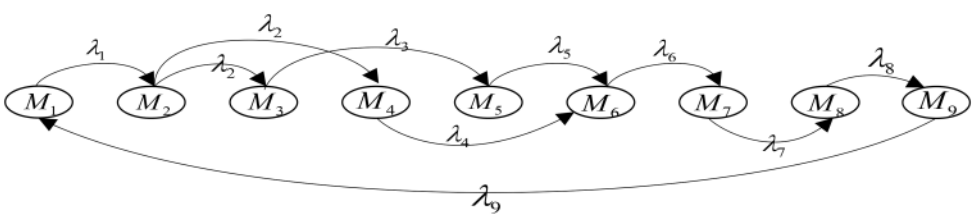

Figure 3. Markov chain for scenario evolution model of hazardous chemical disaster and accident.

Is set p(M_i), (i=1,2,…,9) as the state Mi probability under stable state of the stochastic Petri net model in the evolution process of chemical disaster accidents. Thus, the following relationship between state probabilities can be obtained:

$$\begin{cases} \lambda_1 p(M_1) = \lambda_9 p(M_9) \\ \lambda_2 p(M_2) + \lambda_2 p(M_2) = \lambda_1 p(M_1) \\ \lambda_3 p(M_3) = \lambda_2 p(M_2) \\ \lambda_4 p(M_4) = \lambda_2 p(M_2) \\ \lambda_5 p(M_5) = \lambda_3 p(M_3) \\ \lambda_6 p(M_6) = \lambda_4 p(M_4) + \lambda_5 p(M_5) \\ \lambda_7 p(M_7) = \lambda_6 p(M_6) \\ \lambda_8 p(M_8) = \lambda_7 p(M_7) \\ \lambda_9 p(M_9) = \lambda_8 p(M_8) \\ \sum_{i=1}^{9} p(M_i) = 1 \end{cases}$$

By solving the above linear equations, the steady-state probability of hazardous chemical disaster accidents in a possible state can be obtained. From the steady-state probability, it can be found that how to change some links to reduce the harmfulness of hazardous chemical disaster accidents has important practical significance for improving the emergency decision-making efficiency of hazardous chemical disaster accidents.

4 SCENARIO DYNAMIC INFERENCE SIMULATION ANALYSIS

Taking the "11.22" oil pipeline explosion accident in Qingdao as an example, the evolution simulation is carried out, this paper assumes the average implementation rate of change of change t_1 is $\lambda_1 = 3$; the average implementation rate of change of change $t_2, \ldots, t_9$ respectively is $\lambda_2 = 2, \lambda_3 = 3, \lambda_4 = 4, \lambda_5 = 2, \lambda_6 = 1, \lambda_7 = 2, \lambda_8 = 4, \lambda_9 = 1$, scenario inference simulation is carried out by changing the average implementation rate of change λ_1, λ_5.

Scenario 1 Incomplete (change λ_1) changes in pipeline risk identification.

The model assumes that $\lambda_2, \ldots, \lambda_{11}$ is constant. Through change λ_1, the evolution situation can be obtained as shown in Figure 4.

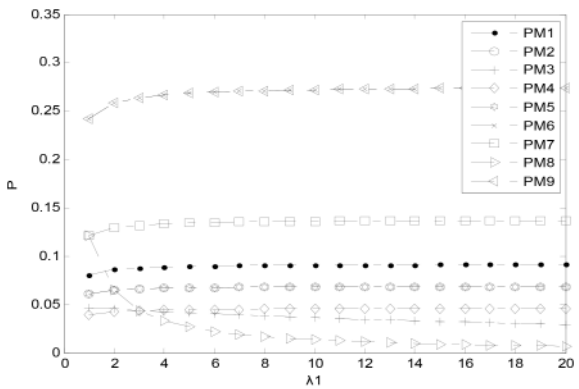

Figure 4. Steady state probability of fire and explosion of hazardous chemicals under λ_1 change.

As can be seen from Figure. 4, when the value changes from 1 to 20, that is, the problem of incomplete investigation of hidden dangers of oil pipelines becomes increasingly prominent, the probability of oil leakage and oil explosion increases significantly, and the probability of completion of fire extinguishing and rescue also decreases, indicating that the difficulty of rescue increases

with the severity of hidden dangers of pipelines. In order to avoid the occurrence of oil pipeline explosion, it is necessary to strengthen the supervision of oil pipeline. First of all, enterprises should develop strict inspection systems and procedures to ensure that no oil leakage occurs in the crude oil pipeline. Secondly, the government departments to strengthen supervision, from the origin to prevent the occurrence of special major explosion accidents.

Scenario 2 Changes in the extinguishing degree (change λ_5) of fire areas such as oil pipeline fire, oil-polluted sea fire and road fire, etc. The model assumes $\lambda_1, \ldots, \lambda_4, \lambda_6, \ldots, \lambda_{11}$ is constant, the evolution can be obtained through the change λ_5, as shown in Figure 5.

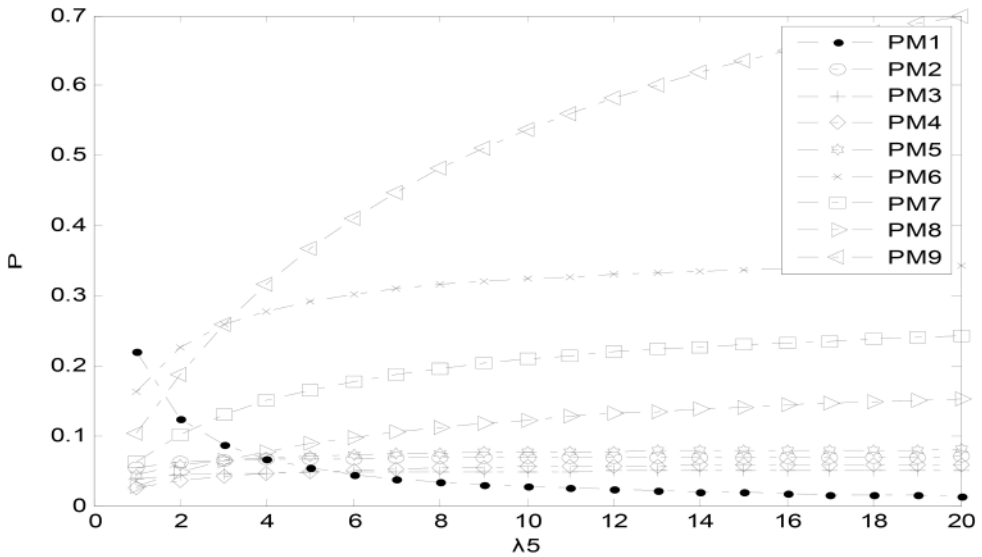

Figure 5. Steady state probability of fire and explosion of hazardous chemicals under λ_5 change.

As can be seen from Figure 5, when the change from 1 to 20, namely, with the increase of the extinguish degree of fire, the probability of oil leakage interception and the probability of oil leakage being cleaned up obviously increases. As the fire is put out, more areas can be cleaned up quickly, allowing booms to be isolated and cleaning agents added to contain the spill more quickly. In the initial stage of fire, the enterprise should choose the right extinguishing agent to extinguish the fire quickly and take various measures to prevent oil leakage. Government departments actively organize professional rescue teams for dangerous chemical fire accidents and formulate effective rescue plans.

5 CONCLUSION

Based on the "scenario-response" research perspective, this paper studies the scenario construction and dynamic deduction of major hazardous chemical disaster accident: 1) Based on the scenario analysis and structured description theory, the evolution process of hazardous chemical disaster accident is described from the logical structure dimension of "scenario state (S)- element attribute (I)- emergency response (R)". On this basis, the construction expression of hazardous chemical disaster accident scenario was abstracted to collective representation, and the dynamic causal relationship among the scenario elements was further discussed, and the evolution process of hazardous chemical accident scenario was constructed. 2) The stochastic Petri net model and equivalent Markov chain model for the evolution of chemical disaster accident scenarios are constructed by

using the modeling and analysis method based on stochastic Petri net, according to the isomorphism relation between stochastic Petri net and Markov chain, and the stable state probability of the system is calculated. 3) Taking the "11·22" oil pipeline leakage and explosion accident in Qingdao as an example, the scenarios are deduced and simulated by Markov chain and related mathematical methods, and different evolution states are discussed to study the development and evolution trend of hazardous chemical disaster accidents, and the evolution and change rules are analyzed. Based on the result of scenario deduction, it provides theoretical support for "scenario-response" emergency decision of major chemical disaster accident.

ACKNOWLEDGMENTS

The authors sincerely thank the editor and the anonymous reviewers for their constructive and important comments on the paper. Xunqing Wang's research is partially supported by National Natural Science Foundation of China, grant no.71603109, Natural Science Foundation of Shandong Province, grant no. ZR2021MG025.

REFERENCES

Bhardwajjr, Chawlar Sharmark. Chemical disaster management: Current status and perspectives [J]. Journal of Scientific and Industrial Research, 2007, 66(2): 110.

Lin Chuang. Stochastic Petri Net and System Performance Evaluation[M]. BeiJing: Tsinghua University Press, 2000, 28–35.

Ohtanih, Kobayashim. Statistical analysis of dangerous goods accidents in Japan[J]. Safety Science, 2005, 43(5): 287–297.

Song Yanlin. Disaster handling of hazardous chemicals[J]. Chemical Enterprise Management, 2015(5): 257–257.

Sun Kang, Zhou Wu, CHAI Ruirui. Network Evolution Model of Hazardous Chemical Accident with Domino Effect in Chemical Industry Park[J]. Journal of Electronic Science and Technology (Social Sciences Edition), 2015, 17(5).

Yuan Xiongjun, Bi Haipu, Zhou Ning, et al. Study on Evolution Mechanism for Hazardous Chemical Leakage Accident[J].Industrial Safety and Environmental Protection, 2014, 40(2): 21–24.

Advances in Applied Chemistry and Industrial Catalysis – Saikia (Ed.)

Research and application of instrument and equipment health evaluation method considering state evolution process

Feifeng Wang* & Haoze Zhuo
Electric Power Research Institute of Guangxi Power Grid Co., Ltd., Nanning, P.R. China

Dandan Yan
Guangxi Power Grid Co., Ltd., Nanning, P.R. China

Bin Wang & Tailin Li
Electric Power Research Institute of Guangxi Power Grid Co., Ltd., Nanning, P.R. China

ABSTRACT: At present, in the process of equipment testing, most of the testing institutions carry out a single discrete test. Which cannot effectively compare the performance of similar products of different manufacturers. It cannot achieve the goal of optimizing the categories of instruments and equipment. The existing testing mode is difficult to effectively find the deterioration trend of the performance of a single instrument and equipment. The performance has significantly deteriorated equipment is still in normal use and sent to check according to the cycle. Lead to misjudgment of the performance of the device under test. In view of the present situation, this paper establishes the instrument equipment deterioration model by Gauss Poisson process according to the actual requirements of instrument and equipment health management and evaluation. The partial observability of the Health Status Information and the time continuity of the state evolution process of the instrument and equipment are considered respectively. The Gauss Poisson health status degradation process model is used to classify the health status of the instrument and equipment. That can be used to analyze the stability and reliability of instruments produced by different manufacturers.

1 INTRODUCTION

With the rapid development of power system, more and more testing instruments and equipment are put into use, and the testing workload of instruments and equipment is increasing year by year. At present, most measurement and testing institutions carry out discrete testing in the process of instrument and equipment testing, which cannot effectively compare the performance of similar products from different manufacturers, so it is difficult to achieve the goal of optimizing the category of instruments and equipment. Moreover, the existing detection mode is difficult to effectively find the performance degradation trend of a single instrument and equipment. Although the detection is qualified, the instruments and equipment with obvious performance degradation are still in normal use and submitted for inspection according to the cycle, resulting in the misjudgment of the performance of the tested equipment. Therefore, the research on the health status evaluation method of instruments and equipment needs to be carried out urgently (Peng et al. 2020; Wang et al. 2020).

How to establish the life distribution model of instruments and equipment and evaluate the performance parameters of power components is a very important topic. This problem must be solved before reliability testing. Wei-bull distribution model is one of the traditional effective methods,

*Corresponding Author: wang_ff.sy@gx.csg.cn

DOI 10.1201/9781003308553-77

which can establish the life distribution of instrument components (Dey et al. 2017), which can be used in fields such as inertial confinement fusion facilities. Under normal pressure conditions, the collection of physical quantity degradation data comes from repeated tests in reliability acceptance test, and the degradation data obtained from one type of power components are fitted by curve fitting in the sense of least square to predict service life. Based on these predicted life data, the parameters of Wei-bull distribution can be evaluated.

According to the traditional method, we study the reliability of insulation resistance meter. However, when comparing our own resistance degradation data with similar data from published references, we find that there are some problems in applying this method. For example, the information provided by some atypical data has not been thoroughly analyzed. We believe that the information provided by abnormal data is more important than that provided by normal data. Any technical method to ignore abnormal data is incomplete. In addition, this kind of resistance box is very expensive, and the normal reliability test will affect the service life of the measured resistance; Therefore, the test cost is very high. In this paper, a new model, Gauss Poisson joint distribution model, is proposed to analyze the health evaluation of systems or units. Using this model, we can analyze the normal or abnormal information provided by resistance test, and save cost by reducing life test.

2 FRAMEWORK OF INSTRUMENT AND EQUIPMENT HEALTH MANAGEMENT SYSTEM

At present, the health status of instruments and equipment is mainly judged according to the error value specified in the verification regulations or calibration specifications. If the error value crosses the line, it is judged as a fault, which belongs to the binary judgment of success or failure. The result of this judgment method is simple, which is difficult to effectively reflect the law of the development and change of the health state of instruments and equipment, cannot reflect the development trend of the health state of instruments and equipment, can not judge and identify the deterioration of the operation trend and give early warning of impending faults, and it is difficult to effectively judge the health state of instruments and equipment. Health status assessment expands the status of instruments and equipment from binary to multivariate, covering all stages of its life cycle, and can more accurately reflect the development law of instrument and equipment faults from trend cracking to actual faults.

The purpose of instrument and equipment health management is to evaluate and judge the health conditions related to instruments and equipment through information collection, health status evaluation and fault hidden danger diagnosis of instruments and equipment, so as to improve the reliability and accuracy of instruments and equipment. Among them, the evaluation of health status is the core of the whole health management (Cheng 2008; Li et al. 2011; Xiao 2008; Zhao et al. 2020). The framework of instrument and equipment health management system is shown in Figure 1. It can be seen from the figure that the health status evaluation of instrument and

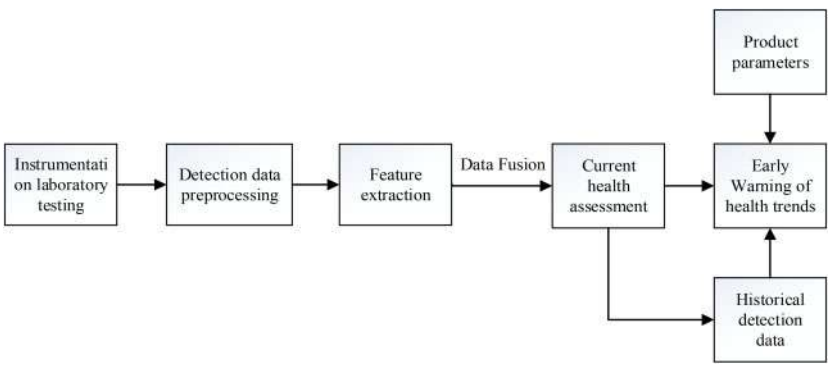

Figure 1. Instrument and equipment health management system framework.

equipment is the most important content of instrument and equipment health management. Proper health assessment results can effectively ensure the stable and reliable operation of instruments and equipment.

3 STUDY ON THE EVOLUTION PROCESS OF HEALTH STATUS OF INSTRUMENTS AND EQUIPMENT

3.1 *Division of health status of instruments and equipment*

The reasonable division of the health status of instruments and equipment is the premise for the implementation of health management and research and judgment in instrument and equipment testing. Due to the simplification of the normal fault state description used in the current instrument and equipment testing results, the health status evaluation model of comprehensive quantitative description and qualitative description is used to evaluate and describe the operation status of instruments and equipment, The health score h is used to characterize the health state S of instruments and equipment. When H is in [1,0.9], [0.9,0.7), [0.7,0.5), [0.5,0.3), [0.3,0), it indicates that the health status of the instrument and equipment is "healthy", "good", "general", "sub-health" and "fault", and it is recorded as S=1, S=2, S=3, S=4 and S=5 respectively. The division of health status and the corresponding relationship between health values are shown in Figure 2.

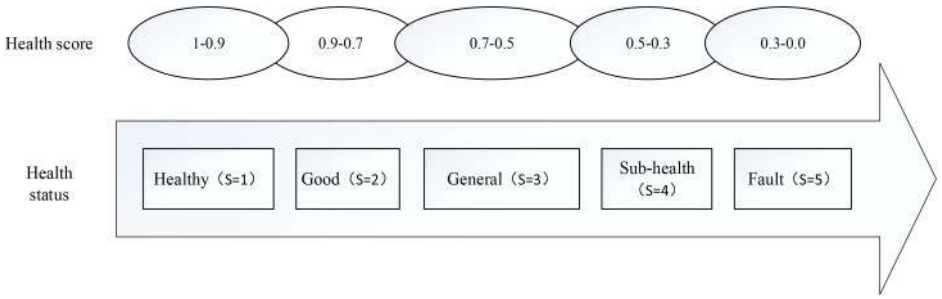

Figure 2. Division of Health Status and corresponding relationship between health values.

3.2 *Deterioration process of health status of instruments and equipment*

In order to more accurately reflect the simultaneous continuous deterioration factors (such as natural aging of components) and sudden deterioration factors (such as collision and moisture) of instruments and equipment, the Gauss Poisson composite process is used to describe the deterioration process of instruments and equipment, and the cracking process of instruments and equipment is discretized into several healthy states (Kimiaki 2009; Sun 2004).

Define the health state set $s = \{1,2,3,4,5\}$ of instruments and equipment as a continuous update process, then the instruments and equipment must be in one of the above five health states at any time in its whole life cycle. Under the condition of no maintenance behavior intervention, the instrument and equipment can only transfer from good state to poor state. Therefore, with the increase of service time, the function failure of the instrument and equipment will eventually occur, that is, the instrument and equipment will have a continuous deterioration process that gradually accumulates with the increase of time. At the same time, in the process of use, because the instruments and equipment will inevitably suffer from random stress, the instruments and equipment in good health also have functional failure, that is, they may also have sudden deterioration during the service period.

To reflect the continuous deterioration and sudden deterioration of instruments and equipment at the same time.

Let $X(t)$ be the natural continuous deterioration at time t. $X(t)$ obeys Gaussian distribution, with mean μ and variance σ Let $Y(t)$ be the amount of paroxysmal deterioration occurring at t up to time. $Y(t)$ obeys Poisson distribution and its mean value is λ. The numerical loss per paroxysmal deterioration is β. C_U is the initial value and is the value at 100% of the initial value.

Set $C(t)$ as the physical quantity value of instrument components at time t. $r(t)$ is the reliability at time t

$$r(t) = \Pr\{C(t) > C_L\} = 1 - \Pr\{C(t) \le C_L\} \tag{1}$$

Let $\Delta C_1(t)$ be the natural loss of the physical quantity value of the instrument component up to time t

$$\Delta C_1(t) = \sum_{i=0}^{t} X_i(t) \tag{2}$$

Let $\Delta C_2(t)$ be the paroxysmal deterioration loss of instrument components at time t

$$\Delta C_2 = \beta \cdot Y(t) \tag{3}$$

From (1)–(3), we can deduce

$$\begin{aligned} &\Pr\{C(t) \le C_L\} \\ &= \Pr\{C_u - C_1(t) - C_2(t)\} \\ &= \Pr\{\sum_{i=0}^{t} X_i(t) + \beta \cdot Y(t) \ge C_u - C_L\} \end{aligned} \tag{4}$$

From the total probability formula, we can transform equation (4)

$$\begin{aligned} &\Pr\{C(t) \le C_L\} \\ &= \sum_{K=0}^{+\infty} \Pr\left\{\sum_{i=0}^{t} X_i(t) + \beta \cdot Y(t) \ge C_u - C_L | Y(t) = k\right\} \end{aligned} \tag{5}$$

So, we can know

$$\begin{aligned} &\Pr\{C(t) \le C_L\} \\ &= \sum_{k=0}^{+\infty} \{\sum_{i=0}^{t} X_i(t) + \beta \cdot k < C_U - C_L\} \cdot \Pr\{Y(t) = k\} \\ &= \sum_{k=0}^{+\infty} \Pr\{Y(t) = k\} \\ &- \sum_{k=0}^{+\infty} \Pr\left\{\sum_{i=0}^{t} X_i(t) + \beta \cdot k < C_U - C_L\right\} \cdot \Pr\{Y(t) = k\} = 1 \\ &- \sum_{k=0}^{+\infty} \Phi\left(\frac{C_U - C_L - k \cdot \beta - \mu t}{\sqrt{t}\sigma}\right) \cdot \frac{(\lambda t)^k}{k!} e^{-\lambda t} \end{aligned} \tag{6}$$

Where $\Phi(\cdot)$ is the standard normal cumulative distribution function.

From (1) and (6), we infer the reliability of instrument components at time.

$$r(t) = \sum_{k=0}^{+\infty} \Phi\left(\frac{C_U - C_L - k \cdot \beta - \mu t}{\sqrt{t}\sigma}\right) \cdot \frac{(\lambda t)^k}{k!} e^{-\lambda t} \tag{7}$$

C_U and C_L are given values and μ, σ, λ and β are parameters.

Define the deterioration amount $Z(\Delta t)$ of the health score of the instrument and equipment in unit time Δt, including natural deterioration amount $X(\Delta t)$ and sudden deterioration amount $\beta Y(\Delta t)$, and the deterioration process of the equipment follows the Gauss Poisson process:

$$Z(\Delta t) = X(\Delta t) + \beta Y(\Delta t) \tag{8}$$

Where: $X(\Delta t)$ is the natural deterioration quantity and follows the normal distribution, i.e. $X(\Delta t) \sim N\left(\mu, \sigma^2\right)$; $\beta Y(\Delta t)$ is the burst degradation amount in unit time Δt,β is the burst degradation amount each time, $Y(\Delta t)$ is the burst degradation times, and obeys Poisson distribution, i.e. $Y(\Delta t) \sim Poisson\ (\lambda)$.

Let the initial health score of the instrument and equipment be 1, after working time t, the natural deterioration amount of the instrument and equipment is $X(t)$, and the number of sudden deterioration times is $Y(t)$, then the health score of the equipment at this time is:

$$H(t) = 1 - \sum_{t=0}^{t} Z\ (t) = 1 - \sum_{t=0}^{t} (X\ (t) + \beta Y\ (t)) \tag{9}$$

Formula (9) the parameters of the health state process of instruments and equipment can be estimated by the error data detected periodically. Let $H_N (N = 1, 2 \cdots n)$ be a group of historical test data of health score, then the 1st ~4th order central moments of health score H of instruments and equipment shown in equation (2) are respectively:

$$E(H) = \mu + \lambda\beta \tag{10}$$

$$D(H) = \sigma^2 + \lambda\beta^2 \tag{11}$$

$$E(H - EH)^3 = \beta^3\lambda \tag{12}$$

$$E(H - EH)^4 = 3\sigma^2 + 3\beta^4\lambda^2 + \beta^4\lambda + 6\sigma^2\beta^2\lambda \tag{13}$$

The 1st~4th order central moments can also be obtained by counting the historical value $H_1, H_2, \ldots H_{\mathrm{n}}$ of the health score of instruments and equipment, and defining the 1st ~ 4th order central moments of H as a_1, a_2, a_3, a_4 respectively, then:

$$a_1 = E(H) = \frac{1}{n}\sum_{N=1}^{n} H_N \tag{14}$$

$$a_2 = D(H) = \frac{1}{n}\sum_{N=1}^{n} (H_N - a_1)^2 \tag{15}$$

$$a_3 = E(H - EH)^3 = \frac{1}{n}\sum_{N=1}^{n} (H_N - a_1)^3 \tag{16}$$

$$a_4 = E(H - EH)^4 = \frac{1}{n}\sum_{N=1}^{n} (H_N - a_1)^4 \tag{17}$$

Therefore, the parameters of the Gauss Poisson process model can be estimated by simultaneous equations (11)~(17):

$$\hat{\mu} = a_1 - \frac{a_3^3}{\left(a_4 - 3a_2^2\right)} \tag{18}$$

$$\hat{\sigma} = \sqrt{a_2 - \frac{a_3^2}{a_4 - 3a_2^2}} \tag{19}$$

$$\hat{\lambda} = \frac{a_3^4}{\left(a_4 - 3a_2^2\right)^3} \tag{20}$$

$$\hat{\beta} = \frac{a_4 - 3a_2^2}{a_3^3} \tag{21}$$

4 EXPERIMENTAL RESEARCH AND APPLICATION EXAMPLES

In order to verify the cracking model of instruments and equipment based on health status, the high resistance box verification device is selected as the standby equipment, and the data verified by its superior legal metro-logical verification unit in recent four years are selected as the research object. The repeatability test results are recorded in the table below.

Table 1. Repeatability test record of high resistance box verification device.

Verification data of superior legal metrological verification organization										
Nominal value	Allowable variation	2018	variation	2019	variation	2020	variation	2021	variation	conclusion
1MΩ	0.002MΩ	0.9990	0	0.9980	0.001	09989	0.0009	1.0002	0.0013	qualified
100MΩ	1MΩ	100.4	0.1	100.4	0	100.5	0.1	100.4	0.1	qualified
1000MΩ	20MΩ	998	4	994	4	1000	6	1002	2	qualified
10000MΩ	500MΩ	10400	400	9996	440	10400	440	10100	300	qualified

It can be seen from table 1 that the change of each gear error of the insulation resistance meter verification device is within the qualified range, but this conclusion can not truly characterize the deterioration trend and actual health state of the device. The change of the maximum gear 10000m of the device is selected as the. According to the analysis of Gauss Poisson process, the historical health scores collected at equal intervals are 0.96, 0.9996, 0.96 and 0.99, When the health values are brought into (14)~(21), it can be estimated that the parameters of the Gauss Poisson process model are $\mu = 0.0451$, $\sigma = 0.0283$, $\lambda = 0.0208$, $\beta = 0.0003$.

The natural deterioration amount $X(\Delta t)$ of the device obeys the normal distribution, i.e. $X(\Delta t) \sim N\left(\mu, \sigma^2\right)$, the first parameter here μ= 0.0226 is the mean value of the random variable subject to normal distribution, the second parameter $\sigma^2 = 8 \times 10^{-4}$ is the variance of the random variable, and the probability law of the random variable subject to normal distribution is take and μ The probability of adjacent values is large, and the value is taken away μ The farther the value, the smaller the probability; The smaller the σ, the more concentrated the distribution is near μ Nearby, the larger the σ, the more scattered the distribution.

$\beta = 0.0003$ is the amount of each burst deterioration, $Y(\Delta t)$ is the number of burst deterioration, and obeys the Poisson distribution. Therefore, the longer the cycle, the greater the total amount of burst deterioration.

In conclusion, the health degree of the device in the next verification cycle is $H = 1 - (0.0451 + 5 \times 0.0003) = 0.9535$, and its health degree is in the range of (1,0.9), i.e. health state. However, from the analysis, the overall stability of the equipment decreases, which is consistent with the decline of health value compared with the past. The reliability and health of other gears of the device can also further verify the model.

5 CONCLUSION

In this paper, a cracking model of instruments and equipment based on health state is proposed. The Gauss Poisson process model is used to describe the health state deterioration process of instruments and equipment. The model takes into account the continuous deterioration factors and sudden deterioration factors of instruments and equipment at the same time. The model is verified by combining the current and historical detection data of actual instruments and equipment. The results show that the model fully meets the actual health status of instruments and equipment, provides specific working methods and ideas for accurately evaluating the health status of instruments and equipment, ensures that all instruments and equipment submitted for inspection can continue to operate only when they are evaluated as healthy, and timely informs the inspection unit for maintenance of instruments and equipment in sub-health and fault status, so as to ensure the accurate and reliable performance of the inspected equipment.

FUND PROJECT

Science and Technology Project of Guangxi Power Grid Co., Ltd. (Research and implementation of full cycle application model of instrument and equipment inspection based on RFID Technology GXKJXM20190719)

REFERENCES

Cheng H.B. Research on health diagnosis and risk assessment method of traction power supply system considering uncertainty [D]. Chengdu: Southwest Jiaotong University, 2008.

Dey S, Sharma V K, Mesfioui M. A new extension of Weibull distribution with application to lifetime data[J]. Annals of Data Science, 2017, 4(1): 31–61.

Kimiaki SAITOA Gauss-Poisson Correspondence and the Levy Laplacian[J]. Interdisciplinary Information Sciences, 2009, 15(3): 431–440.

Li M, Han X.S., Yang M, et al. Research on concept and theory of condition based maintenance of power grid [J]. Journal of electrical engineering, 2011, 31 (34): 43–52.

Peng, L., Dang S.L., Ji Y.L., Zhang Y.W., Deng S. Health evaluation model of metrological verification equipment based on fuzzy theory [J]. Industrial metrology, 2020, 30 (06): 90–92.

Sun, Q, Zhou, J.L, Zhong Z. Guass-Poisson Joint Distribution Model for Degradation Failure[J].IEEE Transaction on plasma Science, 2004, 32(5): 1864–1868.

Wang Q.F., Li Z, Xu S.J., Chen W.W. Research on equipment health evaluation method based on fault case learning [J]. Journal of mechanical engineering, 2020, 56 (20): 28–37.

Xiao L. Research on Modeling and simulation method for maintenance decision of deteriorating system [D]. Changsha: University of Defense Science and technology, 2008.

Zhao ZS, Xu, JH, Wang L, Wang YC. Research on health degree detection of irrigation channel operation based on data mining [J]. Journal of irrigation and drainage, 2020, 39 (11): 130–136.

Advances in Applied Chemistry and Industrial Catalysis – Saikia (Ed.)

Design of solid-liquid fertilizer mixing device for petroleum-contaminated soil organic fertilizer remediation machine

S.F. Liu
College of Mechanical Engineering, China University of Petroleum, Qingdao, China
College of Mechanical and Electronic Engineering, Shandong Agricultural University, Taian, P.R. China

J.X. Wang, Z.Q. Lv, G.L. Zhang & H.X. Wang*
College of Mechanical and Electronic Engineering, Shandong Agricultural University, Taian, P.R. China

ABSTRACT: Aiming at the problems of uneven mixing and poor remediation effect of organic fertilizer remediation machines for petroleum-contaminated soil, this paper designs a solid-liquid fertilizer mixing device for petroleum-contaminated soil organic fertilizer remediation machine. According to particle size analysis of various organic particles and viscosity determination result of solid-liquid mixture, anchor-frame mixer is determined as the basic structure of solid-liquid mixing device. Orthogonal design method was used to design the best reasonable dimension parameter in order to explore solid-liquid mixing uniformity mechanism under the working condition of mixer and determine the best dimension parameter and working state parameters. The experimental results are basically consistent with numerical simulation results. Designed mixer meets the requirements of organic fertilizer solid-liquid mixed. The content of this paper refers theoretical basis for the design of a type organic fertilizer remediation machine.

1 INSTRUCTION

The production, use and transportation of petroleum will pollute the soil and seriously endanger human activities and the natural environment. Bioremediation has gradually replaced physical and chemical remediation methods with its advantages of environmental protection, cost and effect (Flavia 2004; Bao 2016; Shin 2001). Research shows that applying organic fertilizer nutrition system to petroleum-contaminated soil can effectively improve soil physical and chemical properties and degrade petroleum pollution (Akhshik et al. 2015). The development of supporting machinery for organic fertilizer remediation is also an important means to promote the remediation of petroleum-contaminated soil. At present, petroleum-contaminated soil remediation equipment is mainly physical and chemical remediation equipment. Traditional organic fertilizer applicator directly mixes soil with organic fertilizer, but the mixing effect is poor and cannot meet the requirements of petroleum- contaminated soil remediation (Arturo et al. 2017).

According to the technical requirements of petroleum-contaminated soil remediation, aiming at the problems of uneven mixing and poor remediation effect of the current mechanical fertilizer remediation machine, this paper explores the method of solid-liquid fertilizer mixing to make the organic fertilizer become a uniform suspension, so that the organic fertilizer and petroleum-contaminated soil can be fully mixed, and a better remediation effect has been achieved (Tao et al. 2011). The solid-liquid fertilizer blender, which is the key component of the fertilizer applicator, has been designed. This paper uses CFD simulation to analyze the solid-liquid two-phase flow field to study the influence of different solid-liquid mixing ratios, mixer forms, and mixing speeds on

*Corresponding Author: wanghx1899@163.com

DOI 10.1201/9781003308553-78

the fertilizer effect, optimize the fertilizer mixer, and verify the optimized solid-liquid fertilizer on the test bench Reasonable mixer design.

2 DESIGN OF SOLID-LIQUID FERTILIZER MIXER

2.1 *Type selection of solid-liquid fertilizer mixer*

Organic fertilizer is a mixture, which contains water-soluble substances and sand, vegetation, humus and other substances that are insoluble in water and have different densities. Stirring the solid-liquid mixture of organic fertilizer and water involves more complex solid-liquid two-phase fluid dynamics. According to traditional design and calculation methods, it is impossible to design a reasonable shape and size of the mixing blade, and it is impossible to calculate the critical speed and shaft power (Xu & Obbard 2003). Based on the above reasons and the measured viscosity of organic fertilizer, the selected fertilizer mixer requires that organic fertilizer and water-solid mixture should be evenly mixed after stirring and stability, and there should be no large amount of deposition medium at the bottom of the fertilizer barrel.

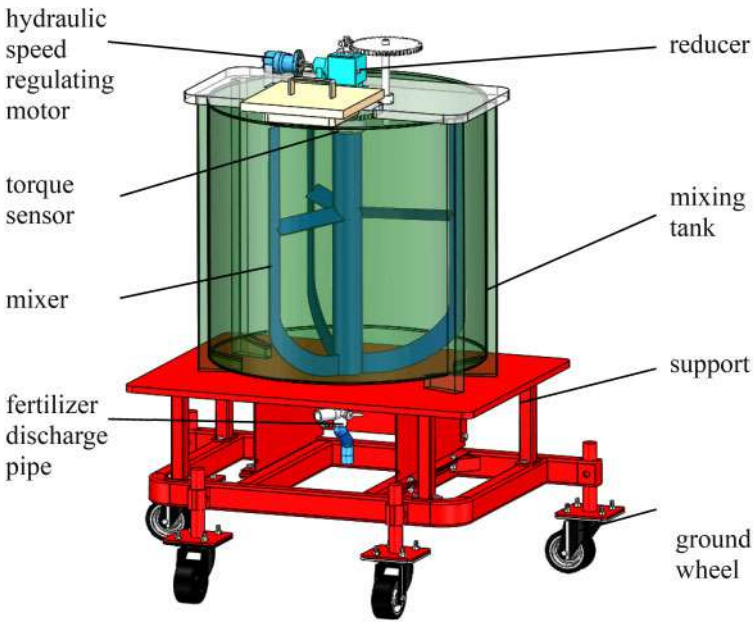

Figure 1. Structure diagram of solid-liquid fertilizer mixing device.

The installation forms of common stirring devices mainly include vertical stirring devices, eccentric stirring devices, inclined stirring devices and side stirring devices. In order to promote the settlement of low density vegetation and reduce the deposition of high density sand soil, vertical stirring device is designed (Li et al. 2021). Common mixers mainly include propeller, Brumakin, paddle, turbine, toothed, screw, screw, anchor, frame, etc. The working environment of the organic fertilizer mixer is the mixture of solid and liquid. According to the parameters of organic fertilizer particles and the viscosity data of solid-liquid mixtures with different mixing ratios, the viscosity range of the mixture is 0.31∼22.37 Pa●s. Combined with the determination and analysis of organic fertilizer parameters and the design of stirring device, and with reference to the design manual, the medium viscosity in the working environment of the mixer should be less than 105 MPa●s. Common speed n = 1∼100 r/min. The structure design of the mixer is the combination of anchor and frame which is anchor frame mixer.

In order to improve the structural strength of the mixer, a horizontal plate is welded between the two blades. In order to improve the mixing effect, install the horizontal plate inclined. Since the average density of organic fertilizer is lower than that of water, the organic fertilizer floats on the water surface at the beginning of mixing. The rotating direction of the mixer is selected along with the inclined horizontal plate, and the flow field is rotated downward in the mixing process.

2.2 *Model establishment of mixing device for solid-liquid fertilizer*

The solid-liquid fertilizer mixing device is an integrated equipment for organic fertilizer water fertilizer mixing test, which is mainly composed of mixing tank, mixer, hydraulic speed regulating motor, reducer, fertilizer discharge pipe, support, ground wheel, etc. The overall structure is shown in Figure 1.

Working principle: organic fertilizer and water are added into the mixing tank according to the test proportion, and the hydraulic speed regulating motor drives the mixer to rotate after decelerating through the gearbox according to the set speed. The torque sensor measures the torque value of the drive shaft of the stirrer. After the stirring and mixing are completed, a sample of the mixture at the sampling point is taken. Drain the solid-liquid mixture through the fertilizer pipe, and rinse the mixing tank and mixer with clean water.

3 FLOW FIELD TEST AND RESULT ANALYSIS OF FERTILIZER MIXER

3.1 *Numerical solution and boundary condition application*

According to the solid-liquid fertilizer mixing process and the experimental design speed, the boundary conditions in the fluid simulation module are added. The wall is set around the mixing tank, and the other sides are automatically generated by the software. The gravity direction y is set as the negative direction, and the rotation speed of the mixer is 15 r/min, 30 r/min, and 60 r/min in turn. Organic fertilizer belongs to small particle flow. Euler-Euler multiphase flow model is used for solid-liquid mixing. Two phase mixture model is set. The first phase is water and the second phase is organic fertilizer. The relevant parameters of organic fertilizer are obtained through the analysis of organic fertilizer particle parameters and the viscosity determination test. The turbulence model is RNG k-ε turbulence model. The constant values of RNG K-ε model are shown in Table 1. The initialization state parameter settings are shown in Table 2. The SIMPLE algorithm is used to solve the problem, and the simulation steps are set to 3000 iterations. The simulation results of 18 groups of orthogonal experiments are different, but they can converge within 3000.

Table 1. RNG k-ε model constant.

σ_k	σ_ε	$C_{\varepsilon 1}$	$C_{\varepsilon 2}$	C_μ	η_0
0.8311	0.8311	1.44	1.92	0.09	4.36

3.2 *Numerical solution and boundary condition application*

Table 2. Parameter setting.

Parameter	Value
Water density (kg/m^3)	1000
Particle diameter of organic fertilizer (mm)	0.3
Density of organic fertilizer (kg/m^3)	580
Volume fraction of second phase (%)	0.55, 0.57, 0.59
Rotating shaft speed (r/min)	15, 30, 60

Because there are many factors affecting the mixer structure, the multi-objective optimization method is used to determine the orthogonal test as the experimental optimization scheme. During the test, it is found that the main factors affecting the mixing effect are as follows: the blade quantity of the mixer A, the inclined angle of transverse plate B, the height of transverse plate C, the speed of the mixer D, the water fertilizer ratio E, the blade width F, and the mixer width G, with a total of 7 factors at 3 levels, as shown in Table 3. The L18 (3^7) orthogonal table can be obtained by looking up the orthogonal table, that is, the experiment with 7 factors and 3 levels, and 18 groups of numerical analysis schemes are carried out. Figure 2 shows the mixer with 4 blades. The inclination angle of transverse plate B, height of transverse plate C, blade width F and mixer width G of the horizontal plate are marked at the corresponding positions of the mixer.

Table 3. Test factors and levels.

Factor	Level		
Blade quantity A	2	3	4
Inclined angle of transverse plate B(°)	30	45	60
Height of transverse plate C(mm)	300	400	500
Speed D(r/min)	15	30	60
Water fertilizer ratio E	1:1	1:1.1	1:1.2
Blade width F(mm)	40	60	80
Mixer width G(mm)	220	270	320

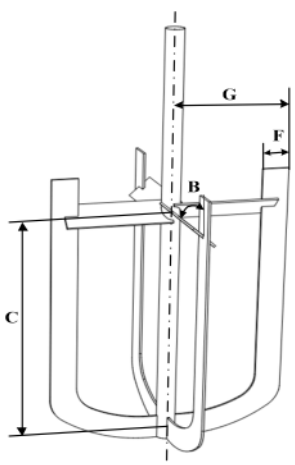

Figure 2. Position labelling of each factor on mixer.

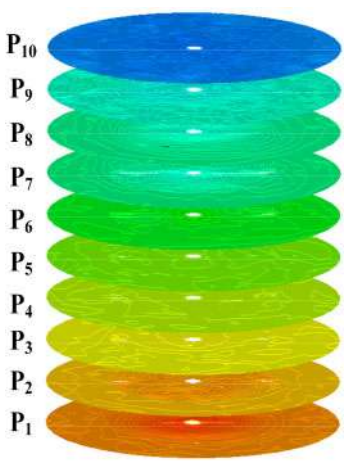

Figure 3. Schematic diagram of 10 cross-sections.

3.3 *Evaluation index of mixer*

The mixer is mainly evaluated from the mixing effect and energy consumption. Because this experiment involves different water and fertilizer mixing proportion experiments, different groups have different densities. In order to eliminate the influence of different densities on the measurement scale and dimension of average density standard deviation, the coefficient of variation is used as the evaluation index of mixing effect. The average density of 10 cross-sections of the flow field analysis results was selected to calculate the standard deviation, and the overall average density of the mixture on the standard deviation ratio was used as the variation coefficient. 10 cross-sections are shown in Figure 3. The mixer shaft power is used as the evaluation index of mixer energy consumption.

3.4 *Analysis of orthogonal test results*

According to L18 (3^7) orthogonal table, 18 groups of simulation experiments are completed, and some simulation results are shown in Figure 4. From the simulation of 10 density cross-section nephogram, it is found that the cross-section mixing of group 3 and 9 is more uniform, and the mixing uniformity of group 1 and 18 is poor.

Table 4. Range analysis and results.

									Test index	
Test number		A Blade quantity	B Inclined angle (°)	C Height of transverse plate (mm)	D Speed (r/min)	E Water fertilizer Ratio	F Blade width (mm)	G Mixer width (mm)	C Coefficient of variation (%)	P Shaft power (W)
1		2	30	500	15	1:1	40	220	3.521	0.77
2		2	45	400	30	1:1.1	60	270	0.279	13.58
3		2	60	300	60	1:1.2	80	320	0.100	169.34
4		3	30	500	30	1:1.1	80	320	0.384	30.31
5		3	45	400	60	1:1.2	40	220	0.174	62.75
6		3	60	300	15	1:1	60	270	1.241	2.40
7		4	30	500	15	1:1.2	60	320	0.028	17.47
8		4	45	300	30	1:1	80	220	0.751	8.55
9		4	60	400	60	1:1.1	40	270	0.109	87.68
10		2	30	300	60	1:1.1	60	220	0.202	44.48
11		2	45	500	15	1:1.2	80	270	2.317	3.50
12		2	60	400	30	1:1	40	320	0.444	15.62
13		3	30	400	60	1:1	80	270	0.140	86.61
14		3	45	300	15	1:1.1	40	320	0.174	22.90
15		3	60	500	30	1:1.2	60	220	0.620	12.28
16		4	30	300	30	1:1.2	40	270	0.214	24.30
17		4	45	500	60	1:1	60	320	0.116	87.11
18		4	60	400	15	1:1.1	80	220	2.507	1.96
C	$(k_{1j})_1$	1.1438	0.7482	1.1643	1.5863	1.0355	0.7727	1.2958	$\sum_{i=1}^{18} C_i = 13.321$	
	$(k_{2j})_1$	0.4555	0.6352	0.6088	0.4487	0.6092	0.4143	0.7167		
	$(k_{3j})_1$	0.6208	0.8368	0.4470	0.1402	0.5755	1.0332	0.2077	$\sum_{i=1}^{18} P_i = 691.61$	
	$(R_j)_1$	0.6883	0.2016	0.7173	1.4461	0.4600	0.2605	1.0881		
P	$(k_{1j})_2$	41.182	33.990	25.240	8.167	33.510	35.670	21.798	D3G3C3A2F2E2B2	
	$(k_{2j})_2$	36.208	33.065	44.700	17.440	33.485	29.553	36.345		
	$(k_{3j})_2$	37.845	48.213	45.328	89.662	48.273	50.045	57.125		
	$(R_j)_2$	4.974	15.148	20.088	81.495	14.788	20.492	35.327		

The range analysis of the simulation results is shown in Table 4. When the coefficient of variation is used as the evaluation index, the optimal combination of the test factors is D3G3C3A2E3F2B2, and the influence order of the factors is D > G > C > A > E > F > B. When the shaft power was taken as the evaluation index, the optimal combination of the test factors was D1G1F2C1B2E2A2, and the order of the influence of the factors is D > F > F > C > B > E > A. The results of variance analysis of coefficient of variation and shaft power are shown in Table 5 and Table 6. The optimal combination of test factors of coefficient of variation is D3G3C3A2F2E2B2, and the optimal combination of test factors of shaft power is D1G1C1F2E2B2A2. In the 75% confidence interval, the speed has a significant impact on the coefficient of variation, the higher the speed, the smaller

the coefficient of variation; in the 90% confidence interval, the speed has a significant impact on the shaft power, the higher the speed, the greater the shaft power.

According to the results of range analysis and variance analysis, the improvement of mixing effect is prior to energy consumption, the coefficient of variation is the main evaluation index, the shaft power is the secondary evaluation index, and the smaller the water fertilizer ratio is, the better. Through comprehensive optimization analysis, the optimal parameter combination of mixer is determined as D3G3C3A2F2E2B2.

4 RESULTS VALIDATION AND ANALYSIS

4.1 *The optimized results are verified by simulation*

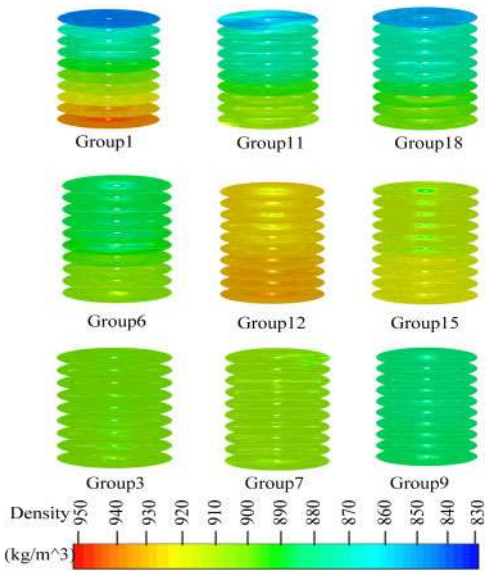

Figure 4. Comparison of simulation results.

Table 5. Variance analysis of variable coefficient.

Source of variance	Sum of squares S	Free degree F	Mean square error S/f	F-value	Critical value Fα	Significance
A	14.365	2	7.1825	0.979	$F_{0.25}(2, 14) = 1.53$	※
B	11.512	2	5.756	0.785	$F_{0.1}(2,14)=2.73$	※
C	14.664	2	7.332	1.000	$F_{0.05}(2,14)=3.74$	(※)
D	26.136	2	13.068	1.782 ※	$F_{0.025}(2,14)=4.86$	[※]
E	12.844	2	6.422	0.876		
F	13.583	2	6.7915	0.926		
G	18.375	2	9.1875	1.253		
Error	17.316	2	8.658	—	—	—
Error δ	85.343	14	7.333	—	—	—
Sum	128.795	16	—	—	—	—

According to the optimal parameter combination of mixer determined by orthogonal test, the flow field model of fertilizer mixing mixer is established. The results of mixture density of 10

cross-sections after optimization are shown in Figure 5. After calculation, the average density of 10 cross-sections is 900.73, and the shaft power is 48.14W. The density distribution of 10 cross-sections after optimization is shown in Figure 6. Compared with the previous 18 groups of simulation results, the coefficient of variation of the average density is the smallest, and the power is relatively small, which proves that the optimized mixer is conducive to improving the mixing effect and reducing energy consumption.

Table 6. Variance analysis of shaft power.

Source of Variance	Sum of Squares S	Free Degree F	Mean Square Error S/F	F-Value	Critical Value Fα	Significance
A	19494.301	2	9747.1505	1.026	$F_{0.25}(2, 14)=1.53$	※
B	21068.415	2	10534.2075	1.109	$F_{0.1}(2, 14)=2.73$	※
C	22468.402	2	11234.201	1.182	$F_{0.05}(2, 14)=3.74$	(※)
D	67111.487	2	33555.7435	3.532 ※※	$F_{0.025}(2, 14)=4.86$	[※]
E	21084.498	2	10542.249	1.11		
F	21993.742	2	10996.871	1.157		
G	26903.441	2	13451.7205	1.416		
Error	33809.263	2	16904.6315	—	—	—
Error δ	133012.799	14	9500.914	—	—	—
Sum	233933.549	16	—	—	—	—

4.2 *Test bench verification*

In order to verify the rationality of the optimization parameters obtained from the numerical simulation, the mixer is processed according to the optimization simulation results, and the organic fertilizer solid-liquid mixed fertilizer mixing device test-bench is built. The experiment was conducted in the laboratory of Shandong Agricultural University on June 13, 2021. The chicken manure compost with numerical simulation parameters was added into the mixing tank according to the water fertilizer ratio of 1:1.1.

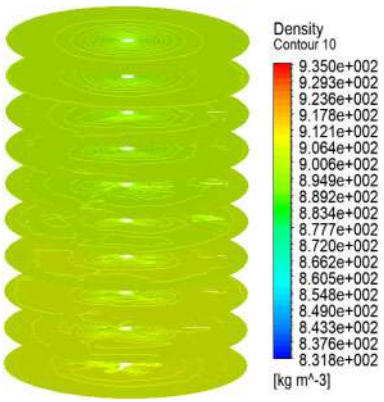

Figure 5. Simulation results after optimization.

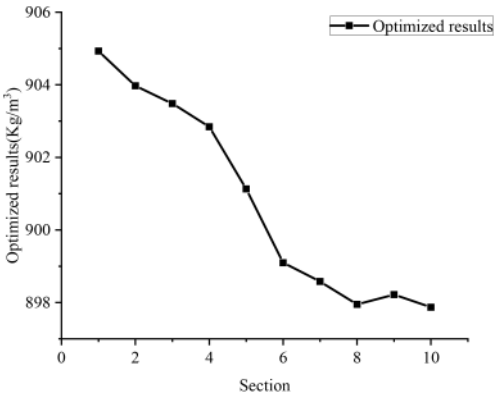

Figure 6. Density distribution results.

The hydraulic motor is driven by the hydraulic control system of the hydraulic comprehensive test-bench, and the speed of the mixer is stabilized at 60 r/min after deceleration. The torque sensor is installed on the intermediate shaft of the gearbox and mixer through the coupling, and reads the torque directly from the control display of the hydraulic comprehensive test bench. After the mixer runs smoothly for 5min, samples are vacuumed at 5 test points on the edge of 10 cross-sections

depths corresponding to the mixing liquid surface by using a coarse straw, and 50ml samples are taken each time. The mass of the samples is measured by an electronic balance to measure the density of the mixture at the test points. Sample test points is shown in Figure 7. The average density of the mixer at five test points corresponding to 10 cross-sections is calculated, and the average value obtained is the average density of the mixture at the corresponding cross-sections. Five repeated tests were carried out under the same test conditions, and the results of the five tests are shown in Figure 8.

The average values of 10 cross-sections of the five test results were calculated as the test bench experimental results, and compared with the optimized simulation values, as shown in Table 7. Results show that the cross-sections density at the upper end of the mixer is smaller than that of the simulation, indicating that the content of organic fertilizer is higher than that of the simulation. The average density of the cross-section of the mixer is higher than that of the simulation results, indicating that the organic fertilizer content is lower than that of the simulation results. Overall analysis shows that the five test results are in good agreement with the optimized simulation results, and the relative errors between the average density and power values of 10 cross-sections and the simulation results are less than 5%, so the numerical simulation results are reliable. Results shows that the best mixing effect and low power consumption can be obtained when the speed of mixer is 60 r/min, the width mixer is 320 mm, the height of transverse plate is 300 mm, the blade width is 60 mm, the water fertilizer ratio is 1:1.1, and the inclined angle of horizontal plate is 45°.

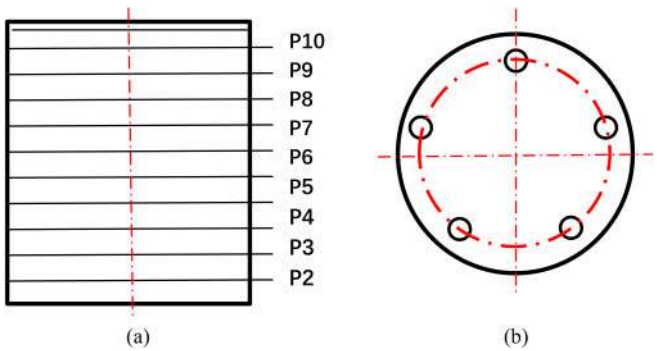

Figure 7. Schematic diagram of test points: (a) axial diagram, (b) sampling points of same section.

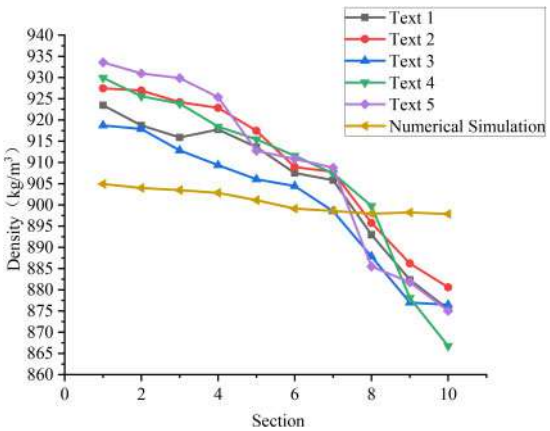

Figure 8. Test bench results.

Table 7. Comparison between experimental results and numerical simulation results.

Item	Experimental results	Numerical simulation results	Relative Error
1	926.63	904.93	2.40%
2	924.02	903.97	2.25%
3	921.33	903.48	1.98%
4	918.76	902.84	1.76%
5	913.05	901.13	1.32%
6	908.66	899.10	1.06%
7	905.66	898.58	0.79%
8	892.36	897.95	0.62%
9	881.07	898.22	1.91%
10	874.85	897.87	2.56%
Average Density (Kg/m^3)	906.64	900.73	0.65%
Power (W)	50.36	48.14	4.61%

5 CONCLUSION

In this study, we designed a solid-liquid fertilizer mixing device for petroleum-contaminated soil organic fertilizer remediation machine.

(1) Through two-phase flow numerical simulation, 18 groups of orthogonal simulation schemes were designed to analyze the mixing effect of organic fertilizer and water in the mixing process of different mixer structures. Results show that the best mixing effect of organic fertilizer and less power consumption can be obtained when the speed is 60 r/min, mixer width is 320 mm, height of transverse plate is 300mm, mixer width is 60 mm, water fertilizer ratio is 1:1.1, and inclined angle of transverse plate is 45°.

(2) A treatment method of solid-liquid mixed fertilizer is proposed. According to the analysis of various organic fertilizer particle parameters and viscosity measurement, the basic structure of anchor frame mixer is designed. Through the uniform mixing mode of water and fertilizer, it provides a theoretical basis for the development of a new organic fertilizer repair machine.

ACKNOWLEDGMENTS

This work was financially by Foundation of Modern Agricultural Technology System Innovation Team Expert in Shandong Province (NO. SDAIT-10-022-10) and The Major Scientific and Technological Projects of CNPC under Grant (NO. ZD2019-184-004).

REFERENCES

Akhshik, S., M. Behzad, M. Rajabi (2015).CFD-DEM approach to investigate the effect of drill pipe rotation on cuttings transport behavior. J. Petrol Sci Eng. 127, 229–44.

Arturo, G. Q., A. R. Pieter, R. K. Shekhar (2017).Design and cold flow testing of a gas-solid vortex reactor demonstration unit for biomass fast pyrolysis. J. Chem Eng. 329, 198–210.

Bao, Y. L. (2016). Analysis of the development and the demands of fertilization machinery. J. China Soils Fertilizers. 03, 1–4.

Flavia, F. E. (2004). Impact of oil contamination and biostimulation on the diversity of indigenous bacterial communities in soil microcosms. J. FEMS Microbiol Ecol. 49, 295–305.

Li, Y. L., G. Q. Yang, S. J. Yao, L. Zhuang (2021). Ecotoxicological effects of petroleum-contaminated soil on the earthworm Eisenia fetida. J. Int Syst Evol Micr .9005025.

Shin, W. (2001). Nutrient enhanced biodegradation of crude oil in tropical salt marshes. J. Water Air Soil Poll. 131, 135–52.

Tao, H. G., H. X. Chen, J. L.Xie (2011). An alternative approach to quantifying fluid flow uniformity based on area-weighted average velocity and mass-weighted average velocity Energ. Buildings, 45: 116–23.

Xu, R., Obbard, J, (2003) Effect of nutrient amendments on indigenous hydrocarbon biodegradation in oil-contaminated beach sediments Environ. J. Quality. 32, 1234–43.

Advances in Applied Chemistry and Industrial Catalysis – Saikia (Ed.)

Adsorption of nitrogen and phosphorus in wastewater by modified biochar

Yizhuo Zhang*
College of Environmental and Ecology, Chongqing University, Chongqing, P.R. China

ABSTRACT: Removal of nitrogen and phosphorus from water is the focus of global environmental research. Biochar is a solid material made by pyrolysis, which has many excellent characteristics, such as high porosity and surface area. It is used for the adsorption, recovery, and reuse of nitrogen and phosphorus in wastewater. Compared with the raw biochar, modified biochar with a larger surface area and various functional groups has better adsorption capacity for nutrients in the water. So far, new modification methods include activation with acid or base, loading metal compounds. In this review, the sources of materials, carbonization conditions, and modification methods of biomass are compared, along with the mechanism affecting the adsorption capacity of biochar for nitrogen and phosphorus was analyzed. Finally, the future application of Engineering biochar for the removal and reuse of phosphate and ammonium from wastewater is emphasized.

1 INTRODUCTION

Sewage discharge from household, industrial and agricultural sources is a global environmental problem. The composition and characteristics of wastewater are related to its source. For example, industrial wastewater has the characteristics of large fluctuation of water quantity and quality, complex composition, and serious pollution. It often contains abundant toxic and harmful pollutants, such as heavy metals, strong acids, strong bases, organic chemical poisons, biologically refractory organic compounds, oil pollutants, radioactive poisons, high concentration nutrients, heat pollution. On the contrary, domestic wastewater usually contains more organic matter.

In the current operation process of the wastewater treatment plants, BOD, COD, turbidity, and other indicators are commonly used to measure the concentration and biodegradability of pollutants in wastewater. In particular, it is noteworthy that nitrogen and phosphorus are listed separately as the main control indicators of sewage treatment. This is because the discharge of nitrogen and phosphorus will easily cause water eutrophication, which will stimulate the growth of algae and result in the degradation of the water ecosystem. The main nitrogen element is ammonia nitrogen, accompanied by a small amount of nitrate nitrogen, organic nitrogen, and nitrogen. So the common indicators include ammonia nitrogen concentration and total nitrogen concentration. Phosphorus mainly exists in the form of organic phosphate, phosphate, and polyphosphate, and total phosphorus concentration is often used as the control index.

This review focuses on the removal of nitrogen and phosphorus, discusses the adsorption effect of biochar and modified biochar on nitrogen and phosphorus, and expounds on the related mechanism.

2 REMOVAL METHODS OF NITROGEN AND PHOSPHORUS

2.1 *Removal methods of nitrogen*

Traditional nitrogen removal methods include biological, chemical, and physical treatment. In the wastewater treatment plant, the biological treatment method is most commonly used. The most

*Corresponding Author: zhangyizhuo@cqu.edu.cn

DOI 10.1201/9781003308553-79

widely operated one is the activated sludge method, which is the use of ammoniating bacteria to degrade the macromolecular organic nitrogen into small molecular ammonia nitrogen first (Ye et al. 2021). Then nitrifying bacteria and nitrobacteria will be used to convert ammonia into nitrate and nitrite under aerobic conditions. Finally, the denitrifying bacteria will convert nitrate and nitrite into gaseous nitrogen and discharge it under anoxic conditions. The physical method of adsorption is easy to operate and is widely used in the lack of large-scale sewage treatment plants. Commonly used adsorbents include biochar, ion exchange resin, alumina, and zeolite. Compared with other adsorbents, biochar has the advantage of high efficiency, low cost, and little negative impact on the environment. So it is regarded as one of the most effective technologies to remove ammonia nitrogen from the water.

2.2 *Removal methods of phosphorus*

The treatment of phosphorus compounds has always been an extremely complex and costly environmental problem. At present, some researchers have put forward relevant methods for the recovery and reuse of phosphorus. So far, the research methods of phosphorus removal can be divided into three categories: physical methods, chemical methods, and biological methods. In wastewater treatment plants, the activated sludge process is most commonly used as the main biological treatment technology (Huang et al. 2021). To be more specific, phosphorus accumulating bacteria release phosphorus under anaerobic conditions, and excessive phosphorus uptake under aerobic conditions to achieve the purpose of phosphorus removal. However, biological phosphorus removal has the defects of strict experimental parameters, long cycles, and unstable effects. Chemical phosphorus removal may lead to phosphorus precipitation and the formation of phosphate-rich sludge, which increases the cost and risk of sludge treatment and disposal. At present, physical adsorption is considered to be one of the most effective technologies to remove pollutants from water because of its low cost, high efficiency, and simple operation (Liu et al. 2013). Therefore, it has been widely studied by scholars. The core of its research and application is adsorbent (Shakoor et al. 2021). The performance of the adsorbent will directly affect the adsorption effect of pollutants.

3 THE PREPARATION OF BIOCHAR

3.1 *Sources of biochar*

The raw material of biochar is the organic matter left in the process of agricultural production, such as corn straw (Jiang et al. 2019), rice straw (Wei et al. 2019), etc. For instance, studies have shown that the ash content of biochar from herbaceous plants is generally higher than that of woody plants (Xu et al. 2018). In addition, the type of raw materials will also affect its pH, specific surface area, yield, etc.

3.2 *The characteristics of biochar*

Biochar is a material with rich carbon content, highly aromatic carbon components, and a stable structure, which has the characteristics of porous structure and large specific surface area. The preparation process is that the organic materials are heated in the retort to the hot state, and the hydrocarbons are distilled out. Besides, the combustion process is maintained by insufficient supply. Therefore, the carbonization process is essentially a pyrolysis process.

The physical and chemical properties of biochar are affected by pyrolysis temperature, contact time, and oxygen content. The changes in physicochemical properties of biochar under different preparation conditions are performed in Table 1.

Table 1. Physicochemical properties of biochars prepared form various feedstocks.

Biochars	Temperature	Contact Time (h)	Surface area (m^2/g)	Ash content (%)	References
Sugar cane	300	20 min	4.93	3.4	Trazzi et al. (2016)
	300	1	9.2	2.5	Trazzi et al. (2016)
	500	20 min	10.8	9.5	Trazzi et al. (2016)
	500	1	20.1	9.4	Trazzi et al. (2016)
	700	20 min	131	12.5	Trazzi et al. (2016)
Miscanthus	300	20 min	6.17	6.5	Trazzi et al. (2016)
	300	1	6.39	7.1	Trazzi et al. (2016)
	500	20 min	21.8	10.0	Trazzi et al. (2016)
	500	1	81	11.3	Trazzi et al. (2016)
	700	20 min	228	13.3	Trazzi et al. (2016)
	700	1	244	14.9	Trazzi et al. (2016)
Undaria pinnatifida	200	2	1.9	32.8	Jung et al. (2016)
	400	2	70.9	41.9	Jung et al. (2016)
	600	2	61.8	48.7	Jung et al. (2016)
	800	2	44.5	50.4	Jung et al. (2016)
Sluge	300	4	2.31		Zhang et al. (2021)
	600	2	4.61		Zhang et al. (2021)

4 MODIFIED BIOCHAR

4.1 *Metal oxides on biochar*

The loading of metal compounds such as Mg, Ca, Al and Fe on biochar can improve the adsorption capacity of biochar for phosphate and ammonia nitrogen. The reasons for the improvement of adsorption capacity can be attributed to the following two aspects.

The first is the improvement of physical adsorption capacity, which shows the increase of specific surface area and porosity. For example, Li used sugarcane leaves as raw materials and soaked them in different concentrations of MgCl2 to improve their specific surface area from 27.9 m^2/g to 218.9 m^2/g, and their total pore volume from 0.038 cm^2/g to 0.372 cm^2/g (Li et al. 2017). This is because metal salts, such as $FeCl_3$, $ZnCl_2$, $MgCl_2$, can be used as activators in biomass pyrolysis. They will release their crystal water at high pyrolysis temperatures. In addition, other substances, such as HCl, are released during the formation of metal oxides. The release of these substances is conducive to the formation of the porous structure. In addition, the original biochar is usually negatively charged, which is not conducive to the adsorption of phosphate ions. The metal oxides and their salts loaded on biochar will ionize metal cations, enhance the electrostatic force between them and phosphate ions, and enhance the physical adsorption capacity of biochar.

The second is the enhancement of its chemisorption capacity, which is reflected by the surface functional groups of biochar and is often characterized by FTIR. There are many absorption peaks on the original biochar and modified biochar, which represent the vibration of functional groups. For example, modified soybean straw biochar with Mg and Al and found O-H stretching vibration, hydrogen bond group, aliphatic group, $-OCH_3$, and Mg-O or Al-O bond on its surface (Yin et al. 2018). In addition, it is found that the surface of modified biochar has more functional groups, which is consistent with Wang et al. (Wang et al. 2015).

Metal-modified biochar has a significant improvement in phosphate adsorption capacity, but improvement in nitrogen adsorption is limited. For example, demonstrated that the maximum adsorption capacity of 20% Mg biochar was more than 398 mg/g for phosphate and 22 mg/g for ammonia nitrogen, respectively. The main adsorption mechanisms were struvite crystallization,

electrostatic attraction, and $\pi - \pi$ interaction (Li et al. 2017). The maximum adsorption capacity of mg Al modified soybean straw biochar prepared by Yin was 0.70 mg/g of ammonia nitrogen and 74.47 mg/g of phosphate ion (Yin et al. 2018). However, it is noteworthy that its maximum adsorption capacity for nitrate ions is 40.63 mg/g. This also reflects the reason why the adsorption effect of metal-modified biochar on ammonia nitrogen is not good. The surface of modified biochar is positively charged, which is difficult to adsorb ammonium ions with the same positive charge. However, it has a good adsorption effect for phosphate and nitrate ions with a negative charge. It can be concluded that the strength of the electrostatic force is the essential factor to determine the adsorption capacity of metal-modified biochar.

4.2 *Other modified methods*

In order to improve the adsorption performance of carbon, one of the ways is to modify carbon with an acid solution, such as nitric acid (Vu, Trinh, Doan, et al. 2017). After the corncob biochar was modified by nitric acid, the adsorption rate of ammonia nitrogen increased from less than 3.5 mg/g to 8.60 mg/g at most. This is mainly due to the increase of surface functional groups on the surface of biochar in the process of being immersed in nitric acid solution. For example, the carboxyl functional groups on the surface of biochar are nearly twice that of the original biochar. These functional groups are beneficial to the adsorption of ammonia nitrogen by biochar. In addition, the acid solution can remove impurities from the surface or pores of biochar, which also means more adsorption pores. However, high acid concentration may lead to a strong redox reaction and destroy part of the structure of biochar, resulting in low efficiency.

5 CONCLUSION

Biochar can be applied to adsorb various pollutants and nutrients in the water. Besides, biochar does not need to be regenerated or recycled. However, because of its abundant nutrients, it can be used as a slow-release fertilizer to improve soil quality. In this review, we discussed the adsorption of phosphate and ammonium by biochar and modified biochar. Converting low-cost and abundant organic wastes (such as agricultural residues) into biochar may be a viable option, which in turn contributes to environmental sustainability. Biochar has the advantages of large surface area, high porosity, improved composition, stable structure, and easy preparation. However, the application of modified biochar to recover nutrients from wastewater is limited to laboratory-scale research and still lacks commercial/industrial implementation. This may be due to the different characteristics of biochar based on various raw materials, and the lack of efficient and economic methods to recover nutrients.

ACKNOWLEDGEMENTS

I would like to express my gratitude to all those who helped me during writing of this thesis. My deepest gratitude goes first and foremost to Professor Huangfu Xiaoliu, for his constant guidance and encouragement. Without his consistent and illuminating instruction, this thesis could not have reached its present form. Second, I would like to express my gratitude to Han Min, who has instructed and helped me a lot.

REFERENCES

Huang J, Xu L, Guo Y, et al. Intermittent aeration improving activated granular sludge granulation for nitrogen and phosphorus removal from domestic wastewater[J]. Bioresource Technology Reports, 2021, 15: 100739.

Jiang Y-H, Li A-Y, Deng H, et al. Characteristics of nitrogen and phosphorus adsorption by Mg-loaded biochar from different feedstocks[J]. Bioresource Technology, 2019, 276: 183–189.

Jung K-W, Kim K, Jeong T-U, et al. Influence of pyrolysis temperature on characteristics and phosphate adsorption capability of biochar derived from waste-marine macroalgae (Undaria pinnatifida roots) [J]. Bioresource Technology, 2016, 200: 1024–1028.
Li R, Wang J J, Zhou B, et al. Simultaneous capture removal of phosphate, ammonium and organic substances by MgO impregnated biochar and its potential use in swine wastewater treatment[J]. Journal of Cleaner Production, 2017, 147: 96–107.
Liu J, Su Y, Li Q, et al. Preparation of wheat straw based superabsorbent resins and their applications as adsorbents for ammonium and phosphate removal[J]. Bioresource Technology, 2013, 143: 32–39.
Shakoor M B, Ye Z-L, Chen S. Engineered biochars for recovering phosphate and ammonium from wastewater: A review[J]. Science of The Total Environment, 2021, 779: 146240.
Trazzi P A, Leahy J J, Hayes M H B, et al. Adsorption and desorption of phosphate on biochars[J]. Journal of Environmental Chemical Engineering, 2016, 4(1): 37–46.
Vu T M, Trinh V T, Doan D P, et al. Removing ammonium from water using modified corncob-biochar[J]. Science of The Total Environment, 2017, 579: 612–619.
Wang Z, Guo H, Shen F, et al. Biochar produced from oak sawdust by Lanthanum (La)-involved pyrolysis for adsorption of ammonium (NH4+), nitrate (NO3−), and phosphate (PO43-)[J]. Chemosphere, 2015, 119: 646–653.
Wei S, Zhu M, Fan X, et al. Influence of pyrolysis temperature and feedstock on carbon fractions of biochar produced from pyrolysis of rice straw, pine wood, pig manure and sewage sludge[J]. Chemosphere, 2019, 218: 624–631.
Xu K, Lin F, Dou X, et al. Recovery of ammonium and phosphate from urine as value-added fertilizer using wood waste biochar loaded with magnesium oxides[J]. Journal of Cleaner Production, 2018, 187: 205–214.
Ye Y, Ngo H H, Guo W, et al. Bio-membrane based integrated systems for nitrogen recovery in wastewater treatment: Current applications and future perspectives[J]. Chemosphere, 2021, 265: 129076.
Yin Q, Wang R, Zhao Z. Application of Mg–Al-modified biochar for simultaneous removal of ammonium, nitrate, and phosphate from eutrophic water[J]. Journal of Cleaner Production, 2018, 176: 230–240.
Zhang L, Deng F, Liu Z, et al. Removal of ammonia nitrogen and phosphorus by biochar prepared from sludge residue after rusty scrap iron and reduced iron powder enhanced fermentation[J]. Journal of Environmental Management, 2021, 282: 111970.

Advances in Applied Chemistry and Industrial Catalysis – Saikia (Ed.)

Study on characteristics of membrane fouling in MBR for liquor-making wastewater treatment and its cleaning

Xingfu Xue*
Sichuan University Jinjiang College, Pengshan, China

ABSTRACT: Membrane bioreactor (MBR) technology has been used in industrial wastewater treatment plants. Membrane fouling still is one of the key problems limiting the stable operation of MBR, the kinds of cleaning reagents on the membrane surface and the cleaning strategies are researched extensively. Focused on the fouled membrane from a liquor-making treatment plant, the influence of chemical cleaning strategies on cleaning efficiency is investigated. Sodium hypochlorite and oxalic acid are two representative cleaning reagents widely used in MBR membrane cleaning. The effect of acid washing followed by alkaline washing is better than that of alkaline washing followed by acid washing, chemical cleaning routine can effectively extend the life of the membrane. The results show that the membrane organic pollutants can be cleaned with the effective chlorine concentration of 2000 ~ 5000mg/L for 2 ~ 3 hours and with the dosage of 2L/each membrane element for 2 hours, the membrane inorganic pollutants can be cleaned with the oxalic acid concentration of 1000mg/L for 1 ~ 2 hours and with the dosage of 2L/each membrane element for 2 hours. Chemical cleaning under 0.8M3/ (M2●h) aeration condition has a better cleaning effect.

1 INTRODUCTION

Most of the liquor has been brewed with sorghum, wheat, and corn as raw materials, the use of an artificial culture cellar, fermentation, distillation, graded storage, carefully blending, and other basic processes. Liquor wastewater refers to the industrial wastewater produced in the process from production to storage and aging. The degree of pollution can be divided into two parts, part of the low-concentration wastewater, including cooling water, bottled water, and site flushing water. The pollutant concentration is far below the national emission standard, and generally can be recycled or directly discharged. The other part is high concentration wastewater, for example, the bottom water of the distillation pot, the wastewater of the koji-making section, the blind ditch-water of the fermentation pond, the surface flushing water of the distillation section, the leakage water of underground liquor store, the raw materials washing, soaking and discharging water in the processes of coarse sand. Its main components are water, starch, low-carbon alcohol, fatty acids, and amino acids. The water is acidic and has a high concentration of pollutants, with a chemical oxygen demand (COD)of up to 100000 mg/L. It must be treated before it can be discharged. With the enforcement of the national standard for discharge of water pollutants in the fermentation alcohol and liquor industry (GB27631-2011), liquor-making enterprises must have the corresponding sewage treatment facilities, the high concentration of wastewater produced in the fermentation and distillation of liquor can not be discharged until it reaches the standard. The commonly used pretreatment methods include filtration, gravity precipitation, air flotation, centrifugation, and neutralization. To avoid the clogging of pipelines and other facilities and to make

*Corresponding Author: xuexingfu1980@163.com

DOI 10.1201/9781003308553-80

the subsequent treatment facilities run smoothly, it is necessary to remove the larger solid waste in the wastewater, usually by setting up centrifuges or air flotation separation devices and primary sedimentation tanks, or by grid filtration. Fermentation wastewater is produced in the fermentation process of fermented grains. Fermentation wastewater is effective in pit maintenance, pit mud production, and bottom pot recovery, but its utilization rate of it in many enterprises is low. At the same time, because the COD is high, the conventional sewage treatment process needs to dilute it with fresh water about 35 times, this will consume a lot of water. The anaerobic process has the advantages of high load, high efficiency, low energy consumption, low investment, and recoverable energy. Biogas can be obtained by anaerobic treatment of high concentration wastewater, and the removal of organic matter also has a certain effect. It is especially suitable for the treatment of liquor wastewater such as pot bottom water, fermentation blind ditch water, and other high concentration organic wastewater. At present, it is mainly around the research and development of various types of reactors and their engineering practices, such as anaerobic biofilter (AF), anaerobic fluidized bed (AFB), anaerobic high-efficiency inner circulation (IC), upflow anaerobic sludge blanket digestion (UASB), anaerobic expanded granular sludge bed (EGSB) or upflow anaerobic hybrid bed (UBF). After anaerobic treatment, due to the influence of melanin and sorghum washing water and soaking water in the brewing process, the wastewater was black-brown and needed further post-treatment. The advanced treatment methods of liquor production wastewater include adsorption, membrane filtration, catalytic oxidation, coagulation, and sedimentation. Combined with the actual work of some domestic liquor-making enterprises in the field of wastewater discharge and treatment with IC reactor and MBR membrane filtration technology as the main processes, this paper mainly expounds on the fouling of the membrane from the liquor-making wastewater and its cleaning methods.

2 RELATED WORK

The rapid development of membrane technology has revolutionized many fields. MBR is a highly efficient biological wastewater treatment process combining the biodegradation function of the traditional biological treatment technology with the highly efficient separation function of the membrane separation technology, it has the remarkable advantages of high pollutant removal efficiency, stable effluent water quality, convenient operation and management, less land occupation and so on, the application prospect of it is wide. Membrane fouling is an inevitable phenomenon in MBR, which leads to the decrease of membrane flux, the increase of membrane filtration resistance, and the shortening of the service life of the membrane module. Generally speaking, there are two basic ways to control membrane fouling: the prevention and control before membrane fouling and the removal after membrane fouling. In the operation of MBR, it is usually considered that there exists a critical membrane flux (constant current operation) or a critical transmembrane pressure difference (TMP) (constant pressure operation). When the system operates below the critical value, the membrane fouling develops slowly. Membrane cleaning is an effective method to control and remove membrane fouling, reduce TMP and restore membrane flux. According to whether the system stops operation, can be divided into online cleaning and off-line cleaning, and according to whether a chemical reagent is used in cleaning, can be divided into physical cleaning and chemical cleaning. Physical cleaning mainly includes aeration, backwashing (air or filtrate), ultrasonic, sponge scrubbing, and water washing. Physical cleaning can keep MBR running at a relatively stable flux without secondary pollution, but it needs to be carried out frequently and increases the operating cost. With the operation of MBR, the irreversible pollution in the membrane will accumulate gradually, which can not be effectively removed by physical methods, so chemical reagents must be used for cleaning. Commonly used chemicals include alkaline cleaning reagents, acid cleaning reagents, oxidation cleaning reagents, and surfactants, such as ethylene diamine tetraacetic acid (EDTA), ammonium fluoride, etc. Alkali cleaning reagents can effectively remove organic and biological pollution, acid cleaning reagents can effectively remove mineral and inorganic pollution, oxidation cleaning reagents can increase the hydrophilicity of organic polymer pollutants, it can also effectively remove the microorganism in the membrane hole, but it may cause

some damage to the membrane material. Surfactants can improve the cleaning effect by improving the contact between the cleaning reagent and the contaminant, while they can also destroy the cell wall of the bacteria and reduce the pollution caused by the biofilm. Chemical cleaning not only can be used for on-line cleaning, but also can be used for off-line cleaning, the membrane flux can be recovered largely, but the waste liquid from cleaning can sometimes cause secondary pollution. The four main factors to be considered in chemical cleaning are cleaning reagent concentration, cleaning temperature, contact time, and mechanical strength of the membrane. Polypropylene (PP) membrane and Zirconia membrane were used to filter alcohol fermentation wastewater in the anaerobic MBR by Kang et al and the online backwashing (55°C, 2h filtration/90s backwashing) was carried out by using HCI of pH=2. The results showed that the flux of PP membrane was nearly doubled, however, the flux of Zirconia membrane recovered little (20°C) or even decreased (55°C), and the flux of Zirconia membrane increased by about 60% after backwashing (55°C) with pH=11 alkaline detergent. It is very important to select suitable cleaning temperatures and cleaning reagents according to different membrane materials and membrane fouling types. In the actual membrane cleaning process, physical cleaning and chemical cleaning methods are often used, which can generally restore the membrane flux to more than 90%. Oxalic acid is an organic compound, the formula is $C_2H_2O_4$, which is a metabolite of an organism. It is a binary weak acid and widely distributed in plants, animals, and fungi, and plays different functions in different living organisms. By comparing the results of two cleaning cases using oxalic acid as a pickling chemical reagent with that of conventional acid pickling reagent (citric acid), Zhu et al revealed that in the process of membrane cleaning of urban sewage treatment with high industrial composition, oxalic acid had a good effect on the removal of industrial inorganic components and metal Fe enriched on the membrane surface, and the membrane flux recovered significantly after cleaning with oxalic acid.

3 MATERIALS AND METHODS

3.1 *Wastewater*

The wastewater from liquor-making in the laboratory comes from the Qingbaijiang district Wanyi wine factory in Chengdu. The distillery mainly uses sorghum to make liquor by fermentation in the distillery. At present, the output of wastewater is about $10M^3/d$ and is discharged intermittently. The COD of the wastewater is up to 94000 mg/L. The wastewater is treated by IC+Anaerobic-Anoxic-Oxic (A^2/O) +MBR process to meet the national standard for discharge of water pollutants in the fermented alcohol and liquor industry (GB27631-2011).

3.2 *Methodology and experimental procedure*

The MBR system is operated by low-pressure constant current and intermittent negative pressure suction. The suction time is 12min, the stopping time is 8min, the hydraulic retention time (HRT) is 6h, the dissolved oxygen (DO) concentration is 4 ~ 6 mg/l, the temperature is 20~25°C, the pH value is 6.5 ~ 7.8. The structural design of the on-line chemical cleaning device of MBR is mainly to design the oxalic acid and sodium hypochlorite cartridge dosing bucket and pump devices and switching of line valves. The complete cleaning process is as follows: make sure the liquid valve is open, adjust the liquid in the liquid storage tank to the given state, stop the filtration operation and close the through water valve (continue aeration), open the cleaning dosing valve slowly and begin to inject a given amount of liquid, a place for a given time (1 ~ 3 hours) after injection, close the liquid valve, open water valve, and resume the filtration operation. The on-line cleaning test device of MBR with chemical reagents has been shown in Figure 1. The cleaning tank is selectively filled with different concentrations of sodium hypochlorite or oxalic acid depending on the situation. The test results of the cleaning effect of different combinations show that the effect of acid washing followed by alkaline washing is better than that of alkaline washing followed by acid washing. In

this study, the scheme of acid pickling followed by alkaline washing is adopted under 0.8$M^3/(M^2 \cdot h)$ aeration intensity. Considering the complexity of the membrane cleaning process, this study only investigates the influence of the kind of cleaning solution and the concentration of cleaning solution on the recovery rate of multi-membrane flux. The cleaning time and the sample quantity under the certain situation of the result are as follows: 2 hours and with the dosage of 2L/each membrane element.

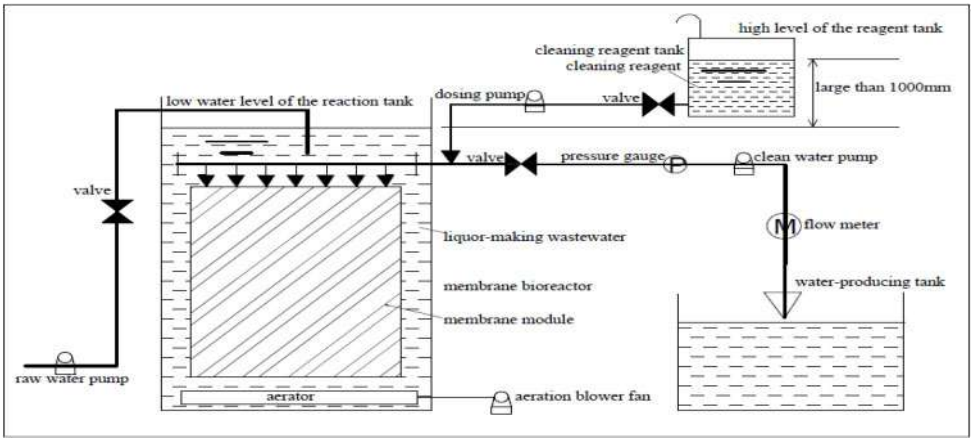

Figure 1. Schematic diagram of MBR membrane chemical cleaning experimental device.

3.3 *Materials and analytical methods*

The membrane of MBR is Polyvinylidene Fluoride (PVDF) hollow fiber membrane which has been produced by Hangzhou Kaiyan membrane technology. The effective area of the membrane is $6M^2$, the height is 1050mm, the pore diameter of membrane closure is 0.05μm, and the flow rate of water production is 6～8M^3/d. The color of the new membrane is milky white, and the color of the fouled membrane is dark brown. The velocity range experimental flowmeter is 0.1～15m/s and the device type of it is ZC-LDG ducted electromagnetic flowmeter produced by Dalian Zhongcheng meter Co., Ltd. The type of pressure gauge is YPF-150B-F, produced by Anhui WeierTai instrument technology Co., Ltd. The aeration fan is made in Chengdu Liangjiang fan Co., Ltd, the type is HF-251S rotary fluid fan which has the following parameters as air volume range 1.44 ～ 1.32M^3/min, blower pressure range 0.1～0.5kgf/cm^2, motor power 0.55kw, diameter 20mm, speed 450rpm and net weight 44kg. Both oxalic acid solution (10%) and sodium hypochlorite solution (12.5%) are purchased from the Chengdu Kelong chemical reagent factory. The purchased chemicals are diluted into cleaning solutions of varying concentrations with certain active ingredients. The membrane flux is calculated by measuring the water output per unit of time. Membrane fouling is characterized by the suction negative pressure of the vacuum gauge. The membrane standard flux is measured by the parameter standard of the commercial membrane and the relative recovery rate of flux is measured by the method described in related research.

4 RESULTS AND DISCUSSION

4.1 *Membrane cleaning effect under oxalic acid cleaning condition*

Oxalic acid, which is more acidic than acetic acid, is a strong acid in organic acids, 0.5% solution of the pH value of 1.62. When oxalic acid is complexed with alkaline earth metal elements such

as Ca, Mg and Ba, its solubility is greatly reduced, such as calcium oxalate is almost insoluble in water. However, when oxalic acid is combined with some transition metal elements such as Fe, Cu, Ni, and Co, soluble complexes can be formed and their solubility is greatly increased. Other studies have shown that oxalic acid concentration is not the higher the better, a high concentration of oxalic acid may lead to secondary pollution, and too low a concentration may lead to a poor cleaning effect, at the same time, in the contamination film surface metal elements of iron accounted for the highest proportion, if the cleaning conditions are not appropriate, it is easy to form stain on the membrane surface, which affects the cleaning effect, so it is necessary to determine the appropriate concentration of oxalate. The results show that when the concentration of oxalic acid increases from 900mg/L to 1000 mg/L, the recovery rate of membrane flux does not change, all the data are stable at about 70%, and the membrane flux recovery rate under different oxalic acid concentrations can be seen in Figure 2.

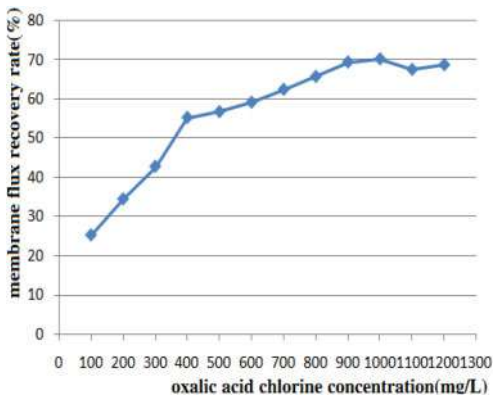

Figure 2. Membrane flux recovery rate under different oxalic acid.

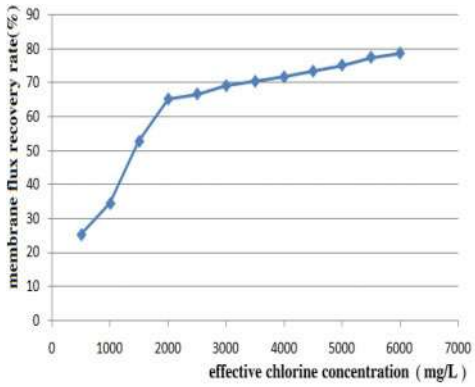

Figure 3. Membrane flux recovery rate under different effective chlorine concentration.

4.2 *Membrane cleaning effect under sodium hypochlorite cleaning condition*

Alkaline cleaning methods are often used to clean the organic matter on the surface of the fouled membrane. Alkaline cleaning agents are sodium hydroxide and sodium hypochlorite. The sodium hypochlorite solution is alkaline, with a pH of 13.75 of 0.5% solution. The alkalis can be saponified with fatty substances on the membrane surface, or they can react with organic pollutants such as a protein on the membrane surface to form soluble substances that can be removed. In addition, the sodium hypochlorite sterilization effect is obvious, and can effectively kill pathogenic microorganisms. However, the water solution of sodium hypochlorite is unstable, and the composition is different with different pH values, resulting in different cleaning effects. When the pH value is 2, most of them exist in CI_2, when the pH value is 2∼3, they mainly exist in CI_2 and HCIO, when the pH value is 4∼5, most of them are HCIO and a little of them are Cl_2 when the pH value is 5∼8, they are mainly HCIO and NaCIO when the pH value is 9, they mainly exist in the form of NaCIO, the oxidation of sodium hypochlorite depends on the CIO^-, HCIO and CI_2, so determining the right pH is important. Other studies have shown that sodium hypochlorite is more stable in alkaline environments and does not decompose easily. Therefore, the effect of sodium hypochlorite pH of 8∼10 on cleaning efficiency is studied. The membrane flux recovery rate under different effective chlorine concentrations can be seen in Figure 3. The experimental results show that the flux recovery rate of the membrane cleaned by sodium hypochlorite increases normally with the increase of the concentration, and increases slowly with the increase of the concentration.

Figure 4. Fouled MBR membrane.

Figure 5. Cleaned MBR membrane.

5 CONCLUSIONS

The following conclusions can be drawn from this study:

The effect of acid washing followed by alkaline washing is better than that of alkaline washing followed by acid washing, chemical cleaning routine can effectively extend the life of the membrane. The membrane organic pollutants can be cleaned with the effective chlorine concentration of 2000～5000mg/L for 2～3 hours and with the dosage of 2L/each membrane element for 2 hours, the membrane inorganic pollutants could be cleaned with the oxalic acid concentration of 1000mg/L for 1～2 hours and with the dosage of 2L/each membrane element for 2 hours. Chemical cleaning under certain aeration conditions has a better cleaning effect, the surface of the membrane cleaned with oxalic acid and sodium hypochlorite has changed from rust stain as can be seen in Fig.4 to white as can be seen in Fig.5. The flux recovery rate of the membrane increases normally with the increase of the concentration and increases slowly with the increase of the concentration.

REFERENCES

CHANG I S, KIM S N. Wastewater treatment using membrane filtration effect of biosolids concentration on cake resistance[J] Process Biochemistry, 2005, 40(3–4):1307–1314.

CHEN V, FANE A G, MADAENI S, et al., Particle deposition during membrane filtration of colloids: transition between concentration polarization and cake formation[J]. J Membr Sci, 1997, 125(1):109–122.

JIANG TAO, KENNEDY MARIA D, VAN DER MEER WALTERr G J, et al.the role of blocking and cake filtration in MBR fouling[J]. Desalination, 2003, 157(1–3): 335–343.

KANG I J, YOON S H, LEE C H.Comparison of the filtration characteristics of organic and inorganic membranes in a membrane coupled anaerobic bioreactor[J]. Water Res, 2002, 36(7):1803–1813.

LI X F, ZHOU Q, CHEN C M, et al. Characteristics of Membrane Fouling in MBR for Treatment of Domestic Sewage and Its Cleaning[J]. CHINA WATER & WASTEWATE, 2016, 32(23):27–30.

PORCELLI N, JUDD S.Chemical cleaning of potable water membranes: a review[J]. Sep Purif T, 2010, 71(2):137–143.

WANG L L, SONG W C.Study on chemical cleaning technology of Membrane Bioreactor [J]. Water Science and engineering, 2008(1):68–70.

WANG P.Membrane cleaning method of fouling membrane in flat membrane sludge thickening process [J]. Water purification technology, 2015, 34(1):82–87.

WANG W L. Research progress on the stability of sodium hypochlorite solution [J]. Inorganic salt industry, 2007, 39(9):12–14.

YAMAMOTO K. HIASA M, MAHMOOD T. et al. Direct solid-liquid separation using hollow fiber membrane in an activated sludge aeration tank[J]. Water Sci T, 1989, 21(4/5):43–54.

YUAN X B. Study on alkaline agent and its performance for ultrafiltration membrane fouling control [J]. MEMBRANE SCIENCE AND TECHNOLOGY, 2013, 33(5):82–86.

ZHANG S T, QU Y B, LIU Y H, et al. Experimental study of domestic sewage treatment with a metal membrane bioreactor[J]. Desalination, 2005, 177(1/2/3):83–93.

ZHU C Q, ZHOU W X, ZHOU Y, et al. Application and analysis of oxalic acid in chemical cleaning of immersed MBR[J]. China water & wastewater, 2013, 29(19):106–108.

Advances in Applied Chemistry and Industrial Catalysis – Saikia (Ed.)

Influence of application frequency and amount of biogas slurry on infiltration liquid

Yue Hu*, Fucheng Li** & Yongcheng Liu***
School of Resource & Environment, Southwest University of Science and Technology, Mianyang, P.R. China

Bo Mei****
Sichuan Xuebao Dairy Group Co., Ltd., Mianyang, P.R. China

Lu Feng*****
School of Resource & Environment, Southwest University of Science and Technology, Mianyang, P.R. China

ABSTRACT: Biogas slurry can increase soil nutrient content and enhance soil microbial activity, but there is a certain threshold for the application of biogas slurry. In order to discuss the appropriate frequency and amount of biogas slurry application, and to provide a theoretical reference for further determining the application amount and fertilization method of biogas slurry in the field, a soil column leaching experiment was adopted with 6 different biogas slurry application rates in this paper, and the single treatment was leached 5 times, and the nutrient content in the infiltrating water was measured after the leaching was completed. This leaching test showed that the content of total phosphorus, total nitrogen, ammonia nitrogen, and nitrate nitrogen in the submerged leachate of the soil increased after multiple successive use of biogas slurry and an increase in the application rate of single biogas slurry, and the greater the application amount of biogas slurry, the nutrient content increases more obviously. Considering the impact of biogas slurry application frequency and application rate on infiltration liquid, in order to avoid the infiltration and pollution of the surrounding water environment, the single application rate should be controlled within 120% of the standard nitrogen demand for plant growth.

1 INTRODUCTION

Biogas slurry is the liquid discharged from the fermentation of biogas project using livestock and poultry manure as raw material. The combined application of biogas slurry and chemical fertilizers can better supplement the nitrogen and phosphorus nutrients required by crops and improve the yield and quality of crops (Abbas & Naveed 2020; Zheng & Ma2020). Although there are many benefits of returning biogas slurry to the field, there are certain thresholds for the application of biogas slurry. In recent years, with the vigorous development of livestock breeding and biogas projects, biogas slurry has gained a lot of favor in planting fertilization. However, due to the continuous increase in the application of biogas slurry in many developing countries, the nutrient utilization efficiency has dropped significantly, the nutrient element content in surface water and groundwater has reached unprecedented levels (Dai & Zhou 2013; Tan & Jiang 2013). A large amount of biogas slurry after returning to the field at will exceeds the range of natural digestion of the biogas slurry in the surrounding land, and finally the biogas slurry is indirectly discharged into the water body and the surrounding environment, forming new secondary environmental pollution (Eltohamy 2021; Svoboda & Taube 2013).Therefore, problems such as crop yield reduction, soil

Corresponding Authors: *757959731@qq.com, **lfckind@163.com, ***1907357693@qq.com, ****934059979@qq.com and *****18881627112@163.com

DOI 10.1201/9781003308553-81

and water environment pollution caused by excessive application and irregular application have attracted much attention, and the rational application of biogas slurry is particularly important.

In recent years, there have been many studies on the effects of biogas slurry applied in farmland instead of chemical fertilizers on crop growth, yield and soil quality, but there have been few studies on the impact of biogas slurry application on the surrounding surface and groundwater environment. In this study, the calcareous purple soil in Xinqiao Town, Mianyang City was used as the experimental object to simulate the leaching test of biogas slurry, dynamically detect the nutrient element content in the infiltration liquid after the biogas slurry leaching, and study the effect of different biogas slurry application rates and application times on the infiltration liquid. The influence of the irradiance provides theoretical support for the rational use of farmland nutrients.

2 MATERIALS AND METHODS

2.1 *Materials*

The limestone purple soil in Xinqiao Town, Mianyang City was selected as the test soil. After being air-dried, the stone residues other than the soil particles were removed, and then used for soil column leaching test filling after passing through a 5 mm sieve. The test biogas slurry was taken from the Hongfeng Ranch of Sichuan Xuebao Dairy Group Co., Ltd. The biogas slurry had a total nitrogen of 1134 mg/L and a total phosphorus of 98 mg/L. The biogas slurry was filtered through a gauze filter to remove large suspended solids for use.

2.2 *Methods*

Put the test soil into the soil column (inner diameter 8 cm, height 40 cm), the height is about 20 cm, the soil bulk density after filling the soil column is about 1.35 $g \cdot cm^{-3}$. According to the local multi-year average rainfall in Mianyang City (the average annual rainfall is 1261 mm, this test is calculated as 1260 mm, 30% is calculated by the surface runoff cycle, and the simulated test rainfall is determined to be 882 mm), the size and the upper surface area of the soil column are calculated as 370 mL for each actual irrigation. The experiment set up 6 treatments (T0, T1, T2, T3, T4, T5), and the single application rate of biogas slurry was set to 36, 54, 72, 90, and 108 mL (the insufficient part was made up with clean water), which was equivalent to each Apply 81.6 (40%), 122.4 (60%), 163.2 (80%), 204 (barley standard nitrogen requirement 100%), 224.8 (120%) kg of nitrogen fertilizer per hectare.

After the soil column was filled, the soil was moistened with deionized water several times, and the test was started after standing for 3 days. Each treatment is divided into 5 times for leaching. During each leaching, first add biogas slurry and then clean water. At the same time, put the soil column in a large 2 L beaker to receive the infiltration liquid, and determine the nitrogen and phosphorus nutrients of the infiltration liquid (TN, TP, NH_4^+-N, NO_3-N).

2.3 *Measurement index*

The total N was measured with the alkaline potassium persulfate digestion and ultraviolet spectrophotometry; total P was determined by the ammonium molybdate spectrophotometry; Ammonium Nitrogen was determined using Nessler's reagent spectrophotometry; Nitrate Nitrogen was measured using ultraviolet spectrophotometry.

3 THE RESULT AND DISCUSSION

3.1 *Effect of application times of biogas slurry on nutrient content of infiltration liquid*

3.1.1 *Total phosphorus*

It can be seen from Table 1 that except for the T0 treatment, after the fifth leaching, the total phosphorus content of the infiltration liquid under the other treatments all increased in different

ranges. The results revealed that excessively increasing the number of leaching will cause the loss of total phosphorus, reduce the utilization efficiency of nutrient elements, and cause pollution to the environment.

Table 1. Changes of total phosphorus content in leachate under different application frequency and application rate of biogas slurry (mg/L).

Treatment of different biogas slurry application rates	T0	T1	T2	T3	T4	T5
1st	0.028	0.043	0.068	0.074	0.085	0.177
2nd	0.021	0.032	0.032	0.221	0.301	0.326
3rd	0.008	0.043	0.030	0.259	0.609	0.631
4th	0.003	0.221	0.241	0.475	0.809	0.791
5th	0.003	0.257	0.459	0.629	1.029	1.147

3.1.2 *Total nitrogen*

The experiment found (Table 2) that the total nitrogen content of infiltration water decreased first and then increased under different application rates of biogas slurry. Different from this experiment, Wang Zhongjiang (Wang & Zhang 2018) believes that the total nitrogen in the leachate does not change significantly in the early stage of the application of biogas slurry, and it rises first and then decreases in the later stage. This is because as the amount of biogas slurry application increases, the nitrogen adsorbed in the soil will be affected because of the decomposition of anaerobic and denitrification. The leaching time in this test was short, and the anaerobic and denitrification conditions were not reached.

Table 2. Changes of total nitrogen content in leachate under different application frequency and application rate of biogas slurry (mg/L).

Treatment of different biogas slurry application rates	T0	T1	T2	T3	T4	T5
1st	7.01	8.87	14.04	15.87	16.87	18.71
2nd	3.33	2.90	11.21	12.75	14.10	21.17
3rd	1.05	1.90	7.72	14.55	16.85	28.17
4th	0.87	3.31	12.28	16.41	17.58	29.56
5th	0.71	5.27	14.70	17.04	18.11	30.68

3.1.3 *Ammonia nitrogen, nitrate nitrogen*

The test found (Figures 1 and 2) that the change trend of ammonia nitrogen content in infiltration liquid was roughly the same as that of nitrate nitrogen. With the increase of the number of leaching, the content of ammonia nitrogen and nitrate nitrogen in the infiltration liquid also increased, and the nitrate nitrogen content of the infiltration liquid under the soil column with higher biogas slurry application rate (T3, T4, T5) in the later stage of the application of the biogas slurry increased rapidly, indicating that with the increase of the number of leaching, the nitrogen content of leachate may be more likely to pollute the groundwater environment at high application rates.

3.2 *Effect of application rate of biogas slurry on nutrient content of infiltration liquid*

3.2.1 *Total phosphorus*

It can be seen from Table 1 that the TP content of the leachate under T5 treatment in a single application of biogas slurry was greater than other treatments, and the more frequency of application, the greater the difference, with the increase of the number of leaching, the total phosphorus content of the leachate under the treatment of low biogas slurry (T1, T2) decreased first and then increased, this is mainly because soil adsorption and crop absorption of TP nutrients occurred in the initial

stage of biogas slurry application, so the TP content in the infiltration water was low, but in the later stage the demand for TP in plants decreased and the soil adsorption reached saturation, so the TP content in the infiltration water increased. This is consistent with the finding obtained by Qiao and Zhang (2013). However, the total phosphorus content of the leachate continued to increase under the treatment with higher biogas slurry application rate (T4, T5). This is because the adsorption saturation was reached in the early stage of the treatment with higher biogas slurry application rate, and there was no significant change in the later period of increase from the previous period.

3.2.2 *Total nitrogen*

It can be seen from Table 2 that after the fifth leaching, the total nitrogen content of the permeate liquid under each treatment from T2 to T5 increased compared with the first time, and the increase ranges were 4.74%, 7.35%, 7.34%, and 64.02%, respectively. In T1 treatment, the total nitrogen content of the infiltrating liquid after the fifth leaching was less than that of the first. It shows that in this experiment, the application amount of T5 treatment exceeded the ability of soil to absorb the biogas slurry and entered the groundwater, causing certain hidden dangers to the water environment. It can be suggested that with the increase of the amount of biogas slurry, the application amount of biogas slurry in T5 treatment was more likely to cause nitrogen infiltration, and this application amount was not suitable for long-term irrigation.

3.2.3 *Ammonia nitrogen, nitrate nitrogen*

Combined with the analysis of Figures 1 and 2, different from the change rule of total nitrogen content of leaching infiltration liquid, the increasing trend of ammonia nitrogen and nitrate nitrogen content in infiltration liquid was more obvious. Under the same leaching frequency, the soil column treated with T0 application rate had the lowest content of ammonia nitrogen and nitrate nitrogen in the infiltration liquid, and the content of ammonia nitrogen and nitrate nitrogen in the infiltration liquid increased with the increase of the application amount of biogas slurry. There was little difference in the content of ammonia nitrogen and nitrate nitrogen in the leachate under the soil column with different application rates of biogas slurry.

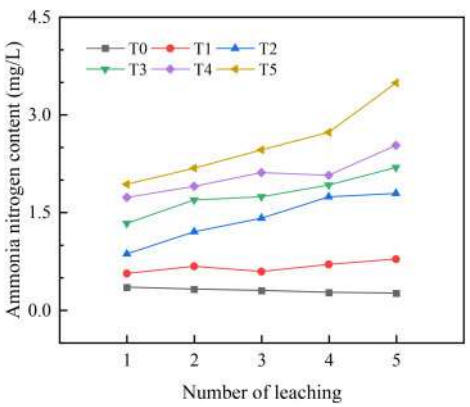

Figure 1. Changes of ammonia nitrogen content in leachate under different application rates of biogas slurry.

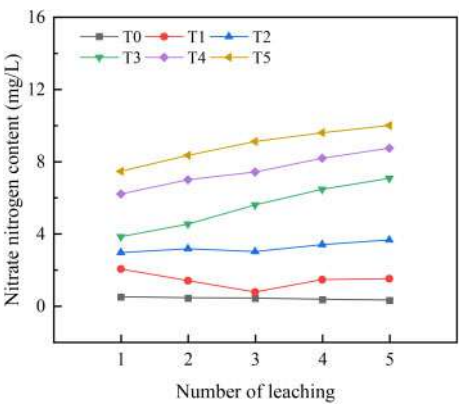

Figure 2. Changes of nitrate nitrogen content in leachate under different application rates of biogas slurry.

4 CONCLUSION

Multiple continuous use of biogas slurry and the increase of the single application rate of biogas slurry will lead to the increase of total phosphorus, total nitrogen, nitrate nitrogen, and ammonia nitrogen in the infiltration liquid. In order to avoid the infiltration and pollution of the groundwater

environment due to unreasonable application of biogas slurry, attention should be paid to reducing the number of continuous applications of biogas slurry and the amount of single biogas slurry application during the application, and the single application rate should be controlled within 120% of the standard nitrogen demand for plant growth.

ACKNOWLEDGMENTS

This work was supported by Sichuan Province Science and Technology Support Program (2021YFN0125), Key Laboratory of Development and Application of Rural Renewable Energy, Ministry of Agriculture and Rural Affairs, China (2020–002) and Mianyang Science and technology project (2018YFZJ019).

REFERENCES

Abbas, A. & M. Naveed (2020) Efficiency of Wheat Straw Biochar in Combination with Compost and Biogas Slurry for Enhancing Nutritional Status and Productivity of Soil and Plant. J. Plants (Basel), 9(11).

Dai, X. L. & X. H. Zhou (2013) Managing the seeding rate to improve nitrogen-use efficiency of winter wheat. J. Field Crops Research, 154: 100–9.

Eltohamy, K. M. & C. L. Liu (2021) An internet-based smart irrigation approach for limiting phosphorus release from organic fertilizer-amended paddy soil. J. Journal of Cleaner Production, 293.

Qiao, X. S. & X. W. Zhang (2013) Risk Analysis of Biogas Slurry Application for Paddy Water Environment. J. China Biogas, 31(04): 21–6. (in Chinese)

Svoboda, N. & F. Taube (2013) Nitrogen leaching losses after biogas residue application to maize. J. Soil and Tillage Research, 130: 69–80.

Tan, D. S. & L. H. Jiang (2013) An in situ study of inorganic nitrogen flow under different fertilization treatments on a wheat–maize rotation system surrounding Nansi Lake, China. J. Agricultural Water Management, 123: 45–54.

Wang, Z. J. & Z. Zhang (2018) Effects of Biochar Combined with Biogas Slurry on Soil Nutrients in Leaching State. J. Transactions of the Chinese Society for Agricultural Machinery, 49(11): 260–7. (in Chinese)

Zheng, J. & J. Ma (2020) Effects of Biogas Slurry Irrigation on Tomato (Solanum Lycopersicum L.) Physiological and Ecological Indexes, Yield and Quality as Well as Soil Environment. J. Applied Ecology and Environmental Research, 18(1): 1013–29.

Advances in Applied Chemistry and Industrial Catalysis – Saikia (Ed.)

Explore the purification effect of constructed wetlands on total phosphorus in water, taking Taihu Sanshan Island Wetland Park as an example

Oujing Wen*
Environmental Science, School of Science, Xi'an Jiaotong-Liverpool University, Suzhou, Jinagsu, China

ABSTRACT: In recent years, due to the intensified eutrophication of water bodies, more and more studies have been conducted on water purification and nitrogen and phosphorus interception based on wetland ecosystems. To understand the ecological impact of lake wetlands on eutrophic lakes and provide more methods and data for optimizing lake wetland management. This experiment selects the Sanshan Island Constructed Wetland Park as the research object to discuss two issues. First, explore the water purification effect of the constructed wetland park. Secondly, the influence of the density distribution of aquatic vegetation on the total phosphorus content of the water body is discussed.

1 INTRODUCTION

Sanshan artificial wetland is located in Taihu Lake, 50 kilometers southwest of Suzhou. It is an artificial wetland park composed of islands and adjacent waters (Wang et al. 2016), belongs to the lake wetland, a type of wetland ecosystem, and its area includes the lake water itself and the periodic flooding areas of its coastal regions. Among the many ecosystems on the earth's surface, the wetland ecosystem is extraordinary. The rich biological resources of the ecosystem determine that wetland has multiple ecological service functions (Zhao & Gao 2007).

In recent years, due to the increase in eutrophication of water bodies, more studies have been conducted on the purification of water quality and interception of nitrogen and phosphorus emissions based on wetland ecosystems. Some domestic scholars' research on lake wetlands in different regions of China, such as Tianmu Lake Wetland, Longgan Lake Wetland, and Yinchuan Yellow River Wetland Park, has also shown that wetlands have an apparent interception and purification effects on pollutants entering the lake (Li et al. 2012). At the same time, many studies have shown that free surface constructed wetland (FWS CW) is the most effective method for phosphorus removal, with an annual efficiency between 73% and 85% (Machado et al. 2017), and the removal rate of continuous groundwater for TP is as high as 60% (Vymazal et al. 2018). In fact, at present, domestic and foreign wastewater treatment technologies in constructed wetlands, a nutrient interception in watershed wetlands, heavy metal retention function, and other aspects have been carried out much work. However, most of the studies that measure the water purification function of lake wetlands express the water purification function of wetlands by comparing the concentration of nitrogen and phosphorus in the water at the inlet and the outlet. On the other hand, there are relatively few studies on phosphorus retention and purification for the open and no clear boundary between the lake wetland and the water body (Xu et al. 2007).

*Corresponding Author: Oujing.Wen18@student.xjtlu.edu.cn

DOI 10.1201/9781003308553-82

Based on the above information, understand the ecological impact of lake wetlands on eutrophic lakes, and provide more methods and data for optimizing lake wetland management. This experiment selected the Sanshan Artificial Wetland Park to study the phosphorus migration between the eutrophic lake water body and the lake wetland. Firstly, put forward the following hypotheses:

(1) Exploring the effectiveness of wetland water purification: the total phosphorus content of water bodies from Taihu Lake to Sanshan Island gradually decreases.
(2) Explore the influence of plant distribution in wetlands on total phosphorus: The total phosphorus content in water bodies where plants are densely distributed is lower than that in water bodies where plants are sparsely distributed.

2 METHODOLOGY

2.1 *Sampling point*

According to the construction time, the Sanshan Wetland Park can be divided into phase I and phase II. The wetland park can be roughly divided into six areas (area 6 is Taihu Lake). The general characteristics of each area are shown in Table 1. Among them, biomass can be used to indicate the magnitude of vegetation in the area.

Table 1. Plants distribution and sampling point information table.

Wetland	Time	Area	Colour	Total sampling points	Plant species and density	Biomass (kg/m^2)
First phase	2008	I	Light blue	1–1 to 1–5	Dense emergent plants, floating leaf plants and submerged plants	7.00
		2	Dark blue	2-1 to 2-6	Dense submerged plants and sparse floating leaf plants	5.80
		3	Light green	3-1 to 3-3	Dense submerged plants	6.00
		4	Pink	4-1 to 4-3	A few submerged plants and no floating leaves	4.80
Second phase	2013	5	Green	5-1 to 5-3	More miniature aquatic plants and the distribution is patchy	3.00
Taihui		6	Blue	6-1 to 6-3	Few aquatic plants and no emergent plants	0.00

Based on the above information, to explore the impact of wetlands on total phosphorus in water, variables should be controlled as much as possible during the sampling process. Therefore, a water sample at a distance of 25 cm from the water surface was collected as a sample to avoid the influence of the silt at the bottom of the lake on the measurement of total phosphorus. For Hypothesis 1, water samples were taken from six areas, according to the direction of water flow. While to obtain the overall total phosphorus content value of the area, three sampling points (one each on the left, middle, and right) are selected for sampling in each area. Among them, since areas 3 and 4 cannot enter the center for sampling during the protection period, and the plant species between 3 and 4 are similar, sampling is carried out on both sides of the reed belt (Figure 1(a)). For Hypothesis 2, to explore the impact of vegetation density on total phosphorus in the water body, area 2 was selected

as the study area. However, due to time and operation constraints, the vegetation distribution density can only be roughly observed through field observation and qualitative analysis (Figure 1(b)).

Figure 1a. Sampling for Hypothesis 1. Figure 1b. Sampling for Hypothesis 2.

Figure 1. Sampling map of Sanshan island wetland park.

2.2 *Data measurement*

The alkaline potassium persulfate digestion spectrophotometry would measure the total phosphorus value, divided into the digestion reaction and the chromogenic reaction.

2.3 *Data measurement*

According to the two hypotheses put forward by the experiment, different methods are used for data analysis. First of all, for Hypothesis 1, samples were collected from six regions, and the chart was used to observe the changing trend of total phosphorus content. Meanwhile, it was compared with the changing trend of biomass in each region to judge the effectiveness of wetland construction for water purification preliminarily. Moreover, to more intuitively observe the sample data of sampling points in different regions, draw a mean value map with a 95% confidence interval, and observe the mean value of the sample data from area 1 to area 6. Then use one-way ANOVA to verify Hypothesis 1. For Hypothesis 2, it was first integrating the sample points of the region into a dense plant distribution group and a sparse plant distribution group. Then, use box plots to observe the data distribution of the two groups of data, and then use one-way ANOVA to study different plant densities to test whether there is a significant difference in total phosphorus content in the following samples. All operations will be used by R.

2.4 *Results*

After measurement, a total of 23 sample points in 6 regions were obtained.

Hypothesis 1

The data of hypothesis 1 is shown in Table 2. By comparing the average total phosphorus value and biomass of the six regions, it can be found that the overall trend of changes is the same (Figure 1). From area 6 to area 1, the total phosphorus content gradually decreased with the increase of biomass and reached the lowest point in area 2.

At the same time, after one-way ANOVA(a=0.05) calculation, it can be seen that the P-value of Hypothesis 1 is 0.00314, which means that the total phosphorus content of water bodies in various regions does have significant differences. Therefore, it can prove that the wetland park has played its role in water purification.

Table 2. The value of total phosphorus (TP) for different areas.

Sampling point	TP value (moi/L)		Sampling means (mol/L)	Area	Area mean (mol/L)	Biomaas (kg/m^2)
	Replicatel	Replicate2				
1-2	0.12	0.14	0.13			
1-3	0.15	0.16	0.16	1	0.14	7.00
1-4	0 11	0.14	0.13			
2-1	0.08	0.11	0.10			
2-2	0.18	0.17	0.18	2	0.12	5.80
2-5	0.08	0.11	0.10			
3-1	0.13	0.19	0.16			
3-2	0.13	0.14	0.14	3	0.14	6.00
3-3	0.13	0.11	0.12			
4-1	0.15	0.15	0.15			
4-2	0.16	0.14	0.15	4	0.15	4.80
4-3	0 17	0.13	0 15			
5-1	0.19	0.24	0.22			
5-2	0.21	0.19	0.20	5	0.20	3.00
5-3	0.19	0.19	0.19			
6-1	0.22	0.21	0.22			
6-2	0.19	0.25	0.22	6	0.21	0.00
6-3	0.19	0.19	0.19			

Hypothesis 2

The data of Hypothesis 2 is shown in Table 3

Table 3. The total phosphorus of different plant densities in Area 2.

Plant Density	Sampling point	TP value (mol/L)		Mean TP value (mol/L)
		Replicate1	Replicate2	
Spaces	2-1	0.08	0.11	0.095
	2-2	0.18	0.17	0.175
	2-3	0.12	0.17	0.145
Dense	2-4	0.15	0.12	0.135
	2-5	0.15	0.12	0.135
	2-6	0.08	0.11	0.095

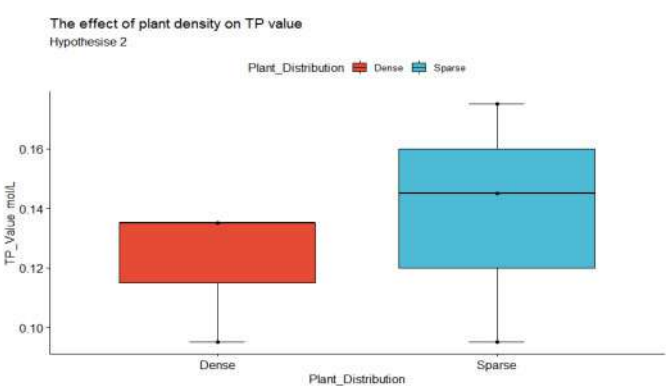

Figure 2. The effect of plant density on TP value.

As mentioned in the method section, through field observation of the water surface in area 2, the 6 sample points can be roughly divided into sparse groups (2-1 To 2-3) and dense groups (2-4 to 2-6). From the box plot (Figure 4), though the lowest value of the total phosphorus content of the two groups is the same, the total phosphorus content of the sparse group is overall higher than that of the dense group. Comparing the area of each box shows that the fluctuation of total phosphorus content is more significant than that of densely distributed plants.

However, through the calculation of single-factor analysis of variance, P-value is 0.569, which is far greater than 0.05, which means that for Hypothesis 2, based on the experimental data, there is no significant difference in the influence of plant distribution density on total phosphorus content.

3 DISCUSSION

Hypothesis 1

Although the measurement results of Experiment 1 are basically in line with expectations, due to the limitations of field sampling, the sampling points in areas 3 and 4 are mainly concentrated on the shore of the reed protection forest belt. There are many fallen leaves on the water surface, and the water body is relatively turbid, which will cause the TP measurement value to be higher (Xia 2015). Therefore, comparing the measurement result of Experiment 1 with the measurement result of Sanshan Island in April 2020, it is found that the overall trend is roughly in line, which once again verifies that the wetland has a specific effect on water purification and interception of TP.

Meanwhile, it should be noted that there is a significant standard error in area 2. When combining the data of the sampling points and the field investigation, it can be found that samples 2-1 and 2-2 belong to the distribution of plants' sparse points, and 2-5 belong to the points with denser plant distribution. Different plant densities have different absorption rates for the total phosphorus content of the surrounding water body. When the density of the water body plants is greater, the absorption rate for total phosphorus will be higher, which may be one reason for the significant standard error in this area.

In addition, one thing that needs to be paid attention to is the investigation of potential pollution sources. For example, there are four sewage outlets near area 1, which regularly discharge domestic wastewater. This may be why the total amount of area 1, even with the highest biomass, the phosphorus content is still higher than in area 2. However, to verify this, it may be necessary to take a mixed water sample based on the discharge time and discharge amount of the location where the sewage discharged from the sewage pipe enters area 1, calculate its average total phosphorus and compare it with the total phosphorus value in the surrounding water samples.

Hypothesis 2

There are two main ways for wetland plants to remove pollutants from water. On the one hand, the plants' root absorption, substrate adsorption, and biochemical transformation of aquatic plants are the main processes for removing pollutants in wetlands (Xi 2006). Secondly, wetland plants can input oxygen from the air into the root zone through their stems and leaves, forming an oxidizing micro-environment in the root zone, providing necessary places and aerobic conditions to survive nitrifying bacteria and the degradation of nutrients, and also for microorganisms. According to Su et al, the composition and diversity of microorganisms greatly influence the ability of wetlands to remove pollutants. Higher community diversity usually indicates an increase in the functional diversity of the microbial community, which in turn increases the number and scope of degradable waste components. Therefore, as the density of wetland fabrics increases, the total phosphorus content of the surrounding water will decrease correspondingly (INAMORI 2008). However, the conclusions from the Hypothesis 2 experiment are not sufficient to support this theory. In this case, the following analysis can be made.

First of all, as mentioned by the result, in the box plot, the maximum number of dense groups coincides with the median. This explains to some extent that the sample data is too small. Therefore, the conclusions drawn based on this data are not indicative. Meanwhile, the distribution of sampling

points in area 2 is mainly concentrated in the right part of the area. Therefore, the distance between sampling points 2-4 and the rest of the sampling points is too far, and the plant belt blocks the middle.

Moreover, the area where the sample points 2-4 are located is a human activity area, and tourists often taxi on cruise ships in this area. Therefore, it should be confirmed whether other potential unknown influencing factors (such as pollutants discharged by cruise ships) in 2-4. The point's total phosphorus content has an impact. Alternatively, re-select the sampling points in the right half of area two.

Secondly, there are also problems with the control of variables. On the one hand, through qualitative analysis and field observation, this experiment roughly divided the six samples into a dense plant distribution group and a plant distribution coefficient group. On the other hand, however, the lack of a description of the specific vegetation quantity at each sample site may cause some errors. In this regard, area 2 should be divided into 2m2m squares of the same area in advance, and the number of vegetation in the area should be counted in turn. Then, on a sequential basis, increase sample points for sampling.

On the other hand, this experiment mainly explores the influence of vegetation distribution density on total phosphorus. However, there are two types of aquatic plants (submerged plants and floating-leaf plants) in area 2. Therefore, the combination of different plants will have a significant impact on the total phosphorus content. Sample points 2-1 and 2-6 may have such problems. In this regard, when collecting water samples, the vegetation type of the sample point should be recorded. When the sample data is subsequently sorted, the control variable method is used to sort and compare according to the classification of vegetation types.

4 CONCLUSION

This experiment chooses the Sanshan Island Artificial Wetland Park to explore two issues. First, explore the effectiveness of artificial wetland parks for water purification. It can be seen that the artificial wetland park has a noticeable effect on water purification. Secondly, it explored the influence of aquatic vegetation density distribution on the total phosphorus content of the water body. According to the data, it is found that the vegetation density does not have a significant impact on the total phosphorus content, however, since there are too little sample data and too many potential unknown variables. Therefore, this conclusion is not representative. In this regard, it is necessary to refine the experimental design and expand the sample data to draw more accurate conclusions.

REFERENCES

Inamori, R. et al. (2008). Seasonal effect on N2O formation in nitrification in constructed wetlands. Chemosphere. 73, 1071–7.

Li Zhaofu et al. (2012). Impact on Nitrogen and Phosphorous Export of Wetlands in Tianmu Lake Watershed Environmental Science. 33, 3753–3759.

Machado, A.I., et al. (2017). Overview of the state of the art of constructed wetlands for decentralized wastewater management in Brazil. J. Environ. Manag. 187, 560, 570.

Vymazal, J. et al. (2018). Removal of nutrients, organics and suspended solids in vegetated agricultural drainage ditch. Ecol. Eng. 118, 97, 103.

Wang Yan et al. (2016). Nutrient removal efficiency of lake wetlands: A case study of Sanshan Wetland in Lake Taihu, eastern China. Journal of Lake Sciences. 28, 124–131.

Xi Ming et al. (2006). Progress in study on the water quality purification functions of wetlands in watersheds Advances in Water Science. 566–573.

Xia Wenwen et al. (2015). Influences of Turbidity on the Measurement of Total Phosphorus Using Different Types of Automatic Monitoring Analyzer. Environmental Monitoring and Forewarning. 28–30.

Xu Delan, et al. (2007). Characteristics of Phosphorus of Sediments with Reed Community in the Littoral Zone of Lake Taihu WETLAND SCIENCE. 133–139.

Zhao Qiguo &Gao Junfeng (2007). Ecosystem services of wetlands and their delineation in China Chinese Journal of Eco-Agriculture. 1–4.

Author index